

(NASA-SP-486) GEOMORPHOLOGY FROM SPACE: A
GLOBAL OVERVIEW OF REGIONAL LANDFORMS (NASA)
737 p

CSCL 08E

N87-18139

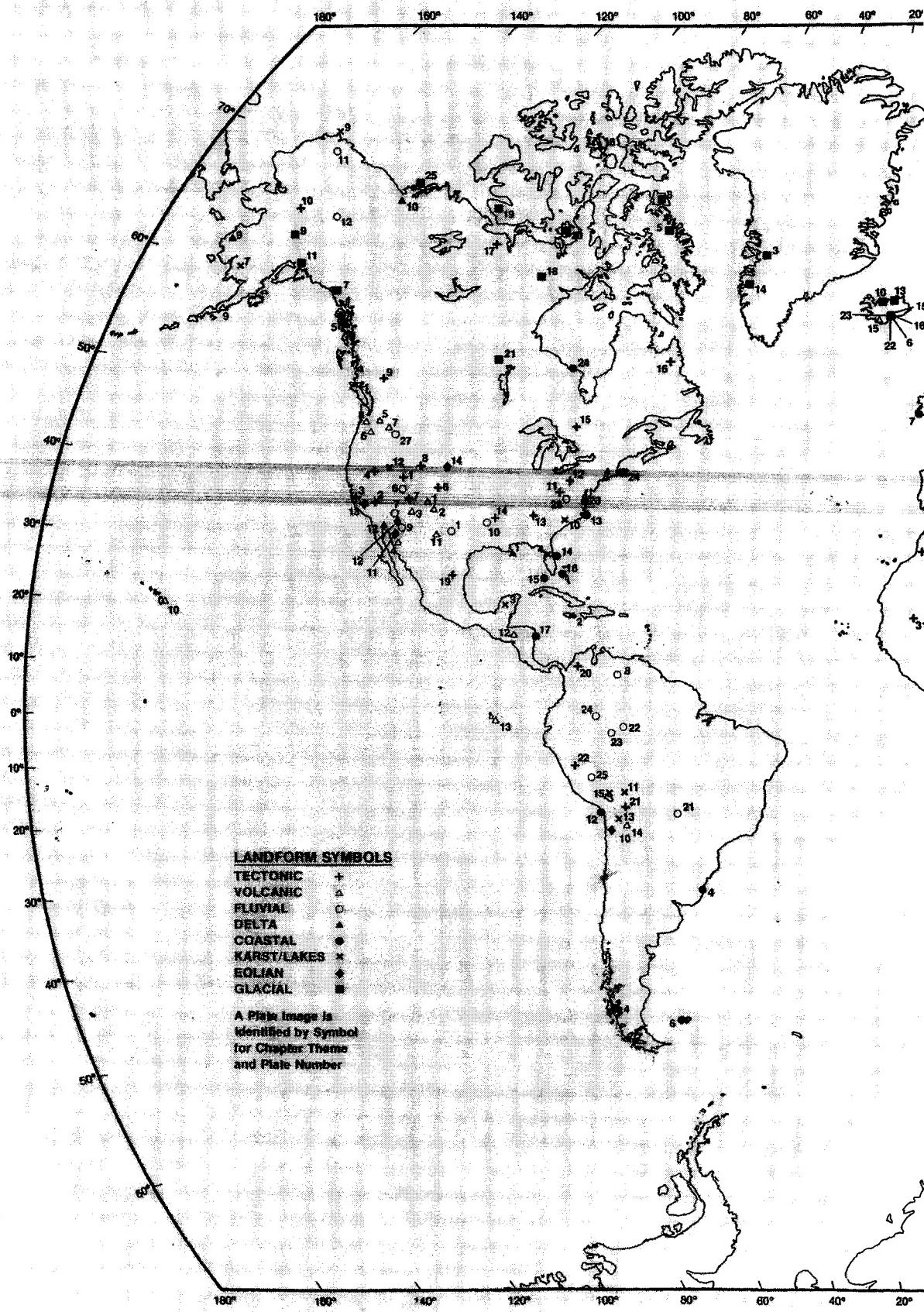
Unclassified

H1/42 43292

GEOMORPHOLOGY

FROM SPACE

LOCATION OF PLATE IMAGES





ORIGINAL CONTAINS
COLOR ILLUSTRATIONS

GEOMORPHOLOGY FROM SPACE

A GLOBAL OVERVIEW OF REGIONAL LANDFORMS

GEOMORPHOLOGY

FROM SPACE

A GLOBAL OVERVIEW OF REGIONAL LANDFORMS

Edited by

Nicholas M. Short
Goddard Space Flight Center
Greenbelt, Maryland

Robert W. Blair, Jr.
Fort Lewis College
Durango, Colorado



Scientific and Technical Information Branch 1986
National Aeronautics and Space Administration
Washington, DC

The Landsat-1 image on the front cover of this book is a full scene (185 by 185 km) in false color that depicts the fold belt of the Anti Atlas Mountains in Morocco (North Africa). The tectonic style shown in this spectacular view (made more impressive because of the sparsity of vegetation and high degree of bedrock exposure) is typical of the deformation of layered sedimentary cover in most major fold belts. See Plate T-30 (pp. 94-97) for a more detailed discussion. Landsat 1103-10413, November 3, 1972, enhanced version courtesy of Earth Satellite Corporation, Bethesda, Maryland.

Library of Congress Cataloging-in-Publication Data

Geomorphology from space.

(NASA SP ; 486)

Includes index.

1. Geomorphology—Remote sensing. I. Short,
Nicholas M. II. Blair, Robert. III. Series.
GV400.42.R4G46 1986 551.4 86-17974

For sale by the Superintendent of Documents, U.S. Government Printing Office
Washington, D.C. 20402

FOREWORD

Science and technology—both have the potential to serve us well if we but use them appropriately. Landsat and its images of Earth are indeed fulfilling that promise, providing new tools for Earth scientists to decipher geologic processes, to better comprehend the evolution of surface features of nature. The new understandings obtained are more than mere satisfiers of scientific curiosity; they are the underpinnings of practical uses of space imagery, be it for determining the causes and extent of desertification, the impact of habitation on the environment, or the creation of an inventory of land use.

Impressive as the uses of space imagery are to date, we must point out that the potential is largely unmined. Too few Earth scientists are facile in the day-to-day working with this new tool. The challenge, then, has been to put within these chapters, authored by the pioneers, the “stuff” with which to awaken the latent interest, to stimulate by analysis and example, and to revitalize the discipline of geomorphology.

I hope that *Geomorphology from Space* serves more than the research community. Teachers of Earth science at all levels should find it an exciting adjunct to their customary texts. The lay person, too, can share the wonderment and beauty of the Earth as seen by our space eyes. To do so can but enhance one’s sensitivity to the need to nurture our one and only Planet Earth.

Noel W. Hinnens
Director
Goddard Space Flight Center

PRECEDING PAGE BLANK NOT FILMED

PROLOGUE

I doubt that any Earth-born space farer could ever tire of looking at our home planet from space. It is a beautiful, wondrously diverse sphere that routinely entralls space crews. Because the number of people living and working in space, for increasingly diverse reasons, is likely to grow rapidly over the next 25 years, the possibility now exists for observations from this unique vantage point to become an element of first-hand "field experience" for many Earth scientists.

Given this potential, it is instructive to compare our approach to learning about the Earth with our approach to other bodies in the solar system. Over many years, our knowledge of our neighboring planets has advanced from the very coarse telescopic views of colored planetary discs to the more detailed views provided by imaging spacecraft. In only one case have we extended our resolution to the mesoscopic and microscopic scales of observation with which we routinely view terrestrial geologic phenomena. In contrast, our understanding of the Earth begins on small personal scales (often childhood rock collections) and only becomes global, in any sense of the word, through years of indoctrination and intellectual synthesis. Now, after 27 years of development, we have the means to venture sufficiently far from our home planet to view it—with both human and electronic eyes—as a single entity, as we first see our neighboring planets. We are just beginning to glean the lessons that this new perspective contains, but it is certain that they will be of tremendous significance to all mankind, in both practical and intellectual terms.

For example, what benefit will this new view bring to our own scientific discipline? The history of geology is full of cases in which access to a new region for direct observations was a vital factor in the formulation of new ideas and the advent of new models. It is exciting to consider what the effect might be on the foundations of current geological thinking if many of us were as directly familiar with the orbital view of our home planet as we are today with our individual field areas.

Nicholas M. Short and his colleagues have assembled an impressive collection of images and detailed supporting data that help us to begin to understand this entity called Earth in a planetary context. This book should be a vital reference for all who find this a stimulating new perspective and especially for those who hope someday to view it with their own eyes.

Kathryn Sullivan
Astronaut—Mission Specialist
NASA STS-17 (Mission 41G)

PRECEDING PAGE BLANK NOT FILMED

PREFACE

The idea that eventually led to *Geomorphology from Space: A Global Overview of Regional Landforms* can be traced back to the moment that its predecessor, *Mission to Earth: Landsat Views the Earth*, was conceived. The senior editor of both books was privileged to be the scientist asked to display the first roll of film on the day the initial images were received from Landsat-1 (then known as ERTS-1*) in late July of 1972. As dozens of managers, scientists, and technicians crowded around a viewing console at NASA's Goddard Space Flight Center (GSFC), the scenes along an orbit across the upper Midwest were quickly scanned until one spectacular cloudfree image captured everyone's attention. This scene was centered on the western end of the Ouachita Mountains in eastern Oklahoma. There, the spectacular landforms carved from open plunging folds and thrust faults in this Appalachian Mountains offshoot stood out sharply against a background of surrounding farmlands and woods (see Plate T-14, this book). After viewing still more superb scenes from the western United States, the present editor was heard to announce to all that, if Landsat images from other parts of the world were like these from the United States, then a picture book documenting these fascinating glimpses of the Earth's surface should be prepared for both the scientific community and the general public. By 1977, *Mission to Earth* had become a reality. During the same period, a companion volume, *ERTS-1: A New Window on Our Planet*,[†] was published. The two books clearly demonstrated the value of repetitive coverage from spaceborne sensors in conducting regional and global studies of our planet as a new means for monitoring and understanding the natural and cultural (manmade) processes that have shaped, and will continue to shape, the Earth's dynamic surface.

Anyone examining the color Plates in both books would soon realize that many images are replete with geologic themes. In fact, two aspects of geology, both geomorphic in expression, dominate most such scenes: structural patterns associated with tectonic actions and water-, wave-, wind-, and ice-generated landforms. Although this is also true for many aerial photographs, the main advantage of space imagery over the larger scale (and more detailed) aerial views stems from the *synoptic* or broad-area coverage possible from orbiting sensors. This means that entire mountain systems, large stretches of rivers and their drainage basins, a whole coastal or inland delta, swarms of sand dunes, clusters of volcanoes, and groups of mountain glaciers as well as polar ice caps and ice sheets can be recorded in single images under uniform solar illumination that is nearly impossible in aerial photomosaics. From such synoptic views, the geomorphic character of a complex diverse terrain is easily studied from a *regional perspective*. This perspective allows one to analyze the impact of multiple geomorphic

*Acronym for Earth Resources Technology Satellite.

[†]R. S. Williams, Jr. and W. D. Carter (Eds.), *ERTS-1: A New Window on Our Planet*, U.S. Geological Survey Prof. Paper 929, 362 pp., 1976.

PRECEDING PAGE BLANK NOT FILMED

~~PAGE VIII~~ INTENTIONALLY BLANK

processes operating over wide areas. Above all, the regional outlook characteristic of space imagery permits effective planimetric portrayal on a global scale of most of the larger landforms that make up the Earth's land surface. With Landsat, for the first time a capability has existed for mapping major geomorphic units over vast areas. One efficient way to accomplish this mapping is to construct a photobase by joining reprocessed Landsat images into mosaics (as, for example, the famed Soil Conservation Service black and white mosaic of the United States, Alaska, and Hawaii).

In the 14 years since the first Landsat launch, more than 150 NASA-funded investigations and many other federal and private studies, both in the United States and worldwide, have defined and evaluated many plausible uses of space remote sensing data (mainly images) for geology. In addition, comparable studies have used data from photography obtained during Gemini, Apollo, Skylab, and Space Transportation System (Shuttle Orbiter) missions and from imaging sensors on Skylab, Seasat, Heat Capacity Mapping Mission (HCMM), and the Shuttle. The principal applications include: (1) reconnaissance-level geologic mapping and editing, (2) rock-type discrimination, (3) stratigraphic facies recognition, (4) detection of hydrothermal alteration zones sometimes associated with mineralization, (5) mapping of fractures and lineaments, (6) regional tectonic analysis, (7) search for surficial indications of subsurface structure, (8) geologic hazards assessment, (9) environmental geology, (10) movements of surging glaciers and sand seas, and (11) geomorphic analysis of landforms.

Surprisingly, the list of studies directly concerned with geomorphic topics is comparatively small. These studies have dealt with glaciation and glacial deposits, volcanism and volcanoes, deltas and coastlines, desertification and sand deposits, and stream systems and fluvial landforms. Most studies were observational and descriptive rather than analytical. A common use of geomorphically rich space images has been to illustrate regional features in introductory geology textbooks. Few investigations have attempted to produce maps of the landforms that are recognizable from space. Indeed, it is ironic to realize that geologic maps of one half to nearly all of four planetary bodies (Venus, Mercury, Moon, and Mars) and parts of 21 moons imaged by camera, radar, and scanners on various planetary probes and spacecraft have now been completed. Yet, only a small fraction of the Earth's surface is comparably mapped from similar photobases produced from Landsat and other sensor data, despite the current availability of worldwide coverage. Small-scale mapping of any planetary surface relies primarily on geomorphological and stratigraphic principles (e.g., on Mars the maps are combinations of landforms and surface units whose relative ages are determined largely from rules of superposition).

The preceding serves as background for the "why" of this book. The purpose of the book is threefold: first, to serve as a stimulant in rekindling interest in descriptive geomorphology and landforms analysis at the regional scale; second, to introduce the community of geologists, geographers, and others who analyze the Earth's surficial forms to the practical value of space-acquired remotely sensed data in carrying out their research and applications; and third, to foster more scientific collaboration between geomorphologists who are studying the Earth's landforms and astrogeologists who analyze landforms on other planets and moons in the solar system, thereby strengthening the growing field of comparative planetology. Additional rationale for the book is developed in the introductory chapter, written to establish the background and status today of the regional approach to geomorphology.

After a decade in which support of active programs connecting research in geomorphology to Earth observations from space remained at a low priority, a new expression of interest from geoscience managers within NASA led to a favorable reception of a proposal

to underwrite preparation and publication of *Geomorphology from Space*. This firm commitment to a revitalized geomorphology program promises to redirect attention to the potential role of space data in supporting both theoretical and applied geomorphology through the combination of pictorial examples of regional scale landforms with astute descriptions of their scientific significance and, when feasible, with examples of their efficacy as analytical devices.

ORGANIZATION AND USE OF THIS BOOK

The first step in preparing *Geomorphology from Space* was to select its contents and to design its format. The core of the book is a *gallery* of space imagery consisting of 237 Plates,* each treating some geographic region where a particular landform theme is exemplified. A Plate usually consists of a two-page spread with the image on the right side, a commentary (an extended caption) on the left, and ancillary (supporting) photographs, index (locator) maps, and sometimes a geologic map at the bottom of both pages. A few four- or six-page spreads are allotted to mosaics or oversized images, or to topics requiring extended text and more photographs. Many ancillary photographs were trimmed to allow a maximum of four per Plate where appropriate; if used as ancillaries, the skewed sides of Landsat images were squared off (less than 10 percent of the rhombic-shaped original image is lost) to maintain a balance of shapes across the photo sequence.

In one sense, this gallery stamps *Geomorphology from Space* as mainly an atlas-like collection of images, except that the emphasis in the commentaries is centered on the scientific information content of the primary image. The arrangement of the gallery is by geomorphic theme: (1) Tectonic (Structural), (2) Volcanic, (3) Fluvial, (4) Delta, (5) Coastal, (6) Karst and Lakes, (7) Eolian, (8) Glacial, and (9) Planetary Landforms. This last topic is in keeping with the current awareness of the importance of (comparative) planetary geomorphology to the NASA space exploration program in general and with the growing realization that understanding of formative processes of surface features on other planets has obvious feedback effects on recognizing many terrestrial counterparts. The number of Plates allotted to each gallery chapter varies from 15 to 27 for all but one chapter. The Tectonic chapter is deliberately made longer for two reasons: (1) the natural diversity of tectonic landforms warrants a larger number of Plates to provide adequate coverage of the variability, and (2) the realization as writing proceeded that the commentaries offer a powerful synoptic overview and summary of the general geology of the entire globe, especially of the major shields and orogenic belts.

The sequence of Plates within each chapter was determined by the author(s) of that section. Two choices were available—arrangement either by geographical distribution (beginning in North America and proceeding through South America, Europe, Africa, and Asia) or according to a thematic classification (e.g., types of deltas) established by the author. That classification, if devised, appears in an introductory section that opens each gallery chapter. This section also reviews the current state of knowledge about the landforms in the chapter theme, aspects of their origin and development, and their appearance at regional scales.

*Throughout the book, any reference to a gallery Plate uses a capital "P" to avoid any ambiguity in the frequent instances where tectonic plates (lowercase "p") may also be mentioned in the text.

The bulk of the images in this book are those taken by the Multispectral Scanner (MSS) on Landsats 1, 2, and 3, the Return Beam Vidicon (RBV) on Landsat 3, and the Thematic Mapper (TM) on Landsats 4 and 5. (See Appendix A for a summary of sensor systems and a brief review of remote sensing concepts and information extraction procedures relevant to the appreciation of the multispectral images appearing in this book.) In general, Landsat images predominate in this book because they have proved to be the most informative, often the most photogenic, and the most readily obtainable. A complete collection of Landsat 1 through 3 images collected through 1978, many Landsat 4 and 5 images, and HCMM and SIR-A images were accessible for inspection at GSFC. The remaining space images include early photographs from Gemini and Apollo and later ones taken from the Shuttle by astronauts using the Large Format Camera or hand-held cameras, as well as radar images obtained by the Seasat SAR and SIR-A and -B (on the Shuttle) and thermal and visible images acquired by HCMM. As a policy, when a non-Landsat scene was available, the final choice of it over Landsat as the primary Plate image was based on its visual superiority, its coverage of an area not matched by Landsat (as in tropical cloud-covered regions), and the new information content and/or different perspective of the scene.

Most of the more than 400 gallery images initially considered for the book were chosen by the editors. The bulk of these were originally processed from film negatives obtained from the EROS Data Center or from the Landsat Browse Facility at GSFC. The candidate images were then pared down to the final 237 by the author(s) of each gallery chapter.

Nearly all Plates are accompanied by three to four ancillary photographs. In many instances, either Landsat or non-Landsat space images were used as ancillaries. Other candidates for ancillaries were oblique and vertical aerial photographs, ground panoramic views, and a few closeup pictures. Most ancillary photographs depict a location somewhere in the image area and show pertinent geomorphic, structural, or other geologic features discussed in the commentary. When ancillaries located within the scene were not available, the editors or authors substituted either representative photographs from outside the image or appropriate maps. Nearly all Plates are accompanied by an index map that identifies major geographic and geologic features, either by name or by a letter, called out in the commentary. All spellings of geographic terms and locations used on these maps and in the text are taken from the 1982 edition of the National Geographic Society Atlas of the World. Landsat MSS images are printed at approximately 1:1000000 scale (18.3 cm or 7.2 inches) but may deviate slightly where layout spacing would lead to crowding.

A word about the illustration numbering system adopted for this book follows. The main image for each Plate is identified in the text by the first letter of the landform type to which a chapter is dedicated and a sequential number. For example, the first three Plate images in the Fluvial Landforms chapter are Plates F-1, F-2, and F-3. The ancillary illustrations are numbered as shown in this example for three such figures in Plate F-2, namely Figures F-2.1, F-2.2, and F-2.3. However, the actual illustrations (usually photographs) are tied to their figure callouts by a single number for each (e.g., 1, 2, and 3, located in the lower left corner of the figure itself). There are no accompanying captions; identification and any description are incorporated directly into the full text for the Plate. Photographs, images, and line drawings in the nongallery chapters and in the introductions to the landform theme chapters (gallery) themselves are designated by the chapter number and the number sequence for the figures. For instance, the fourth figure in Chapter 11 (Geomorphic Mapping) is given as Figure 11-4; captions accompany this category of figures. This diverse numbering system allows for easy recognition of what the figure should highlight whenever cross-referenced; thus, a reader encountering a reference to Figure V-4.2 in a caption for an Eolian chapter Plate

would quickly surmise it to be a volcanic ancillary for the fourth Plate in the Volcanic Landforms chapter. The normal arrangement for an ancillary illustration sequence is the customary 1, 2, 3, 4, left to right across the two facing pages, with the index map on the far right; however, in a few instances, odd illustration sizes or other unusual circumstances prompt variations in this sequence.

The orientation of most space images can be determined in two ways: (1) for Plate images, latitude/longitude tick marks appear along the top and right margins of the accompanying index map, and (2) for ancillary Landsat images, north typically points topwise, slanted left along a line making about an 11° angle with the cropped left/right margin of the illustration. In a few cases, north arrows are imposed on images other than Landsat to specify the orientation. Distance scales are drawn on index maps for images other than those of normal (full) Landsat, HCMM, Seasat, SAR, and SIR-A scenes. For these four observation systems, equivalent dimensions are fixed as follows: Base of Landsat MSS or TM = 185 km across; base of Landsat RBV = 92 km; base of HCMM = 716 km; width of Seasat SAR = 100 km; and width of SIR-A = 50 km.

In preparing this book, acquisition of satisfactory ancillaries proved to be the most formidable problem. Many photographs came from an author's personal collection or from his/her contacts with colleagues having comparable interests. Each author was responsible for finding most of the needed ancillaries; this worked well for the chapters on Volcanic, Delta, and Glacial Landforms, but shortfalls occurred for other chapters, especially that for Tectonic Landforms. A supporting search by the editors to fill these gaps concentrated on sending more than 150 letters of request to organizations and individuals in 39 countries (in all, scenes from 58 countries appear in this book) asking for any appropriate pictures that tied into the images. The percentage of success in this approach was a disappointing 30 percent (approximated). Three factors account for this low return: (1) most of those asked to help did not fully appreciate the value of their contribution or simply did not have the time to go through image files to match their coverage with that of the space images; (2) relatively few panoramic ground or aerial oblique views (such as those taken by John A. Shelton, who is noted for this type of photograph and who is a contributor to this book), are available in the first place; and (3) many countries have strict policies against release of official photos (such as those obtainable from geologic surveys) to other nations.

Nevertheless, many superb contributions were received, as gratefully acknowledged in the credits (including copyright statements) listed in Appendix B. However, the photographs were often submitted as 35-mm color slides that had to be converted to black and white prints that lose detail or sharpness and often internal contrast in the process. Other photographs were those used in the contributors' own publications or books. Many pictures were purchased from the U.S. Geological Survey and the Canadian Geological Survey photolibraries. Still, all in all, the initial hopes for a plethora of "outstanding" ancillaries were not fully realized.

A word about color: *Mission to Earth* owes much of its success to its nearly 400 color plates. Today, with publication costs more of a factor, the number allotted to *Geomorphology from Space* is much reduced. The images finally picked for this special treatment are either mosaics or are simply more "beautiful" in color than in black and white. Generally, *landforms* are characterized more by their shape than by color. Thus, a black and white version communicates almost the same essential geomorphic information as a color one.

The commentaries for the Plates in each gallery chapter were written by the chapter author unless otherwise stated. For the coauthored Tectonic Landforms chapter, the principal writer of a particular commentary is identified at the end of its text. A special situation, involving students at the University of Maryland who contributed background information

for a given scene in the Tectonic Landforms chapter, is explained in its introduction; the person who secured that information is listed in Appendix B. A few guest authors were asked to write commentaries for specific Plates; these individuals are named at the end of the commentary text following the initials GCW (for Guest Caption Writer); then affiliations are given in Appendix B. Literature references used in preparing individual commentaries are cited by author names and year within and/or at the end of the text for each Plate. Full references appear at the end of each chapter.

Besides the gallery, several other chapters complete this book. The opening one is an overview and evaluation of the present status of the regional or synoptic approach to the study of landforms, prepared by Victor R. Baker, a geomorphologist at the University of Arizona. This chapter, which precedes the gallery, reviews the history of "scale" or level of observable detail in the development of geomorphic concepts, defines the newly named subfield of mega-geomorphology and weighs its advantages, and explores the role of space imagery as a viable data source for characterizing and analyzing landforms from a global perspective. The first chapter after the gallery, written by Robert Hayden of George Mason University, examines the evolution of geomorphic unit mapping and demonstrates the applicability of space imagery in producing this type of map.

The closing chapter reviews a conference that was a direct outgrowth of the commitment to this book. Because the book was well under way, Mark Settle, then program manager for geologic studies in the Earth Observations Program within NASA, commissioned the senior editor to organize a Workshop cosponsored by NASA and the International Union of the Geological Sciences on "Global Mega-geomorphology" that would delve into many of the same objectives already outlined in this book. Thirty-two individuals, including all contributing authors of *Geomorphology from Space* and some key workers in landform studies from academia, industry, and the U.S. Geological Survey, met near Tucson, Arizona, on January 13–17, 1985. Some of the principal ideas, conclusions, and recommendations reached at this workshop are summarized in the last chapter by Robert Hayden of George Mason University, Robert W. Blair, Jr., Fort Lewis College, and James Garvin and Nicholas M. Short, Goddard Space Flight Center.

Even as typesetting of this book was nearly complete, a major space event opened up another dimension for the practical use of synoptic imagery in regional geomorphic analysis. The successful launch of the French Système Probatoire pour l'Observation de la Terre (SPOT) spacecraft for the first time will allow worldwide acquisition of high-resolution multispectral *stereographic* images, so that the Earth's landscapes can now be viewed in relief. An Epilogue after the final chapter describes the SPOT system and offers striking examples of this new stereo capability.

ACKNOWLEDGMENTS

The first intensive outside review of *Geomorphology from Space* took place immediately after the Tucson Workshop on Global Mega-geomorphology. Authors of all chapters except that on Planetary Landforms met with other participants who agreed to remain an additional 2 days to evaluate the book in terms of scientific validity and clarity of text. The editors and the chapter authors express gratitude to the following reviewers: Ian Douglas, Physical Geography Department, University of Manchester, England; Clifford Embleton, Faculty of Science (Geography), Kings College, University of London; John Ford, Jet Propulsion Laboratory, Pasadena, California; John S. McCauley, U.S. Geological Survey, Flagstaff, Arizona; Wilton Melhorn, Department of Geological Sciences, Purdue University, West Lafayette, Indiana; and Dale Ritter, Department of Geology, Southern Illinois University, Carbondale, Illinois. A second rigorous review was conducted in March 1985 by the following: Tectonic Landforms Chapter—Kevin Burke, Lunar and Planetary Science Institute, Houston, Texas; Volcanic Landforms Chapter—Charles Wood, Johnson Space Center, Houston, Texas, Peter Francis, Lunar and Planetary Science Institute, and Richard Fiske of the Museum of Natural History, Smithsonian Institution; Fluvial Landforms Chapter—Edward Keller, Department of Geological Science, University of California at Santa Barbara; Coastal Landforms Chapter—Stephen Leatherman, Department of Geography, University of Maryland; Eolian Chapter—Carol Breed, U.S. Geological Survey, Flagstaff, Arizona, and Ronald Greeley, Arizona State University; Glacial Chapter—John P. Schafer and Jane G. Ferrigno, U.S. Geological Survey, Reston, Virginia. A review of the Delta Landforms Chapter was conducted internally at the Coastal Studies Institute, Louisiana State University. The Karst/Lake Landforms Chapter was reviewed by contributors to individual Plates. The Planetary Landforms Chapter was examined by colleagues of the chapter authors. Richard Craig, Department of Geology, Kent State University, and Larry Mayer, Department of Geology, Miami (Ohio) University, offered invaluable insight into aspects of quantitative geomorphology and image processing treated in Chapter 12 and Appendix A.

In mid-1985, the book was subjected to two more special reviews. The entire manuscript and illustrations were examined as a unit by M. Gordon Wolman, a noted geomorphologist who is Chairman of the Geography Department at Johns Hopkins University and, at the time, was President of the Geological Society of America. Some of his helpful suggestions for improving parts of the book have been incorporated in this final version. In September, two xerox copies of the complete book were placed on display at the First International Conference on Geomorphology at Manchester, England. More than 50 attendees inspected segments of the book, with particular attention given to regions of the world especially familiar to each individual. A number of new facts or erroneous statements were pointed out by these critics that have been accommodated in the final version.

Others deserve special acknowledgment for valuable assistance. The credit for producing more than 200 index maps goes mainly to Malcolm Tarlton, Science Applications Research, Inc. Much help in generating high-quality photographs, both of Plates and of ancillary scenes, was provided by Peter Baltzell, Still Photography Branch, GSFC, and by his associates. Barbara Conboy, then Secretary for the Geophysics Branch, GSFC, offered steady aid in the voluminous correspondence in search of ancillary pictures. Mary Kennedy served as assistant to the senior editor during the library research phase of the manuscript preparation. Carole Edwards, Photographic Library, U.S. Geological Survey, Denver, was instrumental in tracking down many ancillary pictures. Staff members at the Earth Satellite Corporation in Bethesda, Maryland, produced some outstanding images for a number of plates. Many more individuals and organizations provided ancillary photographs, as acknowledged systematically when appropriate in Appendix B. Particular thanks are expressed to Mark Settle of NASA Headquarters for his key support of the entire project. Finally, the senior editor is especially grateful to Anne Schmidt of Engineering and Economics Research, Inc. for her vital assistance in editing and in coordinating the production of the book in its present form.

CONTENTS

Foreword	v
Prologue	vii
Preface	ix
Organization and Use of This Book	xiii
Acknowledgments	xvii
1 Introduction: Regional Landforms Analysis	1
<i>Victor R. Baker</i>	
2 Tectonic Landforms	27
<i>John R. Everett, Marie Morisawa, and Nicholas M. Short</i>	
3 Volcanic Landforms	185
<i>Nicholas M. Short</i>	
4 Fluvial Landforms	255
<i>Victor R. Baker</i>	
5 Deltaic Landforms	317
<i>James M. Coleman, Harry H. Roberts, and Oscar K. Huh</i>	
6 Coastal Landforms	353
<i>Arthur L. Bloom</i>	
7 Karst Landforms and Lakes	407
<i>Robert W. Blair, Jr.</i>	
8 Eolian Landforms	447
<i>Alta S. Walker</i>	
9 Glaciers and Glacial Landforms	521
<i>Richard S. Williams, Jr.</i>	

10	Planetary Landforms..... <i>Paul D. Lowman, Jr., and James B. Garvin</i>	597
11	Geomorphological Mapping..... <i>Robert S. Hayden</i>	637
12	Global Geomorphology: Outlook for the Future..... <i>Robert S. Hayden, Robert W. Blair, Jr., James B. Garvin, and Nicholas M. Short</i>	657
	Epilogue	675
	Appendix A: Remote Sensing Principles Applied to Space Imagery..... <i>Nicholas M. Short</i>	679
	Appendix B: Sources of Illustrations and Tables Appearing in This Book.....	689
	Index.....	709

1

INTRODUCTION: REGIONAL LANDFORMS ANALYSIS

*Victor R. Baker**

THE NATURE OF GEOMORPHOLOGY

Definitions

Geomorphology is the study of landforms and landscapes, including the description, classification, origin, development, and history of planetary surfaces. During the early part of this century, the study of regional-scale geomorphology was termed "physiography" (Salisbury, 1907). Unfortunately, physiography also became synonymous with physical geography, and the concept became embroiled in controversy surrounding the appropriate concerns of that discipline. Some geomorphologists held to a geological basis for physiography and emphasized a concept of physiographic regions (Fenneman, 1938). A conflicting trend among geographers was to equate physiography with "pure morphology," divorced of its geological heritage. In the period following World War II, the emergence of process, climatic, and quantitative studies led to a preference by many Earth scientists for the term "geomorphology" in order to suggest an analytical approach to landscapes rather than a descriptive one.

In the second half of the twentieth century, the study of regional-scale geomorphology—the original physiography—was generally neglected. Russell (1958) attributed the decline of physiography to its elaborate terminology and to its detachment from evidence acquired by other disciplines, chiefly geology. Although the concept of physiographic regions endured among geologists (Thornbury, 1965; Hunt, 1967), geographers became much more interested in the details of man/land interactions and in the applications of modeling and systems analysis (Chorley and Kennedy, 1971) to geomorphology.

In the exploration of planetary surfaces by various space missions, the perspective of regional geomorphology has been the required starting point for scientific inquiry. Global studies of Mars (Mutch et al., 1976), the Moon (McCauley and Wilhelms, 1971), Mercury (Strom, 1984), and Venus (Masursky et al., 1980) resulted in the identification of "surface units" or physiographic provinces. The Colorado Plateau (Plate I-1) is an excellent example of a terrestrial physiographic province. Plate I-1 illustrates the use of a large-scale perspective to focus on this naturally defined region.

The term "mega-geomorphology" was introduced in March 1981 at the 21st anniversary meeting of the British Geomorphology Research Group. The proceedings of that meeting (Gardner and Scoging, 1983) reveal that the concept was not well defined. It clearly involves a return by geomorphologists to the

study of phenomena on large spatial scales, ranging from regions to continents to planets. It also involves large time scales. Nevertheless, mega-geomorphology is merely a convenient term, unencumbered by past philosophical trappings, that emphasizes planetary surface studies at large scales.

The interrelation of temporal and spatial scales in geomorphology is illustrated by the tentative classification shown in Table 1-1. Of course, such a hierarchical ordering of geomorphic features is far from satisfying. As stated by Sparks (1971), classifications are arbitrary constructions designed to facilitate the discussion of diverse phenomena at the risk of some distortion of the truth. The scheme merely illustrates what was well known to the great geomorphologists at the last turn of the century. The large first-order features, continents and ocean basins, persist and evolve over long time scales. Small high-order features are transient. Fundamental units appear at different orders. The old concept of physiographic regions was used to designate second-order forms, such as entire mountain ranges or coastal plains. Massive entities within a physiographic region might constitute a third-order form, such as a domal uplift. The details of the classification are unimportant as the analysis moves on to exploring the explanation of phenomena.

This book explores mega-geomorphology. The parent science of geology has long emphasized large-scale features in its central discipline of tectonics. Although early proponents of large-scale crustal mobilism, such as Alfred Wegener, were decidedly renounced by the mainstream scientific community, their ideas provided the stimulus for work that eventually transformed the Earth sciences. The plate tectonic model that emerged in the late 1960s was but a quantitatively geophysical confirmation of the elegant hypothesis developed by careful attention to large-scale structural patterns on the Earth's surface. Of course, this is not intended to imply that microscale studies are unimportant in structural geology. Such studies tell much about the details of rock deformation and the fabric of resulting materials. The lesson here is that significant science occurs at all scales of study. Scientists neglect the study of one spatial scale to the peril of their advancement to understanding.

Scales of Study

Cailleux and Romani (1981) believe that there are two major trends in modern geomorphology: toward quantification and toward more varied extensions. In the latter, they see an extension of concern to other scientific disciplines, to applied problems, to longer time scales, and to more ancient features. They also see an extension to greater spatial scales.

The operative temporal and spatial scales of geologic phenomena span an immense range (Figure 1-1). Note that fluvial

*Department of Geosciences, University of Arizona,
Tucson, Arizona 85721.

Table 1-1
A Hierarchical Classification of Terrestrial Geomorphological Features by Scale

Order	Approximate Spatial Scale (km^2)	Characteristic Units (with examples)	Approximate Time Scales of Persistence (years)
1	10^7	Continents, ocean basins	$10^8\text{--}10^9$
2	10^6	Physiographic provinces, shields, depositional plains	10^8
3	10^4	Medium-scale tectonic units (sedimentary basins, mountain massifs, domal uplifts)	$10^7\text{--}10^8$
4	10^2	Smaller tectonic units (fault blocks, volcanoes, troughs, sedimentary subbasins, individual mountain zones)	10^7
5	$10\text{--}10^2$	Large-scale erosional/depositional units (deltas, major valleys, piedmonts)	10^6
6	$10^{-1}\text{--}10$	Medium-scale erosional/depositional units or landforms (floodplains, alluvial fans, moraines, smaller valleys and canyons)	$10^5\text{--}10^6$
7	10^{-2}	Small-scale erosional/depositional units or landforms (ridges, terraces, sand dunes)	$10^4\text{--}10^5$
8	10^{-4}	Larger geomorphic process units (hillslopes, sections of stream channels)	10^3
9	10^{-6}	Medium-scale geomorphic process units (pools and riffles, river bars, solution pits)	10^2
10	10^{-8}	Microscale geomorphic process units (fluvial and eolian ripples, glacial striations)	

(Modified from Tricart, 1965; Chorley et al., 1984)

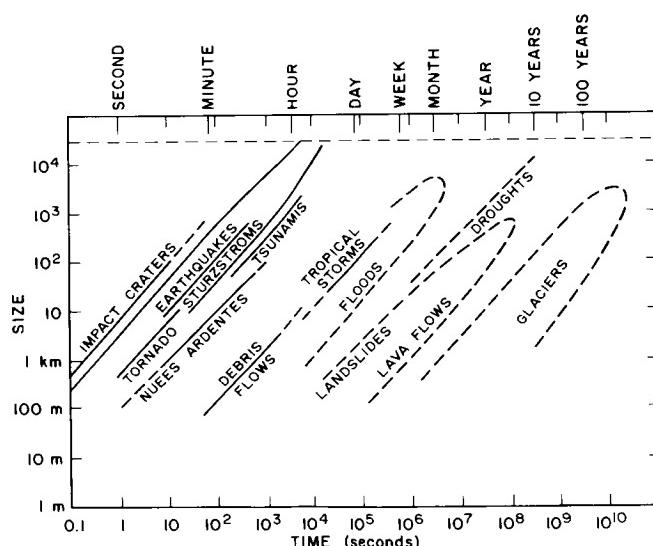


Figure 1-1. Scale relationships for various geomorphic processes. The relationships are illustrative and are based on the work of Carey (1962).

phenomena (floods) occupy an intermediate position in this scaling. The various phenomena all follow the general equation:

$$S = aT^b$$

where S is the size of the feature, T is the time (duration), and a and b are constants. The constant b is generally a scaling fac-

tor (equal to about 1.0), showing that big phenomena tend to last longer. The constant a seems to relate to the intensity of the process (i.e., how rapidly it expends energy per unit area).

Despite the utility of such scaling relationships, summarized in the concept of allometry (Bull, 1975), problems arise at very large spatial and temporal extrapolations (Church and Mark, 1980). However, perhaps more important than the details of scaling is the intellectual excitement of multiscale thinking. In his insightful review of geomorphological processes on planetary surfaces, Sharp (1980) observed that one of the lessons from the comparative study of landforms on different planets is to "think big." The same can be said of the application of space-age global remote sensing technology to the study of terrestrial landforms. At the turn of the century, geomorphologists are once again ready to think big.

Time scales are also important in defining the nature of geomorphic investigations. The role of time scales in geomorphology is discussed more fully by Schumm and Lichaty (1965) and Cullingford et al. (1980). The macroscale of geomorphic time is that over which major phases of erosion or deposition occur. These phases, which may be cyclic, are controlled by the geological processes of regional warping, mountain building, and crustal plate movement. The scientific questions arising at the temporal macroscale concern the evolution of the planetary surface over millions of years. Many of the approaches to this time scale are historical, using elements of the landscape to reconstruct past events.

The mesoscale of geomorphic time is that which treats major changes in landforms and landscapes over hundreds to

thousands of years. Examples include the growth and recession of glaciers, the aggradation and degradation of rivers, and the progradation and recession of shorelines. These changes generally involve a complex interplay between tectonic and climatic controls on geomorphological processes. This is perhaps the most fertile area of geomorphic analysis, since it involves continual intellectual feedback between historical reconstruction and the study of modern processes.

The microscale of geomorphic time is that over which the major variables of tectonism and climate are assumed to be constant. The processes that characterize sand dunes, glaciers, rivers, or beaches are assumed to reflect only the short-term events that dictate local flow physics. This is the temporal view of both the engineer and the process geomorphologist. Because of the ability to measure events that occur at the approximate scale of a year, this temporal scale is the richest source of quantitative geomorphic data. The ability to fashion predictions from studies at this scale also makes such studies immensely useful in application. People inhabit the dynamic surface of the Earth and must interact with its surficial processes.

Reasoning from one scale to another is an instinctive mental exercise for scientists. The geomorphologists of the 19th century generally perceived the details of landforms from foot, horseback, or even hands and knees. From such detail, they generalized to the larger synthesis of landscape form and processes. Nevertheless, they also realized the importance of a broad view. The great vistas of the Alps, Appalachians, and Colorado Plateau inspired regional assessment of landscape types.

The reasoning from distant views to the details of site-specific investigation is perhaps no better illustrated than in G.K. Gilbert's study of the Henry Mountains in Utah (Gilbert, 1877). Gilbert's brilliant concept of the laccolith structure and its modification by erosional processes was conceived *before* he visited the scene! His field notes show that he conceived the rela-

tionships from distant views as he approached the mountains along the Waterpocket Fold (Pyne, 1980, pp. 66-67).

Fundamental Concepts

Most geomorphologists would agree that certain fundamental assumptions underlie all geomorphological investigations. Whether termed "fundamental concepts" (Thornbury, 1969), "philosophical assumptions" (Twidale, 1977), "paradigms" (Ollier, 1981), or "basic postulates" (Pitty, 1982), these ideas constitute a "conventional wisdom" for the science. One such fundamental concept involves the inherent complexity of landscapes. This concept has impeded the development of grand theories that survive the test of explaining numerous local features. Another basic assumption involves climatic morphogenesis, emphasizing the role of climatically controlled processes of landform genesis. Several of these concepts have yielded major intellectual controversy, such as the role of cataclysmic processes in shaping the landscape. These concepts apply to geomorphology of all scales. Table 1-2 outlines some important concerns.

Role of Geomorphic Studies

There is no question that geomorphology is a science of fundamental importance. We inhabit, indeed all life evolved at, a dynamic interface between a rocky planetary surface and its atmosphere and hydrosphere. However, geomorphology is also a science in transition, in which serious questions arise concerning basic methodology and philosophy. During the last half of this century, many geomorphologists neglected the macroscale concept of landscape development over time by the action of processes on geologic structure. Instead, they emphasized the study of process alone and the short-term response of landforms to processes. When most geomorphologists abandoned the Davisian

Table 1-2
Fundamental Concepts of Geomorphology

Concept	Description	Alternatives
Uniformitarianism	Similar geomorphic processes that operate today operated throughout geologic time.	Unusual processes without modern analogs occurred in the geologic past.
Gradualism	Relatively frequent, modest-sized processes dominate in the progressive changing of the landscapes over long time periods.	Cataclysmic processes and changes are most important in landscape evolution.
Orderliness	Erosional agents on a planetary surface produce an orderly sequence of landforms as a function of time.	Some landscapes arise from disorderly processes.
Morphoclimatic Zonation	Landscapes reflect the influence of certain climatic processes by developing a characteristic assemblage of landforms.	Geologic structure predominates over climate in influencing landform assemblages.
Youthfulness of Topography	Most of the Earth's topography is no older than Pleistocene.	In stable tectonic areas, extensive landscapes of Tertiary, or even Mesozoic, age are preserved.
Legacy of the Pleistocene	The geologic and climatic changes of the Pleistocene were critical in the shaping of most landscapes.	Relict landscape elements persist despite Pleistocene changes and comprise palimpsests.
Modernism	Geomorphology is primarily concerned with present-day processes that shape present-day landscapes.	Geomorphology attains its maximum usefulness by historical extension, analyzing ancient conditions.
Simplicity	It is necessary to search for simplicity in geomorphological systems.	Complexity of geomorphic systems is more common than simplicity.

model and its attendant concern with denudation chronology, many embraced a systems approach, with emphasis on statistical analysis and predictive modeling of process/response phenomena on the Earth's surface. However, this change in methodology also engendered a change in the scale of phenomena studied. Small-scale features and short-acting processes proved to be most amenable to the new methodology. The global concern with long-acting denudation was ignored, not because of its importance, but because of methodological inadequacies in its past study.

The dominance of process studies in geomorphology is exemplified in the following statement of Thorne and Brunsden (1977, p. 116): "The current paradigm is one in which process studies prevail effected principally and increasingly through mathematical and stochastic models." In contrast, Church (1980) writes, "Contemporary process studies are of little worth in evaluating landscape evolution." The fact remains that landscape evolution remains a critical concern for geomorphology, despite past problems in the implementation of its study. Thornbury (1969) made a key point when he noted that geomorphology, although concerned primarily with present-day landscapes, attains its maximum usefulness by historical extension. Although some upward extrapolation is possible (Church and Mark, 1980), a balanced approach to these problems demands research on very large temporal and spatial scales.

It can be argued that the greatest advances in science occur not by reaction to present concerns—embellishing models established in current paradigms. Rather, major advancement comes from a concentration on the anomalies in the present scientific understanding—the points at which models fail. The clear inability of small-scale process studies to be extrapolated to large-scale geomorphic concerns should not be viewed as a failure of geomorphic theory. Indeed, it is an opportunity. Geomorphologists need to engage in large-scale studies, employing the most modern research techniques of remote sensing, computer modeling, and geochemical dating. It would be refreshing to see what comes of some downward extrapolation.

TYPES OF GEOMORPHIC ANALYSIS

Regional landforms analysis can be approached with several different emphases. Since these derive from traditional geomorphic subdisciplines, this section will review several frameworks for study.

Process Studies and Systems Analysis

Process geomorphologists employ field, laboratory, and analytical techniques to study processes presently active on the landscape. The work relies heavily on the incorporation of other disciplines, including pedology (the study of soils), soil mechanics, hydrology, geochemistry, remote sensing, hydraulics, statistics, geophysics, civil engineering, and geology. To organize the complexities of process interactions, most geomorphologists utilize systems analysis. The landscape is idealized as a series of elements linked by flows of mass and energy. Process studies measure the inputs, outputs, transfers, and transformations that characterize these systems. Although systems analysis does not constitute a true theory for geomorphology, it does serve the useful purpose of organizing process studies into a framework that allows modeling and prediction, especially when data are fed into digital computers.

The systems approach to geomorphology has been extensively reviewed by Chorley and Kennedy (1971) and by Chorley et al. (1984). Table 1-3 summarizes some of the most important systems terms and their usage.

Climatic Geomorphology

Climatic geomorphology developed as an alternative to Davisian theory for landscape evolution. Climatic geomorphologists hold that modern relief-forming mechanisms differ as a function of climate and that their relief products define major morphoclimatic zones on the globe. Climatic geomorphologists systematized the various process combinations that occur in the morphoclimatic zones. Major practitioners include J. Tricart and A.

Table 1-3
Terminology of Geomorphic Systems

Term	Usage	Example
Cascade	A type of system through which energy and mass flow from one subsystem to another.	Movement of water and sediment through a drainage basin.
Feedback	Output to one system acts as input to itself. The effect can be self-enhancing (positive feedback) or self-regulating (negative feedback).	As river bar is eroded, it becomes more streamlined in shape, which reduces erosion (negative feedback).
Equilibrium	A balance between form and process.	Hillslopes form as a balance between rock resistance and erosional processes.
Threshold	A condition that must be achieved for a system to pass from one state to another.	A landslide can occur only when the driving forces exceed the resisting forces.
Equifinality	The derivation of similar final states in different ways from diverse origins.	Polygonal ground may form from desiccation, freezing, or volcanism.
Dynamic Equilibrium	An equilibrium state maintained by a balance of fluctuations around a constantly changing system condition.	Rivers maintain an equilibrium of channel form as they continue long-term degradation.
Steady State	An equilibrium state maintained around a time invariant system condition.	Soil clay content increases by weathering until it reaches constant value.

Callieux of France and J. Budel of Germany. German geomorphology is especially dominated by the approach of Budel (Bremer, 1984).

A related concept is climato-genetic geomorphology (Budel, 1982), which emphasizes the study of exogenic forces and especially climatic change as controls on the evolution of relief. Many climatic geomorphologists hold that little of the extant relief on the Earth is the product of modern relief-forming processes. Most is instead inherited from past morphoclimatic controls. The study of relief generations or landscape evolution therefore consists of interpreting climatic changes in relation to certain diagnostic landscape features.

An example of a useful designation of a morphoclimatic region is the periglacial zone. The term "periglacial" has come to mean the complex of cold-climate processes and landforms, including, but not limited to, those near active glaciers. A key feature is frost action, especially the freezing and thawing of ground. A related, but not necessarily coincident, phenomenon is permafrost (perennially frozen ground). Permafrost covers 20 to 25 percent of the Earth's land surface. It manifests itself on the landscape when large quantities of ground ice are present. This ice may form wedges that penetrate vertically into the regolith, growing with seasonal meltwater flow into tension cracks. Polygonal patterns characterize the ground surface.

Where ice-rich permafrost is degraded by geomorphic, vegetational, or climatic change, it forms a complex landscape known as thermokarst. Depressions form where zones of ground ice are removed by melting. In extreme cases, such as near Yakutsk in eastern Siberia, large valleys may form by the coalescence of thermokarst depressions.

During the coldest periods of the Pleistocene, the periglacial zone extended to cover 40 percent of the Earth's land surface. Hillslopes were mantled with frost-shattered rubble that moved downslope during seasonal freezing and thawing. Patterned ground (polygons and stripes) developed as the frost rubble was further sorted by seasonal changes. Even huge streams of rubble and ice-cored rock glaciers formed in areas of especially high debris production. The relicts of this periglacial activity characterize many of the modern humid-temperature zones, such as Pennsylvania, Wisconsin, England, and Poland.

Structural Geomorphology

Structural geomorphology derives from the fundamental observation that geologic structure dictates the resistance of Earth materials to degradational processes. The role of structure may be passive, in which case the composition of rocks or their discontinuities (joints, faults, and bedding) dictate the details of erosion. In this way, structure provides the boundary conditions for landscape denudation. Structure may also play an active role when tectonic processes create primary landforms and landscapes. Thus, volcanoes, fault-block mountains, grabens, and domes comprise fundamental elements of planetary surfaces.

The cuesta landscape of Riyadh, Saudi Arabia, is an excellent example of classic passive control degradation by rocks of varying resistance to erosion. Plate I-2 illustrates the use of this quality of regional degradation to prepare a geologic map of the Riyadh area.

Morphostructural analysis is a variety of tectonic geomorphology that has achieved paradigm status in the Soviet Union and eastern Europe. This concept derives from the work of I. P. Gerasimov, who defined various structural units, called "morphostructures." Morphostructures consist of relief generated by a combination of tectonic activity and climate. They exist in a hierarchical arrangement, ranging from megamorphostructures, such as the Fennoscandian Shield, to micromorphostructures, such as a fault-controlled valley. Various morphostructures are produced by alternating periods of uplift (with resulting dissec-

tion) and stabilization (yielding planation surfaces) that reflect regional tectonism. The approach of morphostructural analysis, summarized by Gerasimov (1946, 1959) and Metcherikov (1968), uses river terraces, planation surfaces, and correlative deposits as key sources of data.

Climatic geomorphology organizes regional studies by global climatic classifications, and structural geomorphologists consider regions of broadly similar tectonic style or rock type. For the latter, it is possible to analyze the characteristic landforms of granite rocks (Twidale, 1982), volcanic rocks (Ollier, 1969), or karstic limestone (Sweeting, 1973). Controversy surrounds the interpretation of specific landforms as diagnostic of climatologic process controls or as merely associated with structure. For example, Twidale (1983) disputes the conventional geomorphological wisdom that pediments are developed in low latitude regions under semiarid conditions, that peneplains are typical of humid temperate regions, and that the morphology of various residual hills varies with climate. Instead, he argues that both hillslopes and planate surfaces reflect structural control.

TECHNIQUES FOR MODERN LARGE-SCALE GEOMORPHIC ANALYSIS

It can be argued that the methodologies of a science are reflected in the research techniques of its practitioners. Indeed the recent review by Goudie (1981) clearly demonstrates the methodological focus of geomorphology on small-scale short-duration process studies. However, proper techniques do not guarantee proper results. Büdel (1982) provided a parable of a misguided process geomorphologist "of a generation who no longer read A. Penck." This fictitious scientist studied processes on Alpine upland surfaces by "modern" methods, including soil analysis, grain-size distributions, clay mineralogy, slopewash monitoring, morphometry, and statistical analysis. Büdel observes: "His conclusion was that these processes created the trough shoulders of the Alps. His evidence for the certitude of these results was the indubitable precision of the analysis." The neglected fact was that the measured modern processes are all completely ineffective in modifying landforms that are relict from ancient times and that were formed by processes controlled by a completely different climate from that prevailing today.

Quantification

Quantification began to sweep geomorphology after the publication of R. E. Horton's visionary studies of drainage basin analysis (Horton, 1945). Some attempts at quantification were decidedly innovative. In the case of M. A. Melton (1958a, 1958b), the work was so ahead of its time that only a few geomorphologists appreciated its implications. The extensive work on drainage basin and hillslope quantifications by Strahler (1950, 1952, 1956, 1957, 1958) and his students (Melton, 1957; Morisawa, 1962; Schumm, 1956) inspired a flowering of geomorphic research in the 1960s. Similarly, the detailed studies of small-scale fluvial processes by Luna Leopold and colleagues at the U.S. Geological Survey also led to an abundance of related studies (Leopold et al., 1964). Such process studies were decidedly advanced by technological developments that allowed for relatively easy measurement and long-term monitoring of processes in the field. Morphometric studies proved amenable to automatic data processing procedures by computer.

Quantification has been described as a revolution in geomorphology. Although its use certainly superseded the qualitative approach of William Morris Davis, it is clear that quantification never constituted a revolution in the accepted sense of scientific philosophy (e.g., Kuhn, 1962). Quantification is a tool of study, one that indeed adds great power to the simplification of complexity. Nevertheless, it remains a mere technique, not a fundamental framework of thought.

One exciting aspect of quantification in mega-geomorphology derives from the ability of computing systems to handle the immense data sets necessary to describe terrain. The manipulation of these very large data sets will generate new and interesting research questions.

Role of Space Technology

Modern macrogeomorphology makes extensive use of global observations from spacecraft that employ a variety of imaging and sensing systems. These include vidicon imaging, multispectral scanning, radiometers, and radars. Modern image processing of digitally formatted data has revolutionized the interpretation of large-scale planetary landscape scenes. These topics are discussed in other chapters of this book. Here, the following question is posed: why have geomorphologists been slow to appreciate the global perspective afforded their planet by these advances?

The question probably has many answers. The technology of remote sensing has only recently advanced to the point at which many geomorphologists can appreciate its relevance. The technology requires training in disciplines not normally considered in the training of geomorphologists. Even more interesting is the requirement placed on the user to have a large-scale view of problems.

Consider the perspective of a fluvial geomorphologist interested in floods. One approach might be to measure in excruciating detail the flood events he can easily access from his temperate climate university. This provides an impressive data set, but a problem remains. What of the immense rare floods that affect the great tropical regions of the planet? Figures 1-2

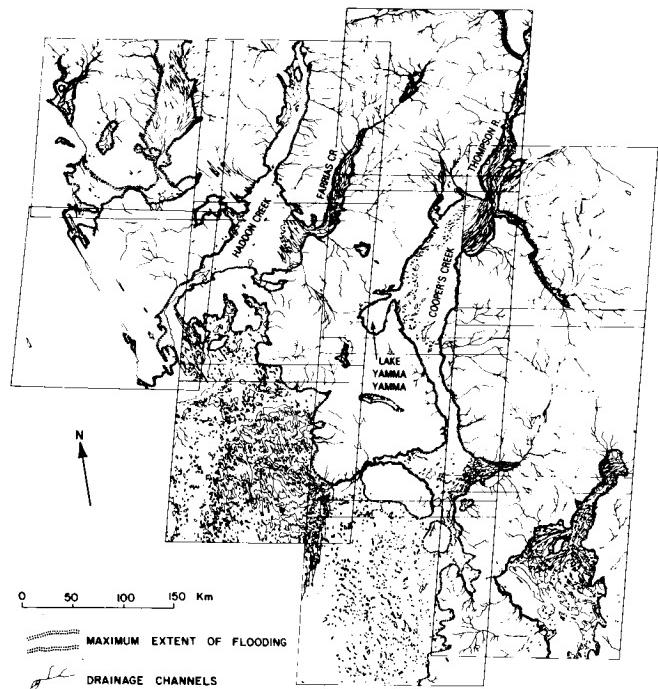


Figure 1-2. Map of inundation in the channel country of southwestern Queensland, Australia, produced by monsoonal flooding in early 1974. The map was prepared from a mosaic of 12 Landsat frames and covers an area approximately 640 by 640 km. The individual Landsat frames were acquired in February 1974. An example is presented as Plate F-15 in Chapter 4, Fluvial Landscapes.

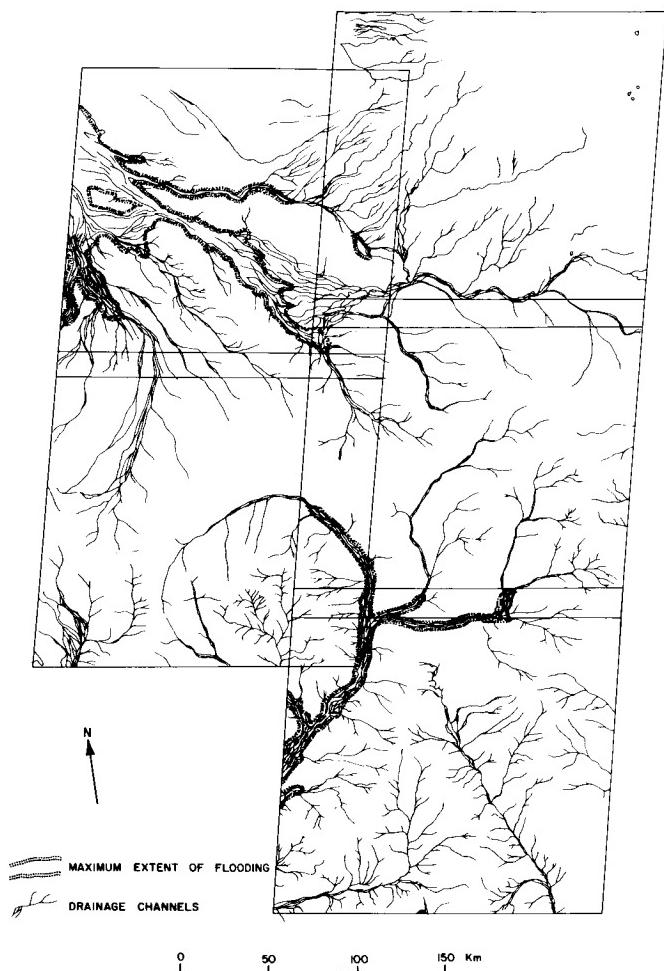


Figure 1-3. Inundation map of the area immediately north of that shown in Figure 1-2. January 1974 rainfall on the divide between the Diamantina River (bottom half of scene) and the Flinders River (top half) was in excess of 800 mm.

and 1-3 show the immensity of flood effects in southwestern Queensland that followed phenomenal rains in 1974 (see Plate F-15). Without satellite images, this scale of flooding could not have been measured at all.

Another solid example of the utility of appropriately processed space imagery is strikingly portrayed in Figure 1-4. This Landsat image of block (horst) mountains and basin fill in the Mojave Desert on the California and Arizona sides of the Colorado River between Lake Mohave and an agricultural development south of Parker. It has received both computer enhancement and special photographic reproduction. The resulting color composite brings out both pronounced and subtle color tones and patterns in the alluvial fill and pediments. In some parts of the scene, individual wash or fan patterns can be traced back to immediate source rock areas. Three broad color classes of unconsolidated surface materials can be recognized: (1) light buff to tan material commonly in lower levels of the basin, (2) reddish-brown material (probably indicative of iron enrichment), and (3) dark gray to blue gray material, forming aprons around many eroding ranges and generally overlapping the first class. Although this false-color rendition departs from the normal colors observed in the field or in natural color aerial photography, it can be interpreted in terms of parent lithologies. Both the color emphasis and the interactions among alluvial deposits emanating from

ORIGINAL PAGE
COLOR PHOTOGRAPHY



Figure 1-4. Landsat false-color composite (MSS Bands 4, 5, and 7 in blue, green, and red) of scene 1285-17445, May 4, 1973, enhanced and color-printed to emphasize compositional differences among alluvial fans in the Mojave Desert around Parker, Arizona.

the mountain uplifts are far better displayed and interpreted synoptically than has been possible from aerial photographs, even after these are joined in mosaics.

In any science, new techniques are not important of themselves. It is rather the new discoveries made possible because of those techniques that stimulate scientific progress. A profound example of such a new discovery in terrestrial geomorphology came in November 1981 when the shuttle Columbia trained a

space-age instrument on the Earth. The Shuttle Imaging Radar (SIR-A) carried by Columbia produced radar images of the hyperarid Selima Sand Sheet on the eastern Sahara (Elachi et al., 1982). The radar penetrated the sand cover to reveal fluvial valleys now filled by eolian sand (Plate I-3). The valleys discovered by radar interpretation show a regional drainage system formed when the modern eolian-dominated landscape was subject to extensive fluvial erosion, probably during pluvial episodes of the Pleistocene and Tertiary (McCauley et al., 1982).

Geomorphological Mapping

Geomorphological mapping is discussed at length in Chapter 11. Most of the interest in geomorphological mapping has centered on the development of various mapping systems for use in environmental management (Cooke and Doornkamp, 1974). The most detailed systems have been developed in Europe, where different countries utilize different procedures (Salomé et al., 1981). Despite attempts at international standardization (Demek, 1972; Demek and Embleton, 1978), the major problem remains the correlation of various mapping schemes. Global remote sensing has great promise for generating geomorphic maps at large spatial scales.

Figure 1-5 illustrates the use of the SIR-A system to define terrain categories for geomorphic mapping in Indonesia (Sabins, 1983). The terrain types are recognized through interpretation of radar interaction with the ground surface, especially the surface roughness, vegetation, and topography. The radar information is made even more remarkable because the mapped areas are characterized by dense tropical forest cover and persistent clouds.

FUTURE DIRECTIONS

In 1982 in Vienna, the United States proposed at the United Nations Conference on Peaceful Uses of Outer Space that an international cooperative research program be organized to understand the Earth as a system. This program was initially named "Global Habitability" and was formulated to involve the central role by NASA in the observation of system parameters and changes (NASA, 1982). In a sense, the program constitutes a "mission to planet Earth" (Edelson, 1985) in which spaceborne remote sensing is applied to studies of dynamic processes in the atmosphere, biosphere, geosphere, and hydrosphere. The Global Habitability concept will probably be integrated into the broader efforts of the proposed International Geosphere-Biosphere Program (National Research Council, 1983) to be coordinated by the International Council of Scientific Unions.

In his keynote address to the World Conference on Earthquake Engineering, the President of the National Academy of Sciences proposed an "International Decade of Hazard Reduction" (Press, 1984). A major component of such an initiative must be the global analysis of hazardous geomorphic processes.

What do such initiatives mean for geomorphology? The following sections present some geomorphic problems that require a global perspective. A more extensive discussion of future directions in mega-geomorphology is presented in Chapter 13.

Global Tectonic and Climatic Systems

Tectonic geomorphology involves the interactions among landforms, landscapes, and tectonics. Tectonics, the branch of geology dealing with regional structures and deformation features, occupies a central role in the Earth sciences. The discipline has achieved great importance through the unifying role of the plate tectonic model in explaining the large-scale surface features of our planet.

Major advances in tectonic geomorphology have been made in the last decade, mainly because of an increased ability to evaluate the time factor in landscape development (Bull, 1984). Thus, through the use of geochemical means of dating and computerized models of landform change, it is now possible to evaluate differential rates of uplift (or subsidence). It is also possible to determine the magnitude and frequency of displacements along faults.

Perhaps the most important new development for climatic and climatogenetic geomorphology is the use of analytical models to characterize the global interactions of the land surface, atmosphere, and oceans. Most interesting are the general circulation models (GCMs) that simulate global atmospheric processes (Washington and Williamson, 1977). For climatic geomorphology, these models have shown profound feedback relationships operating between soil moisture and precipitation (Shukla and Mintz, 1982), carbon dioxide and climate (Hansen et al., 1981), and anthropogenic changes in the albedo and climate (Charney, 1975; Sagan et al., 1979). An example of an especially useful climato-genetic reference point is provided by the CLIMAP (1976) reconstruction of the 18000 years B.P. global climate from a compilation of the Earth's ocean surface temperatures. A preliminary extension of the analysis to continental areas revealed numerous problems of local variability (Peterson et al., 1979). Such comparisons between general atmospheric conditions, as modeled by GCMs, and paleogeomorphic reconstructions hold great promise for understanding large-scale climate/landscape interactions. The goal here is to generate a self-enhancing spiral of understanding, with models pointing to key geomorphic questions and geomorphic data refining the models.

Ancient Landscapes

At the end of the 19th century, geomorphology achieved an important theoretical synthesis through the work of William Morris Davis. Davis (1899) conceived a marvelous deductive scheme of landscape development by the action of exogenetic processes acting on the basic materials and structures to produce a progressive evolution of landscape stages through time. Unfortunately, this theoretical framework was somewhat abused by those who employed it solely for landscape description and classification. By the middle of the 20th century, evolutionary geomorphology fell from favor among Earth scientists, who focused their primary efforts on the study of various geomorphic processes.

An unfortunate by-product of the controversy over Davisian geomorphology was the general abandonment, especially in Britain and the United States, of studies that concerned ancient landscapes and landforms. The development of radiometric dating has rekindled interest in this topic by identifying the antiquity of landscapes. For example, Young (1983) has shown that upland surfaces in southeastern Australia originated as early as Mesozoic and Early Tertiary, with the landscape assuming its approximate present-day form by the Miocene. Twidale et al. (1974) also identified Mesozoic landscapes in South Australia.

Olier (1979), in an analysis of ancient landscapes in Australia, concluded that conventional approaches to geomorphic change suffer from inadequate appreciation of broad scales of time and space. He proposed an evolutionary approach to geomorphic features, such as that applied by geologists to tectonic features (Windley, 1984).

Low-relief plains cutting across varied rocks and structures are common features on the Earth. Such surfaces have long been of interest to geomorphologists, and many scientific controversies have arisen over their explanation. The genetic implications are contained in the many names for the surfaces; peneplains, pediplains, panplains, etchplains, exhumed plains, and paleoplains. To avoid the problems inherent in these controversies, it is perhaps best to simply call these features planation surfaces.

Figure 1-6 shows a spectacular planation surface that bevels sandstone cuestas in the fold belt of the Amadeus Basin in central Australia. An analysis of the regional geomorphology of this area is presented in Plate I-4. The question of regional planation surfaces obviously awaits a modern global analysis. Perhaps the classic syntheses of King (Table 1-4) can be reevaluated by the use of the new techniques described in this volume (Figure 1-7).

ORIGINAL PAGE IS
OF POOR QUALITY

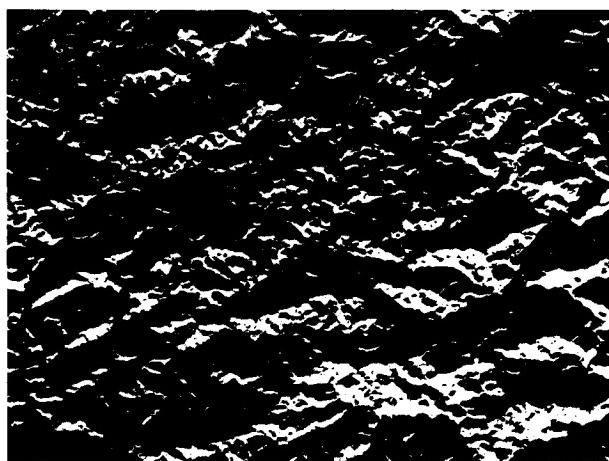
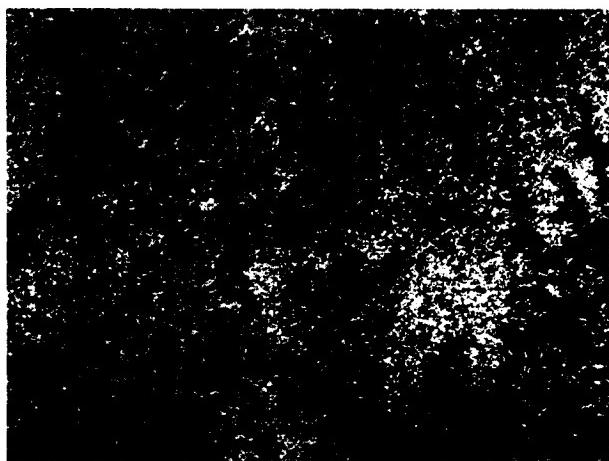
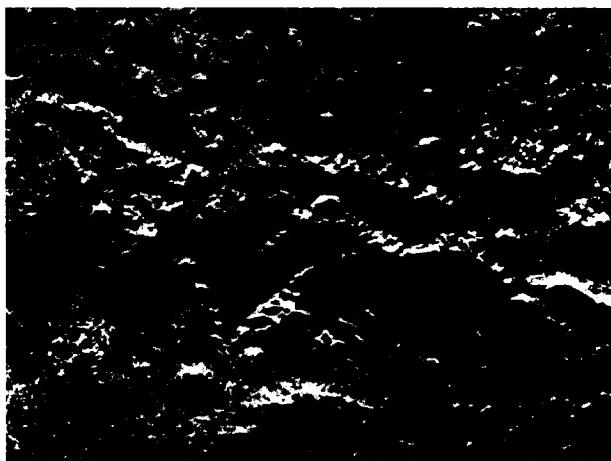
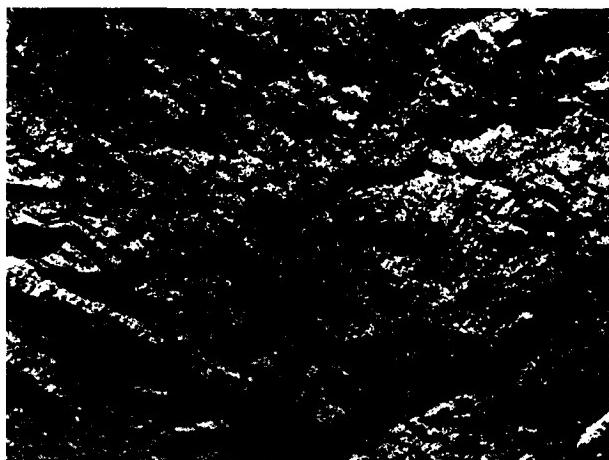


Figure 1-5. Shuttle Imaging Radar (SIR-A) images of typical Indonesian terrain types (from Sabins, 1983). Each image is 28 km wide. The radar look direction is from top to bottom of each image. Upper left: carbonate terrain (karst topography). Upper right: clastic terrain (cuestas and hogbacks); middle left: volcanic terrain (cinder cones); middle right: alluvial terrain (river patterns); lower left: melange terrain (tectonic chaos); lower right: metamorphic terrain (high relief and angular ridges).



Figure 1-6. Planation surface cut across dipping Paleozoic sandstone, James Range of central Australia.

It would be refreshing to accomplish such a study with automated data collection procedures, free of the raging controversy that so hampered the highly personal interpretive studies of the past.

The identification and dating of various planation surfaces have become important components of tectonic geomorphic analysis. Deformation of such surfaces by faulting, folding, or broad warping can be calibrated by the displacement of a planation surface from its original attitude.

Planetary Geomorphology

Some geomorphologists hold that their science is properly restricted either to the dynamic geology or to the physical geography of the Earth's surface. Indeed, more argument would probably be expended on the relative "geologic" or "geographic" content of geomorphology than whether any consideration should be given to bizarre alien landscapes. Such a view ignores two fundamentals. First, any science of the Earth must recognize that Earth is a planet. We learn more about that planet by studying analogs to its mysteries on other planets. Second, science derives

its greatest excitement and its most important advancement through discovery.

A century ago geomorphology was a science filled with wonder and excitement. The stimulus for its rapid growth in this time period was the discovery of landscapes that then seemed as bizarre and alien as those on other planets. The great plateaus of the western United States, the hyperarid deserts of the eastern

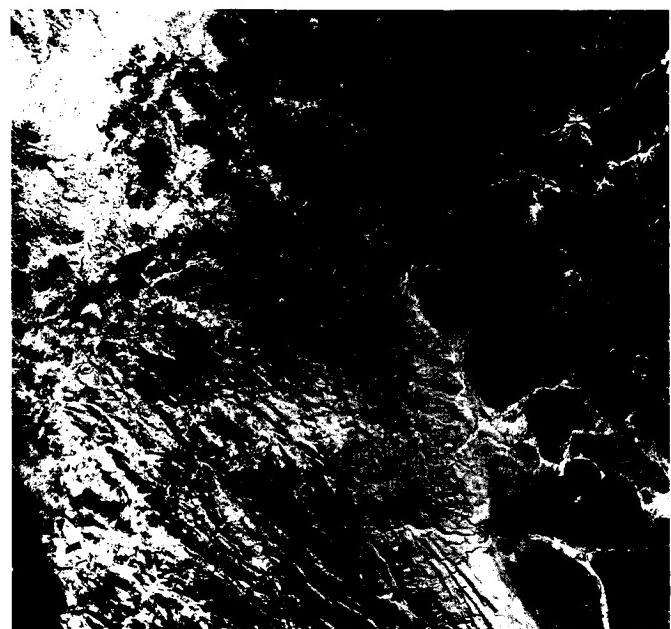


Figure 1-7. Landsat image of western South Africa (latitude 31°45' South, longitude 19°15' East). The area shows the classic cyclic denudational land surfaces interpreted by King (1967). Most of the eastern (right) portion of the image is the African Surface (Table 1-4) developed on Karoo System shale, sandstone, and tillite. Local high areas are Gondwana and post-Gondwana remnants. The plains to the northwest represent the Miocene Post-African Surface developed on Archean granite. Younger Quaternary valleys are dissecting this surface.

Table 1-4
Widespread Planation Surfaces

Name	Age	Comments
Gondwana	Jurassic	Related to Pangea and its breakup
Post-Gondwana or Kretacic	Early to Mid-Cretaceous	Related to Pangea and its breakup
African or Moorland	Late Cretaceous to Early Cenozoic	Extensive surface created by stripping weathered material from older surfaces
Post-African or Rolling	Miocene	Undulating surface developed above younger valleys
Widespread	Pliocene	Global surface common near coastal areas
Youngest	Quaternary	Latest valley formation

(King, 1962, 1967, 1976, 1983)

understood terrestrial processes. Sharp (1980, p. 231) emphasizes this benefit as follows:

"Planetary exploration has proved to be a two-way street. It not only created interest in Earth-surface processes and features as analogues, it also caused terrestrial geologists to look on Earth for features and relationships better displayed on other planetary surfaces."

Because many planetary surfaces have been relatively stable for billions of years, they preserve the effects of extremely rare, exceedingly violent processes. Such processes include impact cratering, sturzstroms (large avalanches of rock and debris), and cataclysmic flooding. On Earth, the evidence of such catastrophes is meager because of rapid crustal recycling through plate tectonics and relatively high denudation rates. However, on the other terrestrial planets, the results of these processes can be studied in great detail, commonly in large-area images (see Chapter 10) similar to those obtained by Earth-observing sensors in space. This is of profound importance for Earth studies. When cataclysmic processes have occurred on Earth, their influence has been profound. The extinction of numerous organisms at the end of the Cretaceous because of a meteor impact is a case in point (Alvarez et al., 1980).

The steppes of central Asia, the karst of Dalmatia, and the inselbergs of Australia and Africa all posed anomalies in the prevailing geomorphic theory. The explanation of the new landscapes led to an expanded and improved explanation for landscapes already described. Of course, this reflects an obvious quality of all science: there are no bounds, geographic or otherwise, for inquiry into the origin of phenomena. If a geomorphologist can learn more about the surface of Earth by studying other planetary surfaces, then that extraterrestrial study can no longer be dismissed as merely an interesting intellectual diversion. It becomes an absolutely essential part of geomorphology. An Earth-centered view of geomorphology is as limiting as a pre-Copernican view of the solar system.

Not all geomorphologists have shared the modern reluctance to consider the study of extraterrestrial relief forms. In 1892, the U.S. Geological Survey suffered a drastic cut in research funds. The Chief Geologist of the Survey at that time was geomorphologist Grove Karl Gilbert. Without support for his field work, Gilbert undertook a study using the U.S. Naval Observatory telescope in Washington, D.C., to compare surface features

on the Moon with counterparts on Earth. Despite the prevailing view that gradual and prolonged volcanism explained lunar surface features, Gilbert (1893) concluded that cataclysmic impact processes best explained the ubiquitous lunar craters. He applied the term "meteoric" to his impact theory, which had to wait over 70 years for verification by the Apollo program of lunar landings and sample returns. Among the many lessons that geomorphology can trace to Gilbert's example (Baker and Pyne, 1978)—that of studying other planets besides Earth—has yet to be fully appreciated.

The study of planetary surfaces relies heavily on analogic reasoning to reconstruct the complex interactions of processes responsible for the observed landforms (Mutch, 1979). Thus, the photointerpreter of planetary images must rely on this experience with terrestrial landscapes. Moreover, the geomorphic interpretation of other planets produces a kind of intellectual feedback: some planetary surfaces contain excellent analogs for little-

CONCLUSIONS

Regional landforms analysis, once termed "physiography," was the major concern of geomorphologists until the middle of this century. Landscapes and landforms were analyzed at regional and global scales in terms of their structure, processes of formation, and evolutionary sequence of development. Although regional landforms analysis continues in Europe (Embleton, 1984), it has generally fallen from favor in Britain and the United States. In the latter countries, attention in recent decades focused on the small-scale landforms and short-acting processes that were most amenable to quantitative measurement, statistical analysis, and incorporation into a systems analytical framework.

A resurrection is occurring in regional landforms studies. The impetus for this resurrection comes from many quarters. In the theoretical realm, unifying models of global tectonics and climatic systems are providing the appropriate scientific framework for large-scale studies. In the technology realm, the use of orbital remote sensing systems and geochemical tools for dating Earth history is quantifying the measurement at large spatial and temporal scales. In the discovery realm, geomorphology is being stimulated by the need to explain enigmatic landscapes, newly explored on the sea floor and on the surfaces of other planets.

PLATE I-1

The mosaic of color Landsat scenes on pages 00 and 00 shows in remarkable detail the geomorphic features of the northern Colorado Plateau region of the western United States. The mosaic is centered near the "four corners area" of Arizona, Utah, Colorado, and New Mexico. The region is characterized by spectacular high desert scenery, including plateaus, deep canyons, and broad valleys with great sandstone inselbergs (Hunt, 1969). The structure is predominantly horizontal, but the sedimentary strata are locally deformed into gently dipping monoclines, broad domes, and basins.

The top center of the mosaic shows the complex relationships associated with the transition from the Rocky Mountains to the Colorado Plateau. Grand Mesa is capped by Late Tertiary basaltic lava flows. Broad upwarps were created on the plateau during the so-called Laramide Orogeny of the Early Tertiary. The folding affected drainage in many ways (Hunt, 1969). The Gunnison River, for example, cut deeply into Precambrian rock at Black Canyon. Parts of this canyon are filled with Oligocene volcanic rocks from the San Juan Mountains. Thus, the valley is 35 000 000 years old. At Unaweep Canyon, the Gunnison River, and probably the Colorado River, flowed through the Uncompahgre Plateau. However, continued uplift of the plateau eventually diverted the river northward. The canyon was probably abandoned in the Late Pliocene. Its floor now stands over 400 m higher than the modern Gunnison and Colorado Rivers, indicating considerable Pleistocene uplift.

Farther downstream, the Colorado River maintained its course across rising domal uplifts. The river crosses the Monument Upwarp at Cataract Canyon. The San Juan River maintained its course across the same structure. Such relationships of streams to structure are classic examples of antecedence.

Several major deformational structures are spectacularly displayed by differential erosion of the exposed sediments. Waterpocket Fold (Figure I-1.1) is an excellent example of a monocline. Paradox Valley, just east of the La Sal Mountains, is an anticlinal structure that formed by the intrusion of plastically deformed bedded salt of the Permian Paradox Formation. The San Rafael Swell exposes Pennsylvanian sandstone and carbonate units in its core. These are surrounded by great cuestas of dipping Triassic and Jurassic sandstone and shale units. Uplift of the swell began in the Early Tertiary but continued for a prolonged period, as indicated by arched Tertiary formations at the north fold's northern end.

Note that the Colorado and Green Rivers have pronounced incised meanders upstream of their confluence. In this area, they are flowing upstructure (i.e., against the regional dip). In Cataract Canyon, the river becomes much less sinuous as it crosses the crest of Monument Upwarp. The San Juan River shows a similar phenomenon as it approaches the Monument Upwarp (Figure I-1.2). This results in the famous "goosenecks" (Figure I-1.3). Farther downstream, the Colorado River displays a spectacular cutoff meander, the Rincon, where it crosses the Waterpocket Fold.

The region near the Colorado/Green junction is known as the Canyonlands section. The rivers have an inner gorge about 150 m deep (Figure I-1.4), developed in Upper Paleozoic rocks. A broad bench is developed on the Permian Cutler Formation. Triassic and Jurassic shale and sandstone units have retreated over 10 km from this inner gorge to form the bench. Charles Hunt

COLORADO PLATEAU MOSAIC

(1969) suggested that the upper bench formed over a long period, extending back to at least the Miocene. The inner canyon is believed to have formed since the late Pliocene, and presumably, about three-quarters of the depth was achieved in the Quaternary.

Prominent laccolithic domes (Gilbert, 1877) are responsible for several of the mountain areas in the southwestern part of the mosaic. These include the Henry Mountains, Abajo Mountains, La Sal Mountains, Navajo Mountain, Ute Mountain, and the Carrizo Mountains (Hunt, 1956). Doming generally occurred in the Early Miocene about 25 million years ago. Unlike the Laramide fold structures, the major rivers do not cross these domes. Rather, they flow around the large igneous structures. The domes are drained by radial patterns of streams.

The right portion of the mosaic shows the Rio Grande depression, a series of downfaulted grabens between the Colorado Plateau and the Sangre de Cristo Range of the southern Rocky Mountains. The Ortiz Mountains and Sandia Mountains are fault blocks in this portion of the basin and range province. A prominent fault marks the western boundary of this zone at the Nacimiento Mountains.

The spectacular Valles Caldera was produced by cataclysmic Pleistocene eruptions of ashflow tuffs. Subsidence after the eruption was followed by resurgence as more lavas entered the caldera to form a ring of small domes.

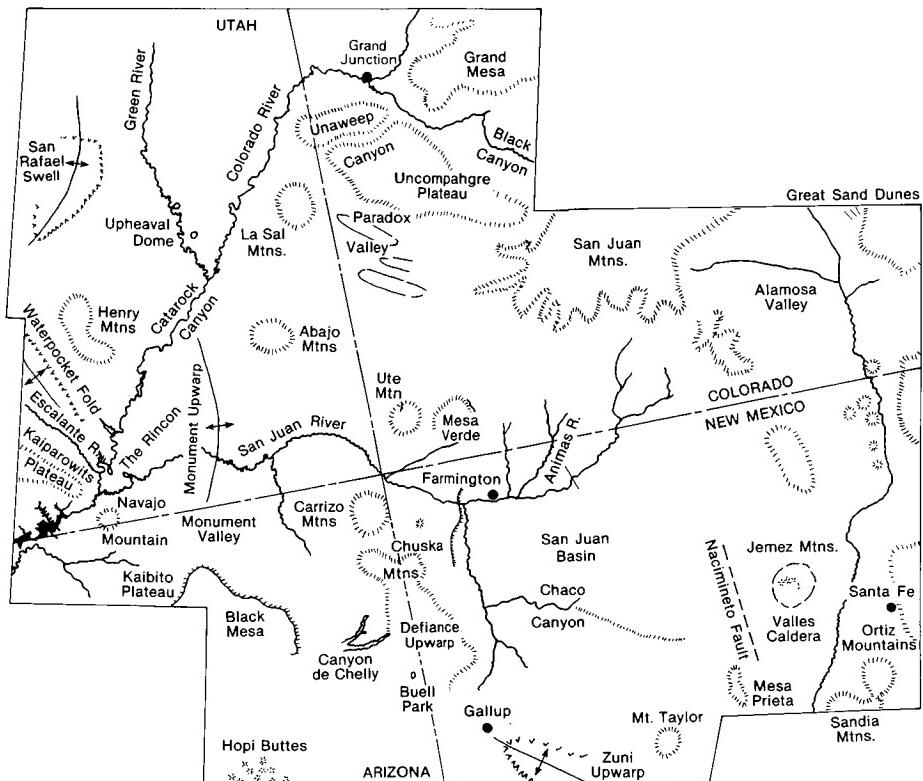
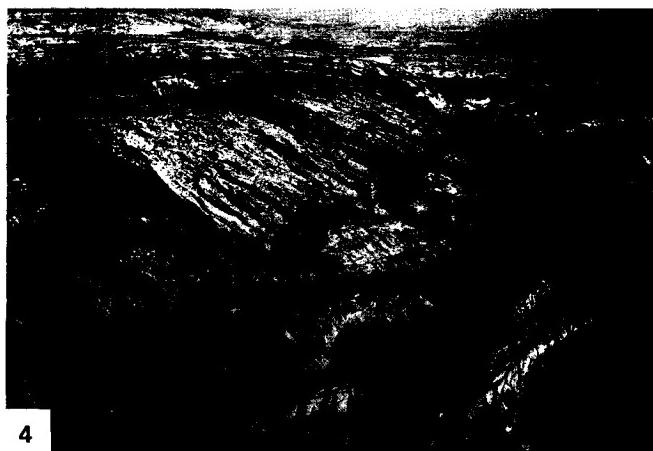
The San Juan Mountains, at the northeastern margin of the plateau, consist of older Tertiary ashflow tuff units. Deep erosion highly modified the original volcanic structures. Glacial troughs and cirques occur at the highest elevations, which were extensively glaciated during the Pleistocene.

The San Juan Basin, immediately south of the mountains, contains a thick fill of Cretaceous and Tertiary rocks. At Chaco Canyon, the drainage has breached Chaco Cuesta, a sandstone-capped cuesta. Mesa Verde exposes littoral-marine Cretaceous sandstone capping a thick sequence of Mancos Shale. The sandstone cliffs at both Mesa Verde and Chaco Canyon were highly desired occupation areas for the Anasazi culture of Indians approximately 1000 years ago.

Among the younger volcanic fields of the Colorado Plateau are the Hopi Buttes, a swarm of cones and eroded volcanic pipes of Tertiary age. Mount Taylor comprises a stratocone reaching 3340 m (11 300 ft) in elevation. Its volcanic field also includes a basalt-capped mesa (lower right of the mosaic) and a prominent outlier, Mesa Prieta. The volcanism was Late Tertiary in age.

The mosaic also shows some interesting small circular structures. Buell Park, at the bottom center, is a caldera-like basin eroded from soft volcanic tuff at the crest of the Defiance Upwarp. It is one of more than 30 volcanic explosion pipes (diatremes) that have been recognized nearby. Upheaval Dome, near the Green River in the upper left of the mosaic, was once thought to be the result of salt deformation, similar to the origin of the Paradox Basin. This structure has recently been reinterpreted by Eugene Shoemaker, who finds it to conform to the expected properties of a deeply eroded astrobleme. As much as 2 km of overlying beds may have been removed by erosion since the impact, which Shoemaker infers to be latest Cretaceous or Paleocene in age. The original crater may have been 10 km in diameter before its modification by deep erosion. The required impacting body would have been on the order of 500 m across.

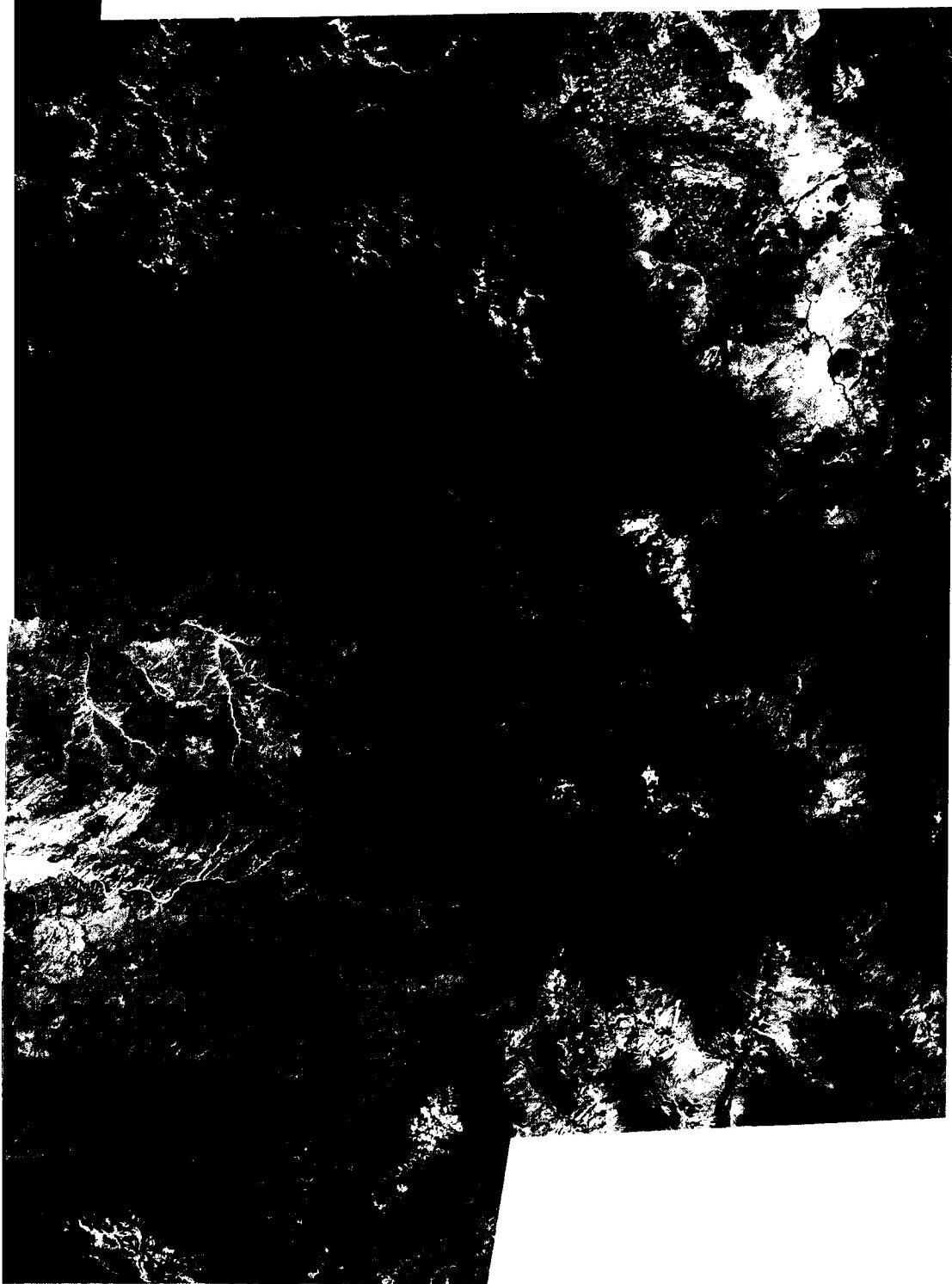
ORIGINAL PAGE IS
OF POOR QUALITY



ORIGINAL PAGE
COLOR PHOTOGRAPH



ORIGINAL PAGE
COLOR PHOTOGRAPH



This striking example of image processing illustrates the lithologic control of a cuesta landscape in east-central Saudi Arabia. Riyadh is situated at an elevation of 600 m in a zone of uplands characterized by a northwest to southeast trending series of ridges developed on Jurassic and Cretaceous carbonate units. The western boundary of the uplands is marked by a prominent west-facing escarpment, the Jabal Tuwayq. Lowlands to the west of the escarpment are filled with eolian sand, including the Nafūd-Qunayfidhah dunefield. To the northeast of the Upland is the Ad Dahna sand sea, a small portion of which is visible at the top right corner of the image. Prevailing wind directions can be inferred from the dune development along a northwest-to-southeast pattern of sand drift (McKee, 1979).

The cuesta landscape is developed on an eastward-dipping sequence of Mesozoic shelf-platform sediments that overlie the Precambrian crystalline rocks of the west-central Arabian Peninsula. Limestone units comprise resistant ridges with west-facing escarpments. Sandstone units comprise the intervening valleys. The lowest troughs are occupied by sandy desert.

The resistant rock units are dissected in a striking erosion pattern that leaves relatively flat sloping surfaces on the gently dipping bedding planes (Figure I-2.1). Valleys have relatively flat floors, and steep slopes separate the upland surfaces from the valley floors. Such slopes, with a faceted appearance, characterize resistant rock types in arid and semiarid regions.

The climate of north-central Saudi Arabia is extremely arid. Average annual rainfall at Riyadh is 75 mm. The aridity explains the resistance of various limestone units, which in a humid climate might be less resistant because of solution processes. Granular disintegration of sandstone may be facilitated by salt-weathering processes in an arid climate, whereas a sandstone of similar composition may be more resistant in a humid climate. Whatever the details of differential resistance to erosion, the resulting landscapes produce an excellent response of geologic units on remote sensing imagery. The simple index map prepared from the image conveys nearly as much geologic information as a detailed geologic map based on considerable ground-based field mapping. **Landsat 10171-06530, January 10, 1973.**



ORIGINAL PAGE
COLOR PHOTOGRAPH



Q_a Sand Dunes
Q_d Piedmont Gravel
Q_w Wadi Deposits
K_a Aruma Limestone
K_w Wesia Sandstone
K_b Biyadh Formation
(Sandstone & Shale)
K_{bou} Buwaib Limestone
K_y Yamana Limestone
K_s Sulaiy Limestone
J_a Arab Formation
(Anhydrite)
J_j Jubaila Limestone
J_n Hanifa Limestone
J_m Tuwaig Mtn. Limestone
J_d Dhruma Limestone
J_{km} Minjur Sandstone
J_{kj} Jilh Formation
(Sandstone & Shale)

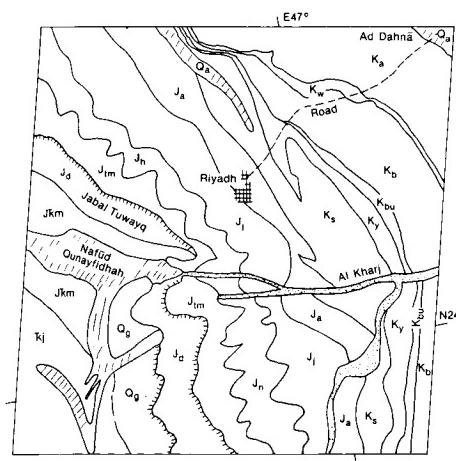


PLATE I-3

SELIMA SAND SHEET, SUDAN

This scene is a strip of SIR-A radar imagery placed over a Landsat-simulated, true-color image of the Selima Sand Sheet region in northwestern Sudan. The study area is located in the core of the largest expanse of hyperarid terrain on Earth. It lacks surficial traces of active fluvial processes and is dominated by eolian erosional and depositional features. The bedrock is predominantly Cretaceous Nubian sandstone overlying Precambrian granite of the African Shield.

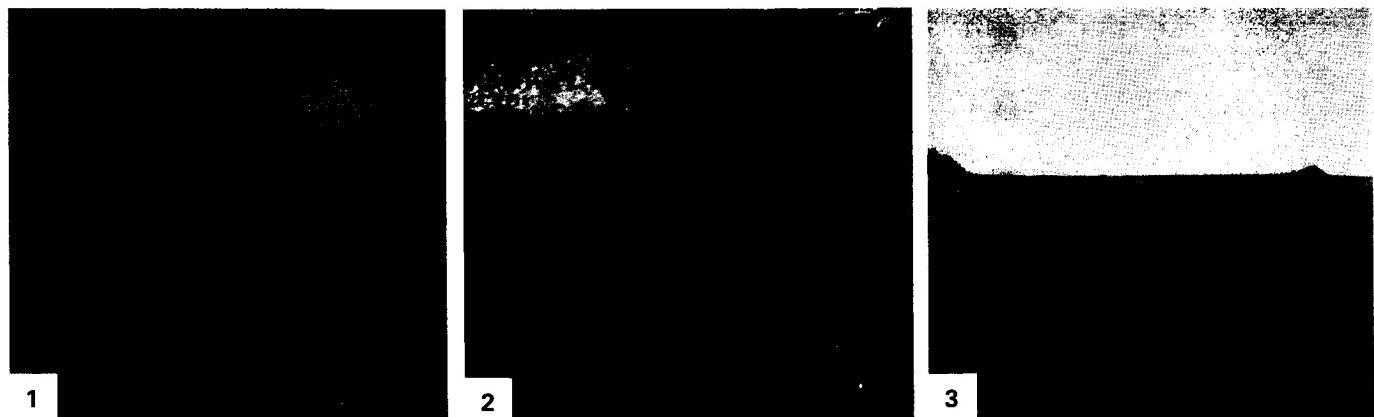
The radar penetrated up to several meters of extremely dry drift sand to reveal previously unknown buried valleys and other relict fluvial features (McCauley et al., 1982). The valleys seem to be a part of Late Tertiary systems that drained the eastern Sahara during relatively wet conditions before the onset of general aridity in the Pleistocene. The bright responses on the radar images consist of very rough bedrock surfaces, such as the former valley walls (Figure I-3.1). Note that ground photographs (Figure I-3.1) convey little impression of the relict fluvial networks that characterize the regional terrain.

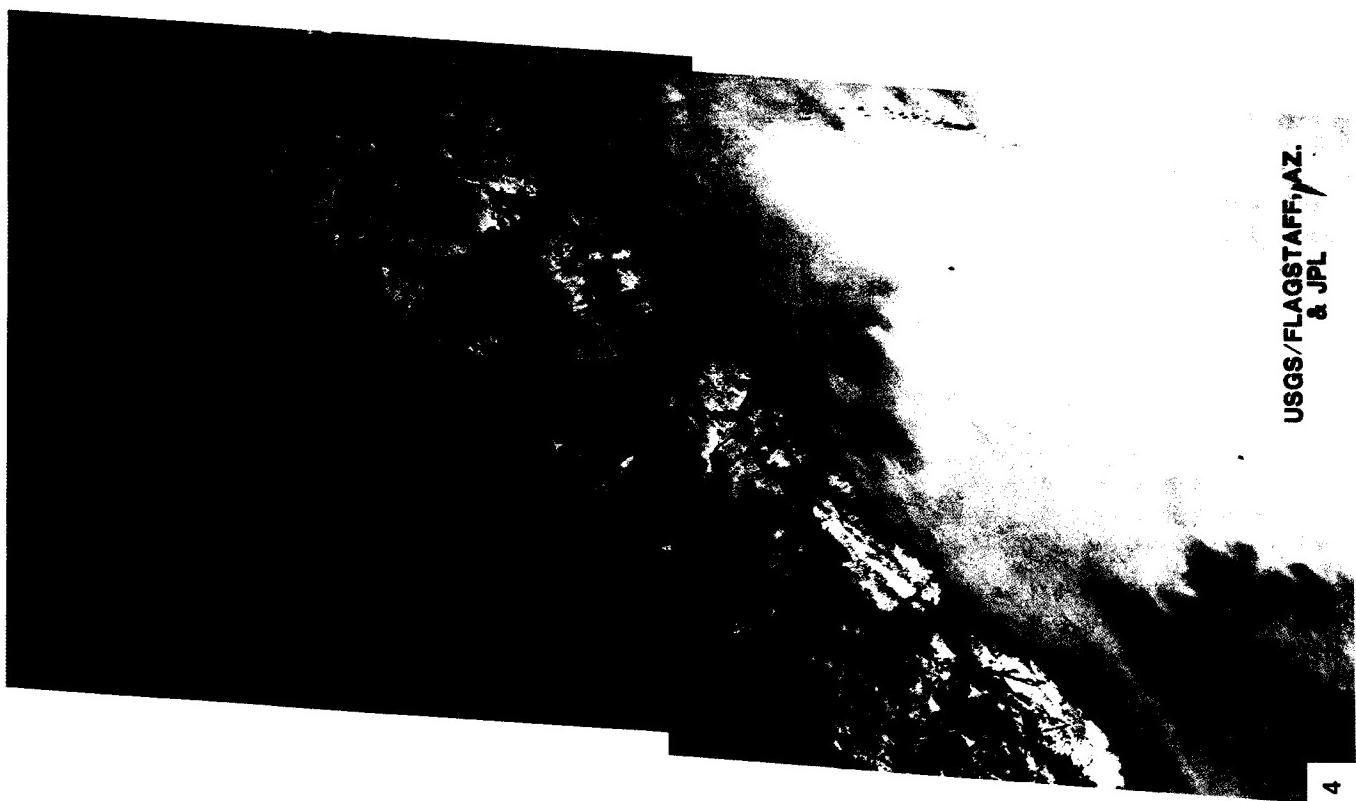
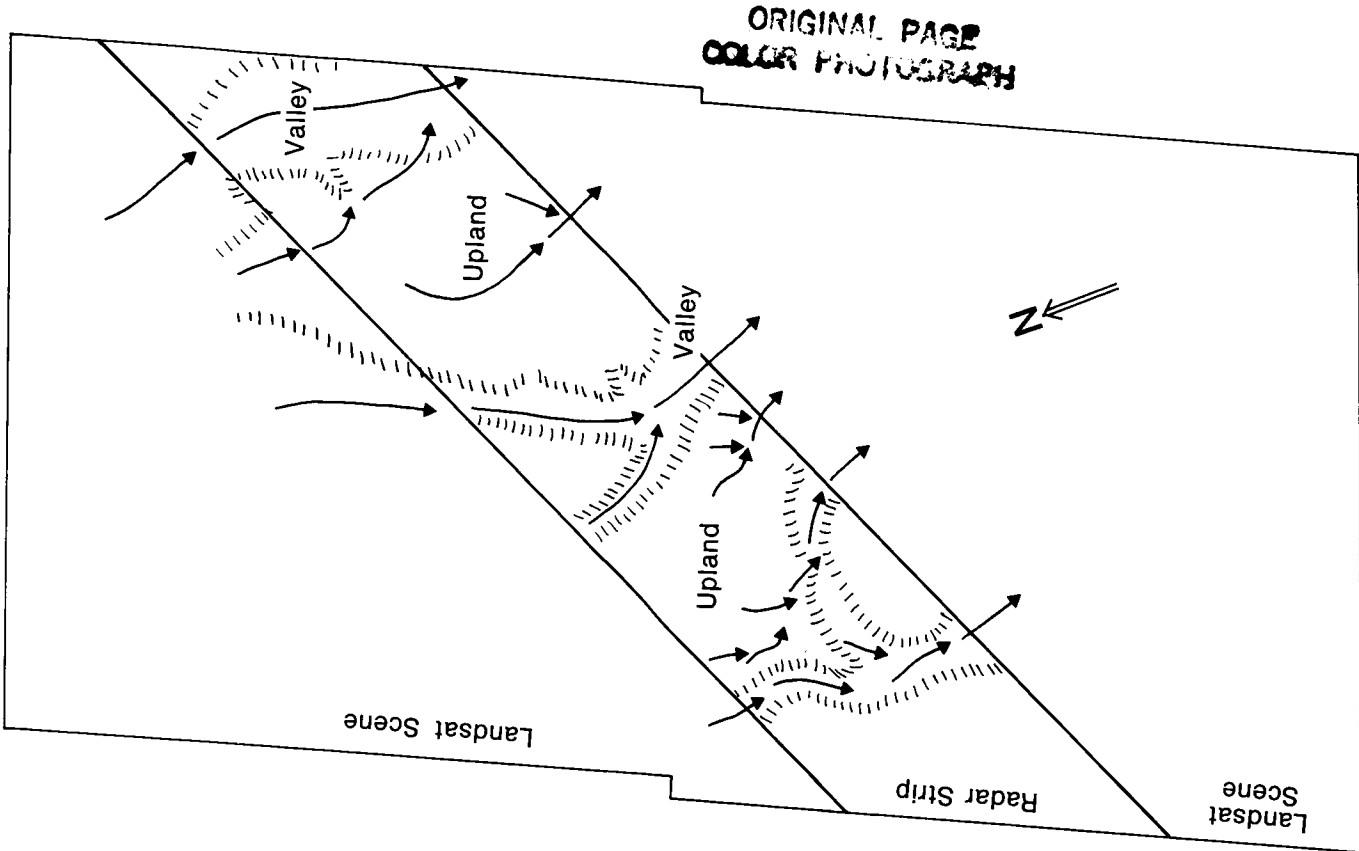
The dark areas on the radar images can be considered "radar-smooth" because they reflect incident radar waves specularly in a direction away from the receiver. Excavation during field exploration has shown that these areas of the Selima Sand Sheet are underlain by thick alluvial fills of sand and gravel (McCauley et al., 1982). Drainage was locally from the Gilf Kebir Plateau, which lies to the northwest of the study area. The southeastward-flowing streams established their courses by Late

Tertiary time, before the reorientation of drainage northward by the Nile River systems in the Quaternary.

Some of the alluvium-filled valleys are nearly as wide as the modern Nile Valley. Underfit and incised dry wadis are locally superimposed on the large valleys. In places, the old Tertiary drainage lines are marked by playas, many of which are now buried by active sand. It is believed that the wadi and playa activity represents pluvial episodes of the Quaternary. The radar imagery has been used to map these pluvial features in order to locate evidence of occupation by early man in migration routes northward across Africa.

Figure I-3.2 shows an area 400 km northeast of the region discussed above. This area is on the eastern edge of the Selima Sand Sheet. Note the braided river channels near the top right. These relict features are completely concealed beneath the sand sheet. The direction of former streamflow seems to have been from left to right (eastward). To the south of the channels are wind-eroded bedrock outcrops that give a bright radar response. "Tarma" (*Tamarisk* sp.) vegetation grows along some of the relict channelways. This vegetation survives in a hyperarid precipitation regime by tapping shallow ground water with deep roots. Figure I-3.3 shows two small sand mounds in this area caused by the trapping of windblown sand by these plants. The radar-located channels have proved to be valuable ground-water reservoirs. **SIR-A Radar Image, November 1981.**





0 50 Km

PLATE I-4

The east-west fold belt of central Australia contains some of the world's most fascinating desert scenery. The folding occurred during Late Devonian and Carboniferous time and affected a thick sequence of Late Proterozoic through Carboniferous rocks comprising the Amadeus Basin (Wells et al., 1970). The principal mountain areas include the Macdonnell, James, and Krichauff Ranges. Relatively tight anticlines and broad synclines are clearly indicated by the differential erosion of the various sedimentary rocks.

The oldest rocks on this image occur in the northeastern corner, where the Chewings Range stands as a resistant member of the Lower Proterozoic Arunta Block. During the Upper Proterozoic, this block became the source area for sedimentation into the Amadeus Basin to the south. Oldest of the sediments deposited in this basin is the Heavitree Quartzite, which forms magnificent resistant ridges breached by spectacular gorges such as Ellery Big-Hole (E on the sketch map) and Ormiston Gorge (O). Deposition of the Heavitree Quartzite was followed by the emplacement of a thick sequence of sediments ranging from Adelaidean to Devonian in age (850 to 400 million years ago). The Macdonnell and James Ranges expose older rocks in this sequence, while the Krichauff Range and the Pernjarrar Hills (PH) expose younger Devonian/Carboniferous rocks. The latter consist mainly of sand and conglomerate shed during the Alice Springs Orogeny, which occurred about 350 million years ago. The orogeny resulted in the spectacular folds of the James Range and the lesser ranges to the south.

Figure I-4.1 is a detailed geomorphic map of a portion of this Landsat image that was prepared from standard low-altitude aerial photography. The location of the mapped area is shown as a box in the northwest corner of the index map. The map was prepared from photographs NT465-853, NT465-855, NT-465-857, and NT465-859, which were flown in 1978 and produced at 1:53 000 for the Australia national mapping program. Figure I-4.2 shows photograph NT465-855, which was used in this exercise. The stippled areas mapped in Figure I-4.2 are dissected remnants of debris-mantled pediment surfaces of Middle Tertiary age. These surfaces comprise remnants of a deeply weathered Tertiary landscape that existed in the valleys between the resistant ridges (Figure I-4.4).

The Mesozoic and Tertiary history of this region was a prolonged episode of denudation, during which multiple erosion surfaces evolved. Fluvial action and deep weathering were both important during this period. In a sense, the structures were "etched" by the differential erosion (Figure I-4.3). Less resistant rocks were preferentially removed to comprise low plains. During the Tertiary, a wet climate promoted the development of lakes in some of the plains. Changing climate also promoted an episode

CENTRAL AUSTRALIA

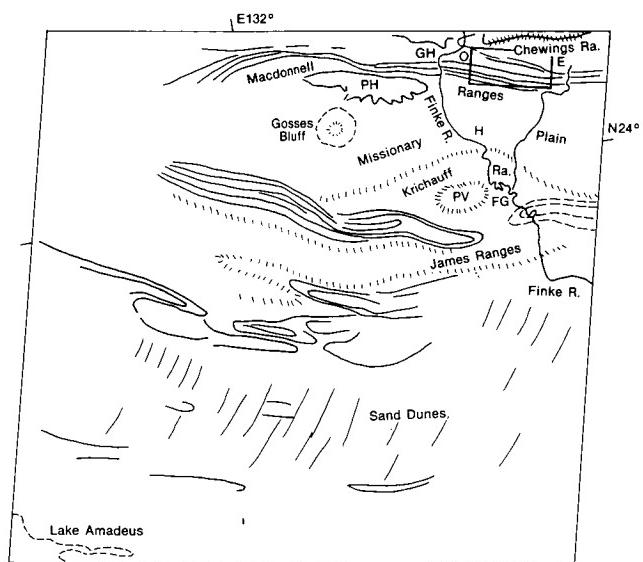
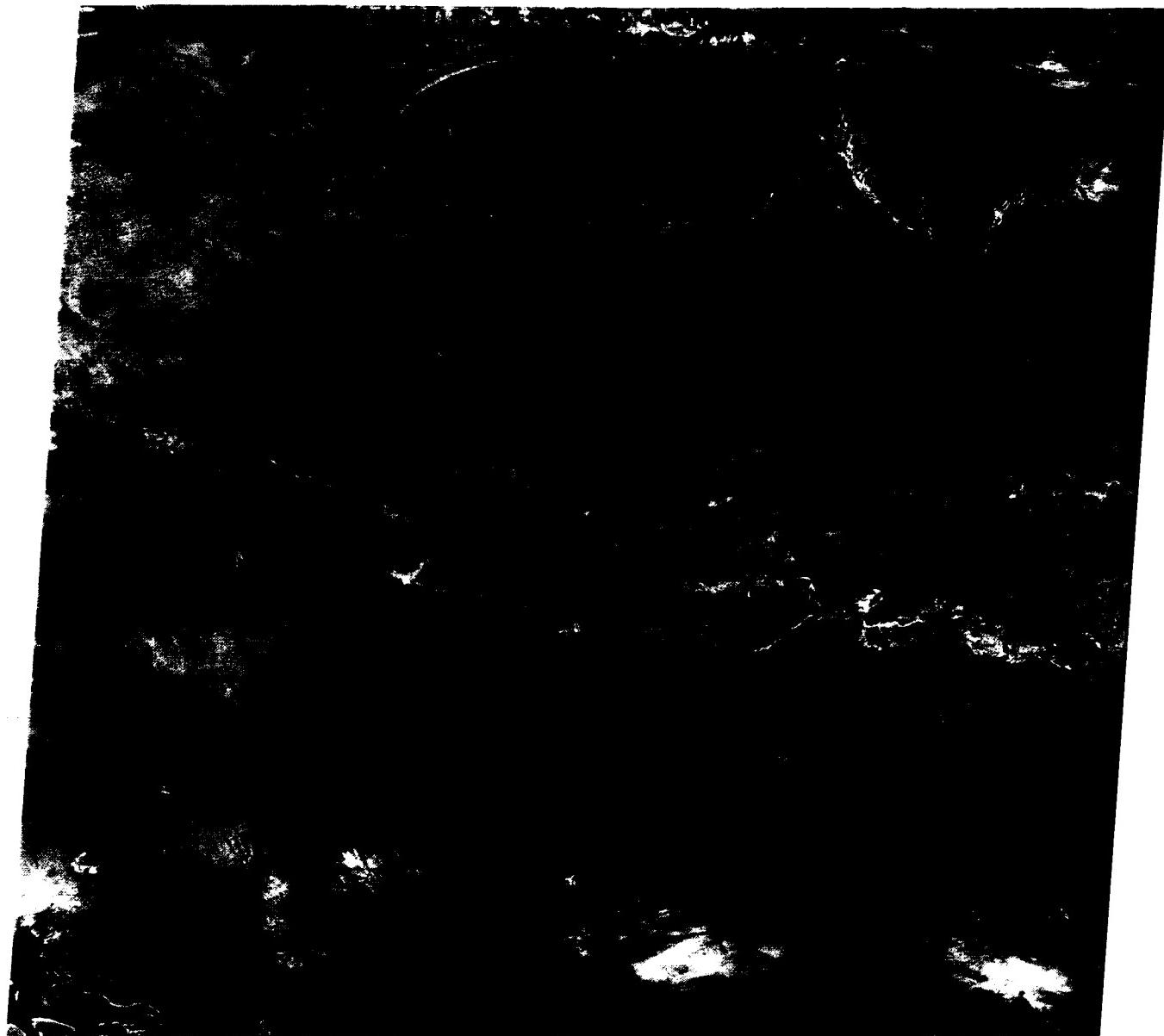
in the Miocene of extensive silification on the landscape. This produced siliceous duricrusts called silcrete. The latest Tertiary and Quaternary was marked by progressively more arid conditions. Extensive sand sheets and dunes developed during the Quaternary.

The central ranges line up with a pattern of high-amplitude highs and lows in the free-air and Bouguer gravity anomaly pattern over Australia. Gravity highs occur over the thrust-bounded cratonic blocks, such as the Arunta Block, and lows occur over sedimentary basins, such as the Amadeus Basin. The pattern is thought to be consistent with north-south lateral compression. This compression could have either: (1) deformed the central Australian lithosphere into a series of buckle-like undulations, or (2) broke the lithosphere into juxtaposed blocks through mechanical failure. The Devonian/Carboniferous Alice Springs Orogeny was presumably the major manifestation of the compression. The gravity anomalies show that the cratonic blocks are uncompensated today, suggesting that lateral compression may still be maintaining the Amadeus Basin. The combining of geophysical data sets with orbital imagery thus provides an important perspective on regional tectonic geomorphology.

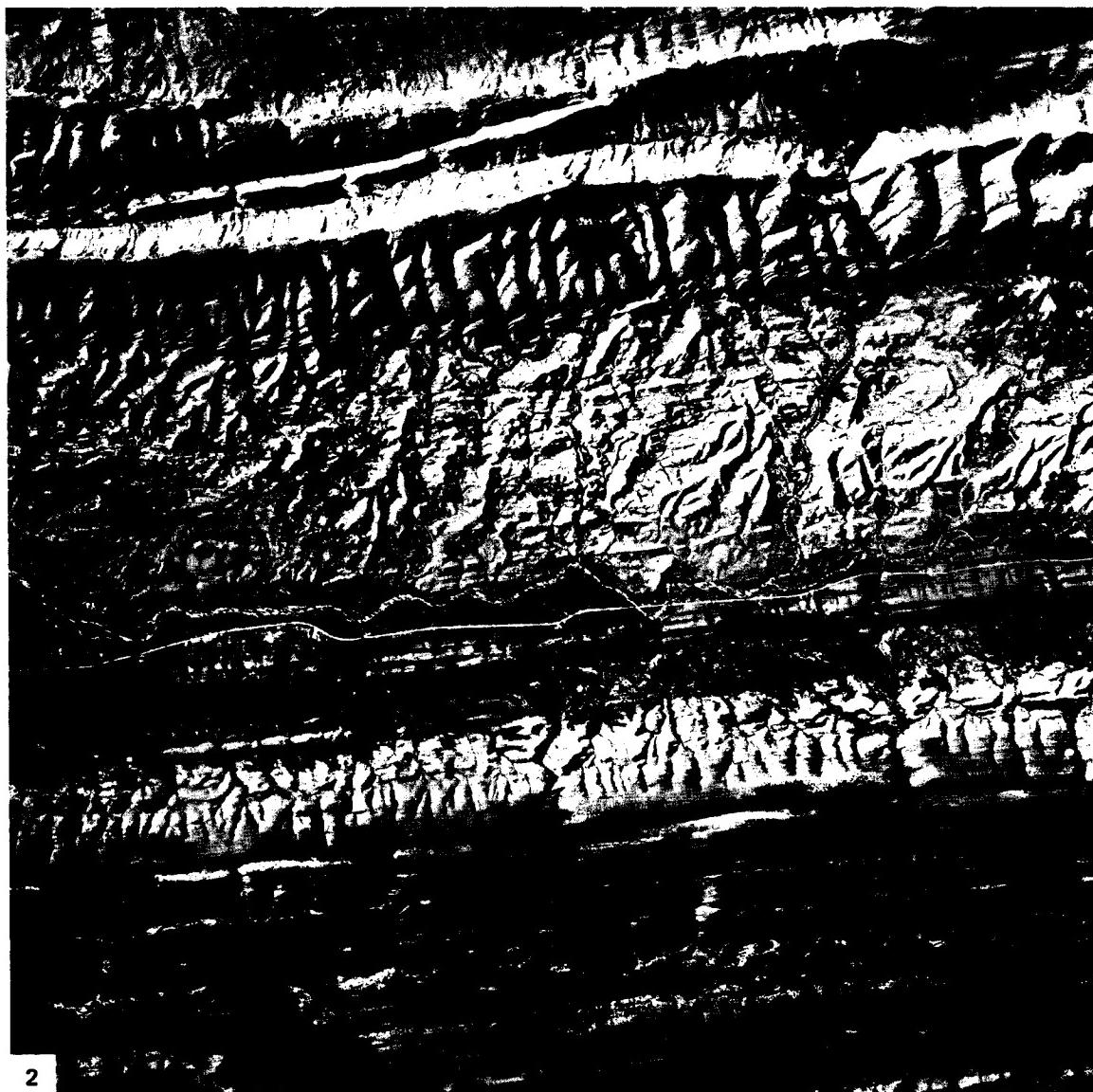
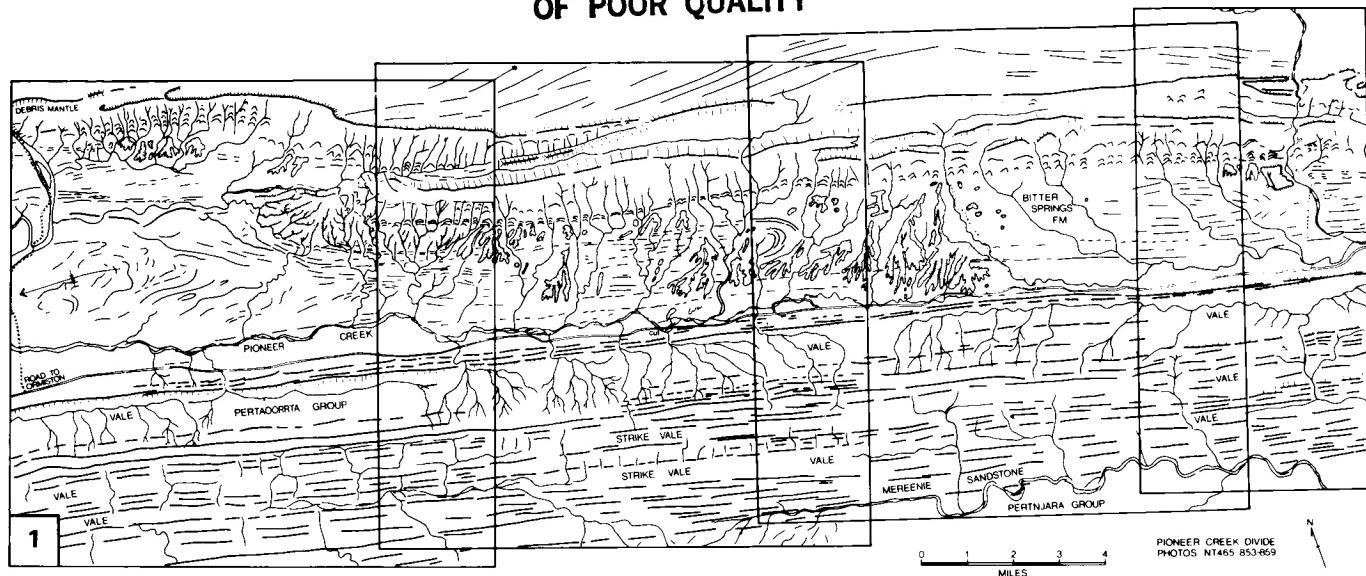
Perhaps the most striking structure in this region is the Gosses Bluff astrobleme. This impact structure formed during the Early Cretaceous, about 130 million years ago (Milton et al., 1972). Deep erosion has exposed a deformed zone 20 km in diameter (dashed pattern on the index map). The central uplift (Figure I-4.5) is a ring of vertically dipping sandstone units. Less resistant sandstone and siltstone comprise the central depression, and brecciated sediments form the outer zone on the Missionary Plain. Thus, erosion has preferentially removed the breccia, but little of the coherent bedrock. Gosses Bluff is an excellent example of a partially eroded impact structure.

The prominent meandering valley of the Finke River cuts directly across the mountain trends. The Finke River Gorge (Figure I-4.6) is an example of this cross-axial or discordant drainage. Other gorges and water gaps are well displayed in the Macdonnell Range. The discordance of drainage with regional drainage has been attributed by various investigators to superimposition, antecedence, and inheritance from the ancient erosion surface. Speculation that the Finke was antecedent to the Devonian/Carboniferous folding has led to its popular description as the "world's oldest river." However, there is no evidence to associate the river with its present course any time earlier than the Cretaceous. Current hypotheses suggest that the drainage of central Australia developed since the Cretaceous through a complex combination of inheritance, local superimposition, and stream capture (Mabbutt, 1966). **Landsat 1373-00364, July 31, 1973.**

ORIGINAL PAGE
COLOR PHOTOGRAPH



ORIGINAL PAGE IS
OF POOR QUALITY

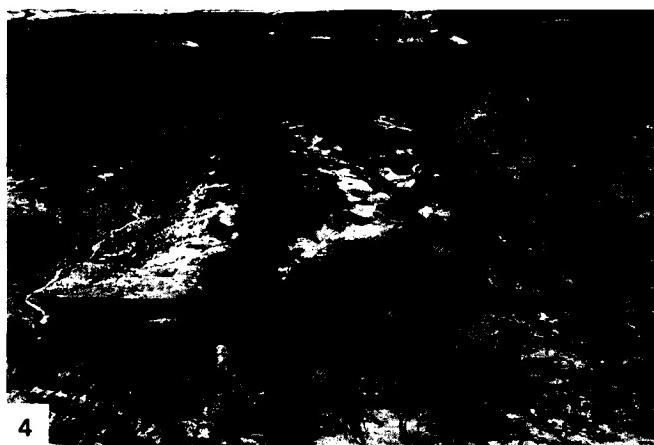


2

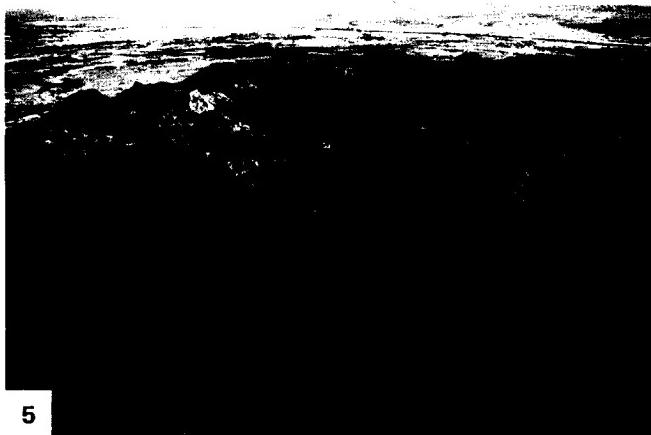
ORIGINAL PAGE IS
OF POOR QUALITY



3



4



5



6

REFERENCES

- Alvarez, L. W., W. Alvarez, F. Asaro, and H. V. Michel, Extraterrestrial cause for the Cretaceous-Tertiary extinction, *Science*, **208**, 1095-1108, 1980.
- Baker, V. R., and S. Pyne, G. K. Gilbert and modern geomorphology, *Amer. J. Science*, **278**, 97-123, 1978.
- Bremer, H., Twenty-one years of German geomorphology, *Earth Surface Processes and Landforms*, **9**, 281-287, 1984.
- Büdel, J., *Climatic Geomorphology*, 444 pp., Princeton University Press, Princeton, New Jersey, 1982.
- Bull, W. B., Allometric change of landforms, *Geol. Soc. Amer. Bull.*, **86**, 1489-1498, 1975.
- Bull, W. B., Tectonic geomorphology, *J. Geol. Education*, **32**, 310-324, 1984.
- Callieux, A., and L. Romani, Modern trends in geomorphology, in *Perspectives in Geomorphology*, edited by H. S. Sharma, pp. 9-20, Concept Publishers, New Delhi, 1981.
- Carey, S. W., Scale of geotechnic phenomena, *J. Geol. Soc. India*, **3**, 97-105, 1962.
- Charney, J. G., Dynamics of deserts and drought in the Sahel, *Quart. J. Roy. Meteorol. Soc.*, **101**, 193-202, 1975.
- Chorley, R. J., and B. A. Kennedy, *Physical Geography: A Systems Approach*, 370 pp., Prentice-Hall, London, 1971.
- Chorley, R. J., S. A. Schumm, and D. E. Sugden, *Geomorphology*, 605 pp., Methuen, London, 1984.
- Church, M., Records of recent geomorphological events, in *Timescales in Geomorphology*, edited by R. A. Cullingford, D. A. Davidson, and J. Lewin, pp. 13-29, John Wiley, New York, 1980.
- Church, M., and D. M. Mark, On size and scale of geomorphology, *Progress in Physical Geography*, **4**, 342-390, 1980.
- CLIMAP Project Members, The surface of the ice-age Earth, *Science*, **191**, 1131-1136, 1976.
- Cooke, R. U., and J. C. Doornkamp, *Geomorphology in Environmental Management*, 413 pp., Oxford University Press, London, 1974.
- Cullingford, R. A., D. A. Davidson, and J. Lewin, (Eds.), *Timescales in Geomorphology*, 360 pp., John Wiley, New York, 1980.
- Davis, W. M., The geographic cycle, *Geographical J.*, **14**, 418-504, 1899.
- Demek, J., (Ed.), *Manual of Detailed Geomorphological Mapping*, 344 pp., Academia, Prague, 1972.
- Demek, J., and C. Embleton, *Guide to Medium-Scale Geomorphological Mapping*, 348 pp., E. Schweizerbartsche Verlagsbuchhandlung, Stuttgart, 1978.
- Edelson, B. I., Mission to planet Earth, *Science*, **227**, 367, 1985.
- Elachi, C., W. E. Brown, J. B. Cimino, T. Dixon, D. L. Evans, J. P. Ford, R. S. Saunders, C. Breed, H. Masursky, J. F. McCauley, G. Schaber, L. Dellwig, A. England, H. MacDonald, P. Martin-Kaye, and F. Sabins, Shuttle Imaging Radar experiment, *Science*, **218**, 996-1003, 1982.
- Embleton, C., *Geomorphology of Europe*, 465 pp., Macmillan, London, 1984.
- Fenneman, N. M., *Physiography of the Eastern United States*, 714 pp., McGraw-Hill, New York, 1938.
- Gardner, R., and H. Scoging, (Eds.), *Mega-Geomorphology*, 240 pp., Oxford University Press, Oxford, 1983.
- Gerasimov, I. P., Attempt at a geomorphological interpretation of a general scheme of the geological structure of the U.S.S.R., *Izv. Akad. Nauk SSR*, **12**, 33, 1946.
- Gerasimov, I. P., Structural features of the relief of the Earth's crust in the U.S.S.R. and their origins, *Izv. Akad. Nauk SSR*, **25**, 99, 1959.
- Gilbert, G. K., *Report on the Geology of the Henry Mountains*, U.S. Geological and Geological Survey of the Rocky Mountain Region, 160 pp., 1877.
- Gilbert, G. K., The moon's face: a study of the origin of its features, *Philosophical Soc. Washington Bull.*, **12**, 241-292, 1893.
- Goudie, A., (Ed.), *Geomorphological Techniques*, 395 pp., George Allen and Unwin, London, 1981.
- Hansen, J., D. Johnson, A. Lacis, S. Lebedeff, P. Lee, D. Rind, and G. Russell, Climatic impact of increasing atmospheric carbon dioxide, *Science*, **213**, 957-966, 1981.
- Horton, R. E., Erosional development of streams and their drainage basins: hydrophysical approach to quantitative morphology, *Geol. Soc. Amer. Bull.*, **56**, 275-370, 1945.
- Hunt, C. B., Cenozoic geology of the Colorado Plateau, U.S. Geol. Surv. Prof. Paper 279, 1956.
- Hunt, C. B., *Physiography of the United States*, W. F. Freeman, 480 pp., San Francisco, 1967.

- Hunt, C. B., Geologic history of the Colorado River, *U.S. Geol. Surv. Prof. Paper*, **669**, 59–130, 1969.
- King, L. C., *The Morphology of the Earth*, 699 pp., Oliver and Boyd, Edinburgh, 1962.
- King, L. C., *The Morphology of the Earth*, 726 pp., Hafner, New York, 1967.
- King, L. C., Planation remnants upon high lands, *Zeitschrift für Geomorphologie*, **20**, 133–148, 1976.
- King, L. C., *Wandering Continents and Spreading Sea Floors on an Expanding Earth*, 232 pp., Wiley-Interscience, New York, 1983.
- Kuhn, T. S., *The Structure of Scientific Revolutions*, 172 pp., University of Chicago Press, Chicago, 1962.
- Leopold, L. B., M. G. Wolman, and J. P. Miller, *Fluvial Processes in Geomorphology*, 522 pp., Freeman, San Francisco, 1964.
- Mabbutt, J. A., Landforms of the western Macdonnell Ranges, in *Essays in Geomorphology*, edited by G. H. Dury, pp. 83–89, Heinemann, New York, 1966.
- Masursky, H., E. Eliason, P. G. Ford, G. E. McGill, G. H. Pettengill, G. G. Schaber, and G. Schubert, Pioneer Venus radar results: geology from images and altimetry, *J. Geophys. Res.* **85**, 8232–8260, 1980.
- McCauley, J. F., G. G. Schaber, C. S. Breed, M. J. Grolier, C. V. Haynes, B. Issawi, C. Elachi, and R. Blom, Subsurface valleys and geoarcheology of the eastern Sahara revealed by shuttle radar, *Science*, **218**, 1004–1020, 1982.
- McCauley, J. F., and D. E. Wilhelms, Geological provinces of the near side of the Moon, *Icarus*, **15**, 363–367, 1971.
- McKee, E. D., (Ed.), A study of global sand seas, *U.S. Geol. Surv. Prof. Paper*, **1052**, 1979.
- Melton, M. A., An analysis of the relations among elements of climate, surface properties and geomorphology, *Office of Naval Research, Geography Branch*, Tech. Rep. 11, 102 pp., 1957.
- Melton, M. A., Geometric properties of mature drainage systems and their representation in an E4 phase space, *J. Geol.*, **66**, 25–54, 1958a.
- Melton, M. A., Correlation structure of morphometric properties of drainage systems and their controlled agents, *J. Geol.*, **66**, 442–460, 1958b.
- Metcherikov, J. A., Les concepts de morphostructure et de morphosculpture: un nouvel instrument de l'analyse géomorphologique, *Annals Geographie*, **77**, 539, 1968.
- Milton, D. J., B. C. Barlow, R. Brett, A. R. Brown, A. Y. Glikson, E. A. Manwaring, F. J. Moss, E. C. E. Sedmik, J. V. Son, and G.A. Young, Gosses Bluff impact structure, Australia, *Science*, **175**, 1199–1207, 1972.
- Morisawa, M. E., Quantitative geomorphology of some watersheds in the Appalachian Plateau, *Geol. Soc. Amer. Bull.*, **73**, 1025–1046, 1962.
- Mutch, T. A., Planetary surfaces, *Rev. Geophys. Space Physics*, **17**, 1694–1722, 1979.
- Mutch, T. A., R. E. Arvidson, J. W. Head, III, K. L. Jones, and R. S. Saunders, *The Geology of Mars*, 400 pp., Princeton University Press, Princeton, New Jersey, 1976.
- NASA, Global change: impacts on habitability, Report of the Executive Committee of a Workshop at Woods Hole, Massachusetts, June 21–26, 1982, *NASA Jet Propulsion Laboratory*, Document 95, 15 pp., 1982.
- National Research Council, *Toward an International Geosphere-Biosphere Program: A Study of Global Changes*, 81 pp., National Academy Press, Washington, D.C., 1983.
- Ollier, C. D., *Volcanoes*, 177 pp., MIT Press, Cambridge, Massachusetts, 1969.
- Ollier, C. D., Evolutionary geomorphology of Australia and Papua-New Guinea, *Transactions of the Institute of British Geographers*, pp. 516–539, 1979.
- Ollier, C. D., *Tectonics and Landforms*, 324 pp., Longman, London, 1981.
- Peterson, G. M., T. Webb, III, J. E. Kutzbach, T. Van Der Hammen, T. A. Wijmstra, and F. A. Street, The continental record of environmental conditions at 18 000 yr B.P.: an initial evaluation, *Quaternary Res.*, **12**, 47–82, 1979.
- Pitty, A. F., *The Nature of Geomorphology*, 161 pp., Methuen, London, 1982.
- Press, F., The role of science and engineering in mitigating natural hazards, Keynote Address at the Eighth World Conference on Earthquake Engineering, San Francisco, California, July 23, 1984, 15 pp., 1984.
- Pyne, S. J., *Grove Karl Gilbert: A Great Engine of Research*, 306 pp., University of Texas Press, Austin, Texas, 1980.
- Russell, R. J., Geological geomorphology, *Geol. Soc. Amer. Bull.*, **69**, 1–22, 1958.
- Sabins, F. F., Jr., Geological interpretation of Space Shuttle radar images of Indonesia, *Amer. Asso. Petrol. Geol. Bull.* **67**, 2076–2099, 1983.
- Sagan, C., O. B. Toon, and J. B. Pollack, Anthropogenic albedo changes and the Earth's climate, *Science*, **206**, 1363–1368, 1979.
- Salisbury, R. T., *Physiography*, 770 pp., Henry Holt, New York, 1907.
- Salomé, A. I., H. J. Van Dorsser, and P. L. Rieff, A comparison of geomorphological mapping systems, *ITC Journal*, **1981-2**, 272–274, 1981.
- Schumm, S. A., Evolution of drainage systems and slopes in badlands at Perth Amboy, New Jersey, *Geol. Soc. Amer. Bull.* **67**, 597–646, 1956.
- Schumm, S. A., and R. W. Lichty, Time, space and causality in geomorphology, *Amer. J. Science*, **263**, 110–119, 1965.
- Sharp, R. P., Geomorphological processes on terrestrial planetary surfaces, *Ann. Rev. Earth and Planet. Sciences*, **8**, 231–261, 1980.

- Shukla, J., and Y. Mintz, Influence of land-surface evapotranspiration on the Earth's climate, *Science*, **215**, 1498–1500, 1982.
- Sparks, B. W., *Rocks and Relief*, 404 pp., Longman, London, 1971.
- Strahler, A. N., Equilibrium theory of erosional slopes approached by frequency distribution analysis, *Amer. J. Science*, **248**, 673–696, 800–814, 1950.
- Strahler, A. N., Hypsometric (area-altitude) analysis of erosional topography, *Geol. Soc. Amer. Bull.*, **63**, 1117–1142, 1952.
- Strahler, A. N., Quantitative slope analysis, *Geol. Soc. Amer. Bull.*, **67**, 571–596, 1956.
- Strahler, A. N., Quantitative analysis in watershed geomorphology, *Trans. Amer. Geophys. Union*, **39**, 913–920, 1957.
- Strahler, A. N., Dimensionless analysis applied to fluvially eroded landforms, *Geol. Soc. Amer. Bull.*, **69**, 279–300, 1958.
- Strom, R. G., Mercury, in *The Geology of the Terrestrial Planets*, pp. 12–55, NASA SP-469, 1984.
- Sweeting, M. M., *Karst Landforms*, 362 pp., Columbia University Press, New York, 1973.
- Thornbury, W. B., *Regional Geomorphology of the United States*, 609 pp., John Wiley, New York, 1965.
- Thornbury, W. B., *Principles of Geomorphology*, 594 pp., John Wiley, New York, 1969.
- Thornes, J. B., and D. Brunsden, *Geomorphology and Time*, 208 pp., Methuen, London, 1977.
- Tricart, J., *Principes et Methodes de la Géomorphologie*, 496 pp., Masson, Paris, 1965.
- Twidale, C. R., Fragile foundations: some methodological problems in geomorphologic research, *Revue de Géomorphologie Dynamique*, **26**, 81–95, 1977.
- Twidale, C. R., *Granite Landforms*, 372 pp., Elsevier, Amsterdam, 1982.
- Twidale, C. R., Pediments, peneplains and ultiplains, *Revue de Géomorphologie Dynamique*, **32**, 1–35, 1983.
- Twidale, C. R., B. Daily, and A. R. Milnes, The age of the laterised summit surface on Kangaroo Island and adjacent areas of South Australia, *J. Geol. Soc. Australia*, **21**, 387–392, 1974.
- Washington, W. M., and D. L. Williamson, A description of the NCAR global circulation models, in *General Circulation Models of the Atmosphere*, edited by J. Chang, pp. 111–172, Academic Press, New York, 1977.
- Wells, A. T., D. J. Forman, L. C. Ranford, and P. J. Cook, Geology of the Amadeus Basin, Central Australia, Australia Bureau of Mineral Resources, *Geol. and Geophys. Bull.*, **100**, 1970.
- Windley, B. F., *The Evolving Continents*, 404 pp., John Wiley, New York, 1984.
- Young, R. W., The tempo of geomorphological change: evidence from southeastern Australia, *J. Geol.*, **91**, 221–230, 1983.

2

TECTONIC LANDFORMS

John R. Everett,* Marie Morisawa,† and Nicholas M. Short‡

W. M. Davis (1899) viewed *structure*, *process*, and *time* as the three pillars of geomorphology. Although there has been great progress in geomorphology since the fundamental work of Davis, his "trio" of structure, process, and time (stage) remains a useful starting point for any treatment of landforms, be they earthbound or extraterrestrial. Structure is generally agreed to be the most important of the Davisian trio. "Structure," as used by Davis and most later geomorphologists (e.g., Thornbury, 1969), includes not only deformational features like folds, faults, and joints, but any characteristics of the rock bodies such as their mineralogy and fabric that govern their relative resistance to erosion. In this chapter, we normally use "structure" in its deformational or tectonic sense.

One of the most profound realizations after looking at the Earth from space, where vast areas are seen in a single image, is that, over much of the land surface, the major control of the landscape is its underlying structure (Wolman, in preparation). From the vantage point of space, one seems to "see through" the modifying effects of process and stage to reveal this intrinsic control. The role of process and stage is more obvious at local scales. The synoptic views of tectonic landforms presented in this chapter offer strong support of the concept that, in the Davisian trio, structure is the "first among equals."

"Tectonic landforms" are structural landforms of regional extent. These landforms make up extensive landscapes whose topography is strongly influenced by the structure of underlying rocks that have undergone (or are undergoing) some degree of deformation (and possible associated metamorphism and igneous intrusion). Landscapes developed on orogenic belts, uplifts, domes, basins, and shields can all be thought of as tectonic landforms. There is a continuum of tectonic landforms ranging from recently formed fault scarps to physiographic provinces (e.g., Valley and Ridge Province of the Appalachian orogen) that have evolved over many millions of years by differential erosion on older structures that themselves took millions of years to form. Bloom (1969) points out that one rarely sees pristine tectonic landforms (i.e., those surface features formed solely by crustal deformation such as fault scarps) because they are constantly being modified by erosion as deformation proceeds so that their shapes originate both by endogenetic and exogenetic processes.

A minor problem in categorization arises in connection with landforms cut on nearly horizontal, essentially undeformed strata

where uplift and erosion have combined to create substantial and often spectacular relief. The Colorado Plateau and the Grand Canyon are obvious examples, but the midcontinent region of the United States and the Siberian Platform also fall into this category. In many such areas, fractures or other structural features control or strongly influence erosion, so that the term "structural geomorphology" (Bloom, 1978) can be appropriately applied. Degree of deformation in this definition is incidental.

The organization of the gallery sections of this book, in which chapters are based on geomorphic *process* (e.g., glacial, eolian, and volcanic), tends to obscure the fact that almost every large region has been shaped by many processes, in most instances operating through several geomorphic cycles, all controlled by structure. Chapter titles are thus pragmatic categories that do not necessarily represent the actual evolution of the landscapes shown. A physiographic province such as the Canadian Shield is thus a sort of palimpsest or montage, in which "complexity of geomorphic evolution is more common than simplicity" (Thornbury, 1969). Physiographic provinces are a useful means of grouping regional landforms; Fenneman's physiographic maps, for example, although dating from the 1920s, are still basically valid.

Geomorphic classifications of structural features at local scales are uncommon, and regional scale classifications (beyond the physiographic province concept) apparently do not exist (C. D. Ollier, Australian National University, personal communication). A search of the literature (Bloom, 1978; Butzer, 1976; Chorley et al., 1985; King, 1967; Morisawa and Hack, 1984; Ollier, 1981; Small, 1978; Sparks, 1972; Twidale, 1971, 1976) reveals several possible reasons for this situation.

For tectonic (and volcanic) landforms, the materials, processes, and subsurface geometry are mainly endogenic and three-dimensional. In contrast, landforms related to fluvial, eolian, and other processes are primarily exogenic and essentially two-dimensional. These same processes, of course, etch out features established by endogenic processes. The point is that, although a large collection of specific classes and descriptive terms exist for exogenic landforms, there is no comparable vocabulary for endogenic ones. Instead, much terminology for these landforms is adapted from that used for them in a structural (or volcanic) sense. Thus, such terms as anticline, thrust sheet, fault, and nappe (or stratocone, caldera, and shield volcano) are used interchangeably between endogenic structures and associated landforms. Some structural terms are used with modifiers (e.g., breached anticline, anticlinal ridge, perched syncline, and fault-line scarp) to clarify particular geomorphic aspects. Other terms such as cuesta, hogback, inselberg, mesa, ribbed ridge, and stream offset are geomorphic but have structural connotations.

Because of these problems in classification and nomenclature, the text for Plates in this chapter and the next (volcanic

*Earth Satellite Corporation, 7222 47th Street, Bethesda, Maryland 20815.

†Department of Geoscience, State University of New York-Binghamton, Binghamton, New York, 13901.

‡Geophysics Branch, Code 622, Goddard Space Flight Center, Greenbelt, Maryland 20771.

ORIGINAL FIGURE IS OF POOR QUALITY

landforms) may appear to neglect the geomorphic aspects of the chapter themes in that structural and volcanic terms are applied to landform description. The situation is aggravated, paradoxically, by the main advantage of orbital remote sensing—its wide areal coverage—that inherently best shows the very large features for which terminology and classification are generally lacking.

Earth scientists received their first glimpses of the Earth from space in photographs from sounding rockets and early manned missions in the early 1960s (Lowman, 1985) at about the same time that interest blossomed in seafloor spreading and what became known as plate tectonics. Thus, a new paradigm and the tools for studying that paradigm fortuitously emerged at about the same time. Since 1972, the high-resolution (79 m), nearly global Landsat imagery has had a great impact on the scientific understanding of the geology of isolated, poorly mapped land areas (e.g., the African Rift, studied by Mohr (1973) with Landsat data). Weather satellites, the Heat Capacity Mapping Mission, Seasat radar, and Shuttle Imaging Radar (SIR-A and B) have provided additional means for refining and integrating the regional perspective, although Landsat remains the most widely used comprehensive space data set for the Earth sciences. Lowman (1981) used Landsat and manned mission imagery, along with published maps, to compile a map of global tectonic and volcanic activity during the last 1 Ma (Figure 2-1) that is a useful

framework for the geotectonic applications of orbital imagery discussed in this chapter.

The work of Molnar and Tapponier (1975) and Tapponier and Molnar (1976, 1977, 1979) powerfully demonstrates the value of space-acquired data for regional tectonic studies (Tapponier et al., 1982). Using Landsat imagery together with existing geologic information and seismic data, they reinterpreted the recent tectonics of China in terms of the collision of India with Eurasia (Figure 2-2). What emerged is a new insight into the extremely widespread structural consequences of continent/continent plate collisions. An integrated pattern of fold and thrust belts, strike-slip faults, and grabens is spread over much of south-central and eastern Asia. Many features mapped by these workers (largely based on geomorphic interpretation of Landsat images) were recognized for the first time as major tectonic elements. Geomorphic features and tectonic modeling implied displacements on faults of magnitudes that have since been confirmed in several areas by field work (W. S. F. Kidd, personal communication, 1985). This series of Landsat investigations is a *tour de force* of interpretation, tectonic modeling, and regional synthesis.

Plate-tectonic theory provides a conceptual framework within which to examine tectonic landforms. Stress fields, resultant strain fields, and regional deformation patterns reflect the plate-tectonic setting in which they formed. Tectonic landforms

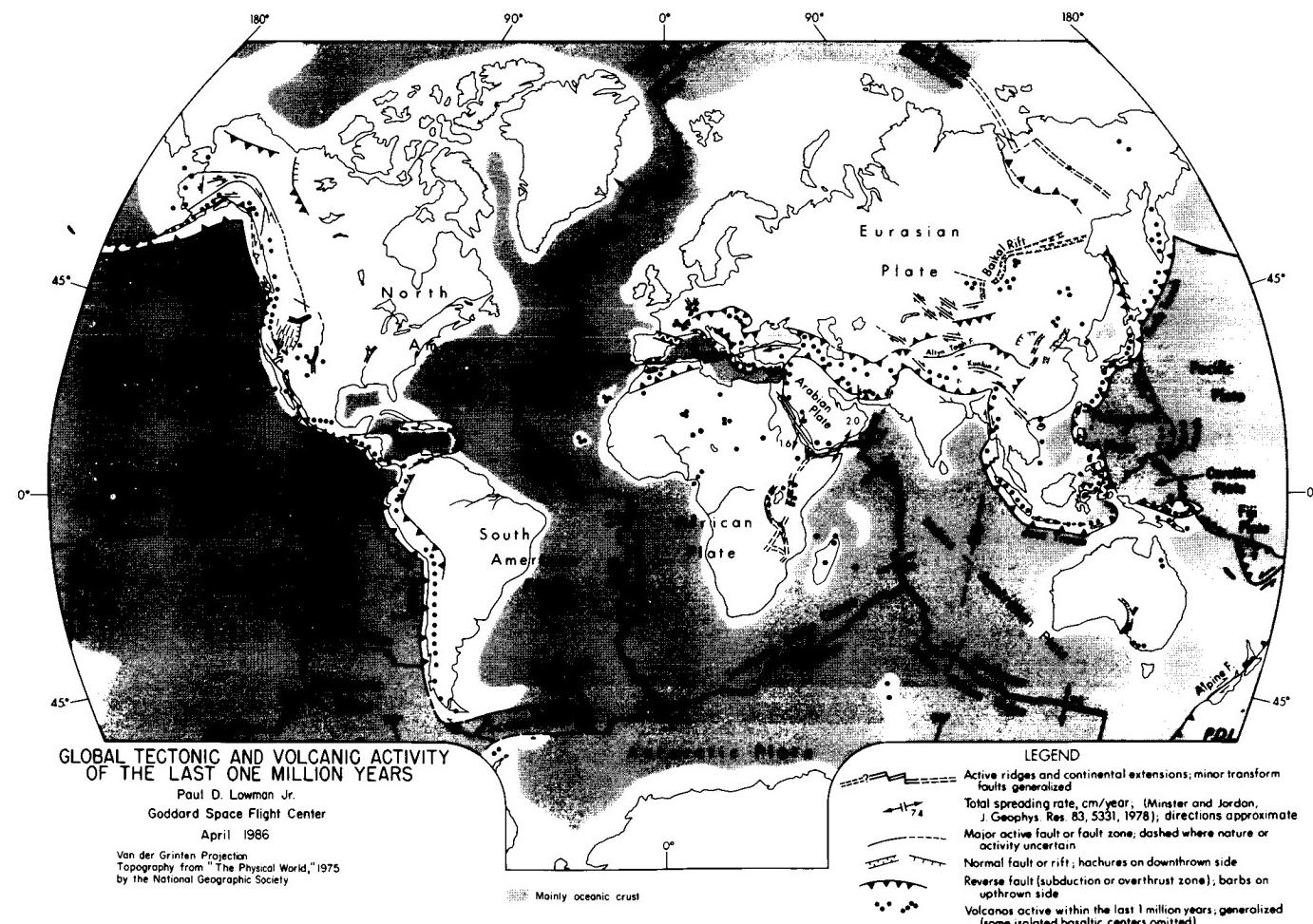


Figure 2-1. Map of global tectonic and volcanic activity of the last one million years (Lowman, pers. comm.). The map provides a current tectonic context for the Plates in this chapter.

ORIGINAL PLATES TO
OF POOR QUALITY

visible on space imagery can thus aid in deciphering the structural history of an area in context with adjacent areas. In examining the Plates comprising this chapter, it will be helpful to associate landforms with a plate-tectonic setting (Table 2-1).

Although tectonic setting is a recurrent theme in the description of the images, it serves better as a context for discussion than as a basis for classification of tectonic landforms. Superficially similar deformation packages may have formed in different tectonic settings. The sequence of structural overprinting in many areas is difficult or impossible to determine from morphology alone. Consequently, in some instances, knowledge of deformational and depositional events is necessary to infer plate motion history. Some plate settings are not associated with unique or spectacular structures (e.g., passive continental margins). Others are covered with water: midocean ridges, submerged continental fragments, and subduction zones. Still others, such as convergent plate boundaries, hotspot tracks, and midcontinent rift

zones, are expressed as volcanic landforms, which are covered in Chapter 3.

Most of the landforms depicted in this chapter were formed primarily by differential erosion acting on structures produced by endogenic processes. Although there are variations due to climate and previous erosional history (including different processes, rejuvenation, earlier planation, etc.), tectonic landforms in different parts of the world have enough in common to be recognized as variations on several common themes. Thus, the Flinders Range of Australia (desert), the Ouachita Mountains of Arkansas (humid and forested), and the Labrador Trough (glaciated) are all clearly fold belts. The essential control of tectonic landforms is *tectonic history*, including cycles of sedimentation, deformation, and igneous or metamorphic events. For this reason, commentaries on the Plates in this chapter (and most of the references cited) tend to stress the tectonic regimes depicted rather than geomorphic processes.

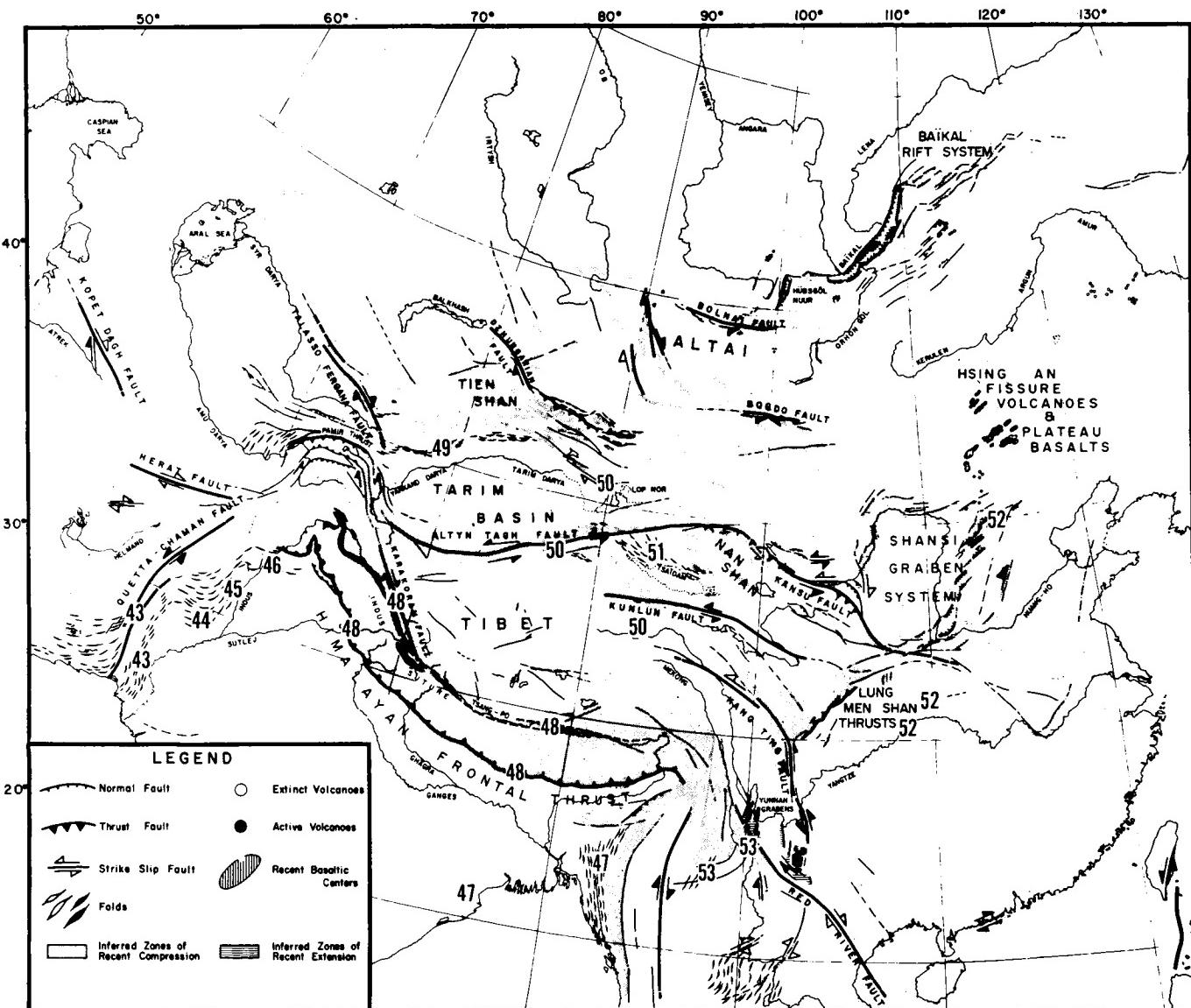


Figure 2-2. Map of the major structural features related to the collision of India with Eurasia during the Tertiary (Molnar and Tapponnier, 1975). The map is based on the analysis of Landsat imagery and available geological and geophysical data. Numbers indicate areas covered by Plates in this chapter.

Table 2-1
Plate-Tectonic Setting Classification*

-
- | | |
|-----|--|
| A. | Divergent plate boundaries (plates moving away from each other with creation of new lithosphere) |
| 1. | Intracontinental rifts (T-37) |
| 2. | Oceanic spreading centers (V-13) |
| 3. | Trailing continental margins (C-4; T-37) |
| 4. | Failed rifts (aulacogens) (V-2) |
| B. | Convergent plate boundaries (plates moving toward each other with consumption of lithosphere) |
| 1. | Ocean/ocean (V-9) |
| 2. | Ocean/continent (T-58) |
| 3. | Continent/continent (T-43) |
| 4. | Accreted margins (T-9) |
| C. | Transform zones or shear plate boundaries (plates slide past each other; lithosphere is conserved) |
| 1. | Trench/trench (T-39) |
| 2. | Ridge/trench (T-43) |
| 3. | Ridge/ridge (T-3) |
| D. | Plate interior settings |
| 1. | Ancient metamorphic terranes (shields) (T-59) |
| 2. | Flat-lying sediments overlying stable craton (F-10) |
| 3. | Intracratonic uplifts (T-7) |
| 4. | Posttectonic magmatic intrusions (T-60) |
| 5. | Normal faults related to "downslope" gravity sliding of uncompacted sediments (D-1) |
| 6. | Evaporite diapirs (T-42) |
| 7. | Hotspot tracks and aseismic ridges (V-10) |
| 8. | Submerged continent fragments — |
| 9. | Anomalous uplift of extant deformation belts (T-21) |
| 10. | Intraplate faulting related to reactivation of ancient fault zones (T-23) |
| 11. | Dike swarms and related fractures (T-17) |
-

*An example of each type, shown in this or other chapters, is called out by Plate (scene) number in parentheses.

The space-acquired images in this chapter display a variety of tectonic features distributed over six continents. After reviewing many examples of different types of space imagery from many sources, we based our selection on several criteria that sometimes conflicted. An obvious goal was to display a diversity of tectonic provinces and structural styles, and images that boldly portrayed geomorphic/tectonic features in an instructive manner were preferred. Although we sought a diversity of tectonic styles and settings, some important but bland or nonphotogenic settings (e.g., stable sediment-covered cratonic interiors) are underrepresented, whereas tectonic "spectaculars" such as shields and fold belts may be overemphasized. In addition to diversity, we attempted to use examples from many parts of the world, including those regions important in the development of fundamental insights and basic principles of geology and geomorphology. We realize that areas within optimum viewing environments, such as deserts and semiarid regions, get more attention than those in high or low latitudes where cloud cover and vegetation pose problems. Our own experience colored our choices; other workers would have made different and equally valid selections in attempting to strike a three-way balance among aesthetics, diversity, and scientific interest.

In the interest of space and ease of reading, we have kept citations within the text to a minimum. The references in the text and the list are far from exhaustive and are meant to provide a point of entry into the literature rather than comprehensive documentation.

The Plates in this chapter are arranged geographically rather than by tectonic style, partly to avoid surfeiting the reader

with a repetitive sequence of the same theme (e.g., a half dozen shield scenes in a row). Because the continents themselves are products of large-scale tectonic processes, the continent by continent grouping establishes a coherent thread that connects and relates many of the tectonic features in a given region. For example, the closing of the Tethys Sea as several crustal plates collided provides a large number of our examples that sprawl from the Anti Atlas through the Alps, the Anatolides, and the Zagros to the Himalaya Mountains.

The deformation field produced by the Indian plate as it impinges on the Eurasian plate offers several striking examples of tectonic landforms. This region contains excellent examples of many of the different tectonic styles associated with a single type of plate interaction—continent/continent collision. Deformation styles include compressional folds and thrust faults of the frontal Himalayas, ridge-trench transform (strike-slip) faults (Chaman/Quetta Fault), large-scale strike-slip faults (e.g., Altyn Tagh and Kunlun Fault), and tensile regions like the Shanxi Graben system. The magnitude and recency of the Indian collision event, coupled with the climate of the area, make the images of this area particularly spectacular.

The Appalachian images, from New England to Georgia and Oklahoma, reveal the anatomy of a fold belt produced by periodic accretionary collisions, culminating in a continentwide convergent collision. Previously existing geologic structures and differences in depositional history along the system produce a variety of features that are characteristic of large-scale continent/continent convergence and whose recognition may be useful in the study of other similar systems.

Western North America was an area of plate convergence throughout most of Mesozoic and Early Tertiary time. About 30 Ma B.P., a segment of the East Pacific Rise, the spreading center that had driven plate convergence against the west coast, began to impinge on the subduction zone that lay along the west coast. As portions of the spreading center were subducted, a ridge/ridge transform fault gradually developed, linking the ends of the surviving sections of the East Pacific Rise (Atwater, 1970). The American and the Pacific plates began to slide past each other, changing the ambient stress field from one of convergence-driven compression to right-lateral shear. The consequences of both these large-scale stress fields extend far beyond the immediate zone of plate interaction and are evident in the structure and resulting geomorphology of the region. Images covering a few to many thousands of square kilometers shed light on this complex story.

The series of illustrations dealing with the African Rift, Afar Triangle, Gulf of Suez, etc. offer insight into the initiation of rifting, continental breakup, and separation. The geologic record preserves a number of these features, frozen in various stages of development. It is clear that few rifts grow large enough to become oceans and that a host of events can interrupt the process, some forming failed rifts or aulacogens (Burke, 1977). Study of these features provides a better comprehension of the early genesis of oceans and rifted continental margins.

A fascinating aspect of this chapter as a whole is the recurrence of certain tectonic/geomorphologic motifs. Shield areas in Canada, Brazil, India, Australia, and Africa have a surprising number of features in common. The whaleback folds of the southern Zagros of Iran are morphologically similar to the décollement folds of the Sichuan Basin of China, despite notable differences in the climate, tectonic setting, and ages of the rocks involved. The same is true for the Shanxi Grabens of northeast China and those of the Basin and Range Province of the western United States or the folds of the Atlas Mountains of North Africa and the Appalachians of eastern North America. These similarities can be both informative and deceptive. They enable us to extrapolate insights gained from well-studied to less-studied areas. In some instances, of course, apparent similarities may mask critical differences. This points up some of the benefits and pitfalls of using space imagery to efficiently interrelate widely separated features and the critical role of field work.

Another informative aspect of viewing geomorphology globally is the wide distribution of features that are believed to be unusual or rare. Large strike-slip faults control topography over vast areas of China, the west coast of the United States, and the Levant. Alluvial fans, some astoundingly large, are common, widely distributed landforms. This suggests that a considerable amount of insight is to be gained from studying the Earth in a holistic way similar to the global-scale exploration of a growing number of extraterrestrial bodies by deep space probes.

Few Plates in this chapter deal solely with a single tectonic or geomorphic process. This substantiates the increased scope that synoptic observations from space bring to the geosciences; at

the regional level even more than locally, the concern must be with intricate patterns of surface and subsurface features wrought by a variety of processes acting serially and in concert. Geomorphologists are still developing appropriate descriptive and analytical tools to handle the wealth of new information about our planet returned from an increasing number of space systems (see in particular Chapter 12 and Appendix A). What will be learned promises to broaden, improve, and almost certainly alter the conceptual framework from which major paradigms in geomorphology specifically and geology in general will continue to evolve.

ACKNOWLEDGMENTS

In addition to the expressions of gratitude given in the Acknowledgment section at the beginning of this book, the authors wish to call special attention to certain individuals who offered invaluable assistance in the preparation of this chapter.

The authors of this chapter shared the work of assembling the imagery and preparing the text. Two of them, J. R. Everett and N. M. Short, are identified at the end of the text by initials (JRE) and (NMS) as responsible for organizing most of the Plates and their written material; guest caption writers are identified by name at the close of the text they developed and again in Appendix B, along with their addresses. Marie Morisawa played a special role throughout this chapter by reviewing and editing the text of all Plates and has infused geomorphic observations into this text wherever the other authors "leaned too far" toward the purely tectonic aspects of a scene. Paul D. Lowman, Jr., of NASA/Goddard Space Flight Center, was instrumental in refocusing the emphasis and approach initially chosen for the chapter introduction, several sections of which are incorporated as he rewrote them.

Members of Paul Lowman's Structural Geology class (Spring 1984) at the University of Maryland participated in a term project designed to help themselves in the learning process, as well as to assist us at a critical time during the early preparation of the commentaries. Each student was assigned to analyze one of the candidate tectonic landform images and to summarize the results in a report that included illustrations and references. These contributors are listed in Appendix B.

A turning point in our conception of this chapter arose from an insightful critique of the first full draft by Kevin Burke of the Lunar and Planetary Institute. It was he, more than anyone, who led us to realize that this chapter not only comprises a comprehensive survey of tectonic landforms *per se* but also is, in a sense, a summary of the geology of the entire Earth insofar as that depends on the nature and distribution of orogenic belts and shields as a framework.

Finally, especially deserving of thanks are members of the Earth Satellite Corporation for their assistance, in particular, Max Miller and others in the Photolab, Coetta Withgott and her word-processing crew, and Fanny Barrett for her patience in coordinating preparation of the captions through several rewrites.

PLATE T-1

Computer-enhanced Landsat Multispectral Scanner (MSS) images can be joined into mosaics at continental scales. This Plate displays the geomorphology of the western third of the National Geographic Society's U.S. Bicentennial mosaic (vegetation rendered in natural color by projecting IR band 7 through a green filter). Major physiographic divisions (Hunt, 1974) appear below in the index map. The mosaic serves as a small-scale visual framework for relating present geomorphic expression to the geologic evolution of the Cordillera, synopsized as follows (Condie, 1982; King, 1976; Windley, 1984); and especially Ch. 13 in Suppe, 1985:

1. Development in Late Precambrian of a miogeoclinal clastic sedimentary prism along a trailing continental edge, thickening off craton (west of present Wasatch Front of Utah) as a Proto-Pacific ocean opened (Stewart, 1972); later carbonate deposits through Devonian affected by possible subduction (with polarity reversal) and arc-continent collision in Early Carboniferous (Antler orogeny; Roberts Mountain thrust belt in Nevada); Late Paleozoic block-faulting in Colorado/New Mexico (Ancestral Rocky Mountains); Permo-Triassic collision of arcs, eliminating inland basins, during Sonoma orogeny; eastward thrusting (Golconda allochthon) in Great Basin; westward thrusting around Klamath Mountains (Burchfiel and Davis, 1972); cratonic deposits into Cretaceous in eastern Cordillera.

2. Early Mesozoic shift in megastructural trend from NNE to NNW as Pangaea breaks up and North America again moves westward; during Jurassic/Cretaceous, the Kula/Farallon plates subduct under continental margin (inland California today), leading to paired orogenic belts of (1) a western high P-low T Franciscan Group (ophiolites, pelagic sediments, and continental margin turbidites, intermixed as mélange; also blueschists) and (2) an eastern high T pervasive batholithic assemblage and arc volcanism (160 to 130 Ma) in Sierra Nevada/Klamath regions; forearc basin fill from eroding belts (Great Valley of California) and Coast Ranges affected by westward thrusting atop under-thrust oceanic plate; tectonic climax during Nevadan orogeny.

3. Orogeny intensifies inland during Cretaceous, leading to major eastward thrusting during Sevier orogeny (105 to 75 Ma) along a zone extending through Utah, western Wyoming, and Montana, passing into Canadian Fold and Thrust belt and Alaska; subsequent broad deformation with folding and thrusting during Laramide orogeny (80 to 60 Ma) over most of U.S. and Canadian Rocky Mountains and Mexican Sierras; extensive plu-



WESTERN UNITED STATES

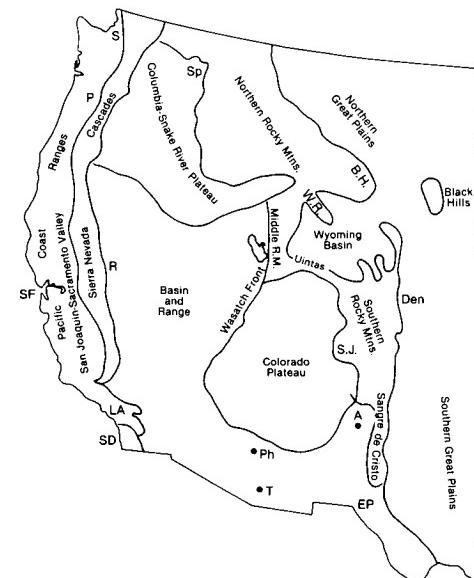
tonism in Rockies and southern California/Arizona; basement uplift along thrust faults in Middle and Southern Rocky Mountains forms large mountain blocks and intermontane basins; erosion products build up in basins and Great Plains.

4. Throughout later Paleozoic and entire Mesozoic, much of western Cordillera experiences numerous collisions with oceanic plateaus, arcs, microcontinental fragments, and other terranes rafted on oceanic plates from beyond North America; accretionary terranes expand Cordilleran margin, comprising much of present land masses and causing or moderating orogenies (see also Plates T-9 and T-10).

5. In Cenozoic, most of Farallon plate consumed along shallowing subduction zone; ~30 Ma ago, North American plate encounters Pacific plate, whose spreading ridge (East Pacific Rise (EPR)) is being progressively overridden; two triple junctions where separated remnants of Farallon plate (Gorda (Juan de Fuca) plate in north; Cocos plate in south) meet the North American/Pacific plate boundary; lengthening boundary becomes Proto-San Andreas (SA) fault where northward spread of Pacific plate initiates right-lateral slip along Mendocino transform; Salinas terrane (Los Angeles sliver) and Baja California detach from North America along SA fault, and Gulf of California opens along decoupling zone; other faults subparallel to continental margin allow various accreted terranes to continue northward movements.

6. Initial widespread calc-alkaline volcanism in Early Tertiary changes ~16 Ma ago to basaltic outpourings in Columbia Plateau; younger basalts in Snake River Plains and silicic lavas over hotspot now beneath Yellowstone; basalt-rhyolite volcanism in Great Basin; Basin and Range begins ~19 Ma ago as crustal thinning causes extension, inducing grabens/horsts along normal faults; general regional uplift within Cordillera, including largely undeformed cratonic sediments of Colorado Plateau; calc-alkaline volcanism confined to active subduction boundaries inboard from Cocos (Mexico), Juan de Fuca (Cascades), and Pacific (Alaska) plates.

Figure T-1.1 shows details visible in a computer enlargement of a small part (subset) of a single Landsat frame (Paylor et al., 1985) covering Casper Arch south of the Bighorn Mountains in Wyoming. Homoclinal dipping resistant beds of Pennsylvanian through Cretaceous age give rise to hogbacks and cuestas. Parallel consequent and resequent drainage has developed on the longer dip slopes. (NMS) Landsat Mosaic.



ORIGINAL PAGE
COLOR PHOTOGRAPH

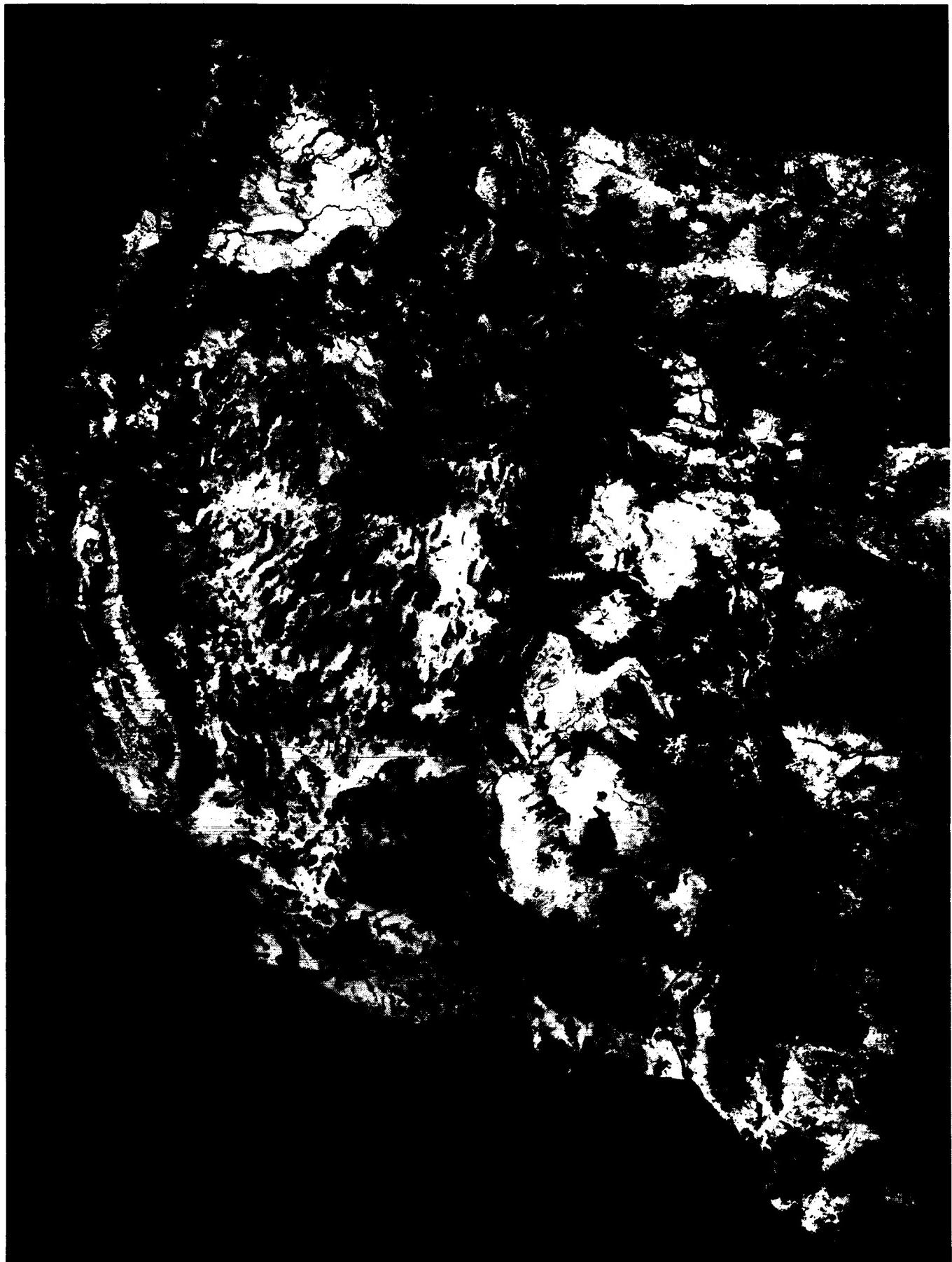


PLATE T-2

The striking differences in topography within this area of southern California and Nevada dramatically reflect the region's tectonic provinces. This mosaic of Landsat MSS imagery displays the regional relationships among the San Andreas fault (an active transform fault boundary between the Pacific and North American plates), the Great Valley (a forearc basin), the Sierra Nevada (an old volcanic arc), and the Great Basin (an extensional province).

Over much of this area, the physiography is the direct result of tectonic processes, with resulting landforms only slightly modified by erosion. In the Coast Ranges, the Great Valley, and the Basin and Range, much of the relief is the result of deformation rather than erosion.

The Sierra Nevada consists of the roots of an ancient (Jurassic) volcanic arc that was similar to the present Andes of South America. The Sierra formed as a volcanic arc above the Pacific plate as it descended beneath the western edge of the North American plate in Jurassic time (Schweickert, 1981). Resistant rocks of the Sierras stand high (approximately 3000 m) above the adjoining geomorphic provinces. Jurassic and Cretaceous Franciscan mélange rocks that accumulated in the trench west of the Sierra Nevada and serpentines that mark old sutures underlie the Great Valley (San Joaquin and Sacramento valleys) and much of the Coast Ranges. Fragments of Sierran rocks that have moved northward along the San Andreas and related faults underlie other parts of the Coast Ranges.

The Cretaceous and Tertiary rocks of the Great Valley sequence that comprise the fill in the San Joaquin Valley accumulated in a forearc basin west of the Sierran Arc and are deposits of debris eroded from the rising Sierras. Stresses related to plate convergence and subsequent right-lateral transform movement have produced several large folds and numerous faults that constitute traps for hydrocarbons within the Great Valley.

The northwest-trending linear fabric of the Coast Ranges results from a large strike-slip fault zone. One can trace the San Andreas system from the Gulf of California to Cape Mendocino, a distance of almost 1400 km. The aligned pattern of linear ridges and depressions separate markedly different terranes (the Great Valley to the east and the Coast Ranges to the west; see Plate T-3). Just north of Los Angeles, the topographic trace of the left-slip Garlock fault is evident, branching eastward from the San

SOUTHWESTERN UNITED STATES

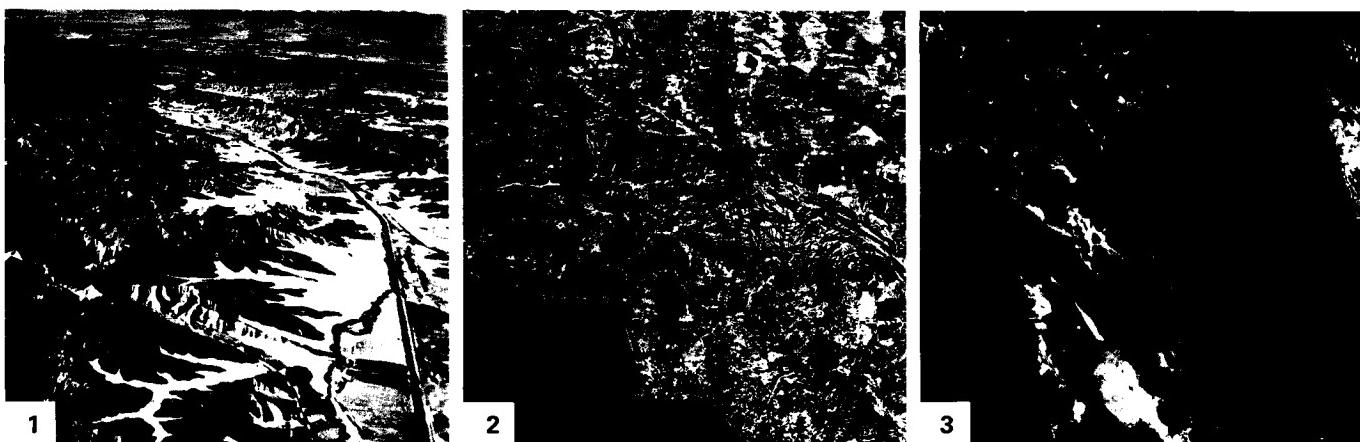
Andreas fault (Allen, 1981; Atwater, 1970; Dickinson, 1977). Figure T-2.1 shows intricately dissected topography developed on recently uplifted terrain adjacent to the San Andreas fault near Palm Springs.

This mosaic shows the pronounced linearity of the San Andreas fault in central and southern California, which marks the southern boundary of the Mojave Desert Basin. This fault is shown in more detail in a remarkable aerial photograph mosaic (Figure T-2.2), which required more than 8000 individual re-processed large-scale aerial photographs to cover about the same area as a single Landsat image.

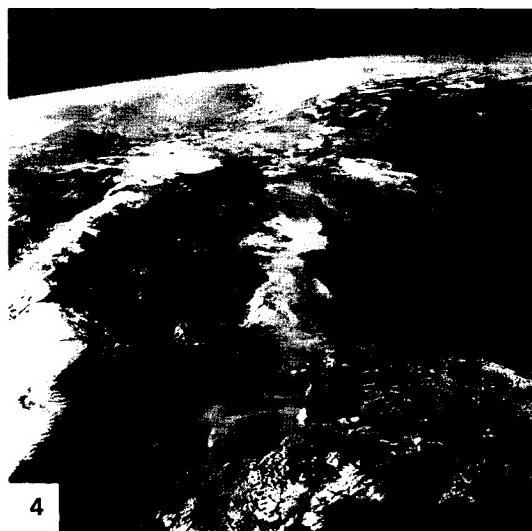
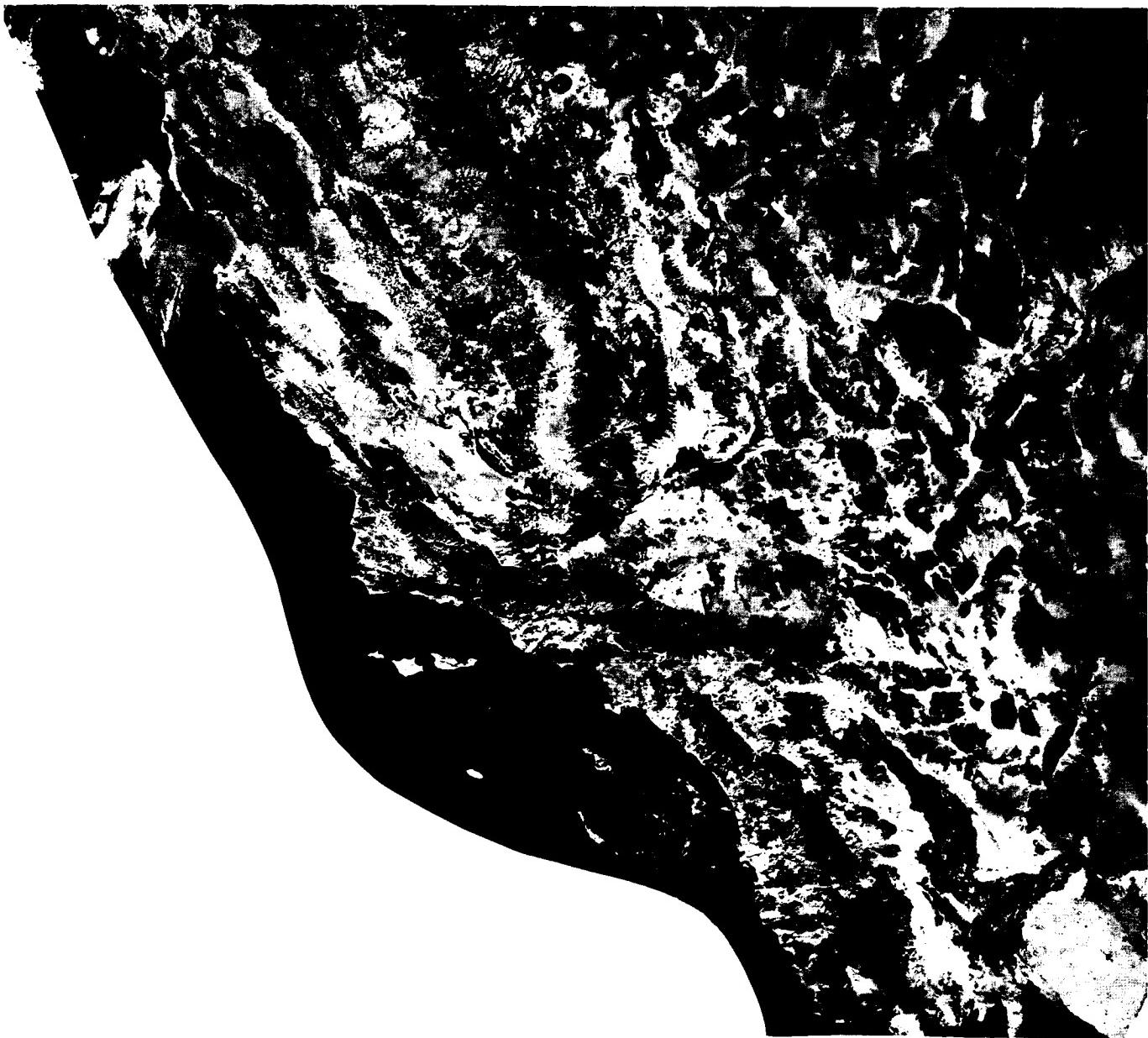
The San Andreas fault system is an active transform boundary between the Pacific plate to the west and the North American plate to the east. This fault system is a ridge/ridge transform that connects the north end of the East Pacific Rise in the Gulf of California and the south end of the Juan de Fuca Ridge off the coast of Oregon. The Pacific plate is moving northwestward (at about 2.5 cm per year) relative to the Northern American plate. As the Pacific plate moves northwestward, a gap (actually a new ocean basin similar to the Red Sea) is forming between the two plates (Atwater, 1970). The Salton Sea (the large lake) and the Gulf of California (the body of water at the bottom center of Figure T-2.3, a daytime visible band image made from the Heat Capacity Mapping Mission (HCMM) sensor) occupy this gap. Figure T-2.4, an oblique Apollo photograph of the Salton Sea, distinctly shows the scarp that marks the linear eastern edge of the Salton trough and the merging of both margins with the San Andreas fault to the north.

To the east of the Sierra Nevada is the Basin and Range (Great Basin) province, one of the largest areas of regional extensional tectonics on Earth. In the near-surface Tertiary, Mesozoic, and Paleozoic rocks, high-angle normal faults accommodate the extension. Extension exceeds 100 percent over most of the province (i.e., the region is about twice as wide as it used to be (Zoback et al., 1981)).

The Coast Ranges (T-3), the Great Basin (T-4), and Death Valley (T-5) Plates discuss specific portions of this area in substantially more detail and include additional illustrations. The Rocky Mountain Plate (T-6) discusses the area east of the Great Basin. (*JRE Additional References: Burchfiel and Davis (1975), Ernst (1981), Smith and Eaton (1978). Landsat Mosaic.*)



ORIGINAL PAGE IS
OF POOR QUALITY



4

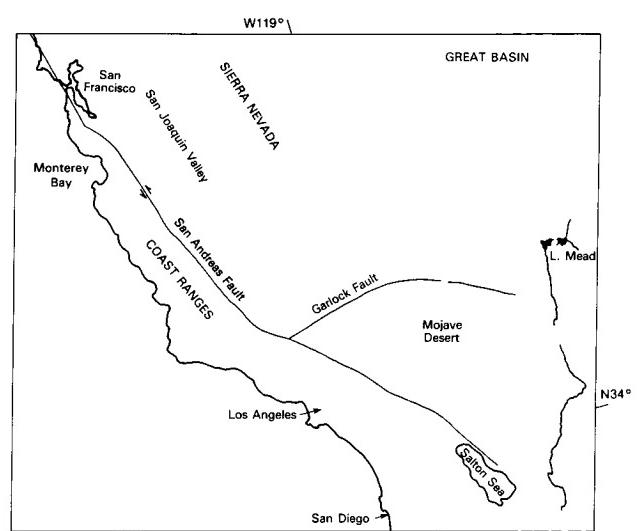


PLATE T-3

One of the major types of interaction that lithospheric plates exhibit is sliding past each other. This happens along transform faults, which are major strike-slip fault systems. These fault zones characteristically exhibit landscapes with linear valleys and ridges and evidence of "drag" of the structural fabric in the area adjacent to the fault zone. In active zones, this structural drag affects very young and transient features, offsetting streams, fans, and ridge spurs. Such an active fault zone may also include sag ponds, small closed drainage basins, and anomalous drainage patterns (Blake et al., 1978; and Ernst, 1981).

The Thematic Mapper (TM) image of the Coast Ranges of California, which lie along the San Andreas fault between the San Joaquin Valley and the ocean, displays an excellent example of the topography within a major strike-slip zone. (Plate T-2 provides the regional context for this image.) In this active zone, much of the topography, the direct result of movement on the faults, is only slightly modified by erosion. Strike-slip movement commenced in the area as the westward-moving North American plate began to overrun a spreading ridge at about 30 Ma ago (Atwater, 1970). Strike-slip faults joined portions of the spreading ridge lying north and south of the overrun part of the ridge. As subduction of the ridge continued, strike-slip movement extended progressively inland. Through time, movement was concentrated on the Hosgri (off shore), Sur-Nacimiento, and Rinconada fault systems and, finally, the San Andreas (Dibblee, 1976; Graham, 1978). Although the majority of movement now takes place on the San Andreas (about 2.5 cm/year), some movement continues to occur on the older zones. After the Coalinga earthquake of 1983, aftershocks occurred along the Rinconada system, as well as the San Andreas.

The main trace of the San Andreas fault zone is clearly visible as a lineament, partly ridge and partly valley, running diagonally northwest across the scene. Figure T-3.1 shows the remarkable linearity and crispness of the San Andreas fault trace in the Carizzo Plain near the southeast corner of the image. The uplifted area is dissected by a system of parallel streams, some of which have been offset by very recent right-lateral movement on the fault. To the east of the fault, elliptical and linear ridge patterns indicate several large folds developed in an area of relatively easily deformed Franciscan basement. These appear to swing into the San Andreas as if dragged. To the west of the fault is the Salinian block with a more brittle granitic basement. West

COAST RANGES, CALIFORNIA

of the San Andreas, numerous linear valleys, which mark fracture traces, also appear to trend into the major fault.

The northern reaches of the Salinas River occupies a valley that lies between the welt created by the San Andreas on the east and the welt of the older Rinconada/Jolon fault zone to the west. The valley itself probably marks the trace of a major fault. The ridge to the west of the northern section of the Salinas River is an excellent example of a fault scarp with a steep, short northeast face and a gentler western backslope on which longer streams have developed. Some triangular facets (interstream spurs) are also visible along this ridge front, further evidence of its fault origin. The abrupt right-angled change in flow direction of both the San Antonio and Nacimiento Rivers above their junctions with the Salinas is a result of faulting. West of the Rinconada zone is the Sur-Nacimiento zone, a darker area adjacent to the Pacific Coast. This heavily forested region includes numerous outcrops of Franciscan (trench, mélange, and serpentine) rocks. Even though major strike-slip movement on this zone ceased several Ma ago, the terrain still displays a very strong northeast lineation parallel to the strike of the faults.

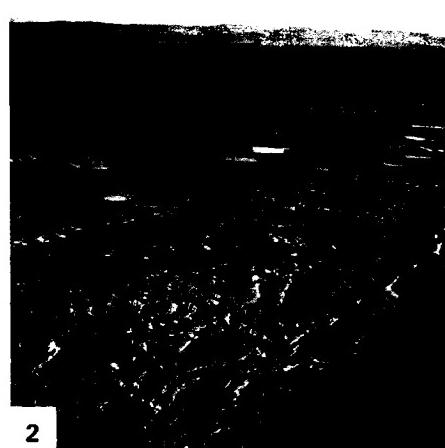
Figure T-3.2 is a view of the Kettleman Hills, a large doubly plunging anticline, seen near the east-central edge of the TM image. The inward-facing cuesta-form ridges outline the edges of the breached anticline. Subsequent strike valleys have formed where less resistant beds outcrop along the dipping strata so that a trellis pattern is beginning to develop. Linear and curved ridges and valleys at the southeast edge of the Cholame Hills (middle distance) illustrate structural drag.

Figure T-3.3 is a view of this region taken from the Shuttle. The San Andreas fault zone runs diagonally across the center of the photograph, with several splays toward the upper right corner. The strongly linear topography of the entire region is quite evident.

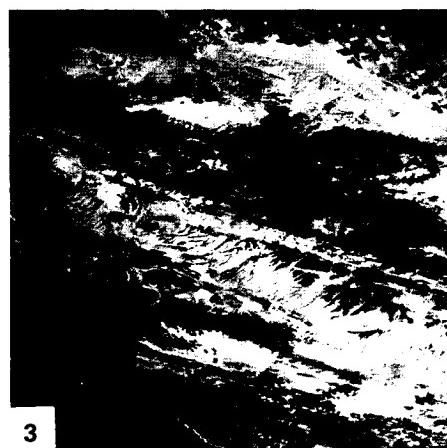
Figure T-3.4 is a photograph looking northeast from the Salinas Valley toward the topographic high west of the San Andreas fault. The streams that drain the upland are "shuttered": right-lateral movement on several small faults paralleling the San Andreas has successively shifted segments of the interstream promontories to the right, creating shutter ridges that obscure, or shut off, the stream valleys from view. (JRE) Landsat TM 40145-18084, December 8, 1982.



1



2



3

ORIGINAL PAGE
COLOR PHOTOGRAPH

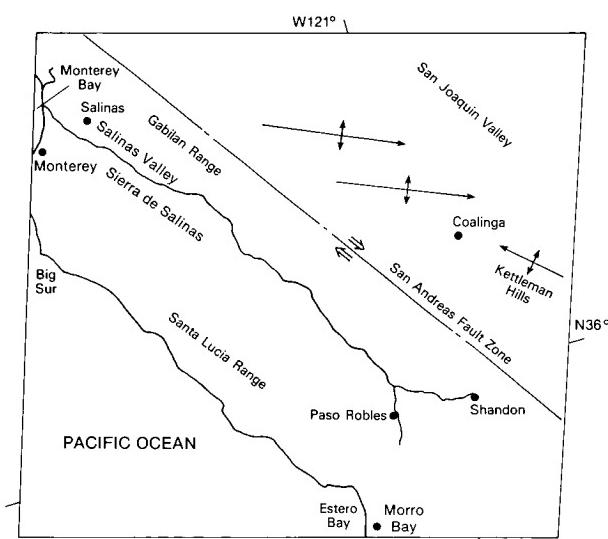
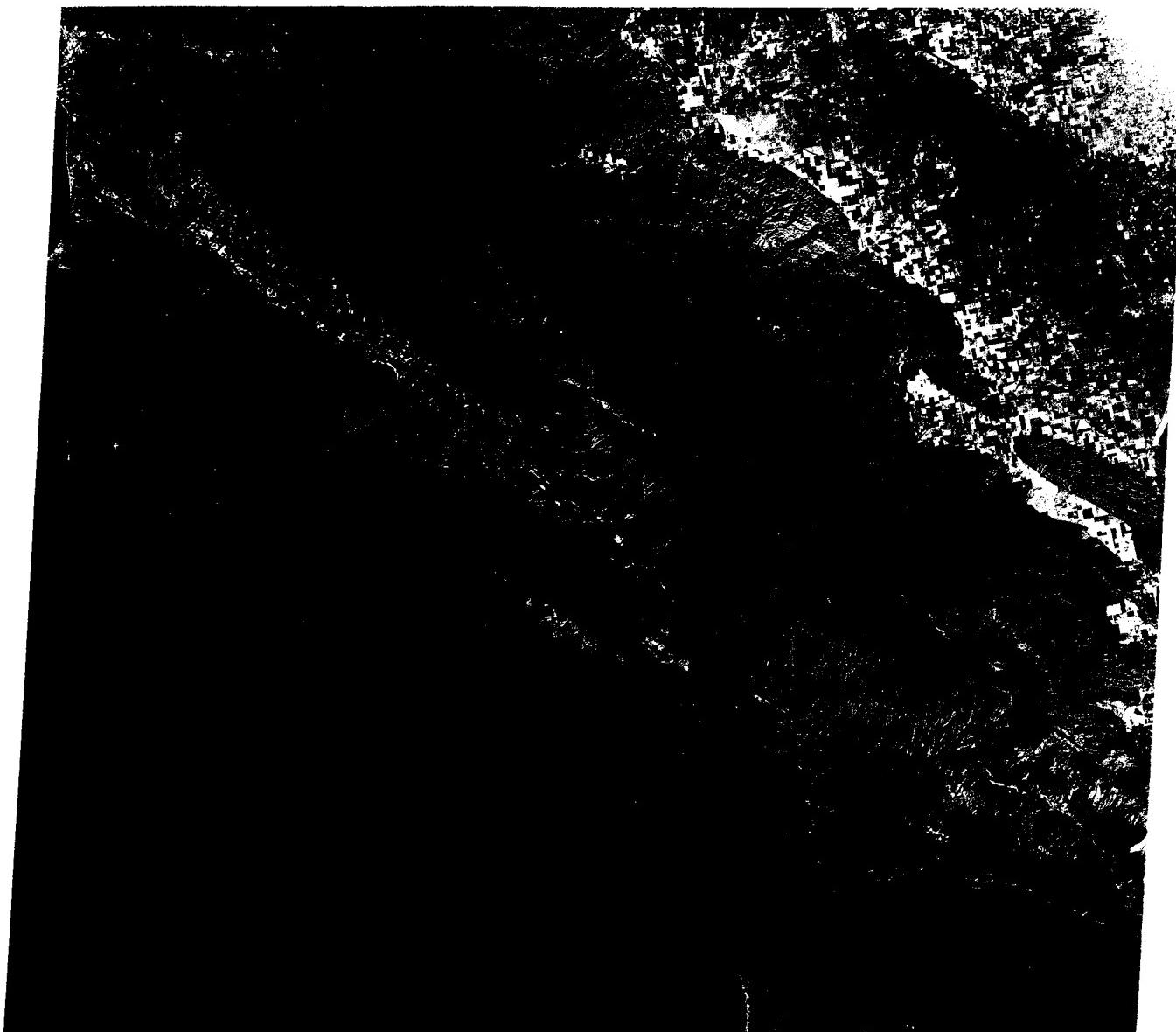


PLATE T-4

GREAT BASIN

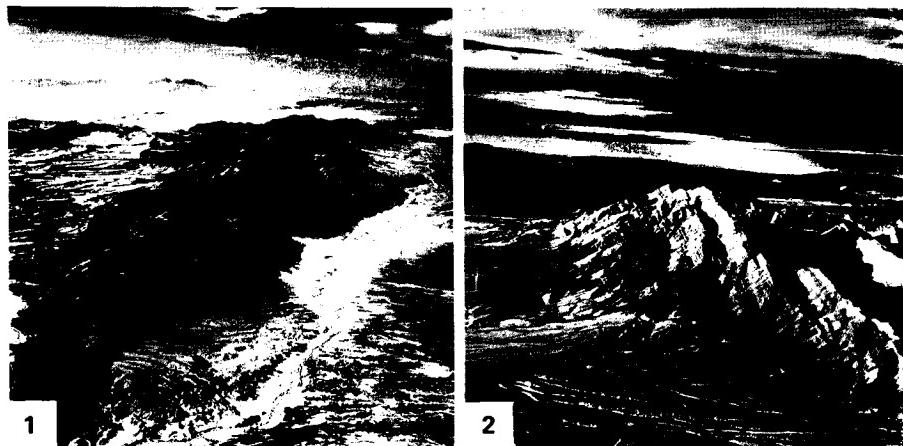
Elongate, generally north-trending, fault-bounded high mountain ranges and intervening dry, alluvium-filled, flat-floored valleys characterize the Great Basin or Basin and Range Province, which C. E. Dutton described as giving the appearance of "numerous caterpillars crawling toward Mexico" to a map of the region. The mosaic of Landsat images covering the state of Nevada dramatically illustrates this pattern, with the dark "caterpillar" ranges separated by light-colored valleys. The province is a vast area of extensional tectonics in the southwestern United States and northwestern Mexico.

The region is arid because it lies in the rain shadow of the Sierra Nevada. A few of the highest ranges (e.g., White Mountains, Toyabe Range, Spring Mountains, and Ruby Range) support conifer forests at higher altitudes. Because of the recent tectonic activity that produced the fault-bounded ranges and valleys and the general aridity of the region, almost all of the drainage is internal. Relatively short streams end in salt flats or playa lakes. Even the Humboldt River eventually dies in Carson Sink.

The area was not always so dry. Episodically during the Pleistocene, large lakes occupied many of the basins, which accounts for the exceedingly flat basin floors. Some old lake terraces are 100 m or more above the adjacent lake beds.

Recent tectonic activity also accounts for extremes in elevation, with Mt. Whitney (4418 m) in the Sierra Nevada and Death Valley (-86 m) less than 120 km apart. Two thousand meters of relief between adjacent ranges and valleys is not uncommon.

The precise processes and mechanics of tectonic extension are not entirely clear. Several factors seem to operate. A pervasive pattern of north- to north-northeast-trending normal faults bounds the ranges and valleys. Some of the ranges are horsts; others are tilted fault blocks. Several very long northwest-trending shear zones, such as Walker Lane and the Central Nevada Shear Zone, that parallel the San Andreas and display a similar sense of right-lateral movement, interrupt this pattern. The overall fracture pattern indicates a substantial component of right-lateral shear that appears to be the result of a right-lateral couple imposed on the region as the Pacific plate continues to slide northwestward relative to the North American plate along the San Andreas and related transform faults. The subduction zone, lying between the coast of Washington and Oregon and the Gorda and Juan de Fuca rises offshore to the west, acts as a free face that accommodates the resultant northwestward extension of the Basin and Range section of the North American plate. This northwestward expansion forces the subduction zone to the northwest, closer to the spreading rises. Similar extension of the continental plates over tectonic free faces appears to occur in western Turkey and eastern China and produces structure and topography analog-



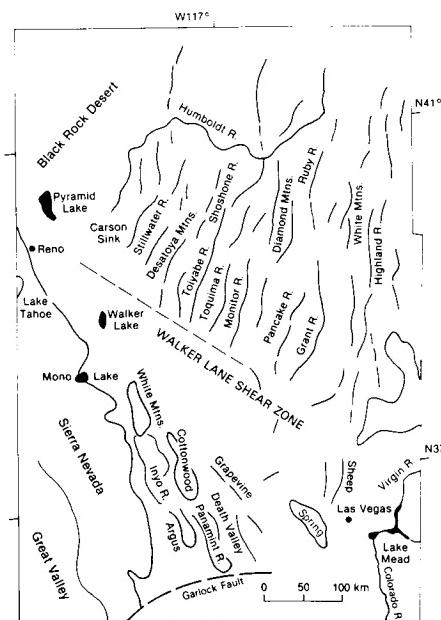
ous to that of the Basin and Range (Livicciari, 1979; Livicciari et al., 1982; Nelson, 1981; Zoback et al., 1981).

Internally within the Basin and Range, the extension results as a combination of attenuation of the lower crust and normal faulting of the more brittle upper crust. Attenuation of the lower crust (crustal thickness is approximately 10 km versus greater than 30 km elsewhere) occurs through a combination of low-angle brittle shear and viscous flow. Many of the upper crustal normal faults are listric, which accounts for the tilting of many of the fault-bounded ranges (Burchfiel and Davis, 1975; Smith and Eaton, 1978; Wernicke and Burchfiel, 1982).

In some instances, asymmetry of the mountains indicates scarp and dip slopes. Steeper topography with short streams develops on scarp faces; gentler gradients and longer streams form on back (dip) slopes. On other ranges (horst types), dip slopes are not discernible, and the ranges are symmetrical. Most ranges are straight, at least at the base where the steep mountain sides abruptly intersect the basin floor. The steep slopes are heavily raved with sharp V-shaped gorges. Triangular facets are common on interfluves between valleys. The ancillary photographs illustrate well the abrupt transition from flat-floored playas and gently sloping bajadas to the steep abrupt range fronts (Figures T-4.1 and T-4.2).

Figure T-4.1 is an oblique view looking south toward the Arrow Canyon Range, Nevada. The tilted nature of the fault block is evident. Note the difference in stream length, depending on steepness of the dip of strata. Landforms on the east and west sides of the range are different. On the west, the steep range front is being covered with debris that is now being trenched, with the material removed into the center of the basin. Recent deformation has resulted in deep entrenchment and deformation of the fan on the north end of the range.

Figure T-4.2, looking north at Frenchman Mountains (east of Las Vegas, Nevada), shows another tilted fault block, in which differential erosion of hard and soft layers is quite evident. The alluvial fans are being actively entrenched. This entrenchment, as well as the linearity of parts of the front and what appears to be a recent fault cutting several fans, indicates active faulting. (JRE) Additional Reference: Christiansen and McKee (1978). Landsat Mosaic, prepared by the U.S. Geological Survey, Flagstaff, Arizona.



ORIGINAL PAGE
COLOR PHOTOGRAPH



PLATE T-5

DEATH VALLEY

This TM scene shows the southwestern portion of the Great Basin (Basin and Range province) where it abuts the northern Mojave Desert along the Garlock fault (A on index map). The center of the scene straddles the California/Nevada border about 150 km west of Las Vegas. In the upper left part of the image lies Death Valley, within which is the lowest surface point (-86 m) in North America, the Badwater basin. Only about 120 km farther to the west across the Owens Valley, along the eastern front of the Sierra Nevada, stands Mt. Whitney (4418 m), the highest point in the conterminous United States. Compare the detail present in part of the TM scene with the equivalent area from a 1973 Skylab photograph (Figure T-5.1). It is also instructive to compare a subscene from a June 1984 TM image (Figure T-5.2) that has been enhanced to bring out details of the stratigraphic/topographic sequence in Tucki Mountain, which overexposes the saline deposits in Cottonball Basin (I), with an aerial oblique photograph of much the same area (Figure T-5.3).

Like other ranges of the Basin and Range, normal faults are frontal to or otherwise bound the blocks (e.g., west side of the Funeral Range and the Black Mountains) that comprise the mountain ranges in this area, as demonstrated by the linearity of the mountain base. Because divides here trend northwest to north-northwest, they differ from most similar ranges in Nevada, which have north to north-northeast trends (Plate T-4). Many ranges in another structural unit, the Mojave Desert, are oriented east-west. Here, the northwest alignment is controlled in part by the orientation of several major strike-slip fault zones such as the Furnace Creek Zone (B) and the Las Vegas Shear Zone (C), all of which are right-lateral faults. The Las Vegas Shear Zone is an eastern branch of the Walker Lane wrench zone that continues to the northwest for some 200 km; the faults along the Grapevine and Funeral Range join the same zone.

Most of the ranges consist of Paleozoic miogeoclinal sedimentary units and some Mesozoic sedimentary rocks. Folding and strong eastward thrusting affected these rocks during the Antlerian (Mid-Paleozoic) and Sonoran (Mid-Mesozoic) orogenies. Numerous imbricated thrust sheets make up much of the eastern Panamint Range. Tertiary volcanic rocks occur in the Owlshead Range, around the Granite Mountains and the Greenwater Ranges, and in the Spectre Range and Black Mountains. Silicic volcanic rocks remain along the eastern side of the Grapevine Mountains and along eastern Tucki Mountain. Rhyolites and basalts have been emplaced during the last 10 Ma in the valley and elsewhere (F, Devils Playground).

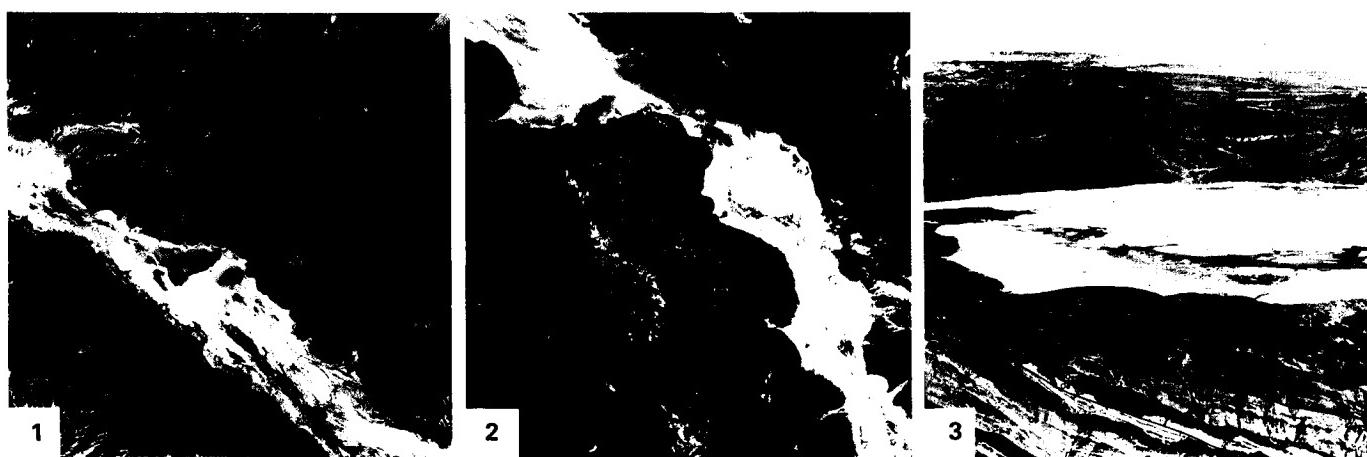
The present structure and its topographic expression in this part of the Great Basin began to develop about 10 Ma ago with

initiation of movement on the Furnace Creek fault system. Miocene/Pliocene lacustrine beds indicate that, as movement occurred, lakes formed along the downfaulted zone. During that time, uplift, faulting, and erosion, accompanied by volcanism, produced thick sediment accumulation (gravels and muds) in the incipient basin depression. In Late Pliocene (5 to 3 Ma ago), the region became transtensional, allowing rocks to adjust differentially along high-angle faults, some of which previously showed right-lateral movement. Movement continued on several of the right-lateral faults and accelerated on the left-lateral Garlock fault to the south. The strong vertical movement and subsequent erosion produced the present topography.

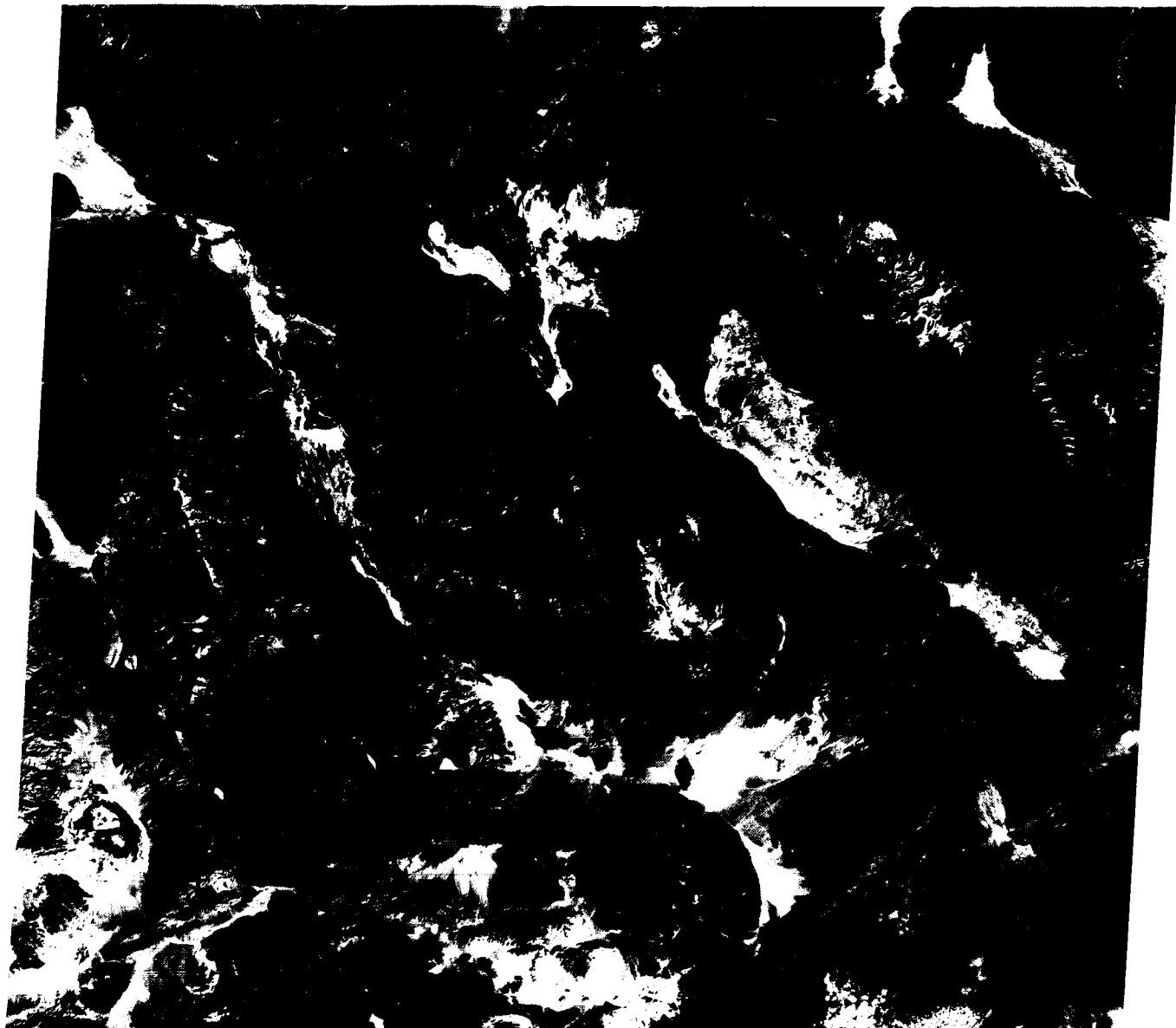
The linearity of the mountain base in the Panamint and Funeral Ranges indicates faulting. The Slate Range is separated from the Panamint Range by a fault valley. The Furnace Creek fault zone is marked by the depression occupied by Death Valley. "Wineglass" valleys, with the flaring basins and fans joined by the "stem" where the stream debouches the mountains through a narrow gorge, are common and provide evidence of faulting. Alluvial fans themselves are a result of watershed erosion along a steep scarp face produced by faulting. Triangular facets (spurs), although eroded, can be identified, again indicating faulting. Several "turtlebacks," smooth curved surfaces, can be seen along the Black Mountains front. These were formed by fault movement. Arcuate ridge forms in the central Black Mountains are controlled by faulting. Some valleys are offset and shuttered.

Death Valley, Panamint Valley (H), and other low areas include outstanding examples of arid landforms. Most conspicuous are the playas and salt pans. Cottonball Basin (I) is a remarkable example of saline deposition that includes sodium borates and sulphates, gypsum, encrustations of rock salt, salt-cemented mudstones, carbonates, and lake and floodplain sediments. The valleys also contain excellent examples of pediments, alluvial fans, and bajadas. Many fans have distributaries that are emphasized in the imagery by darker material spread over lighter and older materials. Both color and amount of dissection appear to differentiate fans of different ages.

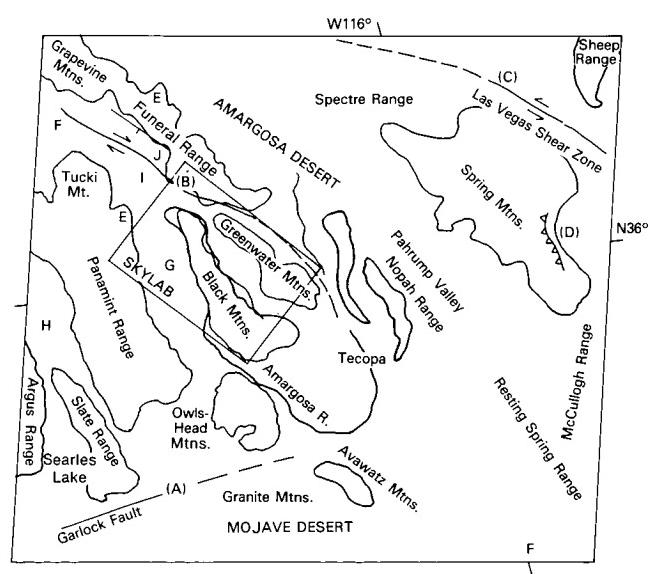
Several generations of fans are evident in Figure T-5.4. The higher dissected surfaces are older, then an intermediate fan, and finally, the fan presently in process of construction. This series of coalescing fans is called a bajada (bahada). Conspicuous triangular facets lie at the interplains between fans. (NMS) References: Hildreth (1976), Hunt and Mabey (1966), Streitz and Stinson (1977), Thornbury (1965). Landsat TM 40124-17495, November 19, 1982.



ORIGINAL PAGE
COLOR PHOTOGRAPH



4



41

PLATE T-6

THE ROCKY MOUNTAINS

Together the two Heat Capacity Mapping Mission images (Plate T-6 and Figure T-6.1) span the Rocky Mountains and include part of the Basin and Range (Plate T-4) on the west and the Great Plains on the east. Most of the present-day topography is the result of erosion of rocks deformed and uplifted in Late Cretaceous through Middle Tertiary time. Some geologists refer to the area as the Laramide Rockies, implying that most of the structure is the result of the Laramide orogeny (Cretaceous Campanian through Tertiary Eocene). Although in general, this is true, previously established structural grain has influenced the effects of Laramide and post-Eocene deformations, and igneous activity has obscured the effects of the Laramide deformation in some areas.

To the east, the rocks underlying the Great Plains are relatively undeformed. To the west, Middle to Late Tertiary extension of the Great Basin has disrupted and obscured many of the trends established during the Laramide. In between lies a complicated mosaic of generally broad basins (Powder River, Big Horn, Green River, Shirley, Uinta, etc.) (light-toned in Plate), separated by abrupt basement-cored uplifts (dark-toned, from vegetation) sprinkled with smaller basins, such as Washakie and North Park, and isolated uplifts like the Rock Springs uplift and San Rafael Swell (Plate T-7). A major overthrust belt (Wyoming Thrust Belt/Hingeline), a zone of extensive décollement, overthrusting, and folding, lies along the western margin of the province. Figure T-6.2, a Landsat band 7 image, shows some of the detail of these complexly folded and thrusted rocks where the Snake River Plain interrupts the Thrust Belt.

Several structural trends are prominent in the region: north, Front Range and Wyoming Thrust Belt; northwest, Wind River Mountains and Uncompahgre uplift; west-northwest, Owl Creek Mountains and Shirley Basin; west, Uinta and San Juan Mountains; and northeast, San Rafael Swell and the margins of several basins and uplifts. There are regional lineaments parallel to each of these directions.

Taken as a whole, the region is a portrait of large-scale continental collapse resulting from prolonged normal (B-type) subduction along the western edge of North America and consequent intracontinental thrusting west of the Overthrust Belt along the older Precambrian continental margin during Mesozoic and Early Tertiary time. Folding and thrusting in the west began in Late Jurassic time. Through the end of Cretaceous time, convergence, and consequently the maximum compressive stress axis, was oriented east to east-northeast. This produced north-trending thrust faults, west-northwest-trending left-slip faults, northeast-trending right-slip faults, and east to east-northeast-trending tensional features. During Eocene time, convergence became more northerly (northeast to north-northeast), producing a new stress

field and a new suite of structural features. The new stress regime made use of many previously existing structural trends, modifying or changing the sense of movement on them. This reorientation of stress fields, coupled with a strong northwest trend established during Late Paleozoic deformation, has produced a complex regional structural fabric.

Several post-Eocene features affect parts of the area. The San Luis Valley (and perhaps North and South Park) is a down-faulted intermontane depression within the Late Tertiary Rio Grande Rift. The Snake River Plain and Absaroka volcanic field are part of a widespread Tertiary episode of extension and extrusion. The Middle to Late Tertiary extension in the eastern Great Basin reversed the sense of movement of some of the thrust faults of the western Overthrust Belt.

Topographically, a northwest-trending lineament marks a fault along the edge of the Medicine Bow Mountains, extending southward along the northeastern border of the North Park basin. Other faults are indicated by the linearity of the edges of many anticlinal ranges such as the Sawatch, Elk, Mosquito, and Sangre de Cristo Mountains. Both North and Middle Parks also show topographic linearity resulting from faults.

Many ranges are deeply eroded, faulted anticlines. Erosion of the sedimentary cover has resulted in monoclinal ridges called cuestas, hogbacks, or flatirons, depending on steepness of dip of the strata. (Cuestas are eroded on gently dipping sediments, flatirons on steeply dipping sediments.) Figure T-6.3 depicts the alpine geomorphology of the Rocky Mountains in this view of Loveland Pass, Colorado. Broad undissected upland "flats" can be seen, despite numerous sharp arêtes and horns carved by glaciers. The high rugged terrain with steep valley sides and broad glacial cirques and troughs makes beautiful mountain scenery. In addition, asymmetry of the folds is evidenced by differences in steep scarp faces and gentle back slopes (e.g., Laramie Mountains).

The problem of antecedence or superposition arises where rivers of the region cut across mountain ranges (i.e., the Laramie, Arkansas, and North and South Platte Rivers). Although these rivers were previously thought to be antecedent, they are now considered to be superimposed.

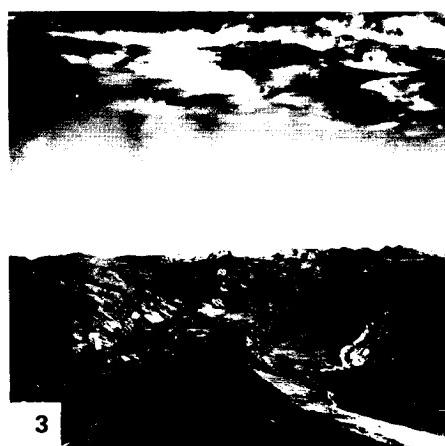
Figure T-6.4 is a view of differential erosion of the uplifted rocks along the Front Range at Morrison, Colorado. Resistant sandstones hold up these hogbacks. (*JRE References: Anderson et al. (1975), Dickinson (1977), Gries (1981, 1983), Hunt (1974), King (1977), Lowell and Gries (1983), Matthews (1978), Rocky Mountain Association of Geologists (1972), Suppe (1985), Thornbury (1965, pp. 287-405). HCMM 0528-19310-1, October 6, 1979.*)



1

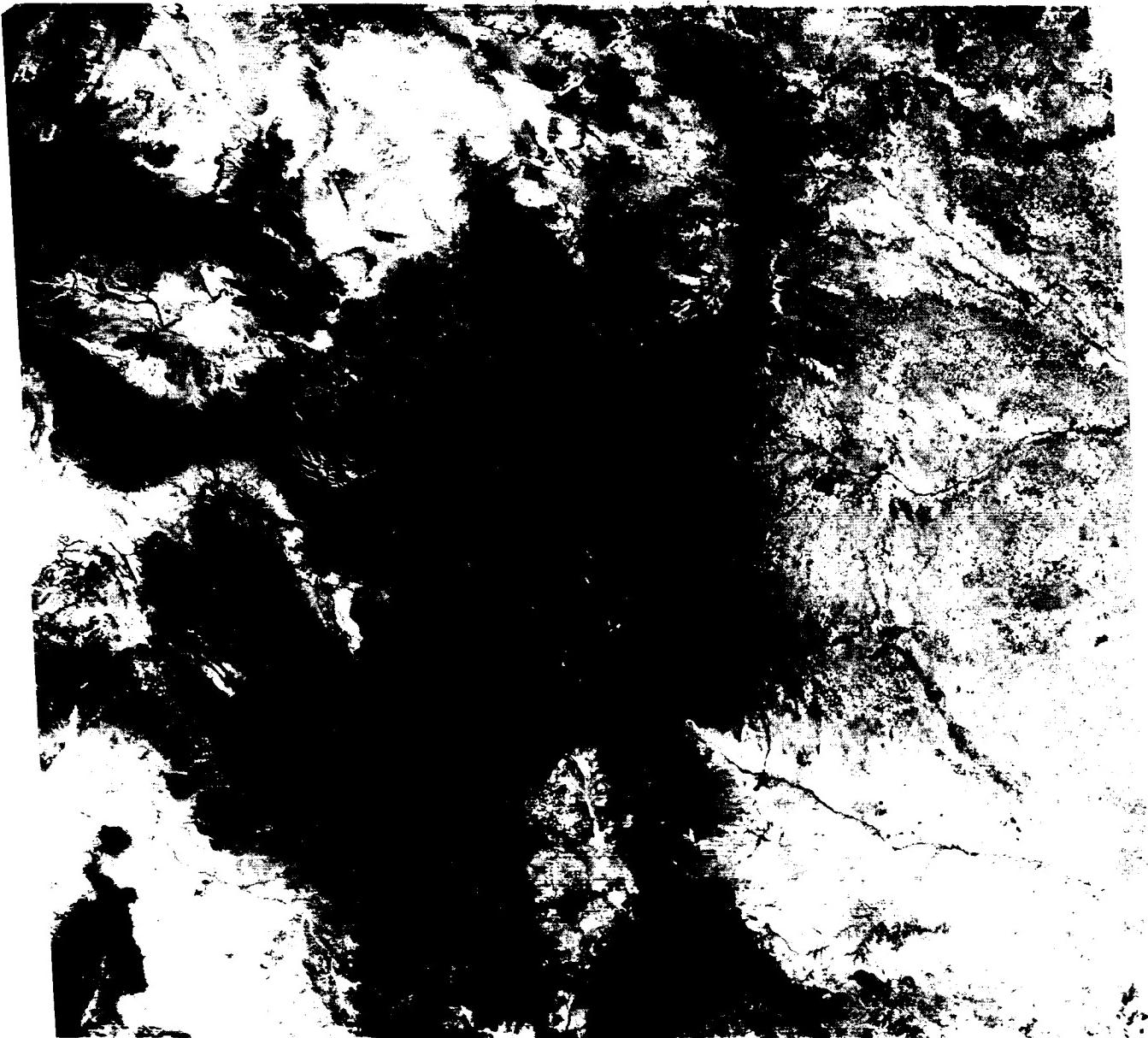


2

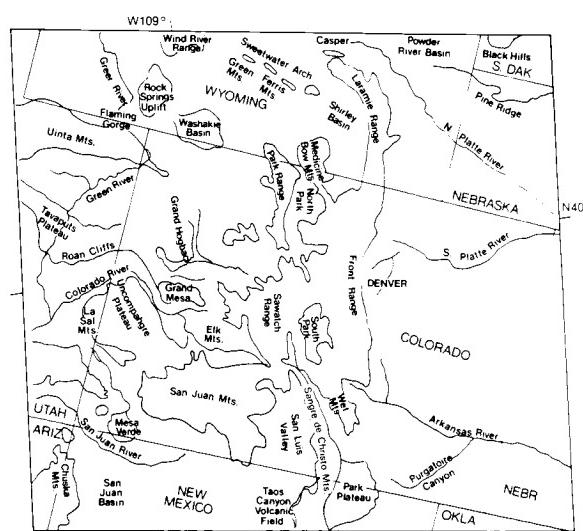


3

ORIGINAL PAGE IS
OF POOR QUALITY



4



The San Rafael Swell is one of the best-exposed broad anticlinal flexures of Laramide age that dot the Rocky Mountains of the western United States. An arid climate, the degree of erosion, and marked contrasts in resistance to erosion of the sedimentary section combine to produce a spectacular exposure of the interior structure of the archlike swell. Resistant rock units that range from Permian (the highly fractured unit slightly east of center of the swell) to Early Tertiary age (the dark units north of the Roan Cliffs, east of the swell) form a series of roughly elliptical concentric inward-facing hogback ridges and strike valleys that define the fold. Jurassic Navajo sandstone forms the upper part of the bold cliff that defines the culmination of the structure and comprises much of the smooth-stripped structural surface around the northern, western, and southern flanks of the structure. The steeper inward-facing scarp contrasts with the gentle dip slope (Figure T-7.1). The difference in dip of the rocks on east and west is shown by the wider bands of exposure on the more gently dipping west side and the less pronounced scarp face. Beyond the swell, two regional escarpments, the outer Book Cliffs and inner Roan Cliffs, formed by erosion of resistant sedimentary layers extend across the companion Landsat image (Figure T-7.2) along the outer edge of the swell and outline the southern tip of the Tavaputs Plateau. The short, steep scarp face and gentler backslope define a slight dip to the northeast and then north as the Roan escarpment is traced from west to east (Thornbury, 1965; King, 1977).

A narrow graben (Joe's Valley graben) lies along the western side of the swell. Careful examination of the northeast flank of the swell reveals a small asymmetric parasitic fold manifested as an elongate (banana-shaped) feature. The dark spots near the south end of the swell mark relatively young volcanic centers. These centers lie generally on trend with the narrow graben mentioned above and may mark the locus of a deeper seated fracture that controls both graben formation and the volcanic activity, each of which postdates the swell.

Close examination of the topography in the core of the swell reveals linear and rectangular patterns, indicating sets of joints that erosion has emphasized by etching. Joints trend north-south, northwest, west-northwest, and northeast. Several small faults parallel these joints. The joints appear to be related to the processes that produced the fold.

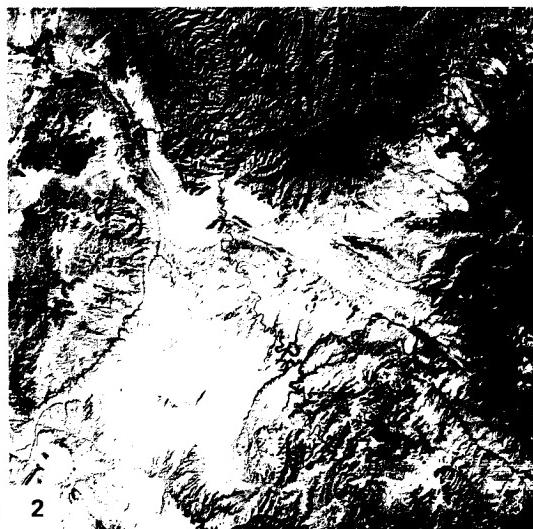
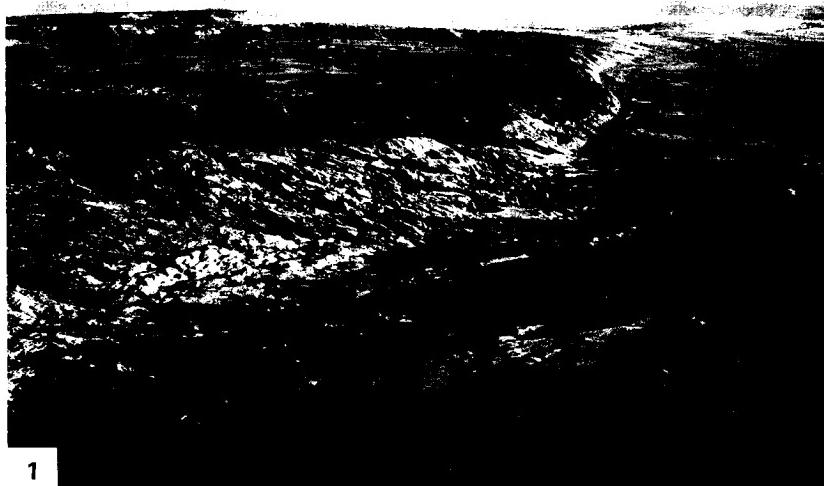
In flowing across the axis of the swell, the San Rafael River disregards both structure and rock type. This suggests that it is

either antecedent (developed its course before the formation of the fold) or superimposed (developed its course on an unconformable overlying cover that erosion has subsequently stripped away).

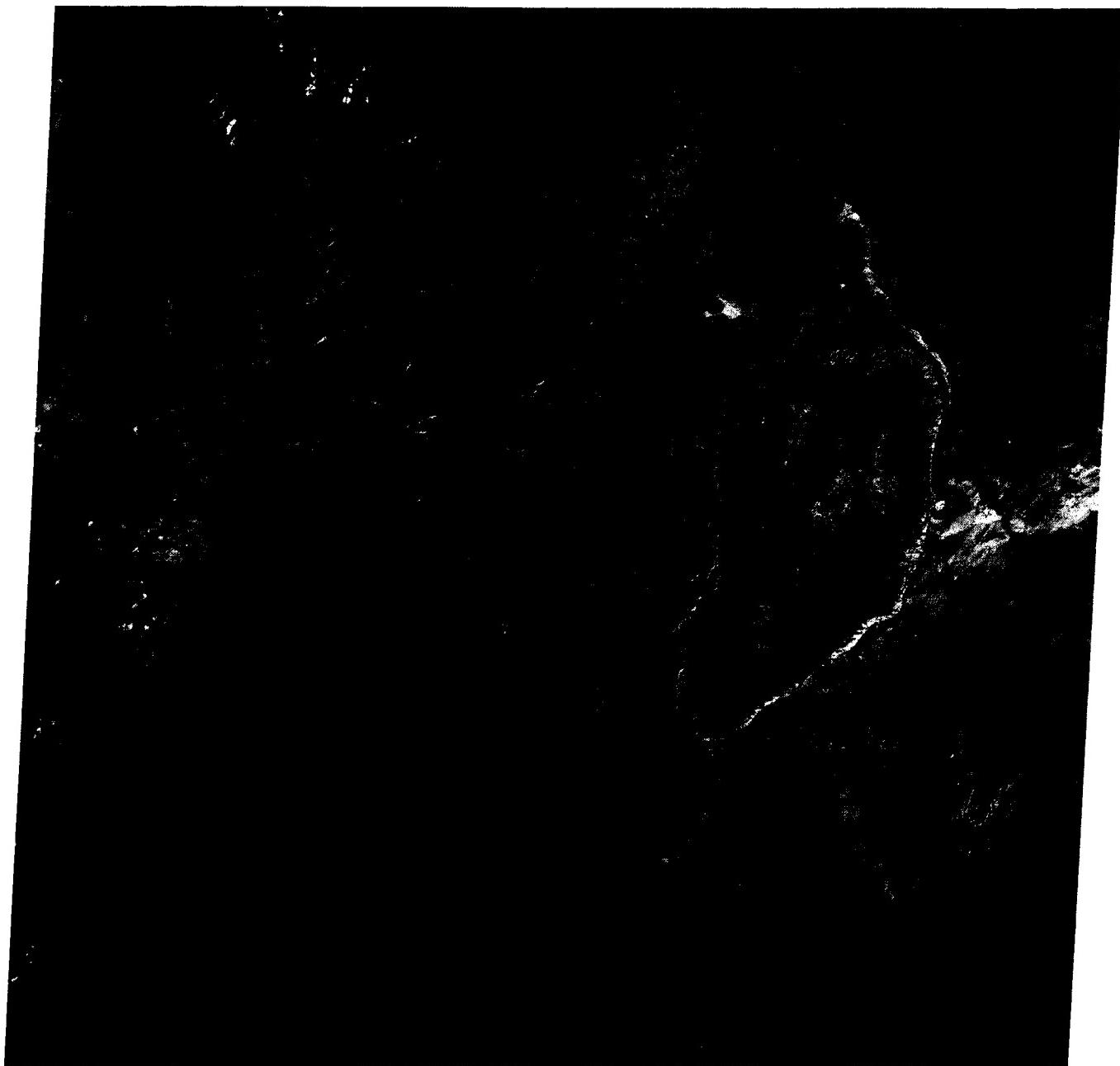
East of the swell in the vicinity of the La Sal Mountains lie the folded and faulted rocks of the Paradox basin. The folds in the Paradox basin are much tighter and are evidently décollement folds. The zone of detachment (*décollement*) follows the Pennsylvanian Paradox salt and related evaporite rocks (Rocky Mountain Association of Geologists, 1972).

Figure T-7.3 is a section of a Large Format Camera scene that shows the Black Hills of Wyoming and South Dakota, another well-defined dome lying to the east of the main Rocky Mountains. The tree-covered Precambrian crystalline rocks that core the uplift and the tree-covered resistant ridges of the overlying sedimentary rocks stand out as dark areas in this scene. Ridges formed of more resistant strata and valleys carved in weaker rocks outline the structure around this central core. These completely encircle the dome, giving an annular drainage pattern. A north-trending monocline and/or fault zone is clearly visible as a lineament near the west side of the core area. The dark sedimentary ridges outline several folds in the immediate vicinity of the uplift. The orientation of these folds suggests a component of left-lateral slip along the northwest-trending margin of the uplift. Although the Black Hill uplift is much larger than the San Rafael Swell, the two uplifts are similar in that both are large, rather simple, doubly plunging anticlinal uplifts of Laramide age and both appear to be related to faulting at depth.

The isolated nature of the broad folds of the Colorado Plateau and Rocky Mountains in general sets them apart from the tight parallel folds normally associated with collision of continental lithospheric plates. It appears that the San Rafael Swell and similar Rocky Mountain uplifts are related to deep-seated thrust or strike-slip faults related to long-sustained (Mesozoic and Early Tertiary) underthrusting along the western margin of North America that took place without collision of continental plates. To the west, this convergence produced folds, thrust-faults, and A-type subduction. East of the western Overthrust Belt, the deformation is manifested as fault-bounded uplifts, many of which are basement-cored (see Plate T-1, western United States). (JRE) Additional References: Gries (1981), Livicari (1979), Lowell and Gries (1983), Matthews (1978), Suppe (1985). Landsat MSS 1068-17364.



ORIGINAL PAGE
COLOR PHOTOGRAPH



3

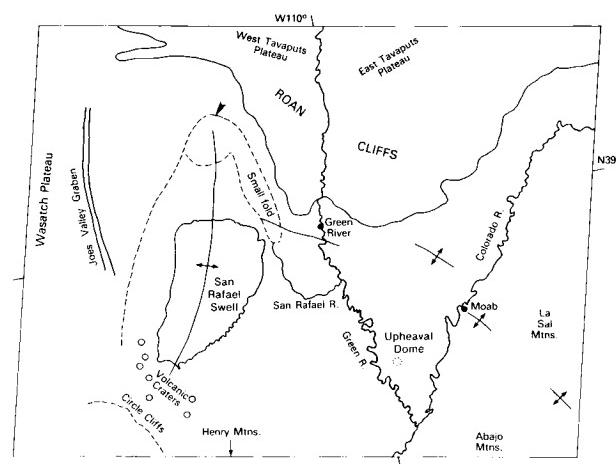


PLATE T-8

The late stages of development of the western U.S. Cordillera (Laramide orogeny) produced intermontane structural basins and adjacent mountain blocks in the foreland. Foreland deformation of this style seems to be typical of continental plates adjacent to convergent margins of long duration that have not sustained continent/continent collisions. This tectonic setting produces a pattern of compressive uplifts and basins, with most of the deformation confined to block edges. Twelve kilometers of structural relief between basins and adjacent uplifts is not uncommon. The basins contain several thousand meters of Paleozoic and Mesozoic sedimentary rocks that predate the Laramide orogeny. As much as 5000 m of Cretaceous and Tertiary sediments filled these orogenically defined basins. Deformed Paleocene and Eocene deposits record continuing orogenic activity.

During the Laramide orogeny, basin floors and mountain summits were much closer to sea level than today. After the seas retreated from the Rocky Mountain region, floodplains, swamps, and vast lakes developed in the basins. Drainage systems imposed at that time persist today. Since the Oligocene, episodic epeirogenic uplift gradually raised the entire region, including the Great Plains, to present altitudes. Most of the modern topography is the result of Pliocene/Pleistocene events, including additional uplift, glaciation of the high country, and denudation and dissection of older Tertiary surfaces in the basin by fluvial processes.

In the United States, these distinctive intermontane basins occur principally in the central Rocky Mountains from Colorado and Utah (Uinta basin) to Montana and are best developed in Wyoming, with the Big Horn, Powder River, and Wind River being the largest. Topographically, the basin floors resemble the surface of the western Great Plains, except for vistas of surrounding mountains.

At most boundaries, Paleozoic through Early Tertiary units dip steeply into the basins off uplifted blocks cored by Precambrian rocks. The eroded steeply dipping units form hogbacks and flatirons. Many of the boundaries are thrust or reverse faults. Although other boundaries appear to be monoclinal flexures, faulting is suspected at depth. Most bounding faults show evidence of at least two episodes of Laramide (Late Cretaceous and Eocene) movement, suggesting both thrust and strike-slip types of displacement.

Plate T-8 shows the interior of the Green River basin, one of the largest basin complexes in Wyoming. The mosaic includes nearly all the Green River basin. This basin is bounded on the west by the Wyoming Overthrust Belt (Figure T-6.2), in which folded miogeosynclinal Paleozoic and Mesozoic rocks have been pushed eastward in a series of fault slices that now stand out as parallel mountain ranges. On the south, the basin abuts the east-west-trending Uinta Mountains uplift. To the north and northeast, the Green River basin is hemmed in by the Gros Ventre and Wind

WYOMING INTERMONTANE BASINS

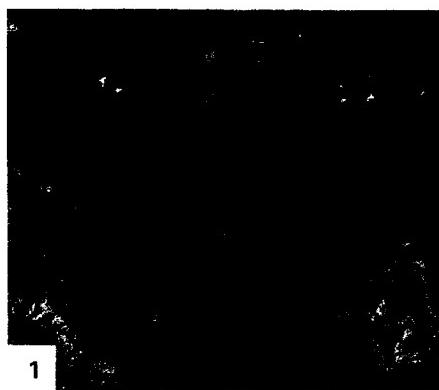
River ranges; the latter is a tilt block with a thrust fault on the southwest flank and monoclinal hogbacks on the northeast side. Eastward around the Rock Springs uplift, the basin merges with the Great Divide basin, which, in turn, is bounded by the up-arched Sweetwater block and Rawlins uplift and merges with the Washakie basin (synclinal) to the south.

Figure T-8.1, a color composite of three ratio bands that enhances differences in lithologic and weathering colors among the surface units (iron-rich surface in orange, vegetation in blue), contains three intraplate structures. The Rock Springs domal uplift is rimmed by inward-facing cuestas carved from Upper Cretaceous (Mesaverde Formation) strata. To its east is the synclinal Washakie basin, with its outward-facing cuestas held up by Lower Tertiary units. North of these structures is the Red Desert (Great Divide) basin, partially encircled by an eastward-facing escarpment. Playas have developed in this basin of interior drainage, along with the Kilpecker dune field, a narrow sand and silt surface that stretches east-west.

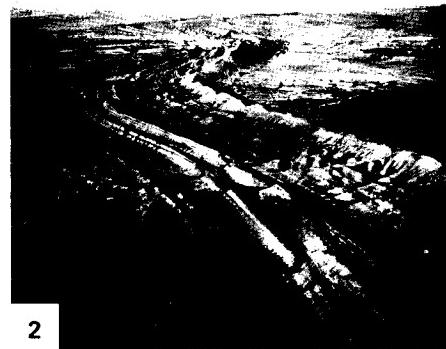
Drainage of the Wyoming basins is problematical because the rivers appear to disregard the structure. The Sweetwater River cuts across the Wind River Range and Sweetwater Mountains, the Big Horn River takes a difficult course across the Big Horn Mountains instead of going around them, and the Green River has eroded a deep canyon through the Uintas. Hence, the question of antecedence or superposition once again arises. Subsequent drainage must also be considered. For example, the Green River makes a sharp bend eastward to flow along the strike of uparched beds on the north edge of the Uintas before it cuts southward across the nose in another strike valley. Such drainage anomalies are typical in eroded folded terrane.

Figure T-8.2 highlights differential erosion of tilted beds near Rawlins, Wyoming. This monoclinal structure zig-zags because of changing direction of tilt. Convergent closure of the water gaps indicates the direction of dip. A trellis drainage is well developed on this structure.

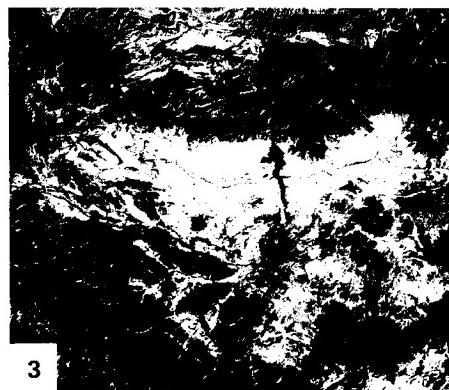
Figure T-8.3 is a Landsat view of the Wind River basin, another large intermontane depression that occupies the center of the state between the Wind River Mountains on the west, the Casper Arch on the east, the Owl Creek/Bridge Mountains on the north, and the Sweetwater Arch to the South. The dip of the flanking ridges around Little Dome in the Wind River basin can be readily determined in Figure T-8.4. The offset linear ridges and valleys on the east side of the dome indicate faulting. The partly annular, partly trellis drainage patterns also reflect a change in structure. Steeper dips of rocks on the east flank are evident. (NMS) References: Armstrong and Oriel (1965), Abrams (1985), Gries (1981, 1983), King (1977), Lowell et al. (1983), Matthews (1978), Suppe (1985), Thornbury (1965). Landsat Mosaic.



1



2



3



ORIGINAL PAGE
COLOR PHOTOGRAPH

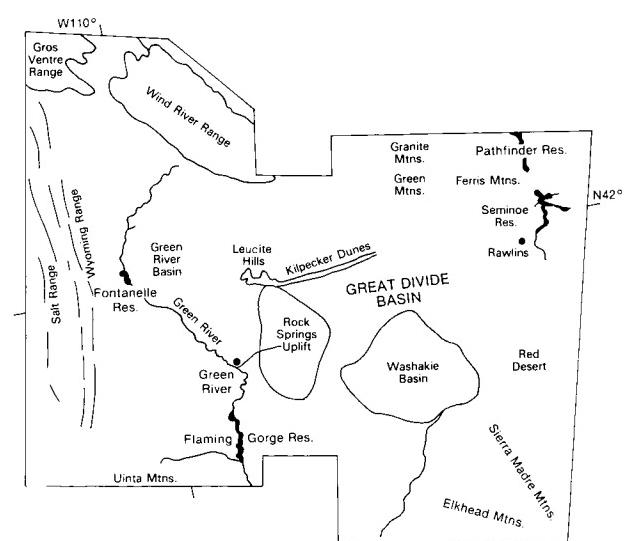


PLATE T-9

CORDILLERAN ACCRETIONARY TERRANES

This Plate, a nighttime HCMM thermal image, records a scene that extends 700 km across the southern Canadian Cordillera from the Pacific Ocean almost to the eastern edge of the Rocky Mountains (Wheeler et al., 1972). The tonal patterns, directly tied to sensed temperatures, broadly coincide with different topographic expressions that, in turn, are controlled by structure. These notable variations in topography are surficial evidence of abrupt changes in underlying structures that result from accretion of suspect or exotic terranes to the west side of North America (Jones et al., 1982).

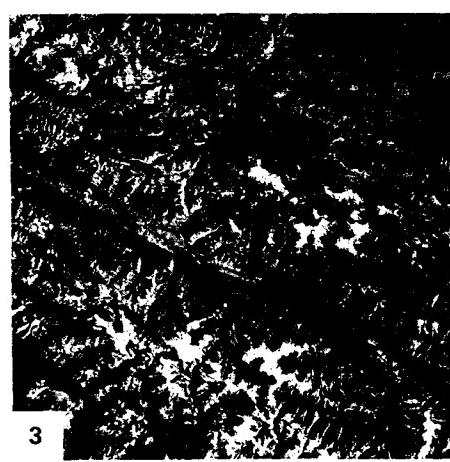
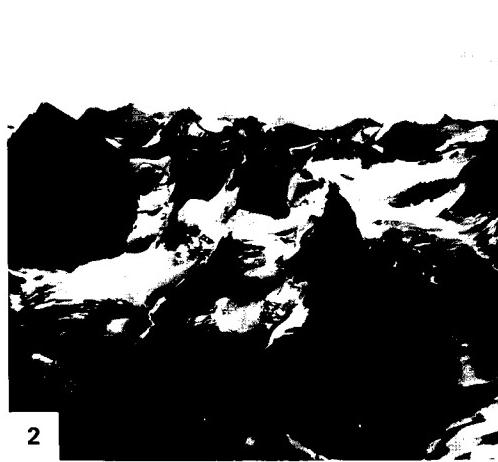
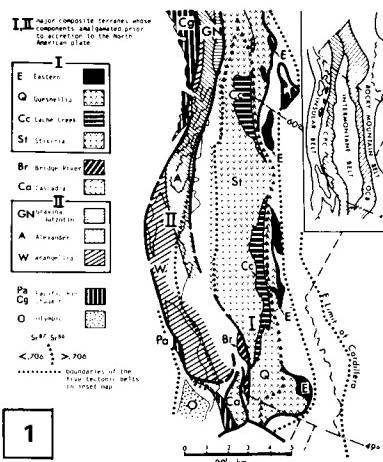
British Columbia has been subdivided into five structural belts (Figure T-9.1 taken from Monger et al., 1982). Westernmost is the seismically active Insular Belt, made up of Upper Cambrian to Neogene volcanic rocks and sedimentary strata, which includes Vancouver Island. The Coast Plutonic complex, which comprises the Coast Ranges, consists principally of Cretaceous and Tertiary granitic rock with some eugeosynclinal sedimentary and volcanic rocks of Late Paleozoic to Tertiary age, probably intermingled with some Early Paleozoic and Precambrian units. These high mountains, with typical rugged alpine crags (Figure T-9.2) resulting from intense glaciation in the Pleistocene, are still snow-covered in late spring (dark (cool) tones in the HCMM image). The strongly glaciated terrane is marked by cirques, arêtes, glacial troughs, and finger lakes (Figure T-9.2). Broad glaciated valleys appear as light (warm) tones; these may be submerged by seawater, approaching their western termini, thus producing fjords that extend well inland beyond the coast (see Plate C-5). The dendritic drainage near the coast changes to structurally controlled patterns and then changes again to more randomly oriented drainage farther inland (Holland, 1964).

Somewhat lower, more subdued topography is represented in the Intermontane Belt, composed of volcanic and sedimentary rocks emplaced from Late Paleozoic to Late Tertiary time. Granitic intrusions are comagmatic with the volcanic rocks. The belt was deformed at various times from Early Mesozoic to the Neogene. This belt is separated from the Omineca Crystalline Belt to the east by the Fraser and Pinchi faults that mark change in crustal structures. The Omineca Belt consists of highly deformed, metamorphosed miogeosynclinal rocks of Mid-Proterozoic to Mid-Paleozoic ages above Precambrian crystalline basement. The belt is overlain by metamorphosed Paleozoic and Lower Mesozoic volcanogenic and pelitic rocks and Tertiary volcanic rocks. Considerable thrusting has rearranged these units; Jurassic and Cretaceous plutons intrude over wide areas.

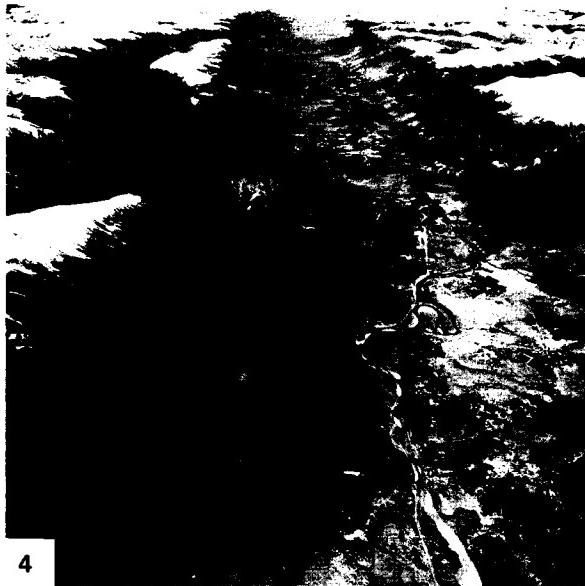
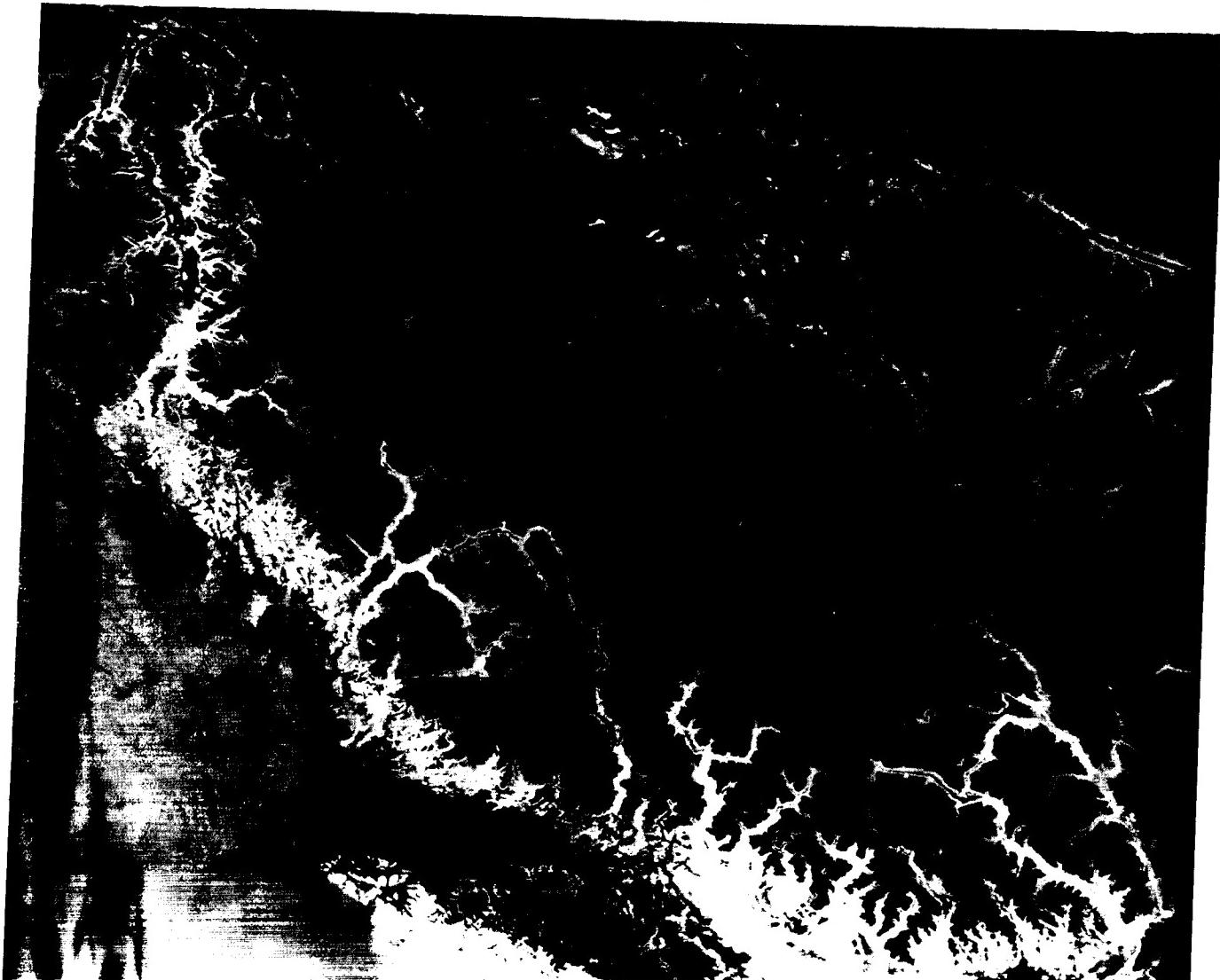
The eastern border of the Omineca Crystalline Belt largely coincides with the Rocky Mountain trench. This low, linear valley with high mountains on either side is strikingly expressed

in a Landsat-2 image (Figure T-9.3) and an oblique aerial photograph (Figure T-9.4). The western boundary of this graben-like structure is a normal fault (McLeod fault). Its east margin is bounded by the Back Range fault, the first of a series of west-dipping thrusts that characterize the Rocky Mountain Belt. This belt is composed of Devonian to Jurassic miogeosynclinal sedimentary rocks and overlying Upper Jurassic to Paleocene exogeosynclinal Cordillera-derived clastic rocks. Compression toward the northeast displaced belt units up to 200 km onto the craton during the Laramide orogeny. The crust under this belt is relatively thick (45 to 50 km) against the edge of the North American craton, compared with 30 to 35 km thicknesses for belts to the west. In Figure T-9.3, the regions on either side of the trench appear similar topographically, even though quite different structurally and lithologically, due in part to the superposed influence of mountain glaciation that has carved comparable glacial valleys on both terranes.

Much of British Columbia is constructed from several accreted terranes. Ocean-floor crust was plastered on the craton in places by a series of plate collisions driven by seafloor spreading. Obduction occurred rather than subduction. The crustal blocks, separated by faults, are distinguished by different rocks, geologic histories, and internal structural fabrics. As many as 12 allochthonous terranes are distributed among the five geologic subdivisions of the Canadian Cordillera (Figure T-9.1). More than one suspect terrane may be present in a belt and can straddle belt boundaries. Five of these terranes occur within the HCMM image: (1) the Cache Creek (Cc) terrane, a Mississippian to Upper Triassic mélange of tectonically disrupted chert, argillite, basalt, alpine-type ultramafics, extensive carbonates, and local blueschist; (2) the Eastern (E) terrane, Upper Paleozoic and Lower Mesozoic (?) basalt, alpine ultramafics, chert, and argillite; (3) the Quesnellia terrane (Q), Upper Paleozoic and Lower Triassic volcanics, volcanoclastics, and carbonates, Upper Triassic and Lower Jurassic volcanics, clastics, and argillites; (4) the Stikinia terrane (St), possibly Upper Precambrian basement, with Mississippian and Permian volcanoclastic rocks, basic to silicic volcanic flows, and carbonate rocks, locally deformed and intruded in Middle to Late Triassic time, overlain by Upper Triassic to Middle Jurassic andesitic volcanic strata; and (5) the Wrangellia terrane (W), an Upper Paleozoic volcanic complex composed of flows, breccias, and volcanoclastic rocks overlain by limestone, clastic rocks, chert, and Upper Triassic pillow and subaerial basalt flows succeeded by Triassic to Jurassic limestone, cherty limestone, and clastic and volcanic rocks. (NMS) Additional References: Price (1981), Price and Mountjoy (1970), Saleby (1983). HCMM 0036-10540-3, June 1, 1978.



ORIGINAL PAGE IS
OF POOR QUALITY



4

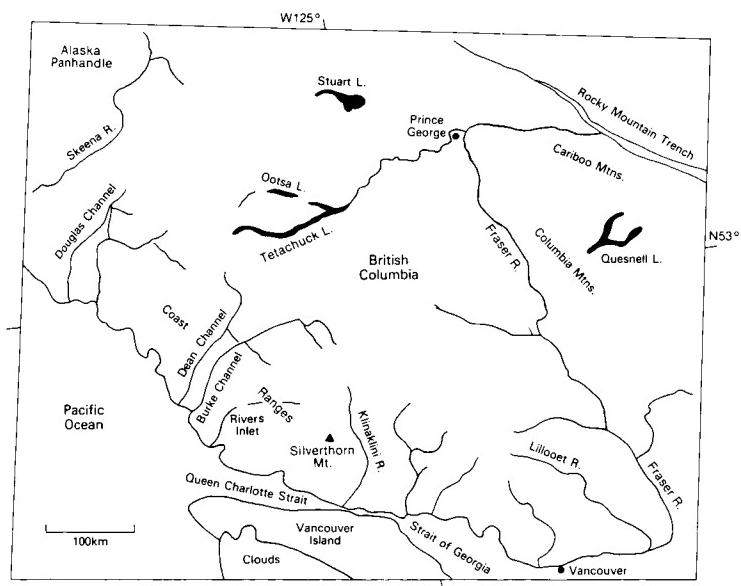


PLATE T-10

ALASKA

This mosaic of Landsat MSS images covers some 1.5 million km², providing a view of most of the state of Alaska that would have been almost impossible to obtain before the availability of space imagery. Changes in geomorphic character differentiate the various geologic provinces (Thornbury, 1965, Ch. 28). Some of these geologic provinces have counterparts in the Canadian and U.S. Cordillera. The rugged Pacific Border Ranges (highest peaks > 6000 m) consist of the St. Elias Range (southeast of the mosaic) and the Chugach Mountains, farther west. They are a continuation of the Coast Ranges of British Columbia, Washington, and Oregon. The arcuate (convex north) Alaska Range and the Talkeetna and Wrangell Mountains are considered correlatives of the Cascades/Sierra Nevadas in the United States. The interior Alaska lowlands and highlands, drained by the Yukon/Tanana/Porcupine River system and characterized by downfaulted troughs containing Eocene and younger sediments, correspond somewhat to the Basin and Range province. The Brooks Range is analogous to the Rocky Mountains, and the North Slope is comparable to the western Great Plains.

Prominent right-lateral wrench faults and the juxtaposition of rock units quite different in lithology, age, and origin suggest that far-traveled allochthonous terranes make up the bulk of Alaska and the adjoining Cordillera of Canada (Jones et al., 1982; Monger and Price, 1979; Jones and Silberling, 1979). Generalized locations of most of the larger recognized and named terranes are set forth on the index map, as indicated by the following abbreviations: AGM = Angayucham, Ch = Chugach, End = Endicott, Kyk = Koyukuk, NXF = Nixon Fort, OS = Overlap Sequence ("hiding" subjacent terranes), PN = Peninsular, POR = Porcupine, PW = Prince William, RB = Ruby, SEW = Seward, TOG = Togiak, TOZ = Tozina, WR = Wrangellia, YT = Yukon/Tanana, and Y = Yukon. The only autochthonous part of Alaska, which has remained part of North America since the Precambrian, is a small triangular area in the northeast corner of the state. This area, the Yukon Flats, is bounded by both the Yukon and Porcupine Rivers and is centered around the Fort Yukon area. The rest of Alaska, including the highly deformed Brooks Ranges, has moved to some extent, although the amount, nature, and timing of movement is poorly understood and highly controversial. Marked paleontological and stratigraphic discontinuities, coupled with paleomagnetic studies, indicate that most Mesozoic rocks now in Alaska originally formed at more southerly latitudes (Jones and Silberling, 1979).

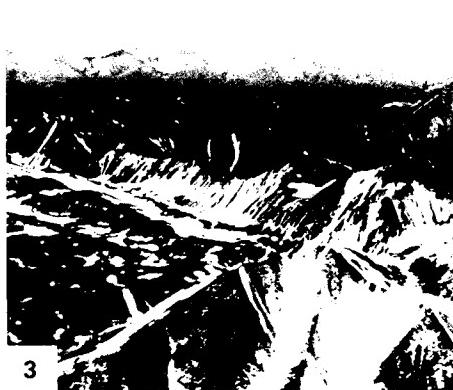
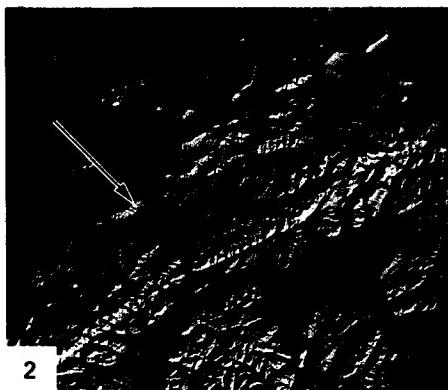
Hallmarks of the Alaskan tectonic regime are the several major strike-slip faults that roughly parallel the principal mountain chains (Lathram et al., 1974). These faults, plotted on the index map by number, are: (1) Yukon Flats fault, (2) Kaltag (RL (right lateral)), (3) Tintina (RL), (4) Denali system (RL): 4a =

Farewell, 4b = Hines Creek, 4c = McKinley, 4d = Shakwak Valley segments, (5) Togiak/Tikchik (RL and reverse), (6) Border Ranges (RL and reverse), (7) Fairweather (RL), and (8) Chugach/St. Elias fault. Several are visible in the Landsat mosaic. The Border Ranges fault defines the western front of the Kenai Mountains, where these rise more than 1300 m (Figure T-10.1) from the downdropped coastal plains (MacKevett and Plafker, 1974).

After earlier orogenic events in the Jurassic, climax deformation of the Brooks Range occurred in the Cretaceous, with strong northward thrusting of thin-skinned tectonic displacements. More orogenic activity took place in the Late Tertiary and Quaternary, further distorting the range to its present concave northward bend. The Brooks Range contains both open and tight folds; it now rises to altitudes of almost 3000 m and displays a moderately rugged topography accentuated by glaciation. The Foothills (400 to 1000 m high) to its north are underlain by Devonian to Cretaceous sediments and mantled by Pleistocene morainal deposits.

The Yukon/Tanana Uplands consist of moderately folded Paleozoic/Mesozoic sedimentary units and a distinct east-central metamorphic zone. Dissected plateaus are present. The Tintina Trench, a possible extension of the Rocky Mountain Trench (Plate T-9), divides the Uplands from the Yukon Flats Lowlands underlain by highly folded Mesozoic units. To the west, a vast region of alternating highlands (Kuskokwim, Norton Sound, and Seward) and lowlands are built of Late Paleozoic through Tertiary metamorphic sedimentary and volcanic rocks and Quaternary continental beds.

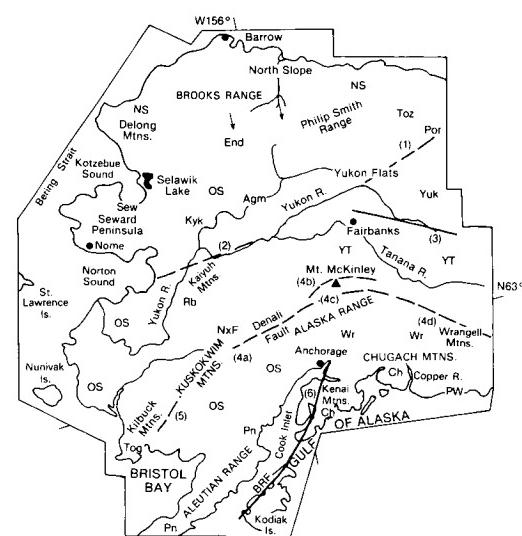
Most of southern Alaska is characterized by narrow arcuate zones of strongly folded and faulted metamorphic and intrusive rocks and zones of compressed strata, much of whose structure is mainly the result of subduction. The Alaska Range is a large synclinorium of uplifted rocks cut by numerous faults, accentuated by active glaciers. Most of its peaks are under 4000 m, but Mt. McKinley reaches 6194 m. A Landsat image (Figure T-10.2) includes Mt. McKinley (arrow) and the south-facing mountain front along the arcuate Denali strike-slip fault (Figure T-10.3). Triangular facets are prominently displayed along the scarp face at interfluves. Volcanic rocks make up much of the Wrangell Mountains to the southeast. (Mt. Wrangell is an active volcano.) The Alaska Peninsula and Aleutian arc (Plate V-9), a line of active arc-continent collision, also include many volcanoes (more than 80: 36 active, 20 forming calderas). The Chugach Mountains along the Gulf of Alaska exceed 4000 m in altitude inland, with spectacular scenery created by the intense sculpturing of Pleistocene and modern glaciers (Figure T-10.4). (NMS) Additional Reference: Williams (1958). Landsat Mosaic.



ORIGINAL PAGE IS
OF POOR QUALITY



4



51

PLATE T-11

APPALACHIAN MOUNTAINS

The daytime HCMM image records all of the central Appalachian Mountains and part of the southern Appalachians, extending 850 km from the edge of the Catskills in New York (Plate T-12) to the Pine Mountain thrust in Tennessee and North Carolina (Plate T-13). The folded rocks record the convergence of two continental plates in Pennsylvania/Permian time. Part of much of the same area, centered on central Pennsylvania and upper New York state, stands out in a Day-thermal HCMM image (Figure T-11.1) taken on September 26, 1978, in which the dark tones correlate with higher standing resistant stratigraphic units in the fold mountains that are mantled with heavy vegetation; the lenticular light-toned pattern in center right is the Wyoming Valley syncline, covered with dark wastes from anthracite mining that absorb solar energy and reradiate it at temperatures higher than the adjacent uplands. The dark northeast-pointing finger-like apophyses near the center of the thermal image (shown in more detail in Figure T-11.2, a Landsat MSS band 5 image) are gentle synclinal mountains along the north edge of the Appalachian Plateau. Spectacular large-scale trellis drainage has developed on these broad folds and persists well to the northeast of the dark “fingers.”

Both HCMM scenes highlight several of the Appalachian physiographic provinces—the fold belt consisting of the Valley and Ridge, the Blue Ridge and its eastern extension into the Reading Prong, the carbonate rocks in the Great Valley including the Shenandoah Valley in Virginia and its Pennsylvanian counterpart, and the low rolling hills of the Piedmont. The flat-lying terrain imposed on Paleozoic sediments of the Appalachian Plateau and Interior Lowlands can be seen to the northwest. To the southeast, the landscape is carved from Late Mesozoic/Cenozoic sediments of the Atlantic Coastal Plains that lap unconformably over the Piedmont. In these images, one can easily see the regional geomorphic differences between the much-eroded and rejuvenated Appalachian Mountains and the flatlands on the east and dissected plateau on the west.

The Appalachians are one of the regions from which modern ideas of tectonics and mountain-building have evolved. The concept of the geosyncline arose from studies in the 1800s of the depositional and subsequent deformational events recorded in the central Appalachians. The advent of plate tectonic concepts has modified and refined these ideas so that the Appalachians are now used as a type example for the Wilson cycle (the opening and closing of an ocean).

The Appalachians of eastern North America stretch northeast 3200 km from Alabama to Newfoundland and have an exposed width between 150 and 600 km. Before the opening of the Atlantic Ocean, the region was continuous with the Caledonides of northwestern Europe and eastern Greenland. At its southern tip in northern Alabama, it bends westward in a buried fold belt extending across to Arkansas, where it joins the Ouachita belt (Plate T-14) that, in turn, extends southwestward in the subsurface to the Marathon fold belt of west Texas and northern Mexico. The illustration at the bottom of the next page is a map prepared by R. Hatcher and G. Viele (1982), outlining the subdivisions of the Appalachian orogen.

This map suggests that structural and age units of the Appalachians north of a hinge line in southeastern New York are different from those to the south, although there is some correlation. Pre-Late Paleozoic deformational events dominate the northern segment, and rocks are more intensely metamorphosed, where more deeply buried, and have sustained more viscous deformation than those to the south. Figure T-11.3 shows the western side of the New England Appalachians along the Green Mountains of Vermont (right side), as they abut against the Champlain

Valley and the Adirondack Mountains to the west. The Green Mountains consist of Taconic thrust sheets of Lower Paleozoic eugeosynclinal metasediments carried over miogeosynclinal carbonates and other sedimentary rocks in the Champlain/Hudson lowlands. To their east are additional thrusts emplaced during the Acadian deformation. Lake Champlain lies along a fault system separating the domal uplift of the Adirondacks (an outlier of the Grenville section of the Canadian Shield (Plate T-15)) from the New England Province. Faults are indicated by the linearity of the lake and associated river valleys, but erosion was certainly facilitated by the presence of Cambrian/Ordovician carbonates that underlie the lowlands. The topographic grain of the Adirondacks shows a strong structural influence in a northeast-southwest direction. Lineaments (expressed primarily as valleys) are a result of erosion along fractures. Crosscutting faults are indicated by lineaments in both provinces.

Much of the terrane in New England is equivalent to that of the Piedmont; both are root zones of metamorphosed Lower to Mid-Paleozoic sediments, volcanic rocks, and plutons that have been exposed by erosion of 5 to 15 km or more of overlying rock. The Piedmont region comprises deeper continental crust that contained island-arc and arc-trench gap deposits, some parts of earlier shelf, and later foreland basin deposits, together with mélange and ophiolite suites. These were compressed and moved toward the continent (westward) as flowage nappes and overthrusts.

The Piedmont of the United States and parts of the Canadian Appalachians contain zones that represent either segments of ancient continental margins or suspect terranes (rafted in on oceanic plates or crustal fragments detached from the continental crust elsewhere and transported laterally along transcurrent faults) that eventually accreted to the orogen. There are abrupt differences in lithology, stratigraphic sequence, and tectonic style across the boundaries of these terranes with adjacent assemblages. A prominent band of ophiolites extends from Atlanta to southeastern Quebec in the western Piedmont (mainly to the east of the Blue Ridge and the surface traces of the thrust sheets). This may mark suturing of oceanic sediment and upper basaltic crust along a subduction zone.

Like many other orogenic belts, the Appalachians have a long complex history. It has been interpreted in terms of the Wilson Cycle, the opening and closing of oceans (Condé, 1982; Windley, 1984, Ch. 12) as follows: (1) Late Proterozoic rifting of Laurasia; (2) initiation of subduction in Late Precambrian; and (3) closure of the proto-Atlantic (or Iapetus) Ocean by the Middle Devonian. A more recent interpretation (Williams and Hatcher, 1982) accounts for the several orogenic events (Taconic (450 to 500 Ma ago), Acadian (350 to 450 Ma), and Alleghanian (250 to 300 Ma)) by the accretion of several terranes to the continental margin, culminating in the closure of the Atlantic by the end of the Paleozoic as the African and North American plates collided. Each orogenic event involved folding and thrusting.

The thrust sheets that characterize Appalachian tectonics are mainly décollements in which older sequences override younger rocks. The thrusting of folds and their westward transport is the response of supracrustal rock to subduction of lower crust. The entire allochthonous sequence slides over basement rocks along one or more thrust zones. Most thrust planes parallel bedding in low-viscosity rocks such as shale (particularly the Mid-Cambrian Rome Formation) and salt beds. Individual thrust plates imbricate in slices bounded by high-angle surface-reaching reverse faults that change into lower angle thrusts with depth. Sny- and post-orogenic intrusions cut the plates, especially in the Piedmont.

ORIGINAL PAGE IS OF POOR QUALITY

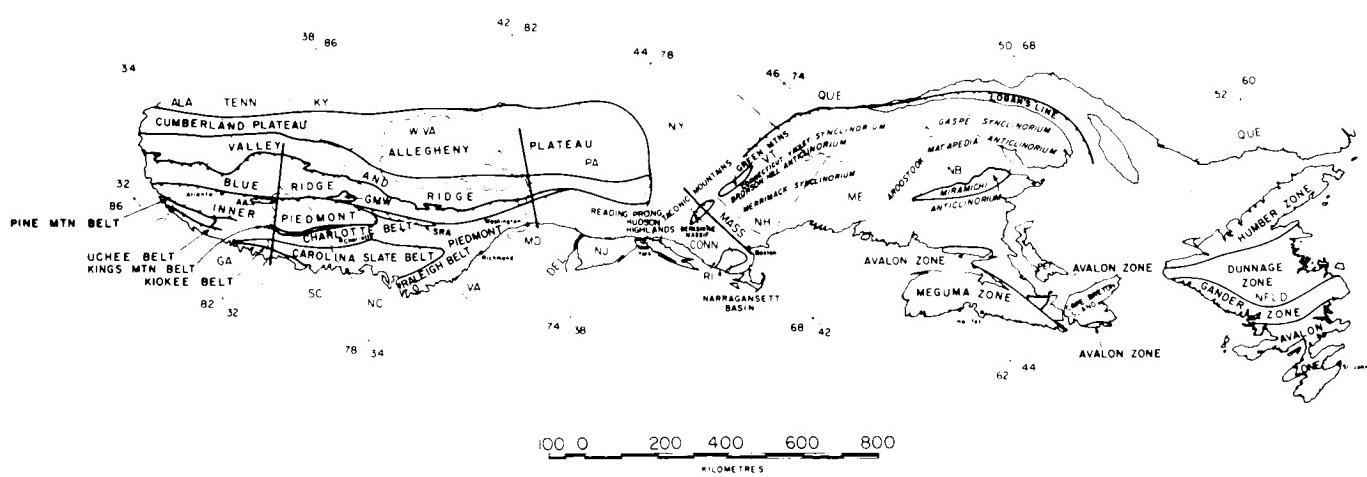
The folded Valley and Ridge Province is part of foreland and miogeocinal sedimentary sequences. Deformation in this province grades from thrusts and tight to overturned folds in the east to more open, gently plunging folds to the west. The western side of this fold belt is bounded either by a thrust zone or by an escarpment that separates the steep dips of the fold belt from the gently warped, generally westward-dipping Upper Paleozoic strata of the plateau. The Appalachian (Allegheny + Cumberland) Plateau to the west contains mainly Mississippian to Permian beds that were uplifted without notable deformation.

The fold belt itself lies within a series of thrusts carried up onto the continent during the final closing of the Iapetus (pre-Atlantic) ocean as the African plate converged on the North American plate. Although earlier orogenic events during the Taconic (Ordovician) and Acadian (Devonian) stages of Appalachian history had affected the region, the activity that produced the folding we see today happened during the Alleghenian (Permian) orogeny. All three orogenies produced slices of basement and overlying sedimentary crust that moved as allochthons along decollements (slip zones) in several lower viscosity units (e.g., the Rome Formation in the southern Appalachians). Foreshortening of the crust during the Alleghenian orogeny amounted to 60 to 80 km or more.

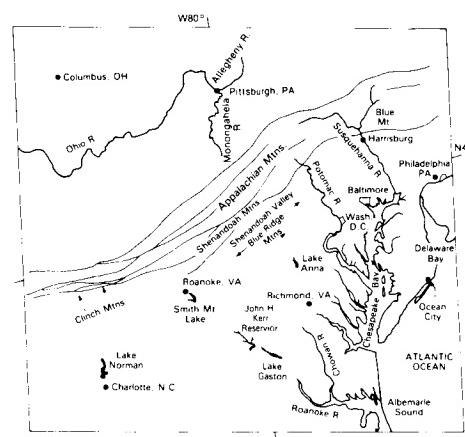
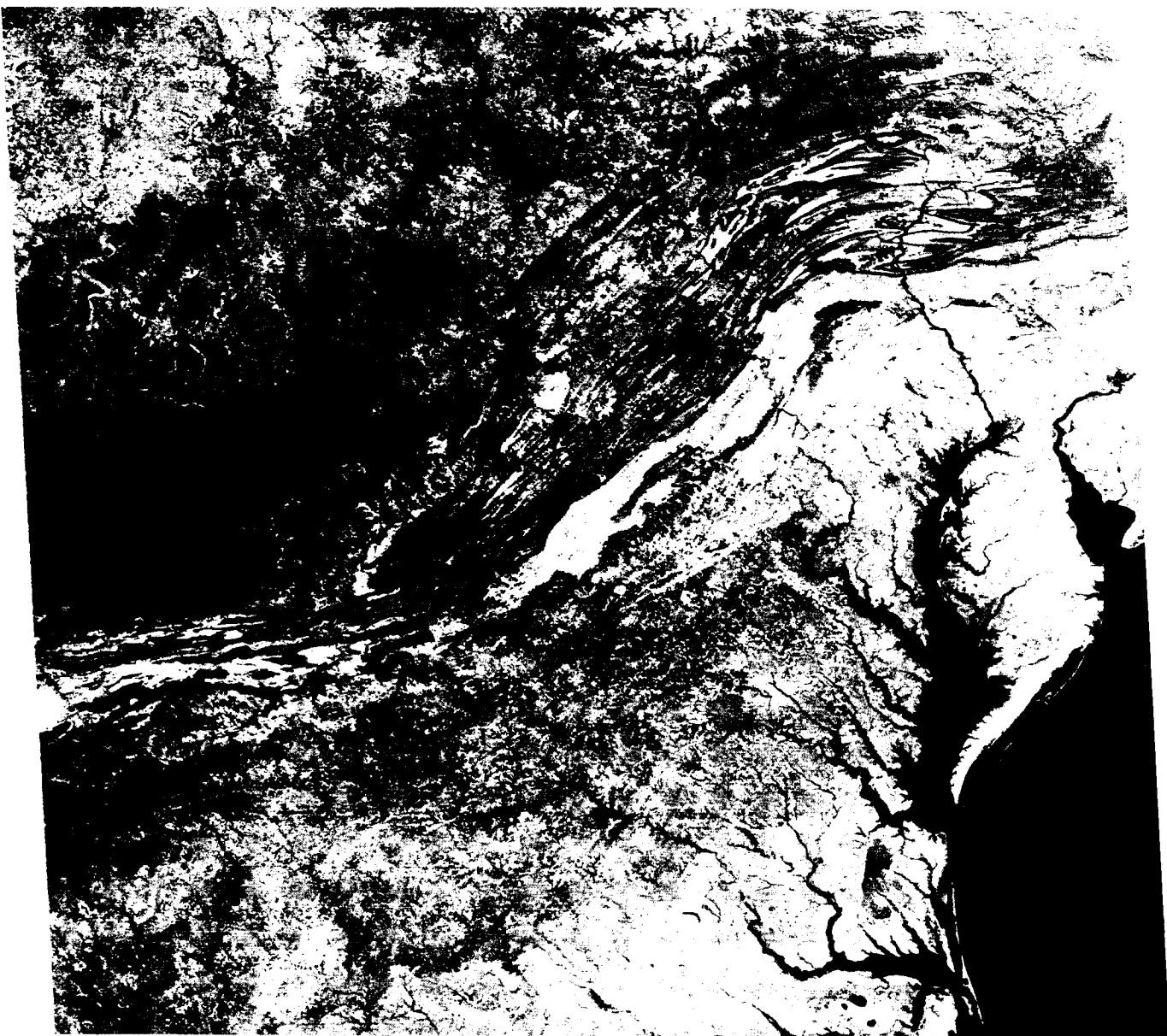
The Appalachian landscapes clearly demonstrate the relation of tectonics and structure to geomorphology. The topographic expression of four structural units is readily apparent in the low-Sun-angle Landsat view of the southern Appalachians of Tennessee/North Carolina around Asheville and the Great Smokies

(Figure T-11.4). The Valley and Ridge fold belt (upper left corner) shows the effects of differential erosion on beds of differing hardness. The long linear ridges are etched out of steeply dipping sandstone units that are resistant to erosion. The broad exposure of carbonates in the Great Valley, just southeast of the fold ridges, reveals the continuation of the strong folding, but the more uniformly resistant lithology gives rise to much more subdued, low-relief ridges whose zig-zag patterns reveal tight plunging folds. Diagonally across the scene is the mountainous terrain (including the Great Smokies) that is an extension of the Blue Ridge of Virginia. This province is bounded on the southeast by the Brevard fault zone that separates it from the western Piedmont (lower right corner), a complexly dissected terrain marked by low hills grading to rolling country farther eastward.

Figure T-11.5 shows still another segment of the central Appalachians, centered on Roanoke in western Virginia. Here also, the Valley and Ridge fold belt is conspicuous. To the south, the Blue Ridge is discontinuous. North of Roanoke, where it is more coherent, it helps to enclose the southern end of the Shenandoah Valley. Isolated linear ridges in the Piedmont define its main structural trend. In West Virginia, the Appalachian Plateau is well dissected with rugged topography, generally high-relief decreasing westward, narrow valleys, and closely spaced interfluves. (See Plate F-26.) The New River drains the Plateau here before cutting across water gaps in the folded Appalachians. (NMS) Additional References: Bird and Dewey (1970), Harris and Bayer (1979), Hatcher and Viele (1982), Hunt (1974, Ch. 11), King (1977, pp. 522-531), Suppe (1985), Williams and Hatcher (1982). HCMM 570-17380-1, November 17, 1979.



ORIGINAL PAGE IS
OF POOR QUALITY



ORIGINAL PAGE IS
OF POOR QUALITY

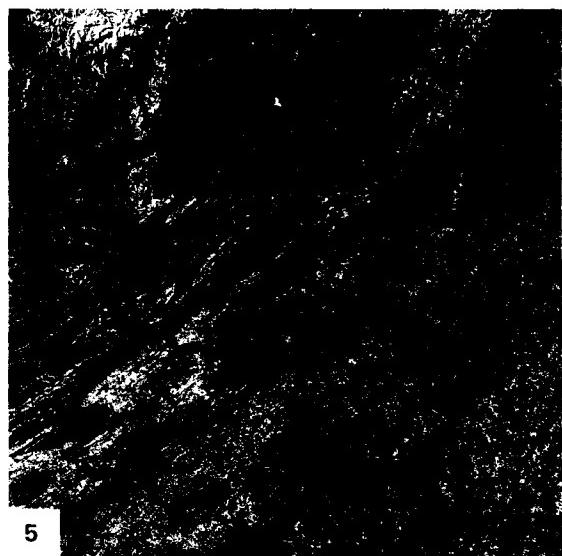
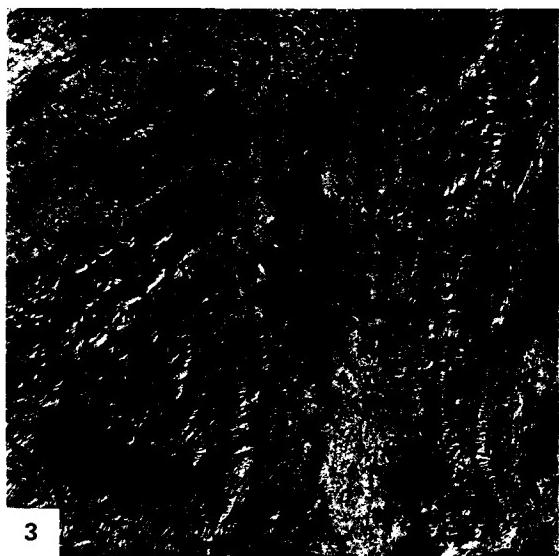


PLATE T-12

The mental picture of the Appalachian Mountains most of us have is that of long linear ridges and valleys that form a belt some 25 to 100 km wide through Pennsylvania/Virginia/West Virginia and the Carolinas. With relief of 300 to 1000 m or more, these ridges stand out as mountains, particularly obvious where they must be crossed by car on older highways. On a trip across the belt along the Pennsylvania Turnpike and other Interstates, one can observe the structural forms that have made the Valley and Ridge Province of the Appalachians synonymous with folded mountains. Outcrops almost invariably consist of inclined Paleozoic strata. Individual ridges may show reversal of dip, usually associated with secondary or smaller scale folding, but more commonly, the dips in a given ridge are essentially homoclinal, comprising only one limb of a larger anticline or syncline. The exact nature of the structure must usually be inferred or reconstructed by examining the stratigraphic sequence and bedding attitudes in successive ridges.

The Plate covers the well-exposed central Pennsylvania segment of the Valley and Ridge Province of the Appalachians. This foreland province, wedged between the Piedmont/Blue Ridge Provinces and composed of strongly metamorphosed rocks on the east and the uplifted but only mildly deformed sediments of the Appalachian Plateau on the west, runs the length of the Appalachian orogen from northern New York to Alabama. Within the belt, exposed rocks generally become increasingly older from west to east, but age discontinuities exist in parts of the belt because of complex thrusting and differential erosion. In the sections exposed in Pennsylvania, there are fewer thrusts than in the southern Appalachians and the southern end of the central Appalachians around Roanoke, Virginia (see Figure T-11.5). To the northeast, the diagnostic fold forms of the Valley and Ridge Province diminish rapidly in the vicinity of the Pocono Mountains of Pennsylvania and Catskills of New York (Plate T-11). A structural style similar to the folded Appalachians has developed along the Hudson/Champlain valleys, with differential erosion forming the "Little Folded Mountains," or Helderbergs, with the characteristic linear ridge forms.

Plate T-12 illustrates beautifully the effects of fluvial erosion on strata of unequal resistance that have been folded by continental collision. The long linear monoclinal ridges, held up by resistant sandstones and conglomerates, become zig-zag mountains as they wind around plunging fold noses; the short stubby zags are canoe-shaped synclinal noses, and the long gentle cigar-like noses are anticlines. The major ridge makers are the Tuscarora (T), Pocono (Po), and Pottsville (Pt) Formations. Benches (subsidiary ridges) can be seen on the inner sides of the main outlining ridge in anticlinal structures and on the outside

FOLDED APPALACHIANS

in synclines. Most ridges are monoclinal, and the dip of many can be determined by the difference in scarp and dip slopes. However, at many locations, strata dip so steeply that slopes on both sides of the crest are equal. The grain of the ridges makes it obvious that folding is much tighter on the east side of the province and broader and more open to the west. Offsets of some ridges indicate cross faults.

Nittany Valley and Morrison Cove, eroded anticlinal valleys (coves), near the western edge of the fold belt shown here, and Broadtop Mountain (a syncline east of Morrison Cove) are examples of inverse topography, which is common in this geomorphic province. Anticlines became breached, and the overlying sediments eroded down to the weak Cambrian/Ordovician carbonate strata, forming valleys. Synclinal structures, protected by the resistant Pottsville and Pocono Formations, become higher as less resistant rocks are eroded away around them.

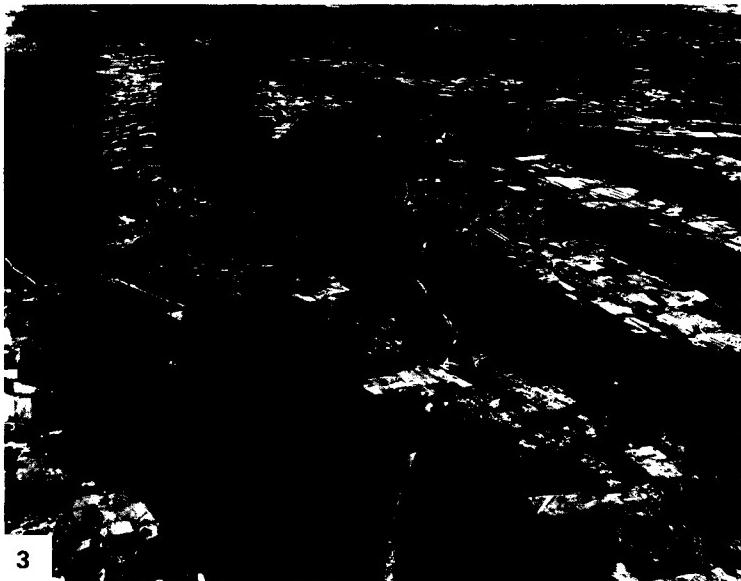
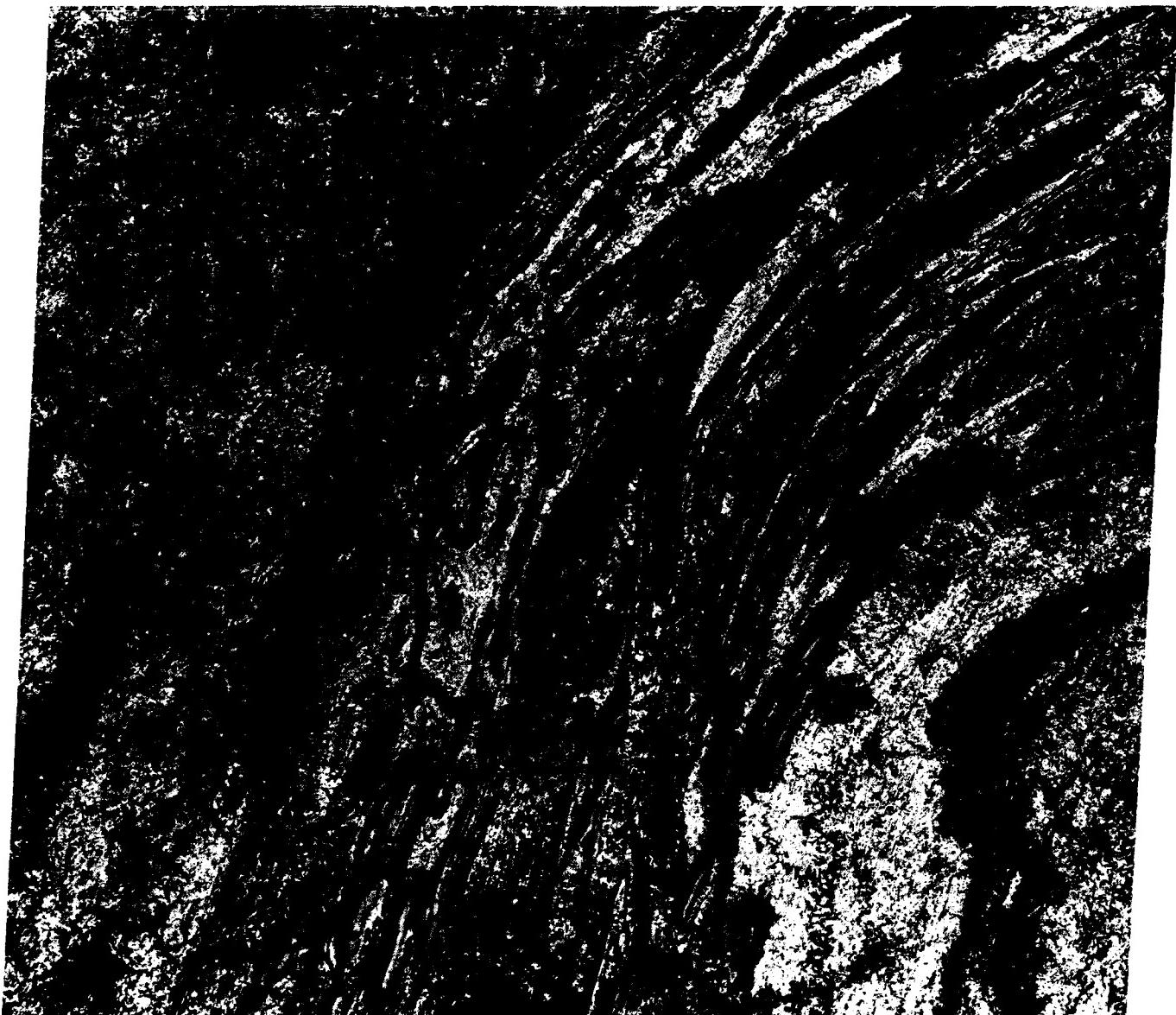
The overall trellis drainage pattern can be traced by careful scrutiny of the Plate and of a Seasat SAR image (Figure T-12.1, near Harrisburg) and an aircraft radar (X-band) image (Figure T-12.2, near Altoona), shown together for comparison. One of the major geomorphic problems of the folded Appalachians is the anomalous drainage, with transverse streams flowing across the structure, creating wind and water gaps. The Susquehanna River, the major river in the Plate and Figure T-12.1 seems to pay very little attention to structure and cuts right across major ridge-forming strata. However, note that the river does dodge around or cut close to the end of plunging noses as it makes its way southward (Figure T-12.3). In places, its major tributary, the Juniata, does the same. Both the Juniata and the Susquehanna are partially subsequent where they flow along strike valleys (oriented northeast-southwest). Moreover, it is also possible that the rivers are subsequent where they cut across a resistant ridge in a water gap. There are cross faults (offsets in the ridges), and the river may have discovered and utilized this weakness in carving its channel. In other places, the river channel may have been locally superimposed onto the underlying stratum. Another possibility is that the major southeast-flowing rivers were all superimposed from a regional coastal plain cover that extended westward (to the Appalachian Plateau?).

Another long-standing problem of the folded Appalachians is the origin of the accordant ridge summits and their evenness over long distances. Do these characteristics represent relic peneplains or are they the result of erosion on equally resistant beds? The question has not yet been resolved satisfactorily for all geomorphologists. (*NMS*) References: Fisher et al. (1970), King (1977), Rogers (1970), Suppe (1985), Thornbury (1965). Landsat 5377-14424-7, April 30, 1976.



ORIGINAL PAGE IS
OF POOR QUALITY

ORIGINAL PAGE
OF POOR QUALITY



3

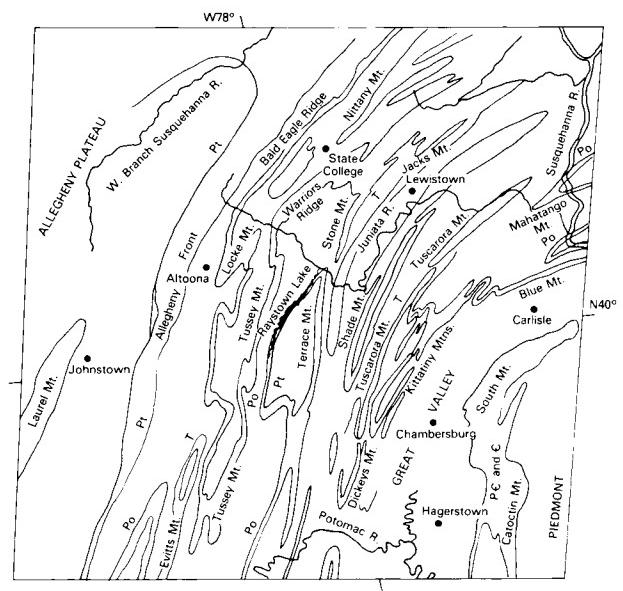


PLATE T-13

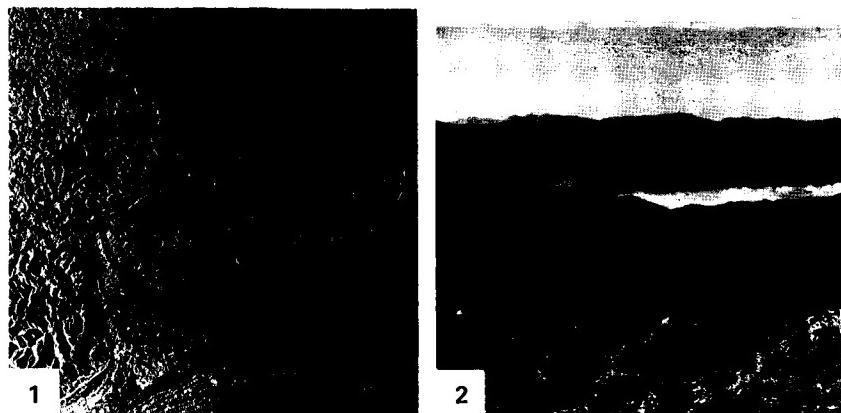
PINE MOUNTAIN THRUST

This two-frame mosaic of the northern end of the southern Appalachians further demonstrates the close relationship of topography and underlying structure in this orogen. Three major structural provinces—the Cumberland Plateau to the northwest, the Valley and Ridge, and the Blue Ridge at the southeast corner—coincide with physiographic provinces of the same names. Although the Valley and Ridge Province in Pennsylvania consists of plunging folds in a large anticlinorium, that province here includes numerous imbricated thrust sheets (see index map). The stratigraphic section exposed in this southern segment contains mainly Lower Paleozoic sedimentary rocks; the folds in Pennsylvania include younger units.

Deformation in much of the Appalachians is related to a master décollement zone that extends from under the continental shelf westward below the eastern Appalachian Plateau. Over most of the area, the detachment zone is a sole thrust just above crystalline basement. Imbricated thrust sheets, with east-dipping fault planes, developed progressively westward during at least two episodes of continent/continent convergence (Mid-Ordovician and Late Paleozoic time), carrying successive slices of older rocks over younger rocks. Although deformation in the Valley and Ridge Province is thin-skinned and apparently does not involve basement, it is characterized by folds and faults in the sedimentary cover.

The dominant feature in this scene is the Pine Mountain block, a rectangular structure about 200 km long and 40 km wide, thrust to the northwest along the Pine Mountain fault (PM). The Jacksboro (J) and Russell Fork (RF) strike-slip faults and Wallen Valley (WV) fault further bound the block. The master décollement thrust faults are stratigraphically controlled, rising in abrupt steps at ramps. The thrust planes are concentrated in thick fine-grained sediments of low viscosity and permeability (the Rome Formation, the Conasauga Group, and the Reedsville and Chattanooga Shales).

Topographically, Pine Mountain on the northwest and Cumberland Mountain on the southeast outline the fault block. The scarp slope on Pine Mountain faces northwest, with dip slope to the southeast; the steeper face on Cumberland Mountain faces southeast. The mountains thus form a syncline (the Middlesboro syncline) containing gently dipping Pennsylvanian coal beds. Within this structure is a 9-km circular depression, centered on the town of Middlesboro, that is an astrobleme (eroded impact crater). Southeast of the syncline, the Powell Valley anticline is a broad fold above a structural ramp with Cambro-Ordovician carbonate rocks at the surface. Drilling indicates that the Pine Mountain sole thrust is about 2 km higher under the rootless anticline than east of the ramps.



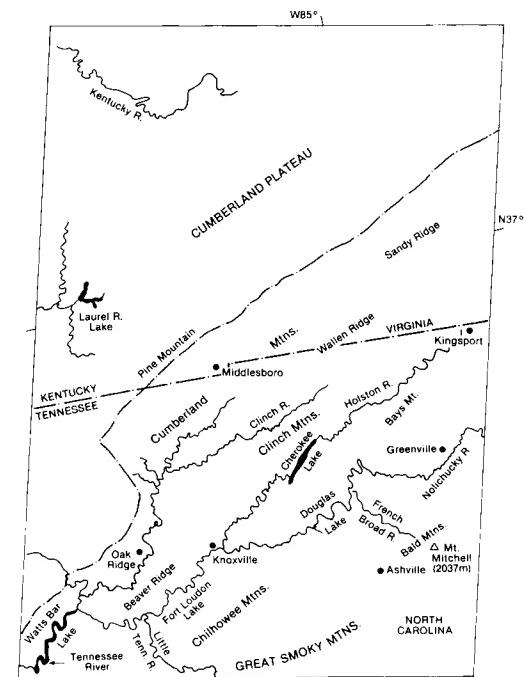
A Seasat radar image (Figure T-13.1) presents a different perspective on the topography in and around the Pine Mountain fault zone (Ford, 1980). In particular, it emphasizes differences in drainage texture between the thrusts and folds to the east and the flat-lying rocks of the Appalachian plateau to the west.

In the Valley and Ridge Province extending northeast across the image, resistant sandstones form strike ridges roughly parallel to the thrust planes. Each successively eastward fault carries older rocks over younger units to the west. These faults probably merge with the master décollement at depth. Numerous cross faults cause offsets or disappearances of ridges. The Great Valley of Tennessee is approximately equivalent to the Shenandoah Valley in northern Virginia; both are controlled by the presence of more erodible limestones.

The southeast corner of the scene shows the Great Smoky and Holston Mountain faults that comprise the northwest boundary of the Blue Ridge Province. The crystalline Blue Ridge block of Precambrian to Lower Paleozoic metamorphic rocks is a single allochthonous thrust sheet 10 to 20 km thick that overrode previously emplaced Valley and Ridge units (visible as whitish terrain in the image where several windows (e.g., Caves Cove) cut through the overlying thrust).

The Smoky Mountains are among the most spectacular in the Appalachians (Figure T-13.2). Mount Mitchell (2037 m) and Clingman's Dome (2025 m) are the highest in the Appalachians. The high relief and dendritic drainage result from deep downcutting into relatively homogeneous crystalline rocks.

Present topography throughout the Appalachians has developed mainly in the last few million years. Although larger streams cross structural units, the landforms in each province are well adjusted to the dominant lithologies and structures on which the drainage networks are imposed. Historic Cumberland Gap, shown as a reentrant on Cumberland Mountain, is a wind gap. Whether it was formed by a north- or south-flowing stream is debatable. (NMS) Additional References: Harris and Bayer (1979), Harris and Milici (1977), King et al. (1968), Rich (1933). Landsat Mosaic.



ORIGINAL PAGE
COLOR PHOTOGRAPH



PLATE T-14

ORIGINAL PAGE COLOR PHOTOGRAPH

OUACHITA MOUNTAINS

The second great segment of the depositional/deformational trough that lay along the convergent Paleozoic eastern and southern margins of the North American craton is the Ouachita orogenic system (Viele, 1973). The segment begins at a structural recess now buried under the eastern side of the Mississippi Embayment, swings northwestward, and then turns westward through the 360-km long Ouachita mountain belt of Arkansas and eastern Oklahoma, the western portion of which is seen in this Plate. It then turns southwestward (the change in trend is visible near the center of the Plate) through central Texas and extends west to the Marathon uplift. The Sierra Madre Oriental of the northeastern Mexican Cordillera truncates the trend in northern Mexico.

Both segments have considerable thicknesses of Lower Paleozoic carbonate sediments (in the scene, about 2000 m) with decreased deposition during the Middle Paleozoic, although thick clastic wedges built up on the interior side of the central and southern Appalachians. In Paleozoic times, convergence, and consequently orogenic activity, progressed from northeast to southwest. In the Ouachita segment, subsidence increased progressively through Mississippian to Mid-Pennsylvanian times, leading to the accumulation of as much as 10000 m of clastic sediments. These turbidite deposits were derived from land areas to the southeast and east (Europe/Africa). Orogenic activity culminated in Late Pennsylvanian/Permian time.

The scene here shows the western end of the exposed Ouachita Mountains around McAlester in eastern Oklahoma, where mountains exceed 800 m in elevation, and local relief may be up to 500 m. The northern edge of unconformably offlapping Cretaceous sedimentary units, which dip south, abruptly obscure Ouachita structure along the southern edge of the mountains. These Cretaceous rocks also bury the eastern section, the Ardmore basin, of the Wichita aulacogen.

The structure across the Ouachitas, beautifully etched out by differential erosion, resembles the deformation patterns of the southern Appalachians (Plate T-11). Several major faults are named in the index map. A series of thrust sheets carry Mississippian and Pennsylvanian units, usually over younger beds. Traces

of the thrust faults that join sole faults at depth are especially evident. One major thrust detachment overlies Lower Paleozoic rocks; elsewhere, these units are brought to the surface by folding. Spacing between individual imbricated sheets is greater to the south and decreases to the north in the Pennsylvanian units southeast and east of McAlester. The Upper Paleozoic strata are strongly folded (with some overturning) within each sheet, giving rise to closed plunging anticlines (A) and synclines (B and C). Most of the linear ridges associated with folds and thrusts are resistant units of the chert-bearing Pennsylvanian Jackfork formation. The Potato Hills are an inlier of Devonian rocks exposed probably as a fenster through a thrust sheet on an anticlinal node. Cambrian/Devonian rocks, including ridge-forming cherts, also crop out around Broken Bow Lake and form an extensive central core to the anticlinorium in the Arkansas section of the Ouachitas.

North of the Choctaw thrust, the structure changes to a synclinorium with gentler, more open folds developed in the Atoka, Stanley, and Jackfork shales and sandstones of Pennsylvanian age. There, in the Arkoma basin, the Arkansas River valley follows the general east-west trend of the fold axes. Both folding and faulting decrease northward as this section of the Ouachitas gradually merges with the homoclinal south flank of the Boston Mountains. Relief also diminishes, but some mountains still exceed 700 m in elevation.

Topography is similar to that of the folded Appalachians with homoclinal and generally linear ridges, but curved around plunging noses. Although it is difficult to determine dip on homoclinal ridges in the anticlinorium because of steepness of dip, scarp and dip slopes are more easily determined in the gentler folds. Trellis drainage is prevalent with subsequent strike valleys and crosscutting water gaps. Many ridges are breached at faults, manifested by offsets of the ridge line. These details are apparent in a real aperture airborne radar image (Figure T-14.1) and a Seasat SAR image (Figure T-14.2) of an area in Arkansas to the east. (NMS) References: Cebull and Shurbet (1980), Keller and Cebull (1972), King (1977), Thornbury (1965, Ch. 15), Viele (1973). Landsat 1146-16300-7, December 16, 1972.



1

ORIGINAL PAGE
COLOR PHOTOGRAPH

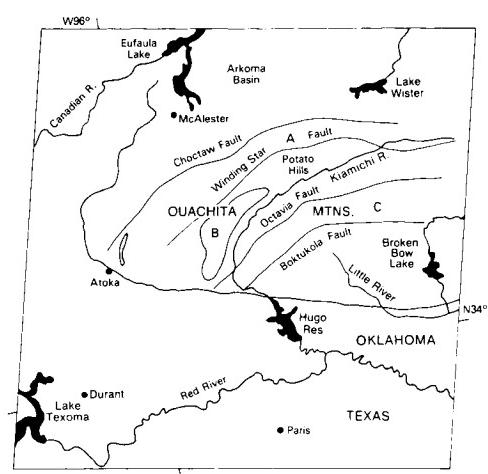
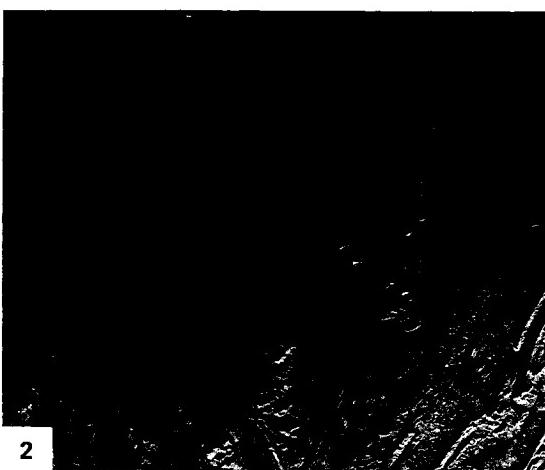


PLATE T-15

This scene boldly portrays the fault-controlled boundary between the oldest (Superior) and youngest (Grenville) structural provinces of the Canadian Shield. When viewed regionally, the two provinces differ in the number (density) and orientation of megalineaments, and as revealed here, the tectonic zone of contact between them appears to show its own characteristic fracture patterns. Prominent megalineaments in the Superior Province trend north-northeast, and those of the Grenville trend north-northwest. Both sets of lineaments are separated by a region with a dominant east-northeast topographic grain. Folds are indicated by the topographic patterns along the southern border of the image.

Terrain developed on the rocks of the Superior Province in this part of western Quebec is a low, nearly flat erosional plain reduced over the last 2.5 Ga by stream erosion and glaciation. Although today's surface has been strongly affected by Pleistocene glacial events, it is actually an ancient peneplain that has undergone only moderate erosion since the Superior cratonic nucleus stabilized at the close of the Archean. The relative smoothness of the surface suggests that the underlying rocks are more homogeneous in terms of resistance to erosion than those of the Grenville Province. Most rocks making up this segment of the province are igneous and medium grade (greenschist to amphibolite) metamorphic bodies derived 3.4 to 2.5 Ga ago. Supracrustal sediments (graywackes, shales, and iron formation) and volcanics were laid down in active mobile troughs or sags, many controlled by faults. In the north of this scene are metavolcanics of the Keewatin greenstone belts that probably once underlaid an island arc. Metasediments are dominant in the Pontiac Gneiss belt whose K/Ar ages of about 2.5 Ga relate them to metamorphism accompanying the Kenoran orogeny that climaxed the history of the province.

Following this orogeny and subsequent episodic uplifts, intensive erosion for the next 600 to 700 Ma swept away great volumes of weathered material from the initially mountainous terrain. Some of this material accumulated in basins in what is presumed to be the Grenvillian basement. The Grenville Province underwent deformation and igneous intrusion during the Hudsonian orogeny (~1.8 Ga). Anorthosites were emplaced over several limited time spans centering around 1400 Ma ago. The Grenville Province assumed its present character starting about 1200 Ma ago, with orogenic climax in the interval 1050 to 950 Ma ago, which transformed the sedimentary rocks and older volcanic, intrusive, and metamorphic rocks in the region into a metamorphic assemblage that attains amphibolite to granulite facies levels, along with migmatites and new intrusives. The entire province seems to have been shoved northward against the Southern

GRENVILLE FRONT

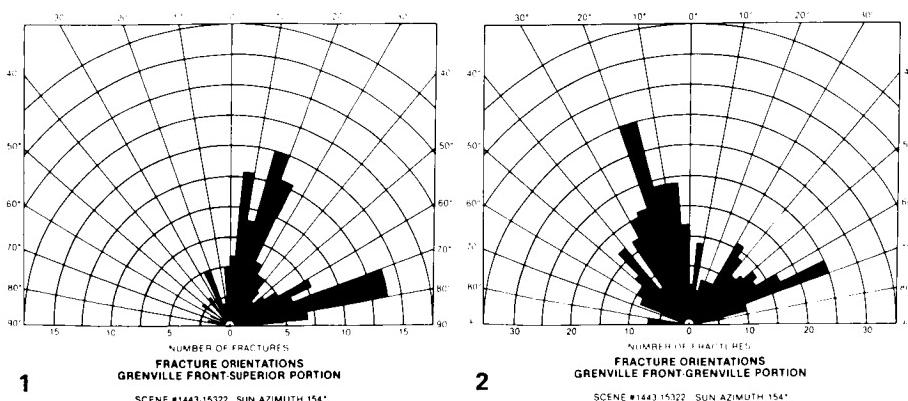
Superior, Churchill, and Nain Provinces along a vast accretionary zone along the southeast and east margins of the North American proto-continent.

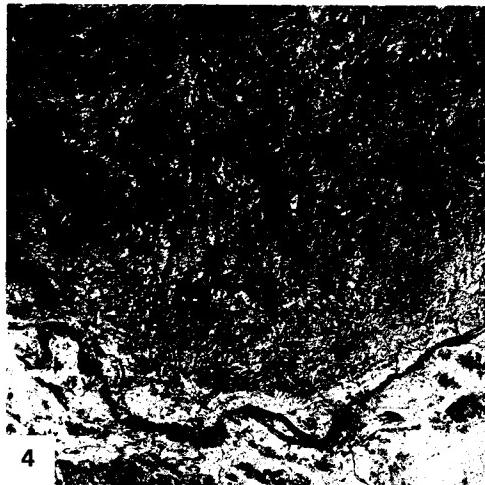
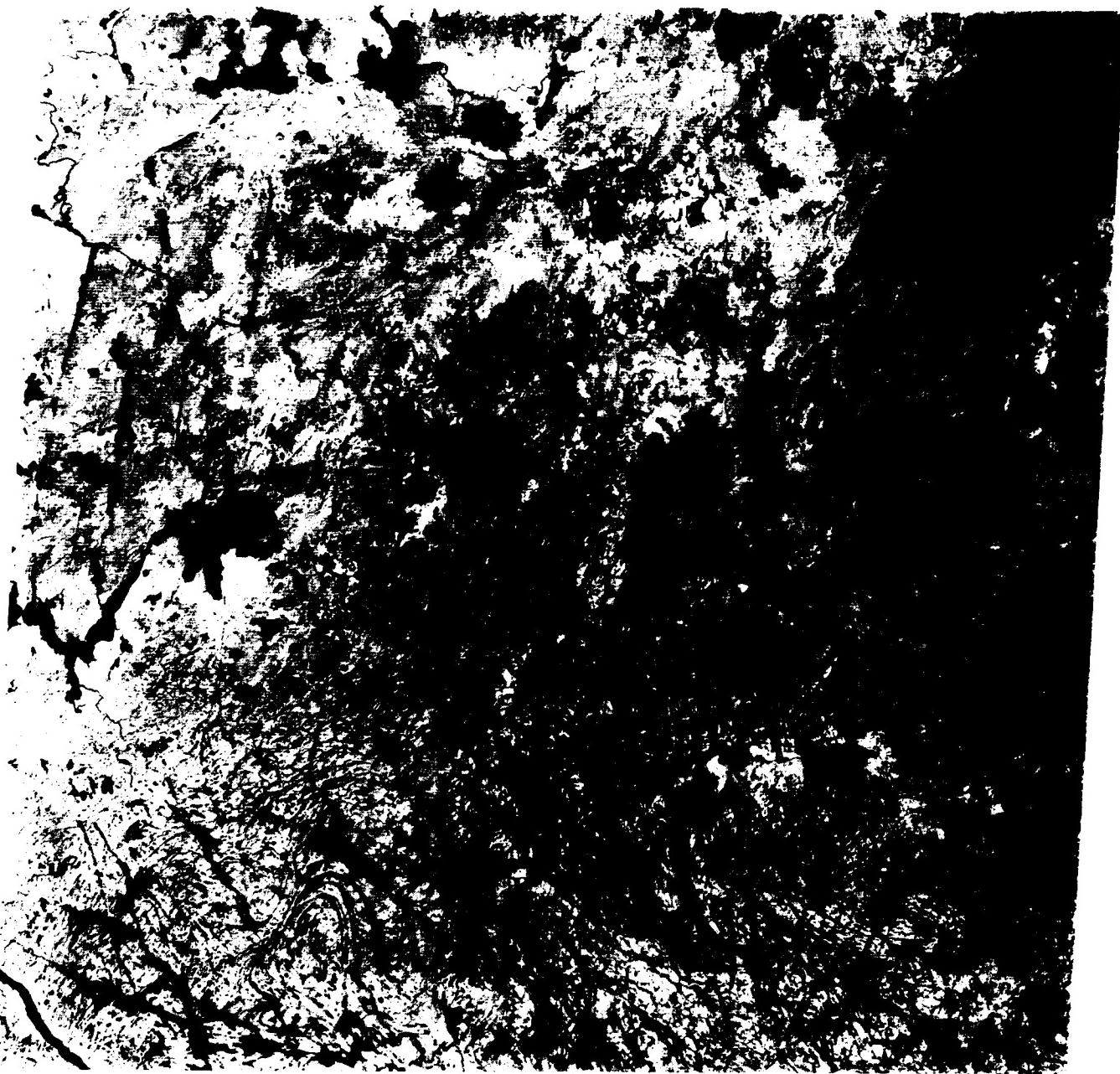
In the northern part of the image, the Quebec Gneiss belt typifies the Grenville Province in structure and lithology. Near Cabonga Reservoir, a swirled body of plutonic rocks is surrounded by foliated metavolcanic and metasedimentary rocks. To the southwest, the Ontario Gneiss belt is dominantly meta-sedimentary. The Kipawa syncline block is a conspicuous plunging steep fold with kyanite-garnet gneisses and quartzites in the core.

The Grenville Front itself is a zone from 20 to 30 km wide, with increased metamorphic effects in rocks on both the Superior and Grenville sides. In places, a recognizable fault zone with mylonites—the Boundary fault—defines the actual contact. The fault varies between a high-angle reverse and a thrust that dips southeast. Elsewhere, the best evidence for the discontinuity comes from abrupt changes in metamorphic grade, with higher intensities in the Grenville Province. Foliation, as well as a number of megafractures, trends northeast.

A plot of megalineament orientations (Figure T-15.1 and T-15.2) within the two principal provinces reveals significant differences. A north-northeast trend in strike characterizes Superior rocks and a north-northwest trend marks those of the Grenville. The east-northeast secondary trend noted in the two rose diagrams is associated with the boundary zone between provinces. Most visible lineaments owe their expression to glacial scouring of zones of weakness (such as close-spaced fractures), which produced depressions later filled with lakes (Figure T-15.3) (black in Landsat IR images) or bogs (darker gray).

Elevations in the Grenville Province range between 350 and 650 m, with relief sometimes exceeding 150 m locally. Rounded ridges and knobs are common; these have been partially shaped by glaciation. Low areas contain glacial fill. Forests consist of maple and pine in the south that give way to spruce and fir northward. A typical Grenvillian landscape of more rugged hills is shown in Figure T-15.4, which is a Landsat-4 Thematic Mapper (TM) image of the edge of the Shield north of Ottawa, west of the Laurentian Mountains. This image is southeast of the previous Landsat images and shows how erosion has differentially etched out the folded metasediments. The fracture density in this TM scene is almost double that identifiable in a Landsat Multispectral Scanner (MSS) image, taken 7 years earlier on almost the same date, owing to the better resolution and a light dusting of snow. (NMS) References: Baer (1981), Irving and Donaldson (1972), Osborne and Morin (1962), Wynne-Edwards (1972). Landsat 1443-15322-7, October 8, 1973.





4

ORIGINAL PAGE IS
OF POOR QUALITY

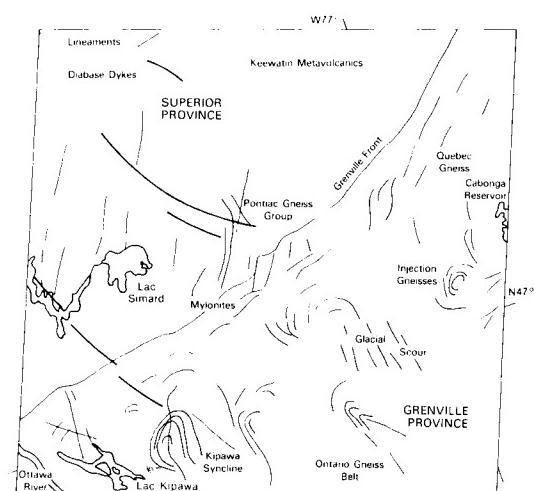


PLATE T-16

Like much of the Canadian Shield, the region in this image and in Figure T-16.1 is one of low relief, resulting from eons of erosion and Pleistocene glaciation. The effect of structure and lithology on erosional topography (Bird, 1972) is brought out in a low-Sun-angle midwinter Landsat-4 image (Figure T-16.1). Glacial scour along bedding contacts in the fold belt produced most of the linear lakes, thus emphasizing the form of folding through the tonal contrast between water or snow and rock (Figures T-16.2 and T-16.3; vertical and oblique aerial photographs, respectively). Glacial cover overlies and "smooths" some of the surface. Fractured terrain of the Churchill Province (upper right corner of the Plate) is quite similar to that of the Superior Province (lower left). Both have low knobby hills. As seen from Landsat, the interaction of fracture-producing tectonism, differential stream erosion, and glacial action in this part of the shield is well expressed by the topography evident in the two Labrador Trough images and in the neighboring Nain Province to the east (Figure T-16.4).

Although one cannot identify the rock types present in the Landsat scenes, the topographic texture clearly distinguishes four major groups of rocks—those in the Superior Province, the juxtaposed miogeosynclinal and eugeosynclinal facies of the Trough, and the Churchill Province. Both topographic orientation and texture suggest that the Churchill and Superior rocks are much more integrated (metamorphically homogenized) than either of the geosynclinal units and that contrasts in erosional resistance are greater among sedimentary rocks of the miogeosyncline than those of volcanic origin in the eugeosyncline.

It is interesting to compare the appearance of the Labrador Trough to that of the other orogens in this chapter, particularly the Appalachians to the south. In general, the rocks of the Labrador Trough are more tightly folded and have a finer grained topographic texture than those of the Appalachians. The Labrador orogen is much narrower than younger orogens. The fine versus coarse texture of eugeosynclinal versus miogeosynclinal appears to be true of other orogens.

This Proterozoic orogen is unusual in that it represents deformation of a sedimentary sequence that accumulated entirely

LABRADOR TROUGH

on continental crust (Gastil et al., 1960). Although ophiolite-like assemblages are present, the crust in this part of the Canadian Shield did not rift enough to allow emplacement of new oceanic crust. Thus, the Labrador Trough is more akin to intracratonic basins like the Michigan Basin than to the Appalachians.

The Labrador Trough constitutes the eastern segment of the Circum-Ungava belt that wraps around much of the northern Superior Province of eastern Canada (Dimroth, 1970). It was a linear deposition basin that lay between the Archean Ungava craton on the west and the eastern continuation of the Churchill Province. The Grenville Province overrides (?) the trough on the south and does not quite abut against the southwestern edge of the Nain Province.

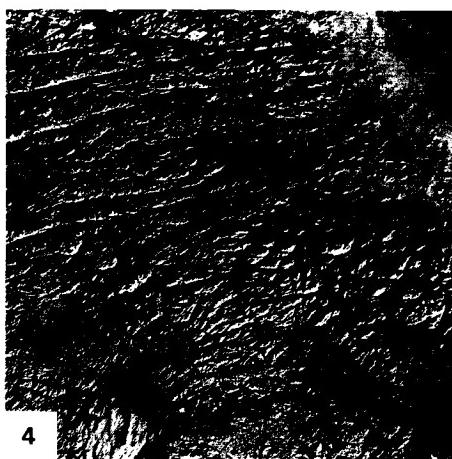
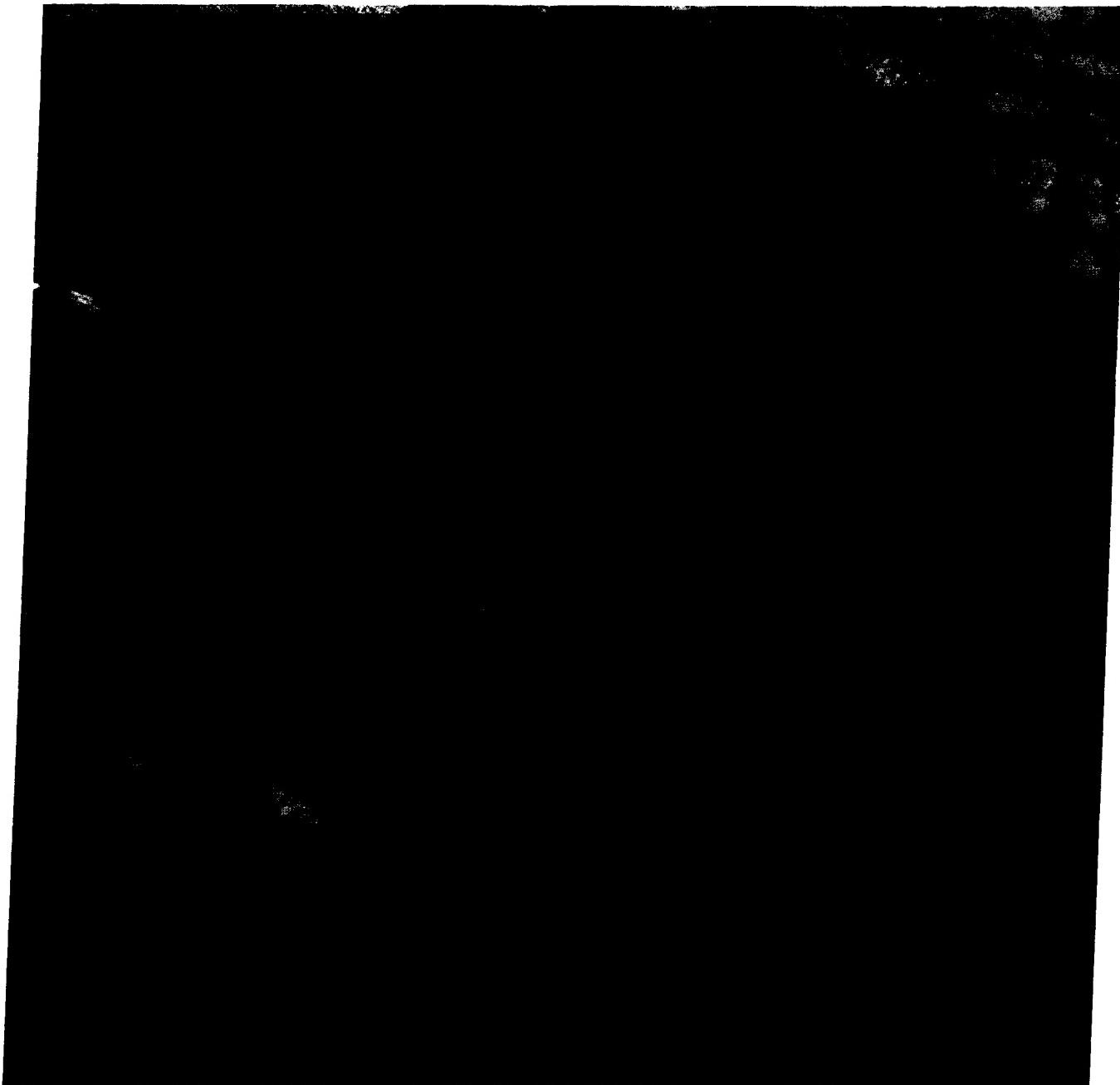
As subsidence progressed slowly, a well-defined miogeosyncline formed on the west side, with a eugeosyncline of similar width on the east. Sediments dominate the miogeosyncline, whereas volcanic rocks are predominant in the eugeosyncline. These facies accumulated through most of the Aphebian Era of the Lower Proterozoic, and all rest on crystalline sialic basement of Archean gneisses. The miogeosynclinal rocks include some banded iron formation (BIF), which occurs in huge deposits around Schefferville.

Deformation of the trough (initially about 200 km wide) was contemporaneous with the Hudsonian orogeny (1800 to 1600 Ma). This converted the eastern zone into a large synclinorium with strong folding in the miogeosynclinal zone, compressing the trough to its present width of 80 to 120 km. Folds range from open to tight (isoclinal), and many are doubly plunging (conspicuous patterns in the space images and aerial photograph). High-angle thrusting is common in the western zone, in places producing repeated sequences, with eugeosynclinal units overriding westward. A major low-angle thrust forms a tectonic boundary between the geosynclinal facies. Field relations, including the presence of staurolite, kyanite, and sillimanite (diagnostic of higher pressure mineral assemblage), indicate a continent/continent collision. (NMS) Landsat 1438-15013-6, October 4, 1973.

ORIGINAL PAGE IS
OF POOR QUALITY



ORIGINAL PAGE IS
OF POOR QUALITY



4

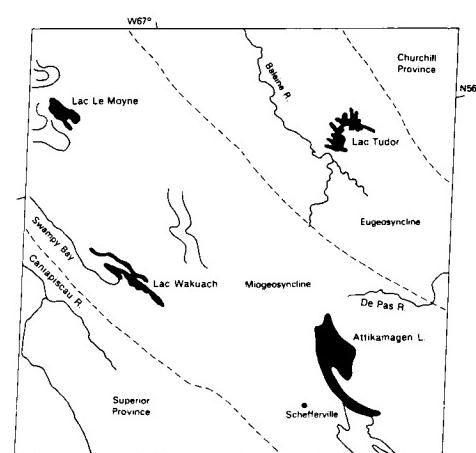


PLATE T-17

WESTERN CANADIAN SHIELD

This extraordinary image convincingly conveys the value of the combination of low (winter) Sun angle (09°) and snow cover in accentuating the fracture patterns in an ancient craton or shield terrane. The scene lies athwart the Arctic Circle (hence, almost no forest) south of the Coronation Gulf, Northwest Territories of Canada, across from Victoria Island. Two of the seven major age provinces of the Canadian Shield—Bear Province (left) and Slave Province (right)—are juxtaposed along a sharp boundary (suture line?) that also stands as a topographic scarp, the result of differential erosion. These provinces differ in several respects:

1. Surface rocks in the Slave Province are mainly Archean. Isotopic ages cluster around 2500 Ma—the Kenoran orogeny that marked the end of the Archean in North America. Ages of rocks in the Bear Province average 1750 Ma—the Hudsonian orogeny.

2. As evident from the index map, rocks comprising the Slave Province represent a high grade of metamorphism, intrusion, and basement remobilization typical of Archean terranes. Many of these rocks are metamorphosed members of the sedimentary Yellowknife Supergroup. Rocks of the Bear Province are mainly metasedimentary and volcanic, deformed in the Aphebian Era. A few outliers of these Lower Proterozoic rocks remain on the Slave Province, particularly around Lake Contwayo.

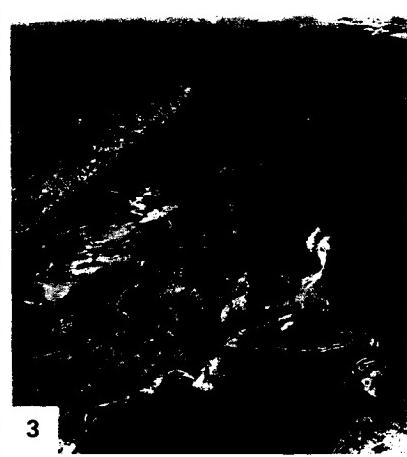
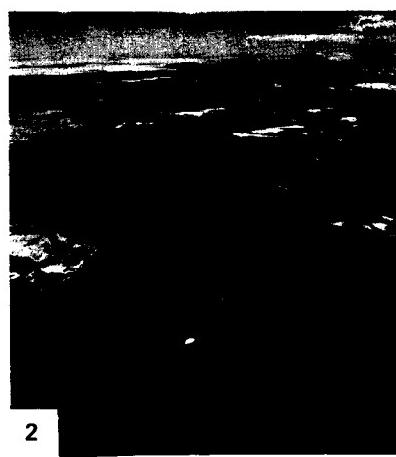
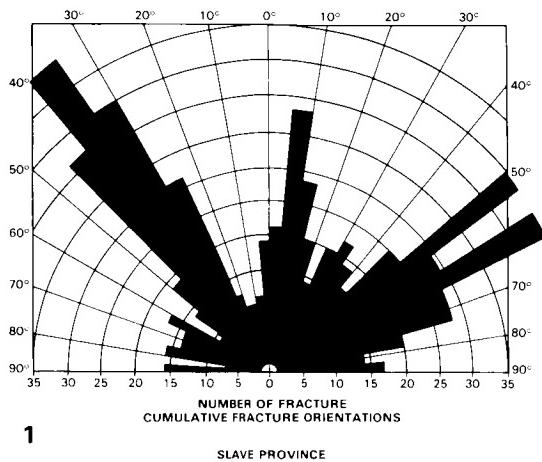
3. The structural style in the Slave Province is that associated with deep crustal units. Migmatites, batholithic intrusives, and granulitic metamorphic rocks show foliation and compositional banding, but the rocks are rather uniformly hard and so thoroughly deformed that little foliation is expressed in landforms at this scale. Most Yellowknife Supergroup metasediments are tightly folded (isoclinal) or occur in plunging anticlines (see lower right corner). The Bear Province rocks are both folded and strongly foliated (approximately parallel to fold-axis trends), giving rise to a pronounced north-south grain that has a subdued but strongly linear topographic expression.

The lineaments in the Slave Province are clearly expressed because of glacial scouring which removed most of the soil cover and excavated the bedrock along lines of weakness. The density of fractures is the highest the writer has seen at this scale in Landsat imagery. Orientation measurements (Figure T-17.1) reveal three dominant directions (Lowman et al., 1986). Many lineaments can be traced for 50 km or more; where intersections are

observable, offsets are rarely seen, supporting the hypothesis that these are tensional fractures without planar slip. A prominent zone of lineaments running vertically through the image center corresponds to a dike-like intrusion of metamorphosed volcanic rocks. The rose diagram for the Bear Province shows almost identical orientations (adjustments were made for the foliation trends) but much lower densities. Note the large “patch” of Archean rock along the Coronation Gulf; its identity is disclosed by its fracture density. In both provinces, the principal orientation trend is northwest; in the field, numerous younger (1100 to 1200 Ma) Proterozoic diabase dikes (not distinguishable from fractures in image) occupy lineaments of that trend.

Both provinces have surfaces of low relief (Figure T-17.2), but the average elevation of the Slave Province is higher (up to 670 m) than the lowlands of the Bear Province (relief 100 m). The present surface is an exhumed Precambrian erosion surface (slightly modified) developed at the end of the Archean, now exposed after removal of later Aphebian and Phanerozoic cover rocks. Ridges with steep slopes are produced from resistant Late Archean diabase/gabbro intrusions along linear zones within the eastern section of the Bear Province. Erosional remnants of large sills appear as flat plate-like plateaus along the Gulf.

The southern edge of the Slave Province 600 km to the south abruptly meets the younger (1.6 Ga) Churchill Province (farther south) along the MacDonald fault, a major crustal break traceable for more than 500 km into the shield. This fault (Figure T-17.3) stands out at the surface as a conspicuous scarp more than 100 m high in places. The same scarp can be followed in a Landsat image as a bold trace, without apparent relief, along the southeast side of the Great Slave Lake (Figure T-17.4). There, most of the rocks in the Slave Province are granitic with subordinate Yellowknife metasedimentary and volcanic rocks. The rocks in the Churchill Province are also primarily granites and gneisses, but Aphebian metasediments occur in isolated patches, such as along Taltson Lake (lower right). The arc-like units within Great Slave Lake are Aphebian and Helikian (younger) basin sediments and intrusive gabbros. As is typical in glaciated shield terrain, glacial plucking has emphasized the linear fractures, and water now fills the topographic lows. (NMS) Additional References: Fraser et al. (1970), Hoffman et al. (1970), McGlynn and Henderson (1972). Landsat 1206-18381-7, February 14, 1973.



ORIGINAL PAGE IS
OF POOR QUALITY

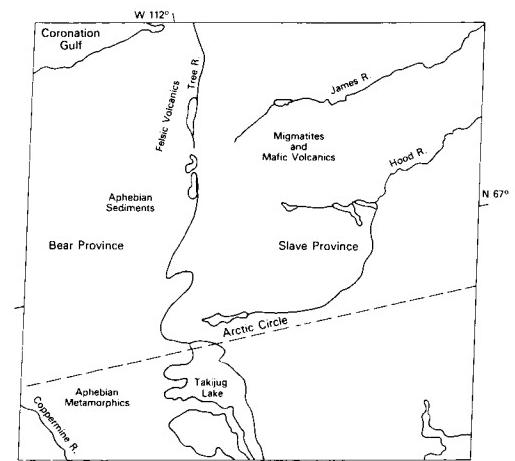
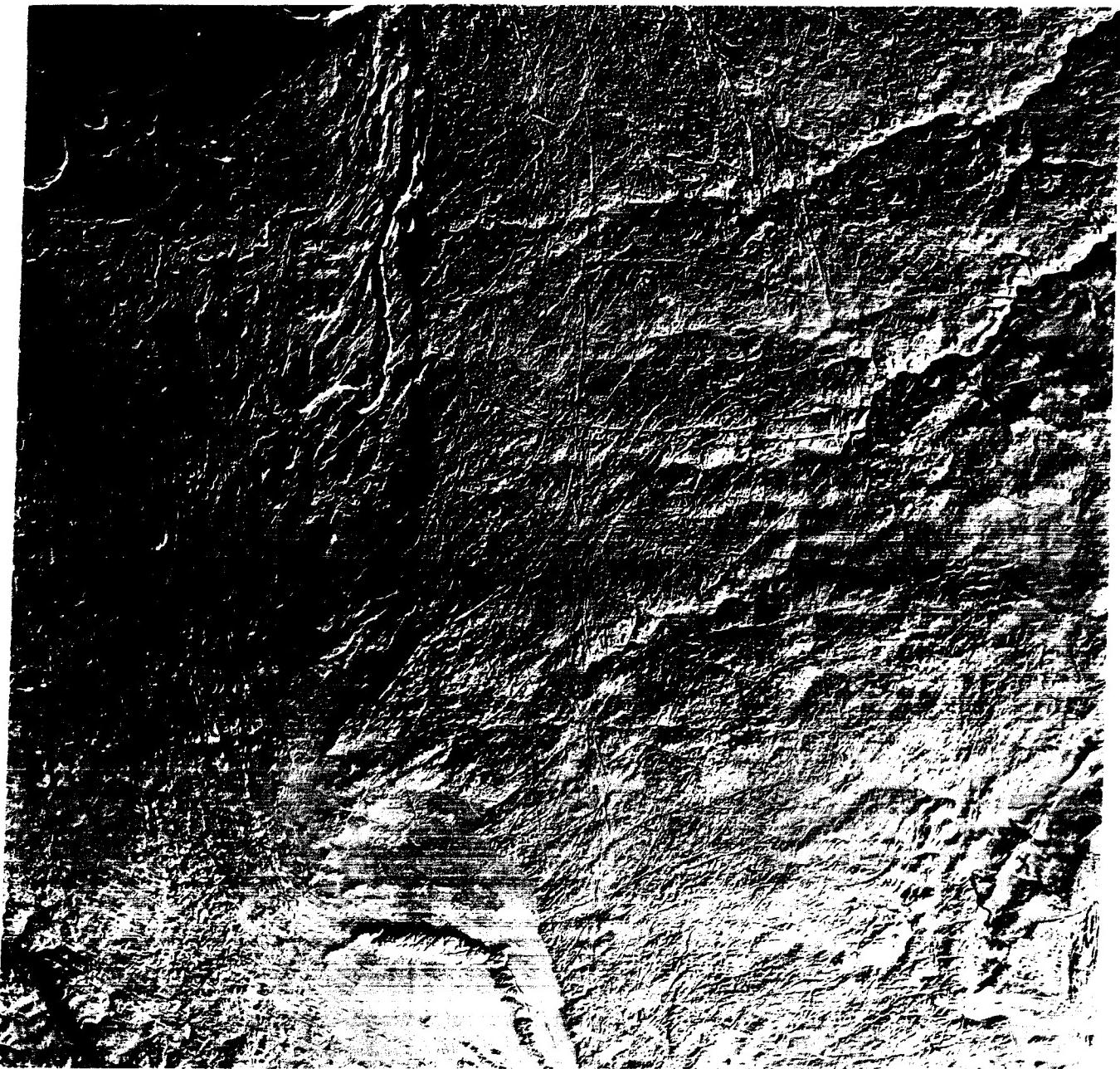


PLATE T-18

Contrast in rock types, lack of soil, and sparseness of vegetation makes the Bathurst Island Group a superbly exposed example of the interference of two fold belts. These islands lie near the center of an extensive group of islands north of mainland Canada known collectively as the Arctic Archipelago. The Bathurst group, approximately 17500 km² in area, is centered about 76° latitude and 100°W longitude (Dunbar and Greenaway, 1956).

Vegetation on the island is restricted to lichens, mosses, and a few hardy species such as sedge and Arctic willow that grow only a few inches in height. Although the environment is extremely harsh, substantial vegetative cover is present on parts of the island. Clearly, some lithologies provide a more favorable environment for plant growth than others. The limestones and dolomites are essentially barren. Sandstones tend to support lichens, and the siltstones and shales support grasses and shrubs.

Structurally, Bathurst Island lies at the eastern terminus of the Parry Island fold belt, a unique 450-km long structural province consisting of uniformly folded broad synclines and narrow anticlines. The axes of several of these structures exceed 300 km in length.

These east-northeast-trending structures, so prominent in the western portion of the island, end abruptly near the east side of the island against north-south-trending folds and faults (Kerr and Temple, 1974). Figure T-18.1, an aerial oblique photograph, shows the relationships very well. The anticline adjacent to Stuart River (right center) is faulted along its axis so as to join subsidiary anticlines on either side of the river. The north-trending folds are on the west flank of the Cornwallis fold belt, a sediment-covered northward extension of the Boothia uplift, whose major structural features had their origin in Precambrian time. Unconformities show that repeated periods of uplift have occurred in the Cornwallis fold belt; several during the Devonian, but also as late as Pennsylvanian/Permian time (Kerr and Christie, 1965).

The younger Parry Island fold belt was formed by compressive forces in essentially a north-south direction during the Ellesmerian orogeny. The folding was accentuated by décollement movement in a Middle Ordovician evaporite sequence more than 1000 m deep.

Strata exposed on the island consist of dolomite, limestone, shales, siltstone, and sandstones. On the Landsat image, the rocks

BATHURST ISLAND GROUP

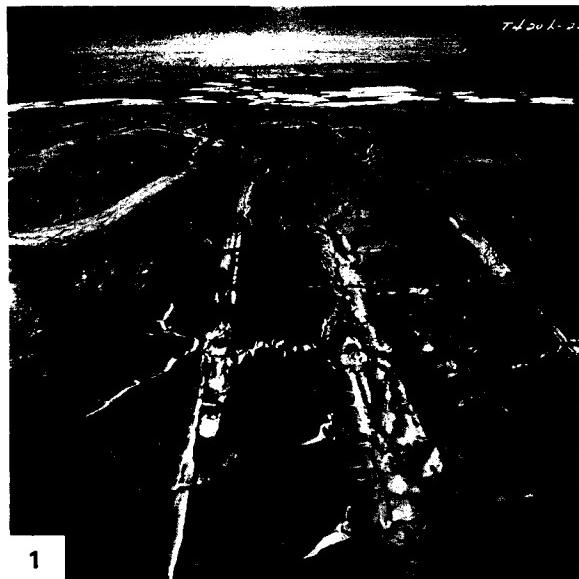
shown are almost entirely Devonian with minor exposures of Ordovician beds in the cores of a few of the anticlines around May Inlet.

The prevalent rock type in the southern and eastern portions of the island is dolomite. The light-toned resistant beds exposed on the flanks of the structures near the upper end of Erskine Inlet are quartz sandstone. In this area, the dark grays, normally indicative of shales, are predominantly sandstones. The dark color undoubtedly results from an extensive growth of black and green lichens that favor the resistant sandstone outcrops. The light-colored quartz sandstone is too friable to form the hard, enduring substrate necessary for the slow-growing lichens.

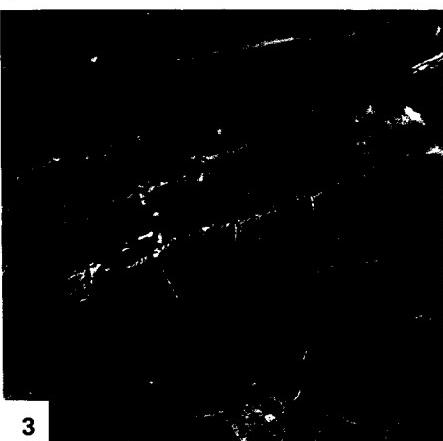
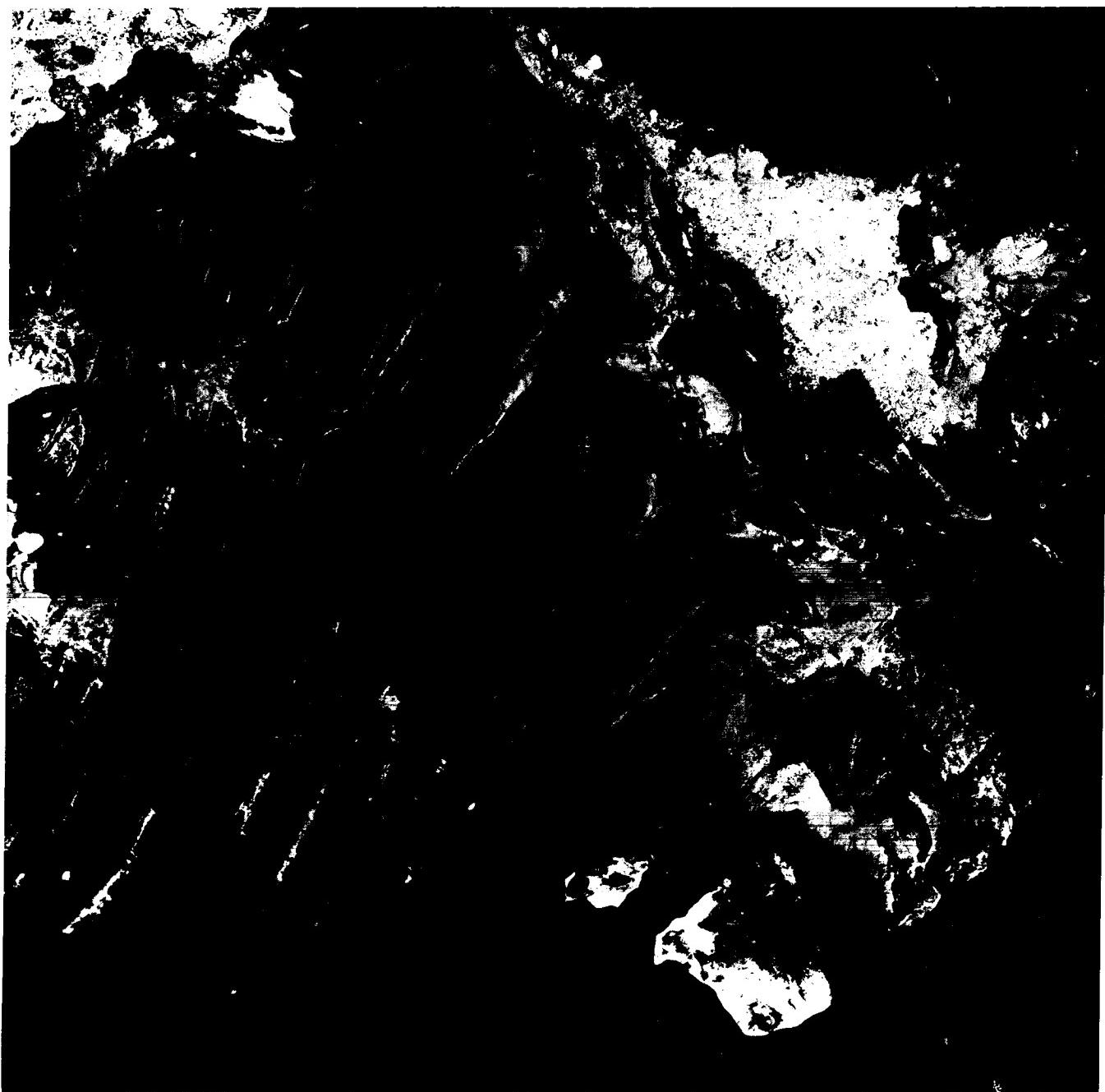
Two physiographic units appear in this image; a Southern Plateau lying south of a line extending from just south of Bracebridge Inlet eastward to the central portion of McDougall Sound, and a Folded Upland comprising the rest of the island group.

The Folded Upland is characterized by low rounded ridges and valleys resulting from differential erosion of the tilted strata of the Parry Island fold belt (Figures T-18.2 and T-18.3). Dips can be determined by scarps infacing on anticlines and outfacing on synclines. Much of the secondary drainage is controlled by and parallels the strata, giving rise to a trellis pattern. At least two major drainage systems on the island flowed northward during the Ice Age when the sea level was at least 100 m lower. These drainage systems are now drowned and are known as Erskine and May Inlets.

Hills in the uplands are generally smooth and broadly rounded and rarely exceed elevations of 300 m. They are dissected by deep steep-walled gullies and canyons, an erosional form common in much of the Arctic, as evident in the ancillary figures. Although the Landsat image shows excellent definition of lithologic units, good *in situ* exposures are absent on the ground. Deep mechanical weathering has broken, scattered, and disintegrated outcrop material to the extent that much of the surface is composed of fields of boulders called *felsenmeer*. Ironically, in this area, one can delineate geologic units better from 900 km above the ground than on the surface. (Actual identification of the mapped units would depend on ground work.) Some stream captures have occurred on the broad upland; others are imminent. (GCW: O. R. Russell) Landsat 20943-18161-7, August 8, 1977.



ORIGINAL PAGE IS
OF POOR QUALITY



3

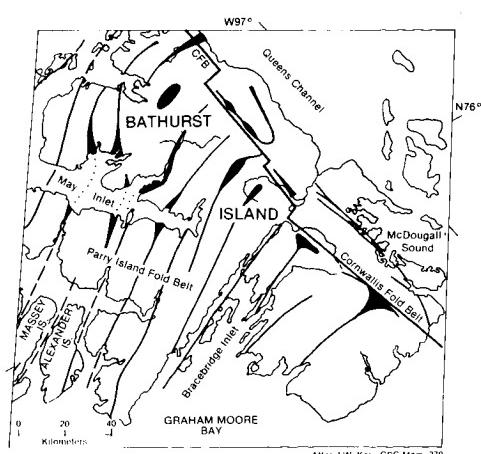


PLATE T-19

ORIGINAL PAGE IS
OF POOR QUALITY

SIERRA MADRE ORIENTAL

This low-Sun-angle scene, which straddles the Mexican states of Coahuila and Nueva León, depicts graphically the prominent structural features associated with the Sierra Madre Oriental. The Sierra Madre Oriental in this region is an excellent example of the wrinkled-rug style of décollement folding produced above a relatively shallow detachment zone. This orogenic belt represents the easternmost extension of the North American Cordillera. In Mexico, the Cordillera divides into the western Sierra Madre Occidental and the eastern Sierra Madre Oriental, separated by the southern extension of the Basin and Range and the Central Mesa before joining with the Sierra Madre del Sur, which then passes into the Central American orogenic belt. The Sierra Madre Oriental trends northwest over most of its length, but splits abruptly in this scene into a western branch and the Cross Ranges, then northward to rejoin the trend in the Basin and Range section.

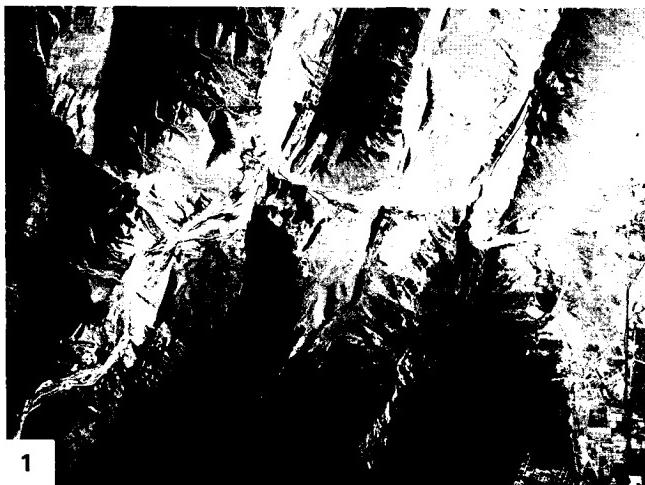
The scene contains Jurassic to Cretaceous age rock units and younger basin fill. Paleozoic rocks presumably underlie the exposed Mesozoic units. After limited Triassic sedimentation (mostly in grabens), this region gradually submerged as the Atlantic opened to form the Mexican geosyncline, which ties into the depositional troughs of the U.S. Cordillera to the north. The eugeosyncline lay to the west (roughly where the Sierra Madre Occidental exists today) of the miogeosynclinal zone now occupied by the Sierra Madre Oriental. Deformation (thrusting and gravity slide folds) affected the eugeosyncline in Jurassic times, even as the present Gulf of Mexico began to open up to the east. Molasse sedimentation characterizes Jurassic deposits in eastern Mexico. By Mid-Cretaceous, marine waters had inundated most of Mexico, depositing carbonates (including reef units) and evaporites. Metamorphism and uplift of the eugeosyncline (Baja California region) in the Late Cretaceous provided coarser clastics carried eastward as flysch that spread over the shallowing miogeosyncline. The scene lies athwart a broad foreland basin that filled with clastic and carbonate rocks from the Jurassic to Early Eocene. The Eocene Hidalgoan orogeny, coeval with the late phase of the Laramide orogeny, produced the folds and thrusts evident in this image. Graben faulting followed, with flysch deposits accumulating in the structural basins while molasse clastics spread over the eastern coastal plains into the Gulf.

Several structural styles are discernible in this scene. Differential erosion has etched out less resistant rocks, leaving resistant ridges that outline the folds. Synclinal noses are broad arcs; anticlinal noses are sharper and longer. Many breached anticlines are evident. Gentler dipping synclinal beds show scarp and dip slopes. South of Monterrey is a belt of tight folds, part of an

anticlinorium, dominated by east-west anticlinal mountains (up to 3500 m high) composed of predominantly limestone units that dip steeply in exposed vertical to overturned folds (Figures T-10.1 and T-19.2, a vertical aerial and a ground photograph, respectively). These structures are made up mostly of Lower Cretaceous rocks with Jurassic rocks exposed in breached plunging anticlines and Upper Cretaceous rocks in intervening synclines. To the west, the Parras basin, which extends from Saltillo westward beyond the image, contains Upper Cretaceous sandstones and carbonates that form ridges whose outlines define open plunging synclines. Even broader synclines (Figure T-19.3) are found in the Paredon basin (Plate image center). The main belt of the northwest-trending folds in the Sierra Madre Oriental spreads across the top of the image. Most of the individual mountain units are anticlinal. Erosion has breached several (e.g., S. del Fraile) of these to varying extents. Sierra de Minas Viejas and others have Jurassic units exposed in their cores as salt-gypsum evaporite beds. The Sierra de La Paila is a broad domal arch of Lower Cretaceous rocks over a Tertiary intrusion.

Conjecture abounds on the reason for the deflection of fold trends in this part of Sierra Madre Oriental. Although the style of folding around Saltillo, Monterrey, and Paredon is clearly that of décollement, the underlying cause of the deflection is unclear. Several factors may have played a role, including gravity sliding off uplifted basement blocks, the distribution of evaporite units in the area, and, possibly most important, movement on the west-northwest-trending Torreon/Monterrey fracture zone. This left-lateral fault system that developed in the Early Mesozoic may have influenced distribution of the evaporite basins and controlled the deflection of the fold trends. Regardless of origin or mechanism, the resulting structures in this scene make up one of the most striking displays of tectonic landforms anywhere on the North American continent.

Figure T-19.1 is a vertical air photograph of the area south of Monterrey that shows the near vertical ridge of Cretaceous limestones. The syncline is ringed by out-facing scarps. Rivers anomalously cut across the structure. Figure T-19.2 highlights some of these ridges in the Huasteca Canyon area. Figure T-19.3 is a vertical aerial photograph of the small basin to the east-northeast of Paredon and shows the spectacular degree to which differential erosion has etched out the complicated structure of this arid area. (NMS) References: Baker (1971), McBride *et al.* (1974), Mitre-Salazar (1981). Landsat 1508-16410-6, December 13, 1973.

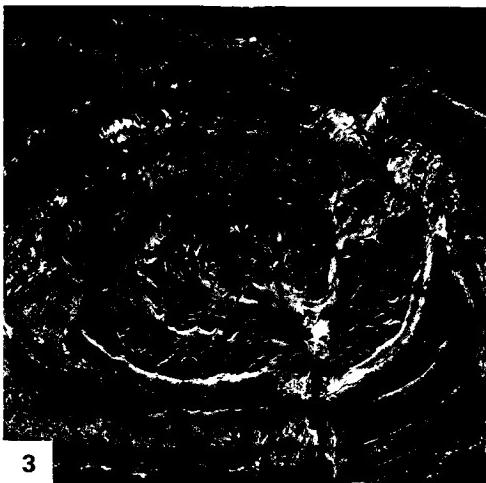


1



2

ORIGINAL PAGE IS
OF POOR QUALITY



3

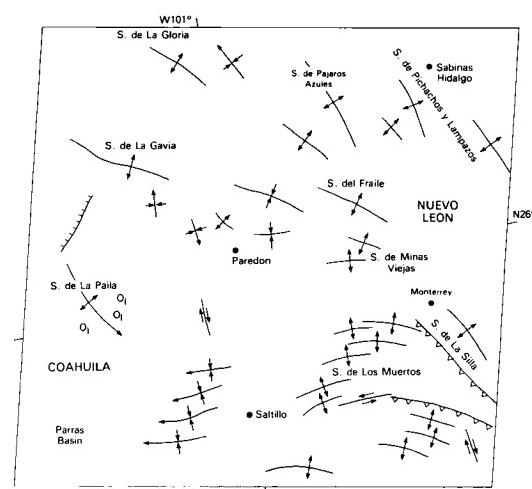


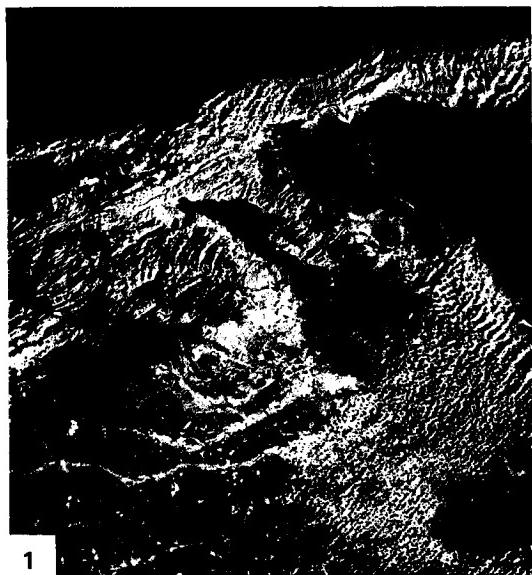
PLATE T-20

The terrain displayed in this Landsat mosaic of the northern coast of Colombia is dominated by the Sierra Nevada de Santa Marta. At 5800 m, the Sierra Nevada de Santa Marta is the highest point in Colombia, although it is immediately adjacent to the ocean. Truly an impressive feature, the Sierra is the result of recent and continuing tectonism of very large scale. The oldest exposed rocks in the Sierra are Precambrian plutonic rocks. The remainder of the core is made up of Triassic and Jurassic plutonic, volcanic, and sedimentary rocks. The mountain mass has moved (in a relative sense) in a northwest direction so that it now sits over a portion of Caribbean oceanic crust. The movement has occurred along the right-lateral Oca Fault and the left-lateral Santa Marta/Bucaramanga fault system. As readily seen in the imagery, the transition from mountainous terrain to flat lowland occurs abruptly across these two major fault systems. Behind the mountain to the southeast lies the valley of the Rio Cesar. This is a low-relief valley whose center lies at less than 100 m above sea level. It separates the Sierra Nevada de Santa Marta from the Serrania de Perija, whose major peaks rise to 3600 m. The valley of the Rio Cesar is a tectonic depression bounded perhaps by a series of faults with predominantly normal displacement. However, there is evidence of a component of strike-slip motion, especially on the faults that bound the south side of the valley. This evidence consists primarily of en echelon folds and minor thrusting on the north flank of the Serrania de Perija. The formation of the Serrania de Perija seems to be wrench-controlled and related to the formation of the Cordillera Oriental of Colombia, whose main body lies to the south. In contrast, the Sierra Nevada de Santa Marta is related to convergence of this portion of South America with the Caribbean plate. The Sierra would

SIERRA NEVADA DE SANTA MARTA

therefore be the result of underthrusting of the Caribbean plate, causing uplift of the mountain mass with attendant strike-slip motion along the Oca and Santa Marta/Bucaramanga fault systems. In the scene, the Sierra are being jammed into the corner formed by intersecting conjugate strike-slip faults (Bonini et al., 1984; Burke et al., 1984; Giegengack, 1984). Figure T-20.1 is a Landsat image of the eastern end of the right-lateral fault system that runs across northern South America. The Bocono/Araya/Paria faults, although separate from the Oca fault, have the same trend and sense of movement.

The other dominant feature on this image is the extensive lowlands area adjacent to the Sierra Nevada de Santa Marta that extends westward to the Rio Magdalena. Much of these lowlands, especially adjacent to the river, is swampy. East of Barranquilla, Cienaga Grande is a prime example of one of these swamps in what appears to be depressions formed by extensional tectonics. The structural relations seen on the image indicate that these swamps are not simple floodplain features, but rather water blockages controlled by extensive normal faulting. Figure T-20.2 pans across one of these depressions to the Sierra Nevada de Santa Marta. This faulting creates a series of graben features adjacent to the Rio Magdalena within which the swamps form. Although considerably smaller, these areas appear to have the same type of structural control that gives rise to the rhombic graben shape of the Gulf of Venezuela and Lake Maracaibo to the east. This system of graben features is typical along the course of the Rio Magdalena at least as far upstream as Barrancabermeja. In fact, much of Colombian oil production comes from fields related to these structures along the middle reaches of the Magdalena. (GCW: S. J. Prucha) **Landsat Mosaic.**



1



2

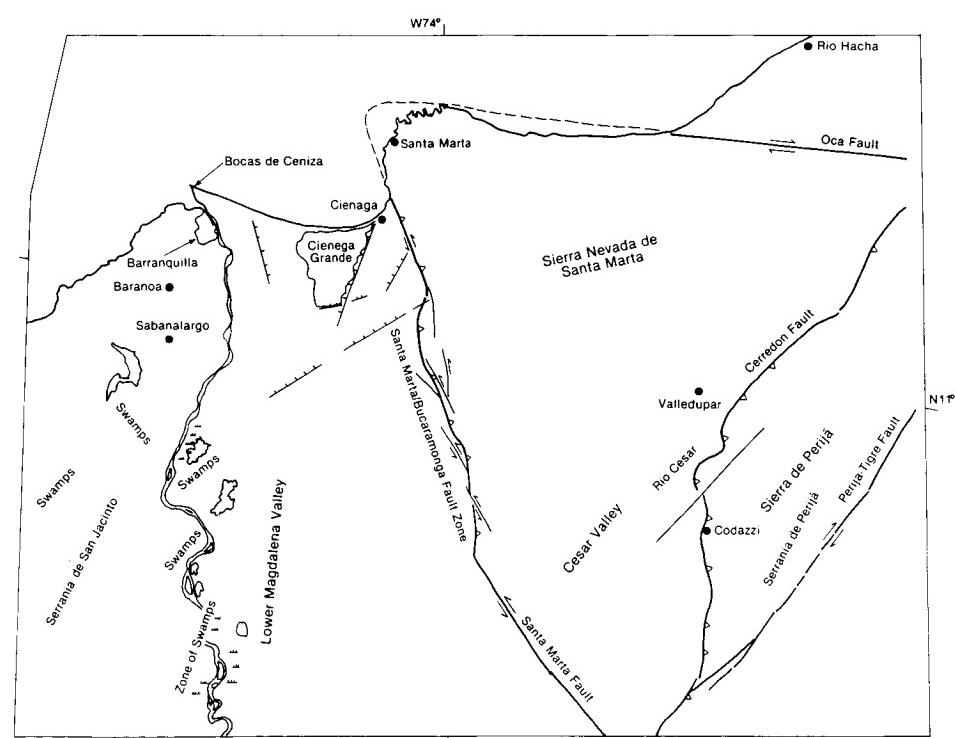


PLATE T-21

BOLIVIAN ANDES

The Peru/Chile trench, a major tectonic feature extending some 8000 km from the coast of western Colombia to Tierra del Fuego, marks the convergent boundary between the Nazca and South American plates. The Andean Cordillera rimming the western edge of the continent appears to be a textbook example of a simple plate tectonic model. Topographically, the Andes are essentially a post-Miocene feature; however, as a structural entity, they were not uniformly built up in either time or space, but are a complex of orogenic belts superimposed on each other since the Precambrian. At present, it is not clear how uplift is related to the subducting Nazca plate; crustal thickening, volcanism, plutonism, and thermal expansion all appear to play a role.

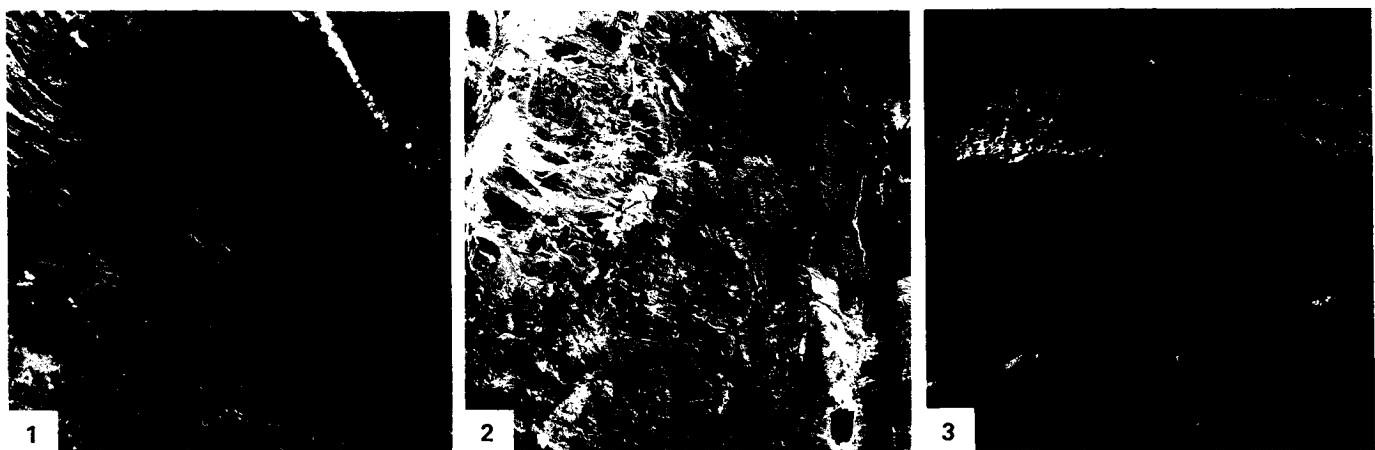
The subducting plate consists of a series of tongue-like sections 300 to 1000 km wide, with varying degrees of dip. The complexities of the subduction zones are clearly reflected in the tectonics of the leading edge of the continent. The Andes consist of one to three ranges or cordillera. In several locations, the ranges are cut transversely by large east-west deflections or megashears. These offsets may reflect the shape of the presubduction continental margin or postsubduction offset of the subduction zone.

Near the border between Peru and Chile, both the coastline and interior Andean ranges change from an approximately north-south trend in Chile to a northwest-southeast trend in Peru, a change of over 45° . This bend has been called the Arica Elbow and appears to be a major deflection zone running inland from the Chilean coastal town of Arica. The Plate is a Landsat Mosaic (28 frames) that encompasses the Andean Cordillera around this great bend. The overlap shows parts of four South American countries lying within the scene. The major geological provinces of the central Andes have been superimposed on this scene in lieu of an index map. Line A-A locates a strip of SIR-A radar imagery, placed under the mosaic, that provides more structural and topographic detail across the Eastern Cordillera. Figure T-21.1 highlights part of this elbow zone east of the Altiplano in south-central Bolivia. The northward-trending Chilean/Argentinian Andes along the left side of the image bend northwestward to form the Peruvian Andes that continue essentially in this direction to the Ecuadorian border. From southwest to northeast, the mountains are primarily composed of highly folded and faulted Ordovician, Silurian, and Devonian sedimentary rocks. The topographic grain that sweeps around this elbow in a large "S" curve is the result of differential erosion etching out many imbricate thrust faults and the tilted and folded sedimentary rocks involved in the faulting. In the southwest corner of the scene,

younger volcanic and volcanoclastic rocks mask the underlying structure. Much of the younger faulting parallel with the trend of the cordillera in this section is either high-angle normal or reverse associated with uplift. Farther to the east in the Andean Foredeep area, the faulting becomes exclusively high-angle reverse. The relatively flat terrain in the bottom left quadrant consists of Tertiary volcanics on the eastern edge of the Altiplano southeast of Lago Poopo. The Bolivian city of Sucre is located in the lower left center of the image. The important mining center of Potosí appears at the bottom center edge of the image on a bulge caused by a Tertiary intrusion, which is the source of the rich mineralization.

Figure T-21.2, another Landsat view of the Bolivian Andes lying south of the Figure T-21.1 scene, shows an area where the cordillera starts to swing uniformly northwest. Two large faulted basins are evident, with interior drainage and large alluvial fans. The lake (lower right) just inside Argentina lies on the Altiplano (Puna) in one of the faulted basins between ridges of folded and thrust-faulted sedimentary rocks. West of the deformed sedimentary rocks are several large volcanic edifices (one of which shows excellent radial drainage), numerous small craters, and wide areas of smooth topography that include large alluvial fans and pediments, tuff sheets, and basin fill.

An oblique photograph (Figure T-21.3), taken during the Apollo 7 mission, looks east over Chile toward Argentina at the region just south of the mosaic. Lying on the South American plate adjacent to the Antarctic plates, this area also exhibits tectonically controlled geomorphology. This photograph shows a strong topographic zonation due to successive deformational events affecting the rocks of the plate margin. The band of topography behind (east of) the Salar de Atacama (center left margin) is a result of differential erosion of basic volcanic rocks topped by numerous recent volcanoes. These volcanoes and the associated effusive rocks are Pliocene to Quaternary in age. Both west and east of this band are belts of rocks deformed at the plate margin. Perhaps the most notable morphologic feature in the photograph is the right-lateral Atacama fault (near the coast), which forms a sharp topographic low along its length. The fault, as it cuts along the peninsula, is delineated by a linear ridge. Figure T-21.4 shows the same peninsula, fault, and inland Desierto de Atacama from the vertical perspective of Landsat. (GCW: R. Allenby) References: Cobbing and Pitcher (1972), Lohmann (1970), Kulm et al. (1981), Zeil (1979). Landsat Mosaic.



ORIGINAL PAGE IS
OF POOR QUALITY

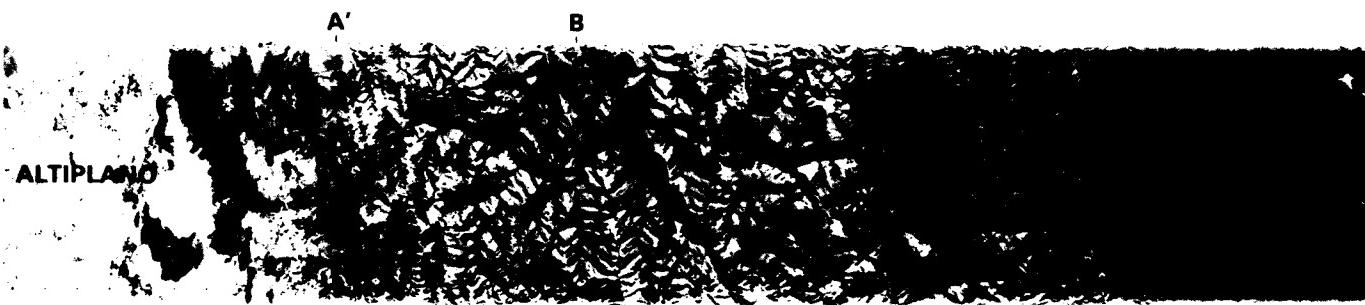
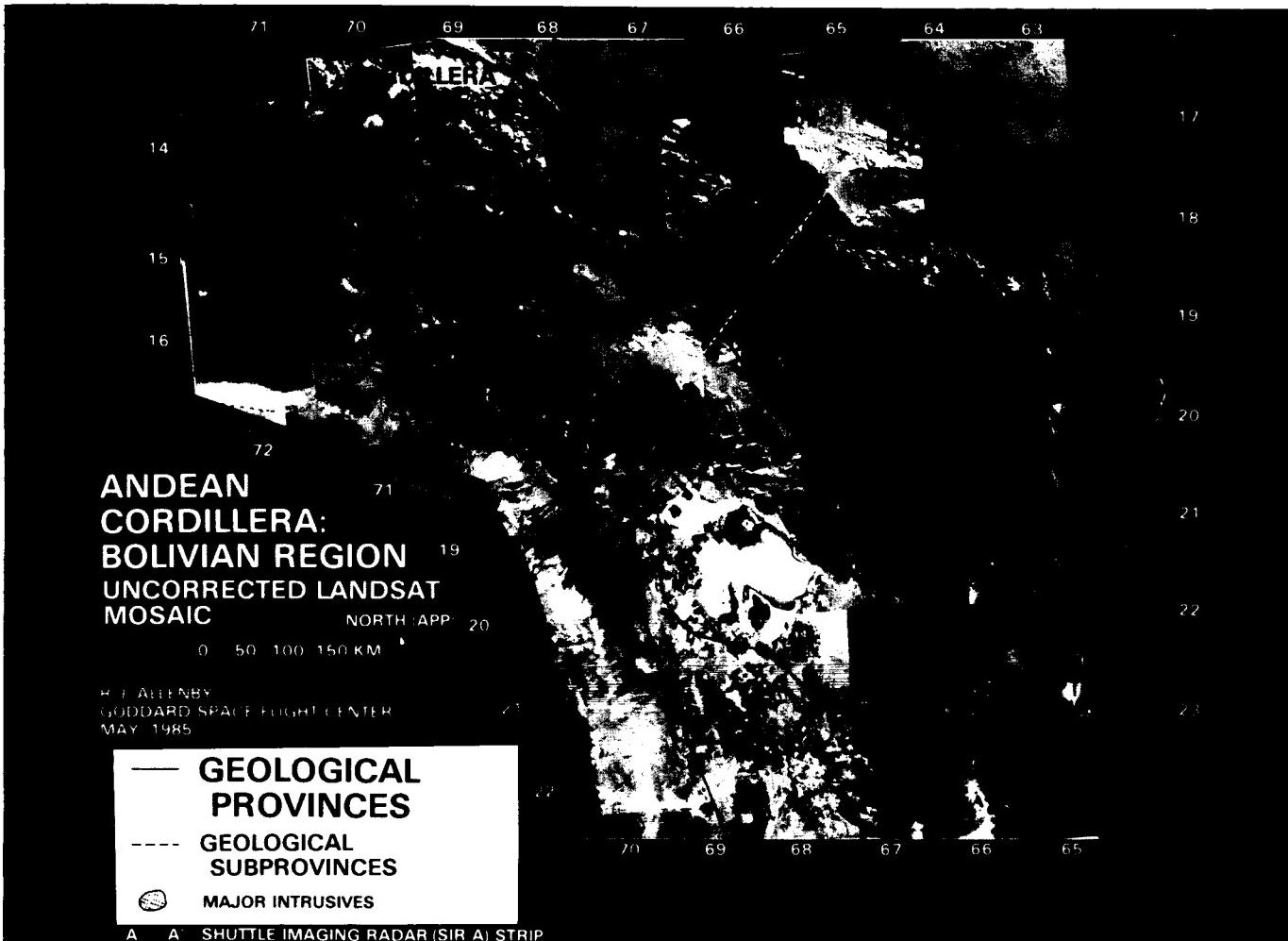


PLATE T-22

ANDEAN CORDILLERA

This Plate covers a portion of western Peru in the Western Cordillera. Virtually all of the landforms encompassed by the image can be related to plate interactions. To the west, the Nazca plate is subducting beneath this portion of the South American plate. This action has produced a progression of events well portrayed in the geology and geomorphology of the area. The image shows five distinct northwest-trending morphotectonic bands, which correspond to differing rock types and ages of deformation that ultimately form the spectacular landforms in this segment of the Andes Chain.

The first band, the Cordillera Central, drained by the Rio Huallaga, contains the oldest rocks in the scene. These Precambrian rocks were first deformed in the Middle and Late Paleozoic. Andean tectonic activity subsequently has deformed the same area. This multiplicity of events has so churned these phyllites and schists that they now have a fine-grained nondescript geomorphic texture with only a few through-going structural features. However, one northwest-trending and several east-trending lineaments indicate faults. Separated from the foredeep to the northeast by a thrust fault along the Rio Huallaga, this area experienced the first Andean deformational pulses during subduction of the Nazca plate in this part of South America.

The Rio Marañon flows along a fault trace for most of its length on the image, separating these older rocks from younger, less deformed rocks to the west. Jurassic, Cretaceous, and younger strata dominate this second band of rocks between the Rio Marañon and the Cordillera Blanca farther west. These rocks have been affected by fewer deformational pulses than the areas to the northeast and consequently appear to have more coherent structure that can be traced across the image in the topography. The main deformational event for this region is known as the Inca Phase and spans Middle Eocene to Early Oligocene time. The deformation has produced long northwest-trending folds, as well as a number of east-directed thrusts. Erosion along the thrust traces and less resistant beds has given rise to a geomorphology characterized by long northwest-trending linear mountains with relatively little crosscutting drainage (Figure T-22.1). The area is not as finely dissected as the area northeast of the Rio Marañon.

The third morphotectonic band on the image is the Cordillera Blanca. This mountain range, the highest in the area,

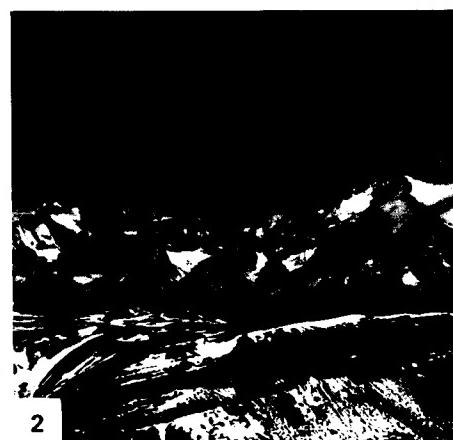
reaches 7000 m. The Cordillera Blanca is composed mainly of Tertiary intrusive rocks. It is part of the Coastal Batholith, emplaced by generation of magma from the subducting Nazca plate. The intrusive rocks of the Cordillera Blanca have been uplifted along normal faults and glaciated (Figure T-22.2). Some glaciers and a substantial amount of snow still cover the peaks (thus, the name Cordillera Blanca).

The fourth distinct band on the image is sandwiched between the Cordillera Blanca to the northeast and Cordillera Negra to the southwest. This band of mainly Quaternary volcanic rocks comprises most of the eastern portion of the Rio Santa Valley. Referred to as the Callejon de Huaylas, this valley is one of the more densely inhabited and cultivated valleys of Peru. Earthquakes related to subduction of the Nazca plate are frequent destructive events that can cause large mudslides composed of saturated soils derived from the Quaternary volcanic material on the eastern side of the valley. The earthquakes also start snow avalanches that come into the valley from the snow-covered Cordillera Blanca. Close examination of the image reveals several avalanche tracks, the most notable of which is seen in the lower left corner.

The fifth and southwesternmost band of structures in the Plate image is the Cordillera Negra, seen also from the road to Huanuco (Figure T-22.3). The rocks of this mountain range are mainly Late Cretaceous. Of the units on the image, the Cordillera Negra has experienced the most recent large-scale deformation. In addition to Inca Phase deformation, the Cordillera Negra has undergone a Middle Miocene/Early Pliocene Quechua Phase deformational event. Although folding is common here, with minor amounts of thrust faulting, overall the deformation has progressed less in this area than between the Cordillera Blanca and the Rio Marañon. Characteristically, the western slopes of the mountains have distinct watersheds that drain the area toward the nearby Pacific Ocean. The exposed Andes orogen, where expressed by mountainous terrain, narrows to less than a 200-km width farther to the south in Chile/Argentina (Figure T-22.4). Volcanoes (including V. Llaima and V. Villarrica) once more become prominent. (GCW: S. J. Prucha) References: Geologic Map of South America (1964), Rutland (1974), Tectonic Map of South America (1978), Zeil (1979). Landsat 2194-14351-6, August 4, 1975.



1

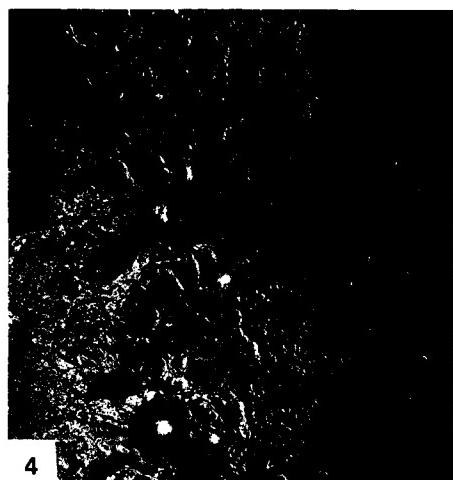
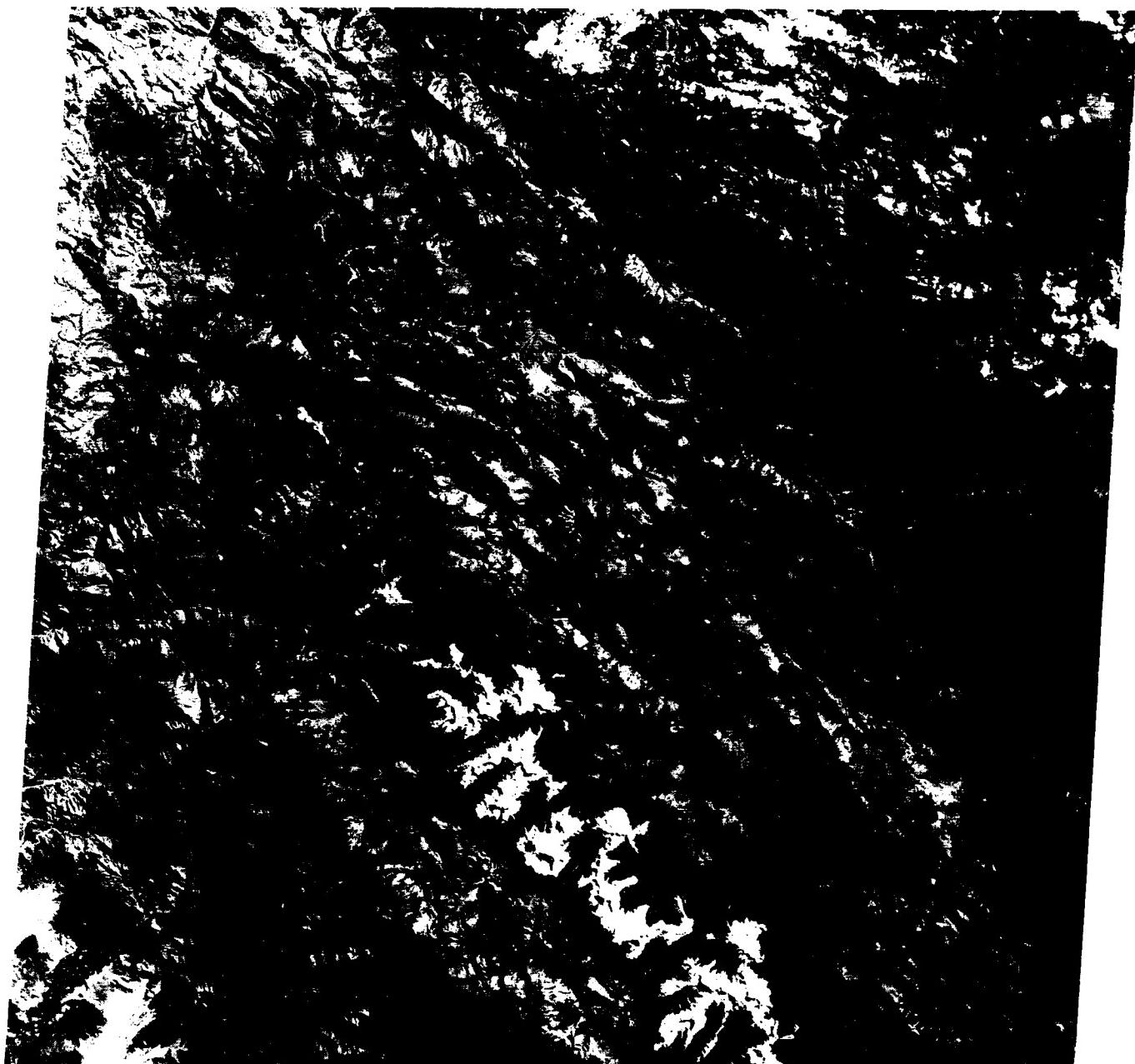


2



3

ORIGINAL PAGE IS
OF POOR QUALITY



4

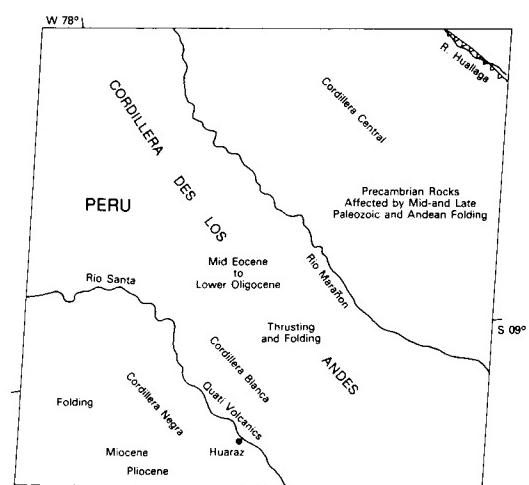


PLATE T-23

The topography in this scene of northwestern Scotland is deceptive because it suggests relatively simple underlying geology (Price, 1976). In fact, the Plate fails to reveal some very interesting aspects of this region that is so important to the development of geologic concepts. Here, G. Barrow first arrived at his concepts of metamorphic zones and index minerals in the Dalradian schists. The region is also noted for excellent exposures of ring dikes and cauldrons and its assemblages of Precambrian and Lower Paleozoic crystalline rocks. It is also the type of locality for the Caledonian orogeny. The Highlands can be correlated with the Scandinavian Highlands (Norway) and the northern Appalachians, which once formed a continuous belt before the breakup of Pangaea.

In the Plate, the most prominent topographic feature is the long linear depression along which several lakes, including Loch Ness (Figure T-23.1), are aligned. This feature is a valley developed in a 1-km wide zone of weakness associated with the Great Glen fault (Anderson, 1978). Devonian rocks in the valley suggest that it is quite ancient (initial erosion must be Pre-Devonian). The fault is left-lateral transcurrent with a cumulative horizontal displacement of 104 km (with some vertical movement). The Great Glen fault separates two geomorphic units, the Northern and the Grampian Highlands. The southeast edge of the latter lies along the Highland Boundary Fracture Zone, a normal fault that borders the Midlands graben.

Precambrian assemblages comprised a craton against which much of the Caledonian tectonic activity was directed (Anderson, 1978). The Caledonian Front is marked by the Moine thrust (roughly along the left edge of Plate). Behind the Front, the rocks of the Highlands consist mainly of the Moine schists (Late Precambrian, with some activity perhaps as young as 410 Ma) distributed about equally on either side of the Great Glen fault. West of the fault, the terrane is sliced by a series of westward-directed thrust sheets associated with autochthonous nappes, which impart a northeast lineation to the topography. Valley adjustment is guided by these faults. These sheets consist of Lewisian, Torridonian, Moinian (mostly metasedimentary), and some

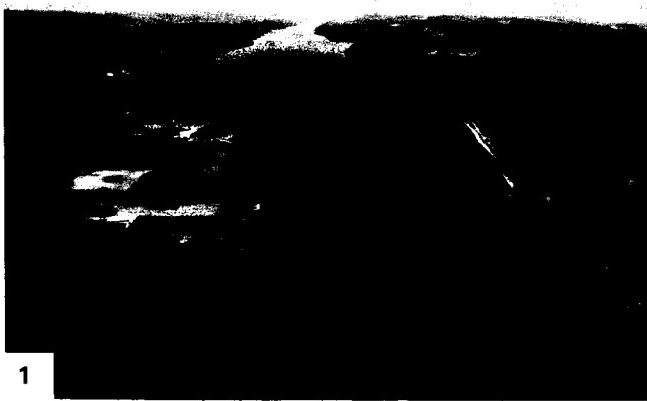
SCOTTISH HIGHLANDS

Cambrian units; most displacements carry older rocks over younger ones. In parts of this subregion (e.g., around Inverness) are deposits of Devonian Old Red Sandstone, moderately deformed, that rest unconformably on the older metamorphic assemblages.

The Late Precambrian-Cambrian Dalradian metamorphic rocks occupy roughly the eastern third of the Grampian Highlands. In the Grampian Highlands, in addition to Moinian and Dalradian units and deformed Old Red Sandstone beds, there are remnants of sediments laid down in the Carboniferous, Permo-Triassic (New Red Sandstone), and the Lias. Structurally, the older metasedimentary rocks (and the underlying Lewisian units) were affected by at least three or four major folding phases, commencing probably in Mid-Ordovician and culminating with the first stage of the Caledonian orogeny in Late Silurian that continued into Late Devonian. Kyanite and sillimanite grade metamorphism affected all older rocks.

The landscape of the Highlands (Embleton, 1984) is rugged, bleak, and strangely beautiful. The highly dissected terrain indicates great differences in rock resistance. Steep-sided towers of Torridonian sandstones, as well as cuestas and plateaus cut from other rocks, add diversity to the vistas (Figure T-23.2). The mountain on the right, towering above the exhumed Sub-Torridonian surface of low relief, is an erosional remnant, an outlier of the Moine thrust. Bare rock is common, with a cover of forests, heath, and brush. Rounded knobby hills and monadnocks and mountain ranges above 1000 m alternate with low moors. The land was largely covered by Late Pleistocene glacial ice. The high plateau area has been glacially eroded to form cirques, arêtes, sharp ridges, and broad glacial troughs, many of which are filled by lakes. Many valleys are ice-sculptured weak zones along faults. Fjord-like inlets (firths) on the west coast are also ice cut.

A Seasat radar image (Figure T-23.3) of the Fort Williams area gives another perspective on the narrow ridges and valleys imposed on the resistant Moine rocks. (NMS) Landsat 1233-10564-7, March 13, 1973.

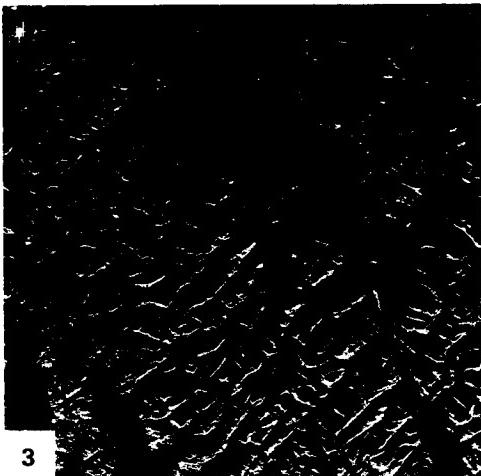


1



2

ORIGINAL PAGE IS
OF POOR QUALITY



3

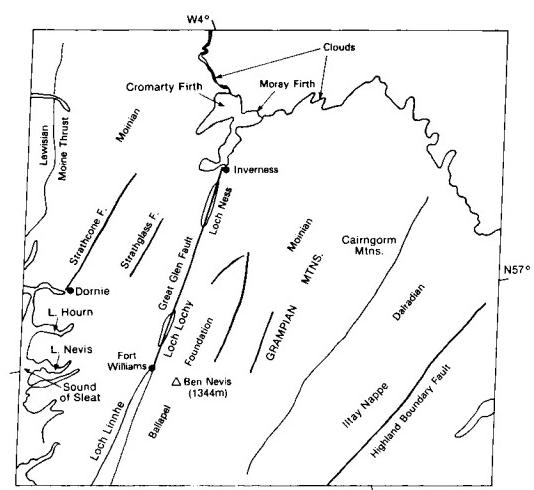


PLATE T-24

ORIGINAL PAGE IS
OF POOR QUALITY

PARIS BASIN

Differential erosion of gently dipping (1 to 10°) layered rocks produces cuestas (long gentle dip slopes and steep scarp fronts). Mild deformation sets the stage for development of most cuestas. However, primary depositional dips can also produce cuestas where resistant beds lie between more easily eroded ones.

One of the best-known examples of a stratigraphic cuesta is the series of outward-facing scarps that rim the eastern and southern flanks of the Paris Basin in northeast France (Joly, 1984). This color mosaic illustrates a striking pattern of wide bands, roughly concentric, comprising valleys or low plains cut on less resistant rock and more resistant units marked by topographic rises with out-facing scarps or "côtes" (Figure T-24.1) Sinuosity of the cuestas is a result of gentle folding. Rivers cross the structure without regard to lithology, indicating probable consequent rivers that are antecedent or superimposed on the structure. Drainage adjustment has taken place as shown by wind gaps and river capture. For example, the Seine has captured the headwaters of the Meuse. Epeirogenic uplift has caused incision of river channels to fix them in their paths. To the northwest and west, the drainage has resulted in inverted relief as anticlines eroded.

The Paris Basin is a crudely oval feature of about 140000-km² area with a long axis of nearly 400 km. Much of the area consists of flat valleys and low plateaus lying less than 100 m above sea level; eastward toward the Meuse, elevations reach 350 to 400 m, with relief generally less than 100 m.

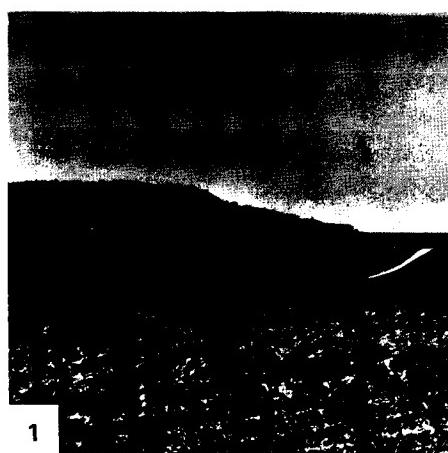
The Paris Basin is an epicontinental depocenter developed on a continental shelf invaded by marine seas from time to time. It is built on a crystalline basement downdropped relative to surrounding crystalline highs of Hercynian age, chief of which are the Massif Central (south), Massif Armorican (west), Massif Ardenno-Rhenan (northeast), and the Vosges (southeast) (Anderson, 1978). Marine sedimentation began in the Permian and continued into the Tertiary (L = Lias; MJ = Mid-Jurassic; UJ = Upper Jurassic). As many as six côtes or cuestas are developed on resistant Jurassic sandstones and limestones. Subsidence decreased somewhat in the Lower Cretaceous (LK), but by Upper Cretaceous (UK), the Tethys Sea to the south had transgressed and covered much of France. (Brunet and LePichon, 1982). The extensive chalk deposits (The Chalk) that outcrop in the Champagne Valley and westward in a ring passing through Amiens, Beauvais, and Chartres mark this transgression. Following a period of subaerial erosion, more episodic encroachments occurred in the Paleogene, with widespread Eocene (Eo) beds overlain

by Oligocene and Miocene (Ol-Mio) units, a sequence of sands, marls, and clays preserved in the Valois, Brie, and Beauce plateaus near Paris.

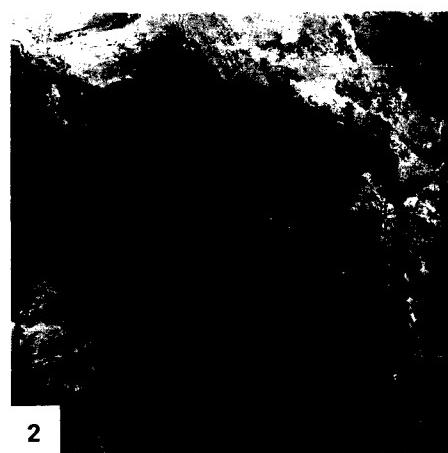
Basement faulting has propagated to the surface, although displacements are not large. Several northwest-trending folds extend from the basin toward the English Channel. The Bray anticline, seen in the mosaic as a cigar-shaped pattern defined by vegetation (reddish), is erosionally breached with inward-facing scarps. Both structural benches and fluvial terraces attest to periodic rejuvenation in response to uplift in the Cenozoic. The Alpine orogeny to the southeast increased stream gradients. Man's clearing of the forest in postglacial time has disturbed the erosion/sedimentation balance of the rivers.

Figures T-24.2 and T-24.3 show two other examples of landforms developed on gently dipping rocks. In the Mariental district of Namibia (Figure T-24.2), the Nama Group (Early Paleozoic) of sedimentary rocks dip at 1 to 5° eastward off a basement block (lower left corner) (Furon, 1963). Shales interbedded with quartzites (center left) form a distinctive pattern of swirls and contortions even though the units are not strongly deformed. Broad bands of the Schwartz Rand and Fish River Formations occupy the center third of the image; darker bands are more argillaceous than the lighter (sandstone) bands. A gentle fold (lower center), breached by an incised stream, causes local dip reversals. Karroo rocks lie unconformably (right in image) on the Nama Group, abruptly terminating the bands along the north side. Calcrete units hold up the scarp-bounded plateau (right and top). Windblown sand deposits, including longitudinal dunes, occupy the right corner.

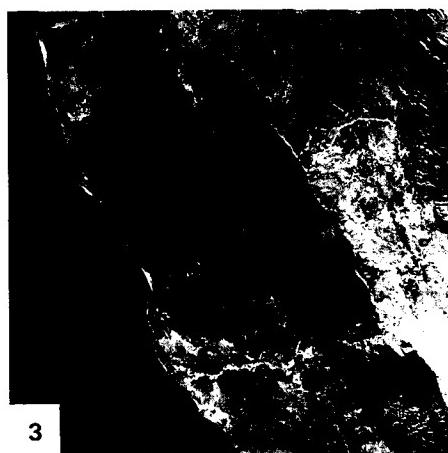
Figure T-24.3 examines the west coast of the central Malagasy Republic (Madagascar). Precambrian crystalline rocks (Tananarive block) underlie about three-fourths of the island (Besairie, 1971). A major north-northwest-trending fault juxtaposes the massif (upper right) against Karroo sediments. A broad valley, drained by the Manambolo River, flows across the Isalo Group (Upper Triassic/Lias). This river then cuts through an upland of Jurassic sedimentary rocks and across a valley containing mainly Cretaceous limestones. The eastern front of the upland is an erosional scarp; another fault controls its western margin. North of the river, a dark band of rocks represents a higher plains unit formed from a sheet of Cretaceous basalt. To the west, this westward-dipping sequence includes sediments of uppermost Cretaceous rocks. (NMS) Landsat Mosaic.



1

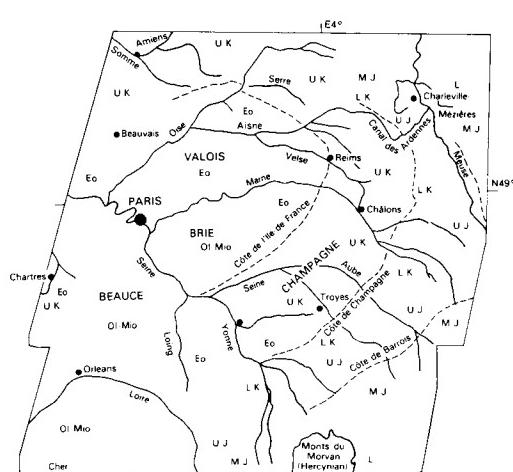
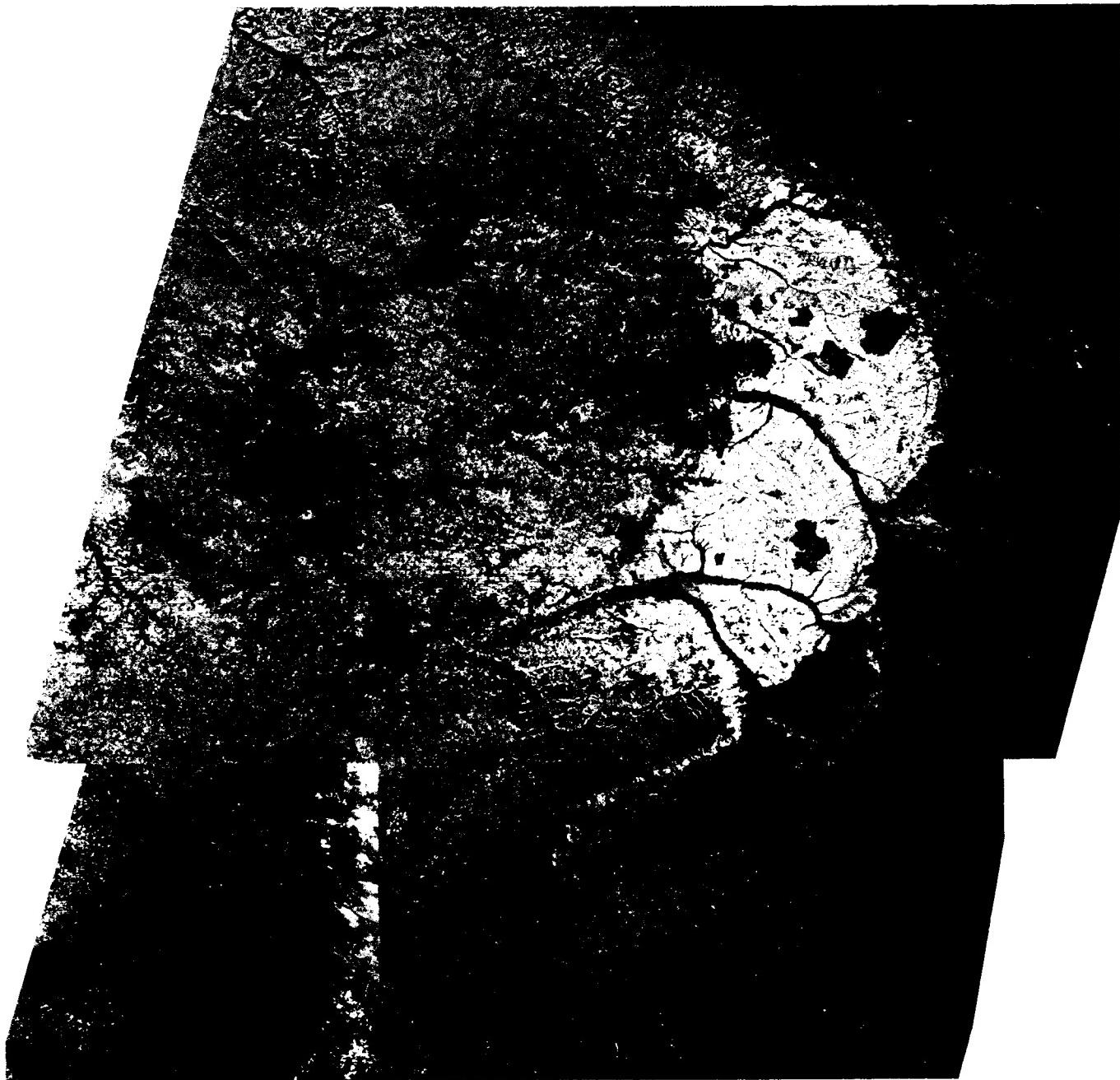


2



3

ORIGINAL PAGE
COLOR PHOTOGRAPH



C - 2

PLATE T-25

This splendid mosaic in quasi-natural color gives a synoptic view of the European Alps and related chains of mountains (see the mosaic of the western United States in Plate T-1). This mosaic provides a context for the more detailed discussions of the tectonics of the Alps and their geomorphic development in Plates T-25 and T-26.

The Alps are part of the belt of deformed rocks that extends across southern Europe into Asia Minor, thence into northern India, Russia, and China. Offshoots from the main alpine trend in Europe include the Apennines, the Dinaride/Pindar belt, and the Carpathians. A series of orogenic events beginning in the Mesozoic and culminating in the Cenozoic deformed sediments accumulated in the Tethys Sea and associated depocenters to generate the Alpine/Himalayan System (Brinkman, 1969). Most of the deformation is related to convergent margin collisions of the continent/continent type. For the Alps, this collision involved northward movement of the African plate against the Eurasian plate, partially closing the Tethys Sea, leaving behind the present Mediterranean Sea. Structurally, much of the Alps now consists of piles of allochthonous thrust sheets or nappes that were carried onto or against older landmasses. Actual tectonic transport involved compression and gravity gliding off the raised tectonic welt. Some of this gliding was submarine. The nappes and décollement folds imply a substantial amount of crustal shortening by subduction.

Folding styles range from open Jura-type décollement folds to complexly deformed recumbent folds. Orogeny began in the Late Mesozoic and culminated in the Miocene. The present rugged character of the High Alps is the result of uplift that continues today and erosion by Pleistocene glaciers.

A synopsis of tectonic events that contributed to formation of the Alps is as follows (Condé, 1982; Dewey et al., 1973; Windley, 1984):

1. As North America began to split from Pangaea about 180 Ma ago, concurrent rifting separated Eurasian and African plates.

2. A series of small plates formed in the rift zone; these have since tended to move individually in different directions and at different rates. A network of spreading ridges, subduction zones, and transform faults bounded the plates. Collapse of these features as Africa closed on Europe produced the complicated tectonic patterns that mark the alpine region.

3. The Iberian Peninsula rifted from the separating European/American plates (100 to 400 Ma ago).

4. During the Cretaceous, Iberia was emplaced along the Betic fault zone and the Pyrenees.

5. Major volcanism and deformation began in Early Tertiary; the Carnics plate began to impinge on the underside of Europe, causing early stages of folding.

6. By Miocene time, the pattern of modern structures had developed; the Turkish/Aegean plate had moved westward along the Anatolian fault zone; the Carnics plate had compressed against Europe, producing great nappe folds and translation of sediments and crustal rocks northward along south-dipping thrusts; and the foreland in Europe developed more open folding.

7. The Apulian and Rhodope plates were joined to the Carnics plate; these experienced north-south deformation as a migrating arc system (present Italian Peninsula) moved eastward in the Late Miocene; Tyrrhenian and Balearic Seas opened.

8. Greece separated from Turkey (6 to 8 Ma ago).

An inset map on the Plate mosaic (from Spencer, 1977) shows the structural divisions of the European Alps that are visible on the mosaic:

- Massifs (e.g., Vosges, Bohemian): crystalline uplifts of pre-Alpine age, mostly Hercynian (Late Paleozoic).

THE ALPS I

- Foreland grabens (Rhine, Bresse) or impactogens (tensional features formed at high angles to the collisional front).

- Swiss Plain: undeformed molasse deposits derived from the advancing Alps in Oligocene/Pliocene times.

- Jura Mountains: foreland folds, part of a thin-skinned décollement driven forward along a thrust plane in low-viscosity salt and gypsum deposits.

- Helvetic/Northern Limestone Alps: great piles of calcareous and other sedimentary rocks contained in nappes sliced up by thrusts; derived from zones between basement massifs to the south; now rootless.

- Pre-Alps: A great klippe of strongly folded and faulted Mesozoic to Early Tertiary strata, subdivided into five nappe units, carried over Helvetic Alps from deeper zone to south.

- Pennine Alps: crystalline and sedimentary rocks (schisté lustrés), with granitic, volcanic, and ultramafic rocks formed originally in eugeoclinal zone, detached (including part of basement from deep zone to south) and pushed northward as ductile nappes.

- Austroalpine Nappes: sheared crystalline rocks, older limestones and dolomites, and still older graywackes, thrust northward from source areas south of Pennine source.

- Tauern Window: a fenster through the Austroalpine unit, exposing underlying Pennines.

- Insubric/Tonale Line: a suture or boundary fault zone, with shearing and some strike-slip movement, separating young (15 to 25 Ma) rocks on north from old (300 Ma) rocks to south.

- Southern Alps: root zone consisting of basement rocks of high metamorphic grade; probable source of some Austroalpine and Pennine nappes.

- Ivrea Zone (west of Turin): ophiolitic ultrabasic rocks; thrusted component of upper mantle near subduction line.

- Po Basin: molasse-filled structural depression containing up to 20 km of sediments derived from inner Alpine arc.

- Subalpine chains: largely folded Cenozoic sedimentary rocks trending north-south to east-west; deformed at lateral edges of Carnics plate.

- Northern Apennines: nappes of turbidite and carbonates of Cretaceous age, deformed in post-Oligocene by action of Carnics/Ligurian plate during eastward migration of arc-subduction zone.

- Dinarides: sedimentary units folded and thrusted as Adriatic plates pushed eastward as Apennines developed.

In general, there is a close correspondence between structural divisions and geomorphological or physical divisions (Embleton, 1984, Ch. 10). Four composite geomorphic zones have been recognized: (1) Pre-Alps (including Jura Mountains and Po Basin), (2) Calcareous Alps, (3) Schist Alps, and (4) High Alps. These form the broad arc that makes up the Alps proper.

The present geomorphology of the Alps is the consequence of interplay among structures established in the Tertiary, active neotectonics including vertical uplift, the continuing action of streams (many structurally controlled before the Pleistocene), and, above all, intense erosion by mountain glaciers, particularly during the Riss and Würm glacial episodes (Watts, 1971).

Structures strongly control the alignment of the main valleys. For example, longitudinal valleys are located along the strike of weaker rocks, along nappe boundaries, in tectonic grabens, or along the axes of breached anticlines. Transverse valleys, which cut across gross structures and rock types, are influenced by faults, old flexures, and axial depressions. These valleys have been widened and deepened by glacial erosion.

The ground and aerial photographs and space image below provide a broader perspective on the structural and physiographic character of the Alps. Figure T-25.1 depicts a horn and other

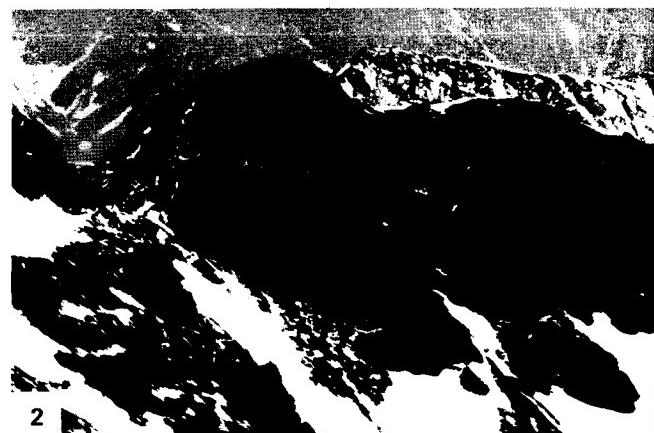
**ORIGINAL PAGE IS
OF POOR QUALITY**

terrain in the Helvetic Alps at the east end of Lac Léman (Lake Geneva). A typical flowage fold within the Pleising nappe in Austria appears in Figure T-25.2. Mountains capped by folds of massive limestone present distinct landforms in the French Alps north of Grenoble (Figure T-25.3). Figure T-25.4 shows a series of parallel ridges separated by deep subsequent stream valleys enlarged by glaciation acting on one of the mountain chains in the Niedere Tauern of Austria, seen in the next figure. Figure

T-25.5 is a Landsat-5 TM thermal image centered on western Austria that illustrates the effects of warmer Sun-facing and cooler shadowed slopes (black tones = snow) in producing a sense of rugged high-relief terrain. Long glacially enlarged valleys cutting through the mountains include those occupied by the Inn, Salzach, Enns, Isel, and Drava Rivers. Figure T-25.6 is an aerial view down the valley of the Inn River east of Innsbruck. (NMS) Landsat Mosaic.



1



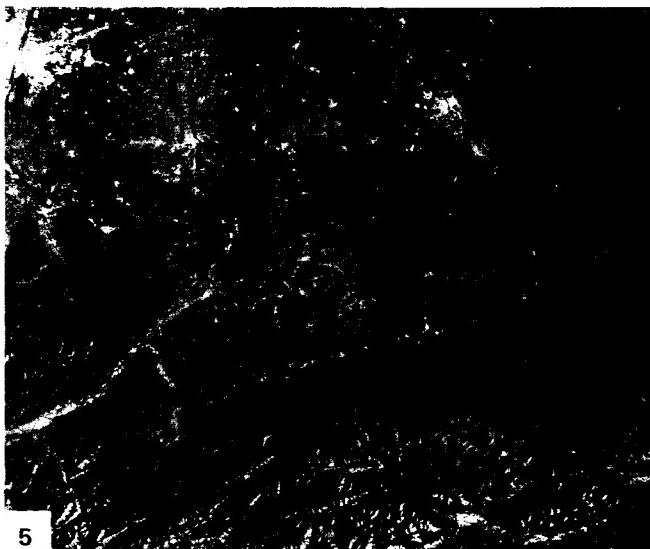
2



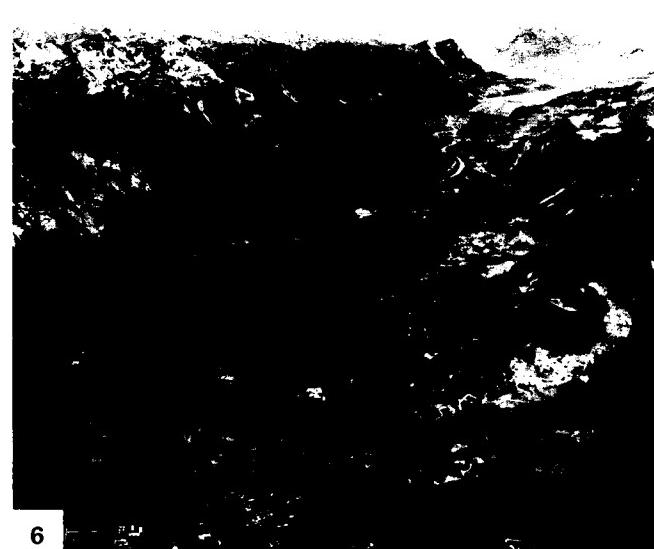
3



4

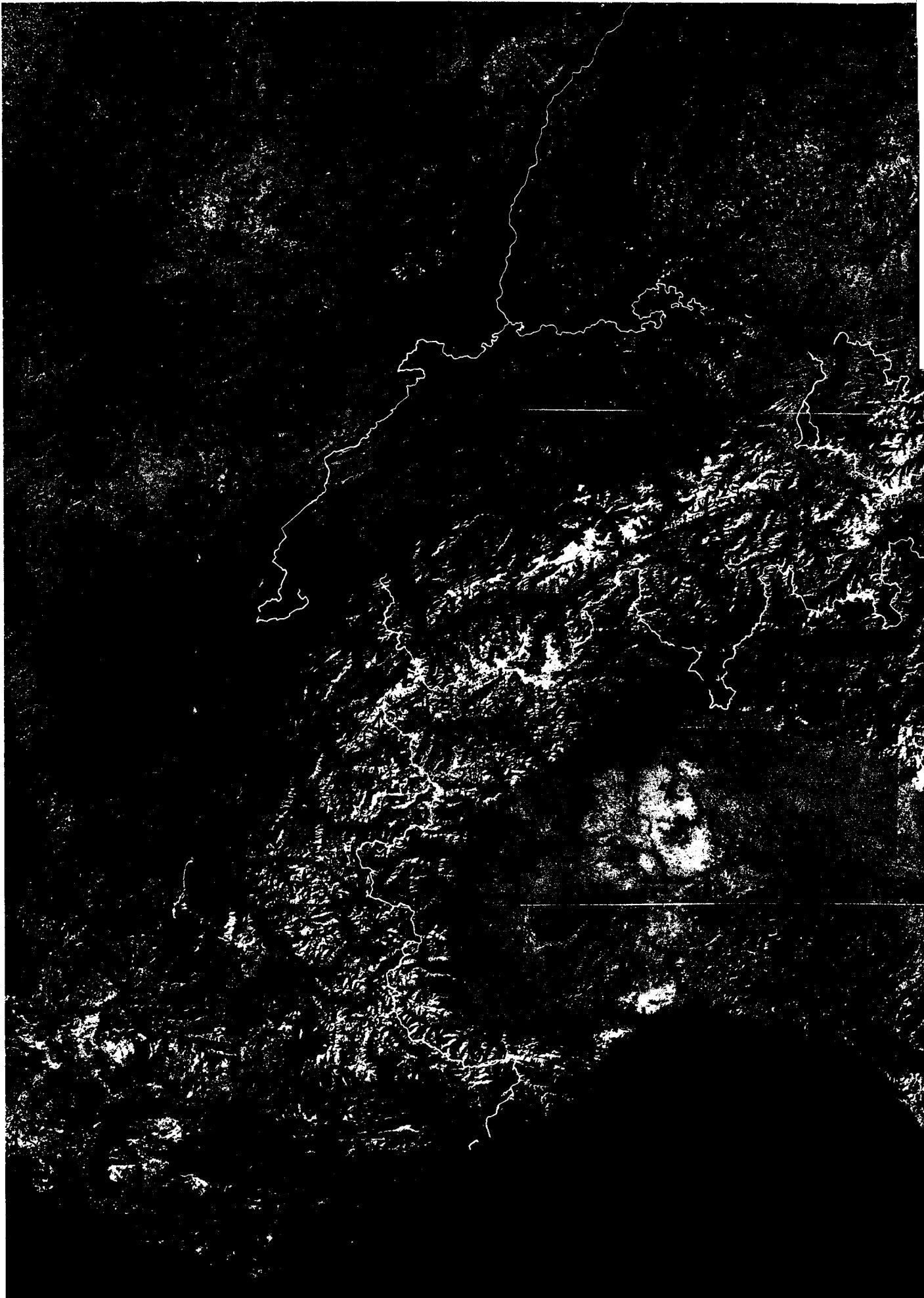


5



6

ORIGINAL PAGE
COLOR PHOTOGRAPH



ORIGINAL PAGE
COLOR PHOTOGRAPH

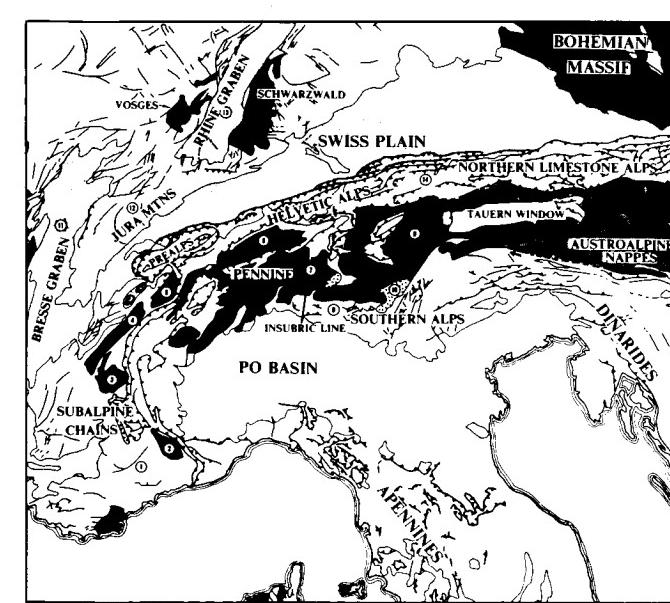
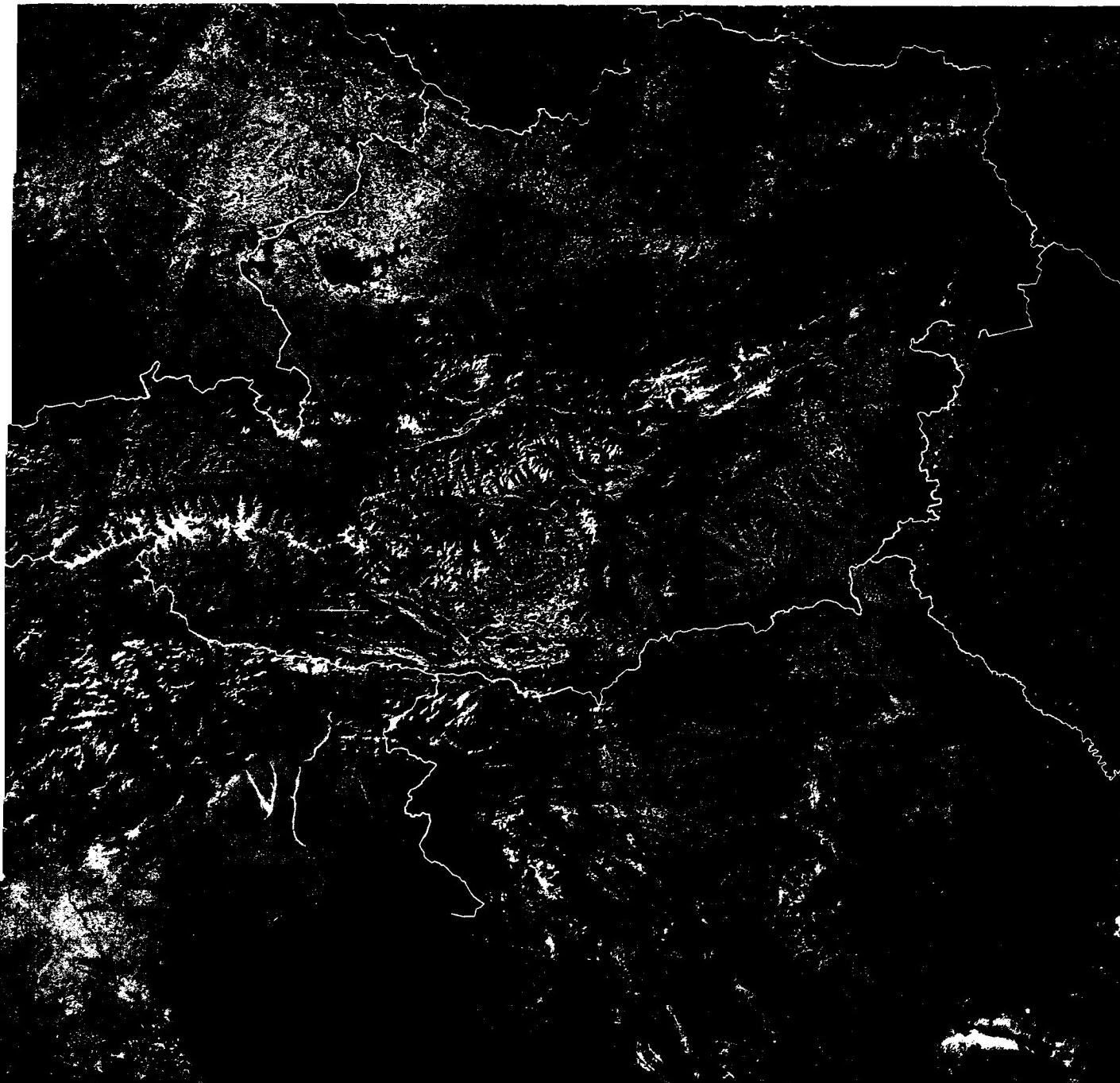


PLATE T-26

THE ALPS II

This scene and its companion to the north (Figure T-26.4) illustrate in more detail several zones in the main arc of the Alps and two major structural units of the foreland—the open folds of a thin-skinned décollement (Jura Mountains) and the older crystalline massifs (Vosges, Schwarzwald), each with its own characteristic topography. Rivers and troughs outline the structural units in the image. The pattern of the ridges also differentiates the tectonic structures. The long linear ridges extending northeast-southwest through the center of the scene are thrust slices and folds. The longitudinal valleys are carved on less resistant rocks, and many lie along the root zone of nappes. Anomalous drainage transverse to the ridges marks locations of faults or flexures. Lakes occupy some of the broad glacial troughs. The visual tour of these structures begins in the lower right corner of the Plate image and moves upward through the top of Figure T-26.4.

The Penninic Alps, in their type area here ("A" on index map), comprise the inner alpine zone. The Pennines here are schists and some gneisses that comprise lower older crystalline basement. They are thrust-bound on the west against the Helvetic Alps (B). Movement of the Pennines began in the Eocene and largely ceased by Mid-Oligocene after up to 140-km northward transport.

The Helvetic Belledonne, Aiguilles Rouges, and Mont Blanc (Figure T-26.1) massifs are also great thrust sheets that moved northward as much as 50 km during Mid-Oligocene to Mid-Miocene onto the molasse units to the west. Parts of the Helvetic Alps are structurally equivalent to the High Calcareous Alps.

The Pre-Alps occupy a belt extending from the east side of Lake Geneva southward west of the Isère River. Tectonically, they are a décollement sheet detached and moved as much as 200 km from the Pennines to the southeast; they show evidence of emplacement episodes from Eocene through Upper Oligocene and were also affected by Helvetic events. They now overlie the Helvetic nappes. South and east of Lausanne, the Pre-Alps are a series of klippen or zones of notable brecciation. Rock units include flysch beds of Cretaceous to Eocene age and Triassic/Jurassic carbonates.

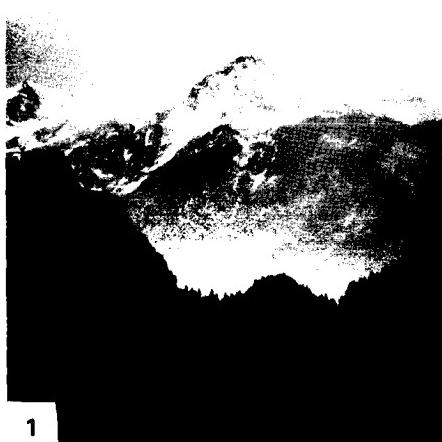
The Pre-Alps reach a height of 1000 to 1600 m. Valleys are narrow and deep, with transverse drainage controlled by faulting. Segments of anticlines and synclines are evidenced by cuestas and hogbacks. The nappes formed partially by gravity

sliding as great sedimentary piles in the orogen were uplifted and laterally stressed. Plate convergence was the driving mechanism, assisted by increased thermal gradients that lowered the viscosity of rocks in the roof zones.

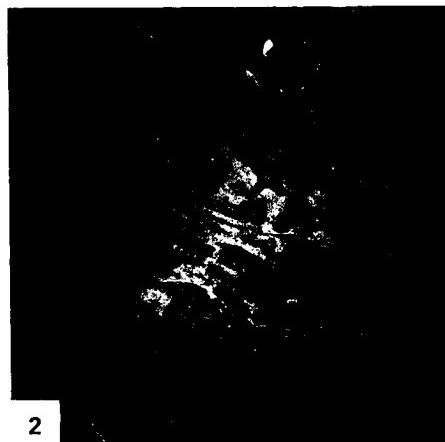
Lake Geneva (developed by glacial scouring) lies near the southern end of the Swiss Plains, a molasse basin that extends eastward through Bern, Zurich, Munich, and Linz. The basin received up to 6 km of fluvial, lacustrine, and marine sediments derived from alpine sources. Most units are folded and faulted near the juncture with the Pre-Alps. Although a lowlands compared to bordering mountains, they form a hilly landscape modified both by glaciation and postglacial erosion.

The last major mountain unit of Alpine origin is the Jura Mountains that lie to the northwest. South of Chambéry, the Jura meets the Chaines Subalpines of France. To the west in this scene is the Bresse graben. Rocks in the Jura foreland include Triassic through Cretaceous marine units on a crystalline basement (not exposed) and are overlain unconformably by Tertiary molasse. Two principal subdivisions are evident here: The Jura Blisse, a flexure belt of open to tight anticlines and synclines (Figure T-26.2, an aerial photograph) east of the Ain River, grades westward into the Jura Plateau, consisting of more open folds and gentler relief (Figure T-26.3). This folding began in the Late Miocene and climaxed in the Pliocene. The Jura is a décollement (one of the first places this style of deformation was recognized).

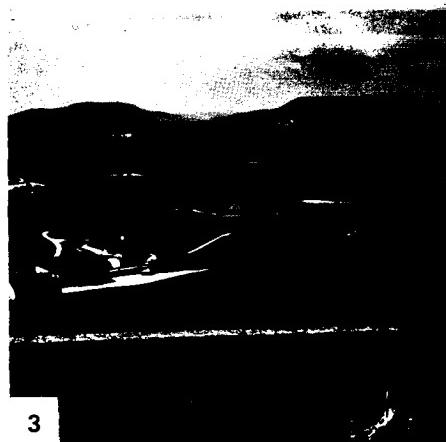
Figure T-26.4 depicts the northern half of the Jura where these mountains swing to the northeast. The change in style of folding from tighter to more open folds westward is clear. A third subdivision, the Jura Tabulaire, occupies a thin belt just above the northernmost folds. Rock layers there are nearly horizontal, with little apparent deformation (somewhat analogous to the Appalachian Plateau (Plates T-11 and F-26)). Near the top of the scene, the Rhine graben separates two dark areas, the crystalline massifs of the Vosges (center) and Schwarzwald (right corner). Because drainage of the Jura was incised across the developing folds, many transverse valleys or "cluses" are antecedent to the larger anticlines. The later drainage is accordant to the structure (subsequent). Products of accordant drainage are the "combes," longitudinal valleys formed by erosion of less resistant layers in isoclinal folds. (*NMS*) References: *Ager and Brooks (1977)*, *Anderson (1978)*, *Leser (1984)*. Landsat 1078-09555-7, October 9, 1972.



1

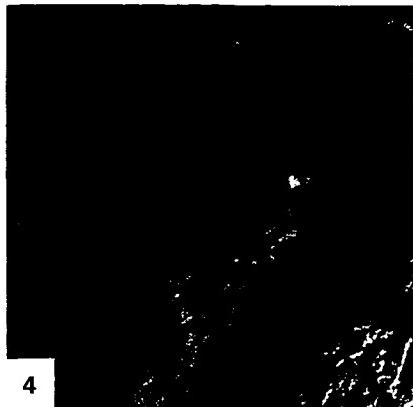


2



3

ORIGINAL PAGE IS
OF POOR QUALITY



4

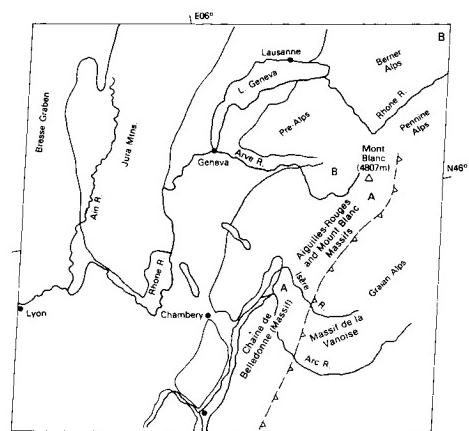


PLATE T-27

This scene depicts another segment of the complex tectonic terrane that makes up the alpine mountain system. The Dinaride Alps (Plate KL-5), run southeast along the western side of the Balkans and pass through Yugoslavia into Macedonia, where they join the Hellenide segment. The Plate image shows the Pindus Mountains of central and northwestern Greece (Epirus Mountains in Albania).

Following the breakup of Pangaea, there were several microplates between the Eurasian, African, and Arabian plates. During the Mesozoic and Cenozoic convergence, the microplates were caught between the major plates and underwent a complex series of deformations in the Eastern Mediterranean. The Italo/Adriatic plate moved eastward against the Balkan segment of the Eurasian plate to create the Dinaric orogenic belt. To the south, various microplates (e.g., the Messina, Macedonian, Ionian, Aegean, Turkish, and Levantine plates) became involved along subduction and transform boundaries. The Macedonian microplate that underlies the terrain appearing in the Plate image is bounded on the west and north by suture zones.

As in much of the western Alps, the developmental sequence in the southern Balkans began with rifting, release of flood basalts, and formation of new crust in the Triassic. This was followed by building of platforms in the Jurassic, on which shallow carbonates accumulated, that were separated by deeper water basins containing pelagic (radiolarian) sediments and extensive flysch deposits. Then, convergence of plates started in the Cretaceous with destruction of oceanic crust (ophiolites) at trenches, closure of marginal basins, and formation of thrust belts, nappes, and metamorphic zones during general closing and collision between Europe and Africa, which continued into the Oligocene. Deformation continues to the present (Dewey and Sengor, 1979).

A series of tectonic zones trend roughly north-northwest across this part of Greece. Because most zones are actually thrust sheets, thrust faults form the zone boundaries. Most fault planes dip eastward, with westward directions of tectonic transport (shortening of 130 to 200 km) imposed when oceanic crust was consumed under the continental plate along the east-dipping subduction zone. These tectonic zones contain sedimentary rocks and associated oceanic basalt flows of the types found in depositional

BALKAN ALPINE SYSTEM

troughs along active plate margins: the deposits have been telescoped into imbricate slices within the zones (Temple, 1968).

The index map names and delineates these zones as defined by Zimmerman and Ross (1976). In general, rocks are older and more metamorphosed to the east. The Pindus zone (high mountains and rough texture) is an allochthonous block separated from the Frontal Folds by a shallow-dipping (30°) thrust fault that extends from northern Albania to the southern Peloponnesus. The block itself is cut into numerous slices by subsidiary thrusts that further offset tight folds and nappes. The High Pindus Mountains reach elevations above 2000 m. A fenster (scene center) exposes underlying frontal zone strata. The Othris (sub-Pelagonian) zone, whose western margin is another sole thrust, is an old oceanic trench that contains Cretaceous ophiolites and mélange underlying Tertiary molasse deposits and overlying siliceous oceanic sediments. The Pelagonian zone, which includes Cretaceous volcanic, metamorphic, and sedimentary rocks, probably represents an island arc that was caught up in the complex subduction.

The most remarkable attribute of this scene is the close correlation between the individual structural zones (mostly imbricated thrust sheets) and the differences in their geomorphic expression. In the image, one is immediately impressed by the variability of these allochthonous terrains in terms of variations in slope and relief, drainage texture, and tonal changes. This can probably be quantified by measurements of such parameters as stream or divide lengths, densities, and orientations. The important point is this: the landforms themselves express the structural configuration and lithologic makeup of each zone and graphically display the tectonic framework of the entire deformed belt.

Ground views help to give a "feel" for these distinctive terrains. Figures T-27.1 and T-27.2 portray allochthonous blocks and imbricate slices as landforms in the Greek Pindus Mountains. In Figure T-27.3, jumbled terrain has been cut from an autochthonous block of Cretaceous limestones in the comparable Dinaride Alps in southern Yugoslavia (see Plate KL-5). (NMS)
Additional References: Demek et al. (1984), Zimmerman (1972), Zimmerman and Ross (1976). Landsat 1102-08491-7, November 2, 1972.



ORIGINAL PAGE
COLOR PHOTOGRAPH

ORIGINAL PAGE
COLOR PHOTOGRAPH



2



3

PLATE T-32

DAMARA MOUNTAIN BELT

The Damara Mountain Belt is an outstanding example of a Late Precambrian/Early Paleozoic ocean basin whose shelf or trailing edge and deep-water or trench deposits remain well preserved. The belt occupies an extensive outcrop area in central and northern Namibia (South-West Africa) trending northeastward from the coastline inland some 400 km. It may continue beneath the Cretaceous/Tertiary Kalahari sedimentary rocks in Botswana and the Pan-African suture zone of the Zambezi Valley. This belt of ancient sedimentary rocks, now regionally metamorphosed, accumulated between two continents, the Congo on the north and the Kalahari on the south.

Deposition in the Damara basin began perhaps as early as 700 Ma ago. The shelf rocks lie in Angola to the north of this scene. Most of the Damara consists of the Swakop facies, mainly graywackes and shales more than 10000 m thick that are metamorphosed to schists and gneisses. Some deformation is as old as 680 to 580 Ma, but the major collisional activity took place during the Pan-African Tectonic Episode from 450 to 550 Ma ago. This Damaran orogeny imposed a strong northeast structural fabric on the region, with folds locally overturned, intrusions commonplace, and extensive faulting in places.

Deformation and metamorphism show maximum intensity in the areas around A, B, and C on the index map. High-grade metamorphosed rocks associated with abundant intrusions of anatetic granites and pegmatites characterize these crystalline terranes. The folding is expressed by the resistant ridges and eroded valleys. In the southern zone around the Eiseb River and the Naukluft Mountains (highest point 2245 m), complex folds, nappes, and thrust faults with reactivated granitic cores and other basement plutons are typical (D). The Auas Mountains (maximum elevation 2465 m), a transverse range held up by the Quartzite Series, are now eroded into a dissected plateau.

The conspicuous Khomas Highlands plateau (average elevation of 2100 m), is an older erosion surface cut on the same Damaran rocks as the more dissected area to the east. The structural trends visible in the plateau in the area to the west are more subdued. Because of a great degree of planation and weathering, it is easier, in many locations, to trace the stratigraphy from the space imagery than on the ground. On the surface, graphitic schists serve as marker horizons. A well-defined narrow black line (E and F) is actually a serpentinite that marks the suture zone.

It is known in the region as the Matchless Belt, within and around which are a number of base metal mines. The Khomas Highlands are also distinguished by prominent lineaments in two dominant sets, north-south and northwest. Most of these are joints, but a few are traces of faults that offset marker units. The Hakos Mountains, a large northeast-plunging anticline made up of crystalline Swakop facies, lie south of the highlands.

Both these mountains and the Highlands are bounded on the west by the Great Escarpment (G and H) of southern Africa, a post-Eocene erosion feature not as well developed here as in the Cape Province of South Africa (see Figure 1-7). The scarp is the result of the current cycle of erosion cutting headward into an older erosion surface. In fact, four of L. C. King's (1967) lateral erosion surfaces, each interrupted by a regional uplift event (cymatogeny), are found over the scene; the Jurassic Gondwana surface cuts across much of the Khomas Highlands; the African surface occupies most of the lower right part of the image; the younger post-African surface extends along the lower left of the image; and the youngest Congo surface lies along the Kuiseb River valley. Tertiary to Recent alluvium and sands extend to the west. In the lower right corner of the scene are sedimentary beds of the Nama System, which were broadly folded during the late phase of the Damara collision.

In Figure T-32.1, the outcrops of Damara facies rocks define an asymmetrical plunging syncline with a characteristic sharp short nose. Figure T-32.2 is a fine example of a bornhardt (der grosse Spitzkopf) or erosion remnant standing on a pediplain. Figure T-32.3 shows how erosion is guided by foliation in metamorphic rocks (relict bedding?) along the Kuiseb River.

The conspicuous large joints and faults cutting across the Khomas Highlands form weaker areas where erosion is concentrated and which guide the paths of rivers. This same control is beautifully displayed in Figure T-32.4, a Landsat-4 TM subscene (enlargement) of a plateau traversed by the Zambezi River near Victoria Falls, some 1500 km northeast of Windhoek. This river and its tributaries have sharp angular bends where their downcutting has carved canyons along the intersecting joints that crisscross the karroo basaltic units capping the plateau. (NMS) Additional References: Burke and Dewey (1970), de Villiers and Simpson (1974), Furon (1963), Truswell (1970), Viljoen and Viljoen (1975). Landsat 1382-08205-7, August 9, 1973.



1

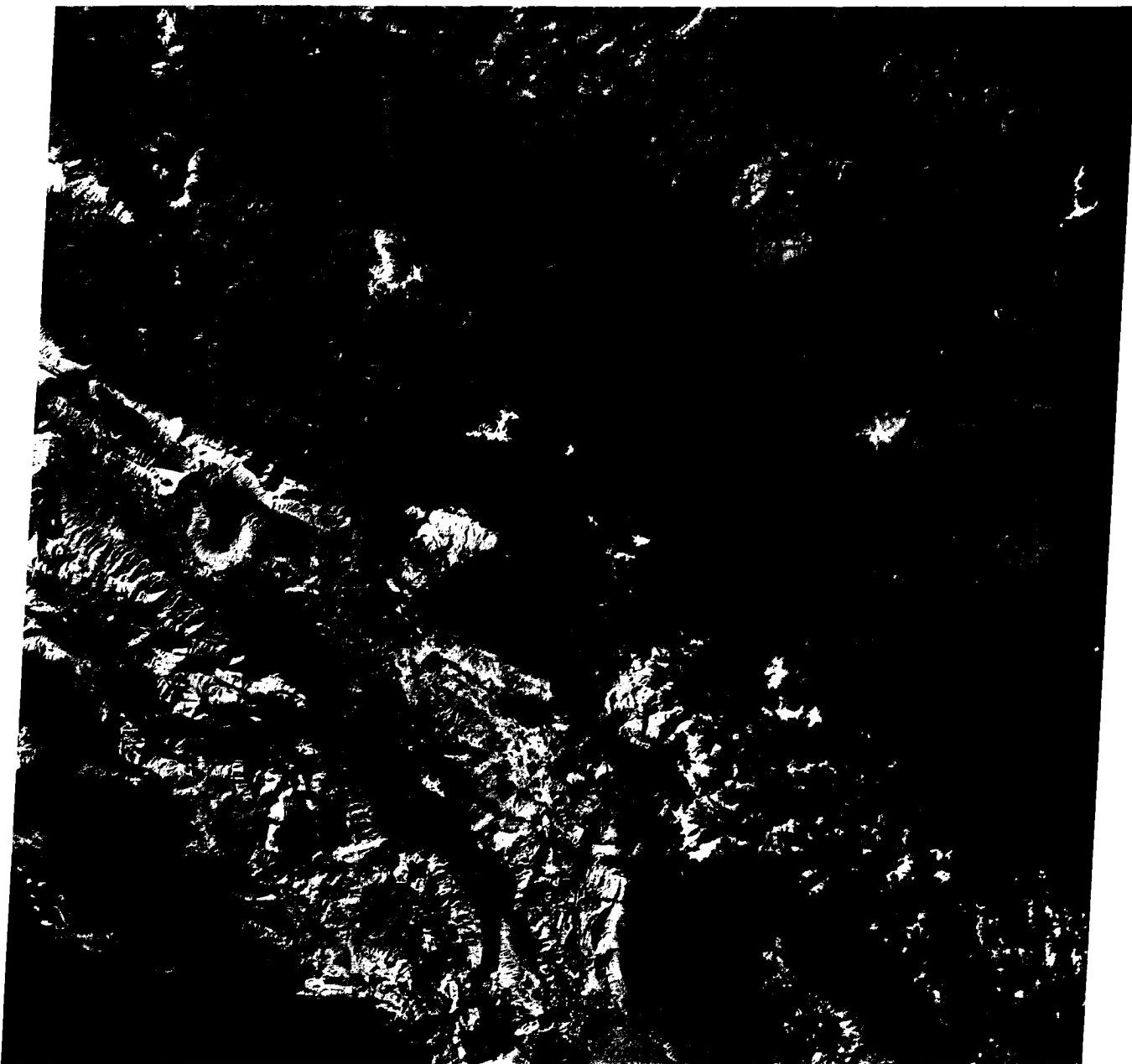


2



3

ORIGINAL PAGE IS
OF POOR QUALITY



3

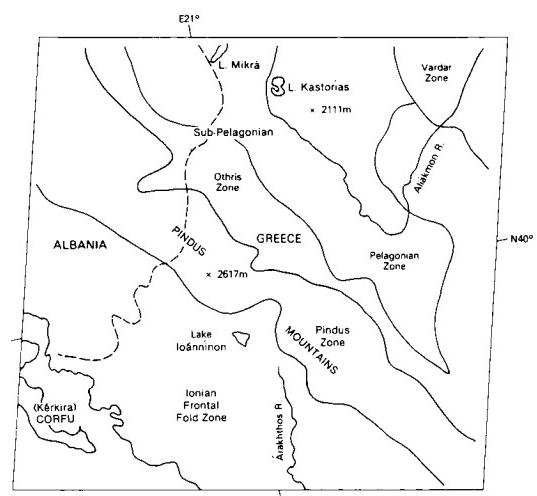


PLATE T-28

The Ural Mountains are an excellent example of deformation associated with collisions of two continents, and they bear a striking resemblance (structurally, and to some extent, morphologically) to the Appalachians. They form a continuous belt 150 to 300 km wide and more than 4000 km long. Beginning near 48°N latitude, they run nearly parallel to 60°E longitude until they deflect northeastward (Polar Urals), then northwestward (Pay Khay), then northeastward again through Novaya Zemlya. They are overthrust to the west and cover the eastern part of the little deformed Russian (East European) platform. On the east, they abut the West Siberian lowlands, which contain mildly deformed post-Paleozoic sedimentary rocks, now largely covered by Quaternary deposits.

The Plate covers part of the widest zone of the South Urals, just northwest of the industrial city of Magnitogorsk. The mountains here reach 1663 m (at A), with relief of 400 to 500 m. In the western half, elongate ridges predominate; those near the scene edge are part of an anticlinorium made up of Middle Paleozoic sedimentary rocks. Rivers anomalously cut across these folds through water gaps controlled by faults. The easternmost edge of the slightly folded Permian rocks (in the Cis-Urals) crosses the upper left corner of the scene. Rocks in the central section of the image are mainly Late Proterozoic and Early Cambrian metasediments. A fault zone near Beloretsk (an iron-mining center) separates the central Urals (part of the miogeosynclinal segment) from the eugeosynclinal Trans-Urals to the east. These eastern rocks range from Ordovician to Carboniferous age. Middle Paleozoic (Caledonian) ultrabasic rocks near Beloretsk and synorogenic (Hercynian) intrusive granite massifs farther east intrude these units. Much of the Trans-Urals is now eroded to a surface of low relief, much like the Piedmont of the eastern United States. Erosion of the crystalline rocks presents quite a different topographic texture (as seen in the aerial oblique photograph of the Urals (Figure T-28.1)) than erosion of the dipping sedimentary rocks.

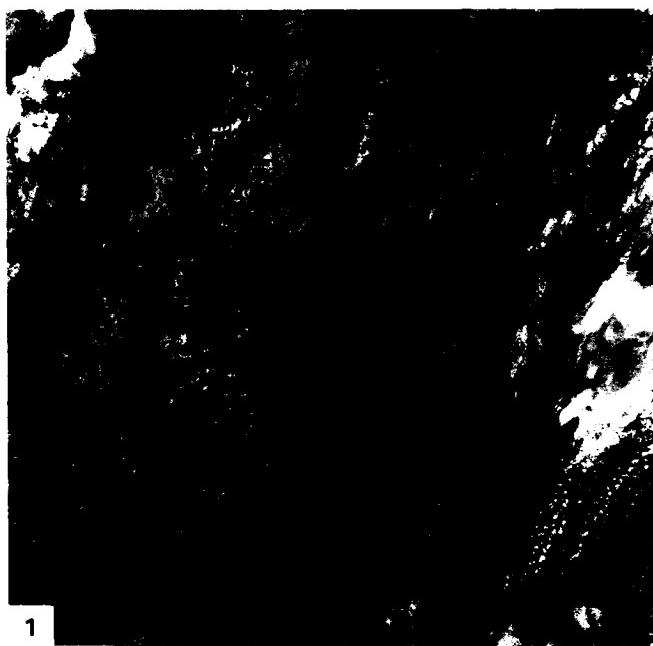
Figure T-28.2 (a Landsat MSS scene) shows a segment of the Polar Urals near 65°N where the mountainous terrain narrows to a belt only 50 km wide that contains (oceanic) ultramafics rocks

URAL MOUNTAINS

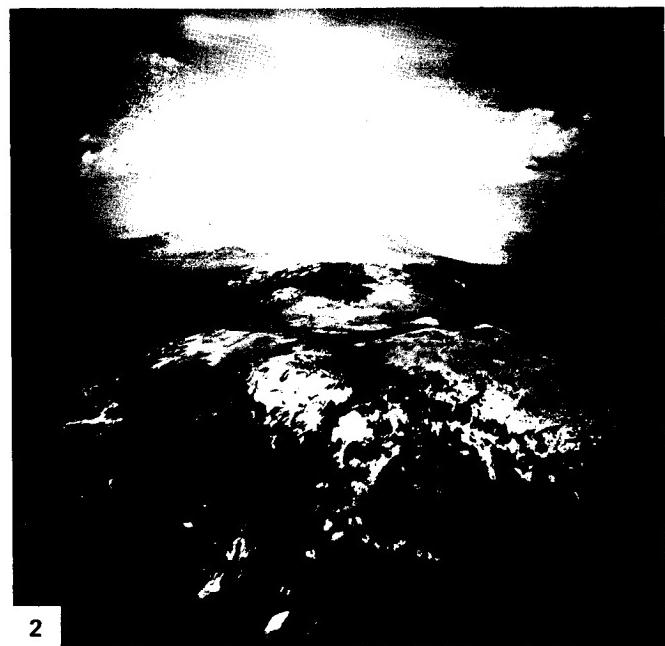
and granites intermixed with Proterozoic to Ordovician rocks. To the right are plains of Quaternary sediments and glacial cover drained by the Synya and Voykar Rivers that empty into the Ob River (upper right) (see Plate KL-8).

The Urals are the western side of a wider zone of deformation, the Uralides, which underlie the West Siberian platform (a foreland basin) and eastward crop out again along the western edge of the Siberian platform. The Uralides underwent maximum deformation during the Late Paleozoic (Hercynian time) as the Russian and Siberian continents converged and sutured, sweeping up island arc and other essentially oceanic fragments caught between them (evidenced by spilites, radiolarian cherts, and other ophiolitic assemblages). Convergence during the Hercynian produced folding that diminishes to the west, along with strong westward thrusting of slices of the eugeosynclinal rocks onto the western shelf. (The two terranes meet along the Main Uralian fault, a shear zone up to 20 km wide.) Right-slip faulting deformed the Variscan basement and indicates either nonorthogonal convergence or an earlier period of deformation.

Figure T-28.3 covers another of the best known orogenic complexes in the Soviet Union. The Great Caucasian chain, or Caucasus, is a northwest-trending orogen that lies along the northeast segment of the Mediterranean geosynclinal belts, which includes the Alpine, Carpathian, Hellenide, and Anatolian mountain systems. Rocks from Precambrian through Tertiary/Quaternary ages are exposed in the Caucasus, with Jurassic and Cretaceous units reaching thicknesses of 15 km or more. Two major epochs of deformation have shaped the modern Caucasus: the Kimmerian (Upper Triassic/Lower Cretaceous), in which the Caucasian anticlinorium was produced, and the Alpine (Cenozoic), in which earlier tectonic structures were, and still are, being further deformed. The Caucasus now has heights exceeding 5000 m (Mount Elbrus = 5633 m), which fostered a well-developed system of glaciers in the Pleistocene. Parallel drainage systems flowing northward form an incipient trellis pattern. (NMS) References: Bashenina (1984), Dumistrasko (1984), Hamilton (1970), Nalivkin (1960). Landsat 2922-06040-7, August 1, 1977.

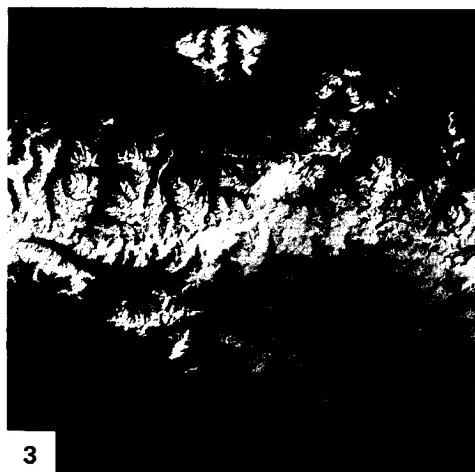
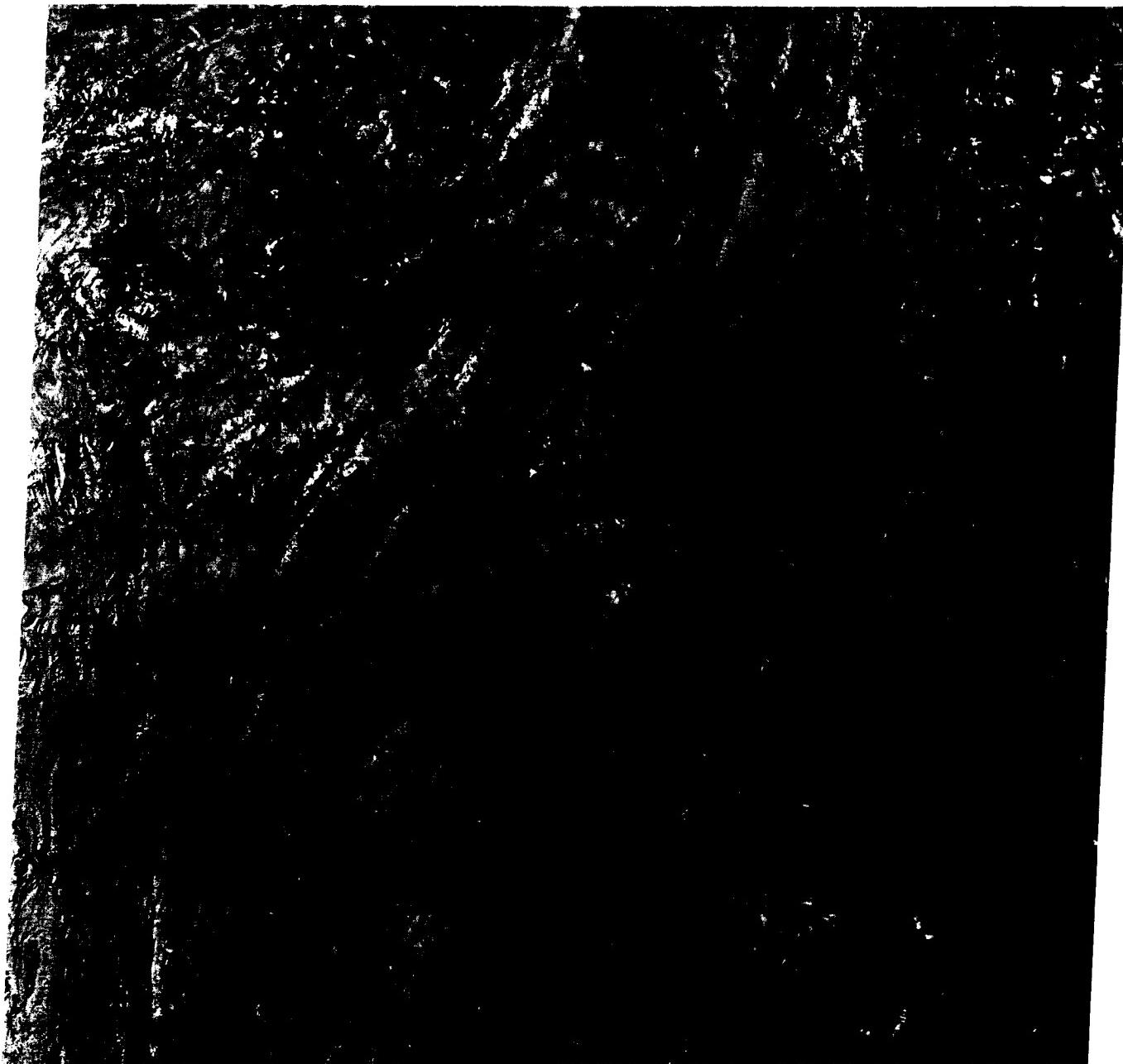


1



2

ORIGINAL PAGE IS
OF POOR QUALITY



3

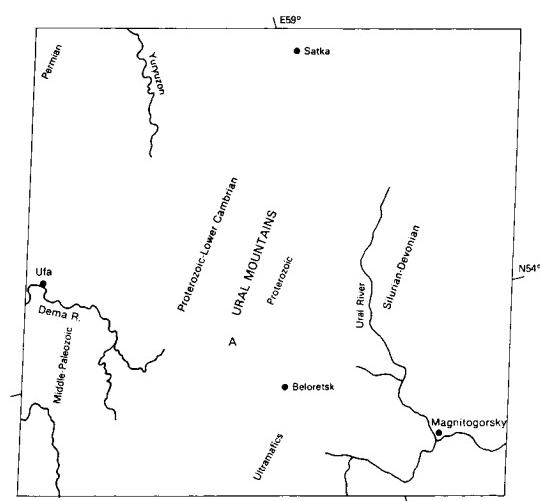


PLATE T-29

SIBERIAN RANGES

Much of eastern Siberia is mountainous, the eroded products of Mesozoic and Cenozoic orogenies that affected a vast depositional region that Russian geologists call the Pacific Ocean geosyncline. This region is further subdivided into the Kimmerian subregion (within which this scene is included), in much of which orogenic activity culminated in the Cretaceous and, farther east, the Alpine subregion, with activity continuing from Cretaceous to the Recent.

The scenes in the Plate and Figures T-29.1 and T-29.2 depict the Verkhoyanskiy orogenic belt, a series of compound oroclines concentrated in the central part of the Verkhoyanskiy continental shelf. To the southeast, most of this shelf area consists of Jurassic and Cretaceous sedimentary rocks that remain largely undeformed.

The scene in this Plate lies near the north end of the main Verkhoyanskiy Range, just east of the Lena River and a few hundred kilometers south of its great delta (Plate D-11). Along the left margin are mildly deformed Cretaceous and Quaternary rocks that comprise a flat terrain influenced by Lena drainage. Slivers of Triassic and Jurassic sedimentary rocks occupy the fault-controlled west end of the Verkhoyanskiy Range. The majority of units in this scene are north-striking beds of Permian age, with Triassic units appearing around the Omoloy River at the right margin. These clastic sediments (12 to 15 km in thickness) were derived from Siberian Mountains that had been folded, uplifted, and eroded in late phases of the same Hercynian orogeny that also affected the Uralides and parts of the Siberian platform.

Figure T-29.1 depicts almost the same area, but was taken in late July when the snows had vanished. Together, these scenes provide a broader insight into the character of the mountains. They have a distinctive expression that is characteristic of other ranges in this part of the Kimmerian region (Figure T-29.2). The mountains tend to be rather low (below 2400 m), with about 1500 m of relief. On the west, linear ridges are carved from steeply dipping units. This strike-dominated fabric persists through the Permian units, which appear to contain repeated sections. Larger rivers have rather wide floodplains (glacially expanded?). Except for the Omoloy River, the major rivers are consequent, flowing eastward transverse to the structure. Although uplift has caused

incision of the main channels, enabling them to maintain their paths irrespective of underlying rock and structure, the drainage shows some secondary trellis patterns in conformity to the north-easterly structural trends. Well-developed terraces can be seen along the rivers. Note that several rivers have captured other drainage, and for others, stream piracy is imminent. The lack of respect of major drainage for structure suggests that it is superposed on or antecedent to the mountains.

About 800 km to the southeast, another major mountain chain, the Chersky Range (Figure T-29.3), rises to similar heights (3000 m). Triassic sedimentary rocks occupy the lower half of the scene. To the north is a belt of Jurassic rocks and a band of Lower Cretaceous intrusive granites and, near the top, older units of Silurian/Devonian age. Similar patterns of hill erosion, strongly influenced by bedding planes, are evident here. Several northeast-southwest-trending valleys seem to be fault-controlled, as evidenced by their linearity and the presence of triangular facets along the mountain face. Other ridges are broken by cross faults where rivers have cut across the topographic trend.

The northernmost part of the Kimmerian region is located along the Chukchi Peninsula. The smaller area, higher resolution Landsat RBV image in Figure T-29.4 captures a part of the snow-covered Chukchi Mountains (1400- to 1800-m altitudes), whose forms are emphasized by the low Sun angle. A window of Triassic rocks, invaded by Mesozoic intrusives, is dissected by the Pegtymel River. Most rocks in the scene are Upper Carboniferous volcanic deposits, emplaced during the early phases of the Alpine orogeny. The lack of bedding with contrasting resistance accounts for the somewhat "rounder" appearance of the hills.

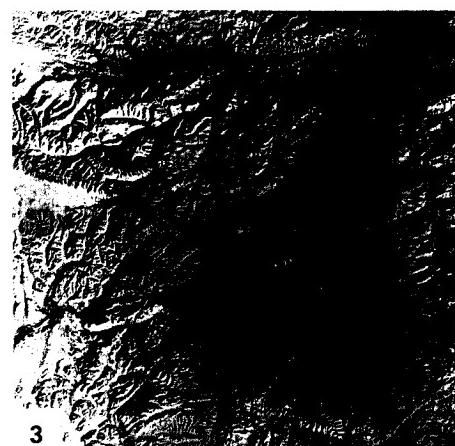
The Trans-Baikal region of southernmost Siberia (Plate KL-14) extends across the eastern end of the Paleozoic Angara geosyncline to the southern end of the Kimmerian region. This is one of the widest belts of continuous intrusive rocks in the world. Multiple intrusions range from Proterozoic (mainly on west side), through Caledonian and Variscan (mostly central Trans-Baikal), to Mesozoic (east side). Elevations in this region are generally below 1200 m, but reach to 1700 m in the Yablonovyy Range. (NMS) References: Nalivkin (1960), Suslov (1961). Landsat 1221-02505-6, March 1, 1973.



1

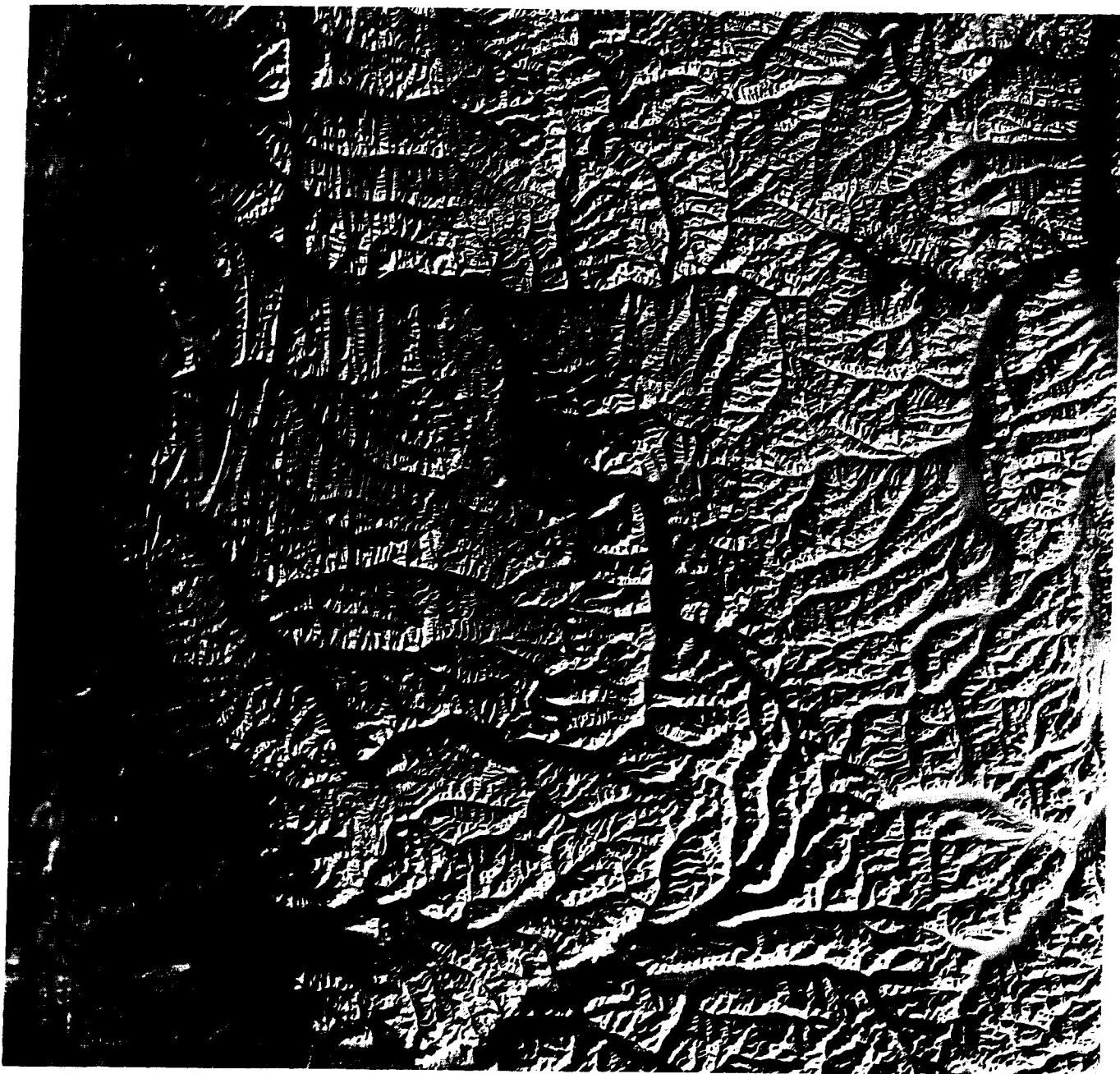


2



3

ORIGINAL PAGE IS
OF POOR QUALITY



4

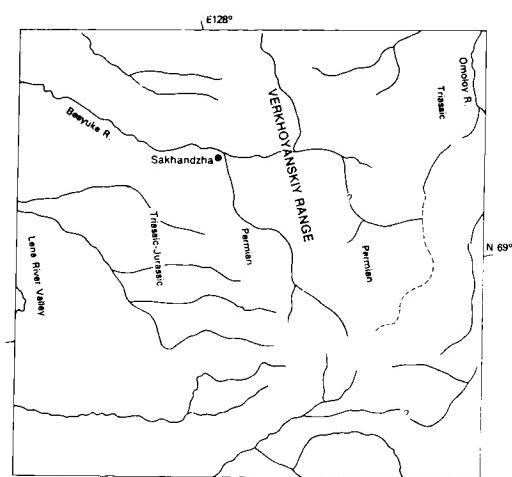


PLATE T-30

The deformed rocks of the Atlas mountain system (Anti Atlas, High Atlas, and Rif Mountains of Morocco) and the neighboring mountain ranges of southern Spain (Betic Cordilleras) record the collision of Africa and Eurasia—the final stage of the closing of the Tethys Sea. The Atlas system is the only Cenozoic orogenic belt in Africa and, by virtue of the climate, degree of erosion, and contrast in rock types (both in terms of erodibility and spectral response), one of the most spectacularly exposed fold belts in the world. The structures are clearly outlined by the resistant beds because erosion has removed the softer layers. The earliest Alpine deformation began in latest Cretaceous time and continues to the present. Like other Alpine mountain belts, the extreme degree of nappe formation, overthrusting, and folding of platform sedimentary rock attests to the consumption of a substantial (150 km wide at a minimum) section of continental crust in the course of the continent/continent collision (Choubert and Faure-Muret, 1974; Dewey et al., 1973; Manspeizer et al., 1978; Trumpp, 1983; Wildi, 1983).

The day-visible band Heat Capacity Mapping Mission (HCMM) image below (Figure T-30.1) provides a regional context for the spectacular Plate scene on pages 96 and 97, taken from the full Landsat image used on the cover of this book. (The small rectangle on the index map tied to the HCMM image shows the location of this image in the region.) The presence of an east-west-trending fault is suggested by the deformation style along a zone that bisects the area shown on the HCMM image for a linear distance of some 640 km. This zone is parallel to the right-slip Agadir fault to the north (Dewey et al., 1973). Offsets in gross outcrop patterns of Saharan platform rocks suggest that this suspected fault, like the Agadir, has at least some component of right-lateral movement. The orientation of the folds, north of Gebel Ouarkziz (well displayed on the color composite), confirms this sense of movement.

The Plate image displays topographically several characteristics of continental collision orogenic belts. Most obvious is that the rocks are complexly folded and thrust-faulted. Rock sequences are repeated, anticlines encroach upon anticlines, and synclines encroach upon synclines. These exemplify extreme compressive deformation and imply substantial crustal shortening. Figures T-30.2 and T-30.3, aerial photographs taken over the Moroccan Atlas, offer two striking examples of the zig-zag ridges and plunging anticlinal (long, gentle) and synclinal (short, steep) noses formed by resistant rock strata. This style of deformation is common to the layered sedimentary cover of all major fold belts.

Numerous zones of structural discontinuity or disharmonic folding are particularly obvious in the Plate image. In general,



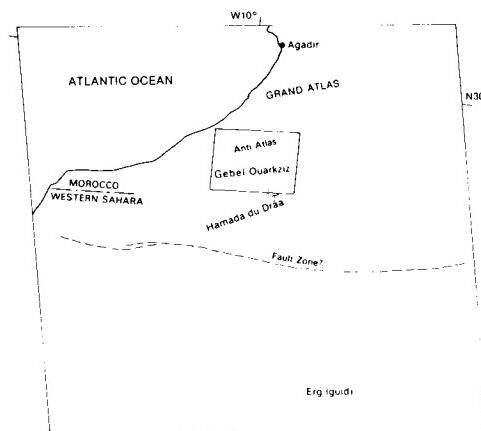
ANTI ATLAS MOUNTAINS

the older rocks to the northwest appear to be more highly deformed than the younger rocks to the south and southeast. The lighter colored yellowish brown Precambrian rocks in the northwest are tightly folded, highly fractured, intruded, and metamorphosed. The high degree of deformation and reorganization of the Precambrian rocks is a function of extreme compression, their deep burial and intrusion, and their greater age. This implies that these rocks might have sustained several periods of deformation before the closing of the Tethys Sea. The younger Cambrian through Silurian rocks are disharmonically folded about this Precambrian core.

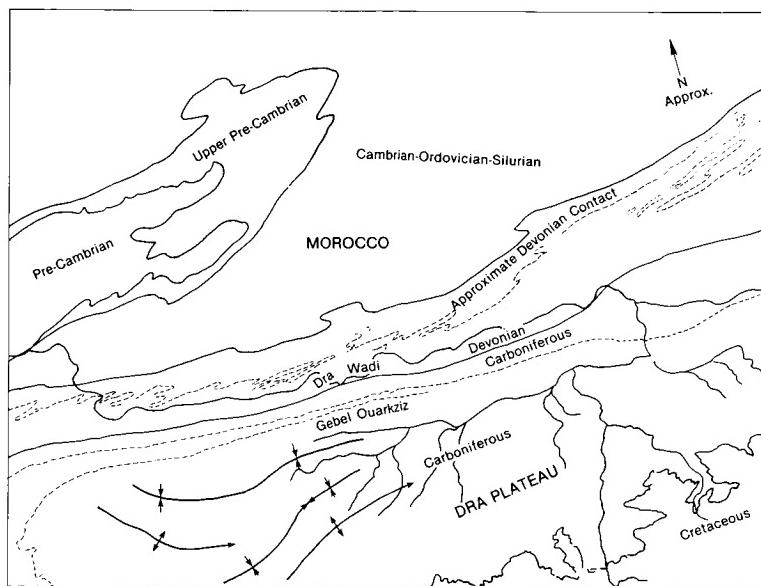
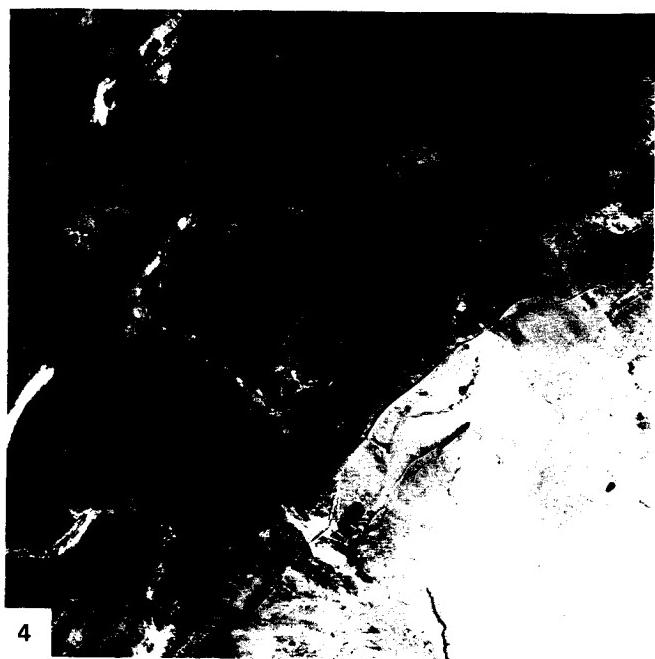
There are several zones of disharmonic folding within the Paleozoic sedimentary section. The most obvious zone is the drag-folded Devonian rocks—the narrow band of contorted, intensely folded black rocks that extend diagonally across the center of the image just north of Gebel Ouarkziz. By comparison, the Carboniferous rocks of Gebel Ouarkziz are rather gently deformed and dip to the south, forming the northern limb of a broad synclinorium. The very tight east-northeast-trending folds in the black Devonian rocks north of Gebel Ouarkziz and similar trends of more gentle folds in the Carboniferous and Triassic rocks to the south of the Ouarkziz imply that a major zone of right-lateral transcurrent, or right-slip, movement lies just north of Gebel Ouarkziz. This zone is also parallel to the Agadir right-slip fault to the north and the previously mentioned suspected fault zone to the south (Wildi, 1983).

The trends and changes in trends of structures and the major zones of apparent right-lateral strike-slip movement call attention to two other features common within most major zones of plate convergence: first, convergence is not generally orthogonal (i.e., movement vectors of convergent plates are not parallel to each other or are not perpendicular to the plate margins or suture zones), which implies translational as well as compressive strain at the suture (Wildi, 1983), and second, the previously existing structural fabric of the tectonic plate may play an important role in determining the style and orientation of deformation features. It is difficult to separate the effects of these two general conditions without field work.

Farther to the east, the style of deformation in the Atlas orogen changes somewhat, as evidenced in the Landsat images (Figures T-30.4 and T-30.5), which show two regions along the Moroccan/Algerian border. Darker Jurassic (and isolated outcrops of older rocks) are more strongly folded than lighter toned Cretaceous rocks. This disharmony is partially the result of a Late Jurassic folding event in which decoupling took place on an Upper Jurassic salt unit. (*JRE*) Landsat 1103-10413, November 3, 1972.



ORIGINAL PAGE IS
OF POOR QUALITY



ORIGINAL PAGE
OR PHOTOCOPY



ORIGINAL PAGE
OF THE PHOTOGRAPH



PLATE T-31

RICHÂT STRUCTURE, MAURITANIA

The bull's-eye target pattern of the Richât structure on the barren Gres de Chinguetti Plateau in the Adrar region of central Mauritania is an eye-catching feature when seen from space, as is evident in the color Plate photograph taken looking south from the 17th Shuttle mission. Sand has drifted northward and encroaches on part of the southern half of the 38-km wide structure. The Makteir desert abuts the plateau to the north (Figure T-31.1). Although reminiscent of multiringed impact structures on the Moon, Mercury, and Mars, field and laboratory evidence suggests that the Richât structure is a dome of endogenic origin.

Richât, slightly elliptical and with its long axis oriented northeast (upper right corner in Figure T-31.2, a vertical air photograph), lies in a depression in which drainage is annular and radial and topographic relief is about 100 m. The strata dip outward, so that weathering and erosion of the alternating resistant and nonresistant Late Precambrian and Early Paleozoic rocks have produced a series of inward-facing cuestas (Figure T-31.3). Quartzite forms the resistant circular ridges, and less resistant rocks underlie the intervening annular depressions, some of which contain seasonal lakes. The center of the structure, the Guelb er Richât (Figure T-31.3), exposes flat-lying limestone and some meta-arkose surrounded by a massive ridge of chert and chert breccia. The overlying part of the stratigraphic section, well exposed outward in the dome, consists of Upper Precambrian/Lower Paleozoic shelf facies rocks.

The quaquaversal dip of the beds increases inward 20 to 25°; locally, dips are as great as 35°. Some minor radial and tangential faults occur in the outer parts of the structure. The north part of the structure is cut by a fault system oriented N30°E that appears to be unrelated to the formation of the dome. Reconstruction of the eroded beds of the structure suggests that they were uplifted 3 to 4 km to form the dome.

Reconnaissance gravity data do not support the presence at a reasonable depth of an igneous or diapiric intrusive mass nor do they suggest the presence of low-density breccia layers characteristic of impact structures. However, deep erosion could have removed the brecciated lens. Thus, the gravity data neither confirm nor preclude an impact origin for the structure.

Dolerite sills and dikes crop out at several localities within the structure. Associated analcime-rich rock has been interpreted by some to be the result of hydrothermal alteration of rhyolite sills and dikes. No evidence of volcanic activity exists at Richât.

Some geomorphologists have interpreted Richât as an impact structure because of the nearly circular "bulls-eye" pattern, the reported presence of coesite, the uniqueness of the structure in the region, its interior drainage, and the presence of nearby

impact structures—Aouelloul, some 150 km to the southeast, and Tenoumer to the north (Plate T-61). Most geomorphologists now consider Richât to be an endogenic structural dome of purely terrestrial origin. An impact origin is discounted by Monod and Pomerol (1973) for these reasons:

1. Dips of strata are relatively gentle; strata are even flat-lying at the center of the structure. Nowhere are beds severely disrupted and contorted.

2. Although breccia is abundant in the structure, the breccia does not have the characteristics of that produced by impact.

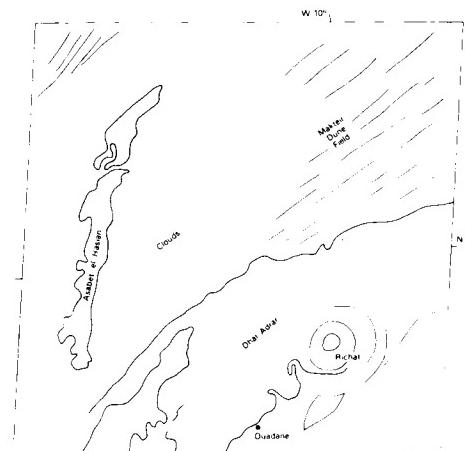
3. Injection breccia and pseudotachylite-like material, shatter cones, and other shock-metamorphic effects have not been identified.

4. The coesite reported from the rocks of the structure is almost certainly barite that was misidentified (Fudali, 1969).

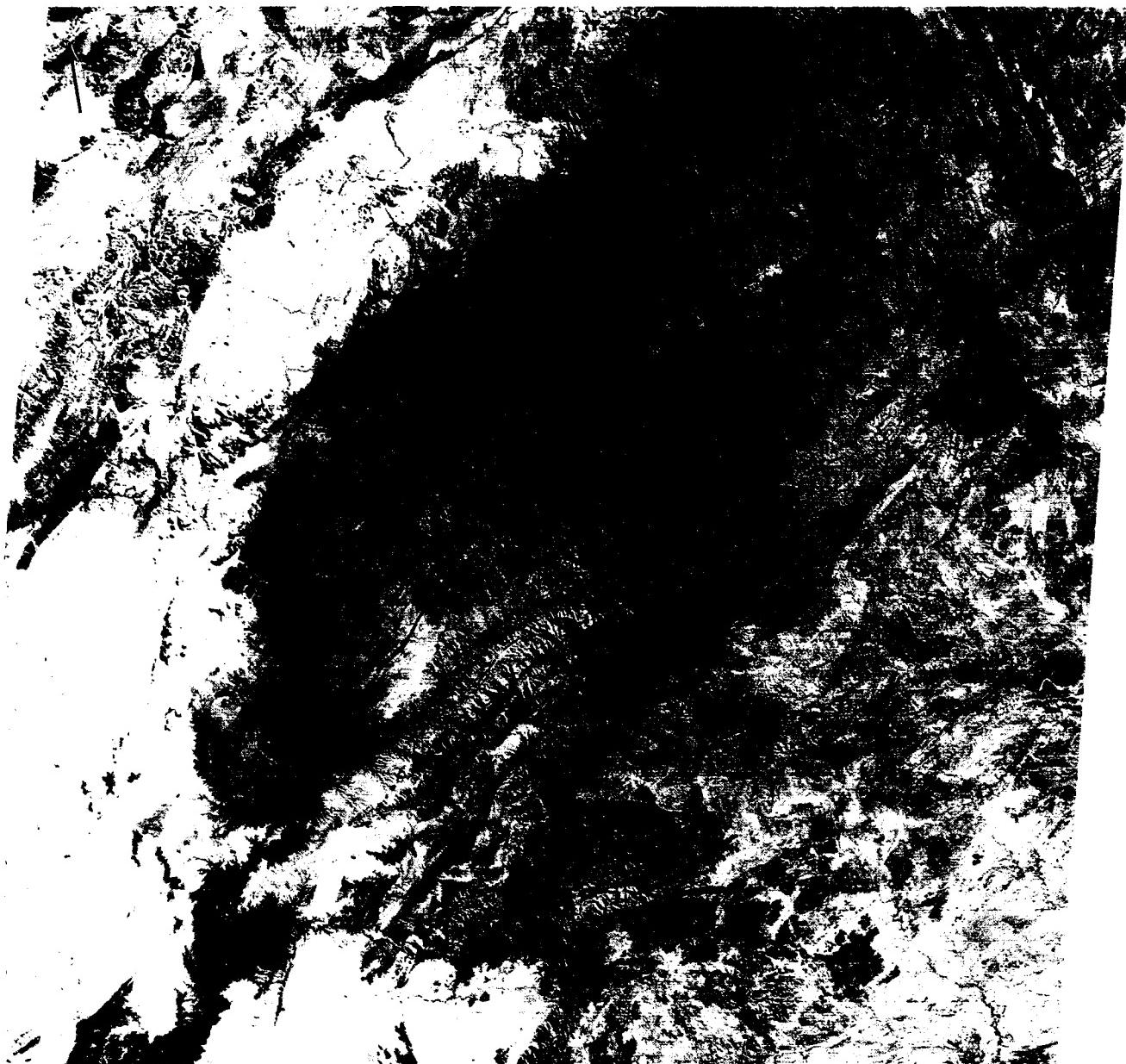
5. An unrealistic amount of erosion would be needed if Richât were an impact structure in order to remove shock-metamorphic effects. Studies elsewhere have indicated that severe effects extend downward below the base of a typical impact crater to about one-fifth its diameter; less severe shock-metamorphic effects extend even deeper. At Richât, then, detectable shock-metamorphic effects might be expected to extend to a depth of perhaps 10 km. The fact that none is observed in the rocks of the structure argues for at least 10 km of erosion if, in fact, Richât is an impact structure. Geologic history of the region does not allow the possibility of that degree of erosion nor does the structure itself show evidence of secondary uplift or deformation, or both. Reconstruction of the beds suggests a maximum uparching of 3 to 4 km, which is a reasonable upper limit to the amount of erosion that has occurred at Richât.

6. The proximity of Aouelloul and Richât is coincidental; they are of significantly different ages. Aouelloul, a small bowl-shaped crater, is probably of Quaternary age, whereas Richât is an ancient structure that has undergone significant planation.

Semsiyat dome, 50 km west-southwest of Richât and centered at latitude 21°0'N and longitude 11°50'W, has a diameter of 5 km. Although the style of deformation is similar to that of Richât, Semsiyat is barely detectable on the ground. The structure lies on the Chinguetti Plateau and has only a few meters of topographic relief. Strata dip so slightly that field measurement is difficult. Exposures are poor, and the rocks are extremely weathered. No evidence of shock metamorphism has been discovered at Semsiyat; like Richât, it is believed to be a dome of endogenic origin (Dietz et al., 1967). (GCW: J. R. Underwood) STS-61A.



ORIGINAL PAGE
COLOR PHOTOGRAPH



4

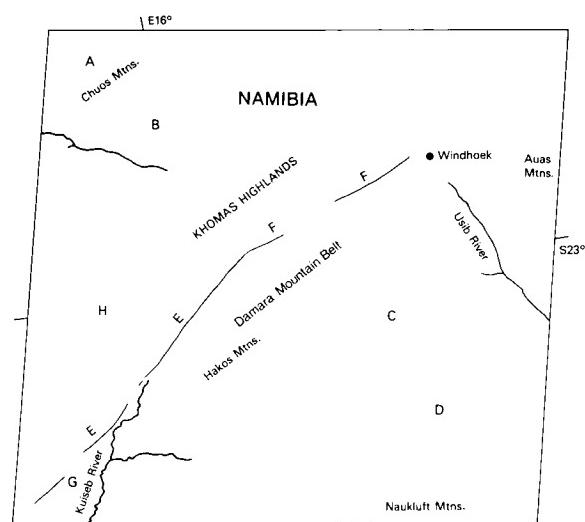


PLATE T-33

The largest of the ancient shield nuclei in the African continent is located in eastern South Africa. Known as the Transvaal or Kaapvaal Craton, this shield contains plutonic, metamorphic, and metasedimentary rocks older than 2.5 Ga. Although younger Precambrian units cover much of the southern and western parts of the craton, the old basement complex, including Archean granite/greenstone belts, crops out along the eastern and much of the northern parts of the craton.

The Plate covers the part of the craton lying slightly west of Johannesburg and Pretoria (just off the right-central margin) and just north of the Vaal River. Two physiographic regions, the South Africa High Veld (lower part of the image) and the Transvaal Plateau Basin (upper) appear in the scene, which itself extends across sections of the Witwatersrand and Bushveld geologic provinces. Elevations in these regions are between 1500 and 1600 m. The High Veld is mainly undulating grass country; the Transvaal Plateau contains eroded plains (Figure T-33.1, an aerial photograph) and ridges (Figure T-33.2) of resistant quartzite whose distribution is controlled by the Bushveld structure. Most of the terrain is a pediplain within the Late Cenozoic/post-African denudation surface, but a remnant of the Early African surface cuts across the lower half of the image.

Outcrops of the Basement (or "Old") Granite in the Swazi Erathem System are limited to the areas around A on the index map, but land-use patterns obscure their expression in the image. The next younger group of rocks comprise the Early Proterozoic Witwatersrand Supergroup. This triad includes the Dominion Reef Group, the overlying Witwatersrand Group (exposed at B, C, and D), and the Ventersdorp Group (exposed at E, F, and G). Within the Witwatersrand are the "reef" units, layers of quartzose conglomerates that carry both disseminated and nugget gold, which makes this region the greatest world supplier.

In this scene, a quadrant of the near-circular Vredefort Dome (G) contains Ventersdorp units along with inner Witwatersrand beds surrounding the Old Granite in its core (off the lower right corner). This structure, with its overturned rimming strata, has been explained as a diapiric intrusive plug, but the discovery of shatter cones and other shock-induced metamorphic features in its central granite suggests that it possibly originated as an ancient impact crater now eroded to an astrobleme.

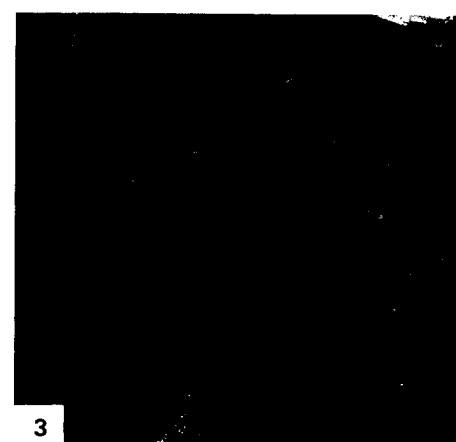
Strongly folded Proterozoic Transvaal Supergroup rocks appear in the central part of the image, where they dip northward toward the Transvaal basin, and at an inlier around J. The

TRANSVAAL, SOUTH AFRICA

Dolomite Series (at H and I), 1000 to 2000 m thick, includes darker chert-poor and lighter chert-rich stratigraphic zones. Overlying it is the Pretoria Formation, up to 8000 m of shales and quartzites, some of the latter holding up ridges and escarpments as at K and L. Numerous regional fractures, some of which truncate or offset the units, cut both series (Figure T-33.3). These faults and joints also localize water, as is evident during the rainy season when linear vegetation marks them (see Short et al., 1976, Plates 353 and 354).

Transvaal deposition ended with emplacement of the Bushveld Complex about 1950 to 2000 Ma ago. This huge igneous terrain (66000 km^2), once supposed to be a great lopolith, covers the upper third of the image, but extends over an even larger area to the northeast. The Bushveld event began with extrusion (east of scene) of felsites and granophyres, with concomitant subsidence of Transvaal units as magma withdrawal weakened support. The Main Plutonic phase involved emplacements of several funnel-shaped intrusions into both the felsites and Transvaal (Pretoria) units from at least five centers. This first produced gabbros, then pyroxenites and norites, that attain thicknesses in excess of 9000 m. Basic intrusions occupy areas around M, N, O, and P. Within these are differentiated cumulate layers of magnetite and chromite. Later granite rocks of the Acid Intrusive Phase intruded between the ultrabasics and felsites; these form a plains around Q and R. About 1.4 Ga ago, several alkaline intrusions penetrated the Transvaal craton. The largest, the Pilanesberg (S), consists of syenite and foyaite that form concentric hills.

Figure T-33.4, a Landsat image, depicts the ancient terrane (older than 3.0 Ga) carved from the Barberton Mountain Land greenstone and other units exposed on the east edge of the Transvaal Craton. The infolded greenstones were derived from volcanic rocks and chert-rich sediments (Onverswacht Series, which contains spheroidal and filamentous micro-organisms), graywackes and shales (the Fig Tree Series, which contains primitive algae and other life-forms), and feldspathic sandstones and shales of the Moodies Series. Erosion has accentuated the folds, faults, and fractures in this terrane. Compare this greenstone/pluton belt with the Archean terranes of Western Australia (Plate T-55). (NMS) Additional References: Anhaeuser and Robb (1980), Fripp et al. (1978), Simpson (1978), Windley (1984), Furton (1963), Hamilton and Cooke (1959). Landsat 10230-07370-7, March 10, 1973.



ORIGINAL PAGE
COLOR PHOTOGRAPH

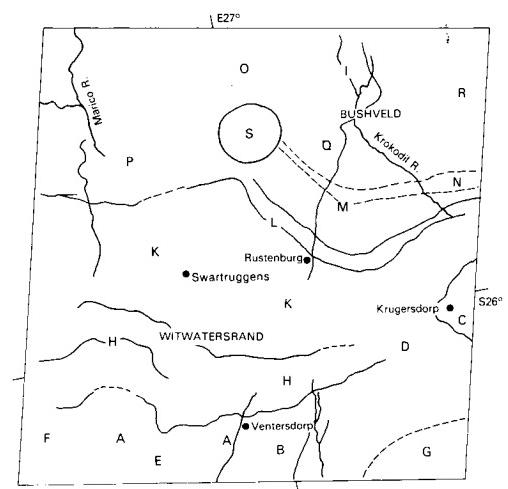
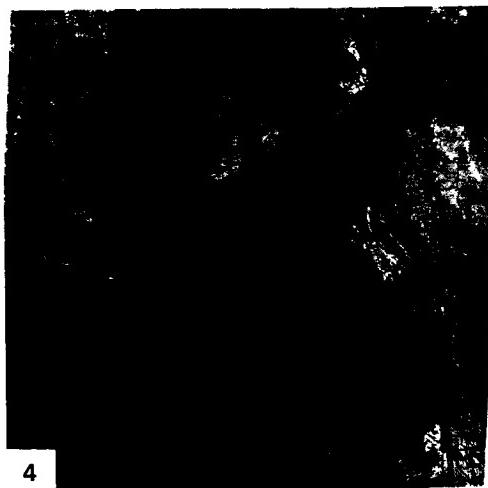
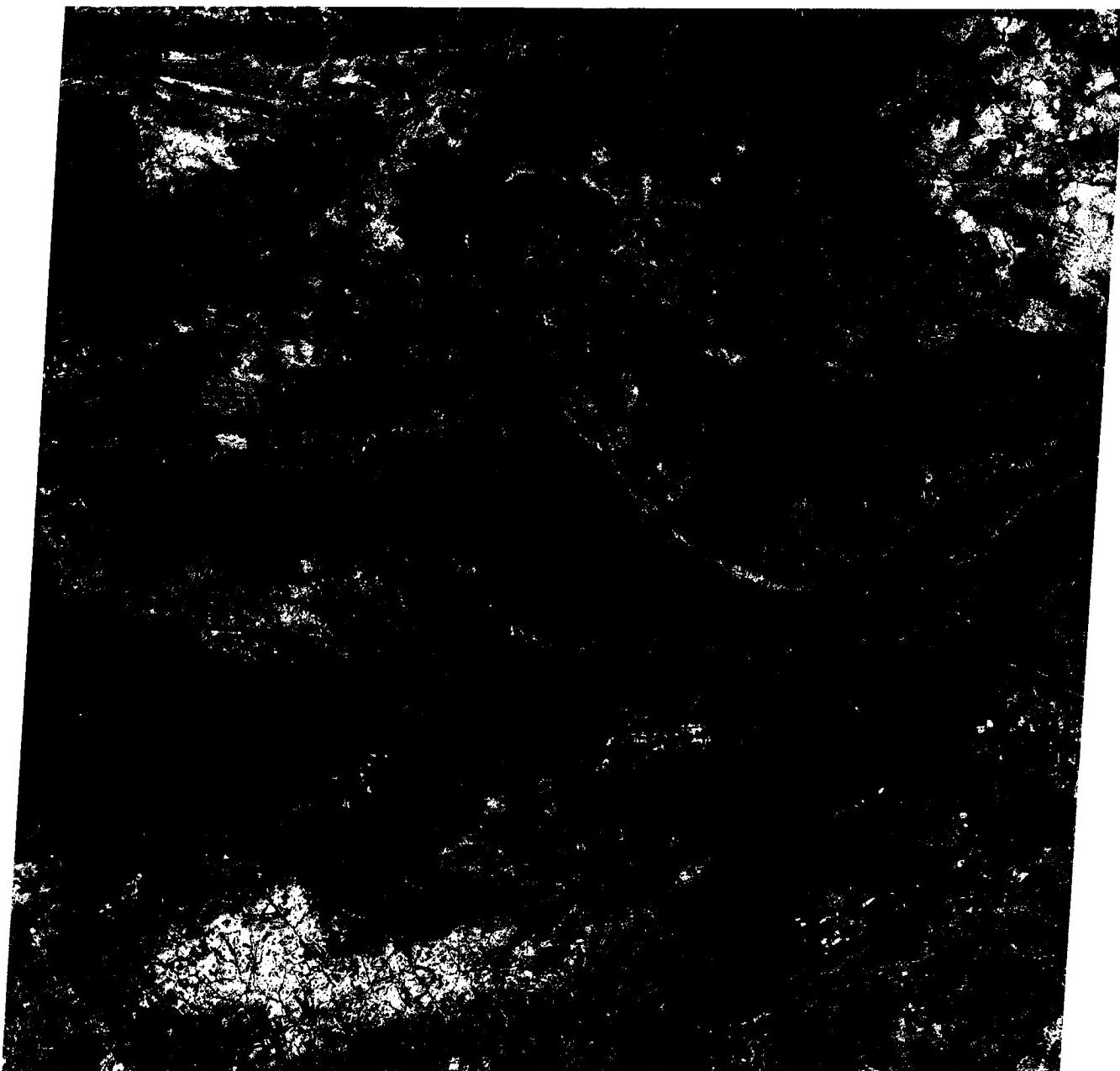


PLATE T-34

Southern Africa contains extensive exposures of the African Shield, a cratonic complex consisting of accreted arcs and microplates that have built up from collisional terranes. These terranes are replete with sutures, infolded sedimentary rocks, and intrusions of granitic rock. Isotopic ages range from 3800 to 500 Ma. The Plate scene shows the southern Zimbabwe (Rhodesian) Craton and one of the most remarkable intrusive bodies in the world, the Great Dike of Zimbabwe (also referred to in older reports as the Great Dyke of Rhodesia).

On the south, the Limpopo Mobile Belt, a 900-km long, 200-km wide ancient mountain belt (including metasediments as old as 3.8 Ga and clastic sediments as young as 2.5 Ga), separates the Zimbabwe Craton from the Kaapvaal Craton in the Transvaal of South Africa (Plate T-33). Highly deformed greenschists, anorthosites, and gneisses (seen on the index map at A and B) were thrust from the south against the Zimbabwe Craton about 2700 Ma ago.

The Zimbabwe cratonic terrane is an excellent example of an Archean greenstone/granodioritic complex (MacGregor, 1951). Volcanic rocks, graywackes, cherts, banded iron formation, and other sedimentary rocks have been metamorphosed into low-grade schists and amphibolites. These comprise strongly deformed, arcuate, synformal belts enclosed within older rocks. "Gregarious batholiths" (MacGregor, 1951), diapiric granites/tonalites, including the Chibi batholith at C and segments of the Shangani and Malopo batholiths at D and E, occupy large parts of the image.

The Plate scene and Figure T-34.1, another Landsat frame that depicts the craton around Salisbury and to the east, illustrate the terrain typical of the region. The greenstone belts (Sebakwian Group (~3.3 Ga), Bulawayan Group (2.7 Ga); with contorted infolds at F, G, H, and I; Shamvaian Group (2.65 Ga)) are conspicuous, but the gneisses, granulites, and granites form featureless low-relief topography. The savannah veld contains obscuring patterns of land use, including large light-toned cleared areas that superficially resemble plutons. In Figure T-34.2, the northeast corner of Zimbabwe, circular clusters of castle kopjes (degenerate bornhardts)—rocky hills of resistant granite—are remnants of several plutons (e.g., Mtoko near the center). The arrangement of the kopjes suggests that weathering and erosion proceeded along fractures (joints) that enlarged over time.

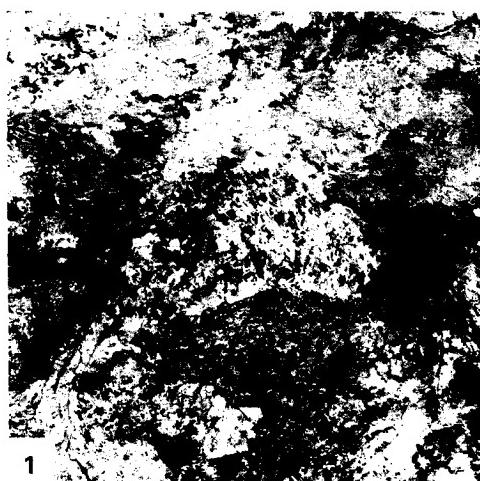
The Great Dike itself, conspicuous on the image and in an aerial photograph (Figure T-34.2), is a topographic ridge of low relief with linear outer ridges developed on cumulate layers that dip gently inward near the contact of the dike with the coun-

GREAT DIKE OF ZIMBABWE

try rock. The dike (average width of 6 to 8 km) runs about N15°E for nearly 500 km across Zimbabwe. The term "dike" for this structure is somewhat misleading in a strict sense. The narrow linear dark band seen in the Plate is actually the feeder conduit for four contiguous lopoliths intruded about 2.5 Ga ago into several north-trending fractures within the craton during an extensional tectonic phase. The intrusions spread subhorizontally in one or more thick, dense units. Later faulting (normal with some strike-slips along west-northwest or east-west trends) offsets the lopoliths and their feeders, easily seen in the Plate (at J, K, L, M). Subsequent deep erosion over the last 2.5 Ga has stripped off most of the spread-out lopolithic mass, leaving only its feeder roots in the form of the largest "dike" known on Earth. Smaller subsidiary dikes, Umvimeela and East, also served as feeders.

Each of the lopoliths' feeder segments, the Wedza and Selukwe complexes in the Plate and the Hartley and Musengezi Complexes to the north, is characterized by similar distinctive petrology and internal structure. Where exposed or drilled, each of the lopoliths is layered with a gentle syncline bend perpendicular to the dike axis. The topmost unit is usually gabbroic, seen in the Landsat images as patches of lighter toned rock. Lower units consist of cyclic bands (cumulates, often many meters thick) of orthopyroxenite, picrite, harzburgite, and chromite seams. Structural relations and gravity distribution suggest that the "dike" is a permissive intrusion with vertical contacts emplaced in an extensional stress field; it seemingly is not the initial phase of continental rifting.

The Zimbabwe shield ends abruptly along a suture line against the Zambezi belt to the north. This is strikingly evident in a Landsat image (Figure T-34.3) that shows darker tones where the Zambezi belt meets the shield. An escarpment marks the contact, and both topography and structural grain are somewhat different in this northern terrane. (The irregular light-toned patches result from land cultivation practices.) The Zambezi River here flows eastward from Zambia to Mozambique. (NMS) Additional References: Bichan (1970), Furon (1963), MacGregor (1951), Pritchard (1979), Stagman (1978), Worst (1960). Landsat 10103-07291-7, November 5, 1972.



1



2

ORIGINAL PAGE IS
OF POOR QUALITY

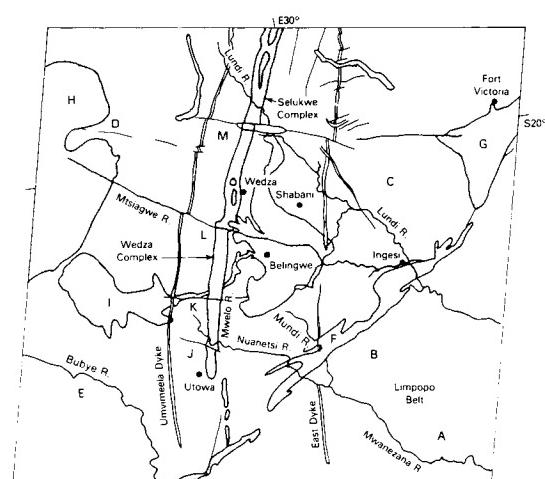
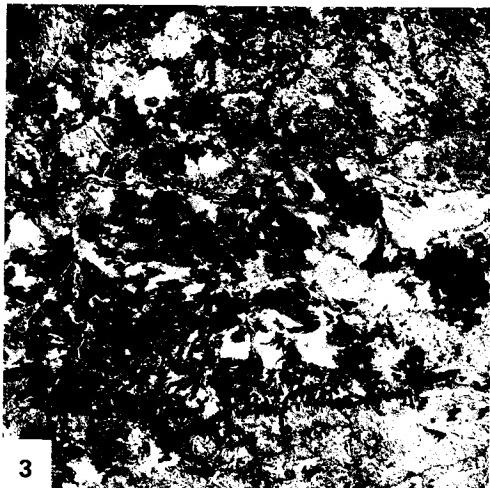


PLATE T-35

AFRICAN RIFT

The African rift system is one of the most spectacular geologic features on the face of the Earth. It extends from the Red Sea in the Afar region of Ethiopia (about 10°N) (Plate T-36) to beyond the Zambezi River (15°S) (Plate T-32) a distance about 4000 km (Willis, 1936). Over much of this distance, young volcanic and sedimentary rocks (Miocene to Recent) fill the rift, which lies within old (Precambrian) shield rocks (McConnell, 1972; Pallister, 1979). Like the Red Sea and Gulf of Aden rifts, the African rift marks the locus of the divergence of continental plates. Movement on this African rift is only a few millimeters per year versus centimeters per year on the other rifts. The process of continental divergence has proceeded much farther in the Red Sea rift and Gulf of Aden rift, which constitute the other two arms of a triple rift junction, than in the African rift. The African rift offers a unique opportunity to observe the initiation of plate divergence in a continental environment (Baker et al., 1972).

It was nearly impossible to study the rift in its entirety until the advent of space-acquired imagery because of its size (Mohr, 1973, 1974). One of the long-standing controversies about the rift is the extent to which preexisting Precambrian structural trends control the location and trend of the rift. Examination of imagery covering the entire rift shows that, in some locations, the rift parallels preexisting structural trends and, in other places, the rift is clearly independent of Precambrian trends. In the area shown on this Plate mosaic, the rift appears to be independent of Precambrian structures (i.e., the trend of the rift and the strike of the Precambrian structure are divergent).

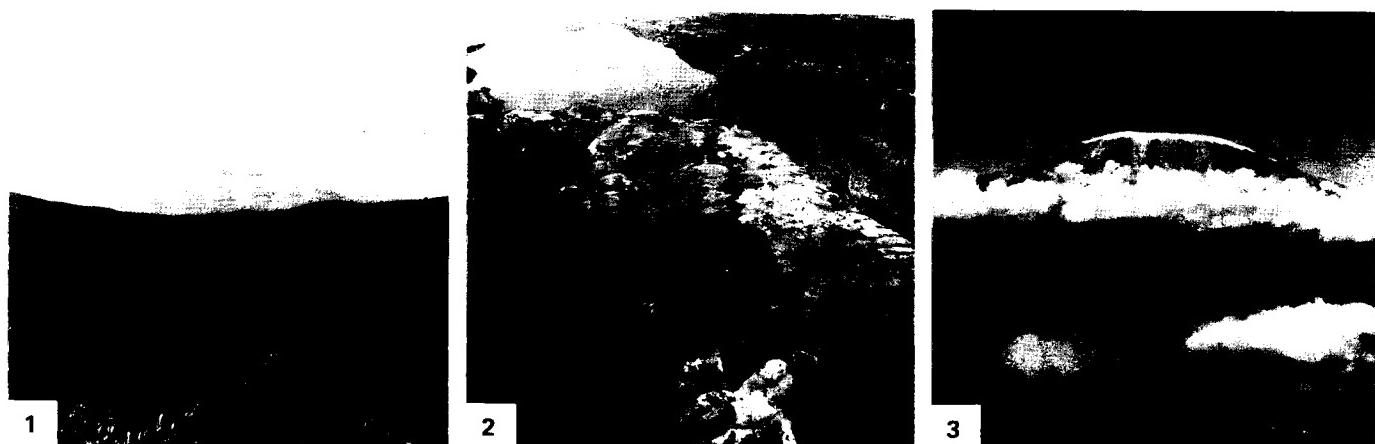
The mosaic, which covers about 500 km of the rift, displays many of the features typical of the rifting process. Bold scarps mark the faults that bound the rift. The crisp topographic character of many of these scarps indicates very recent movement on the associated faults. The ground photographs (Figures T-35.1 and T-35.2) indicate the abruptness and freshness of the valley walls on both sides. Over much of their length, these scarps separate the more moist upland forests (bright red) from the arid, barren, lava-covered floor of the rift. Soda lakes (e.g., Lake

Natron) and parallel north-trending extensional fractures characterize the floor of the rift. The parallel fractures and bounding faults accentuate the tensional nature of the rift and emphasize the divergence of the continental plates.

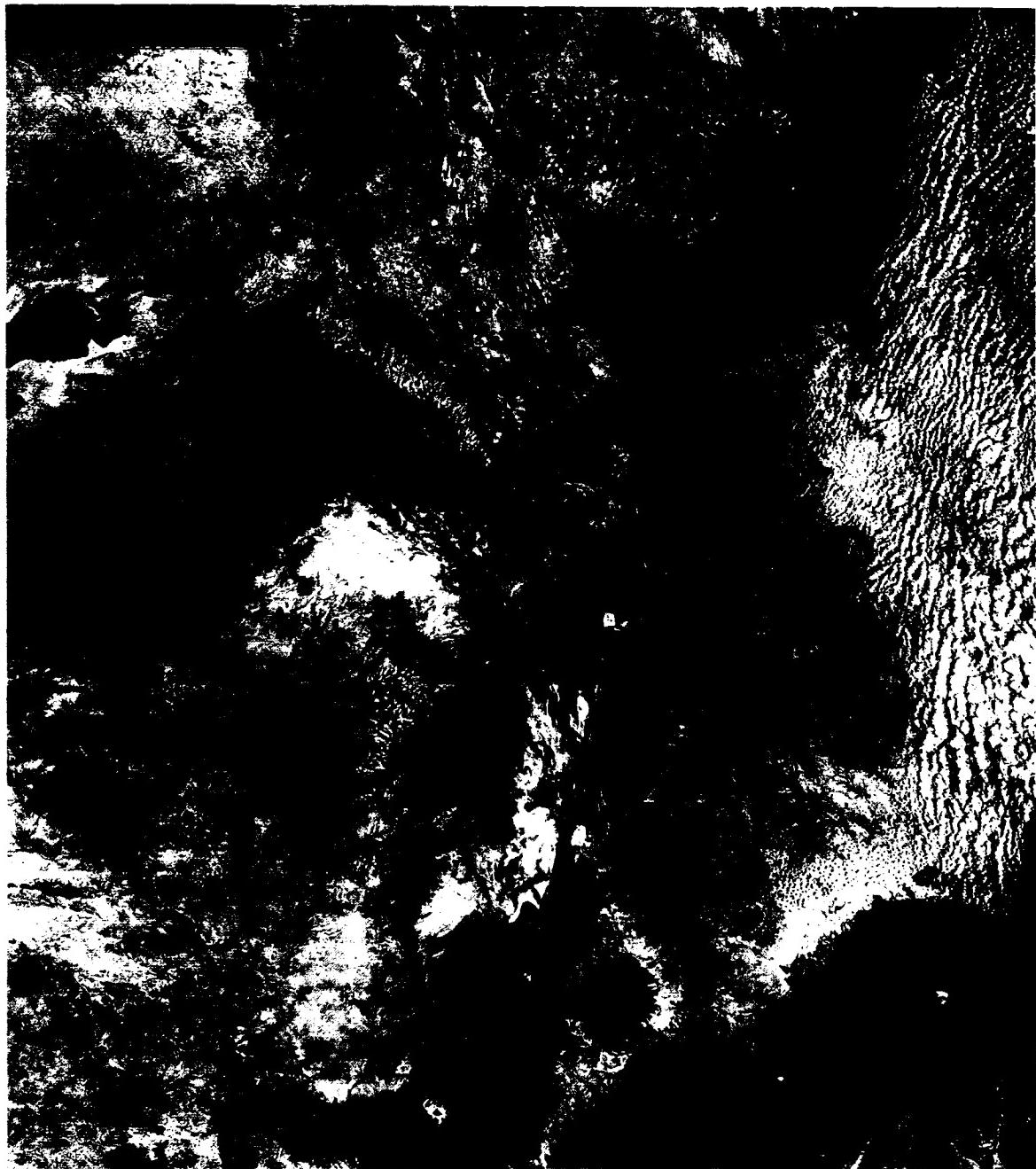
The mosaic includes the two highest mountains in Africa, Mt. Kenya (5199 m) and Mt. Kilimanjaro (5895 m; Figure T-35.3), both of which are large volcanic edifices. The volcanoes, with their circular structures and radial drainage patterns, are easily identified. Part of the lower section of the scene is shown elsewhere in Figure V-19.2. That Landsat image shows volcanoes and craters in various stages of erosion. Many of the abundant volcanoes in and near the rift have erupted extremely basic (silica poor) lavas, which suggests intimate relationship to the mantle and a paucity of partial melting of the crust. For instance, Ol Doinyo Lengai erupts nepheline lavas. Other volcanoes have carbonatite flows, equilibrated at great depth, associated with them (Baker et al., 1978).

The complex structure of the Precambrian rocks that comprise the uplands is clearly visible on both sides of the rift near the center of the mosaic. Within the area of the mosaic, the uplands slope away from the rift on both sides, suggesting that the rift bisects a broad crustal bulge. This uparching is similar to the general structure present along the Red Sea and Gulf of Suez (Plates T-36 and T-37) and probably is thermally driven.

To the north, the Gregory rift joins the Ethiopian rift, which extends into the Afar Triangle (Plate T-36). To the south, the Gregory rift fans out and loses its distinctive character in the Tanzanian shield. The Western rift appears to take up the extension where the Eastern rift plays out. Figure T-35.4 shows a portion of Lake Tanganyika, which occupies a segment of the Western rift. The trough, containing the lake, appears to be offset in a right-lateral sense. The offset is more apparent than real, and the graben probably originated in this geometric arrangement without major lateral displacement (B. Rosendahl, personal communication). Here, as to the northeast, the uplands on either side slope away from the rift, suggesting a large topographic bulge. *(JRE) Landsat Mosaic.*



ORIGINAL PAGE
COLOR PHOTOLASH



4

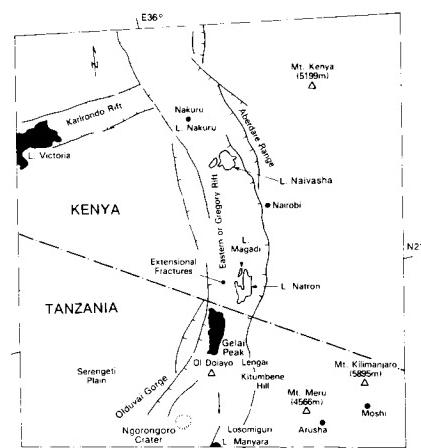


PLATE T-36

This mosaic displays the incipient breakup of a continent along rifts with concomitant invasion of magmas to form new oceanic crust. Indeed, this scene is the outstanding example of a growing spreading center and a rift/rift/rift (RRR) triple junction. The rift arms—the Red Sea, the Gulf of Aden, and the Ethiopian section of the East African Rift—diverge from a center near Lake Abbe. The first two separate Africa from Arabia, whereas the third, the African Rift, seemingly initiates splitting of the continental crust of northeastern Africa. As a consequence, Arabia moves to the northeast, bounded on the northwest by the Dead Sea Rift zone and the Owen/Quetta/Chaman Fault zone to the southeast, to collide with Eurasia along the Zagros Mountains of Syria, Iraq, and Iran along a northeast front. Easternmost Africa appears to be separating eastward along the East African Rift, but movement is very slow and is hindered by westward spreading from the Carlsberg Ridge in the Indian Ocean.

Precambrian rocks (reddish brown in the mosaic (A)), once part of a single shield, border the rift arms and rise to +3000 m along abrupt scarps to form the Ethiopian (west) and Somalian (east (B)) plateaus and the mountains of Yemen (C). Old erosion surfaces and capping Mesozoic rocks (lighter areas in Yemen (D)) slope away from the rift. Tertiary and Quaternary extrusive rocks fill the Afar Depression at the intersection of the three rift systems. Here, elevations vary from +1000 to -100 m. Alkali salts and eolian sand fill some of the lower areas and appear white against the dark-gray and black lavas on the mosaic.

Thermally driven uplift and domal arching of the crust began in the Oligocene (perhaps earlier), accompanied by attenuation and eventual rifting in the Gulf of Aden and Red Sea regions. Lateral spreading of ascending mantle material helped to generate linear or axial zones of weakness along which rifting progressed. Early stages of volcanism (Eocene) extruded alkalic basalts of the Trap Series ($150\,000 \text{ km}^3$) that range in thickness from a few hundred to 2000 m. Somewhat later, an extensive (thickness $>4000 \text{ m}$, volume $120\,000 \text{ km}^3$) series of flood basalts filled the protorift trough within the Afar. By the Miocene, alkali olivine basalts poured from large shield volcanoes at various local centers, releasing up to $70\,000 \text{ km}^3$ of widespread extrusive material. Some extrusions were peralkaline in the Pliocene. Many of the deposits resulted from violent eruptions that discharged large

AFAR TRIPLE JUNCTION

volumes of silicic welded tuffs both on plateaus and in rifts. Rifting in Ethiopia and southward began in the Miocene and intensified in the Pliocene. Eruption of oceanic tholeiites began in Middle Miocene and became the dominant rock type erupted through the Holocene. (Some peralkaline activity continued.) True oceanic lavas, confined mainly to the oceanic rift arms, were first emplaced from 25 to 15 Ma ago. The median troughs of the Gulf of Aden and Red Sea reached widths of 200 and 50 km, respectively. Although neither rift floor has evolved into a spreading ridge, transform faults cut the proto-oceanic crust of the Gulf. This crust shows some magnetic polarity striping from which a spreading rate of 2 cm/year has been calculated.

Deformation within the Afar Triangle (Plate V-21) tends to be greatest adjacent to the margins of the rift (marked by bold scarps). Faults of large throw control the inner boundary of the margins. These zones contain marginal grabens, 4 to 6 km wide, offset by cross-rift transcurrent faults. On its east side, the Afar Triangle is separated from the Red Sea and Gulf of Aden by the Danakil and Aysha horsts, strongly deformed blocks of Precambrian and Mesozoic rocks now largely covered by Afar volcanic rocks. Many normal fault belts trend northwest parallel to the Red Sea across the eastern portion of the Afar. Northeast transcurrent faults and associated secondary en echelon faults cut the floor of the main rift (Figure T-36.1).

In the Afar, Holocene volcanic cones, mostly of silicic composition, lie on tensional crest lines (Figure T-36.2). These axial ridge volcanoes line up in the central zone along an extension of the Wonzi fault belt that occupies the middle of the Ethiopian Rift zone to the south. The structural trend of this rift is north-northeast, but en echelon fault displacements give it an apparent northeast trend in the topography.

Figure T-36.3, a Landsat image of the Danakil Depression northwest of Djibouti, shows details of the complex pattern of recent volcanic flows (black), salt deposits in depressions (white), and large numbers of small normal faults. From the pattern, it is easy to visualize the crust stretching, faulting, and spreading with magma oozing up through the fractures to form flows and volcanoes. (GCW: H. Blodgett) References: Al-Shanti (1979), Bannert (1972), Greenwood and Bleackley (1967), Mohr (1970). Landsat Mosaic.



1



2

**ORIGINAL B&W
COLOR PHOTOGRAPH**

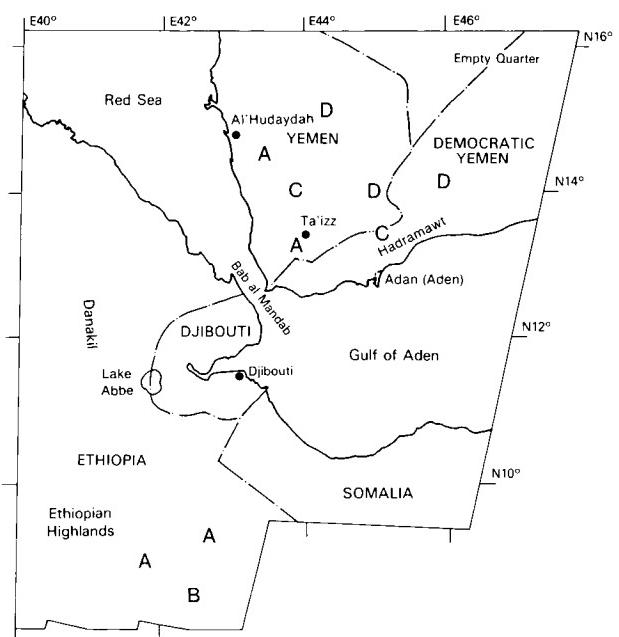
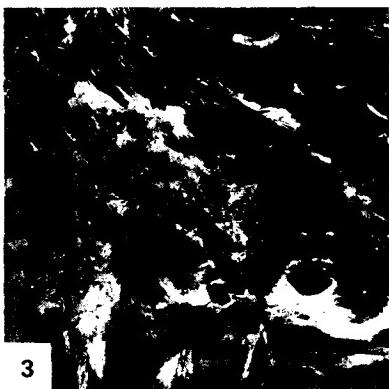


PLATE T-37

ORIGINAL PAGE IS
OF POOR QUALITY

The Plate, an oblique photograph taken from Apollo 7, clearly illustrates the division of the Red Sea at its northern end into two linear depressions flanking the Sinai Peninsula. These depressions, the Gulf of Suez and the Gulf of Aqaba, and the Red Sea itself are products of active tectonism. About 40 Ma ago, Arabia was an integral part of the African continent, but by Late Oligocene time, rifting had begun along the future site of the Red Sea. This rifting resulted in the formation of the Arabian plate that broke away from the African plate and began to move northward independently (see Plate T-36).

An active spreading center in the axis of the Red Sea joins another in the Gulf of Aden at the Afar junction where the East African Rift extends southward into the continent. Separation of the two plates is greater in the south along the Red Sea, and true ocean floor does not extend all the way to the Gulf of Aqaba.

The Gulf of Suez is 30 to 50 km wide compared to over 160 km for the northern Red Sea. The trend of the Gulf of Suez is the same as that of the Red Sea; it can be thought of as an extension of the Red Sea Rift. The Dead Sea fault system is an active left-lateral strike-slip fault with local extensional and compressional segments. Cumulative displacement of a little over 100 km since the Miocene has been reported (Freund et al., 1970).

About 40 Ma ago, a large area in northeastern Africa and the Arabian Peninsula was covered by seas, and thick limestones were deposited. As rifting progressed, the shoulders of the rift, not only along the Red Sea but also along the Gulf of Suez and much of the Dead Sea transform fault, were elevated several kilometers. Garfunkel and Bartov (1977) report as much as 4 km of vertical displacement along faults in the Sinai near the southern end of the Gulf of Suez. Intensive erosion of these uplifted areas removed the sedimentary cover, exposing the underlying crystalline rock. These are the dark-toned highly fractured areas seen in the Plate and Figure T-37.1, a Landsat view, on the southern end of the Sinai Peninsula, along the Gulf of Aqaba and adjacent to the Red Sea and Gulf of Suez. Relief in these rugged highly dissected areas exceeds 2000 m at Gebel Musa (Mt. Sinai) near the center of the crystalline rock outcrop in Sinai. An adjacent peak, Gebel Katherina, is more than 2500 m high. Gebel Gharib, near the northern end of the dark zone, is less than 1800 m high.

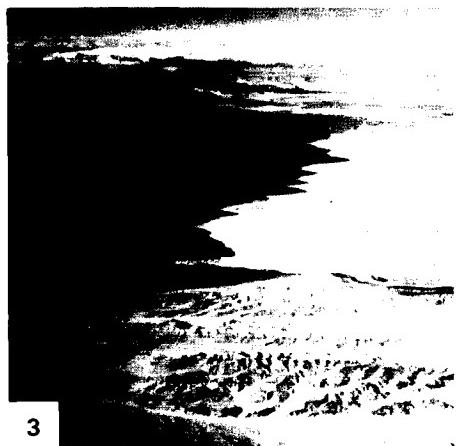
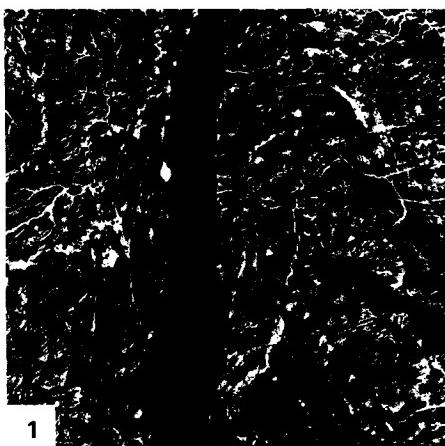
Uplift of the border area along the Gulf of Suez was not uniform, but diminished northward, thus preserving Tertiary and older sedimentary rocks around the northern end of the Gulf, and in the interior of the Sinai Peninsula. The lighter toned areas on each side of the Gulf of Suez are Miocene sediments dropped

GULF OF AQABA/GULF OF SUEZ

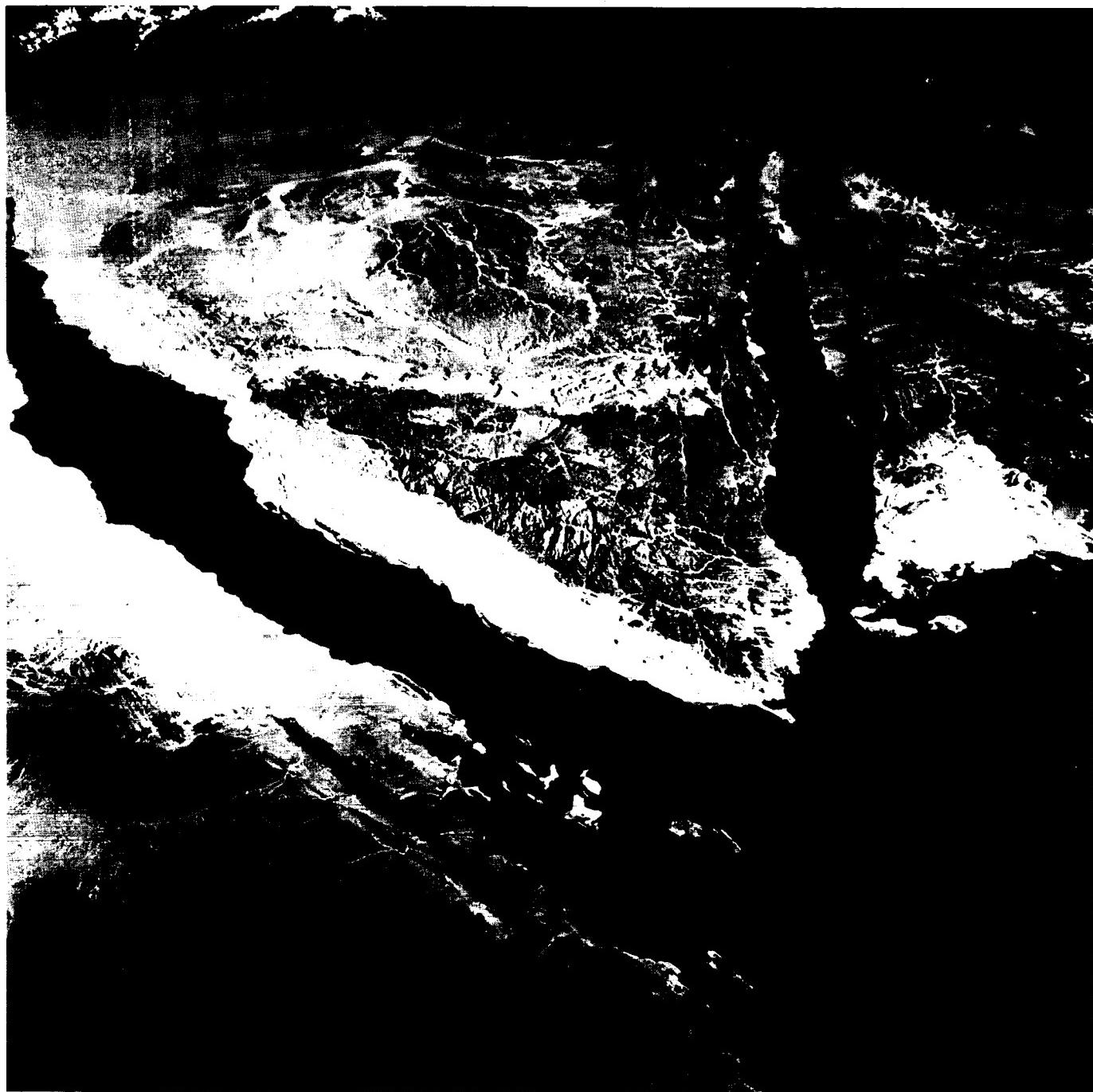
down on normal faults and preserved. These rift shoulders are partly covered with erosional debris from the mountains deposited as alluvial fans and wadi channel fill. Figure T-37.2 shows the abrupt topographical contrast between Miocene and Quaternary sediments and crystalline rocks that form the rift walls.

Although the topographic features adjacent to the rift are impressive, those under water are equally spectacular. As extension progressed in the Red Sea and the Gulf of Suez, deep chasms formed, and large elongate blocks broke from the adjacent walls and slumped into the void. Some blocks are several kilometers long and a few kilometers wide. As extension continued, the bottom of the rift subsided, mainly in response to sediment loading, by as much as 5 or 6 km in the Gulf of Suez (Bayoumi, 1983) and by even more in the Red Sea. Topographic differences in the rift bottom never approached these values because slump blocks and erosional debris from the adjacent landmasses partially filled the depression as it subsided.

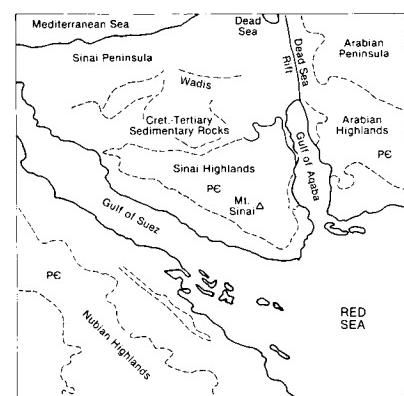
The Gulf of Aqaba can be considered a complex of pull-apart grabens associated with the great Levant transform fault that extends well to the north of the Dead Sea (Plate T-38). Erosion along the uplifted margins of the Gulf has produced a number of deltas, which line the shore (Figure T-37.3). The faulting associated with this graben system can be seen in the Plate image as straight lines extending from the Gulf of Aqaba to the Dead Sea. The graben is complex in that the surface does not consist of a single down-dropped block, but is cut by numerous cross faults. A topographic high creates a drainage divide near Gebel el Khubeij. From this point both northward and southward, elevations drop to below sea level. Several isolated deeps have been mapped in the Gulf of Aqaba, and one, located about midway along the Gulf, is more than 2000 m below sea level. The Dead Sea (Figure T-37.4, near Wadi ah Arabah) represents another major pull-apart graben along the strike-slip fault. The water surface is approximately 400 m below sea level, and water depths exceed 300 m in places. Sediment fill in the Dead Sea is several kilometers thick. The linear edge of the graben between the Gulf of Aqaba and the Dead Sea is quite evident in the Plate and Figure T-37.1. Sediments are being poured into the graben from both sides, forming fans and bahadas. The distinctive uplands terrain, a dissected plateau, east of the fault valley in Jordan (upper right corner of Plate image), is depicted in Figure T-37.4 (Ordovician sedimentary rocks near Mahattat al Mudawwarah). (GCW: O. R. Russell) Additional References: Bartov et al. (1980), Ben-Avraham et al. (1979), Coleman (1974), Eyal et al. (1981), Garfunkel (1981), Garfunkel et al. (1981), Quennell (1958). Apollo 7 7-5-1623.



ORIGINAL PAGE IS
OF POOR QUALITY



4



ORIGINAL PAGE
COLOR PHOTOGRAPH

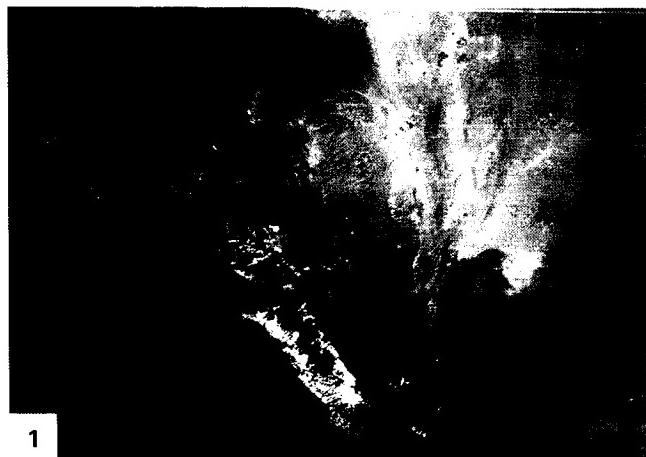
PLATE T-38

Along the eastern margin of the Mediterranean Sea, a major left-lateral transform fault extends from a spreading center at the northern end of the Red Sea through the Gulf of Aqaba, the Dead Sea, and the Sea of Galilee to a zone of continent/continent collision in the Taurus/Zagros Mountains in southern Turkey (Plate T-39). This fault is known by different names along its extent, but should probably be called the Levant fault zone. It is approximately 1000 km long and bounds the western edge of the Arabian plate. As can be readily seen on the Landsat mosaic and Figure T-38.1, an Apollo-Soyuz photograph, the fault is not straight, but exhibits angular bends that have produced zones of pull-apart grabens (Gulf of Aqaba, Dead Sea, and Sea of Galilee) and compressive bulges (Lebanon, Anti-Lebanon, and Palmyra Mountains). This has resulted in impressive differences of topography. The Jordan River Valley and the Sea of Galilee (G) lie 200 m below sea level in a pull-apart basin. In contrast, the elevation of the Lebanon Mountains, the focal point of compression at a bend, exceeds 3000 m above sea level. These mountains receive the largest quantities of snow and rainfall in the Levant area, and the runoff to the sea only 30 km away has carved several deeply incised channels and gorges on the western slopes of the mountains.

The part of the Levant fault portrayed in the mosaic has been subjected to intermittent volcanism since Mesozoic time, and flows of various ages ranging from Pliocene to Recent (particularly Pleistocene) are extensive (Garfunkel et al., 1981). Much of the area east of the Jordan Valley and south of Damascus is covered by basaltic lavas. Several cinder cones of Recent age can be seen on the Golan Heights, a plateau, and on Gebel ad Drouz. East of Damascus is an extensive field of cinder cones. Many of these cinder cones have formed along fissures up to 15 km in length.

Another basaltic flow west of Homs, Syria, forms the Shin Plateau. This flow extends across the Levant fault zone nearly to the Mediterranean Sea (Ponikarov, 1967). Southwest of the Sea of Galilee, a basaltic flow forms the resistant plateau that accentuates the differences in relief of greater than 500 m to the valley floor of the Jordan River.

Near the Lebanon/Israeli border, the Levant transform fault deviates from the Jordan Valley trend by about 25° to the east. This change in trend marks the transition along the fault from a transtensional to a transpressional regime. This zone of compression coincides with the development on the east side of the fault of a series of subparallel faulted anticlines and synclines known as the Anti-Lebanon, and farther east, the Palmyra Moun-



1

ORIGINAL PAGE
COLOR PHOTOGRAPH

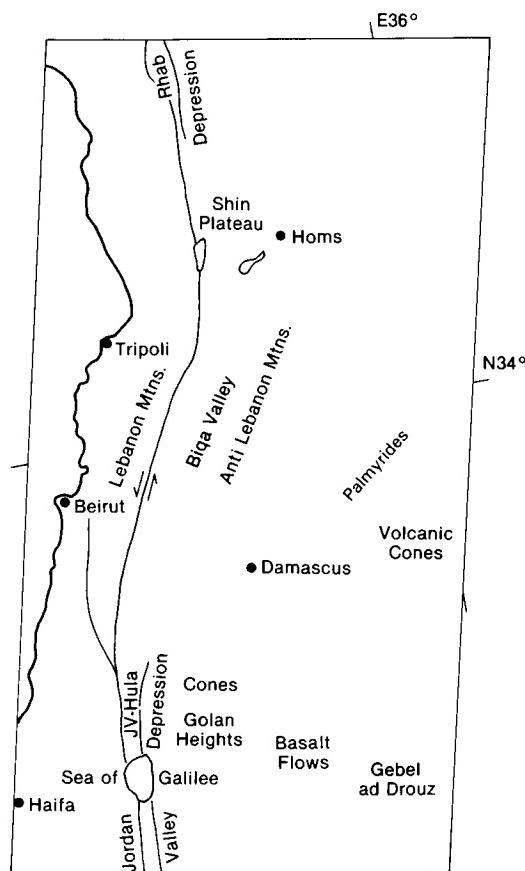
LEVANT FAULT

tains. The first major structure east of the fault is the Biqa Valley, a broad synclinal structure. This valley is flanked by a large faulted anticlinal fold more than 20 km wide, with elevations exceeding 2600 m, that is part of the Anti-Lebanon Mountains (Dubertret, 1955).

In the Palmyrides, both the widths and heights of the structures are less imposing. The anticlinal folds are tighter, and many of the crests appear to be longitudinally faulted.

At the northern end of the Lebanon Mountains, the trend of the Levant transform fault nearly parallels the Jordan Valley segment. The compressive bulge along the fault abruptly diminishes at this point. Evidence of tension is suggested by the presence of a probable rhomb graben at the west side of the Shin Plateau. Evidence for the graben is confused by a large elongate volcanic ridge that was apparently the source for the extensive basaltic cover that formed the Shin Plateau. Farther north along the fault, the Rhab depression is definitely a graben structure with a width exceeding that of the Jordan Valley. The Apollo-Soyuz photograph (Figure T-38.1) shows the extension and change of direction of the lineament northward and the folds on the east of the fault.

The Levant fault is an instructive example of a major left-lateral strike-slip fault. Differences in the width of the Red Sea and the Gulf of Suez and the orientation of the folds in the Anti-Lebanon and Palmyra Mountains indicate the sense of movement. Transitions from zones of transtension (where the trace of the fault is locally more westerly) to zones of transpression (where the fault trends more easterly) are characteristic of many major strike-slip faults. (GCW: O. R. Russell) **Landsat Mosaic.**



ORIGINAL PAGE
COLOR PHOTOGRAPH

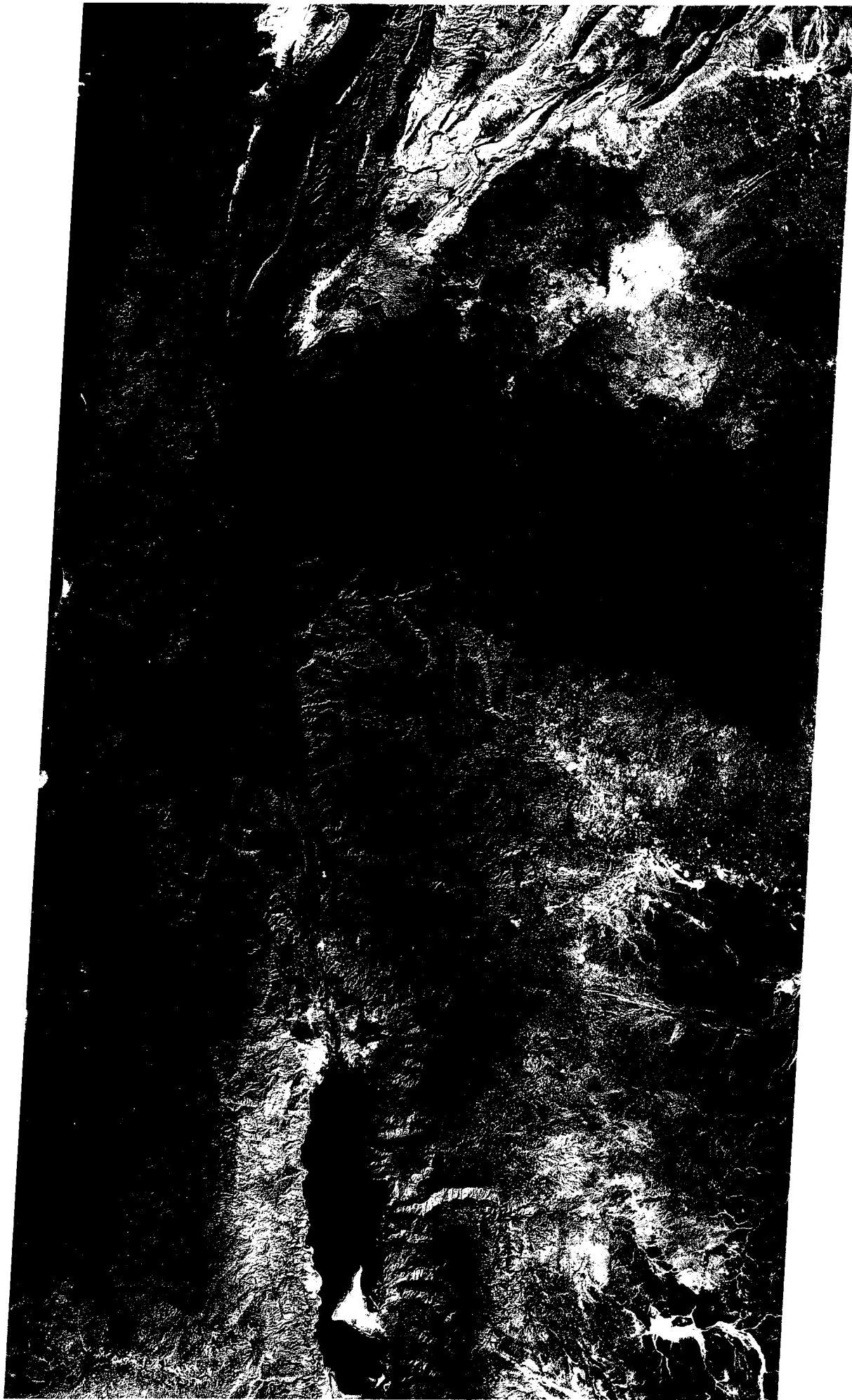


PLATE T-39

The mosaic (next pair of pages) and the accompanying ancillary images show the North Anatolian (NAT) and East Anatolian (EAT) transforms, the faults bounding the northern and southern edges of the Anatolian plate located in southeastern Turkey (Figure T-39.1, from Sengor and Yilmaz (1981)). Much of this part of Turkey and adjacent countries typifies the geomorphology of an active plate boundary where two continental blocks are colliding. Continental collision began in the Miocene as the result of closure of a Neo-Tethys Ocean (Dewey and Sengor, 1979; Sengor and Yilmaz, 1981). The Neo-Tethys began to close in Late Cretaceous time and continued through the Early and Middle Tertiary. This closure resulted in Miocene collision of the Arabian plate and the Eurasian plate (locally, the Black Sea plate) along the Bitlis-Zagros (BS-ZS) suture. This continent/continent collision formed an accretionary terrane, "welding together" several smaller continental blocks and an associated accretionary prism of ophiolite mélange between the two larger continental plates. Convergence continues today, forcing the pie-shaped Anatolian plate westward along the North and East Anatolian transform faults. The westward movement of the Anatolian plate is taken up along a subduction zone (i.e., free face) to the south and west (Figure T-39.1). Extension over the free face produces a series of grabens similar to the Great Basin (Plate T-4).

The North (right-lateral) and East (left-lateral) Anatolian transforms typify strike-slip faults that bound continental plates. These faults are generally vertical, cutting the entire continental crust, and therefore have a linear trace over many hundreds of kilometers marked by valleys (Figure T-39.2) or linear lakes. Close-in inspection of geologic and geomorphic features on opposite sides of such linear valleys are commonly offset and appear to have been dragged against the fault. These faults may juxtapose entirely different geologic terranes. For example, the East Anatolian transform fault juxtaposes rocks (mainly igneous and metamorphic) of the Anatolian plate against accretionary prism rocks (crystalline rocks) and ophiolite mélange in thrust contact with Arabian plate strata (folded and thrusted sediments). Minor curvatures along these faults produce either transpressional (folds and uplifts) or transtensional features (pull-apart grabens).

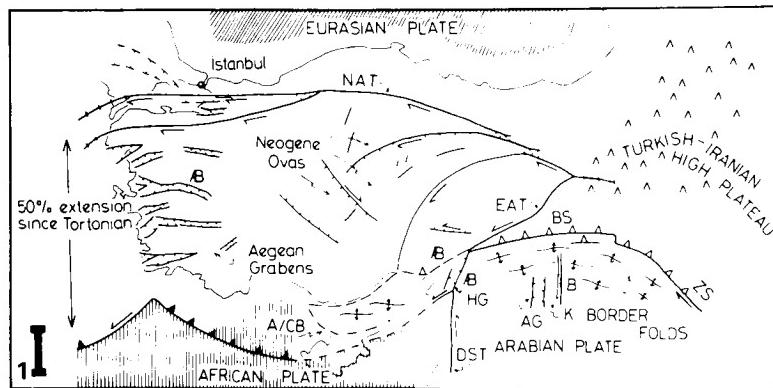
The geologic terrane south of the East Anatolian transform is a good example of a continent/continent suture zone. This

ANATOLIAN FAULTS, TURKEY

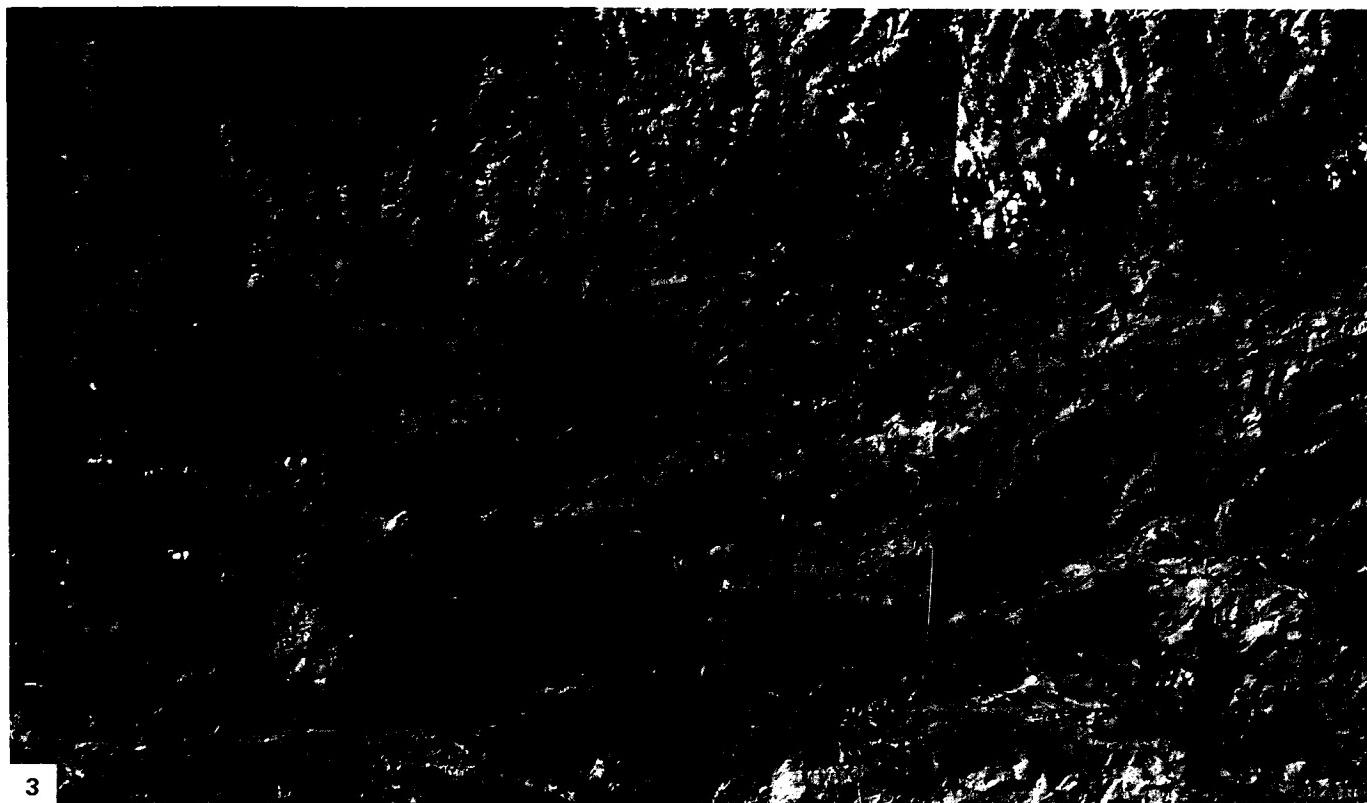
region consists of an accretionary prism of ophiolite mélange and remnants of small continental plates (e.g., Bitlis and Poturge Massifs) that were "welded" onto sediments of the large continental (Arabian) plate to the south (Sengor and Yilmaz, 1981). The actual suture is marked by the Frontal Thrust of the Bitlis Suture. A segment of the Frontal Thrust Zone is visible across the mosaic as an undulating line separating sedimentary rocks to the south from principally crystalline rocks to the north. This thrust exposes crystalline rocks of the Bitlis and Poturge Massifs, as well as ophiolite mélange in thrust contact overlying Eocene sediments of the Arabian plate. The upper plate of this thrust has moved at least 15 km southward since the beginning of continental collision in the Miocene (Livaccari and Merin, 1986). Southeast of the thrust are the Border Folds, a zone of imbricately thrusted and folded sediments marking the northern edge of the Arabian plate. North of the thrust are remnants of small continental blocks (Poturge and Bitlis Massifs) located within an ophiolite mélange (i.e., the East Anatolian accretionary prism). One such ophiolite assemblage is the Guleman (see index map).

A portion of the East Anatolian transform is visible on this image as a northeast-trending linear valley located just north of the Poturge Massif and ophiolite mélange. Large segments of the Euphrates and Murat Rivers follow this valley. Lake Hazar (this Plate) marks a small graben (i.e., Hazar pull-apart) associated with this left-slip fault. Arpat and Saroglu (1972) documented 22 km of left-slip offset along this fault and movement of 5 to 10 cm that occurred in places along this fault during a 1971 earthquake.

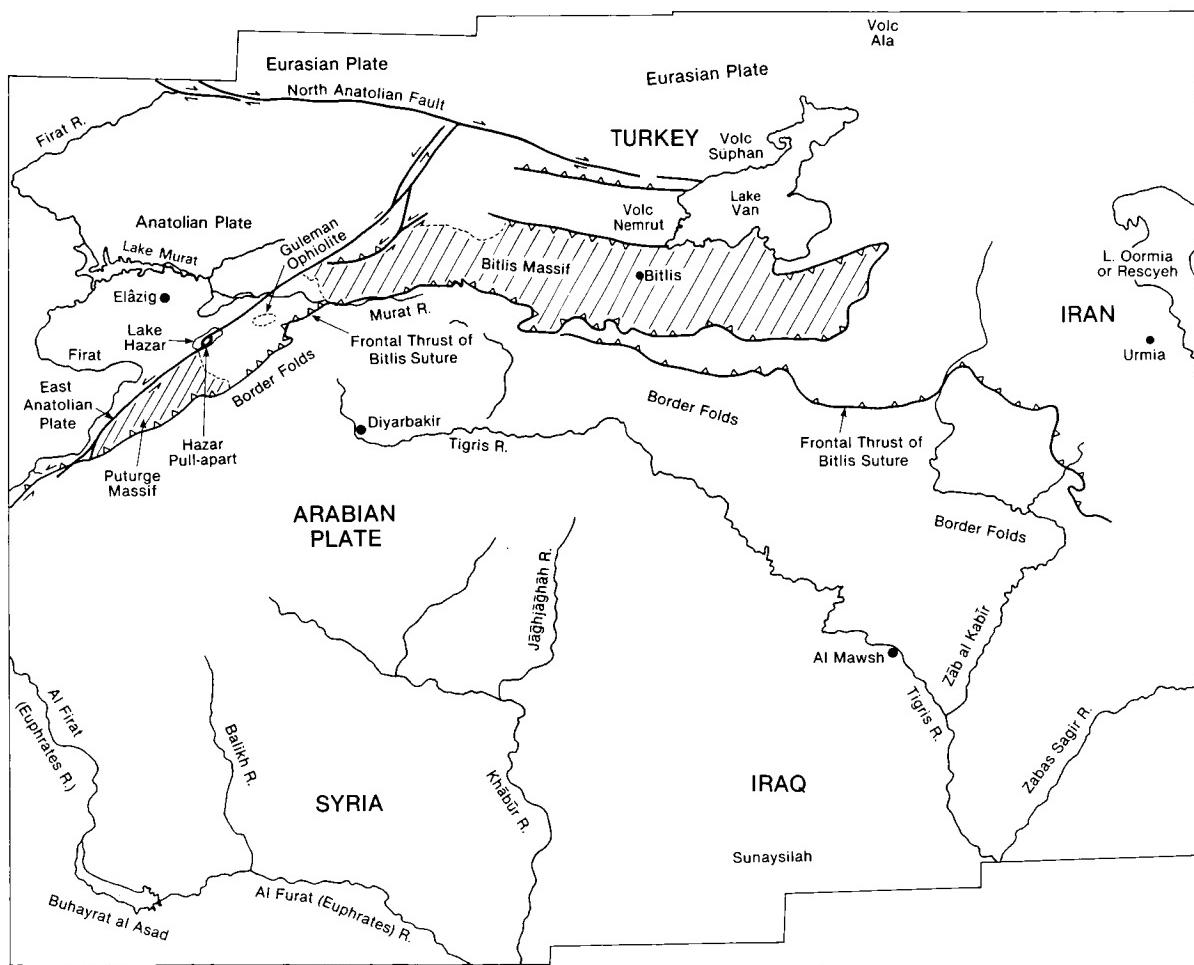
A segment of the 1200-km long North Anatolian transform to the west of the mosaic is visible as a linear valley trending west-northwest in the two-image mosaic of Figure T-39.3. North of the fault are the Pontids structural unit; to its south are the Anatolids, which have more ophiolites and olistostromes. Portions of the Euphrates and Yesil Rivers follow this valley. Dewey and Sengor (1979) reported that this fault has 85-km right-slip displacement and, based on earthquake data, is currently active. (GCW: I. S. Merin) Landsat Mosaic.



ORIGINAL PAGE
OF POOR QUALITY



3



**ORIGINAL PAGE
COLOR PHOTOGRAPH**



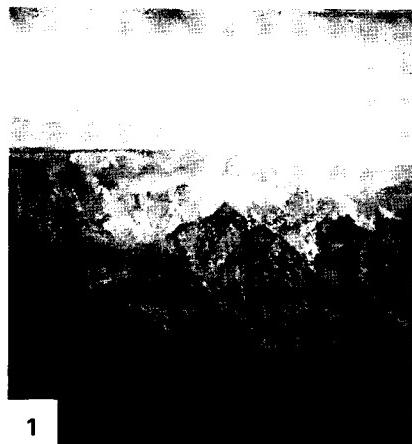


**ORIGINAL PAGE
COLOR PHOTOGRAPH**

PLATE T-40

This controlled Landsat MSS mosaic includes all or parts of twelve enhanced color-composite scenes that have been geocorrected to Lambert Conformal Conic Projection. The mosaic encompasses southwesternmost Saudi Arabia and the contiguous northwestern portion of the Yemen Arab Republic along the east side of the Red Sea rift. Jizan, Saudi Arabia's major southern Red Sea port, is across from the small tombolo located slightly south of the thin north-south-trending Ras At Taria Peninsula. The major cultivated areas (bright red hues) are developed on the alluvial fan deposits associated with the major drainages. These include Wadi Qadim in the southeast corner, the Najran oasis to the north where the Wadi Najran extends into the southwest corner of the Rub Al Khali, and several wadis on the coastal plain that extend seaward from the Red Sea escarpment. Water from the infrequent rains flows along the intermittent streams (wadis) and, in part, infiltrates the underlying alluvium. These aquifers can be tapped by shallow irrigation wells to provide water for fairly intensive but localized cultivation.

The darker rocks that are exposed in the northwest quadrant and transect the photograph in southeasterly direction form the southern section of the Arabian shield. The old erosion surface (partially exhumed) developed on these crystalline rocks inclines eastward into the Rub Al Khali basin where it can be seen to be overlain by gray and tan alluvial sediments and light brown to light yellow eolian sands. The bold fault-line scarp that separates the Tihama (coastal plain) from the highlands marks one of the major bounding fault zones of the Red Sea rift. The east-northeast slope of the old erosion surface demonstrates the arching and tilting of crustal blocks associated with rifting. Along the right edge of the Plate, the wind-deposited sands tend to be concentrated in local depressions along the eastern margin of the shield or as elongate "seif" dunes farther toward the basin. Along the south edge of the mosaic, deformed Mesozoic sedimentary rocks overlie the basement. Just to the north of the southeast corner, a major northwest-trending fault separates the dark highly jointed crystalline rocks on the north from yellow-brown Jurassic limestones on the southeast.



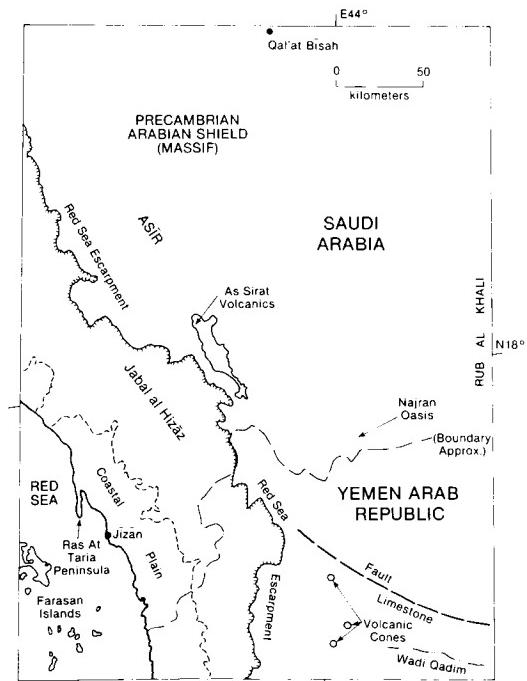
SOUTHERN ARABIAN SHIELD

The eroded south-southeast-trending Red Sea escarpment is clearly visible starting slightly below the upper left corner of the mosaic. Elevations along the scarp edge average 2200 m, but local prominences exceed 3000 m (Figure T-40.1). The scarp drops rapidly toward the Red Sea, and elevation averages 30 m where the basement slopes intersect the narrow coastal plain.

Crystalline rocks of the shield consist of complexly folded, metamorphosed, and granitized rocks that are locally intruded by Upper Proterozoic igneous bodies ranging from syenite to gabbro. These intrusions have a regular, near-circular form (see Plutons, Plate T-60). Erosion has reduced parts of the shield to low hills (Figure T-40.2). On the west, erosional remnants of Cambro-Ordovician sandstone locally unconformably overlie the basement; this basement is encroached upon locally by Recent alluvium and eolian sands. The southeast-trending Y-shaped As Sirat volcanic field (harrat) located just to the left of the center of the mosaic provides evidence of the large-scale volcanic eruptions associated with the Red Sea rifting. This is the southernmost and smallest of the 13 flood basalt flows in Saudi Arabia; it covers an area of about 750 km², and comprises 20 separate flows. Its maximum thickness is 580 m. Isolated volcanic cones are scattered over the lower half of the mosaic area. Those most easily recognized appear as small, very dark, near-circular features superposed on the light-brown Mesozoic limestones.

The coastal plain separating the shield from the Red Sea averages 40 km in width. It consists primarily of fan and terrace deposits composed of silt to gravel-sized clastics and coastal salt-mud flats. Narrow, shallow coral reefs closely parallel much of the southern shoreline.

The islands in the southwest corner are part of the Farasan Group. The coral reefs that comprise these islands grew over salt domes and were subsequently uplifted. (GCW: H. Blodget) References: Al-Shanti (1979), Brown and Jackson (1959), Geukens (1966). Landsat Mosaic.



ORIGINAL PAGE
COLOR PHOTOGRAPH



PLATE T-41

SEMAIL OPHIOLITES

Ophiolites represent the anomalous superposition of oceanic crust on top of continental crust. Few geologic features more clearly reveal the dynamic effects of seafloor spreading. Rather than a single rock type, an ophiolite is a stratified group of three separate rocks types, known as the "Steinman Trinity." The lowermost members consist of ultramafic peridotites, above which are layered to massive gabbros that in turn are source to and overlain by a volcanic member composed of sheeted dikes and pillow basalts. Ophiolite rocks are formed at the spreading ridges as reduced pressure allows partial melting in the Earth's mantle, generating the gabbro plutons which then feed the pillow basalts through fissures opened during spreading.

This scene covers much of the Semail ophiolite nappe comprising the Oman Mountains in northern Oman. Peridotites (P) are clearly visible as large dark massive rocks with a characteristic highly dissected drainage pattern. The gabbros (G) are not well represented on this image. Most are easily differentiated by their light color and coarser drainage pattern. Volcanic units (V) rimming the northern perimeter of this south-dipping nappe are distinctive in their dark color and characteristic low relief due to their lack of weathering resistance.

The northern edge of Oman and the rest of the Arabian platform broke away from the land areas to the north in the Early Triassic. For most of the Mesozoic, the Neo-Tethys seaway continued to open, creating a thick miogeosynclinal section of carbonates on the passive margin of the Arabian platform (lightest tones in the image). Lower Cretaceous age fossils in chert intercalated with the pillow basalts date the formation of the Semail ophiolites. The Neo-Tethys began to close in the Early Cretaceous. By Late Cretaceous time, accelerated by an anomalously high worldwide spreading rate, the old spreading center of the Neo-Tethys collided with the Arabian platform. The result of the collision was the emplacement of the Semail nappe on the Arabian craton (Glennie et al., 1973; Glennie, 1974; Welland and Glennie, 1975; Coleman, 1981).

Sima (oceanic) crust is considerably more dense than sialic (continental) crust, with average specific gravities of 3.3 and 2.7, respectively. The isostatic imbalance created by superposition of massive sima crust on the Arabian platform is one explanation for the formation of the large folds observed in the autochthonous shelf carbonates of the Hajar (Hj) Super Group (Mesozoic). These have been domed up and eroded to expose the underlying pre-Permian (P) units at the Siat-Hatat in the northeastern corner

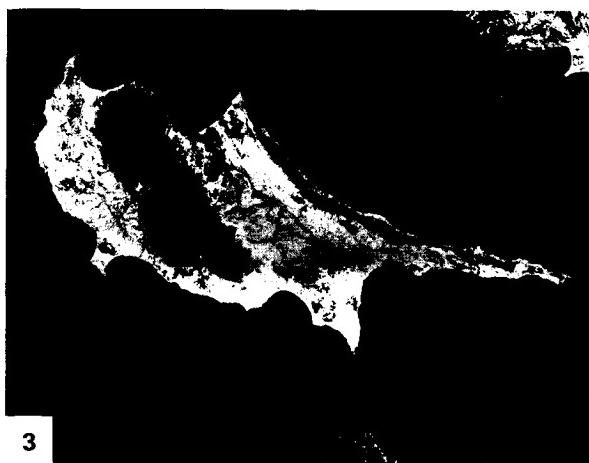
of the scene. Nearby folding in response to diapirism extends westward until it takes an almost 90° left turn to the south for 20 km and then takes another 90° turn to the west, where it widens to form the Gebel Akdar window. At first glance, the apparent left lateral offset the Siat Hatat and Gebel Akdar might be interpreted as a transcurrent fault. However, close inspection of the imagery and in the field reveal no evidence of large-scale faulting within the autochthonous sections. These areas are interpreted instead as large-scale folding in response to crustal diapirism. Under the awesome loading created by the superimposed ophiolite, the crust began to buckle, probably along zones of weakness in the overlying ophiolite nappe. As erosion progressed, the ophiolite cover in the areas of the present folds became thinner, causing a positive feedback situation in which the more the folds rose, the more the ophiolite was unloaded. The final result is the high-standing Gebel Akdar, whose breached rim with inward-facing scarps stands over 3 km above sea level. Figure T-41.1 is an outcrop of a steeply dipping resistant unit within the ophiolite sequence. Figure T-41.2 depicts the contact of the ophiolites with the older shelf rocks (Dykstra and Russell, 1980).

The Oman salt basin, an offshoot of the Infracambrian Hormuz salts of Iran, extends up to the southern edge of the Oman Mountains. An arcuate fold of dark Tertiary limestone (T) formed as a salt pillow rose in response to the ophiolite loading. A more equidimensional salt dome (K) is clearly visible near the southeast corner of the scene, which also contains some excellent examples of braided river channels and coalescing alluvial fans. Young (post-obduction) limestones (L) stand out as light-colored patches overlying dark ophiolites.

Figure T-41.3 is taken from a Large Format Camera photograph of another of the world's famous ophiolites, the Troodos Massif of Cyprus, best known for its mineral deposits of copper and chrome, first mined in the Bronze age. The geologic environment at spreading centers, where ophiolites are formed, is conducive to the formation of two general types of ore deposits: massive sulfide copper deposits and layered chrome deposits. Sulfide deposits in the Troodos ophiolites are produced as exhalative deposits where mineral-rich brines are exhaled on the seafloor and intercalated with the pillow basalts (Constantinov and Garrett, 1973). The Semail nappe also has several massive sulfide and chromite deposits; however, none of the chromite and only one of the massive sulfide deposits are of economic grade. (GCW: J. D. Dykstra) Landsat 10127-06080, November 27, 1972.



ORIGINAL PAGE
COLOR PHOTOGRAPH



3

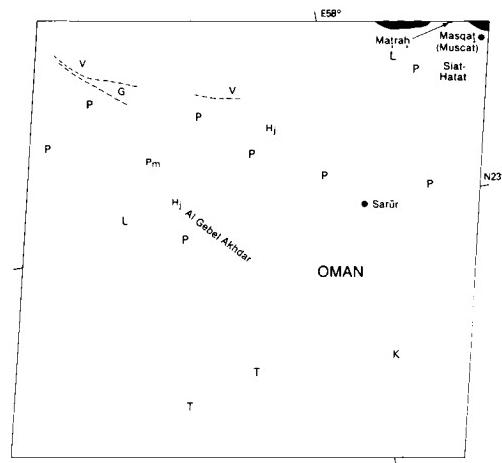


PLATE T-42 THE ZAGROS MOUNTAINS: ARABIAN/ASIAN COLLISION

The morphology of Iran and Pakistan north of the Straits of Hormuz spectacularly expresses the surficial traces of several plate boundaries. These boundaries are the tectonic effects of the collision of the Arabian platform with the Asian landmass to the north, or more accurately, with a microcontinent fragment of the Asian landmass known as the Central Iranian Microcontinent (CIM). The CIM block split away from the Asian continent and drifted slowly southward during the Triassic opening of the Neo-Tethys ocean. By the Jurassic, the Neo-Tethys began to close so that the CIM block was caught in a tectonic vise during the Cretaceous. At the same time the Arabian platform was suturing to the southern margin of the CIM block, the Asian continent was being sutured to the northern margin of the CIM block. The series of units making up the "colored mélange," delineated on the index map by dark patterns, are characteristic of interstructured groups of flysch and ophiolitic rocks associated with the northern margin of the suture zone between the CIM block and the Arabian platform. The mélange separates the "worm-like" anticlinal folds to the south from obviously complex geology of the CIM to the north (Stocklin, 1968, 1974; Roohi, 1976).

The Central Iranian Microcontinent is divided by the north-easterly striking Nayband fault (clearly visible in the mosaic) into two areas of distinctly different structure. The eastern, more stable platform area is called the Lut Massif; the western, highly faulted area is known as the Tabas Block. The Lut Massif has a relatively low degree of Cretaceous Alpine deformation. Most of the area is covered with Tertiary continental sediments and volcanic rocks with scattered outcrops of Mesozoic and Paleozoic rocks. In marked contrast, the Tabas block includes a succession of arcuate fault-bounded grabens with Precambrian basement exposed within the intervening horsts. The arcuate normal faulting that controls the horst and graben structures is convex to the west, with increasing curvature from east to west. The extreme western fault marks the curved western boundary of the CIM block (Dykstra and Birnie, 1979; and Stocklin, 1974).

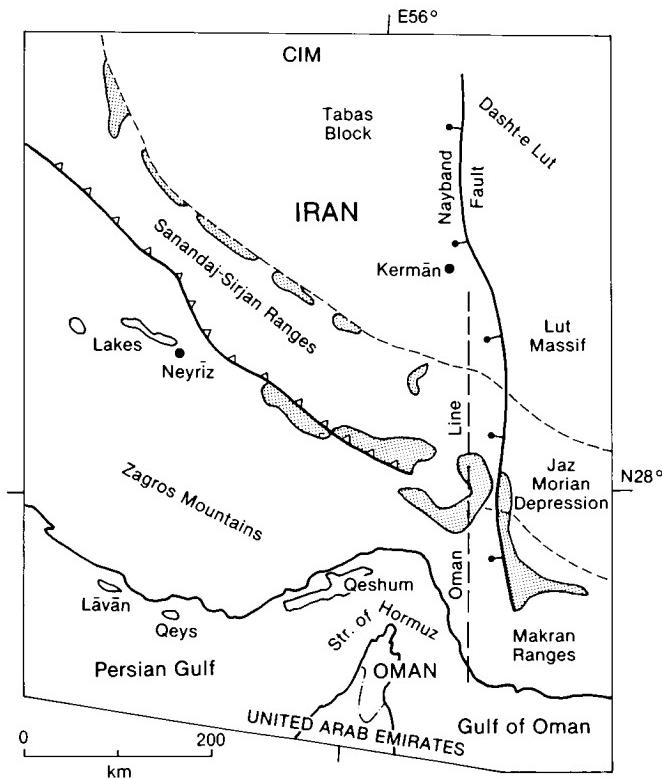
The Nayband fault continues south and becomes an integral part of a broad structural discontinuity known as the "Oman Line" that extends northward from Oman across the Straits of Hormuz. This line divides the flysch-rich eugeosynclinal sediments of the Makran Ranges on the east from the miogeosynclinal shelf sediments of the Zagros Mountains to the west. To the west of the Oman Line, the Zagros Crush Zone marks the location of a continent/continent-style active margin where the Arabian platform collided, and continues to collide, with the CIM block. To the east, the active margin is a continent/ocean-style boundary with the oceanic lithosphere of the Indian Ocean being subducted beneath the CIM and other more easterly microcontinental blocks. The Oman Line can therefore be interpreted as marking the eastern boundary of the Arabian platform. The close association of the Nayband fault and the Oman Line reflects the marked structural contrast across the Nayband fault. This probably indicates that, west of the fault, the CIM block is caught in a highly compressive continent/continent-style collision, whereas to the east, the Lut Massif section of the CIM block is affected by the smaller compressive forces associated with the subduction along a continent/ocean margin. The continued subduction of oceanic lithosphere east of the Oman Line has led to the flysch-rich accretionary prism comprising the Makran Range of southern Baluchistan (Glennie, 1974; Glennie et al., 1973; Stocklin, 1974).

Part of the southern Zagros Mountains is shown in detail in a Landsat scene (Figure T-42.1) and again from an oblique perspective in a Gemini photograph (Figure T-42.2). These mountains consist predominantly of miogeosynclinal shelf sediments of Mesozoic and Lower Tertiary age. The sediments were deposited largely on the northern edge of the Arabian platform.

During the Maastrichtian, after the beginning of the continent/continent collision, the Zagros and regions immediately to the north were uplifted. This, in association with the lateral forces generated by the continental collision, created southward thrusting and folding of the Zagros sediments (Dykstra and Birnie, 1979). The shortening has been estimated as approximately 50 km with a probable decollement surface along the Hormuz salt beds of Infracambrian age. Several salt diapirs have pierced the folded sediments and are clearly visible on the Landsat imagery as salt glaciers (circular masses of darker colored material). Figure T-42.3 zeros in on one of these diapirs.

Plunging anticlines in all stages of dissection are visible, some appearing as if layers were peeled off (Oberlander, 1965). Tilted resistant beds in the anticlines are eroded to form hogbacks, triangular flatirons, and infacing scarps. Synclinal basins, where eroded, have out-facing scarps. These folds have not reached the degree of dissection of the folded Appalachians. Figures T-42.4 through T-42.7 offer striking views of anticlinal landforms in both the central and southern Zagros Mountains, as these are experiencing various stages of breaching. The structural style so evident in Figure T-42.1 is clearly reflected in the topography and drainage patterns. The V's where streams cross tilted beds form scalloped cuestas. Fans and braided rivers are abundant.

In the central Zagros, the folds are closed, as evident in a Landsat RBV view (Figure T-42.8) of structures in the main petroleum fields between the head of the Persian Gulf and Esfiahān. The folds of the main belt in the northern Zagros Mountains (Figure T-42.9) are more tightly spaced and elongated, without obvious plunging, where this orogen approaches the Anatolian plate along the Bitlis Suture (Plate T-39). South of this belt are well-exposed but seemingly isolated plunging folds separated by valley fill that now covers other structures. (GCW: J. D. Dykstra) **Landsat Mosaic.**



ORIGINAL PAGE
COLOR PHOTOGRAPH



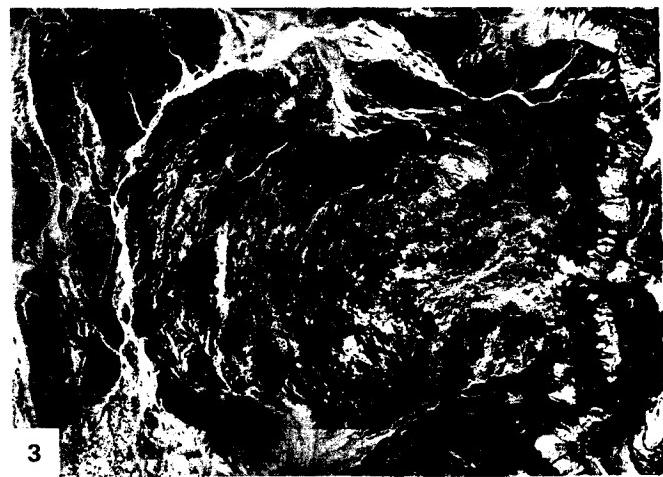
ORIGINAL PAGE
COLOR PHOTOGRAPH



1



2



3

ORIGINAL PAGE
COLOR PHOTOGRAPH

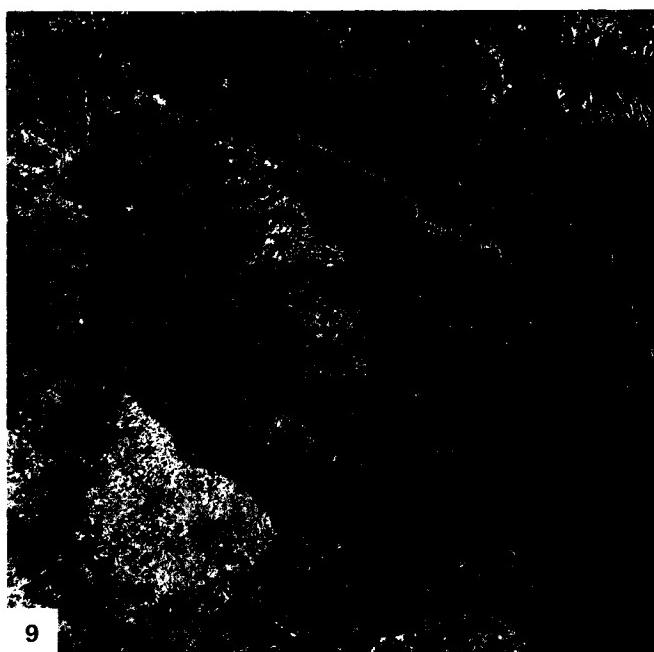
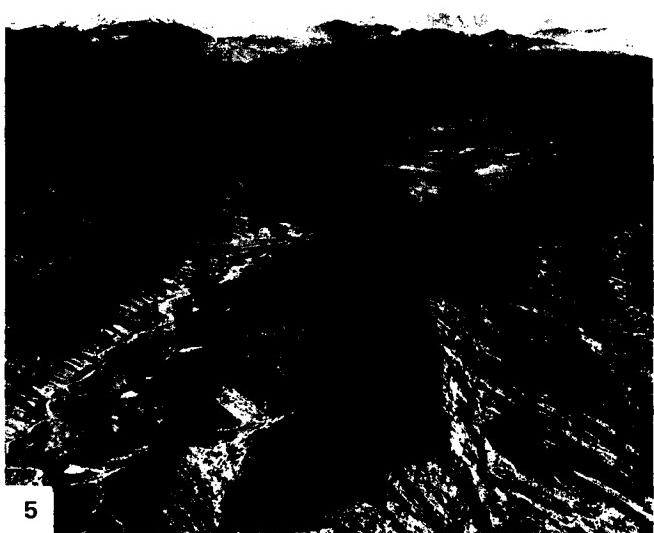
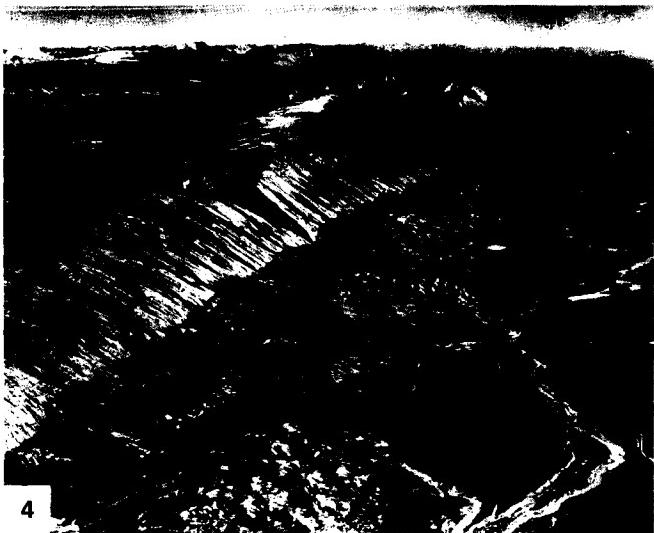


PLATE T-43

SOUTHWEST ASIA

The mosaic on pages 128-129, made up of more than 130 individual Landsat scenes, displays the morphology associated with large-scale crustal deformation along the western end of the continental collision belt across southwest Asia (Stocklin, 1974). The mosaic includes all of Pakistan, most of Afghanistan, and parts of Iran, Oman, the U.S.S.R., India, and China. During the Late Paleozoic, the southern continents were gathered together as the Gondwana supercontinent. The south Asian section of Gondwana broke up in two stages during the Mesozoic. First, a small slice known as the Cimmerian continent split off in the Permo-Triassic and moved north to collide with previously accreted Asia in the Mid-Jurassic, leaving the Paleo-Tethys seaway in its wake. Then, about 130 Ma, India broke away from eastern Gondwana and began to drift north toward Asia. As the Paleo-Tethys was consumed in front of India, the Neo-Tethys was formed behind it. Their ancient ocean crusts are now recorded by ophiolites and related rocks along suture lines between continental fragments. Major tectonic features associated with these collisions are located on the index map inset on the mosaic.

This mosaic might well be subtitled "the suturing of microcontinents." The tonal patterns clearly discriminate between relatively stable areas and deformed orogenic belts. On the north are the Tarim and Turpan platforms, which were intruded by Triassic batholiths that formed beneath island arcs in the north Paleo-Tethys. To the south is the Indian subcontinent, and to the southwest is a corner of the Arabian Peninsula, each with obducted ophiolites on its northern edge. In between are fragments of the Cimmerian continent: the Lut and Dasht-I-Margo/Afghan blocks to the west, the Lhasa block to the east, and an unnamed, poorly known block north of the Main Karakoram Thrust and south of the Pamirs. Ophiolites (shaded patterns on the index map) along the Neh fault, on the Kabul block, and along the Karakoram fault mark the edges of these microcontinents.

The cores of these blocks, platforms, and continents have been little affected by the collision, whereas areas between them are intensely deformed. The northern suture with remnants of the Paleo-Tethys extends from northern Iran, along the Helmund fault, through the Pamirs, and on to east along the North Tibet suture. The southern suture lies in two bands across the western portion of the mosaic. One is seen in Oman and then along the northwest edge of the Kirthar/Sulaiman Ranges. The other borders the Murien depression, passes through the Ras Koh, and continues along the southern edge of the Kabul block. These two bands are separated by deep marine sediments (flysch) present in the Makran Ranges and between the Chaman and Ghazaband faults (Figure T-43.1, an Apollo oblique photograph looking north across the Makran along the faults). These faults join together in the intense collision zone north of India along the Main Mantle thrust and the Indus suture.

The Cenozoic collision of the Indian subcontinent with Asia about 50 Ma ago caught the Cimmerian blocks in a tectonic vise, creating crustal compression with both convergent and lateral components. Between 20 Ma and the present, continuing northward movement was accompanied by clockwise rotation of the Indian subcontinent, leading to the formation of the Himalaya Mountains rimming India on the north, the Hindu Kush ranges to the northwest, and the highly deformed suture zone between the Dasht-I-Margo and Indian platforms.

The images on the next page and the three Plates (numbered on index map) that follow illustrate deformation typical of the western collision zone. A Landsat view (Figure T-43.2) of the Kirthar Range (A on index map) focuses on highly deformed Tertiary and Upper Mesozoic carbonate and clastic rocks east of the Oranach-Nal fault (just off left edge of the scene) that separates

these units from imbricated north-dipping thrust sheets of flysch sediments in the Makran Range where it swings northward.

Figure T-43.3, another Landsat image (B on index map), concentrates on the Chaman fault, which trends north near the left edge. This fault extends from near Kabul in Afghanistan, thence some 900 km south-southwestward to the northern edge of the Makran Range. Movement along the fault in 1892 offset the Quetta-Chaman railroad 75 cm in a left-lateral sense, the consequence of continuing northward movement of the Indian subcontinent. West of the fault are darker volcanic rocks in the eastern extension of the Ras Koh Mountain Range. Similar rocks appear again at the north edge of the image just west of the Chaman fault. Slaty cleavage is well developed in the mountainous terrain east of the fault, with the tectonic fabric of the entire range being controlled by stresses that produced the fault. The Ghazaband fault lies within the right half of the image; on the west side are the folded flysch units caught in a shear couple between the Chaman/Ghazaband faults, and to the east are Indian plate shelf beds.

The remaining four photographs on the facing page give a sense of the rugged terrain and structure of the mountain country of Pakistan. Figure T-43.4 looks south along the Chaman fault about 35 km south of the town of Nushki. The fault runs from the lower left to the top center of the photograph. Looking east across this fault (Figure T-43.5), one can see the Khojak hills (Eocene and Oligocene) in the distance and the low ground of the fault zone itself in the middle ground. Pliocene/Pleistocene sediments from the Ras Koh occupy the foreground. Anticlines and synclines (Figure T-43.6) outlined by differential erosion lie just west of the Chaman fault zone and are large-scale drag features in the rocks of the Makran. Figure T-43.7 is a view south along the Indus River near the mouth of the Astor River looking toward Nanga Parbat, a peak typical of the Hindu Kush. The valley is occupied by the active Raikot fault. This picture also includes glacial terraces along the river; in this tectonically active area, there are folds in Pleistocene to Recent glacial till with overturned limbs. (*GCW: R. L. Lawrence; J. D. Dykstra*) Additional References: Andrieux and Brunel (1977), Farah and De Jong (1979), Farah et al. (1984), Gansser (1980), Lawrence et al. (1981), Molnar and Tapponnier (1977), Sengor (1979, 1984), Stoneley (1975), Yeats and Lawrence (1984). **Landsat Mosaic.**



ORIGINAL PAGE
COLOR PHOTOGRAPH



LANDSAT MOSAIC OF PAKISTAN & VICINITY
SOUTH ASIA

by

Robert D. Lawrence and Robert O. Rogers
Oregon State University
Corvallis, Oregon 97331
U.S.A.

ORIGINAL PAGE
COLOR PHOTOGRAPH



**ORIGINAL PAGE
COLOR PHOTOGRAPH**

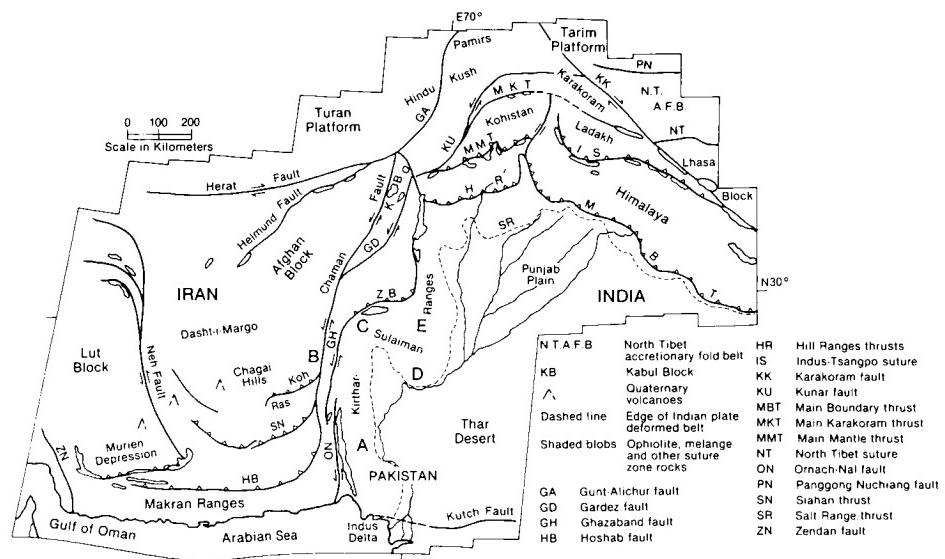


PLATE T-44

This and the next two Plates show different aspects of the tectonic effects of the collision between the Indian subcontinent and Eurasia. The collision was frontal in the Himalayas, but in the Kirthar and Sulaiman Ranges of western Pakistan, it was oblique. Assessment of deformational styles shown in Plates T-44 and T-45 (Zhab Valley and Zinda Pir) indicates that oblique collision there resulted in a structural complexity greater than that found in the foothills of the Himalayas (Plate T-46, Kohat). In an oblique collision zone, such structural complexity may be expressed by major strike-slip faulting, overprinting of tectonic domains, and drastic changes in the direction of thrusts and folds over short distances. All of these features can be seen in this Plate.

The city of Sibi is located in a small undeformed basin, presumably the westernmost outlier of the undeformed Indian subcontinent. West of the basin, thrust sheets moved eastward, which is the typical transport direction in the north-south-oriented Kirthar Range. In the extreme southwest corner of the Zhab Valley image is a fault parallel to a group of three or four faults farther west that repeat the sinistral motion along the Chaman fault. The fact that this is an active group of faults is demonstrated by a series of earthquakes (30000 killed in Quetta in 1935). Combined, the two transport directions, eastward-thrusting and sinistral strike-slip along north-south-oriented faults, indicate northwest motion of the subcontinent with respect to the Afghan block.

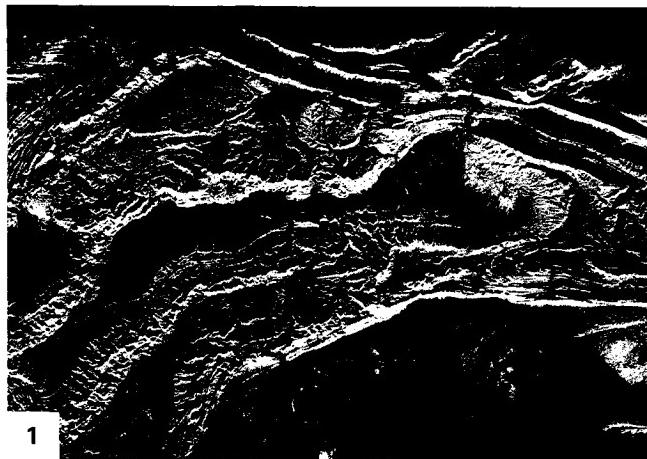
North of Sibi is the Sibi Trough, a triangular area with broad basins (A) separated by narrow tight folds. Details of the intricacies of these fold patterns are strikingly revealed in a SIR-A radar image (Figure T-44.1). The youngest deformed rocks are Pleistocene (Figure T-44.2, Mount Zarghun, 3615 m), implying that this is a trough in the process of being deformed. The accumulation of sediments continues in the southern basins around Sibi. Visible in some of the narrow anticlines are whitish Middle Eocene limestones (B); they, together with the overlying red bed sequence, are detached with respect to the lower strata. The detachment horizon is in Lower Eocene shales. Northeast of the Sibi Trough, Lower Eocene, Cretaceous (C), and Jurassic (D) rocks are exposed in the cores of doubly plunging folds, thus demonstrating that another, much deeper zone of detachment

ZHOB VALLEY

exists in this area. The folds contrast with those of the Sibi Trough, having broad anticlines and narrow synclines; such anticlines farther to the southeast host the major gas occurrences in Pakistan (e.g., the Sui gas field, located in the southernmost anticline visible in the Landsat image just to the southeast (Figure T-44.3). In the southeast corner of the Zhab Valley Plate, complex structures (E) between the broad folds attest to the role of the Lower Eocene shales as a detachment horizon higher in the section.

All deformation discussed thus far is of Late Tertiary, Pleistocene, or even Recent age. Farther to the north, however, spectacular examples of older deformation are visible. For example, near the apex of the Sibi Trough, the existence of a thrust fault can be inferred from the repetition of Paleocene limestone (F) (Kazmi, 1979). The upper slab has been partially eroded and is discordantly overlain by Miocene red beds, which, together with the underlying thrust sheet, are folded in an anticline and syncline. The folds are cut off by a Late Tertiary or Pleistocene thrust fault overlain by a unit with two huge slabs of dark (almost black) rock (G). These are ophiolites, originally part of the mantle and oceanic crust that once separated Eurasia from the subcontinent. The ophiolites were thrust upon the continent before the collision, but not later than Paleocene, since they are overlain by white limestones of Early Eocene age (Abbas and Ahmad, 1979). The ophiolites are underlain by mélanges, chaotic deposits which contain large ophiolitic blocks that are visible in the Landsat image.

North of Muslimbagh (meaning Garden of Muslims; bright red in the Plate), both Eocene rocks and ophiolites are caught in imbricate thrust slices beneath the major thrust fault of the area, the Zhab Valley thrust (H). This fault juxtaposes Tertiary marine rocks, similar to those in the Makran (see Plate T-43), with continental red beds, also of Tertiary age. The marine sediments had been deposited in the gulf between the Afghan block and the advancing subcontinent before they were underthrust by the latter. The telescoping of two different facies domains was preceded by folding, as can be deduced from the syncline that is cut by the Zhab Valley thrust (I). (GCW: K. A. DeJong) **Landsat 30212-05203, October 3, 1978.**

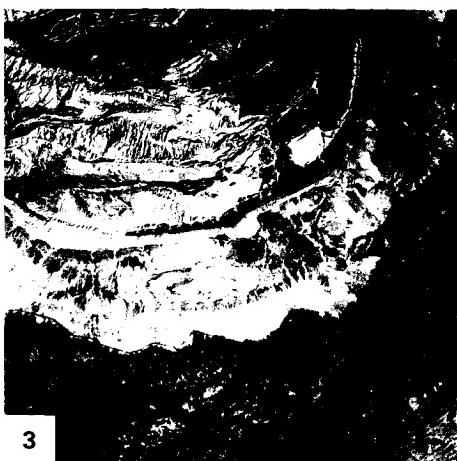


1



2

ORIGINAL PAGE
COLOR PHOTOGRAPH



3

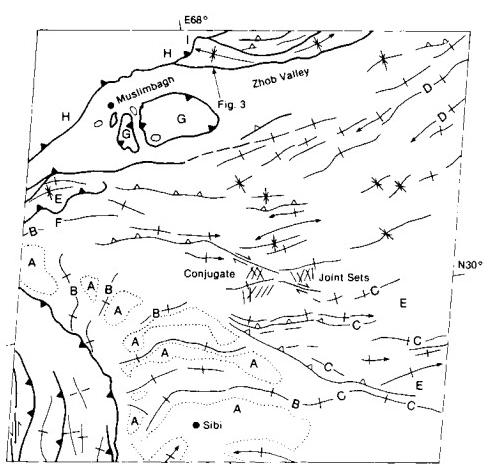


PLATE T-45

ZINDA PIR

As the Indian subcontinent drifted northward, eventually creating the mighty mountains of the Himalaya, the subcontinent also had to push aside the continental blocks to the east and west. The ensuing oblique collision between the Afghan block and the Indian subcontinent formed the Kirthar and Sulaiman Ranges of Western Pakistan. The latter range is partially shown in this Plate, itself the eastern two-thirds of a full Landsat scene. As the mosaic of Pakistan (Plate T-43) shows, the Sulaiman Ranges are oriented north-south, ending southward in a festoon-shaped arc. In this arc, folds and faults are locally associated with strike-slip faults. A good example of such an association can be seen in this Plate. Folds and thrusts at the southwestern end of the Kingri fault (Rowlands, 1978) transfer their compression into sinistral slip along the fault (see index map). The folds on either side of the Kingri fault cannot be correlated across the fault, suggesting that they formed during faulting.

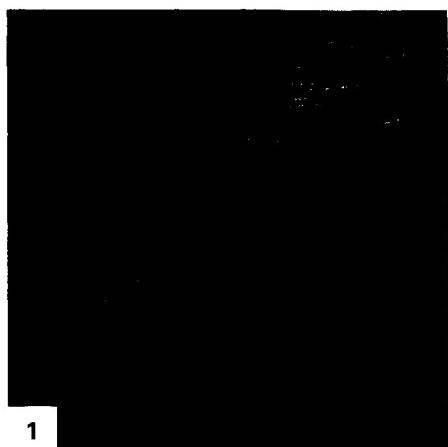
Earthquake studies (Quittmeyer et al., 1984) demonstrate that two recent earthquakes originated in the superficial structures seen in this scene, whereas two other recorded earthquakes resulted from thrusting in the basement. Such a differentiation between earthquakes is only possible when the upper layer of the crust has detached itself from the basement.

The regional structure also indicates that the Kingri fault and associated folds are the result of detachment; the structure is indeed similar to that of other thrust and fold belts characterized by detachment. Typical are the absence of basement rocks at the surface, the similarity between nearby folds, and the presence of imbricate fault structures in the northwest corner. There, light-colored limestone and marl overlain by dark-colored sandstone, both of Cretaceous age and with a total thickness of less than 330 m, have been imbricately thrust into a repetition of at least 20 steeply dipping, fault-bounded panels that later were folded. This remarkable structure (Figures T-45.1 and T-45.2) plunges to the northeast, thus revealing broad folds of Jurassic rocks in the southwest beneath the detachment plane. The imbrication of

the Cretaceous rocks is contemporaneous with the obduction of the ophiolites shown in the Zhob Valley Plate, while the folds in the Jurassic rocks, most other folds shown in this Plate, and the Kingri fault are of Late Tertiary/Recent age. Some of these young folds display an en echelon arrangement indicating a southward slip of the detached layer with respect to the foreland. Farther east, the gently curved Zinda Pir anticline reflects transport to the east, but next to the fold is the left-lateral Chaudhwan fault (Kazmi and Rana, 1982), emphasizing the close relations between compressive features and strike-slip faults in this area.

The festoon shape of the Sulaiman fold belt, together with the en echelon fold structures along its flanks, suggests that indeed the entire lobe is a thin-skinned structure moving along a deeper décollement surface. Thick Infracambrian evaporites, probably correlative to the Hormuz salts of Iran, are present in the near surface within 250 km east of the Sulaiman fold belt. It is likely that a westward extension of these salt units provided the detachment surface for the apparent décollement movements. The southward décollement movement has not occurred across the northerly striking Sibi Trough, a portion of which is seen as the high area in the lower center of the Plate. Indeed, it is the lack of movement within this area, coupled with the extensive southward movement of the fold belt to the east, that gives much of the Sulaiman belt its distinctive festoon shape.

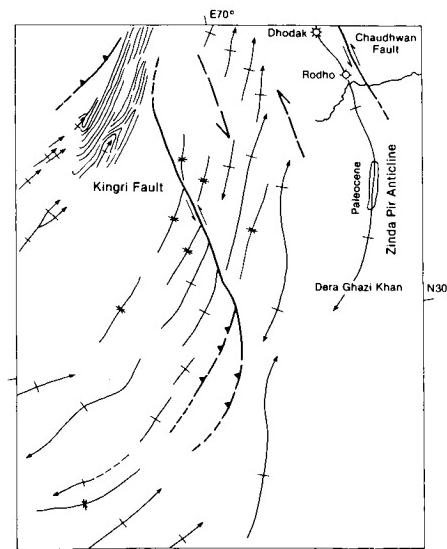
The successive breaching of the multicolored Tertiary formations of the Zinda Pir anticline reveals in its core the same Paleocene rocks that host the gas in the Sui anticline (southernmost anticline in Figure T-44.2). These rocks were the prime target in two wells drilled in the northern end of the anticline where the Paleocene formations had plunged beneath a cover of younger Tertiary rocks. The Dhodak well discovered a giant gas and gas condensate field in 1976; 9 years later this field has not yet been brought into production, in part because of the extremely difficult access to the Sulaiman Range. (GCW: K. A. DeJong) Landsat 30283-05144, December 13, 1978.



1



2



ORIGINAL PAGE
COLOR PHOTOGRAPH



PLATE T-46

KOHAT

This Plate shows the western terminus of the foothills of the Himalaya Mountains. Farther west is the sinistral Chaman Fault (Figure T-43.3), along which the Indian subcontinent moved northward, and to the north are crystalline and Paleozoic formations underthrust by the subcontinent during the Cenozoic. The detachment fault climbs stepwise to the surface and ultimately reaches the surface south of the Salt Range (A) and Surghar Range (B). The two ranges are connected by a dextral strike-slip fault system (C), indicating that movement was in a south-southeast direction. The detachment fault steps upward from a Precambrian or Cambrian salt layer comparable to the Hormuz Salt in Iran. The salt is exposed in the Salt Range, where folds are due to tectonic transport (D) and to salt flowing toward river valleys (E). Other morphotectonic features include topographic breaks related to normal faults (F) visible just north of the valley anticlines.

The abundance of low mountain ridges in Kohat and their absence in Potwar shows a fundamental difference between the structure of the two regions. The ridges are formed by Eocene limestone, and the relatively flat areas by the molasse of the Murree and Siwalik Formations are of Miocene/Pliocene age. The ridges in Kohat indicate the presence of folds or, less commonly, thrust faults formed by detachment and folding of Eocene and younger formations along an evaporite and shale sequence of Middle Eocene age. That sequence is restricted to the Kohat area, which explains the differences in topography and structure between Kohat and Potwar.

The broad folds (G) of the molasse in southwest Potwar involve Mesozoic rocks at depth, and the Dhulian and Khaur brachyanticlines are apparently underlain by pillows of Precambrian/Cambrian salt. The folds in the northwest Potwar are strikingly different. Two recent wells (H) in surficial synclines of Upper Murree rocks bottomed in anticlines of Lower Murree and older rocks. This disharmony is the result of a detachment zone within the Murree Formation, the presence of which can be deduced from observations in the northwest Potwar south of the

Kala Chitta Range. There, the Upper Murree has been folded in three synclines (I) (Figure T-46.1), of which the northern one is partially overthrust by units of the Kala Chitta Range. The Lower Murree is also folded, but the wavelength of these folds, as shown in this Plate, is much smaller than that of the three synclines. This disharmony can be explained by the presence of a detachment zone in the Murree Formation. Another example of disharmonic structure can be found west of the Kohat Plateau. Looking eastward at an angle of about 30° , one sees major thrusts in the Orakzai Mountains (J) below the folds of the Kohat Plateau (K). The Orakzai thrust faults apparently coalesce in the Eocene shales, thus forming a roof thrust with a duplex underneath.

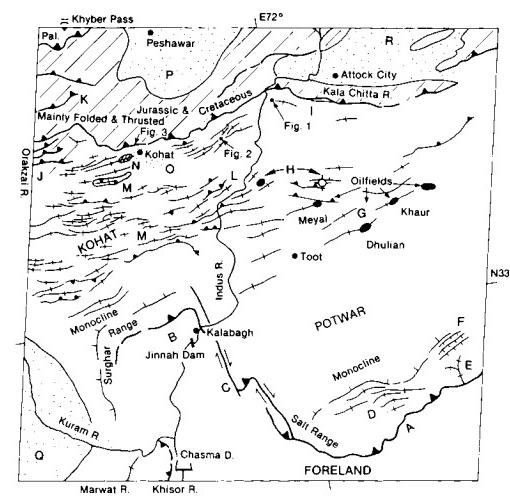
In general, Middle Eocene shales, gypsum, and salt in the Kohat anticlines are overlain conformably by the younger layers. The gypsum and salt form ridges that rose to the surface concomitant with the folding that began during deposition of the Siwalik sequence, with most of the deformation occurring in the Early or Middle Pleistocene. The folds consist of shale and evaporites overlain by Eocene limestones and shales, then sandstones and conglomerates of the molasse. In the semiarid climate, the limestone weathers out to form high ridges (L) (Figure T-46.2). The largest such feature is a tectonic klippe in the Surgul syncline (M). The klippe of Eocene limestone, which slid southward from the Buraka anticline, is folded in the neighboring syncline so that displacements must, therefore, have occurred early in the folding process. During folding, the anticlines flattened, overturning fold limbs such as those west of the city of Kohat, which include a syncline (N) in which an artificial lake is located. This lake irrigates an area that is a recent tectonic depression (Figure T-46.3, as seen from the Kohat Pass) filled by alluvium thousands of meters thick (O). Other large recent tectonic depressions, also characterized by extensive irrigation, include the plains of Peshawar (P), Bannu (Q) and Attock City (R). (GCW: K. A. DeJong) References: DeJong (1981), Gornitz and Seeger (1981), Meissner et al. (1974), Yeats et al. (1984). Landsat 20691-04550, December 13, 1976.



ORIGINAL PAGE
COLOR PHOTOGRAPH



3



India is a large continental mass that drifted northward after breaking off Antarctica (Gondwana) to ultimately collide with southern Asia in the Mid-Tertiary. This shield, known as the Peninsula, is an ancient plateau comprising Archean belts that contain intrusions mixed with high-grade metamorphics, Proterozoic platform belts, Late Paleozoic/Mesozoic sedimentary rocks (Gondwana System) in rifts, and Cretaceous/Tertiary Deccan basalt flows.

The Plate shows the central part of the state of Andhra Pradesh in the southern peninsular shield. The scene (left index map) includes most of the Cuddapah Basin, containing Upper Proterozoic sedimentary rocks deposited on a surface (Eparchean unconformity) carved from much older Archean rocks, the entire assemblage then being considerably deformed. Archean rocks surrounding the basin form low hills and plateaus (A) that are part of the eastern Ghats (Figure T-47.1). At the eastern edge are metavolcanics and schists of the Dharwar Super Group, found mainly in the Velikonda Range.

The Cuddapah System (exposed at B) is composed of 6000 m of shales, sandstones-grits, and limestones grouped in four Series. Proterozoic orogenic activity folded these rocks into a broad synclinorium with greater deformation and mild metamorphism along the eastern basin margin. Dolerite sills (Figure T-47.2) are evident at C. The Kurnool System of less deformed sedimentary rocks lies unconformably on the Cuddapah sequence at D.

Bedi (1982) recognizes four major geomorphic subprovinces in this semiarid (620 to 890 mm of rainfall) region. The exposed Archean rocks underlie a vast, intricately dissected piediplain, in which fractures control the numerous short ephemeral to semi-perennial streams with narrow floodplains. The path of the Dindi River is fault-influenced. Pediment surfaces occur on the low interfluvies. Red soils derived from the gneisses are developed north of the Krishna River; black soils exist around the Tungabhadra River drainage basin. Small fans and baradas (bajadas) are scattered throughout.

The Srisailam Plateau is topped by quartzites and sandstones. Lineaments (as at E and along the Dindi River) break the plateaus into several structural blocks. Steep scarps (F) bound much of the plateau, and cuestas occur in places (G). The Krishna River has cut through resistant cover units to produce a high-walled gorge. The plateau supports both mixed forest and scrub cover.

Cuestas mixed with broad floodplain piedmont surfaces form the black soil-covered areas between Kurnool and Nandyal

(Figure T-47.3). These gently sloped landforms are associated with the Cuddapah rocks, whereas the flatter piedmont terrain is developed from the Kurnool rocks. The Nallamalai Range is characterized by a valley and ridge topography in which the hogbacks are held up by harder quartzites and the valleys are eroded on weaker phyllites and schists.

The state of Orissa, in east-central India along the Bay of Bengal, is another part of the Peninsular Shield. The section of Orissa seen from Landsat in Figure T-47.4 (index map to its right) consists of two physiographic areas—the Utkal Plain and the Garhjat Hills. The latter, mostly 1000 to 1200 m above sealevel, contains the Simlipal Massif, the Baitarani Uplands, and the Keonjhar Plateau.

The Eastern Ghats Group (Archean granulite rocks) serves as the basement for the Iron Ore Group of sediments (western third of image) deposited in a basin bordering the Ghats stable mass. That Group was folded and metamorphosed during the Iron Ore orogeny, about 2700 Ma ago, after which the Singhbhum granite was emplaced. The Keonjhar Plateau includes remnants of older erosion surfaces on the Iron Ore Group (schists/quartzites to the north; volcanics in the south). A spectacular pattern of orthogonal fractures crisscross the Baitarani Uplands. Dolerite (diorite) dikes appear to fill some of the fractures. Erosion and vegetation cause others to stand out boldly.

The forest-covered Simlipal Massif is a Mid-Proterozoic rift basin containing banded iron formation. The massif formed as a broad basinal structure later folded into open concentric folds.

The Baitarani Uplands (lighter toned) are composed mainly of Singhbhum granites. The Uplands comprise an old surface of flat-topped hills. Numerous dolerite dikes (up to 700 m wide) pervade the Uplands, standing out as low ridges (visible as dark lines).

Late Paleozoic block-faulting influences the courses of the present Brahmani and Mahanadi River valleys. Cross-folding accompanying the faulting imposed a northwest topographic grain (the Mahanadi trend) that interrupts the regional northeast Eastern Ghats trend.

Marine transgressions in the Early Tertiary led to formation of the Utkal coastal plain. Alluvial and deltaic deposits from the braided Brahmani and Baitarani Rivers added to the thickness of this marine wedge, which increases toward the Bay of Bengal (just off the image). (NMS) Additional References: Chowdhury, (1974) Drury and Holt (1980), Drury et al. (1984). Landsat 2719-04125-6, January 10, 1977.



ORIGINAL PAGE
COLOR PHOTOGRAPH

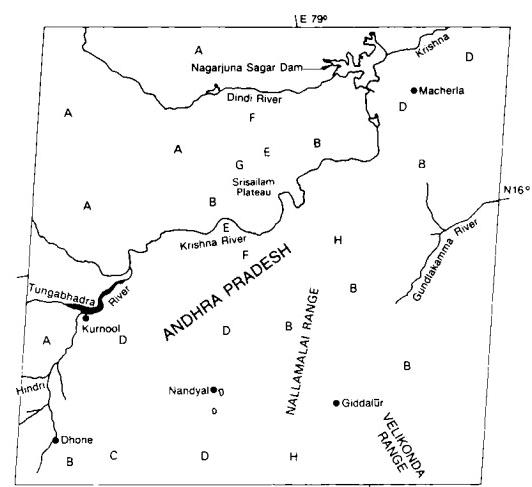
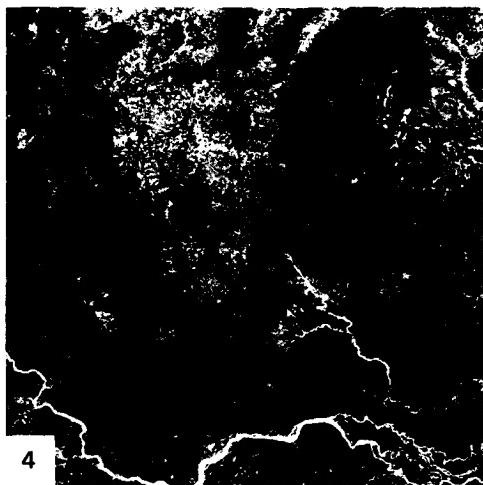


PLATE T-48

HIMALAYAN FRONT AND TIBETAN PLATEAU

The most profound deformational event involving the interaction of lithospheric plates is the collision between continents. The Indian continent began to impinge on the Eurasian continent in the Eocene. The continuing northward compressional movement of India has produced intracontinental thrust sheets responsible for the highest mountains in the world. Mount Everest, the Annapurna Range, and the rest of the Himalayas are still rising, and the region remains seismically active. The effects of this collision are extraordinarily widespread, being responsible for the 2500-km long thrust front of the Himalayas (see Figure 2-2) that extends from the Hindu Kush (Plate T-43) on the west to the Burma Ranges (see Figure T-48.9) on the east and for the creation of tectonically bonded intramontane basins (e.g., Kashmir and Katmandu) developed on the back slopes of the frontal thrusts. In addition, the collision is still producing strike-slip faulting far into western and central China, as well as along the Red River fault of southwest China and Vietnam (Plate T-53) and normal faulting on the Lake Baikal (Plate KL-14) and Shaanxi graben (Plate T-52) systems. The collision has led to 60 to 80 km of crustal thickening beneath the Tibetan Plateau, an area of 600 by + 1000 km, which provides the buoyancy in part necessary to maintain the plateau at an average of 4 km above sea level (Lyon-Caen and Molnar, 1985).

Much of our understanding of the geometry and kinematics of this widespread deformation is derived from studies of Landsat mosaics and their integration with available geologic and geophysical data (Molnar and Tapponnier, 1975, 1978; Ni and York, 1978; Tapponnier and Molnar, 1976, 1977, 1979; Tapponnier et al., 1982). Space imagery is virtually the only tool available to visually span the regions affected by this vast deformation. Other Plates in this chapter that include elements of this widespread deformation field are T-43 through T-46 and T-49 through T-53, whose locations are plotted on Figure 2-2.

On the facing page is a spectacular hand-held camera photograph taken during Shuttle Mission S-17 from a point almost directly above Mt. Everest looking northwest to the Hindu Kush (snow-covered peaks near the midhorizon). (A "boot-shaped" lake (A) is a useful reference in locating several other figures in this Plate.) The Indo-Gangetic Plains (bluish-green), at less than 100 m average elevation, lie to the left, and the haze-filled Tarim Basin occupies the right half of the horizon (see index map below Plate). Over much of the Himalayas, topography strongly mirrors underlying structure. The light- to dark-green transition on the left roughly marks the edge of the Himalayan deformation front and the approximate location of the Main Boundary Fault (Gansser, 1974). Snow delineates the higher Himalayas (many peaks being greater than 7500 m, with Mt. Everest rising to 8848 m); the southern margin of the snow crudely follows the trace of the Central Thrust of the Himalayas.

In the Plate, the extensive area of light-brown (tawny) terrain containing scattered lakes that indicate closed drainage basins is the youthful topography of the Tibetan Plateau. Deformation and uplift, although strong, are so recent that much of the plateau lacks an integrated drainage system. Linear ridges mark fold and thrust belts; faults control many of the linear valleys. The very straight valley near the horizon is cut along the Karakoram fault zone (right-lateral); the Indus suture, or Bangong Nu Chang, representing the collision boundary between India and Asia (Crawford, 1974), occupies a wide light-colored valley that runs diagonally across the photograph. Several straight graben valleys, some containing lakes, trend northward transverse to major compressive features. Other lakes collect in low spots along active strike-slip faults or in valleys dammed by recent volcanic material.

Figure T-48.1 (Large Format Camera photograph 0534) pictures a segment of the Himalaya front from the syntaxis near Islamabad, Pakistan, to Simla, India. The Main Boundary Thrust (MBT) of the Himalayan front marks the boundary between the low relief and relatively gently deformed Tertiary rocks of the highly cultivated Punjab plain and the folded and thrust-faulted Tertiary rocks of the Siwalik Hills (darker toned (forest-covered) topography), beyond which are the more highly deformed Lower Paleozoic and Mesozoic rocks of the lower Himalayas. Most of the Punjab plain is at an altitude of about 100 m, whereas the cloud-covered peaks to the north are above 6000 m (6 km or more of relief over a 60-km horizontal distance). Actually, topographic relief along the front is even more abrupt, with elevations rising to 2500 m in less than 10 km. Discrepancies between land surveys based on celestial and ground measurements in the vicinity of this impressive topographic discontinuity led to an awareness of gravity anomalies and the development in the last century of the Airy and Pratt theoretical models for isostasy.

Another LFC photograph (Figure T-48.2) is a vertical view of much the same area as shown in the center foreground of the Plate photograph (the boot-shaped lake, center of the LFC view, is a good tie point). The scene extends across the main Himalaya in Nepal to the Siwalik Hills and Indo-Gangetic Plain (lower right), with its center about 1500 km southeast of Figure T-48.1. Mt. Everest appears in the photograph toward the upper right. Terrain typical of the Everest region appears in Figure T-48.3.

Despite the great elevations of the Tibetan Plateau, the comparatively gentle topography of much of this plateau (Figures T-48.4 (Landsat) and T-48.5 (ground)), except near its northern and southern margins and in several ranges such as the Tengulla Shan (Figure T-48.6) that lie within it, is strong evidence for recent uplift. Paleontological evidence suggests that most of this uplift is post-Miocene. Indeed, the region is still rising, some places at rates greater than 1 cm per year (Lyon-Caen and Molnar, 1985). Many of the circular features that dot the plateau are young volcanoes (e.g., southeast of the boot-shaped lake in Figure T-48.2) or recent intrusions. Both attest to the geologic youthfulness of the region.

The Kunlun Mountains (see Plate T-49) are another range that divides the Tibetan Plateau. The Kunlun fault, seen in Figure T-48.7, is one of the most active in the Himalayan region. Kidd and Molnar (personal communication, 1985) found evidence, based on pyroxenite clasts in a glacial till, of 27 km of Pleistocene left-lateral movement (a rate of 1 to 3 cm per year). Gash crevices along the fault are deep enough to conceal a standing man (Kidd, personal communication, 1985). The linear fault valley and the "drag" of geologic features into the fault are excellent examples of topography developed along a major strike-slip zone. Topographic relief between snow-covered peaks in this LFC scene and the Qaidam basin to the north (see Plate T-51) is about 5000 m.

Several of the large active faults (Rothery and Drury, 1984) in the Himalaya orogen are evident in the oblique photograph taken from the Shuttle (Figure T-48.8) looking toward the north-northwest. The low look-angle and the snow cover help to make these stand out. The northwest-trending linear valley (occupied by the upper Indus River) traversing the entire frame follows the trace of the right-lateral Karakoram fault (Molnar and Tapponnier, 1975, 1977).

Figure T-48.9, which straddles the intersection of the Himalayan front and the Indoburman ranges, shows a juxtaposition of tectonic styles. The beautifully developed north-trending

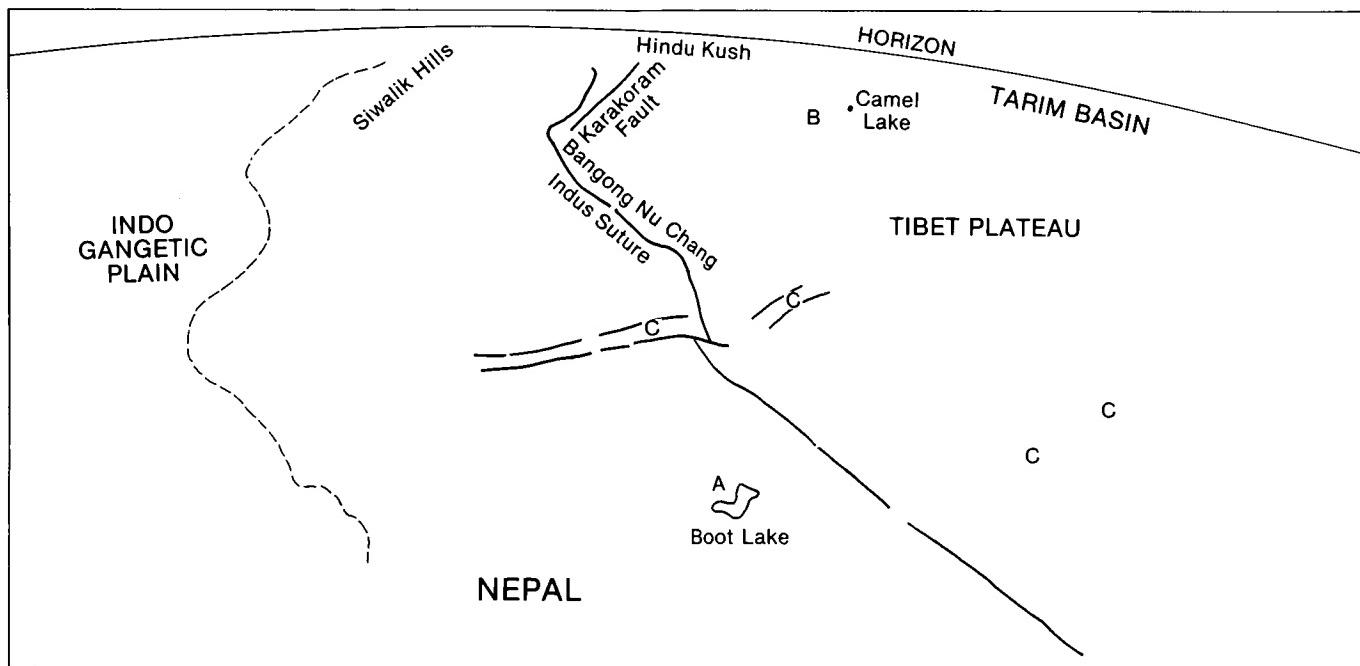
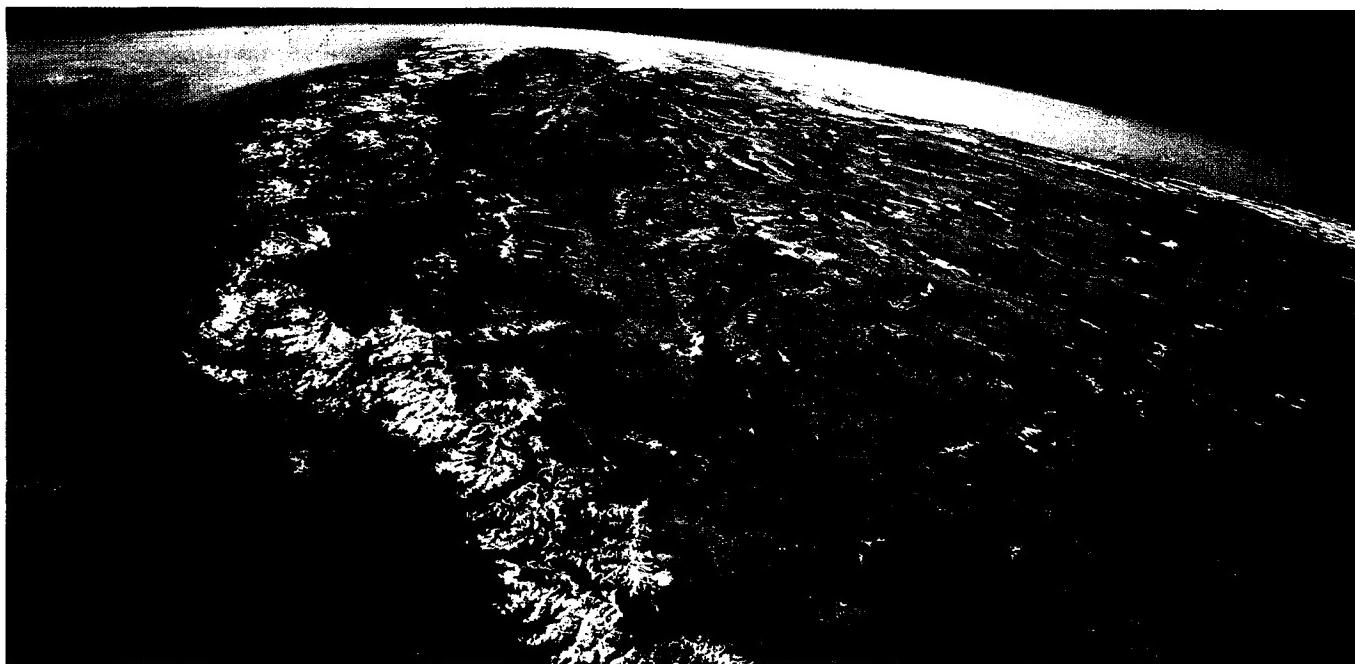
**ORIGINAL PAGE
COLOR PHOTOGRAPH**

décollement folds of the Chin Hills end abruptly against the thrust of the front. The right-angle intersection of the two sets of compressive features, of approximately the same age, is a consequence of the clockwise rotation of India as it plowed into Asia. The same collision was responsible for both the Himalayan and the Chin Hills deformations.

The forested finger-like anticlines that comprise the Chin Hills stand out in this Landsat scene, in stark contrast to the highly cultivated synclinal lowlands. Individual lithologic units of Tertiary age making up the folds are traceable for substantial distances along the strike. To the east, the folds become tighter, and westward-directed thrusting increases. The detachment zone is probably a series of shales that immediately overlie the basement; the folds are produced as the Upper Cretaceous and Ter-

tiary rocks are scraped off the Indian craton while it is being subducted beneath Asia.

The Khasi Hills and Meghalaya Plateau are an uplifted Precambrian crystalline complex (part of India). These rocks were eroded to a very low-relief surface before the beginning of uplift. Much of the older erosion surface is still intact, and many features characteristic of planation surfaces in shield areas are visible. Only the southern portion of this uplifted shield, adjacent to a large southward-directed frontal thrust, has begun to undergo erosion. The freshness of the little-eroded upland surface implies very recent (Pleistocene) uplift. This fresh appearance is particularly remarkable in that the town of Cherrapunji, in the hills north of Syhlet, receives the largest recorded annual rainfall of any place on Earth. Folded alluvial fans suggest that thrusting continues today. (JRE) STS-17-120-022.



**ORIGINAL PAGE
COLOR PHOTOGRAPH**



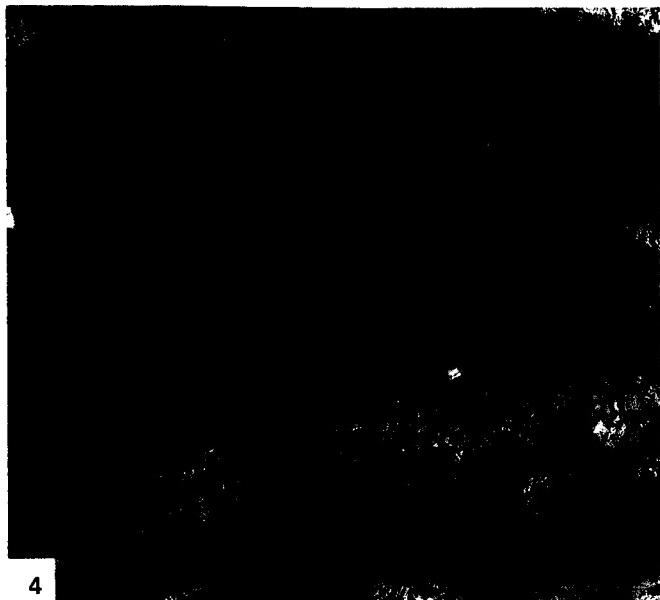
ORIGINAL PAGE
COLOR PHOTOGRAPH



ORIGINAL PAGE
COLOR PHOTOGRAPH



3



4



5



6



7

ORIGINAL PAGE
COLOR PHOTOGRAPH

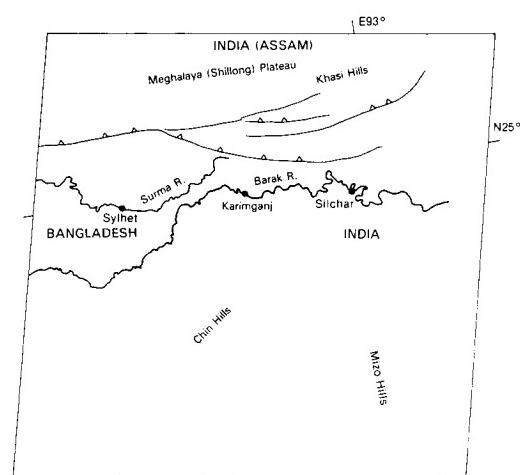
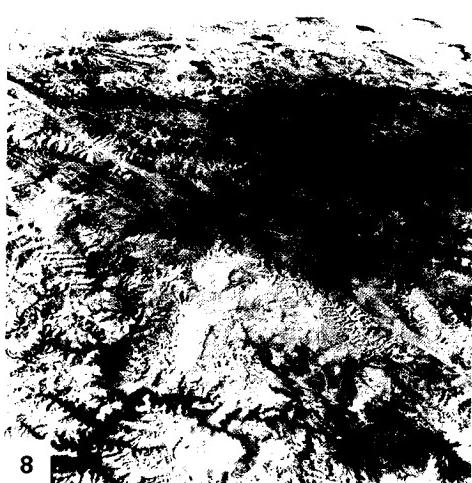
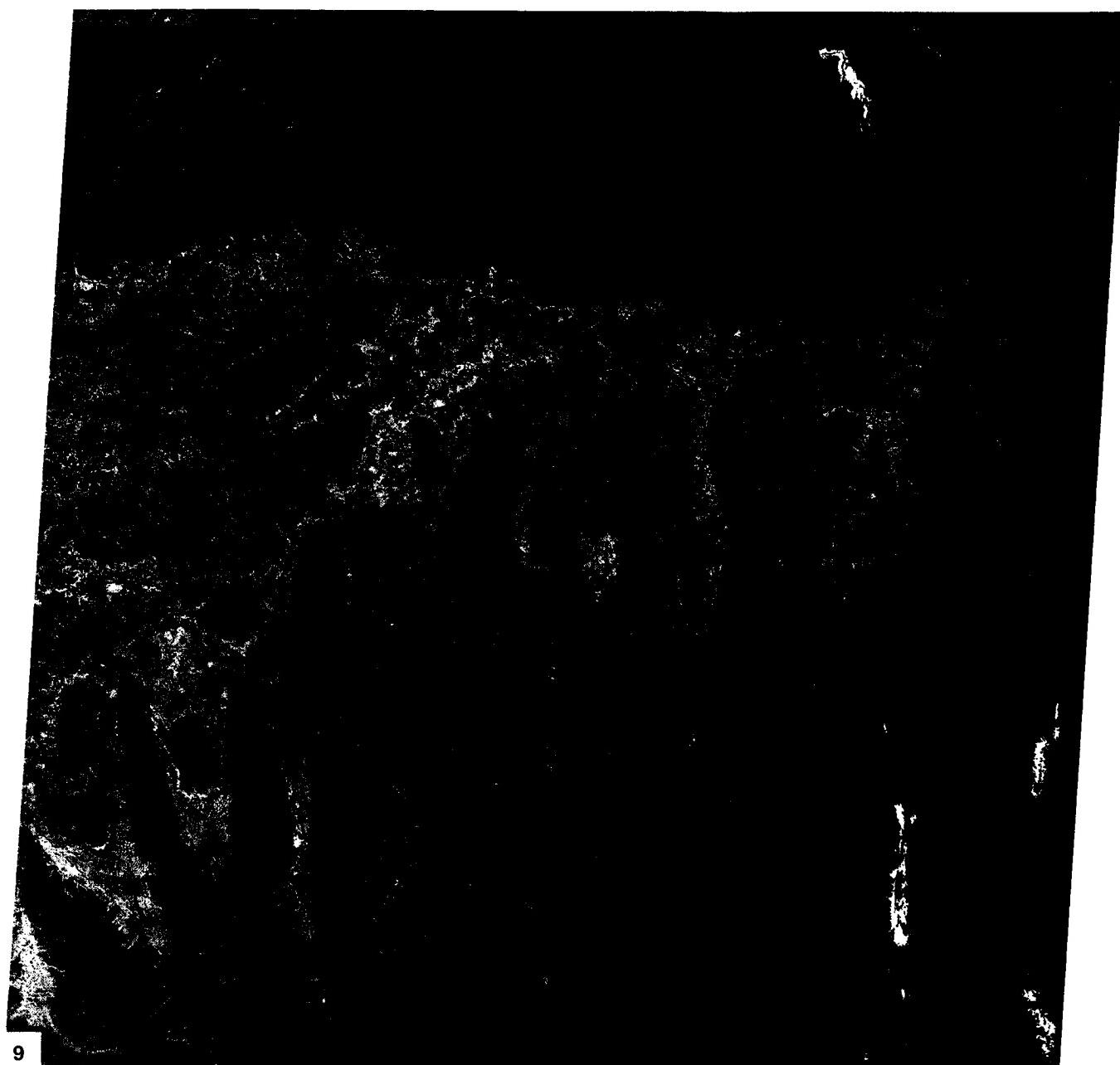


PLATE T-49

KASHGAR KU-CHE FOLD BELT, TIAN SHAN

The Tian Shan is the major mountain belt of central Asia, extending approximately 2500 km from the Kyzyl Kum Desert of western China to the Gobi Desert in Mongolia. It separates the Tarim basin to the south from the Kazakhstan shield and the Dzungarian basin to the north. Arc collisions during the Silurian, Devonian, and Mississippian and, finally, suturing along the Tian Shan in the Late Paleozoic produced most of the structural and metamorphic fabric of the mountain interiors in the northwest part of the Plate scene (Bally et al., 1980; Dewey and Burke, 1973; Gansser, 1974; and Zhang and Liou, 1984). Following a period of quiescence in the Mesozoic and Early Tertiary, tectonic activity resumed in the Eocene in response to the collision of India with Eurasia (Molnar and Tapponnier, 1975; and Tapponnier and Molnar, 1977).

The Kashgar Ku-Che fold belt is an area of conspicuous thrust faulting associated with box folds involving many Silurian and Devonian formations. Linear ridges oriented northeast-southwest, with multiple southeast-facing scarps, denote a series of northwest-dipping strata. These ridges are broken and offset by faulting. The repetition of the sequence of northwest-dipping sedimentary units, coupled with the absence of apparent dip reversal or overturned beds, indicates that the stratigraphic section is being repeated across thrust faults. Fault traces parallel to the interpreted thrust direction can be observed in the alluvium separating the older core of Tian Shan from the thrust belt. This, in conjunction with the juvenile erosional patterns associated with the thrusts and fault blocks south of the new thrust fault, demonstrate recent and continuing deformation.

Two prominent strike-slip faults abruptly offset the thrust belt in the western part of the scene. The westernmost of these north-trending faults transects the entire thrust belt (~75 km) and has an apparent 10-km left-lateral offset. The presence of similarly oriented left-lateral strike-slip faulting can be inferred from outcrop patterns and bedding orientation in the northeastern

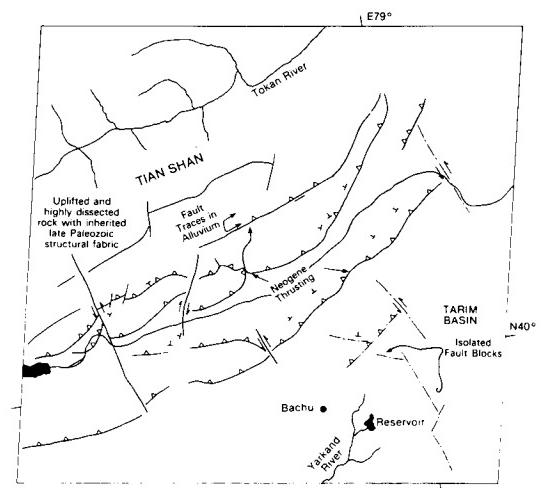
part of the scene and along the margins of the isolated fault blocks in front of the main thrust fronts. The outcropping of older rocks and the apparent continuation of thrust-belt tectonic direction in front of the main thrust front indicate that active compression deformation is occurring to the south within the Yarkand Darya floodplain.

Figure T-49.1 is a SIR-A image of complex folds and thrusts in the southwestern portion of the Landsat MSS image. The folds, which lie on the north edge of the Tarim basin, are overturned to the south and thrust on the south side. The intensity of deformation decreases from north to south across the zone. Radar does a much better job here of highlighting fine details of the fracture pattern edges of the eroded beds that make up the cuestas than the MSS. The radar is actually "seeing through" some of the sand and alluvium that cover the low areas in this arid region. These details of the stratigraphy and fracturing are visible farther down the dip slopes on the radar than on the MSS image. The higher-resolution of the radar brings out many details that are not visible in the MSS image.

This scene falls within the southwestern Tian Shan where it straddles the border between westernmost Sinkiang Province of China, north of the Taklimakan Desert (Plate E-27), and the Kirghiz S.S.R. Several mountain peaks in the scene reach above 6000 m and approach 8000 m both to the west and to the east. The mountains (Figure T-49.2) have been extensively glaciated (see Plate G-26) and in places rival the Himalayan chain to the south in ruggedness and grandeur. Farther west, the Tian Shan chain extends into the Pamirs in the Tadzhik S.S.R., north of the Hindu Kush. Russia's highest mountain, Pikkommunizma (7495 m), is located within the Landsat image seen as Figure T-49.3. The Peter the Great Ridge (Figure T-49.4) is typical of the spectacular scenery of this region. (*GCW: R. C. Michael*) Landsat 1206-05000, February 14, 1973.



ORIGINAL PAGE
COLOR PHOTOGRAPH



The Tibetan Plateau has been the site of convergence and collision of northward-drifting island arcs and continental fragments since the Late Paleozoic (Dewey and Burke, 1973; Zhang and Liou, 1984). These events culminated in the Late Eocene with the closure of the southern Tethys Sea and the consequent collision of the Indian Continent against the underbelly of Eurasia (Gansser, 1974). This collision, which continues today, has produced a belt of deformation that covers an area of over 20° latitude by 70° longitude in central and eastern Asia.

The neotectonic regime of central Asia (see Figure 2-2), including most of the Tibetan Plateau, is dominated by a series of gigantic left-lateral strike-slip faults that are moving successively more southerly slices of Asia eastward away from the northward-advancing Indian plate (Molnar and Tapponnier, 1975). The north-south-oriented normal faults and southeast- and east-northeast-trending strike-slip faults that are characteristic of the Tibetan Plateau accommodate this regional north-south shortening and eastward translation (Molnar and Tapponnier, 1975; Rothery and Drury, 1984).

Mean elevation of the Tibetan Plateau is about 4000 m and locally exceeds 7000 m. The Uula-Muztag, approximately 50 km south of the scene, reaches an elevation of 7724 m. To the north of the Plateau, elevation within the Tarim basin drops to approximately 1000 m.

The Altyn Tagh fault is the most prominent fault of Tibet and western China, extending more than 1500 km from the Karakoram to the Nan Shan. Meeting the Kansu fault in the east, it is part of an even larger system that extends over 2500 km and defines the margins of many of the largest basins and uplifts in central and western China. About two-thirds of the Altyn Tagh fault can be followed in the color mosaic in the upper half of this Plate (next pair of pages). Older igneous and metamorphic rocks are exposed along this fault and presumably continue beneath the Tertiary and Quaternary fill of the Tarim basin.

The Large Format Camera photograph in the lower half of the Plate shows a segment of the Altyn Tagh fault about 500 km west of the center of the mosaic image. The large and small folds north of the main trace of the fault suggest that there is a substantial amount of compression across the fault and perhaps a considerable thrust component to movement at this locality. The snow-covered mountains of the Tibetan Plateau tower 5000 m above the Tarim Basin. The numerous closed basins (lakes) and complex pattern of ridges on the plateau (west end of the Kunlun fold belt) attest to recent deformation.

Considerable evidence for recent movements along the Altyn Tagh fault is apparent from looking at details visible in an individual Landsat image (Figure T-50.1, located near middle of mosaic). Note in particular the discrete linear traces of the fault, the juvenile erosional patterns of adjacent uplifted areas, the left-lateral offset of minor drainage that crosses the fault, and the tilted alluvial terraces along the fault. The Tarim basin lies north of the fault. This isolated rigid block is surrounded on all sides by active intraplate orogenic zones. Compression and depression dominate along the northern margin of the Tarim basin, and strike-slip motion prevails along its southern margin, with the result that the entire basin has tilted northward. South of the

Altyn Tagh fault is an area characterized by broad alluvium-filled valleys and narrow, subparallel, and highly elevated ridges. These ridges consist of folded and fault-bounded sedimentary rocks; the faults exhibit a combination of strike-slip and dip-slip movement.

The most prominent features situated along the southeastern margin of the Tian Shan in westernmost China on the north side of the eastward-moving edge of the China block are the Kuruk Tagh uplift and the Kuruk Tagh fault. The discrete trace of the Kuruk Tagh fault is seen on a Landsat image (Figure T-50.2) where it cuts through folded and metamorphosed Late Paleozoic (?) rocks. The fault trace is sharp and straight, implying a large component of strike-slip motion. The crispness or freshness of the fault trace, disruption of drainage across this fault (e.g., alluvial fans displaced from major streams), and abruptness of relief across this fault line indicate that the Kuruk Tagh fault is currently active. Detached structural blocks, such as the small detached anticline in the western part of the image, also suggest recent movement on the fault.

The Kuruk Tagh fault, which extends for over 250 km in an east-west direction, is only one of several such faults in the Tian Shan. Offset of streams and fans across the fault, "drag" of the tectonic fabric of rocks adjacent to the fault, and displacement of lithologic blocks across the fault demonstrate right-lateral movement. Right-lateral movement along the Kuruk Tagh and similar faults probably began during the Oligocene, with the rate of movement displacement progressively increasing since then. Right-lateral displacement on these faults is part of the kinematic pattern that has accommodated the eastward movement of crustal blocks in the southeastern Eurasian continent away from northward-moving India since the initial Eocene collision.

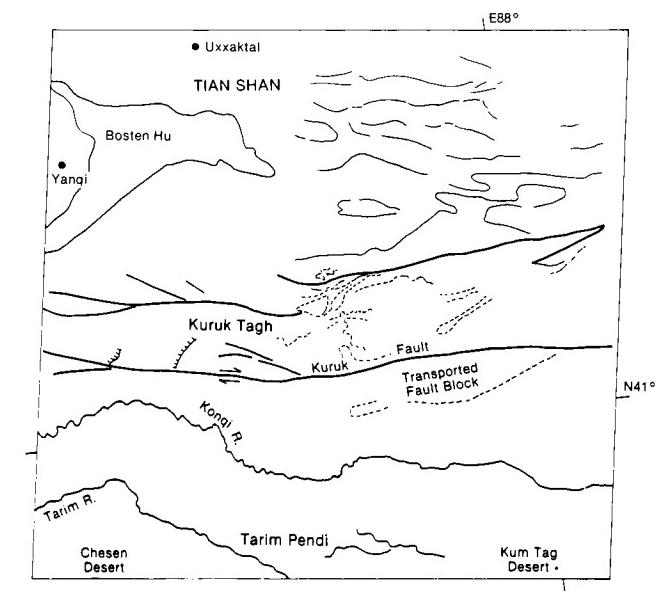
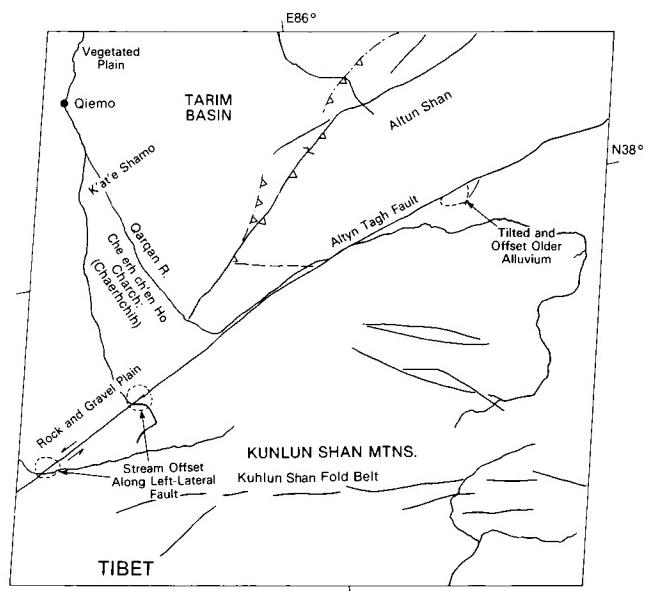
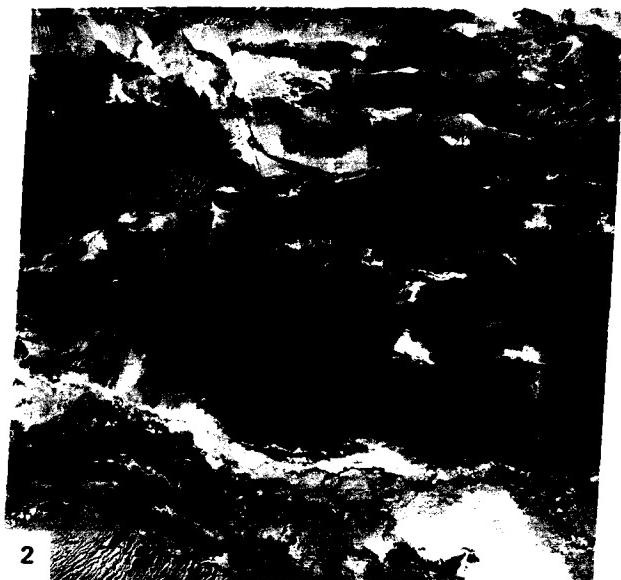
The Bagrash Kol depression (northwest portion of image) is one of several large east-west elongated depressions on the eastern Tian Shan that resulted from the interference between dominant right-lateral strike-slip faults and subordinate left-lateral strike-slip faults.

Earthquake solutions and evidence from Landsat imagery to the east and north of the Kuruk Tagh suggest that many of the faults bounding the individual block uplifts are actually reverse faults (Tapponnier and Molnar, 1977). The recent and continuing uplift of these blocks is attested to by the active system of steep alluvial fans that flank most of the uplifts.

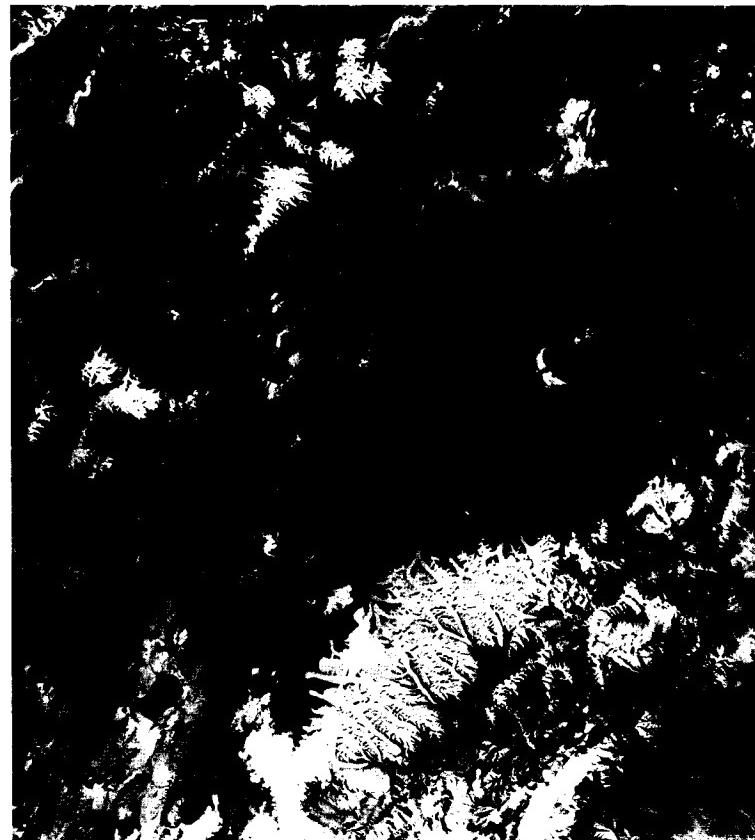
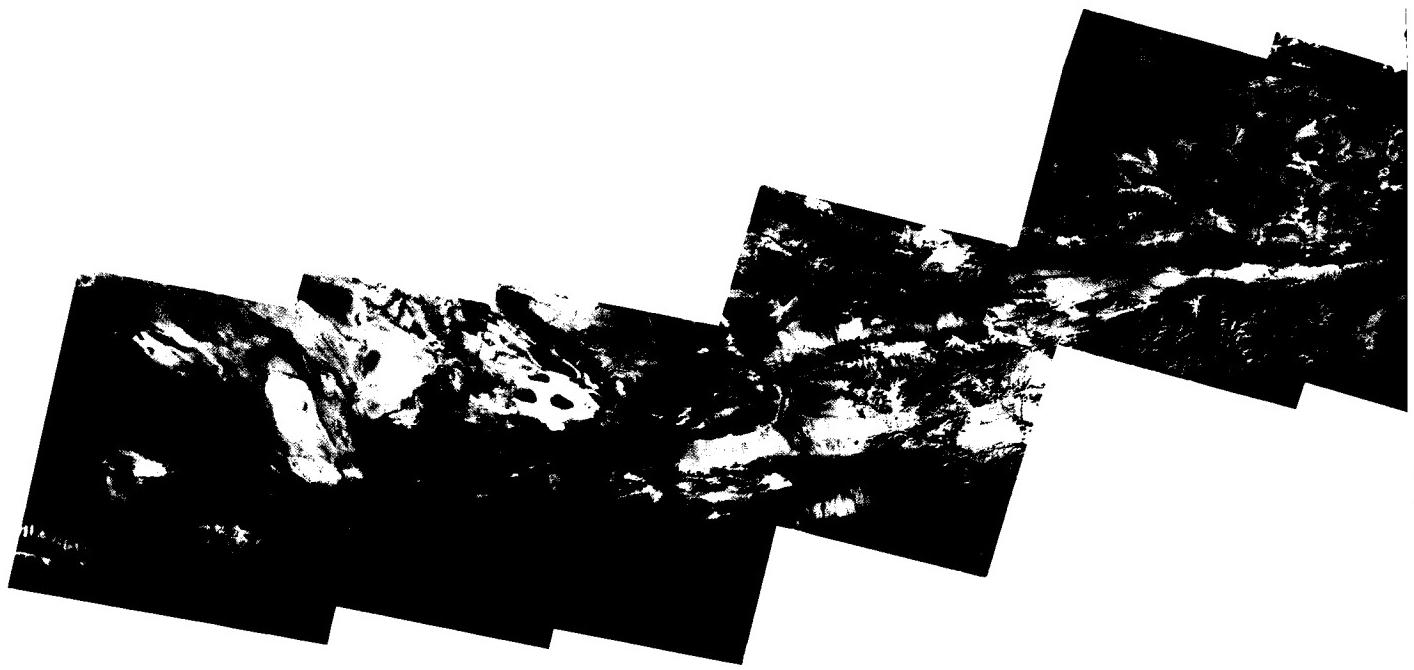
To the south of the Kuruk Tagh are the vegetated floodplains of the Kuruk and Tarim Rivers. Farther to the southwest in this Landsat scene is the northern edge of the Cherchen Desert, which occupies the easternmost portion of the Tarim basin. Note the well-developed compound crescentic dunes and interdune lakes.

The Kunlun fault (Figure T-50.3) and the Kunlun Mountain belt (Figure T-50.4) roughly parallel the eastern half of the Altyn Tagh fault system to the north. This, too, is another strike-slip fault with pronounced left-lateral displacement. The Landsat image shows the Kunlun fault near its western terminus; note the subsidiary faults running in much the same directions. (*GCW: R. C. Michael*) Additional Reference: Bally et al. (1950). Large Format Camera 168, October 6, 1984.

ORIGINAL PAGE
COLOR PHOTOGRAPH



**ORIGINAL PAGE
COLOR PHOTOGRAPH**



ORIGINAL PAGE
COLOR PHOTOGRAPH



PLATE T-51

WESTERN QAIDAM BASIN

The Qaidam basin is a large intermontane basin in west-central China, covering approximately 100 000 km² between 36°N and 39°N latitude and 91°E and 98°E longitude. The Qaidam basin and adjacent physiographic features owe their present configuration to Neogene Himalayan tectonism. The interior of the basin comprises a vast middle-latitude desert that receives only 35 mm of precipitation per year and is subjected to very high winds and long severe winters. As a result, vegetation is extremely sparse and much of the surface is covered by thin eolian deposits and encrusted saline soils. Average surface elevation within the basin is 3000 m. The clear air, lack of vegetation, and abundance of exposed bed rock make the Qaidam an almost ideal subject for study from space.

Viewed synoptically in the six-image mosaic of the Plate, the Qaidam region exhibits coherent structural patterns that result from northeast-oriented principal stress associated with Himalayan tectonism (Bailey and Anderson, 1982). This stress is largely accommodated by movement along major east- to east-northeast-trending left-lateral strike-slip faults, such as the Altyn Tagh and Kunlun fault zones that extend for thousands of kilometers across China. In western China, where movement along these faults is transpressional, marginal uplifts are intensely and complexly deformed. Large intermontane basins, such as the Qaidam basin, form as compressional features between major uplifts that were produced by movement on strike-slip faults (Tapponnier and Molnar, 1977). In the Qaidam basin, the compressional origin of the basin is attested to by the large complex folds that dominate the basin interior.

The western Qaidam basin lies between the Altyn Mountain to the north and the Kunlun Mountains to the south. These ranges comprise Paleozoic and older rocks deformed during Late Paleozoic and Mesozoic times. However, the elongate en echelon, and many places discontinuous, aspect of these ranges strongly suggests that movement of adjacent through-going strike-slip faults of large displacement controls their present configuration. The Altyn Tagh left-lateral fault zone is particularly conspicuous on the mosaic. Evidence on the Landsat imagery for recent predominantly strike-slip movement along this fault includes: (1) the straight, narrow trace of the fault, (2) the sharp trace of the fault within recent alluvium, (3) left-lateral offset of streams crossing the fault and the orientation and, in any instances, truncation of minor related structures along the fault.

The older, repeatedly deformed rocks of the Altyn and Kunlun Mountains also exhibits a superimposed structural fabric

that appears to be related to left-lateral strike-slip faulting. Much of the structural fabric in the northwest Kunlun Mountains parallels the left-lateral east-trending Kunlun fault zone. The structure of the Altyn Mountains, although complex and partially inherited from older orogenies, includes locally prominent features that appear to be related to left-lateral movement along the Altyn fault zone (Tapponnier and Molnar, 1977).

The Qaidam basin proper is filled mainly with Tertiary, and locally Cretaceous, continental sediments. The interior of the basin is pervasively folded, with folding affecting sediments as young as Quaternary age. This suggests that deformation of the basin interior and strike-slip faulting of the surrounding uplands are contemporaneous. Most large folds, trending northwest to west-northwest, that structurally comprise the interior of the basin are asymmetrical. The absence of discernible intervening synclines between anticlines, the local and in many places highly oblique truncation of beds, and the general disharmonic appearance of these folds indicate that many are thrust-displaced. A major thrust-bounded intrabasinal uplift, the Youshashan, is present in the western part of the basin, interior to the apex where the two mountain systems converge (Bailey and Anderson, 1982). The Youshashan uplift exhibits a juvenile erosional texture and is oriented parallel to the major folds and thrust faults.

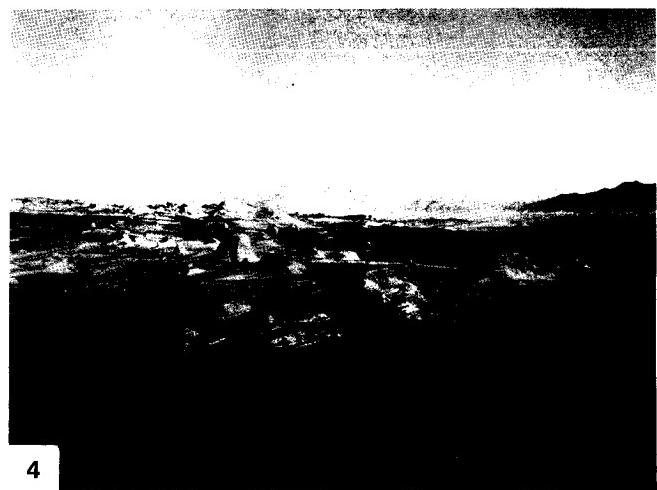
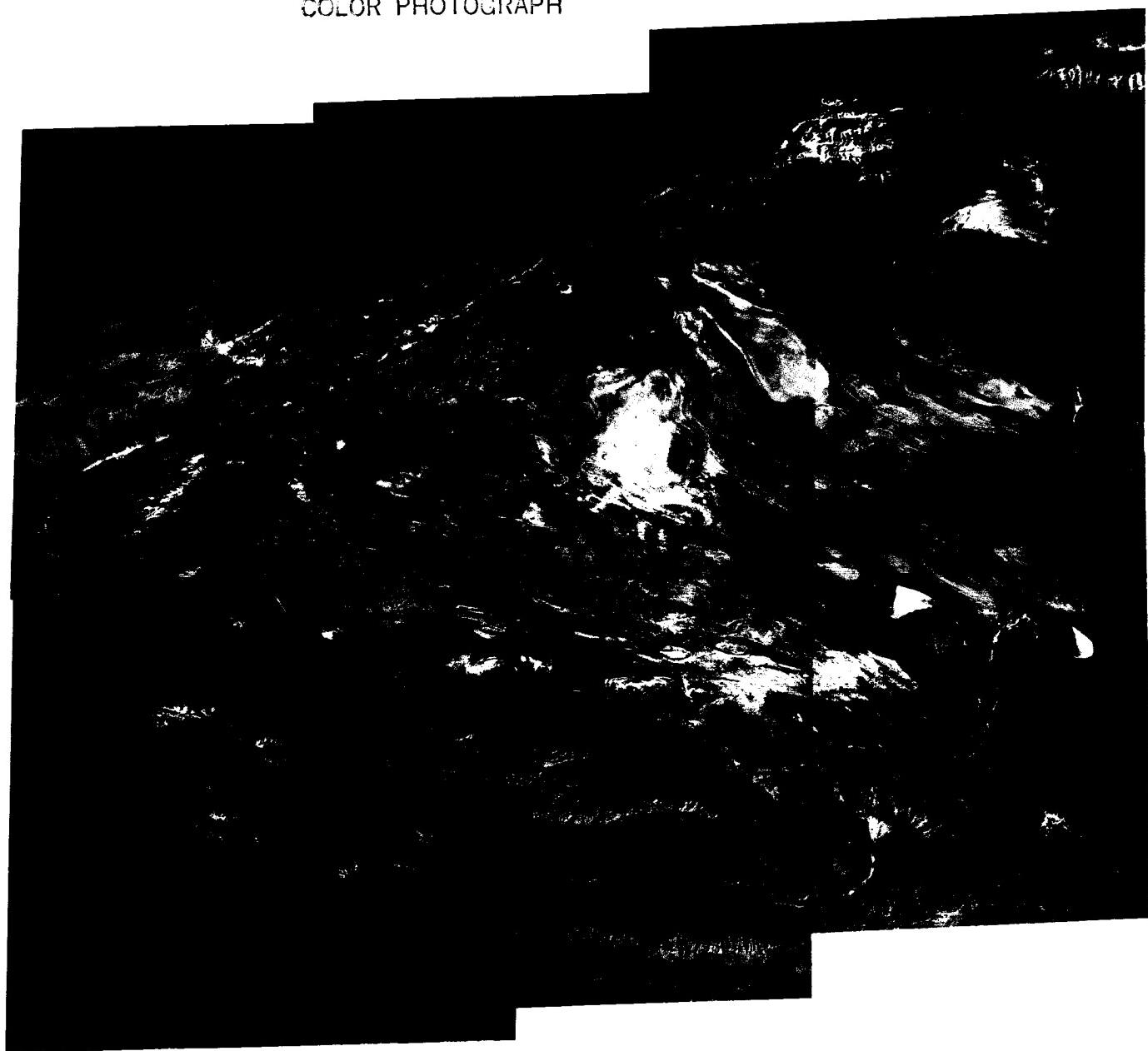
Much of the basin's surface appears to be wind-scoured. Large surficial evaporitic deposits are also widespread. Most of the area, because of sparsity of precipitation, supports little or no vegetation, except in areas of seasonal lakes.

Figure T-51.1 is an east-northeast view along a fault valley of the major left-lateral strike-slip Altyn fault zone. Rock berms in the foreground are used for road construction by the workers in the distance. Figure T-51.2 shows the subdued topography typical of the Qaidam Basin. More resistant remnants of generally nonresistant clastic sedimentary rocks dip to the right in this photograph. Figure T-51.3, from the western part of the Qaidam Basin, shows typical exposures of folded nonmarine clastic sedimentary rocks and illustrates the low topographic relief commonly exhibited by folded rocks in the basin interior.

In the rugged, desolate terrain of the fault bounded Youshashan uplift (Figure T-51.4), the soft silty rocks weather rapidly in the harsh climate, leaving extensive surficial clay residues. The region is devoid of vegetation. In Figure T-51.5, the camp of a Chinese geological field party is seen in the middle ground. (GCW: R. C. Michael) Additional References: Bally et al. (1980), Zhang and Liou (1984). Landsat Mosaic.



ORIGINAL PAGE
COLOR PHOTOGRAPH



4



5

Among its many geologic wonders, China contains some of the most spectacularly exposed and expressed examples of décollement (detachment folds) in the world. The Sichuan basin of central China includes some of the best samples of this style of deformation. Away from the margins of the basins, the folds are relatively simple. Several of the anticlines are more than 200 km long, with widths of less than 10 km. The anticlines are breached, with long gentle plunging noses and flatirons along the outside of the fold. Broad open synclines more than 20 km wide lie between the narrow anticlines. As one approaches the margins of the basin, the structures become tighter and more complex, synclines narrow, anticlines lie upon anticlines, thrust faults replace synclines and even take the place of anticlinal axes so that one is confronted with a series of imbricate thrust sheets. Differential erosion of the Jurassic through Cretaceous rocks that comprise the folds allows one to trace particular lithologic units the entire length of some folds. The presence of a well-developed karst topography on the carbonate sequence provides an excellent regional stratigraphic marker that is easily spotted from space.

Décollement folds are similar to the wrinkles produced in a rug sliding on a smooth floor. All that is required is separation of a (more competent) layer from an underlying (less competent) layer as deformation proceeds. A homogeneous layer of essentially uniform thickness overlying a less viscous layer produces the most spectacular folds. The incompetent layer can be evaporites, shales, or even heated lower crust (i.e., any situation that will provide a viscosity inversion with depth).

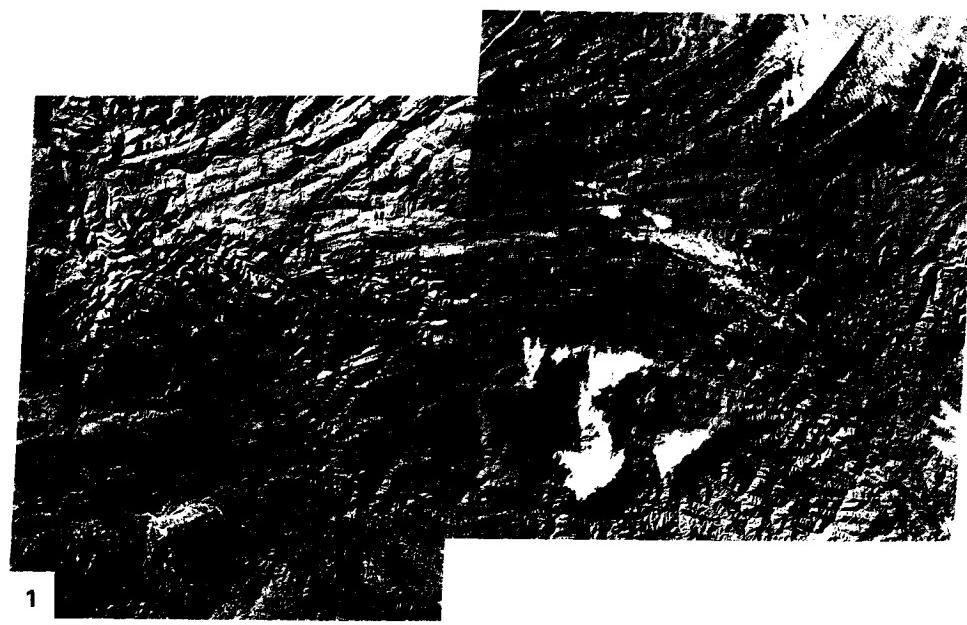
Décollement folds also imply a mismatch in the horizontal dimensions of the layer above the detachment zone and the layer below the zone. The upper layer is larger in at least one dimension. Several sets of circumstances can produce this mismatch: the upper layer can be stretched as in diapiric folds, the upper layer can break away and slide off an uplift, or the lower layer can be shortened by thrusting or subduction. In the Appalachians and the Anti Atlas (Plates T-11 and T-30), subduction attendant to continental collision shortened the lower layer (lower continental crust). In the Western Overthrust Belt of the central Rocky Mountains (Figure T-6.1), continental telescoping and thickening shortened the lower layer. In many basins, shortening is ac-

complished by thrusting at the margins; this is true on the west side of the Sichuan basin and is probably true on the east side as well, accounting for the increased complexity of structure near the eastern margin of the basin.

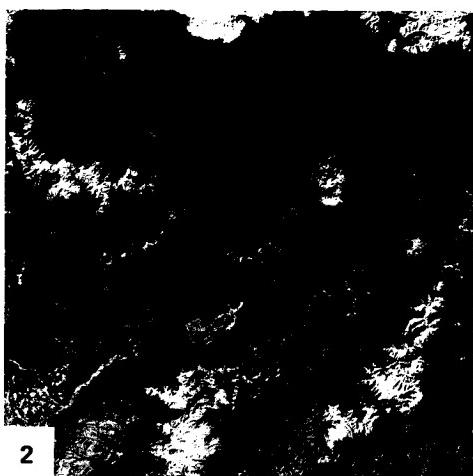
The Sichuan basin has acted as a stable block, with relatively little internal deformation, lying between two large left-lateral faults; the Kansu to the north and the Kang Ting on the southwest (Figure 2-2). The collision of India and Eurasia, beginning in the Late Eocene, reactivated the Lung Men Shan thrusts on the west side of the basin, and the tight folds and thrusts on the east are all structures that were formed in the Mid-Mesozoic. This two-phase deformation history accounts for the apparent anomalies in the strain field (Molnar and Tapponnier, 1975; Tapponnier and Molnar, 1977; Zhang and Liou, 1984).

Figure T-52.1 (a join of two adjacent Landsat frames) shows the complicated structure at the northeast corner of the Sichuan basin. Tightly folded Lower Paleozoic rocks of the Tapa Shan (southern Shanxi and western Hubei Provinces) are juxtaposed with the more gently folded Mesozoic rocks of the Sichuan basin (southwest half of the left image), along a complex system of strike-slip and thrust faults (the extreme eastern end of the Altyn Tagh system). Several thrust/strike-slip faults within the Paleozoic rocks bring together divergent structural trends. The Paleozoic rocks were deformed at least once before the imposition of the current strain field. Fortunately oriented earlier faults are still experiencing movement in the current cycle of deformation (Huang, 1978; Zhang and Liou, 1984). The famed gorges of the Yangtze River (see Figures F-16.3 and F-16.4) are located near the lower edge of Figure T-52.1 and in the Plate image. The river was either superimposed on or antecedent to the complex structure.

Farther to the northeast, the scene in Figure T-52.2 shows several graben of the Shanxi graben system about 1000 km north-northeast of the Sichuan basin scene and some 300 km west of Beijing. These features lie in the tensile sector of the deforming stress field north of the Altyn Tagh fault. The grabens trend northeast. The crisp appearance of many of the scarps suggests recent movement. (JRE) Landsat MSS 2305-02370, November 23, 1975.



ORIGINAL PAGE
COLOR PHOTOGRAPH



2

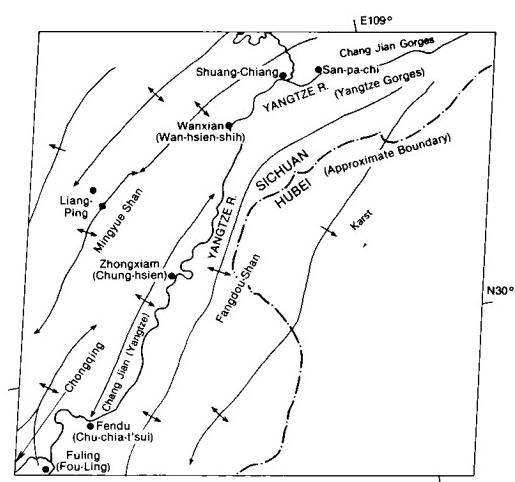


PLATE T-53

RED RIVER FAULT ZONE

Tappognier et al. (1982) proposed a model for the tectonic development of southeastern Asia following the Indian subcontinental collision in which they put forth a concept of propagating extrusion tectonics based on a simple experiment involving the penetration of a rigid block (representing India) into layers of plasticine in a partly confined block (Asia). As indentation proceeded, a series of criss-crossing shear faults eventually gave way to major movement of two principal fault-bounded blocks to the right (eastward) that were elongated by deformational squeezing of internal elements along faults within the blocks. The final result of the model deformation bears a remarkable resemblance to much of southwestern China and Indochina as analogs to these blocks. The two main boundary faults are likewise analogs to the left-lateral Altyn Tagh fault of Tibet (Plate T-50) and the right-lateral Red (Yuan) River fault passing through the Yunnan Province of China. Both are characterized in the model by strike-slip movement of considerable cumulative magnitude.

The Red River fault, crossing diagonally from upper left to lower right in this Plate, extends from the southwest edge of the Yangzi (Yangtze) Platform of north-central Yunnan in a southeasterly direction past Hanoi in Vietnam into the Gulf of Tonkin, a distance of 900 km. Although the fault is generally straight (remarkably so in this image), it bends or deflects upward (north) just to the southeast. The fault plane, where exposed, is near vertical, with subhorizontal slickensides affirming a dominant horizontal movement. On its northeast side is the Central Yunnan Swell, consisting of shallow marine sedimentary units, which is marked by a number of north-south faults; to the southwest are rocks of the Western Yunnan Province, part of the Ailao Shan metamorphic zone, cut by subparallel (northwest-trending) faults.

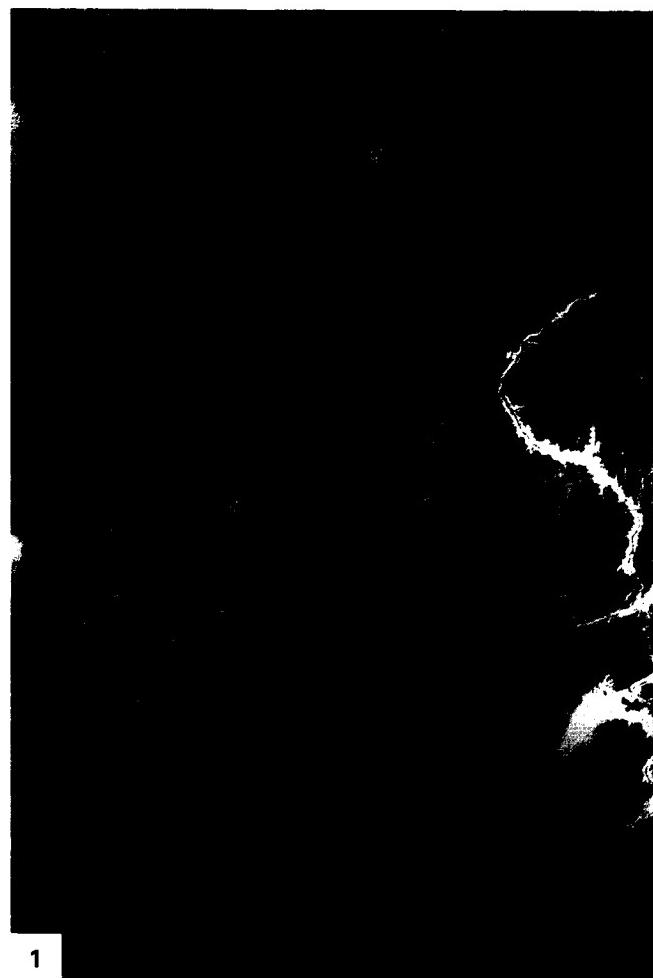
Allen et al. (1984) have studied the Red River fault system both in the field and through the use of the Plate image and other Landsat scenes. Their work confirms earlier information that movement along the fault has been dominantly right-lateral since the close of the Tertiary. The best evidence comes from offsets of tributary streams—visible with close inspection of this image—of up to 5 to 6 km in the last 2 to 3 Ma (amounting to slip rates of 2 to 5 mm/yr); earthquake focal mechanism solutions support this. No significant earthquake has occurred along this fault in the last 2000 years, which is consistent with an estimated 3000-year recurrence interval deduced from the recognition of four notable slip events recorded in Holocene deposits. Within the Plate scene, the fault has split into two subparallel segments. The main (Mid Valley) strike-slip fault lies within isolated Cenozoic river basins, and its trace has been migrating eastward. A second (Range Front) fault is coincident with the Ailao Shan Escarpment on the southwest side of the narrow river valley; curiously, this fault has a large dip-slip component.

Tappognier et al. (1982) surmise reversal of movement on the Red River fault from the initial left-lateral sense during the first 20 to 30 Ma following the onset of the Indian collision. A different regional stress pattern now favors adjustment by dextral slip. The orientation of the fault is consistent with north-south shortening and east-west extension.

About 300 km west of the scene, along the Yunnan/Burma border, the western continuation of the mountain terrain (Figure T-53.1) is cut by a number of smaller faults and several large ones that strike east-northeast. Examination of this Landsat mosaic, but without geologic control, suggests displacement of possibly once contiguous mountain sections in a left-lateral sense. Note the ground fog in a stream valley cutting across the terrain between the two most prominent faults. The relation of these faults

to the Red River fault to the east is not clear, but it is tempting to speculate on a pattern of dominant (first-order) and subsidiary (second-order) slip faults similar to that predicted by Moody and Hill (1956) in their wrench-fault model.

Some of the most rugged terrain in China is distributed over Yunnan Province. Figure T-53.2 shows a typical narrow river gorge (fault-controlled?) enclosed within steep-sided spurred valley walls. (*NMS*) **Landsat MSS 1547-03112-7, January 21, 1974.**



ORIGINAL PAGE
COLOR PHOTOGRAPH

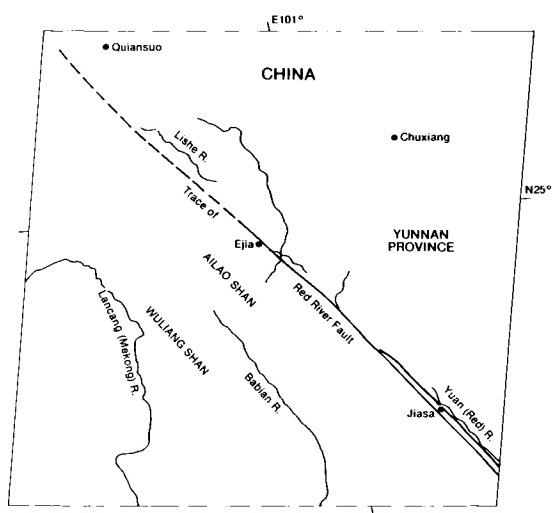


PLATE T-54

THE SETO INLAND SEA

Japan consists of chains of arcuate mountains representing terranes now joined by accretion along subduction zones. Japan is an example of a complex island arc lying on the continental side of a large subduction zone (Sugimura and Uyeda, 1973). South of western Honshu, the offshore Nankai trough, a currently active subduction zone, joins the Ryukyu Trench. A second older subduction zone, the southwest Japan arc, is now a major structural and lithologic boundary that coincides with the Median Tectonic Line (MTL) separating the two major subdivisions of the western half of Japan. The MTL is not truly a "line" but the trace of a series of closely spaced parallel faults that mark the former locus of a plate convergence. The zone underwent southwest-directed thrusting and left-slip movement early in its history (Late Cretaceous), left-slip again during Mid-Tertiary, and right-slip during the Quaternary. The Yoshino River course is controlled by the MTL; southwest of the river, the MTL is marked by a fairly straight sharp scarp line along which several triangular facets can be seen, all evidence of recent movement. Terranes north of the MTL comprise the Inner Zone, composed of metasedimentary rocks (high temperature/low pressure) and intrusives of Later Paleozoic and Mesozoic age that represent the hanging wall of the subduction zone. South of the MTL is the Outer Zone of generally younger rocks, also strongly deformed, consisting mainly of low-grade (low temperature/high pressure) metasedimentary rocks that accumulated in a trench (Miyashiro, 1972; Matsuda and Uyeda, 1971). Volcanism in this part of Japan is confined to the mainland side of the MTL; no active volcanoes are present in this scene.

Geologic units in the Inner Zone are broadly arranged in three belts—the Sangun (A), the Tambia (B), and Ryoke (C)—but outcrop patterns of principal units are rather irregular. Ultramafic inclusions and Cretaceous/Paleocene granitic intrusions (D) occur within these belts. The Ryoke belt here occupies a broad synclinal structure formed during the Cenozoic into which the Seto Inland Sea has invaded. A belt (E) of younger Mesozoic sedimentary rocks (marine turbidites and nonmarine facies) is juxtaposed against the MTL.

The units south of the MTL occur in well-defined belts that parallel both the MTL and the island arc/trench trend. These include the Sambagawa belt (F) which lies in fault contact with the Chichibu belt (G). Most rocks in this belt and the narrow Sambosan belt (H) have undergone folding and thrusting.

The Butsuzo Tectonic Line (BTL) is a structural boundary that separates the Honshu depositional basin from the Late Mesozoic/Paleocene Shimanto basin (I). Near the BTL, rocks are principally Cretaceous eugeosynclinal deposits of marine clastics and submarine volcanic flows. Paleocene sedimentary rocks, also deformed, make up most of the southern third of Shikoku Island.

Japan has therefore been the locus of two major continental margin deposition basins now juxtaposed by plate convergence and strike-slip faulting. Orogenic activity has climaxed several times—Late Paleozoic (Abean orogeny), Early Mesozoic (Akiyoshi orogeny), Late Mesozoic (Sakawa orogeny), Late Cenozoic (Takachiko orogeny), and the Recent.

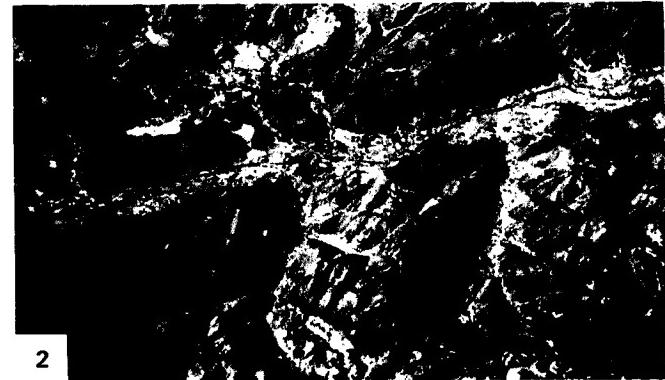
Present topography clearly reflects differences in underlying rocks and major structural features. The strongly linear topographic grain of the Outer Zone suggests both strong folding and strike-slip faulting. The rugged topography indicates recent uplift, and the extremely straight crisp appearance of several river valleys implies recent strike-slip fault movement. Topographic texture adjacent to the flats at the northeast end of Shikoku is interpreted to mean that at least some of the recent movement is right-lateral. Denudation rates are high (up to 1 m/1000 years) in parts of the Outer Zone. Mountains of the zone in this scene are characterized by pronounced linear crest lines and high relief. Most crests trending northeast are approximately parallel to the boundaries of the stratigraphic and metamorphic belts on which they develop. The relatively easily eroded granitic rocks just north of the MTL are areas of low relief. Figure T-54.1 is an aerial view looking southwest at the broad plains inland from the Seto Sea in central Shikoku, against which rise the triangular-faceted fault scarp of the MTL and the high mountains of the Sambagawa belt.

In the Inner Zone, mountains of more subdued relief, expressing denudation at a much slower rate, lack well-defined crests and peaks. Fracture zones, some of which are also faults, produce long narrow valleys (J) and appear to control some of the meandering deflections of several major streams such as the Ashi River. The less "organized" texture of the topography in this zone probably reflects the greater metamorphic homogenization of the rocks. Such topography is evident in Figure T-54.2, a view of granitic rocks in the Tambia belt.

The eastern end of the southwest Japan structural division is shown from Landsat in Figure T-54.3. The region here includes the fringe of Nagoya (lower left) to Takaoka and Toyama (top left) and Matsumoto (east). The Fossa Magna (see Plate V-24) that divides the belts running subparallel to the coastlines in southwest Japan from the northeast Japan division lies along the east side of the image. Zones 2 (Sangun) and 3 (Ryoke), seen in the Plate, continue up to this fault-controlled boundary. Zone 1, the Hida Zone (not present in the Seto Sea region), occupies the upper third of Figure T-54.3. (*NMS Additional References:* Moore and Karig (1976), Shimazaki (1976), Tanaka and Nozawa (1971), Uyeda and Miyashiro (1974), Yoshida (1975), Yoshikawa et al. (1981). **Landsat 1112-01120-7, November 12, 1972.**)

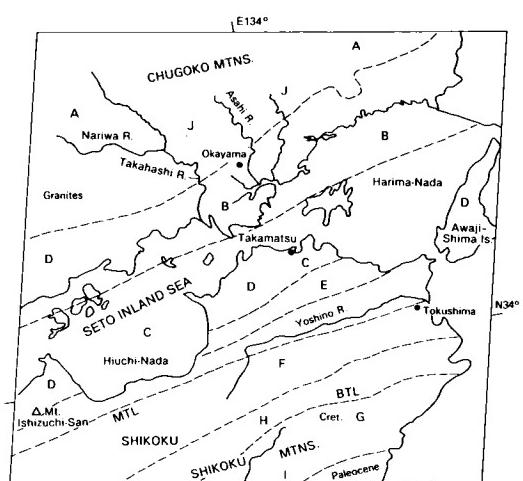
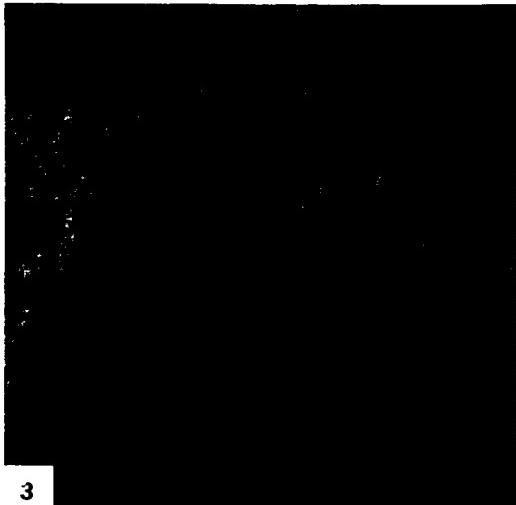
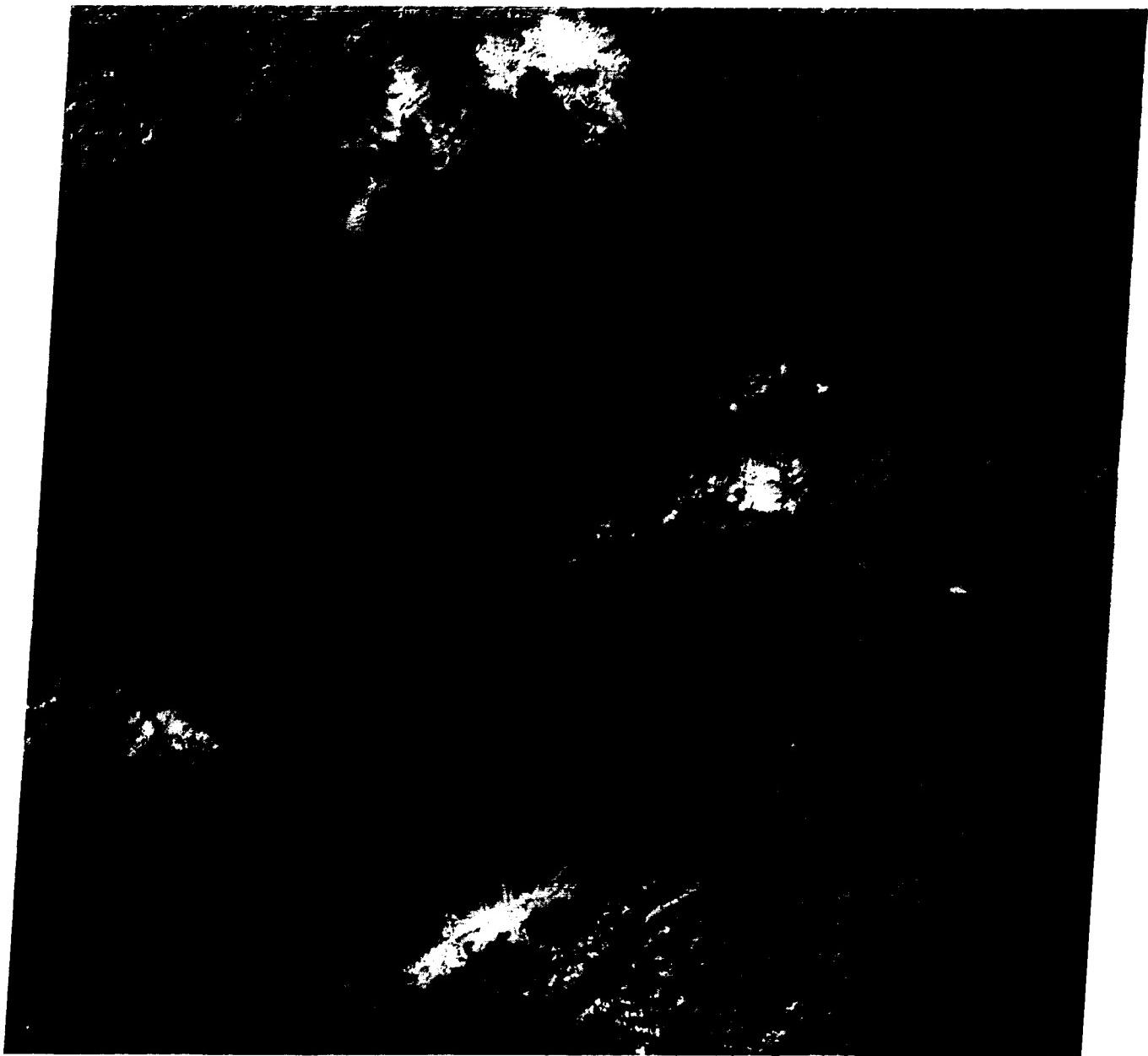


1



2

ORIGINAL PAGE
COLOR PHOTOGRAPH



The remarkable mosaic on pages 160 and 161 reveals the influence of erosion on the Precambrian rocks of an ancient continental shield in a vegetation-sparse environment. The correspondence between different outcrop patterns visible in the mosaic and their counterpart to geologic units is evident when they are compared with the geological map of this part of (northern) Western Australia, reproduced at the top of the next page.

Ages of exposed rocks range from Early Precambrian through Permian (P), Cretaceous (K), and Tertiary (T), with widespread Quaternary (Q) cover in coastal regions. Because soils are generally thin, the structure of the bedrock exerts a strong control on surface morphology. The region has had a complex history of deposition, volcanic extrusion, deformation, metamorphism and intrusion, and periodic uplift.

Much of Western Australia consists of a crystalline shield terrane. The Yilgarn Block, a large structural unit, extends from the southern coast of Australia to a line south of the Gascoyne River just below this mosaic. Rocks as old as 3.5 Ga are found in this cratonic segment. Essentially coeval rocks compose the Pilbara block, whose surface appearance is dramatically displayed in the upper part of the mosaic. Elsewhere, unconformable Lower Proterozoic units (Mt. Bruce Supergroup; 2.3 to 2.4 Ga) fringe the Pilbara Block and also lie to the south in the Nullagine (Hamersley) basin, which contains the Hamersley and Ophthalmia Ranges. These units (Fortescue Group), labeled PF in the index map, are mainly metamorphosed felsic volcanic rocks, basalts, and sedimentary deposits. Widespread units marked PHi and PHs represent the Hamersley Group, rich in jaspilite (Banded Iron Formation), that comprises one of the world's great iron reserves, and sandstones, shales, and carbonates. The youngest units are conglomerates of the Wyloo Group.

The Ashburton Trough contains metasediments and basalts (PN, PW) of ages between 1.9 to 2.0 Ga. Farther south, the extensive Bangemall basin contains sandstones, shales, and cherty carbonates (PM) deposited from 1.1 to 1.0 Ga ago. Wedged between the Yilgarn Block and this basin are older migmatites (AP) and metasedimentary rocks (Pn) of the Gascoyne Province. On either side of these ancient Precambrian blocks are younger depositional basins: the Late Paleozoic/Mesozoic Carnarvon basin and Mesozoic Canning basin. Cenozoic deposits (Cz) inland around the Fortescue River, derived from older units (especially the Fortescue jaspilites), include a variety of ferruginous deposits (pisolithes, laterites, opaline limestones, and ferricrete).

The Pilbara Block stands out as perhaps the best exposed example of an Archean granite (Ag; Am)-greenstone (Ab) terrane anywhere on Earth. Here, the light-toned Granitic Complex (actually tonalites, granodiorites, and adamellites) consists of batho-

liths emplaced as diapirs into the dark-toned greenstones (Figure T-55.1, an outstanding Landsat scene). These consist of the metamorphosed Warrawoona Group, a collection of volcanic lavas (basalts, andesites, and rhyolites), ultramafics, and sedimentary rocks (jaspilites, volcanic clastics, and cherty carbonates), and the overlying Mosquito Creek Group, another volcanic/jaspilite/shale sequence. The pregreenstone assemblage accumulated in shallow water filling an extensive trough along a belt developed by rifting (?) of thin crust. The greenstones have radiometric ages of 3.45 to 2.85 Ga. The batholithic intrusions have Rb-Sr ages of 2.9 to 3.0 Ga, attributable to the time of metamorphism when they were emplaced as gneissic domes. Although melting phenomena are present, some workers believe that these granitic rocks are older (ages now reset) basement that was reactivated during the formation of the dome structures. The Fortescue Group accumulated after the crust stabilized to form the Pilbara Block.

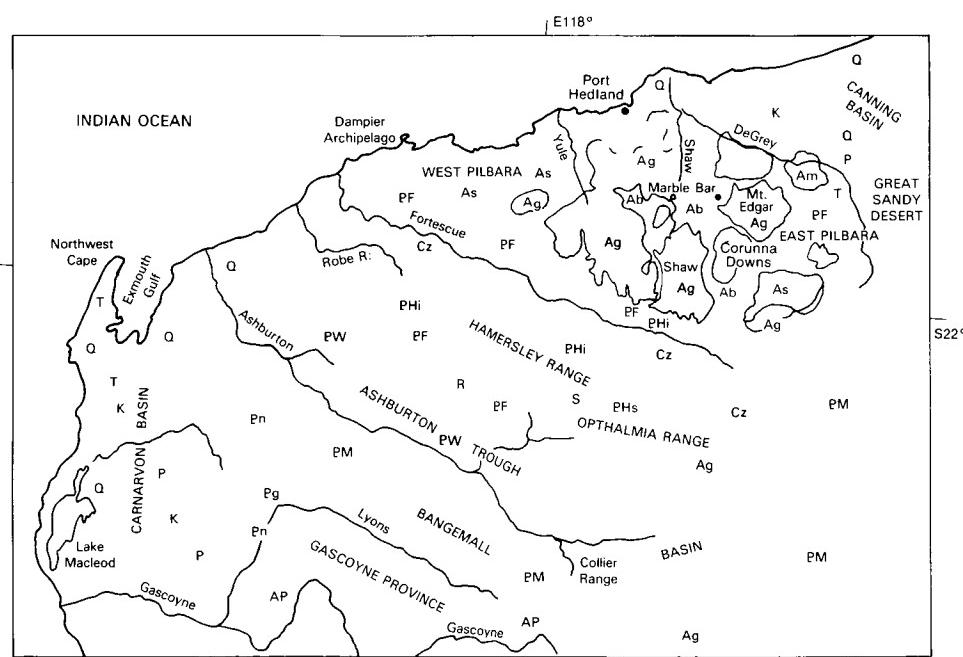
Figure T-55.2 is a computer-enhanced version of part of a Landsat frame that shows in more detail the batholiths and intervening greenstone units. Compare equivalent parts in this version with the 1:86000 aerial photograph (Figure T-55.3) of the northeast corner of the Shaw intrusive and adjacent greenstone belt (in which light units are quartzites and cherty metasediments). Tributary drainage of the two eastern blocks is pinnate. Note the basaltic dikes that fill many of the major fractures.

A SIR-A radar strip (Figure T-55.4) emphasizes the structural control of the terrain across the south-central Hamersley Range. The Rocklea Dome (R) has an Archean granite core, but most other rocks are Proterozoic. Plunging synclines occur at S. The domes are outlined by annular drainage, but major rivers disregard the structure.

Topography throughout northern Western Australia is varied but generally of low relief. Elevations reach a maximum of 1235 m at Mount Bruce in the Hamersley Range. The Pilbara Block is generally flatland, with low ridges among the greenstone. Ridges and hills dot the Hamersley Range. Desert sand cover is conspicuous in the eastern section of this mosaic.

Figures T-55.5 through T-55.8 are ground views typical of the regions in the mosaic. Low domes near Nanotarra appear in Figure T-55.5; Figure T-55.6 shows a close view of Archean rocks near Marble Bar. East of Port Hedlund are granitic inselbergs capped by Lower Cretaceous sandstones that are remnants of an exhumed erosion surface (Figure T-55.7). Gently dipping strata are exposed in dissected hills of the Hamersley Range (Figure T-55.8). (NMS) References: Blake (1984), Brown et al. (1968), Gee (1975), Pidgeon (1974), Viljoen and Viljoen (1975). Landsat Mosaic.

ORIGINAL PAGE
COLOR PHOTOGRAPH

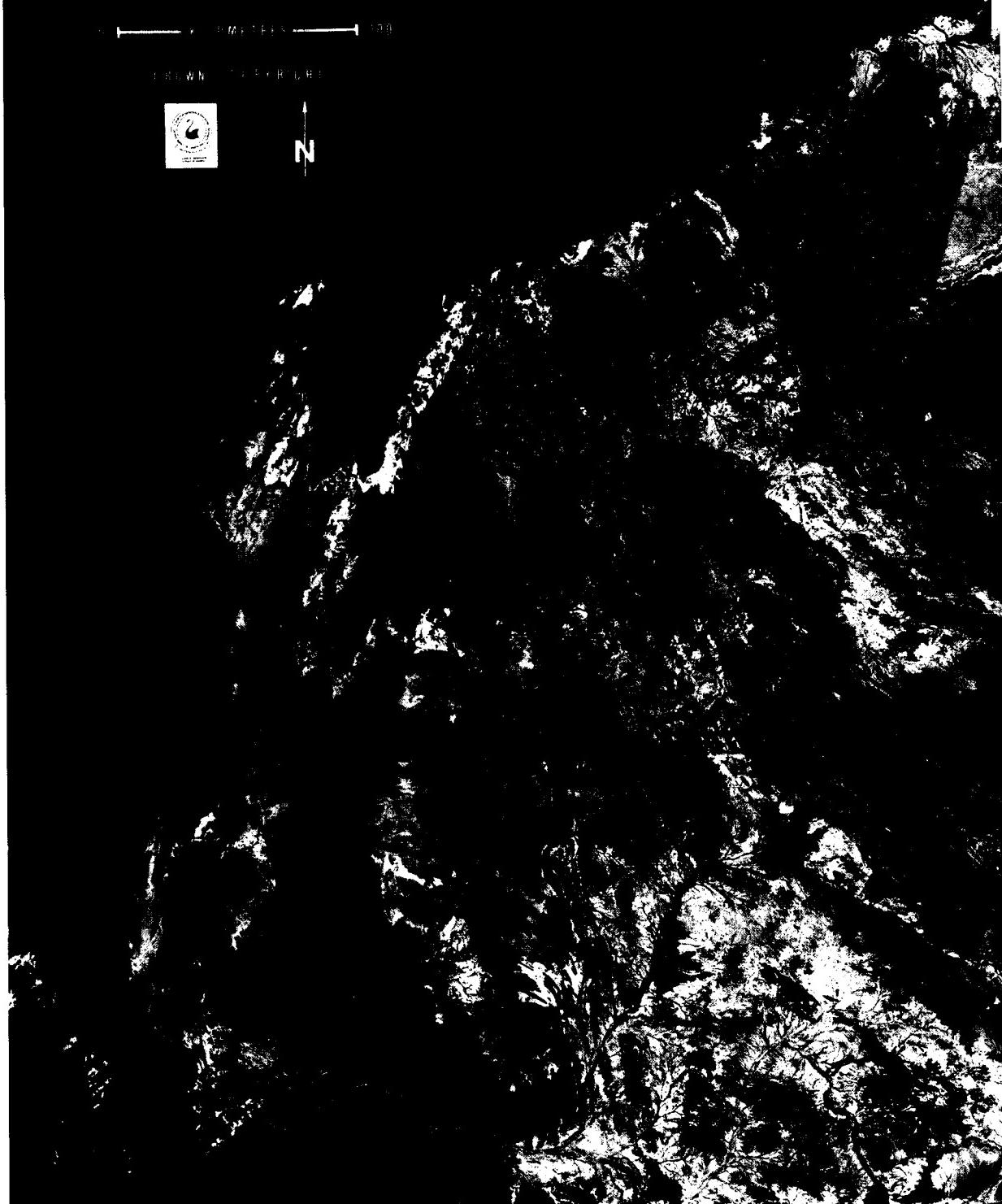


ORIGINAL PAGE
COLOR PHOTOGRAPH

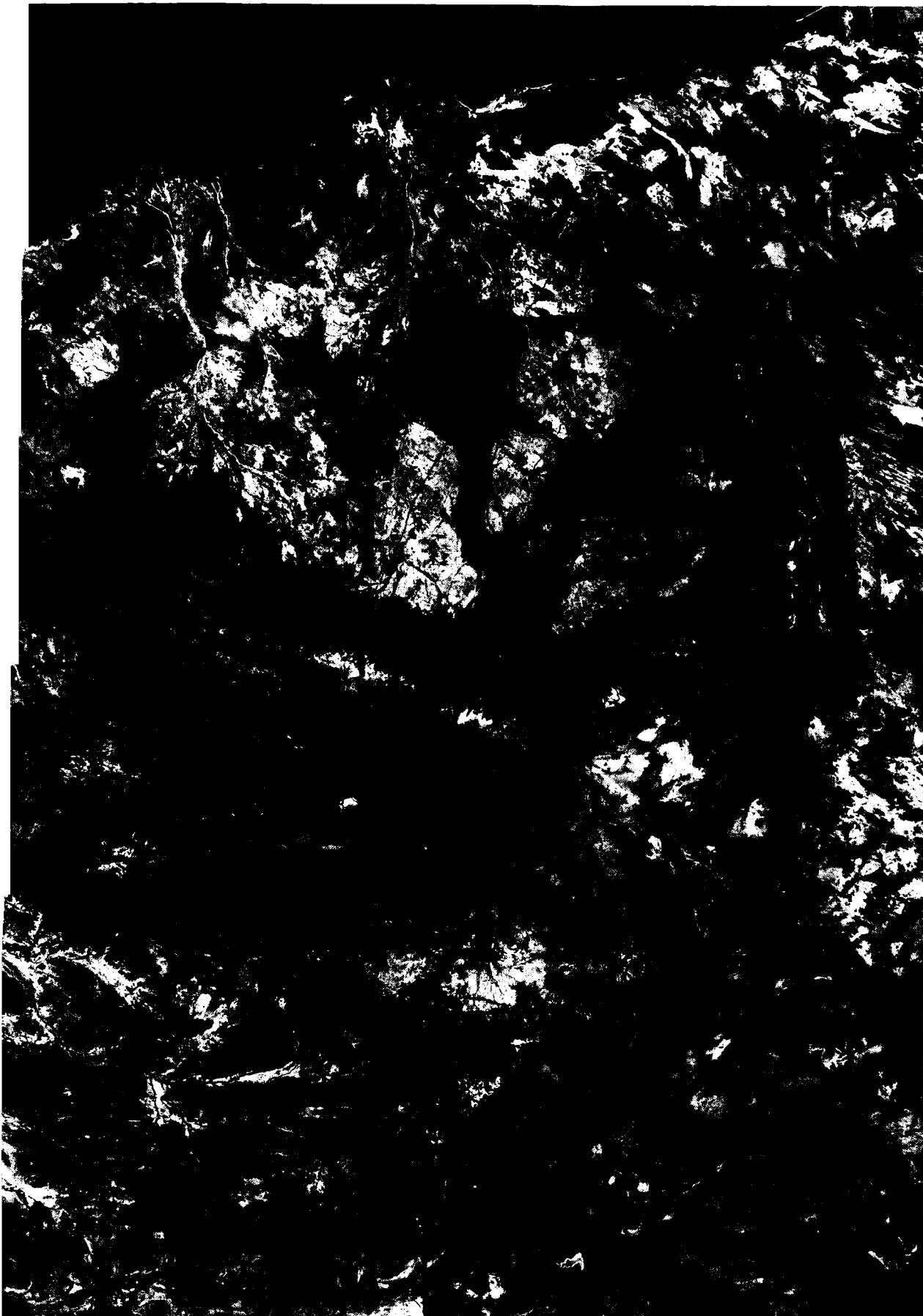
LANDSAT MOSAIC
PILBARA REGION
OF
WESTERN AUSTRALIA

— 100 KILOMETERS —

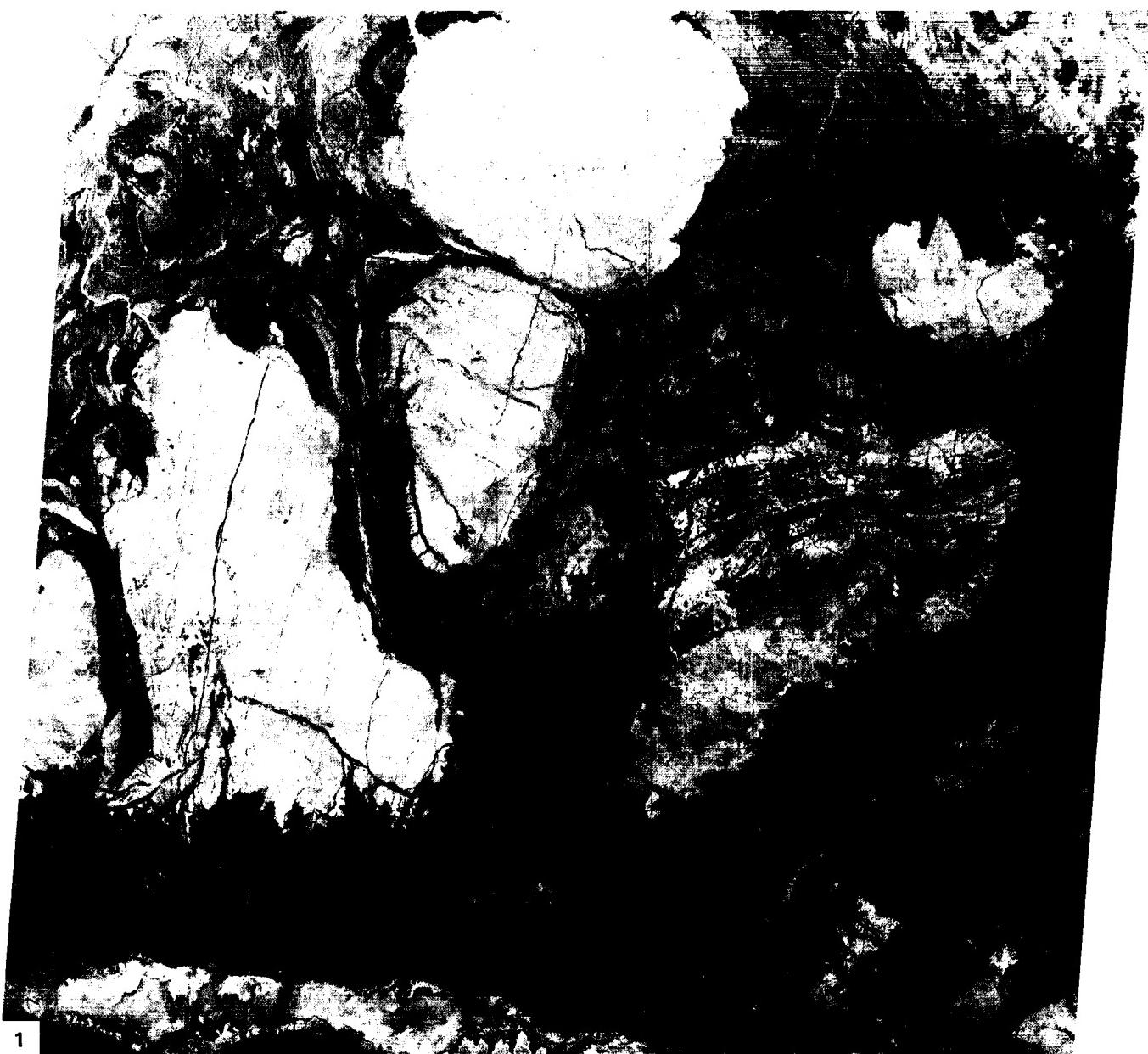
CROWN COPYRIGHT



ORIGINAL PAGE
COLOR PHOTOGRAPH



ORIGINAL PAGE
COLOR PHOTOGRAPH



1

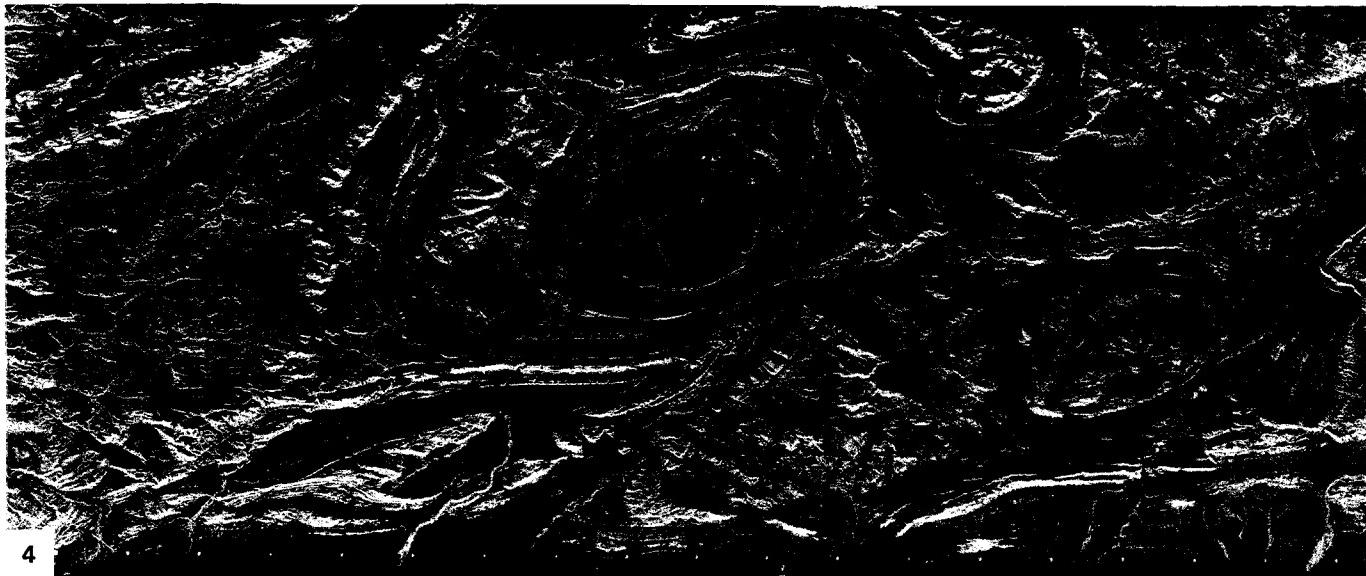


2

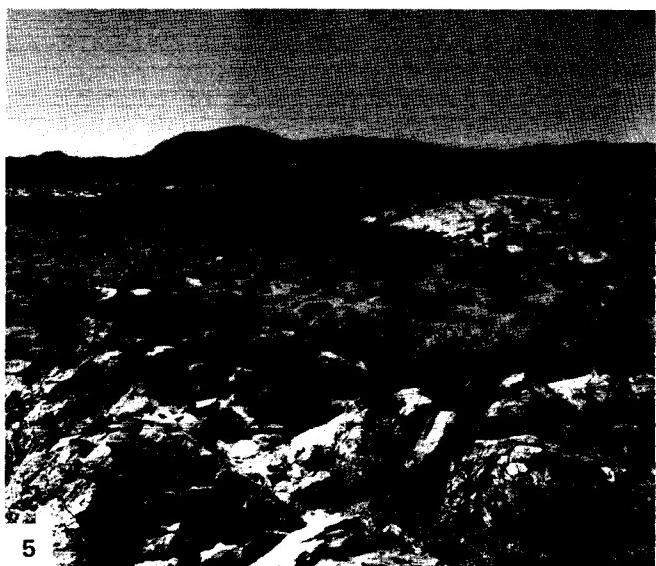


3

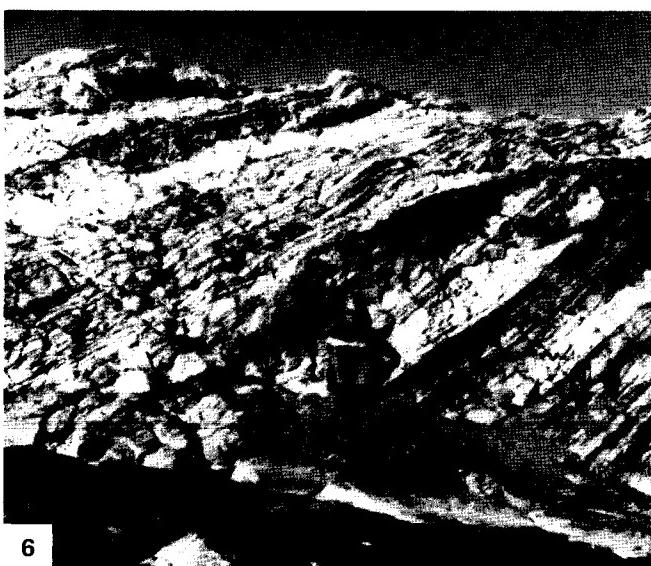
ORIGINAL PAGE
COLOR PHOTOGRAPH



4



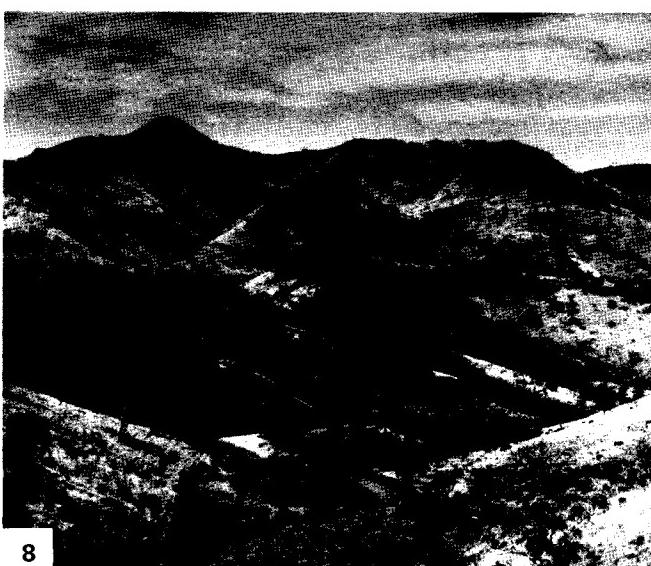
5



6



7



8

This Plate image is graphic proof of the ability of the Landsat MSS to capture geologic details where exposed bedrock is not masked by heavy soil or vegetative cover. The correspondence between different outcrop patterns visible in the image and their counterparts as geologic units is immediately evident when they are compared with a part of the 1:2500000 map of this region of northeastern Western Australia, reproduced below the Plate. Even better than the map, the image shows the effects of abrupt termination of certain units by several large faults.

The Plate is centered about 700 km to the northeast of the eastern edge of the Pilbara Block shown in the previous Plate. The Kimberley Plateau contains parts of three major depositional basins, each of which also evolved into a distinct tectonic unit. Oldest is the Halls Creek Province. This strongly deformed Proterozoic unit wraps around the somewhat younger, less deformed Kimberley basin to the north. Some workers subdivide the Halls Creek Province into the Halls Creek Trough, trending northwest, and, farther east, the Sturt Platform, trending north-northeast. The youngest tectonism affected the Ord basin of Devonian age to the east. These basins are shown in wider perspective in a mosaic (Figure T-56.1) that includes almost all of the Kimberley basin, the upper parts of both arms of the Halls Creek Province, and the northern tip of the Canning basin (left). The upper half of the Plate scene occupies a portion of the mosaic near its lower right corner. This part, shown in the Plate, displays the Halls Creek Group, of "Nullaginian age," that includes basic volcanics, graywackes, shales, and limestones/dolomites. These are intruded by ultrabasic rocks, gabbros, and granites of the Lamboo complex. Accompanying metamorphism ranges from the greenschist to the granulite facies. The oldest units (Px) are felsic volcanic rock dated at 2050 Ga.

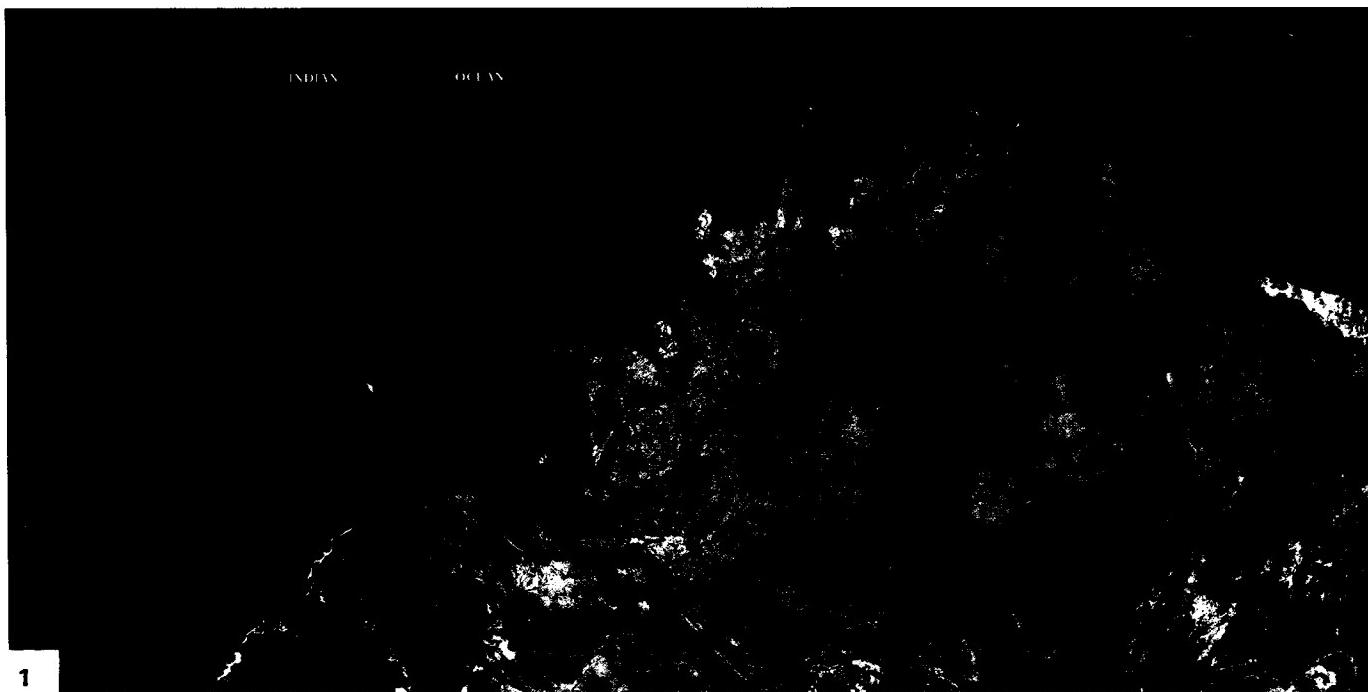
Rocks of the Carpentarian System (1.8 to 1.4 Ga), deposited in the Kimberley basin, seem to have equivalent sequences in the mobile belts comprising the Halls Creek Province but show fewer unconformities. Rocks of Nullaginian age are buried in the Kimberley basin. The basal units in the Kimberley basin consist of about 2000 m of silicic volcanic and tuffs that lie unconformably over the Halls Creek Group. Younger Carpen-

tarian units, the Speewah, Kimberley, and Bastion Groups that reach an aggregate thickness of about 5700 m of sandstones, arkoses, shales, and stromatolitic dolomites, lie mainly to the northeast of the scene. The entire sequence has been intruded by sills of the Hart dolerite, several of which are strongly expressed in this scene. Members of the Adelaidean System occur in scattered outliers in both the Sturt Platform and the Kimberley basin. In this scene, the unit marked PV (~1100 Ma) lies against a wedge of an older unit (PB, 1600 Ma); a still younger unit (PG, 700 Ma), containing tillites, outcrops just to the north.

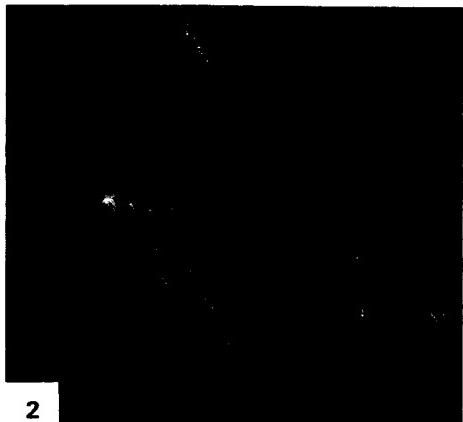
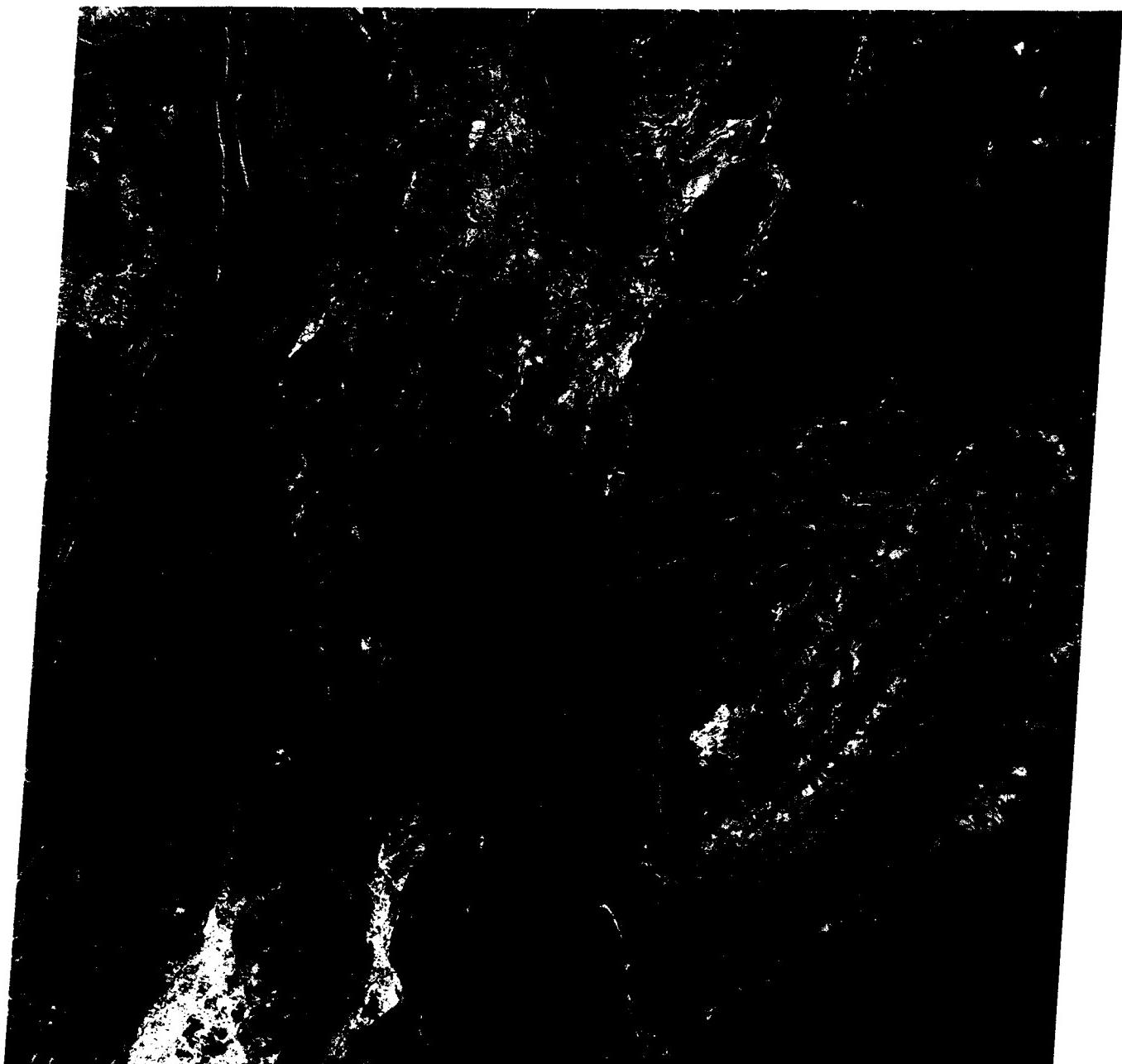
Cambrian units, consisting of basal basalts flows (Ev) and sandstones and dolomites (Ec), rest unconformably along the eastern flank of the Sturt Platform. In the lower right corner of the scene, these dip gently to the southeast. Between the two outcrop areas of this Cambrian sequence is a central area of Devonian (D) sandstones, conglomerates, and reef limestones. The false-color yellow tones of many of these units suggest that they are actually reddish (containing iron oxides).

Three major orogenies affected Precambrian rocks in this scene: one of epi-“Nullaginian” age (~1800 Ma), the second during the Carpentarian time interval, and the last near the close of the Adelaidean event. Additional deformation took place in the Paleozoic.

A high-altitude aerial photograph (scale = 1:86000) provides a closer look at some of the structural landforms. In Figure T-56.2, deformed units, composed of Mid- to Late-Proterozoic and Early Paleozoic sedimentary rocks, stand out as bench-like landforms. These rocks include jointed sandstones, siltstones, shales, dolomites, and tillites. Some units form impressive scarps. Resistant beds clearly show an eastward (to the right) dip through most of the view, except along the western edge where they dip west off the domal structure. Many of the ridges are really escarpments, or cuesta-like. A prominent erosional escarpment can be seen along the right (east) side of the photograph. Drainage channels are discordant in part, where they cut across the structure. Figure T-56.3 shows the terrain along the Ord River from the ground. (*NMS Reference: David (1950). Landsat 1377-00573, August 4, 1973.*)



ORIGINAL PAGE
COLOR PHOTOGRAPH



2



3



PLATE T-57

The Flinders Range is an orogenic belt developed from the Adelaide rift, a large depositional basin containing a thick (15000 to 20000 m) section that records accumulation of sediments from about 1400 to 550 Ma ago. The rift opened first to the north and later to the south. The accumulation in the basin probably constitutes the most complete section of Middle to Upper Proterozoic rocks in the world. Geographically, this is part of the Highland Chain that runs through the state of South Australia from the Musgrave Ranges in the northwest and the Peake and Dension Ranges (north), southward through the Flinders Range, to the Mt. Lofty Range that lies east of Adelaide, and on to Kangaroo Island. The Plate shows the Northern Flinders Range. Most of the Flinders and Mt. Lofty Ranges stand at altitudes from 700 to 900 m (highest peak at 1165 m), with internal relief of 200 to 400 m; the Arrowie basin (east) and Lake Torrens Plain (west) have surfaces that are mainly below 300 m.

Structurally, the Flinders Range is a giant horst block rising above graben blocks on either side. Internally, the range is a refolded fold belt. Lake Torrens to the west is situated on the east side of the Stuart Shelf, a crystalline block (less than 2 km to basement) covered by mainly undisturbed Proterozoic sedimentary rocks and bounded to its southwest by the higher Gawler Block of Early Proterozoic rocks, which are actually a continuation of the ancient shield underlying much of Western Australia.

The great thicknesses of sedimentary rocks—shales, sandstones, and carbonates—in the Adelaide system include a remarkable accumulation of almost 6000 m of glacial deposits, mostly tillites, contained in the basin. The youngest Proterozoic formation in the basin, the Pound Quartzite (once considered basal Cambrian), is famed for its unique fauna—jelly fish, segmented worms, and sea pens (known as the Ediacara assemblage). These were entrapped along a coastline, leaving impressions in the mud.

The basin ceased its gentle downwarping in the Late Cambrian and underwent strong deformation during much of the Ordovician (Delamerian orogeny). The deformation produced a fold belt with plunging synclines and anticlines from this thick prism of sedimentary rocks. Most of the exposed rocks from the lower

FLINDERS RANGE

portion of the sequence are mildly metamorphosed. Crystalline basement was mobilized and emplaced as plastic solids in diapiric intrusions or as melts (dating around 470 Ma) at various places (e.g., in the Mt. Lofty Range). On the western flank of the Flinders Range, a pronounced north-trending lineament, the Torrens Crush Zone, separates the western graben from the Flinders Block. Erosion acting on this orogen since the Ordovician(?) has carved out the present landforms. The region has undergone vertical uplift, beginning in the Mesozoic and continuing through the Holocene (Kosciuskan orogeny). Cretaceous sedimentary units lie in grabens and intermontane basins on the west and to the north of the Flinders Range, as well as around Lake Frome. The present-day structurally controlled ridges, monadnocks, and other topographic prominences in the Flinders Range result from differential erosion that leaves quartzites, sandstones, and granites as resistant high hills in the form of linear ridges and curvilinear noses. Escarpments are developed along the Paralana fault east of Mt. Painter and to the west. Around the Flinders Range, traces remain of a low-relief erosion surface predating the later Mesozoic units. Cenozoic erosion has produced thick gravels, derived from older Tertiary silcrete deposits, that are carried across pediments off the flanks of the mountains into outwash deposits (many are calcreted) extending into the basins (Figure T-57.1). Both Lake Frome and Lake Torrens are now ephemeral and saline as the result of high evaporation rates in the semiarid climate. Oblique air photographs (Figures T-57.2 and T-57.3) highlight the topography (flatirons and hogbacks) formed by erosion of the tilted sediments. Major drainage is inherited with river channels superimposed on the structure.

Overall, the prominently exposed pattern of metasedimentary units discloses that these rocks were folded and then refolded along different trends. (Axial traces of folds are complexly bent.) Despite this complicated structural history, the rocks are neither tightly folded nor complexly thrusted, which suggests that this area may have been some distance from an actual suture zone. (NMS) References: Brown *et al.* (1968), Parkin (1969), Twidale (1969). Landsat 22144-23514, December 5, 1980.

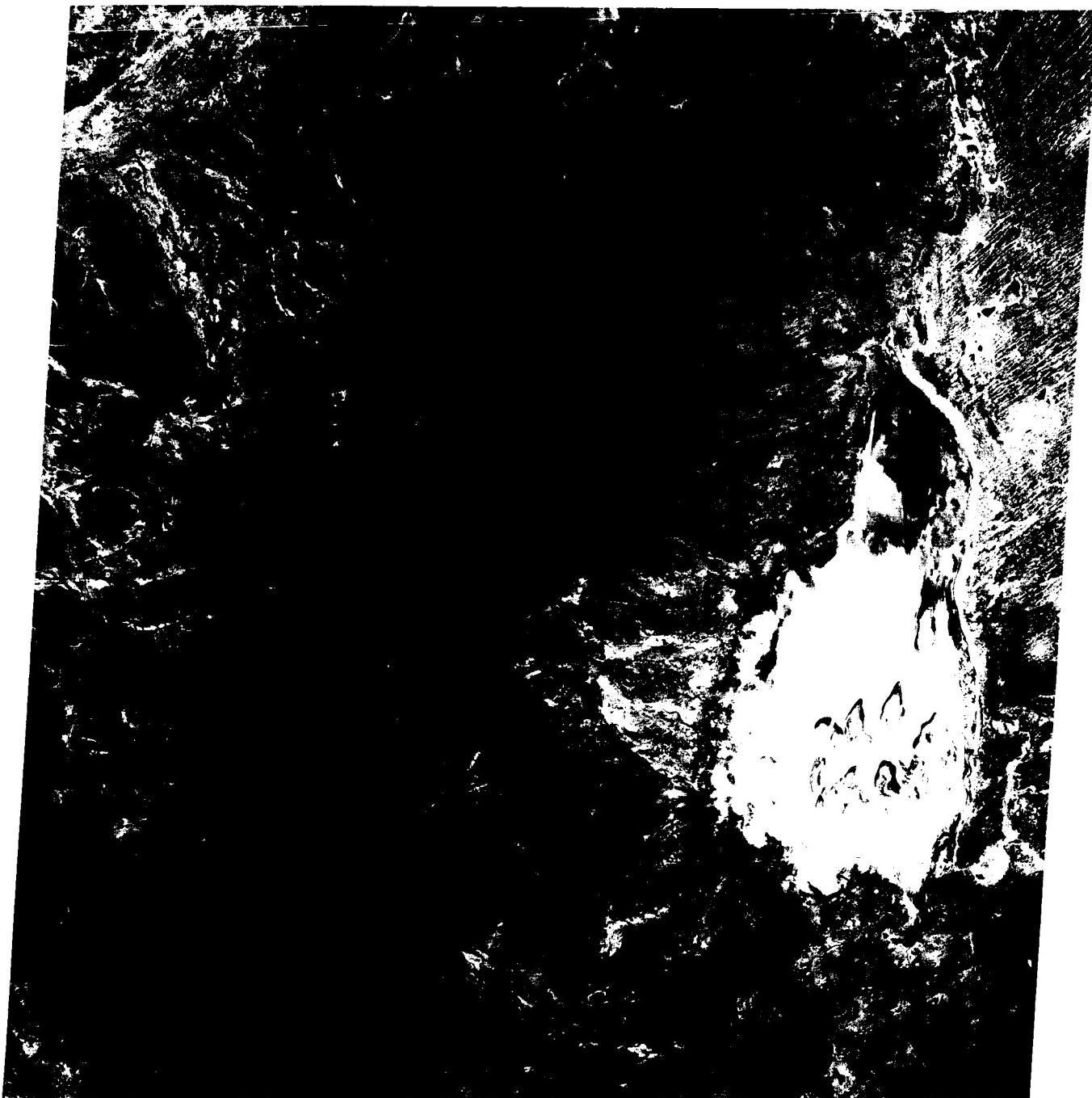


1



2

ORIGINAL PAGE
COLOR PHOTOGRAPH



3

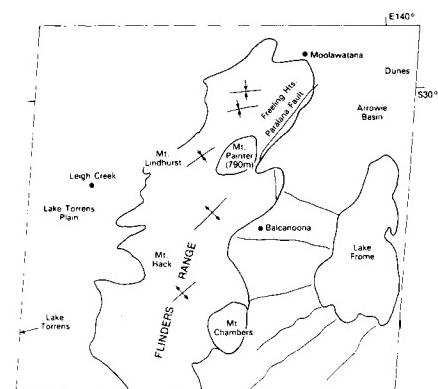


PLATE T-58

New Zealand has been called a geomorphologist's paradise. This Plate (an HCCM Day Thermal IR image, taken during the southern hemisphere winter) captures both the structure and physiography of South Island. Three features are conspicuous: (1) the Alpine fault, which separates the Southern Alps from the low coastal Westlands; (2) the Alps themselves (rising to 3784 m at Mt. Cook), with their glacially sculptured ridges, moraine-dammed lakes, and fjords along the southwest coast; and (3) the Canterbury Plains and Southland, a vast lower area (schists, graywackes, and mudstone) east of the mountains that is still relatively high and hilly in places, but elsewhere is covered by coalesced fans of thick Late Quaternary glacial gravels and outwash carried from the Alps, especially around Christchurch. Inland, these deposits show multiple fluvial terracing (Figure T-58.1). Recent marine terraces are developed along the coast; much older elevated terraces are found along the slopes of the Alps. Overall, South Island remains a monument to the influence of tectonic features in determining morphology.

Before about 80 Ma ago, New Zealand was attached to Gondwanaland near Australia. During Paleozoic and Early Mesozoic times, what is now New Zealand was a series of depositional troughs adjacent to Gondwanaland. These troughs accumulated immense thicknesses of shallow- and deep-water marine sediment (10000 m in an Early Paleozoic cycle and 30000 m during a Late Paleozoic and Mesozoic cycle). Accretion of island arcs (?) (or continental fragments) along the margin of Gondwanaland first deformed these sediments in the Mid-Paleozoic (Silurian/Devonian) and again in the Late Jurassic/Early Cretaceous. During the Cretaceous, the Alpine fault was a suture between the Pacific plate to the east and India/Australia to the west. This fault separates high-pressure/high-temperature Tasman metamorphic rocks on the west from low-temperature/low-pressure Wakatipu rocks on the east.

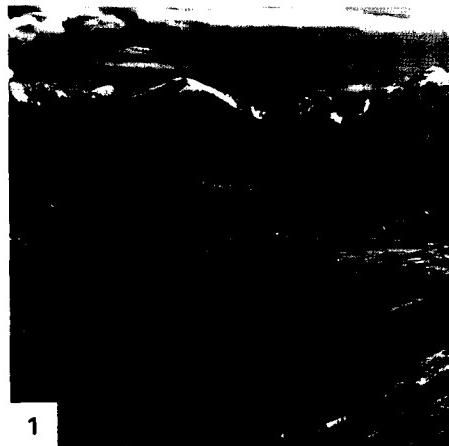
Erosion, deposition of marine and nonmarine sediments (including coal, limestone, and chaos breccias), and periodic folding and faulting prevailed between the Late Cretaceous and

SOUTH ISLAND, NEW ZEALAND

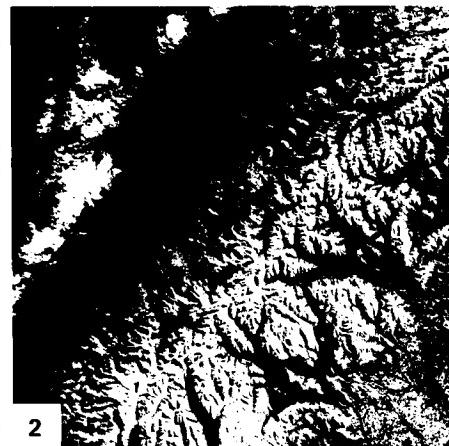
the close of the Oligocene. A third major deformation, the Kaikoura orogeny, then further folded older units and those of Tertiary age. Climaxing in the Miocene, this tectonic activity persists today. The deformation converted the Alpine fault from a suture line (subduction zone) to a trench/trench transform fault on which motion continues today. Although subduction along South Island has ceased, it continues below the Kermadec Trench east of North Island.

As seen by Landsat (Figure T-58.2), the Alpine fault is defined by abrupt truncation of mountain spurs against the Westland plains. Lithologic correlations indicate dextral strike-slip movement estimated to be as great as 800 km, based on somewhat tenuous correlations. The fault splays into four major branch faults—the Wairau, Awatere, Clarence and Hope Faults—in northern South Island (Plate C-11) and is traced as several others cutting across southern North Island. Although it appears to have moved subhorizontally (up to 10 mm/year) over most of its history, the Alpine fault underwent significant vertical movements (with possible thrusting) in the Pliocene/Quaternary interval in which the southern Alps rose to their present heights. The Pacific plate is now being consumed against eastern North Island, and the Australian plate is being subducted south of South Island. The two offset New Zealand Islands are currently drawing apart along the lengthening Alpine transform fault.

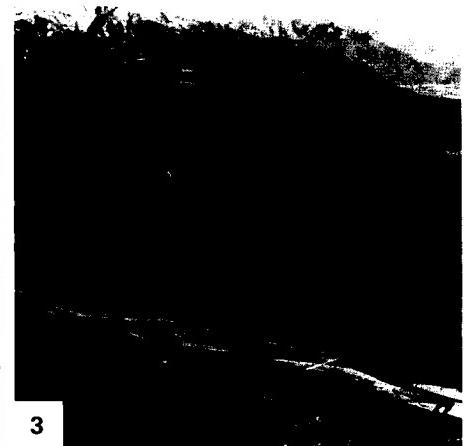
Despite its checkered history, the Alpine fault now exhibits many of the characteristics of a well-behaved strike-slip fault, including a spectacularly straight trace and en echelon splays. Figure T-58.3 (looking south across the Wanganui River) follows the trace of the Alpine fault, cutting across ridge spurs with the Southern Alps on the left. Figure T-58.4 (looking east toward the Southern Alps from the sea at the mouth of the Karangama River) shows the exceptional change in relief across the fault. The straight line of faceted spurs marks the trace of the fault. (NMS) References: Grindley (1974), Kingma (1974), Lillie (1980), Sugate (1978). HCMM 0050-03010-2, June 15, 1978.



1

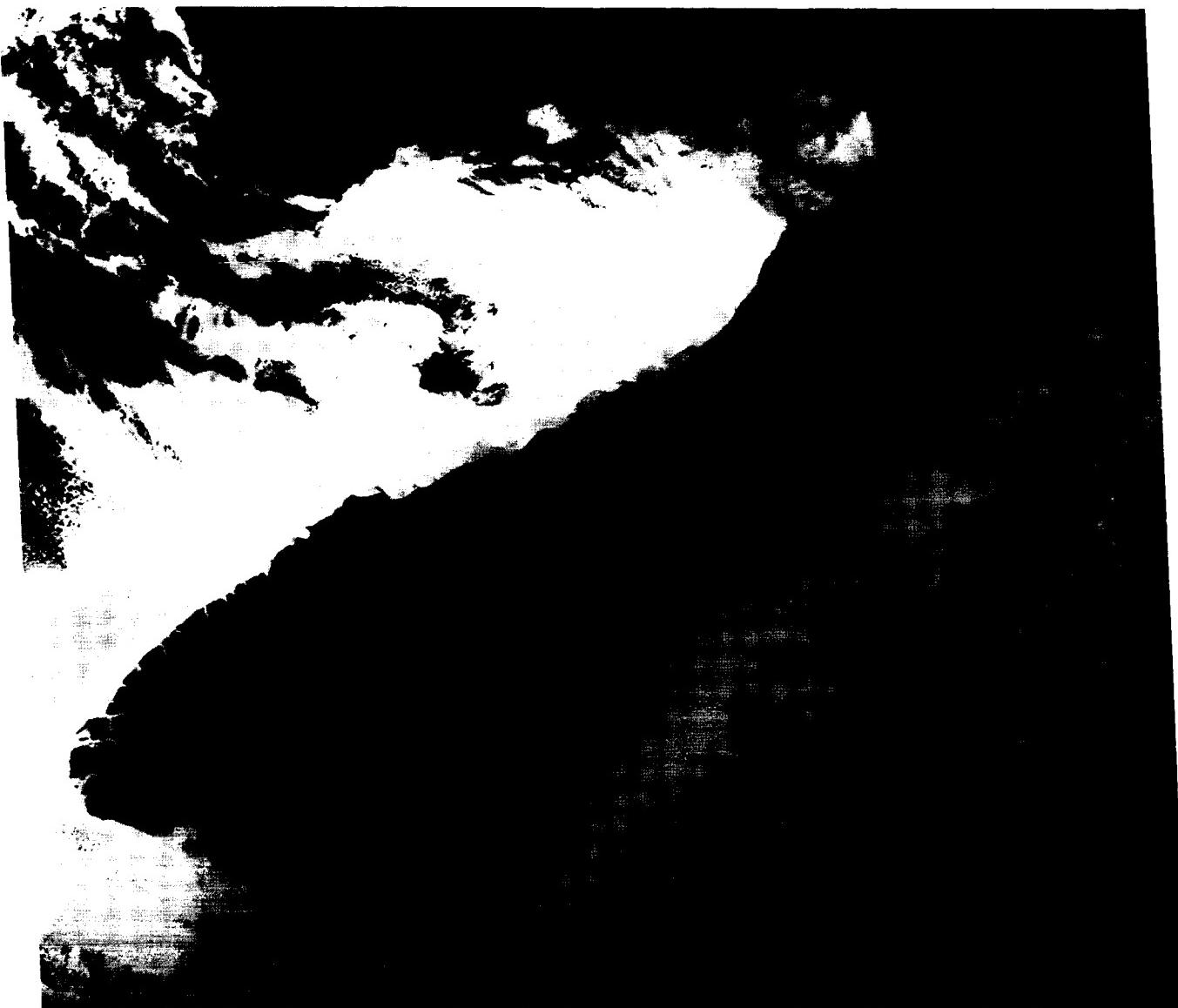


2



3

ORIGINAL PAGE
COLOR PHOTOGRAPH



4

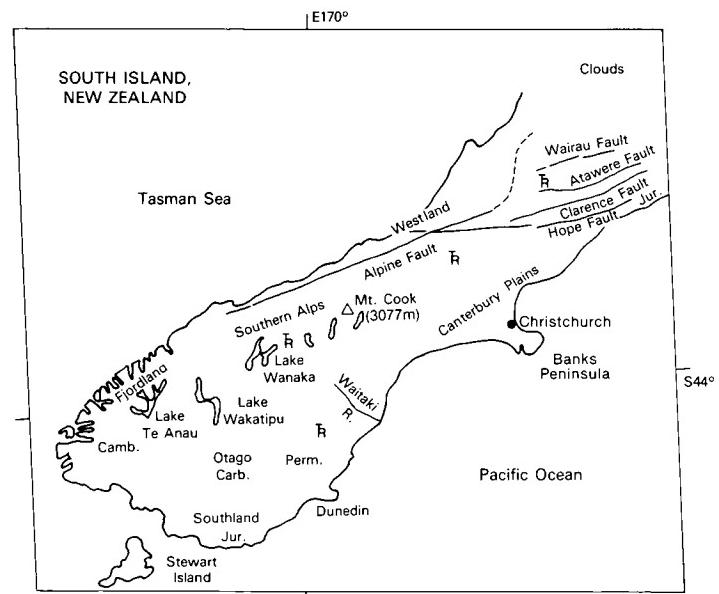


PLATE T-59

SHIELD AREAS

Shields, exposed parts of thick sections of crystalline rocks that comprise the core of continents, contain some of the most complex and interesting geology on Earth. Many of these areas are spectacular when viewed from space. Most of these regions have been geologically stable for a long time with the last major tectonic or metamorphic event having occurred before the beginning of the Paleozoic. Because of this great antiquity, "Precambrian" is almost automatically associated with shields.

Crystalline rocks comprise the bulk of the rocks exposed in shields. Most of these rocks have experienced repeated cycles of deformation, intrusion, and metamorphism in which these processes acted while the rocks were buried at considerable depth. This implies that flow folding and other low-viscosity types of deformation dominated during much of a cycle. Repeated metamorphism and intrusion have affected a substantial degree of welding and integration (and even homogenization) of rocks that were initially quite different in composition and competence. Cratonic shields have served as nuclei for continuing continental accretion as other shields, island arcs, fold belts, etc. are driven against their margins. Most shield rocks record structural overprinting from several tectonic cycles. Later uplift and erosion superimpose tensile fracture patterns over other patterns present. In many areas, intrusion of dikes or equidimensional bodies accompanied a tensile phase (see Plate T-60, Plutons). Details of lithology and history (tectonic, thermal, erosional, etc.) are different from shield to shield, but there are several important general similarities that lead to a characteristic "shield" geomorphology. This "shield" morphology includes complex structural patterns, low relief, and exhumed surfaces.

Plates elsewhere in this chapter (Plates T-15, T-16, T-33, T-34, T-40, T-47, T-55, and T-56) show a variety of these features from a number of different shields of the world, including Australia, Africa, India, and Canada.

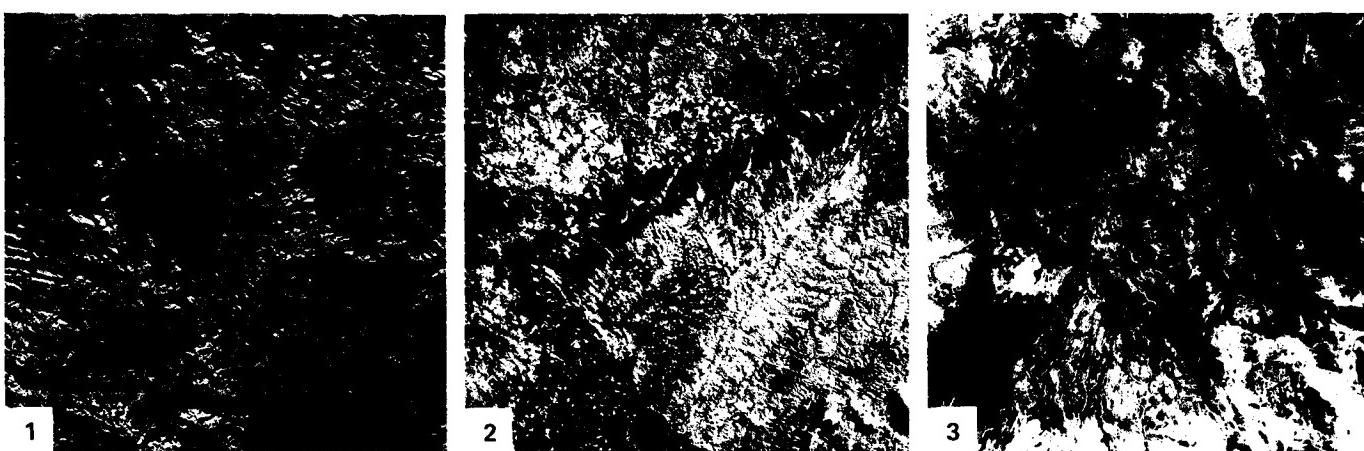
Many shield areas exhibit an almost featureless topography of low relief as a result of long exposure to erosion and the lack of differential resistance of the complex crystalline rocks to erosion. Unconformable strata now overlie many of these ancient surfaces or once covered them in the past. Some of the most prominent characteristics of the shields are projected up through this cover. Erosion of these cover rocks exhumes features of the old erosion surface. Commonly, the most conspicuous features are ancient fractures that extend for many kilometers and that are often strongly etched.

The Plate image brings out the bold fracture patterns visible in the Nigerian shield lying astride the Nigeria/Cameroon

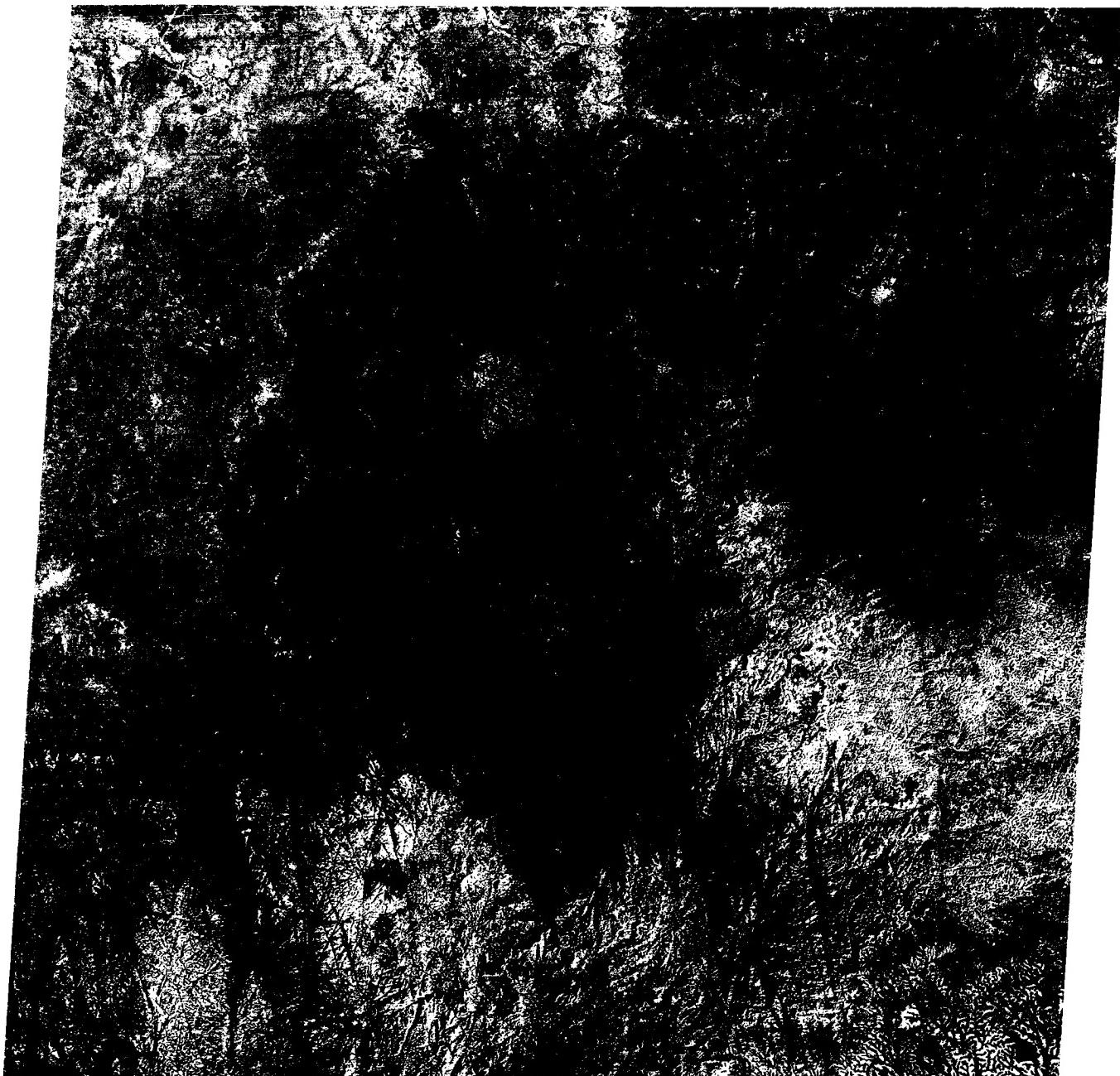
border. These are well-developed near the scarp bounding, an old erosion surface covered in places with younger basalts. At least six systems of joints are expressed in the basalt plateau; some of these fractures are inherited (carry upward from the shield surface). In this semiarid environment, vegetation grows more profusely in the fractures, which act as conduits for ground-water movement, making them stand in strong contrast to the heavily cultivated plateau and surrounding lowlands. Close examination of the fractures reveals that several of the sets are rather strongly curved, whereas fractures of other sets are straight over considerable distances. This condition is common to most shields. (Fracture sets in younger terrain tend to be straight.) Curved fractures may reflect inherently curved strain trajectories of the initial stress field, postfracturing deformation, or fracture associated with domal uplifts or intrusive bodies. Compare the Landsat image with a Side-looking Airborne Radar (SLAR) image of the same area (Figure T-59.1). The latter reveals substantially more detail of actual relief in the area by virtue of shadowing and the sensitivity of SLAR to changes in slope angle. Both the upland and lowland have more relief than the Landsat image suggests.

In southern Brazil, west of São Paulo (Figure T-59.2) Late Precambrian crystalline rocks, part of the Atlantic Shield, are being exhumed (along the right side of the Landsat image), as the Paleozoic cover is stripped away. Note the scarp with reentrants along the arcuate eastern edge of this unconformable cover, erosion surfaces of low relief to the west, and a prominent northwest pattern of fractures (some dike-filled) in the shield rocks that passes through the cover terrain to the west.

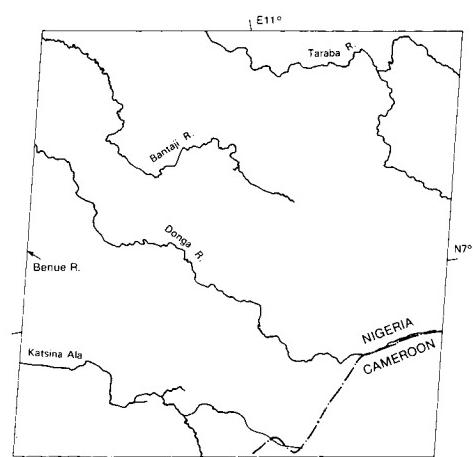
The Ahaggar (Hoggar) Mountains show many of the features of shields, complex fracture patterns, juxtaposition of different trends, equidimensional posttectonic intrusions, and complex foliation patterns (Figure T-59.3). Most of the scene is underlain by Precambrian rocks of the Suggarian Zone (note faults trending northwest; rocks of the Pharusian Zone occupy the western margin. Here, only a few remnants of younger lava flows (dark splotches) mask the older rocks. Jointed volcanic necks and associated flows add to the ruggedness of the terrain (Figure T-59.4). Many joints are strongly etched. Not only has faulting determined the path of several linear valleys, but many streams also show the effect of jointing in the rectangular patterns (including right angle bends) in their channels. (JRE) References: Burke and Dewey (1973), Furon (1963), Pritchard (1979). Landsat 21395-08373, November 17, 1978.



ORIGINAL PAGE
COLOR PHOTOGRAPH



4



One of the most eye-catching structural features of shield areas in widely separated parts of the world are circular or near-circular plutons that seem to float in the contorted and fractured shield rocks like plums in a pudding (see the Southern Arabian Shield mosaic, Plate T-40). The ages of these plutons span a wide range of time. They are patently younger than the shields which they intrude, and they appear to be less structurally complex than the country rock, which likewise suggests that the age difference between country rock and pluton may be substantial. The strikingly smooth circular to elliptical outlines of many of these features suggest that emplacement took place in a horizontally isotropic stress field after the last major deformational event that contorted the shield rocks.

During the emplacement, the magmas that form the intrusions rose buoyantly in the crust to a near-neutral buoyancy equilibrium level. However, the depth of emplacement, as well as depth of subsequent erosion, also seem to vary widely from region-to-region. For instance, the Air Mountain (Niger) plutons (see below) clearly display evidence of having domed the surrounding rocks and appear to be in an early stage of unroofing. In contrast, plutons in Egypt and Sudan (see below) show little or no evidence of having domed the surrounding rock, suggesting a deep level of erosion and, perhaps, emplacement.

The Plate montage on the facing page depicts plutons from opposite sides of the African continent (Egypt above and Mali below) as recorded by two sensors (Shuttle Imaging Radar (left) and Landsat Multispectral Scanner (right) for each pair). Each instrument gathers unique information. In general, the synthetic

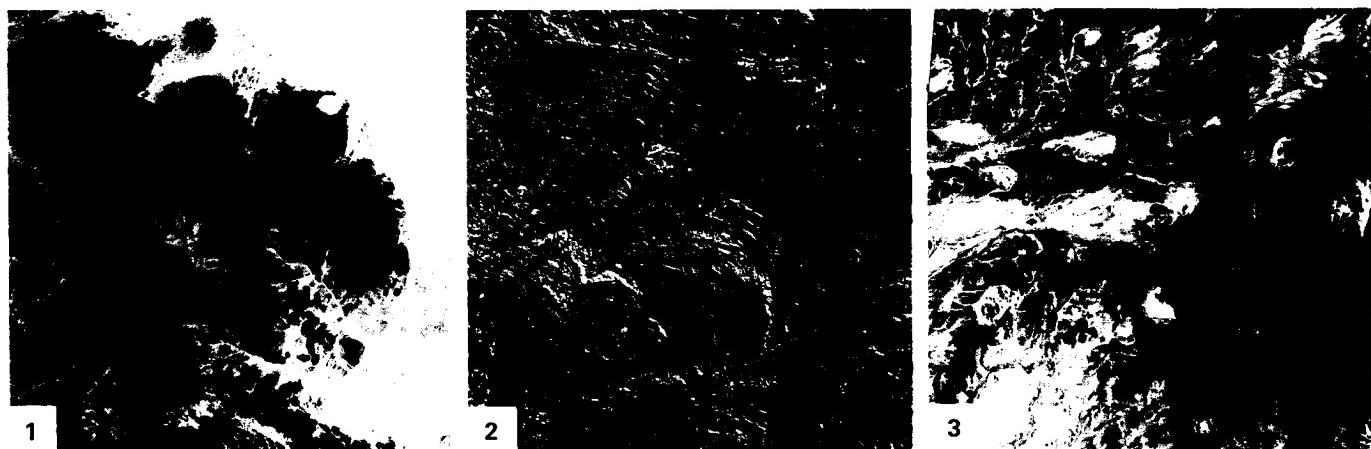
aperture radar records far more textural information so that fractures and foliation stand out strongly. Conversely, the MSS emphasizes tonal variations so that the strongest contrasts are between sand and bedrock. The radar conveys considerable structural information, and in some areas, actually reveals bedrock features beneath a thin dry sand cover that obscures the underlying rock from the MSS (see Plate I-3). But, distribution of the sand in MSS imagery sometimes assists in recognizing the outline of the plutons, which tends to become lost in the structural detail revealed by radar.

Figure T-60.1 shows the Air Mountains of Niger (18.5°N , 9°E). These Precambrian to Devonian plutons intrude and dome lighter toned Precambrian (2750 to 1750 Ma) rocks. Several of the plutons clearly display radial and concentric fracture sets.

Figure T-60.2 records a carbonatite intrusion in the complexly deformed rocks of the Brazilian shield (21.5°S , 46.5°W) near Poços de Caldas. Most of the area is forested. However, the richer soils developed on the carbonatites are intensively farmed.

Figure T-60.3 near Tokar, Sudan (17.9°N , 36.3°E), covers a complexly deformed, highly eroded shield area sprinkled with more than a dozen plutons. Different compositions probably account for the different tones of the various plutons. In fact, the plutons range in composition from sodic syenite to riebeckite granite, with a few being as basic as gabbros. These so-called younger plutons have ages that group at 700, 500, and 100 Ma (Neary et al., 1976). (JRE) (See Appendix B for image ID's.)

SIR-A and MSS Mosaics



**ORIGINAL PAGE
COLOR PHOTOGRAPH**

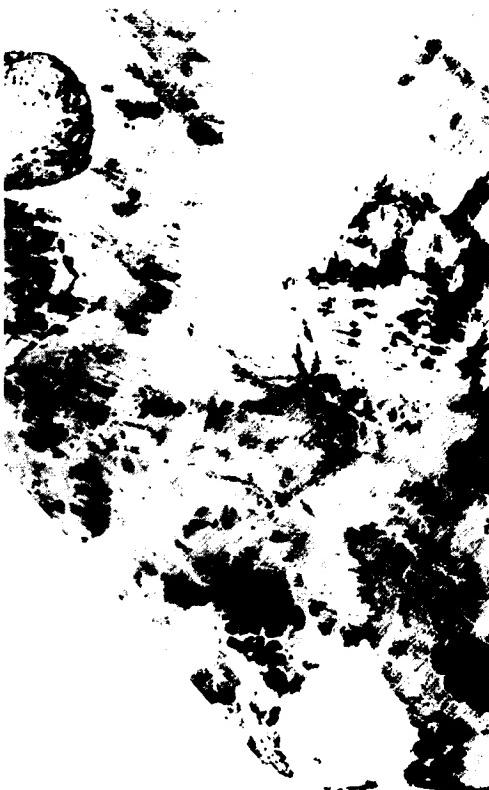


PLATE T-61

IMPACT STRUCTURES

Space imagery has proved, as demonstrated in this Plate, to be a powerful tool in the search for meteorite/asteroid impact sites on the Earth's land surface. More than 200 confirmed, probable, or suspected craters and astroblemes (the eroded scars or roots of the initial impact structure) have been located by conventional means on every continent except Antarctica. The bulk of these were identified from field work and drilling. With the advent of space photography, a number of circular features—most already known but a few seemingly new—were highlighted in the synoptic coverage, prompting renewed interest and, in several instances, actual expeditions to investigate their nature. Although a few indeed were impact structures, that nature generally turned out to be one or more of the following: (1) structural domes, (2) intrusive plutons, (3) fracture patterns, (4) erosional or collapse basins, (5) an artifact of illumination, (6) chance morphological patterns, or (7) simply unexplained. With the worldwide coverage offered by Landsat, new efforts are being directed toward a careful quest for suspicious structures or patterns that could then be field-checked. As an example of the *modus operandi*, the author (NMS) "discovered" the Araguainha Dome in Mato Grosso, Brazil, in a Landsat scene; by coincidence, on the same day, a colleague at GSFC was "discovering" petrographic microscope evidence of impact-induced shock metamorphism in thin sections of rocks from that locality. Even though Landsat did not originally find this structure, the image brought to light the realization that its diameter was almost twice that initially assigned from ground studies.

R. S. Dietz and J. McHone of Arizona State University were among the first to scan through numerous Landsat scenes seeking signs of previously undetected impact structures. Generally, the most common observable features are: (1) pattern circularity (distortions may occur from subsequent tectonic disturbance and/or erosional irregularities), (2) rimmed depressions (if a crater still persists), and (3) central peaks (if large enough); ejecta is almost certainly absent (long since removed) and volcanism is seldom evident.

The collection of image subsets in the Plate has been supplied by J. McHone, who also furnished much of the following abstracted commentary. Scales of the individual insets vary.

A. Manicouagan (Quebec): This astrobleme, impressed on Precambrian rocks, is at least 66 km in diameter. Vestiges of an initial rim cannot be discerned, suggesting removal if formed. A broad central uplift persists; many of the anorthosites making up Mt. Babel in this interior are now converted to maskelynite (feldspar glass). A surrounding depression has since been filled with water following the construction of a hydroelectric dam.

B. Clearwater Lakes (Quebec): This pair of structural depressions (30- and 20-km diameters), east of Hudson Bay, also consists of astroblemes, now much eroded and glaciated, cut in-

to Precambrian crystalline rocks. Abundant evidence of shock damage, impact melt, and shatter cones remain in these rocks. West Clearwater has a central (uplift) rim rising above lake level.

C. Serra da Cangalha (Brazil): Landsat played a large role in pinpointing this ring structure (~12-km diameter), with its central depression. About 50 km to the northeast is the smaller (4 km) Riachao Ring (mounted here as an inset) with its peripheral circle of ejecta. Shock features have been recognized at both sites. An aerial oblique photograph of Cangalha (Figure T-61.1) and an aerial vertical photograph of Riachao (Figure T-61.2) together illustrate the geomorphic expression of impact structures in a typical low-relief setting.

D. Lake Ashanti (also known as Bosumtwi) (Ghana): This part of equatorial Africa is seldom free of clouds, so that this good look at the lake-filled crater (~10-km diameter) is exceptional. Shock criteria, including coesite, place this structure in the meteorite impact category. It is also believed to be the site of origin of the Ivory Coast microtektites.

E. Logancha (Siberia, U.S.S.R.): In the last two decades, Soviet scientists have examined a number of circular structures, some quite evident in space imagery (best example: El'gygytgyn). Because this subsurface occurs on an expansive volcanic plateau, an endogenetic origin is implied. However, reports of shatter cones from its central area make it a candidate impact structure.

F. Zhamanshin (U.S.S.R.): This small astrobleme (~10-km diameter) is greatly eroded and difficult to detect. A variety of shock features are present, including glasses (irghizites) that share much in common with Australasian tektites.

G. Ramgarh (India): This structure, of questionable origin, lies about 300 km south of Delhi in Precambrian/Early Paleozoic terrane. It is a ring (~3-km diameter) analogous to the Gosses Bluff impact structure in central Australia, but no shock features have yet been reported here.

H. "The Spider" (Northwest Australia): This structure consists of a central peak of steep-dipping beds, bearing shatter cones, moved upward and inward from below.

I. Talemzane (Algeria): This Landsat image shows that sand has partially buried this 1.75-km rimrock ring, around which megabreccias have survived.

J. Talemzane (Algeria): This SIR-A radar image shows the crater rim to be a bright backscattering surface owing to blocky fractured bedrock and breccia clasts.

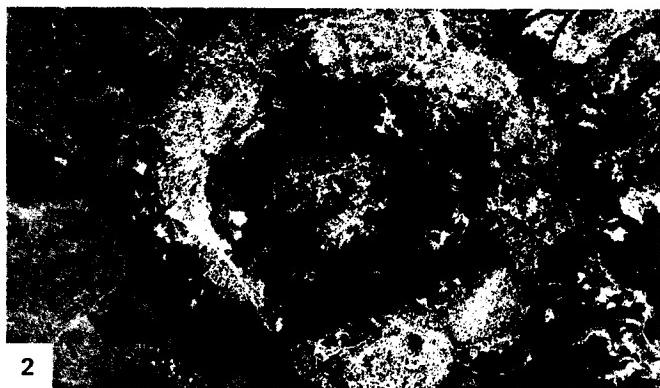
K. Tenoumer Crater (Mauritania): Another rimmed structure, 1.8 km wide, sticks out from a thin veneer of Sahara sands.

In addition to the above, other terrestrial impact structures illustrated in this book are Gosses Bluff (Figure 1-4), Meteor Crater (Plate V-3), and El'gygytgyn (Figures 12-14a-d). (NMS)
Montage of Landsat Subscenes.



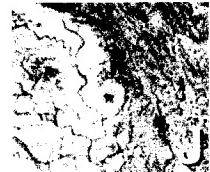
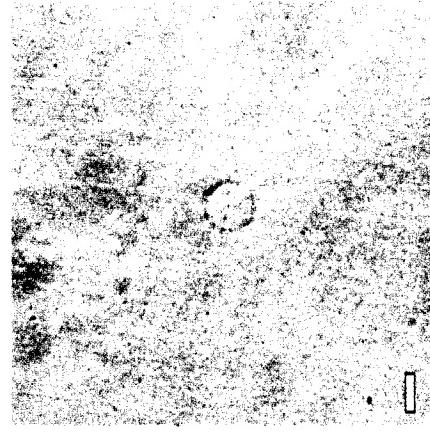
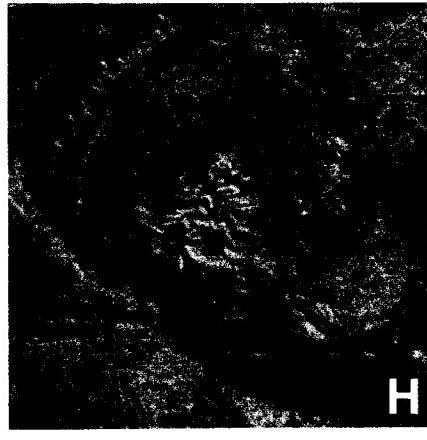
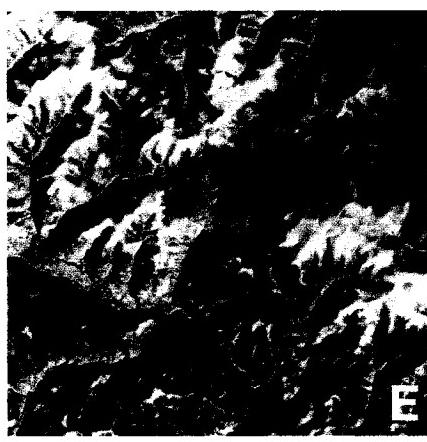
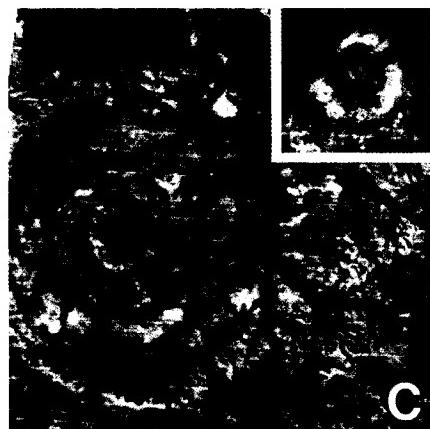
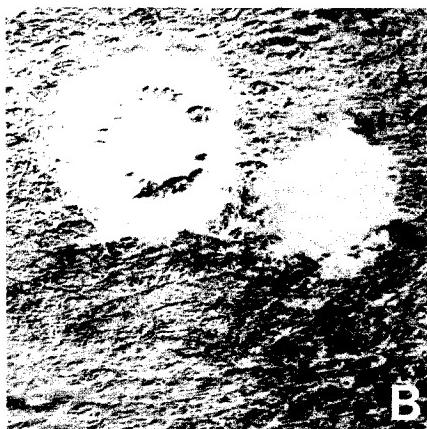
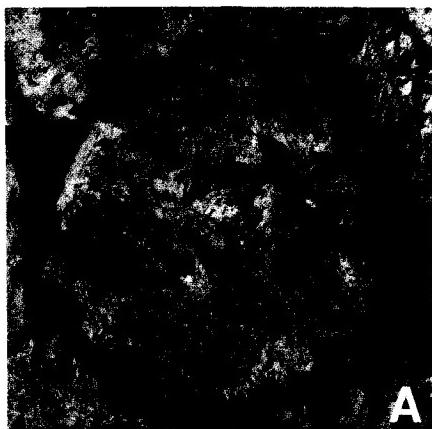
1

C 1



2

ORIGINAL PAGE
COLOR PHOTOGRAPH



REFERENCES

- Abbas, S., and Z. Ahmad, The Muslimbagh ophiolites, in *Geodynamics of Pakistan*, edited by A. Farah and K. A. DeJong, Geol. Surv. Pakistan, Quetta, pp. 243–249, 1979.
- Abrams, M. J., J. E. Conel, H. R. Lang, and H. N. Paley (Eds.), *The Joint NASA/Geosat Test Case Prov.*, 2 vols., AAPG Bookstore, Tulsa, Oklahoma, 1985.
- Ager, D. V., and M. Brooks, *Europe from Crust to Core*, pp. 143–159, John Wiley, London, 1977.
- Allen, C. R., The modern San Andreas fault, in *The Geotectonic Development of California*, edited by W. G. Ernst, pp. 511–534, Prentice Hall, Englewood Cliffs, New Jersey, 1981.
- Allen, C. R., A. R. Gillespie, Han Yuan, K. E. Sieh, B. Zhang, and C. Zhu, Red River and associated faults, Yunnan Province, China: Quaternary geology, slip rates, and seismic hazard, *Geol. Soc. Amer. Bull.*, **95**, 686–700, 1984.
- Al-Shanti, A. M. S., Evolution of and mineralization of the Arabian-Nubian shield, Pergamon Press, Oxford, *IAG Bull.*, No. 3, 1979.
- Anderson, J. G. C., *The Structure of Western Europe*, 250 pp., Pergamon Press, Oxford, 1978.
- Anderson, J. J., P. D. Rowley, R. J. Fleck, and A. E. M. Laird, Cenozoic geology of the southwestern high plateaus of Utah, *Geol. Soc. Amer. Special Paper 160*, pp. 1–51, 1975.
- Andrieux, J., and M. Brunel, L'evolution des chaines Occidentales du Pakistan, *Memoir Hors Service Society Geologique France*, **8**, 189–207, 1977.
- Anhaeuesser, C. R., and C. J. Robb, *Magmatic Cycles and the Evolution of the Archean Granitic Crust in the Eastern Transvaal and Swaziland*, 11 pp., University of Witwatersrand, 1980.
- Armstrong, F. C., and S. S. Oriel, Tectonic development of the Idaho Wyoming thrust belt: *Amer. Assn. Petrol. Geol. Bull.*, **49**, 1847–1865, 1965.
- Arpat, E., and F. Saroglu, The East Anatolian fault system: Thoughts on its development, Mineral Research and Exploration Institute of Turkey, *Bulletin 78*, pp. 33–39, 1972.
- Atwater, T., Implications of plate tectonics for the Cenozoic tectonic evolution of western North America, *Geol. Soc. Amer. Bull.*, **81**, 3513–3536, 1970.
- Baer, A. J., A Grenville model of Proterozoic plate tectonics, in *Precambrian Plate Tectonics*, edited by A. Kröner, pp. 353–385, Elsevier, Amsterdam, 1981.
- Bailey, G. B., and P. D. Anderson, Applications of Landsat imagery to problems of petroleum exploration in the Qaidam basin, China, *Amer. Assn. Petrol. Geol. Bull.*, **66**, 1348–1354, 1982.
- Baker, B. H., R. Crossley, and G. G. Goles, Tectonic and magmatic evolution of the southern part of the Kenya rift valley, in *Petrology and Geochemistry of Continental Rifts*, edited by E. R. Neuman, and I. B. Ramberg, pp. 29–50, D. Reidel, Dordrecht, Holland, 1978.
- Baker, B. H., P. A. Mohr, and L. A. J. Williams, Geology of the eastern rift system of Africa, *Geol. Soc. Amer. Special Paper 136*, 67 pp., 1972.
- Baker, C. L., Geologic reconnaissance in the eastern Cordillera of Mexico, *Geol. Soc. Amer. Special Paper 131*, 1971.
- Bally, A. W., et al., Notes on the geology of Tibet and adjacent areas, Report of the American plate tectonics delegation to the People's Republic of China, *U.S. Geol. Surv. Open-File Report 80-501*, 100 pp., 1980.
- Bannert, D., Afar tectonics from space photographs, *Amer. Assn. Petrol. Geol. Bull.*, **56**, 903–915, 1972.
- Bartov, Y., G. Steinitz, M. Eyal, and Y. Eyal, Sinistral movement along the Gulf of Aqaba—Its age and relation to the opening of the Red Sea, *Nature*, **285**, 220–222, 1980.
- Bashenina, N. V., Ural Mountains, in *Geomorphology of Europe*, edited by C. Embleton, pp. 4404–4412, Macmillan, London, 1984.
- Bayoumi, A. I., Tectonic origin of the Gulf of Suez, Egypt, as deduced from gravity data, in *Chemical Rubber Company Handbook of Geophysical Exploration at Sea*, edited by R. Geyer, pp. 417–432, 1983.
- Bedi, N., Applied geomorphologic studies on Landsat imagery, in *Perspectives on Geomorphology*, **3**, 251–270, 1982.
- Ben-Avraham, Z., G. Almagar, and Z. Garfunkel, Sediments and structure of the Gulf of Elat—northern Red Sea, *Sedimentary Geol.*, **23**, 239–267, 1980.

- Ben-Avraham, Z., Z. Garfunkel, G. Almagar, and J. Hall, Continental breakup by a leaky transform: The Gulf of Elat (Aqaba), *Science*, **206**, 214–216, 1979.
- Besairie, H., Madagascar, in *Tectonics of Africa*, UNESCO Earth Sciences, No. 6, 549–558, 1971–72.
- Bichan, R., 1970, The evolution and structural setting of the Great Dike of Rhodesia, in *African Magmatism and Tectonism*, edited by T. N. Clifford and I. G. Gass, pp. 51–72, Oliver and Boyd, Edinburgh, 1970.
- Bird, J. B., *The Natural Landscapes of Canada*, 191 pp., John Wiley, Toronto, Canada, 1972.
- Bird, J. M., and J. F. Dewey, Lithosphere plate-continental margin tectonics and the evolution of the Appalachian orogen, *Geol. Soc. Amer. Bull.*, **81**, 1031–1059, 1970.
- Blake, M. C., Jr., R. H. Campbell, T. W. Dibblee, Jr., D. G. Howell, T. H. Nilsen, W. R. Normark, J. C. Vedder, and E. A. Silver, Neogene basin formation in relation to plate tectonic evolution of San Andreas fault system, California, *Amer. Assn. Petrol. Geol. Bull.*, **62**, 344–372, 1978.
- Blake, T., Evidence for stabilization of the Pilbara block: Australia, *Nature*, **307**, 721–723, 1984.
- Bloom, A. L., *The Surface of the Earth*, 152 pp., Prentice-Hall, Englewood Cliffs, New Jersey, 1969.
- Bloom, A. L., *Geomorphology: A Systematic Analysis of Late Cenozoic Landforms*, 510 pp., Prentice-Hall, Englewood Cliffs, New Jersey, 1978.
- Bonini, E., R. B. Hargraves, and R. Shagam (Eds.), The Caribbean-South American plate boundary and regional tectonics, *Geol. Soc. Amer. Mem.* **162**, 421 pp., 1984.
- Brinkman, R., *Geologic Evolution of Europe*, Ferdinand Enke Verlag Stuttgart, and Hofner Publications, pp. 70–75 and 109–114, 1969.
- Brown, D. A., K. S. W. Campbell, and K. A. W. Crook, *The Geological Evolution of Australia and New Zealand*, 409 pp., Pergamon Press, Oxford, 1968.
- Brown, G. P., and R. O. Jackson, *Geology of the Asir Quadrangle, Kingdom of Saudi Arabia*, 1:500 000 scale, U.S. Geol. Surv. Miscellaneous Investigations, Map 1-217A, 1959.
- Brunet, M. F., and X. LePichon, Subsidence of the Paris basin: *J. Geophys. Res.*, **87**, 8547–8560, 1982.
- Burchfiel, B. C., and G. A. Davis, Structural framework of the Cordilleran orogeny, western United States, *Amer. J. Science*, **272**, 97–108, 1972.
- Burchfiel, B. C., and G. A. Davis, Nature and controls of Cordilleran orogenesis, western United States: Expansions of an earlier synthesis, *Amer. J. Science (Rogers Volume)*, **275-A**, 363–396, 1975.
- Burke, K., Aulacogens and continental breakup, *Ann. Rev. Earth Planet. Sci.*, **5**, 371–396, 1977.
- Burke, K., C. Cooper, J. F. Dewey, P. Mann, and J. L. Pindell, Caribbean tectonics and relative plate motion, in *The Caribbean South American Plate Boundary and Regional Tectonics*, edited by E. Bonini et al., pp. 31–64, *Geol. Soc. Amer. Mem.* **162**, 1984.
- Burke, K., and J. Dewey, Orogeny in Africa, in *African Magmatism and Tectonics*, edited by T. N. Clifford and I. G. Gass, pp. 583–606, Oliver and Boyd, Edinburgh, 1970.
- Burke, K., and J. F. Dewey, Plume generated triple junctions: Key indicators in applying plate tectonics to old rocks, *J. Geol.*, **81**, 400–433, 1973.
- Butzer, K. W., *Geomorphology from the Earth*, 463 pp., Harper and Row, New York, 1976.
- Cebull, S. E., and D. H. Shurbet, The Ouachita belt in the evolution of the Gulf of Mexico, in *The Origin of the Gulf of Mexico and the Early Opening of the Central North Atlantic*, edited by R. H. Pilger, pp. 17–26, Louisiana State Univ., Baton Rouge, 1980.
- Chorley, R. J., S. A. Schumm, and D. E. Sugden, *Geomorphology*, 605 pp., Methuen and Co., London, 1985.
- Choubert, G., and A. Faure-Muret, Moroccan Rif, in *Mesozoic and Cenozoic Orogenic Belts*, edited by A. M. Spencer, pp. 37–46, Geological Society of London Special Publication, Scottish Academic Press, Edinburgh, 1974.
- Chowdhury, M. K. R., *Geological and Mineral Map of Orissa*, Miscellaneous Publications, No. 30, Part III, Government of India, New Delhi, 1974.
- Christiansen, R. L., and E. H. McKee, Late Cenozoic volcanic and tectonic evolution of the Great Basin and Columbia Intermontane regions, Ch. 13, *Geol. Soc. Amer. Memoir* **152**, 283–308, 1978.
- Cobbing, E. J., and W. S. Pitcher, The coastal batholith of central Peru, *Geol. Soc. London Journal*, **128**, 421–460, 1972.
- Coleman, R. G., Geologic background of the Red Sea, in *The Geology of Continental Margins*, edited by C. A. Burke and C. G. Drake, pp. 743–751, Springer-Verlag, New York, 1974.
- Coleman, R. G., Tectonic setting for ophiolite subduction in Oman, *J. Geophys. Res.*, **86**, 2497–2508, 1981.
- Condie, K. C., *Plate Tectonics and Crustal Evolution*, 310 pp., Pergamon Press, Elmsford, New York, 1982.
- Constantinou, G., and G. J. S. Govett, Geology, geochemistry, and genesis of Cyprus sulfide deposits, *Economic Geology*, **68**, 843–858, 1973.
- Crawford, S. R., The Indus suture line in the Himalaya, Tibet, and Gondwanaland, *Geological Magazine*, **III**, 369–383, 1974.
- David, T. W. E. *The Geology of the Commonwealth of Australia*, 3 vols., Edward Arnold and Company, London, 1950.
- Davis, W. M., The geographical cycle, *Geogr. J.*, **14**, 481–504 (reprinted in 1954 in *Geographical Essays*, pp. 249–278, Dover Publications, New York), 1899.

- DeJong, K. A., Collapsed anticline in Kohat, southwest Himalaya foothills, Pakistan, *Geol. Soc. Amer. (Abstracts and Program)*, **13**, 437, 1981.
- Demek, J., I. Gams, and I. Vaptzarov, Balkan Peninsula, in *Geomorphology of Europe*, edited by C. Embleton, pp. 374–386, Macmillan, London, 1984.
- de Villiers, J., and E. S. W. Simpson, Late Precambrian tectonic patterns in South West Africa, in Contributions to the Precambrian Geology of Southern Africa, edited by A. Kroener, *Bull. Univ. of Cape Town, Dept. of Geol.*, **15**, 141–152, 1974.
- Dewey, J. F., and K. C. A. Burke, Tibetan, Variscan, and Precambrian basement reactivation: Products of continental collision, *J. Geol.*, **81**, 683–692, 1973.
- Dewey, J. F., W. C. Pitman III, W. B. F. Ryan, and J. Bonnin, Plate tectonics and the evolution of the Alpine System, *Geol. Soc. Amer. Bull.*, **84**, 3137–3180, 1973.
- Dewey, J. F., and A. M. C. Sengor, Aegean and surrounding regions: Complex multiplate and continuum tectonics in a convergent zone, *Geol. Soc. Amer. Bull.*, **90**, 84–92, 1979.
- Dibblee, T. W., Jr., The Rinconada and related faults in the Southern Coast Ranges, California, and their tectonic significance, *U.S. Geol. Surv. Prof. Paper 981*, 55 pp., 1976.
- Dickinson, W. R., Paleozoic plate tectonics and the evolution of the Cordilleran continental margin, in *Paleozoic Paleogeography of Western United States: Pacific Section*, edited by J. H. Stewart et al., pp. 137–156, Society of Economic Paleontologists and Mineralogists, Pacific Coast Paleogeography Symposium 1, 1977.
- Dietz, R. S., R. Fudali, and W. Cassidy, Richât and Semsiyat domes (Mauritania): not astroblemes, *Geol. Soc. Amer. Bull.*, **80**, 1367–1372, 1969.
- Dimroth, E., Evolution of the Labrador geosyncline, *Geol. Soc. Amer. Bull.*, **81**, 2717–2749, 1970.
- Drury, S. A., N. B. W. Harris, R. W. Holt, G. F. Reeves-Smith, and R. T. Wightman, Precambrian tectonics and the evolution of South India, *J. Geol.*, **92**, 3–20, 1984.
- Drury, S. A., and R. W. Holt, The tectonic framework of the South Indian crust, *Tectonophysics*, **65**, T1–T15, 1980.
- Dubertret, M. L., *Carte Géologique du Liban*, 1:200 000 scale, Ministère des Travaux Publics, République Libanaise, 1955.
- Dumistrasko, N. S., Caucasian Mountains and Armenian Highlands, *Geomorphology of Europe*, edited by C. Embleton, pp. 393–403, Macmillan, London, 1984.
- Dunbar, M., and K. R. Greenaway, *Arctic Canada from the Air*, pp. 253–263, Canada Defense Research Board, 1956.
- Dykstra, J. D., and R. W. Birnie, Segmentation of the Quaternary subduction zone under the Baluchistan region of Pakistan and Iran, in *Geodynamics of Pakistan*, edited by A. Farah and K. A. DeJong, p. 361, Quetta, Pakistan, 1979.
- Dykstra, J. D., and O. R. Russell, Mineral exploration in ophiolites using digitally processed Landsat imagery, 6th Ann. Pecora Symp., Sioux Falls, pp. 78–80, April 1980.
- Embleton, C., Scotland, in *Geomorphology of Europe*, edited by C. Embleton, pp. 104–114, Macmillan, London, 1984.
- Ernst, W. G. (Ed.), *The Geotectonic Development of California*, 706 pp., Prentice-Hall, Englewood Cliffs, New Jersey, 1981.
- Eyal, M., Y. Eyal, Y. Bartov, and G. Steinitz, The tectonic development of the western margin of the Gulf of Elat (Aqaba) Rift, *Tectonophysics*, **80**, 39–66, 1981.
- Farah, A., G. Abbas, K. A. DeJong, and R. D. Lawrence, Evolution of the lithosphere in Pakistan, *Tectonophysics*, **105**, 207–227, 1984.
- Farah, A., and K. A. DeJong (Eds.), *Geodynamics of Pakistan*, 361 pp., Geological Survey of Pakistan, Quetta, 1979.
- Fisher, G. W., F. J. Pettijohn, J. C. Reed, Sr., and K. N. Weaver (Eds.), *Studies in Appalachian Geology: Central and Southern*, 460 pp., Wiley-Interscience, New York, 1970.
- Ford, J. P., Seasat orbital radar imagery from geologic mapping: Tennessee-Kentucky-Virginia, *Amer. Assn. Petrol. Geol. Bull.*, **64**, 2064–2094, 1980.
- Fraser, J. D., J. A. Donaldson, W. F. Fahrig, and L. P. Tremblay, Helikian basins and geosynclines in northwestern Canadian Shield, in *Symp. Basins and Shields of the Canadian Shield*, Geol. Surv. of Canada, Paper No. 8, pp. 213–238, 1970.
- Freund, R., Z. Garfunkel, I. Zak, M. Goldberg, T. Weissbrod, and B. Berlin, The shear along the Dead Sea rift, *Phil. Trans. Roy. Soc. London*, **267**, 107–130, 1970.
- Fripp, R. E. P., D. A. van Nierop, M. J. Callow, P. A. Lilly, L. U. du Plessis, Deformation in part of the Archaen Kaapvaal Craton, South Africa, *Precambrian Res.*, **13**, 241–251, 1978.
- Fudali, R. F., Coesite from the Richât dome: A misidentification, *Science*, **166**, 228–230, 1969.
- Furon, P., *Geology of Africa*, 377 pp., Oliver and Boyd, Edinburgh, 1963.
- Gansser, A., Himalaya, in *Mesozoic-Cenozoic Orogenic Belts*, edited by A. M. Spencer, pp. 267–278, Geological Society of London, Scottish Academic Press, Edinburgh, 1974.
- Gansser, A., The Peri-Indian suture zone. Geology of the Alpine chains born of the Tethys, *26th International Geological Congress*, **5**, 140–148, 1980.
- Garfunkel, Z., Internal structure of the Dead Sea leaky transform (rift) in relation to plate kinematics, *Tectonophysics*, **80**, 81–108, 1981.
- Garfunkel, Z., and M. Bartov, The tectonics of the Suez rift, *Geol. Surv. Israel Bull.*, No. 71, 1–44, 1977.
- Garfunkel, Z., I. Zak, and R. Freund, Active faulting in the Dead Sea rift, *Tectonophysics*, **80**, 1–26, 1981.
- Gastil, G., R. A. Blais, D. Knowles, and R. Bergeron, The Labrador geosyncline, *International Geological Congress of Mexico*, Part 9, 21–38, 1960.

- Gee, R. D., Regional geology of the Archean Nuclei of the western Australian Shield, in *Economic Geology of Australia and Papua, New Guinea*, edited by P. Knight, pp. 43–54, Monograph Series No. 5, Australian Inst. of Min. Metall., 1975.
- Geologic Map of South America*, scale 1:15000000, prepared by G. S. Goudarzi, U.S. Geol. Surv. MF-868A, 1977.
- Geukens, F., Geology of the Arabian Peninsula-Yemen, *U.S. Geol. Surv. Prof. Paper 560-B*, 23 pp., 1966.
- Giegengack, R., Late Cenozoic tectonic environments of the Central Venezuelan Andes, in *The Caribbean-South American Plate Boundary and Regional Tectonics*, edited by E. Bonini et al., pp. 343–364, Geol. Soc. Amer. Mem. 182, 1984.
- Glennie, K. W., Geology of the Oman Mountains, *Nederland Geologisch Mijnbouwka Genoot. Verh.*, **31**, 423, 1974.
- Glennie, K. W., M. G. A. Bouef, M. W. Hughes-Clark, M. Moody-Stuart, W. F. H. Pilaar, and B. M. Reinhardt, Late Cretaceous nappes in Oman Mountains and their geologic evolution, *Amer. Assn. Petro. Geol. Bull.*, **57**, 5–27, 1973.
- Gornitz, V., and L. Seeber, Morphotectonic analysis of the Hazara arc region of the Himalayas, North Pakistan, and Northwest India, *Tectonophysics*, **74**, 263–282, 1981.
- Graham, S. A., Role of Salinian block in evolution of San Andreas fault system, California, *Amer. Assn. Petro. Geol. Bull.*, **62**, 2214–2231, 1978.
- Greenwood, J. E. G. W., and D. Bleackley, Geology of the Arabian Peninsula: Aden Protectorate, *U.S. Geol. Surv. Prof. Paper 560-C*, 1–82, 1967.
- Gries, R., Oil and gas prospecting beneath the Precambrian foreland thrust plates in the Rocky Mountains, *The Mountain Geologist*, **18**, 1–18, 1981.
- Gries, R., North-south compression of Rocky Mountain foreland structures, in *Rocky Mountain Foreland Basins and Uplifts*, edited by J. D. Lowell, pp. 9–32, Rocky Mountain Association of Geologists, 1983.
- Grindley, G. W., New Zealand, in *Mesozoic-Cenozoic Orogenic Belts*, edited by A. M. Spencer, p. 809, Geol. Soc. London Special Publication 4, The Scottish Academic Press, 1974.
- Hamilton, G. N. G., and H. B. S. Cooke, *Geology for South African Students*, 439 pp., Central News Agency, Ltd., South Africa, 1959.
- Hamilton, W., The Uralides and the motion of the Russian and Siberian platforms, *Geol. Soc. Amer. Bull.*, **81**, 2553–2576, 1970.
- Hamilton, W., Tectonics of the Indonesian region, *U.S. Geol. Surv. Prof. Paper 1078*, 345 pp., 1979.
- Harris, L. D., and K. C. Bayer, Sequential development of the Appalachian orogen about a master décollement—A hypothesis, *Geology*, **7**, 568–472, 1979.
- Harris, L. D., and R. C. Milici, Characterization of the thin-skinned style of deformation in the southern Appalachians and potential hydrocarbon traps, *U.S. Geol. Surv. Prof. Paper 1018*, 40 pp., 1977.
- Hatcher, R. D., Jr., and G. W. Viele, The Appalachian/Ouachita orogens: United States and Mexico, in *Perspectives in Regional Geological Synthesis*, edited by A. R. Palmer, pp. 67–75, D-NAG Spec. Pub. 1, Geol. Soc. Amer., Boulder, Colorado, 1982.
- Hildreth, W., *Death Valley Geology*, Death Valley Natural History Assn., California, 1976.
- Hoffman, P. F., J. A. Fraser, and J. C. McGlynn, The corona-tion geosyncline of Aphebian Age, District of Mackenzie, in *Symp. Basin and Geosynclines of the Canadian Shield*, Geological Survey of Canada, Paper 7240, pp. 201–212, 1970.
- Holland, S. S., *Landforms of British Columbia: A Physiographic Outline*, 138 pp., A. Sutton, 1964.
- Huang, T. K., An outline of the tectonic characteristics of China, *Eclogae Geologicae Helvetiae*, **71**, 611–635, 1978.
- Hunt, C. B., *Natural Regions of the United States and Canada*, 725 pp., W. H. Freeman and Co., San Francisco, 1974.
- Hunt, C. B., and D. R. Mabey, Stratigraphy and Structure, Death Valley, Calif., *U.S. Geol. Surv. Prof. Paper 494-A*, 1966.
- Irving, E., and J. L. Donaldson, Grenville front and rifting of the Canadian Shield, *Nature*, **237**, 1972.
- Joly, F., Paris Basin, in *Geomorphology of Europe*, edited by C. Embleton, pp. 154–160, Macmillan, London, 1984.
- Jones, D. L., A. Cox, P. Coney, and M. Beck, The growth of western North America, *Scientific American*, **247**, 7084, 1982.
- Jones, D. L., and N. J. Silberling, Mesozoic stratigraphy—The key to tectonic analysis of southern and central Alaska, *Open-File Report 79-1200*, U.S. Geol. Surv., 1979.
- Jones, D. L., N. J. Silberling, W. Gilbert, and P. J. Coney, Character, distribution, and tectonic significance of accretionary terranes in the central Alaska Range, *J. Geophys. Res.*, **87**, 3709–3717, 1982.
- Kazmi, A. H., The Bibai and Gogai Nappes in the Kach-Ziaret area of northeastern Baluchistan, in *Geodynamics of Pakistan*, edited by A. Farah and K. A. DeJong, pp. 333–339, Geological Survey of Pakistan, Quetta, 1979.
- Kazmi, A. H., and R. A. Rana, *Tectonic Map of Pakistan*, Geological Survey of Pakistan, Quetta, 1982.
- Keller, G. R., and S. E. Cebull, Plate tectonics and the Ouachita system in Texas, Oklahoma, and Arkansas, *Geol. Soc. Amer. Bull.*, **83**, 1659–1666, 1972.
- Kerr, J. W., and R. L. Christie, Tectonic history of Boothia Uplift and Cornwallis fold belt, Arctic Canada, *Amer. Assn. Petro. Geol. Bull.*, **49**, 905–926, 1965.
- Kerr, J. W., and P. G. Temple, Geology of the Bathurst Island Group, *Memoir 378*, 197 pp., Geological Survey of Canada, 1974.
- King, L. C., *The Morphology of the Earth*, 726 pp., Oliver and Boyd, London, 1967.
- King, P. B., *Evolution of North America* (revised edition), 196 pp., Princeton University Press, Princeton, New Jersey, 1977.

- King, P. B., et al., Geology of the Great Smokey Mountains National Park, Tennessee and North Carolina, *U.S. Geol. Surv. Prof. Paper* 587, p. 23, 1968.
- Kingma, J. T., *The Geological Structure of New Zealand*, John Wiley, 407 pp., 1974.
- Kulm, L. D., J. Dymond, E. J. Dasch, and D. M. Hussong, Nazca plate crustal formation and Andean convergence, *Geol. Soc. Amer. Mem.* 154, 824 pp., 1981.
- Lathram, E. H., et al., Alaska, in Mesozoic-Cenozoic Orogenic Belts, edited by A. M. Spencer, 809 pp., *Geol. Soc. of London Spec. Pub.* 4, Scottish Academic Press, 1974.
- Lawrence, R. D., S. H. Khan, K. A. DeJong, A. Farah, and R. S. Yeats, Thrust and strike-slip fault interaction along the Chaman transform zone, Pakistan, in *Thrust and Nappe Tectonics*, edited by K. McClay and J. J. Price, pp. 363-370, *Geol. Soc. London Spec. Pub.* 9, 1981.
- Leser, H., Western Alps: The Jura, in *Geomorphology of Europe*, edited by C. Embleton, pp. 262-267, 1984.
- Lillie, A. R., *Strata and Structure in New Zealand*, 441 pp., Tohunga Press, 1980.
- Livaccari, R. F., Late Cenozoic tectonic evolution of the western United States, *Geology*, 7, 72-75, 1979.
- Livaccari, R. F., and I. S. Merin, Hydrocarbon exploration within southeastern Turkey, *Oil and Gas Journal*, 88-93, January 20, 1986.
- Livaccari, R. F., R. Michael, and J. R. Everett, Late Cenozoic tectonic evolution of the Great Basin: Implications for hydrocarbon exploration; International Symposium on Remote Sensing of Environment Second Thematic Conference, *Remote Sensing for Exploration Geology*, pp. 651-657, 1982.
- Lohmann, H. H., Outline of tectonic history of the Bolivian Andes, *Amer. Assn. Petrol. Geol. Bull.*, 54, 735-757, 1970.
- Lowell, V., and R. Gries (Eds.), Rocky Mountain foreland basins and uplifts, *Rocky Mountain Association of Geologists Field Conference Symposium Volume*, 181 pp., 1983.
- Lowman, P. D., Jr., A global tectonic activity map, *Bull. Intern. Assn. Engineering Geol.*, 23, 37-49, 1981.
- Lowman, P. D., Jr., *Geology from Space: A Brief History of Orbital Remote Sensing*, Geol. Soc. Amer., Centennial Spec. Vol. 1, 481-518, 1985.
- Lowman, P. D., Jr., N. M. Short, P. J. Whiting, and A. M. Lohmann, Fracture patterns of the Canadian Shield: Implications for plate tectonics and the regmatic shear theory, submitted to *Canadian J. Earth Sci.*, 1986.
- Lyon-Caen, H., and P. Molnar, Gravity anomalies, flexure of the Indian Plate, and the structure, support and evolution of the Himalaya and the Ganga Basin, *Tectonics*, 4, 513-538, 1985.
- MacGregor, A. M., Some milestones in the Precambrian of Southern Africa, *Proc. Geol. Soc. S. Africa*, 54, 27-71, 1951.
- MacKevett, E. M., and G. Plafker, The Border Ranges fault in south central Alaska, U.S. Geological Survey, *J. Research*, 2, 323-329, 1974.
- Manspeizer, W., J. H. Puffer, and H. L. Cousminer, Separation of Morocco and eastern North America; a Triassic-Liassic stratigraphic record, *Geol. Soc. Amer. Bull.*, 89, 901-920, 1978.
- Matsuda, T., and S. Uyeda, On the Pacific-type orogeny in its model-extension of the paired belts concept and possible origin of marginal seas, *Tectonophysics*, 11, 5-27, 1971.
- Matthews, V. (Ed.), Laramide folding associated with basement block faulting in the western United States, *Geol. Soc. Amer. Mem.* 151, 370 pp., 1978.
- McBride, E. F., A. E. Weide, J. A. Wollenben, and R. C. Laudon, Stratigraphy and structure of the Parras and La Popa Basins, northeastern Mexico, *Geol. Soc. Amer. Bull.*, 84, 1603-1622, 1974.
- McConnell, R. B., Geological development of the rift system of eastern Africa, *Geol. Soc. Amer. Bull.*, 83, 2549-2572, 1972.
- McGlynn, J. C., and J. B. Henderson, The Slave Province, in *Variations in Tectonic Styles in Canada*, edited by R. A. Price and R. J. W. Douglas, pp. 454-503, *Geological Association of Canada Special Paper* 11, 1972.
- Meissner, C. R., J. M. Master, M. A. Rashid, and M. Hussain, Stratigraphy of the Kohat Quadrangle, *U.S. Geol. Surv. Prof. Paper* 716-D, 30 pp., 1974.
- Mitre-Salazar, L. M., Las Imagenes Landsat—Una Herramienta Util en la Interpretacion Geologio-Estructural, Un Ejemplo en el Noreste de Mexico, Universidad Nacional Autonomia de Mexico, *Instituto Geologia Revista*, 5, 37-46, 1981.
- Miyashiro, A., Metamorphism and related magmatism in plate tectonics, *Amer. J. Science*, 272, 629-656, 1972.
- Mohr, P. A., The Afar triple junction and sea-floor spreading, *J. Geophys. Res.*, 75, 7340-7352, 1970.
- Mohr, P. A., Structural geology of the African rift system: Summary of new data from ERTS-1 imagery, *Proc. Symp. Third Earth Resources Technology Satellite-1*, Vol. I, Section B, pp. 767-782, 1973.
- Mohr, P. A., Mapping of the major structures of the African rift system, Final Rpt., NASA Contract NAS5-21748, 1974.
- Molnar, P., and P. Tapponnier, Cenozoic tectonics of Asia: Effects of continental collision, *Science*, 189, 419-425, 1975.
- Molnar, P., and P. Tapponnier, The collision between India and Eurasia, *Scientific America*, 236, 30-41, 1977.
- Molnar, P., and P. Tapponnier, Active tectonics of Tibet, *J. Geophys. Res.*, 83, 5361-5376, 1978.
- Monger, J. W., and R. A. Price, Geodynamic evolution of the Canadian Cordillera: progress and problems, *Canadian Journal of Earth Sciences*, 16, 770-791, 1979.

- Monger, J. W. H., R. A. Price, and D. J. Templemanklait, Tectonic accretion and the origin of the two major metamorphic and plutonic welts in the Canadian Cordillera, *Geology*, **10**, 70–75, 1982.
- Monod, T., and C. Pomerol, Contributions à l'étude de l'accident circulaire des Richâts, *Mémoire 28, Sciences de la Terre*, L'Université de Nancy, France, 190 pp., 1973.
- Moody, J. D., and M. J. Hill, Wrench fault tectonics, *Geol. Soc. Amer. Bull.*, **67**, 1207–1246, 1956.
- Moore, J. C., and D. E. Karig, Sedimentology, structural geology, and tectonics of the Shikoku subduction zone, southwestern Japan, *Geol. Soc. Amer. Bull.*, **87**, 1259–1268, 1976.
- Morisawa, M., and J. T. Hack (Eds.), *Tectonic Geomorphology*, 390 pp., Allen and Unwin, Boston, 1985.
- Nalivkin, D. V., The geology of the USSR, *International Series of Monographs on Earth Sciences*, **8**, 170 pp., 1960.
- Neary, C. R., L. G. Gross, and B. J. Cavenaugh, Granitic association of northeastern Sudan, *Geol. Soc. Amer. Bull.*, **87**, 1501–1512, 1976.
- Nelson, C. A., Basin and Range Province, in *The Geotectonic Development of California, Rubey Volume 1*, edited by W. G. Ernst, pp. 206–216, Prentice-Hall, Englewood Cliffs, New Jersey, 1981.
- Ni, J., and J. D. York, Late Cenozoic tectonics of the Tibetan Plateau, *J. Geophys. Res.*, **83**, 5377–5384, 1978.
- Oberlander, T., *The Zagros Streams: A New Interpretation of Transverse Drainage in an Orogenic Zone*, 168 pp., Syracuse Geogr. Ser. 1, Syracuse Univ. Press, 1965.
- Ollier, C., *Tectonics and Landforms*, 324 pp., Longman, London, 1981.
- Osborne, F., and M. Morin, Tectonics of part of the Grenville subprovince in Quebec, in tectonics of the Canadian Shield, *Royal Society of Canada Special Publication 4*, University of Toronto Press, pp. 118–143, 1962.
- Pallister, J. W., The tectonics of East Africa, in *Tectonics of Africa*, pp. 511–542, UNESCO, Earth Sci. Ser. No. 6, 1979.
- Parkin, L. W., *Handbook of South Australian Geology*, 268 pp., Geological Survey of South Australia, 1969.
- Paylor, E., M. Abrams, J. Conel, A. B. Kahle, and H. R. Lang, Performance evaluation and geologic utility of Landsat 4 Thematic Mapper data, *JPL 85-66*, 68 pp., 1985.
- Pidgeon, R. R., 340 Million Years Old, volcanics in the Archean layered greenstone succession of the Pilbara block, Western Australia, *Earth and Planetary Letters*, **37**, 421–428, 1974.
- Ponikarov, V. P. (Ed.), *The Geology of Syria: Explanatory Notes on the Geological Map of Syria*, scale 1:500000, translated by T. F. Lokhova, prepared by the Ministry of Geology, U.S.S.R., for the Ministry of Industry, Syrian Arab Republic, 1967.
- Price, R. A., The Cordilleran foreland thrust and fold belt in the southern Canadian Rocky Mountains, in *Thrust and Nappe Tectonics*, pp. 427–448, Geological Society of London, 1981.
- Price, R. A., and E. W. Mountjoy, Geologic structure of the Canadian Rocky Mountains between Bow and Athabasca Rivers—A progress report, in *Structure of the Southern Canadian Cordillera*, pp. 7–25, Geologic Association of Canada, Special Paper 6, 1970.
- Price, R. J., *Highlands Landforms*, 110 pp., Highlands and Islands Development Board, Inverness, Scotland, 1976.
- Pritchard, J. M., *Landform and Landscape in Africa*, 160 pp., Edward Arnold, London, 1979.
- Quennell, A. M., Structural and geomorphic evolution of the Dead Sea rift, *Geol. Soc. London Quart. J.*, **114**, 1–24, 1958.
- Quittmeyer, R. C., A. L. Kafka, and J. G. Armbruster, Focal mechanisms and depths of earthquakes in Central Pakistan, *J. Geophys. Res.*, **89**, 2459–2470, 1984.
- Rich, J. L., Physiography and structure at Cumberland Gap, *Geol. Soc. Amer. Bull.*, **44**, 1219–1236, 1933.
- Rocky Mountain Association of Geologists, AAPG Field Trip: Energy and Resources of the Southern Rocky Mountains, *Mountain Geologist*, **9**, No. 283, July 1972.
- Rodgers, J., *The Tectonics of the Appalachians*, 271 pp., Wiley-Interscience, New York, 1970.
- Roohi, M., Structural history of the northeastern margin of the Arabian Plate in southwestern Iran, *International Geological Congress (abstracts), Résumés*, **1**, 97–98, 1976.
- Rothery, D. A., and S. A. Drury, The neotectonics of the Tibetan Plateau, *Tectonics*, **3**, 19–26, 1984.
- Rowlands, D., The structure and seismicity of a portion of the Southern Sulaiman Range, Pakistan, *Tectonophysics*, **51**, 41–56, 1978.
- Rutland, R. W. R., Andes: Antofagasta segment, in *Mesozoic-Cenozoic Orogenic Belts*, edited by A. M. Spencer, *Geol. Soc. London Spec. Pub.* **4**, Scottish Academic Press, 1974.
- Saleeby, J. B., Accretionary tectonics of the North American Cordillera, *Ann. Rev. Earth Planet. Sci.*, **15**, 45–73, 1983.
- Schweickert, R. A., Tectonic evolution of the Sierra Nevada, in *The Geotectonic Development of California, Rubey Volume 1*, edited by W. G. Ernst, pp. 87–131, Prentice-Hall, Englewood Cliffs, New Jersey, 1981.
- Sengor, A. M. C., Mid-Mesozoic closure of Permo-Triassic Tethys and its implications, *Nature*, **279**, 590–593, 1979.
- Sengor, A. M. C., The Cimmeride orogenic system and the tectonics of Eurasia, *Geol. Soc. Amer. Spec. Paper 195*, 82 pp., 1984.
- Sengor, A. M. C., and Y. Yilmaz, Tethyan evolution of Turkey: A plate tectonic approach, *Tectonophysics*, **175**, 181–241, 1981.

- Shimazaki, K., Intra-plate seismicity gap along the Median Tectonic Line and oblique plate convergence in southwest Japan, *Tectonophysics*, **31**, 139–156, 1976.
- Short, N. M., P. D. Lowman, Jr., S. C. Freden, and W. A. Finch, Jr., *Mission to Earth: Landsat Views the World*, 459 pp., NASA SP-360, Govt. Printing Office, Washington, D.C., 1976.
- Simpson, C., The structure of the Rim Synclinorium of the Vredefort Dome, *Geol. Soc. S. Africa Trans.*, **81**, 115–121, 1978.
- Small, R. J., *The Study of Landforms*, 2nd Ed., Cambridge University Press, Cambridge, 1978.
- Smith, R. B., and G. P. Eaton, Cenozoic tectonics and regional geophysics of the western Cordillera, *Geol. Soc. Amer. Mem.* **162**, 132–295, 1978.
- Sparks, B. W., *Geomorphology*, 2nd Ed., Longman, London, 1972.
- Spencer, A. M. (Ed.), Mesozoic-Cenozoic orogenic belts, *Geol. Soc. London Spec. Pub.* **4**, Scottish Academic Press, 809 pp., 1974.
- Spencer, E. W., *Introduction to the Structure of the Earth*, 2nd Ed., 640 pp., McGraw-Hill, New York, 1977.
- Stagman, J. G., An outline of the geology of Rhodesia, *Rhodesia Geol. Surv. Bull.*, **80**, 1–122, 1978.
- Stewart, J. H., Late Precambrian evolution of North America: Plate tectonics implications, *Geology*, **4**, 11–15, 1976.
- Stocklin, J., Structural history and tectonics of Iran: A review, *Amer. Petrol. Geol. Bull.*, **52**, 1229–1258, 1968.
- Stocklin, J., Structural correlation of the alpine ranges between Iran and central Asia, *Memoir Hors Service Society Géologique France*, **8**, 333–353, 1974.
- Stoneley, R., On the origin of ophiolite complexes in the southern Tethys region, *Tectonophysics*, **25**, 303–322, 1975.
- Streitz, R., and M. C. Stinson, *Geologic Map of California*, Death Valley Sheet, scale 1:250000, Calif. Div. Mines and Geology, 1977.
- Suggate, R. P. (Ed.), The Geology of New Zealand, Vols. I and II, 820 pp., New Zealand Geol. Surv., Dept. of Science and Industrial Res., E. C. Keating, Govt. Printers, Wellington, New Zealand, 1978.
- Sugimura, A., and S. Uyeda, *Island Arcs: Japan and Its Environment*, 235 pp., Elsevier, Amsterdam, 1973.
- Suppe, J., *Principles of Structural Geology*, 537 pp., Prentice-Hall, Englewood Cliffs, New Jersey, 1985.
- Suslov, S. P., *Physical Geography of Asiatic Russia*, translated by V. D. Gershevsky, 594 pp., W. H. Freeman, San Francisco and London, 1961.
- Tanaka, K., and T. Nozawa (Eds.), *Geology and Mineral Resources of Japan*, Sumitomo Printing and Publ. Co., Tokyo, 1971.
- Tapponnier, P., and P. Molnar, Slip-line field theory and large scale continental tectonics, *Nature*, **264**, 319–324, 1976.
- Tapponnier, P., and P. Molnar, Active faulting and tectonics in China, *J. Geophys. Res.*, **82**, 2905–2930, 1977.
- Tapponnier, P., G. Peltzer, A. Y. Le Dain, R. Armijo, and P. Cobbold, Propogating extrusion tectonics in Asia: New insights from simple experiments with plasticine, *Geology*, **10**, 611–616, 1982.
- Tectonic Map of South America*, scale 1:5000000 (2 sheets), Departamento Nacional da Produção Mineral (DNPM), Divisão de Geologia e Mineralogia, 1978.
- Temple, P. G., Mechanics of large-scale gravity sliding in the Greek Peloponnesos, *Geol. Soc. Amer. Bull.*, **79**, 687–700, 1968.
- Thornbury, W. D., *Regional Geomorphology of the United States*, 609 pp., John Wiley, New York, 1965.
- Thornbury, W. D., *Principles of Geomorphology*, 2nd Ed., 594 pp., John Wiley, New York, 1969.
- Trumpy, R., Le Rif et le Tell-leur place entre les oceans et entre les continents, *Revue de Géologie Dynamique et de Géographie Physique*, **24**, 197–199, 1983.
- Truswell, J. F., *An Introduction to the Historical Geology of South Africa*, 167 pp., Purvill Press, South Africa, 1970.
- Twidale, C. R., Geomorphology of the Flinders Range, in *Natural History of the Flinders Range*, edited by D. W. P. Corbett, pp. 57–137, Publ. Library of South Australia, Adelaide, 1969.
- Twidale, C. R., *Structural Landforms*, 247 pp., Australia Nat. Univ. Press, 1971.
- Twidale, C. R., *The Analysis of Landforms, Part II*, pp. 19–159, John Wiley, North Ryde, New South Wales, 1976.
- Uyeda, S., and A. Miyashiro, Plate tectonics in the Japanese Island; A synthesis, *Geol. Soc. Amer. Bull.*, **85**, 1159–1170, 1974.
- Viele, G. W., Structure and tectonic history of the Ouachita Mountains, Arkansas, in *Gravity and Tectonics*, edited by K. A. DeJong and R. Scholter, pp. 361–377, John Wiley, New York, 1973.
- Viljoen, R. P., and M. J. Viljoen, ERTS-1 imagery: An appraisal of applications in geology and mineral exploration, *Minerals Science and Engineering*, **132–168**, 7, 1975.
- Watts, M. T., *Reading the Landscape of Europe*, 315 pp., Harper and Row, New York, 1971.
- Welland, M., and K. W. Glennie, Late Cretaceous nappes in Oman Mountains and their geologic evolution, *Amer. Assn. Petrol. Geol. Bull.*, **59**, 1686–1688, 1975.
- Wernicke, B., and B. C. Burchfiel, Modes of extensional tectonics, *J. Structural Geol.*, **4**, 105–115, 1982.
- Wheeler, J. O., et al., The Cordillera structural province, in *Tectonic Styles in Canada*, edited by R. A. Price and R. J. W. Douglas, p. 181, *Geol. Assn. of Canada Spec. Paper 11*, 1972.

- Wildi, W., La chaine tello-rifaine (Algérie, Maroc, Tunisie): Structure, stratigraphie et évolution du Trias au Miocene, *Revue de Géologie Dynamique et de Géographie Physique*, **24**, 201–298, 1983.
- Williams, H. (Ed.), *Landscapes of Alaska: Their Geologic Evolution*, 148 pp., University of California Press, 1958.
- Williams, H., and R. D. Hatcher, Jr., Appalachian Suspect Terranes, *Geol. Soc. Amer. Mem.* **158**, 33–53, 1983.
- Willis, B., East African plateaus and rift valleys, *Carnegie Institution Washington Pub.* **470**, 358 pp., 1936.
- Windley, B. F., *The Evolving Continents*, 399 pp., John Wiley, Chichester, England, 1984 (1st Ed., 1978).
- Wolman, G., Structure and scale in geomorphology, Presidential Address, Ann. Mtg. Geol. Soc. Amer., Reno, Nevada, in prep., 1984.
- Worst, B.C., The Great Dyke of Rhodesia, *Southern Rhodesia Geological Survey Bull.* **47**, Salisbury, 1–237, 1960.
- Wynne-Edwards, H. R., The Grenville Province, in *Variations in Tectonic Styles in Canada*, edited by R. A. Price and R. J. W. Douglas, *Geol. Assn. of Canada Spec. Paper 11*, 263–334, 1972.
- Yeats, R. S., S. H. Khan, and M. Akhtar, Late Quaternary deformation of the Salt Range, *Geol. Soc. Amer. Bull.*, **95**, 958–966, 1984.
- Yeats, R. S., and R. D. Lawrence, Tectonics of the Himalayan thrust belt in northern Pakistan, in *Marine Geology and Oceanography of Arabian Sea and Coastal Pakistan*, edited by B. U. Haq and J. D. Milliamn, pp. 177–198, Van Nostrand Reinhold, 1984.
- Yoshida, T. (Ed.), *Outline of the Geology of Japan*, 3rd Ed., 61 pp., Geol. Survey of Japan, Kawasaki-shi, 1975.
- Yoshikawa, T., S. Kaizuka, and Y. Ota, *The Landforms of Japan*, 222 pp., University of Tokyo Press, 1981.
- Zeil, W., *The Andes: A Geological Review*, 260 pp., Gebr. Borntraeger, Stuttgart, Germany, 1979.
- Zhang, Z. M., J. G. Liou, and R. G. Coleman, Plate tectonics of China, *Geol. Soc. Amer. Bull.*, **95**, 295–312, 1984.
- Zimmerman, J., Emplacement of the Vourinos ophiolite complex, northern Greece, *Geol. Soc. Amer. Mem.* **132**, 225–239, 1972.
- Zimmerman, J., Jr., and J. V. Ross, Structural evolution of Varadar Root Zone, northern Greece, *Geol. Soc. Amer. Bull.*, **87**, 1547–1550, 1976.
- Zoback, M. L., R. E. Anderson, and G. A. Thompson, Cainozoic evolution of the state of stress and style of tectonism of the Basin and Range Province of the western United States, *Phil. Trans. Roy. Soc. London*, **300**, 407–434, 1981.

3

VOLCANIC LANDFORMS

Nicholas M. Short*

As perceived from space, entire geomorphic provinces may look volcanic in origin (e.g., Columbia Plateau in the Pacific Northwest section of the United States); in other provinces, volcanism may prevail over a significant but usually spatially discontinuous fraction of the region (as in parts of the Basin and Range province of the United States). The extent to which a regional landscape is controlled by volcanism depends on: (1) the nature of the extruded materials (basic lavas tend to spread over larger areas, producing landforms with more subdued slopes (1 to 5°) than do silicic lavas (20 to 35°); (2) the distribution of vents and fissures; (3) the volume of outpourings, (4) the duration of volcanism, (5) the age(s) of volcanic activity relative to the present and to associated stratigraphic units; and (6) the intensity and stage of subsequent erosional activity. In some regions, volcanic outpourings were confined to a limited time period, leading to flows that cap older nonvolcanic units. The resistance of such volcanic rocks to erosion strongly influences the subsequent history of landscape development as streams penetrate into the underlying more erodible bedrock, causing a distinctive assemblage of lava-capped hills and mesas (as, for example, in the western Siberian Platform of Russia, Figure 3-1). Likewise, lava flows and/or thick tephra deposits that accumulate over larger areas may partially to completely bury preexistent topography.

Most (about 82 percent) currently active centers of volcanism are concentrated on or near convergent margins of continents and island arcs along plate boundaries within the Pacific Basin ("Ring of Fire"). Nearly 14 percent of the world's active volcanoes are located in the Indonesian Archipelago. Another 6 percent lie along the Mid-Atlantic Ridge. Africa, the Mediterranean, and Arabian Peninsula regions account for 5 percent. The remainder occur at other plate boundaries within the ocean basins (e.g., Hawaiian Islands) or continental interiors (e.g., Yellowstone), generally where one or more subcrustal thermal plumes (hot spots) have been identified or postulated. Although the sub-aerial distributions of volcanoes now and in the past are intermittent in time and space, the ocean basins have experienced continuous buildup of volcanic layers since at least the Triassic (and probably much farther back in time). Where not covered by thin sedimentary deposits, the topography of the ocean floor is distinctly that of a basaltic volcanic terrain, with shield volcanoes, ridges, cones, and rifts adding variety to an otherwise rather even low-relief surface.

Most landforms identified as specifically resulting from volcanic action differ in two essential respects from some of the other landform types treated in this book. First, volcanoes and their

derivative surroundings are primarily *constructional* during their active or formative stages. Second, most smaller volcanic landforms tend to develop to their full extent more *rapidly* than many fluvial, tectonic, and other landforms. The net effect due to this and to the high levels of volcanic activity in the last few million years is that large parts of a terrain dominated by volcanism appear to be notably fresher or younger than terrains of a different nature, including those adjacent to the volcanic field. In his textbook on geomorphology, Von Engeln (1942) states:

"Volcanic force is endogenic and, as such, gives rise to constructional landforms. These may be so large as to constitute geomorphic units of first importance . . . The lesser volcanic features may be so numerous as to give a distinct topographic aspect to wide districts (volcanic regions)."

In terms of the traditional (but now obsolete) Davisian sequence of erosional stages from youth through old age, many volcanic forms seem to be young as now observed. While active, volcanoes are usually built up (repaired) faster than destructive forces can reduce them because of replenishment of surface cover by periodic (and often spasmodic) outpouring of materials. Between occasional eruptions, smaller volcanoes covered with ash undergo conspicuous erosion in a matter of years. However, most volcanic forms do not progress into maturity until the activity causing them has either ceased or been long dormant. For some, this may happen catastrophically, as when parts of a structure collapse or are blown asunder during caldera formation. Likewise, flows generally do not experience significant weathering or removal until after the last flows or ejecta have covered them. Surficial forms and features generated by tephra deposits are commonly short-lived because of their ready erodibility. Volcanic structures attain old age when much of their external protective covering has been stripped off, leaving a core of more resistant rock.

Volcanoes develop from extrusion or expulsion of fluids, congealed fragments, and gases that collect or distribute at or near the Earth's surface to produce a variety of forms, chief of which are conical, often mountain-like structures, thin to thick piles of flow sequences, and sheets of airfall deposits of tephra (fragmental particles of volcanic material). The forms are controlled in part by the mode or types of volcanic activity. This ranges from quiet emission to explosive ejection, depending mainly on the gas content and viscosity (related to composition) of the initial magma and resultant lava. The various modes of eruption are identified by reference to an individual named volcano, a regional location, or (in one case) a person (Pliny) associated with the type of activity, as summarized in Table 3-1.

Classifications of volcanic landforms are surprisingly sparse in the literature. Although textbooks and sourcebooks (at least

*Geophysics Branch (Code 622), Goddard Space Flight Center, Greenbelt, Maryland 20771.

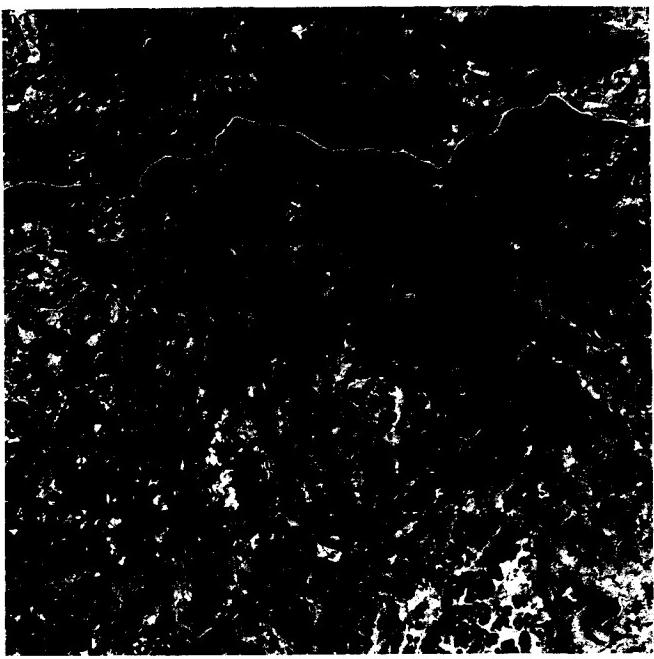


Figure 3-1. Landforms developed by erosion of Permo-Triassic rocks capped by basaltic trap. Area shown in this Landsat image (1097-04465-5; Oct. 28, 1972) is part of the western Siberian Platform drained by the Nizhnyaya Tunguska river. Many hills are flat-topped, reflecting control by the resistant volcanic members. The Platform contains 750000 km² of Mesozoic flood basalts.

those in English) on volcanology (Rittman, 1962; Ollier, 1969; Macdonald, 1972; Bullard, 1976; Williams and McBirney, 1978; Simkin et al., 1981) concentrate on mechanisms of eruption and the petrology of products, they describe most of the large- and small-scale structures and surface phenomena attendant to the volcanism. More recently, Williams et al. (1983) have developed a geomorphic classification of Icelandic volcanoes. Bloom (1978) treats volcanic landforms in a separate chapter early in his textbook on geomorphology. He points out that volcanism can be treated naturally from two viewpoints, either petrologically (including mechanisms of emplacement) or as a landform builder. He notes that classifications are based on one or more defining parameters: (1) chemical composition (and temperatures) of volcanic effluents, (2) state of the ejecta released, (3) history of the volcanic field, (4) shapes/locations of the vents/fissures, (5) nature of the volcanic activity, and (6) characteristic landforms. Bloom erects a classification around two parameters: (1) viscosity (quality of magma) and (2) size of the landform edifices (quantity of magma), yielding the types shown in Table 3-2. Many of these types are expressed pictorially in relation to their plutonic sources in Figure 3-2.

Two other books place their prime emphasis on the volcanic landforms *per se*. These are:

C. A. Cotton, *Volcanoes as Landscape Forms*, 416 pp., Whitcombe and Tombs, Ltd., Christchurch, New Zealand, 1952.

J. Green and N. M. Short, *Volcanic Landforms and Surface Features; A Photographic Atlas*, 519 pp., Springer-Verlag, New York, 1971.

Cotton's book delves at length into development of volcanic landforms by both petrogenetic mechanisms and modifying geomorphic

processes. Numerous worldwide examples are given, but an inordinate number come from his home country of New Zealand. The Green and Short volume is primarily a pictorial atlas with descriptive captions, but an introductory chapter by Arie Poldervaart succinctly summarizes volcanic landform origin and history from the dual standpoints of emplacement and erosion processes.

In his book, Cotton proposes grouping volcanic landforms into two first-order classifications, based on: A. Lava Types = 1. Rhyolitic, 2. Andesitic, 3. Basaltic Landforms; B. Fundamental Physiographic Types = 1. Mountains, 2. Plateaus, 3. Plains, as constructed by volcanic materials. However, Cotton does not formally organize the many landforms treated in his book into any specific classification. The author of this chapter has developed a classification of sorts extracted from the chapter and heading sections and some textual descriptions in Cotton's definitive work. The result violates to some extent principles of scientific taxonomy in that these headings are of mixed character; certain ones refer to structures, others to topographic features, and still others to phenomena or processes accompanying eruption. Nevertheless, the classification as it appears in Table 3-3 (with several modifications from Green and Short) is valuable as a listing of most common larger surface features attributable to volcanism. The table also lists examples of each landform category from selected localities and singles out those landforms (indicated by +) known to be visible from space. (Others on the list, some now being discriminable but not clearly identifiable, may be added as higher resolution stereo sensors provide improved imagery.) Some volcanic landforms exemplified in the space images are so large that they can be easily seen, others nevertheless visible are much smaller (best seen under magnification), and many occupy only a tiny fraction of the scene.

Some specific types mentioned in Tables 3-2 and 3-3 deserve further comment. Domical volcanic landforms (exogenous domes) result from the comparatively high fluidity of basaltic magmas. Smaller dome-shaped mountains, of the Icelandic type, have gentle lower slopes that may increase to angles of 20° or more toward the top. The much larger Hawaiian type (Plate V-10) has slopes around 1 to 3°, rarely exceeding 10°. Individual edifices may have basal dimensions approaching 100 km on a side and heights of 3 to 5 km. (The island of Hawaii is 400 km in diameter at its submarine base and reaches a total height of 10 km.)

Flood basalt plateaus and plains (Plates V-5, V-7, V-20, and V-23) cover areas exceeding 10000 km². While generally of low relief after the final eruptive emplacement of lava onto a thickening pile, the terrain is affected by later erosion that produces notable relief characterized by benches and cliffs. This landscape form is sometimes referred to as "treppen" (step-like).

Composite volcanoes or stratocones comprise one of the most distinctive of all landforms. They occur in isolation (Mt. Etna, Plate V-16), in alignments (Kamchatka, Plate V-25), or in clusters, often numbering more than 100 in a field (Andes, Plate V-14). Stratocones may begin as tephra rings and grow into larger bodies (typically circular in plan view by repeated periodic episodes of eruption of both tephra (ash, lapilli, and blocks) and lavas. These two types of effluents complement each other in building up a stable structure. Outpourings of lava mix with fragmental ejecta to construct a reinforced conical landform about a structural mainframe consisting of dikes, sills, and cone sheets. The main, usually central vent, often topped by a crater at the surface, may also contain one or more endogenous domes (Plate V-8), also known as tholoids, or may extrude a transient spine of congealed lava.

Many larger stratocones eventually self-destruct by some type of explosive eruption, often resulting from introduced sea or ground water or melted snow, that succeeds in blowing away the peak and parts of the framework (Plate V-24). Expulsion of great volumes of ejecta and/or withdrawal of melted rock from the proximate magma chamber commonly robs the upper struc-

Table 3-1
Types of Volcanic Eruptions*

Type	Characteristics
1. Icelandic	Fissure eruptions, releasing free-flowing (fluidal) basaltic magma; quiet, gas-poor; great volumes of lava issued, flowing as sheets over large areas to build up plateaus (Columbia).
2. Hawaiian	Fissure, caldera, and pit crater eruptions; mobile lavas, with some gas; quiet to moderately active eruptions; occasional rapid emission of gas-charged lava produces fire fountains; only minor amounts of ash; builds up lava domes.
3. Strombolian	Stratocones (summit craters); moderate, rhythmic to nearly continuous explosions, resulting from spasmodic gas escape; clots of lava ejected, producing bombs and scoria; periodic more intense activity with outpourings of lava; light-colored clouds (mostly steam) reach upward only to moderate heights.
4. Vulcanian	Stratocones, (central vents); associated lavas more viscous; lavas crust over in vent between eruptions, allowing gas buildup below surface; eruptions increase in violence over longer periods of quiet until lava crust is broken up, clearing vent, ejecting bombs, pumice, and ash; lava flows from top of flank after main explosive eruption; dark ash-laden clouds, convoluted, cauliflower-shaped, rise to moderate heights more or less vertically, depositing tephra along flanks of volcano. (Note: ultravulcanian eruption has similar characteristics but results when other types (e.g., Hawaiian) become phreatic and produce large steam clouds, carrying fragmental matter.)
5. Vesuvian	More paroxysmal than Strombolian or Vulcanian types; extremely violent expulsion of gas-charged magma from stratocone vent; eruption occurs after long interval of quiescence of mild activity; vent tends to be emptied to considerable depth; lava ejects in explosive spray (glow above vent), with repeated clouds (cauliflower) that reach great heights and deposit tephra.
6. Plinian	More violent form of Vesuvian eruption; last major phase is uprush of gas that carries cloud rapidly upward in vertical column for miles; narrow at base but expands outward at upper elevations; cloud generally low in tephra.
7. Peléan	Results from high-viscosity lavas; delayed explosiveness; conduit of stratovolcano usually blocked by dome or plug; gas (some lava) escapes from lateral (flank) openings or by destruction or uplift of plug; gas, ash, and blocks move downslope in one or more blasts as nuées ardentes or glowing avalanches, producing directed deposits.
8. Katmaian	Variant of a Peléan eruption characterized by massive outpourings of fluidized ashflows; accompanied by widespread explosive tephra; ignimbrites are common end products, also hot springs and fumaroles.

*Abstracted and modified from Chapter XII (pp. 305–310) of *Principles of Physical Geology* by A. Holmes, 2nd ed., Ronald Press, 1965, with additional data from *Volcanoes: In History, In Theory, In Eruption*, by F. M. Bullard, University of Texas Press, 1962.

ture of support, leading to collapse and, at times, additional explosive ejection of the fragmented materials. The large craters (>1 km in diameter, up to 10 km or more) are termed calderas; if the rim of this great cavity remains intact, the caldera may fill with water to form a crater lake (Plates V-6 and V-18). Ignimbrites expelled during these events may spread over wide areas, as at the Yellowstone region in Wyoming (Figure 3-3), infilling more rugged terrain to produce an aggradational plateau.

A few added comments concerning the relevant volcanic features that can be recognized in the space images (those taken both from satellites and by astronaut-operated equipment) shown in this chapter closes the introductory section:

1. For the most part, the scenes are mainly a mix of volcanic and other types of landforms. Plate V-4, for example, shows the Pinacate Field in northernmost Mexico as an area of recently active volcanism set apart from the Basin and Range structural landforms that dominate the scene. By contrast, the entire image of the Afar in Ethiopia (Plate V-21) depicts a volcanic terrain exclusively.
2. The most common associations with volcanic landforms are those of tectonic/orogenic origin. This is to be expected inasmuch as anorogenic volcanism is the excep-

tion even on the continents. Volcanism is a characteristic or hallmark of several tectonic regimes. Referring to the classification given in the introduction to Chapter 2, *Tectonic Landforms* (p. 30), one can predict volcanic activity concomitant with lithospheric plate interactions for the following classes (named and then listed by the number-letter code used in that classification):

I. Divergent Plate Margin:

- a. Intracontinental Rift (A-1)
- b. Oceanic Spreading Center (A-2)

II. Convergent Plate Margin:

- a. Ocean-Ocean Plate Margin (B-1)
- b. Ocean-Continent Margin (B-2)
- c. Continent-Continent Margin (B-3)

III. Transform Zone:

- a. Trench-Trench (Dead Sea Type) (C-1)
- b. Ridge-Trench (San Andreas Type) (C-2)
- c. Ridge-Ridge (San Andreas Type) (C-3)

Table 3-2
Classification of Volcanic Landforms*

Quality of Magma	Type of Activity	Quantity of Eruptive Material		
		Small		Large
Fluid, very hot, basic ↓ Increasing viscosity, gas content, and silica percentage	Effusive	Lava flows	Exogenous domes	Basalt plateaus and shield volcanoes
		Scoria cones with flows		Icelandic Hawaiian
		Loose tephra cones and thick flows	Composite cones or Strato-volcanoes	Volcanic fields with multiple cones
	Explosive	Endogenous domes (plug domes, tholoids, spines)	Ruptured endogenous domes with thick lava flows	
		Maars of tephra	Maars with ramparts	Collapse and explosion calderas
		Gas maars	Explosion craters	Ignimbrite sheets

*Adapted from Bloom (1978), as simplified from Rittmann (1962), Tables 4 and 5.

IV. Plate Interior:

- a. Shields (D-1)
 - b. Posttectonic Magmatic Intrusions (D-4)
 - c. Hot Spot Track (D-7)
3. Space imagery is especially effective in placing active, recent, or older, but nearly always Cenozoic, volcanism in context with several types of structural control. Fault zones and rifts are the prevalent types, as exemplified in Plates V-21, V-25, and V-27. Alignments of volcanoes are frequently obvious, but the controlling fracture sets and lineaments are more difficult to discern in many images.
4. Recognition and better definition of many volcanic landforms that stand above their surroundings (cones, domes, eroded dikes, and viscous flows) are significantly enhanced by winter imagery (see Plates V-2 and V-25), owing to both lower Sun angles and occasional snow cover.
5. Again, the synoptic aspect of space imagery helps to call attention to the remarkable range in sizes among such volcanic structures as stratocones (compare Plates V-14 and V-17) and calderas (Plates V-13 and V-18).
6. Some landforms that at least partially owe their existence to volcanism display only subtle evidence of this connection in the imagery. The rounded hills and sculptured divides seen in Figure 3-1 do not readily manifest the

influence of basaltic trap flows that cap underlying sedimentary rocks in the Siberian Platform, nor do the

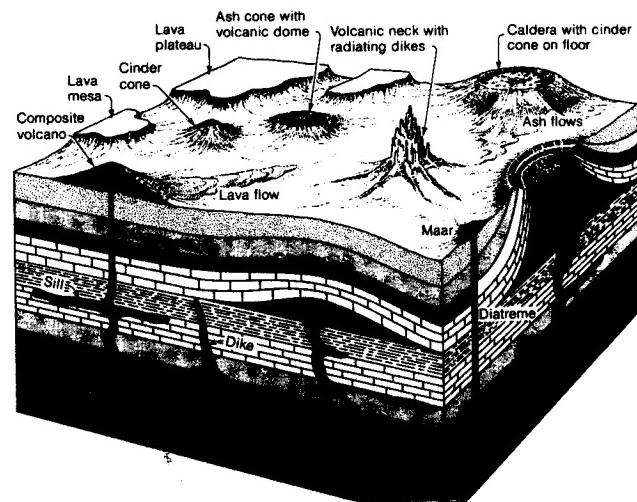


Figure 3-2. Schematic diagram showing characteristic landforms resulting from volcanic action at the surface and their relation to shallow intrusive activity in the crust (in Press and Siever (1982); adapted from R. G. Schmidt and H. R. Shaw, U.S. Geological Survey).



Figure 3-3. Mountainous and flatlands terrain developed on ignimbrites, flows, and ash deposits produced during Late Tertiary and Quaternary volcanic activity in and around present-day Yellowstone National Park in northwestern Wyoming (Landsat 1825-17294-7; October 26, 1972).

Karoo dolerite sills of South Africa (Plate V-20) produce a landscape that makes evident the role these intrusions play in the landform pattern.

7. Other volcanic landforms may be obscured by land-use patterns or soil cover. This is evident in the Deccan Plateau of India (Plate V-23) and the Snake River Plains of Idaho (Plate V-6). Tephra deposits are geologically transient, as indicated in the Mt. St. Helens subimage (Plate V-8), where only a few years of forest growth has diminished the once sharp contrast between tephra deposits and vegetated terrain.

8. As is evident in Table 3-3, space imagery is presently not well suited to recognizing the majority of volcanic features whose critical dimensions are less than the effective resolution of the sensor system. This group of phenomena include pahoehoe, blocky, and aa lavas, plug domes, tholoids, spatter cones, hornitos, pit craters, many dikes (and dike swarms), and nearly all other small features. Some of these are even difficult to locate and identify in aerial photos. Certain other smaller features—maars, diatremes, necks, lahars, and welded tuff units—can frequently be spotted in space images of adequate resolution.

9. Finally, under fortuitous circumstances, space imagery can capture a volcanic eruption “in the act” or can often provide the first direct evidence of the consequences of that eruption shortly thereafter. Plate V-8 offers a dramatic example in its extended coverage of the 1980 eruptions at Mt. St. Helens, during which a NOAA satellite actually picked up the airborne ash clouds in transit and after which Landsat provided the first complete view of the devastated area around the volcano. A lava flow in process of descending from one of the Galapagos volcanoes is visible in Plate V-13. New flows from eruptions at Mt. Etna (Plate V-16) in the 1980s are readily discernible.

ORIGINAL PAGE IS
OF POOR QUALITY

Table 3-3
Volcanic Forms and Features

Types of Surface Features	Selected Examples
Domes and Cones of Basaltic Lava	
Basalt Cones +	San Francisco Volcanic Field, Arizona
Central and Fissure Vents	Haleakala, Hawaii
Flank Outflows of Lava +	Mauna Loa; Etna
Basaltic Lava Shield (small) +	Skjaldbreidur, Iceland
Basalt Dome (shield) Structure +	Mauna Loa; Mauna Kea
Icelandic Spatter Cones	Búrfell, Iceland
Scoria Cones	Búdaklettur, Iceland
Lava Plateaus and Plains	
Ignimbrite Plateaus +	New Zealand; Yellowstone; New Mexico
Basalt Plateaus +	Deccan, India; Columbia, NW U.S.; Drakensburg, South Africa
Fissure Eruptions +	Lakiðígar, Iceland
Phonolite Plains +	Kenya; Dunedin; New Zealand
Basalt Plains +	Snake River, Idaho
Lava Fields	
Lava Tongues +	Galapagos, Ecuador
Ponded Lavas	Keanakakoi, Hawaii
Pahoehoe: Tumulis; Squeeze-ups; Pressure Ridges	Many
Block Pahoehoe	McCarty's Flow, New Mexico
Block aa	Mt. Vesuvius, Italy
Block and Ashflows	Martinique; Merapi, Java
Fire Fountains	Hawaii
Scoria Mounds (cinder cones)	Stromboli, Italy; Teahuahua, New Zealand
Adventive Cones	Mauna Kea, Hawaii
Exposed Intrusive Features	
Laccoliths +	Henry Mountains, Utah
Dikes, Sills +	Spanish Peaks, Colorado; others
Maars and Tuff Rings	
Maars +	Eifel, France; Lago di Nemi, Italy
Ubehebes	Death Valley, California
Basaltic Tuff Rings +	Diamond Head, Hawaii; Mt. Gambier, Australia; Hverfjall, Iceland
Diatremes +	Hopi Buttes, Arizona; Kimberlites, South Africa
Rifts	
Rift Valley +	Africa
Rift Lines +	Mývatn Area, Iceland; Tarawera, New Zealand
Craters and Calderas	
Craters +	Mt. Ubinas, Peru
Pit Craters	Nyirangongo, Kenya; Halemaumau, Hawaii
Calderas +	Mt. Vesuvius, Italy; Fernandina; Aso, Japan
Glencoe	Krakatoa, Indonesia; Aniakchak, Alaska
Krakatoa	Dyngjufjöll, Iceland
Multiple	La Palma, Canary Islands; Mauritius; Banks Peninsula, New Zealand
Erosion Calderas +	

Table 3-3 (Continued)

Types of Surface Features	Selected Examples
Viscid Lavas, Coulées, and Tholoids	
Convex Lava Flows	Ascension Island, United Kingdom; Mono Craters, California
Cumulo Domes (Tholoids)	Mayor Island, New Zealand; Puy de Dome, Auvergne, France; Tarawera, New Zealand
Obsidian Domes	Mono Craters, California
Plug Domes	Usu, Japan; Lassen Peak, California
Spines	Mt Pelée, Martinique
Tephra Showers and Nuées Ardentes	
Vulcanian Ash Phase	Mt. Vesuvius, Italy; Taupo, New Zealand; Katmai, Alaska
Nuées Ardentes (First Order) +	Mt. Pelée, Martinique; Valley of 10000 Smokes, Alaska
Plateau-Building (Ignimbrite Sheets) +	Bishop Tuff, California; Yellowstone Park, Wyoming-Montana
Nuées Ardentes (Second Order)	Mt. Pelée, Martinique; Santa Maria
Tephra-Built Stratified (with lava) Cones	
Ash Cones +	Fujiyama, Japan
Young Cones	Vulcan, Italy; Rabaul, Papua, New Guinea; Paracutín, Mexico
Composite (stratified) Cones +	Merapi, Indonesia; Mayon, Philippines; Agua, Guatemala
Multiple Cones +	Tongariro, New Zealand
Parasol Ribbing	Mt. Vesuvius, Italy; Paracutín, Mexico
Lahars (mudflows) +	Bandaisan; Galunggung, Indonesia
Erosion Features	
Ravine Cuts (Barrancos) +	Popocatepetl, Mexico
Planeze Stage of Dissection +	Cantal, France
Necks and Plugs +	Shiprock, New Mexico; Roche St. Michel, France; Hopi Buttes, Arizona
Erosion Caldera +	Huahine, Society Islands
Eroded Dome	Haleakala, Hawaii
Lava Ridges (Inverted Topography) +	Australia
Lava Palisades	Hudson River, New York

PLATE V-1

VOLCANISM IN SOUTHWESTERN UNITED STATES

This large-area ($490\,000 \text{ km}^2$) HCMM scene provides a synoptic overview of volcanic activity in the last 60 Ma dispersed over the southern Rocky Mountains, Colorado Plateau, Great Plains, and Basin and Range Provinces from Utah/Colorado southward into New Mexico and Arizona. Figure V-1.1 shows the same scene as imaged by the Day IR (thermal) sensor on HCMM. The Jemez Mountains (Valles Caldera) and Mt. Taylor field and the Hopi Buttes and San Francisco volcanic field are described in some detail in the next two plates. Other important fields are considered here.

The most continuous volcanic deposits in the scene are the San Juan Mountains of southwest Colorado (Lipman et al., 1972). There, a great pile (up to 2300 m thick) of lavas and ashflows emitted from various centers from Eocene into Quaternary has been carved by stream and glacial erosion into rugged mountains (elevations to 4361 m) that rival any in the Rocky Mountains in relief (Figure V-1.2). Especially evident in both visible and thermal images are three resurgent calderas—Silverton, Lake City, and Creede—resulting from expulsion of huge volumes of welded ashflows. All three are nested within the San Juan, Uncompaghre, and LaGaita calderas, whose larger collapse structures and outlines are difficult to perceive in the imagery. All told, 17 calderas have been identified in the San Juan field (P. Lipman, private communication).

Even more widespread but scattered volcanism occurs within the Mogollon-Datil field that extends through various mountain ranges in southwestern New Mexico into eastern Arizona. This Mid-Tertiary activity involves calc-alkaline intrusives and outpourings of andesites and rhyolites emplaced during three cyclic spasms, the last of which shows bimodal basaltic and rhyolitic affinities. The location of the volcanic deposits is difficult to discern in the Day VIS HCMM image; the darker patterns, which embrace some nonigneous rocks as well, are governed in part by distribution of vegetation. The thermal image better distinguishes the mountain uplifts, including the Gila and Blue Mountains, owing to cooler temperatures at their higher elevations.

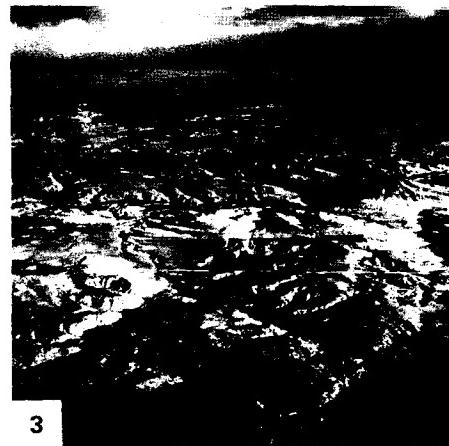
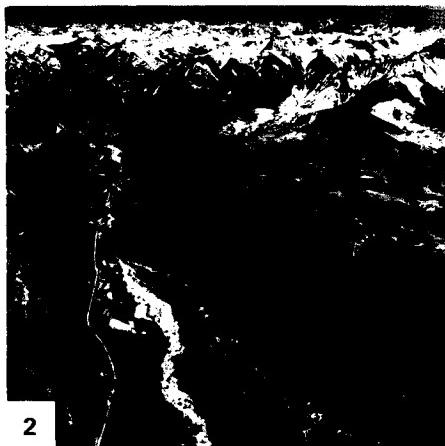
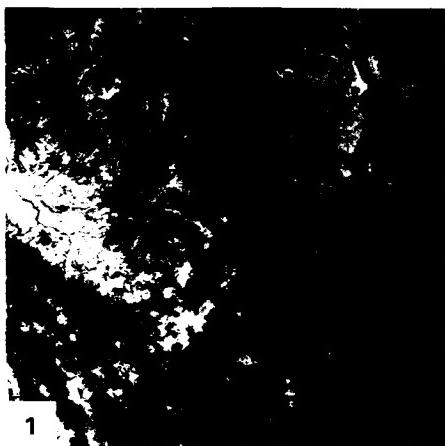
North of these mountains is the Datil Mountains physiographic section of the southeastern Colorado Plateau. Numerous lava-capped plateaus and mesas are common south of the Zuni uplift, where lava fields abound. The Day VIS image depicts one

young-looking series of dark flows (Suwanee and McCarty's flows) that, however, occupy much less of the mapped Quaternary extent of the field; even these are scarcely recognizable in the thermal image. The Mt. Taylor field (Figure V-1.3) is conspicuous in the Day VIS scene, and Mt. Taylor itself stands apart in the Day IR thermal image.

Exposed Tertiary intrusives make up the Navajo Mountains near the Four Corners area. The nearby famed Shiprock diatreme neck, with its radiating dikes, can be clearly seen in the Day VIS image because of the light-toned background, but shows only as a dark spot in the Day IR.

Volcanism is associated with the Rio Grande Rift, in some respects analogous to the East African Rift System. At the scene bottom (best noted in the thermal image) are the Quaternary cones and pipes of the Potrillo Mountains. Near the Rio Grande is the Socorro field, an older Quaternary basalt flow that stands out in lighter (warmer) tones. In the Tularosa Basin east of the rift zone, the Carrizozo basalt flow, a narrow Quaternary flow more than 60 km in length, is sharply contrasted in the Day VIS scene, but shows in only slightly darker tones in the Day IR. The Tertiary intrusives in the Carrizozo complex to the east appear as isolated darker blotches in both images. The Taos Plateau volcanics—a Tertiary field with calc-alkaline affinities—occupies the Rio Grande trench in northern New Mexico/southern Colorado, where a number of large hills carved from andesites and tholeiitic cones and plugs are major features of the landscape. To the east are the older (Eocene) Spanish Peaks (granitic stocks intruded into Tertiary and subjacent Mesozoic units), around which are many radiating dikes that are sharply visible in the enlargement of a Landsat TM band 5 scene (Figure V-1.4). To its southeast are the dissected basalt-capped mesas and plugs of Miocene/Pliocene age in the Raton section of the Great Plains.

This entire region thus offers well-preserved to remnant indicators of intermittent volcanism from Late Cretaceous onward. Volcanic rocks older than about 26 to 28 Ma are usually differentiated from calc-alkaline parent magmas. Christensen and Lipman (1972) and Lipman et al. (1972) have defined a significant shift thereafter to basaltic parents that dominate extrusives to the present. Their model for Cenozoic volcanism as related to plate tectonics is introduced in the next Plate caption. **HCMM 171-20240-1 Day VIS, October 14, 1978.**



ORIGINAL PAGE IS
OF POOR QUALITY

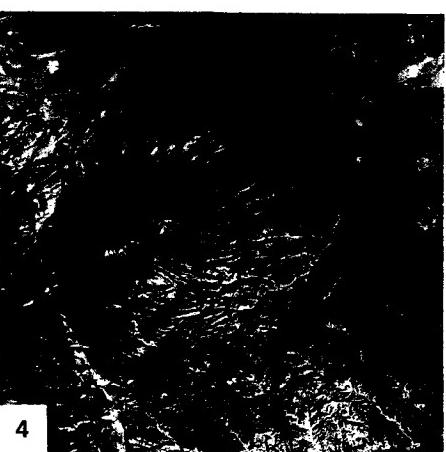
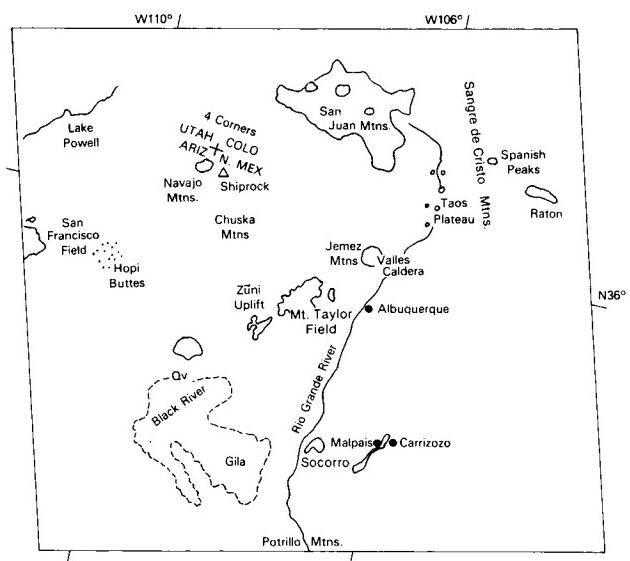
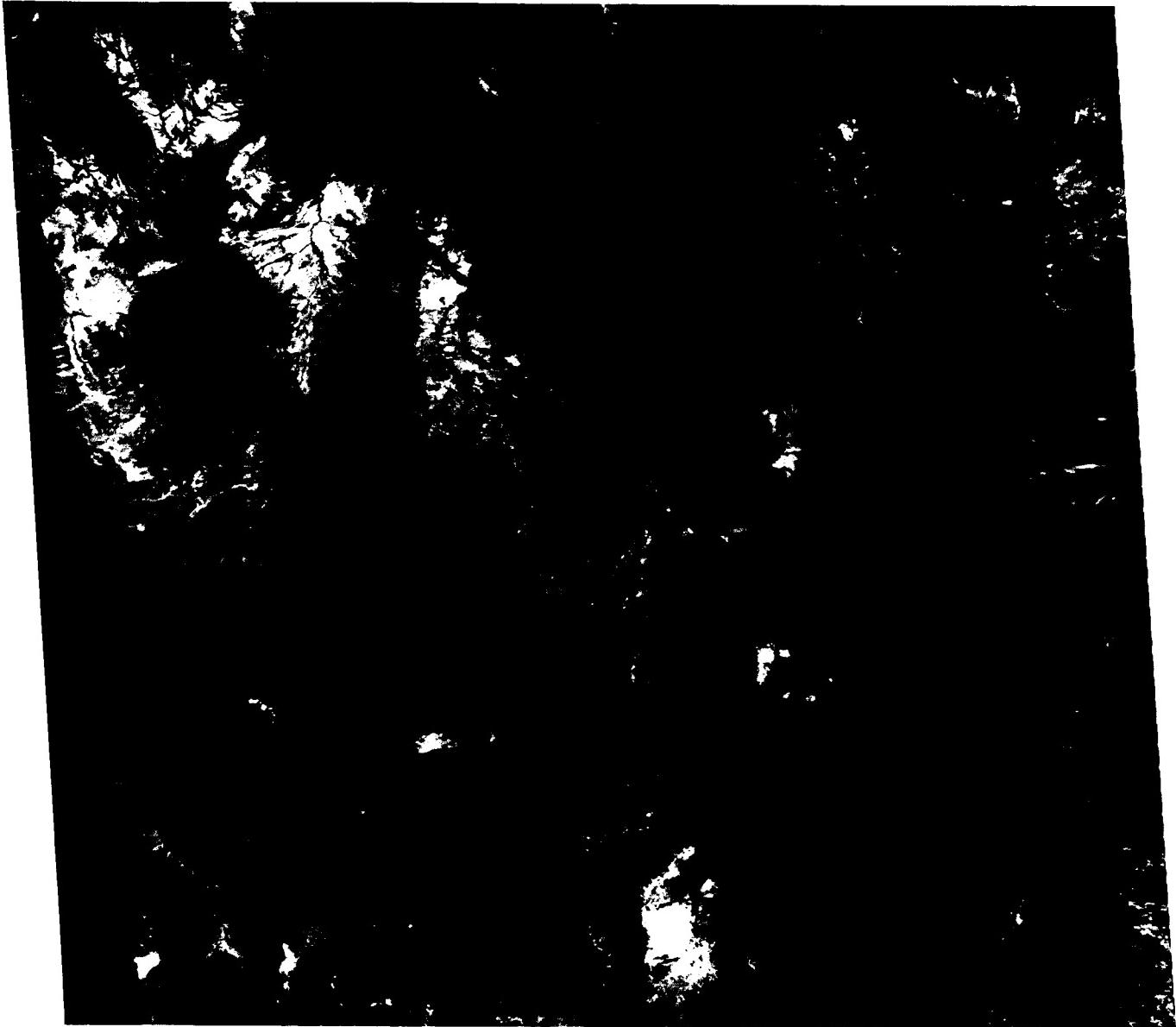


PLATE V-2

ORIGINAL PAGE IS OF POOR QUALITY

This image focuses on volcanic features in north-central New Mexico, the regional setting of which was shown in the preceding Plate. Dominating the scene and that in the oblique space photograph taken during the Apollo 9 Mission (Figure V-2.1) is the subcircular Valles caldera in the center of the Jemez Mountain volcanic complex about 70 km north of Albuquerque (Bailey and Smith, 1978). The central caldera, 19 by 24 km in rim dimensions, is the classic example of resurgent cauldrons as defined by Smith and Bailey (1968).

The Jemez Mountain volcanic complex is built on a basement of Precambrian igneous-metamorphic and Paleozoic/Mesozoic sedimentary rocks on the west and overlaps and interbeds with Cenozoic continental sediments that fill the Rio Grande Rift on the east (Ross et al., 1961). The abrupt escarpment along the western edge of the Sierra Nacimiento adjacent to the Jemez Mountains marks the trace of the Nacimiento Fault, a reverse fault that bounds a block of predominantly Precambrian rocks (Figure V-2.2). The volcanic field itself consists of material erupted from more than 100 vents. A variety of landforms, ranging from maar volcanoes to massive silicic domes, was created.

Jemez volcanism began about 10 to 12 Ma ago with the eruption of basalts, andesites, dacites, and rhyolites that continued until about 3 Ma, building up a broad thick (>1000 m) pile of flow units. Flanking the complex are several basalt fields, including the Santa Ana Mesa (south), Cerros del Rio (east), and Los Setos (north). At 1.7, 1.4, and 1.1 Ma, rhyolite magma erupted explosively, spreading thick ashflow deposits (Bandelier Tuff) that locally attain thicknesses of +300 m (Figure V-2.3) over the flanks of the complex. These successive expulsions of magma caused collapse of the roof of the magma chamber along ring faults, forming three nested calderas. Two of these, the Toledo caldera (1.45 Ma) and the Valles (1.09 Ma) are of nearly equal size. Only the youngest of these (Valles) has a well-defined morphology that forms a prominent depression. The cumulative thickness of volcanic infill within the calderas reaches 1 km on the west and 3.5 km on the east. Following the collapse of the Valles caldera, renewal of magma pressure in the underlying chamber caused uplift of the caldera floor and formation of a central resurgent dome. Accompanying this resurgent uplift, eruption of viscous rhyolite along the caldera ring-fault system resulted in extrusion of an arcuate ring of lava domes around the central resurgent uplift. Redondo Dome is transected by a northeast-

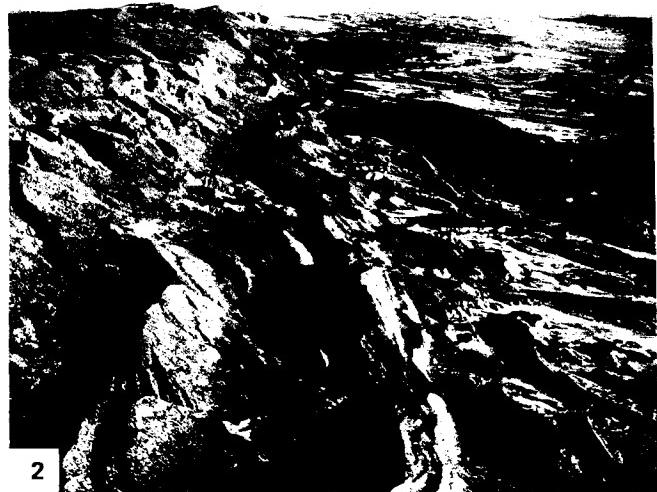
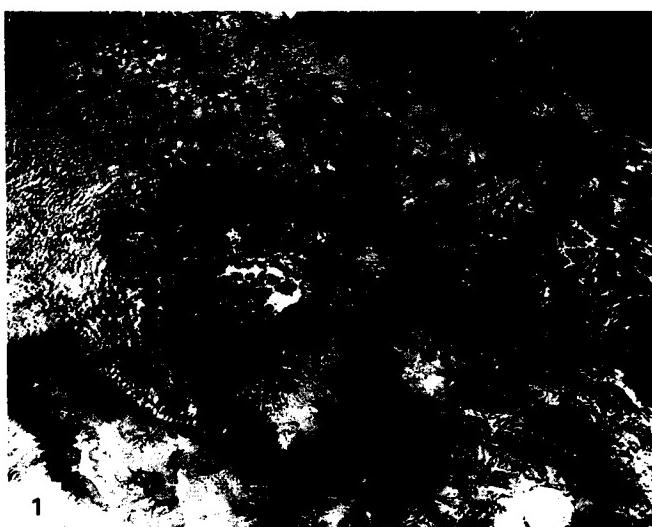
VALLES CALDERA

trending medial graben apparently controlled by older basement structures. Pleistocene erosion has cut deep radial canyons into the flanks of the complex. Cutting of the exceptionally deep San Diego Canyon on the southwest flank caused draining of a former caldera lake.

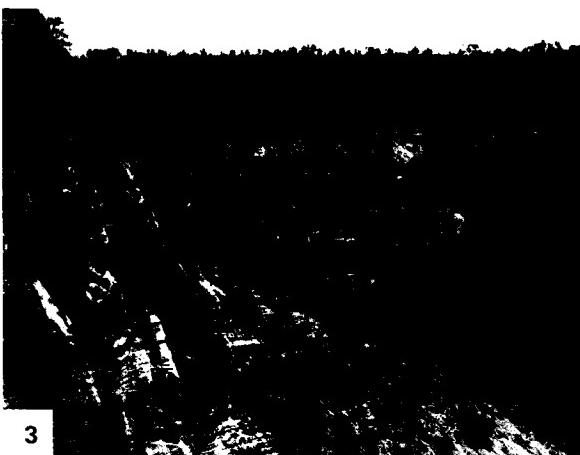
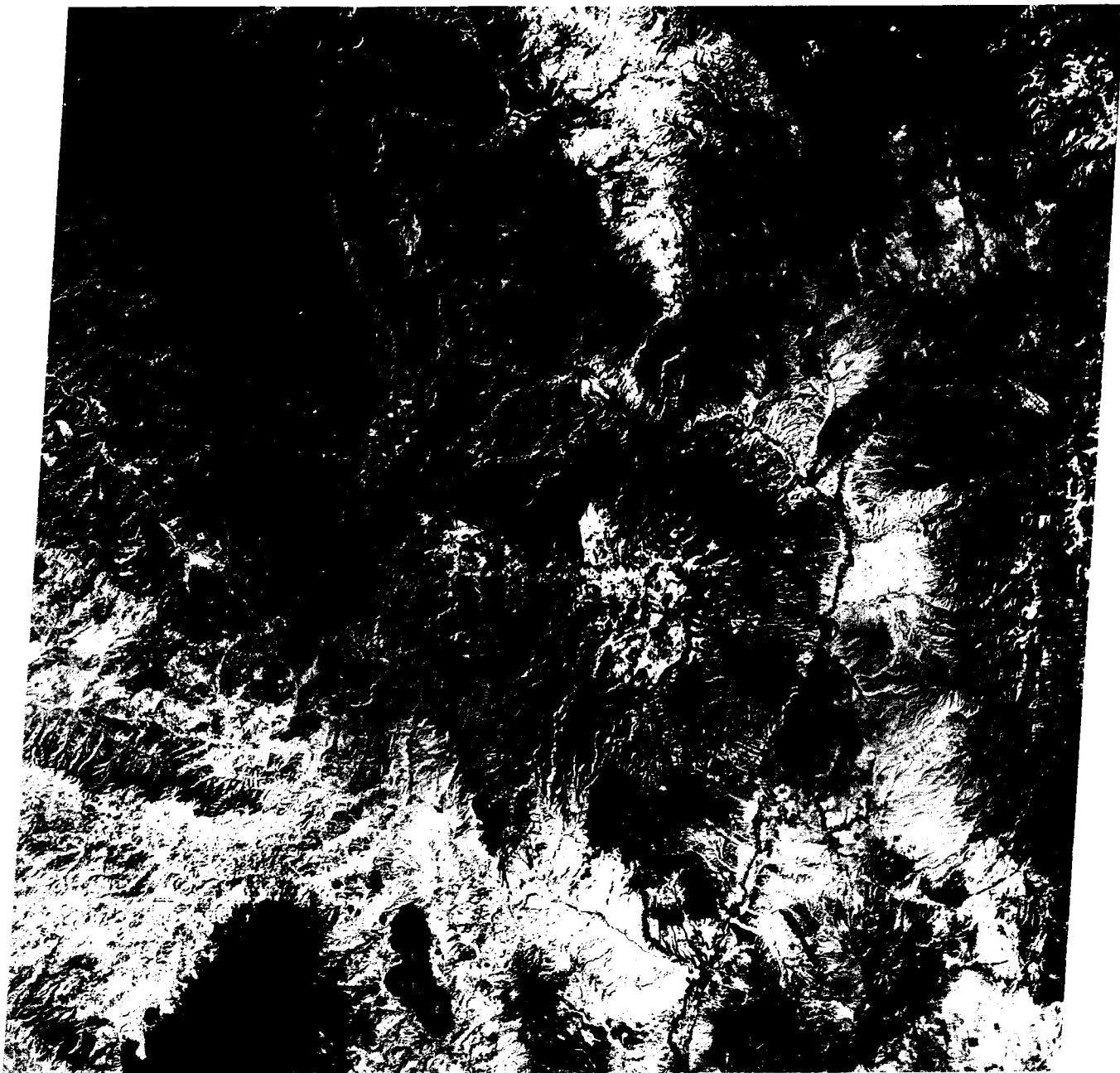
The intersection between the Jemez lineament and the Rio Grande Rift provided a structural control for generation and emplacement of the Jemez magma system. Other volcanic fields, including the Raton basalt field and the Spanish Peaks to the northeast, the Springerville field, and the Mt. Taylor field, lie generally proximate to the lineament. Several domical mountains and cones in the Taos Plateau volcanic field stand just west of the Rio Grande River in the Rift where it extends into Colorado. An Oligocene intrusive complex lies along the eastern rift margin northeast of the Sandia Mountains. North-south Tertiary dikes (barely visible in the image) cut Cretaceous and Tertiary sedimentary rocks along the northeast flank of the San Juan Basin.

The Mt. Taylor volcanic field is another of the large Tertiary outpourings that concentrated along the periphery of the Colorado Plateau since the Miocene (Hunt, 1938). Basalts and other lava types extruded from its many central vents into Cretaceous sedimentary rocks, building up an unbroken plateau—the Mt. Taylor Mesa—that extends 500 m or more above the surrounding terrain (see Figure V-1.3). Mt. Taylor itself (just below the bottom edge of the Plate) is a stratocone-shaped structure that towers to 3500 m above sea level. At the low Sun angle in this late Fall image, individual volcanic cones and necks, some of Holocene age, are discernible in the central mesa. Mesa Prieta is an outlier of this same field.

The Christensen and Lipman (1972) model alluded to in Plate V-1 proposed a plate tectonics control over volcanism in the southwestern United States. Prior to 30 Ma ago, calc-alkaline volcanism associated with the continental side of a subduction zone was predominant. Following deactivation of this zone as the North American Plate began to override the East Pacific Rise, bimodal volcanism—both basaltic and alkalic series—became the norm. However, the Jemez Mountain field may be an exception inasmuch as a wide range of magma types have been emplaced in the last 13 Ma. *Caption modified from comments by R. Bailey (USGS) and G. Heiken (Los Alamos National Laboratory, personal communication). Landsat 10856-17022-7, November 26, 1974.*



ORIGINAL PAGE IS
OF POOR QUALITY



3

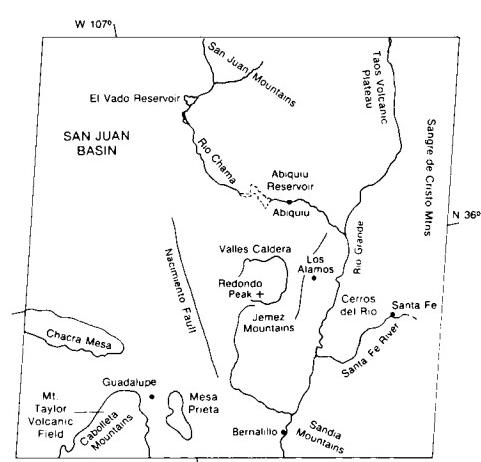


PLATE V-3

Late Cenozoic volcanism along the southern margin of the Colorado Plateau (Eastwood, 1974) produced two of the finest examples of small volcanic fields in the western United States. Large parts of each—the San Francisco and the Hopi Buttes fields—are portrayed in the lower half of the Plate image.

The San Francisco field (Moore et al., 1974; Updike, 1974) extends over 5000 km² in a section of the Plateau around Flagstaff, Arizona, capped by Permian sedimentary rocks. Three segments of volcanic outflows center around the San Francisco Peaks. The best studied of these segments lies east and north of the peaks. There, more than 175 individual cinder cones and associated flow units have developed during the last 6 Ma. These cones exhibit considerable variations in shape and height, depending both on the original morphology after they had completed their active phase and on subsequent erosive degradation. Figure V-3.1 offers a typical panorama of the cinder-cone field in the northeast. Many of the cones appear to be aligned in a north-northeast trend followed by the conspicuous graben at the north end of the Mesa Butte fault, one of several in the region that suggest that lineament control (ultimately in the basement rocks) has governed emplacement of magmas probably derived from mantle sources. This figure also depicts a second morphologic type, the maar depression, represented by Moon Crater in the foreground. The appearance of several cones is splendidly defined in an X-band radar image (Figure V-3.2) taken from an aircraft. The northern part of the field was also imaged by the L-band radar on Seasat. Tonal differences are correlated to some extent with the several ages of the flows; bright tones indicate considerable backscatter from rough fresh surfaces such as SP Crater (S on Figure V-3.3), one of the youngest in the field. Note that the nearby older flow at Black Point (B on Figure V-3.3) reflects as a darker tone that affords less contrast with other flows and surface gravels and alluvium.

Five episodes of volcanism have been identified and dated radiometrically, beginning about 5.5 million years ago and apparently ending in the last 1000 years (Moore et al., 1974). The principal outpourings are alkali olivine basalts. Consanguineous differentiates emplaced mainly in the last 0.7 to 0.2 Ma include andesites, rhyodacites, and rhyolites, extruded as domes, some

NAVAJO COUNTRY VOLCANISM

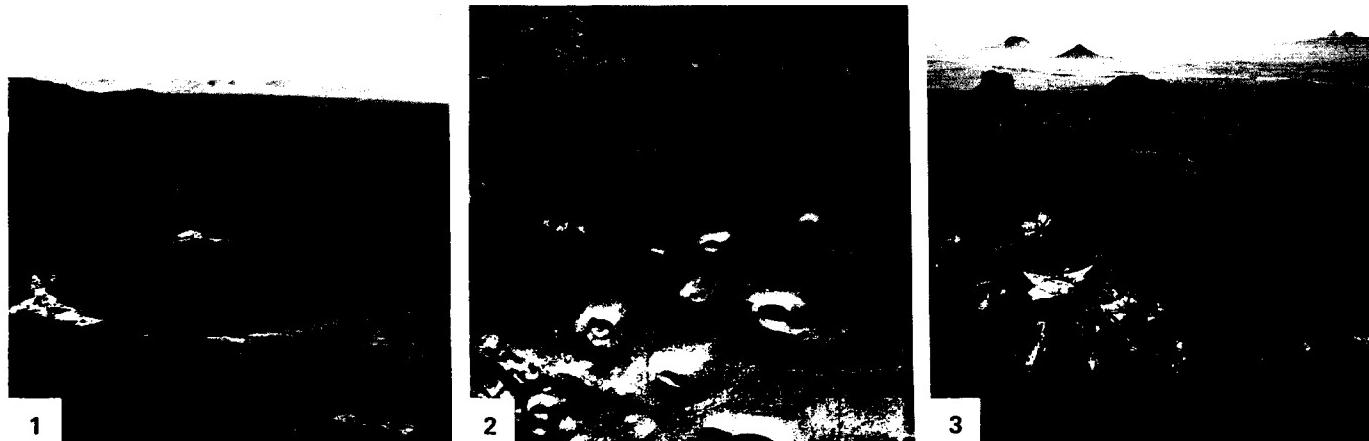
breaking on the surface as flows and pyroclastic deposits. One of several silicic eruptive centers is at O'Leary Peak (upper left in Figure V-3.1); nearer to Flagstaff, a much larger silicic volcano has formed the present San Francisco Mountains, now somewhat eroded by glaciation. A second center is at Elden Mountain, south of Humphreys Peak.

In this image, one can readily see Meteor Crater, a prominent white dot (sedimentary ejecta blanket surrounding the 1.4 km wide central depression). This impact structure is less than 25000 years old.

The Hopi Butte volcanic field (Sutton, 1974; Williams, 1936) stands out against a background of the Late Miocene/Early Pliocene Bidahochi Formation, a fluvio-lacustrine deposit resting on Mesozoic strata in the Painted Desert south of the Cretaceous uplands of Black Mesa. This roughly circular (radius ~30 km) field encloses about 200 individual eruptive centers, most isolated from one another (Figure V-3.4). Most prevalent are necks and plugs of volcanic rocks, now exposed as resistant central cores surrounded by remnants of sedimentary rocks and talus slopes. Buttes of sedimentary rock and volcanic ash capped by lava flow remnants are also common. A few maar craters are scattered through the cluster. Dikes, sills, and domes are also found in the field.

These volcanic features are related to a swarm of diatreme pipes tapping deep below the crust to bring up explosively expelled basic rocks. These rocks are chiefly alkalic lamprophyres (limburgite and monchiquite) that contain olivine, titanaugite, and analcime. During part of their activity, some diatremes erupted into lakes, and maar-type craters were formed. Erosion by the Little Colorado River has stripped away most of the cover, leaving exposed butte-like vent-fill pipes along several levels of valley terracing. Again, lineaments serve to localize the volcanic activity along two prominent northeast and northwest trends.

Note a faint, but traceable northeast streaked pattern on the Painted Desert bench surfaces. This also is suggested by notched indentations along the Echo Cliffs near Tuba City. The surface pattern seems to be affected by prevailing winds; the notch indentations may be a response of joint orientations to wind-affected erosion. Landsat 1103-17323-5, November 3, 1972.



ORIGINAL PAGE IS
OF POOR QUALITY

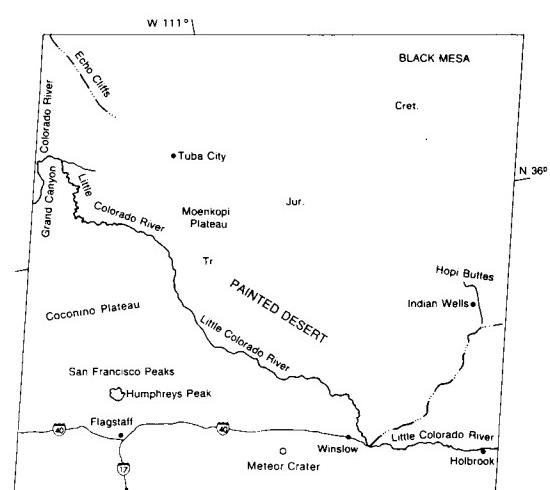


PLATE V-4

PINACATE FIELD

At the edge of the block-fault mountains of the Basin and Range and east of the Colorado River delta, the young Pinacate Volcanic Field intrudes abruptly onto the low desert terrain of northwestern Sonora state in Mexico (Wood, 1974). Seen in this Landsat TM image, the field is characterized by a continuous spread of coalescing basaltic lavas from numerous vents (more than 200 can be mapped on site), many still surviving as cinder cones. The field now extends over some 1500 km^2 in a crudely circular pattern, smoothed at its edges by aprons of erosional debris from the volcanic deposits. Dune sands from the Gran Desierto (see Plate E-11) have encroached from the west, and sand and alluvium reach its eastern side. Parts of the field remain only a few hundred meters above sea level, but the central field rises to a maximum elevation of 1303 m at the twin peaks of Cerro Pinacate (A) (Figure V-4.1). In this figure, note the presence of breached cinder cones, overlapping lava flows, and lava channels.

Of special interest in this field are the 10 larger ringed depressions that have been termed craters. Their names and locations are plotted on the index map, covering part of the scene, as adapted from maps in Jahns (1959). Most of these craters lie in an east-west trending zone along the northern border of the main field. Typical of these craters, although isolated off the zone, is Crater Elegante (B) (Figure V-4.2). This nearly circular depression has a maximum diameter of $\sim 1500 \text{ m}$ and a depth of 243 m. Its rim rises only a few tens of meters above the local level. The crater base consists of covered older volcanic rocks, followed by several basalt flows that dip gently away from the center. Overlying this is a sequence of cinder deposits, scoria, and basalt breccia, then about 50 m of tuff breccias and ash. These make up prominent rim beds that extend beyond the immediate crater, suggesting fallout and surge deposits of ejecta. Within the crater

are deltaic and lacustrine deposits of volcanic debris carried into the crater when it was occupied by a small lake.

Another landmark is Cerro Colorado (C), a young tuff ring with an outer dimension of 1600 m and an irregular rim rising to 110 m on the southeast. Unlike the other craters, this one displays only a series of tuff breccias that contain volcanic bombs and occasional metamorphic and granitic rock fragments. A salt unit lies near the base along the inner southwest wall.

These craters have been identified as maars by some investigators, implying explosive ejection as steam is generated from encounters between rising magmas and ground water. Foundering of the upper structure may have occurred as magma, on reaching the surface, vesiculated violently with escape of volatiles. Cerro Colorado resembles a Hopi Buttes type diatreme and may be just an incomplete step in the eventual collapse sequence. The other craters probably also passed through a diatreme stage before collapse.

The thermal image (band 6) of the Pinacates acquired by the TM 15 days earlier discloses several interesting phenomena (Figure V-4.3). The tonal contrast in band 5 between the (dark) volcanic field and surrounding (light) sands almost disappears in the temperature rendition. Generally, dark basalts absorb more incident solar radiation than lighter-toned rocks, and reradiated thermal energy therefore shows as higher radiant temperatures (light tones in band 6). Some of the fresher recent flow units in the eastern field indeed stand out as lighter thermal tones, but certain other dark flows do not. Individual cinder cones can be spotted in the thermal image because of bright-toned thermal highs along their Sun-facing southeastern slopes. *Caption modified from comments by C. A. Wood, NASA/Johnson Space Center. Landsat 40199-17332-5, January 31, 1983.*



ORIGINAL PAGE IS
OF POOR QUALITY

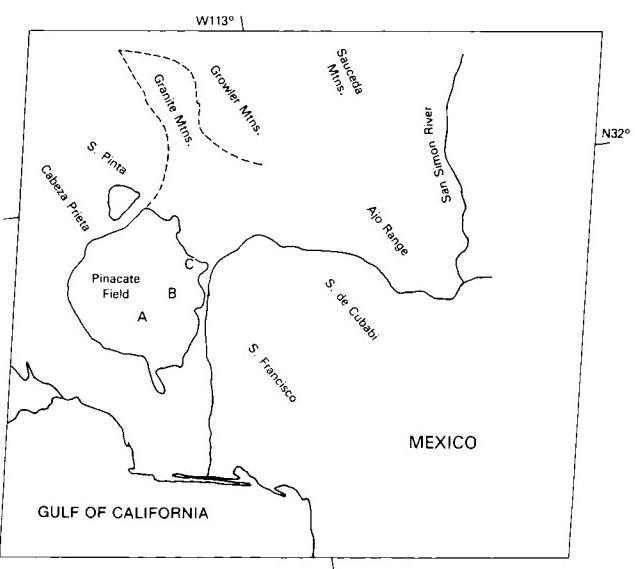
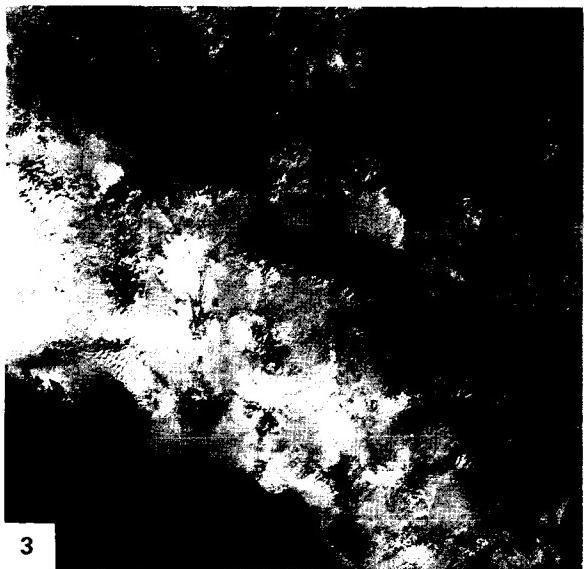
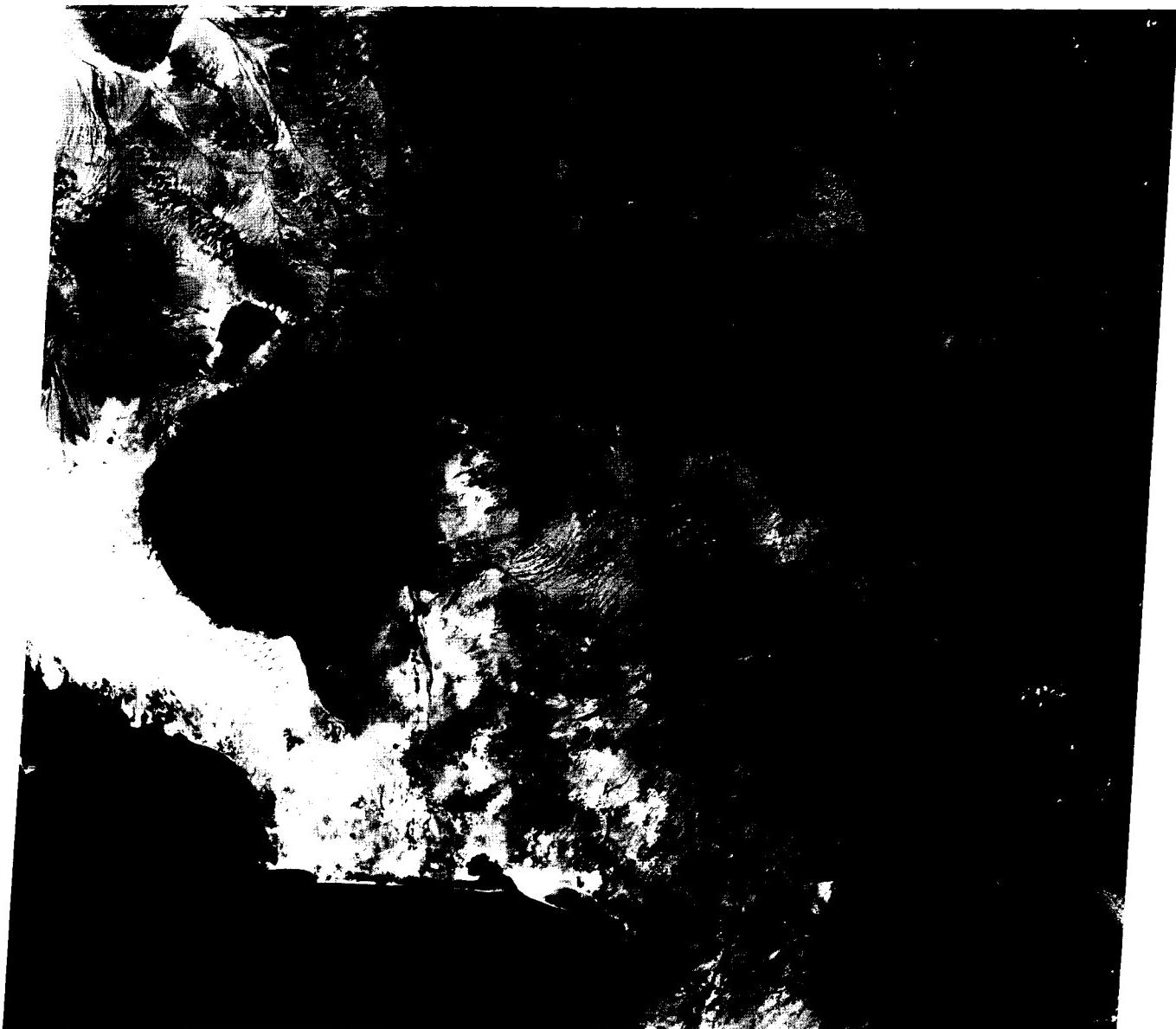


PLATE V-5

CENOZOIC VOLCANISM IN THE PACIFIC NORTHWEST

This large-area mosaic includes nearly all of Oregon and Washington and part of Idaho and southernmost British Columbia. Graphically depicted are much of the Idaho/Montana Rocky Mountains and parts of the Canadian Rocky Mountains on the east and north, the Cascades and Coast Ranges to the west, and the northern boundary of the Basin and Range on the south. The Columbia Plateau and other volcanic geomorphic subprovinces within the mosaic are located in the index map. The region has recorded several extensive episodes of major volcanism during the Late Cretaceous and continuing throughout Cenozoic time (Christiansen and McKee, 1978; Armstrong, 1968).

In the Cenozoic, sections of the Pacific Northwest have been marked by an earlier predominance of calc-alkaline volcanism into the Miocene with a gradual transition in places to bimodal basaltic-rhyolitic magmas. The Western Cascades have remained calc-alkaline since Mid-Miocene. Volcanic eruptions have piled up as much as 1.8 km of lava and tephra in the northern Great Basin, Columbia Plateau, and Snake River depression, covering up lower altitude (mature) topography west of the Idaho Rockies and leaving a few structurally deformed higher Paleozoic/Mesozoic mountain systems mainly in northern Oregon as projections above the general level.

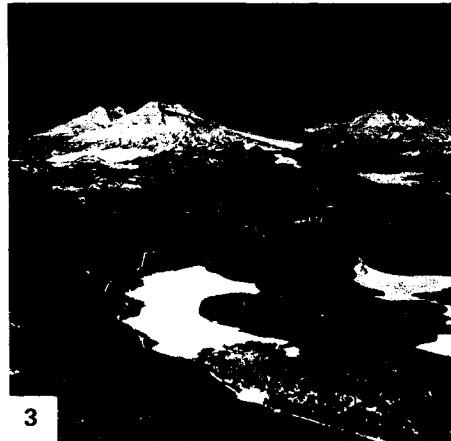
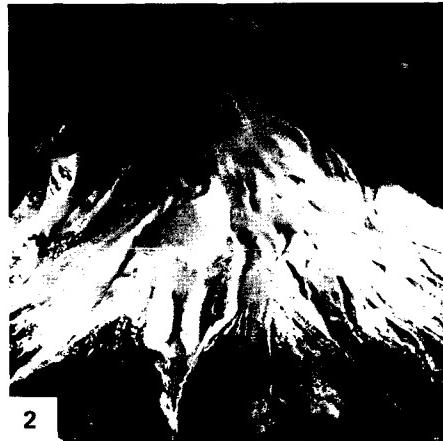
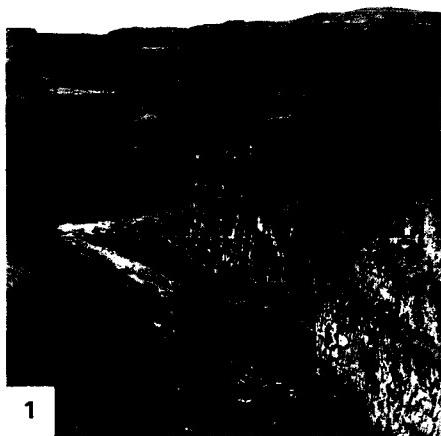
The earliest Cenozoic was generally a volcanically quiet time in the region except for submarine basaltic activity in the ancestral Coast Ranges and the Olympic Mountains. Widespread igneous activity commenced in the Eocene over much of northern Idaho and Washington, spreading southward with plutonic intrusions and large-scale surficial volcanism that culminated in the Challis episode (50 to 43 Ma). This calc-alkaline volcanism extended from the Absaroka Mountains of northwest Wyoming into southwestern Montana, the central Idaho Rocky Mountains and southern British Columbia, central Oregon, and the proto-Cascades and Coast Ranges. Another episode of relative quiescence followed for nearly 20 Ma, but the Cascade volcanic arc began to take on its modern definition, and extensive volcanic ash and welded tuffs of the Oligocene/Miocene John Day Formation covered parts of the Blue Mountains/Ochoco-Wallowa Mountains in northeast Oregon.

Cenozoic volcanism culminated in great floods of tholeiitic basalt, mostly during a brief interval from 17 to 13 Ma ago (90 percent in 1 Ma), centered on vents east of the Pasco Basin of central Washington, which continued to sag as the lavas were

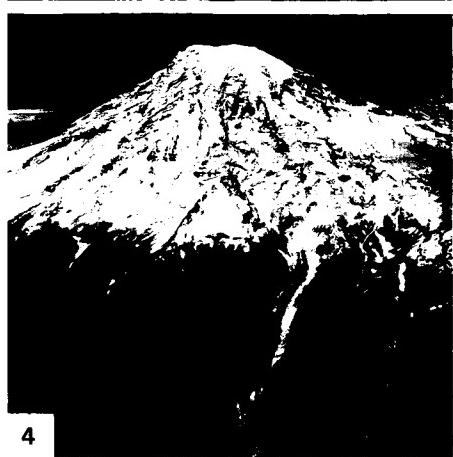
withdrawn. Successive flows, some up to 50 m thick (Figure V-5.1), spread from linear fissures over a wide area (presently, more than 400000 km²), with concomitant bimodal eruptions in eastern Oregon indicative of the transition previously mentioned. In the last 13 Ma, volcanism has concentrated in the southern Oregon/Idaho strip and the Cascades, principally during intervals from 10–8, 7–5, and 2 Ma to the Present. Much of the modern landscape around the volcanic centers evolved during these times. The period also witnessed extensional tectonics in the Great Basin (Basin and Range) to the south, high heat flow and crustal thinning, and subduction-controlled Cascade volcanism (stratocones superposed on shield volcanoes) as the Juan de Fuca/Farallon Plates continued to subduct under the North American plate.

Volcanism continues today, although at a minuscule pace compared with some other segments of the Pacific Ring of Fire. On May 18, 1980, Mt. St. Helens (Figure V-5.2), one of the younger stratovolcanoes of the middle Cascades, blew its top (reducing its height by more than 300 m), after swelling for several months from upwelled magma. Triggered by a sudden failure of the summit's north slope, the volcano violently ejected great quantities of ash as a lateral blast. Other large stratocones, such as the Three Sisters in Oregon (Figure V-5.3) and Mt. Rainier in Washington (Figure V-5.4), have been sites of repeated activity in the last million years and are likely to be reawakened in the future.

From space, the landforms of the flatter sections of the Columbia Intermontane Province show few obvious signs of volcanism. The Columbia Basin is a region of moderate relief, fairly extensive soil cover, glacial erosion and aggradation, and loess deposition, largely masked by wheat farming and natural grass cover. Canyons caused by flood erosion (see Plate F-27) and coulees (now-abandoned fluvial canyons) offer some exposure of underlying lava units. Rugged, often spectacular terrain occurs within high country along the Snake River Canyon (in places more than 1500 m deep) and in the mountains of the Central Highlands. Not until the flows of the High Lava Plains (Plate V-7) are reached is a young volcanic terrain with many preserved primary features imposed on the landscape. *Caption modified from comments by N. H. Macleod, USGS. References: Christiansen and Lipman (1972), Harris (1976), Petersen and Groh (1965), Waters (1961). Landsat Band 5 Mosaic.*



ORIGINAL PAGE IS
OF POOR QUALITY



4

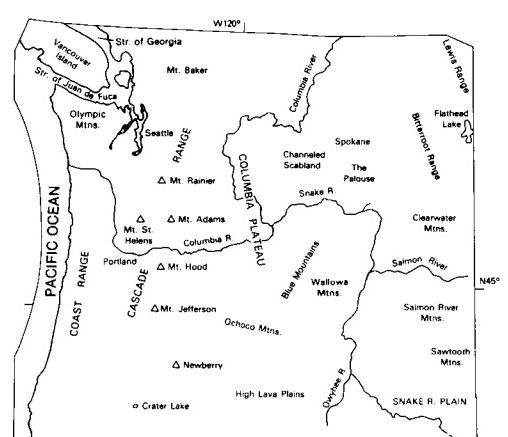


PLATE V-6

The west coastal states of the United States typify the landscape of an active boundary region in which the leading edge of a continent-bearing plate overrides or otherwise adjusts to a colliding oceanic plate. North of Cape Mendocino, California, a subduction zone exists below the nearby margin of the boundary between the North American and Pacific plates, and its presence in the Tertiary is evidenced in the structural and petrologic character of the terrains both at the coast and inland. From the northern Sierra Nevada northward into Canada, Cenozoic volcanism marks the continental edge of the landward side of the North American plate.

The right half of the scene lies at the southwest end of the High Lava Plains (Plate V-7); the southern boundary of the Columbia Plateau is just north of this image. In the Plains, northwest-trending faults and narrow rift fractures controlled the extrusion of volcanic rocks. Rocks of Lower Tertiary age intermix with younger flow and tephra deposits around Glass Buttes. The Fremont Mountains consist of dissected Pliocene flow units involved in extensive normal faulting. A series of close-spaced normal faults at (A) generated west-facing scarps in a higher plateau made up of Pliocene volcanic rocks between the depressions occupied by Summer and Abert Lakes.

The left third of the scene extends over much of the Cascade Range—a line of stratovolcanoes that occupies a position similar to volcanic edifices rising along modern island arc complexes (Harris, 1976). In the Early Tertiary, a series of andesitic eruptives produced during subduction were interposed within geosynclinal sediments to construct a thick pile of chained volcanic islands. Aggradational growth by continuous eruptions, together with intrusion and uplift, built the platform on which the present Pleistocene volcanoes form the High Cascades belt of lofty peaks that have experienced some stream and glacial erosion but retain much of their original form. Although activity seemingly has diminished, several volcanoes have recorded events within historic times.

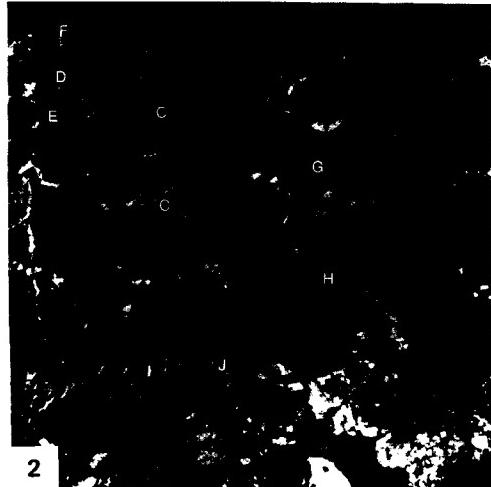
The catastrophic eruption of Mount Mazama about 6500 years ago produced a 9.5-km wide caldera depression now occupied by Crater Lake (Figure V-6.1), almost 610 meters deep, which

SOUTH-CENTRAL OREGON

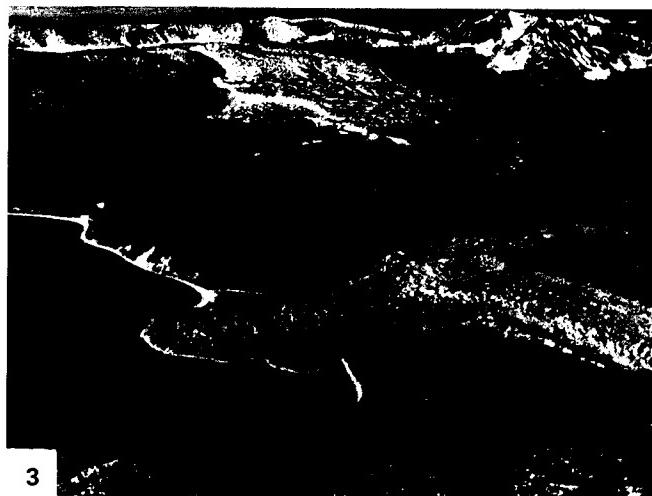
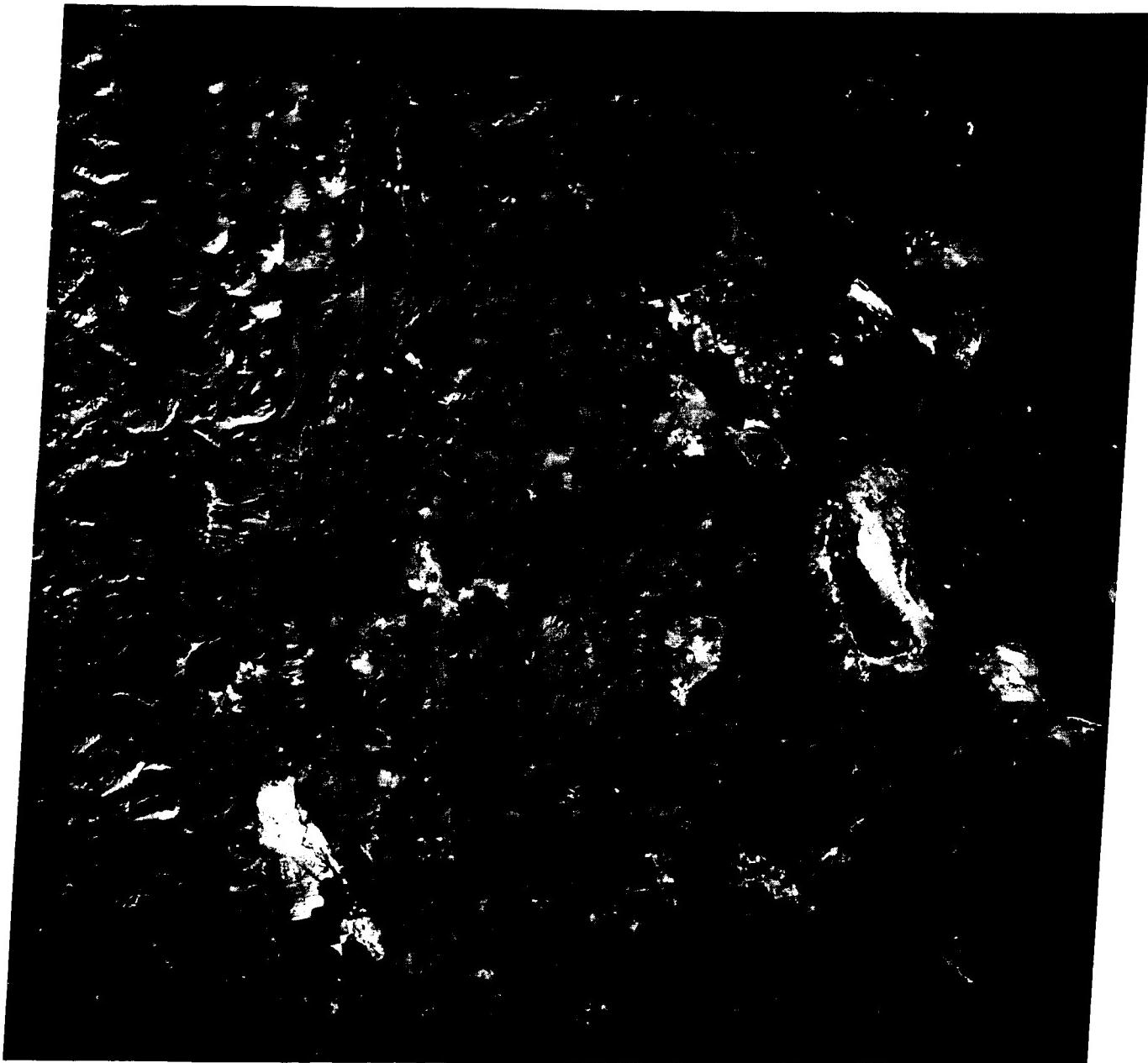
served as the type area from which Howell Williams (1942) developed his classic concepts on modes of caldera formation. Before its eruption, Mazama reached 3600 meters above sea level and had undergone extensive glaciation. Failure leading to climactic eruptions began as explosive ejection of dacitic pumice, along with invasion of lavas that formed domes and outflows. Later, violent eruptions released nuées ardentes and stratospheric ash clouds that carried tephra northeastward over vast areas. Almost 13,000 km² were covered by deposits thicker than 15 cm that still affect present surfaces, as at (B). Withdrawal of more than 70 km of wall rock, magma, and pyroclastics deprived the structure of internal support, causing collapse and further ejection of material.

Figure V-6.2 is a Landsat-1 enlargement of the area around the enormous Newberry Volcano, with a 32-km wide base, a shield structure located east of the main Cascade line (Williams, 1935). At its summit is a steep-walled caldera of 8 km maximum length, partially occupied by the Paulina and East Lakes (Figure V-6.3). The oldest rocks (~0.3 Ma) in its floor consist of rhyolites and basalts; basaltic cinder cones and obsidian flows also lie within. Numerous fissure-controlled basaltic cinder cones (C) populate both its north and south flanks. (Note also the light-toned pumiceous deposits along the south caldera rim.) Three prominent basaltic lava fields—Mokst Butte (D), Lava Cascade (E), and Lava Butte (F)—align along a 32-km long northwest-bearing fissure, from which they emerged about 6100 years ago.

Pleistocene and Holocene lavas extend eastward from Newberry, lapping against hills (kipukas) of older flow units at Pine Mountain (G) and elsewhere (Peterson and Groh, 1965). Even younger Recent pahoehoe flows at the Devil's Garden (H) and to the east retain fresh soil- and vegetation-poor surfaces pockmarked by collapse structures. During pluvial times, parts of these lava plains were filled with shallow lakes. Lavas approaching the surface, on encountering water, set off explosive eruptions that formed maars, as at Hole-in-the-Ground (I). Palagonitic tuff rims survive as eroded ramparts, as at Fort Rock (J). **Landsat 1094-18215-7, October 7, 1972.**



ORIGINAL PAGE IS
OF POOR QUALITY



3

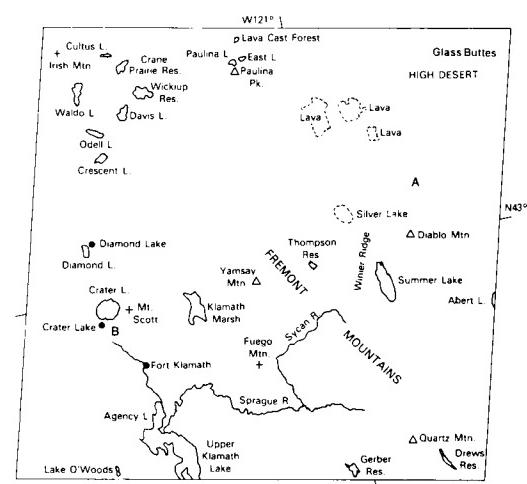


PLATE V-7

HIGH LAVA AND SNAKE RIVER PLAINS

The southern fringe of the Columbia Plateau and beyond contains some of the youngest basaltic flows in the Pacific Northwest. Much has transpired to reshape the landscape in the past 20 Ma. Along a line running from northern California/southern Oregon through southern Idaho into Yellowstone/Wyoming/Montana country, volcanism associated with tectonic deformation has created distinctive landscape elements. Christiansen and McKee (1978) ascribe this activity to the onset of extensional tectonics that ultimately has depended on interactions of the North American, Pacific, and Farallon plates and the northward migration of the Mendocino triple junction. This fostered a chain of heating events accompanied by widespread crustal foundering and block-faulting during regional uplift. This resulted in thinning, lowered rigidity, brittle deformation, basal crustal melting, and widespread outpourings of bimodal lavas (rhyolites and basalts) as extension afforded opportunity for relief of thermal stresses induced at depth. Both the High Lava Plains (Figure V-7.1) and the Snake River Plains (this Plate) to their east are astride the transition between the older Columbia Plateau volcanism and the younger Basin and Range faulting (with its sporadic volcanism) that runs south into Mexico (Christiansen and Lipman, 1972).

The oldest part of this southern volcanic province is the Owyhee Uplands, a series of isolated, dissected mountains and incised plateaus that contain rhyolites and latites. These grade into younger lavas, mainly basalts in the Boise/Malheur section of eastern Oregon/western Idaho, well exposed in deep canyons. The intermittent nature of the volcanic activity is illustrated by fine (often powdery) lake and river sediments interbedded with the basalts.

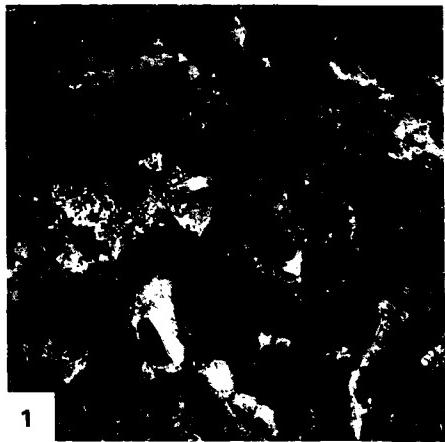
Most of southeastern Oregon contains lavas extruded in the last 10 Ma along northwest fissures cutting through the Harney-High Desert section of the High Plains (Robyn, 1979). The resulting countryside, as seen by Landsat (this Plate), is one of low-relief desert-like surfaces, fresh lava features, including cinder cones and lava-capped buttes (see Plate V-6), and ridges that show prominent fault scarps (step-fault terrain reminiscent of parts of the very young terrain in the Afar Triangle (Plate V-21)). The influence of the northern Nevada/California limits of Basin and Range topography carries over into uplift blocks such as Abert Rim, Hart Mountain, and Steen Mountain. Despite the youthful appearance of the terrain, as in the Great Sandy

Desert shown here, the volcanism traces its history back to about 17 Ma ago, continuing spasmodically until about 1 Ma ago, with subordinate basaltic flows in the Newberry Volcano area and pumice deposits from the Cascades since then.

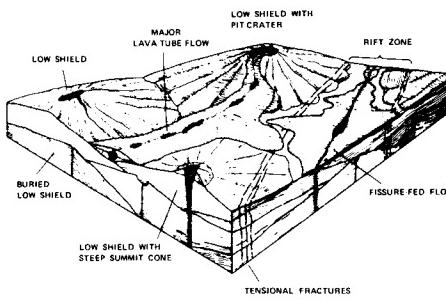
There is a progressive eastward shift in age toward younger volcanic outflows proceeding through the Snake River Plains. The older segment makes up a structural trough trending northward from the Malheur/Boise Basin east to Mountain Home, Idaho. Middle to Upper Miocene rhyolites/basalts have since been covered by lavas through the Late Tertiary. The Plains subprovince undergoes a deflection to the northeast through east-central Idaho, where a downwarp and faulting produced a trough that holds lavas as old as 14 Ma. Mostly olivine tholeiite lavas, several thousand meters thick, have accumulated under the Plains.

R. Greeley (1982a, 1982b) proposes the Snake River Plain as a new category of volcanic activity, which he terms basaltic plains volcanism, intermediate between plateau flood basalt and Hawaiian shield volcanism. This terrain is characterized by low shield volcanoes, fissure flows from point sources rather than linear sources, and tube-fed flows (Figure V-7.2).

Fissures, however, controlled extrusion at the Craters of the Moon Lava Field and the Wapi flow (Prinz, 1970). Lines of cones and spreading lavas (Figure V-7.3) concentrate along the Great Rift and Kings Bowl fracture zones. Details of the constructional surfaces in these quite young lava fields stand out in the aerial photo showing the north edge of the Craters of the Moon National Monument (Figure V-7.4). Flow ages in the larger field are qualitatively separable in the image by variations in darkness or gray level of the surfaces because these weather over time. Vegetation is sparse on these basalts, keeping soils at minimal thickness, as streams readily disappear into the porous fractured lava flows from which high-volume springs emerge. Subordinate rhyolitic volcanism in the Plains progressed eastward with time, culminating in the Island Park caldera complex at the east head of the Snake River Plains and the still-continuing activity at Yellowstone National Park that may have been driven by a mantle plume source at depth (see Figure 3-3 in the chapter introduction). *Caption modified from comments by R. Greeley, Arizona State University. Additional Reference: Leeman et al. (1976). Landsat 1358-17471, July 16, 1973.*



1

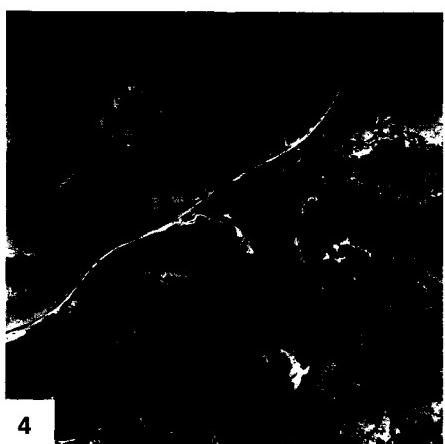
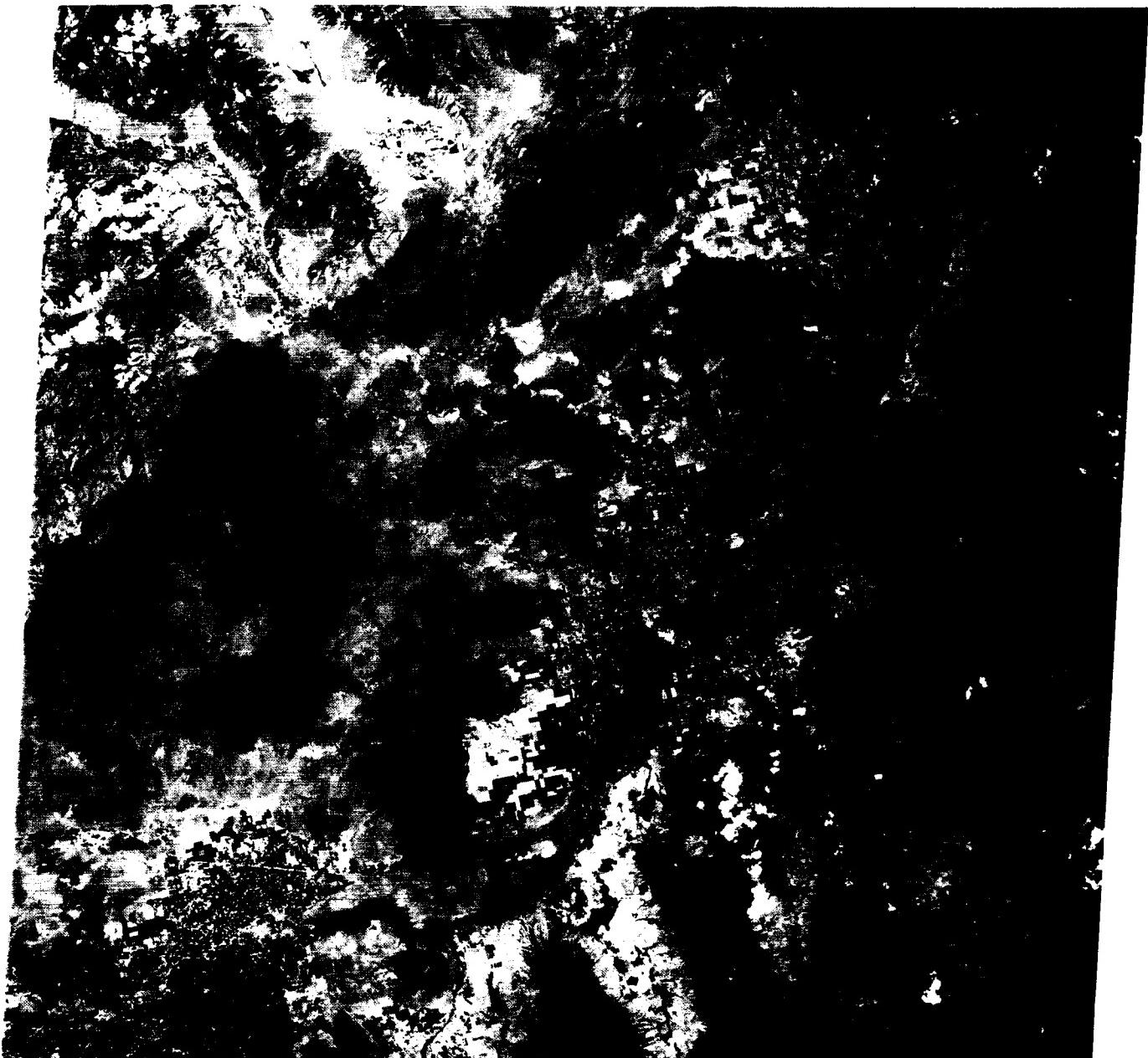


2



3

ORIGINAL PAGE
COLOR PHOTOGRAPH



4

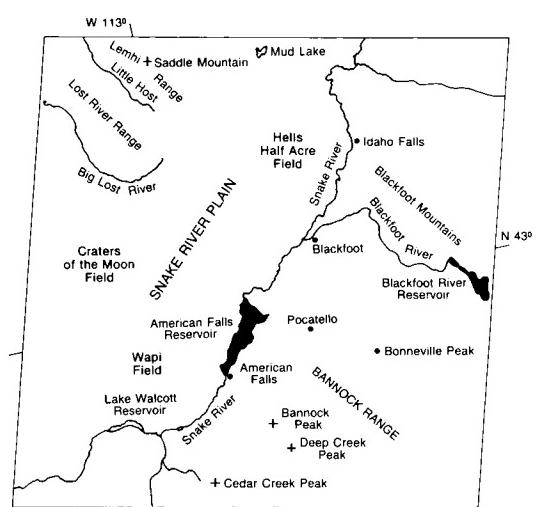


PLATE V-8

These next four pages are dedicated to a more comprehensive review of perhaps the best-documented volcanic eruption in history and of the role that satellite remote sensing has played in this study. On May 18, 1980, in southwest Washington State, on the western slopes of the Cascade Mountains some 75 km northeast of Portland, Oregon, in less than 1 minute, Mount St. Helens (MSH)—the youngest of the active andesitic volcanoes in the Cascade chain—blew its top in a dramatic and awesome sequence of events that took 60 lives, destroyed more than 200 homes, and exacted damage to the Pacific Northwest that exceeded \$1 billion. In addition to camera-wielding ground witnesses (several of whom perished), observers in light aircraft recorded on film the instant of eruption and most of the subsequent activity during the entire eruption phase. Scientists had been monitoring changing conditions at MSH for several months before the fateful day and had carried out numerous measurements during a continuing watch for several previous years. Because the day itself was crystal clear over much of the western United States, a NOAA Weather Satellite successfully tracked the initial and subsequent ash clouds as they progressed hundreds of kilometers to the east. Later that summer, both Landsat and the Heat Capacity Mapping Mission (HCMM) satellites obtained striking visible and thermal images of the scene.

The earliest dated eruptions at MSH began some 40000 years ago. Much of its growth to a composite stratocone reaching a pre-1980 altitude of 2975 m was accomplished in the last 4000 years. It experienced a strong eruption (4 km^3 of airborne ejecta) around 1900 B.C. Its last previous pulse of intermittent activity fell between 1831 and 1857, in which a new summit crater and an exogenous dome were formed. Because its record indicated that MSH commonly experiences major activity every 100 to 200 years, an eruption before the close of this century seemed likely to the several geologists studying this volcano. This threatened to disfigure one of the most symmetrical of the Cascade stratocones. (See Figure V-5.2, and Figure V-8.1.)

The first sign of reawakening was a notable Earth tremor on March 20, 1980, followed by a steam and ash eruption on the 27th that produced a small crater by steam “reaming.” Several phreatic eruptions, originating from the influx of snow meltwater into ascending magma, pulverized parts of the summit. That magma accounts for the gradual swelling (at 1 to 2 m per day) of the northern upper slopes as a magma pocket (or cryptodome) neared the surface. By mid-May, the bulge had risen about 150 m just above the 1857 Goat Rocks Dome, and reference points along it had shifted 100 m or more to the north.

The catastrophic eruption of May 18 began at 8:32:20 PDT with a 5.1-magnitude earthquake that apparently triggered the next reaction some 15 seconds later—a massive landslide or avalanche that tore open the summit as weakened rock slid as a debris flow along a detachment plane. First to fail was ground around Goat Rock Dome, then a second mass that included the pre-eruption crater broke loose, and finally the remaining section of the summit dome itself slid away. At 8:32:41, the first of several expulsions of fragmented rock (some blocks of house size), ash, and steam emerged from the old crater vent and the new gash along the flank (Figure V-8.2). Part of the rising cloud and the lateral blast combined into a surge that proceeded downslope at speeds up to $\sim 1000 \text{ km/hr}$, being directed mainly to the North Fork of the Toutle River, which flows west, and Spirit Lake to the north. The surge raced indiscriminantly over rough terrain for the next 30 seconds (Figures V-8.3 and V-8.4). Out to distances of about 12 km, the Direct Blast Zone is characterized by almost total tree upheaval from the dense coniferous forests along the slopes. Farther out to 19 km, the Channelized Blast Zone is marked by flattened tall trees, many of which fell like “match-

MOUNT ST. HELENS

sticks” in an array of parallel-aligned trunks (Figure V-8.5). For a few kilometers beyond, the lateral blast and surge singed trees in the Seared Zone.

Within 10 minutes of the beginning of the eruption, a mushroom-capped ash plume had risen to 18 km, well into the stratosphere (Figure V-8.6). The dispersing first cloud and a later ejection of ash are evident in the NOAA Weather Satellite image (Figure V-8.7) taken shortly after noon PDT. Parts of central and eastern Washington and neighboring Idaho were quickly blanketed by 3 to 7 cm of fine powdery gray tephra. Measurable traces of ashfall were deposited as far away as Minnesota, New Mexico, and an isolated pocket in Oklahoma. All told, 540 000 000 tons of ash came to rest over about 55000 km^2 . Fine tephra remained suspended in the upper atmosphere for several years.

Mudflows (lahars), formed as volcanic debris mixed with steam and water, moved out from the slopes within the first 20 minutes into nearby drainage channels such as the North and South Forks of the Toutle River to the west (Figure V-8.8) and Pine Creek to the southeast. Even the navigation channel of the Columbia River downstream from the Toutle River/Cowlitz River network was temporarily reduced from 13 to 4 m in depth by the choking mud debris. En route, mudflows may locally have surged up valley walls as much as 100 m, but their final deposits were much thinner. Phreatic craters (Figure V-8.9) formed where pyroclastic flows and lahars encountered pockets of trapped fluids.

After the dust cleared, the devastation wreaked by the May 18 eruption could be fully appreciated. The highest remaining section of the upper peak is now 400 m lower than the original summit; the rock at that summit point was dropped about 1000 m to the crater floor. The avalanche and subsequent blast left a crater 680 m deep and 2 by 3 km wide, readily visible from space (Figure V-8.10). Dispersed deposits from the debris avalanche have an equivalent volume of $\sim 2.8 \text{ km}^3$; another 1 km was entrained in the plume expulsions. The initial eruption devastated an area of about 20 by 30 km (east-west). The full extent of this damage, roughly coincident with the area of tephra deposits of 2 to 5 cm and thicker, is evident in the Landsat-3 image shown in the main plate. Multispectral Scanner (MSS) data from this July 31, 1980, scene were used to construct a supervised classification of several classes of deposits (Figure V-8.11); class colors are: blue = clear water; gray = silty (ash-laden) water; dark green = conifers; light green = other vegetation; aqua = ash-covered terrain, with trees down (also bare soil); purple = ash plus standing trees (deneedled); yellow = avalanche deposits; orange = mudflows; red = pyroclastic flows plus mudflows; and black = pumice flow. Earlier, the HCMM satellite obtained a thermal Night IR image of the MSH area on June 19, 1980. Using an internal calibration lamp within the sensor to estimate ground temperature, C. Bohn of NASA's Goddard Space Flight Center used a computer program to calculate a surface temperature distribution (Figure V-8.12). Highest temperatures (white-coded) occur at the crater and along a lobe (red) extending to Spirit Lake; lowest temperatures (black) are associated with snow still covering part of the peak. A thermal IR image (Figure V-8.13) made with an airborne sensor on July 22, 1980, shows surface temperature variations along a pyroclastic flow lobe. A remarkable airborne SLAR (X-band radar) image (Figure V-8.14) of MSH was obtained from a flight near the volcano just over 2 hours after it had erupted on May 18.

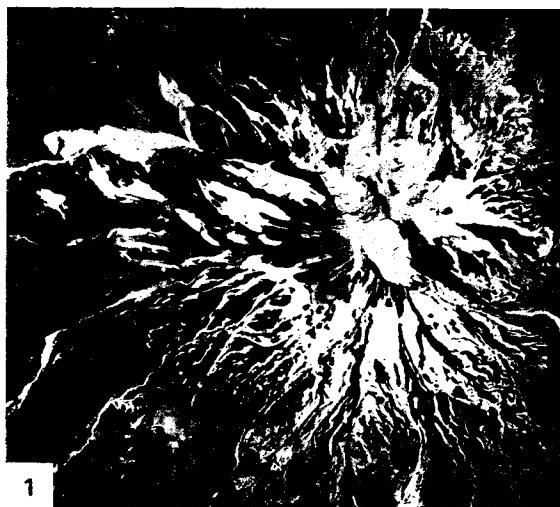
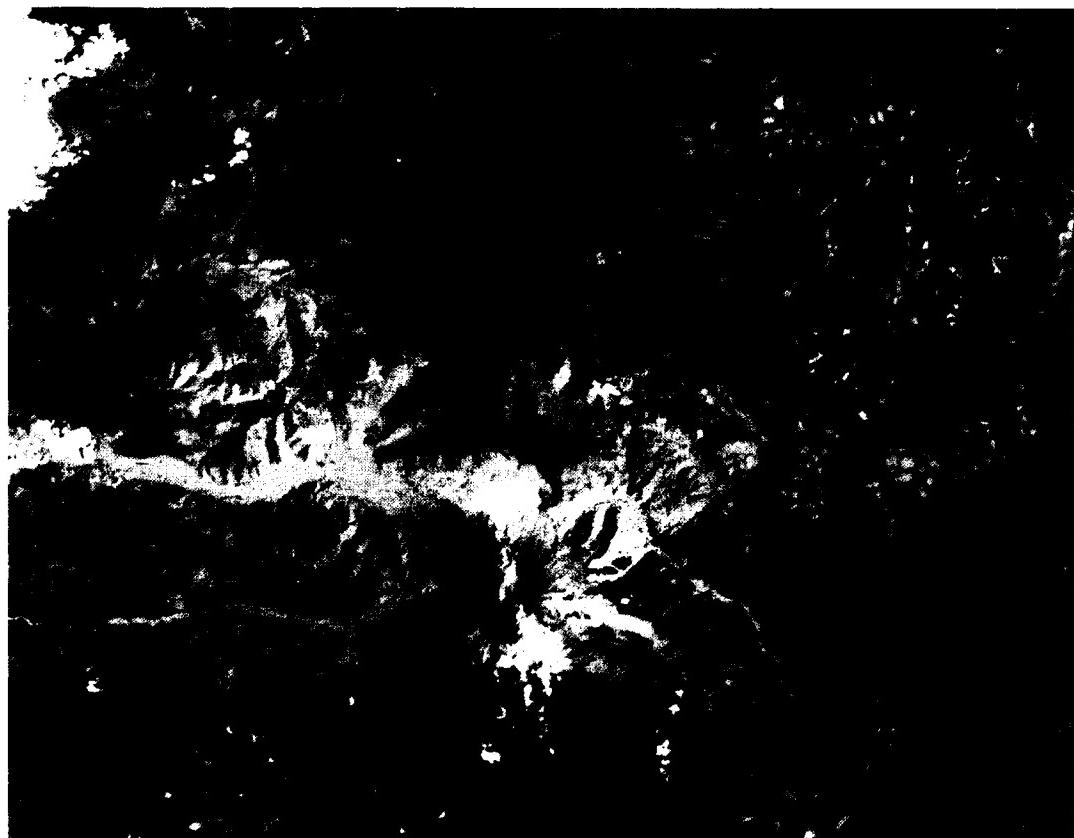
Mount St. Helens has continued to erupt through 1985. Another Plinean eruption took place on May 25, 1980, carrying ash toward Seattle, followed by still more smaller eruptions in June, July, August, and October. By the end of 1980, tephra in the devastation area had built to thicknesses of a half meter or

ORIGINAL PAGE
COLOR PHOTOGRAPH

more close in. By mid-June of 1980, a lava dome began to push up at the surface within the crater and has grown periodically to a height of 600 m since then (Figure V-8.15). The surface heat state of this dome in 1984 is depicted in a Thematic Mapper band 6 thermal image (Figure V-8.16). More than 800 m across, the dome is warmer than its surroundings.

By some standards, MSH was not a large explosive event. It compares with the 1586 eruption of Kelutin in Indonesia and Mt. Pelée (1902) on the Caribbean island of Martinique and was somewhat smaller than the famous 79 A.D. eruption of Vesuvius. It was much smaller (1 km^3 of airborne tephra) than Crater Lake's Mt. Mazama (42 km^3) or the great 1815 eruption of

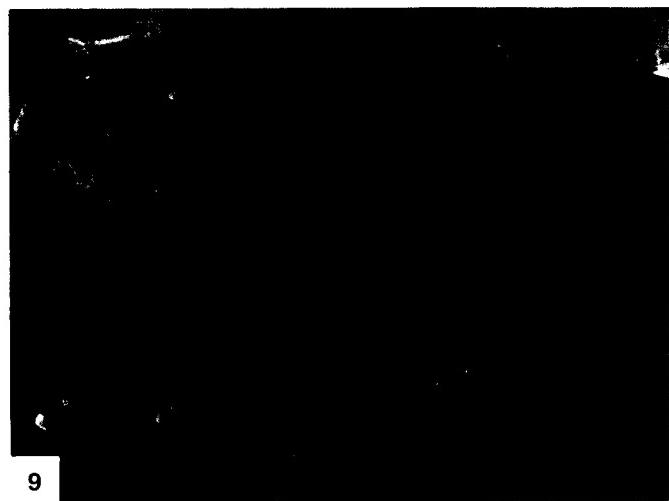
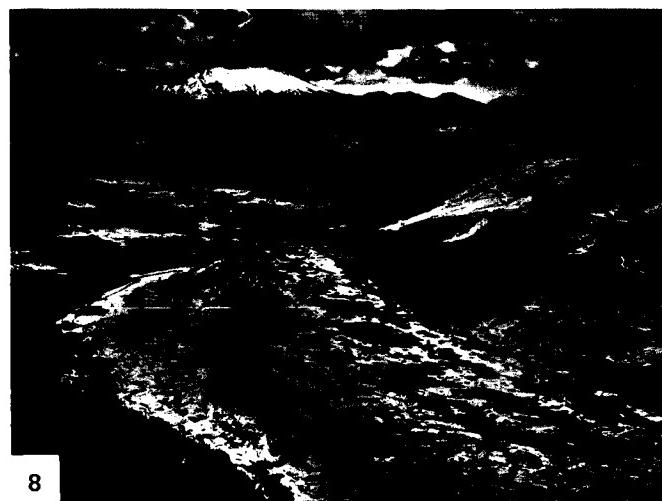
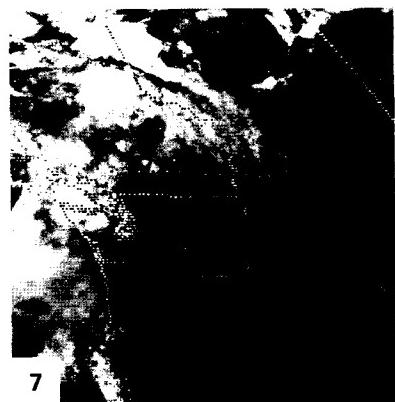
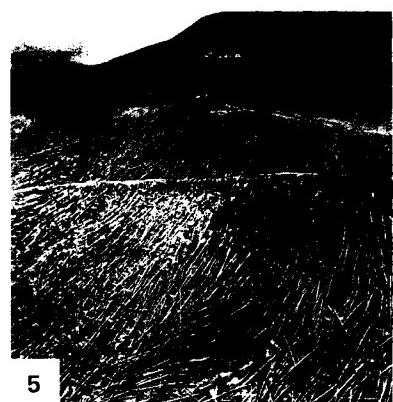
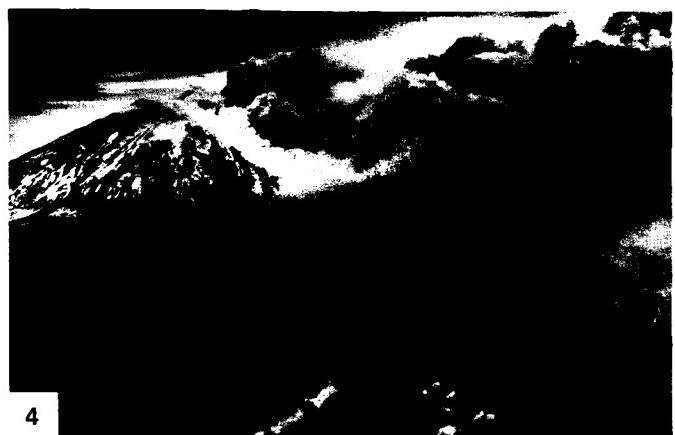
Tambora in Indonesia (80 km^3) and was inconsequential compared to the welded tuff-forming eruptions in the Yellowstone region and at the Valles Caldera in prehistoric times. Nevertheless, it remains in one sense the most spectacular of all famous eruptions in the thoroughness with which it has been recorded and studied. It is likewise a cogent example of how a dominantly constructional landform can convert almost instantly to one that has a look of total destruction around it. After only 5 years, however, the ecology around it has begun to revert to its past state. *Caption modified from comments by N. H. MacLeod, USGS. Additional References: Foxworthy and Hill (1982), Tilling (1984), U.S. Geological Survey General Information Bulletin. Landsat Subscene, July 31, 1980.*



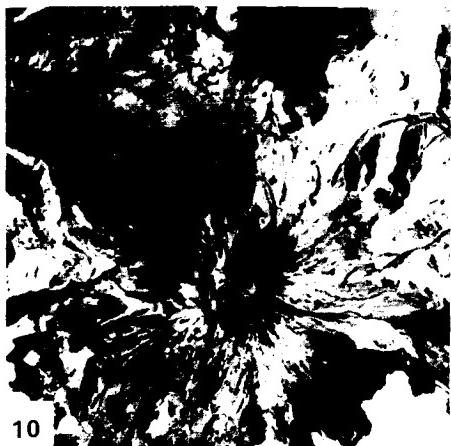
1

2

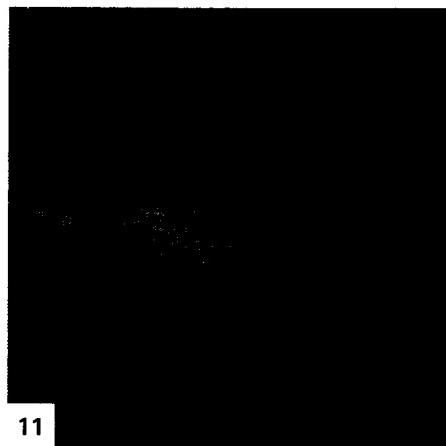
ORIGINAL PAGE IS
OF POOR QUALITY



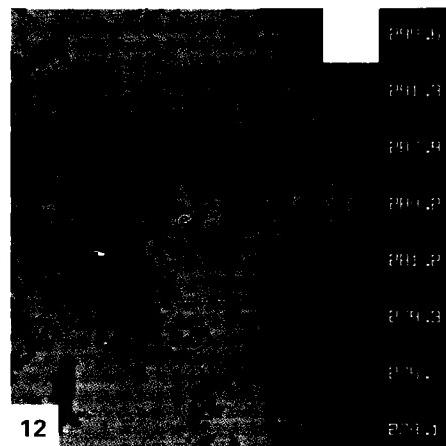
ORIGINAL PAGE IS
OF POOR QUALITY



10



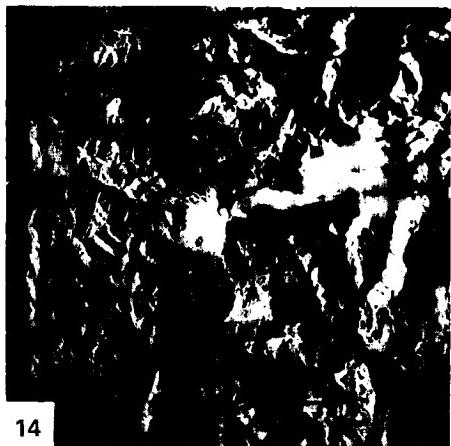
11



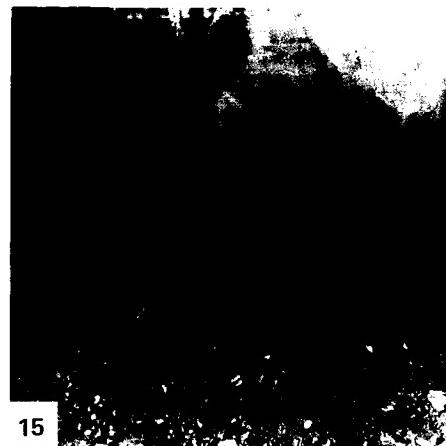
12



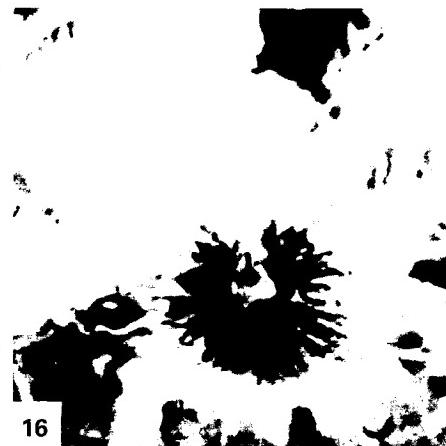
13



14



15



16

PLATE V-9

In several respects, the 3200-km long arc running from the Alaskan Peninsula west almost into Asia at the Kamchatka Peninsula is the classic example of a trench-bordered eugeosynclinal cluster of volcanic islands that fall on the continental side of a major subduction zone. The arcuate Aleutian Ridge, convex southward, rises subaerially to average heights around 650 m along a truncated surface, but on the ridge, the Aleutian Range reaches elevations in excess of 1200 m and some volcanoes exceed 2500 m (Lathram, 1974). The Aleutian Trench, near the top of the Benioff Zone, is deeper than 7000 m in places; in between is the seaward sloping Aleutian Terrace that bottoms around 4000 m at the trench hinge. On the north side of the arc is the Aleutian Basin, a back-arc basin that attains depths of 3500 m in the western Bering Sea. However, this arc/trench system differs from others, such as the Japanese and Indonesian orogenic belts, in lacking a well-defined outer nonvolcanic forearc basin and a paired metamorphic belt.

The present arc complex—the result of the plunge of the Pacific plate under the west margin of the (overthrusting) North American plate—began in the Cretaceous as ophiolites, oceanic sediments, and basalts collected in a constructional pile to thicknesses of 10000 m through the Early Miocene. Volcanogenic sediments and flows since then remain the dominant geosynclinal deposits. As the ridge built up above the sea, sedimentation patterns were shifted with the reduction of the Aleutian Basin. Basaltic volcanism prevailed in the earlier phases, with a period of quiescence in the Miocene except for emplacement of plutons, and resumption of active volcanism (calc-alkaline with andesites and some rhyolites) from Late Miocene to the Holocene. Folding followed by faulting, metamorphism to the greenschist stage, marked intermittent deformation that climaxed in an extended orogeny from Early Miocene to Late Pliocene. The Aleutian Ridge, which has undergone considerable vertical uplift, has remained stable since the Pliocene.

Tertiary volcanic centers and Quaternary andesitic volcanism are concentrated along four arc segments that are subdivided by transform fault zones running north-south in the Pacific Plate (Kay et al., 1982). Most Quaternary volcanoes are stratocones; some now have calderas that developed when ashflows carried

THE ALEUTIAN ARC

away the underlying supporting magmas. In general, the large volcanoes have associated tholeiitic lavas, but not typical island arc tholeiites; smaller volcanoes tend to be andesitic (Kay et al., 1982).

Both this Plate and the superb aerial radar mosaic (Figure V-9.1) highlight the Aniakchak caldera on the Alaskan Peninsula. This still-active volcano, once more than 2000 m high and nearly 40 km wide at its base, sits on a plains just north of the Aleutian Range, a folded sequence of Jurassic, Cretaceous, and Tertiary sediments mixed with volcanic tuffs, agglomerates, and flow units. The eruptive collapse (in Early Pleistocene?) that formed the present 9.5 km diameter, 1000 m relief crater, has expelled ash over 2500 km² to thicknesses of 100 m or greater in the pre-existent gullies and valleys on and beyond the original volcano. Ashflows actually move up onto slopes of the Aleutian Range. The glaciofluvial deposits that mantle the lowlands on the Bering Sea side are covered by this ash near the crater, as evidenced by the sharp decrease in numbers of lakes in the vicinity of Aniakchak. Aniakchak Crater (Figure V-9.2), whose nature was not fully discovered until it was entered by surveyors in 1922, is breached by the Aniakchak River that drains the small Surprise Lake at a gap called the Gates. Other volcanoes including the older Mt. Kialagak and the active Mt. Chiginagak fall along a line that serves as the central axis of this section of the Peninsula.

One of the most graceful cones in the Aleutian chain is Shishaldin Volcano on Unimak Island. This 2858 m high volcano has erupted more than 25 times in the last 200 years. A hint of this conical symmetry is evident in the Seasat L-band radar image (Figure V-9.3), but the layover effect distorts the form. The nearby older Isanotski volcano is more extensively dissected and is topped by an eroded (partially glacial) peak. On the south end of Unimak, Westdahl Peak shows its small circular vent to advantage in the radar view. A huge crater (18 by 11 km and about 1070 m deep), known as Fisher caldera, is possibly a remnant of a stratocone that released great volumes (20 m thick in places) of andesitic ash, pumice, and bombs that spread out in several directions through valleys and even up over the Tugamak Range (top center). Additional References: Miller and Smith (1977) and Smith (1925). Landsat 30341-20591-5, February 9, 1972.



ORIGINAL PAGE IS
OF POOR QUALITY

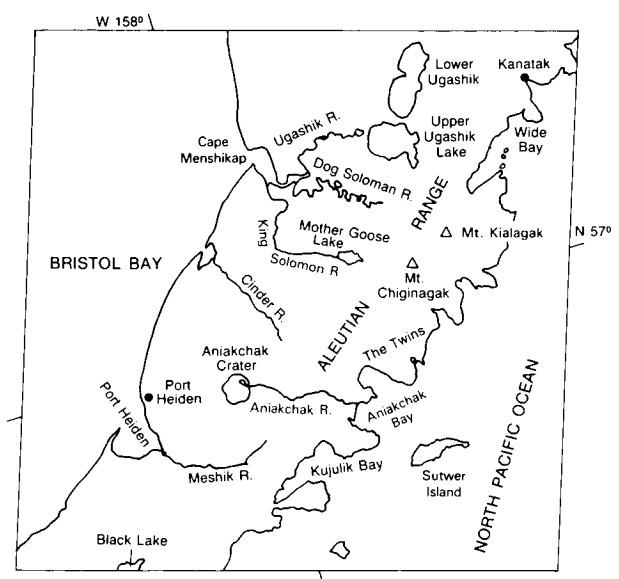
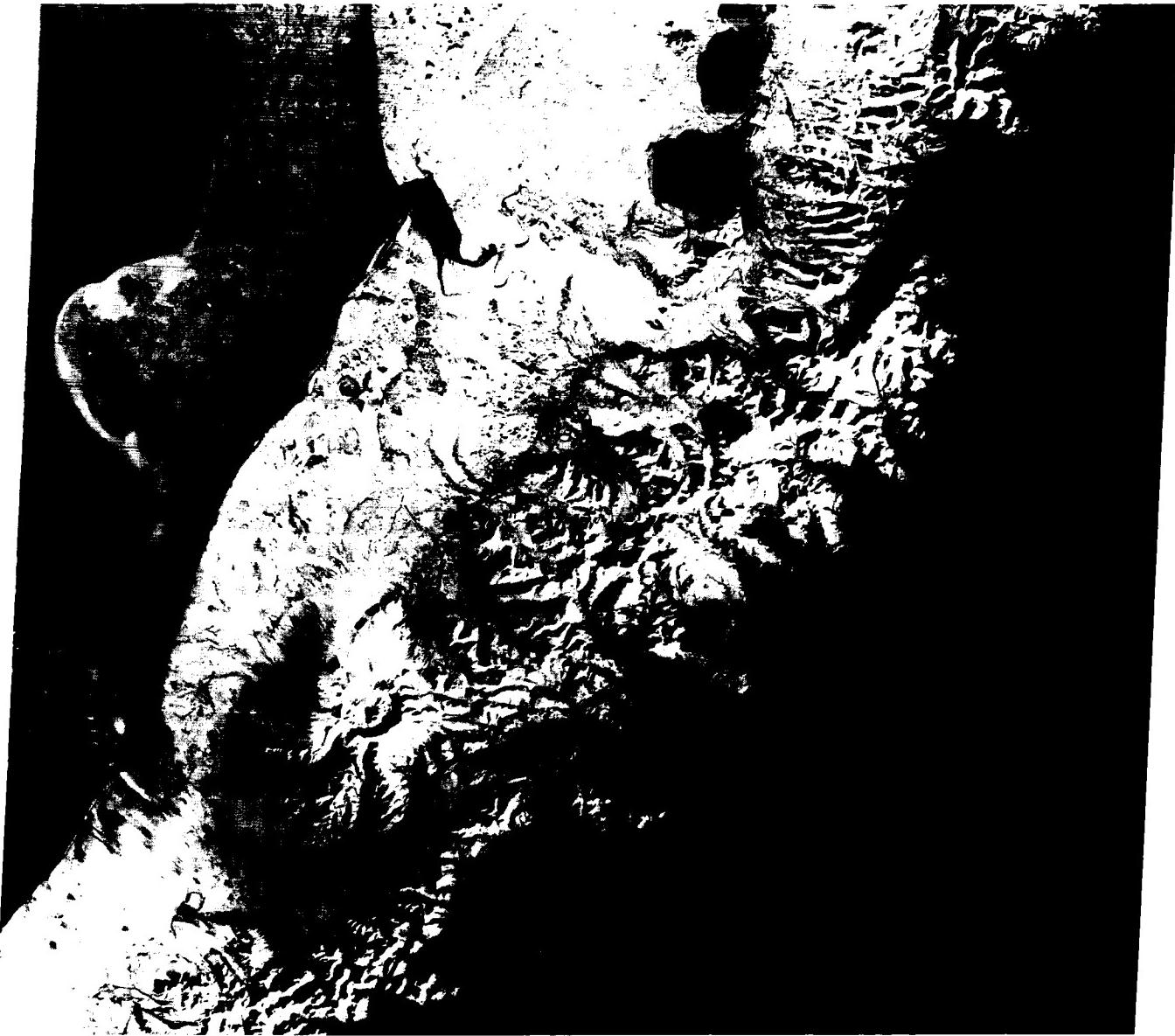


PLATE V-10

An impressive landform when seen from space, Hawaii is famous not only for its esthetic beauty, but also as the largest shield volcano complex on Earth. Its subaerial landmass rises 4135 m above sea level to its present elevation; it also extends 4900 m below the waves to the ocean floor. It is 140 km wide at sea level and even wider at its base and is aptly called the "Big Island."

Hawaii is at the southeastern end of a striking geographical and geologic feature, the Hawaiian archipelago. This consists of a broadly linear chain of more than 50 volcanic islands and submerged mountains stretching 4000 km northwest from Hawaii itself past Midway Island to the Emperor Seamounts, a chain of about 30 submerged volcanoes (Stearns, 1966). These seamounts form an "elbow" with the Hawaiian volcanic chain and then trend north-south for 4800 km, disappearing to the north in the Kamchatka Trench. The 80 or so volcanoes in these two chains came into existence more or less sequentially. Radiometric dating shows ages exceeding 70 million years for the oldest seamounts, but the Hawaiian Islands are far younger. Hawaii, the only island with volcanoes that are active in this century, is the youngest major volcanic pile, with ages under 700 000 years. (Maui has experienced activity in historic times.) Moving northwestward along the chain, the islands become progressively more weathered and decomposed.

Jason Morgan (1971) suggested that the cause or source of these shield volcanoes was a stationary hotspot in the Earth's mantle that created rising columns or plumes of hot light material that broke through weak places in the crust. The Pacific plate on which these volcanoes are built has slowly moved west over the hotspot, leaving a trail of volcanic islands. The bend in the chain where the Emperor Seamounts appear represents a direction change of the plate some 40 Ma ago.

A shield volcano is defined as a great pile of lava flows, normally composed of basaltic rocks, whose gentle slopes (2 to 10°) downward from a central highpoint give it a profile likened to a warrior's shield resting face up—well illustrated by Hawaii (Figure V-10.1). Thousands of layers of tholeiitic lava (higher in silica and lower in alkalis than average basalt) were laid down on the ocean floor until Hawaii reached its present height. This lava, not viscous enough to form steep cones, spread out at high flow rates from narrow surface fissures (rifts) that opened as pressure built up in the subterranean magma chambers.



1

ISLAND OF HAWAII

The island of Hawaii, amalgamated by the coalescence of five smaller shield volcanoes (most of the chain islands are composites), lies near the present position of the hotspot today (possibly under Loihi to the southeast). In chronological order, these volcanoes are: Kohala, Hualalai, Mauna Kea, Mauna Loa, and Kilauea. Erosion has already affected Kohala, but at Landsat MSS resolution, the others appear relatively fresh. The three oldest are apparently extinct, but the last two are very active; in fact, a recent major simultaneous eruption of Mauna Loa and Kilauea (a rare double event) occurred in March-April of 1984.

Many eruptive events on Hawaii over the last few millennia can be seen from space as light (older, more weathered) and darker (younger, fresher) streaks on its surface (Carr and Greeley, 1980). Most large dark lava flows along the flanks of Mauna Loa have happened in the last 150 years. Most Holocene eruptions of Mauna Loa take place as flank flows along rift zones (Figure V-10.2) identifiable at the surface as open fissures and by alignment of cinder and spatter cones constructed by episodic lava fountains. A huge oval steep-walled caldera, Mokuaweoewo, was formed by collapse at Mauna Loa's summit.

Directly to the east of Mauna Loa, a linear seam reveals where Kilauea has been welded to Mauna Loa as it grew. It was added primarily by eruptions from two rift zones, southwestward and eastward from its summit crater (Figure V-10.3). In the image, Kilauea's caldera stands out as an oval shape between dark lava streaks. The caldera formed by collapse of the volcanic pile along ring faults over a shallow magma chamber. Dark dots in the oval represent pit craters on the floor. The pit crater nearest the southwestern edge is Halemaumau (House of Everlasting Fire), which from time to time has contained a lake of boiling lava. Halemaumau is the traditional home of Madame Pele, the Hawaiian goddess of volcanoes. Residents of the island make offerings of her favorite drink, gin, to appease her and save their properties during threatening eruptions. Past eruptions of Kilauea varied from lava lakes in Halemaumau through short-lived lava flows within the crater or flank flows from fissures along the rift zones passing across the volcano. Spectacular lava fountains develop along these zones, sometimes reaching heights of 500 m or more (MacDonald, 1972). Occasionally, seepage of ground water into underlying heated rocks causes steam eruptions. *Prepared by Mary M. Kennedy. Text modified from comments by R. Greeley, Arizona State University. Additional References: Greeley (1974) and Macdonald and Hubbard (1970). Landsat Mosaic.*



2

ORIGINAL PAGE IS
OF POOR QUALITY

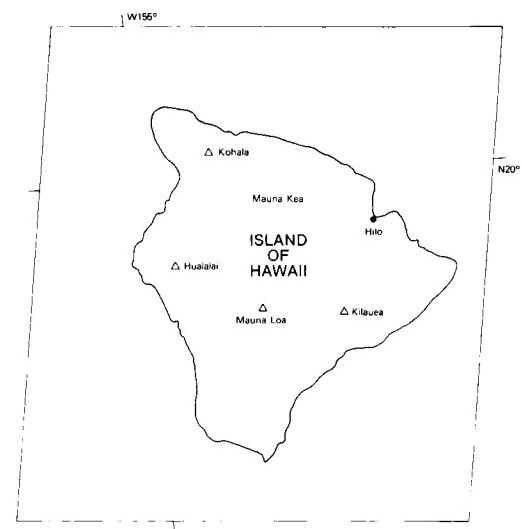
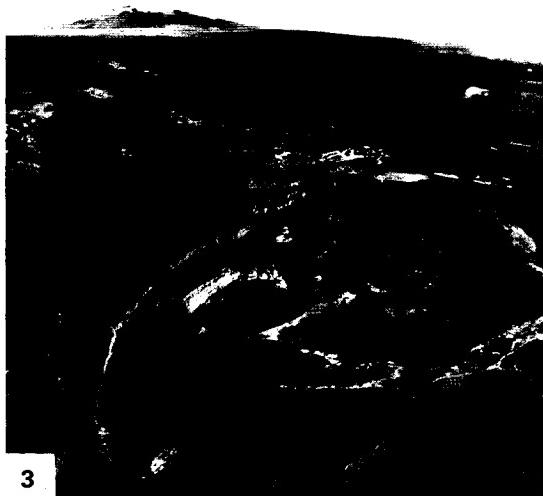


PLATE V-11

This scene displays a composite of landforms that fall into the volcanic, tectonic, and desert categories. Volcanism of Tertiary age abounds in the Big Bend National Park area and surroundings in Texas and extends across the Rio Grande River into northern Coahuilla and Chihuahua states in Mexico.

The tectonic framework for the scene places it in a structurally complex setting. The region lies along the eastern edge of the Mexican Cordillera adjacent to the Sierra Madre Orientale. On the Mexican side, the Sierra del Carmen and other ranges make up the Coahuilla Marginal Fold Belt (A), which lies between the Sabinas Basin (B) and the El Burro-Picachos Massif (C). The basin itself is the eastward extension of the Coahuilla Platform or Shelf (D). Numerous plunging anticlines (E), trending northwest, form strongly dissected mountainous terrain; some anticlines are breached (especially evident in the next scene to the south (Plate T-19). Similar anticlines (F) extend into the Big Bend country.

In the Trans-Pecos Texas area and to the north, three distinct periods of tectonic activity can be deciphered from structural and stratigraphic evidence. Paleozoic sedimentary units were involved in folding and thrust-faulting along a northeast-southwest trend that has been tied to concurrent activity in the Ouachita system. Cretaceous marine and continental sedimentary rocks, including numerous limestone units in the lower sections, and overlying sands and clays were strongly deformed during the Laramide orogeny that closed in the Early Tertiary. This affected beds within the central Park area, the Sierra del Carmen in the United States, and most of the nearby mountains in Mexico. Northeast-dipping thrusts follow the trend of the Santiago Mountains (G). Other contemporary structures include the Terlingua Monocline (H) and Terlingua (I) and Cow Heaven (J) fault zones. Block-faulting also began at this time, resulting in down-dropped segments (Sunken Block (K)) and uplifts (Mesa del Anguila (L)). These tectonic disturbances were accompanied by igneous activity

BIG BEND COUNTRY

expressed as sills and vent extrusions. The Early Tertiary witnessed deposition of clastics derived by erosion of Laramide terrain. From Middle Eocene throughout Oligocene, more than 1600 m of sandstones, clays, tuffs, basalts, and trachyandesites accumulated in the basins. Continuing Tertiary/Quaternary deformation produced broad open folds and normal faults along earlier lines of weakness, further tilting and raising the uplifts.

Most volcanic landforms here owe their inception to Tertiary volcanism that climaxed possibly by the Miocene. The general trend was mafic basalts (Lower Cretaceous to Mid-Eocene) — trachyandesites (Eocene to Early Oligocene) — riebeckite rhyolites (Oligocene and younger). The Chisos Mountains (Figure V-11.1), rising to 2410 m at Emery Peak, consist of pyroclastic and lava flow units mixed with tuffaceous sandstones and clays. These are topped by the Burro Mesa rhyolite and ignimbrite flows. The main event, of post-Burro Mesa age, culminated in numerous intrusions of granite, microgranites, and other silicic rocks into the Chisos Mountains (Sierra Quemada (M) and Ward Mountain (N)) and surrounding locations in the McKinney Hills (O), Paint Gap Hills (P), Grapevine Hills (Q), Rosilla and Chalk Mountains, and elsewhere. In Figures V-11.2 and V-11.3, the Solitario (R), a classic laccolithic dome, is shown close up from the air and the ground. Quicksilver deposits around Terlingua are associated with the volcanic activity. In the Cenozoic, extrusive volcanism was also widespread in northern Mexico, as around the Llano de Los Ranchos, and intrusives, including El Conejo, occur at (S) and (T).

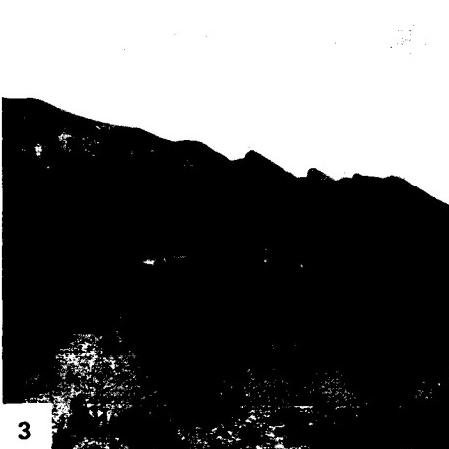
The volcanic areas show a variety of landforms developed by erosion of laccolithic hills and of caprock formed from resistant flow units. Spectacular scenery in and around the Big Bend is highlighted by several steep-walled canyons (Figure V-11.4) such as Santa Elena (U), Marsical (V), and Boquillas (W). Additional Reference: Maxwell and Dietrich (1972). Landsat 1816-16430, October 17, 1974.



1



2



3

ORIGINAL PAGE IS
OF POOR QUALITY

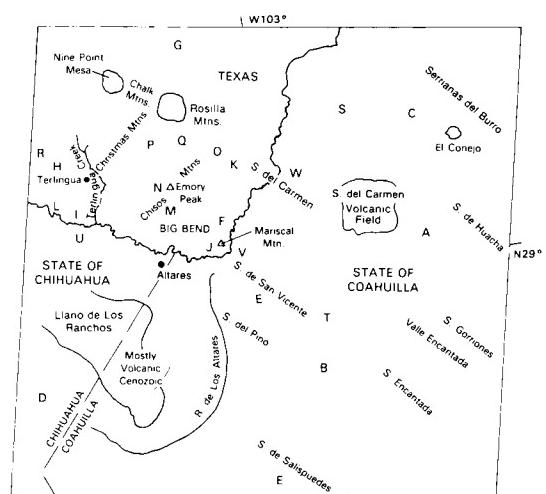
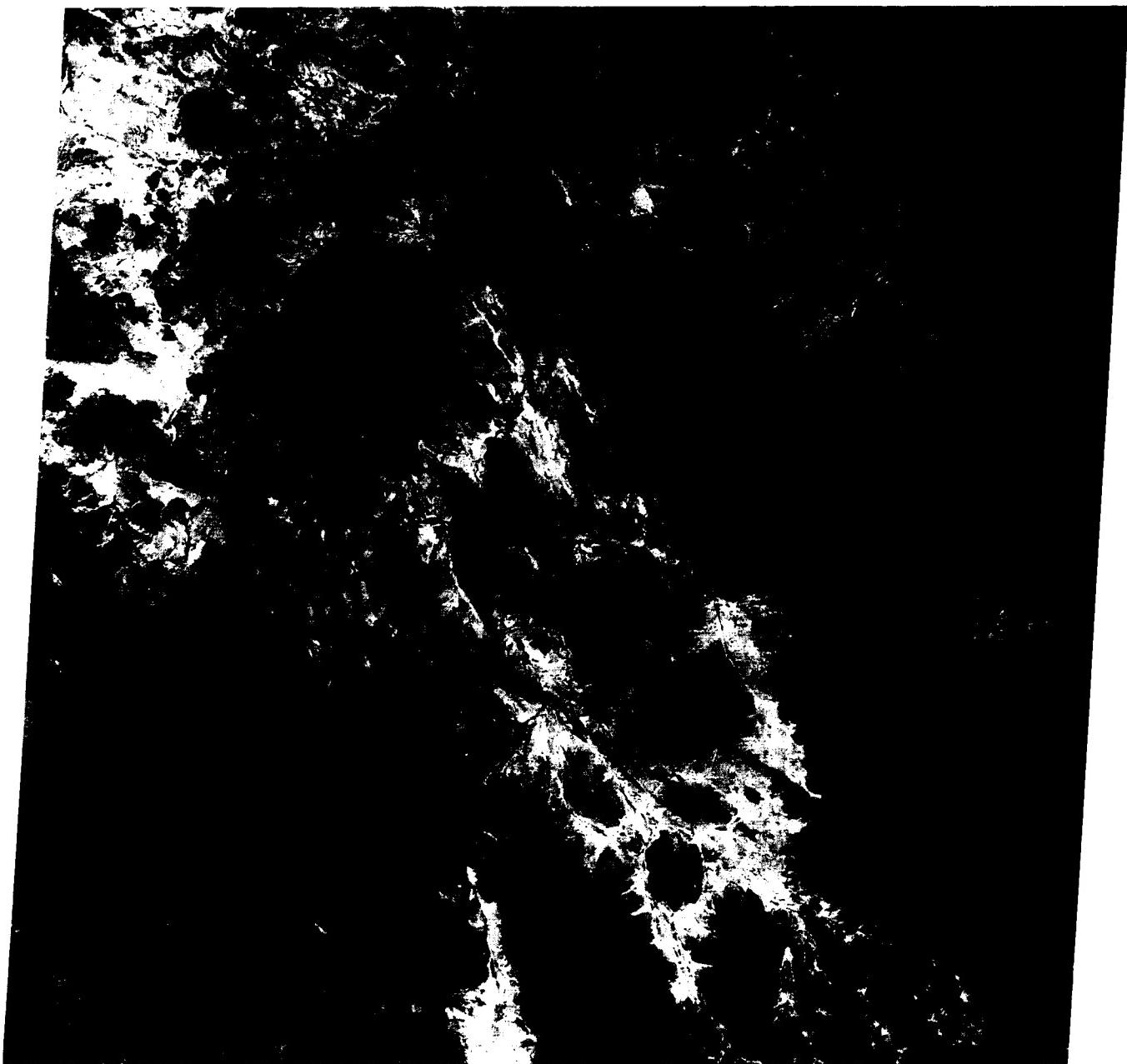


PLATE V-12

CENTRAL AMERICA

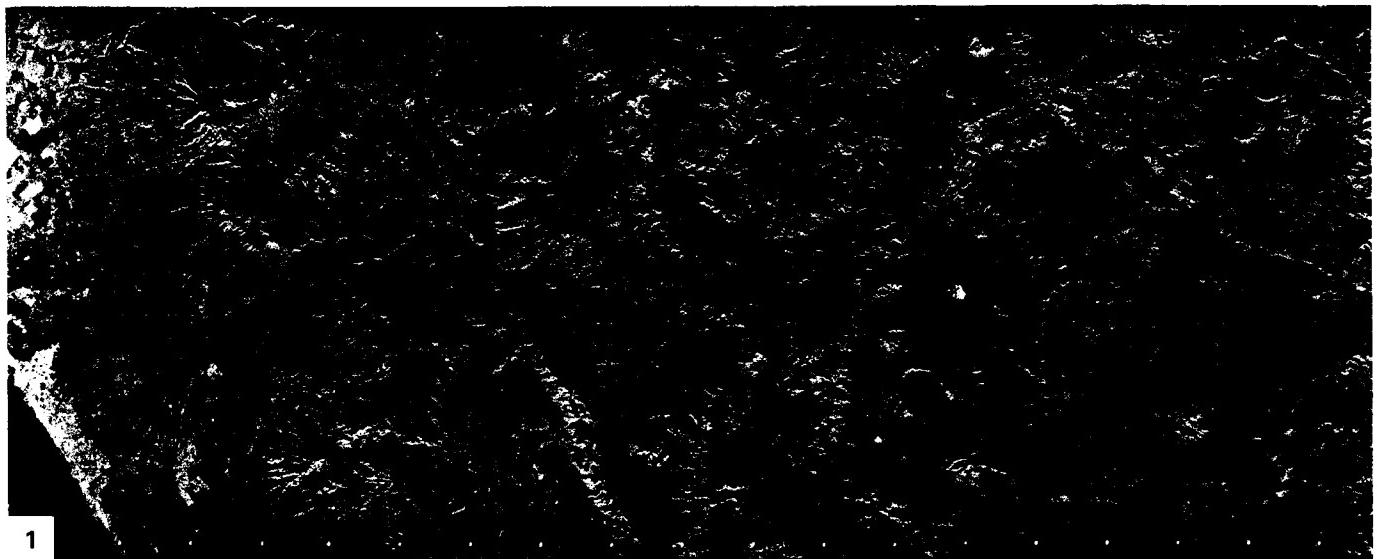
This image and the SIR-A Radar strip (Figure V-12.1) that traverses its eastern side are of volcanoes along the so-called Andesite Line that parallels the Pacific Basin. Here in southern Guatemala, a country roughly the size of Ohio, the small Cocos Plate east of the East Pacific Rise is subducted under a regional sliver of the Caribbean Plate (Nagle et al., 1977). The zone of subduction lies offshore approximately coincident with the Middle America Trench. Onshore, a eugeosynclinal belt (A) of Paleozoic sedimentary rocks (mainly graywackes) has been metamorphosed (upper greenschist facies) to slates and phyllites, accompanied by diabase and basalt. The grade increases to produce schists, gneisses, and amphibolites farther north (B). Granitic to dioritic plutons dated from 345 Ma ago (Pennsylvanian) through Cretaceous intrude this complex at several places (C). A major shear zone, the Motagua Fault (D), cuts across these older exposures of the Caribbean plate; its surface expression is a deep valley that localizes the Rio Motagua. Strong deformation during the Late Cretaceous to the Eocene imposes an east-west grain on this crystalline basement (Guatemalan Massif) in the Central Guatemalan Cordillera which, in this region, is an extension of the Cayman Trough traceable across much of the western Caribbean. Metasediments give way to folded sedimentary units along the northern boundary. To the north, this boundary (just off the scene) is the Polochic fault zone, a left lateral system that separates the Caribbean and North American plates. There and northward into the Petén Basin, the rocks comprise gently folded Cretaceous carbonates and Tertiary clastic and evaporite deposits.

Extensive volcanism began in the Tertiary along fracture zones associated with a structural trough or graben (Bonis, 1967). Activity in the Miocene consisted of fissure-type eruptions predominantly of rhyodacitic composition that covered the older basement. These, together with ignimbritic units, volcano-clastic units, and laharic deposits, comprise a broad belt (E) that oc-

cupies the southern margin of the Cordillera (Williams and McBirney, 1964). By the Quaternary, volcanic style had shifted to buildup of large composite stratocones that straddle the south side of the earlier volcanic belt. Most of these lie between 2600 and 4210 m in elevation. The volcanoes expel primarily pyroxene andesites as ash, ignimbrites, and other pyroclastic material that concentrated to the south (F), along with dacitic pumice that collected northward in lower areas (G) owing to prevailing offshore winds. Rhyolitic obsidian in domes and basaltic cinders and flows around cinder cones also were emplaced at this time.

A major caldera formed earlier is now occupied by Lake Atitlan. A smaller subsidence structure has localized Lake Ayarza (V₁₁). Explosive volcanoes distribute in several clusters (Figure V-12.2) controlled first by northwest trend of the trough and also by north-south cross faults. Holocene eruptions have been observed at Volcano Santa María (V₈; 1902, 1922, 1969), Cerro Quemado (V₉; 1783), Atitlan (V₆; 1856?), Acatenango (V₁; 1926-27), Fuego (V₂; 1971), and Pacaya (V₄; 1970) (Macdonald, 1972). The Santa María event (which actually took place from a subsidiary domal vent named Santiaguito) included release of a nuées ardentes, as well as lava flows and lahars. Other volcanoes, such as Agua (V₃), Tolimán (V₅), San Pedro (V₇), and Tecuamatz (V₁₀), have not been active since the Spanish Conquest.

The Pacific Coastal Plain Province, up to 70 km wide, is constructed largely from detritus carried in by the debris-choked streams coming off the Volcanic Highlands Province. Sands and gravels, mixed with pumiceous ash and extensive laharic deposits, form coalescing alluvial fans. Much of the population of Guatemala lives on this plain, which hosts most of the agricultural production. *Additional Reference:* Sapper (1925). **Landsat 21449-15304-7, January 10, 1979.**



ORIGINAL PAGE IS
OF POOR QUALITY

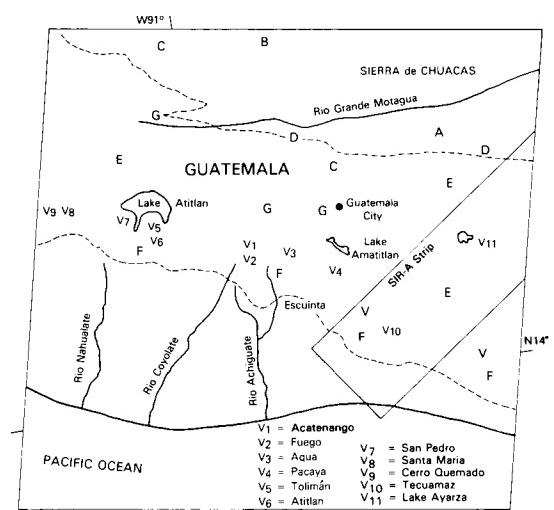


PLATE V-13

THE GALAPAGOS ISLANDS

The Galapagos Archipelago achieved fame in the 19th Century because its remarkable fauna played a key role in Charles Darwin's thinking on the evolution of living creatures (Darwin, 1844). These volcanic islands also impressed Darwin with their wealth of information on the nature of volcanism. His writings on the geology of this region are another monument to his profound insights.

The Galapagos are a cluster of islands lying along the Equator about midway (900 km) between the Ecuadorian coast to the east and the submerged ridge marking the spreading center of the East Pacific Rise (EPR) to the west (Durham and McBirney, 1975). The islands (highest point 1689 m) emerge from a basaltic base, the Galapagos Platform, that rises out of nearby oceanic deeps from -1200 to -3500 m. This platform merges eastward into the Carnegie Ridge and lies at the southwest end of the northeast-trending Cocos Ridge. The islands are located just south of the east-west Galapagos Spreading Ridge (rate: 3 cm/yr). The volcanoes align along a northwest-southeast set of fractures; northeast-southwest fractures and an east-west set also exert some control over the distribution of eruption centers (Nordlie, 1973). Since their emergence more than 3 million years ago, the islands have been moving eastward along the spreading direction established at the EPR. The oldest volcanics are found in the center, whereas the youngest lie near the western margin. Petrologically, the extrusives are mainly tholeiitic and alkalic basalts of the oceanic type, with minor amounts of trachytes and pyroclastic basaltic tuffs (often altered to palagonite) (McBirney and Williams, 1969). The islands have been formed within a plate that has moved over a surface hotspot fed by a mantle plume, an origin analogous to the Hawaiian Islands. The Carnegie and Cocos Ridges are older now-submerged volcanic piles that resulted from the passage of the Cocos and Nazca plates over this plume.

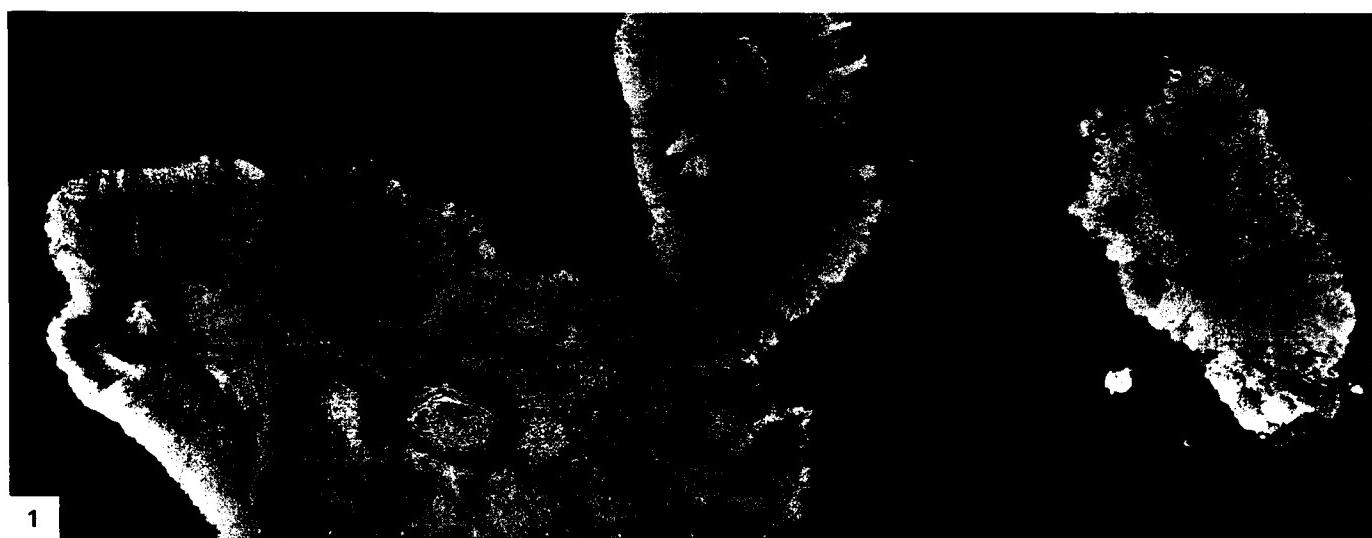
The volcanoes on the western islands are among the most active in the world (39 eruptions since 1700 A.D.; Macdonald, 1972; see also Simkin, 1984). Seven days before this scene was imaged by Landsat, the Sierra Negra volcano, whose caldera is evident at (D), began to erupt. A light-toned streak (orange in a color composite) along the flank fixes the path of the main lava flow; a vapor cloud from this activity is also evident.

The scene also reveals nearly cloud-free glimpses of the major eruptive centers on the big island of Isabela (Albemarle Island

as named by British explorers). Its J-shaped outline is closely allied to the northwest- and northeast-trending fault zones. Three of Isabela's large calderas are visible. The northernmost is the summit of Wolf Volcano that rises to 1710 m. The top is broad and relatively flat, but the upper slopes steepen to 35°. The central caldera measures 6 by 4.5 km and is more than 600 m deep. At least 10 eruptions since the late 1790s have been recorded there. A nearly circular (4.5 km diameter) caldera tops Darwin Volcano, along whose flanks are many lava flows emanating from both radial and concentric fractures. No historic eruptions are known from Darwin. Alcedo Volcano (1130 m) has erupted at least once during this century. Along the western shores of Isabela Island are the breached and down-faulted Ecuador Volcano (A) and the smaller tuff ring structures of Tagus Cone (B) and Beagle Cone (C). These were built by explosive (phreatomagmatic) action; most of the larger shield volcanoes on this island were generated from rather quiet effusive outpouring, but pyroclastic deposits on their upper slopes indicate occasional more violent eruptions at each. The two remaining large calderas, Sierra Negra (partly visible) and Cerro Azul (just off the image) are shown in Figure V-13.1, a SIR-A radar image taken from the Space Transportation System (Shuttle) in November 1981.

A single volcanic edifice, exceeding 1350 m in elevation, comprises Isla Fernandina (Narborough). Its gentle lower slopes (3 to 6°) steepen locally to 35° near its flattened upper bench. Extensive aa lava flows in all directions attest to repeated eruptions in the past few thousand years. The central caldera (Figure V-13.2) is elliptical (6 by 4 km). The lake shown in Figure V-13.2 was totally evaporated by a large eruption in 1958 (T. Simkin, private communication). Another eruption in 1968 led to collapse within the caldera, during which its floor dropped 350 m, and a new lake has developed, into which later lava flows have entered, including one just 15 months before the date of this Landsat pass.

Erosion of the islands results from a mix of surface water runoff (from rainfalls up to a maximum of 260 cm on Santa Cruz), ground-water action as rainwater enters porous basalts, and persistent wave action along the coast. Gully-forming erosion is especially active along surfaces covered by fine ash compacted to an impervious cover (e.g., around Beagle Cone). *Text modified from comments by T. Simkin, Smithsonian Institution. Landsat 30624-15340-7, November 19, 1979.*



1

ORIGINAL PAGE IS
OF POOR QUALITY



2

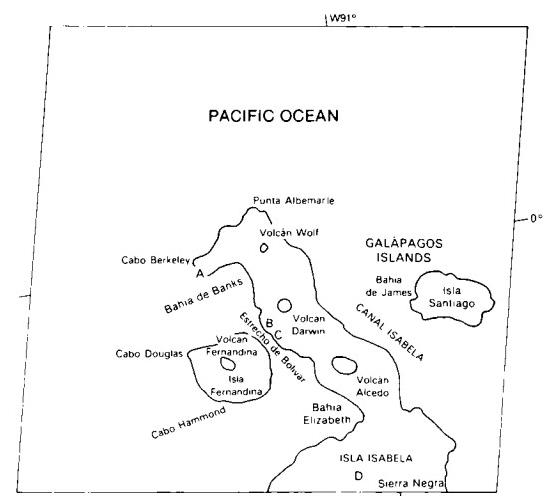


PLATE V-14

ORIGINAL PAGE IS OF POOR QUALITY

ANDEAN VOLCANISM

The Andes Mountains of South America extend the entire length of the western side of the continent, making up a spectacular continuous (>4100 km) segment of a convergent plate margin along the Pacific Ring of Fire. The geologic setting of this orogenic belt has been described in Plate T-21 (see also Rutland, 1974). This Plate concentrates on the volcanic aspects of this great mountain chain (Casertano, 1963).

The pictures shown on these two pages lie within the central section of the Andes between latitudes 15 and 30°S, along the borders of Bolivia, Chile, and Argentina. This region hosts the largest number—more than 600—of stratocones (Figure V-14.1) exceeding 5000 m in elevation above sea level anywhere on Earth (Zeil, 1979). These stratocones were emplaced during the Late Tertiary through the Recent. Most are now extinct (indicated by C, for Cerro, before each name), some may be dormant (indicated by V), and a few remain active, but overall, present activity is low relative to other parts of the Andes. The stratocones are mainly andesitic in composition; the emergent materials are distributed in both lava flows and abundant ignimbrite deposits.

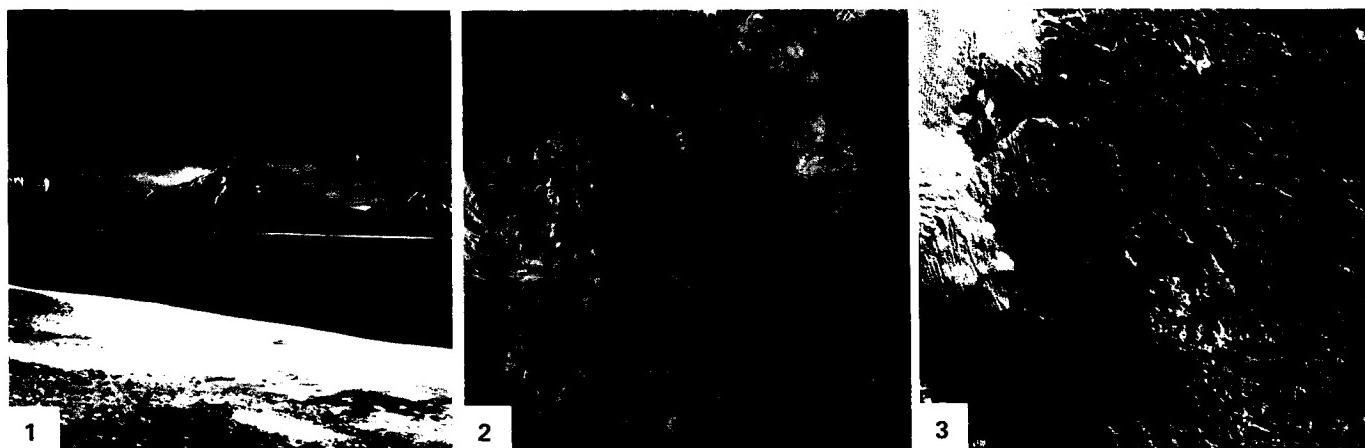
This part of the Andes, known as the Antofagasta segment, lies south of the northwestward bend of the coast near the Peruvian border. Offshore, the Nazca plate begins subduction (at east-dipping angles from near flat to 30°, from seismic evidence) along the active Peru/Chile Trench (Kulm et al., 1981). Subduction and associated volcanism and seismicity are strongly diminished at the north and south ends of this segment where the Nazca (north) and Juan Fernandez (south) Ridges impinge at high angles onto the South American plate; consumption of these ridges retards the penetration of the Nazca plate under the continent at these gaps, with the intervening segment (Benioff Zone dips $>30^\circ$) south of this scene now slowed down so that once-extensive volcanism has subdued.

The scene is filled with numerous smaller calc-alkaline volcanoes scattered across the Puna-Altiplano Zone—the section of the High Cordillera within which lie most of the volcanoes in this segment. This zone was once the site of Mesozoic platform sedimentation. It began to experience deformation in the Cretaceous, followed by development of synorogenic to post-orogenic con-

tinental basins in the Tertiary. Volcanism proceeded eastward through this area, with culmination in Late Tertiary times. This belt of stratocone volcanism is unusually wide here, exceeding 200 km in places, suggesting a shallower dip for the underlying Benioff Zone. An older belt of volcanism, containing mainly rhyolites and dacites, extends westward from the eastern reach of the Rio Loa and is also present elsewhere (A, B) within the scene.

This scene, then, is dominated by the Puna Plateau, with its sedimentary basins largely filled by Tertiary/Quaternary debris, so that most present surfaces lie above 4000 m (Zeil, 1979). Major relief is controlled by the newer volcanic peaks and by partially buried low north-south ranges of folded Paleozoic sedimentary rocks (C). Many basins are landlocked and serve to localize drainage that evaporates into salt-crusted salars and salinas (some containing sodium nitrate). The Rio Lipez is a typical ephemeral stream that empties into the Salar de Uyuni (see Plate KL-13). In general, the shape of the salars in this scene may differ notably from their shapes on published maps. This variability results primarily from periodic infilling following rains in the normally very dry climate. Figure V-14.2 is a near-vertical photo taken in September 1983 with a handheld camera by an astronaut during the 8th Space Transportation System (Shuttle) mission. It shows (arrow) the second highest volcano in the Andes, Ojos de Salado (6880 m), on the Chile/Argentine border (S 27°) and several others. The sharply dissected nature of this volcanic terrain is accentuated by the low Sun angle at that time.

Andean volcanism persists intermittently to the south until it dies out beyond S 45°. Highest elevations in the Andes diminish to less than 4000 m in southern Chile. In the Sur Chico (Little South) region shown from Landsat in Figure V-14.3, the High Cordillera (most peaks less than 2500 m) is a zone of Mesozoic granites and Upper Tertiary/Quaternary volcanics that dies out east of the Longitudinal Valley Zone, a structural depression filled with Quaternary sediments and now occupied by the Golfo Corcovado. The active Volcán Osorno (topmost volcano in Figure V-14.3; closeup view in Figure V-14.4) reaches 2661 m; this, the Volcán Hornopiren (below it), and several others in the scene here fall within a narrow line rather than widely dispersed as are the volcanoes in the Plate. **Landsat 2419-13440-7, March 16, 1976.**



ORIGINAL PAGE IS
OF POOR QUALITY

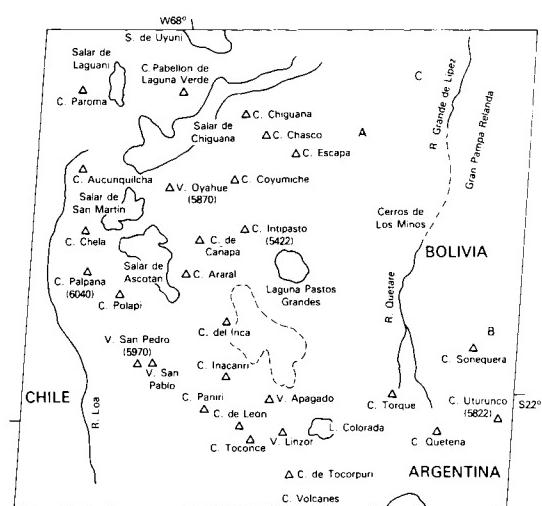
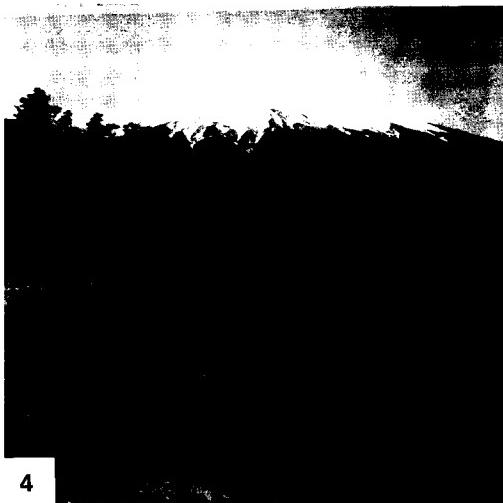
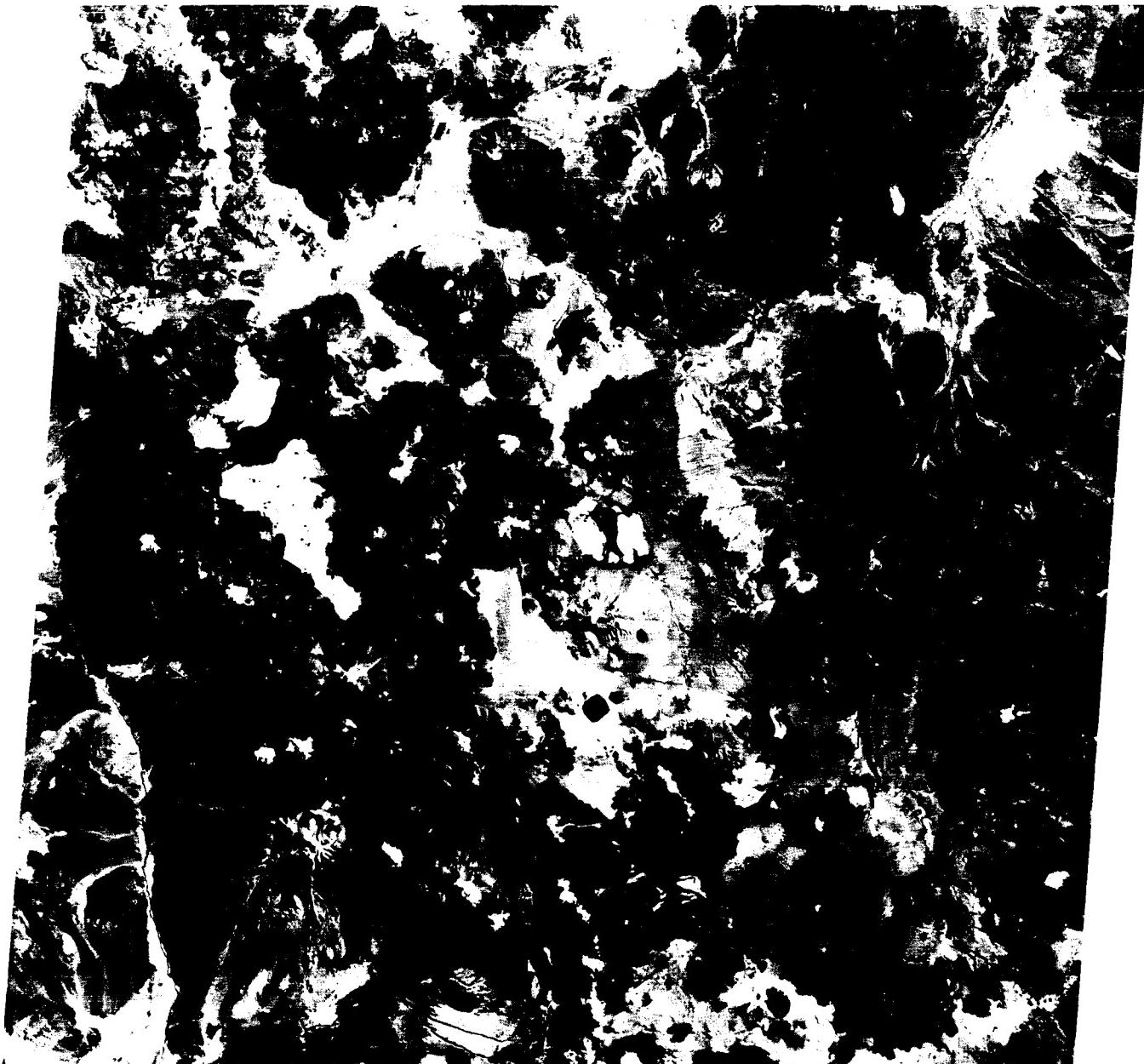


PLATE V-15

Iceland is one of two places on the Earth's face (the other is the Afar, Plate V-21) where geologists can take a close subaerial look at the morphology of a large part of an active oceanic spreading ridge. This volcanic island lies astride the Mid-Atlantic Ridge at the intersection between its Reykjanes and Kolbeinsey segments and the Iceland Transverse Ridge. This latter structure, seismically inactive, extends east-southeast from the Greenland shelf through the Iceland Block, thence southeast along the Iceland/Faeroe Ridge. Iceland itself is the highest topographic section of the Mid-Atlantic Ridge. Here the oceanic crust is anomalously thick (8 to 18 km), giving rise to a strong gravity high. Icelandic-type crust, made up of oceanic tholeiitic basalts typical of the MORB (Mid-Ocean Ridge Basalts) suites, displays thicker counterparts of normal oceanic layers 2 and 3 observed at submarine ridges, whereas layer 1 is replaced by igneous units. Seismically, anomalously low sub-Moho velocities exist beneath Iceland. High heat-flow values on Iceland suggest that the island sits atop a mantle plume or an expression of upwelling convection currents along the crossing ridges.

The island developed well after the opening of the North Atlantic; the oldest rocks emplaced in Iceland date 16 Ma. In the Late Tertiary, rifting increased, accompanied by intermittent volcanism that persisted through maximum glacial activity during the Pleistocene into the present stage of reduced icecap cover. In the last 11000 years, the 400 km³ of volcanic effluents, including 55 km³ of tephra, now cover 11000 km² of the island (Thorarinsson, 1959). Since the 1500s, Iceland's volcanoes, 3 percent of the active ones on Earth, have produced 24 percent by volume of the extruded lavas worldwide (Macdonald, 1972). The sequence of units in Iceland (Preusser, 1976) begins with the Tertiary Basalt Fm, covered by the Gray Stage Basalts, then the Old Gray Basalts (Pliocene/Pleistocene), the Young Gray Basalts (Pleistocene interglacial), and the most recent Móberg or Palagonite Fm, consisting of tuff breccias, pillow lavas, and basalt glass altered from sideromelane glass. Sediments interspersed with these units are mostly tillites and glaciofluvial deposits.

As expected for a spreading ridge, halves of Iceland are diverging at a rate of 0.6 to 2.0 cm/year from the Central Axial Graben. In this scene, two arms of the graben (Western and Eastern Volcanic Zones) extend northeast-southwest before joining in a single north-south branch just above the image. Here the plateau

SOUTHWEST ICELAND

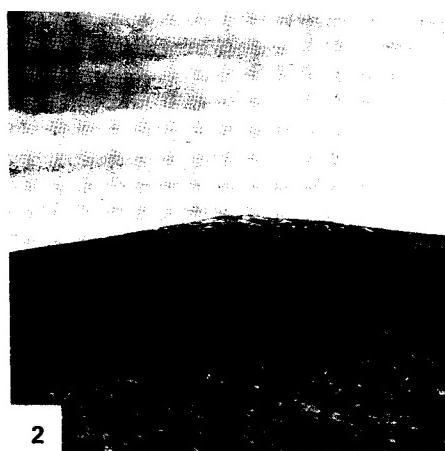
basalts are broken into a series of tilted blocks (horsts/grabens) of shallow depth and moderate vertical displacements. Mainly within the rift zones are numerous en echelon fissures (*gjár*) (A) from a few meters to 1 km in width; sheet basalts with innumerable vertical dikes are common within and beyond the faults.

Iceland hosts a variety of unique landforms developed by extrusion under the ice caps (Preusser, 1976; Williams et al., 1983). A dominant form is the serrated ridge produced by subglacial eruptions where lava enters long fissures under the ice. Another is the *stapi* or table mountain, of which those at Eiríksjökull (Figure V-15.1 (B)), Thórisjökull (C), Geitlandsjökull (D), Bláfell (E), and Hrútafell (F) are outstanding examples that cluster about the icecap, Langjökull. A *stapi* results from "intrusion" of lava into glacial ice cover which, on melting, helps to mold the volcanic materials against the ice-wall void. *Stapis* have steep slopes and flat tops built from palagonite breccias capped by subaerial basalt. Another landform, the shield volcano, is represented by Skjaldbreidur (G) (Figure V-15.2) and by the even larger Ok (H). These structures form primarily during interglacial times, with several having smooth undissected profiles originating in the last interglacial period. Typical of Iceland are crater row volcanoes (Figure V-15.3) that align along linear fractures, as at the Laki-gigar row of some 100 cones along a 25 km zone (I). Larger linear composite volcanoes, such as Hekla (J) with its elongate (8 km) crestal fissure (Figure V-15.4), are another distinctive form. Hekla erupts frequently, including several times in the 20th century, sending tephra long distances from Iceland. Hekla is the site of many small lava flows, or *hraun* (K); others in the scene include the Hallmundarhraun (L), the Lambahraun (M), and the Veidivatnahraun (N) in the northwestern lava fields west of the Laki fissure that expelled 12 km³ of lava and ash in 1783, with accompanying poisonous gases, killing much livestock and causing a devastating famine. An older flow, the Thjórsá field, extends up to 70 km wide for 130 km before reaching the sea in the southwest lowlands (O).

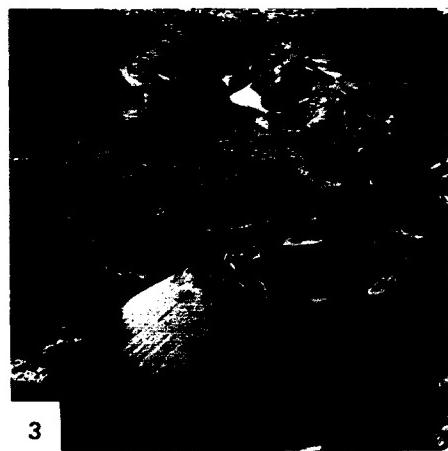
Other geomorphic features of interest are: (1) the southern highlands (palagonites and Young Gray Basalts) (P), rising to 1000 m against the Mýrdalsjökull/Eyjafjallajökull icecaps; (2) the Torfajökull Highlands (Q), with cone-shaped mountains, obsidian lava fields, and 30 solfataras; and (3) Hvalfjördur (R), a 35-km long fjord. **Landsat 1392-12191-7, August 19, 1973.**



1



2



3

ORIGINAL PAGE IS
OF POOR QUALITY

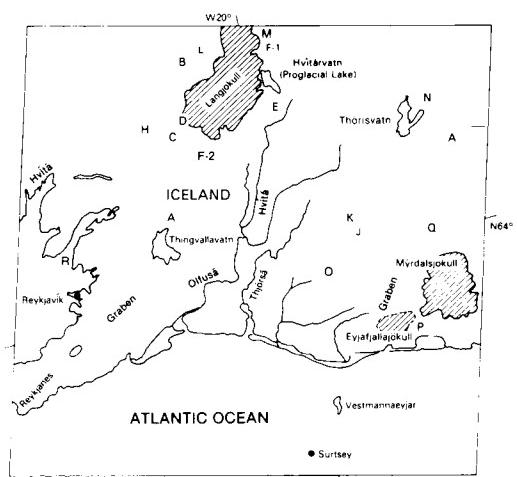
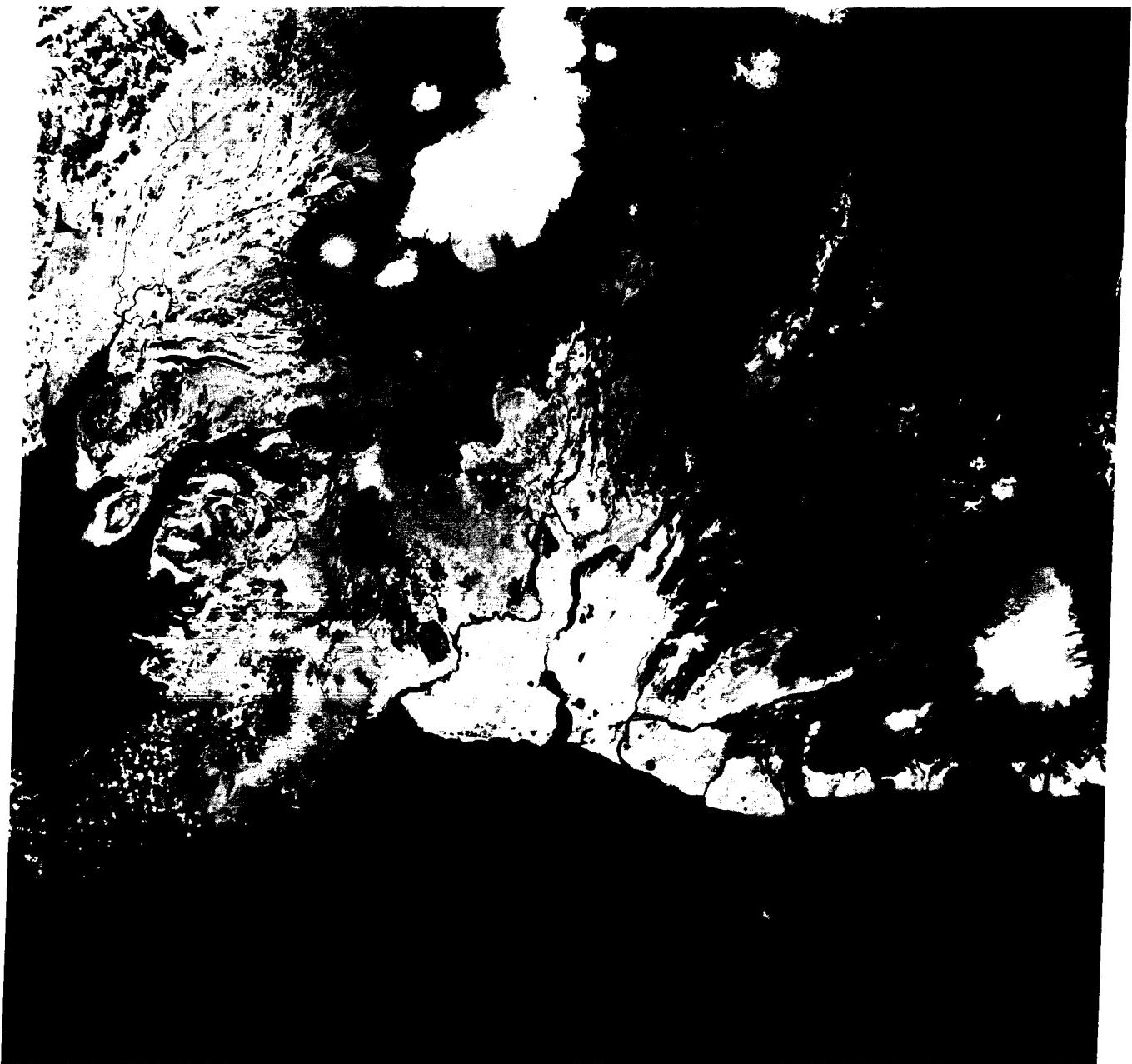


PLATE V-16

Volcanism in Europe during historic times has occurred in France, Germany, Greece (Santorini Island), and Italy (Rittman, 1973). Central Mediterranean volcanism is concentrated in a zone along the west coast of the Italian peninsula, through the Aeolian Islands (Stromboli, Vulcano), and at Mt. Etna in eastern Sicily (Barberi et al., 1973). This activity expresses continuing interaction between the eastward-moving Ligurian microplate and the Adriatic microplate, which contains the Apennines, that involves migration of an arc-subduction zone resulting from late stage shifts in Cenozoic alpine deformation. As evident in a Landsat subscene of central Italy (Figure V-16.1; Rome near bottom), lake-filled calderas mark a line of now extinct volcanoes (Monte Albani, Sabatini, Cimini, Vulsini, and Amiata) that spewed forth potash-rich lavas (leucite- and nepheline-bearing (Alvarez, 1975)); similar volcanic products characterize Vesuvius to the south. These and the Aeolian Island volcanoes release sialic magmas contaminated by continental crust rocks. Etna's lavas come from deep sources in the upper mantle, as evidenced by their low $\text{Sr}^{87}/\text{Sr}^{86}$ ratios (Tangay and Kieffer, 1976-77).

Mount Etna, Europe's largest active volcano, stands in sharp contrast to the surrounding sedimentary units in northeast Sicily. Most Sicilian rocks are Mesozoic or Cenozoic in age, with limestones and shales dominant, many being flysch deposits. The present island was once simultaneously connected with the Atlas and Barbery chains of North America and the Apennines to the north. Now detached from the African Berberides, Sicily is part of the Tyrrhenian arc that remains structurally higher than the present Tyrrhenian marine basin. From Oligocene to Miocene, as the Alpine orogeny culminated, thrusting affected much of Sicily. Etna itself is built on a horst that utilized northeast fracture lines extending across the Strait of Messina.

Etna's base extends 40 km east-west and nearly 60 km north-south. Lavas from its many eruptions (average of 15 per century) cover nearly 1000 km². These lavas are described as andesitic basalts, with trachyandesites, tephrites, phonolitic tephrites, mugearites, and hawaiites as differentiates produced in fissures owing to variations in rates of ascent. The Etna eruptions can be classed into three types: (1) subterminal effusion, taking place at the central cone vent (Figure V-16.2) (after degassing, the lavas outflow quietly without building any structure), (2) lateral eruption, involving simultaneous venting of ash at the central

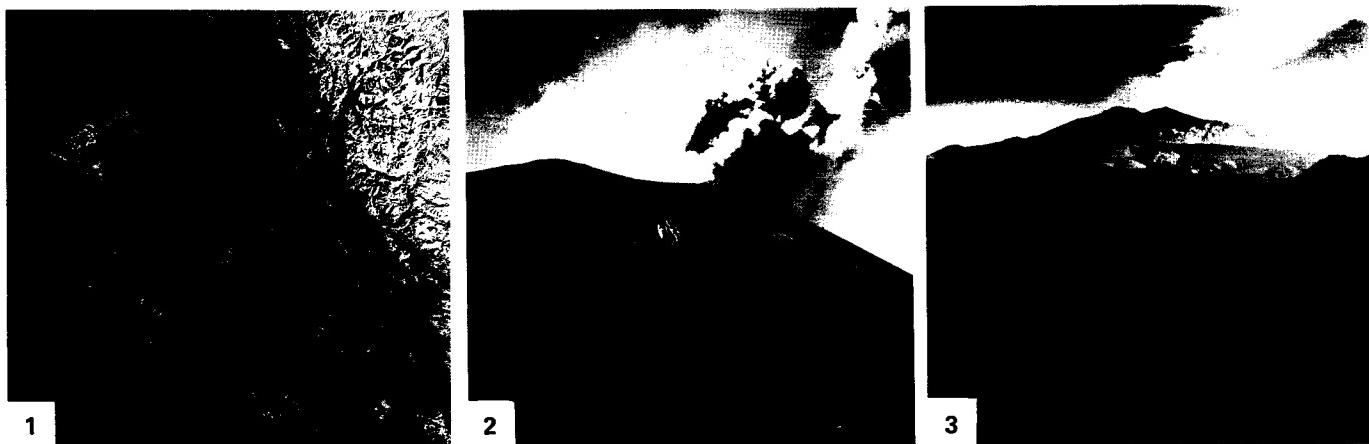
MEDITERRANEAN VOLCANISM

cone and eruption along the volcano flanks as lavas escape through a radial fissure (a row of cinder cones lines the fissure intersection with the surface), and (3) eccentric eruption, controlled by a separate noncentral vent that breaks out on the flank and constructs parasitic cones (Walker, 1968). Lavas predominate on the lower slopes, with pyroclastics more in evidence near the summit (Figure V-16.3).

This Plate shows a 1983 eruption in progress. Comparison of flow patterns around Etna in this Plate with a Landsat view taken in 1977 (Figure V-16.4) reveals the location and shape of the new 1983 lava flow and the 1981 eruption to the north.

The extensive dark areas seen in these images are Etna's young lava flows, mostly those extruded since about 1150 A.D. Although the majority originate from vents high on the flanks, a few, notably that of 1669 which flowed through the town of Catania and partially filled its harbor, escape from lower flank fissures. Lavas entering low-lying ground tend to disappear under vegetation cover. In marked contrast to 19th and 20th century flows, those of 1651 and 1566 (A.D.) flow on the northeast flank, the 1537? flow on the northwest, the 1591 flow on the west, and the 1169 flow on the southwest are almost totally vegetated. The lower slopes of Etna are densely populated; the highest villages, forming an incomplete ring around the flanks, are localized by the upper limit of available water. On the average, about three flows per century reach the populated areas and cause damage. This has happened five times during this century—in 1923, 1928, 1947, 1971, and 1982. One of Etna's lavas is said to have blocked Hannibal's army in Roman times.

Etna had a profound influence on scientific belief in Renaissance times and was important in the development of understanding volcanism in the early days of modern geology. In the early 19th century, Charles Lyell observed that the historic lava flows, although extensive, were but a thin veneer on the great bulk of the volcano, and that few of the 150-odd cinder cones such as Monte Rossi were known to have been produced by historic eruptions. These observations demonstrated to Lyell that Etna, though very young in relation to the geologic record, must be very old in relation to recorded history, thus laying the foundations for our present ideas on the immensity of geologic time. *Text modified from comments by G. P. L. Walker. Landsat, April 23, 1983.*



ORIGINAL PAGE IS
OF POOR QUALITY

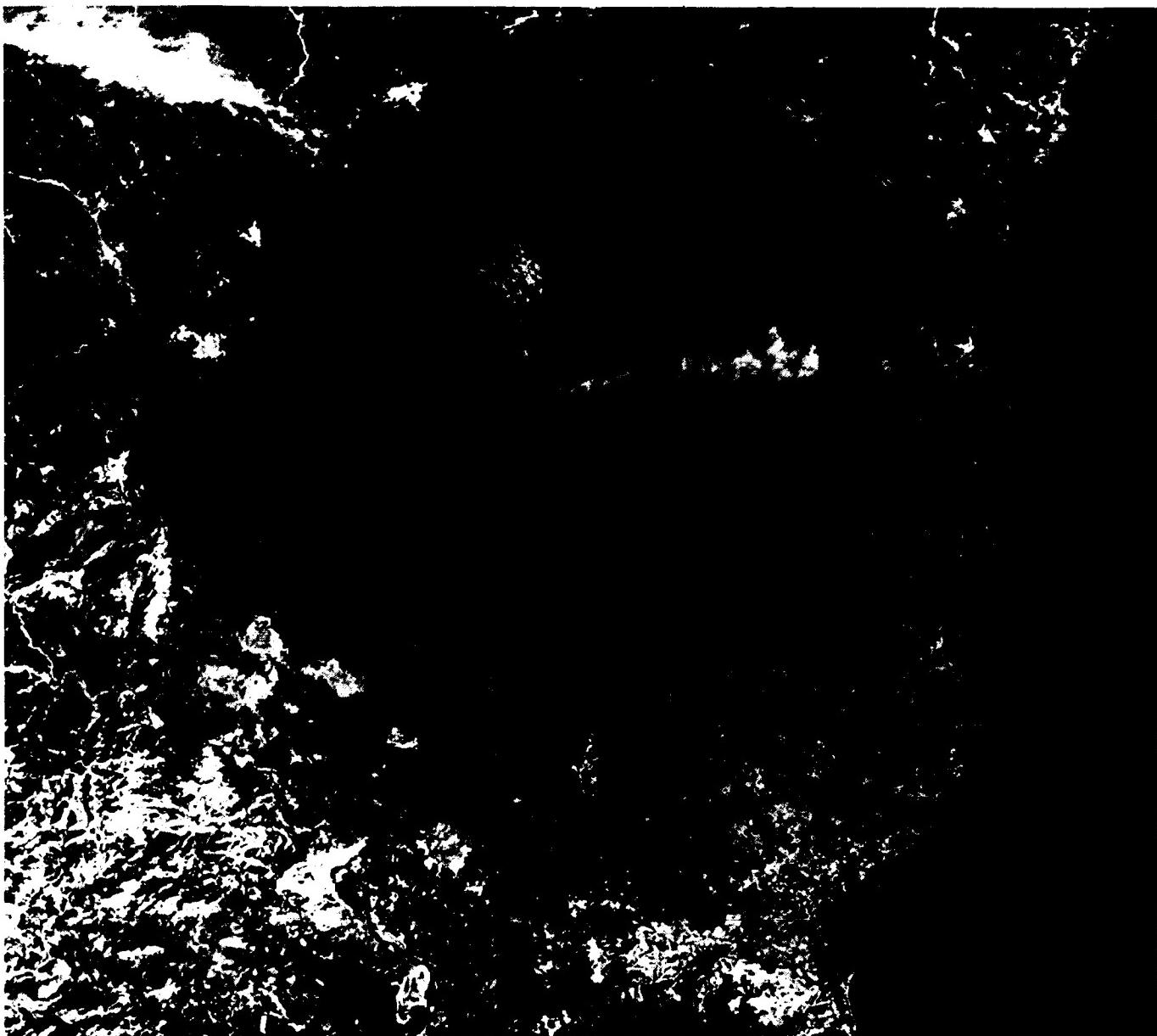


PLATE V-17

As stated in the introduction, most of the active volcanoes worldwide lie along the convergent margins of the Pacific Ring of Fire or along the network of spreading ridges that traverse the oceans. Another great line of convergence is marked by the Alpine/Himalayan belt system along which at least four major plates continue to move against one another. Surprisingly, Neogene volcanism throughout this belt has been relatively sparse compared with the Pacific Ring. In the Mediterranean region, only a few volcanoes are active today, mainly in and around Italy, with other centers in France, Germany, and the Aegean Islands. At its eastern end, now extinct but apparently recent volcanoes have been discovered (some through Landsat) on the Tibetan Plateau north of the high Himalayas. A third region of sporadic activity extends from Armenia in eastern Turkey eastward through the Central Volcanic Belt of Iran (Boccaletti et al., 1977).

This region is located mainly within a zone of intense lithospheric crushing where the Arabian Plate is moving northeast against the Eurasian Plate (see Plate T-39). On the west and east sides of the point of convergence near Lake Van are two other plates, the Anatolian and the Iranian, which are considered microplates by some tectonicists. The Anatolian Plate is being squeezed westward along the North and East Anatolian transcurrent faults. Likewise, the Iranian Plate is being pushed to the southeast along similar faults that pass through the Elburz Mountains north of Tehran and through the suture (Main Recent Fault) of the Zagros Crush Zone. Some of this deformation began in Late Cretaceous/Paleocene times, intensified in the Miocene/Pliocene, and continues unabated.

Lambert et al. (1974) studied the tectonic, petrologic, and geochemical setting of the region that encloses Mt. Ararat, a large stratocone (more than 35 km wide at ground base) near the corner at which Turkey, Iran, and Soviet Armenia meet. Here, in the aforementioned crush zone (considered a discrete microplate—the Van plate—by Dewey et al. (1973)), crustal shortening along a northeast line gives rise to a northwest tensional line of fractures that control volcanic emplacement. This group includes Nemrud at the west end of Lake Van, Suphan, Tendurek, and Ararat itself at the northeast end. The crush zone sits astride the intersection between east-west tectonic trends in Turkey and the northwest-southeast Zagros structures (Plate T-42). Dewey et al. (1973) and

MT. ARARAT, TURKEY

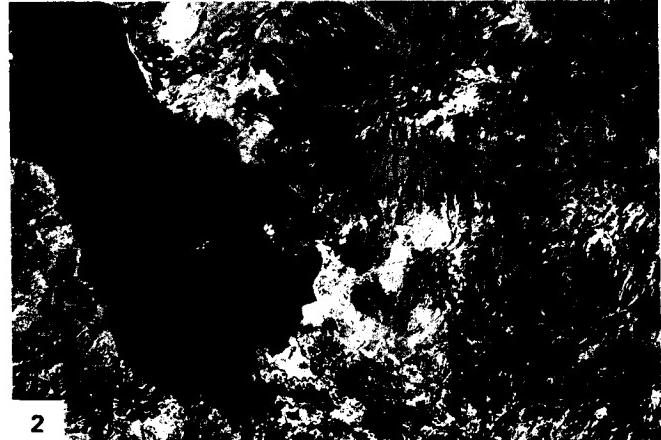
other investigators postulate consumption of the Arabian Plate along a subduction zone under the Van microplate. Lambert et al. (1974) and McKenzie (1972) point to the absence of intermediate to deep earthquakes as evidence against subduction today.

Highest of the northeast line of volcanoes is Ararat (Altinli, 1964). As seen (looking southward) from the ground (Figure V-17.1), Greater Ararat (right) at 5156 m towers above Little Ararat (3903 m) some 12 km to the east. Both peaks are evident in the thematic mapper subscene that constitutes Plate V-17. This unusual color rendition results from a combination of bands 1 (blue), 4 (green), and 7 (red). This effectively separates clouds above Greater Ararat from an ice cap (in blue), both of which appear white in visible wavelength images. Much of the lava and ash deposits along the slopes appears as a purplish-brown (as does some derivative Quaternary slope debris). Some of the younger basalts to the northeast take on a purplish-blue hue. Bright red markings superficially resemble fresh lava flows but are brush fire burn scars (bright in band 7). Older tuffs exposed in the Cehenna Gorge cut into the north flank are not recognizable, being largely in shadow, but still older volcanics to the west are rendered yellow-brown. The darker orange-brown along the upper slopes of Ararat results from the color mix related to bright returns from vegetation (forests) for band 4 and rock and vegetation for band 7. Especially distinctive in the image are lava channels and gutters; adventive cones and possibly domes may also be present on the slopes. Dissected volcanic terrain gives way to a plains along the Rizdan River to the north and to Devonian/Permian sedimentary rocks in mountains to the southeast.

Ararat is typical of the calc-alkaline volcanism that led to the expulsion of dacites and andesites in the region. Younger outpourings consist of alkali basalts. Related volcanism extends eastward into northern Iran, culminating in the dormant Damavand (5671 m) volcano near Tehran. Another large stratovolcano, Sahand (3710 m) south of Tabriz, is prominent in the Landsat image shown as Figure V-17.2; a smaller volcanic structure, Shaki (2189 m), extends as a peninsula into Lake Urmia. Both show extensive slope erosion, forming barrancos or gorges that help to emphasize the pronounced radial drainage. This pattern is especially brought out in the SIR-A radar image of Sahand seen in Figure V-17.3. **Landsat TM 50209-07140, September 9, 1984.**



1



2

ORIGINAL PAGE IS
OF POOR QUALITY

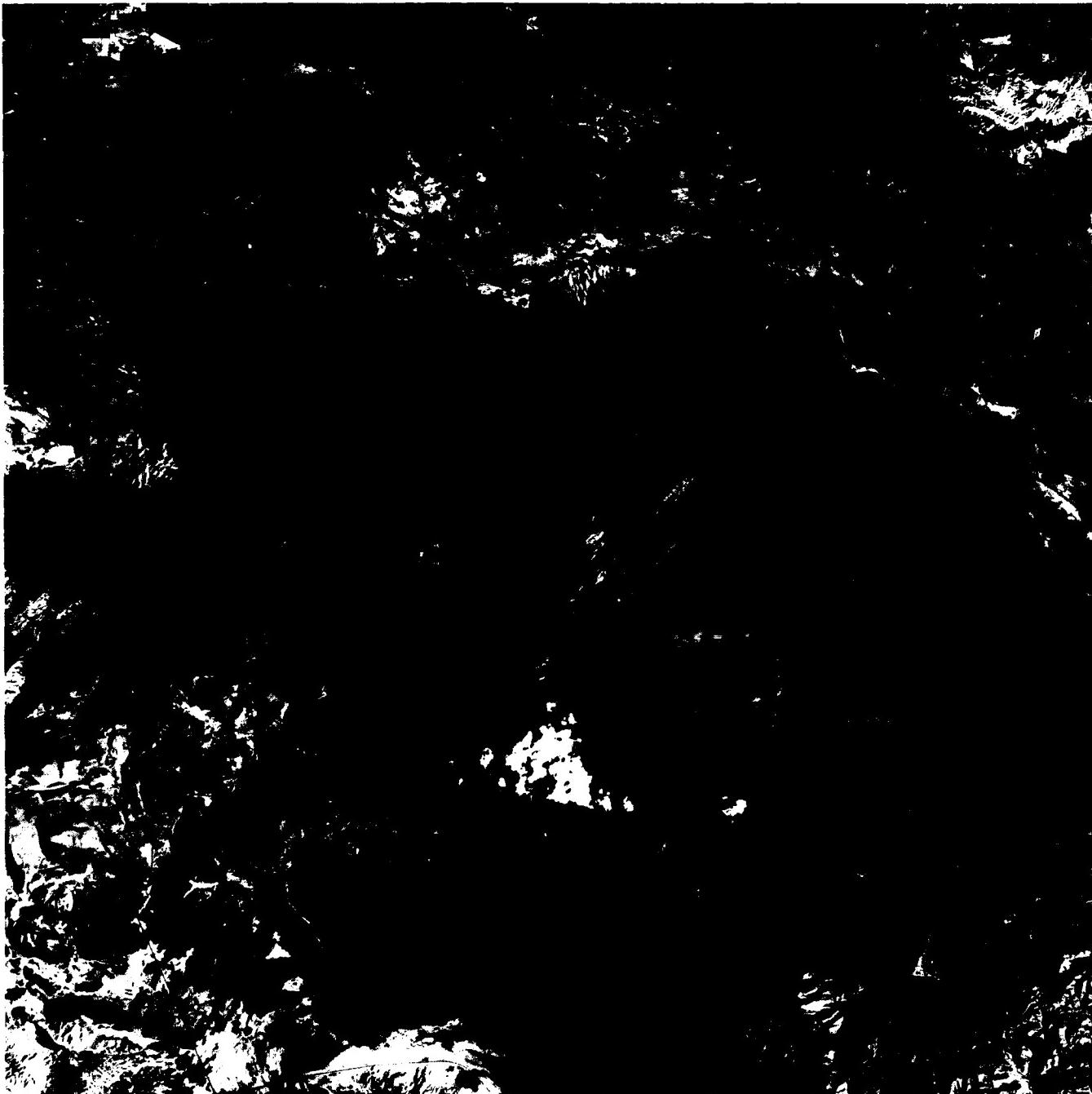


PLATE V-18

The Tibesti Massif in northern Chad (Vincent, 1970) is a large epeirogenetically uplifted crustal block of Precambrian crystalline rocks capped by Cenozoic volcanic flows and pyroclastic deposits. The present topography (Figure V-18.1) of the Tibesti complex is one of stepped plateaus, low dissected ridges cut into volcanics, and volcanic cones with minimum slopes of 2 to 4° and seldom exceeding 15° (Prichard, 1979). The entire massif now extends over 100 000 km², of which about 30 000 km² consist of volcanic rocks. The older Precambrian units (A) contain migmatites and granitic intrusions within metamorphic complexes. The more widespread younger Precambrian (B) is a collection of quartzites and phyllites. Sandstones dominate an unconformable Lower Paleozoic sequence that spreads around the periphery of the Tibesti Plateau (C). A Nubian sandstone unit (D) of Early Cretaceous age lies along the edge of the crystalline basement. The massif has been intermittently raised, with arching of overlying sedimentary units, since Mid-Paleozoic times. Later, sets of northeast and north-northeast faults (E), following Precambrian trends, cut these units. The structure, then, is that of a major block broken by several horst/graben segments, tilted north-northeast, and capped by a broad flexure with a northwest-trending axis.

Intense volcanic activity began in the region during the Early Tertiary. One view holds that the Tibesti volcanoes represent continental volcanism over a hotspot tied to a deep-seated mantle plume. In several respects, the volcanic complex can be compared as a continental analog to the Island of Hawaii, although there are considerable petrologic differences. A great pile of plateau flows forms the volcanic base on which shield-like volcanoes, some made of ignimbrites intercalated with basalt flows and most topped by calderas, are superposed. Volcanism was quite active during the Quaternary, with numerous explosive ejections of pyroclastics, but currently the activity has abated so that only one volcano, presently dormant, has shown recent stirrings.

The oldest volcanics, the First Black Series, are alkaline olivine basalts that flooded the terrain. Associated trachytes and phonolites form plugs. Later, the Second Black Series, mostly tholeiitic basalts with alkaline rhyolites, built up the shield volcanoes (Toon, Oyoye, and Yega), together with rhyolitic elevated domes (Abeki) and cumulo-domes (Sosso) of viscous rhyolitic glass. Another type of volcano, called a "shield sheet," is repre-

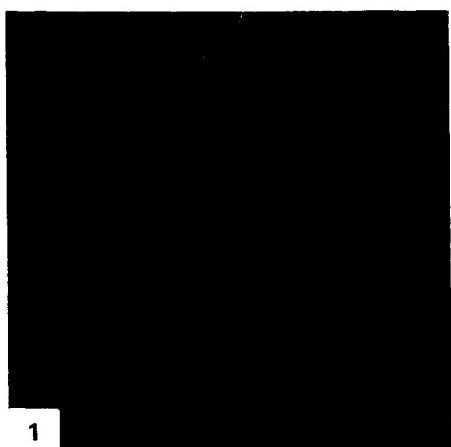
TIBESTI MOUNTAINS, CHAD

sented by Tarso Voon. This unusual structure consists of a wide apron of poorly indurated pumiceous pyroclastic deposits (sillars) that extend without an apparent "root" (vent channel) across previous valley terrain and pinch out laterally from a deeper center (Vincent, 1970). Within this cupola-like structure, a large (18 by 11 km) summit caldera collapsed into the central interior.

The most recent volcanism added both alkali basalts and trachyandesites to the surface. The distinctive dark pattern around Tousside (possibly still active; 3265 m high) associates with a fresh low-reflectance surface composed of trachyandesitic ignimbrites with some flows. Nearby is the smaller explosion-collapse caldera (8 by 6 km) atop the Trou au Natron, on whose floor are deposits of sodium carbonate (natronite) surrounding small cones (Figure V-18.2; Green and Short, 1971). At the southeast end of the volcanic terrain stand the massive Emi Koussi (Figure V-18.3), largest and highest (3415 m) of the central caldera volcanoes from which pyroclastic deposits have spread outward many kilometers. In the same image is the older, more dissected Tieroko Volcano. As photographed by an astronaut during the STS-17 (Shuttle) Mission, Emi Koussi (Figure V-18.4; north to right) bears a striking resemblance to Klysim Mons and, to a lesser extent, Olympus Mons (Plate P-6; Malin, 1976).

Several of the volcanoes, particularly Toon and Abeki, show a concentration of feeders along boundary faults within and beneath the walls of their calderas. These are analogous to the classic cone-sheet structures described by Anderson (1936) for Scottish volcanic roots. The faults are directed inward and steepen with depth, producing a convergent feeder system. Radial dikes also occur in these structures.

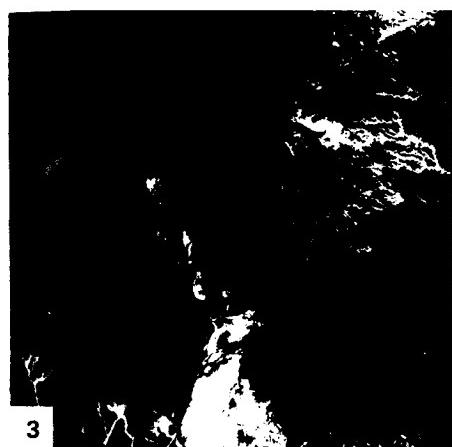
Volcanism began as the region underwent flexuring in the Mid-Eocene. Tensional fractures parallel to a northwest flexure axis, and probably controlled in part by basement lineaments, localized the feeders. The NNE-NE fracture systems did not serve to channel the lavas. Sources of the older alkaline lavas and the younger tholeiites were probably independent of each other and came from different depths. The rhyolites are believed to have resulted from partial fusion of the crust rather than direct differentiation. Although the older basalts are widespread in this part of Africa, being found at the Haroudj and Eghei and elsewhere, the rhyolites are confined to the Tibesti region. **Landsat 2367-08343-7, January 26, 1976.**



1

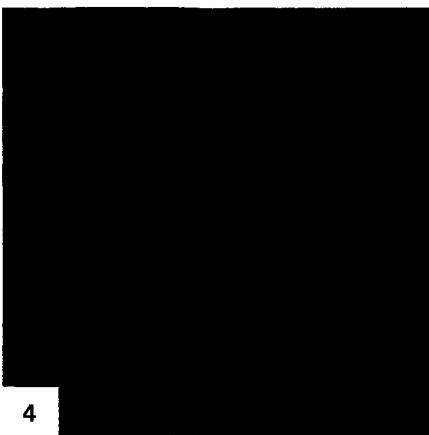


2



3

ORIGINAL PAGE
COLOR PHOTOGRAPH



4

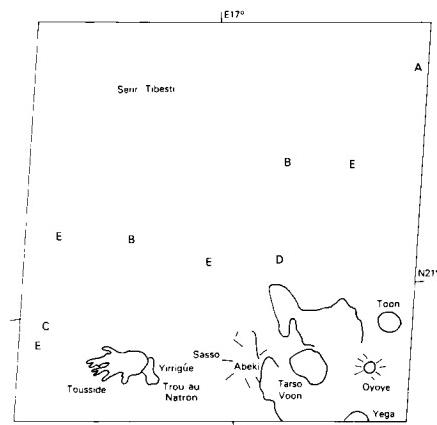
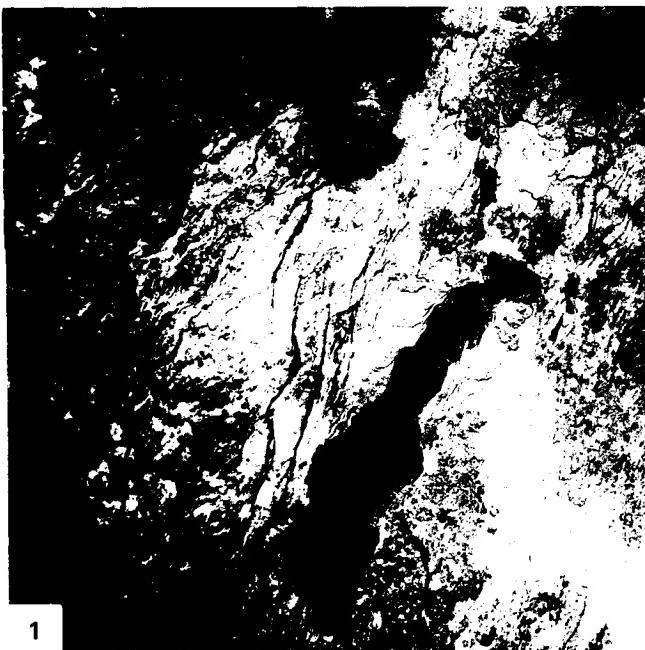


PLATE V-19

This scene lies almost entirely within the north-central section of Tanzania. The central part of the image is athwart the southern extension of the east or Gregory arm of the Great Rift Valley described in detail in Plate T-35 (Baker et al., 1978). Surficial evidence of rifting is less conspicuous in this segment than farther to the north, except for occasional step-fault traces (A) (Figure V-19.1) and the north-south elongation of the three lakes shown. In this part of East Africa, the rift has split into an Eastern (shown here) and a Western Rift owing to deflection of the main fracture system by the Tanganyika craton (Fiarhead, 1980). In the image, the Eastern Rift south of the Nguruman Fault has further split into two segments that pass by the elongate shores of Lake Manyara and Eyasi. The rift farther south becomes less well defined as it intersects on a southwest-trending structural lineament reaching almost from the Indian Ocean down to Lake Malawi, where it joins the Western Rift. Rifting in East Africa is associated with uparching of the Kenya Arch. Directions followed by most rift fractures appear to be closely controlled by lineaments in the underlying Precambrian. The eastern side of the Eastern Rift is a step-faulted downwarp; sharper faults line the western side. Although large throws (1000 to 3000 m) have been measured, the present topography is held to elevations around ~600 to 900 m, and relief is subdued.

The western third and isolated sections elsewhere in this image are part of the Serengeti Plain, underlain mainly by Precambrian crystallines and metasedimentary rocks. This plain is a remnant of an Early Cenozoic erosion surface. Drainage presently moves westward toward Lake Victoria and the Western Rift, with the divide near the east side of the image. Lateritic soils have developed over these and younger volcanic rocks. The shallow lakes of the region are examples of interior drainage in which water levels fluctuate considerably and salts are concentrated by evaporation. Lake Natron, for example, contains thick deposits of sodium carbonate.

Volcanism began in the Tertiary and continues even now (Goles, 1980). Many volcanoes are found within the rift zone, but it is often difficult to associate a given volcano with individual faults. Several of the volcanoes, however, lie outside the primary zone of rifting (e.g., the space view of Mt. Kenya (Figure V-19.2)



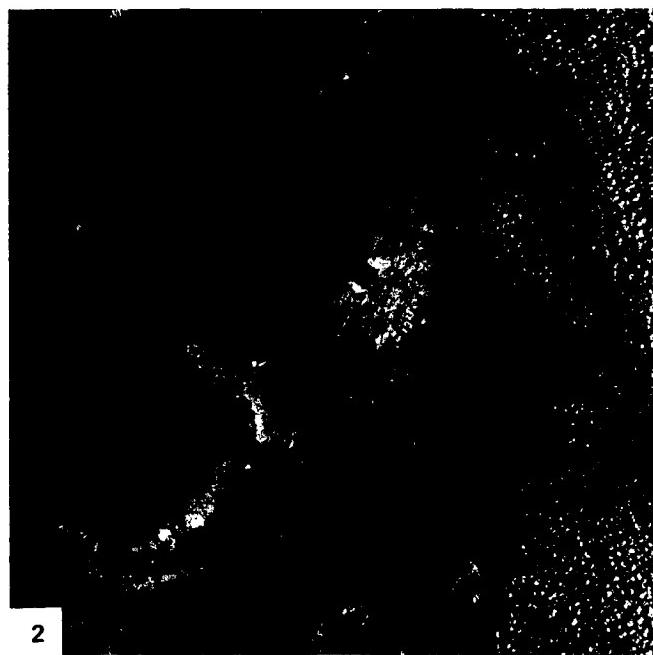
1

EAST AFRICAN VOLCANISM

and Mt. Kilimanjaro elsewhere to the east off image). Inception of the first significant volcanism roughly coincided with the start of major rifting in the Miocene (Baker and Wohlenberg, 1971). Volcanic outpourings nearly fill most of the rift depressions and, in this scene, spill beyond westward and for 150 km to the east. Two series of compositional trends are distinguished: one is notably alkaline, is marked by nepheline, and evolves into phonolites; the other is less alkaline and nepheline-free, with rhyolites and trachyandesites as end products. Basalts and nephelinites emerged first, some from central volcanoes. Vast floods of phonolite followed, building up a plateau of flow units that extends beyond the main zone of rifting (Goles, 1980). A succession of trachytes, nephelinites, and phonolites, then more basalts, and finally trachytic pyroclastic units closed out the Tertiary activity. Quaternary volcanism began with fissure eruptions of basalt and basanite lavas, and then trachytes, rhyolites, and phonolites erupted from central vent volcanic edifices located within late-forming grabens of the rift zone.

A cluster of peaks and calderas dots the aptly named Crater Highlands northeast of Lake Eyasi. Dominant among them is the shallow caldera of Ngorongoro, with its satellites, Oldeani and Lemagarut, and the smaller crater of Olmoti. These now extinct volcanoes erupted trachytic flows and large quantities of pyroclastic materials that in places are recognized by their lighter tones. Tephra from these sources play a role in geochronology at Olduvai Gorge, where skeletal remains of early hominids are preserved.

Volcanoes Essimingor and Gelai follow the nephelinite/phonolite trend. That small conical volcano, Oldestyo Lengai (2880 m above sea level; Figure V-19.3), and the nearby caldera-topped Kerimasi have expelled ash of carbonatite composition and sodium-rich flow material is well known from Oldestyo (note bright spot in its interior). This is the only active volcano in this region of the rift, having erupted more than eight times in the last 300 years. These volcanoes are the principal suppliers of the soda that accumulates in the Lake Natron lacustrine deposits. Kitumbeine to the southeast is a smaller version of Mt. Kenya and is the source of phonolite and basalt flows and ash (LeBas, 1977). *Text modified from comments by G. Goles, University of Oregon.* Landsat 2368-07040-6, January 25, 1976.



2

ORIGINAL PAGE
COLOR PHOTOGRAPH

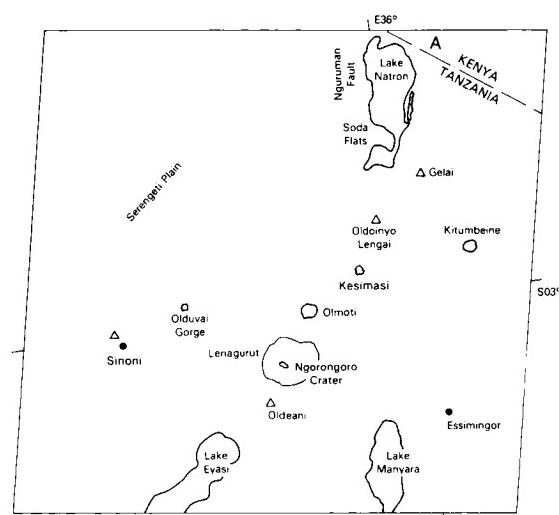
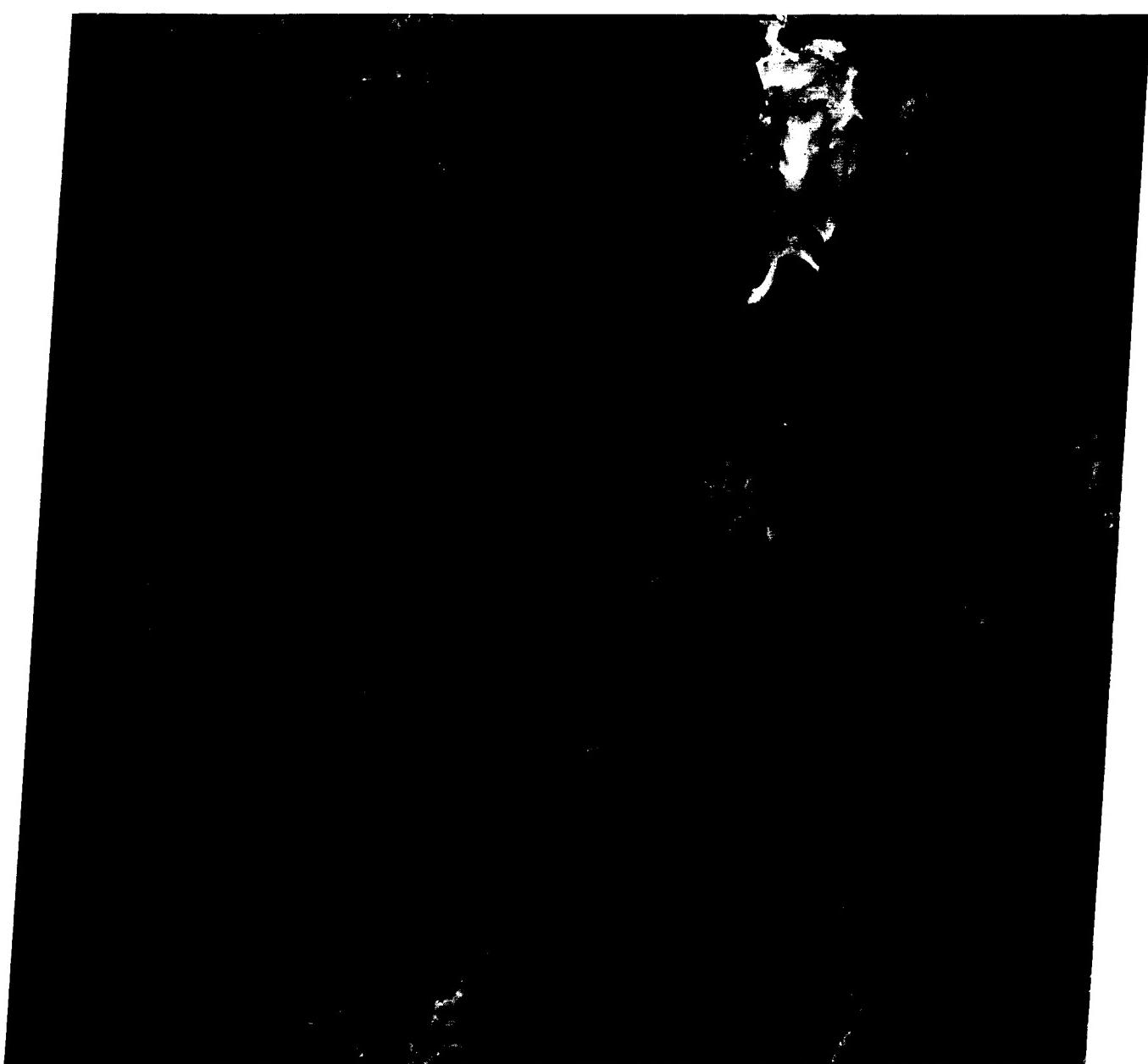


PLATE V-20

This Plate encompasses part of the southeastern Great Karroo Basin in the Cape Province of South Africa (Furon, 1963) to the southwest of Lesotho. The Great Kei River, visible near the lower right corner, has formed conspicuous entrenched meanders.

Southwest of the image are the east-west-trending Cape Ranges, a Paleozoic fold belt deformed in the Permian. Unexposed basement within the scene is part of the Precambrian Namaqua-Natal mobile belt (gneisses-granulites) peripheral to also-covered much older Kaapvaal Craton block. This ancient terrane lies at the base of a northwest-trending basin that received up to 8000 m of sediment between Late Carboniferous and Early Jurassic times. Four divisions of the basin infilling sediments of the Karroo System comprise a supergroup of depositional units. The older Dwyka and Ecca units do not outcrop in the scene. Most of the southern two-thirds of the image is occupied here by the Beaufort Series, a stratigraphic succession of arenaceous and argillaceous fluvial channel sands laid down during the Middle Permian/Early Triassic. The Beaufort Series is noted for its fine assemblage of amphibian and reptilian remains and land plants, indicating a depositional environment of low marsh surfaces periodically affected by shallow seas (Kitching, 1978). Parts of the northern third of the scene are topped by sediments of the Stormberg Series (type locality at the Stormberg (2168 m)), including white and red sandstones and grayish shales, that contain distinctive dinosaur remains. The youngest part of the Karroo succession is represented by the Drakensberg Volcanics (Early Jurassic), basalt flow lavas over basal tuffs and agglomerate. In the top right of the image, a mountainous plateau (elevation to 2700 m), with its fringing escarpment, is capped by this unit. A second escarpment, cut into the Stormberg Series, crosses the image (see index map); a lower cliff (dashed line) bounds rugged terrain below the Great Kei River.

Roughly coeval with the Drakensberg plateau basalts are the Karroo dolerites, lavas with calcic plagioclase laths, pyroxene, and sometimes olivine. These lavas were intruded at hypabyssal depths into the Beaufort Series. They inserted first through steep dikes and then concordantly along bedding planes (usually in shales or at shale contacts) as sills. Many sills are a few meters thick at most, but thicknesses up to 300 m are reported. More than 570000 km² in this part of the Karroo basin were affected

SOUTH AFRICAN SILLS

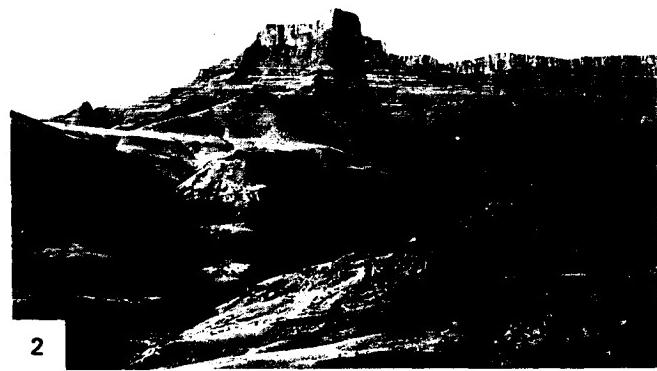
by this intrusion, which actually covers much larger areas in various parts of southern Africa. In the image, the sills are more abundant in a lowlands between two major scarps.

Distinctive landforms (called "koppies" by the South Africans) have developed from these sills. On the ground, the sills usually appear as cappings for the mesa-like hills (Figure V-20.1). In the satellite image, the koppies tend to stand out as curved (crudely circular to irregular but usually closed) dissected ridges with both outward- and inward-facing scarps. They ring Beaufort Series sedimentary units exposed within the curved ridges and beyond. These units have been gently folded with the curvature of the caprock contributing to the present interior "basins" tapping some koppies. Although this folding postdates the close of the deformation that produced the Cape Ranges, it may relate to continuing compression. Intrusion during subsequent regional tension may have been under post-orogenic conditions similar to those leading to injection of Triassic trap lavas in the eastern Appalachians. The dolerites were probably emplaced within the time interval in which the supercontinent of Gondwana began to break apart. Their mobilization from depth into shallow sills and surface outpourings appears to be consistent with comparable lava extrusions during early stages of rifting and consequent spreading (Bristow and Saggerson, 1983).

At the time of the Gondwanaland split, a general erosion surface—describable both as a pediplain and a peneplain—had been imposed on this part of the supercontinent (King, 1951). A remnant of this surface may be preserved in terrain seen at the top of this image. The next cycle of erosion, the post-Gondwana, continued into the Cretaceous. Subsequent cycles, named the African (Early Cenozoic) and post-African (Late Cenozoic), affected areas around this scene. Especially prominent is the south-facing Great Escarpment (near bottom of image), which overlooks the Cape Ranges. This escarpment takes on a dramatic face in eastern Lesotho and neighboring Natal, where its front displays relief up to 1500 m or more (Figure V-20.2). The appearance from space of this volcanic terrain is presented in Figure V-20.3. The upper or African surface was developed on Karroo volcanics. The lower but younger post-African surface that extends almost to the coast below Durban was produced by erosion following regional uplift. **Landsat 1049-07315-6, September 10, 1972.**



1



2

ORIGINAL PAGE IS
OF POOR QUALITY

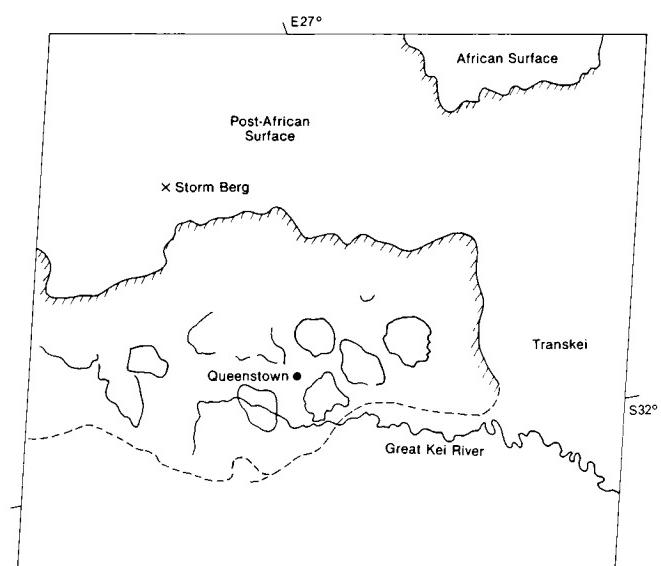
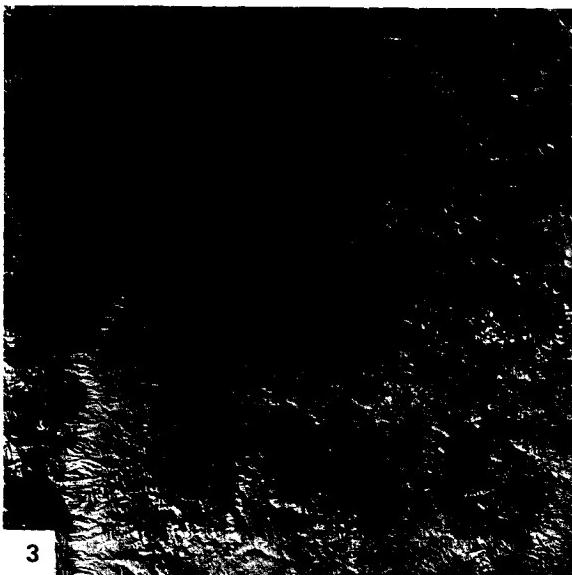
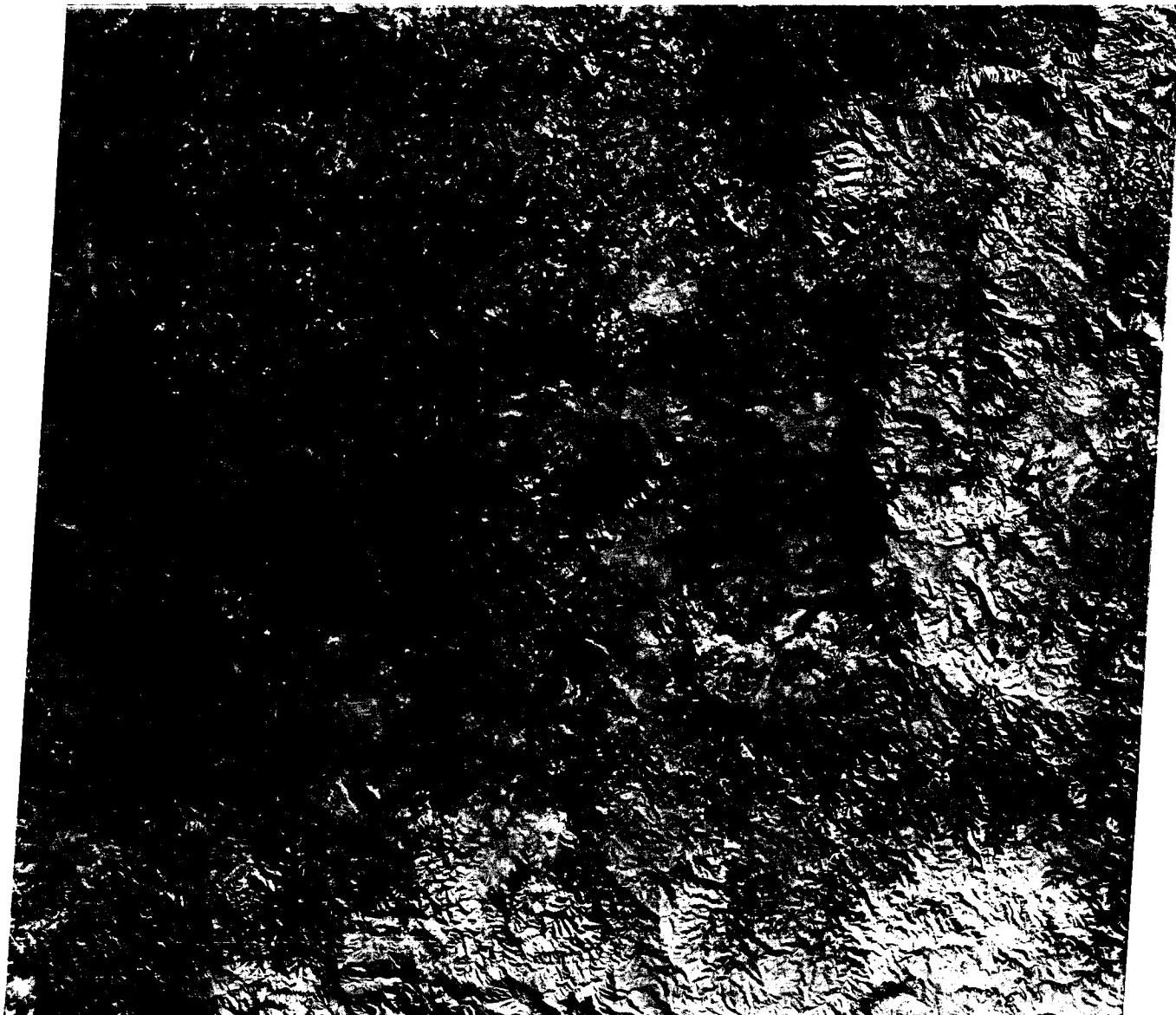


PLATE V-21

ORIGINAL PAGE IS
OF POOR QUALITY

VOLCANISM IN THE AFAR

This superb Large-Format Camera (STS-41-G) scene might better be retitled "Birth of an Ocean," except for the missing water. The Afar Triangle lies at the most obvious triple junction (between the African and Arabian tectonic plates) visible anywhere on the Earth's surface. Here, three arms of an aulacogen—represented by the Gulf of Aden/Red Sea/African Rift Valley—meet in an almost classic intersection with angles between arm pairs approaching 120° . The nature of this junction is reviewed, along with a broader treatment of the regional geology in Plate T-36. Oceanic crust has formed over the last 4 Ma in both arms now invaded by the sea (Barberi et al., 1972). At the Afar, oceanic basalts similar to those in the two marine arms have poured over older basalts and continental crust intermittently in the last 2 Ma. Thus, the surface seen in this plate displays many characteristics assumed to be typical of a newly formed volcanic crust proximate to a spreading center (see Iceland, Plate V-15).

The Afar occupies a relatively low region of northeast Ethiopia and extends to the district of Djibouti at the head of the Gulf of Aden, which terminates at the small Gulf of Tadjoura. Structurally, it is a lowlands located between the Ethiopian Plateau (west), the Somalian Plateau (south), the Aisha Horst (east), and the Danakil Horst (northeast). Parts of the Afar, such as the Danakil Depression, now lie below sea level (Gibson, 1969).

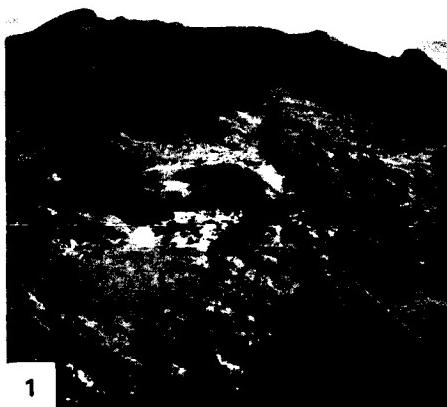
In places within the Afar, especially to the north, Precambrian basement, which is prevalent in the Ethiopian Plateau, is exposed. Marine sediments covered most of the region in the Mesozoic. This general region of East Africa/Arabia began to rise in a broad swell, the Afro-Arabian Dome (with Nubian, Somalian, and Arabian segments), in the Early Tertiary. This coincided with partial melting in the mantle, generating magmas that moved up along one or more thermal plumes. The first effusive lavas in the Eocene are represented by the basaltic Trap Series, which can be subdivided into an earlier, more alkaline phase and a later peralkaline phase (erupting during Miocene/Pliocene times; Mohr, 1983). These basalts show high Na/Si and $\text{Fe}^{+3}/\text{Fe}^{+2}$, high water content, and low TiO_2 .

As the dome was subjected to extensional stresses during arching, great fissure systems developed that were precursors to the current fault zones associated with the arms. Graben tectonics

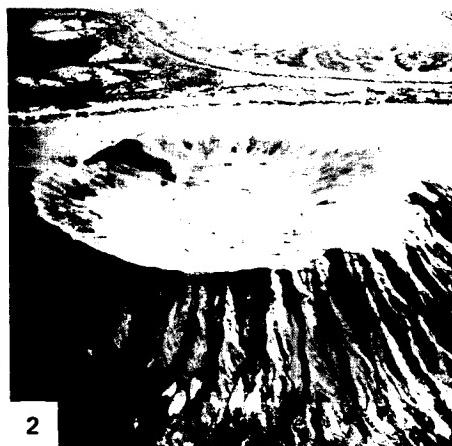
prevailed, with normal faults often antithetic (Baker, 1972). Tholeiitic basalts first invaded the "oceanic" arms, then in Late Pleistocene/Recent times, spilled out within the Afar and in parts of the Ethiopian Rift to the south. Silicic crust may be completely separated where the new Arabian plate (moving northeast) has split off, with the basalts now filling a fracture system deep into the lithosphere. Where the crust experienced strong attenuation, a tholeiitic lava type has emerged; elsewhere, coeval low-alkali basalts were extruded as the Aden Series. Later, tholeiites emplaced from fissures became the dominant type in the Afar; these layered flows comprise the Stratoid Series. The lavas flowed widely over the landscape, but here and there, small shield volcanoes, such as Dame Ale, calderas such as Fantale (Figure V-21.1), and guyot-like cones (Figure V-21.2), have built up.

The present scene is remarkable for the numerous step faults (throws seldom exceeding 100 m) that cut through the Trap (largely buried), Aden, and Recent basalts (Mohr, 1975). These extensional faults, some producing rotated blocks, make distinctive cliffs (Figure V-21.3) within the topography. The principal trends of these faults are subparallel to the three aulacogenic arms. Over much of the Plate scene, the fault zone strikes northwest, but northeast of Lake Abbe (part of which is visible at bottom center), the trend is east-west; southwest of that lake is the northern end of the Wonji Fault Belt that connects with the main African Rift Zone. The lake itself lies quite near the "point" at the triple junction. To the west, faults and lineaments follow a north-south trend, roughly parallel to the contact with the highest Ethiopian Plateau. Transform faults have been postulated for the Afar, but significant horizontal offsets are not evident in the image; their surface expression may be sets of en echelon faults. Several grabens in the scene (e.g., Gawa) have curved boundaries, suggesting progressive rotation, with en echelon cross-faulting, perhaps controlled by movements of the Danakil horst. These and other depressions create internal drainage conditions, with entrapped waters becoming brackish to strongly alkaline; the white tones in the image coincide with gypsum and halite deposits.

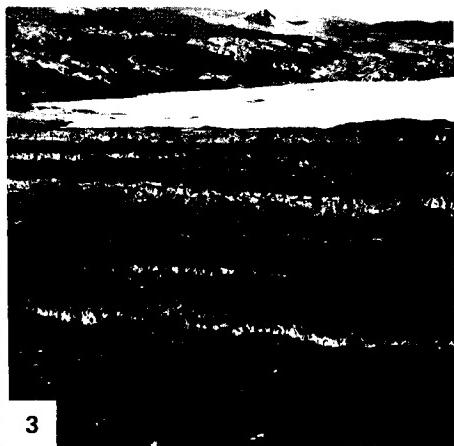
Contributor: Timothy Stacy, University of Maryland. Additional References: Barberi and Varet (1970) and Mohr (1975). Large Format Camera, October 31, 1972.



1



2



3

ORIGINAL PAGE IS
OF POOR QUALITY



PLATE V-22

Volcanic rocks and intrusive magmatic-metamorphic crystalline rocks are frequently coassociated in terranes in which these several rock types are emplaced contemporaneously or in a succession related to stages in an orogenic cycle. It is unusual, however, to find young volcanic structures and products resting directly on ancient stable cratons. The Plate scene and Figure F-22.3 testify to the occasional condition in which Tertiary/Quaternary volcanism can develop on supposedly stable Precambrian shields, producing flows and ejecta deposits that have escaped primarily from fissure feeders that utilize deep crustal fractures. Striking examples of dark basaltic flows are found on heavily jointed crystalline surfaces in North Africa and the Arabian Shield.

The main Plate is a color-ratio composite made from the combinations of bands 5/4 (blue), 6/5 (green), and 7/6 (red) for this Landsat MSS scene. This rendition enhances certain rock units and improves their overall recognition. To assess the quality of discrimination, compare these units with their corresponding equivalents in part of the 1:250 000 Al Madinah Quadrangle (Sheet 24) map prepared by the U.S. Geological Survey for the Kingdom of Saudi Arabia as reproduced below at reduced scale in lieu of an index map (Pellaton, 1982).

Three groups of Upper Proterozoic rocks are present in this shield region, but the oldest, the Hulayfah Group, lies outside the scene. Next are members of the Al Ays Group, with lithologies ranging from pyroclastic rocks, andesites, rhyolitic tuffs, epiclastic sandstones, graywackes, and other sedimentary types. These are overlain by the Furayh Group, which is composed of a lower conglomerate/sandstone, next a unit containing other sedimentary lithologies, then an andesite-basalt lava and pyroclastic sequence, and a basin-filling section of mature sedimentary deposits. During Proterozoic time, these groups were periodically invaded by intrusions ranging from gabbros through granodiorites and tonalites after the Al Ays Group was emplaced, and a variety of igneous bodies (including alkalic to peralkalic granites) subsequent to the Furayh Group. Late Precambrian/Early Cambrian orogenic events led to low-grade metamorphism (greenstone facies) and tectonic fracturing.

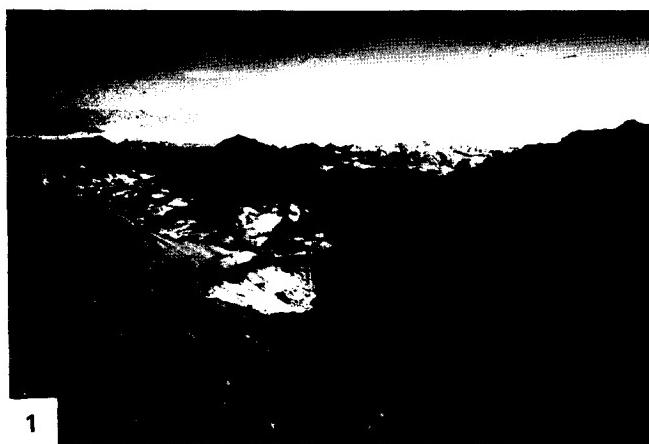
ARABIAN SHIELD VOLCANISM

Except for localized remnants of Cambro/Orodovalian sandstones, the region persisted as a stable landmass until the Tertiary. Then, a series of olivine basalt flows (b1, b2), followed by trachypholitic rocks (b3, tr), and finally Quaternary basalts (b4, b5) (all labeled on the color map) were extruded from fissures and conical vents. Upwards of 400 m of volcanics piled up between the earliest phase, some 11.1 ± 0.8 Ma ago and flows as young as the 13th century A.D.

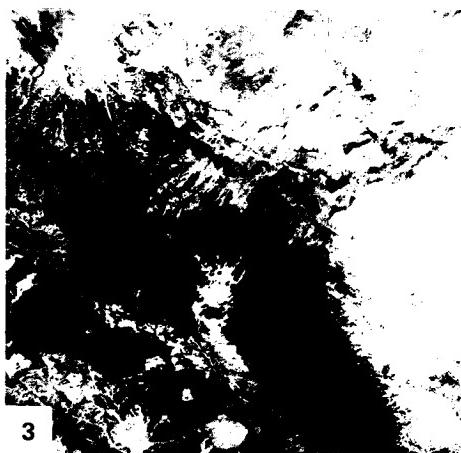
In the color composite, most of the flow units can be distinguished from each other by sharp to subtle differences in color tones (best seen on the original). Unit b1 appears light brown; b2, dark yellow to medium brown; b3, tan-brown; b4, orange; and b5, black to orange. These differences relate more to extent of weathering over time than to compositional variations. Precambrian clastic/volcanic units show up as brownish-black. Crystalline igneous rocks usually are varying tones of bluish-white to light tan. Quaternary sabkhas (saline clay beds) are rendered in light blue, which can be confused with similar tones for some granitic rocks.

Topography (Figure V-22.1) is characterized by dissected plateaus between the Hijaz Mountains to the west and a peneplain farther east. Basalt plateaus (Figure V-22.2) are known as harrads. Prominent in the Landsat scene is Harrat Rahat (lower right), a convex upland whose relief is produced mainly by volcanic craters and cones. Several internal-draining wadis (ephemeral desert channels) cut steep gorges where they pass over mountainous terrain (upper left in Plate).

Figure V-22.3 illustrates similar terrain on the Arabian Shield inland from the coast farther north (Gass and Mallick, 1966), again as imaged by Landsat. Precambrian units at the lower left are exposed where remaining Paleozoic cover (upper right) was stripped off. The prominent Harrat al 'Uwayrid runs northwestward near the line of unconformity. In the center of the image are numerous cones and craters giving vent to young dark basalts. **Landsat 1446-07195, October 12, 1973.**



**ORIGINAL PAGE IS
OF POOR QUALITY**



3



PLATE V-23

The Deccan Plateau ranks as the world's fourth largest (volumetrically) subcontinental outpouring of plateau basalt lavas extruded at unstable margins during active plate tectonic movements. Once covering more than 1 000 000 km² with an average thickness of 1 km, its present subaerial volume of 500 000 km³ is 2.5 times larger than the Columbia Plateau basalts, but smaller than flood basalts associated with the Karroo lavas of Africa, the Siberian Plateau in Asia, and the Paraná Plateau of South America (Windley, 1984).

This scene shows a part of the surviving Deccan cover along the west coast of the peninsula section of India. On land, about 500 000 km² of these flows remain following Cenozoic erosion. Nearly the entire continental portion occurs within a single continuous mass extending eastward from Bombay (just off the image at left center), but outliers have been correlated with these basalts in Madhya Pradesh, Orissa, and the East Coast. A further continuation of the flows is known from drilling and seismic records for the Arabian Sea to the west; one postulate considers this section to have been down-dropped by faulting of part of the Indian block after the lavas were emplaced and probably during the collisional phase following the northward drift of India into Asia.

Much of the peninsula is a Precambrian shield containing mainly Archean rocks. As such, it was part of the great landmass of Gondwana that began to break up during the Mesozoic. India itself began its northward traverse about 80 Ma ago. The Deccan extrusions commenced in the Late Cretaceous (Cenomanian) and proceeded for 10 to 20 Ma into the Eocene. Eruptions from fissures were relatively quiet and periodic, being classed as Hawaiian type, with associated lower viscosity flows. At least 40 separate flow units can be distinguished, most of them under 30 meters thick but some much greater. Maximum aggregate thicknesses around 2000 m are attained on the western side, as in this Landsat scene. The flows remain nearly horizontal, with a slight eastward inclination. Lithologically, they are continental tholeites

THE DECCAN PLATEAU

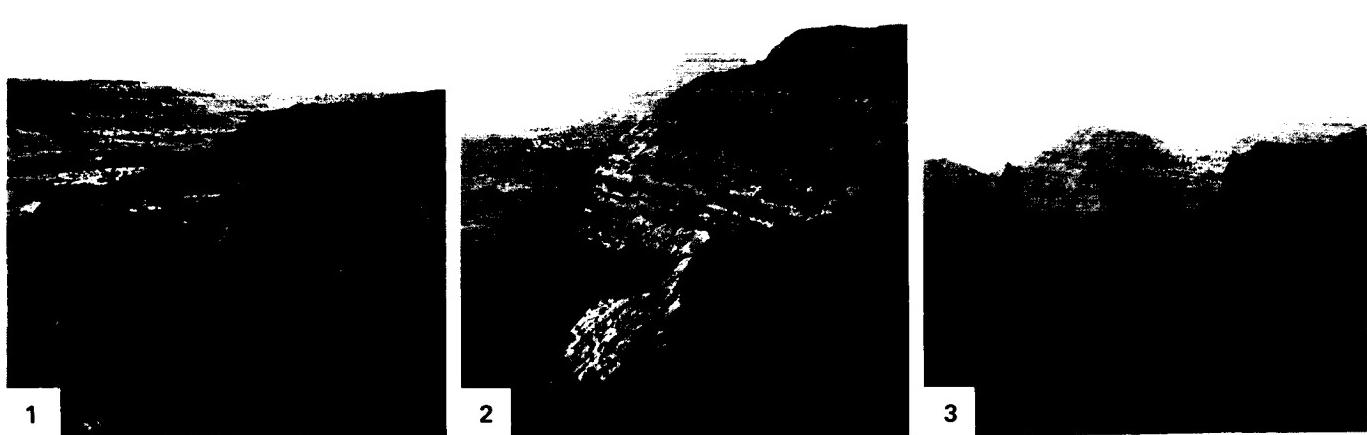
(with labradorite (An_{65}), enstatite, augite, some olivine, and secondary zeolites; ophitic textures are common). Interbeds of fluvial and estuarine limestones and shales (Lameta beds) and sandstones (Infra-Trappean beds) attest to periods when volcanic activity was quiescent.

The regional physiography is one of flat-topped hills and ridges and broad valleys (Figure V-23.1) whose surfaces conform to lava layer boundaries. The darker, almost dendritic drainage patterns evident in Figure V-23.1 are characteristic of a plateau topography controlled by horizontal units. In the Plate image, a series of embayed escarpments (Figure V-23.2) are evident near the coastline. This topography is typical of the Western Ghats, a dissected terrain with considerable relief and elevations up to 1000 m (Figure V-23.3). These are "mountains" of denudation rather than of deformation. "Ghats" refers to steps or terraces that are brought about by erosion along different flow units. The term "Deccan trap" denotes a similar concept, with "trap" being a Swedish term for a terraced plateau.

A remarkable drainage pattern is exhibited in this image and elsewhere along the peninsula, such as that shown in the Landsat scene to the southwest (Figure V-23.4). Rivers such as the Krishna and Bhima, and the Godavari to the north, have their headwaters in the western Ghats within 40 to 100 km of the Arabian Sea. Because of the eastward tilt of the Peninsula, these rivers flow for up to 1000 km to the Bay of Bengal along the east coast rather than across the Ghats divide for short journeys to the west.

Most of the basalt trap rocks are now strongly weathered to *regur* soils, a deep brown to reddish residue rich in Fe, Mg, Ca, alkalis, and organic matter that is exceptional for growing cotton. Laterites also develop over the region. Vegetation is of the savannah type over most of the plateau. Additional References: Krishnan (1949, 1963), Mehdirata (1962), Narain (1968), Sukheswala and Poldervaart (1958). Landsat 30278-04492-5, December 8, 1978.

ORIGINAL PAGE IS
OF POOR QUALITY



ORIGINAL PAGE IS
OF POOR QUALITY

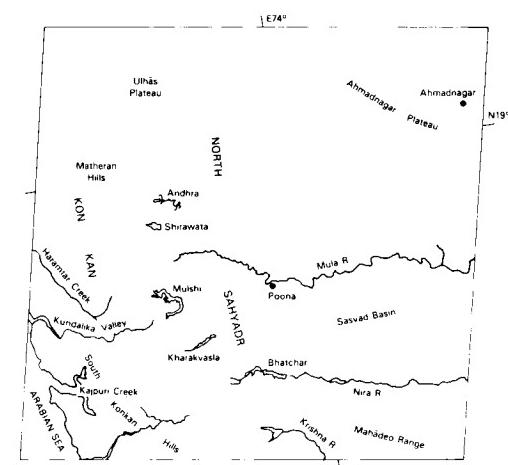
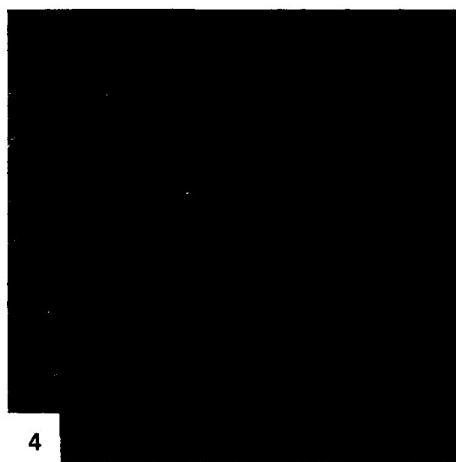


PLATE V-24

KYUSHU, JAPAN

The reader is referred to Plate T-54 for a background synopsis of the geology of the Japanese Islands (see also Tanaka and Nozawa, 1977; Yoshida, 1975). The southwestern island of Kyushu contains many of the same petrologic, structural, and age units described earlier for the Inland Seto Sea scene. Kyushu is part of the Ryukyu Arc system, which meets the Southwest Japan Arc north of Oita. The southwestern extension of the Median Tectonic Line (MTL) once again divides this island into the older Inner Zone (metamorphic terrane) and the younger Outer Zone (sedimentary terrane). Various belts within these two zones cross the island. Their approximate positions as deduced from published maps are shown in the index map but, except for the MTL, neither the actual boundaries nor the different terranes are well expressed in the image.

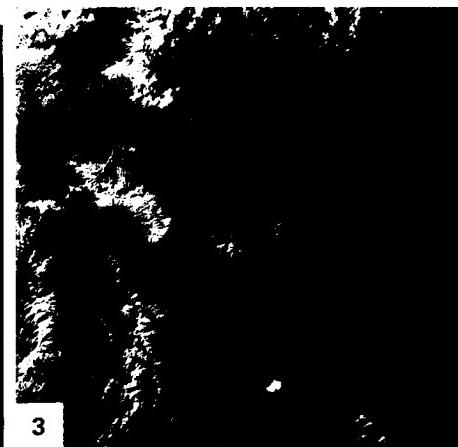
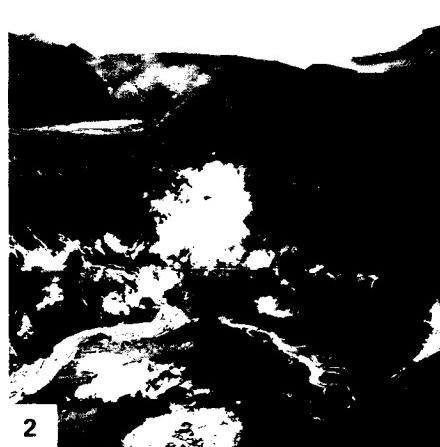
The contact between the Sangun and the Ryoke metamorphic belts appears to run through the giant Aso caldera (see below). Cretaceous granites intrude into the Sangun belt. The western termination of the Sambagawa belt lies just below Oita. In the Outer Zone, the Chichibu belt is characterized by linear ridge crests. Patches and inliers of Silurian/Devonian, Carboniferous, Permian, and Triassic units occur mainly in this belt. The narrow Sambosan belt and its southern boundary fault, the Butsuzo Tectonic Line (BTL), seem to have a faint expression. To the southeast are Cretaceous sedimentary units of the Shimanto Belt. Paleocene rocks make up the surface at the lower right corner; an inlier of this age occurs to the north, and Paleocene units cover most of Amakusa Island. High-pressure crystalline schists comprise the north-south-trending Nishisonogi belt around Nagasaki, which may be a continuation of the Sambagawa belt.

The volcanoes of Kyushu (Matumoto, 1963) lie along the West Japan Volcano Belt that extends southwestward through the Nansei (Ryukyu) Islands. The Aso Volcano is a Valles-type caldera (20 km maximum dimension) formed by multiple collapses as pyroxene andesites ashflows were ejected during Late Tertiary through Pleistocene times. Ignimbritic ashflows, pumice, and other pyroclastics (some water-saturated, producing so-called "mud lavas") filled river valleys and extend almost across the island (light tones near caldera walls are ashbeds) (Yoshikawa et al., 1981). Views of Mount Aso, a post-collapse crater within

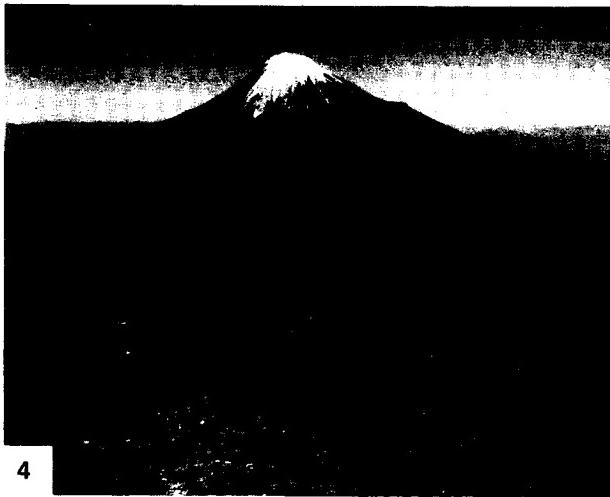
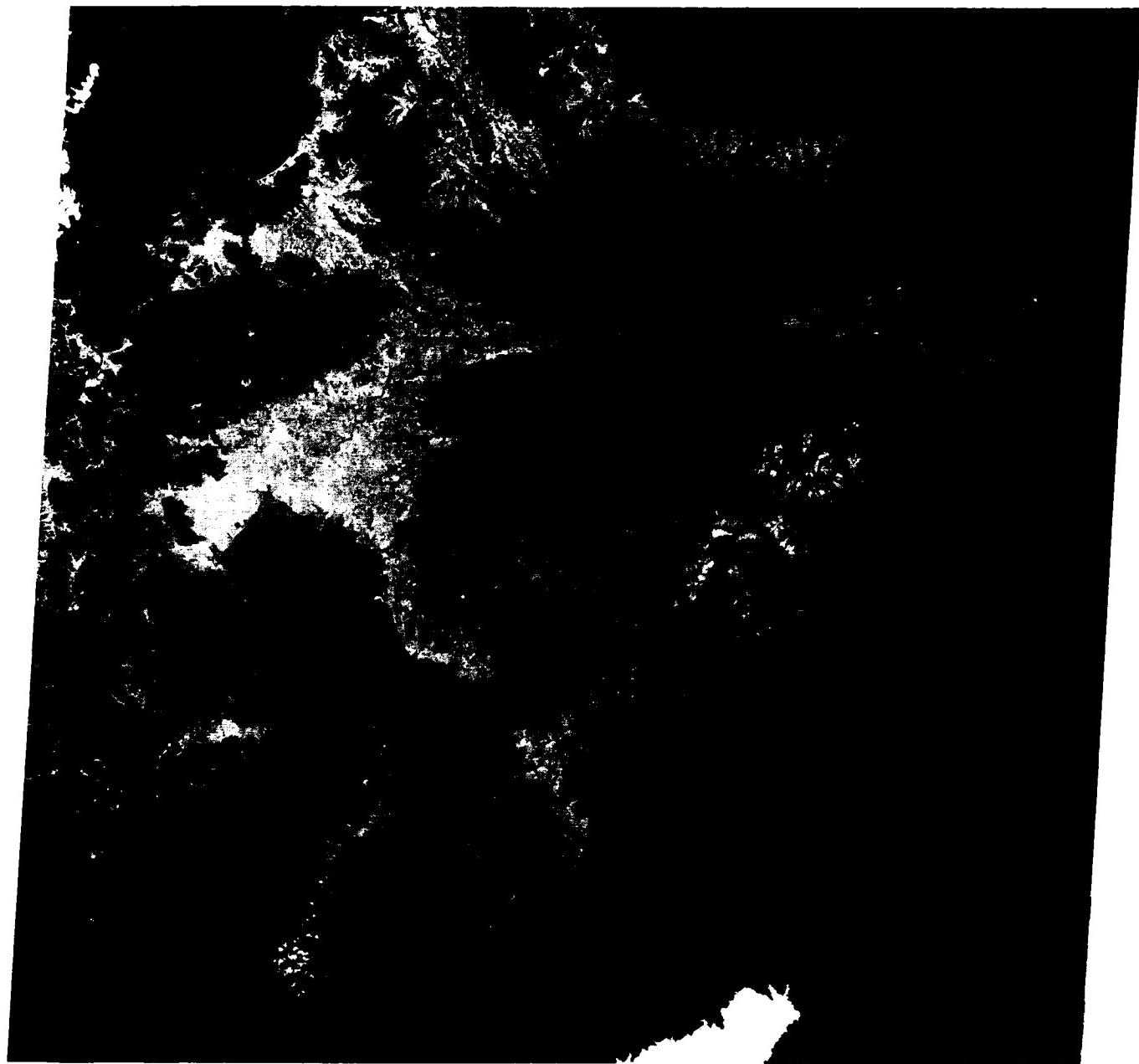
the caldera, are presented in Figures V-24.1 and V-24.2. Mt. Unzen, Mt. Kuju, and others in the Landsat scene, marked by V's, are dissected Quaternary stratocones that erupted lavas and ash of hornblende andesite composition.

Figure V-24.3 is a Landsat scene taken on December 15, 1972. The three prominent rivers (from left to right) are: Tenryu, Fuji, and Tone Rivers. This is a critical section in the Japanese Arc geologic framework because it marks where the Island of Honshu is separated into two geologic regions (Southwest and Northeast Japan Arcs). In this area is a rupture zone known as the Fossa Magna, whose western border is denoted by the Itoigawa/Shizuoku Tectonic Line (upper left to lower center). To its east are the Kanto Mountains and Kanto Plain. (Part of western metropolitan Tokyo appears here.) The Akaishi and Kiso ranges to the southwest are on either side of the north-south Ina tectonic valley. Parts of the Sambagawa, Chichibu, Sambosan, and Shimanto belts lie to the south of the Tone River. The Median and Butsuzo Tectonic Lines continue through the scene but are deflected northward around the Fossa Magna (a folded zone containing Neogene sediments and Neogene/Quaternary volcanics) before turning east again. North of these lines (near the top of the scene) are three Inner Zone terranes—the Joetsu, Ashio, and Tsukubawa belts. A province of the Green Tuff region, an assemblage of altered volcanic rocks and clastic sediments laid over older rocks in the Miocene, then folded, metamorphosed, and intruded by granites, occupies much of the western half of the scene.

In the Fossa Magna scene, the famed Mt. Fuji (Figure V-24.4), a composite cone, has erupted lavas, ash, and tephra of basaltic to mafic andesitic composition. To its southeast, the Hakone volcano is a caldera formed from collapses of an old and a young cone after numerous pumice and lava eruptions. The older Ashitaka volcano falls at the third (south) apex of the triangle of volcanoes that stand at the head of the Izu Peninsula. Older dissected stratocones are visible in the image north of the Fuji River and west of the towns of Takasaki/Maebashi on the Tone River. Still farther west is frequently active Asama-yama, site of a disastrous eruption in 1783 that produced two nuées ardentes and a lava flow. **Landsat 30277-01130-5, December 7, 1978.**



ORIGINAL PAGE IS
OF POOR QUALITY



4

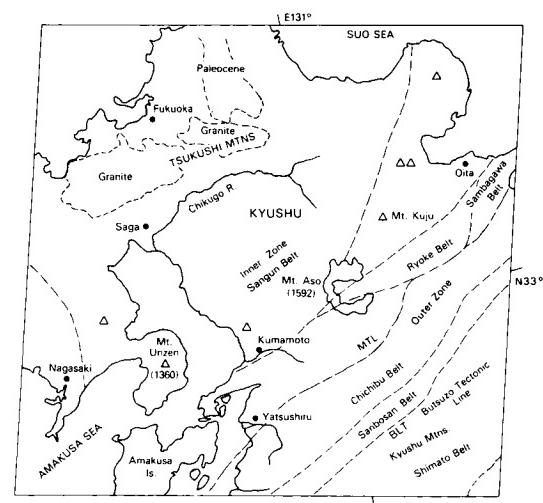


PLATE V-25

The Kamchatka Peninsula in eastern Siberia is a segment of the famed Pacific Ring of Fire. Together with Java, it ranks as one of the most active volcanic segments along the ring, and one of its volcanoes, Klyuchevskaya, is claimed to be the most active in the world (Markhinin, 1971). The peninsula is approximately 1200 km (750 miles) long and varies in width from 485 km (300 miles) to a minimum of 97 km (60 miles). At its southern tip, it ties in with the Kurile Islands, another volcanic chain. Tectonically, this peninsula is akin to an island arc, analogous to those in Indonesia, except for its continuity with the Asian mainland. In some respects, its closest analog on the ring is the Cascade Range of western North America (Coster, 1963). The Kamchatka Peninsula connects with the great arc system of the Aleutian Islands at a juncture near latitude 58°, but the two arcs lie parallel to trenches that meet at nearly 90°, just offshore from the central part of the peninsula.

The backbone of Kamchatka is the Shredinny Khrebet, subdivided into the western and eastern ranges, composed of Mesozoic gneisses and granites, Cretaceous/Paleocene volcanics and clastic and siliceous sediments. Miocene tuffs, all strongly folded in the Pliocene, were followed by volcanic renewal through the Quaternary to the Holocene. Erlich (1979) describes the structure of Kamchatka as a geanticlinal-volcanic island arc belt that underwent abrupt uplift in the Quaternary, during which an en echelon system of anticlinal horsts and synclinal grabens developed; present volcanism is concentrated in these grabens, which as intermontane troughs have partly backfilled with alluvial deposits. More than 100 volcanic edifices are recognized on the peninsula, of which at least 15 comprise currently active vents. Most older volcanoes occupy the western half of the peninsula; by Quaternary time, the main belt of volcanoes had shifted to the eastern third. The eastern zone is structurally controlled by lineaments that parallel the northeast alignment of the ranges. A second lineament trend, northwest, approximately in the direction of the Aleutian Trench, also influences the distribution of some volcanoes. The majority of volcanoes are composite stratocones, some now topped by calderas built mostly of pyroxene andesite tephra mixed with some lava flows (Zavaritski, 1977).

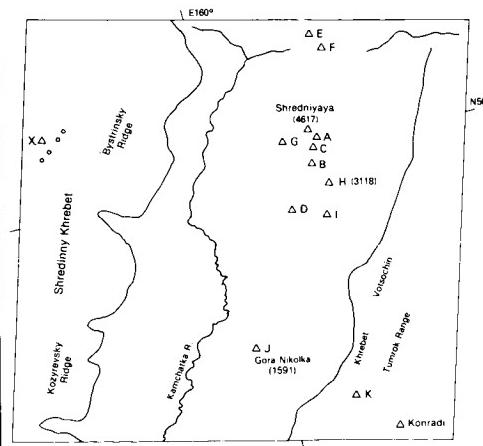
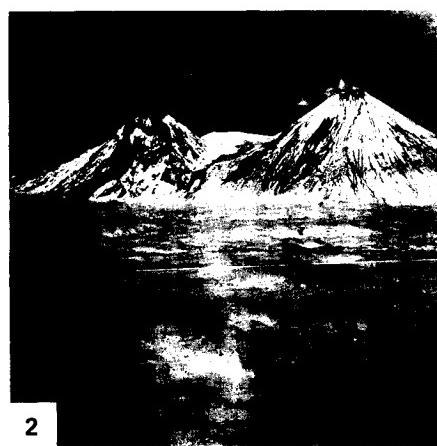
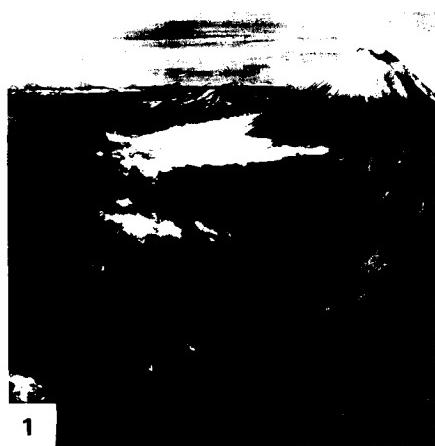
The main cluster (Klichii Group) of volcanoes seen in the Plate, dominated by Sopka (Volcano) Klyuchevskaya (A), 4850 m high, lie within the intersection of sets of northeast-northwest lineaments (Erlich et al., 1972). These volcanoes occur within a

KAMCHATKA PENINSULA

broad structural trench or graben through which flows the Kamchatka River and whose surface is 500 to 1500 m above sea level. The elegant profile of Klyuchevskaya (Figure V-25.1) attests to its continuing eruptions (more than 75 since 1700 A.D.; a major one in 1915), which add materials to its constructional surface faster than erosion can dissect it. Aligned with Klyuchevskaya along a northeast line are the nearby volcanoes, Bezmyanny (B) and Kamen (C) (4617 m) (Figure V-25.2), Tolbachik (D) (active; 3682 m), Kharchinsky (E) and the breached crater of Zarechny (F), and the active Shiveluch (off the image just to the north); Shredinaya lies in the shadow of Klyuchevskaya. The inactive Ploskaya (G) (4030 m), with a prominent central caldera, and the Zimina group (H) (Figure V-25.3) form along a northwest trend. The Udina volcanoes (I) complete the cluster. To the south, Sopka Kinchkolak (J), also known as Gora Nikotka, has been much dissected into barrancos (consequent stream-cut ravines). In the uplands above the graben, in the Tumrot Range, stands the active Sopka Kizimen (K) (2375 m relief).

Another major line (almost 400 km long) of volcanoes, the North Kamchatka/Olyutorsky Group, occupies a graben valley on the west side of the Shredinny Range. Near the left edge of the Plate is a cluster of these volcanoes, including a stratocone at X, that corresponds to a segment of the group including Eggela, Budul, Kapkan, and Anuan.

A joined pair of Landsat images (Figure V-25.4) depicts the southern end of the Kamchatka Peninsula. Here the locations of most volcanoes near the eastern side of the peninsula are clearly defined. Active volcanoes include Ksudach (L) (1095 m), Zheltovsky (M) (1953 m), Ilinsky (N) (1578 m), and Koshelev (O) (1863 m). Older sopkas are represented by Vilyuchik (P) (2175 m), Asacha (Q) (1137 m), Svetly (R), the Khodutka group (S), and Kambolnaya (T) (2160 m). Off the main trend are the still-active Opala (U) (2475 m), the huge strongly dissected Ipelka (V) (1911 m), and Tomalchev (W) volcanoes. Some Russian volcanologists consider Kurilskoye Lake to be a large collapsed caldera. Between Asacha and Vilyuchik, and just off the mosaic, is another group, shown in a photograph (Figure V-25.5) taken during the STS-9 (Shuttle) mission. The large caldera, with its tiny crater-capped central cone, is Gorely. To its south is Mutnovsky and to its east is Falshiv. Tomalchev appears once again near top left. **Landsat 1477-23543-6, November 12, 1973.**

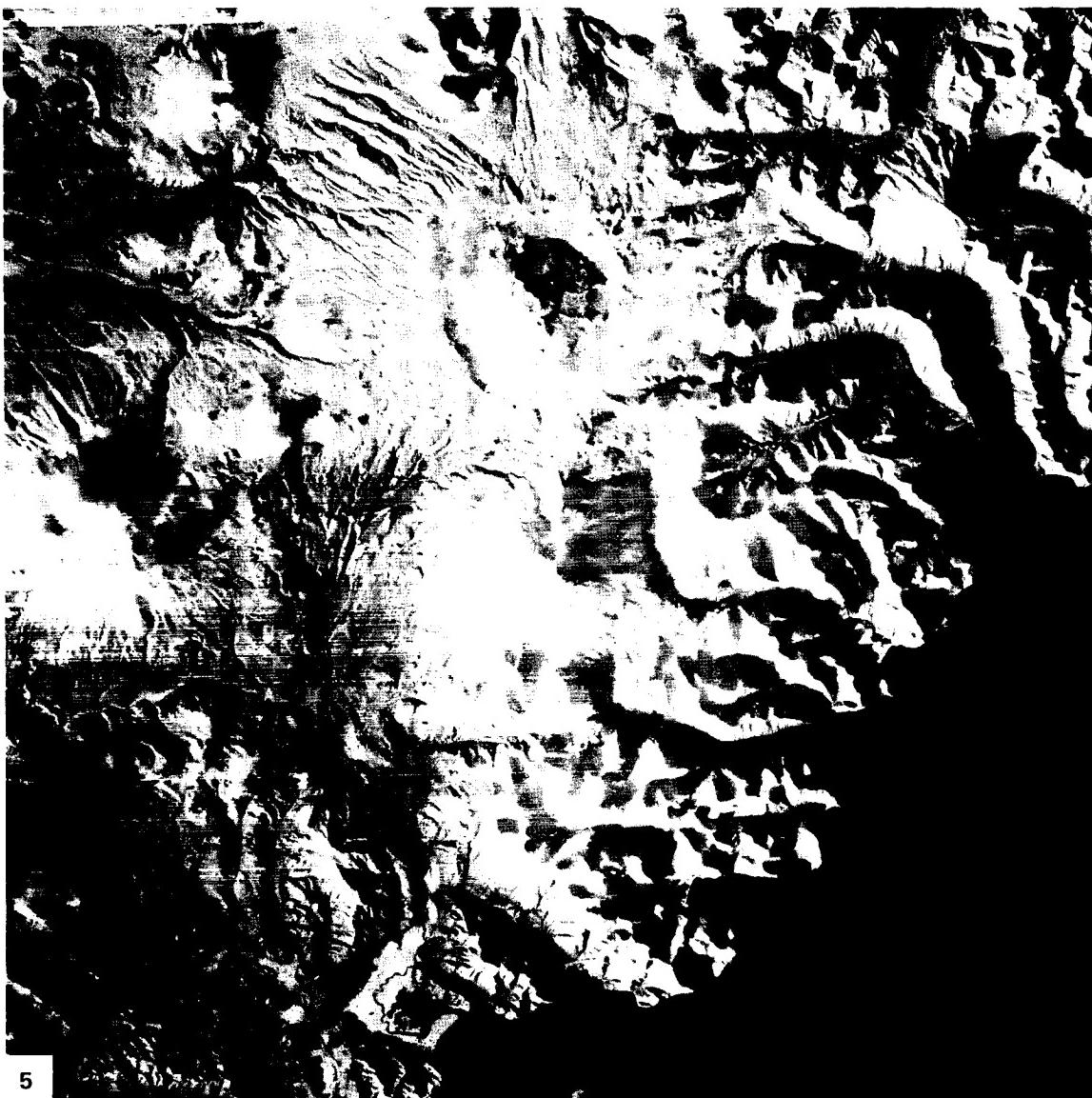


ORIGINAL PAGE IS
OF POOR QUALITY



ORIGINAL PAGE IS
OF POOR QUALITY

ORIGINAL PAGE IS
OF POOR QUALITY



5

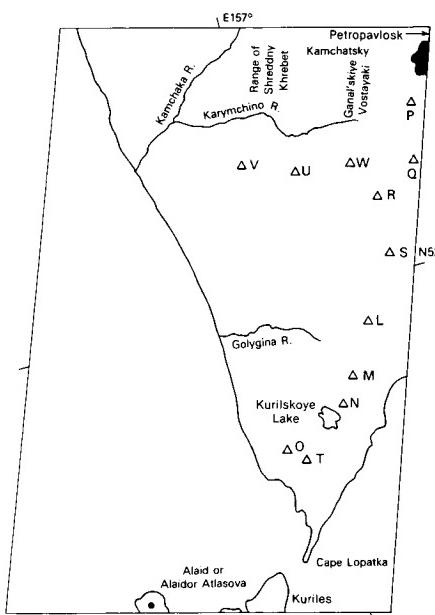


PLATE V-26

CENTRAL JAVA

Java, the main island of the Indonesian archipelago, is a prime example of an island arc terrane that is still in process of evolution (Hamilton, 1979). The Indonesian landmass, convex to the southwest, lies next to the northward-dipping subduction zone along the line of convergence between two colliding oceanic plates. Behind the outer arc rises a line of active and Quaternary (dormant/extinct) andesitic volcanoes extending some 4200 km from Sumatra on the west through the Sunda Islands and those in the Banda Sea to the east. The main islands, including Java, are relatively recent uplifts of geosynclinal sediments, deposited on older terrane, that continue to emerge on the Asian mainland side of the southernmost segment of the Eurasian Plate now being underthrust by the Indian/Australian plate. The volcanoes, mostly composite stratocones, run along a narrow axis through the island center.

In more detail, this part of the Indonesian arc system, typical of the islands as a whole, consists of the following segments from north to south (Hamilton, 1979):

1. Bawean and Kangean Basins: Karimuniawa and Bawean arches; in the Java Sea, back-arc basins and geanticlines.

2. Java Central Trough: Chain of sedimentary foreland basins (now largely land), with up to 6000 m of Cenozoic sediments (terrigenous clastics (flysch type) including volcanogenic and turbidite deposits, and foraminiferal marly limestones), beginning in Early Miocene and culminating in the Pleistocene. The Kending Mountains and Rembang Hills (Figure V-26.1) contain an inner zone of Miocene/Pliocene sedimentary facies fringed by Pleistocene sediments. The rocks now are folded into east-west anticlines, cut by north-south faults, resulting from deformation from Miocene through the Holocene.

3. Sunda Quaternary Volcanic Arc: In hinge zone between (2) and (4); intermediate to silicic calc-alkaline volcanic suites; began in Mid-Pleistocene.

4. Sunda Tertiary Magmatic Arc: A shallow basement belt of Pre-Tertiary metamorphic rocks, Upper Cretaceous melange deposits, and intrusives overlain by Paleogene clastic deposits, reef limestones (Eocene/Pliocene), and "Old Andesites," extrusives of Oligocene/Middle Miocene age, and accompanying intrusives; makes up much of the Southern Mountains.

5. South Central Java Basin: A submarine basin just off the coast, containing up to 4000 m of Cenozoic sediments.

6. Java/Lombok Trough: An interarc basin containing 6000 m of largely undeformed Cenozoic deposits.

7. Java Ridge: A submarine rise within the nonvolcanic outer arc composed of strongly deformed mélange deposits, with thrust and imbricate structure.

8. Java Trench: The subduction line, south of which the basaltic floor covered by Jurassic pelagic sediments of the North Australian basin encroaches against the Eurasian plate.

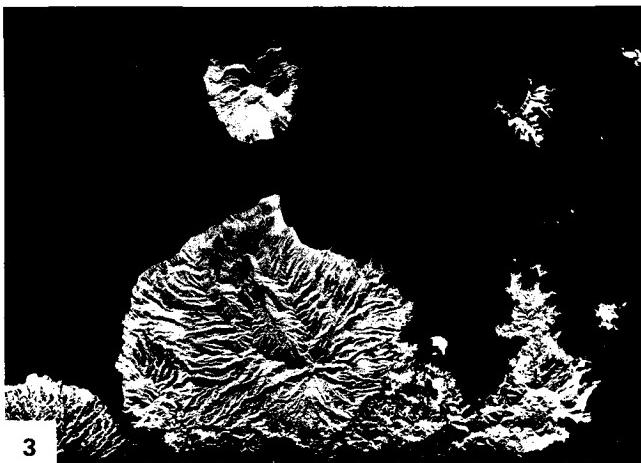
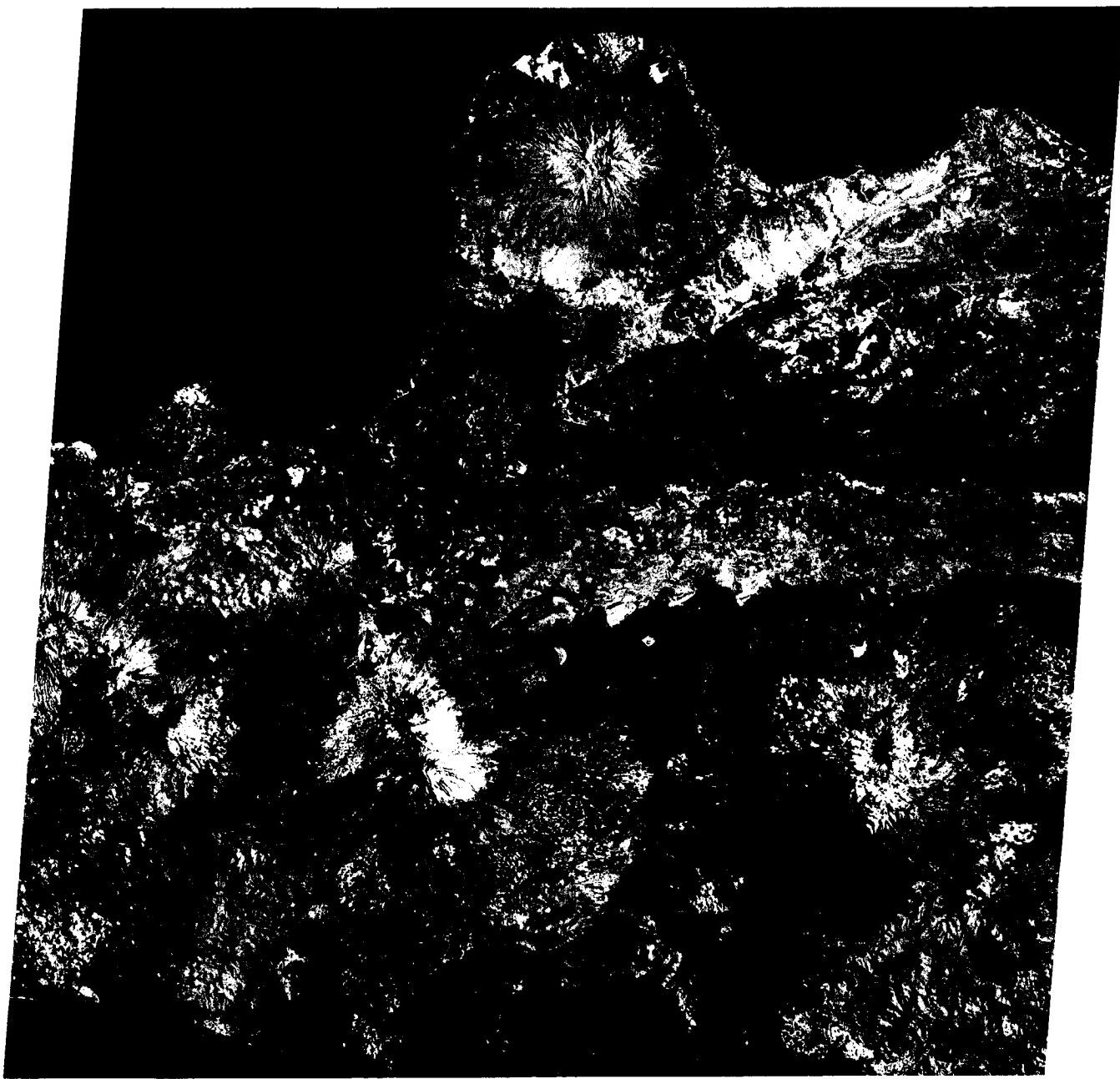
From the above, the general pattern of sedimentation and structural deformation with age shows a progressive northward shift toward younger events. Volcanism likewise shifts to the north from more basic to more silicic. Along the main volcanic belt, most volcanic rocks are pyroxene andesites and high-Al basalts. Off the main belt, Volcano Muria, now inactive, has produced leucite-bearing eruptive rocks of potassic alkalic composition. The explosivity index (ratio of pyroclastic tephra to total expelled materials) for the Indonesian volcanoes ranges up to 99, the highest values along the Pacific Ring of Fire (Macdonald, 1972).

In the volcanic landforms classification devised by van Bemmelen (1949) for Indonesia, several of the volcanoes (Merapi, Merbabu, Lawu, Ungaran) in this scene have experienced eruptions involving partial collapses triggered by sideward sliding along crescentic rifts or "barrancos." Volcano Ungaran also has developed a small central caldera developed after loss of support following magma extrusion. Some of these volcanoes have proved to be especially dangerous to life and property. Merapi (Figure V-26.2) erupts frequently, with lava flows, nuées ardentes, and mudflows providing hazards to the nearby densely populated region.

Eastward, the same geologic terranes extend through the Lesser Sunda Islands. Figure V-26.3 is a SIR-A radar image of parts of the Sunda Islands. Mt. Maria on Sumbawa (south) is now extinct and is much dissected. Mt. Api on Sangeang is still active. A remnant of a caldera (similar to the present appearance of Krakatoa) is visible along the north shore of the small Banta Island. Landsat 1067-02145-7, September 28, 1972.



ORIGINAL PAGE IS
OF POOR QUALITY



3

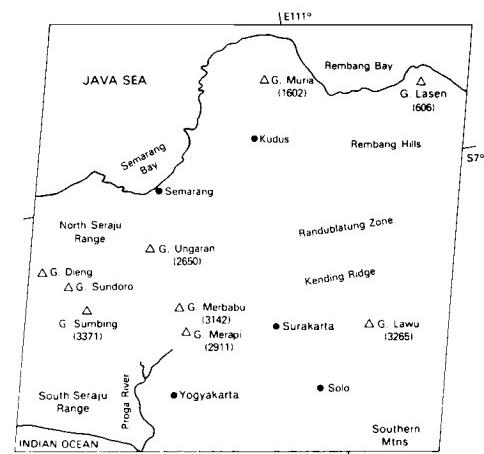


PLATE V-27

The North and South Islands of New Zealand lie on the active boundary between the Pacific and Indian/Australian plates (Brown et al., 1968). On South Island, much of the current plate motion occurs along the northeast-trending dextral Alpine transcurrent fault zone (see Plate T-58), which extends into North Island, passing southeast of this Landsat image. North Island itself is bordered along its east coast by the Kermadec Trench, a southward extension of the Tonga Trench. In Central North Island, a chain of andesitic volcanoes (part of the Circum-Pacific Andesite Line) erupts lavas from a melting zone (estimated depth around 150 km, based on earthquake hypocenters in the west-dipping subduction zone).

North Island was part of the New Zealand geosyncline that received sediments from the Carboniferous through Jurassic (Torlesse Supergroup) (Sugitate, 1978). By Early Cretaceous, these deposits were strongly folded during the Rangitata Orogeny. In this Landsat image, Jurassic/Triassic rocks, mainly graywackes, form the distinctive mountain terrains of the Kaimanawa and Hauhungaroa Ranges. Much of west-central North Island is covered by Tertiary (mainly Pliocene) shallow marine sediments that eroded into the fine drainage network in the mainly forested Matemateaonga Range. These sediments have been warped and locally folded by the Kaikoura Orogeny that began in the Miocene and continues even now.

The chain of volcanoes trending north-northeast in the eastern center of the image is confined to a narrow structural trough variously interpreted as a tectonic graben related to major rifting or as a shallow linear (elongate) 50 by 250 km depression caused by collapse following magma withdrawal (Hazen, 1965). Volcanic activity has marked this line from the Pliocene to the present. This area, referred to as the Taupo (or Central) Volcanic Zone, takes its name from Lake Taupo (mostly cloud-covered), an irregular caldera-like depression developed both by collapse and by explosion at multiple volcanic centers. The Wairakei geyser field is located just north of this lake. The greatest eruptions in the Taupo Zone have been from the silicic volcanic centers of Taupo, Okataina, and Maroa, generating more than 15000 km³ of welded ignimbrites and other ejecta. These ignimbrites form gently sloping plateaus on either side of the Zone, covering more than 30000 km². The smooth form of the Kai'ngaroa Plateau west of Lake Taupo is particularly evident in the Landsat image;



1

NEW ZEALAND VOLCANOES

the "fields" on the plateau at A are clear-cut and reforested stands of conifer trees, which flourish in pumiceous soils. The western plateau is more stream-furrowed. The Taupo Center has been described as an inverse volcano (Walker, 1980). Its eruptions are exceptionally powerful, causing wide dispersal of its disgorged products. The thick deposits of this material form a great bowl-shaped depression (filled with mist in this scene) some 30 km in diameter. The rhyolite dome-cluster of Tarawera Mountain (visible in the upper right corner of the image) is one of several in the Okataina Center; 150 people were killed by a violent fissure eruption of basaltic material in June 1886 that cored out the explosion craters seen in Figure V-27.1. A zone of prominent extensional faults, with the tilted horst of Paeroa Mountain among them, connects both centers. A cluster of rhyolitic domes in the Maroa Center is visible in a gap within the mist clouds.

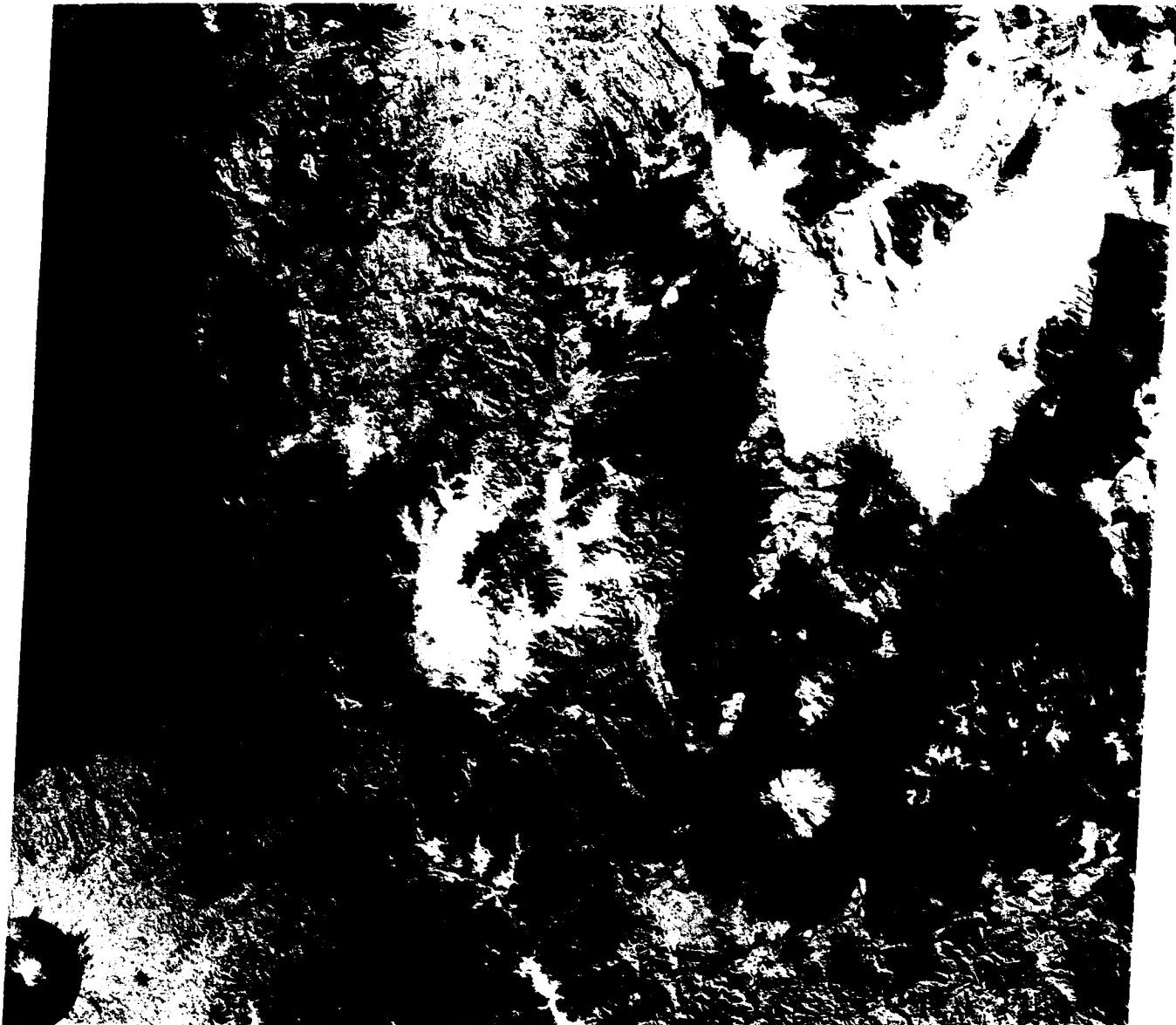
South of Lake Taupo are three prominent andesitic volcanoes, shown from the air in Figure V-27.2: Tongariro (1986 m), with its conspicuous North Crater in the foreground, Ngauruhoe (2291 m), the conical stratocone in the middle ground, and Ruapehu (2797 m), the broad stratocone in the background. Only Tongariro has not erupted in this century; Ngauruhoe is the most active, commonly producing tephra showers, pyroclastic flows, and lava flows (Topping, 1973); Ruapehu has occasionally produced steam explosions and lahars from its glacier-girdled crater lake. A "ring plain" of lahar and rock avalanche deposits lies to the southeast of Ruapehu. The volcanoes in the Tongariro Volcanic Center are older than the ignimbrite plateaus to the north. Note the prominent structural lineaments trending east-northeast along the eastern flank of this center.

In the lower left corner of the Plate image is the lofty snow-capped Mount Egmont (2630 m) (Figure V-27.3), the youngest (and largest) of three volcanoes (others not visible) formed along a north-northwest line on the Taranaki Plains east of Cape Egmont. This andesitic volcano (last active 250 to 400 years ago) was built on Pliocene marine sediments in the Pleistocene. The dark circular area around Mt. Egmont is a temperate rain forest preserve surrounded by an enclosing fence that excludes grazing animals from the higher slopes. *Text modified from comments by R. Bailey, USGS, and G. P. L. Walker, University of Hawaii.* Landsat 30844-21121-6, June 26, 1980.

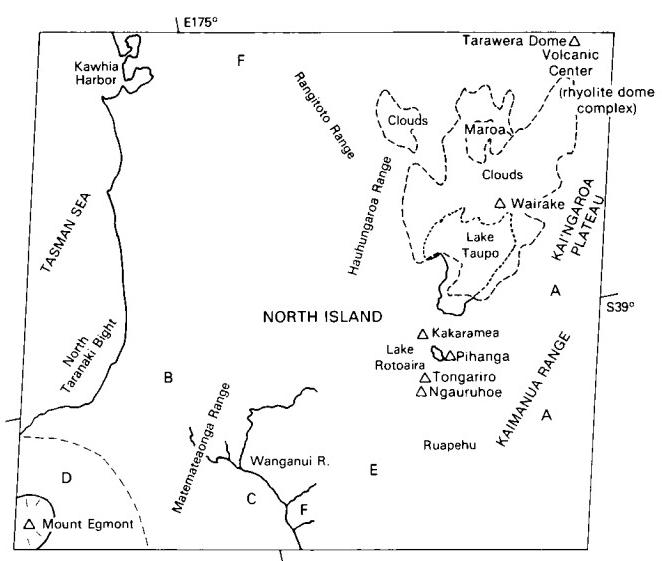


2

ORIGINAL PAGE IS
OF POOR QUALITY



3



REFERENCES

- Altinli, I. E., Explanatory Text of the Geological Map of Turkey, Van. Mineral Exploration and Research Inst., Ankara, pp. 41-90, 1964.
- Alvarez, W., The Pleistocene volcanoes north of Rome, in *Geology of Italy*, edited by T. Squires, pp. 305-377, 1975.
- Anderson, E. M., The dynamics of formation of cone, sheets, ring-dikes, and caldron-subsidence, *Proc. Royal Soc. Edinburgh*, **56**, p. 158, 1936.
- Armstrong, R. L., Cenozoic igneous history of the U.S. cordillera from latitude 42 to 49° north, *Geol. Soc. Amer. Mem.*, **152**, 256-282, 1968.
- Bailey, R., and R. L. Smith, Volcanic Geology of the Jemez Mountains, Valles Guidebook, New Mexico Bur. Mines Circ., **163**, 184-196, 1978.
- Baker, B. H., Geology of the Eastern Rift Systems of Africa, *Geol. Soc. Amer. Paper*, **136**, 1972.
- Baker, B. H., R. Crossley, and G. G. Goles, Tectonic and magmatic evolution of the southern part of the Kenya Rift Valley, in *Petrology and Geochemistry of Continental Rifts*, edited by E. R. Neumann and I. B. Ramberg, pp. 29-50, D. Reidel, Dordrecht, 1978.
- Baker, B. H., and J. Wohlenberg, Structure and evolution of the Kenya Rift Valley, *Nature*, **229**, 538-549, 1971.
- Barberi, F., F. Innocenti, and L. Villari, Volcanism of the Southern Tyrrhenian Sea and its geodynamic implications, *J. Geophys. Res.*, **78**, 5221-5232, 1973.
- Barberi, F., and J. Varet, The Erta Ale Volcanic Range (Danakil Depression, Northern Afar, Ethiopia), *Bull. Volcanologique*, **34**, 848-917, 1970.
- Barberi, F., J. Varet, and H. Tazieff, Volcanism in the Afar Depression: Its tectonic and magmatic significance in East African Rifts, *Tectophysics*, **15**, No. 1-2, 1972.
- Bloom, A., *Geomorphology: A Systematic Analysis of Late Cenozoic Landforms*, 510 pp., Prentice-Hall, Englewood Cliffs, N.J., 1978.
- Boccaletti, M., et al., Neogene and Quaternary volcanism of the Bijar Area (Western Iran), *Bull. Volcanologique*, **40-2**, 121-133, 1976-1977.
- Bonis, S. B., Summary of the Regional Geology of Guatemala, *Guatemala Instituto Geografico Nacional Bull.*, **4-5**, 71 pp., 1967-69.
- Brown, D. A., K. S. W. Campbell, and K. A. W. Cook, *The Geological Evolution of Australia and New Zealand*, 409 pp., Pergamon Press, 1968.
- Bullard, F. M., *Volcanoes of the Earth*, 579 pp., Univ. of Texas Press, Austin, 1976.
- Carr, M. H., and R. Greeley, *Volcanic Features of Hawaii: A Basis for Comparison with Mars*, 221 pp., NASA SP-403, 1980.
- Casertano, L., General characteristics of active andean volcanism and a summary of their activities during recent centuries, *Bull. Seism. Soc. Amer.*, **53**, 1415-1433, 1963.
- Christiansen, R. L., and P. W. Lipman, Cenozoic volcanism and plate-tectonic evolution of the Western United States, II. Late Cenozoic, *Phil. Trans. Roy. Soc. London*, **271**, 249-284, 1972.
- Christiansen, R. L., and E. H. McKee, Late Cenozoic volcanism and tectonic evolution of the Great Basin and Columbia Intermontane Regions, *Geol. Soc. Amer. Mem.*, **152**, 283-312, 1978.
- Coster, A. S., *The Kamchatka Peninsula of the U.S.S.R. and Some of Its North American Analogs*, 167 pp., Dunlap, Stamford, Connecticut, 1963.
- Cotton, C. A., *Volcanoes as Landscape Forms*, 2nd Ed., 416 pp., John Wiley, New York, 1952.
- Darwin, C., *Voyages of the Beagle*; reprinted by Doubleday (Biblio Distribution Centre), Garden City, N.J. (1979 ed.), 1844.
- Dewey, J. F., W. C. Pitman III, W. B. F. Ryan, and J. Bonnin, Evolution of the Alpine System, *Bull. Geol. Soc. Amer.*, **84**, 3137-3180, 1973.
- Durham, J. W., and A. R. McBirney, Galapagos Islands, in *Encyclopedia of World Regional Geology*, edited by R. Fairbridge, p. 285, 1975.
- Eastwood, R., Cenozoic volcanism and tectonism of the Southern Colorado Plateau, in *Geology of Northern Arizona*, Guidebook for GSA Rocky Mountain Section Meeting, edited by T. Karlstrom et al., pp. 238-250, 1974.
- Erlich, E. N., Recent structure of Kamchatka and position of Quaternary volcanoes, *Bull. Volcanologique*, Special Volume: Quaternary Volcanism and Tectonics in Kamchatka, **42**, 13-42, 1979.
- Erlich, E. N., I. V. Melekestsev, A. A. Tarakanovsky, and M. I. Zubin, Quaternary calderas of Kamchatka, *Bull. Volcanologique*, **36**, 222-237, 1972.
- Fiarhead, J. D., The structure of the cross-cutting volcanic chain of Northern Tanzania, *Tectonophysics*, **65**, 193-208, 1980.

- Foxworthy, B., and M. Hill, Volcanic Eruptions of 1980 at Mount St. Helens: The First 100 Days, *U.S. Geol. Surv. Prof. Paper*, **1249**, 125 pp., 1982.
- Francis, P., *Volcanoes*, 368 pp., Pelican Books, 1976.
- Furon, R., *Geology of Africa*, 377 pp., Oliver & Boyd, Edinburgh, 1963.
- Gass, I. G., Volcanism and structure of continental rift valleys, *J. Geol. Soc. London*, **132**, 345-360, 1976.
- Gass, I. G., and D. J. Mallick, Acid volcanism of the Saudi Arabian coast, *Bull. Volcanologique*, **29**, 449-453, 1966.
- Gibson, I. L., Structure and volcanic geology of an axial portion of the Main Ethiopian Rift, *Tectonophysics*, **8**, 561-565, 1969.
- Goles, G. G., Volcanism and tectonics of the Kenya Rift System, in *Symposium Volume "Deccan Volcanism and Related Basalt Provinces in Other Parts of the World," Memoir Geol. Soc. India*, pp. 128-142, 1980.
- Greeley, R., *Aerial Reconnaissance over the Island of Hawaii*, pp. 113-184, NASA CR-152416, 1974.
- Greeley, R., Style of volcanism in the Eastern Snake River Plain, Idaho, in *Cenozoic Geology of Idaho*, edited by B. Bonnichsen and R. M. Breckenridge, pp. 407-421, *Idaho Bur. Mines & Geology*, Bull. 26, 1982a.
- Greeley, R., The Snake River Plain, Idaho: Representative of a new category of volcanism, *J. Geophys. Res.*, **87**, 2705-2712, 1982b.
- Green, J., and N. M. Short, *Volcanic Landforms and Surface Features: A Volcanic Atlas and Glossary*, 522 pp., Springer-Verlag, New York, 1971.
- Hamilton, W., Tectonics of the Indonesian Region, *U.S. Geol. Surv. Prof. Paper*, **1078**, 345 pp., 1979.
- Harris, S. L., *Fire and Ice: The Cascade Volcanoes*, 320 pp., The Mountaineers, Seattle, Washington, 1976.
- Hazen, H. A., Geological Notes on Volcanoes in New Zealand Volcanology: Central Volcanic Region, 1965.
- Hunt, C. B., Igneous geology and structure of the Mount Taylor volcanic field, New Mexico, *U.S. Geol. Surv. Prof. Paper*, **189B**, 51-80, 1938.
- Jahns, R. H., Collapse depressions of the Pinacate volcanic field, in *Arizona Geol. Soc. South Arizona Guidebook*, **2**, 1959.
- Kay, S. M., R. W. Kay, and G. P. Citron, Tectonic controls on tholeiitic and calc-alkaline magmatism in the Aleutian Arc, *J. Geophys. Res.*, **87**, 4051-4072, 1982.
- King, L. C., *South African Scenery*, Oliver and Boyd, Ltd., Edinburgh, 1951.
- Kitching, J. W., The stratigraphic distribution and occurrence of South African fossil amphibia in the Beaufort Beds, *Palaeontol. Afr.*, **21**, 101-112, 1978.
- Krishnan, M. S., *Geology of India and Burma*, 2nd Ed., 544 pp., Madras Law Journal Office, 1949.
- Krishnan, M. S., Deccan trap volcanism, *Bull. Volcanologique*, **26**, 273-296, 1963.
- Kulm, L. D., J. Dymond, E. J. Dasch, and D. M. Hussong (Eds.), Nazca Plate: Crustal formation and Andean convergence, *Geol. Soc. Amer. Mem.*, **154**, 816 pp., 1981.
- Lambert, R. St. J., J. G. Holland, and P. F. Owen, Chemical petrology of a suite of calc-alkaline lavas from Mt. Ararat, Turkey, *J. Geol.*, **82**, 419-438, 1974.
- Lathram, E., Aleutian Arc, in *Mesozoic-Cenozoic Orogenic Belts*, edited by A. M. Spencer, pp. 533-561, *Geol. Soc. London Spec. Publ.* 4, The Scottish Academic Press, 1974.
- LeBas, M. J., *Carbonatite-Nephelinite Volcanism*, 347 pp., John Wiley, New York, 1977.
- Leeman, W. P., C. J. Vitaliano, and M. Prinz, Evolved lavas from the Snake River Plain: Craters of the Moon National Monument Idaho, *Contr. Mineral. Petrol.*, **56**, 35-60, 1976.
- Lipman, P. W., H. J. Prostka, and R. L. Christiansen, Cenozoic volcanism and plate tectonics of the Western United States, I. Early and Middle Cenozoic, *Phil. Trans. Roy. Soc. London*, **271**, 217-248, 1972.
- Macdonald, G. A., *Volcanoes*, 510 pp., Prentice-Hall, Englewood Cliffs, N.J., 1972.
- Macdonald, G. A., and D. H. Hubbard, *Volcanoes of the National Parks of Hawaii*, 59 pp., Hawaii Natural History Assn., 5th Ed., 1970.
- Malin, M. C., Comparison of volcanic features of Elysium (Mars) and Tibesti (Earth), *Geol. Soc. Amer. Bull.*, **88**, 908-919, 1976.
- Markhinin, E. K., *Pluto's Chain*, 213 pp., Progress Publ., Moscow, 1971.
- Matumoto, T., Calderas, volcanoes, and pyroclastic flows of Kyushu, *Bull. Volcanologique*, **26**, 401-414, 1963.
- Maxwell, R. R., and J. W. Dietrich, Geologic summary of the Big Bend Region in *Geology of the Big Bend Area*, pp. 11-33, West Texas Geol. Soc. Field Trip Guide, 1972.
- McBirney, A. R., and H. Williams, Geology and petrology of the Galapagos Islands, *Geol. Soc. Amer. Mem.*, **118**, 197 pp., 1969.
- McKenzie, D. P., Active tectonics of the Mediterranean Region, *Geophys. J. Roy. Astr. Soc.*, **30**, 109-185, 1972.
- Mehdirata, R., *Geology of India, Pakistan and Burma*, 203 pp., Atma Ram Publ., Delhi, 1962.
- Miller, T. P., and R. L. Smith, Spectacular mobility of ash flows around Aniakchak and Fisher calderas, *Geology*, **5**, 173-176, 1977.
- Mohr, P., The Afar triple junction and sea-floor spreading, *J. Geophys. Res.*, **75**, 7340-7352, 1975.

- Mohr, P., Ethiopian flood basalt province, *Nature*, **303**, 577-584, 1983.
- Moore, R. B., E. W. Wolfe, and G. E. Ulrich, Geology of the Eastern and Northern Parts of the San Francisco Volcanic Field, Arizona, in *Geology of Northern Arizona*, edited by T. Karlstrom et al., pp. 465-494, Guidebook for GSA Rocky Mountain Section Meeting, 1974.
- Morgan, W. J., Convection currents in the lower mantle, *Nature*, **230**, 42-43, 1971.
- Nagle, F., J. Rosenfeld, and J. J. Stipp, *Guatemala, Where Plates Collide*, 72 pp., Field Trip Guide, Dept. of Geology, Univ. of Miami, 1977.
- Narain, H., K. L. Kaila, and R. K. Verma, Continental margins of India, *Canadian J. Earth Sci.*, **5**, 1051-1061, 1968.
- Nordlie, B. E., Morphology and structure of the Western Galapagos and a model for their origin, *Geol. Soc. Amer. Bull.*, **84**, 2931-2956, 1973.
- Ollier, C. D., *Volcanoes*, 177 pp., Australian Nat. Univ. Press, Canberra, 1969.
- Pellaton, C., *Explanatory Notes to the Geologic Map of the Al Mandinah Quadrangle, Sheet 24D, Kingdom of Saudi Arabia*, French Bureau de Recherches Geologiques et Minieres, 1982.
- Peterson, N. V., and E. A. Groh (Eds.), *Lunar Geological Field Conference Guide Book: Bend, Oregon*, 51 pp., State of Oregon Department of Geology and Mineral Industries, 1965.
- Press, F., and R. Siever, *Earth*, 613 pp., W. H. Freeman and Co., San Francisco, 1982.
- Preusser, W., *The Landscape of Iceland: Types and Regions*, Dr. W. Junk b. v. Publ., The Hague, 1976.
- Prinz, M., Idaho rift system, Snake River Plain, Idaho, *Bull. Geol. Soc. Amer.*, **81**, 941-948, 1970.
- Pritchard, J. M., *Landform and Landscape in Africa*, 160 pp., Edward Arnold, London, 1979.
- Rittman, A., *Volcanoes and their Activity*, 305 pp., Wiley-Interscience, New York, 1962.
- Rittman, A., Structure and evolution of Mount Etna, *Phil. Trans. Roy. Soc. London*, **274**, 5-16, 1973.
- Ross, C. L., R. L. Smith, and R. A. Bailey, Outline of the geology of the Jemez Mountains, in *Guidebook of the Albuquerque County 12th Field Conference*, edited by S. A. Northrop, New Mexico Geological Society, 1961.
- Rutland, R. W. R., Andes: Antofagasta Segment (20-25 S), in *Mesozoic-Cenozoic Orogenic Belts*, edited by A. M. Spencer, pp. 733-746, Geol. Soc. of London Spec. Publ. 4, The Scottish Academic Press, 1974.
- Sapper, K., *The Volcanoes of Central America*, 144 pp., Verlag Max Niemeyer, Halle, 1925.
- Simkin, T., Geology of Galapagos Islands, in *Galapagos (Key Environments)*, edited by R. Perry, 15-41, Pergamon Press, Oxford, 1984.
- Simkin, T. L., Siebert, L. McClelland, D. Bridge, C. Newhall, and J. H. Latter, *Volcanoes of the World*, 233 pp., Hutchinson Ross Publ. Co., Stroudsburg, Pa., 1981.
- Smith, R. L., and R. A. Bailey, Resurgent cauldrons, *Geol. Soc. Amer. Mem.*, **116**, 613-662, 1968.
- Smith, W. R., Aniakchak Crater, Alaska Peninsula, *U.S. Geol. Surv. Prof. Paper*, **132-J**, pp. 139-149, 1925.
- Stearns, H., *Geology of the State of Hawaii*, 266 pp., Pacific Books, Palo Alto, 1966.
- Suggate, R. P. (Ed.), *The Geology of New Zealand Vol. I & II*, 880 pp., E. C. Keating, Govt. Printer, Wellington, 1978.
- Sukheswala, R. N., and A. Poldervaart, Deccan basalts of the Bombay area, India, *Geol. Soc. Amer. Bull.*, **69**, 1475-1494, 1958.
- Sutton, R. L., The geology of Hopi Buttes, Arizona, in *Geology of Northern Arizona*, edited by T. Karstrom et al., pp. 647-671, Guidebook for GSA Rocky Mountain Section Meeting, 1974.
- Tanaka, K., and T. Nozawa (Eds.), *Geology and Mineral Resources of Japan*, Sumitomo Printing & Publ. Co., Tokyo, 1977.
- Tangay, J. C., and G. Kieffer, The 1974 eruption of Mount Etna, *Bull. Volcanologique*, **40**, 199-252, 1976-77.
- Thorarinsson, S., The postglacial volcanism, in *On the Geology and Geomorphology of Iceland*, *Geografiska Annaler*, **41**, 143-150, 1959.
- Tilling, R. I., *Eruptions of Mount St. Helens: Past, Present, and Future*, 46 pp., General Interest Publication, U.S. Geol. Surv., 1984.
- Topping, W. W., Tephrostratigraphy and chronology of Late Quaternary eruptives from the Tongariro Volcanic Center, New Zealand, *New Zealand J. Geol. Geophysics*, **16**, 397-423, 1973.
- Updike, R. G., The volcanic history of the San Francisco Mountains, Northern Arizona, in *Geology of Northern Arizona*, edited by T. Karlstrom et al., pp. 547-556, Guidebook for GSA Rocky Mountain Section, 1974.
- van Bemmelen, R. W., *The Geology of Indonesia*, 732 pp., Govt. Printing Office, The Hague, 1949.
- Vincent, P. M., The evolution of the Tibesti Volcanic Province, Eastern Sahara, in *African Magmatism and Tectonics*, pp. 300-319, Oliver & Boyd, Edinburgh, 1970.
- Von Engeln, O. D., *Geomorphology: Systematic and Regional*, 655 pp., MacMillan Co., New York, 1942.
- Walker, G. P. L., Mount Etna, *Geograph. Mag.*, **40**, 929-935, 1968.
- Walker, G. P. L., The Taupo pumice: Product of the most powerful known (ultraplinian) eruption, *J. Volc. Geotherm. Res.*, **8**, 69-94, 1980.
- Waters, A. C., Stratigraphy and lithologic variations in the Columbia River basalts, *Amer. J. Science*, **259**, 583-611, 1961.

- Williams, H., The Newberry volcano of central Oregon, *Geol. Soc. Amer. Bull.*, **46**, 253-304, 1935.
- Williams, H., Pliocene volcanoes of the Navaho-Hopi Buttes Country, *Geol. Soc. Amer. Bull.*, **47**, 111-172, 1936.
- Williams, H., *Geology of Crater Lake National Park*, 162 pp., Carnegie Inst. of Washington, Publ. 540, 1942.
- Williams, H., and A. R. McBirney, Petrologic and structural contrasts of the Quaternary volcanoes of Guatemala, *Bull. Volcanologique*, **27**, 61, 1964.
- Williams, H., and A. R. McBirney, *Volcanology*, 397 pp., Freeman, Cooper, & Co., 1978.
- Williams, R. S., Jr., S. Thorarinsson, and E. C. Morris, Geomorphic classification of Icelandic volcanoes, *Jökull*, **33**, 19-24, 1983.
- Windley, B. F., *The Evolving Continents*, 2nd Ed., 399 pp., John Wiley, New York, 1984.
- Wood, C. A., Reconnaissance geophysics and geology of the Pinacate Craters, Sonora, Mexico, *Bull. Volcanologique*, **38**, 149-172, 1974.
- Yoshida, T. (Ed.), *Outline of the Geology of Japan*, 3rd ed., 61 pp., Geol. Survey of Japan, Kawasaki-shi, 1975.
- Yoshikawa, T. S., S. Kaizuka, and Y. Ota, *The Landforms of Japan*, 222 pp., Univ. of Tokyo Press, 1981.
- Zavaritski, A. N., *The Volcanoes of Kamchatka*, 81 pp., Publ. House Acad. Sci., U.S.S.R., 1977.
- Zeil, W., *The Andes: A Geological Review*, 260 pp., Gebr. Borntraeger, Stuttgart, 1979.

4

FLUVIAL LANDFORMS

*Victor R. Baker**

Rivers flowing to the oceans drain about 68 percent of the Earth's land surface. The remainder of the land either is covered by ice or drains to closed basins. Areas draining to the sea are common in humid regions, whereas those draining to interior closed basins occur in arid regions or in areas of active tectonic subsidence. Some areas of the planet lack surface streams because of extremely low rainfall or because lithologic conditions promote infiltration.

Data on the large rivers of the world are subject to numerous problems of measurement and reliability. The most recent summary (Milliman and Meade, 1983) discusses these problems, but it also reveals some startling facts (Table 4-1). Only a score of the world's great rivers are responsible for delivering over half the fresh water and total sediment load to the world's oceans. The Amazon River alone carries about 15 percent of all the water annually discharged by the world's rivers. The annual delivery of suspended sediment to the ocean is about 13.5×10^9 metric tons. Over one-tenth of this is delivered by one system, the Ganges-Brahmaputra. Even more remarkable is the second most prolific source of sediment, the Huang He (Yellow River) of China, which yields 1.08×10^9 tons per year. The Huang He has one-half the drainage area and one-twentieth the water discharge of the Ganges-Brahmaputra.

Although there are several excellent textbooks in fluvial geomorphology (Gregory and Walling, 1973; Leopold et al., 1964; Richards, 1982), all place an emphasis on small-scale processes. This chapter will introduce the mega-geomorphology of rivers in the hope that it will stimulate a new perspective on the science.

SCENE CLASSIFICATION

The various regional study areas in this chapter are classified in terms of either their drainage pattern or their channel pattern (Table 4-2). The classification is used merely to facilitate discussion, since numerous aspects of the various study areas will be described in the plate descriptions. Especially important are the process parameters (climate, streamflow, and sediment loads) and the evidence of relict features that indicate major past changes in the process parameters.

DRAINAGE BASINS

The fluvial dissection of the landscape consists of valleys and their included channelways organized into a system of con-

nexion known as a drainage network. Drainage networks display many types of quantitative regularity that are useful in analyzing both the fluvial systems and the terrains that they dissect (Abrahams, 1984). One very useful property is the pattern of dissection (Figure 4-1). Howard (1967) has summarized the geological significance of various drainage patterns (Table 4-3). Dendritic patterns evident in a SIR-A (Shuttle Imaging Radar) image (Figure 4-2) are named for their similarity to branching organic forms. Indeed, the conveyance qualities of such networks make them morphologically similar to blood circulation systems, tree branching, and landscape drainage. Excellent examples of dendritic patterns occur in the absence of structural control, as on the Edwards Plateau of Texas (Plate F-1) and the Loess Plateau of China (Plate F-2). Areas of trellis and rectangular drainage include central Yemen (Plate F-5) and the Colorado Plateau (Plate F-6), respectively. The Al Jafr area of Jordan (Plate F-4) illustrates a centripetal pattern. An example of a drainage pattern not shown in Figure 4-1 but readily recognized at a regional scale in Landsat imagery (Figure 4-3) is the pinnate pattern seen in tributaries to the Dnestr River in the Moldavian S.S.R.

Drainage networks exist in spatially limited systems known as drainage basins. The drainage network in a basin conveys water and sediment according to the controls of climate, soils, geology, relief, and vegetation. One measure of the network's efficiency is the drainage density, defined as the summation of channel lengths per unit area. The study areas reveal a broad variety of drainage densities.

STRUCTURE AND TECTONICS

Drainage may adjust passively to varying resistance of geologic materials, or it may be actively induced to follow a particular course by tectonism. Examples of the latter include faulting, as in the Ganges-Brahmaputra delta region (Plate F-13). Growing folds and domes have affected drainage in the Colorado Plateau (Plate F-6) and central Australia (Plate F-15). Subsidence has been important in the Mississippi (Plate F-10) and Pantanal regions (Plate F-21).

Streams that emerge from mountain fronts onto surrounding plains display a fascinating array of structural and tectonic controls. Where mountain fronts are erosional because of a complex interplay of geomorphic variables, they may develop flanking surfaces of planation called pediments (Plate F-9). Deposition at the mountain front produces alluvial fans because of the tremendous increase in width as a stream emerges from a mountain canyon. Examples include the Tian Shan (Plate F-18), Kosi (Plate F-19), and Pantanal (Plate F-21) areas.

*Department of Geosciences, University of Arizona, Tucson, Arizona, 85721.

Table 4-1
Characteristics of the World's Ten Largest Rivers*

River	Drainage Area (10^3 km^2)	Length (km)	Water Discharge (m^3/s)	Sediment Discharge (10^3 t/yr)
Amazon	6150	6275	200 000	6300
Zaire (Congo)	3820	4670	40 000	1250
Orinoco	990	2570	34 880	1100
Ganges-Brahmaputra	1480	2700	30 790	971
Yangtze	1940	4990	28 540	900
Mississippi-Missouri	3270	6260	18 390	580
Yenisei	2580	5710	17 760	560
Lena	2500	4600	16 300	514
Mekong	790	4180	14 900	470
Parana-La Plata	2830	3940	14 900	470

*Milliman and Meade, 1983

Table 4-2
Classification of Study Areas Illustrating Fluvial Landforms

Drainage Patterns	
Dendritic	Edwards Plateau, Texas (Plate F-1) Loess Plateau, China (Plate F-2) Huang He, China (Plate F-3)
Centripetal	Elat and Al Jafr (Plate F-4)
Structurally Controlled	Central Yemen (Plate F-5) Colorado Plateau, Utah (Plate F-6) Grand Canyon, Arizona (Plate F-7) Rio Caroní, Venezuela (Plate F-8)
Pediments	Tucson, Arizona (Plate F-9)
Channel Patterns	
Meandering	Mississippi River (Plate F-10)
Braided	Colville River, Alaska (Plate F-11) Yukon River, Alaska (Plate F-12) Brahmaputra River (Plate F-13)
Anastomosed	Burke and Hamilton Rivers (Plate F-14) Cooper Creek (Plate F-15) Yangtze River (Plate F-16)
Distributary	Fans of Southeast Iran (F-17) Tian Shan, China (Plate F-18) Kosi Fan (Plate F-19) Niger River, Mali (Plate F-20) Pantanal, Brazil (Plate F-21)
Transitional	Amazon River System 1. Manaus (Plate F-22) 2. Solimões River (Plate F-23) 3. Japurá River (Plate F-24) 4. Ucayali River (Plate F-25)
Paleochannels	Teays River (Plate F-26) Channeled Scabland (Plate F-27)

Passive adjustment to structure is a quality of nearly all the study areas. Perhaps the most interesting situations, however, are drainage anomalies, where streams cut across structural zones. Some streams appear to take the most difficult routes possible through fold belts. In his studies of the Appalachians and the

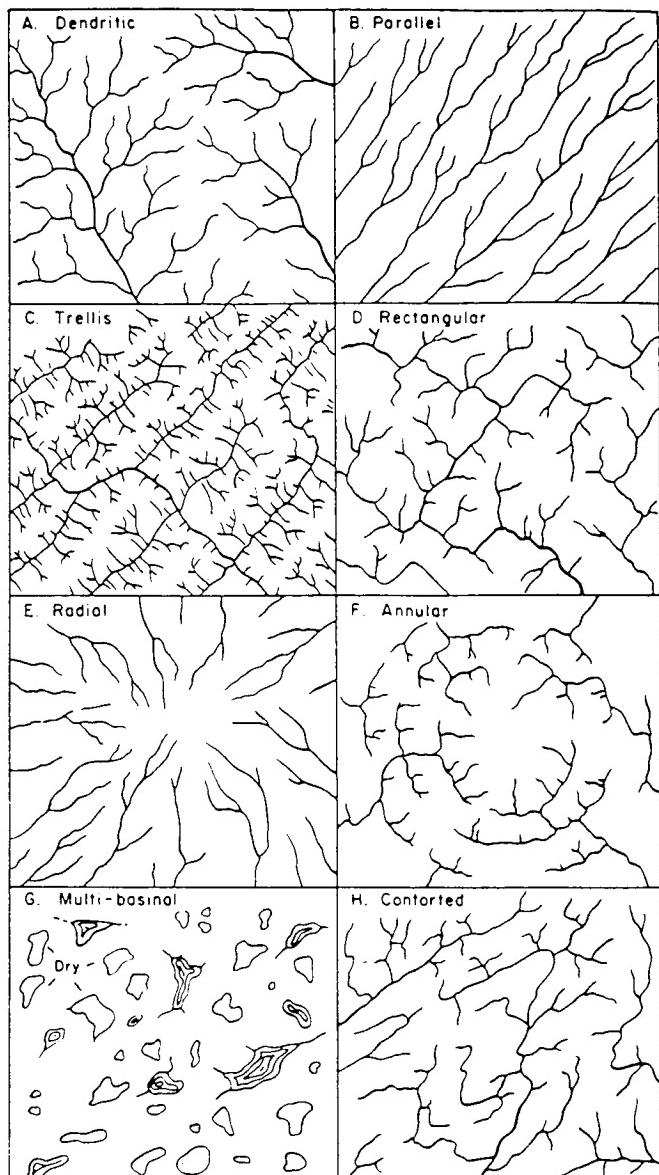


Figure 4.1. Major types of drainage patterns (Howard, 1967).

Zagros Mountains, Oberlander (1985) has applied the term “obstinate streams” to this phenomenon. The Finke River, described in Chapter 1 (Plate I-4), is an excellent example. The Colorado River (Plates F-6 and F-7) provides other examples.

CHANNEL PATTERNS

Rivers display a remarkable variety of channel patterns (Figure 4-4) that are especially amenable to study using spaceborne remote sensing systems. The patterns relate to large-scale conditions of climate and tectonism that can only be appreciated on a global perspective. It is remarkable that, despite the geologic dominance of “big rivers” (Potter, 1978), it is precisely those rivers that have received the least study.

Experimental work by Schumm (1977) has done much to increase our understanding of channel patterns. Pattern adjustments, measured as sinuosity variation, are closely related to the type, size, and amount of sediment load. They are also related

ORIGINAL PAGE COLOR PHOTOGRAPH

to bank resistance and to the discharge characteristics of the stream. Many of the morphological dependencies of river patterns can be summarized in the following expressions:

$$Q_w \propto \frac{W, d, \lambda}{S} \quad (4-1)$$

$$Q_s \propto \frac{W, \lambda, S}{d, P} \quad (4-2)$$

These relationships are expressed by a large number of empirical equations treating the important independent variables,

Table 4-3
Classification of Drainage Patterns*

Pattern	Significance
Dendritic	Horizontal sediments or uniformly resistant crystalline rocks; gentle regional slope at present or at time of drainage inception
Parallel	Moderate to steep slopes; also in areas of parallel elongate landforms
Trellis	Dipping or folded sedimentary, volcanic, or low-grade metasedimentary rocks; areas of parallel fractures
Rectangular	Joints and/or faults at right angles; streams and divides lack regional continuity
Radial	Volcanoes, domes, and residual erosion features
Annular	Structural domes and basins, diatremes, and possibly stocks

*Modified from Howard (1967).

Q_w , a measure of mean annual water discharge, and Q_s , a measure of the type of sediment load (ratio of bedload to total load). The dependent variables are the channel width, W, depth, d, the slope of the river channel, S, the sinuosity, P (ratio of channel length to valley length), and the meander wavelength, λ (spacing of two successive bends in a meandering river).

The relationship of channel slope to sinuosity in an experimental river was elaborated by Schumm and Kahn (1972). The data display a clear threshold phenomenon (Figure 4-5), in which steep low-sinuosity streams may change, somewhat abruptly, to somewhat less steep high-sinuosity streams. The former comprise the bedload-type streams that yield braided patterns, whereas the latter yield the familiar meandering patterns associated with streams that transport a high suspended load. The shift between these two stable pattern configurations is illustrated by several study areas, including the Yukon (Plate F-12), Kosi (Plate F-19), Pantanal (Plate F-21), Japurá (Plate F-24), and Ucayali (Plate F-25).

On the basis of the foregoing experimental work, a variety of pattern classifications can be proposed (Schumm, 1981). However, the immense complexity of natural fluvial systems appears to defy our present understanding (Baker, 1978a; Hickin, 1983). For this reason, the classification employed in Table 4-2 must be considered tentative.

Meandering Pattern

Meandering is the most common river pattern, and meandering rivers develop alternating bends with an irregular spacing along the valley trend. Such rivers tend to have relatively narrow, deep channels and stable banks. The system adjusts to varying discharge by vertical accretion on its floodplain and/or by lateral migration of its channel. A vast complex of floodplain depositional features is associated with such rivers, as illustrated by the Mississippi River study area (Plate F-10).

Braided Pattern

Braided rivers have channels divided into multiple thalwegs by alluvial islands. Braided rivers tend to have steeper gradients, more variable discharge, coarser sediment loads, and lower sinuosity than meandering streams. Their channels tend to be relatively wide and shallow. Braided patterns are "... developed



Figure 4.2. SIR-A radar image of dendritic drainage in east-central Columbia. Most of the image shows an area of dissected plains with a grassland cover that yields low radar return (dark tones). The drainage pattern is strongly enhanced in radar return (bright tones) because the forested stream channels reflect the radar energy back to the receiver.



Figure 4-3. Pinnate drainage developed on tributaries to the Dnestr River in parts of Moldavian S.S.R. and Ukrainian S.S.R. Landsat E-2436-08080-7, April 2, 1976.

depositionally within a channel in which the flow obstructions are sand and gravel deposited by the water moving around them" (Garner, 1974, p. 435). Midchannel bars are emplaced because of local flow incompetence. The resulting braid channels formed by splitting the flow are more competent than the original channel for conveying the load downstream (Leopold et al., 1964). Another way of describing braiding is that it is caused by channel widening that increases the boundary resistance of rivers with noncohesive banks (Church, 1972, p. 74). To maintain enough velocity for sediment transport in a wide, shallow cross section, the channel must divide and form relatively narrow and deep secondary channels through incision. Excellent examples of braiding occur in gravel-transporting rivers, such as Yukon, Colville, and upper Kosi (Plates F-12, F-11, and F-19, respectively). Braiding can also occur in sand-transporting rivers, like the Brahmaputra (Plate F-13). The latter experience more frequent and more complex modification of original bar forms.

Anastomosed Pattern

Many multichannel rivers have relatively low gradients, deep and narrow channels, and stable banks. Such river systems have been termed "anastomosed" (Smith and Smith, 1980). The terminology is a bit confused because "anastomosis" is a general designation for interconnected channelways whether in alluvial or in bedrock rivers. Thus, Garner (1974, p. 435), following Bretz (1923), defined an *anastomosing channel system* as ". . . an erosionally developed network of channels in which the insular flow obstructions represent relict topographic highs and often consist of bedrock." Anastomosis is extensively developed in the Channeled Scabland (Baker, 1978b). Therefore, anastomosing patterns can be considered to be composed of multiple interconnecting channels separated by relatively stable areas of floodplain (in the case of alluvial streams) or bedrock (in the case of bedrock streams). In contrast, braided patterns are single-channel,

multiple-thalweg systems with bars of sediment or vegetated islands around which flow is diverted in the channel.

Excellent examples of anastomosed streams occur in the plainslands of east-central Australia (Rust, 1981). The Burke and Hamilton Rivers (Plate F-14) and the Cooper Creek (Plate F-15) study areas illustrate these arid-region varieties. Anastomosis also characterizes very large tropical rivers, such as those in the Amazon Basin (Baker, 1978a). The Solimões and Japurá study areas (Plates F-23 and F-24) illustrate such rivers.

Distributary Pattern

Distributary patterns occur where fluvial systems are spreading water and sediment across depositional basins. Two varieties are fans and deltas. Fans (Bull, 1977) develop in piedmont areas under the influence of both tectonic and climatic controls. Arid-region alluvial fans are constructed by infrequent depositional events that include both debris flows and water flows. Typical arid-region fans occur in the Tucson and Tian Shan study areas (Plates F-9 and F-18). Cold-climate alluvial fans occur in areas of glacial outwash and in periglacial regions. An excellent example is the Sheenek Fan in the Yukon River study area (Plate F-12).

Humid-region alluvial fans are constructed by seasonal or perennial fluvial flows. The Kosi Fan of Nepal and India (Plate

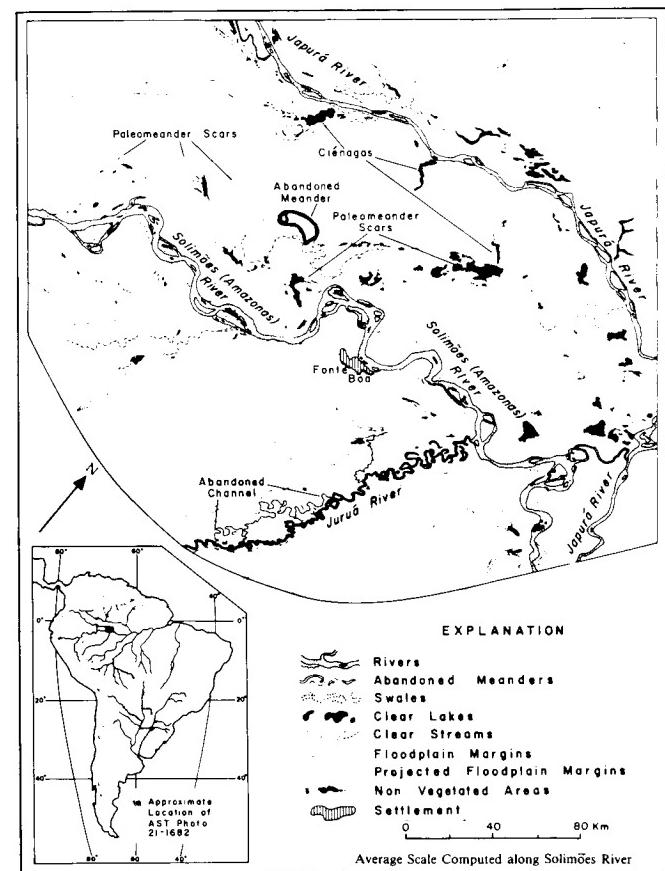


Figure 4-4. Geomorphic map of the fluvial landscape in northwestern Brazil near Fonte Boa on the Solimões (Amazonas) River. Major tributaries are the Japurá and Juruá Rivers. The map was prepared from an oblique color orbital photograph (AST 21-1682) taken in July 1975, during the Apollo-Soyuz space mission (Holz et al., 1979).

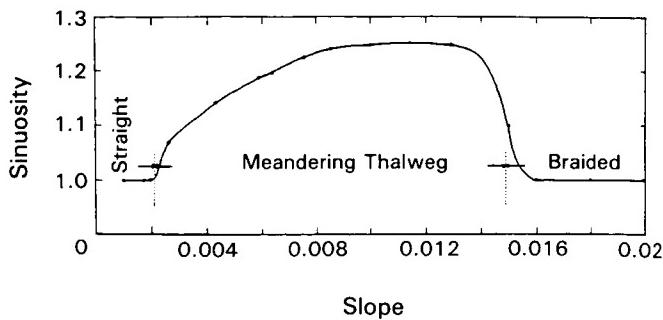


Figure 4-5. Experimental relation between slope and sinuosity for an alluvial channel, showing threshold changes between channel pattern types (Schumm and Kahn, 1972).

F-19) is an example from an area of active mountain building. The Pantanal study area (Plate F-21) illustrates some large fans in the savanna tropics of Brazil.

Deltas are the subject of another chapter in this volume since most deltas involve the interaction of ponded water systems (lakes and oceans) with sediment delivered to a river mouth. However, some basins of deposition in arid regions lack ponded water. Rivers entering these basins may produce typical deltaic morphologies, as in the case of the Niger River study area in Mali, West Africa (Plate F-20).

Transitional Patterns

Five study areas from the Amazon Basin illustrate the complexity of tropical river systems. Many of these complexities arise because the fluvial system is not merely an entity that is totally adjusted to the vagaries of modern conditions. Rivers possess a heritage in which they inherit elements of ancient conditions. Thus, old buried structures, relict alluvium, and progressive development contribute detail to the modern fluvial landscape. The understanding of modern rivers requires an understanding of their past history.

FLOODPLAINS AND TERRACES

Floodplains are the relatively broad and smooth valley floors constructed by active rivers and periodically covered with floodwater during periods of overbank flow. The floodplain is

thus a part of the active erosional and depositional activity of river channels. Floodplains consist of a great variety of depositional materials, including colluvium (debris from valley sides), channel deposits (sand and gravel), and vertical accretion deposits (clay and silt deposited by overbank flows). In addition to fascinating channel patterns, the following study areas illustrate many floodplain features: Mississippi River (Plate F-10), Yukon River (Plate F-12), Brahmaputra River (Plate F-13), Cooper Creek (Plate F-15), Yangtze River (Plate F-16), Manaus (Plate F-22), Solimões (Plate F-23), Japurá (Plate F-24), and Ucayali River (Plate F-25).

River terraces are abandoned floodplains that formed when their associated rivers flowed at high levels in the past. Many alluvial valleys contain complex flights of river terraces, as in the Huang He region of China (Plate F-3). Such terraces reflect numerous possible controls on river gradients, sedimentation, and erosion, including climatic changes, tectonism (uplift or subsidence), sea level changes, and other controls on base level. Distinguishing among these various causative elements can be a very difficult problem in geomorphology.

PALEOCHANNELS

A remarkable diversity of ancient river courses can be identified on large-format imagery. Many of the rivers responsible for these paleochannels have experienced immense adjustments of discharge and sediment load, major drainage diversions, and/or episodes of cataclysmic flooding. River adjustments were especially pronounced in the transitions from glacial to interglacial climates (Baker, 1983). The ancient Teays River system (Plate F-26) and the Channeled Scabland (Plate F-27) are two study areas that illustrate these phenomena.

The ability of orbital sensors to detect the regional associations of paleochannels on a global basis should open fascinating opportunities for paleohydrology. Pattern changes between paleochannels and modern channels should be especially interesting. Schumm (1977) has termed such changes "river metamorphosis." The directions and, in some cases, the magnitudes of change can be deduced from various empirical relations and classifications summarized by Schumm.

CONCLUSION

The study area descriptions that follow will elaborate the details of several river systems. Although this chapter is but a brief introduction to fluvial mega-geomorphology, it is hoped that it will convey the worthwhile perspective on rivers afforded by considering them on large spatial and temporal scales.

PLATE F-1

The Edwards Plateau consists of flat-lying Cretaceous carbonate and shale units at elevations of 600 to 900 m, which blanket much of south-central Texas. Amistad Reservoir on the Rio Grande River marks the southern limit of the plateau, where it terminates at the Balcones Escarpment. This escarpment is developed along a zone of Late Cretaceous and Cenozoic monoclonal folds and normal en echelon faults. The zone separates the relatively elevated and resistant Cretaceous limestone units of the plateau from the lower and more erodible Upper Cretaceous and Cenozoic sediments of the Coastal Plain to the south and east.

Rivers such as the Pecos and Devils are entrenched 100 to 200 m into the plateau surface (Figure F-1.1). The streams of the plateau include ephemeral varieties such as the Dry Devils River (left in Figure F-1.2) and perennial channels such as the lower Devils River (right in Figure F-1.2). Flow in the latter is maintained by ground-water discharge from the limestone.

The climate and geology of the Edwards Plateau combine to produce dynamic fluvial processes dominated by rare cataclysmic floods. The harsh semiarid conditions result in little human impact on the rocky limestone surface. The few towns include Ozona (O), Comstock (C), and Langtry (L)—famous for Judge Roy Bean's "law west of the Pecos." Annual rainfall averages between 30 and 60 cm, with values increasing along a west-to-east gradient. However, rainfall is extremely variable. Droughts of several years are common, and single storms can locally exceed the annual rainfall. Daily summer temperature maxima typically exceed 37.7°C (100°F) for most of June, July, and August.

The flat-lying rocks of the Edwards Plateau are dissected in overall dendritic patterns. Careful inspection of the scene will reveal local linear trends for some channel segments. These result from joints that developed during gentle warping of the brittle rocks in this region.

Among the geomorphic factors that enhance runoff concentration from rains in this region are the thin soils, relatively high local relief, steep hillslopes, relatively impermeable bedrock, and high drainage densities. Morphometric studies of drainage networks in this region by R.C. Kochel (1980) showed drainage densities of 4 to 6 km/km². Drainage density is determined as the summation of channel length in a given area. Similar morphometric studies of plateau areas characterized by lesser flood

EDWARDS PLATEAU, TEXAS

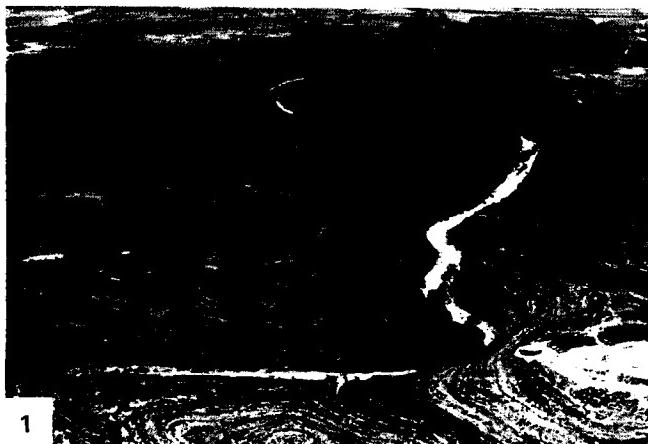
response in Indiana and the Appalachians determined drainage densities of 2 to 4 km/km² (Patton and Baker, 1976). Note that the highest drainage densities occur in the Devils and Pecos River regions to the left center of the image. Lower drainage densities occur in the less dissected core of the plateau to the upper right. The high drainage density is readily discerned because the thin layers of carbonate rocks produce an erosional effect that resembles a topographic map (Figure F-1.3).

Central Texas experiences some of the most intense rainstorms and floodflows in the United States. Maximum rainfall is generated by summer thunderstorms and by late summer tropical disturbances that migrate into an otherwise semiarid environment (Baker, 1977). An extreme example of the former is the cloudburst of May 31, 1935, which yielded 56 cm of rainfall in 2 hours 45 minutes near the Balcones Escarpment at D'Hanis, Texas. National record floodflows for small drainage basins have been recorded at Carta Valley (V) and at Loma Alta (A).

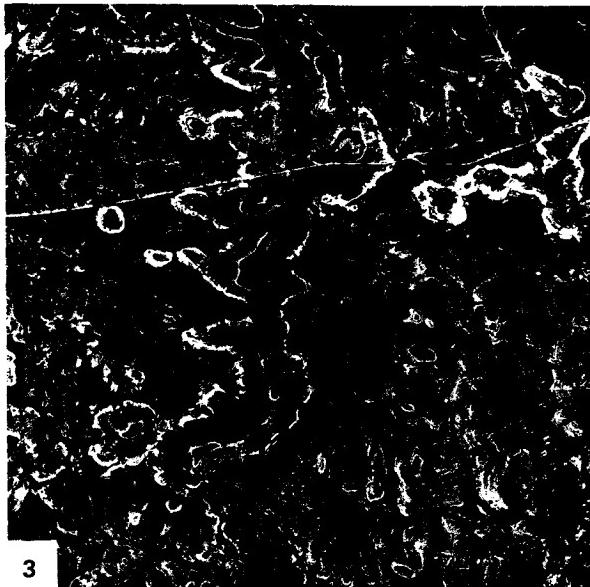
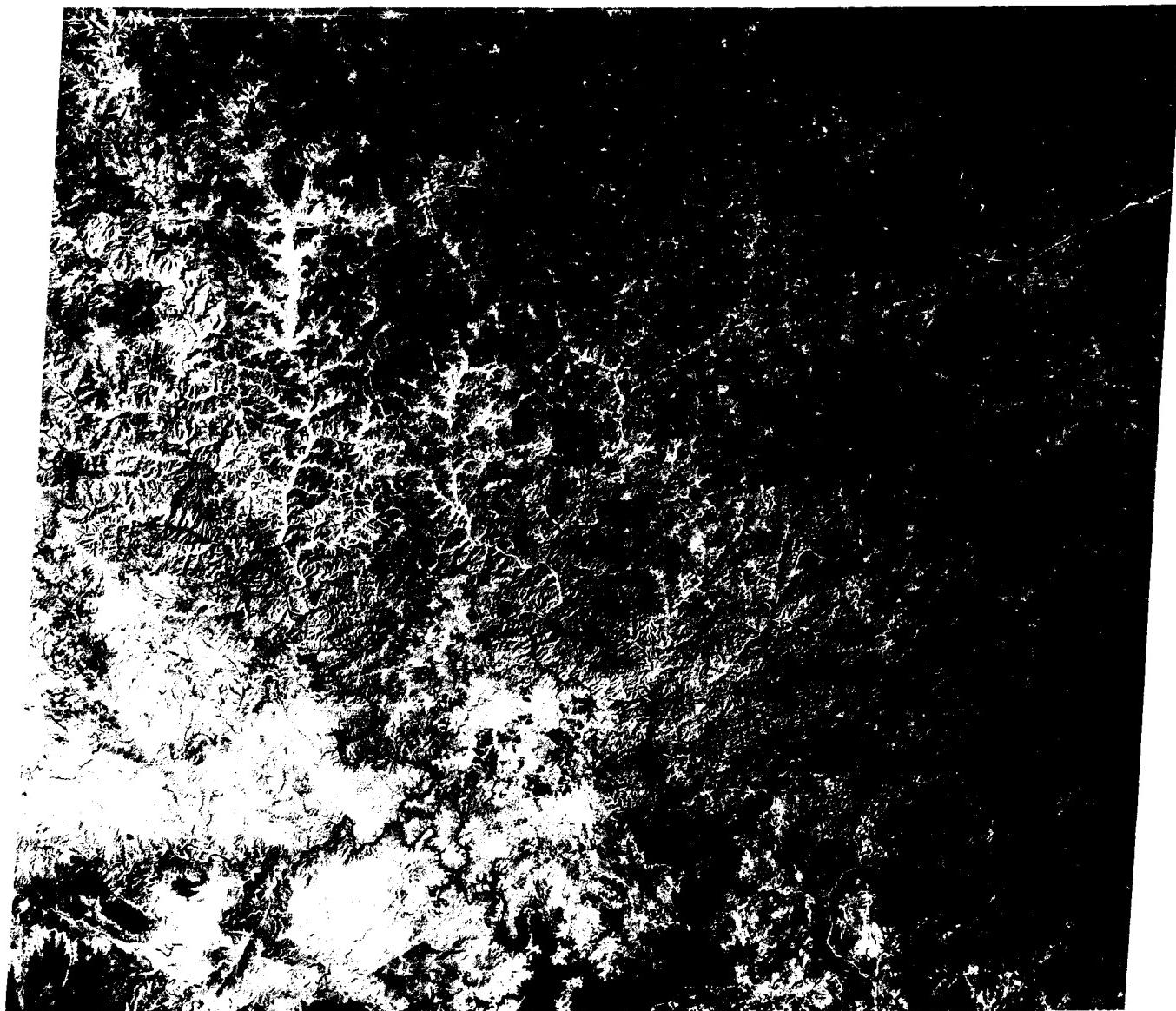
One of the most spectacular floods in the United States struck this region in June 1954, when Hurricane Alice migrated inland from the Gulf of Mexico and centered its precipitation on the Pecos-Devils divide. Rainfall in excess of 1 m was generated over a 2-day period. This produced a flood peak on the lower Pecos River of 27400 m³/s (980000 cfs). The flood stage in the Pecos River Canyon near Langtry (L) exceeded 30 m. In some areas, floodwater actually spilled out of the canyon onto the adjacent plateau surface. The 1954 Pecos Flood was nearly an order of magnitude larger than any flood recorded in the previous 50 years. Paleoflood hydrologic studies of ancient Pecos River floods (Kochel and Baker, 1982) show that the 1954 flood was on the order of a 2000-year event (i.e., it has a 0.0005 probability of occurrence in a given year).

During these rare large floods, the bedrock channels of Edwards Plateau streams are scoured of their bouldery alluvium, exposing fresh white limestone bedrock along channel beds and banks. The high albedo of the valley floors results in the clarity of drainage depiction by this Landsat image (Figures F-1.1 and F-1.2). The gray patina of the plateau limestone on interfluves, plus local soil and vegetation cover, provide a marked contrast to the flood-dominated channel floors when viewed from orbit.

Landsat 21711-16314-7, September 29, 1979.



ORIGINAL PAGE IS
OF POOR QUALITY



3

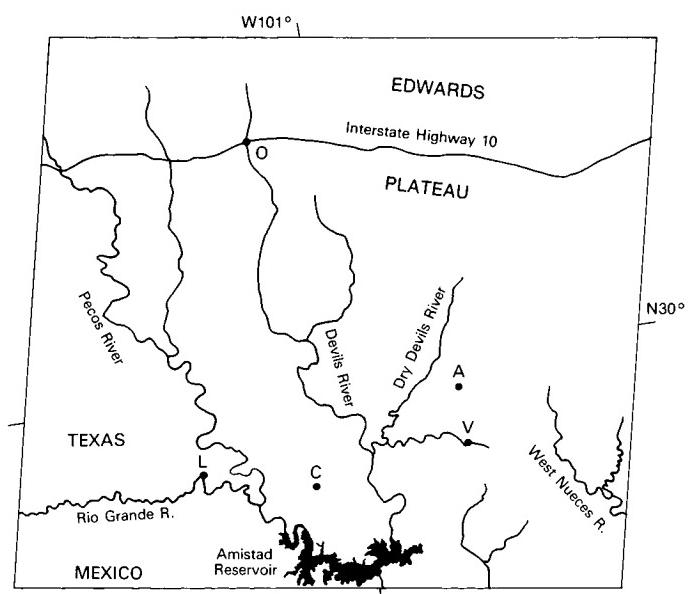


PLATE F-2

LOESS PLATEAU, SHANXI PROVINCE, CHINA

This scene shows the Fen River (Fen He) valley near the major steel-making center of Taiyuan (pop. 2 725 000), Shanxi Province, China. The major river valleys here expose Triassic sedimentary rocks. The Taiyuan Basin is filled with Cenozoic lakebeds and alluvium of the Fen River. To the west is the Lüliang Shan, a mountain range that uplifts Paleozoic units and Late Precambrian crystalline rocks. The Huo Mountains to the southeast are a tilted block of Paleozoic sediments that reach an elevation of 2545 m.

The climate of this region is hot and dry. The lowlands receive about 500 mm of annual rainfall, but the Lüliang Shan receives over 750 mm. The rains come principally in the summer. Population densities along the river bottoms are about 50 people per km². Farming is the principal activity, but industrial areas occur at the northern end of the image.

Except for the Lüliang Shan, the entire region is blanketed with loess. Indeed, the Loess Plateau of central China is probably the greatest single pile of terrestrial eolian silts. The loess mantles about 320 000 km² in the Chinese provinces of Shanxi, Shaanxi, Gansu, and Ningxia. It thickens markedly to the east, where one section near Lanzhou City is 335 m thick.

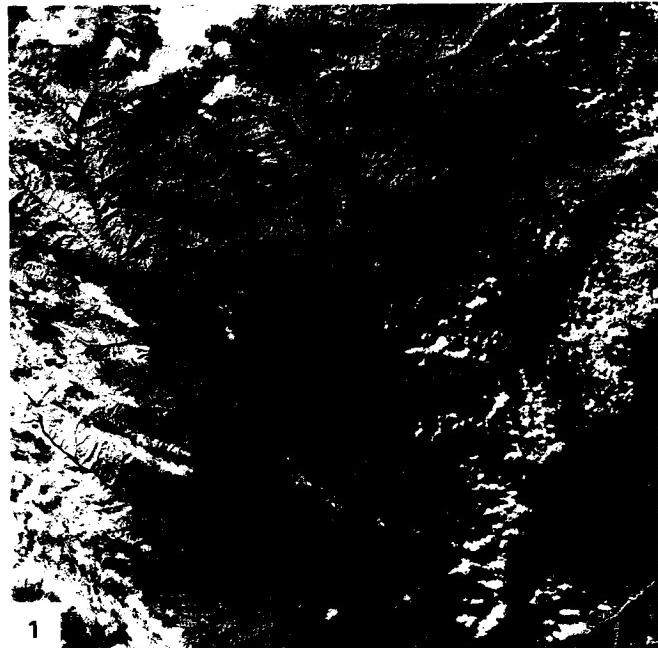
A Landsat scene immediately to the North (2287-02344-7) is shown in Figure F-2.1 The prominent river in the center of the image is the Huang He (Yellow River). Because of its huge sediment load, the river appears as lighter gray tones, even on this Landsat band 7 image. In the Lüliang Shan, the transition from lowland grassland to upland broad-leaved forest follows the 1500-m contour.

The SIR-A radar scene (Figure F-2.2) is centered on the Huang He approximately 60 km north of the Landsat scene. In this picture, the Lüliang Shan gives a bright radar response because the forest canopy is rough relative to the radar wavelength. The very bright spot near the lower right is the city of Lanxian. The city of Xingxian is the bright spot at the right center of the image.

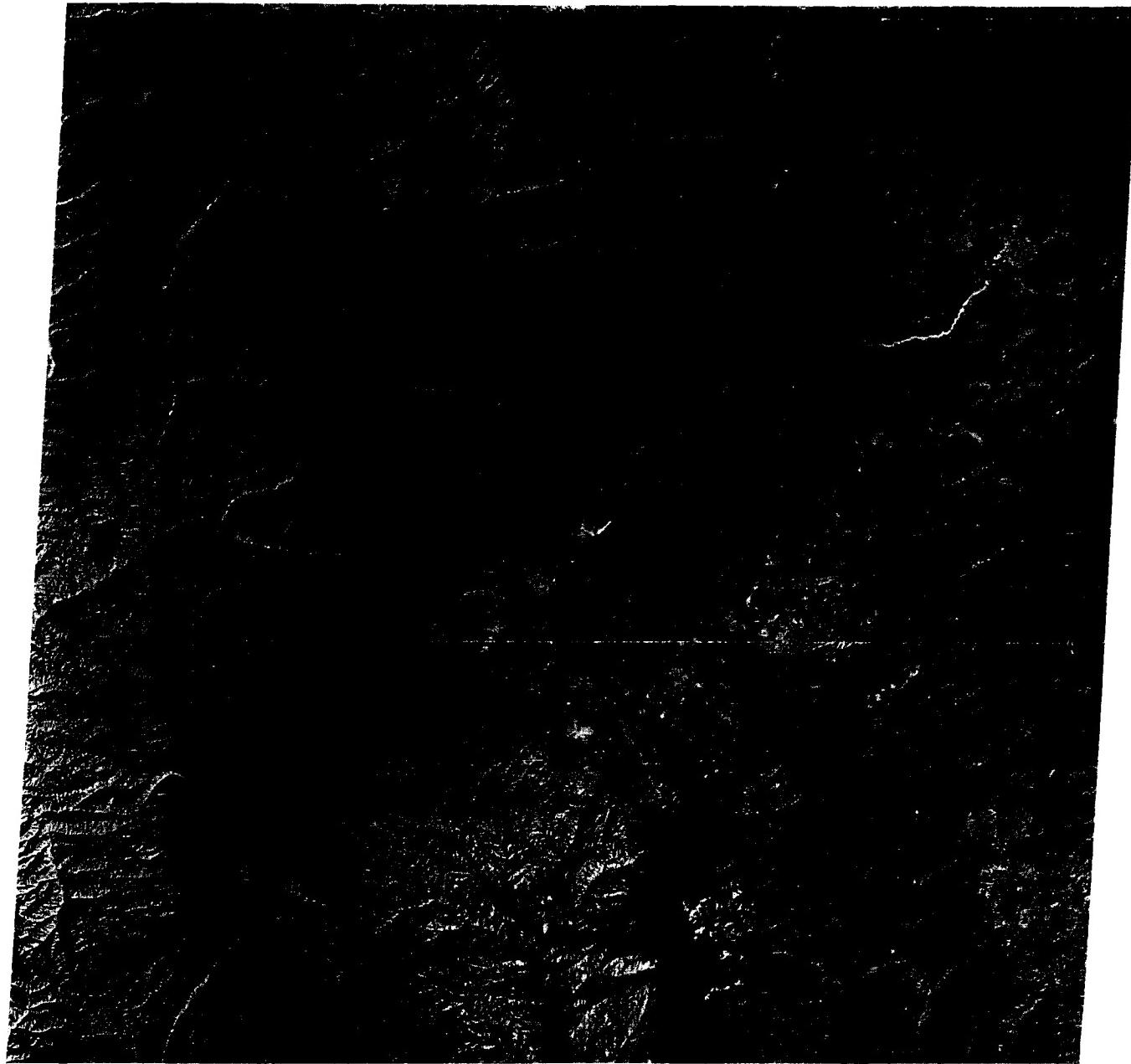
The radar provides an excellent depiction of two major types of loess plateau morphology (Derbyshire, 1983). The far western (left) end of the image shows areas of flat undissected plateau, which are called "yuan." The highly dissected loess at the center of the image consists of elongate ridges between gullies.

The ridge topography, as seen in an oblique aerial photo (Figure F-2.3), is called "liang." Another type of loess topography, not shown here, consists of hemispherical hills known as "mao."

Both the yuan and liang are being dissected by headwardly extending gullies. The gullies are box-shaped and have very low gradients. They deepen until reaching bedrock and extend themselves through large-scale piping. Approximately 236 km² of the Loess Plateau is subject to this type of accelerated erosion. Drainage basins may yield over 30 000 metric tons of sediment per km². During storms, the loess will flow in slurries that are 50 to 60 percent sediment by weight. Such tremendous erosion contributes phenomenal amounts of sediment to the principal rivers. **Landsat 1524-02394-7, December 29, 1973.**



ORIGINAL PAGE IS
OF POOR QUALITY



3

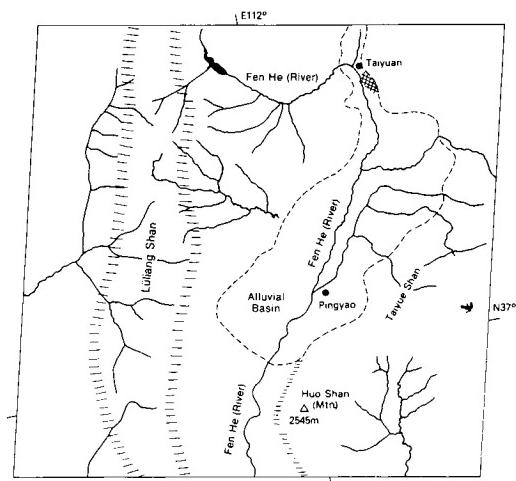


PLATE F-3

ORIGINAL PAGE IS
OF POOR QUALITY

HUANG HE, SHANXI PROVINCE, CHINA

This specially processed Landsat scene, produced by Earth Satellite Corporation, shows the Fen River (Fen He) valley immediately south of the Taiyuan Basin. The Fen He has developed a broad alluvial plain that has terraces overlain with thin loess. Flat loess areas (yuan) dominate in the lower left of the scene, where the Fen He flows into the Huang He (Yellow River). Highly dissected "liang" topography forms a sharp contact with the yuan surface.

The Landsat scene immediately to the west (E-1525-02455-7) is shown in Figure F-3.1. It shows the Huang He valley through typical liang surfaces of the Loess Plateau. Figure F-3.2 depicts the Huang He and its valley elsewhere in the region. The dissected uplands shown in Figure F-3.3 are characteristic of nearby loess plateaus.

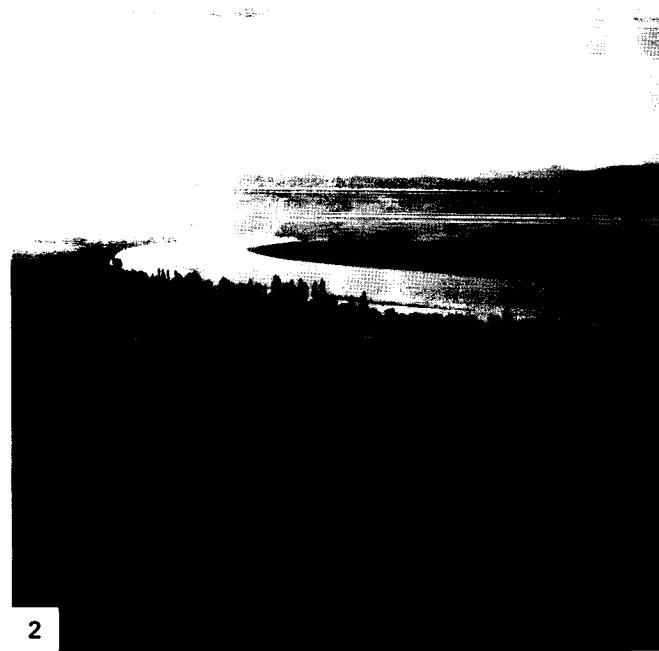
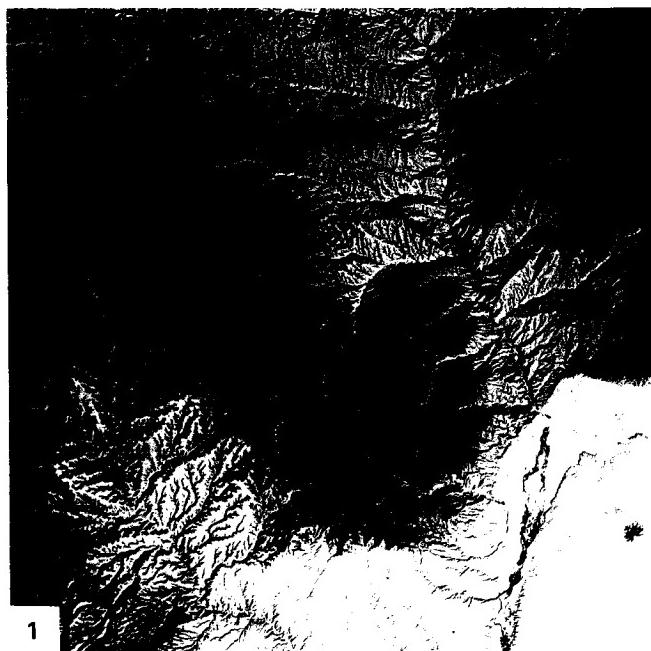
The contrast between the alluvial plains and the dissected loess plateau is especially striking on the imagery. The alluvial plains are characterized by modern floodplains and terraces. Terraces are abandoned floodplains formed when rivers flowed at higher levels than at present. Changes in river position within the valley occur because of changes in the major controls on channel gradients and patterns. In the Loess Plateau, it is probable that past changes in discharge and sediment load were induced by major climatic changes during the Pleistocene. The rivers responded by cycles of aggradation and degradation that were superimposed on the long-term trend of valley incision. Terraces formed when floodplain levels were abandoned by subsequent river incision.

Traditional opinion inside China, going back to at least 32 B.C., has consistently held that the loess is primarily an eolian

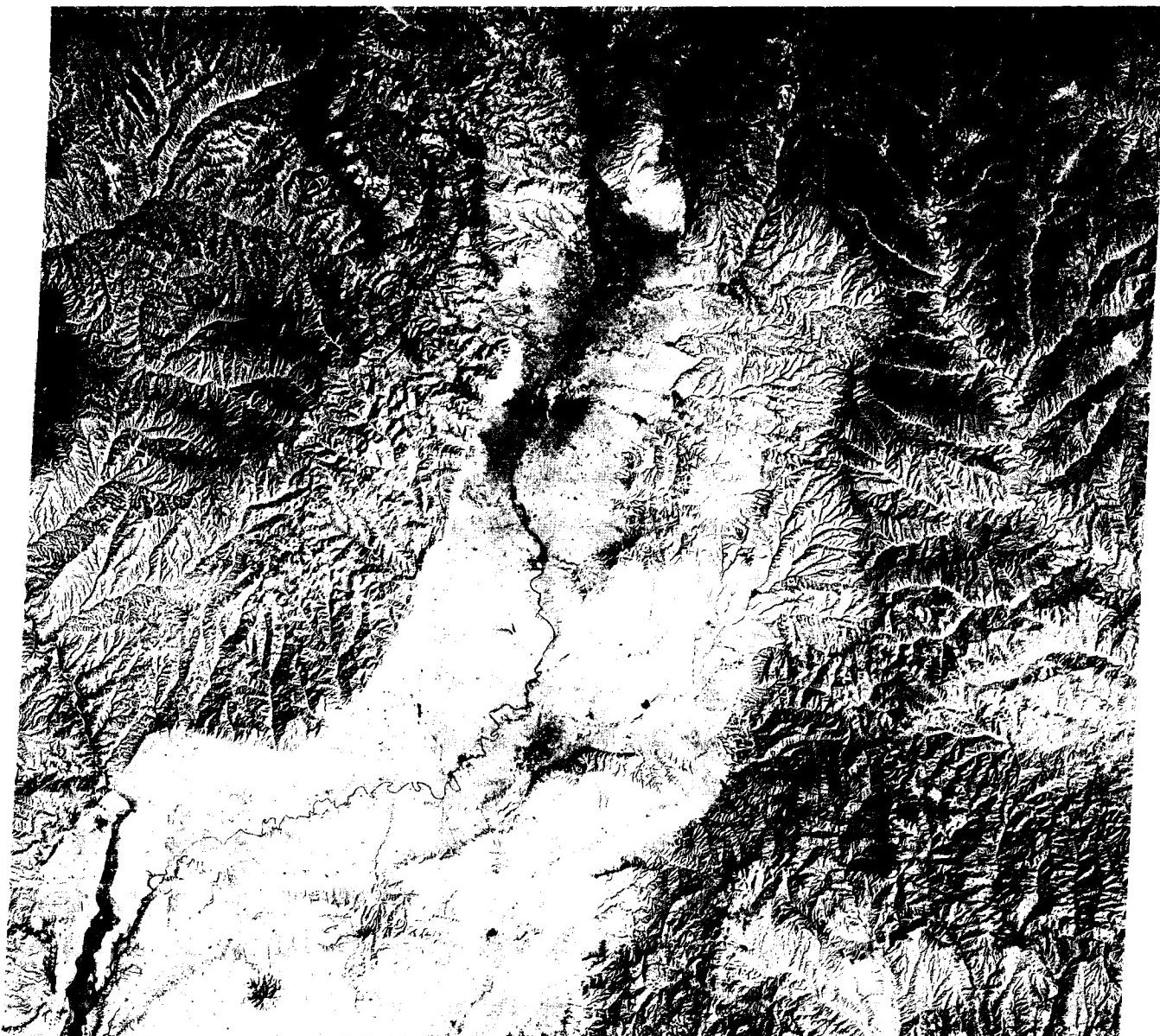
sediment derived from the deserts to the north and west. Recent work has confirmed this hypothesis, showing that loess accumulation followed the desiccation of the high central Asian plateaus in the early Pleistocene. A severe periglacial environment prevailed during glacial periods, associated with prevailing northwesterly winds. The dust blowing from the cold dry plateaus was trapped by the southeasterly climatic gradient toward humid subtropical monsoonal areas of China.

Loess is perhaps the most easily erodible material available to moving water. As a result, the sediment loads of the Huang He are greatly in excess of those for any other large river in the world. Where it leaves the loess plateau, the Huang He is estimated to transport between 1.5 and 1.9 billion metric tons of sediment per year. Much of that load is transported to the Yellow River delta (Figure 5-1) and the Gulf of Bo Hai. The Yellow Sea, of which the gulf is the western arm, derives its name from the immense load of sediment that is delivered to it.

Interestingly, the river delivers its immense load with a relatively small water discharge: $49 \text{ km}^3/\text{yr}$ or an average of $1550 \text{ m}^3/\text{s}$ (Milliman and Meade, 1983). This contrasts with the nearby Yangtze River (Chang Jiang), which does not drain loess. The Yangtze delivers less than one-third the sediment, but its discharge is nearly 20 times as great. The unique qualities of the Huang He give it the highest sediment concentrations of any major river. Average yearly concentrations of sediment in Huang He water are as great as 48 g/liter and average monthly concentrations can exceed 70 g/liter. **Landsat 30597-02293-7, October 23, 1979.**



ORIGINAL PAGE IS
OF POOR QUALITY



3

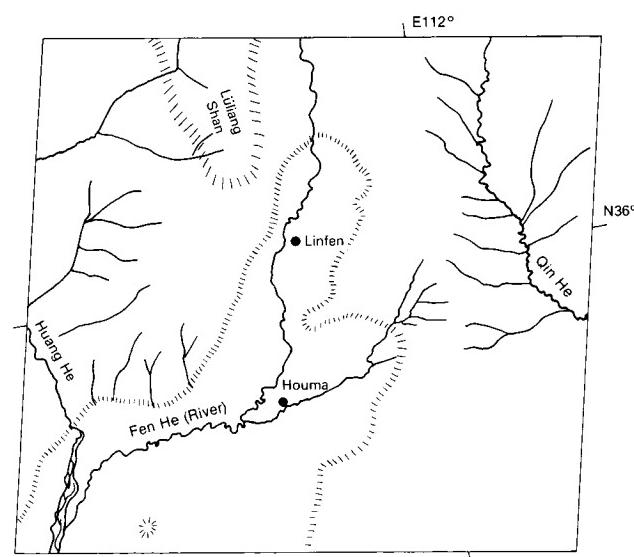


PLATE F-4

ELAT AND QA AL JAFR, ISRAEL-JORDAN

This Landsat scene shows the extreme northern end of the Gulf of Aqaba, which occupies the Dead Sea Rift extending northward across the center of the scene. The rift is a branch of the larger Red Sea spreading axis that separates the Arabian and African Plates. Crustal extension and normal faulting have characterized the rift zone throughout the Neogene. The rift divides two zones of mountains. The Elat Mountains to the west are developed in Precambrian igneous-metamorphic basement rocks overlain by Paleozoic/Mesozoic sandstone ("Nubian" sandstones) and Cretaceous/Tertiary carbonates. To the east, the Precambrian granitic rocks of the Rift/Border Mountains are overlain by thick Paleozoic sandstone units. Northeast of the Ras en Naqb Escarpment, the sandstones are overlain by Lower Cretaceous limestone.

The Dead Sea Rift margins are bounded by extensive talus aprons and alluvial fan bajadas. Israeli geomorphologists have documented the formation of these aprons during wet phases (pluvials) of the Quaternary. The wet phases also involve soil formation, with the production of fines from coarse debris. The fines then serve as matrix for debris flows that develop from rainstorms and abundant sediment. The coarse debris thus passes to mountain-front alluvial fans, which are abundant along the rift valley margin. Because of coarse sediment influxes, these "pluvial" fan surfaces are steep in gradient.

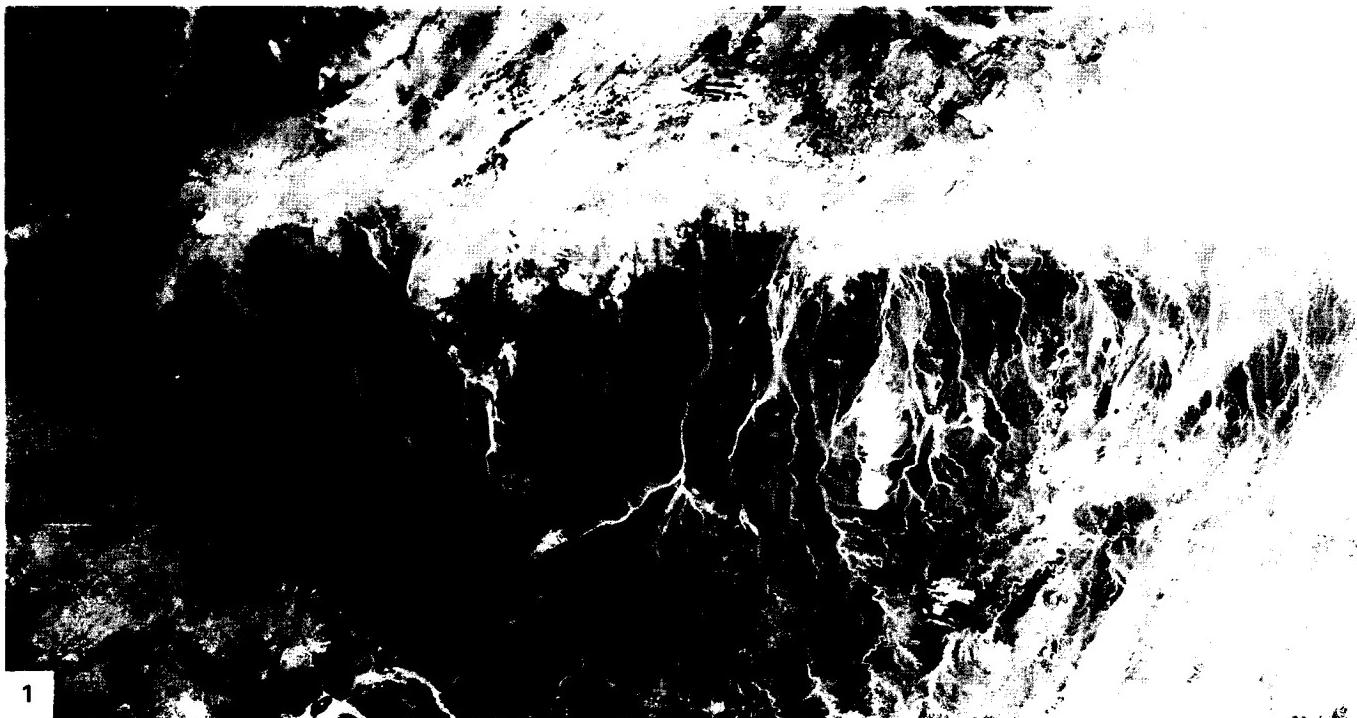
The present environment is an "interpluvial" arid regime. The modern mean annual precipitation is 30 mm, with a standard deviation of 20 mm. The transition of this extremely arid regime profoundly changed the mountain fronts. Because talus production was slowed, the slopes were eroded, exposing bedrock. This, in turn, promoted rapid runoff from the rare rainstorms. Less sediment was yielded from bare rock, so the streams entrenched

the "pluvial" fans and moved fine sediment in narrow valleys to floodplains or playas beyond the alluvial fan bajadas. Repetition of the foregoing processes probably occurred several times during the Quaternary.

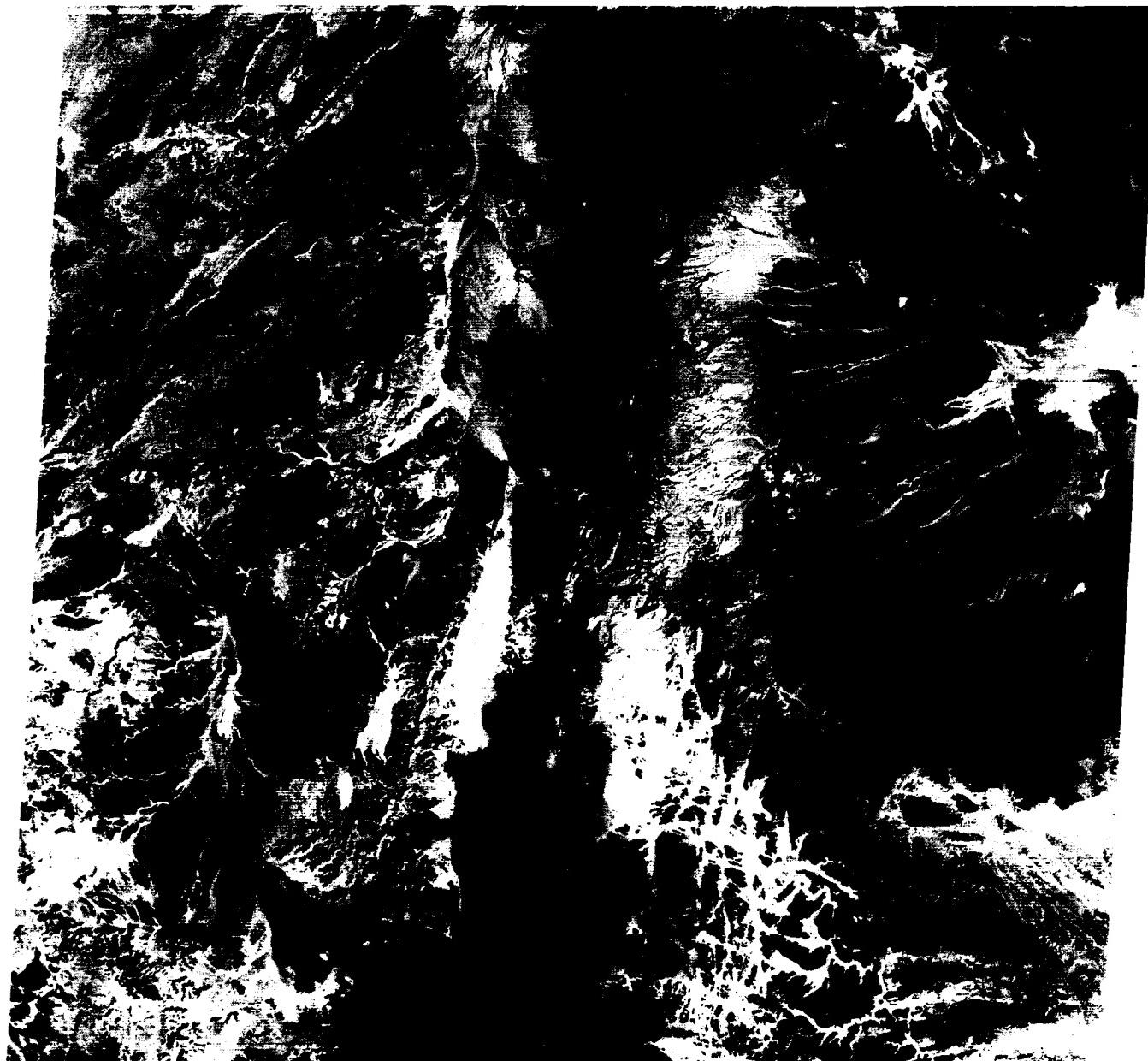
The south-central part of the image shows a striking structural control of drainage. Residual sandstone interfluves stand out as dark hills that rise as much as 800 m above the light-toned drainages. The latter are aligned along an intersecting fracture system. As the valleys coalesced by weathering, mass movement, and fluvial removal of debris, they comprised a lower level surface with great sandstone residuals rising above it (Osborn, 1985). Such landscapes are termed "inselberg" landscapes.

To the northeast of Qa Al Jafr is still another center for internal or landlocked drainage, the Wadi as Sirhān (Figure F-4.1). A series of linear ephemeral streams, draining from Ard as Sawwan in Jordan, empty into an elongate bajada that lies against low hills cut from volcanic flows just inside northernmost Saudi Arabia.

The prominent centripetal drainage system at the right of the Plate is shown more completely in Figure F-4.2, a Return-Beam Vidicon (RBV) scene showing an area of 98 by 98 km. The RBV system on Landsat 3 had a resolution of 30 m per pixel, as compared to 79 m per pixel for the Multispectral Scanner System. The result is a much more detailed rendition of the drainage features surrounding Qa Al Jafr, an immense playa. The overall pattern is centripetal with ephemeral channels incised into old, dark alluvial surfaces that mantle the Cretaceous limestone bedrock. The major highway from Jordan to Saudi Arabia also shows prominently as a linear bright swath across the dark alluvial surfaces. **Landsat 30289-07322-6, December 19, 1978.**



ORIGINAL PAGE IS
OF POOR QUALITY



2

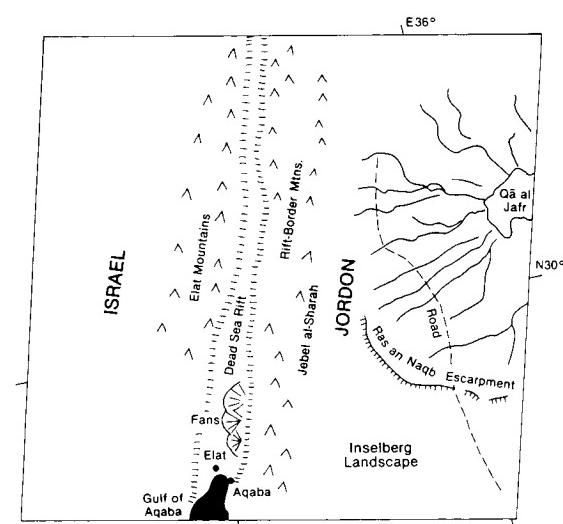


PLATE F-5

CENTRAL YEMEN

The nation of South Yemen (or Aden) is located at the southern end of the Arabian Peninsula. This Landsat scene shows a portion of the Hadhramut Plateau of central Yemen. The plateau is underlain by Early Tertiary sediments that dip northward toward the Rub'āl Khālī Basin. The sediments represent Paleocene transgression that emplaced a sequence of limestones, the Jeza Formation, overlain by an evaporite sequence, the Rus Formation. These two units have extensive exposure and very different patterns of dissection and erosion.

The Hadhramut Plateau was deformed in the Tertiary into several broad anticlines and synclines. The major drainage, Wadi Masila (or Al-Masilah), flows along the general axis of a syncline before turning to the coast to the right of the image. Note that the dendritic pattern of the plateau is modified to a trellis pattern at the lower center of the image, reflecting the presence of these broad folds.

The Landsat scene to the west (E-2362-06242-5) shows the headwater areas of the Wadi Masila (Figure F-5.1). This image, from January 19, 1976, shows the continuation of the drainage along the prominent open syncline in the relatively resistant Jeza Formation. The Wadi Masila derives sufficient flow to maintain irrigated agriculture in the narrow valleys of the right-center image. Upstream of this point, the valleys are much broader, and the drainage is named Wadi Hadhramut. In the left center of the image, the valleys have been widened, and the Wadi Hadhramut actually opens farther westward into the Rub'āl Khālī Basin. This unusual valley widening in a headwater area results in a continuous lowland, the Ramlat Sab'atayn, connecting the Rub'āl Khālī to the Wadi Hadhramut.

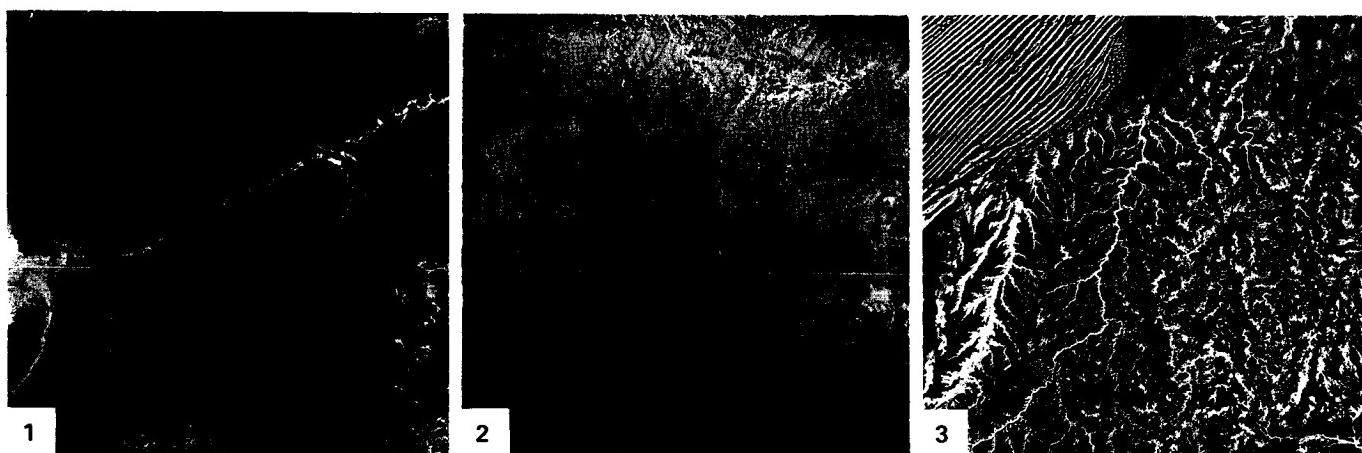
It seems probable that much of the well-developed dendritic drainage of the Hadhramut Plateau (seen from the Space Shuttle, Figure F-5.2) is relict from past wetter conditions, perhaps extending to the Tertiary emergence of the landmass. As the climate changed to an arid one, perhaps in the Early Pleistocene, processes of slope retreat came to dominate along the western

margin of the plateau. As interfluves were destroyed, the western drainage divide of the Wadi Hadhramut/Wadi Masila system was breached. The upstream part of the system experienced pronounced valley widening by lateral slope retreat away from the relict drainageways. The Ramlat Sab'atayn is a desert piedmont etched from the former dendritic pattern of a fluvial landscape.

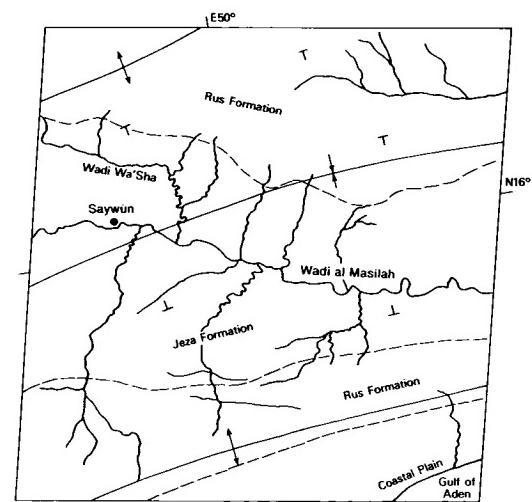
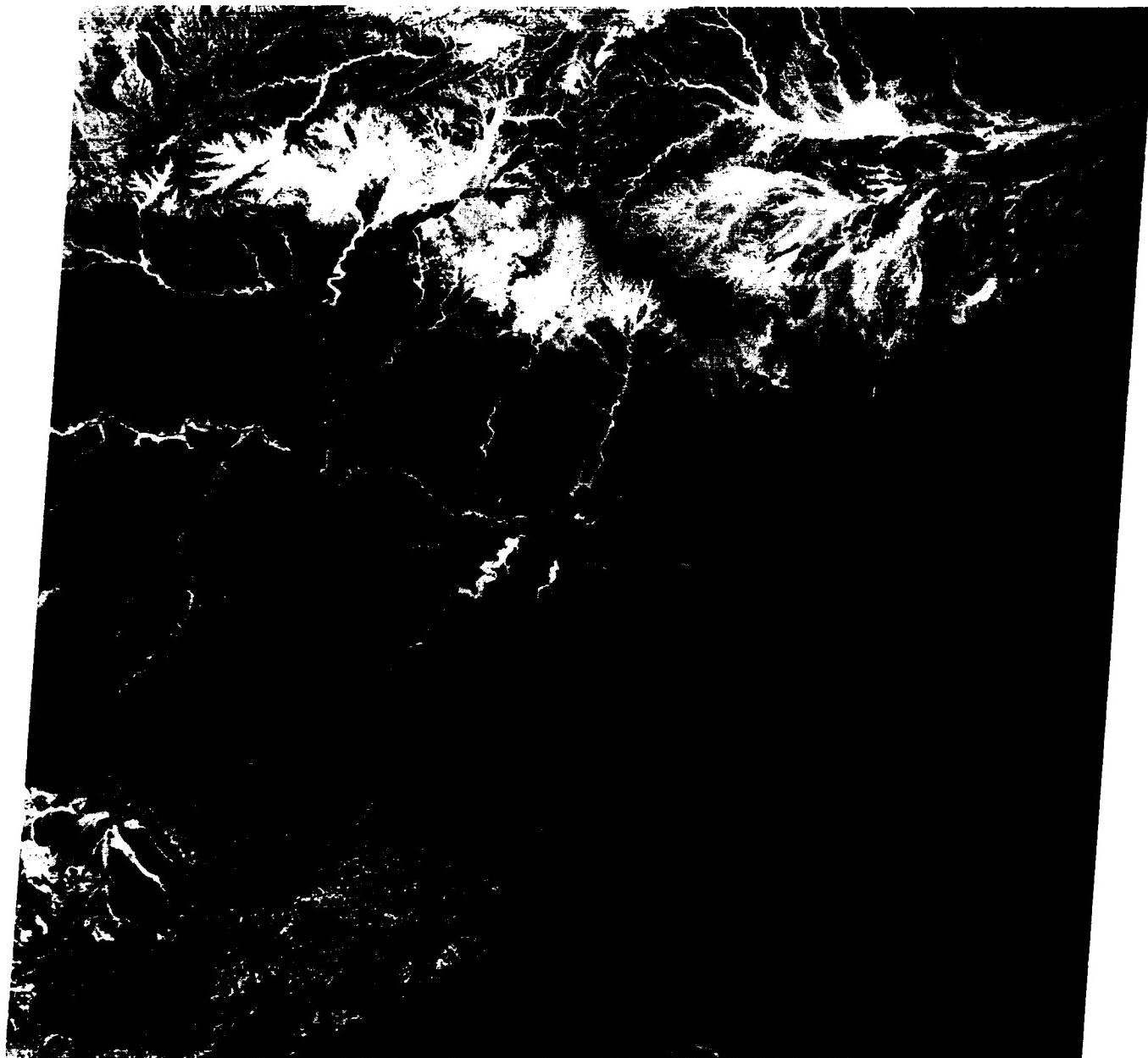
The Landsat scene to the northwest (Figure F-5.3) was imaged on January 19, 1978. It shows several northward-flowing drainages, including Wadi Aywatal Sayer, flowing from the lower left to the zone of linear sand dunes in the sand sea of Rub'āl Khālī (upper left). Note that Wadi Aywatal Sayer is probably a smaller example of the drainage transition noted above for the Wadi Hadhramut/Wadi Masila system. Slope retreat has widened the valley floor, isolating a plateau underlain by the Jeza Formation at the left center when the drainage divide was breached. The Wadi Aywatal Sayer is now a continuous lowland, an extension of the Rub'āl Khālī desert floor.

Another major drainage, the Wadi Makhya flows from the lower left of the image (Figure F-5.3) to a great floodout fan that deflects the linear sand dunes at the top center. Note that this drainage on the Jeza Formation is well developed and dendritic. The drainage on the right (eastern) part of the image is the Wadi Khudra. Note that this area of Rus Formation evaporites has a rather poorly defined pattern of dissection. Highly tortuous meandering channels occur at the right center of the image. Dissolution of Rus gypsum units during wetter climatic conditions may have contributed to the striking patterns.

Farther to the east, in the Zufār Region of Western Oman (Figure F-5.4), almost the entire ephemeral drainage is inland toward the southern edge of the Rub'āl Khālī. The headwaters of these streams in places have nearly reached to within 20 to 30 km of the coastline. From there, short streams cutting into the dissected plateau terrain form a second set of drainage channels that in places have not yet been captured by the interior system. **Landsat 1167-06324-6, October 3, 1973.**



ORIGINAL PAGE IS
OF POOR QUALITY



This Return-Beam Vidicon image shows the region of the Glen Canyon in south-central Utah. An extensive sedimentary sequence is exposed, including the Cretaceous sedimentary rocks along the Straight Cliffs escarpment of the Kaiparowits Plateau. The underlying Jurassic rocks include massive cliff-forming units of the Glen Canyon Group. Narrow sinuous bedrock canyons are especially well developed in the Glen Canyon Group, which includes the Navajo Sandstone. The Circle Cliffs expose underlying Triassic sandstone, shales, and conglomerate units (Figures F-6.1 and F-6.2).

The Henry Mountains (Figure F-6.3) comprise a classic locality where Grove Karl Gilbert (1877) developed the concept of updoming of sedimentary rocks by laccolithic domes. As with other laccolithic mountains on the Colorado Plateau, doming is assumed to have occurred in the Early Miocene, about 25 million years ago (Hunt, 1956). Growth of the domes led to drainage adjustment. It is interesting that, while major rivers flow across folds, they tend to flow around the large igneous structures of the Colorado Plateau.

Cataract Canyon, in the upper right part of the scene, is a relatively low sinuosity section of the Colorado River where it crosses the crest of the broad Monument Upwarp. Because of flooding by Lake Powell below the Dirty Devil River Junction, the details of the Glen Canyon are difficult to discern along the mainstem Colorado. However, preimpoundment surveys reveal that the river gradient through Cataract Canyon is 1.9 m/km (10 ft/mi), changing to 0.3 m/km (1.5 ft/mi) in the Glen Canyon. The meandering patterns are associated with the gentler gradients, and the steeper gradients are associated with the cores of upwarps. One theory holds that these relationships derive from the antecedent history of the river (Hunt, 1969). According to this theory, the Colorado River in the later Tertiary and Quaternary was in-

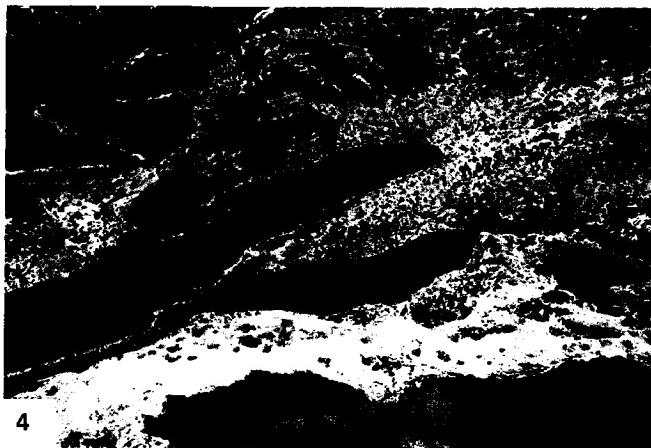
cising this part of the Colorado Plateau as various anticlinal folds and upwarps were growing. A relevant analogy is to a saw into which a log is being pushed. The saw represents the continuing cutting of a river, and the log represents growing folds.

This part of the Colorado Plateau contains numerous examples of natural bridges, alcoves, and arches. These are features of inner canyons along the Colorado Glen Canyon and major tributaries such as the Escalante River. These features are all presumably Pleistocene in age.

Valleys in the massive sandstones of the Colorado Plateau show steep-walled theater-like terminations (Figure F-6.4). Here, an excellent example is an unnamed canyon where ground-water seepage in the Navajo Sandstone contributes to the local disintegration of bedrock and subsequent backwearing of cliffs, a process termed "sapping." Spring sapping is the concentrated variant of the process in which ground-water outflow undermines slopes, generally along joint- and fault-controlled zones, resulting in the headward growth of valleys. Canyons formed by sapping have prominent structural control, vertical to overhanging walls, flat floors, elongate shape, low drainage density (leaving undissected uplands), relatively short tributaries to main trunk valleys, irregular variation in valley width as a function of valley length, and theater-like valley heads. Many of the Colorado Plateau sapping valleys are probably relict features, since lowered water tables and/or dessicating climatic conditions have probably resulted in reduced ground-water flow to the valley floors at present. During wetter climatic episodes of the Quaternary, probably coinciding with periods of mountain glaciation, spring sapping activity would have been more pronounced. Under modern climatic conditions, the results of past spring-sapping processes are obscured by the modifying action of nonsapping morphogenetic processes. **Landsat 30914-17091-A, September 4, 1980.**



ORIGINAL PAGE IS
OF POOR QUALITY



4

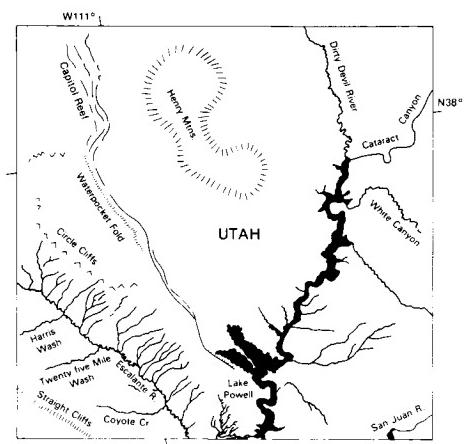


PLATE F-7

The Grand Canyon is a spectacular example of river incision. Here, the Colorado River crosses a broad upwarp of Paleozoic sedimentary rocks, reaching elevations in excess of 2700 m (9000 ft) on the forested Kaibab Plateau (here dusted with spring snow). The canyon measures 1.6 km in depth and 19 km from rim to rim. It exposes relatively flat Paleozoic sediments unconformably overlying Proterozoic sediments and Archeozoic schist and gneiss (Figure F-7.1).

The rim of the Grand Canyon is held up by the resistant Permian Kaibab Limestone that underlies extensive areas of the Kaibab and Coconino Plateaus. Marble Canyon of the Colorado River is named for the exclusive incision into this unit (Figure F-7.2). At Echo Cliffs and Vermillion Cliffs, the brightly colored Triassic units are exposed, including the Moenkopi and Chinle Formations. The cliffs rise to massive caprocks of the Triassic/Jurassic Glen Canyon Group, which underlies the Kaibito and Paria Plateaus.

Two young volcanic fields developed within the sedimentary sequence. The San Francisco Peaks at the lower right include a 3700-m high core surrounded by cinder cones. Volcanic activity occurred through the Quaternary. The youngest cones are less than 1000 years old. The Mount Trumbull/Uinkaret Plateau area at left center also includes Quaternary volcanism. Volcanic flows from this field actually entered the Grand Canyon from the north, forming a dam in the inner gorge 180 m high. The river had cut to within 15 m of its present depth when this dam formed, 1.2 ± 0.6 million years before the present.

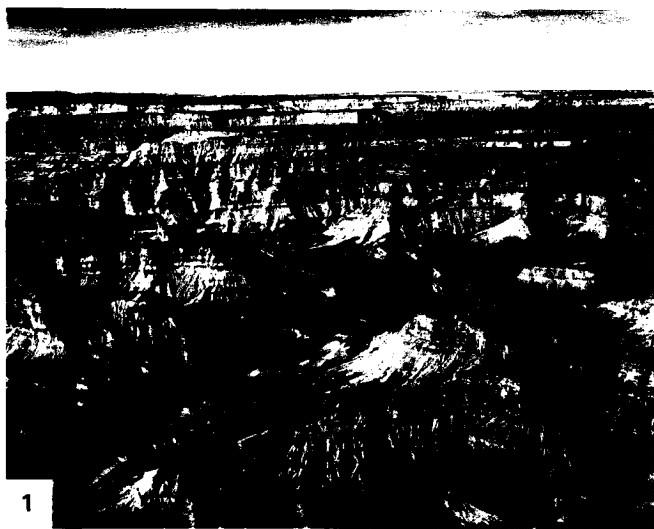
The history of the Colorado River at the Grand Canyon is quite complex and remains unresolved. The view of Charles B. Hunt (1969) is that an ancestral Colorado River (mainly from the San Juan drainage) was antecedent to the Kaibab Upwarp. Gravels on the Kaibito Plateau show that this river was in existence by Late Miocene time. This river joined with the ancestral Little Colorado River to exit the Colorado Plateau south of the present Colorado's course to Lake Mead.

GRAND CANYON, ARIZONA

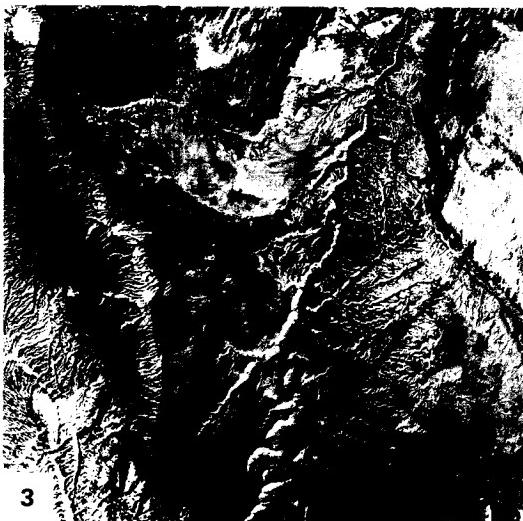
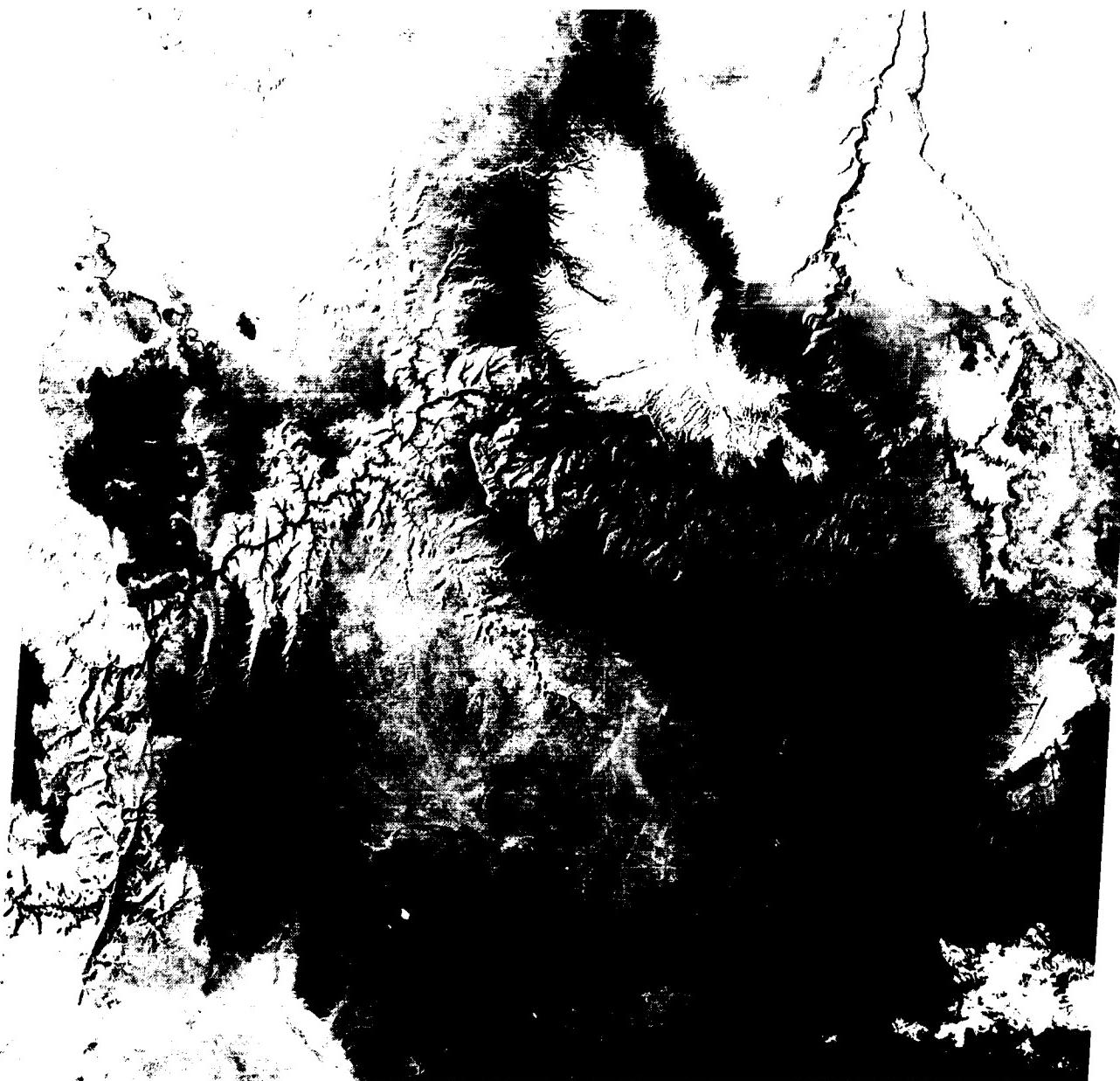
Because of extensive basin-and-range faulting in the Miocene and Pliocene, much of the original landscape has been greatly modified. Ponding of drainage by shifting fault blocks, filling of basins with water and sediment, and spillage of water across developing divides may have all contributed to the complex history of the river downstream of the Grand Canyon. As the Basin and Range province to the west became low-lying, the Colorado Plateau rose. The immense relief of the Grand Canyon developed from this tectonic disparity, but the details of the story remain to be found.

Figure F-7.3 is a Landsat 4 image of the Marble Canyon. Note the structural control of drainage on the Kaibab Limestone. A prominent fault scarp can be seen in the southwest quadrant of the image. It is also unusual that the tributaries appear to be barbed, forming V-junctions that point north (toward the top of the image). In fact, the river flows southward at Marble Canyon toward the Kaibab/Coconino Uplift.

The Colorado River channel falls from an elevation of about 1000 m at the northeast corner of this scene to less than 300 m at Lake Mead, 50 km west of the scene. This reach of 450 river kilometers has 161 rapids, which generate nearly all the elevation change (Howard and Dolan, 1981). The rapids are preferentially located where the river crosses regional and local fracture zones, many of which are visible on this Landsat image. Side canyon tributaries, which are mostly structurally controlled, deliver extremely coarse debris to the main canyon floor through floods and debris flows. The resulting debris fans produce rapids composed of such immense boulders that only extremely rare floods are capable of significantly altering their form. The rapids result in constricted flow in the Colorado River. The high-velocity constricted flow of the main channel induces scour, producing deep pools immediately downstream of the rapids. Pools as deep as 25 m (35 m at high flow) are generated by this process. These sedimentation and erosion features of the canyon floor are familiar to the thousands who annually visit this region through river-rafting expeditions. **Landsat 1284-17384, May 3, 1973.**



ORIGINAL PAGE IS
OF POOR QUALITY



3

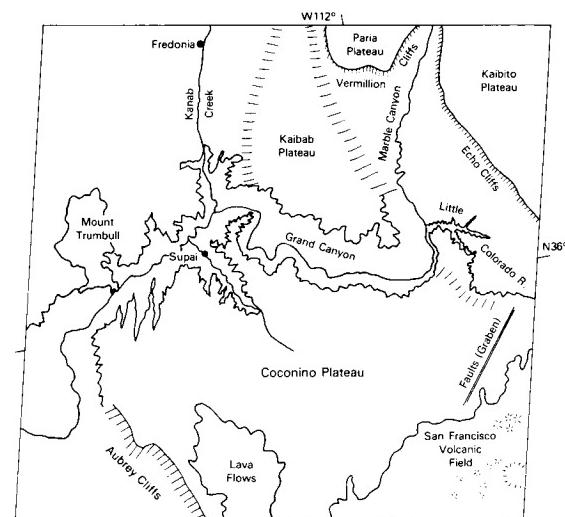


PLATE F-8

This scene shows portions of the Rio Caroni drainage in the Guiana Highlands of southeastern Venezuela. The Caroni flows northward, joining the Orinoco 250 km north of this image. The bedrock in this region consists predominantly of Precambrian crystalline rocks comprising the Guiana Shield. These are unconformably overlain by a thick section of generally flat-lying Mesozoic sedimentary rocks, known as the Roraima Series. The latter comprise striking flat-topped mesas and small plateaus in this region, known as La Gran Sabana. One of these mesas is Auyán-Tepuí, which rises to an elevation of 2950 m (Figure F-8.1). Local relief exceeds 1200 m, and from the edge of this mesa, Angel Falls (A) drops nearly 1000 m to a tributary of the Rio Caroni (Figure F-8.2). This is the highest single-drop waterfall on the Earth.

The Guiana Shield is characterized by dense tropical rainforest cover, but structural control of topography is pronounced and extremely important to geologic interpretation. The SIR-A radar image of Siapa River headwaters in the Casiquiare drainage (Figure F-8.3) illustrates this quite well. This area is located in southern Venezuela, 600 km southwest of Angel Falls. However, it is similarly characterized by rugged uplands of Roraima Group sediments overlying the Precambrian shield complex. Slope effects locally modulate the radar backscatter to produce bright tones on foreslopes and dark tones at backslopes. Radar imagery is especially useful in tropical rainforest areas because of its ability to penetrate the cloud cover that so commonly obscures Landsat images of the same regions.

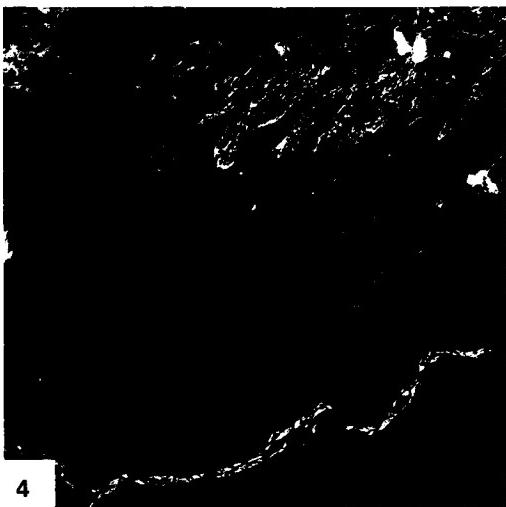
RIO CARONÍ, VENEZUELA

Some tributary junctions of the Paragua River system (lower left of image) are barbed (i.e., they join at a sharp angle that points upstream). Such junctions are not unusual in tropical rivers, which may reverse directions over their geologic history, even crossing divides from one basin to another. One of the most famous of such complexities occurs in the upper reaches of the Orinoco, about 450 km southwest of Angel Falls. The Orinoco splits into two downstream branches, the major one continuing northward through Venezuela and the other giving rise to the Casiquiare River, which flows to the Rio Negro and Amazon in Brazil.

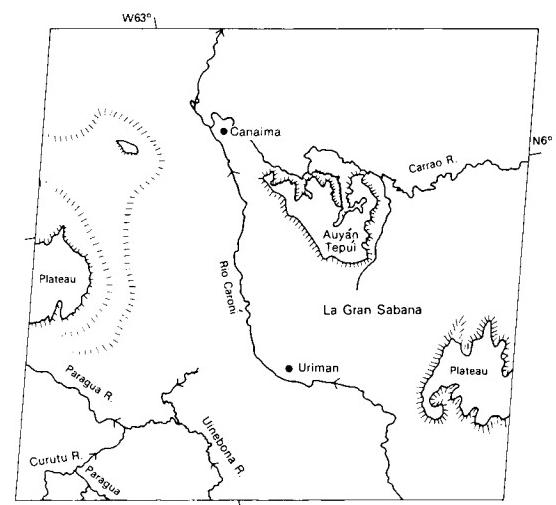
One theory for the channel patterns in this region holds that the rivers are carving trunk channels through relict arid landscapes. This concept, developed by H. F. Garner (1966), considers the Caroni and similar streams to be "rivers in the making." During past arid climates, presumably corresponding to full-glacial conditions, this tropical region was much drier than it is at present. Modern evidence for this is suggested by the occurrence of relict parabolic dunes north of the Meta River in Southwestern Venezuela (Figure F-8.4), in a region now shown on maps as swampy and heavily vegetated. Drainage was directed into local depressions, and considerable derangement characterized the landscape. The subsequent shift to tropical conditions has allowed the rivers to integrate these former deranged patterns, but relicts persist in the overall drainage. **Landsat, 21446-13324-7, January 7, 1979.**



ORIGINAL PAGE IS
OF POOR QUALITY



4



The Tucson area of southern Arizona illustrates the erosional landforms developed on the remnants of block-fault mountains that evolved approximately 10 to 30 million years ago. The area is typical of the Basin and Range physiographic province. Coincident with uplift of the ranges, intervening basins subsided as they accumulated the debris shed from the eroding mountains. Volcanism immediately preceded, and was coincident with, this Late Tertiary tectonism.

Many of the mountain fronts are no longer tectonically active. The piedmonts that surround them are erosional, formed by the headward retreat of the mountain front itself and by continued planation of rock and sediment downslope of the mountain front (Bull, 1984). Such erosional surfaces are termed "pediments." The northeastern front of the Tucson Mountains (Figure F-9.1) is an excellent example.

The Tucson Mountains consist of Tertiary volcanic rocks overlying Mesozoic sediments. Basin- and range-faulting produced a mountain front that retreated during subsequent pedimentation. Note on Figure F-9.1 that the pediment is characterized by a dense pattern of shallow drainageways. During rare intense rainstorms, these drainages are filled, and water moves slowly by sheetflooding on the pediment surface. Under present climatic conditions, only relatively fine sediment is conveyed across the pediment to the trunk drainageway, which is the Santa Cruz River at the bottom of Figure F-9.1.

Note also on Figure F-9.1 that the retreat of the mountain front may leave isolated hills surrounded by pediment surface. These hills are erosional residuals, or inselbergs. Their presence can be useful in mapping the extent of pedimentation.

Where mountain fronts have been active tectonically and/or where climatic change has resulted in sufficient sediment loads, alluvial fans may develop. Figure F-9.2 shows the Madera Canyon Fan at the western front of the Santa Rita Mountains. The fan is composed of coarse debris shed from the quartz monzonite core of the mountains. Most of the fan is relict from the Early Pleistocene, as indicated by its pronounced dissection (Figure F-9.2) and by the strongly developed soil profile beneath its surface.

The relatively active tectonism of the Santa Rita Mountain front is indicated by the two fault scarps visible at the left center of Figure F-9.2. These are Quaternary faults, since they cut the Pleistocene fan surface. Detailed study of trenches across these faults indicates that the youngest movement was Late Pleistocene in age (Pearthree and Calvo, 1982).

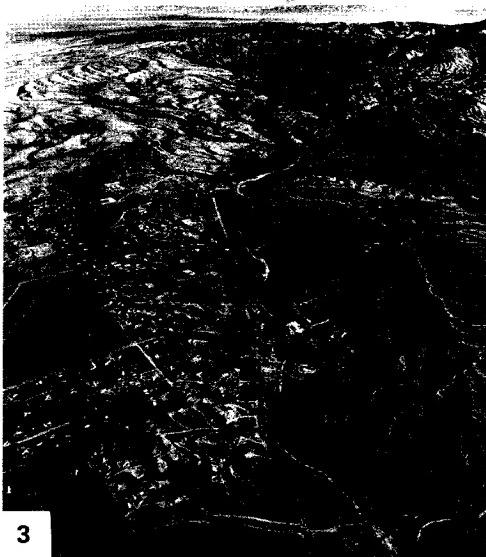
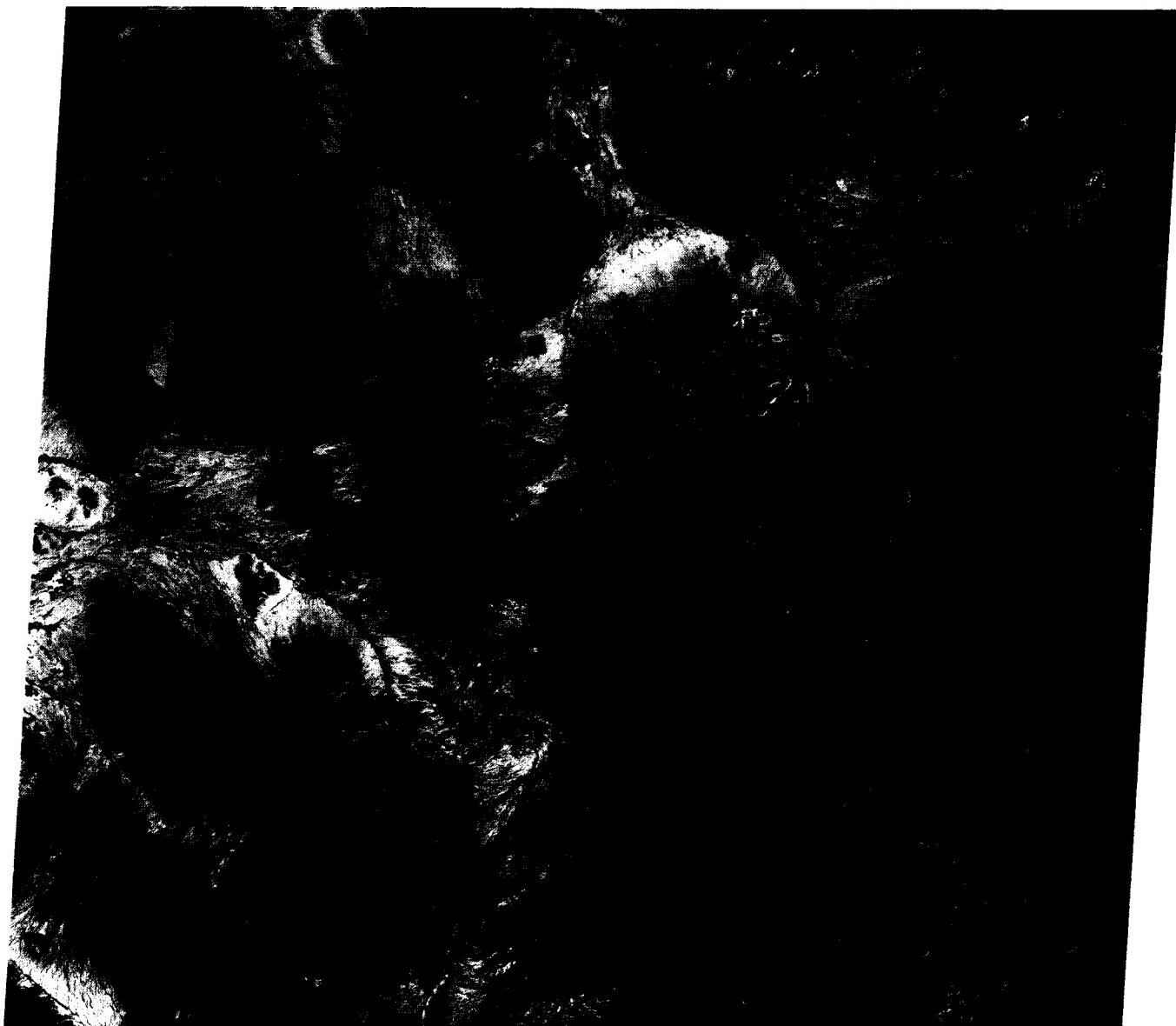
In the northern part of the study area, the great mountain massifs of the Catalina and Rincon Mountains dominate the topography. These are metamorphic core complexes that formed in a compressional phase that preceded basin- and range-faulting. Uplift of these mountains occurred in domal fashion, with covering sediments sliding off along low-angle faults to expose cores of gneiss and granitic rocks. As streams incised from the covering sediments, they cut deep canyons along prominent fractures.

Along the Canada del Oro Valley (CDO on the index map), a stream has incised into a graben northwest of the Catalina Mountains. The result was the exhumation of a pediment at the north end of the mountains (top of Figure F-9.3). Downcutting was episodic. During periods of stability, the stream was able to shift laterally, producing strath terraces. Filling during periods of high sediment yield produced phases of aggradation. Continued downcutting then led to the abandonment of the former strath and aggradation surfaces (McFadden, 1978). The result was a series of terraces (Figure F-9.3). The higher, older terraces in the valley are dissected, whereas the lower, younger terraces preserve much of their original morphology.

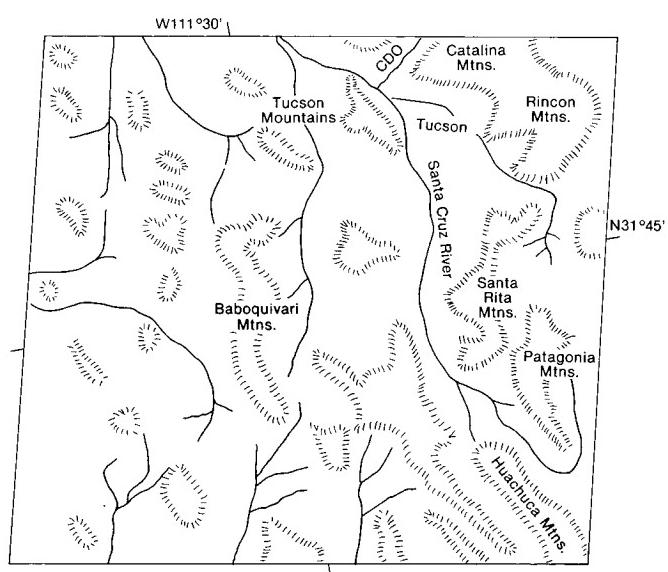
During the initial phases of basin- and range-faulting, many of the basins in the study area were closed. Deep wells have penetrated evaporites and lake sediments beneath the basin fills (Pierce, 1984). As the basins filled with sediment, they were also integrated by drainage systems such as the Santa Cruz River (Figure F-9.1). The modern streams are ephemeral, flowing after desert rainstorms. Major flow events are associated with summer convective storms, winter frontal systems, and occasional tropical disturbances that migrate from the Sea of Cortez in late summer or early fall. Although the lowland climate is arid, the mountain areas receive appreciable rainfall. Higher ranges, such as the Catalina and Santa Rita Mountains, support dense coniferous forests and have appreciable winter snowpacks. **Landsat 40176-17270, January 8, 1983.**



ORIGINAL PAGE IS
OF POOR QUALITY



3



C-4

This scene covers most of the Mississippi River valley from just above the delta in Louisiana (bottom) to Cairo, Illinois, at the junction with the Ohio River (upper right). The image was produced by the Heat Capacity Mapping Mission (HCMM) flown by NASA in 1978–1980. It is a visible-near-infrared picture that corresponds roughly to the panchromatic rendition of familiar black-and-white aerial infrared photographs. The image is especially interesting for comparison to the daytime image in the thermal infrared band (Day-IR) (Figure F-10.1). On the latter, relatively cooler temperatures are indicated by dark tones. The thermal contrasts highlight some important rock and soil types that reflect the fluvial evolution of the Mississippi valley.

Macon Ridge, near Monroe, Louisiana, appears as a prominent bright area on the visible-near-infrared (VIS) HCMM scene, but it is dark (cool) on the daytime thermal-infrared (Day-IR) scene (Figure F-10.1). This may result from evapotranspiration of crops on the rich soils of this alluvial surface. Similarly, Crowley's Ridge in the northeast part of the scene is almost invisible on the VIS scene, but it stands out prominently on the Day-IR picture. The ridge is underlain by Tertiary sedimentary rocks. Note that several cities also stand out prominently because of their warm thermal signatures on the Day-IR picture (Figure F-10.1).

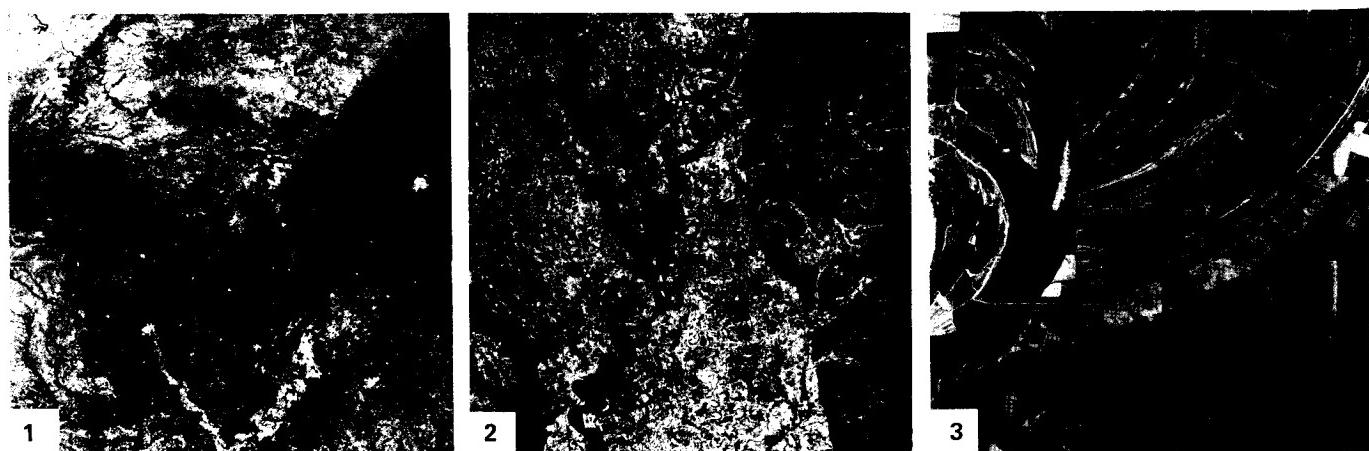
A Landsat TM scene of the Yazoo Basin is shown in Figure F-10.2. A cross section through the floodplain would show the highest elevations at the crests of natural levees flanking the river channel. The levee backslopes flatten away from the channels toward backswamp basins, as in the Yazoo area. These basins receive the fine-grained overbank deposits of floods. High water tables in the basins promote irregular lakes and swamps. Oxbow lakes, produced by neck cutoffs on meander bends, and the scroll topography of meander migration mark the main channelway of the active Mississippi River through a basin area (Figure F-10.3). Oxbows filled with clay can form resistant plugs that hold the river to its general course across the floodplain.

The buildup of levee crests may reach 10 m or more above adjacent backswamps along certain portions of the Mississippi.

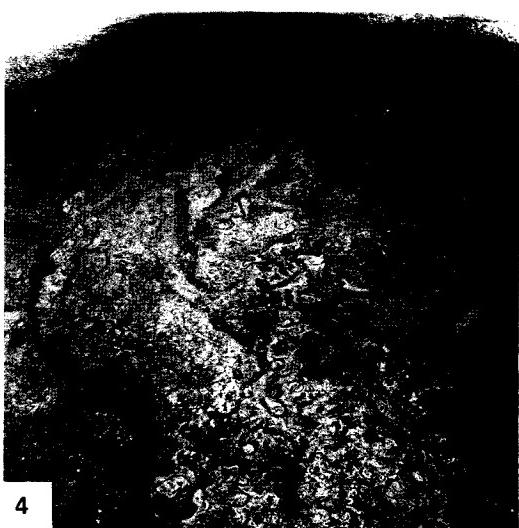
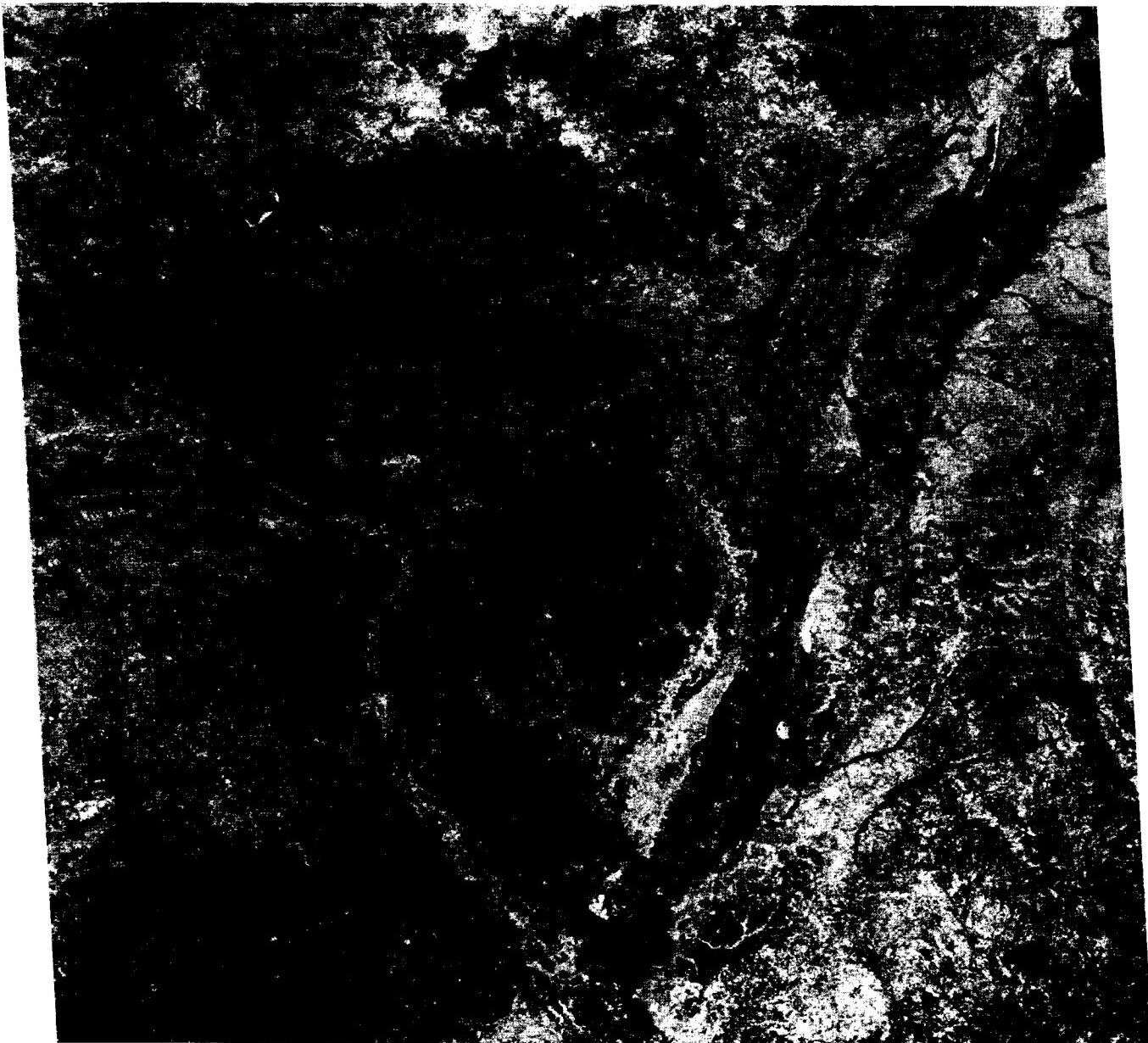
Because of this, less energetic tributaries such as the Yazoo River (center of Figure F-10.2) may flow great distances parallel to the main river before they breach the levee to join it. During floods, the main river may breach its own levee, spilling bedload through the gap to form a crevasse splay of sandy deposits in the backswamp area. Occasionally, the main river may completely abandon an entire channel trend by breaking into the backswamp and initiating a new course in the lower elevation portions of its floodplain. Such avulsions occur after several centuries have resulted in immense disparities between the levee heights and the adjacent backswamps.

A regional view from Apollo 9 of the central Mississippi valley (Figure F-10.4) illustrates the major elements of Late Quaternary fluvial events in the region (Baker, 1983). At the onset of the Wisconsin glacial stage, about 80 000 years ago, the sea level began to fall in the Gulf of Mexico. This induced incision in the lower Mississippi valley, while simultaneously the continental glaciation of the northern headwaters induced aggradation in the upper Mississippi. Prominent braided stream surfaces show that the Mississippi then flowed through the Western Lowlands region west of Crowley's Ridge (Saucier, 1974). Part of the same aggradation cone is also preserved as Macon Ridge. The latter actually dammed the lower Ouachita River, forming a Late Pleistocene lacustrine plain near Monroe, Louisiana (Saucier and Fleetwood, 1970).

About 17 000 years ago, the central Mississippi valley experienced a major diversion. The river abandoned its valley train in the Western Lowlands and cut a gap across the northern end of Crowley's Ridge. The zone of outwash deposition then shifted eastward to the present alluvial valley. Also at this time, the sea level began to rise because of globally melting ice sheets. The lower Mississippi valley aggraded, filling the irregular trench created by its earlier incision. Coarse-grained braided stream deposits were gradually buried by fine-grained sand, silt, and clay as the glacial influence waned and the river assumed its modern meandering character. **HCMM 344-19040-1, April 5, 1979.**



ORIGINAL PAGE IS
OF POOR QUALITY



4

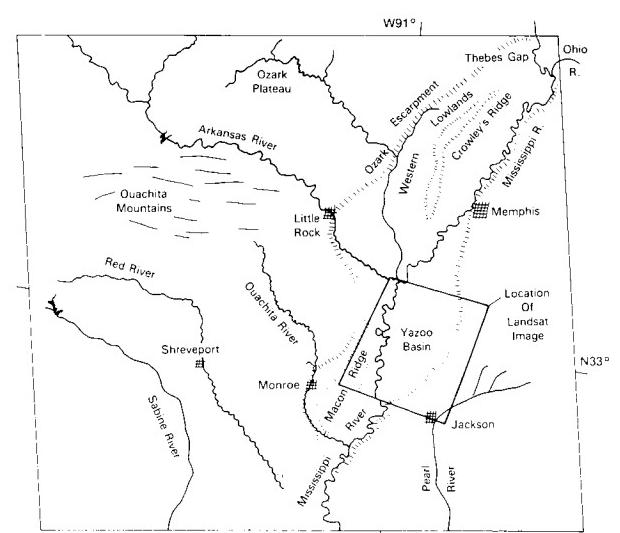


PLATE F-11

COLVILLE RIVER, ALASKA

This scene is centered on the Colville River near Umiat, Alaska. The Colville is the largest of the rivers draining from the Brooks Range to the Arctic Ocean. It assumes an east-trending course for 360 km along the northern Brooks Range before turning north downstream of Umiat, at the center of the picture. This early summer scene shows active streamflow across its prominent braided course. During the winter, when the mean daily minimum temperature here is -29°C (-20°F), the gravel flats of the river become covered with sheets of anchor ice that freeze to the riverbed.

The Colville River crosses the Arctic Coastal Plain at the top center of this scene, changing from a braided pattern to a meandering one. Typical scroll topography and oxbow lakes can be seen in the downstream reaches. At the very top of the picture, the first distributary channels of the Colville delta are visible.

The coastal plain is a relatively smooth plain separated from the Arctic Foothills by an abrupt scarp 15 to 60 m high (Wahrhaftig, 1965). Drainage is extremely poor, with marshy conditions prevailing in summer, as shown here. The small streams west of the Colville, such as Fish Creek, display exceptionally high sinuosity and have valleys shallowly incised into the coastal plain. Elongated thaw lakes are prominent at the upper right of the scene. Permafrost underlying the coastal plain exceeds 300 m in thickness. Higher resolution pictures would reveal a network of ice-wedge polygons on the coastal plain surfaces.

Figure F-11.1 shows a typical Arctic coastal plain river with tortuous meanders. The polygonal pattern of ice wedges in the permafrost shows the influence of ground ice in this area. Subsidence over melting ground ice contributes to slope adjustments by these rivers.

Figure F-11.2 shows a larger river in the area with prominent scroll topography and degraded ice-wedge polygons. River

meandering in permafrost may produce steep calving banks by thermal erosion of ground ice. Steep banks may occur on both the inside and outside of meander bends (Figure F-11.3).

East of the Colville River, the coastal plain is dominated by scattered groups of low hills (Figure F-11.4). This area, known as the White Hills, is largely obscured by cloud cover at the upper right of the image. A reduced number of thaw lakes also characterizes this region.

The Arctic Foothills are shown in the lower half of this scene. The northern foothills rise from an altitude of about 100 m at the Coastal Plain margin to 200 m at the Brooks Range foothills. The latter display local relief of 600 m or more, with buttes, knobs, mesas, and strike-oriented rivers. Diverse sedimentary rocks of Devonian to Cretaceous age underlie this terrain. Tight folding and overthrusting to the north produce the east-west grain in the topography. The folds are locally truncated by regional erosion surfaces. Eolian silt overlies much of the foothill topography.

Much of the Colville River basin would be classified as polar desert. Mean annual precipitation is between 200 and 100 mm, predominantly as snow. Despite elevation of 2500 m in the Brooks Range, modern active glaciers are rare.

Alaskan rivers that drain active glaciers have much larger sediment loads than those that do not. Thus, the Colville River delivers a load of only 5 to 10 million metric tons per year to the Arctic Ocean. In contrast, the Copper River, which drains the numerous glaciers of the Wrangell Mountains and Chugach Mountains, yields 70 million metric tons from a similar-sized drainage basin. Even more impressive is the fact that the Copper River, with a drainage area of 60000 km^2 , yields more sediment than the Yukon River, with a drainage area of 840000 km^2 .
Landsat 1344-21290-7, July 2, 1973.



ORIGINAL PAGE IS
OF POOR QUALITY

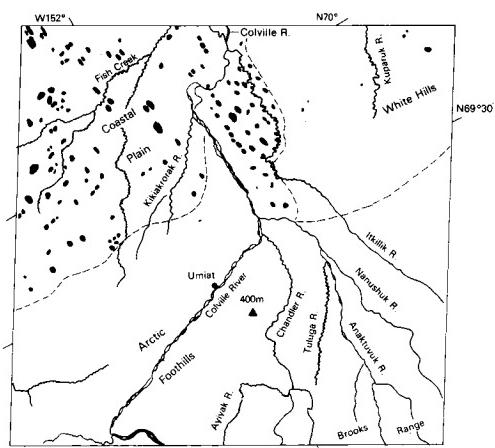
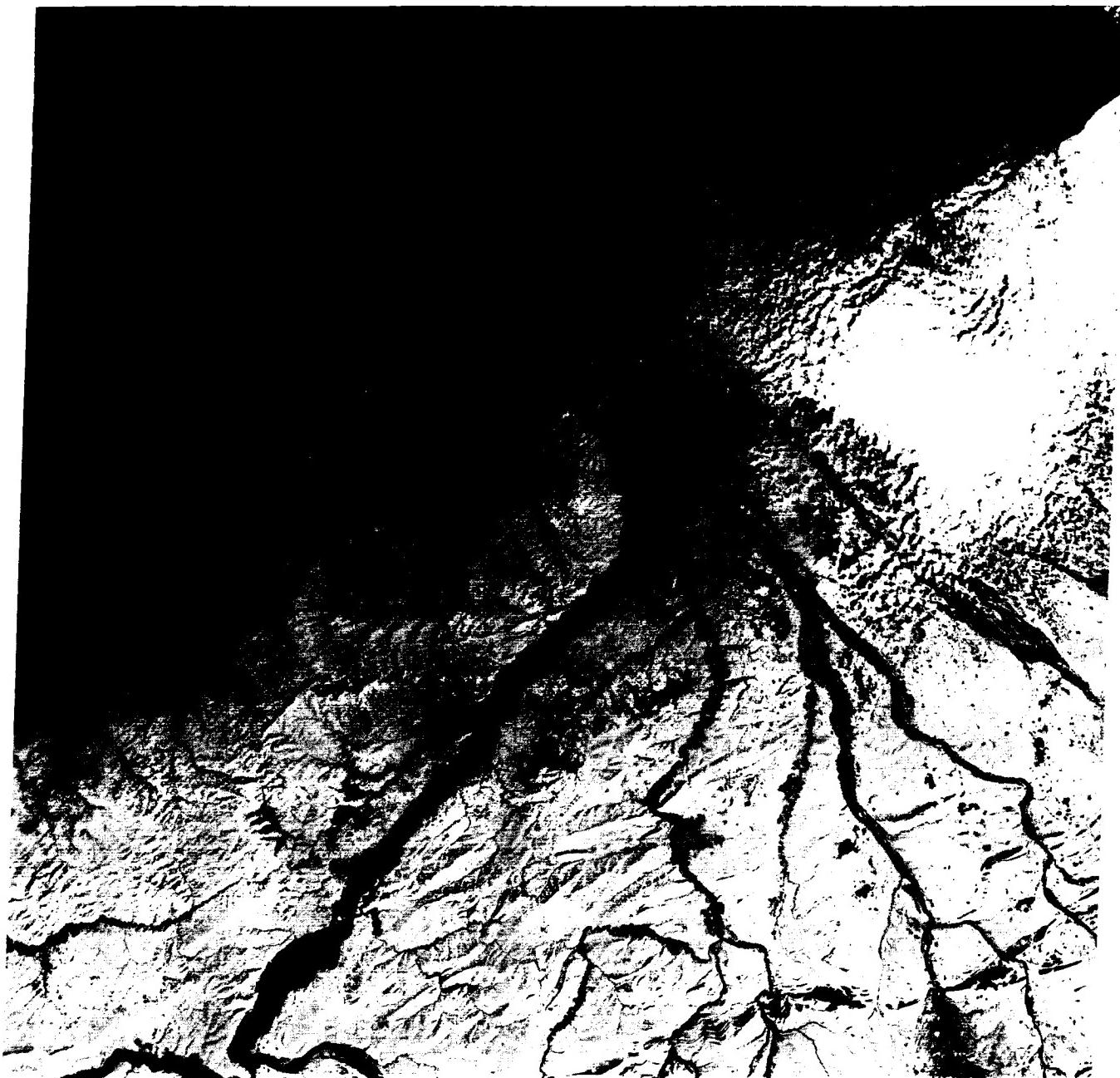


PLATE F-12

YUKON RIVER, ALASKA

Fort Yukon, located at the junction of the Porcupine and Yukon Rivers, is the only major settlement on this image. The Yukon is the largest river in Alaska, draining an area of 840000 km² between the Alaska and Brooks Ranges and into the Yukon Territory of western Canada. The river arc in this image is the northernmost point (66°50'N) reached by the river, just across the Arctic Circle.

The Yukon channel shows a typical braided pattern as it flows over lowlands of Quaternary alluvium known as the Yukon Flats. In this late summer scene, the river is at high flow, transporting snowmelt from nearby mountain ranges. Approximately 700 km to the west, at its junction with the Koyukuk River, the Yukon no longer has a braided pattern. Instead, meander scrolls and anastomosing side channels dominate the lower Yukon (Figure F-12.1).

The dissected plateau on the eastern side of the image is underlain by Mesozoic sedimentary rocks. The highly sinuous Black River traverses this plain in a relatively narrow valley. Where it emerges on the alluvial plains, the Black River floodplain widens and displays numerous cutoffs and oxbow lakes.

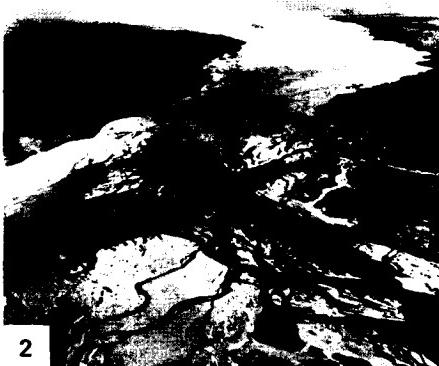
Farther north, the plain becomes the Porcupine Plateau, underlain by moderately deformed Paleozoic and Mesozoic sedimentary rocks (Wahrhaftig, 1965). The Porcupine River crosses this plateau in a narrow cliff-lined canyon up to 150 m deep, named the "Ramparts." The Porcupine River drains an extensive region of the northern Yukon Territory, immediately east of this image. The river may have imposed itself on the Ramparts because of extensive lakes that developed during the Quaternary in several downwarped basins of the northern Yukon. The ancestral Porcupine may have flowed northeastward to the Beauford Sea.

Two large outwash fans, those of the Sheenjek and Christian Rivers, are prominent at the upper left of the image. These rivers deliver sediments from parts of the Porcupine Plateau and

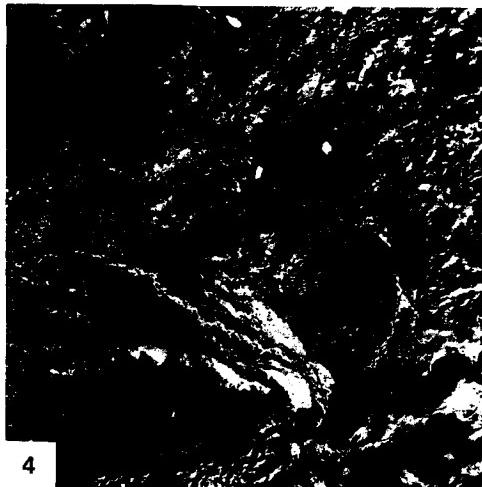
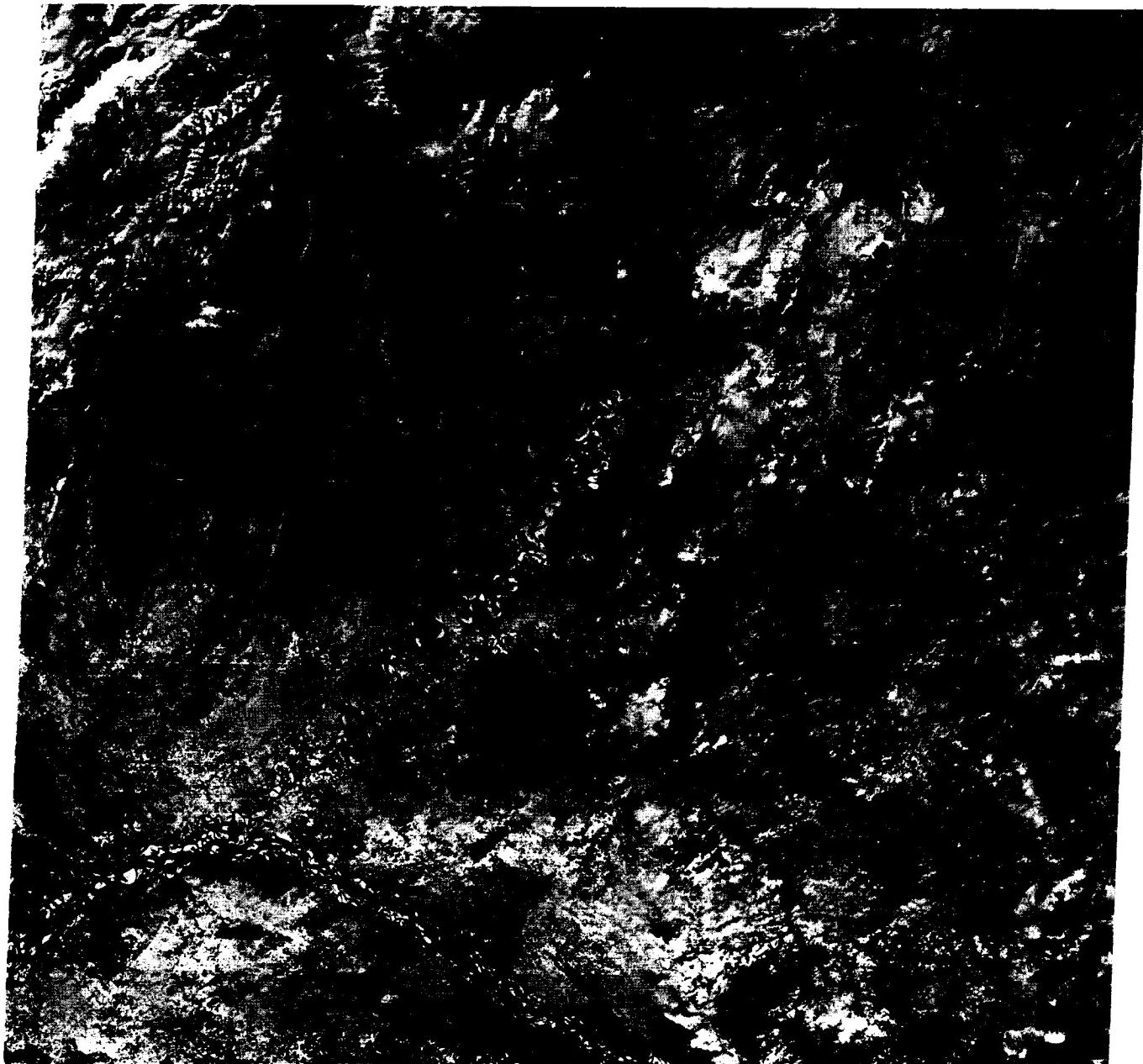
Brooks Range to the north. The Yukon itself comprises a fan here, although its extent is not visible on this scene. The braided Yukon presumably deposits considerable load in this reach, since the pattern changes to meandering downstream of the region shown. The occurrence of up to 100 m of Pliocene/Pleistocene lake sediments beneath 45 m of Quaternary alluvium and eolian sand indicates that the Yukon Flats may have been the site of a Late Tertiary lake that occupied a downwarped basin. Silts blown by wind off active braided rivers (Figure F-12.2) were a major source of Pleistocene eolian sedimentation in the region.

A typical forested floodplain of the Yukon in the Yukon Flats appears in Figure F-12.3. The Yukon Flats display numerous thaw lakes, presumably formed by subsidence as ground ice melted in the permafrost that underlies this region. Beaded drainage also indicates melting of permafrost ground ice, resulting in the transformation of a formerly continuous stream channel into a linear chain of thaw lakes. Other prominent lakes appear to have developed when outwash fans such as the Sheenjek advanced, blocking meltwater flow from adjacent uplands. Such fan-building activity may have been most pronounced at the termination of the last full-glacial period, when extensive sediment was available for transport in the Brooks Range and other highlands. Similarly, the shift to an interglacial climate may also explain the extensive evidence of permafrost disruption.

Figure F-12.4 shows a Landsat scene (1102-20441-7) of approximately the same region, dated November 2, 1972. Many of the lakes that appear dark on the primary scene show up as bright on Figure F-12.4 because they are now frozen. The exceptionally low Sun angle (8°) for this figure helps to emphasize some subtle topographic features that were not evident on the primary scene. Note also the greater extent of bright alluvium in the Yukon River channel. This is the result of decreased flow as water becomes frozen during the winter. **Landsat 1408-20430-7, September 4, 1973.**



ORIGINAL PAGE IS
OF POOR QUALITY



4

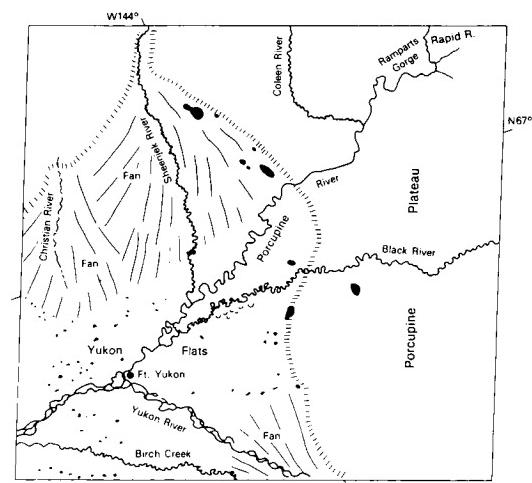


PLATE F-13

The Brahmaputra is one of the world's great rivers. During its 1962 flood, it achieved a discharge of $72460 \text{ m}^3/\text{s}$ (2560420 cfs). However, its minimum recorded dry-season flow was only $3280 \text{ m}^3/\text{s}$ (116000 cfs) in 1960. Draining an immense region of the Himalaya Mountains (see Plate T-46), the Brahmaputra flows in a great arc before reaching the head of the Bay of Bengal. There, just to the south of this Landsat scene, it combines with the Ganges and the Meghna to form the world's largest delta (Plate D-00), which covers an area of 60000 km^2 (23000 mi^2). The mean water surface slope of the Brahmaputra is 0.07 m/km (0.35 ft/mi).

This scene shows the curve of the Brahmaputra around the Shillong Plateau, also known as the Assam Plateau, which consists of horizontal Eocene sandstone and limestone overlying Precambrian crystalline basement. The plateau rises to elevations of 1400 to 1800 m. South and west of the plateau is the Bengal Basin, which is floored with Quaternary sediments contributed by the Brahmaputra and Ganges Rivers.

This picture shows river conditions approximately 1 month after the end of the monsoon season. The Darjeeling Hills at the foot of the Himalaya Mountains, which serve as the headwaters for the Tista, Jaldhara, Godadhar, and other major Brahmaputra tributaries, receive up to 3000 mm of rain during the summer monsoon. The rains begin in May or early June, and the wet season lasts to October. From June to September, the rains occur nearly daily. The river responds by a rapid increase in discharge that peaks in mid-June. A period of fluctuating high flow follows, usually with peaks in July and September. The last peak is followed by a long recession into December and January.

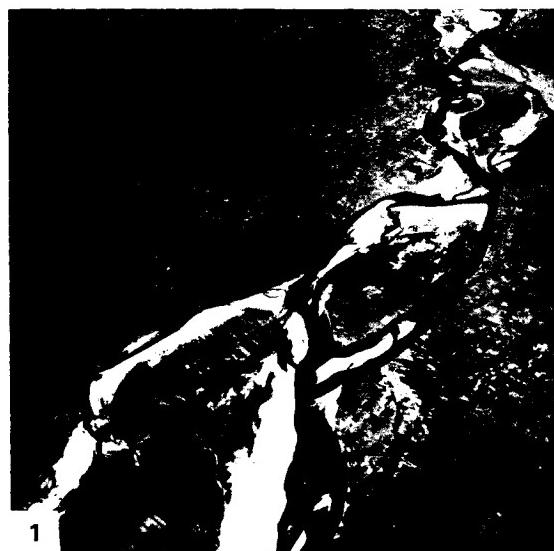
The highest discharges for the smaller rivers in this region occur following tropical storms. One such storm in the headwaters of the Tista River yielded local totals in excess of 1000 mm for October 2-5, 1968 (Starkel, 1972). Throughout the Darjeeling Hills, intensities of 50 mm/hr were achieved for prolonged periods. The discharge of the Tista River rose to exceed $20000 \text{ m}^3/\text{s}$ in the vicinity of Jalpuiguri following these rains.

BRAHMAPUTRA RIVER

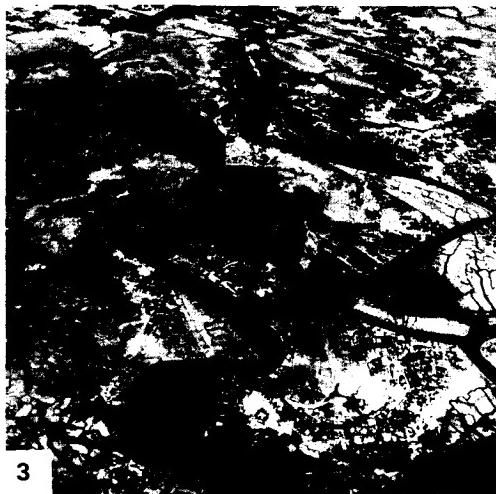
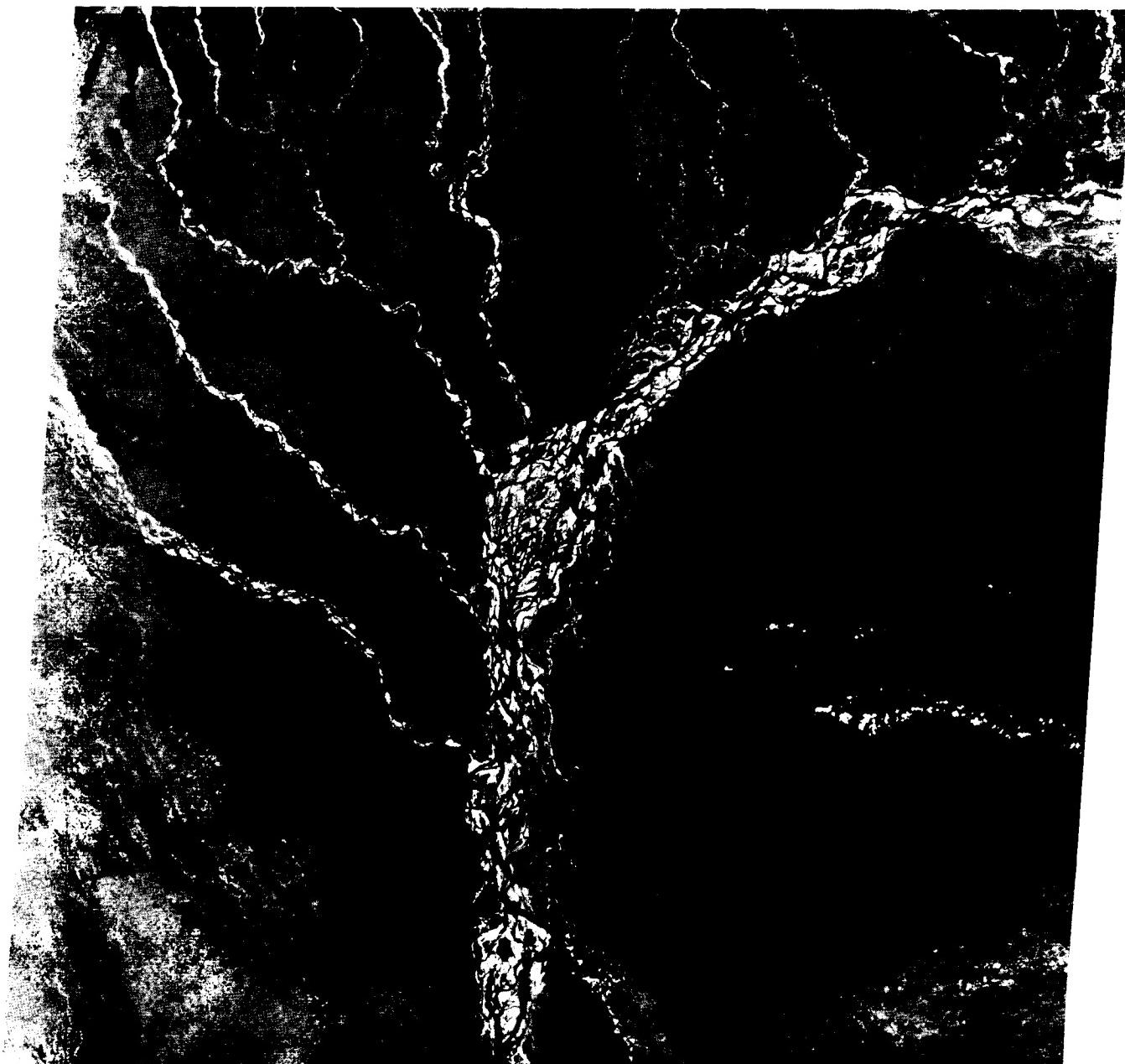
The rises and falls of the river lead to a dynamic sequence of channel adjustment throughout the year. Several varieties of bank failure occur during these flow changes, resulting in channel movement as great as 800 m (2600 ft) per year (Coleman, 1969). The most significant bankline modifications occur during falling river stage, when excess bedload (predominantly fine sand) is deposited as channel bars, inducing changes in local flow direction and migration of the thalweg in a classic braided pattern (Figures F-13.1 and F-13.2). These sandbars, which are called "chars" in Bangladesh, are diamond-shaped and appear as dark islands on the Landsat scene. The dark tones result from vegetation growth induced by the local inhabitants (Figure F-13.3). Once exposed following a flood, the arable land of a char is quickly occupied and put under cultivation.

The sandbars of the Brahmaputra shift even at moderate flow. The relatively fine bedload (mean size 0.172 mm) can be entrained at relatively low velocity. Large floods are capable of inducing spectacular changes in the river cross section and in channel configuration. Major shifts of channel course can occur by avulsion, as one whole channel route is abandoned in the Bengal Basin. The "Old Brahmaputra," seen at the bottom center of the image, is a pre-1800 course of the river that was so abandoned. During major floods of the modern river, some flow is still directed down this older course, producing its visible meandering pattern.

The southwest corner of the scene shows a region known as the Barind. It consists of relatively old Pleistocene alluvium, which has a bright tonal response on the imagery because of its oxidized state and its distinctive vegetative cover. This older alluvium has been elevated by a Quaternary normal fault upthrown to the southwest. The fault partially controls the course of the Karatoya River. Drainage south of the fault is southwestward, consistent with the tilting action by the fault. Relatively high seismic activity and the deformation of Quaternary alluvial units indicate an unusually active neotectonic influence on the rivers of this region. **Landsat 1123-04010-5, November 23, 1972.**



ORIGINAL PAGE IS
OF POOR QUALITY



3

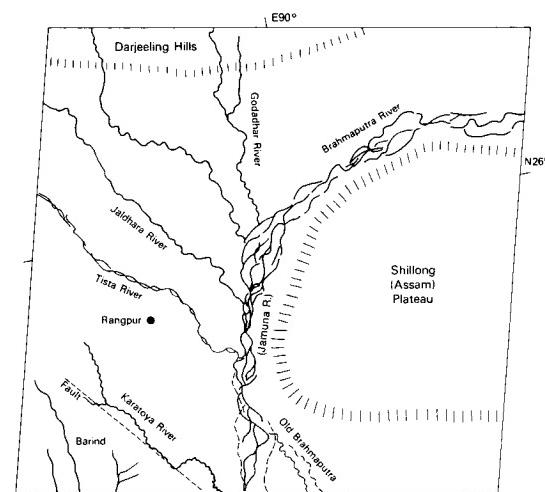


PLATE F-14

The portions of the Burke and Hamilton Rivers shown on this Landsat image are typical of the low-gradient multichannel alluvial systems that are common in southwestern Queensland, Australia (Rust, 1981). This region of 1.3 million km² is known as the "Channel Country" (Figure F-14.1). Channel Country stream systems are characterized by extremely low gradients and clay substrates. Tributaries are organized locally into high-density networks on the relatively impermeable soils (Figure F-14.2). The image shows an area where rivers emerge from highlands surrounding the Lake Eyre drainage basin. The highlands are semiarid to seasonal humid tropical, reaching 50 cm annual rainfall in the Great Dividing Range east of this scene. Rainfall in the headwaters occurs predominantly during the summer monsoon season. The streams are ephemeral, flowing only in discrete flood seasons that are separated by long droughts. Between flows, stagnant water is retained in the deeper channel reaches. Such waterholes are critical elements in the ecosystem and in the grazing economy.

The Burke, Hamilton, and other Channel Country rivers flow toward Lake Eyre, a playa covering 9200 km² in the driest part of Australia. Lake Eyre can be as much as 17 m below sea level and receives a mean annual rainfall of less than 10 cm. The Landsat scene is approximately 600 km northeast and upstream of Lake Eyre, in a region with 25 cm mean annual precipitation. The Channel Country rivers lose water through evaporation and infiltration as they flow toward Lake Eyre. Lake Eyre justifies its name only during exceptionally wet periods. In this century, the lake filled briefly in 1949–1950 and more extensively in 1973–1978. The relatively high river flows that sustained the lake in the middle 1970s probably were the result of global climatic aberrations, which affected the monsoonal patterns over the highlands.

The multichannel systems of the Burke and Hamilton Rivers include sinuous larger elements and a reticulate network of relatively straight short segments. The latter are related to

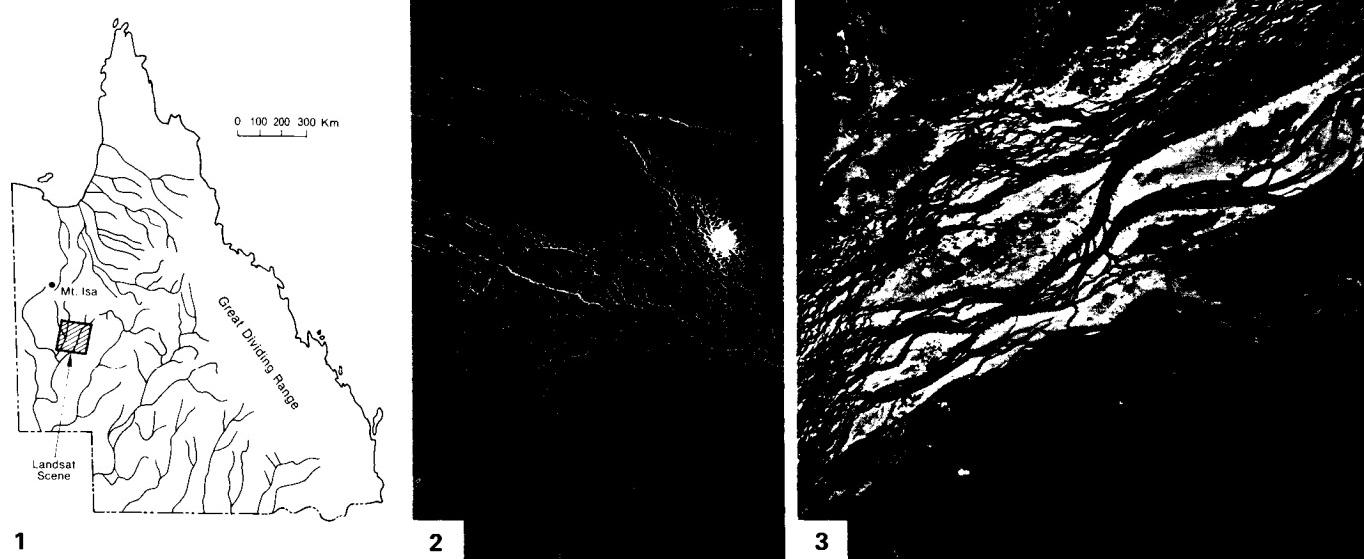
BURKE AND HAMILTON RIVERS, QUEENSLAND, AUSTRALIA

desiccation cracks that develop in the abundant swelling clay that is transported by the rivers. Channel migration in these anastomosing systems occurs mainly by avulsion, rather than by gradual migration as in meandering systems. Figure F-14.3 is a low-altitude aerial photograph of the reticulate pattern in the Hamilton River drainage.

The Burke River drains a large portion of the southern Isa Highlands, which are underlain by Precambrian crystalline rocks. The highlands include considerable areas 300 to 600 m in elevation. The Hamilton River drains much less of the highlands, which may account for the fact that it does not show a large fan as it emerges from the higher country to the north. In contrast, the Burke River has an immense low-gradient fan, which displays braided paleochannels.

Augering by Australian geologists has revealed that the surficial clay emplaced by western Queensland streams constitutes a thin sheet less than 5 m thick. The clay is regionally underlain by a sand sheet that was deposited by relict braided streams (Veevers and Rundle, 1979). Thus, a major shift occurred in the fluvial regimen for Channel Country rivers. An older braided system emplaced sandy braid bars, and this system was altered to one characterized by anastomosing sinuous channels that covered the relict braids with overbank muds. Figure F-14.4 is a low-altitude aerial photograph showing the anastomosing channels and relict braid bars of the Burke River system.

Climatic change appears to be the most likely explanation for the pattern metamorphosis of the Channel Country rivers. The mud veneer could be associated with a shift from relatively wetter conditions in the Early Holocene, 7000 to 5000 years B.P., to relatively drier conditions at present. The system is still in adjustment because the relict braid bars continue to influence the modern fluvial system. Smaller anastomosing channels flow as underfit streams within the larger relict braided channels (Figure F-14.4). **Landsat 30170-23570-B, August 22, 1978.**



ORIGINAL PAGE IS
OF POOR QUALITY



4

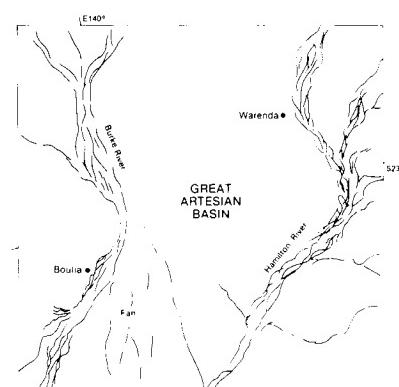


PLATE F-15

COOPER CREEK IN FLOOD, QUEENSLAND, AUSTRALIA

The Channel Country streams of southwestern Queensland experienced spectacular flooding in the monsoonal season of early 1974. Rainfall totals for January show that up to 1 m of rain fell in the headwaters of various Channel Country rivers. The monsoon of that year displayed exceptional strength and southward penetration. The rainfall was as much as four to six times the annual average.

The areal extent of flooding in Queensland shows the enormity of this meteorological phenomenon and its consequences (Figure F-15.1). The extremely low gradient plainslands experienced their greatest (peak) flooding in recorded history. The 1974 maximum discharge for Cooper Creek has been estimated at Collamurra Waterhole, just over the South Australia border upstream from the settlement of Innamincka. The flow was $4000 \text{ m}^3/\text{s}$ (141 000 cfs), with a depth of 16 m in the deepest section of the channel. The mean flow velocity of 0.85 m/s was capable of transporting gravel through the reach.

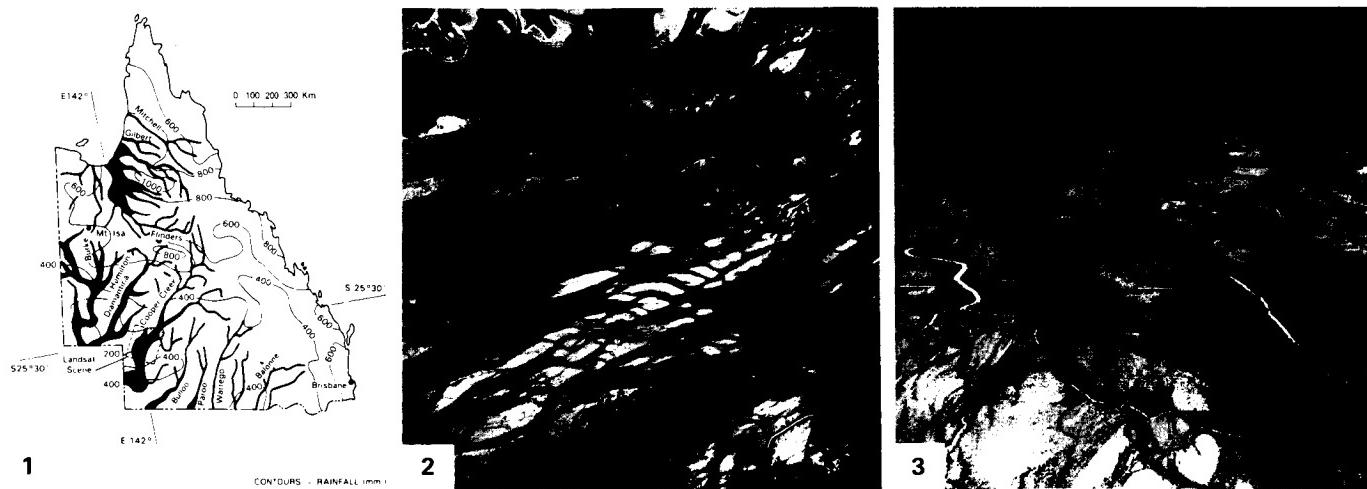
Unfortunately, the Innamincka reach is somewhat anomalous for Cooper Creek. The channel is relatively narrow and deep because it is confined in a valley of duricrust and bedrock across the Innamincka Dome, a Miocene fold. The reach shown in the Landsat scene is exceptionally broad and shallow. Floodwater has spread over a maximum width of 60 km. Flow depths are highly variable, ranging from perhaps 7 or 8 m over the deepest channels to only 1 or 2 m over extensive interchannel highs. The latter are mainly braid bars formed during past climatic conditions in which Cooper Creek was a sandy braided stream conveying a higher average discharge than at present. Figures F-15.2 and F-15.3 show these relict braid bars at two times of low flow (low-altitude aerial vertical and oblique photographs). Note the anastomosing channels that comprise the active fluvial system. Figure F-15.4 shows a small area along Cooper Creek during the height of the 1974 flood.

The gradient of Cooper Creek in the study area is extremely low, approximating 0.2 m/km . Coupled with the broad shallow character of flooding, this results in very slow passage of the flood peak. The peak at the northeastern corner of the Landsat scene was observed on February 2, 1974. However, it took 13 days to reach the South Australian border, 481 km downstream. Thus, the rate of travel for the flood peak averaged 37 km per day or 1.54 km/hr . Using this figure, the Landsat scene taken on February 6 shows the flood peak in the vicinity of Lake Yamma Yamma. The falling flood stage is occurring north of Lake Yamma Yamma, and the rising stage is occurring to the south.

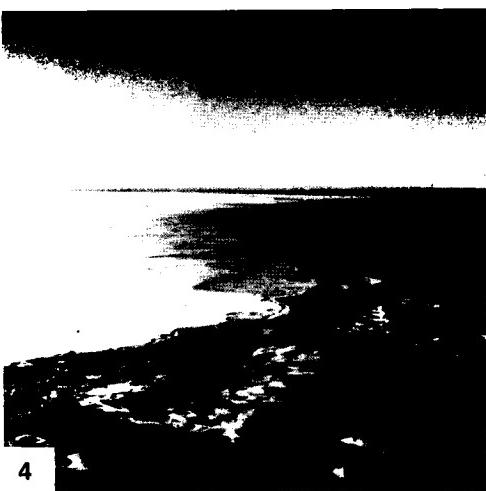
The channel of Cooper Creek is structurally controlled. Its course on the Landsat image corresponds to a broad syncline, lying on a south to northeast trend between the Mount Howitt Anticline and the Curralle Dome. These structures seem to have developed in the Miocene, deforming a sequence of Cretaceous and Tertiary sediments and associated duricrusts. Silcrete, a crust rich in silica, forms many of the resistant elements in the areas between active stream channels. The streams generally shifted as the structures formed, although Cooper Creek crosses the Innamincka Dome as previously noted.

Lake Yamma Yamma is a playa that occupies a structural depression. Floodwater entering the basin has entrained sediment from its floor, carrying it to the southwest, where it appears as a bright area on the image.

Another anomalous color feature of the image is the presence of extremely dark areas within the zone of flooding. These have a streamlined shape, and they parallel the southward flow of Cooper Creek floodwaters. C. J. Robinove (1978) of the U.S. Geological Survey has interpreted these anomalies as wet but unflooded areas of dark alluvial soil. Several high areas correspond to areas of high elevation, but other areas do not. Perhaps zones of water laden with sediment derived from the same dark soils provide some of the anomaly. **Landsat 1563-23530, February 6, 1974.**



ORIGINAL PAGE
COLOR PHOTOGRAPH



4

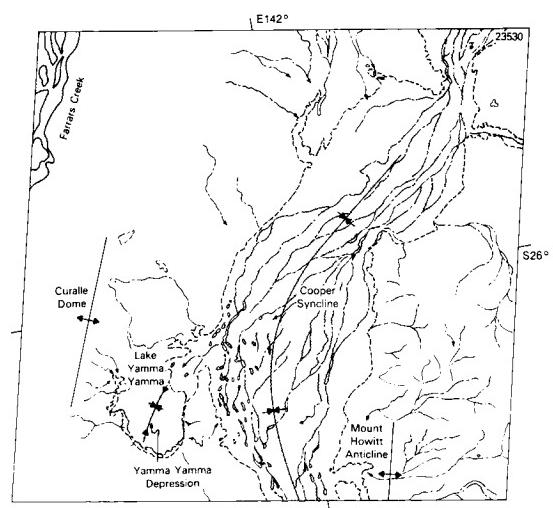


PLATE F-16

YANGTZE RIVER, CHINA

The lower Yangtze River (Chang Jiang) valley of east-central China consists of a broad alluvial plain flanked by uplands of crystalline rocks, the Dabie Shan to the northwest, and the Huang Shan to the southeast. Relatively recent subsidence in the sedimentary basin is indicated by numerous large lakes on the alluvial plain, including Wuchang Hu, Daguan Hu, and Long Hu.

This Landsat scene shows an area 400 km west of the Yangtze delta at Shanghai. The river is navigable for 2900 km from its mouth, and oceangoing vessels of 10000 tons can reach major inland ports such as Anqing (north center of scene), Nanjing (260 km downstream of Anqing), and Wuhan (300 km west of Anqing). The river's watershed includes one-fifth of the land area and two-fifths of the population of China. Boat traffic operates through a magnificent network of lakes and rivers in central China.

The Yangtze headwaters in southwestern China receive peak flows in the rainy season of July and August. Floods of the lower Yangtze are augmented by typhoons in July through September. The result is the world's fifth largest fluvial discharge averaged from an annual basis. The Yangtze transports 1.5 times as much water and 2.3 times as much sediment per year as the Mississippi/Missouri Rivers (Millman and Meade, 1983). Its total length is 5500 km.

As with many large rivers, the Yangtze near Anqing has an anastomosed pattern. Large alluvial islands of relatively stable floodplain are common. One theory for the formation of such patterns in large rivers holds that large discharges of water and suspended sediment are best accommodated in relatively narrow, deep channels. Although width can easily increase as river size scales upward, depth cannot. The depth of scour is limited by the nature of the alluvial valley fill. Therefore, very large rivers with high suspended sediment loads must split their channels, maintaining several channels of optimum width-depth ratio. Anastomosed rivers have relatively fine sediment loads and gentle gradients.

Note that anastomosed rivers of this type are very different from braided rivers, despite similar sinuosity and the presence

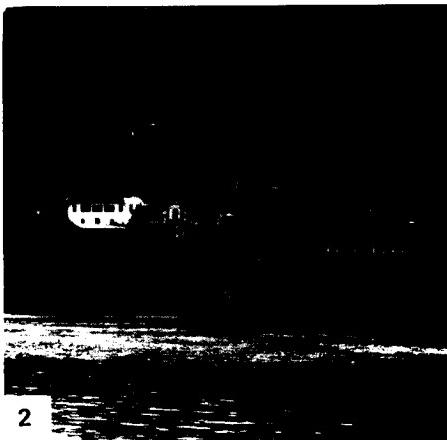
of islands. Braided rivers possess wide, shallow channels that are optimum for transporting relatively coarse sediment as bedload. The "islands" in braided rivers, such as the Brahmaputra or the Yukon, form initially as bars during periods of floodflow. As the stage drops during recession of the flood hydrograph, the bars become obstructions, splitting the flow into narrower, more efficient secondary channels. The former bars may eventually stabilize to become temporary islands. However, these can be easily reworked during a subsequent major flood.

Although the islands of anastomosed rivers are more stable than those of braided rivers, they experience continual modification. The scroll patterns on the Yangtze River islands show that progressive channel migration occurs in a similar manner to that in meandering rivers.

Upstream of Anqing, the Yangtze and its tributaries flow in great inland basins that are intensively cultivated for rice. Largest of these is the Dongting Swamp (Figure F-16.1). The swamp was probably once occupied by the Yangtze, which has now migrated to the north. Rivers entering from the south flood this basin with water. The basin also acts as a flow regulator for the great Yangtze floods. The largest city in the area is Changsha (pop. 850000), visible as a dark spot on the right bank of the Xiang River at the lower right of Figure F-16.1.

Upstream of the Dongting Swamp, the Yangtze flows through three spectacular gorges: Qutang Gorge, Wu Gorge, and Xiling Gorge. The river narrows abruptly in these gorges. Because the great discharge must be conveyed through narrow cross sections, the flow depths become enormous. At one point, the depth reaches 150 m, making the Yangtze the deepest river in the world.

Figure F-16.2 shows Huangling Temple in Xiling Gorge. Floods have entered this building three times in the last 400 years, in 1788, 1860, and 1870. The 1970 flood was 110000 m³/s (3880000 cfs). During such floods, the Yangtze has been known to rise as much as 30 m, stranding river streamers on rock bars in the gorges. Figures F-16.3 and F-16.4 show two views of the Yangtze gorges during moderate discharge conditions in October 1985. **Landsat E-1519-02131-6, December 24, 1973.**



ORIGINAL PAGE IS
OF POOR QUALITY



4

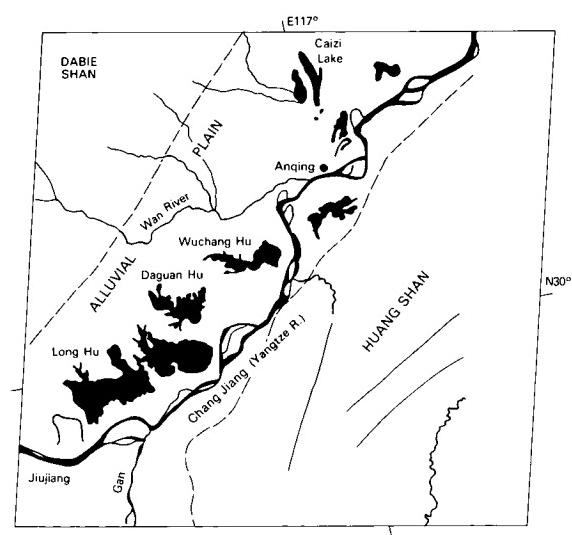


PLATE F-17

ALLUVIAL FANS OF SOUTHEAST IRAN

The rugged terrain of southeastern Iran is an extension of the Zagros Mountain ranges that parallel and are responsible for the eastern margin of the Persian Gulf (Plate T-41). This fold belt has ridges frequently exceeding 1500 m high that are arranged in a general northwest-southeast direction consistent with the long dimension of the Gulf. These ridges and the somewhat more complicated mountains of southeast Iran (see A on index map) are commonly anticlinal features that formed during the Pliocene/Pleistocene Zagros orogeny. Throughout most of the Zagros Mountain trend, the linear topographic highs represent huge folds with steeply dipping flanks, the result of orogenic movements directed toward the Gulf. Many of these large anticlines contain hydrocarbons and form the foundation for Iran's petroleum reserves.

Across the Gulf from southeastern Iran are the Oman Mountains (Plate T-40), which developed during the Late Tertiary into the Recent as a large rugged range that sweeps around from a northwest-southeast orientation to a north-south trend as it approaches Iran at the Strait of Hormuz. The northern plunge of the range into southeast Iran is reflected in the complexity of the Iranian mountains of this region where the Zagros and Oman trends meet. In such a complicated mountainous region, numerous intermontane basins like the one shown in the Landsat scene are being filled by alluvial deposits derived from erosion of surrounding mountains. The process of basin-filling is to a large extent controlled by climate.

The region around the Persian Gulf is characterized by an arid climate with an average annual rainfall of about 5 cm for the Arabian side, whereas the mountains of Iran receive from 20 to 50 cm, which favors numerous small mountain streams (B) and small rivers. One aspect of this type of drainage system in an arid to semiarid climate is its sporadic discharge. High relief and a lack of organic material in the surface sediments favor rapid runoff or flash floods when rains occur. These violent events can transport boulder-sized particles down well-defined and steep-sloping routes through the mountains to the basin. Alluvial fans (C) are the result of this sedimentation process (Figure F-17.1). The term "fan delta" is sometimes used when these coarse sediments are deposited in standing water of a lake or the sea. Regardless of the climatic setting, these features occur adjacent to areas of high relief (A), as is clearly visible on the image.

The typical shape of alluvial fans results mainly from increased frictional resistance as the relatively deep confined intermontane stream network (D) enters a basin, where the streams change to a braided system of shallow channels on the fan (E). Figure F-17.2 illustrates the stream beds that consist of coarse sediment, which are typical of arid and semiarid source areas where runoff tends to be an infrequent but violent event. Because of the high relief of source areas and the hydraulic characteristics, such as sporadic discharge, alluvial fans are commonly composed of coarse gravel and boulder-sized sediment near the mountain fronts. Grain size decreases rapidly downfan. In the Landsat scene, the dark proximal parts of the alluvial fans are the accumulation areas for gravel- and boulder-sized sediments. Figure F-17.1 shows very coarse debris associated with the proximal area of a small alluvial fan complex very much like some of the small fans of the Landsat scene. Note the small dunes that commonly form in association with arid alluvial fan complexes.

Intermontane basins are commonly the sites of playa lakes and their sedimentary counterparts (F). In the Persian Gulf/Iranian mainland area, strong winds, arid to semiarid conditions, and seasonally high temperatures promote high rates of evaporation. These conditions induce the drying of lakes that develop as a product of the enclosed drainage system. In this process, the deposits of these playas are characterized by great lateral continuity of fine-grained sediments, little vegetation, desiccation cracks, and the occurrence of evaporite minerals. Environments of deposition that fit this description are sometimes referred to as continental sabkhas. Because alluvial fans (C) at the basin's edge trap most of the coarse sediment, deposits of the basin interior are generally fine-grained (terrigenous clay and silt) with carbonate and evaporite precipitates. Figure F-17.3 illustrates the surface of a continental sabkha covered with evaporite minerals (largely salt) and carbonates precipitated as the lake dried. The white areas in the Landsat scene are similar deposits in this arid intermontane basin of southeast Iran. Although most sediments that fill the central parts of these basins are fine-grained, occasionally large flash-flood events will deliver coarse sediments to the playa. Strong winds blowing across these arid regions also concentrate sand-sized sediment in the form of dunes that can migrate over the playa surface. (GCW: J. M. Coleman) Landsat 1127-06065-7, November 27, 1972.

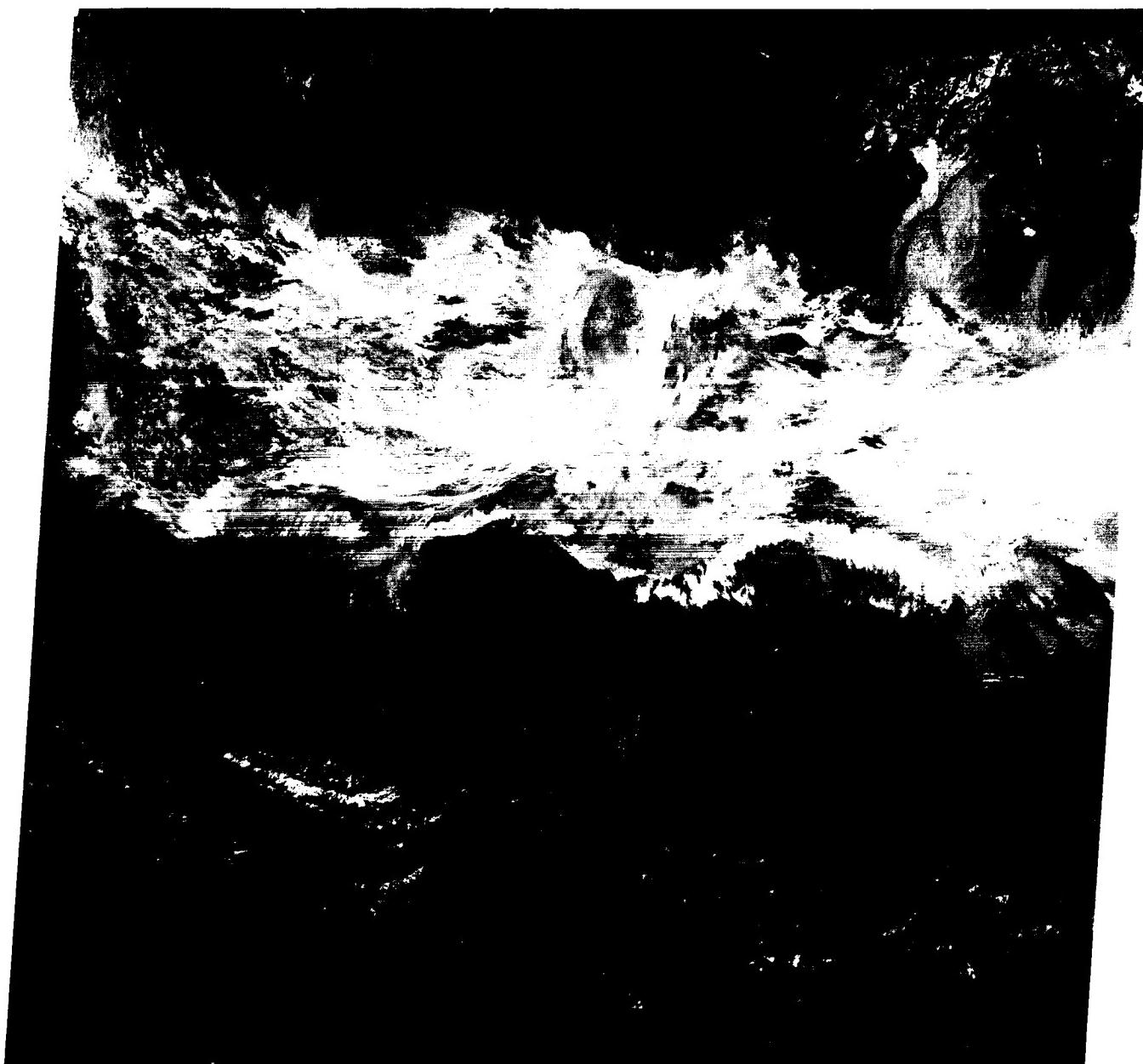


1



2

ORIGINAL PAGE IS
OF POOR QUALITY



3

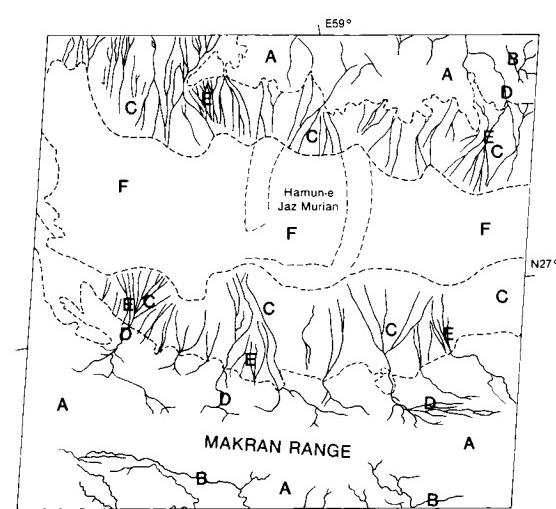


PLATE F-18

The Tian Shan is a series of east-west parallel ranges averaging 3000 m above sea level in extreme northwest China, Province of Xinjiang. The fold belt was generated in a Late Paleozoic orogeny. Sediments from Mesozoic uplift were shed into the Kucha sedimentary basin to the south. Renewed uplift in the Cenozoic produced the present dichotomy between the Tian Shan and the Tarim Basin that is evident on this Landsat scene.

The Tarim Basin is named for the Tarim River, which is fed by snow and glaciers of the Tian Shan, the Kunlun Mountains of northern Tibet, and the Pamirs of the China/Afghanistan/U.S.S.R. border region. The river flows through a great inland basin, which includes the Taklimakan Desert (Petrov, 1976). Elevations average about 1000 m and drop eastward to 760 m at Lop Nur, the playa at the river's terminus, about 700 km east of this scene.

The Taklimakan has an arid continental climate with long cold winters and short hot summers. Continentality is achieved by its location in interior Asia and by near enclosure of the basin by some of the highest mountains on Earth. Although annual rainfall averages less than 100 mm, the flow of the Tarim River maintains riparian woodlands, as shown at the bottom center of the Landsat scene.

Melting snow of the Tian Shan supplies water to the piedmont surfaces north of the Tarim River. The piedmont is underlain by Mesozoic sedimentary rocks that are mantled by alluvial fans flanking the mountain front. The fans comprise a dark-toned bajada, which is made up of surfaces of varying ages, probably reflecting alternating episodes of incision and aggradation through the Quaternary. The adjustments may have been induced by climatic change, tectonic activity at the mountain front, or a combination of both. Younger fan surfaces are inset into older ones, which undergo weathering when they no longer receive active sedimentation. The old fan surfaces are dark on this Landsat image, probably because of the accumulation of desert varnish (mainly manganese oxides) on the coarse particles of the fan surfaces.

Several areas of irrigated farmland are located at distal sites on the Tian Shan alluvial fans. These areas have finer grained

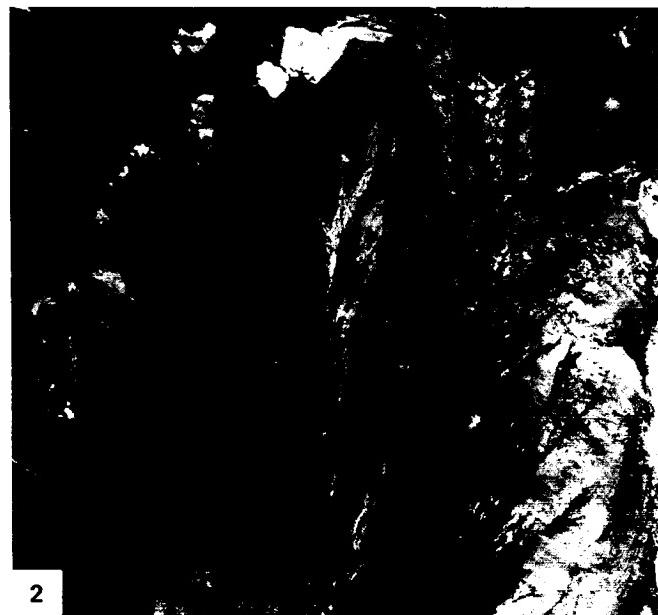
ALLUVIAL FANS IN ASIA

soils and more continuous water supply than the higher and proximal fan surfaces. Cotton is the dominant crop.

Figure F-18.1 shows another Chinese alluvial fan. The fan is shown on another Landsat scene (2621-03235-6, October 4, 1976). This fan is derived from flows out of the Qilian Shan Mountains at the bottom of the image. The fan occurs in Gansu Province, approximately 500 km east of Lop Nur. As with the Tian Shan fans, the active drainage has entrenched older, darker fan surfaces.

Figure F-18.2 shows the Ruo Shui River in the western Badain Jaran Desert, which feeds one of the largest known alluvial fans in the world. The river originates in the Nan Shan Ranges to the south and drains into the Badain Jaran Desert. The entrenched alluvial fan shown in Figure F-18.3 lies on the south slope of the Hajar Range (Oman Mountains) located on the eastern side of the Arabian Peninsula. The dark tone of the alluvial slope is produced largely by desert varnish coating chert fragments. This is no longer a plain of accumulation and is now being eroded by water and wind action. The toe of the fan has been completely removed, exposing lighter toned Tertiary strata.

The causes of fan entrenchment, producing the abandonment of old fan surfaces, remain the subject of considerable debate among geomorphologists. Classic observations in the Gobi Desert by Huntington (1914) led to the hypothesis that high sediment production and low stream discharges resulted in aggradation during relatively dry climatic phases. This was then followed by downcutting when wetter climates led to the stabilization of slopes by vegetation. During wet phases, called "pluvials," streams with increased flow augmented their sediment load by bed incision. Alternatively, some geomorphologists in the western United States have argued that fan-building required a wetter climate to transport accumulated debris (Lustig, 1965). Others note that transitional climatic phases are critical. Weathered mantles produced in a humid phase are mobilized by rare events when the climate changes to an arid one (Hunt and Mabey, 1966). It has also been proposed that fan erosion and sedimentation go hand in hand as elements of a steady-state system. (Denny, 1965). This last hypothesis holds that there is no reason to invoke environmental change to explain alternations of process on alluvial fans. **Landsat E-1400-04352-7, August 27, 1973.**



ORIGINAL PAGE IS
OF POOR QUALITY



3

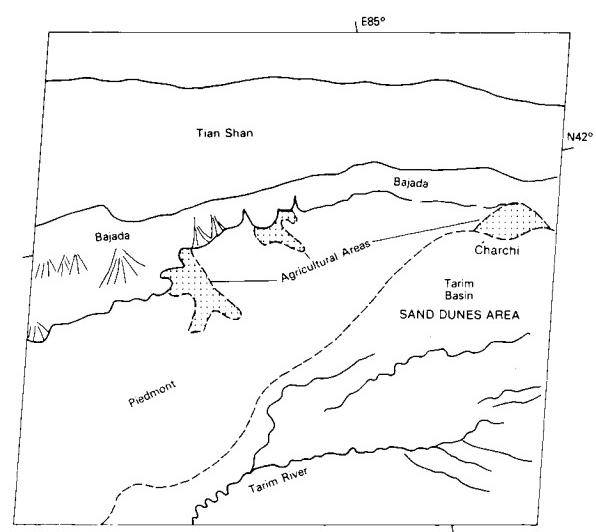


PLATE F-19

The Ganges River plain drains the Himalaya Mountains immediately to the north of this Landsat scene. Belka Hill is a part of the Siwalik Hills, which mark the southern margin of the Himalaya Range. These hills are generally 1000 to 1300 m above sea level and consist of dissected Miocene and Pliocene continental fluvial sediments deposited as the Himalayas formed by the continental collision of the Indian subcontinent into Asia.

The northern quarter of this scene is in Nepal and shows the emergence of the Kosi River from the mountainous extreme eastern end of that nation. The drainage basin includes the highest portion of the Himalayas, with many peaks rising 6000 to 8000 m above sea level. Mount Everest, the highest point on Earth at 8848 m, is within the source basin. Annual precipitation in the source area ranges from 130 to 165 cm/yr. However, 80 to 95 percent of this precipitation occurs during the summer monsoon (June to September).

Monsoons are tropical weather phenomena involving reversals of the prevailing wind directions between winter and summer. The reversals arise from a latitudinal migration of wind belts with the season. The winter monsoon of the eastern Ganges plain is a dry subsiding air current directed from the northeast. The Himalayas shield India from the cold continental air of inland Asia north of the Tibetan plateau. In summer, a deep trough develops over northern India, and a southwesterly flow of warm wet air from the Indian Ocean produces the summer monsoon. The warm wet air generates maximum precipitation under the orographic influence of the Himalayas. The resulting summer floods can cause the Kosi River to attain a width of over 30 km on the nearly flat Ganges plain. During the flood of 1968, the Kosi River achieved a maximum discharge of 25 840 m³/s (about 900 000 cfs). This flow from a catchment area of 59 540 km² is comparable to a moderate flood on the Mississippi River, which drains 327 000 km².

The Kosi River emerges from the Siwalik Hills near the town of Chatra, where old fan surfaces and adjacent hills have a savanna forest cover (Figure F-19.1). The channel pattern near Chatra is braided, and the sediment load is dominated by boulders transported during wet-season flooding (Figure F-19.2). The Landsat scene shows dry-season conditions, with the low flows

KOSI FAN, INDIA AND NEPAL

visible as black and the braided wet-season channels as bright patterns immediately to the west. A dam is located downstream of Chatra, and a diversion canal is clearly visible extending eastward from the river barrier. Near Saharsa (Figure F-19.3), the sediment load is predominantly sand, and the pattern is anastomosed with fine-grained sediment banks. Farther downstream, the pattern becomes meandering as sediment size is reduced and gradient decreases.

The Kosi Fan, outlined by the dashed lines on the index map, covers an area of approximately 15 000 km² (Gole and Chitale, 1966). The fan has an extremely low gradient. The slope at its apex, near Chatra, is 1 m/km, and this decreases distally to less than 0.2 m/km near the Ganges River. The paleochannels at the fan apex have diffuse patterns that indicate probable braiding when they flowed. Near the fan toe, the abandoned paleochannels are meandering. High-water-table conditions and local (non-Himalayan) rainfall result in some continuous flow in these channels. Some sandy point bars are present, but most of the sediment is suspended clay.

Between 1736 and 1964, the Kosi River shifted 110 km from east to west, reworking all the land in between (Gole and Chitale, 1966). Unlike arid-region alluvial fans, which show somewhat random shifts of erosion and deposition, the Kosi Fan developed by a progressively shifting channel. The shifting occurred as deposition raised the active portions of the fan and the river moved to lower terrain on the inactive portions. Because this process is now occurring on the extreme western end of the fan, there is a strong possibility that migration will now begin toward the east. A major shift to the east by avulsion would also be possible, were it not for massive artificial levees constructed to stabilize the river in its present position.

Braiding in the active western channel of the Kosi extends much farther down the fan than the braiding in the paleochannels to the east. It is probable that extensive deforestation of the headwaters in recent decades (Figure F-19.1) resulted in increased coarse sediment loads to the river. Water diversions may have also contributed to the increased braiding of the modern Kosi River. **Landsat 2751-03455-7, February 11, 1977.**

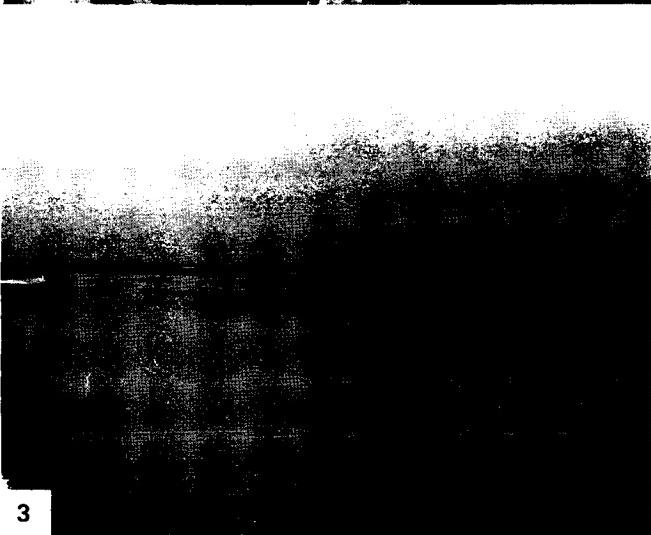
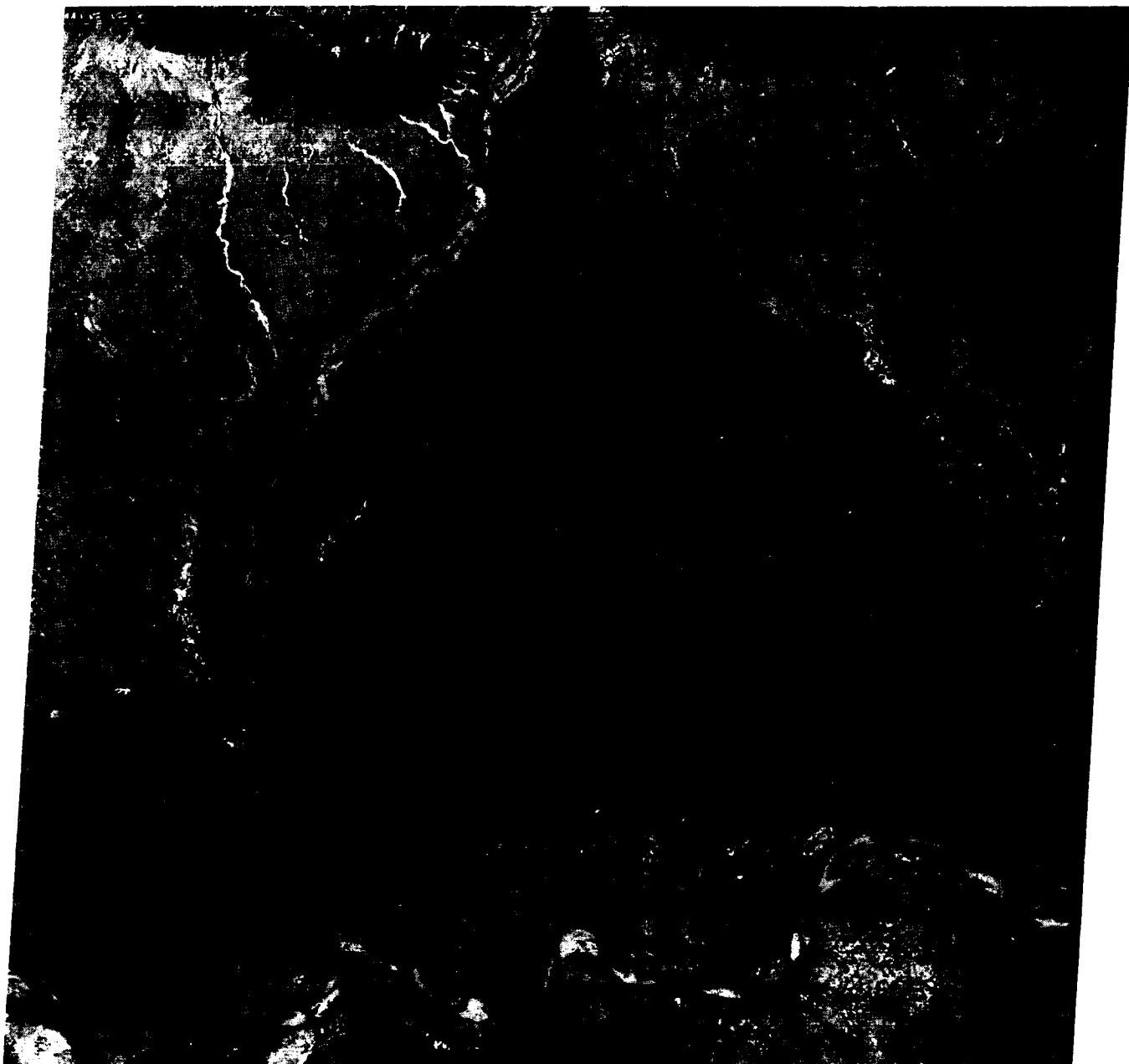


1



2

ORIGINAL PAGE
OF POOR QUALITY



3

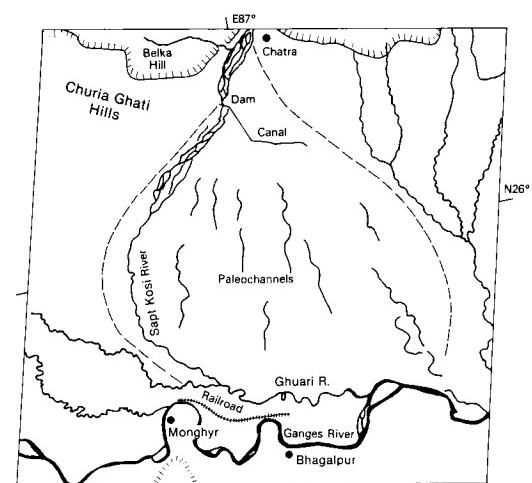


PLATE F-20

NIGER RIVER, MALI

This region of the central West African nation of Mali shows the proximal portion of the Niger River's inland delta. Flowing northeastward from the Guinea Highlands, the Niger derives a relatively large discharge from these tropical uplands. In central Mali, the climate becomes semiarid. The mean annual precipitation is approximately 500 mm at Mopti, the major town of the region. It decreases to less than 200 mm at Timbuktu, located 300 km northeast of Mopti. Rainfall is quite variable, and droughts, such as the catastrophic Sahel drought of 1968–1973, are an unfortunate occurrence for the region's inhabitants.

The distributary pattern of channels shows that this region is a great inland delta (Figure F-20.1). A great cratonic basin, the El-Djouf or Taoudene, receives the northeasterly flowing Niger and its tributary, the Bani River, which has its confluence at Mopti. The delta extends to the northeast of this Landsat scene, covering an area of about 40000 km².

The Niger inland delta serves to spread out the seasonal flows of the river. During the summer flood season, high discharges enter the delta apex. Large areas of open and shallow water are visible north of Mopti. One of these is Lac Debo at the top center of the scene. The flood crest may take 3 months to pass through the marshes, lakes, and channels of the delta.

The dark tones of the delta region correspond to the wetland vegetation, which contrasts markedly with the semiarid region outside the river's influence (northwest portion of the image). Desert pavement surfaces, also called reg or hamada, characterize this area. Sand dune development, which is minimal here, increases northward as precipitation decreases. A great sand sea, the Azaouâd, occurs north of Timbuktu, and the Niger turns to the east at this point, locally following the east-west dune trend (McKee, 1979), as is evident in the view from the Apollo 9 spacecraft (Figure F-20.2).

During the Quaternary, the Niger River was profoundly influenced by climatic change. At the glacial maximum for the northern hemisphere, approximately 18000 years B.P., cooling of the Atlantic Ocean induced an intensification of the trade

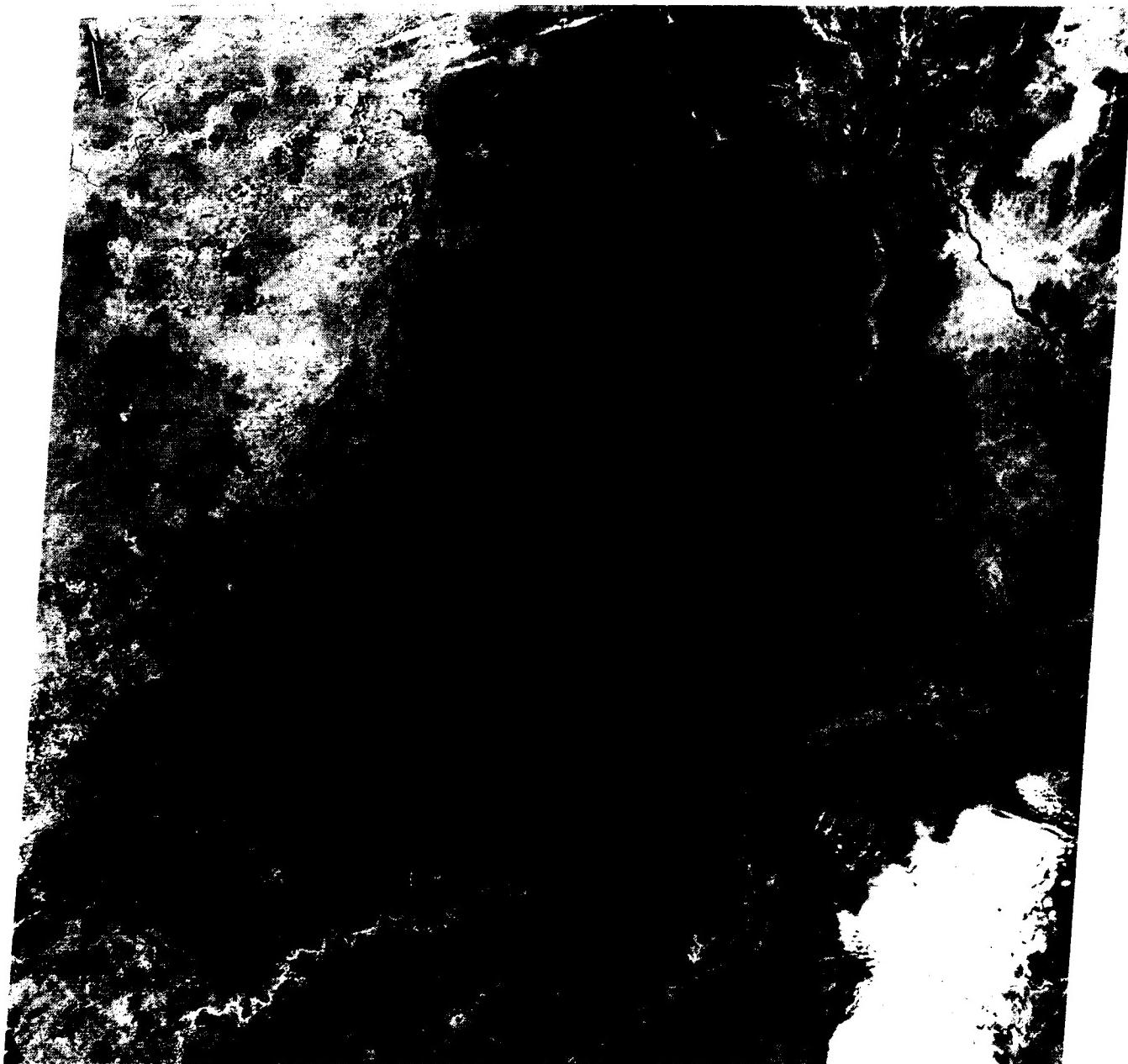
winds. In addition, the migration of the polar front toward the Equator effectively pushed the Saharan arid zone southward into the present Sahel. Reduction of summer rains in the savanna regions further contributed to aridity. Higher wind velocities and greater aridity allowed active sand dunes to extend southward, effectively blocking the Niger River near modern Timbuktu, 300 km northeast of Mopti. Reduced seasonal discharges for the river then resulted in a temporary termination at the Niger at its inland delta. Thus, the sediments of the inland delta represent an alternation of climatically controlled conditions. Delta sediments also contributed to dune development by eolian winnowing during dry periods.

After the full-glacial period of maximum aridity, a more humid period ensued, reaching its maximum development 5500 to 5000 years ago. The dune sands were weathered and stabilized, and in the wetter areas of the delta, the river eroded them away (Figures F-20.3 and F-20.4). The modern Niger continues in a great arc that turns southeastward near Timbuktu, flowing toward the humid tropical coast of Nigeria.

The Niger has a remarkable basin. It rises at only 800 m in the Futa Djallon Plateau of Guinea, and its headwaters are only 250 km east of the Atlantic at Sierra Leone and Liberia. Nevertheless, it flows northeastward in its great arc of 4200 km before reaching the same ocean at Nigeria. One theory for the development of this pattern is that the Niger headwaters were easily captured and diverted on the tropical planation surfaces of the Guinea Highlands. Its flow into the great cratonic basin of central East Africa, the El-Djouf, resulted in a lake, Lake Arouâne. This lake eventually overspilled low divides southeast of Timbuktu to complete the great arc. Climatic change in the Quaternary has now resulted in the unusual pattern of a river that flows from a humid tropical coastal upland into a desert basin, reverses itself, and flows from the desert basin back to the humid tropical coast. The inland delta reflects this heritage since it is developed on plains derived from the sediments of ancient Lake Arouâne. **Landsat 1529-10075-5, January 3, 1974.**



ORIGINAL PAGE
COLOR PHOTOGRAPH



4

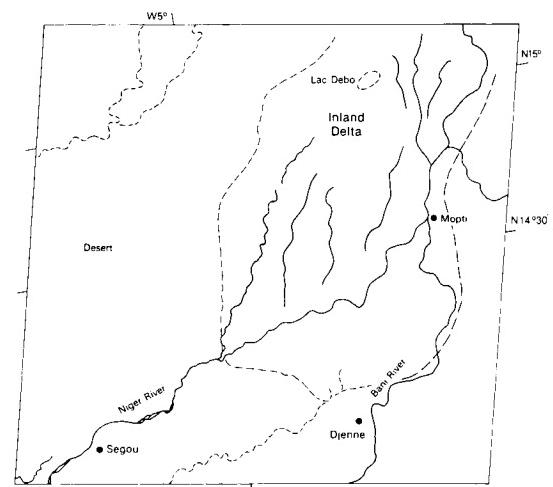


PLATE F-21

PANTANAL, BRAZIL

The rivers in this Landsat two-scene mosaic are tributaries to the Paraguay River in the Brazilian state of Mato Grosso (Holz et al., 1979). This portion of west-central Brazil lies in the savanna climatic zone south of the great Amazon rain forests. Mean annual rainfall is approximately 1250 mm, with one-half generally coming in the summer wet season. Harsh temperatures, poor soils, and periodic extensive flooding result in a low population density. Principal land use consists of grazing and subsistence agriculture. There are no major towns in this scene.

The scene is separated into two physiographic regions (Pantanal Plains on west; Central Plateau) by a prominent escarpment of the Devonian Chapada Group sandstones that underlie the Paraná sedimentary basin to the east. West of the escarpment is the Pantanal Basin, which is underlain by up to 100 m of Quaternary alluvial deposits covering post-Triassic sedimentary rocks. Streams crossing the escarpment, known locally as Serra de São Lourenço, fall several hundred meters from the plateau upland to the basin floor. Gradients of 0.5 to 1.5 m/km occur at the escarpment, while gradients of 0.01 m/km characterize rivers in the Pantanal Basin.

The Brazilian Ministry of Interior reports a maximum daily discharge of the Rio Piquiri immediately west of this scene at 405 m³/s. The minimum daily discharge was 73 m³/s, and the mean annual discharge is 131 m³/s for gage records in 1968-1971. Despite the pronounced seasonality of the climate, baseflow is maintained in the eastern Pantanal rivers through ground-water discharge from extensive sandstone aquifers.

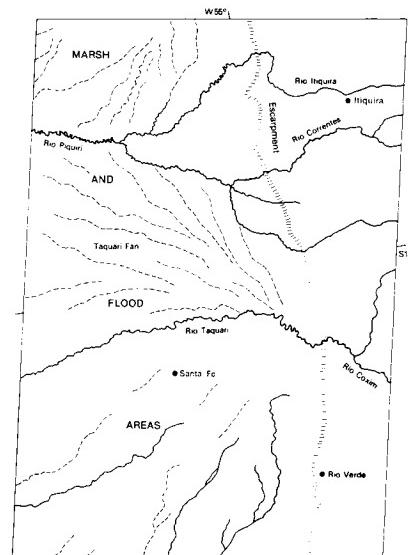
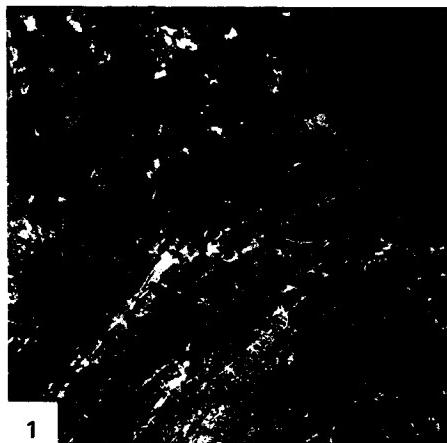
The most striking fluvial features in this image are the great alluvial fans that lie immediately west of the Serra de São Lourenço. The largest of these is related to the Rio Taquari, which appears in the lower part of the mosaic. The Taquari fan covers an area of approximately 50000 km², only part of which is shown in the lower part of this image. Portions of the smaller São Lourenço fan are visible at the top of the picture. These fans consist of sands derived from the Paraná Basin and deposited by low-sinuosity anastomosing channel systems in the relatively recent geologic past (Holz et al., 1979). Note that the modern active rivers crossing the escarpment have high-sinuosity meandering patterns. Their clearly defined floodplains are a marked contrast to the splaying pattern of ancient paleochannels.

This mosaic shows the sinuous Rio Taquari emerging from the escarpment just west of the town of Coxim. Note the splaying pattern of paleochannels developed to the southwest of the Rio Taquari. Crosscutting relationships indicate a succession of channel abandonment on the fan surface.

Note the decrease in sinuosity for the Rio Taquari in a downstream direction (right to left). This occurs because of decreasing mean annual flow and increasing flow variability in the downstream direction. Water is lost by infiltration into the sandy fan sediments underlying the river. This recharge feeds an extensive ground-water system that is directed toward the Paraguay River 200 km to the west.

The pronounced differences in channel patterns for this region probably resulted from Quaternary climatic change. During the glacial conditions that characterized much of the Quaternary, the climate of this region likely changed from its present tropical savanna conditions to semiarid conditions. The modern Brazilian savanna vegetation, known as "Cerrado," was replaced with xeric plants that were less capable of preventing erosion on interfluves. Stream regimens probably changed from their present uniformity to ephemeral conditions characterized by rare but intense floods that carried immense loads of sand washed from adjacent slopes. The sediment-charged streams deposited their load on the immense fans along the Pantanal escarpment. The subsequent climatic change to interglacial time resulted in a shift to modern channel conditions. The expansion of savanna vegetation resulted in greater protection of slopes from erosion. Somewhat more uniform and wetter climatic conditions facilitated the present flow regimen of the rivers. Present stream loads are dominated by suspended fines, and the appropriate channel pattern is that of a through-going meandering stream.

The escarpment cut from the Central Plateau continues northward farther into Mato Grosso until it encounters exhumed Precambrian rocks around the Cuiabá River (Figures F-21.1 and F-21.2 (scarp of the Serra do Aquapei)). These rocks, consisting of molasse metasediments and igneous-metamorphic complexes, are strongly deformed (note anticlines near right side of the image). Post-Paleozoic units lie against this orogenic belt along its north side. The Rio Arinos drains northward into the Amazon Basin from the Planalto do Mato Grosso; the Rio Cuiabá moves southward from the divide into the Paraguay and ultimately the Parana rivers. **Landsat 281149-125759-7, May 29, 1981.**



ORIGINAL PAGE IS
OF POOR QUALITY



PLATE F-22

MANAUS, BRAZIL

This scene shows the confluence of two of the world's largest rivers, the Rio Negro and the Solimões River, which join in the central Amazon basin to form the Amazon River ("Amazonas" in Brazil). The major city of this region, once called "Amazônia," is located at the confluence. Originally built as a colonial fort in 1669 by the Portuguese, the site evolved to the town of Manaus, with continual settlement since the 18th century.

The Amazon is the world's largest river. At the Óbidos Narrows, 600 km east of Manaus, the river channel is over 2 km wide and 60 m deep. This cross section is compared to that of the Mississippi River at Vicksburg in Figure F-22.1. The river flow measured on June 5, 1972, was $255000 \text{ m}^3/\text{s}$ (9000000 cfs), the largest freshwater flow measured on Earth (Sternberg, 1975). Since several major tributaries enter downstream of Óbidos, it is clear that the Amazon experiences much larger flows. The 6300 km^3 of water that it delivers to the ocean each year is approximately 15 percent of all fresh water passing from the continents to the oceans. Figure F-22.2 is a Landsat scene showing a large sediment plume being discharged at the Amazon mouth. Paradoxically, the Amazon river, with its huge discharge and sediment load, does not form a delta of any consequence. This is apparently because of strong offshore currents that prevent sediment accumulation at the river mouth.

The discharge of the lower Amazon is remarkably uniform in time. During an average year, the maximum water discharge can be expected to exceed the minimum by a factor of only 2 or 3. This uniformity results from the river's near-equatorial position. The northern hemisphere Amazon tributaries achieve their peak flows several months later each year than the southern hemisphere tributaries, thus evening out the annual hydrograph. Moreover, the immense floodplains modify floodflows by slowly storing water during rising river stages and slowly releasing it during falling stages.

The upper left of the scene shows the Rio Negro emerging from uplands underlain by Lower Paleozoic sediments related to the Guiana Shield. The river widens markedly as it emerges on the Amazon Plain, a sediment-filled structural basin or trough lying between the Guiana Shield to the north and the Central Brazil Shield to the south. The island-studded expansion of the Negro may be fault-controlled, since buried structures beneath the Amazon Plain sediments influence river patterns in this region. The river depth exceeds 90 m in this reach.

The Rio Negro (Figures F-22.3 and F-22.4) is believed to contribute about 40 percent to the aggregate volume of Amazonas flow just below the confluence. The river drains a large area of

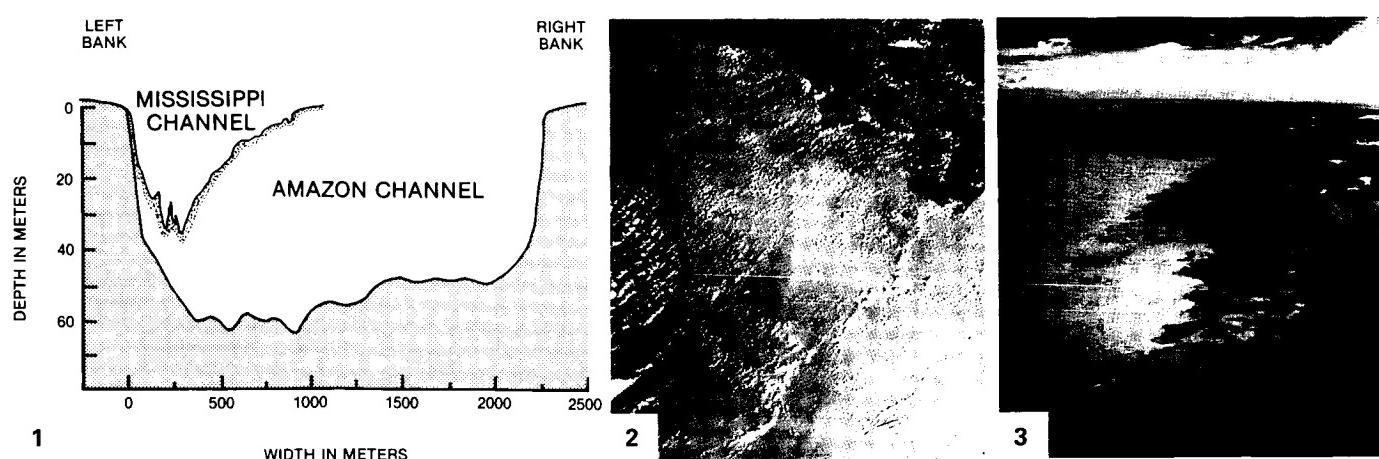
equatorial north-central South America, including much of the southern Guiana Shield. Annual rainfall in much of the basin is 3 m per year. The Rio Negro derives its name from the unusual optical properties in its deep lower courses. The water contains a yellow-brown water-soluble pigment that is derived from decomposed plant material. The pigment can extinguish 8/10 of incoming light at a depth of 25 cm. A lack of significant suspended sediment further contributes to water that has been described as being "black as ink."

The confluence of the dark warm sediment-free Rio Negro and the bright cooler sediment-laden Rio Solimões produces a spectacular effect near Manaus. The "white" water of the Solimões underruns the "black" water of the Negro. The optical contrast persists for several tens of kilometers downstream, with the warm Rio Negro waters hugging the northern bank of the Amazonas. Studies of dissolved salts and isotopic chemistry show that water from the two rivers fails to achieve thorough lateral mixing even 120 km downstream of the confluence.

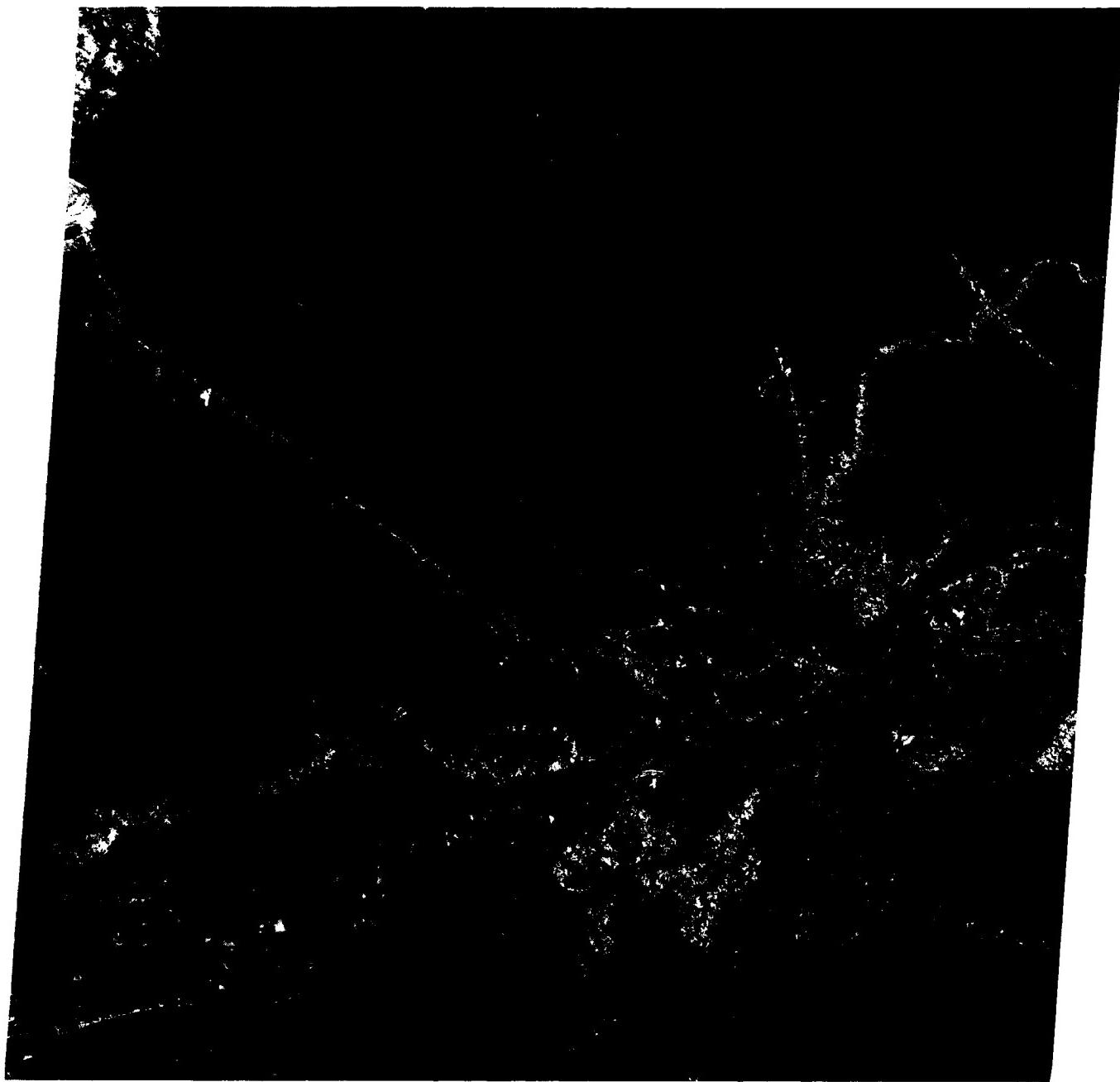
The ecological significance of the Rio Negro geochemistry is immense. The black slow-moving water is much less productive than that of the sediment-rich Solimões. The river is also relatively free of certain insect pests that are common in other Amazon tributaries.

The slope of the lower Amazon is one of the lowest for any terrestrial river, about 2 to 3 cm/km for the 1400 km downstream of Manaus. The reason for this low slope is that the river exhibits delta, rather than floodplain, channel patterns. This is the result of Holocene filling of a great estuary that extended into northern Brazil when the sea level rose rapidly at the end of the Pleistocene. Filling of the estuary by deltaic sediment progressed rapidly as heavy loads were supplied by the Solimões, Japurá, and Madeira Rivers (all of which drain the Andes Mountains). Alluviation was so rapid that tributary arms to the former estuary were dammed and converted to elongate wedgelike dikes, which are named "rias fluviales." Two huge examples occur at the respective mouths of the Tapajós and Xingu Rivers.

Several highways of the Amazônia highway network show up as distinct strips through the rainforest vegetation. The bright response on the imagery is the result of farms provided to new settlers by the Brazilian government. Clearance of the rainforest for farming is an ominous trend, since the forest has little capability of regenerating itself on the lateritic soils of the region. The delicate ecological balance of the region is easily upset. **Landsat 77212-13081-7, July 31, 1977.**



ORIGINAL PAGE IS
OF POOR QUALITY



4

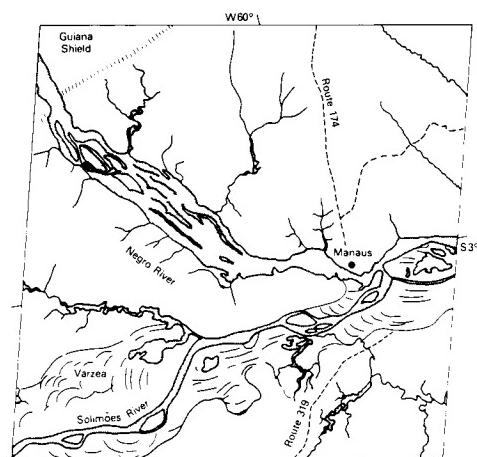


PLATE F-23

SOLIMÕES RIVER, BRAZIL

This Landsat scene shows the natural color of an area centered approximately 300 km southwest of Manaus. Figure F-23.1 is a hypothetical cross section through the Holocene floodplain (Baker, 1978a). The important features are levees (*restingas*), alluvial islands (*ilhas*), second-order channels (smaller channels on the *varzea*), landslides (*terrás caídas*), and tributaries draining sediment-deficient uplands (*terrás firmes*) to lakes at the *varzea* margin (*riás fluviales*). Figure F-23.2 is an older Landsat scene of the same area in band 7 (Landsat 1008-13481-7, July 31, 1972). Note the effect of sediment load (bright response) on the color image.

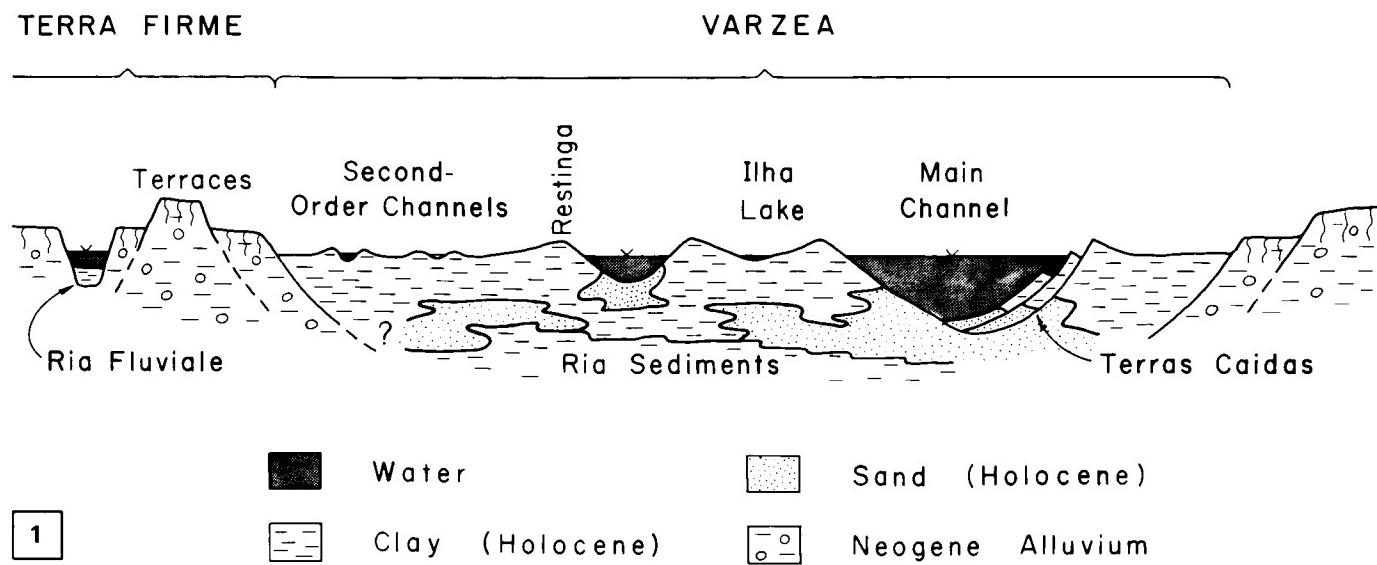
The two major rivers, the Solimões and Purus, have developed Holocene floodplains, which in Brazil are named "varzeas" (Baker, 1978a). The floodplains are inset into uplands underlain by deeply weathered Neogene sediments. These are termed "terrás firmes".

The dominance of the Solimões in Holocene sedimentation history is indicated by the immensity of its *varzea*. The Purus has been forced to hug the eastern margin of the Solimões at the upper right of the picture. The index map records the location of the *varzea* and several *riás fluviales* in the northern part of the scene.

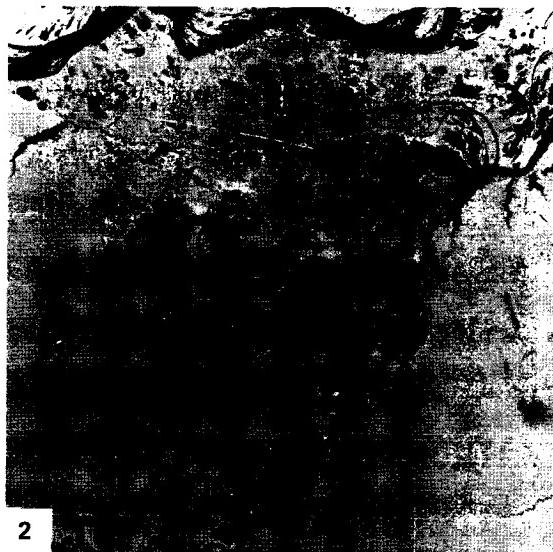
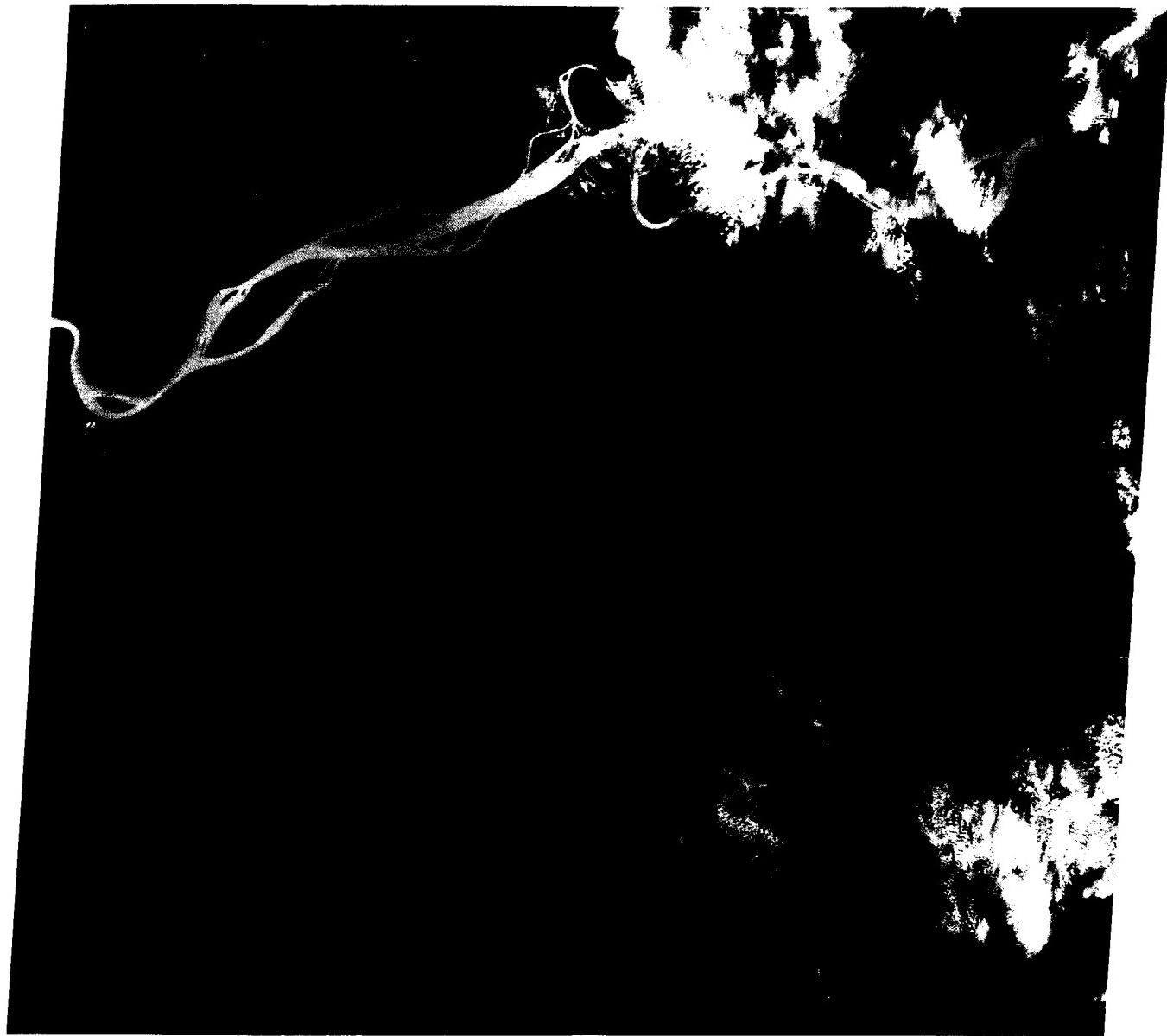
The "riás fluviales" are clear-water lakes formed where streams draining the rainforest of the *terrás firmes* are dammed at the *varzea* margins. Lake Aiapuá, at the center of the image, is a typical example. Such lakes may have small deltas at their heads, but generally they receive very little sediment.

The anastomosing pattern of the Solimões River is very prominent. The river has a low sinuosity and a high width-to-depth ratio for its channel. Sediment load data show that the river transports mainly suspended load. The river apparently maintains several active thalwegs because of its very high discharge. Islands between the channels are maintained by the rapid plant colonization of overbank sediments. Their long-term stability is indicated by archaeological material, which on one island was dated by radiocarbon at 2050 ± 120 years B.P. (Sternberg, 1959). One conclusion about the dynamics and morphology of Amazon Basin rivers is that they cannot be understood by merely scaling up our concepts of smaller rivers.

Recent studies of suspended sediment concentrations and discharges of Amazon Basin rivers have been conducted by Robert H. Meade, Carl F. Nordin, and others of the U.S. Geological Survey. The pattern of sediment storage and remobilization downstream of Manaus is dominated by the Madeira River, which transports the largest sediment load of any Amazon tributary. Since the Madeira reaches its peak discharge 2 months earlier than the Amazon mainstream, the main river stores sediment on its rising stages and remobilizes it during its falling stages. The Madeira drains the Andean Cordilleras of southern Peru and western Bolivia. More than 75 percent of the suspended sediment provided to the Amazon system comes from the tributaries that directly drain the Andes. Sediment is probably derived from the erosion of older Quaternary terrace alluvium in the Andean foothills. **Landsat 50115-13475, June 14, 1984.**



ORIGINAL PAGE
COLOR PHOTOGRAPH



2

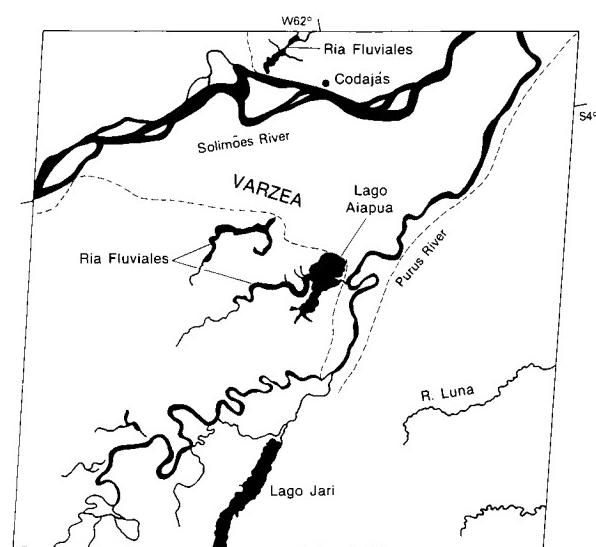


PLATE F-24

JAPURÁ RIVER, BRAZIL

The SIR-A radar image (top of Plate) shows Ilhas (islands) Macuapanim between the Japurá and Solimões Rivers (index map; middle of Plate). The radar highlights the contrast between the terra firme, with its rainforest cover, and the seasonally flooded varzea. The scene is dominated by the varzea topography with numerous cutoffs and scroll topography. Lake Amaúna is a prominent ria fluvial.

The scroll bars and long narrow arcuate lakes indicate relatively rapid lateral migration of the rivers through the varzea, or floodplain. The spectacular response of water to the radar (black on the image) highlights these patterns because the intervening forest canopy has a diffuse scattering (bright on the radar image). The scroll topography can be used to estimate the size and shape of former river meanders.

Channel migration on the Solimões occurs during times of varying discharge. At rising stage, the river can undercut its banks, reworking sediment that has been stored there. Huge landslides, called "terre caídas," can develop during falling stage (Sternberg, 1975).

The Rio Japurá shows a transitional anastomosing-to-meandering pattern. Islands in its channel are elongate and vegetated. The nonvegetated islands of typical braided streams are lacking. The Japurá may be less anastomotic than the Solimões because of its smaller size. R. J. Gibbs (1967) estimates that the discharge of the Solimões is about 3.3 times greater than that of the Japurá at their confluence. It has also been proposed that the lower Japurá is influenced by buried structures beneath the Neogene sedimentary fill. It has a series of linear segments that could reflect fault control.

The Japurá carries a considerable sediment load from the Andes Mountains and their forelands in Columbia. It generally flows on alluvial plains that are free of rapids. The varying sediment loads of Amazon Basin rivers are probably the most important controls on fluvial geomorphic features (Baker, 1978a). In the local descriptive language, the sediment-charged rivers are called "rios blancos" (white rivers). The color, really more a muddy-yellow than a white, is caused by very large suspended loads. Both the Japurá and the Solimões are prolific conveyors of sediment.

Rivers that do not drain the Andes are relatively impoverished in sediment. The "black" rivers, like the Rio Negro, and the "green rivers," including the Tapajós and Xingu, drain crystalline shield areas. The latter provide a sandy bedload but almost no suspended load. Because of the immense varieties of sediment

loads, discharges, and source terrains, the Amazon River Basin contains a fascinating complex of different types of river systems.

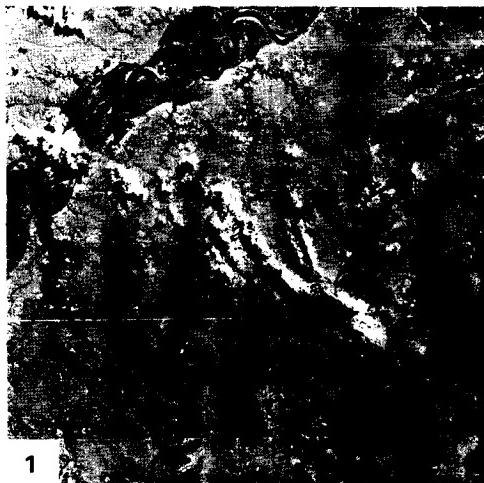
Figure F-24.1 shows another area of the western Amazon Basin, 800 km south of the one described above. The Landsat scene (50129-14022-4, July 8, 1984) shows the Madre de Dios River in northern Bolivia. On its southwest (lower left) to northeast (upper right) course, its pattern changes from low sinuosity, single-channel to low sinuosity, multichannel (anastomosed) to high sinuosity. The Beni River, which flows northward on the east (right) half of the image also shows a marked downstream increase in sinuosity. Both rivers have pronounced varzeas with scroll topography, oxbows, and paleochannel patterns. The terra firme uplands have angular tributary patterns that may indicate structural control.

For comparison, Figure F-24.2 is a Landsat scene of the Zaire (Congo) River in west-central Africa (Landsat 50126-08320-4, July 5, 1984). The Zaire is the world's second largest river in annual discharge and is found at a similar latitude and environment as the Solimões. It has a pronounced anastomosed pattern with large alluvial islands. (Savat, 1975)

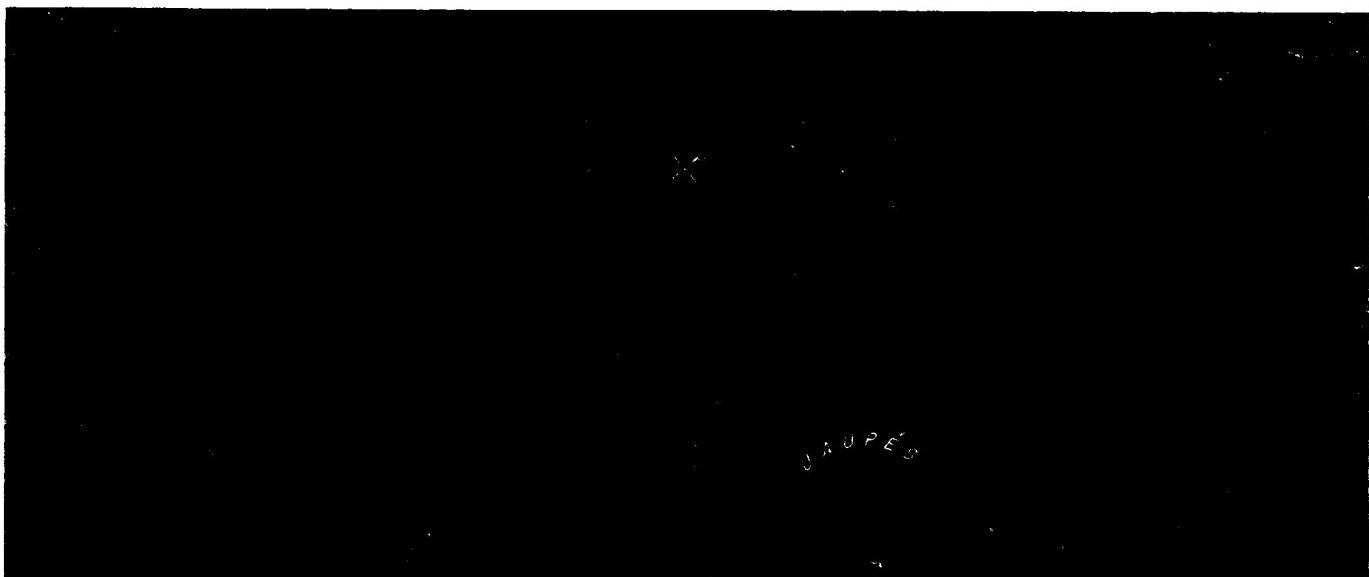
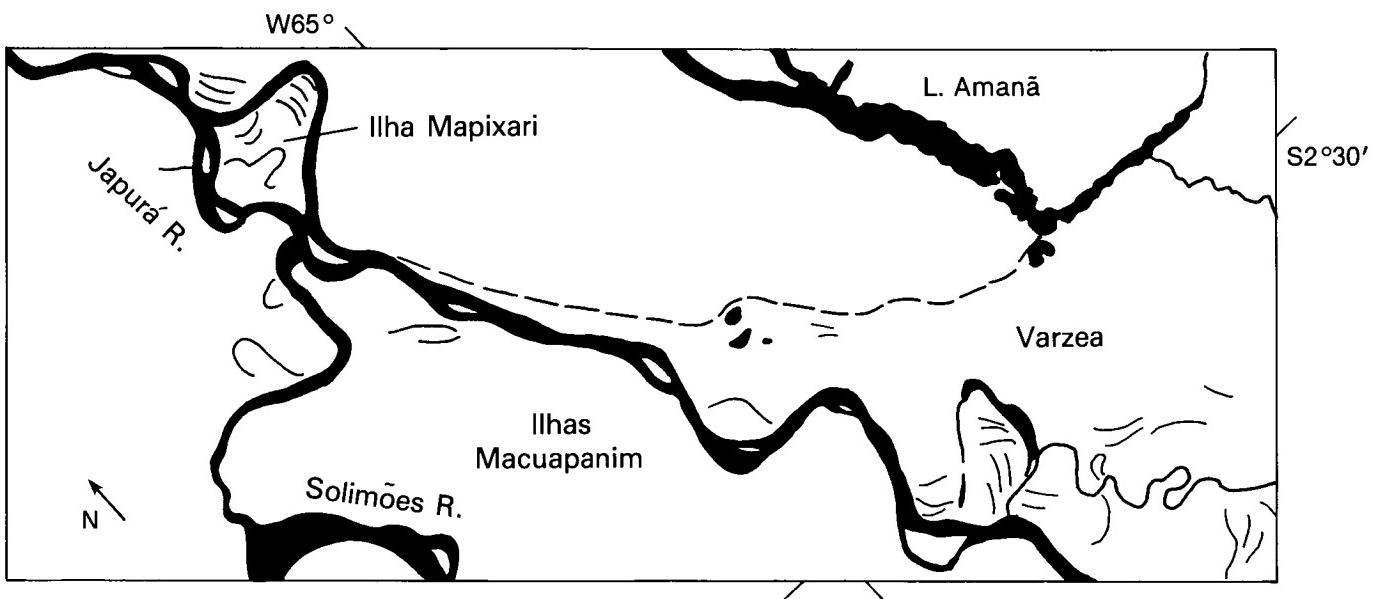
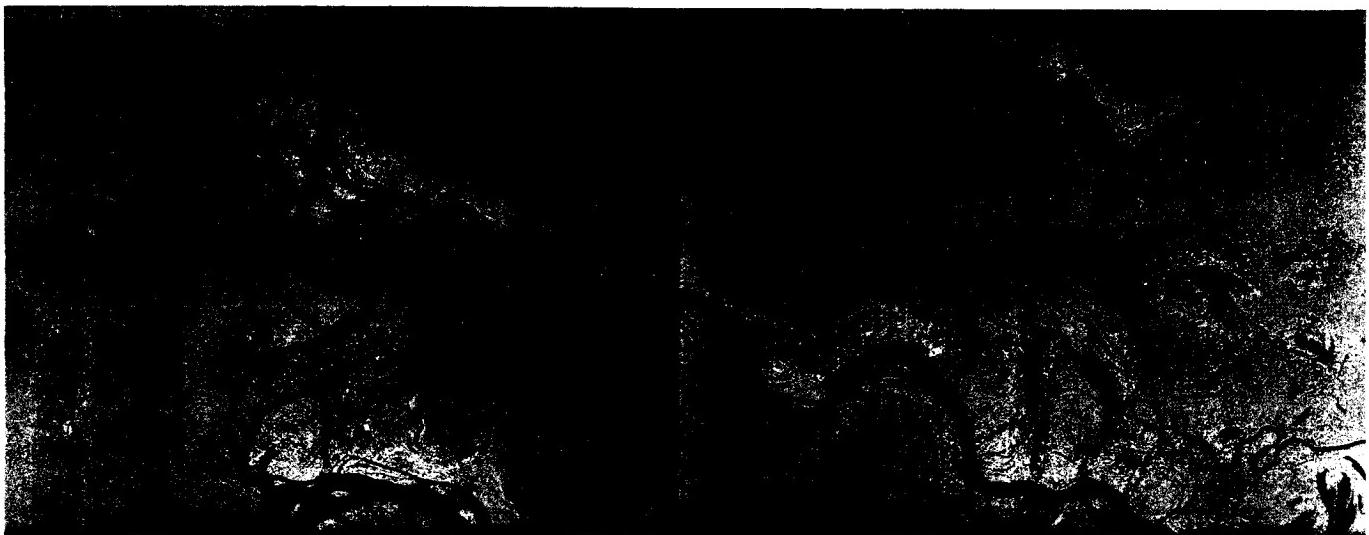
At the bottom of the Plate is a RADAM (Radar Amazon) image (sheet NA19-2-C) in X-band (3-cm wavelength) acquired with a depression angle less than 15° and at a resolution of 12 m from a commercial airborne radar. RADAM was a Brazilian program in airborne radar mapping centered on a 5 million km² region of the Brazilian Amazon. The project included ground-truth collection at thousands of study sites and resulted in a wealth of data for development plans in the region.

The image depicts an area of small Amazon tributaries near the Uaupés River, a Rio Negro tributary in far northeastern Brazil. Note the detail of surface topography generated by the RADAM image as a result of the radar shadowing effect that occurs at the relatively low depression angle. The much larger depression angle (40°) of the SIR-A system does not give this effect.

The intricate dissection pattern emphasized by RADAM has been interpreted by Tricart (1975) as evidence for a relict drainage. He proposes that the relatively dry full-glacial episodes of the Pleistocene were sufficient to change the land cover from rainforest to savanna. The uplands were then subject to intense fluvial dissection, yielding high sediment loads to the Amazon tributaries. The change to interglacial conditions in the last 10000 years has resulted in the stabilization of the dissected interfluves as rainforest returned. **SIR-A Image, Data Take 24G, 1981.**



ORIGINAL PAGE IS
OF POOR QUALITY



ORIGINAL PAGE
COLOR PHOTOGRAPH

PLATE F-25

UCAYALI RIVER, PERU

This specially processed Landsat scene shows the Ucayali River in central Peru, immediately east of the high Andes at Cerro de Pasco. The Ucayali originates at the confluence of the Tambo and Urubamba Rivers. The latter both have low to moderately sinuous channels. The Urubamba contains several vegetated islands and some nonvegetated channel deposits, but point bars are not apparent. The river drains the folded and faulted Andean Foreland in the vicinity of the famous Inca sites of Machu Picchu and Cusco.

Downstream of the confluence, the Ucayali displays a progressive change in channel pattern. For the first 50 km, it has a complex of anastomosing channels, meanders, abundant non-vegetated islands, and elongate vegetated islands. Downstream of that point, islands become far less abundant, and meandering dominates. Bright spots on the image along the river show that nonvegetated channel deposits are less abundant and occur primarily as point bars. Since no major tributaries enter this reach, the change in channel pattern for the Ucayali probably results from downstream decreases in channel slope and sediment size. The river may experience the threshold change from braiding to meandering that was postulated by S.A. Schumm (1977) on the basis of flume experiments.

A change in floodplain character accompanies the change in channel pattern for the Rio Ucayali. The upper low-sinuosity anastomosing reach does not have a clearly developed floodplain. Where meandering begins, there is evidence of lateral migration. Abandoned meanders, scroll topography, and backswamp features all appear. The general tone of vegetation on the floodplain becomes distinctly lighter than that of the surrounding forest. Moreover, the floodplain and the meander tract both widen in

a downstream direction. Figure F-25.1 is a SIR-A radar image of the lower Ucayali River (350 km north of Atalaya) showing how the pattern of meander migration continues downstream. Figure F-25.2, taken of a tributary to the Ucayali River near Iquitos, Peru, shows dense vegetation of the rainforest and its relationship to channel geometry.

Because the Ucayali parallels the Andean foreland, it separates the Amazon lowlands of the north and east from mountainous terrains to the west and south. The transitional tropical-to-mountain environments of the foreland are prolific sources of sediment. Note that the small tributaries that descend from the highlands are closely spaced and display relatively low sinuosity until they join the Ucayali in the lowlands. In contrast, the tributaries flowing from the tropical lowlands are widely spaced and highly sinuous. The predominant sediment loads are entering from the west.

The Ucayali derives its enormous sediment load from the Andean foreland and feeds it to the Solimões River. However, it is clear from studies of ancient sediments that both the Juruá (upper right of image) and Purus Rivers formerly drained the same sections of the Andean Foreland. It is likely that the Ucayali has captured the mountainous headwaters of these rivers, resulting in a profound change in their sedimentation histories.

Professor Jean Tricart (1977) attributes the numerous cut-offs on Amazon basin streams to the throughput of suspended load. The sand that settles out on concave banks is easily eroded, especially through undermining at rising flood stages. However, deposition of suspended load on convex banks is minimal. Meanders migrate and distort until they fail through neck cutoffs.

Landsat 78224-14193-7, August 12, 1978.



1

ORIGINAL PAGE
COLOR PHOTOGRAPH

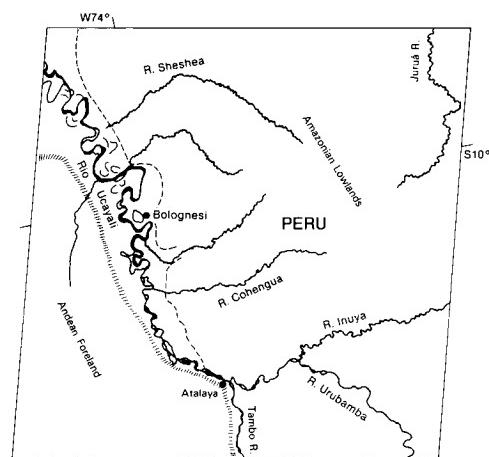
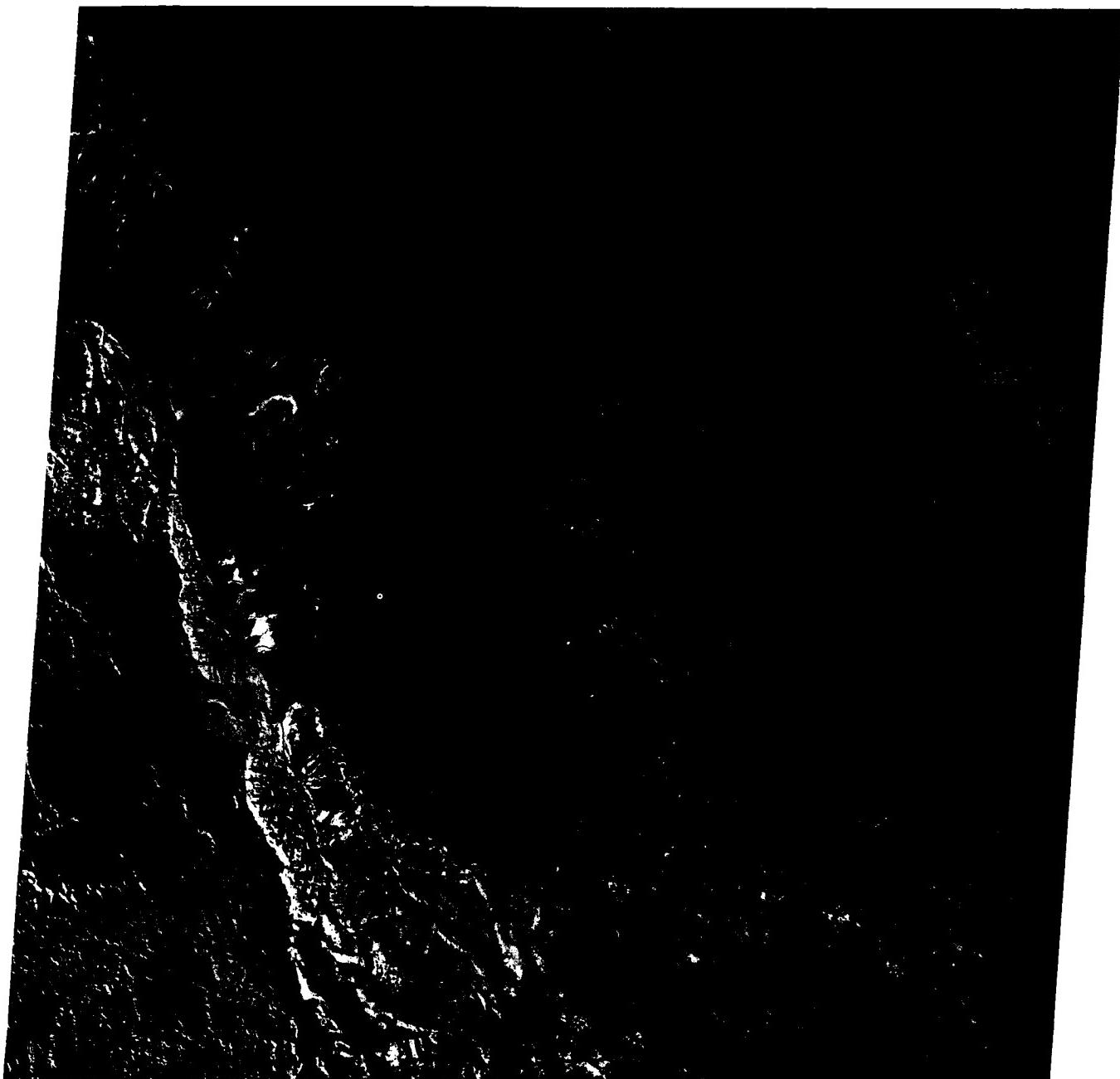


PLATE F-26

TEAYS RIVER, HUNTINGTON, WEST VIRGINIA

This enhanced Landsat mosaic shows the region where the states of Ohio, Kentucky, and West Virginia join near Huntington, West Virginia. The distinctive high-density dissection of the uplands results from intricate dendritic drainage on the generally flat-lying sediments of the western Appalachian Plateau. Almost all the rocks are Paleozoic sandstones, siltstones, and shales, which are easily eroded in the humid-temperate climate. Figure F-26.1 is an aerial photograph showing such topography in great detail, and Figure F-26.2 is an oblique low-altitude photograph.

The Appalachian Plateau dissection noted above can be considered to display a mature phase of erosion. In the idealized concept of fluvial dissection of a landscape, proposed by W. M. Davis (1899), youthful topography is characterized by broad undissected interstream tracts and divides. Steep gullies may be actively eroding as in the Loess Plateau of China. In mature dissection (Figures F-26.1 and F-26.2), the drainage divides are reduced to sharp ridges, resulting in a minimum of interstream uplands. This produces the maximum possible relief. In old age, the divides are reduced, although some high-relief areas may be left as erosional residuals. Removed of its genetic implications, the scheme can provide a useful description of drainage evolution.

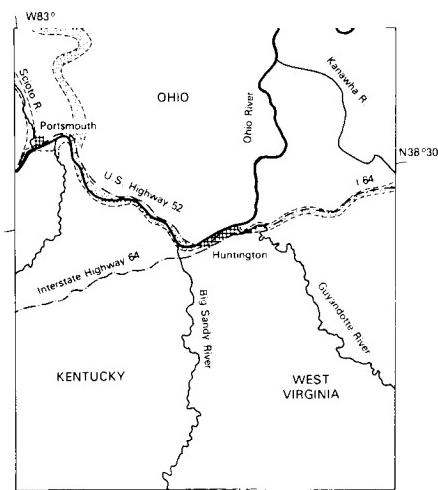
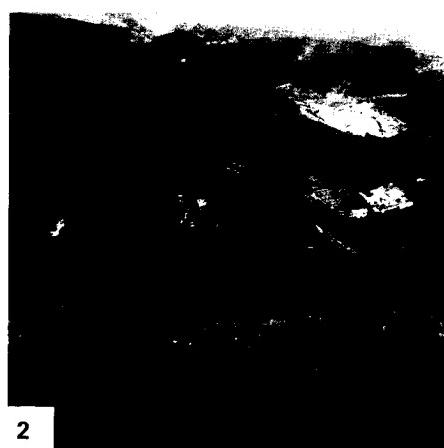
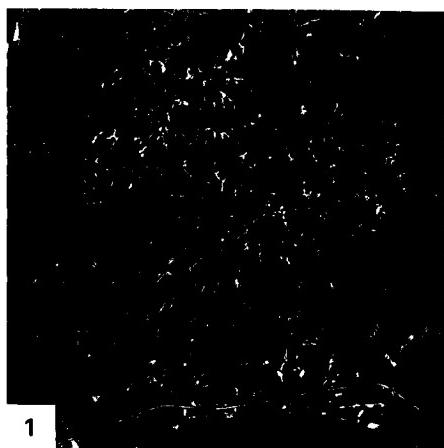
The Ohio River is the major drainage element in this study area, but it has only occupied its present position since the Late Pleistocene. A prominent paleovalley (stippled pattern on the location map and "bands" without ribbon of river in photo) represents the ancestral trunk river in this region. This paleovalley is part of the Teays River system, the preglacial drainage from

which the present Ohio River evolved. The preglacial Teays drained northwestward from the Blue Ridge of Virginia across West Virginia and Ohio. Its course can be traced by numerous wells in Ohio, Indiana, and Illinois, where its westward-trending valley is buried by glacial drift (Thornbury, 1969).

The advance of Pleistocene ice over the Teays River course caused the drainage to shift from the Teays route to a route roughly paralleling the glacial boundary. The modern Ohio River does the latter. However, the timing of the shift is uncertain because of difficulties in dating the complex sequence of drift in the region. Paleomagnetic studies of fills in the Ohio portion of the Teays Valley indicate an age greater than 0.7 million years.

The portion of the Teays Valley extending east-west from Huntington is filled with Late Tertiary alluvium and Early Pleistocene lacustrine clay. The data indicate that the Teays was an active system until Early Pleistocene glacial ice dammed its upper course. Then, either the divide near Portsmouth was overtapped by the lake or piracy from the evolving Ohio system captured the Teays headwaters. Paleomagnetic data indicate that the lake existed from approximately 1.7 to 1.0 million years ago.

The final result was the shift of Appalachian Plateau drainage to the Ohio River course. The modern Ohio River Valley carries the later Pleistocene fluvial record of this region. The uppermost sediments of the Teays paleovalley consist of loess, emplaced by eolian activity during the cold/dry phases of the Pleistocene. **Landsat 2386-15280 and -15282, February 12, 1976.**



ORIGINAL PAGE
COLOR PHOTOGRAPH



PLATE F-27

CHANNELED SCABLAND, WASHINGTON

This Landsat scene shows a region that was subjected to perhaps the most remarkable fluvial processes on the planet Earth. The Columbia Basin of eastern Washington is a lowland surrounded by the Cascade Mountains to the west, the Okanogan Highlands to the north, the Rockies of Idaho to the east, and the Blue Mountains to the south. The bedrock comprises the Columbia River Basalt Group, tholeiitic flood basalts erupted between 16.5 and 6 million years B.P. (Swanson and Wright, 1978). Deformation of the basalt surface during the Late Neogene produced anticlines and monoclines that deformed the basalt surface.

During the Pleistocene, the basalt surface became thickly mantled with loess comprising the Palouse Formation. Because of the rain shadow effect of the Cascade Mountains, the Columbia Basin has an arid to semiarid climate during the present interglacial period. However, full-glacial conditions were extremely cold and dry. The loess, which displays a patchwork pattern of wheat farms on the Landsat scene, was emplaced by glacial period winds.

The northern margin of the Columbia Basin, shown in this image, is actually a tilted plateau in which the basalt dips to the southwest. Glaciers advanced over much of the Okanogan Highlands, reaching portions of the plateau during the last major glaciation. The glaciation impounded great lakes in the Columbia River drainage. Largest of these was Lake Missoula, held by an ice dam in northern Idaho. Lake Missoula covered a large area of western Montana and temporarily held as much as 2×10^{12} m³ of water. The glacial dam in northern Idaho failed repeatedly, releasing the lake water in discharges as great as 2×10^7 m³/s. The resulting floods were the greatest that can be documented in the geologic record of river activity (Baker and Bunker, 1985). The floods spilled across the northern rim of the plateau, eroding a great plexus of flood channelways. The channels appear as darker grays on the Landsat scene because the loess cover was locally eroded, exposing the dark basalt (Figure F-27.1).

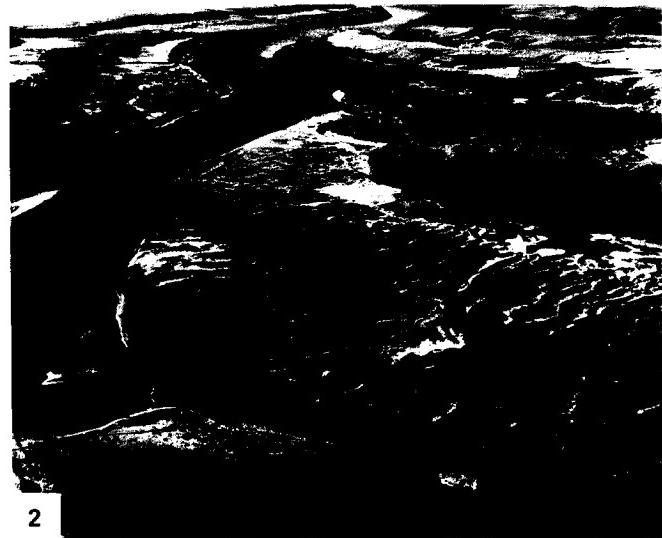
In the 1920s, a University of Chicago geology professor, J Harlan Bretz, did extensive studies in this region, which he named "Channeled Scabland." In a fascinating scientific debate during the 1920s, Bretz encountered vehement opposition to his contention that the Channeled Scabland was the product of catastrophic flooding (Baker, 1978b). He insisted that great Late Pleistocene floodflows had filled pre-flood stream valleys to overspilling, thereby producing divide crossings that converged to comprise an anastomosing complex of channelways scoured in rock and loess.

Bretz was able to convince the critics of his theory by careful documentation of the overwhelming evidence for flood-produced landforms in the Channeled Scabland. These features were subsequently shown to be consistent with the flow physics of cataclysmic flooding. Immense bars of boulders and gravel formed wherever large flow separations were generated by various flow obstructions or diversions. Hills of loess were streamlined by the floodflows (Figure F-27.1), and the basalt bedrock was eroded to form a bizarre landscape, known collectively as "scabland," and consisting of erosional grooves, potholes, rock basins, inner channels, and cataracts. Of hydraulic significance are the giant current ripples, composed predominantly of gravel and commonly over 5 m high and spaced 100 m apart (Figure F-27.2). The giant current ripples are directly related to the shear stresses, mean velocities, and stream powers exhibited by the floodflows (Baker, 1973).

Some of the most spectacular erosional topography in the Channeled Scabland can be seen at Dry Falls (Figure F-27.3), located immediately west of the left center of the image. This cataract is 5.5 km wide and 120 m high. It formed by the recession of a great inner channel that was incised into the basalt layers by the hydraulic plucking action of the deep high-velocity floodwater. **Landsat 1039-18143, August 31, 1972.**



1

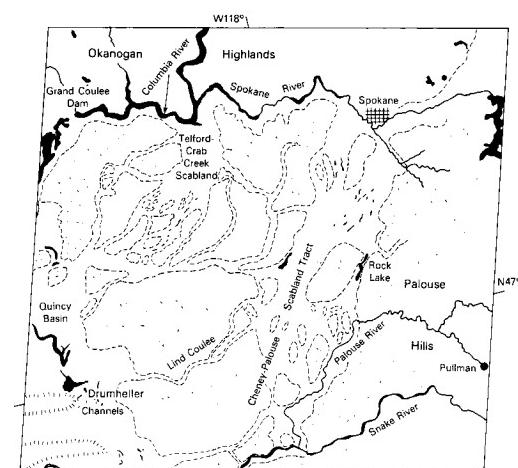


2

ORIGINAL PAGE IS
OF POOR QUALITY



3



REFERENCES

- Abrahams, A. D., Channel networks: A geomorphological perspective, *Water Resources Research*, **20**, 161-188, 1984.
- Baker, V. R., Paleohydrology and sedimentology of Lake Missoula flooding in eastern Washington, *Geol. Soc. Amer. Special Paper*, **144**, 79 pp., 1973.
- Baker, V. R., Stream-channel response to floods with examples from central Texas, *Geol. Soc. Amer. Bull.*, **88**, 1057-1071, 1977.
- Baker, V. R., Adjustment of fluvial systems to climate and source terrain in tropical and subtropical environments, *Canadian Soc. Petroleum Geologists Mem.*, **5**, pp. 211-230, 1978a.
- Baker, V. R., The Spokane Flood controversy and the Martian outflow channels, *Science*, **202**, 1249-1256, 1978b.
- Baker, V. R., Late-Pleistocene fluvial systems, in *Late Quaternary Environments of the United States*, vol. 1, edited by S. C. Porter, pp. 115-129, Univ. Minnesota Press, Minneapolis, 1983.
- Baker, V. R., and R. C. Bunker, Cataclysmic Late Pleistocene flooding from glacial Lake Missoula: A review, *Quaternary Sci. Rev.*, **4**, 1-41, 1985.
- Bretz, J. H., The Channeled Scabland of the Columbia Plateau, *J. Geol.*, **31**, 617-649, 1923.
- Bull, W. B., The alluvial-fan environment, *Progress in Physical Geography*, **1**, 222-270, 1977.
- Bull, W. B., Alluvial fans and pediments of Southern Arizona, in *Landscapes of Arizona*, edited by T. L. Smiley, J. D. Nations, T. L. Péwe, and J. P. Schafer, pp. 229-252, Universities Press of America, Lanham, Maryland, 1984.
- Church, M., Baffin Island sandurs: A study of arctic fluvial processes, *Geol. Surv. Canada Bull.*, **215**, 208 pp., 1972.
- Coleman, J. M., Brahmaputra River channel processes and sedimentation, *Sedimentary Geol.*, **3**, 129-239, 1969.
- Davis, W. M., The geographical cycle, *Geographical J.*, **14**, 481-504, 1899.
- Denny, C. S., Alluvial fans in the Death Valley region, California and Nevada, *U.S. Geol. Surv. Prof. Paper*, **466**, 1965.
- Derbyshire, E., On the morphology, sediments, and origin of the loess plateau of central China, in *Mega-geomorphology*, edited by R. Gardner and H. Scoging, pp. 172-194, Oxford Univ. Press., Oxford, 1983.
- Garner, H. F., The derangement of the Rio Caroni, Venezuela, *Revue de Géomorphologie Dynamique*, No. 2, pp. 50-83, 1966.
- Garner, H. F., *The Origin of Landscapes*, 734 pp., Oxford Univ. Press, New York, 1974.
- Gibbs, R. J., The geochemistry of the Amazon River system, Part 1: The factors that control the salinity and composition and concentration of suspended solids, *Geol. Soc. Amer. Bull.*, **78**, 1203-1232, 1967.
- Gilbert, G. K., Report on the geology of the Henry Mountains, *U.S. Geological Survey of the Rocky Mountain Region*, 160 pp., 1877.
- Gole, C. V., and S. V. Chitale, Inland delta building activity of Kosi River, *Amer. Soc. Civil Engineers, J. Hydraulics Division*, **HY-2**, 111-126, 1966.
- Gregory, K. J., and D. E. Walling, *Drainage Basin Form and Process: A Geomorphological Approach*, 456 pp., Edward Arnold, London, 1973.
- Hickin, E. J., River channel changes: retrospect and prospect, International Assn. of Sedimentologists Special Publication No. 6, pp. 61-83, 1983.
- Holz, R. K., V. R. Baker, S. M. Sutton, Jr., and M. M. Penteado-Orellana, South American river morphology and hydrology, in *Apollo-Soyuz Test Project Summary Science Report*, edited by F. El-Baz and D. M. Warner, pp. 545-594, NASA SP-412, 1979.
- Howard, A. D., Drainage analysis in geologic interpretation: A summation, *Bull. Amer. Assn. of Petrol. Geol.*, **51**, 2246-2259, 1967.
- Howard, A., and R. E. Dolan, Geomorphology of the Colorado River in the Grand Canyon, *J. Geol.*, **89**, 269-298, 1981.
- Hunt, C. B., Cenozoic geology of the Colorado Plateau, *U.S. Geol. Surv. Prof. Paper*, **279**, 99 pp., 1956.
- Hunt, C. B., Geologic history of the Colorado River, *U.S. Geol. Surv. Prof. Paper*, **669**, pp. 59-130, 1969.
- Hunt, C. B., and D. R. Mabey, Stratigraphy and structure, Death Valley, California, *U.S. Geol. Surv. Prof. Paper*, **494-A**, 162 pp., 1966.
- Huntington, E., *The Climatic Factor as Illustrated in Arid America*, Carnegie Inst., Washington, Publ. 192, 341 pp., 1914.
- Kochel, R. C., Interpretation of flood paleohydrology using slackwater deposits, lower Pecos and Devils Rivers, southwestern Texas. Ph.D. dissertation, Univ. Texas, Austin, 360 pp., 1980.
- Kochel, R. C., and V. R. Baker, Paleoflood hydrology, *Science*, **215**, 353-361, 1982.

- Leopold, L. B., M. G. Wolman, and J. P. Miller, *Fluvial Processes in Geomorphology*, 522 pp., W. H. Freeman, San Francisco, 1964.
- Lustig, L. K., Clastic sedimentation in Deep Spring Valley, California, *U.S. Geol. Surv. Prof. Paper*, **352-F**, pp. 131–192, 1965.
- McFadden, L. D., Soils of the Canada del Oro Valley, southern Arizona, M.S. thesis, Univ. Arizona, Tucson, 116 pp., 1978.
- McKee, E. D. (Ed.), A study of global sand seas, *U.S. Geol. Surv. Prof. Paper*, **1052**, 429 pp., 1979.
- Milliman, J. D., and R. H. Meade, World-wide delivery of river sediment to the oceans, *J. Geol.*, **91**, 1–21, 1983.
- Oberlander, T., Tectonics and stream deformation, in *Tectonic Geomorphology*, edited by J. T. Hack and M. Morisawa, Allen and Unwin, London, 1985.
- Osborn, G., Evolution of the Late Cenozoic inselberg landscape of southwestern Jordan, *Paleogeography, Paleoclimatology, Paleoecology*, **49**, 1–23, 1985.
- Patton, P. C. and V. R. Baker, Morphometry and floods in small drainage basins subject to diverse hydrogeomorphic controls, *Water Resources Res.*, **12**, 941–952, 1976.
- Pearthreee, P. A., and S. S. Calvo, Late Quaternary faulting west of the Santa Rita Mountains south of Tucson, Arizona, M.S. prepublication manuscript, Univ. Arizona, Tucson, 49 pp., 1982.
- Petrov, M. P., *Deserts of the World*, 447 pp., John Wiley, New York, 1976.
- Pierce, M. W., Some Late Cenozoic basins and basin deposits of southern and western Arizona, in *Landscapes of Arizona*, edited by T. L. Smiley, J. D. Nations, T. L. Péwé, and J. P. Schafer, pp. 229–252, Universities Press of America, Lanham, Maryland, 1984.
- Potter, P. E. Significance and origin of big rivers, *J. Geol.*, **86** 13–33, 1978.
- Richards, K., *Rivers: Form and Process in Alluvial Channels*, 358 pp., Methuen, London, 1982.
- Robinove, C. J., Interpretation of a Landsat image of an unusual flood phenomenon in Australia, *Remote Sensing of the Environment*, **7**, 219–225, 1978.
- Rust, B. R., Sedimentation in an arid-zone anastomosing fluvial system: Cooper's Creek, Central Australia, *J. Sedimentary Petrology*, **51**, 745–755, 1981.
- Saucier, R. T., Quaternary geology of the lower Mississippi Valley, Arkansas Archeological Surv. Res. Series 6, 1974.
- Saucier, R. T., and A. R. Fleetwood, Origin and chronologic significance of Late Quaternary terraces, Ouachita River, Arkansas and Louisiana, *Geol. Soc. Amer. Bull.*, **81**, 869–890, 1970.
- Savat, J., Some morphological and hydraulic characteristics of river-patterns in the Zaire Basin, *Catena*, **2**, 161–180, 1975.
- Schumm, S. A., *The Fluvial System*, 338 pp., John Wiley, New York, 1977.
- Schumm, S. A., Evolution and response of the fluvial system: sedimentologic implications, *Soc. Economic Paleontologists and Mineralogists Special Publication* 31, pp. 19–29, 1981.
- Schumm, S. A., and H. R. Kahn, Experimental study of channel patterns, *Geol. Soc. Amer. Bull.*, **83**, 1755–1770, 1972.
- Smith, D. G., and N. D. Smith, Sedimentation in anastomosed river systems: Examples from alluvial valleys near Banff, Alberta, *J. Sedimentary Petrology*, **50**, 157–164, 1980.
- Starkel, L., The role of catastrophic rainfall in the shaping of the relief of the Lower Himalaya (Darjeeling Hills), *Geographia Polonica*, **21**, 103–147, 1972.
- Sternberg, H. O'R., Radiocarbon dating as applied to a problem of Amazonian morphology, 17th International Geographical Congress, CR 2, pp. 399–424, 1959.
- Sternberg, H. O'R., *The Amazon River of Brazil*, 74 pp., Franz Steiner Verlag GMBH, Wiesbaden, Germany, 1975.
- Swanson, D. A., and T. L. Wright, Bedrock geology of the northern Columbia Plateau and adjacent areas, in *The Channeled Scabland*, edited by V. R. Baker and D. Nummedal, pp. 37–57, Planetary Geology Program, NASA, Washington, D.C., 1978.
- Thornbury, W. D., *Principles of Geomorphology*, 594 pp., John Wiley, New York, 1969.
- Tricart, J., Influence des oscillations climatiques récentes sur le modèle en Amazonie orientale (Région de Santarém) d'après les images radar latéral, *Zeitschrift für Geomorphologie*, n. f., **19**, 140–163, 1975.
- Tricart, J. Types de lits fluviaux en Amazonie brésilienne, *Annales de Géographie*, **84**, 1–54, 1977.
- Veevers, J. J., and A. S. Rundle, Channel country fluvial sands and associated facies of central-eastern Australia: modern analogues of Mesozoic desert sands of South America, *Paleogeography, Paleoclimatology, Paleoecology*, **26**, 1–16, 1979.
- Wahrhaftig, C., Physiographic divisions of Alaska, *U.S. Geol. Surv. Prof. Paper*, **482**, 52 pp., 1965.

5

DELTAIC LANDFORMS

*James M. Coleman, Harry H. Roberts, and Oscar K. Huh**

Since ancient times, river deltas have been of fundamental importance to civilization. Owing to their early significance as agricultural lands, deltas received considerable attention from ancient scholars such as Homer, Plato, and Aristotle. The term "delta" was first applied by the Greek historian Herodotus in approximately 450 B.C. to the triangular deposit of riverborne sediments at the mouth of the Nile River in Egypt. Deltas in general, as for the Nile in particular, have been areas of special importance to civilization as sites of habitation, agricultural activity, navigation, and fishing. These coastal lowland areas, however, have special problems as well. They are subject to severe catastrophes, including floods from the landward side and sea-level surges, extreme wave erosion, and storm winds from the seaward side. They are major sedimentary depocenters, the surfaces of which are highly sensitive to changes in climate, marine conditions, fluvial hydrology, foliage development, and tectonism. In modern times, they have taken on new importance. Subsurface deltaic facies have played a paramount role in accommodating the world's energy needs; ancient deltaic sediments have provided source beds and reservoirs for a large percentage of known petroleum reserves.

A delta can be defined as a coastal sedimentary deposit with both subaerial and subaqueous expression that has been derived from riverborne sediments deposited in and at the edge of a standing body of water (mainly oceans but also lakes). A delta is one component of a river system which, in totality, includes the drainage basin, the alluvial plain, the subaerial delta plain, and the subaqueous delta/abyssal fan of the receiving basin. Included are those riverborne sediments molded into marine deposits by agents such as waves, currents, and tides of the receiving (marine) basins. Deltas are complex and fragile assemblages of coastal landforms that may include distributary channels, estuaries, river-mouth bars, subaerial/subaqueous levees, interdistributary bays, tidal flats, tidal ridges, beaches, dunes, swamps, marshes, and evaporite flats.

The forms of modern-day deltas vary considerably around the globe and exist in a wide variety of geotectonic, geomorphic, oceanographic, and climatic settings. Delta development is governed by: (1) climatic effects on water/sediment yield and organic/evaporite sediment availability, (2) seasonal and interannual variability in water discharge regime, (3) variations in sediment yield, especially proportions of sand and fine-grained sediment, (4) river-mouth processes controlled by inertial, buoyant, and frictional forces, (5) balance between wave-power regime (weak to

dominant) and fluvial seaward extension of deposits, (6) tidal processes creating multiple channels, (7) wind-driven processes responsible for shallow-water currents and dune formation, (8) effects of nearshore currents, deep-water oceanic currents, and density currents, (9) influence of coastal configuration, particularly shelf slope and topography, (10) receiving basin geometry, and (11) tectonics of receiving basin (Coleman, 1976). Tidal-, wave-, or river-dominant processes impress shore-normal channels, smooth contours of barrier islands, or the digitate/lobate river distributary forms, respectively. The possible combinations are infinite, and each delta is a separate case but with analogous components.

Great deltas form at the mouths of great rivers, and these have been observed to debouch into the sea from cratonic areas of the continental plates (Potter, 1978). In terms of plate tectonic elements, the great deltas of the globe occur predominantly along trailing-edge coasts or marginal seacoasts (Inman and Nordstrom, 1971).

Deltas are regions of rapid and significant change in their surface form. Fundamental scientific problems are encountered in determining which changes are most influential in the steady-state evolution of deltas and what are the process changes resulting from tectonism, important climate shifts, or human activity. How, for example, will these sedimentary systems respond to fluctuations of climate, hydrology, and oceanography under conditions of ice age renewal or global warming? Intellectually, these and other questions will remain major challenges to present and future scientists, even though they will be armed with the timely results of superb new technological and conceptual advances. Pragmatically, the continuous demand for hydrocarbon fuels, agricultural land, and renewable resources will drive expanding human activity in deltas throughout the world. Efforts to explore, understand, manage, and exploit these complex coastal sedimentation sites will most certainly be maintained and will likely intensify in the coming years.

Imagery from spaceborne sensors is even now being used to monitor, analyze, and understand these important sedimentary deposystems. The prime advantage of space imagery to the study of deltas is that entire deltas can be examined in single scenes in context with their surroundings. Many deltas just about fit within a full Landsat image. This match in scales is one reason why deltas warrant a separate chapter (placed naturally between Fluvial and Coastal Landforms) in this book.

The montage of delta images in Figure 5-1 illustrates both this advantage of the small-scale satellite remotely sensed images and some major variations among deltas. The classical Nile River delta is shown at two scales in Figures 5-1a and 5-1b. In 5-1a, visible-IR range (0.4 to 1.1 μm) imagery obtained by a Defense

*Coastal Studies Institute, Louisiana State University, Baton Rouge, Louisiana 70803.

ORIGINAL PAGE IS
OF POOR QUALITY



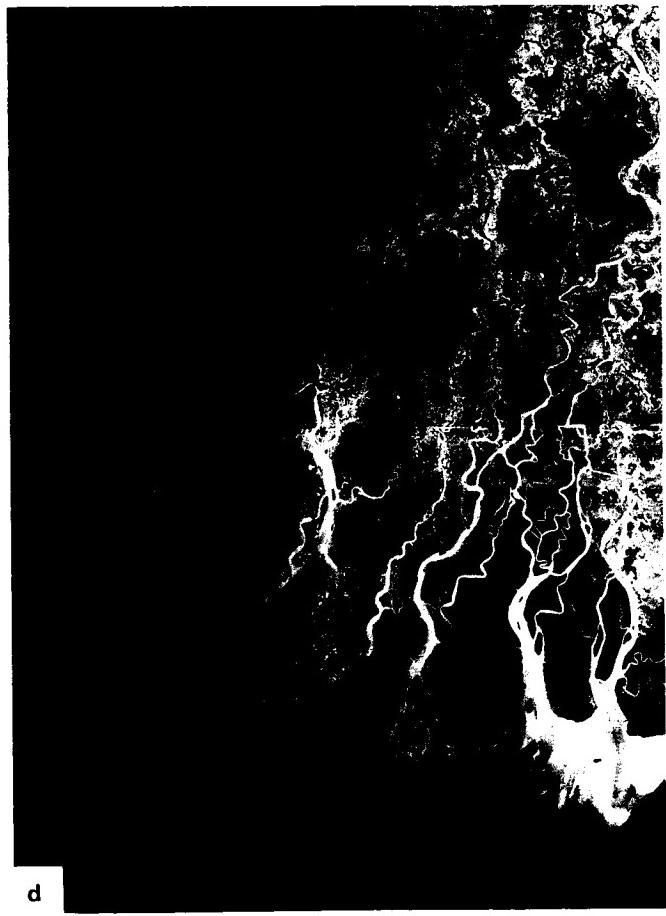
a



b



c



d

Figure 5-1. Images of several major deltas as viewed from space: (a) Defense Meteorological Satellite image of the Nile River from a point near Kerma, in the Sudan, through all of Egypt to its delta termination on the Mediterranean Sea. Length of image covers about 1900 km. (b) Near-vertical photograph of the Nile Delta and surrounding desert, taken by a hand-held Hasselblad camera during the STS-4 Shuttle mission in summer 1982. (c) Part of a Landsat image showing the Huang He (Yellow River) delta. (d) The delta of the Irrawaddy River in Burma as imaged in a two-frame Landsat mosaic, 30263-03235-5 and 30263-03242-5, November 23, 1978.

Meteorological Satellite captures the entire river delta, the upstream drainage basin, and regional geomorphic features in eastern Egypt. The once- to twice-daily repetition rate in coverage is invaluable in monitoring large-area changes across the delta region, but the low spatial resolution (0.6 km) seriously limits this and other meteorological satellite systems (e.g., NOAA orbital satellites at greater than 1-km resolution and geostationary satellites at 2 to 8 km) for geomorphic observations. The most critical deficiency is that the essential relatively fine-scale geomorphic detail is missing. Figure 5-1b is a photograph taken by astronauts Mattingly and Hartsfield during the STS-4 Shuttle mission in summer 1982 using a 70-mm hand-held camera. Images at scales and resolutions similar to this (e.g., the Landsat MSS) are necessary for effective studies of the world's deltas and are used predominantly in this chapter. Figures 5-1c and 5-1d are Landsat images of the Huang He (Yellow River) and the Irrawaddy River deltas. Note the lobate distributary mouths of the Huang He delta and the well-developed bell-shaped channel mouths in the Irrawaddy delta. The differences are due to the enormous silt load carried in a microtidal marine embayment in the Yellow Sea versus the modest sediment load introduced into a mesotidal marine basin off Burma.

Even better high-resolution, more frequent multispectral, and, where possible, all-weather imagery is needed for future studies in deltaic environments. The primary value of such imagery is in direct observation of active processes through a range of time and space scales. Such time-lapse monitoring of environment will detect active versus dormant processes, as well as continuous versus discrete processes, and will provide synoptic detail on the progress and extent of catastrophic changes (as after a hurricane). Synoptic data are particularly valuable in providing plan-view observations that aid in the deployment of systems/personnel for making critical, much more detailed data gathering. Satellite-borne sensors can facilitate observations along the entire river system, from the upper drainage basin down to sea level and the offshore mudstreams. Certain types of imagery, such as that obtained by the Synthetic Aperture Radar (SAR) carried on the Shuttle, the visible-near-IR Landsat Multispectral Scanner and Thematic Mapper, the NOAA Advanced Very High Resolution Radiometer (AVHRR), and the Nimbus Coastal-Zone Color Scanner (CZCS), offer a range of capabilities. They can be analyzed for information about geomorphic changes in delta shapes, vegetation conditions on the subaerial surfaces, primary productivity (plankton blooms) on the shelf, and offshore mudstreams in surface/near-surface waters of the receiving basin. Indirect evidence on circulation in the waters adjacent to the delta is available from analysis of turbid and thermal discharge plumes.

Satellite imagery has already proved beneficial in recognizing similarities and differences in modern world deltas in that, for the first time, a wide variety of delta types has been covered repeatedly in time by the same sensor systems. The uniformity of data scale, quality, and characteristics offers a premium opportunity for change detection, so essential to scientific study of deltaic processes. However, change occurs on many time scales and is sensitive to many causes. Sorting out these factors provides an awesome scientific challenge.

The collection of images discussed in this chapter covers not only the variety of landforms that exist in deltas worldwide, but also attempts to show the variability in the environmental basin settings in some modern deltas. Cloud cover, delta scale, and image availability did not allow all types of deltas to be included in this review, but the 15 Plates treated here will portray

most of the major variations that exist. The following listing of the deltas covered presents a "thumbnail" synopsis of their environmental settings and characteristics:

- *Plate D-1:* Mississippi River Delta (U.S.A.)—Large delta, temperate climate, fine-grained sediments, low wave energy, low tidal range, constant shifting of delta lobes, bifurcated channels.
- *Plate D-2:* Danube River Delta (Romania)—Cold temperate climate, low tide, moderate wave energy, abundant freshwater lakes and marshes, debouching into a semi-enclosed receiving basin.
- *Plates D-3 and D-4:* Ganges/Brahmaputra Rivers Delta (Bangladesh and India)—Large tropical delta, high tide range, low wave energy, high utilization by man for agricultural purposes, large sediment load, complex channel patterns.
- *Plate D-5:* Chang Jiang (Yangtze) River Delta (China)—Humid subtropical delta, high tide, low wave energy, bell-shaped river mouths, high utilization by man for agricultural purposes.
- *Plate D-6:* Hsi River Delta (South China)—Tropical climate, low wave energy, low-to-moderate tide, strong tidal currents around islands and channels, topographically complicated and narrow receiving basin, highly modified by man.
- *Plate D-7:* Mekong River Delta (Vietnam)—Humid tropical delta, high tide, moderate wave energy, bell-shaped river mouths.
- *Plate D-8:* Volga River Delta (U.S.S.R.). Dry subtropical delta, extremely low wave energy, low tide, changing water levels in basin, complex distributary patterns, strong persistent winds.
- *Plate D-9:* Yukon River Delta (Alaska)—Arctic climate, erratic discharge, moderate wave action, low tide, strong littoral currents.
- *Plate D-10:* Mackenzie River Delta (Canada)—Arctic climate, heavy tree cover, abundant freshwater lakes, low tide, low wave energy, complex distributary channel patterns.
- *Plate D-11:* Lena River Delta (U.S.S.R.)—Arctic climate, tundra cover, high wave action, complex ice processes in delta plain, erratic discharge.
- *Plate D-12:* Colorado River Delta (Mexico)—Arid climate, extremely high tide, evaporite sequences, low wave energy, strong currents, narrow receiving basin.
- *Plate D-13:* Shatt el Arab Delta (Iraq)—Arid climate, lack of vegetation, high tide, low wave action, narrow receiving basin.
- *Plate D-14:* Indus River Delta (Pakistan)—Arid climate, narrow receiving basin, high tidal range, moderate wave action, funnel-shaped mouths.
- *Plate D-15:* Amu Darya River Delta (U.S.S.R.)—Arid climate, moderate wave energy, strong littoral currents, low tide, evaporite sequences.

PLATE D-1

MISSISSIPPI RIVER DELTA, U.S.A.

The Mississippi River, the largest river system in North America, drains an area of 3344560 km²; this broad drainage area lies between the Appalachian Mountains (east), the Rocky Mountains (west), and the pre-Cambrian Shield of Canada (north) (Figure D-1.1). The average discharge of the river at the delta apex is approximately 15360 m³/sec, with a maximum and minimum of 57900 and 2830 m³/sec, respectively. Sediment discharge has been estimated to be about 2.4 billion kg annually. The sediment load brought down by the river consists primarily of clay, silt, and fine sand (approximately 70 percent of the load).

During the past 7000 years, the sites of maximum deltaic sedimentation (delta lobes) have shifted and occupied various positions. Figure D-1.2 (Kolb and Van Lopik, 1966) shows the generalized location of these delta lobes during this time, as well as the satellite data coverage outline of Plate D-1. Plate D-1 and the index map show three of the Mississippi delta lobes, the currently active Birdfoot or Belize delta (I), the oldest abandoned delta lobe, the St. Bernard (A), and the youngest abandoned delta lobe, the Lafourche (B). In Recent times, the seaward progradation and lateral switching of the deltas has led to the construction of a broad coastal or deltaic plain that has an area of 28568 km², of which 23900 km² is subaerial.

In the abandoned St. Bernard delta, inactive for approximately 3000 years, the geomorphic forms displayed result from transgressive processes or subsidence and marine inundation. After the delta stopped receiving sediments, seaward progradation ceased, and subsidence and wave and current reworking processes became dominant. Along the seaward margins of the delta, the elongate distributaries are reworked by wave processes, concentrating small barrier islands at the tips of the channel mouths. In the interior of the delta, the marsh surface, no longer replenished by overbank sedimentation, begins to break up and small bays begin to form. Increased salt-water encroachment changes the marsh from a freshwater environment to a saline marsh. The salt marsh cannot keep pace with subsidence, and the former delta surface gradually subsides below sea level, forming a broad marine sound. During this period of time, wave reworking and along-shore sediment transport have resulted in the formation of an elongated offshore barrier island chain (C) (Figure D-1.3). In the protected back-barrier sound, where barrier biological processes abound, currents rework the shell-rich sound sediments into broad coquina or shell banks (D).

In the younger Lafourche delta (B), the transgressive processes did not have as much time to operate; it has been abandoned for less than 1000 years. Wave and current reworking of the ends of the distributaries resulted in formation of coastal barriers still connected to the mainland (E) (Figure D-1.4). The delta plain has been undergoing subsidence, opening up small bays (G) of brackish water not yet the size of those in the St. Bernard delta. The abandoned distributary channels (F) in both of these relict deltas are well displayed, along with freshwater lakes. Land loss is quite high, amounting to some 100 km² per year during the past decade over the entire delta plain. Although a rising sea level has contributed to this loss, subsidence, wave reworking, and modification by man, causing salt-water intrusion, have been responsible for a high percentage of this total land loss. On the landward side of the bays and sounds, ragged marsh remnants (H) indicate continuing encroachment of the marine waters.

The modern Birdfoot or Belize delta (Figure D-1.5, a Landsat TM subscene) of the Mississippi River is the youngest of the Recent delta lobes; it commenced its seaward progradation some 600 to 800 years ago (Fisk and McFarlan, 1955). This newest delta

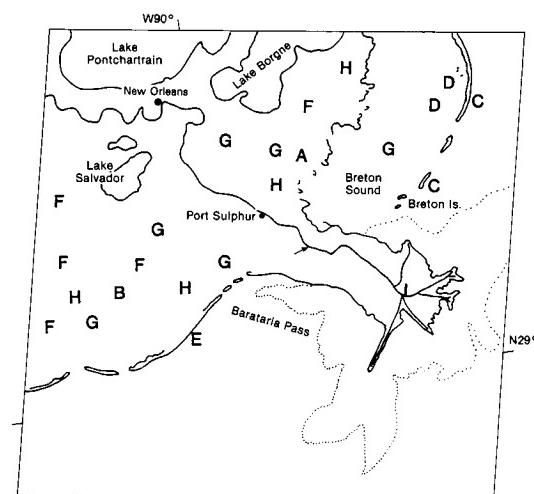
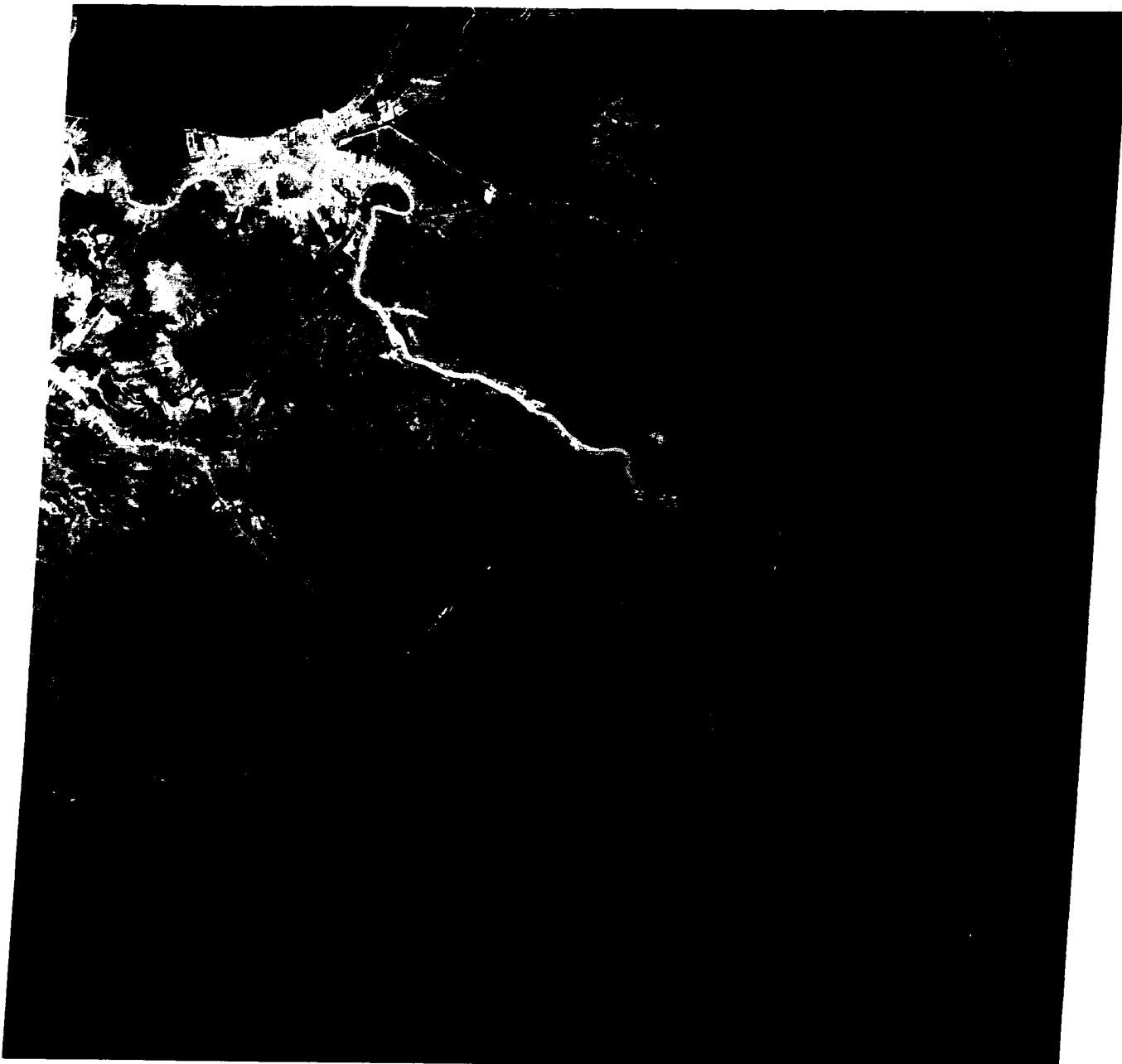
has prograded over a relatively thick sequence of prodelta clays and, as a result of differential sediment loading, has built a relatively thick but laterally restricted deltaic sequence. In contrast, the older Recent deltas, mostly built over shallow bay and shelf deposits, are laterally widespread and relatively thin. The main channel of the river (A; index map 2) is almost 2 km wide, is 30 to 40 m deep, and displays relatively well-developed natural levees (B). At image top, the natural levees are up to 1 km wide and have heights of 3 to 4 m. Along the active distributaries (C) in the lower delta, the natural levees narrow considerably, to widths less than 100 m, and display heights generally less than 0.5 m.

The channels of actively prograding distributaries in the delta display bifurcated patterns (D) both upstream and near their mouths (Figure D-1.6). This type of pattern normally is associated with extremely low offshore slopes and low wave energy. Situated between the channels are interdistributary bays (E) displaying a variety of sizes and shapes. These bays are usually extremely shallow (generally less than a few meters) and contain brackish to normal marine water during periods of low flooding and fresh water during periods of high flooding. Sedimentation rates are relatively low. The bays receive sediment only during periods of overbank flow associated with floods.

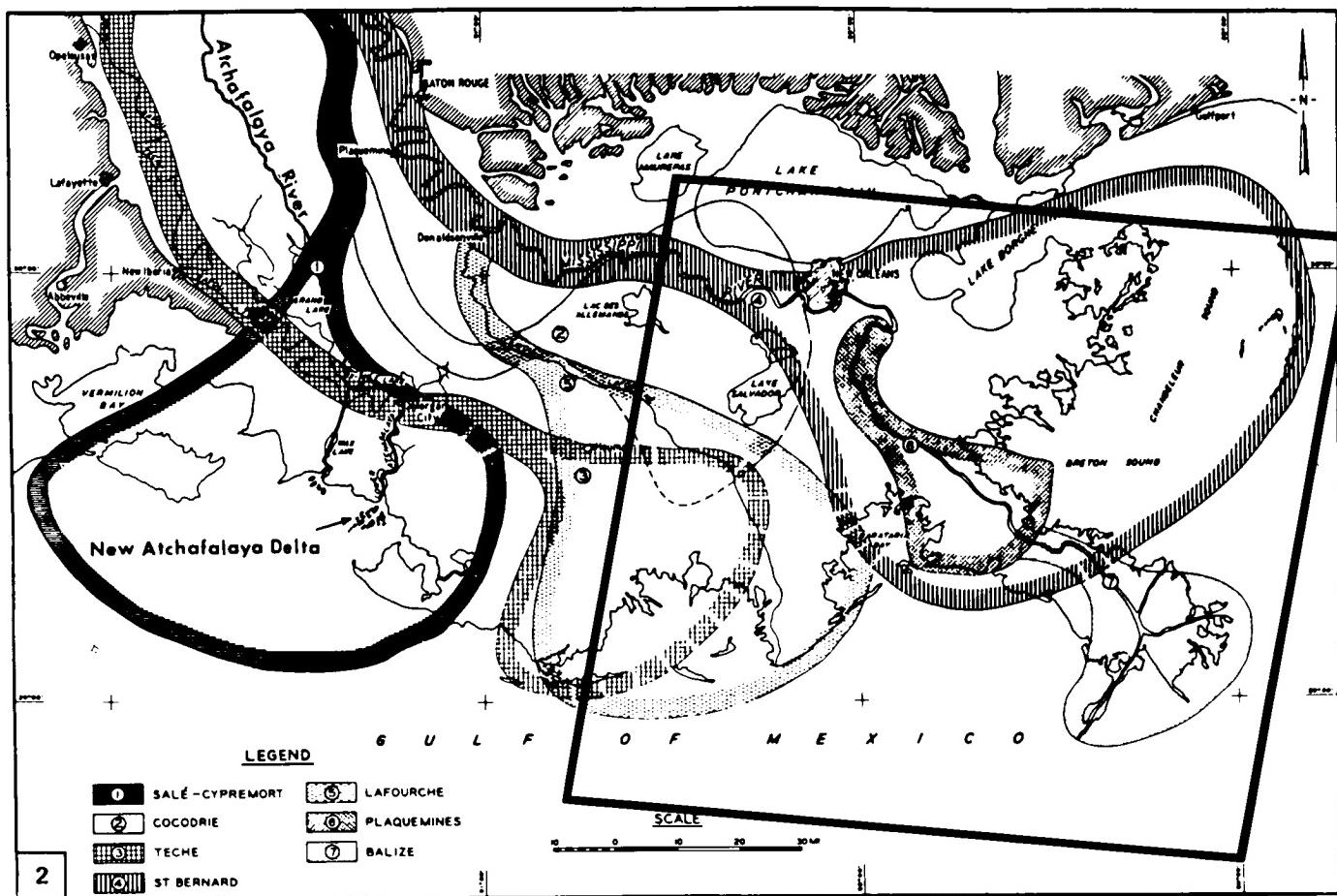
Breaches (crevasses) in the distributary levees result in the formation of subdeltas in the bays (Figure D-1.7). Ultimately, these result in large, complex bay fills or subdeltas of the delta distributary (F-1....F-4) (Figure D-1.8). The smaller breaches are referred to as overbank splays (G) and are active for only short periods, generally less than 10 years (Coleman and Prior, 1980). The bay fills comprise the most common geomorphic landforms in the active delta. Each bay fill forms initially as a break in a nearby major distributary natural levee during flood stage, gradually increases in flow through successive floods, reaches a peak of maximum deposition, wanes, and becomes inactive. Owing to continued subsidence, the marsh surface (H) of the bay fill is inundated by marine waters, reverting to a bay environment and thus completing its sedimentary cycle. The mass of sediment resulting from this crevassing process can vary in thickness from 5 to 20 m, covers an area of 150 to 300 km², and requires 100 to 200 years to complete a cycle. West Bay (F-1) formed by a break in the levee in 1938, Cubits Gap (F-2) in 1962, Garden Island Bay (F-3) in 1872, and Baptiste Collette (F-4) in 1874. Today, these bay fills are undergoing rapid land loss, with destruction of marshes and swamps (Figures D-1.9 and D-1.10), as a result of subsidence and compaction. New bay fills are no longer being formed, due to diking by man to maintain flow in the major navigation channels. Dredged canals (I) are present throughout the image and are constructed as access canals for subsurface hydrocarbon exploration and production. The circular patterns represent well sites associated with buried salt diapiric intrusions.

Immediately seaward of the actively prograding distributaries are the turbid river-mouth effluent plumes (J) (Wright and Coleman, 1971). Deceleration of a turbid plume as it spreads laterally allows the coarser sediment being transported to be deposited, forming the distributary mouth-bar and delta-front environments. The finer grained sediments remain suspended and spread laterally over broad distances, forming a turbid plume (K) that fronts the entire offshore delta; as these fine-grained sediments are deposited, they form the prodelta platform as the distributaries build seaward at rates of 100 to 150 m per year.
Landsat 1177-16023-5, January 16, 1973.

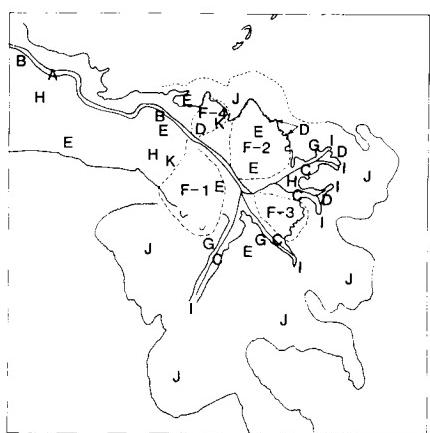
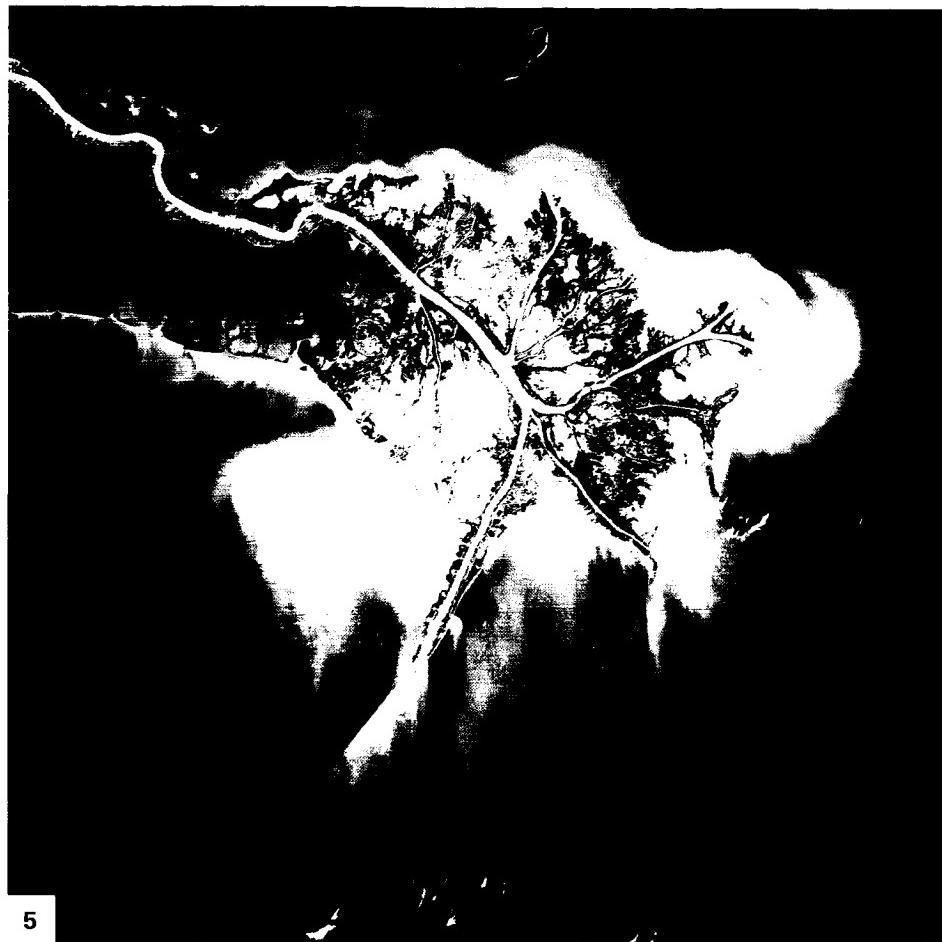
ORIGINAL PAGE IS
OF POOR QUALITY



ORIGINAL PAGE IS
OF POOR QUALITY



ORIGINAL PAGE
COLOR PHOTOGRAPH



9



10

PLATE D-2

ORIGINAL PAGE COLOR PHOTOGRAPH

The Danube River was known to the Greeks as the Ister River, and Herodotus called it "the greatest of rivers"; Napoleon referred to it as the "king of rivers." The Danube is the second largest river in Europe; it is approximately 2900 km long and drains an area slightly larger than 817000 km². It rises in the Black Forest Mountains of Germany and empties into the Black Sea. At the Romanian border, the river once cut a channel through the mountain ridge that joins the Carpathian arc with the Balkan Mountains, and a large interior sea was formed. Not until Recent geologic times has the Danube lowered its channel through the gap to drain this interior sea. The delta area (4345 km²) of the Danube was created in these times. Mean annual discharge is 6500 m³/sec, and maximum discharge up to 10 times that amount has been documented. Sediment discharge averages 122 million tons/year, of which 54 million tons consist of bed load (Samajlov, 1956).

To the north and west of the river delta, primarily Pliocene and Miocene sedimentary rocks form north-south-trending low hills (A) capped by Pleistocene loess up to 200 m high. East of the river and south of the delta, Paleozoic and Mesozoic sediments form high rolling hills (B) that attain elevations of 450 m. The present density of farmlands, however, effectively masks the relief in the Landsat Plate mosaic.

The main channel of the Danube (C) is highly migratory within its alluvial valley, so that numerous meander scars (D) are present within the valley. Small stretches of river braiding are found along the valley course. As the Danube turns abruptly east to form its delta plain, sedimentation has blocked numerous valleys of the north-south-trending topography, forming elongated freshwater lakes (E). Lakes found in the Mackenzie River delta of Canada are formed in the same manner (Figure D-2-1). The major distributaries of the Danube (F) consist of three major channels, the St. George to the south, the Sulina in the middle, and the Kilia to the north (Almazov et al., 1963). The St. George arm is 120 km long and has widths ranging from 200 to 500 m, while the Sulina arm, prior to 1860, had a length of 100 km and a width of 250 m. The Sulina was artificially diked in the period 1860-1895 for navigation purposes. Kilia, the youngest of the distributaries, having formed within the past 600 years, now receives the major part of the flow. It is slightly longer than 100 km and ranges in width from 300 to 700 m. The distributary channels are bordered by well-developed natural levees that are quite narrow, generally less than 250 m wide. Downstream, the natural

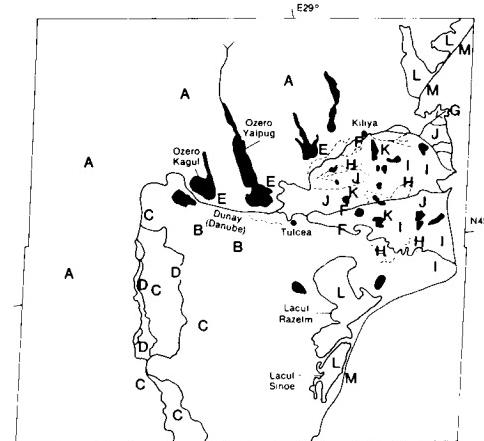
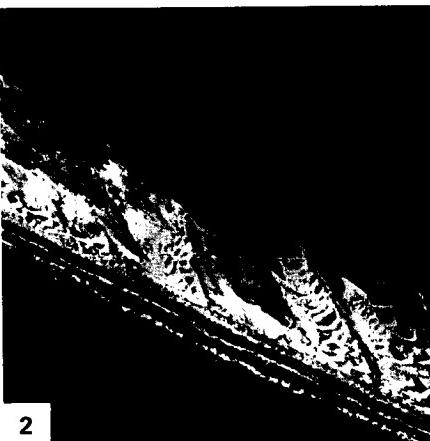
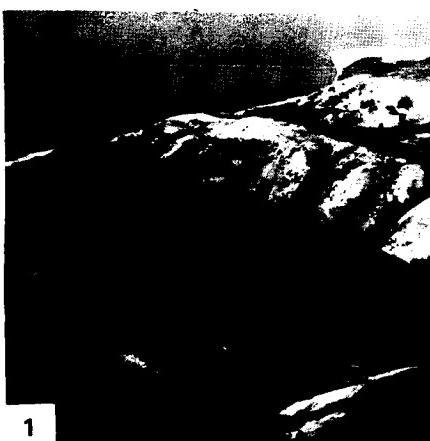
DANUBE RIVER DELTA, ROMANIA

levees decrease in width and height. Sinuous distributary channels result from migration as the channel cuts through former beach-ridge trends. Like distributaries in many deltas, migration of the channel is controlled by the presence of coarser material. The Kilia distributary to the north is the youngest part of the delta. Numerous bifurcated channels and overbank splays (G) are present, most of which are too small to show up in the satellite image. Offshore of these young prograding distributaries, slope is extremely low, the coastline is very muddy, and beaches are entirely absent.

Several abandoned distributary channels (H) are present within the delta plain. They indicate that the channels shift with time in response to subtle changes in slope, supplying sediment to all parts of the delta. In general, the delta consists of an older upstream part and a younger downstream part. Separating the two units is a large beach-ridge complex (I). These beach ridges display both progradational and transgressive characteristics. They are obviously associated with the prograding river mouths of the St. George, Sulina, and older distributaries. Once the Kilia distributary became the dominant channel, wave reworking of the older distributaries resulted in the formation of transgressive beaches at these river mouths. Similar transgressive beach deposits are shown in Figure D-2-2 from the São Francisco River, Brazil. The Danube beach ridges have heights of 5 to 10 m, and many contain coastal eolian dunes.

Predominant in the delta plain are roseau cane (marsh cane, *Phragmites*) marshes (J) and freshwater lakes (K). The marshes are an important resource of the delta, providing a major nesting place for waterfowl. The roseau cane forms thick root mats and results in organic content being exceptionally high in the delta deposits. Much of the delta area is occupied by freshwater lakes up to 3 to 4 m deep. These lakes are initially filled by overbank flow of organic-rich clays. As filling with organic-rich clays proceeds, the lakes become isolated from the overbank splays, and thick floating organic mats form the final fill.

Alongshore drift north and south of the delta has built linear barrier islands and spits (M), which enclose broad brackish and marine estuaries and lagoons (L). The barrier islands have relatively steep shorefaces, and many are characterized by coastal eolian dunes. The estuaries are important biological environments in that they form the spawning ground for many economically valuable marine species. **Landsat Mosaic, 2904-07510-7 and 2904-07504-7.**



ORIGINAL PAGE
COLOR PHOTOGRAPH

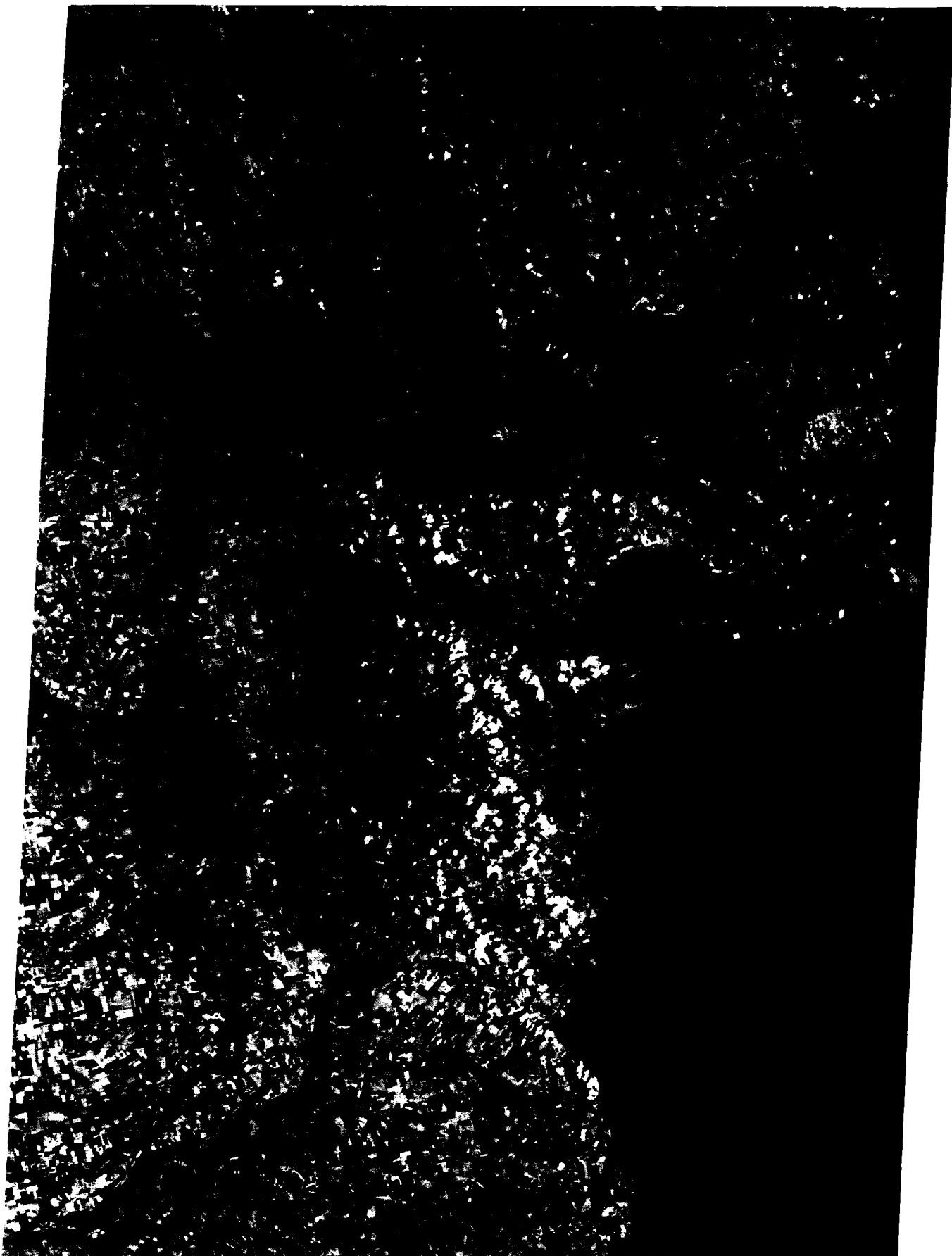


PLATE D-3

EASTERN GANGES/BRAHMAPUTRA RIVERS DELTA— THE ACTIVE DELTA

The Ganges and Brahmaputra Rivers combined have formed one of the largest deltas in the world, comprising approximately 105 640 km². The Bengal Basin, into which this delta has prograded, is bordered on the west and northwest by Lower Jurassic volcanics and on the east by Eocene sandstones and limestones. The southern boundary is the Bay of Bengal. The Ganges River originates near the Tibet/India border, and then flows southeast across India to combine with the Brahmaputra in the country of Bangladesh. The Brahmaputra River has its source in Tibet along the northern slope of the Himalayas, and flows across Assam into Bangladesh. The drainage basin, approximately 1.6 million km² in area, is geologically young, with large volumes of unconsolidated sediment available for transport (Morgan and McIntire, 1957, 1959).

The Ganges is primarily a meandering river, while the Brahmaputra is primarily a braided channel (Plate F-13). Their combined discharge into the Bay of Bengal is approximately 82 000 m³/sec during flood. Sediment load is extremely high, with suspended sediment load during flood stage reaching as high as 13 million tons per day (Coleman, 1969). Figure D-3.1 is a band 5 version of the lower Landsat image in the Plate mosaic that highlights the vast sediment load beyond the mouths of the Ganges. Because the climate within the delta is monsoonal, rainfall is seasonal. Vegetation is highly varied and generally dense in areas that have not been reclaimed for agriculture. The Bengal coast is mesotidal, with an average tidal range of 2 m. Wave energy modifying the coast is relatively low because of the extremely low offshore gradients that front the active delta.

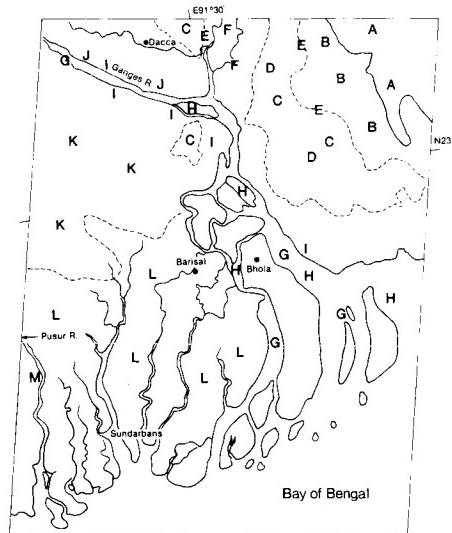
The mosaic covers the eastern active deltaic part of the Ganges/Brahmaputra Rivers and illustrates those landforms that are characteristic of a rapidly migrating channel system partially modified by tidal processes. The Tripura Hills (A) that bound the delta to the east consist of highly weathered Tertiary sediments that show abundant dissection resulting from the high annual runoff. These hills are a southerly extension of the folds seen in Plate T-48 with topography that is highly irregular and relief ranging from a few tens of meters to several hundred meters. Emanating from these highlands are a series of heavily vegetated alluvial fans (B) and small river terraces. During the Pleistocene, large volumes of sediment were delivered to the Bengal Basin, and former Pleistocene terrace surfaces are common along the valley of the river systems. The Tippera surface (C) has been assigned a Late Pleistocene age and consists of an extremely flat terrace composed of highly oxidized and deeply weathered clays and silts. The surface is easily mapped on aerial photographs because it displays a distinctive rectangular drainage pattern (D) resulting from man's modification for agriculture practices. The surface has an elevation of several meters above the Recent fluvial

and deltaic floodplain. During the Pleistocene and even in Holocene times, faulting (E) has been active in this earthquake-prone area, and many of the boundaries of Pleistocene surfaces are marked by relatively straight fault-controlled boundaries. Smaller rivers, such as the Meghna (F), have cut into these Pleistocene surfaces, forming rather extensive meander belts of abandoned channel scars.

The major part of the image shows the Recent delta surface of the Ganges/Brahmaputra Rivers. The main river channel displays a braided and anastomosing channel pattern (G). Figure D-3.2 illustrates this type of channel morphology, showing part of a midchannel island with large bed forms in an active distributary of the Brahmaputra River. Note the large number of active channels and the innumerable midchannel islands or sand bars (chars) that are characteristic of this type of channel pattern (H). These sand bars separate the flow into several channels, resulting in the braided pattern of the river. In such rivers, the sediment bedload is abnormally high, and rapid aggradation in the channel is common, constantly forcing the channel to migrate laterally. Recent channel scars (I), often unvegetated, can be observed along the margins of the active channels. During flood stage, these sand bars are generally eroded on their upstream end, with deposition on the downstream end, causing significant downstream migration of the islands from year to year.

The range of river stage varies considerably from low to flood stage, and adjacent channel banks are often characterized by many overbank splays (J). These splays are responsible for building up rather thick and broad natural levees that border the active channels.

In the northwest part of the image, the morphology of the delta plain is dominated by the abandoned channel scars of former river courses (K). These abandoned courses display evidence of both migratory braided and meander channel scars. These surfaces form the bulk of the rice- and jute-farming areas of Bangladesh. In the southeastern part of the image, the delta surface elevation becomes low enough to be inundated by tidal waters, and much of this area displays tidal plain morphology. A large percentage of the region has been diked (L), and the land has been reclaimed for agricultural purposes. The undiked regions (M), in the southwesternmost part of the image, are dominated by mangrove vegetation. Large tidal channels and tidal drainage networks characterize this part of the delta plain. **Landsat Mosaic 30303-03450-7 and 30303-03452-7.**



ORIGINAL PAGE IS
OF POOR QUALITY



PLATE D-4

WESTERN GANGES/BRAHMAPUTRA— THE ABANDONED DELTA

This color image covers the western abandoned and tidally dominated part of the Ganges/Brahmaputra River delta. Throughout Pleistocene times, the site of active deltaic sedimentation has switched. Today, the Ganges merges with the Brahmaputra, and the site of active sedimentation lies to the east (illustrated on Plate D-4). The major area of abandoned deltaic plain lies in the northwestern part of the image. More of this abandoned delta to the north appears in Figure D-4.1. Numerous abandoned channel scars (A) dominate the surface morphology. These scars are apparently remnants of former courses of the Ganges River and many of its distributaries. Most of the scars indicate that a meandering channel (Figure D-4.2) was dominant, now extensively modified by man. Channel scars are of similar size to channels presently active along the Ganges and its distributaries. Many of these former riverine channels are now tidally dominated (B). The Hooghly and Pusar Rivers are good examples of former major courses of the Ganges that have now become tidally dominated. Some well-defined meander belts display excellent examples of "ridge and swale" topography (C). Oxbow lakes (D), remnant meander channels that have been isolated by river cutoffs, are common on the abandoned delta surface. Much of the original channel morphology has been modified by man for agricultural purposes (Figure D-4.2), and in some cases, the modifications have nearly obliterated the original river-plain morphology.

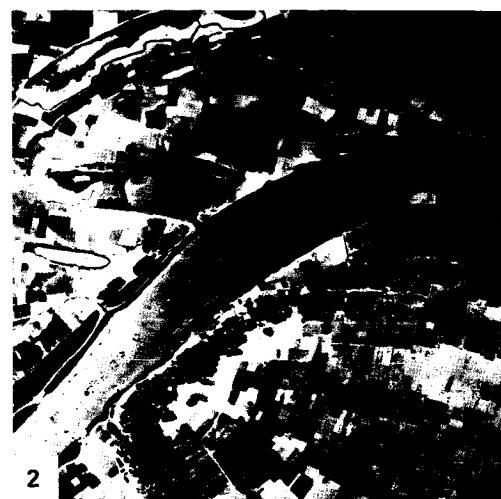
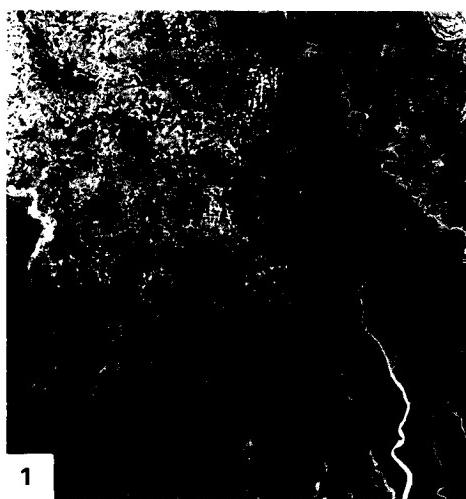
The inland part of the tidal plain has been diked, and the former saline lands have been converted to various agricultural and marine farming practices. This reclaimed land (E) has retained some of the general morphology of the original deltaic channel scars, but it has been modified by tidal drainage networks. Originally, this surface formed an extreme expanse of mangrove forests referred to as the Sunderbans. The only remaining large expanse of tidally dominated mangrove forests is shown on the image by the dark-red color (E), and here dense stands of many species of mangrove exist. The mangrove swamp is dissected by an intricate network of tidal drainage channels (G). Figure D-4.3 illustrates an intricate, dendritic, tidal drainage pattern on an abandoned delta surface of the Ganges/Brahmaputra delta. The channels display a variety of morphologies, ranging from highly sinuous patterns to straight, rectangular networks.

The larger tidal channels (H) form bell-shaped estuaries that are quite deep, and many of them serve as major transport

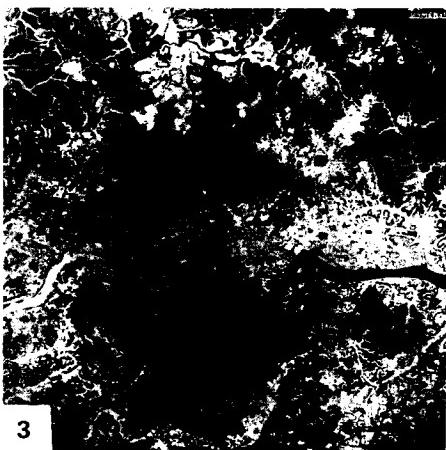
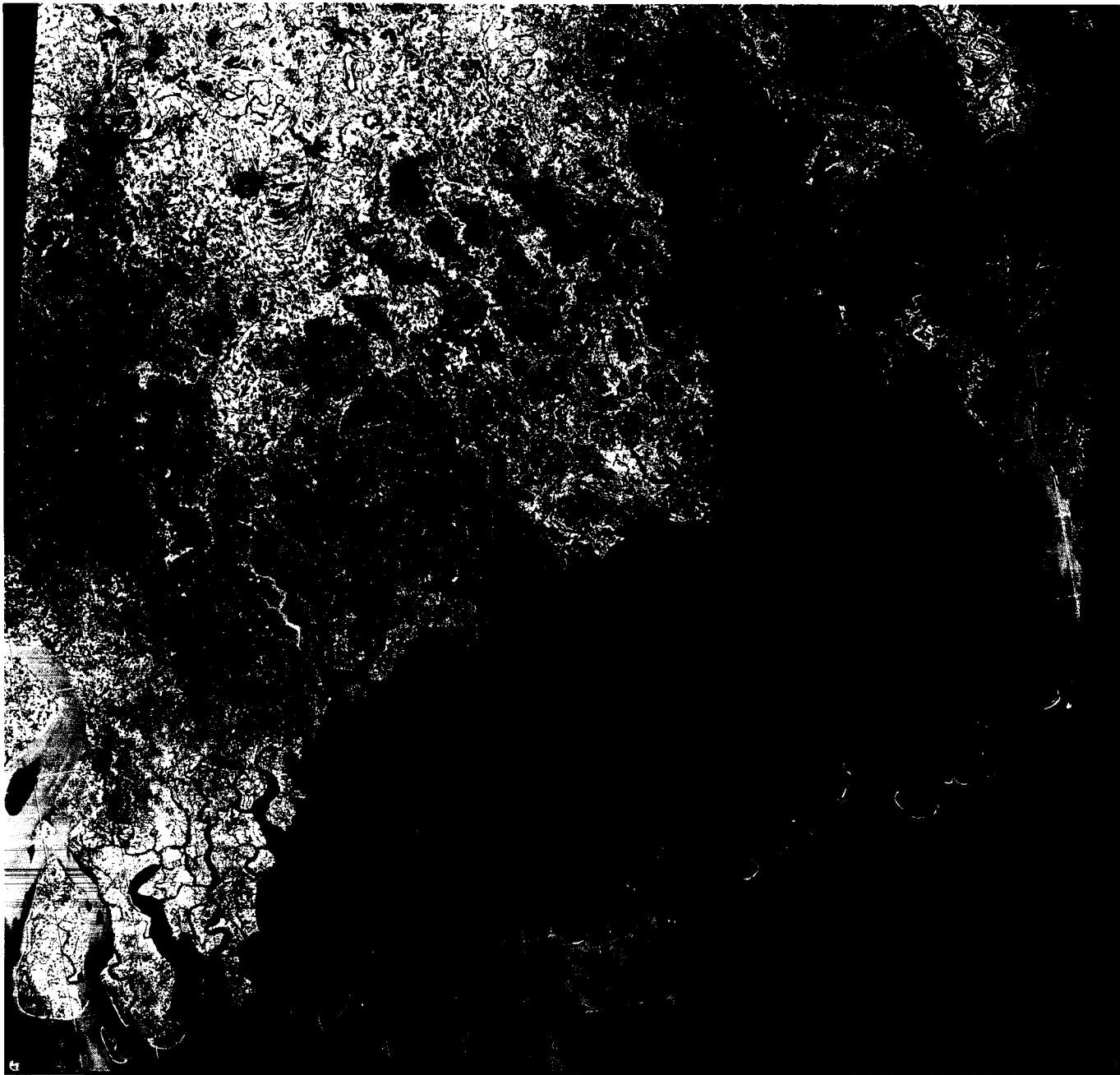
arteries. Inland, the estuarine channels display highly sinuous channel patterns, but appear to be stable rather than migratory. Comparison of old maps and aerial photographs with present-day imagery indicates that some major channel patterns have not changed in tens of years. Figure D-4.3 illustrates some of the delicate and efficient drainage networks that have been established on this former delta surface, nearly obliterating the original delta morphology.

Typical of many high tidal estuaries is the bell- or funnel-shaped river mouth. The tidal range varies considerably along this coast—mean tidal range is 1.7 m (spring, 2.3 m) at the mouth of the Pusar River, and 2.0 m (spring, 2.7 m) at the mouth of the Hooghly River. Tidal range increases inland as the tidal discharge moves into a much smaller cross section associated with decreasing channel widths. Inland from the mouth of the Hooghly River, the mean tidal range increases to 3.7 m (spring, 4.9 m).

The coastline is extremely irregular as a result of the large number of tidal channels that dissect the coast. Broad mud and silt flats border the coast (I). On the image (acquired at high tide), these mudflats are shown as highly turbid plumes. At low tide, many of these flats are exposed as fluid mudbanks. Most of the banks display elongated patterns, aligned in an onshore-offshore direction. This type of subaqueous morphology is common along many high tidal estuaries, and these shoals have been called "tidal ridges." The Bay of Bengal has relatively low offshore wave energy, and this, combined with the generally low offshore gradients, results in a low-wave-energy coastline. Much of the coast is blanketed by the mudflats, and only at isolated regions is any expanse of beach ridges found. The beach deposits (J) are most commonly composed of reworked shell debris and fine sand. These types of beach ridges have been referred to as cheniers on other delta coasts. Note that they are most commonly developed in the southeastern part of the image, opposite the Swatch of No Ground. This submarine feature is a broad canyon that was formed during Pleistocene low sea levels, feeding fluvial sediment to a large submarine fan. As a result of its presence along the coast, the offshore gradients are somewhat higher than on adjacent coasts, and the relatively higher wave energy results in the formation of these coarser grained deposits. **Landsat-2 MSS Scene, Thailand Landsat Station, November 21, 1981.**



ORIGINAL PAGE IS
OF POOR QUALITY



3

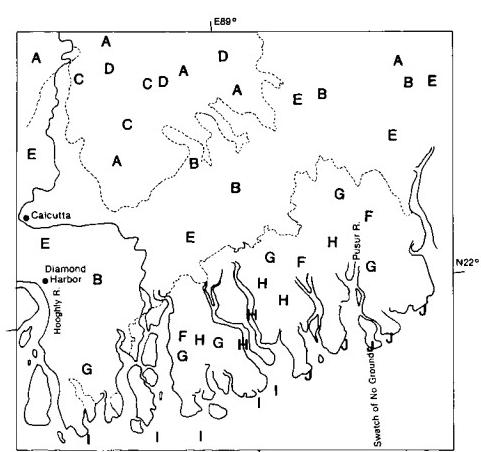


PLATE D-5

CHANG JIANG (YANGTZE) RIVER DELTA, CHINA

The Chang Jiang or Yangtze is the longest river in China. It originates in the Tibetan highlands province on the southern flank of the Kunlun Mountains of southwestern China. The river's course takes it from the Kunlun Mountain region (elevation approximately 5100 m) to the East China Sea through variable terrain for a total length of 5590 km (for the main river). The Yangtze drainage basin, which extends over 1830000 km², can be roughly divided into two sections (Samajlov, 1956). Rugged mountain terrain is characteristic of the western part, which lies within and south of the Szechwan Basin of west China where the main river has its source. It flows through valleys and spectacular steep-sided gorges (Plate F-16) for 3790 km before it encounters a vast alluvial plain beginning some 950 km from the coast. This alluvial area is one of the most fertile and populated regions of China. The river is fed primarily by snow melt in the upper 75 percent of its course. Rainfall averages 970 mm/yr over the middle and lower parts of the catchment basin. Because of the narrow river valleys and erratic discharge, river stage can rise rapidly (as much as 10 m/day). The stage ranges between 20 and 30 m, but sometimes reaches a maximum of 40 m.

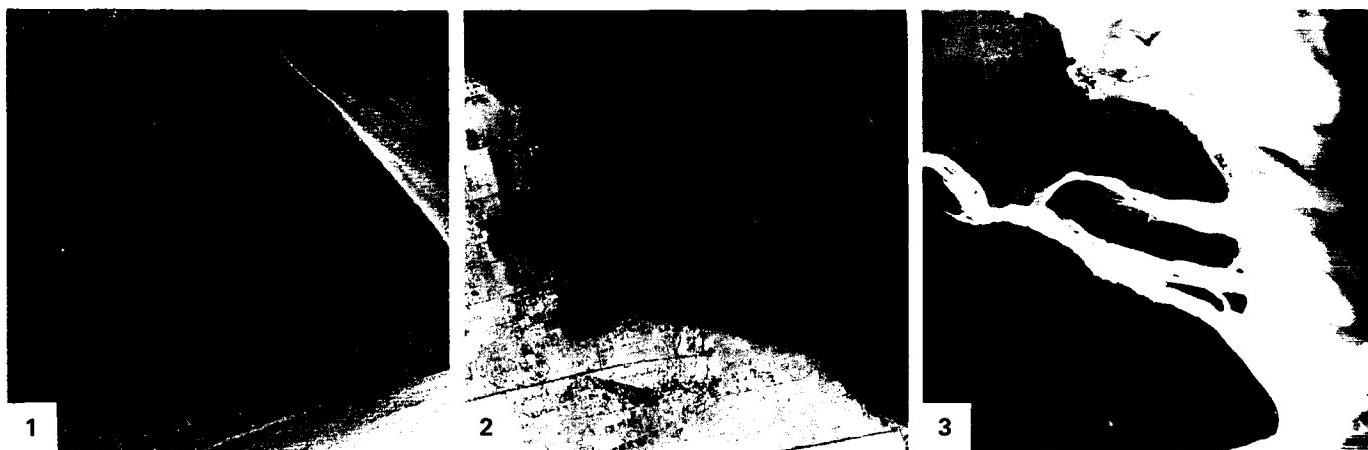
The eastern part of the Yangtze River basin is primarily a vast alluvial plain with numerous lakes situated along the main course. The most easterly end of this series of lakes is located around (A) on the index map. The coastal lowlands along the natural outlet of the huge basin are extensively cultivated and are irrigated by a rectangular grid of canals (Figure D-5.1, a Landsat subscene; note the city of Shanghai, a dark zone in the northwest corner of the figure). In this vicinity, the Yangtze is building a delta that is prograding into the East China Sea at an estimated rate of about 2 km per century.

In most delta classifications, the Yangtze would be categorized as a tidally dominated type because it has a semidiurnal tide of 3.7 m. Like other deltas (e.g., Shatt el Arab, Plate D-13) that are exposed to low levels of wave energy (e.g., the Colorado Delta, Plate D-12) but are building into basins with a high tide range, the channel mouths in this scene are bell-shaped. Other features common to deltas that are shaped mainly by tidal forces are the elongate sandy tidal bars (B), tidal flats (C), and lineated sediment plumes (D), all evident in the Landsat subscene shown in Figure D-5.2. These reflect similarly shaped seafloor topography. The tidal flats, as well as the subaerial coastal plains, are

cut by numerous tidal channels (E). Because of the incredible demands on the subaerial parts of the lower delta to support a massive population, the surface is a maze of intersecting canals (F), many of which serve the triple purpose of drainage, irrigation, and transportation. The speckled pattern (G) that occurs over the entire subaerial delta, especially evident in Figure D-5.1, represents inhabited and cultivated areas segregated by the aforementioned network of manmade canals and a few natural channels.

The Yangtze River discharge is about 690 km³/year (22000 m³/sec) at its mouth. Associated with this discharge is a heavy load of silt. The magnitude of this load is better revealed in a Landsat MSS band 5 image (October 1976) that emphasizes the offshore sediment plumes introduced from the Yangtze and other sources (Figure D-5.3). It is estimated that more than 142 million m³ of sediment pass down the Yangtze every year. Although subsidence is taking place in the delta, deposition occurs at a more rapid rate, resulting in progradation. As sedimentation continues in the delta, reclamation dikes are built that contain sluice gates to allow inflow during flood tide and the settling out of mostly silt- and clay-sized particles. Much of the coastline along the northern flank of the delta, as well as in the main channel, has actually been built by man's intervention. The effects of active reclamation projects along the northern flank of the delta are readily surmised from the geometric appearance of this coast, as seen in the Landsat subimage of Figure D-5.2. Land recently reclaimed (I) by this process is now under extensive cultivation and habitation. Coastal protection with seawalls and rip-rap is widely used to preserve the coastal beach and agricultural lands from both marine and fluvial erosion (Figure D-5.4). These areas are dominated by tidal processes. Only the southern flank of the delta maintains the balance between wave action and sedimentation to create active but narrow beaches (J). The remainder of the coast is fronted by tidal flats (C) and tidal bars (B).

The combination of rich lower deltaic plain sediments, a hot wet summer, and a shallow water table leads to heavy cropping. Rice is by far the most important summer cereal. Other summer crops are cotton, soybeans, and corn. Rice is grown in rotation with winter wheat. Not only the lower delta serves as an important agricultural area, but also the entire alluvial plain, which extends inland some 900 km. **Landsat 30067-01462-7, May 11, 1978.**



ORIGINAL PAGE IS
OF POOR QUALITY



4

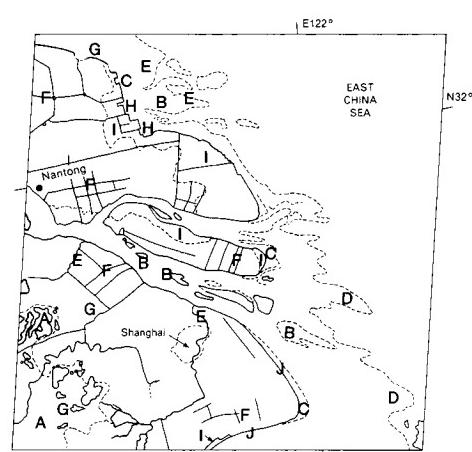


PLATE D-6

HSI (PEARL) RIVER DELTA, SOUTH CHINA

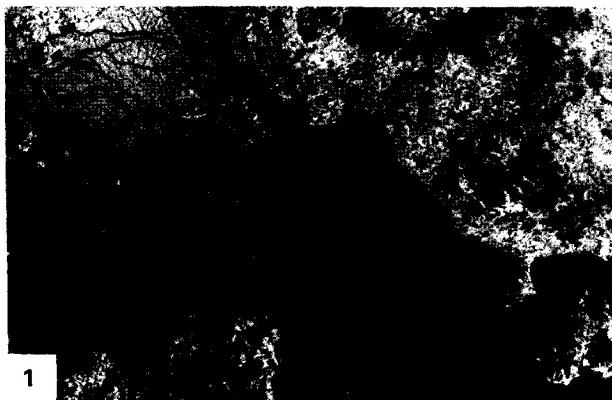
The Hsi River delta is also commonly referred to as the Canton delta or the Pearl River delta. Fed by three rivers at or near its head, the Hsi River delta is building into the Chu Chiang estuary (A), which interfaces with the South China Sea. These three rivers are the Si-Kiang or Hsi River (B), the Bei-Kiang (C), and the Tung-Kiang (D). Each is clearly visible in the Plate. However, together with their distributary networks, a very complicated deltaic morphology has developed. The distributaries of these rivers are separated by a large and rather circular mountainous block, the Chung Shan (E), around which deltaic sediments are being deposited as the deltaic plain progrades to the southeast.

Tributaries that contribute to the delta vary considerably in length, discharge, and sediment load. The Si-Kiang (West River) is the most important with regard to these parameters. It is nearly 2000 km long and can be considered South China's equivalent to Central China's Yangtze River (Plate F-16) and the Huang He River (Plate F-3) of Northern China. The Hsi River is an important artery of commerce because it is navigable by ship traffic over most of its length. Total discharge of this river system (the three major rivers and the smaller ones) is approximately $302 \times 10^9 \text{ m}^3/\text{year}$, or an average of over $9500 \text{ m}^3/\text{sec}$. Of this total discharge, about 78 percent is contributed by the Si-Kiang (Hsi River) and its distributaries. Of the other two major tributaries, the Bei-Kiang (North River) accounts for about 12.8 percent of the total, and the Tung-Kiang (East River) contributes 8.5 percent. Smaller tributaries such as the Liu Qi River form part of the riverine network that builds the Hsi (Pearl) River delta, but their combined contribution to the total discharge throughout the system is only about 0.5 percent. Maximum discharges of the Hsi River system are over $70000 \text{ m}^3/\text{sec}$, which, in the whole of China, is second only to that of the Yangtze. Discharge is highly seasonal with nearly 78 percent of the annual volume occurring between April and September. The main contributor, the Hsi River, rises in East Yunnan province and flows east through Kwangsi and Kwangtung provinces to the region shown in this Plate where effluents from the aforementioned rivers and their distributaries flow into a shallow bay commonly known as the Pearl river estuary or Chu Chiang. Eight major channels and numerous smaller ones debouch sediment-laden fresh water into this water body, causing rapid seaward progradation of subaqueous shoals and the deltaic plain. It has been estimated that, during the summer peak-flow months, approximately 95 percent of the annual suspended load (~ 72500000 metric tons) is discharged through the delta. Although impressive, this suspended load is only about one tenth of that carried by the Yangtze, even

though their total discharges are similar. Despite this lower load, the Hsi and other contributors to the Pearl River system have succeeded in constructing a delta over 100 km long during the past 4000 to 5000 years. In the process of delta-building, many former bays (F) became sediment-filled and have now become a part of the low-relief delta plain. Local topographic highs (G) of the present low-lying deltaic plain were once islands in the bays that have subsequently been filled with deltaic deposits.

The seaward end of the subaerial delta comprises a complicated network of tidal creeks and major distributary channels with bell-shaped mouths typical of tide-dominated distributaries. These wide river mouths, although characterized by shifting shoals, allow excellent access to important inland ports such as Canton (H) by shallow draft ships and a variety of local fishing boats. An excellent example of this intricate alluvial morphology with numerous small channels can be seen at the distal margin of the Tung-Kiang (I). Although sedimentary processes produce complicated delta morphology under low wave energy, moderate tide, and river-dominated conditions, much of the present delta actually represents reclaimed land produced by a combination of manmade embankments and natural sedimentation forced by tidal flow. An enlarged image of part of the deltaic plain and Pearl River estuary (Figure D-6.1) shows the geometric pattern of manmade canals that irrigate and help to deliver sediment for building these fertile lower delta lands. Note the square-appearing land reclamation plots at the distal ends of prograding deltaic wetlands.

Historical records suggest that man has been cultivating the deltaic lands of this region of South China for well over 1000 years. Not only did man expand his agricultural territory as a consequence of natural advancement of the delta, but he learned to build new land by constructing dikes to accelerate reclamation. Many of these dikes are constructed so that the structure is submerged at high tide. This procedure allows tidally raised turbid water to enter the diked area and be trapped during the ebb-tide part of the cycle. This produces a new increment of sedimentation to the diked area with each tidal cycle. By 1950, the lower delta had over 1300 km of levees and dikes, some as much as 7 m high and 4 m wide. Since then, many others have been added. The net result has been to enhance agricultural production by increasing protection against the destructive effects of floods and by producing new land at a faster rate than the natural delta accretion process. Major crops of the lower delta are rice, sugarcane, and mulberries. Figure D-6.2 shows part of a canal and dike in a foliage-covered reclaimed portion of the delta where sugarcane is the main crop. **Landsat 1520-02210-5, December 25, 1973.**



ORIGINAL PAGE IS
OF POOR QUALITY

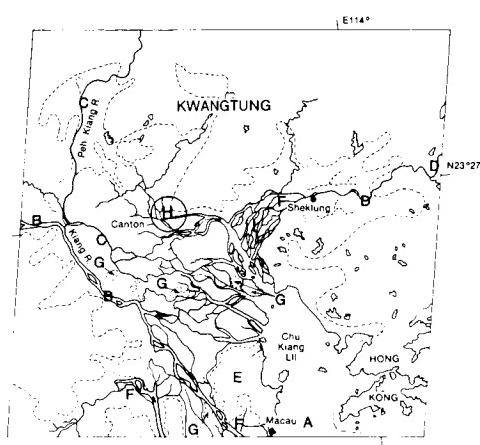
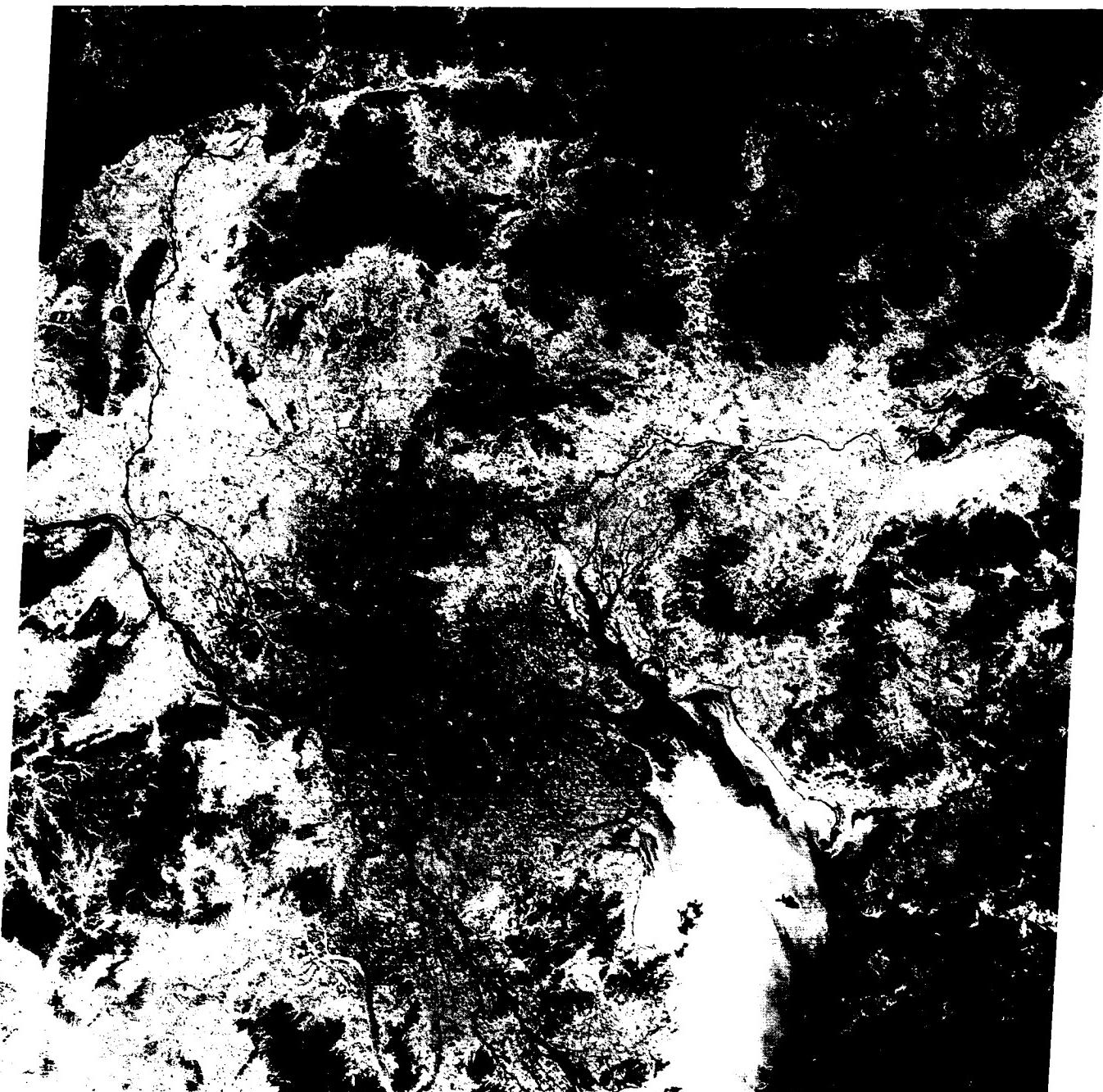


PLATE D-7

The Mekong River is one of the larger rivers in southeast Asia. The river's headwaters are located in the Tibetan Plateau and cover an area of 800000 km². From its source in southern Qinghai Province of China, the Mekong follows a length of 4300 km and displays a low gradient, as slight as 2.5 cm/km in the lower reaches. The river empties into the South China Sea, where offshore wave energy is moderate, resulting in wave reworking of the delta front sediments. Tidal range at the mouth of the Mekong is 3.2 m; the high tidal range, combined with monsoonal weather patterns, sets up relatively strong littoral currents that pass generally to the south. This high tidal range strongly influences the river channel, and shifting water-level effects extend up the main channels to Phnom Penh, a distance of 388 km. Discharge is highly concentrated during the monsoonal period of August through October, with an average of 39000 m³/sec. Low water discharge is 1700 m³/sec. The annual yield of 170 million metric tons is quite large.

The Mekong delta covers an area of 13470 km² in Vietnam (Gagliano and McIntire, 1968). This image of the delta is somewhat obscured by cloud cover that is common in the tropics. The delta is bounded to the northwest by pre-Quaternary surfaces, only a small area of which appears on the image (A). Pleistocene terraces border the river and delta; in the lower delta, these terraces (B) gradually dip below the modern deltaic plain (C). To the southwest of the delta plain lies the Trans Bassac depression (D), a lowlands that parallels the main southern distributary, the Bassac. This region is one of the natural overflow basins of the Mekong system through which large volumes of river flow move westward to the Gulf of Thailand. This relatively featureless flat plain has been constructed by sediment drifting southwest along the coast from the river mouths and by overbank flooding. Much of the area consists primarily of brackish water marshes and small tidal channels bordered by mangrove vegetation. Some of the area has been reclaimed for agricultural purposes, and many of the long straight scars on the image represent irrigation canals.

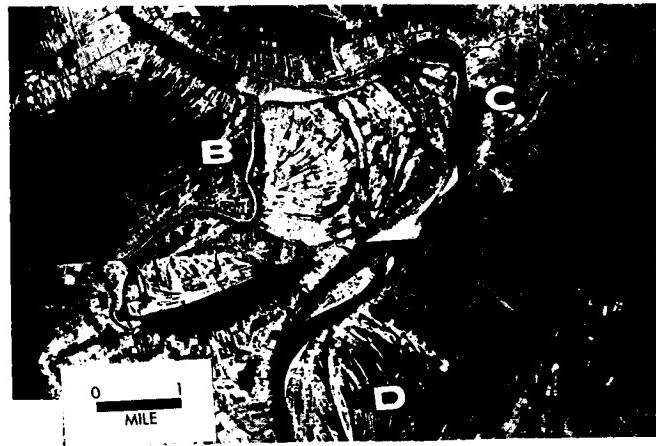
The largest basin in the delta is the vast, primarily uncultivated Plain of Reeds (E), which has an area of 4560 km². Cultivation is restricted mainly to the small channel banks of sluggish streams and along the long manmade canal banks that are used for drainage. The vegetation of this plain consists mainly of numerous species of *Juncus*, a fresh to brackish water marsh plant.

MEKONG RIVER DELTA, VIETNAM

The major distributaries (F) of the delta plain (Figure D-7.1) are characterized by a braided pattern, with channel division around alluvial or midchannel islands. Migration of channel banks is quite high and often erratic in nature, as shown by ridge and swale topography (Figure D-7.2). Most of the midchannel islands have been diked and are cultivated. Among the most conspicuous landforms in this delta are the broad natural levees (G) that border the active channels and surround the interdistributary basins (called bengs in Vietnam). These levees are relatively high, averaging several meters above the adjacent marshy interdistributary surface. Overbank splays are quite common and tend to form small erosional channels across a natural levee. These overbank channels are generally markedly straight and parallel to one another. The high tide, which constantly causes reversals in flow near the river mouths, results in well-developed bell-shaped river-mouth morphology (H) containing numerous bars and spits that obstruct the river mouth. This type of channel-mouth morphology is quite common on most high-tide-dominated river deltas. Discharge down a particular distributary has varied with time, thus introducing pulses of sedimentation at a specific river mouth.

As a result of alternating progradation and coastal retreat, the morphology of the lower delta plain exhibits alternating stranded beach ridges (I) and mudflats (Figure D-7.3). This beach-dune ridge plain extends inland to distances up to 60 km. These stranded beaches or cheniers are composed of sand and shell, parallel the coastline, and display elevations up to 5 m above the adjacent swales. The swales are normally occupied by small tidal channels and salt-tolerant vegetation such as mangrove and Nipa palm. Coastal mudflat sediments underlie the salt marshes and swamps. The elevations of these ridges make them ideal sites for habitation and cultivation of oil palms. The delta shoreline is normally fronted by broad tidal mudflats (J) that are exposed at low tide (Figure D-7.3). Large volumes of organic debris that accumulate on these mudflats are extremely rich biologically.

Mangrove vegetation (K) is spread throughout the lower delta plain and on the banks of the numerous small tidal channels. The bulk of the mangrove area, however, is situated in the tidal estuary (L) southeast of Saigon. This basin lies "updrift" of the delta and is deprived of sediment nourishment from the adjacent river mouths. An intricate network of interconnected tidal channels cuts through the mangrove and Nipa palm swamps and marshes. Landsat 1163-02450-7, January 2, 1973.



ORIGINAL PAGE IS
OF POOR QUALITY



3

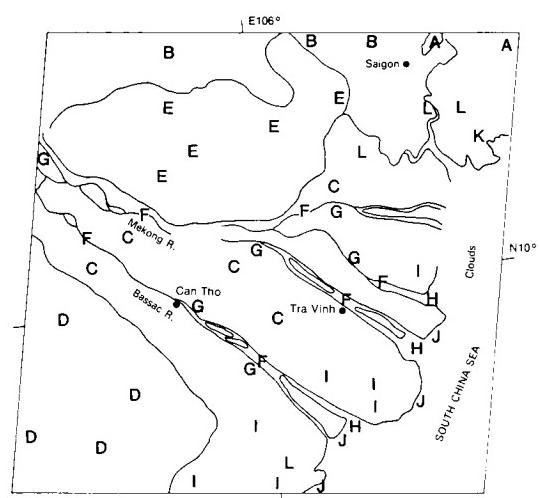


PLATE D-8

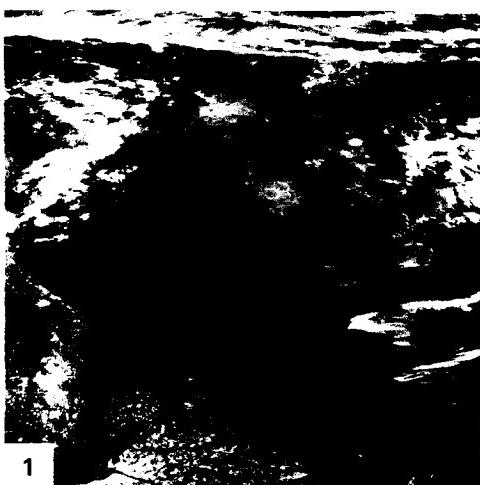
The Volga River, the largest river system in Europe, rises in the Valdai Hills northwest of Moscow and flows through its 3370-km length to discharge into the Caspian Sea. It has a drainage area in excess of 1.3 million km². Over much of this drainage area, the river traverses a broad, often swampy basin, surrounded by low morainic hills. Within its basin lives nearly 25 percent of the total population of the U.S.S.R., and the river and its tributaries carry about two-thirds of all the riverborne freight in the country. Today, much of the flow is regulated through a series of dams and reservoirs. The Volga is fed mainly by snowmelt. High discharge, in May and June, varies from 20000 to 36000 m³/sec, and low discharge, from August through March, is rather constant at 3000 to 5000 m³/sec. Prior to damming, the river delivered 25.5 million tons of suspended sediment and an unknown quantity of bedload to the Caspian Sea (Zenkovich, 1967). On entering the Caspian Sea—a landlocked, once marine body now brackish from freshwater dilution—this load has formed a large (10400 km²) delta, shown in both the Plate mosaic and a southeast-looking oblique photo (Figure D-8.1) taken during the STS-18 (Shuttle) Mission 51B.

The river system can be described as an erratically discharging river, flowing into a receiving basin whose water level has varied consistently during the Recent. Within the receiving basin, wave and current energy is extremely low. The level of the Caspian Sea has been fluctuating significantly, and in the last 150 years, water level has fluctuated over 6 m; during the period 1930 to 1963, water level dropped 2.6 m. This water-level fluctuation has led to three zones in the delta proper. The higher areas of the first zone are referred to as "Behr's mounds," linear ridges of clayey sands ranging from 400 m to 10 km in length and averaging 8 m in height. Between the ridges are elongated depressions (*ilmens* in Russian) that fill with water and become either fresh or saline bays. It is believed that these ridges and swales represent coastal banks now stranded by the falling level of the Caspian Sea. The delta proper, comprising the second zone, displays low relief (generally less than 1 m) and is the site of active and abandoned channels, interdistributary regions (often containing saline water), small dunes and algal flats, and small, partially vegetated eolian dunes (Figure D-8.2) that derive their sediment from the exposed dry channel courses. The third zone is the submarine part of the delta, which forms a broad platform extending 30 to 60 km offshore.

VOLGA RIVER DELTA, U.S.S.R.

The main eastern distributary, the Sumnitsa (A), enters the delta north of the city of Astrakhan and immediately forms a complex anastomosing channel pattern (B) consisting of numerous dry and abandoned channels, as well as active channels. Flow in the channels is so erratic that, for much of the year, little or no water flows in the channels. Strong winds erode the channel floors and form linear dunes on the overbank areas. The left side (after turning) of the Plate shows the natural levee of the main river channel across which small eolian dunes have been deposited; the source of the sand is the adjacent channel. The active channels that contain river flow are ice bound during the period December through March. Before the construction of dams, these complex channels constantly shifted their position with each flood. North and west of the delta are broad coastal dunes (C), many of which have been stranded inland by the falling level of the Caspian Sea. Many of these show little or no orientation and are generally devoid of substantial vegetative cover. The zones marked "D" are areas of Behr's mounds. A similar extensive system bounds the western flank of the delta, in which interdune areas enclose elongate lakes. The sand ridges have been stranded by the falling level of the Caspian Sea and consist of marine sands reworked by eolian action; they generally contain a high shell content.

In the lower delta, the small distributaries display well-developed, complex, bifurcated channel patterns (E), and because of this process, the few major distributaries that enter the head of the delta have split, producing more than 80 active river mouths in the delta (Figure D-8.1). This figure shows the complex distributary channel patterns of the river mouth and the adjacent mudflats. At the river mouths, many shoals and triangular river-mouth bars (called middle ground shoals in the Mississippi River delta) are the most common geomorphic landform. Relief is very low, rarely exceeding 0.5 m. Immediately offshore is another complex system of subaqueous channels (F) and shallow shoals that forms the delta-front platform, or the foredelta. Because of their small size, most of these are barely visible in the image. All along the front of the delta, mudflats, coquina banks, and muddy sand shoals (G) are present, associated with the rapid progradation of the channels before damming. On the lateral margins of the delta are algal flats and salt pans which have accumulated in those parts of the delta that are no longer active or in depressions that have been stranded by the falling level of the Caspian Sea. Landsat TM 50115-06582-4 (right), June 24, 1984; TM 50122-07044-4 (left), July 1, 1984.



ORIGINAL PAGE IS
OF POOR QUALITY

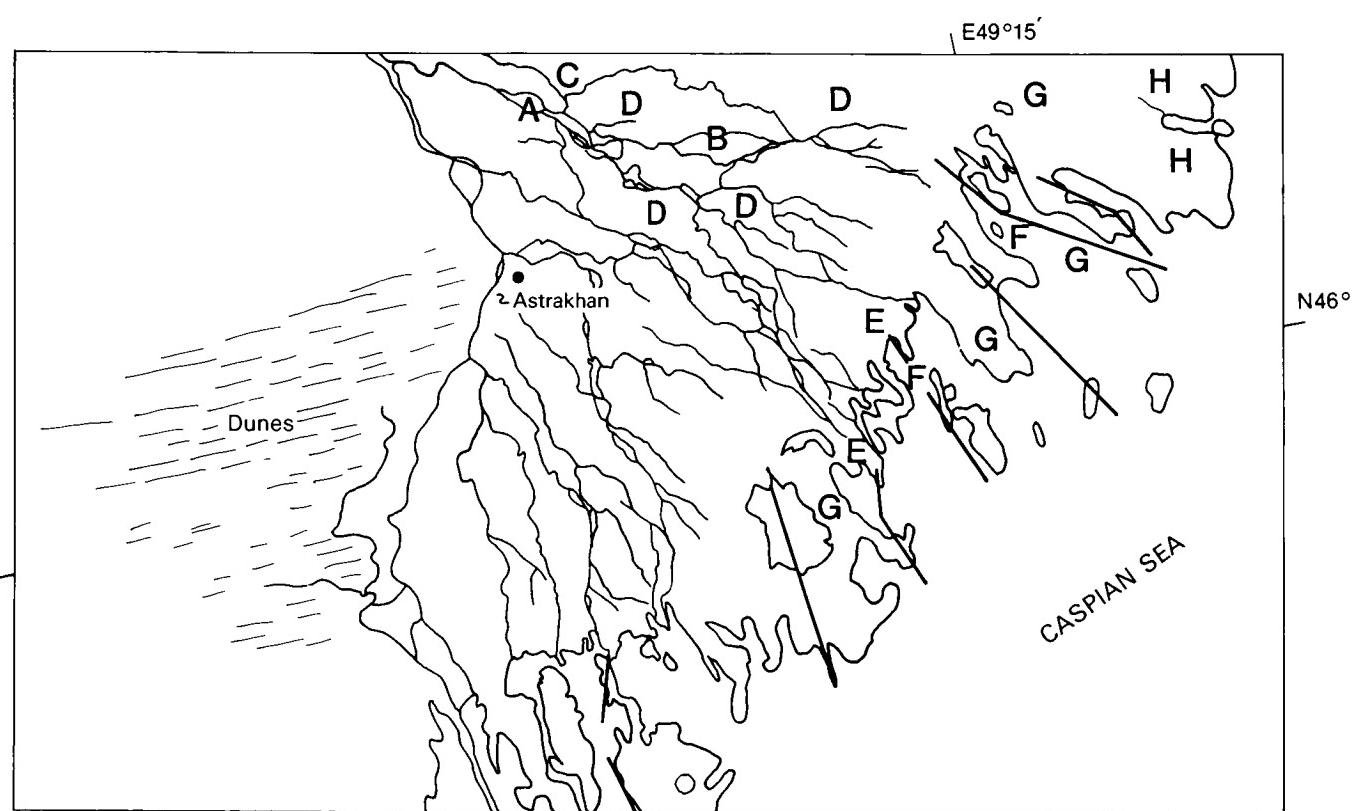
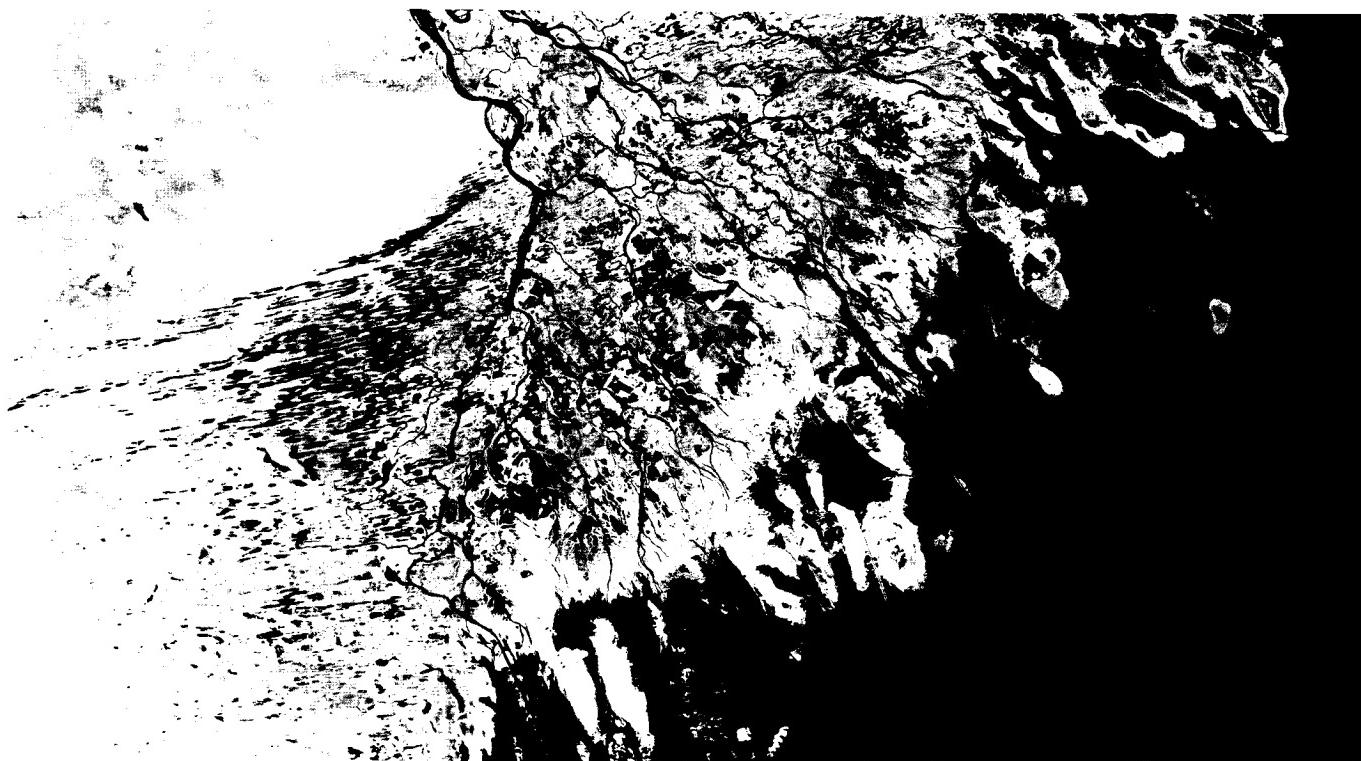


PLATE D-9

The Yukon River, the fifth longest river system (3185 km) in North America, has its headwaters in a group of lakes on the border between the Yukon Territory and British Columbia in Canada. After flowing across central Alaska, it empties into Norton Sound in the Bering Sea. Within its alluvial valley, the river is a complex meandering and braided river system that transports a large volume of extremely coarse sedimentary debris. The valley is flanked on both sides by bluffs composed either of mainly Pleistocene unconsolidated sediment or of Precambrian schists, Cretaceous sandstones and shales, or extrusive rocks. The river system drains an area of approximately 855 000 km² and has a discharge of 6220 m³/sec during breakup. Suspended sediment discharge has been estimated to range from 30 to 90 million tons per year. This river delivers approximately 90 percent of the sediment entering the northeastern Bering Sea (Eardley, 1937).

The source area extends across a region of continuous to discontinuous permafrost in which the effects of mechanical weathering prevail. The sediment is dominated by silts and fine sands containing an abundant percentage of feldspars. The channels and offshore delta region are ice-bound from late October through late May. During breakup, much of the sediment bypasses the delta fringe and is deposited offshore by a combination of over-ice flow and sub-ice flow through a series of channels that extend up to 25 km offshore. Tides in Norton Sound range from 1 to 1.5 m, and tidally induced currents are active throughout the year. In the late summer and early fall, frequent southwesterly winds and waves associated with major storms control the transport of sediment. High wave energy and decreasing sediment discharge from the river result in significant coastal erosion and reworking of the deltaic sediments (Williams, 1952).

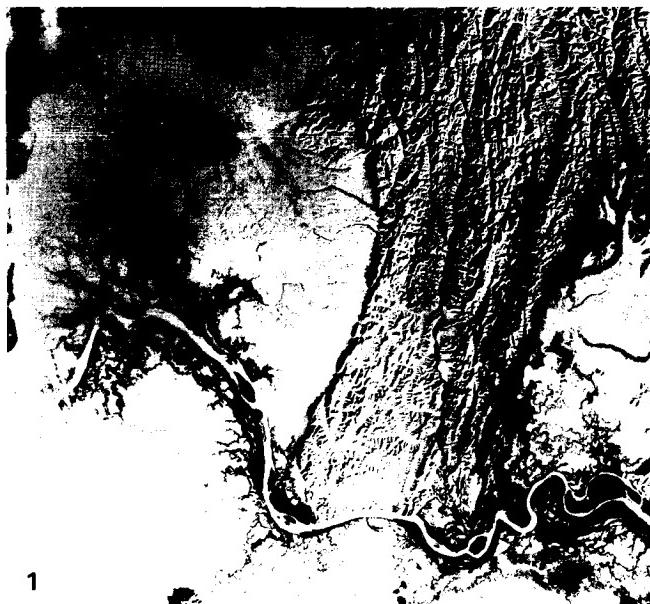
The delta of the Yukon River is a relatively young geologic feature, having begun to form not earlier than 2500 years ago when the river shifted its course to where it presently enters Norton Sound. East of the Yukon delta is a series of Cretaceous highlands that attain elevations ranging from 300 to 600 m. A well-developed trellis drainage network has developed in these sandstones and shales. The fluvial channel (B) of the river is a highly complex meandering river with numerous stretches of intense braiding. Just before entering the delta, the channel displays

YUKON RIVER DELTA, ALASKA

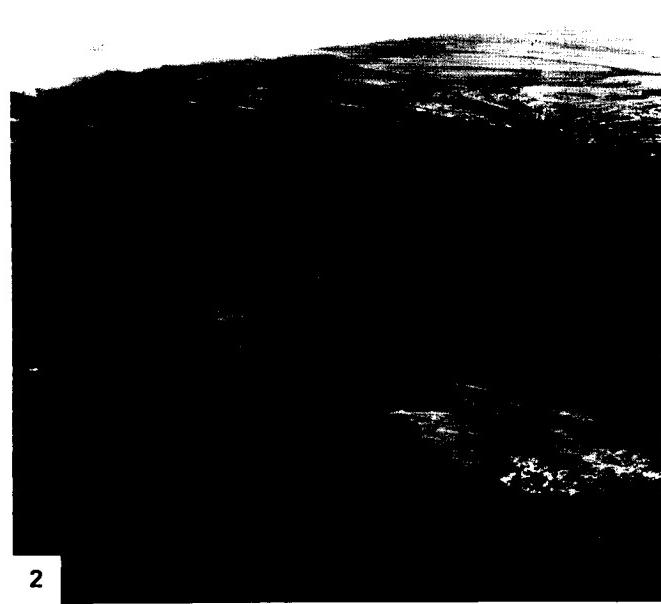
an extremely complex braiding pattern with numerous midchannel islands and braid bars. Farther down the delta, the distributary pattern displays a highly complex anastomosing pattern (D). This is highlighted in Figure D-9.1, a winter (February 7, 1979) Landsat scene in which snow cover contrasts with the still-flowing distributary channels. In the summer, numerous overbank splays break the channel margin and flow into the adjacent interdistributary lows. Near the distributary mouths, the channels bifurcate to form numerous small channels (E) that prograde out onto the delta front that previously served as the subice platform or the shorefast ice zone. The delta plain is fringed by prograding tidal flats and slightly coarser zones associated with the distributary mouth bars.

The subaerial delta plain (F) contains a complex assemblage of active and abandoned distributary channels, natural levees (which are extremely small), interdistributary marshes, and numerous small freshwater lakes (Figure D-9.2, showing the similar Colville River delta, Alaska (see also Plate F-11)). The active distributaries display relatively high sinuosity, and channel migration is rather common as a result of the abundant coarse material in the delta plain. Interdistributary marshes are characterized by poorly sorted peaty silt and mud. Older parts of the delta (G) are often capped by freshwater peats up to 1 m thick. Numerous small freshwater lakes are present on this surface. Incipient permafrost development has resulted in the formation of peat mounds at the sites of former lakes. Many small shallow lakes are present in the delta plain, with most now in the process of being infilled with vegetation.

The delta-front platform consists of prograding tidal flats, distributary mouth bars, and sandy low-relief beach ridges resulting from reworking by major storms (Figure D-9.3). Tidal flats are typically 100 to 1000 m wide and consist of poorly sorted sandy silt. Poorly sorted silty sand forms the progradation linear beach ridges (H) present on the southwestern side of the modern delta. South of the delta are a series of well-developed linear beach ridges (I); between the ridges, small linear lakes have developed in the swales. **Landsat 2505-21303-7, June 10, 1976.**



1



2

ORIGINAL PAGE IS
OF POOR QUALITY



3

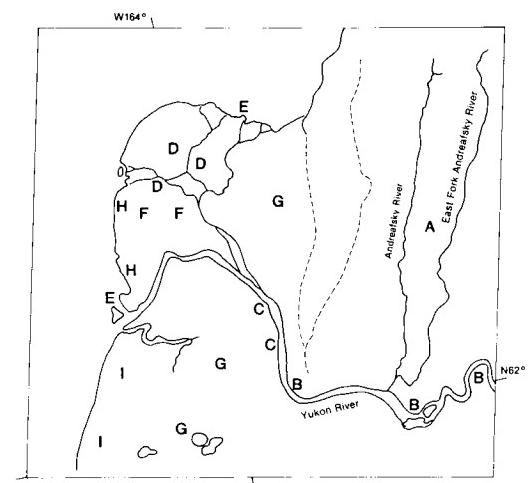


PLATE D-10

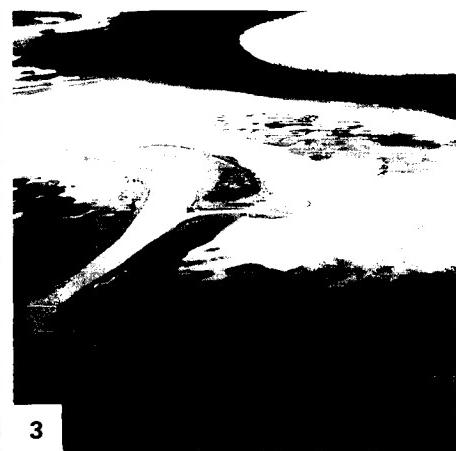
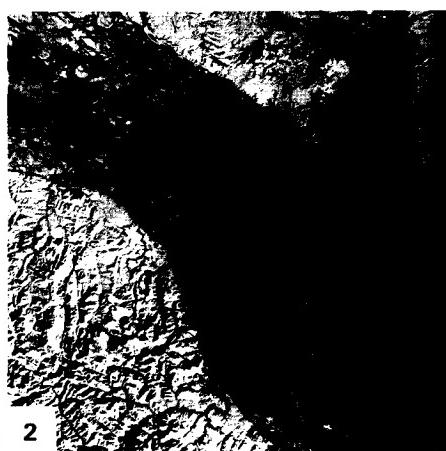
MACKENZIE RIVER DELTA, CANADA

The Mackenzie River is the longest river in Canada, the second longest in North America, and one of the ten longest rivers in the world. The river drains a basin of approximately 1.8 million km² in central Canada and has a total length of 4210 km. Its delta can be classified as an arctic delta; it is ice-free for approximately 3 to 4 months a year. The satellite image illustrates the northern portion of the delta plain that has formed between the foothills of the Richardson Mountains to the southwest and the elevated Pleistocene terrace surface to the east (A). The Pleistocene surface is composed primarily of permafrost or frozen ground on which numerous poorly oriented lakes (B) and polygonal or patterned ground (C) has developed (Samajlov, 1956). Permafrost again began to affect the region approximately 10000 to 11000 years ago and, in some instances, extends to depths of 100 to 130 m. Once permafrost commenced forming, pore water expelled from the encroaching frozen ground domed up the permafrost zone, pushing up ice-cored hills called pingos (D) (Figure D-10.1). These hills often attain extremely high elevation (100 to 150 m above the deltaic plain) and are typically conical in shape. Although many of these are located primarily on the Pleistocene surface, others are found within the modern or Holocene delta deposits (E). Many of these pingos are believed to be on the order of 10000 to 11000 years old, and more than 1350 of them have been mapped. Despite their sizes, pingos seldom show up well in Landsat images.

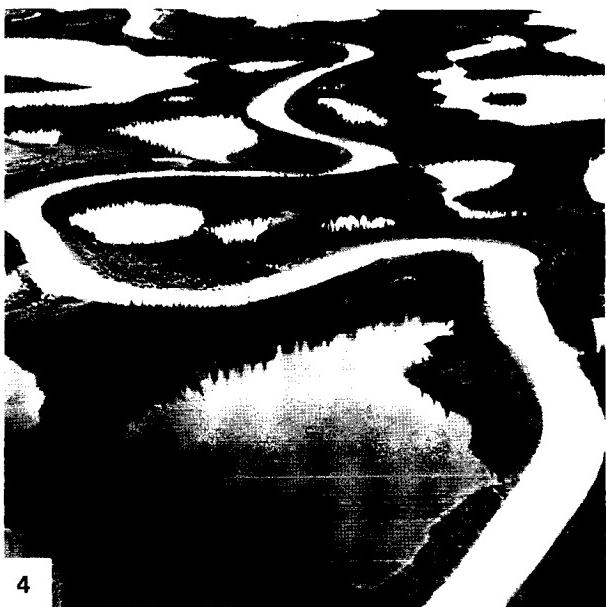
The Holocene delta of the Mackenzie River covers an area of 4700 km². Only the northern or lower delta plain is shown in the image. The discharge of the river averages 11300 m³/sec, 63 percent of which occurs during the ice-free months of May through August. The sediment load is approximately 15 million metric tons per year, a relatively small amount for such a large

river. One of the most notable attributes of the Mackenzie is its large number of anastomosing distributaries (F). These channel patterns often show extremely high angles at the point of bifurcation. The natural levees bordering the distributaries are well developed, and the interdistributary regions are dominated by lakes (G). Myriads of lakes and additional river channels are spread over the entire Mackenzie floodplain (up to 60 km wide) upstream for at least 150 km, as seen in a mid-fall (October 23, 1973) Landsat image (Figure D-10.2). Ice jams and the late thaw of the delta relative to the river thaw cause extreme localized high-water levels in the distributaries; overbank crevassing and formation of splays are common features extending into the freshwater lakes (Figure D-10.3). In the upper delta plain, woody trees, such as spruce, dominate the natural levees and interdistributary regions, forming large woody swamps (H) (Figure D-10.4). In the lower delta, low grasses and shrubs cover the tundra landscape (I).

At the river mouths, broad sandy and silty shoals (J), often completely barren of vegetation (except for algal mats), are common. Low wave energy along the delta front on the sub-ice platform results in a lack of any wave-reworked landforms, and these bars often display highly irregular patterns. The river carries copious amounts of organic material, especially a large number of tree trunks. Organic accumulations (K), often referred to as "coffee grounds," are present along the shoreline. In some instances, logs accumulate to considerable thicknesses along the shoreline. A turbid river plume (L) can be seen on the image. The presence of offshore ice often controls the distribution of the plume, and early in the breakup, turbid river water frequently overrides the shore-fast ice (M) to spread large amounts of sediment on top of the ice. During breakup, this sediment is redeposited offshore. **Landsat 21985-20125.**



ORIGINAL PAGE
COLOR PHOTOGRAPH



4

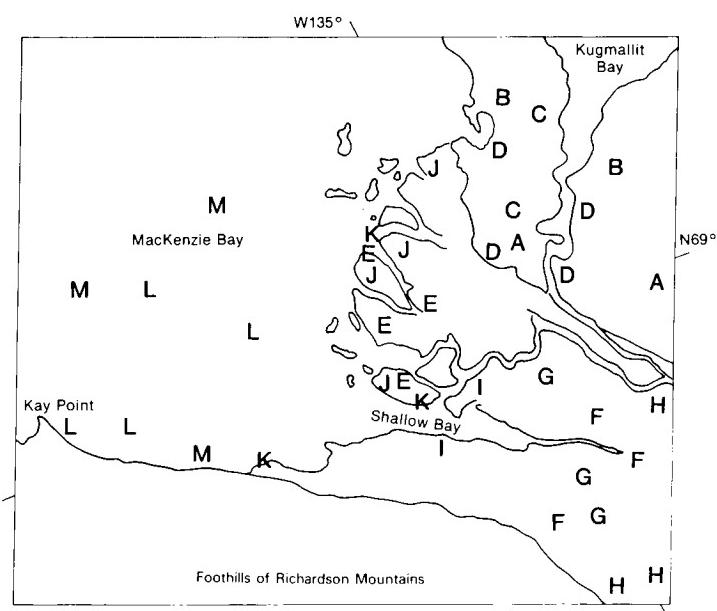


PLATE D-11

The Lena River, with a length of 4250 km, is the longest river in the U.S.S.R. A great delta has formed where it empties into the Laptev Sea, a part of the Arctic Ocean (Figure D-11.1) (Suslov, 1961). The river rises a few kilometers west of Lake Baikal, on the western slopes of the Baikal Mountains, at an elevation of 1800 m. Throughout much of its course, the river widens into broad braided stretches 3 to 4 km wide and then narrows as it cuts through more resistant strata. Near its delta, the river narrows considerably (A) as it cuts through the Kara Ulak Mountains (B), which are composed of Permian and Cretaceous sediments. Even in this stretch, narrow Pleistocene river terraces are present along the Lena's course. Its drainage basin area is quite large at 2478000 km². To the south of the delta, the basin waters tend to thaw and deliver their sediment-water discharge prior to breakup in the delta region. This melting results in extremely large numbers of ice jams and very high water levels along the river's course, as well as in the delta proper. Thus, the discharge is extremely erratic; average discharge is 50870 m³/sec, but the maximum discharge is 393850 m³/sec (Samajlov, 1956).

Emerging from the highlands, this long north-flowing river crosses the taiga of Siberia, one of the most extensive forests on the Earth. After passing through the narrow gorge near its delta, the Lena cuts through broad coastal Pleistocene terraces (C), many remnants of which are present as isolated highs within the delta. The fan-shaped delta covers some 28500 km² and is a maze of small distributaries. The river splits off into several distributaries, the only one of significance being the Trotimorskaya, which flows into the eastern part of the delta. The delta can be divided generally into two major parts, the western delta and the eastern delta (Antonov, 1959). The western delta (not shown on the satellite image) is relatively high, is moderately crossed by distributary channels, and has had many of its lakes tapped and drained, resulting in dry land or former lake surface over approximately 85 percent of the delta. The presently more active eastern part of the delta is characterized by relatively low elevations and a large number of anastomosing channels and sand bars. In both parts of the delta, the ground is permanently frozen, often to depths in excess of 15 m.

At the apex of the delta, the Lena River is complexly braided (D), with many large braid bars and small channels. Within the delta plain, the major channels split and rejoin, forming a maze of anastomosing channels; see (E) and Figure D-11.2 (Suslov, 1961). Near the distal ends of the distributaries, where

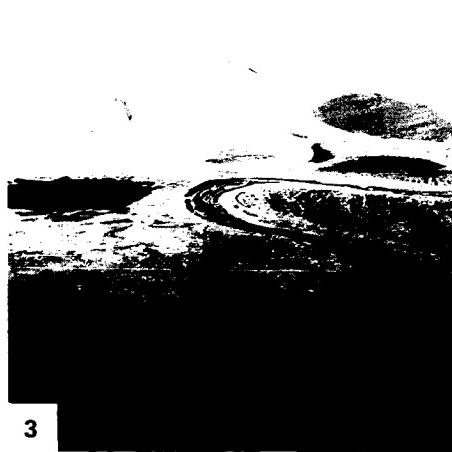
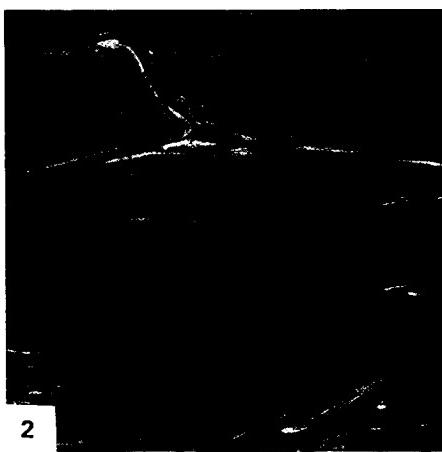
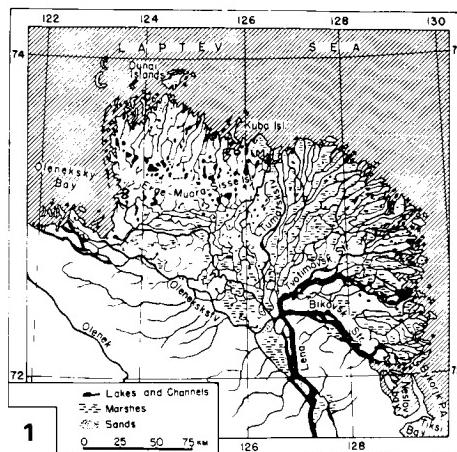
LENA RIVER DELTA, U.S.S.R.

the channels often broaden out, the river mouth bars (F) are composed of barren sand and mudflats. Tidal range is low, generally less than 40 cm, and does not significantly influence the sediment distribution pattern. Wave action at the coast can be considerable, with wave heights up to 2.5 m being quite common. As a result, small beaches and complex offshore barriers are present at most of the river mouths of arctic deltas; see Figure D-11.3, showing the Colville Delta, Alaska, U.S.A. The channels in the lower delta are often quite deep, on the order of 15 to 18 m, being much deeper than the upstream segments. Sediment load is quite high during the short flood season, with the suspended load reaching 11.7 million tons per year. Offshore currents are relatively low and generally flow to the northwest, carrying large quantities of fine-grained sediment westward along the coast.

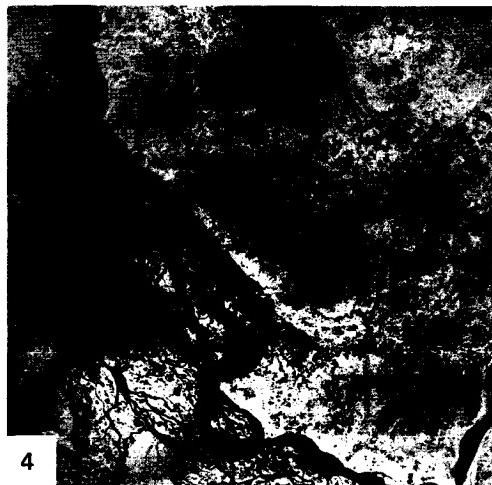
The delta plain (Figure D-11.4) consists of a maze of anastomosing channels, between which are broad areas of tundra surfaces containing patterned ground (Figure D-11.4) or polygons, freshwater lakes, and overbank splays (G). The tundra surface is composed of relatively large and complex patterned ground, which results from the annual freezing and thawing process. Ice wedges and other similar arctic landforms are present. As a result of thawing, many small freshwater lakes now dot the tundra surface. Because ice jams in the distributary channels cause abnormally high water in the delta, overbank splays are quite common, often filling many of the small lakes. After the major flood has subsided, water levels drop considerably, exposing a large number of sandy midchannel bars. Wind erosion removes the finer sands and forms small oriented dunes along the channel margins, often extending onto the adjacent tundra surface and into the lakes. The river traverses large taiga forests and thus carries large quantities of woody debris. This organic debris is often left stranded on the midchannel bars and within the channels.

On the Pleistocene surface (G), oriented lakes (H) are present, similar to those found along most of the Arctic tundra. Pingos (I) or "ice-core hills" are also found on this surface. Broken pack ice (J), which is nearly always present, can be seen offshore of the delta.

The third (largest) of the tundra deltas in the U.S.S.R. is that of the Yenisey River (Figure D-11.4, a Landsat scene), some 1200 km to the west where it empties into the Kara Sea. There, the delta (about one-tenth the area of the Lena delta) lies at the inner end of a narrow gulf and thus does not fan out like the Lena. **Landsat 1368-03062-7, July 26, 1973.**



ORIGINAL PAGE IS
OF POOR QUALITY



4

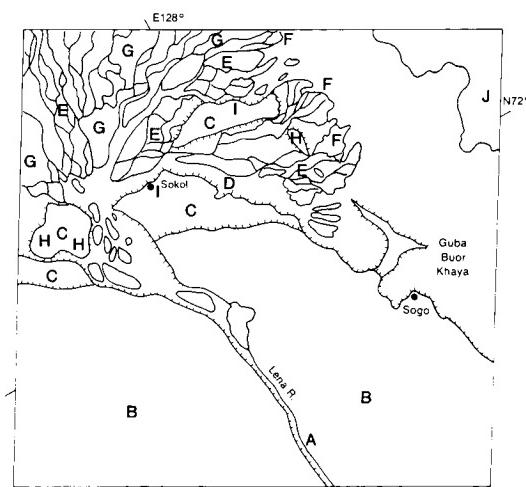


PLATE D-12

COLORADO RIVER DELTA, MEXICO

At the northern end of the narrow elongate Gulf of California, the Colorado River has been depositing sediment for centuries to form a river delta. During the Quaternary alone, the delta has prograded farther into the basin to form a cone of sediment that covers more than 7700 km². The delta is located entirely within the country of Mexico and is divided between the Mexican states of Baja California to the west and Sonora to the east.

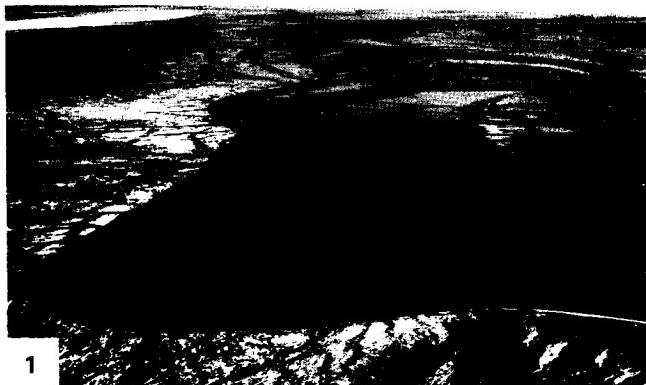
The basin into which the Colorado delta is building is bound by two major fault zones that form its east and west margins. East of the Gulf of California, a family of lateral faults has caused a small escarpment that separates the elevated (120 to 180 m) Sonoran Mesa (upper right part of the scene) from the basin. This mesa is desert land composed of relatively undisturbed Pliocene/Pleistocene strata overlain by dunes (A) and alluvium (B). The western boundary of the basin is marked by large normal faults that create an abrupt transition from the Sierra de Juarez of the Peninsular Ranges (a Mesozoic plutonic complex) to the basin floor. Three other mountain ranges of lesser importance extend into the basin (see index map). All of these ranges are located to the left or west of an imaginary dividing line up the center of the Gulf of California in Plate D-12. As is common with fault-controlled tectonic troughs, elevation changes over short distances can be extreme. In this case, relief up to 1200 m is attained in some areas over a distance of about 6.5 km; however, elevations of about 700 m are most common for the mountains that form the western boundary of the basin.

Because of the elongate configuration of the Gulf of California, the Colorado River delta deposits are subject to distribution and reworking by strong currents (over 200 cm/sec) associated with an enormous tidal range (greater than 10 m). In comparison to tidal effects, the importance of wave action in this delta is small (McGowen and Garner, 1970). As a result, a vast area of tidal flats (C) and tidal bars (D) has developed. Some tidal bars, such as Montague Island, are exposed at low tide. Others that have the same elongate shape remain subaqueous features throughout the tidal cycle. Since the entire area is arid (less than 76 to 100 mm/yr), vegetation is sparse, often allowing topographic lows in the upper tidal plain to develop into salt pans (E). When

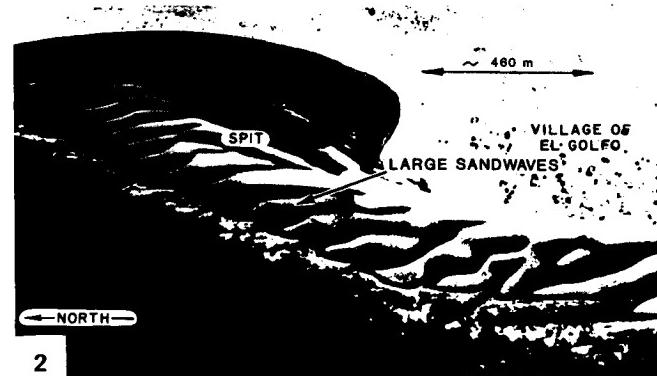
unusually high-water events occur, such as during the passage of a hurricane, marine water inundates the supratidal flat (above the influence of the normal tides), where evaporation and salt accumulation take place. In the valley fill north of the supratidal flats (F), the soil remains moist with fresh water and supports plant growth. This region is extensively cultivated (G), as is apparent in the upper left corner of the scene. The channel patterns (Figure D-12.1) are complex and show the result of modification by tidal processes. Migration of the channels is common, and at low tide, these barren sand flats are the site of small dendritic drainage channels.

In addition to the sediment contributed to the basin directly by the Colorado River, erosion of the steep mountain fronts provides abundant coarse debris to form alluvial fans. Between the mountain front of the Sierra de Juarez and the San de los Cocopas Mountains to the east, alluvial fans from these respective sources have helped to form a miniature basin where a playa lake (I) has developed.

Numerous smaller scale features occur along the coast (Meckel, 1975). These include tidal channels (J), daily providing fine-grained sediment and marine water to the tidal flats; narrow sandy beaches (K); stranded beaches and beach ridges, commonly called cheniers (L); tidal deltas (M); and basinward-building coastal barriers (N), some of which have large sand waves in the intertidal zone (Figure D-12.2). In this figure, large sand waves have formed in the intertidal zone along the Sonoran coastline. Longshore currents, from right to left in the photograph, have created a spit that has effectively sealed a small coastal bay at low tide. Figure D-12.3 represents a part of the Colorado River on the Baja California side. In this photograph, waves are breaking on the thin transgressive beach in the foreground. Behind this sandy coastal ridge (chenier) are the channels of a tidal delta and its associated tidal flats. White areas in the background represent salt pans of the supratidal surface. Alluvial fans originating in Cretaceous granites form the landward margins of the supratidal environment. These coarse detrital fans are prograding across the supratidal surface. Landsat 2335-17311-7, December 23, 1975.



1



2

ORIGINAL PAGE IS
OF POOR QUALITY

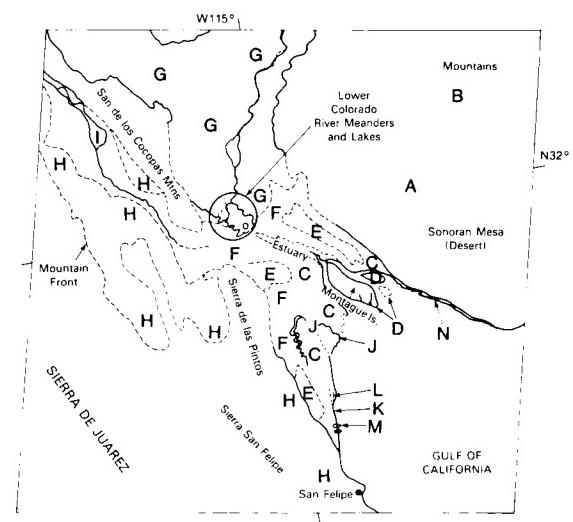
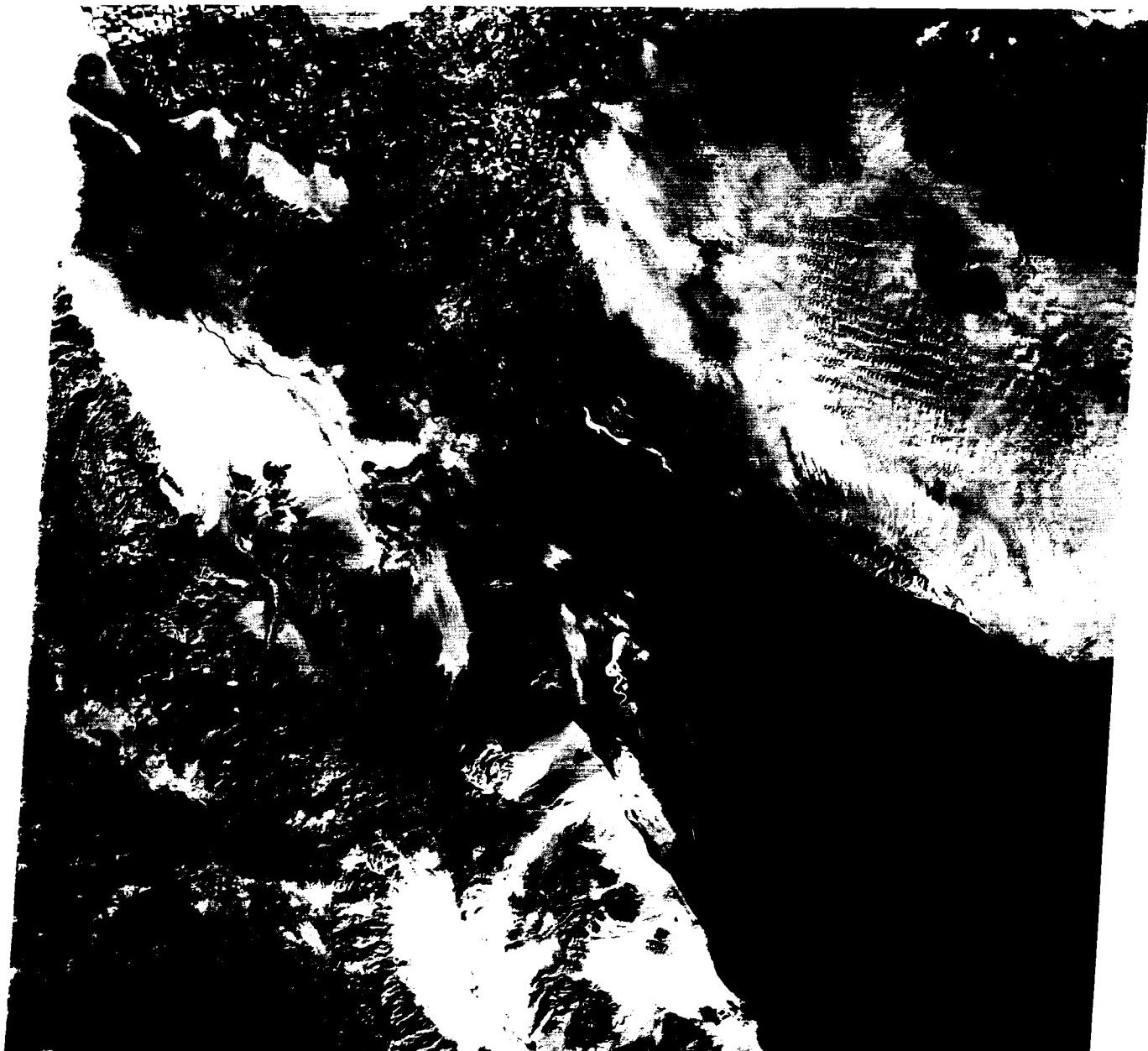


PLATE D-13

The Shatt el Arab delta has built up at the northern extremity of the Persian Gulf (Figure D-13.1, an oblique view from Apollo 7). The Shatt el Arab River (A) that feeds it is only 180 km long and is formed by the confluence of the Tigris and Euphrates Rivers (about 2700 km long), which flow through central and eastern Iraq. It is navigable to Al Basrah (B), the chief port of Iraq. Although the Shatt el Arab River owes its origin to these two historically important rivers, the delta is actually formed from the sediments of three rivers. The Karun River (C) rises in west-central Iran and, like the Tigris, drains the Zagros Mountains, which trend northwest-southeast through western Iran. The Karun is probably the primary contributor to the present delta. One meandering branch of the Karun intersects the lower reaches of the Shatt el Arab where the Iranian port of Abadan (D) is located. Each contributor to the delta has extremely erratic discharges, a variability shared by most rivers in arid midlatitude climates. The drainage basin of these three rivers is 792000 km in area, with an average elevation of 453 m (Samajlov, 1956).

The Tigris/Euphrates Basin, as well as its extension, the Persian Gulf, occupies a zone of subsidence flanked by mountains and/or desert. This elongate depression was formed during an era of mountain building initiated early in the Tertiary that continues with the movement of the Arabian plate against the stable landmass of Asia.

The delta exists today in an arid climate, with extremely high rates of evapotranspiration and notable fluctuations in temperature and wind, controlled mainly by topographic variations outside the delta. The Shatt el Arab delta is located at the northern end of an elongate shallow sea where semidiurnal tidal variations reach about 2.5 m. Although much of the delta is made up of broad marshes and associated lowlands (Figure D-13.2) that are valuable as agricultural lands, most coastal regions are tidal flats and sabkhas devoid of extensive vegetation where salts are deposited. Dark gray areas (E) that border the bell-shaped river mouths and tidal channels (Figure D-13.3) correspond to fine-grained sediment deposits that periodically experience tidal inundations. They support a growth of salt-tolerant vegetation (mainly blue-green algal mats). Most marshlands tied to the delta and its river systems lie northwest of the Plate scene. However, freshwater wetlands around the Haur al Hawizeh marsh just northwest of Basrah are visible (F). This area of active subsidence receives

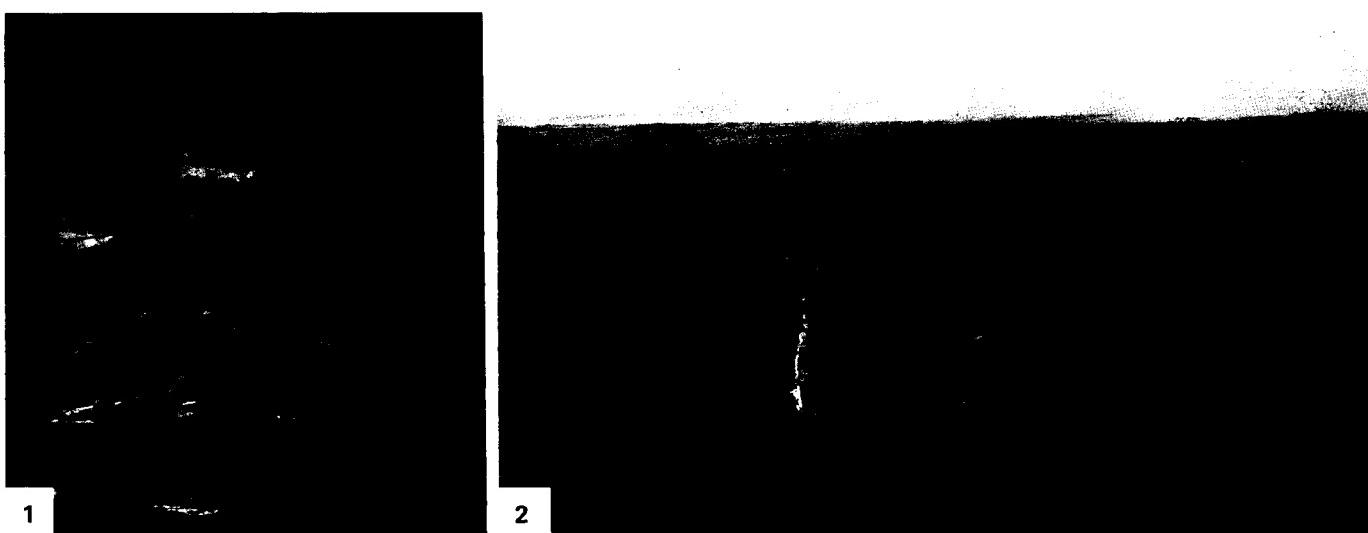
SHATT EL ARAB DELTA, IRAQ

a large percentage of the sediments of the Tigris and Euphrates Rivers. The marshlands contain broad expanses of floating cane marsh and bullrush and are inhabited by a unique group of people commonly referred to as the Marsh Arabs.

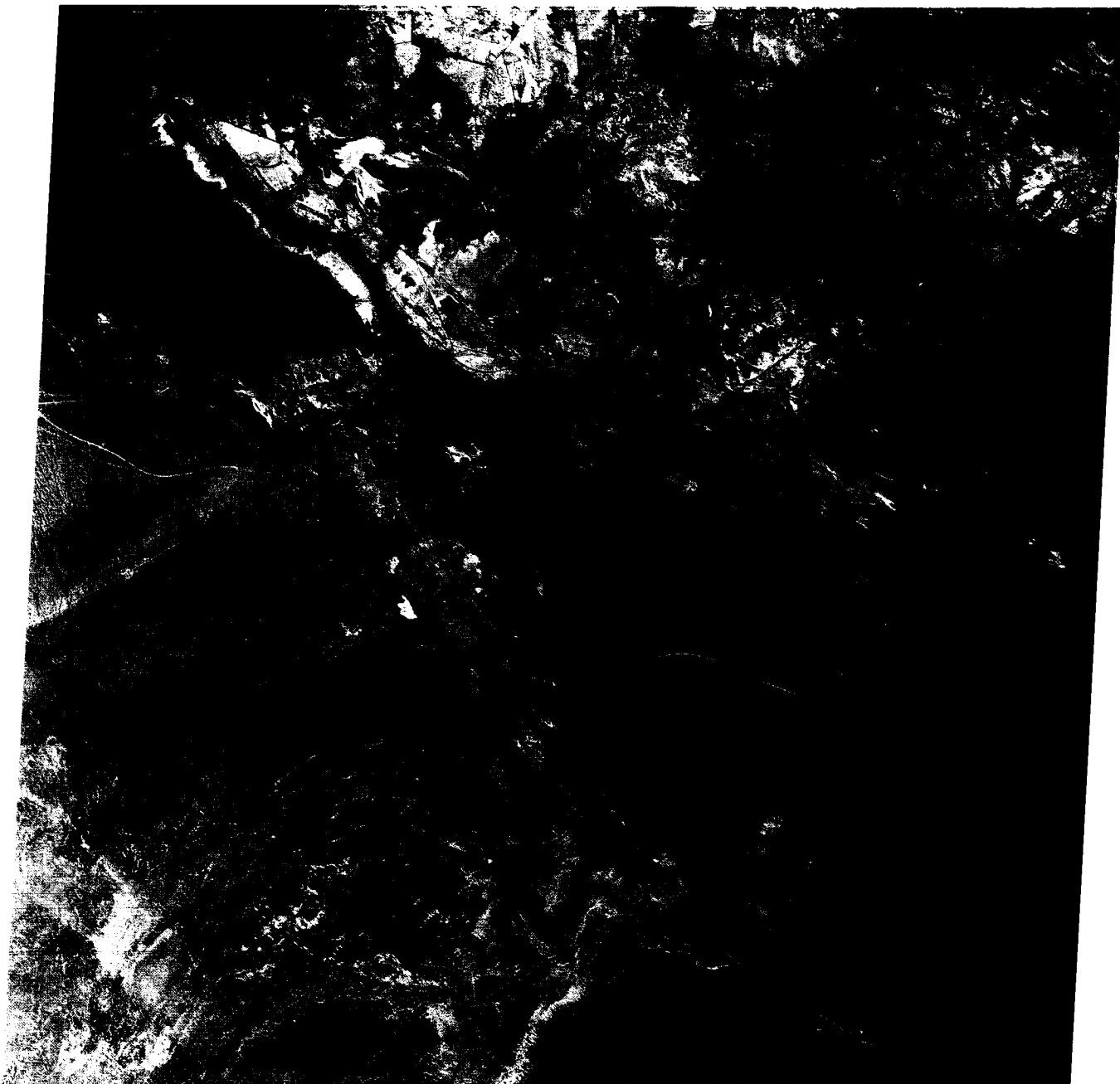
The amounts and quality of water and sediment delivered to the delta by the Shatt el Arab channel are largely dependent on conditions in the marsh both at and above the confluence of the Tigris and Euphrates Rivers. In the Holocene, these conditions varied between two extremes: the first where only marsh waters and the second where only river waters enter the channel. The rate of upstream subsidence is the process controlling the dominance of one extreme over the other.

In many ways, the Shatt el Arab delta is like the Indus delta on the Pakistan/India coast (Plate D-14). Both deltas are developing under arid climatic controls, the discharges are of the same order of magnitude, tidal ranges are the same (between 2 and 3 m), and except for small stands of mangrove trees, their deltaic plains are largely devoid of vegetation. One sharp difference is the extremely low wave energy attacking the Shatt el Arab delta. Due to low wave energy, only narrow beaches (G) and small dune systems lie along the leading edge of the delta. Mudflats and sandbars dissected by tidal channels (H) dominate the prograding delta front. Where seawater is trapped during very high (storm) tides, salt pans (I) develop. White areas in the scene are barren regions of salt deposition along with gypsum/anhydrite. Cultivated areas (J) in the lower delta generally follow the Shatt el Arab and Karun channels. Offshore, elongate turbidity patterns (K) and island shapes (L) associated with the flaring channel mouths indicate that subaqueous as well as subaerial parts of the lower delta are being molded by strong bidirectional tidal currents, the primary transport agents.

Man has profoundly affected the Shatt el Arab and its delta. The network of irrigation ditches in the delta region appears to be responsible for a nearly 64 percent water loss after contributing sources reach the main channel. Most loss is accounted for by evapotranspiration in the irrigated fields (M) of the lower basin and the Hawizeh marsh. In the desert west of the delta, man's activity in producing hydrocarbons is evidenced by the long black lines trending roughly northwest-southeast, which represent smoke plumes from gas flares at oil facilities around the rich fields in Iraq and Kuwait. **Landsat 2653-06291, December 30, 1980.**



ORIGINAL PAGE IS
OF POOR QUALITY



3

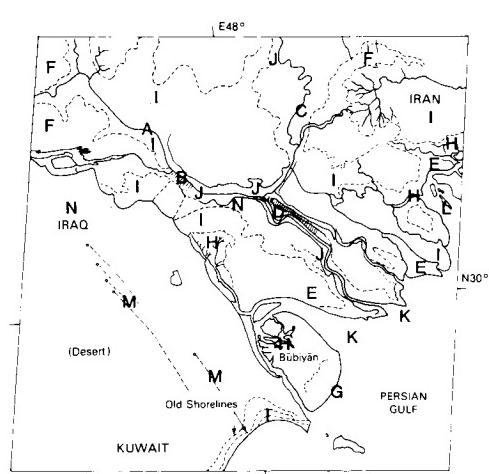


PLATE D-14

The 2900-km long Indus River rises in the Himalaya Mountains of western Tibet at an elevation of about 5183 m. It follows a precipitous course west through Tibet and then northwest across Kashmir. In western Kashmir, it flows down a narrow passage nearly 396 m deep in places through the mountains until it enters Pakistan and proceeds almost due south to the point where it is joined by the Panjab River. Shifting to the southwest, the Indus follows a contorted path before emptying into the Arabian Sea and creating a complicated protuberance of terrigenous clastic sediments known as the Indus delta.

In its upper valley, the Indus flows primarily as a braided stream because of a high gradient associated with the river course and an erratic pattern of discharge. The southern limit of braiding in the Indus can be seen in the river patterns and associated alluvial morphology in the top-central part of the scene (A). As the river approaches the Arabian Sea, it becomes a meandering system in its lower reaches (B). In historic times, the Indus River has switched its location, thus contributing to the construction of a broad deltaic plain, the largest part of which does not receive active sedimentation from the modern river (Wells and Coleman, 1984). Within the abandoned deltaic plain (right-central part of the scene), many remnants of once-active distributaries (C) and their associated alluvial features are still apparent. Oxbow lakes, meander loops, and abandoned channels (D) (Figure D-14.1), plus ridge-swale scrollwork (E) associated with the deposition of coarse point-bar sediments, are formed during the lateral migration of the river. These products of a meandering river system are also very much a part of the alluvial morphology being created by the modern active Indus River (Holmes, 1968).

The delta has formed in an arid climate under conditions of high river discharge (~400 million metric tons of sediment per year), a moderate tide range (2.6 m), extremely high wave energy (14×10^7 ergs/sec/m), and strong monsoonal winds from the southwest in the summer and from the northeast in the winter. The resultant rather coarse-grained delta, which has acquired a lobate shape, is lacking in luxuriant vegetation and is dissected by numerous mangrove-lined tidal channels (F) (Figure D-14.2) in the lower deltaic plain. Estimates of delta building over the last 5000 years indicate an average progradation rate of approximately 30 m/year. Morphology of the Indus lies midway between that of a fluvially dominated delta, with distributaries that protrude into the basin of deposition, and a wave-dominated system, with little expression along the coast, except where characterized by beach and dune deposits.

Plate D-14 clearly shows the distinction between the Indus delta's abandoned and active deltaic plains, as well as the desert uplands (upper left sector of the scene) that form the delta's western boundary. Once the river ceases to deliver sediments as a product of natural diversions or of man's intervention by



1

INDUS RIVER DELTA, PAKISTAN

building artificial levees and other structures, this area of the delta will become an abandoned deltaic plain. In recent years, a high proportion of water from the Indus has been diverted for irrigation, thus considerably reducing the effective discharge. Water storage areas (G) and manmade canals (H) for diverting Indus River water are apparent along the west margin of the delta.

The lower or active deltaic plain is roughly delineated by the landward boundary of salt-water intrusion, the position of which is easily seen on Plate D-14. This lower deltaic plain is crossed by a complicated network of meandering tidal channels (I) that daily inundate the region with salt water and fine-grained suspended sediment. Figure D-14.2 shows that the margins of these tidal channels are commonly lined by salt-tolerant mangrove vegetation on a sand to silt substrate, while barren flats are common in the interchannel areas. Along the creek margins, small crevasses/splays build sediment wedges into interchannel regions. These features are generally too small to be clearly delineated on the Plate image. Even though the tide range of the Indus is not extreme (~2 to 3 m), when combined with the effects of the storm tides of the southwest monsoon in summer, vast areas of both the active and lower abandoned deltaic plain are inundated with salt water. As a result of this yearly cycle, combined with an arid climate, low-relief areas trap salt water that evaporates to create rather extensive salt flats (J). The bell-shaped channels (K) associated with river mouths and tidal creeks are other indicators of tidal influence on this delta's morphology.

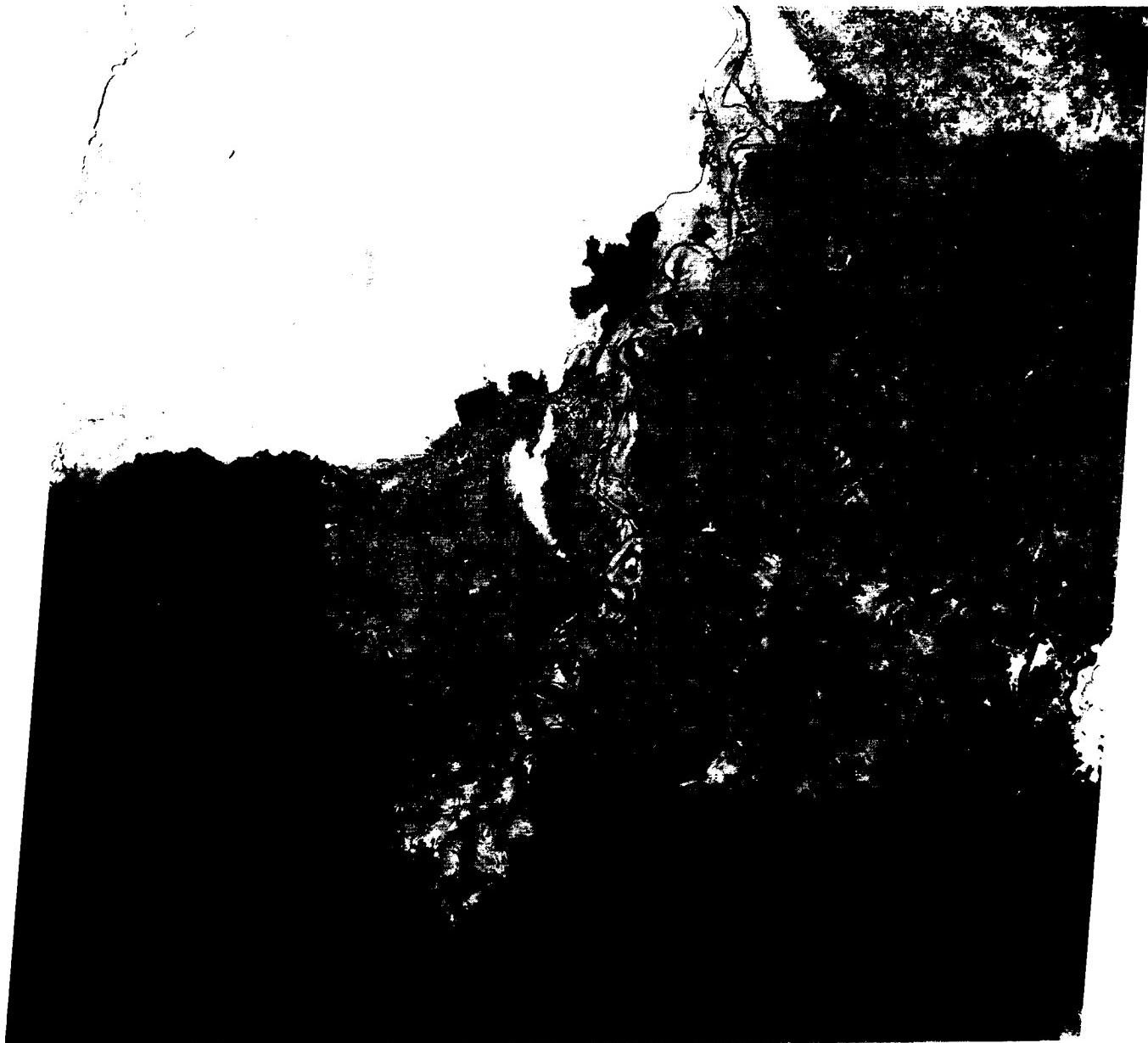
Waves are the single most important process variable in shaping the Indus delta. Intense monsoonal winds arriving from the southwest (May–September) are responsible for an abnormally high level of wave energy at the coast. The effect of this wave energy has been to concentrate the coarse sediments at the shoreline, produce strong longshore currents, and generally straighten the configuration of the coastline. The result has been the development of beach, barrier, and dune complexes (L) at the leading edge of the subaerial delta. Figure D-14.3 illustrates the redistribution of sandy sediments that were originally concentrated at the shoreline by wave activity and then transported into dunes by eolian processes. These dunes reach heights of several meters and are in a state of active migration. They occur along the seaward and western margin of the Indus delta.

Because of man's intervention in the natural delta-building processes of the Indus, this delta's future is uncertain. Extensive use of fresh water for irrigation during the 20th century has decreased the Indus River discharge approximately fourfold. If this trend continues, we can expect the delta to evolve into a more wave-dominated form characterized by extensive beach, beach ridges, and dune formation, probably accompanied by substantial coastal retreat. **Landsat 1228-05274-7, March 8, 1973.**



2

**ORIGINAL PAGE IS
OF POOR QUALITY**



3

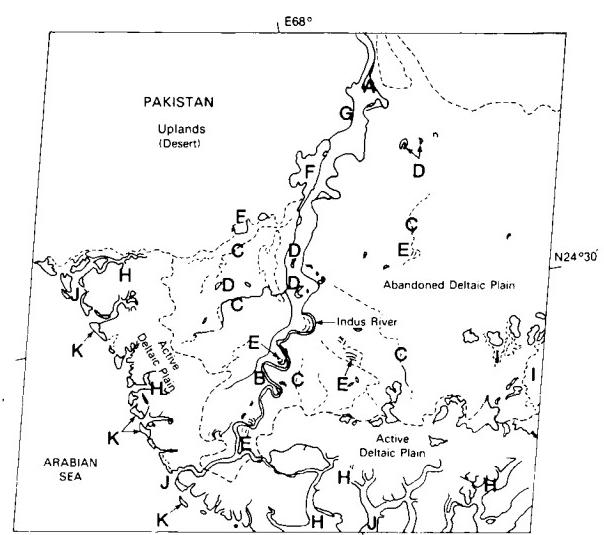


PLATE D-15

AMU DARYA RIVER DELTA, U.S.S.R.

The Amu Darya River, known in ancient times as the Oxus, is the largest river in central Asia. It extends some 2550 km from its headwaters in the high mountains of Afghanistan and Soviet Tadzhikistan to the end of the delta (Samajlov, 1956). In ancient times, at approximately 500 B.C., it is believed that the river flowed into the Caspian Sea and later changed to its present course into the Aral Sea. The receiving basin, the Aral Sea, is some 64000 km² in area and experiences less than 1100 mm of annual precipitation. Evaporation is dominant, with approximately 1 m of water stripped from the surface annually. This water is replaced by inflow from the two major rivers that drain into the Aral, the Amu Darya and Syr Darya. Because water from both of these rivers is used for irrigation, the water level has decreased and the salinity is increasing.

In its alluvial valley, the river flows through the extremely arid Turan lowlands, where evaporation removes a high percentage of the total flow, resulting in extremely high sediment concentrations. The delta, illustrated in the Landsat image, is bordered by the Kara Kum desert on the west and the Kyzyl Kum desert on the east. The Kara Kum consists of a denuded desert plain (A) with abundant salt flats, soft sediment bluffs (Figure D-15.1), and karst topography. The initial flow of the river was into a low depression of this desert referred to as the Sarykamys Depression. Some of the former river courses that fed into this depression can still be discerned on aerial photographs. To the east lie the eolian sand fields of the Kyzyl Kum desert. Quaternary linear dune fields, some of them presently active, are shown in the image (B). Note that many of these linear dune fields have been inundated by the Aral Sea, giving a striking example of the linearity of the dune fields (C).

The modern channel displays active meandering (D) within the upper delta plain; in the lower delta plain, the channel bifurcates, and many distributaries feed water and sediment to the Aral Sea (E). The presently active part of the delta (F) is characterized by relatively small bifurcated channels that deliver a high volume of sediment to the Aral Sea annually. The turbid river plumes are dramatically shown in the image (G). The river has

an average discharge of 1500 m³/sec, with a peak flow of 3380 m³/sec during flood. The image was obtained near the end of May, a period of spring flooding just before the major floods that occur in June and July as a result of glacial melt. Sediment load is extremely high in the active channel; in excess of 100 million metric tons of suspended sediment and 5 million metric tons of bedload is delivered to the delta annually.

The relatively inactive abandoned delta plain (H) dominates much of the scene in the image. The various abandoned channel courses (I) are well defined and consist of abandoned meander scars. In many instances, land reclamation in this arid delta follows these courses, and irrigation schemes are abundant along their courses. Modifications by man are not as prominent on the Plate scene as on low-level photographs. However, the general trend of the former courses can be easily discerned and mapped from the satellite imagery. The eastern part of the delta was active until the 10th century, when the major courses shifted to the west. The modern course began to form in the late 17th and early 18th centuries.

A large percentage of the delta plain is composed of evaporation flats and salt playas (J). Figure D-15.2 examines similar tidal flats of the Ord River delta, Australia, which is comparable in many respects to the Amu Darya. In most instances, these flats are present in the interdistributary regions. Some of the lower lying depressions, formed during the prior delta progradation, have not been totally infilled and now exist as high-salinity algal flats and saline lakes (K). Other partially filled depressions are barren of higher vegetation and consist of algal flats and salt marshes (L). Along the coast, waves and currents have reworked parts of the older delta plains into a series of beach-barrier complexes (M), often covered with small coastal dunes and backed by salt and algal flats. Figure D-15.3 pictures a typical reworked barrier sand spit on the fringes of the Ord River delta, Australia, that acts as an analog to those around the Amu Darya delta. Along the fringes of the older abandoned delta are coastal sand and mud flats (N). *Landsat 1310-06192, May 29, 1973.*

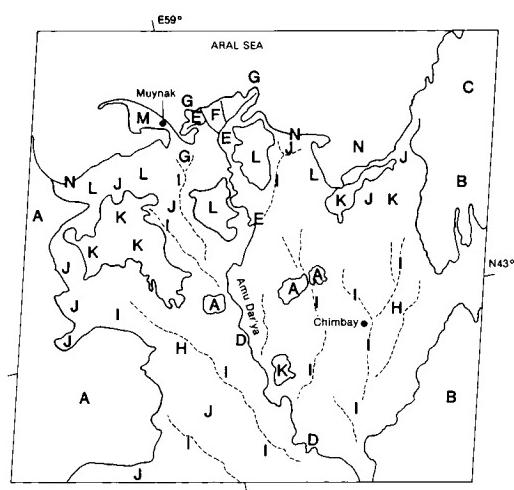
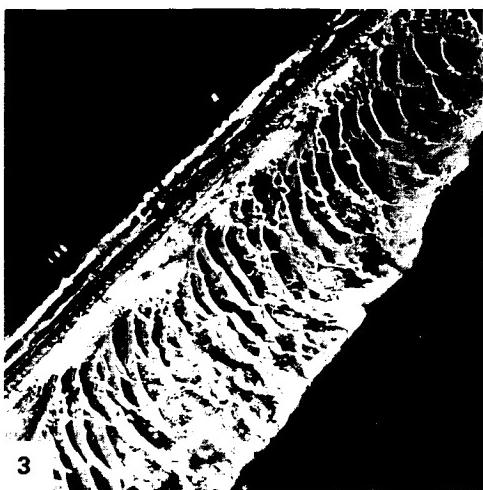


1



2

ORIGINAL PAGE
COLOR PHOTOGRAPH



REFERENCES

- Almazov, A. A., C. Bondar, C. Diaconu, V. Ghederim, V. N. Mikailov, P. Mita, I. A. Nichiforov, I. A. Rai, N. A. Rodionov, S. Stanescu, V. Stanescu, and N. Vaughn, *Zona de varsare a Dunarii, Monografia Hidrologica*, Institutul de Studii si Cercetari Hidrotehnice, Bucuresti, 1963.
- Antonov, V. S., Delta of the Lena River, Academija nauk SSSR, Okeanograficheskaja Komissija, *Trudy*, 6, 25-34, 1959.
- Coleman, J. M., Brahmaputra River: Channel processes and sedimentation, *Sediment. Geol.*, 3, 129-239, 1969.
- Coleman, J. M., *Deltas: Processes of Deposition and Models for Exploration*, IHRDC, Boston, Massachusetts, 1976.
- Coleman, J. M., and D. B. Prior, *Deltaic Sand Bodies*, AAPG Continuing Education Course Note Series 15, 171 pp., Amer. Assoc. Petrol. Geologists, 1980.
- Eardley, A. J., Sediments and topography of Lower Yukon, *Bull. Geol. Soc. Amer.*, 49, 304-341, 1937.
- Fisk, H. N., and E. McFarlan, Jr., Late Quaternary deltaic deposits of the Mississippi River, in *Crust of the Earth, A Symposium*, Spec. Paper 62, edited by A. Poldervaart, pp. 272-302, Geol. Soc. Amer., 1955.
- Gagliano, S. M., and W. G. McIntire, Reports on the Mekong River delta, *Tech. Rept. 57*, Coastal Studies Inst., Louisiana State Univ., Baton Rouge, 1968.
- Holmes, D. A., The Recent history of the Indus, *Geog. J.*, 134, 367-381, 1968.
- Inman, D. L., and C. E. Nordstrom, On the tectonic and morphologic classification of coasts. *J. Geology*, 79(1), 1-21, 1971.
- Kolb, C. R., and J. R. Van Lopik, Depositional environments of the Mississippi River deltaic plain, southeastern Louisiana, in *Deltas*, edited by M. L. Shirley and J. A. Ragsdale, pp. 17-62, Houston, Texas Geological Society, 1966.
- McGowen, J. H., and L. E. Garner, Physiographic features and stratification types of coarse-grained point bars: Modern and ancient examples, *Sedimentology*, 14, 77-111, 1970.
- Meckel, L. E., Holocene sand bodies in the Colorado delta area, northern Gulf of California, in *Deltas, Models for Exploration*, edited by M. L. Broussard, pp. 239-265, Houston Geological Society, 1975.
- Morgan, J. P., and W. G. McIntire, Geological studies in the Bengal Delta, *Res. Reviews*, Office of Naval Research, pp. 1-7, 1957.
- Morgan, J. P., and W. G. McIntire, Quaternary geology of the Bengal Basin, East Pakistan and India, *Bull. Geol. Soc. Amer.*, 70, 319-342, 1959.
- Potter, P. E., Significance and origin of big rivers, *J. Geology*, 86, 13-33, 1978.
- Samajlov, I. V., *Die Flussmundungen*, 647 pp., Veb Hermann Haack, Germany, (translated from the Russian original Ust'ia Rek), 1956.
- Suslov, S. P., *Physical Geography of Asiatic Russia*, 594 pp., W. H. Freeman, San Francisco, 1961.
- Wells, J. T., and J. M. Coleman, Deltaic morphology and sedimentology, with special reference to the Indus River Delta, in *Marine Geology and Oceanography of the Arabian Sea and Coastal Pakistan*, Van Nostrand Reinhold, 1984.
- Williams, J. R., Effects of wind-generated waves on migration of the Yukon River in the Yukon Flats, Alaska, *Science*, 115, 519-522, 1952.
- Wright, L. D., and J. M. Coleman, Effluent expansion and interfacial mixing in the presence of a salt wedge, Mississippi River delta, *J. Geophys. Res.*, 76(36), 8649-8661, 1971.
- Zenkovich, V. P., *Processes of coastal development*, edited by J. A. Steers, 738 pp., Intrascience Publishers, New York, 1967.

6

COASTAL LANDFORMS

Arthur L. Bloom*

A shoreline is the demarcation between subaerial and subaqueous landforms. A coastline specifies an oceanic shoreline. In the more general sense, a *coast* refers to a zone of indefinite width on both sides of the coastline, so we freely speak of coastal shipping, coastal highways, etc. By that usage, coastal landforms are those that are in any way influenced or controlled by proximity to the sea, such as the inland extent of salt spray that affects plants or soil (Bloom, 1978, pp. 435–437). Beyond that general statement, coastal landforms are difficult to classify. Many coasts are simply drowned portions of a subaerial landscape or exposed portions of the sea floor, on which the position of the coastline is the random result of land uplift or subsidence or of a rise or fall of sea level.

Although hard to define and transient in time and space, a coastline has profound geologic implications. Above sea level, all land must be eroded by rain, rivers, wind, and glaciers. The coast marks the line at which the erosion products are dropped and become new marine sedimentary deposits. Thus the coastline denotes the transition from net erosion to net deposition on our planet.

Coasts are also the loci of a unique assemblage of erosional and depositional processes (Shepard and Wanless, 1971). A global survey of wave and current energy in the coastal zone showed that there is 58 000 times more energy available to transport mud and sand in the nearshore marine environment than there is sediment to be transported (Inman and Brush, 1973). All this wave and current energy that is expended on coasts is normally restricted to a vertical zone between only about 10 m above and below mean water level. The upper limit is determined by tidal range and exposure to storm waves. The lower limit is determined by the rapid exponential decay of wave energy at relatively shallow depth. There is no “wave base” in the older sense of the term, but below a depth of about 10 m, most wave motion is too weak to transport sediment.

Because of the relatively narrow vertical range of coastal processes, a small change in the level of either land or sea can initiate an entire new cycle of coastal landform development and leave former coastal features as relict on emerged or drowned topography. Especially during the last 2 million years of perhaps twenty ice ages, sea level has fluctuated through more than 100 m each time glaciers expanded and retreated. Few if any coastal landforms show the morphologic relief of a single set of processes. Almost every coast shows a complex history of emergence and submergence, each episode putting its unique imprint on the land.

The events of the last 125 000 years are especially well recorded on coasts. The last Pleistocene interglacial age was about that long ago, and sea level was probably a few meters higher than: 6 m is an often-cited estimate. That interglacial period may have lasted about as long as the present “postglacial” or Holocene Epoch. Landforms were eroded and built on a scale very similar to those now forming, but at a slightly higher level. With the onset of the last ice age, sea level fell in a series of oscillations to a minimum of perhaps –120 m only about 18 000 to 15 000 years ago. Interglacial coastal sediments were vegetated, weathered, soil-covered, blown away, or dissected by erosion. As the sea has returned almost to its previous level, it has partly reoccupied the coastal zone of the last interglacial age. If the Pleistocene deposits had been lowered only a few meters by tectonic subsidence or erosion, they would have been reworked by Holocene coastal processes and buried by Holocene deposits. In other places, Pleistocene barrier beaches or wave-cut cliffs are separated by only a low scarp or step down to their modern analogs. Few coasts preserve the record of interglacials older than the last one. Perhaps the last interglacial of 125 000 years ago was slightly higher than earlier ones, and that contributed to its common preservation. Numerous examples are cited in the Plate captions for this chapter.

No classification of coasts is widely accepted because the forms are almost always compound in their origin. One proposed by Shepard in 1937 and subsequently modified (Shepard, 1973) is followed in a general way in this chapter. He recognized the global impact of the Holocene rise of sea level and distinguished *primary coasts* as those that had simply been drowned with minimal modification by marine processes and *secondary coasts* as those that were subsequently modified by marine erosion or deposition.

Another current classification of coasts is based on their plate/tectonic setting (Figure 6-1) (Inman and Nordstrom, 1971). *Collision coasts* are at the colliding or converging margins of continents or island arcs. *Trailing-edge coasts* of several types evolve on passive continental margins, initially as rift-bounding fault-scarp coasts, then later as maturely dissected fault scarps fronted by narrow coastal plains, and still later in the evolutionary sequence as broad sedimentary coastal plains. *Marginal sea coasts* are primarily on the depositional edges of shallow marginal or epicontinental seas. Based on the tectonic environment, Inman and Nordstrom devised a morphologic classification of coasts (Figure 6-2) that uses simple descriptive phrases for the gross regional landscape of each tectonic type. The classification has problems; for example, there is no collision in progress along the western side of South America, yet the Andes Mountains are actively rising. Also, to label the entire coast of the Arctic Ocean

*Department of Geological Sciences, Cornell University, Ithaca, New York, 14853.

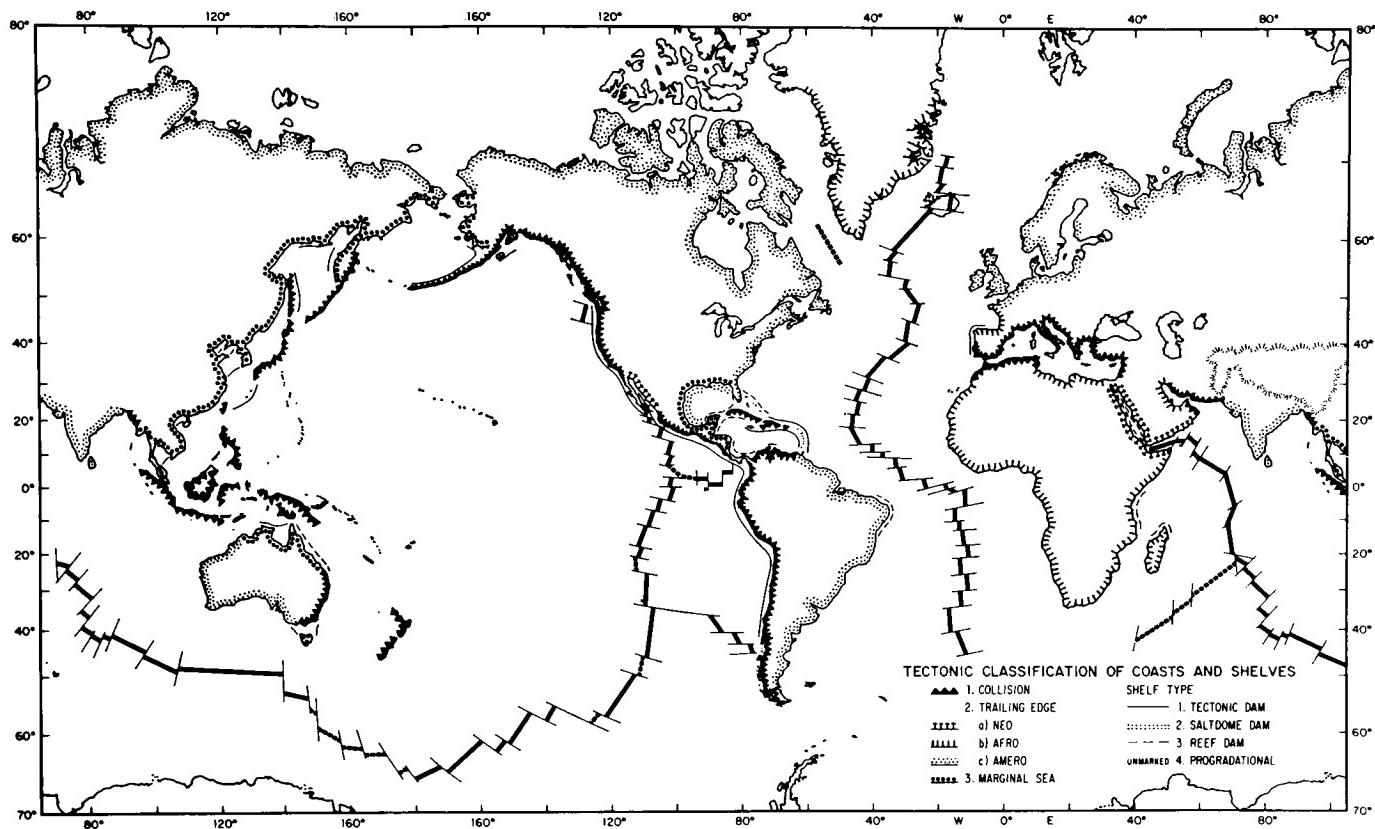


Figure 6-1. Worldwide distribution of tectonic coastal and shelf types.

as "glaciated" is neither true nor consistent with the variety of tectonic activity in the region. Nevertheless, the classification of Inman and Nordstrom is useful and important because it links coastal landforms to important categories of tectonic landforms.

The simplest coasts are probably those on continental shields or cratons, where in many places long continued subaerial erosion has reduced the landscape to near sea level, and the sea, in its present postglacial time of relatively high level, has drowned a fluvial, glacial, volcanic, depositional plain, or other landscape (Plates C-1, C-2, C-3, C-4, and C-5). In such places, coastal landforms are the result of a minimal impact of nearshore marine processes. For the most part, they are simply the result of sea level coming to rest against a preexisting landscape. Lowland drainage systems are particularly susceptible to drowning as sea level rises, producing estuaries that severely indent otherwise regular coastlines (Plate C-23). Mountain ridge crests or hill summits then create peninsulas or islands, separated by drowned former valleys (Plates C-6, C-7, and C-11). If the valleys were shaped by glaciers, their drowned counterparts have become fjords (Plate C-5). Many of our most scenic coastal landscapes (New England, Norway, Ireland, and New Zealand) owe their beauty to the rapid changes when a subaerial landscape suddenly became coastal at the end of the last ice age, only about 10000 years ago.

Structural and tectonic lineaments in a subaerial landscape also control the shoreline shape, especially where the land is partly drowned (Plate C-7). The Atlantic type of coast (Plate C-7) was defined a century ago by the German geologist, E. Suess (1888), who recognized the truncated structures now explained by continental separation and ocean-floor spreading. Other coasts, such as in Peru or the Dalmatian Coast of Yugoslavia (Plates C-8 and

C-12), are of the Pacific type, in which active mountain building is creating folds and faults parallel to the coast. Islands on such coasts as the Makran region of Iran and Pakistan are the crests of fault blocks or rising anticlines that are uplifting and folding the seafloor at converging continental margins (Plate C-9).

On the passive trailing coastal margins of continents, rivers drop their loads of sediments, which are then shaped into deltas or a variety of progradational landforms. Mud may be trapped by vegetation to form extensive coastal salt marshes (Plates C-13 and C-14) or tropical mangrove swamps (Plates C-3, C-4, and C-15). Sand is more likely than mud to move laterally along coasts to build a variety of beach landforms (Plates C-4, C-13, and C-14). Approximately 13 percent of the world's coasts are said to be sandy barrier beaches, primarily constructional in nature (Zenkovich, 1967, pp. 288 and 390).

An extremely abundant but nevertheless remarkable coastal landform type is that built by biogenic deposits of shallow-water marine animals such as corals (Plates C-16 through C-19). Entire island archipelagos and a very large percentage of the world's coasts have been constructed of coralline limestone (Davies, 1980, p. 5), forming reefs that fringe or protect other coastal landforms. The largest of these, the Great Barrier Reef of Australia (Plate C-18), extends for 2300 km along the tropical northeast coast of Australia, inhibiting wave erosion of the mainland coast and creating a huge but unique coastal landform assemblage.

The reader interested in more information on the coastlines of all continents should consult the recently published *The World's Coastlines* (E. C. F. Bird and M. L. Schwartz (Eds.), 1071 pp., Van Nostrand Reinhold Co., New York, 1985).

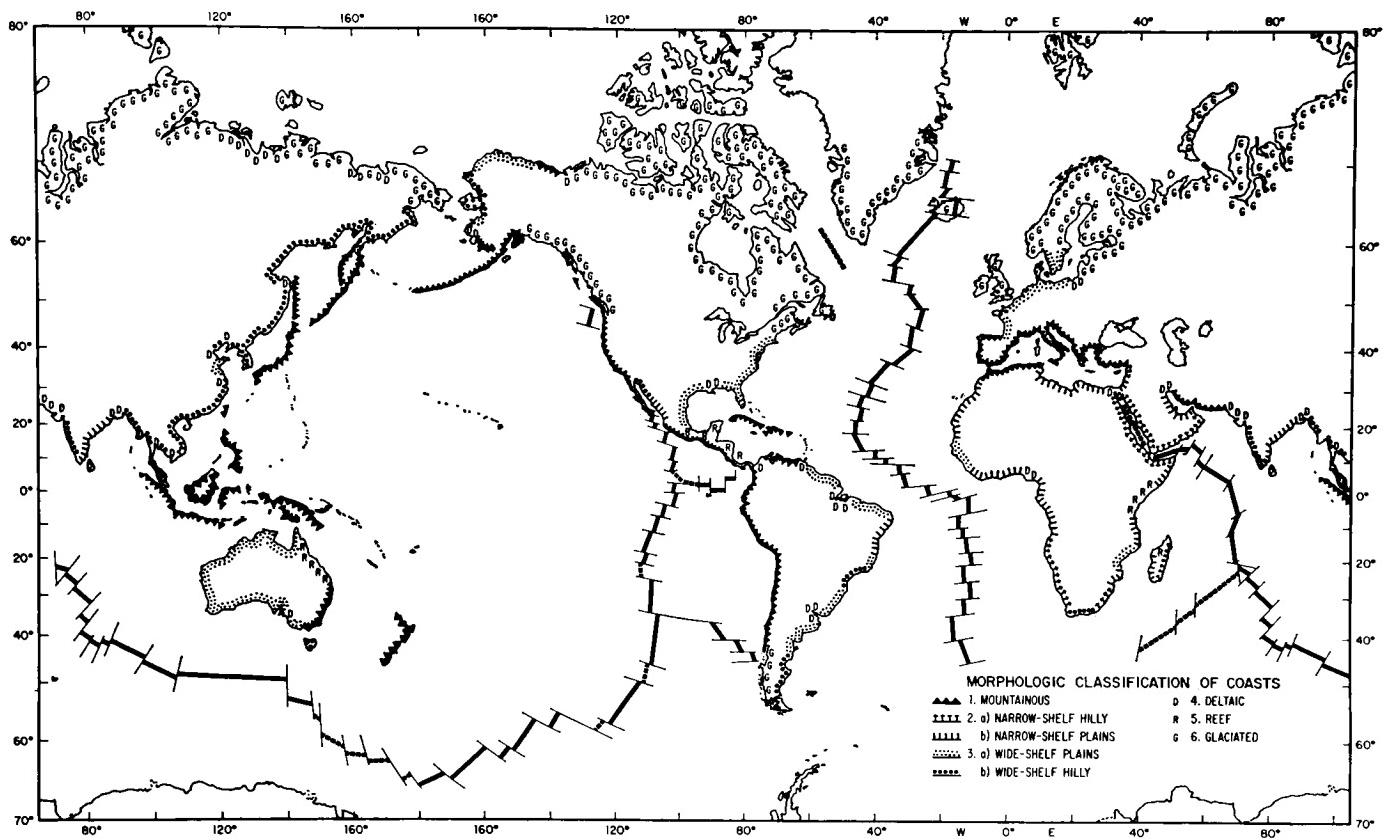


Figure 6-2. Worldwide distribution of morphologic coastal types.

PLATE C-1

WEST COAST, KOREA

The western side of the Korean peninsula is a Cretaceous granitic batholith intruded into Paleozoic metamorphic rocks. All the rocks are coarsely crystalline and weather to sand-size detritus called *grus*. Weathering is deep, with residual subspherical masses of relatively fresh granite forming hilltops above boulder-strewn slopes down into sandy river valleys (Figure C-1.1). Rivers are *braided* to carry massive bedloads. After centuries of deforestation and a recent war, erosion is a major problem. Summer monsoon rains cause avalanches and mudslides on many slopes. Valley floors are almost completely terraced into rice paddies.

The Yellow Sea coast is known for its high tides, which reach 12 m near Inch'on (A). Ships enter tidal basins at high tide and, after the massive gates are closed, unload safely at dockside. Low tide exposes several miles of mud flats far offshore from the basins. Powerful tidal currents ebb and flow among the offshore islands and into the river-mouth estuaries. Sea walls and dikes have permitted reclamation of much rice paddy land from former tidal flats in smaller valleys. In fact, the coast has been extensively straightened by dikes across most of the smaller valleys. Salt is reclaimed from evaporation basins behind sea walls, producing white rectangular patches (B).

Most of the Yellow Sea is less than 60 m deep. Although the tide range is as high as anywhere in the world, wave energy on the west Korean coast is low because of the shallowness and restricted area of the sea. Only a few sandy beaches have formed to bridge the headlands and islands. Most of the sand derived from the erosion of the granite mountains is trapped in deltas at the heads of estuaries. In spite of the strong tidal currents, low wave energy and the deeply embayed nature of the coast combine to inhibit longshore sand movement that would develop beaches, although vegetated sand dunes are formed in places (Figure C-1.2). Extensive intertidal mud flats extend far offshore (Figure C-1.3).

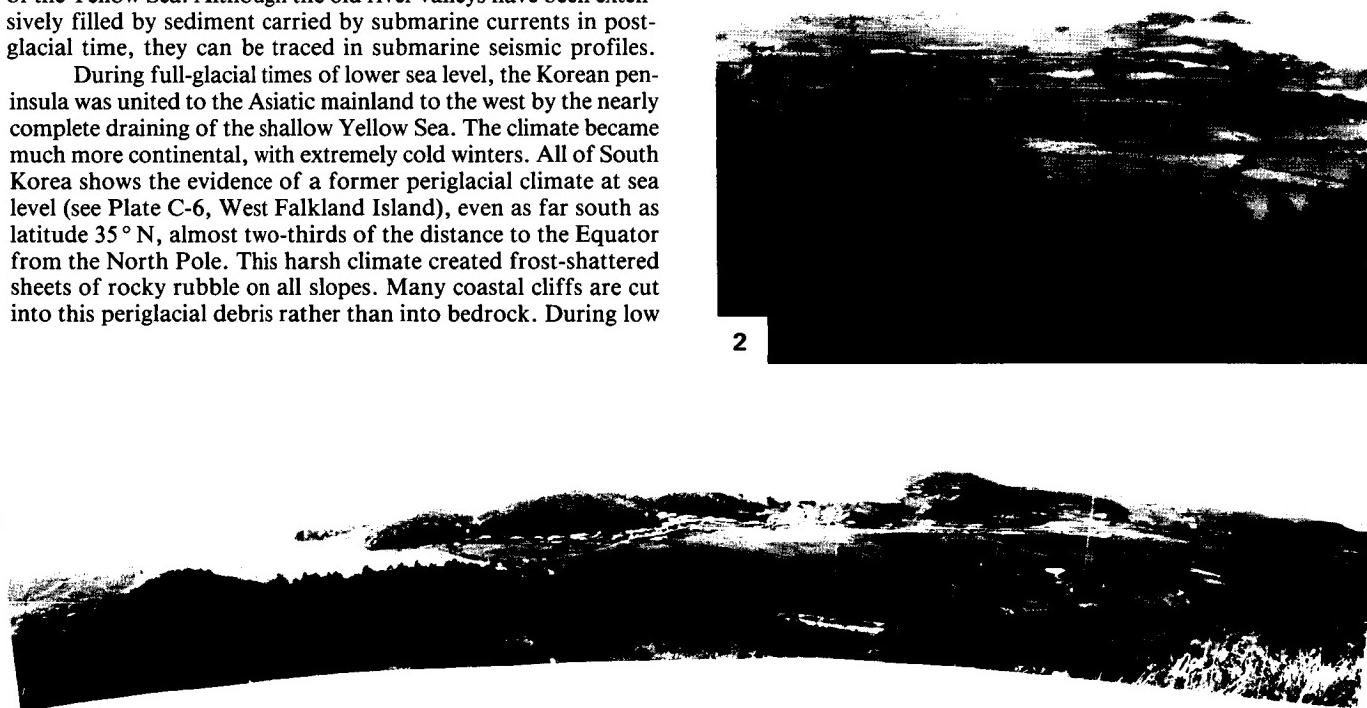
This is a type of *ria* or drowned coast (Guilcher, 1976). During glacial times, river valleys extended out across the floor of the Yellow Sea. Although the old river valleys have been extensively filled by sediment carried by submarine currents in post-glacial time, they can be traced in submarine seismic profiles.

During full-glacial times of lower sea level, the Korean peninsula was united to the Asiatic mainland to the west by the nearly complete draining of the shallow Yellow Sea. The climate became much more continental, with extremely cold winters. All of South Korea shows the evidence of a former periglacial climate at sea level (see Plate C-6, West Falkland Island), even as far south as latitude 35° N, almost two-thirds of the distance to the Equator from the North Pole. This harsh climate created frost-shattered sheets of rocky rubble on all slopes. Many coastal cliffs are cut into this periglacial debris rather than into bedrock. During low

sea level, the exposed floor of the Yellow Sea was a vast plain of silt, carried from the China mainland by the Yellow River (out of view to the west). Both the sea and the river are named for their massive muddy sediment load. This river is said to be 40 percent mud by weight in times of flood. The exposed seafloor plains and the cold westerly winds from Siberia combined to create massive glacial-age dust clouds over Korea. Windblown silt (*loess*; see Chapter 8) draped the hills of the peninsula and washed back down to mix with the coarse solifluction debris. The modern rivers carry this mixture back to the coast, where the mud flat sediments show the complexity of their polygenetic sources.

Tidal currents of 15 km per hour scour constricted channels between islands and in river mouths, but when the currents slacken at each high tide, there is an interval of up to 1 hour when mud can settle onto the flooded tidal flats. During the next low tide, these new layers of mud can become sun-dried and hard or can be attached to a sticky algal layer on the mud surface. The tidal flats have accreted upward to near high-tide level even while deep channels are eroded among them by ebbing and flooding currents. Relatively clear ocean waters along the axes of the tidal channels are clearly visible on the image (C). Plumes of muddy water swirl over the shallow interchannel areas.

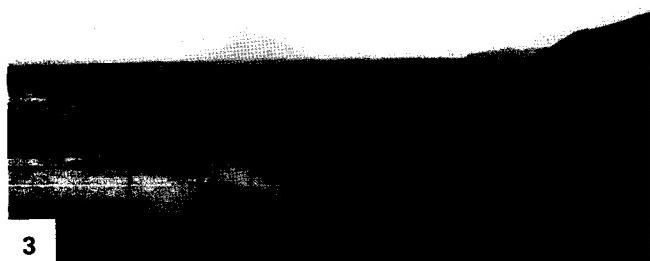
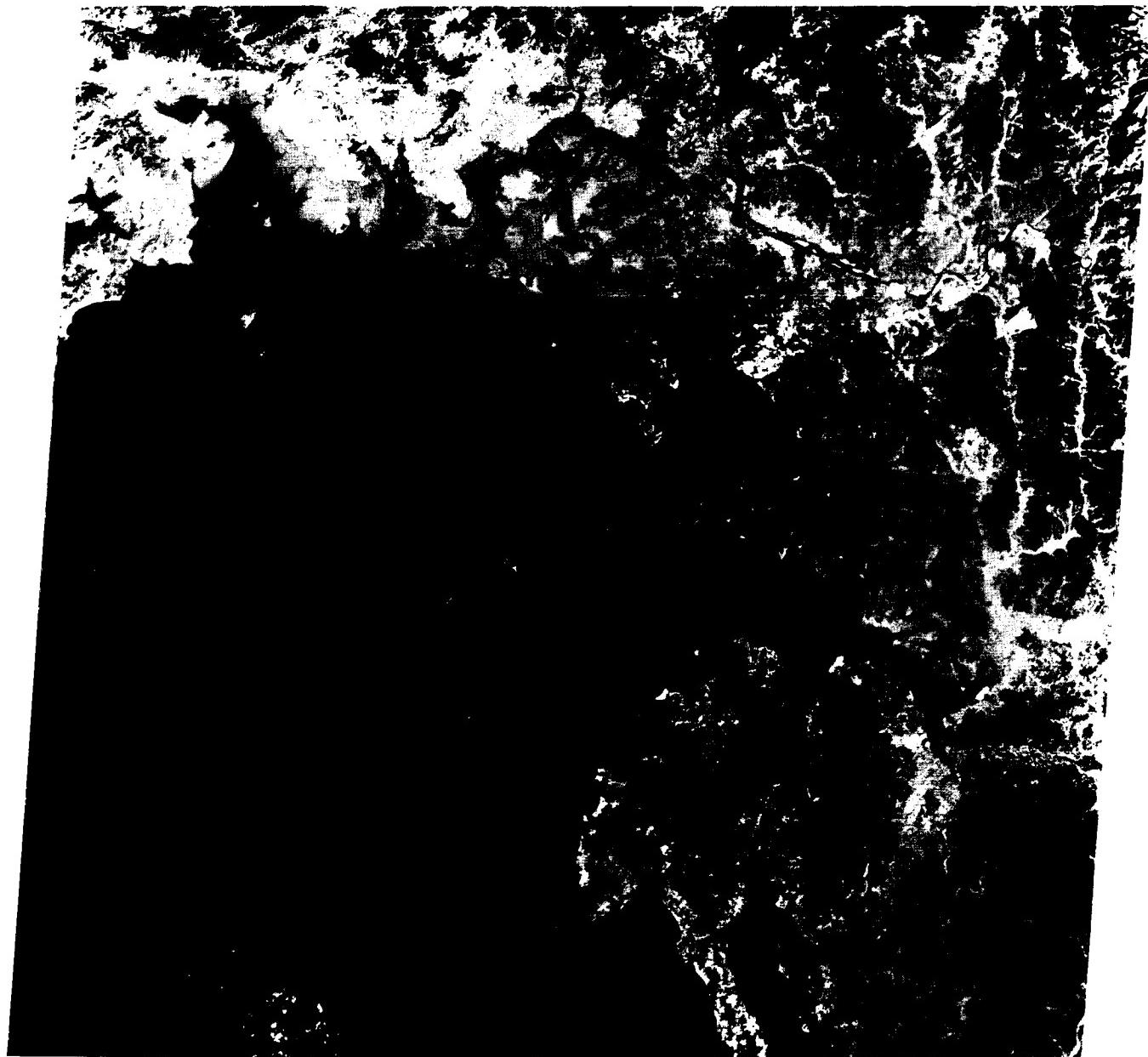
Seoul, a city of at least 8 million people, fills the valley floor of the Han River about 16 km inland from its seaport, Inch'on. The river valleys are useless for dock facilities because of the powerful tidal currents, shifting gravel bars, and submerged mud flats. Landsat 1100-01453-5, October 31, 1972.



1

2

ORIGINAL PAGE IS
OF POOR QUALITY



3

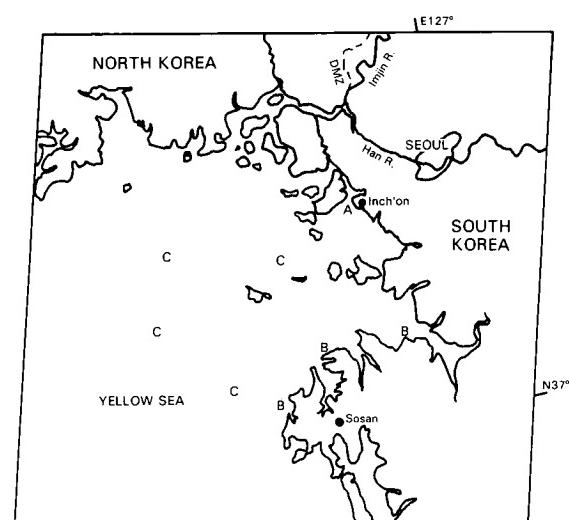


PLATE C-2

NEW SOUTH WALES, AUSTRALIA

The New South Wales coast of southeastern Australia is underlain by Paleozoic and Mesozoic platform sedimentary rocks, mostly sandstones. In the northern half of this view, relief is low, valleys are broad and shallow, and the drowned entrances at the coast are also broad and shallow (A). In the south, dissection of more resistant sandstone created narrow, entrenched meandering valleys (Figure C-2.1) that, when drowned, become steep narrow branching estuaries such as Broken Bay (B). Port Jackson, the harbor of Sydney and one of the world's great harbors (D), was actually overlooked by James Cook in 1770 because of its narrow mouth.

The continental shelf off New South Wales is less than 40 km wide and is deeper than the world average. Wave energy on this coast is high. Winds from the south and southeast blow unobstructed across the Tasman Sea from New Zealand or Antarctica. The tide range is only moderate, less than 2 m.

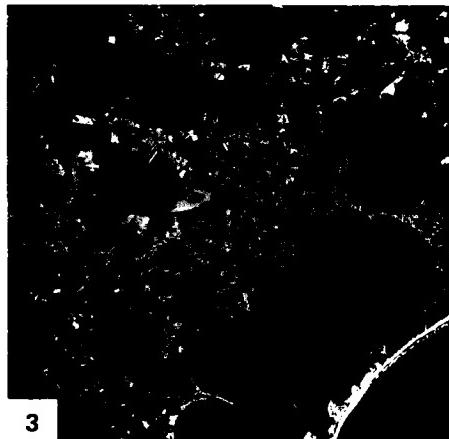
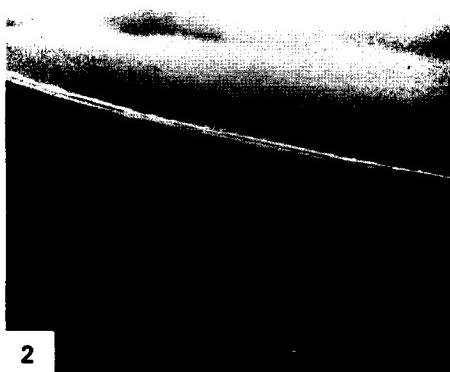
The broad shallow estuaries north of Newcastle (33° S) are enclosed or protected by sand barriers of two different ages. The Pleistocene beach and dune systems date from the last interglacial time, about 135 000 to 120 000 years ago. They are soil- and vegetation-covered and are somewhat degraded by erosion. The younger beach and dune barriers are Holocene in age and show in the image by their very bright tones (D). The older beach ridges record a long period of subaerial exposure to water and wind erosion during the most recent ice age, when sea level was much lower than at present, before the return of the sea to this coast only 6000 to 6500 years ago (Thom et al., 1981).

The beaches show a tendency to form perpendicular to the dominant southeast swell even though the rocky coast trends more nearly north-northeast. Most beaches have a *zetaform*, or logarithmic-spiral plan view, with sharp concave curvature immediately north of a projecting headland and a progressively more open curvature facing to the north (Figure C-2.2). The pattern can be easily explained by the refraction of waves moving onshore obliquely against the regional trend of the coast.

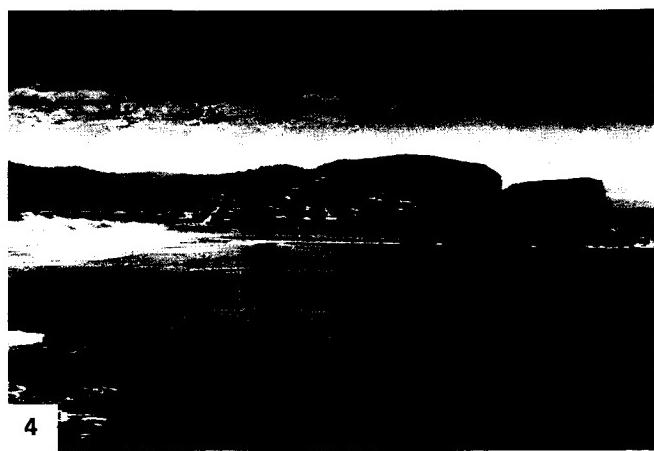
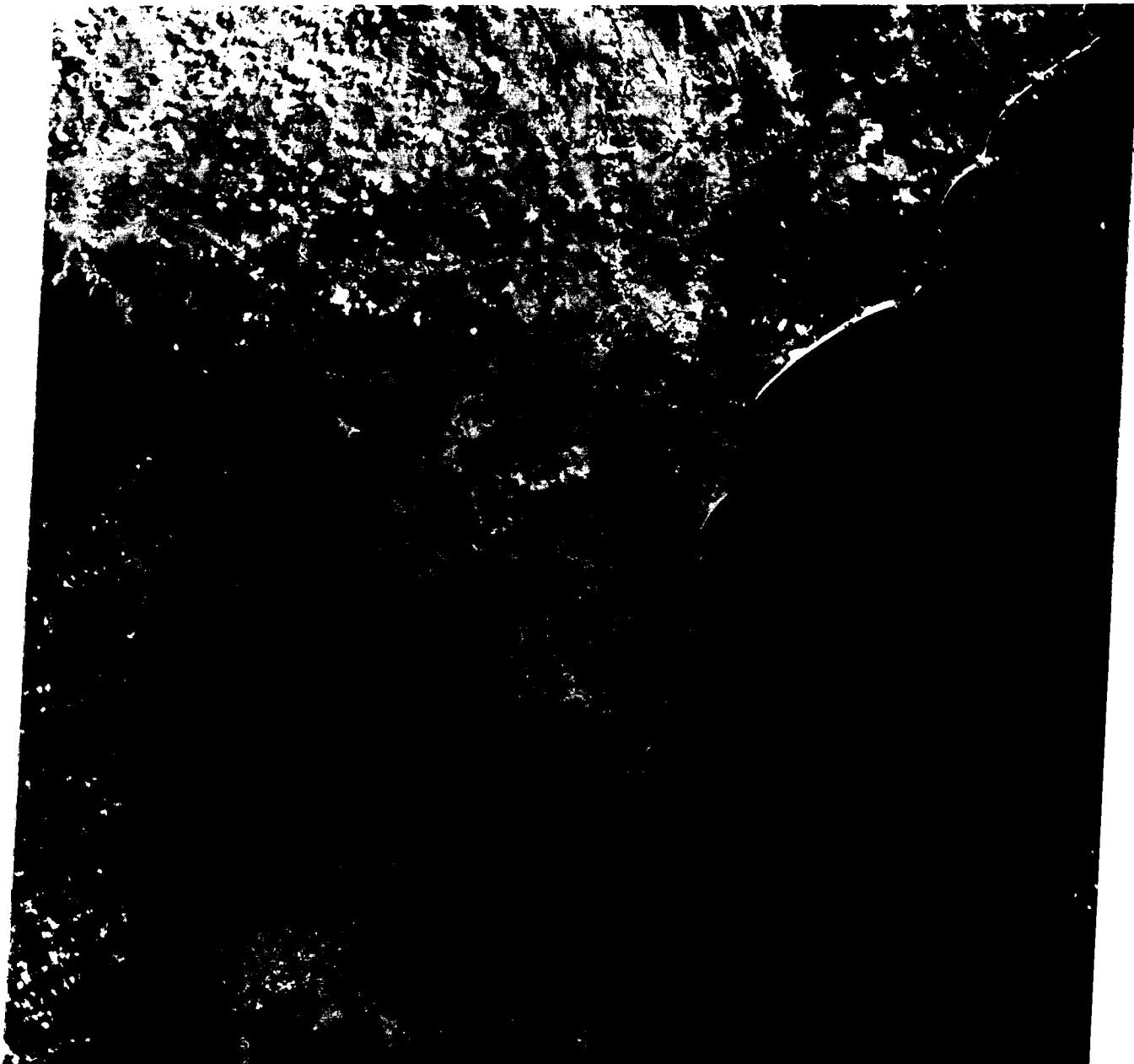
The drowned meandering valley of Broken Bay (B) just north of the city of Sydney is an excellent example of a subaerial valley that has been submerged by rising sea level without substantial marine modification. The same dendritic and meandering pattern can be seen upstream from the head of submergence and in the drowned part. The lower tributaries have been dismembered or *betrunked* by submergence so that each now enters the sea instead of the trunk river. Such a pattern, common also in Chesapeake Bay (Plate C-23), is a diagnostic feature of submergence of a fluvially eroded landscape.

As the last ice age ended and sea level rose toward its present level about 6500 years ago, the shallower estuaries in the north developed new barrier beaches, partly from sand supplied by reworking of the older beach ridges in the embayments. The initial effect of submergence was a marine *transgression*, with seawater flooding into the embayments and depositing onlapping marine sediments. After a few thousand years of relatively stable sea level, younger beach ridges accreted in front of the older ones, and the coast prograded by deposition. For the last 2000 to 3000 years, the beach ridges have stabilized; sediment supply from offshore and alongshore is balanced by wind transport off the beaches into dunes. Some of the beaches are now in an equilibrium condition, poised between erosion and accretion. Figure C-2.3 illustrates this at Tuggerah Lake, a lagoon enclosed by a sand barrier, with elongate distributary levees extending along small stream channels. Vegetation-covered parabolic dunes back the northern end of the barrier beach.

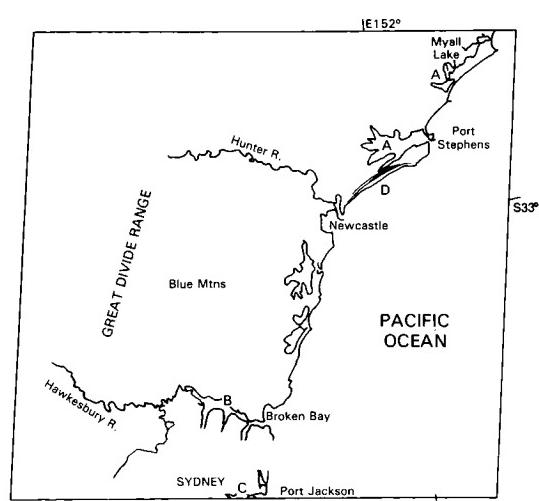
In the south, the deeper narrower estuaries have accumulated fewer and smaller beaches. The coast is more irregular, with bold headlands of rock and narrower harbor entrances (Figure C-2.4). Longshore littoral transport is inhibited by the more rugged coast and deeper water immediately offshore. Landsat 2263-23003-6, October 12, 1975.



ORIGINAL PAGE IS
OF POOR QUALITY



4



COBOURG PENINSULA,
NORTHERN TERRITORY, AUSTRALIA

The northernmost part of Australia (Arnhem Land) faces onto the Arafura Sea toward the eastern Indonesian archipelago. The shallow epicontinental sea, poorly charted and strewn with isolated reefs and waterless islands, was mostly dry land during the low sea level of the ice ages.

The ancient shield of the Australian continent has been eroded to its roots. On the Cobourg Peninsula, a thin cover of Mesozoic sandstone covers the crystalline basement. Nowhere is the relief greater than 500 m, and several kilometers inland, the land may be only a few meters above sea level.

The vegetation of the Northern Territory is a dry savanna. Torrential rains fall during the summer cyclone (= hurricane or typhoon) season, but during much of the year, the plains are hot and dry. Eucalyptus trees and acacias grow in sheltered places below rock ledges. The rocks are deeply weathered, often to an iron-oxide residue called *laterite* that in some places is pure enough to be loaded directly into ships as iron ore. Elsewhere, a comparable residual soil rich in aluminum oxide is the commercial ore of aluminum, bauxite.

As evident in this Plate and in Figure C-3.1 (Cape Wessel, 300 km to the east), the subdued deeply weathered continental relief has been drowned by the postglacial rise of sea level. No extensive valley systems have developed because of the brief seasonal runoff and the subdued topographic relief, but a few valleys are outlined by the dark red reflectance of trees in this false-color image. In particular, areas of intertidal *mangrove swamp* (A) fringe the shoreline and fill two extensive tidal basins on the south side of the peninsula.

In the more humid tropics, mangroves form a thick forest within the intertidal zone. These remarkable trees, members of several plant families, have convergently adapted to life in a saline environment with varying degrees of tidal flooding (see also Plate C-15). Root structures are adapted to provide oxygen through spike-like upward projections. Prop roots support the trees in soft mud. Some species even hold their seeds on the tree until the seed has sprouted two leaves and a substantial protoroot so that, when it falls into the sea upright and floats off, perhaps it will ground in a mud flat and begin a new life. These are among

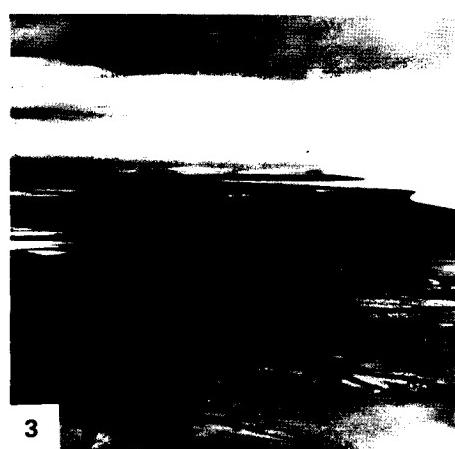
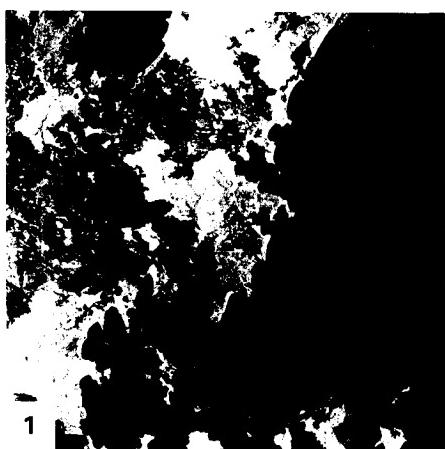
the few plants that can be said to be *viviparous*, or bearers of live young.

In the dry savanna region of northern Australia, evaporation in tidal pools creates high salinity and temperatures that even mangroves cannot tolerate. There, a thin border of mangrove jungle, sometimes only a few trees wide, fringes the shoreline, perhaps rooted in a sandy beach ridge where rainwater can occasionally dilute the saline ground water. Immediately behind the mangrove fringe are harsh white salt-encrusted tidal flats that may be several kilometers wide (B) (Figure C-3.2, an aerial photograph covering the left-most land in Plate C-3). Near the center of Plate C-3, episodic high water floods 30 km inland to fill a shallow basin almost 16 km in diameter. In this view, the tidal creeks and the edge of the basin are outlined by a thin line of red-reflecting mangroves. Figure C-3.3 shows a similar scene from the air near Princess Charlotte Bay.

This is one example of a drowned subaerial landscape in which the lower parts of dendritic branching river valleys are submerged and only the former headwaters remain above present sea level. The pattern is called *skeletal* because only the branching ridge crests are exposed. Cobourg Peninsula shows progressively more submergence from east to west, possibly because of recent westward downwarping.

In the Arafura Sea north of the peninsula, this late September (springtime) scene shows ribbons or streamers of algae streaking the surface. Strong easterly trade winds blow at this time of year, creating the ocean surface pattern.

Minor coral reefs fringe the rocky coast wherever mud is not brought in by tidal creeks. Especially on the north coast of Cobourg Peninsula, small fringing reefs are abundant (Figure C-3.2). Multiple beach ridges have extended some of the headlands, as in the north center of Figure C-3.2, and other headlands have wave-cut platforms (Figure C-3.4). Elsewhere, prograded beach ridges enclose and smooth the outline of bay heads. The beaches have probably formed in Holocene time, with a chronology similar to those on the coast of New South Wales (Plate C-2). Landsat 1069-00442, September 30, 1972.



ORIGINAL PAGE
COLOR PHOTOGRAPH

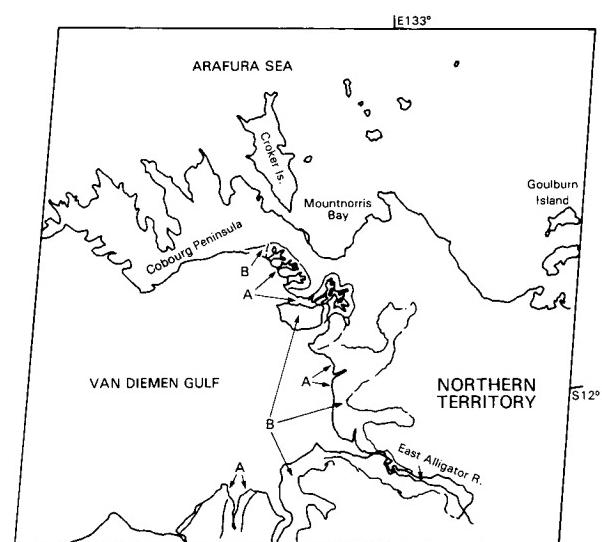
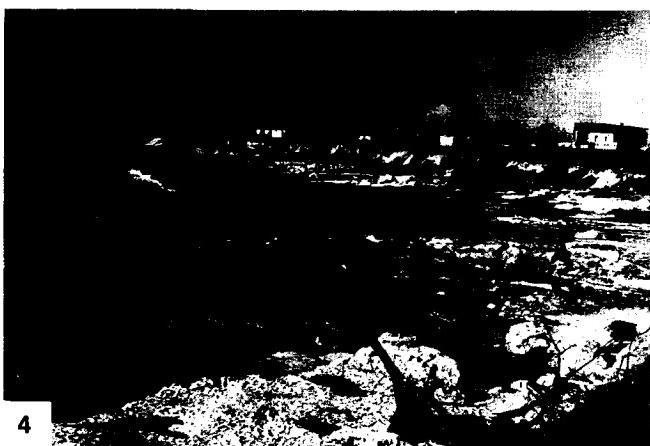


PLATE C-4

RIO GRANDE DO SUL, BRAZIL

The coast of the large southernmost Brazilian state of Rio Grande do Sul is another example of the sea reaching onto the margin of old eroded continental crust. Inland, the relief rises to 1000 meters. River valleys are not prominent. Offshore, the continental shelf is narrow, and a sharp submarine scarp marks the scar where South America rifted from Africa.

On the narrow coastal plain of Rio Grande do Sul, a very large, complex sand barrier spit has built southward for about 240 kilometers, enclosing a large lagoon called Lagoa dos Patos. Eighty kilometers north of the image margin is the southern Brazilian seaport of Porto Alegre, approached by a long voyage up the lagoon from the inlet at its southern end. The barrier, in places 100 km wide and extending 640 km from the city of Torres southward to the Uruguay border, is part of one of the world's longest sandy beaches. Another long barrier beach, approximately 500 km in length but much narrower, lines the Texas coast along the Gulf of Mexico (Figure C-4.1, a Landsat image showing Padre Island). Unlike the Brazilian Coastal Region, the Texas barrier has developed along a coastal plains of low relief.

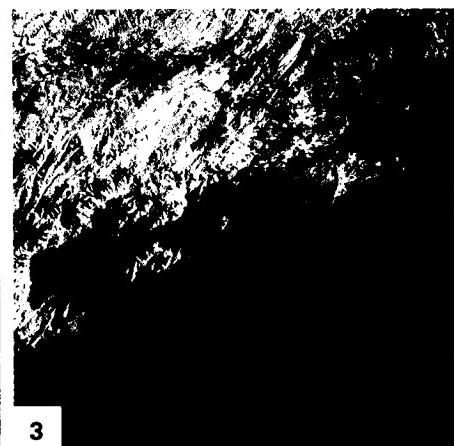
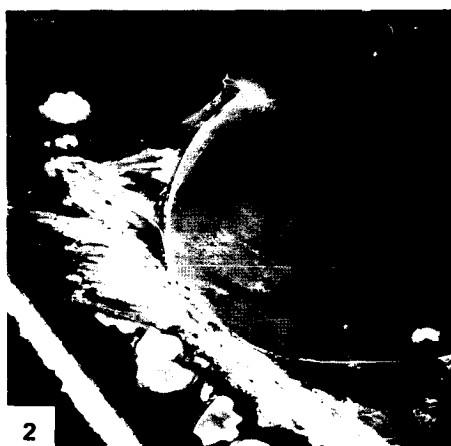
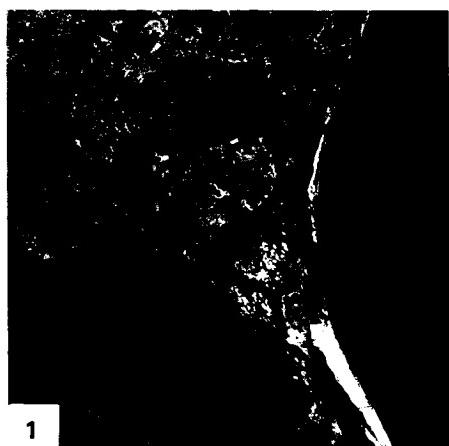
The most striking features of the Lagoa dos Patos are the *cuspate spits* that segment it (Figure C-4.2). The image clearly shows plumes of sediment carried southeast from the cuspate headlands on the inland shore of the lagoon as the surface currents are deflected into the lagoon from each point. On the southeast shore of the lagoon, along the barrier spit, the current is generally northeastward, creating even more sharply defined asymmetric cusps.

The sediment-transporting circulation system of the lagoon seems to develop as a series of counterclockwise rotating ellipses with north-south long axes. A combination of winds and tidal currents maintain the alternating cuspate spits in a north-south orientation in spite of the generally northeast trend of the outer coast. A similar pattern has been noted in Laguna Madre, behind

the Padre Island barrier of Texas (Figure C-4.1), and in southeastern Australia (Bird, 1971).

The great outer barrier of Lagoa dos Patos shows a complex growth history. The crystalline rocks of the shield and their overlying Mesozoic basalt lava flows were eroded to low relief, and buried under a thin cover of Tertiary sediments. These sediments are known only from subsurface borings through a thin cover of Pleistocene sand and gravel that forms the floor of the lagoon. More than one cycle of Pleistocene sea-level fluctuations may be recorded in the Pleistocene sediments. At some time in the Late Pleistocene, interglacial sea level rose to 5 m above its present level and built a barrier system similar to the present one (Delaney, 1962, 1966). About 10000 km² of the present barrier belongs to this Pleistocene system. The barrier and dune sands are now weathered to red and yellow colors, are lightly indurated, and form a low plain with low fixed sand dunes and shallow ponds. A good working hypothesis is that this barrier formed about 125000 years ago, during the last interglacial episode, as has been verified on the coast of New South Wales, Australia (Plate C-2). Subsequently, sea level fell during the most recent ice age, and the old beach ridges and dunes were weathered and eroded. When sea level rose again in the Holocene Epoch, a straight cliff was cut in the Pleistocene barrier, and the red sands were mixed with fresher sand to build the modern barrier, which in itself covers an area of 7000 km² and is up to 15 km wide in places. The straight low scarp that separates the Pleistocene and Holocene barrier is easily visible on Plate C-4 because of the line of ponds and lagoons along it.

Up the coast some 1000 km to the northeast, near Rio de Janeiro, the rugged irregular coastline reflects the interaction between a rising Holocene sea level and mountainous terrain just inland (Figures C-4.3 and C-4.4). The only major barrier developed in this scene is the elongate spit that has reached an offshore island. **Landsat 21468-12235-6, January 29, 1979.**



ORIGINAL PAGE IS
OF POOR QUALITY



4

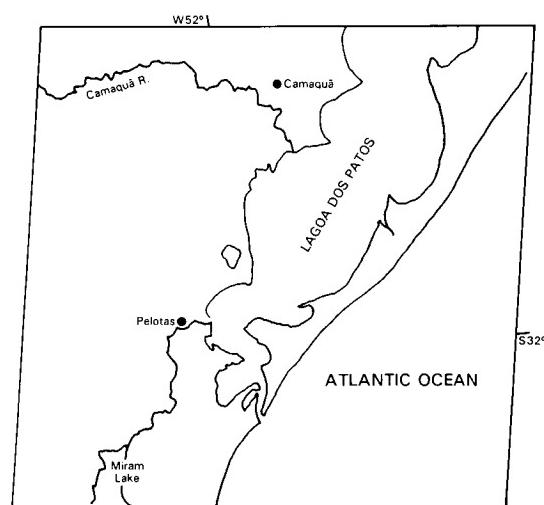


PLATE C-5

GLACIER BAY, ALASKA

Glacier Bay National Monument, northwest of Juneau, Alaska, is a vast area of mountain ice fields, glaciers, and fjords. It covers about 14000 km², including most of the eastern half of the scene north of Icy Strait. Since their European discovery in 1794, some of the tidewater glacier termini have shrunk more than 100 km. Glacier Bay was completely filled with ice to its junction with Icy Strait in 1794. By the time the area was visited by the noted naturalist, John Muir, in 1879, the ice front had retreated 77 km and had divided into numerous tidewater tributary glaciers. By the first decade of this century, there were 11 tidewater glaciers, but some that had been popular tourist attractions were no longer accessible (Tarr and Martin, 1914). Now there are about 16 separate tidewater ice fronts, as continued shrinkage of the ice dismembers the former great ice streams. From time to time, one or more of the glaciers has surged forward for a few years, then resumed its general retreat.

The fjords of Glacier Bay (Figure C-5.1) are strongly controlled by tectonic and structural lineaments. The Chatham Strait fault nearly bisects the image from top to bottom slightly oblique to the 135th west meridian. Right-lateral strike-slip faulting totalling 200 km has been suggested for this fault (Lathram, 1964). The Chugach/St. Elias fault has formed a zone of crushed and weakened rocks parallel to the coast across the southwest corner of the scene.

South of the scene, the two faults merge into the Fairweather fault, a major tectonic boundary between terranes that have no obvious genetic relation to each other, and may have been translocated thousands of kilometers northward to be accreted onto the western edge of North America by lithospheric plate motions (see Plate T-9).

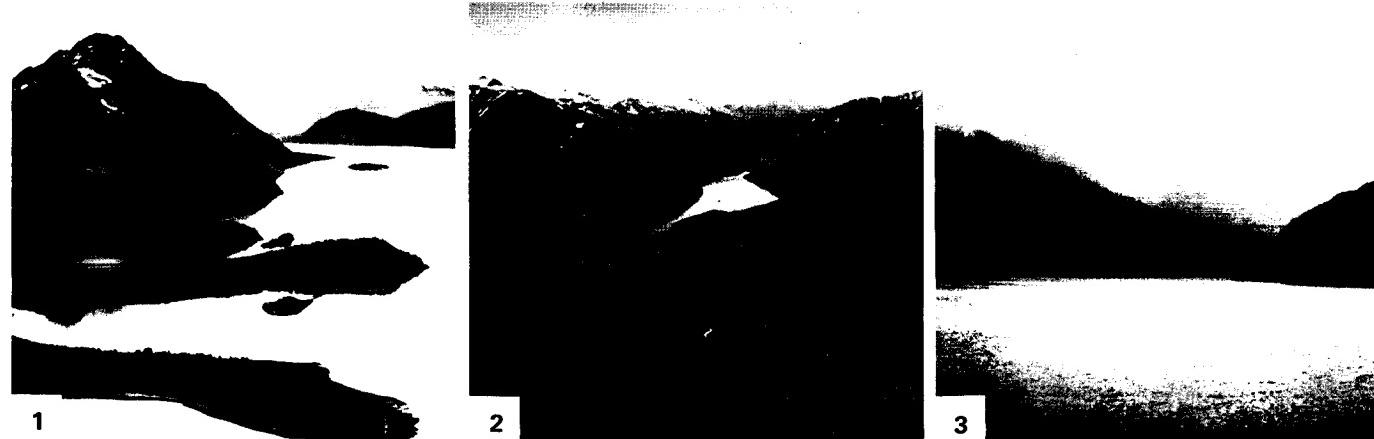
Erosion by rivers and glaciers has carved deep trough-like valleys along the tectonic lineaments. Some valleys extend radially from the centers of the large Glacier Bay and Taku Ice Fields. *Fjords* are glacier troughs, eroded below sea level and now submerged. An excellent example is Tracy Arm (Figure C-5.2) off the lower right edge of the Plate.

Tides in Glacier Bay range up to 7 m in amplitude. The combination of deep fjords, powerful tidal currents, and very recent deglaciation has produced a coastal landscape devoid of any depositional landforms except for outwash deltas at the fronts of some retreating glaciers. There are almost no beaches except for gravel pockets in coves. Icebergs breaking from the receding glaciers are a sight witnessed by thousands of tourists each year, mostly from the safety of a ship well offshore passing along an inland passage (Figure C-5.3) such as Chatham Strait.

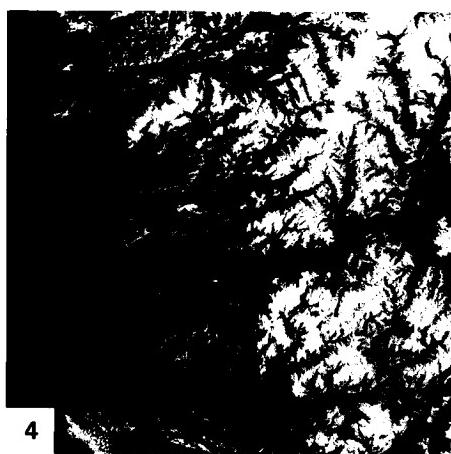
It is typical of tectonic coasts to have strong structural lineations, in this region accentuated by glacial erosion. When such lineations are parallel to the coast, Suess (1888) designated the coast as a *Pacific* type, as in this scene and in Plates C-9 and C-10. We now interpret Suess's Pacific-type coasts as typical of converging plate margins, where active tectonic compression is deforming the edge of the continental crust.

Because of either rapid postglacial isostatic uplift or active tectonism, the region of Glacier Bay is experiencing exceptionally rapid emergence in recent decades. Sites of tide gages that were installed in the late 1930s had risen more than 60 cm when the sites were reoccupied in the 1960s (Clark, 1977; Hicks and Shofnos, 1965). Maximum uplift rates near the center of the National Monument approached 4 cm per year. Studies are in progress to determine if the uplift is an isostatic response to the recent rapid reduction in the mass of glacier ice or if it is possibly precursory movement prior to a major earthquake in the region.

Figure C-5.4 is a Landsat view of western Norway, from whence the name "fjord" has been given to drowned coastal glacial valleys. Here the fjords are narrower, but some extend inland for more than 150 km. Because the structural grain of the Norwegian terrain is oblique or perpendicular to the coast, many fjords extend far inland rather than paralleling the outer coast as they do on the Pacific-type coast of Alaska. **Landsat 1175-19330-7, September 6, 1974.**



ORIGINAL PAGE IS
OF POOR QUALITY



4

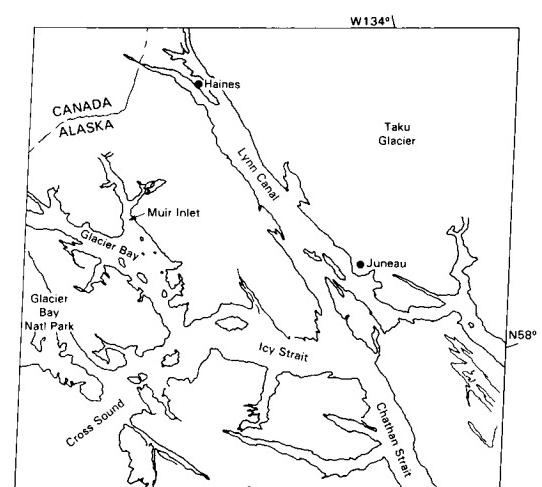


PLATE C-6

WEST FALKLAND ISLAND

West Falkland Island is a "skeleton island," defined as an embayed island, "characterized by a narrow and serrate axial ridge or backbone with slender lateral spurs or ribs; and the ribs enclose open bays" (Davis 1928, p. 197; Cotton, 1969). The island is continental in structure, a fragment of the ancient Gondwana supercontinent that broke up in the Mesozoic Era. The Falkland Islands are a piece of continental crust that was left behind as South America moved westward from Africa. The surface rocks are Paleozoic and Mesozoic quartzites and sandstones, folded and faulted in an intricate pattern that controls the outline of the two large Falkland Islands and innumerable smaller ones.

The intricate skeletal outline of West Falkland Island shown in the image is primarily the result of subaerial erosion, drowned by the postglacial rise of sea level. During glacial times, the Falklands were a range of hills on the emerged Argentine continental shelf 600 km east of Patagonia in southern Argentina. The climate of the Falklands then was even colder than now, yet the present islands were only lightly glaciated by small cirque glaciers on the highest peaks (Clapperton, 1971). The islands were intensely affected by periglacial process, however. The term "solifluction" was coined by Andersson (1906) to define the dominant slope process of the Falkland Islands.

The combination of folded arenaceous sedimentary rocks and intense solifluction created broad low gradient valleys, residual ridge crests capped by tors or low cliffs, and cirque-like "theater-headed" semicircular valley heads (Figure C-6.1). The lowlands were engulfed by masses of saturated sediments that flowed down from higher slopes (Figure C-6.2). When drowned

by the postglacial rise of sea level, the valley systems were dismembered, with ridge crests of resistant rock becoming islands or long sinuous peninsulas. The image clearly shows islands and peninsulas that can be traced into strike ridges across the interior of West Falkland Island. Between them are broad shallow valleys full of ponds and marshes. Major fracture systems that were etched out by subaerial erosion create deep narrow coves along the coast and on the shores of the inland lakes. An especially prominent rock outcrop forms a nearly continuous coastal ridge along Falkland Sound on the northern two-thirds of the east side of West Falkland Island (Figure C-6.3). The small village of Port Howard is on a long narrow harbor behind the prominent ridge.

Like the coast of Ireland (Plate C-7), the coast of West Falkland Island is of the *Atlantic* type, in which structural ridges are truncated by the present shoreline as though fragments from a preexisting mass. The much finer erosional texture of West Falkland Island is due to the unique response of the rock types to intense frost action and solifluction. Even relatively narrow intersecting fracture zones (A) were etched out and are now narrow branching marine coves.

Intense glaciation would have smoothed the outline of West Falkland Island and created deep straight-sided fjords (as in Plate C-5) instead of narrow crooked inlets. Why the Falkland Islands escaped glaciation is not clear, when Patagonia and nearby sub-Antarctic islands carried full ice caps. Perhaps the exposed Argentine shelf and the rain shadow of the Patagonian ice cap blocked moisture from reaching the islands. **Landsat 31510-12502-6, April 23, 1982.**

ORIGINAL PAGE IS
OF POOR QUALITY

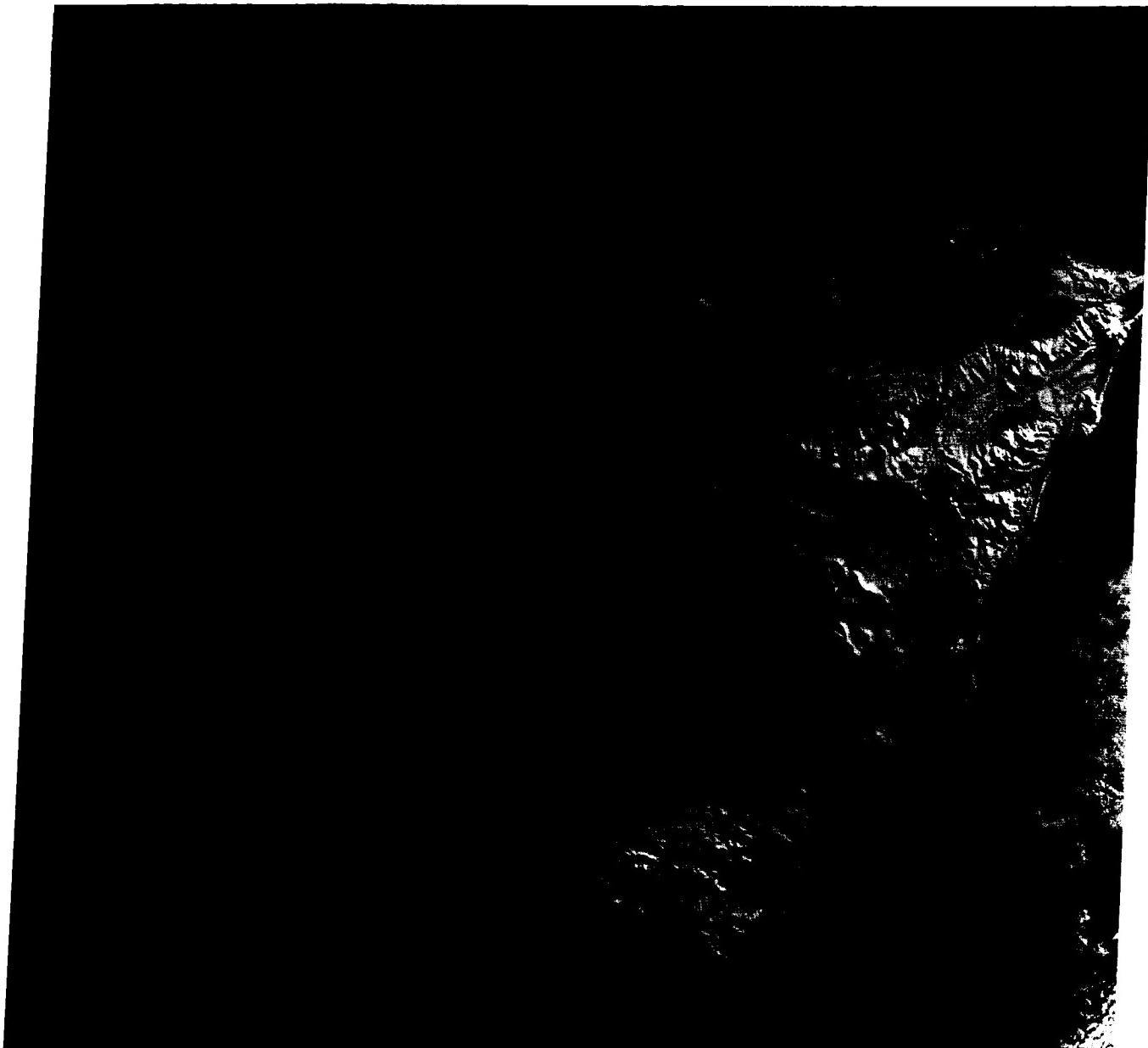


1



2

ORIGINAL PAGE
COLOR PHOTOGRAPH



3

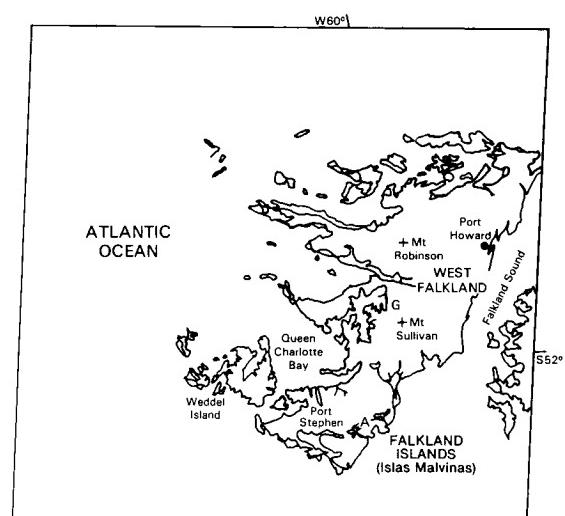


PLATE C-7

SOUTHWEST IRELAND

The southwest corner of Ireland is the classic example of an *Atlantic* type of continental margin, with the coast cutting obliquely across the Hercynian (Appalachian) orogenic trends and breaking the strike ridges of Paleozoic rocks. Somewhere in eastern North America, perhaps covered by Mesozoic and Cenozoic continental shelf sediments, these same strike ridges resume, torn apart by the Mesozoic rifting and opening of the Atlantic Ocean basin. The straight northwest-southeast alignment of the ends of the peninsulas is parallel to the faulted margin of a Tertiary basin about 20 km offshore (Stephens, 1970, p. 134).

Relatively few islands extend from the tips of the peninsulas, showing that the Paleozoic fold axes plunge so steeply that, within a few miles after they enter the sea, they are completely submerged. Similarly, the bays between the headlands are deep and open, although wave energy in them is quickly damped by refraction.

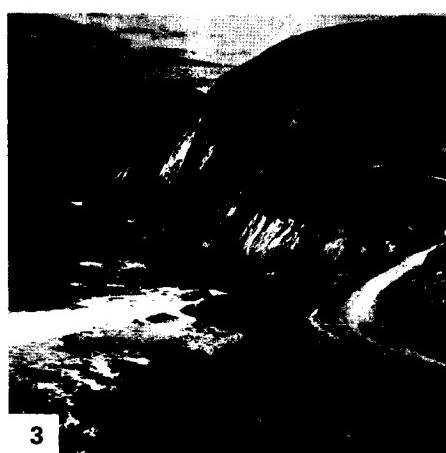
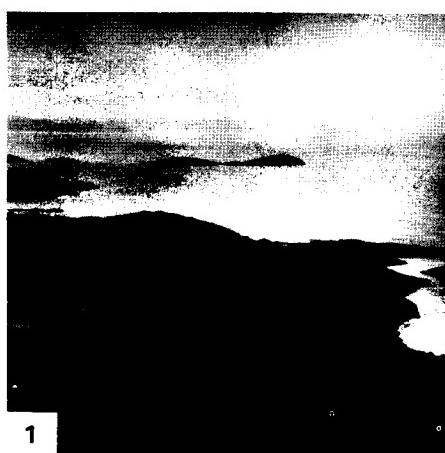
The Armorican Highlands of southwestern Ireland lie south of a line extending east from the head of Dingle Bay. They were lightly glaciated by a small ice cap, not part of the Fennoscandian ice sheet or the late-glacial Scottish ice cap. Ice flowed down the structural valleys to the sea, but did not create distinctive glacial troughs. Some drumlins in the glaciated valleys are now islands. Near present sea level, the slopes were subjected to intense periglacial frost action and mass wasting. Thick deposits of periglacial solifluction debris, angular rock fragments mixed with silt and clay, cover the lower valley walls. This "head," as it is locally known, gives a smooth rounded aspect to the landscape, although ridge crests tend to be rugged with *tors*, residual masses of bedrock that have been exposed by downhill solifluction as at Hag's Head, south of Galway (Figures C-7.1 and C-7.2). The area has been

deforested by grazing and woodcutting, and erosion is severe. Peat bogs or lakes fill many of the small depressions, and peat "blanket bogs" mantle many of the gentle lower valley walls.

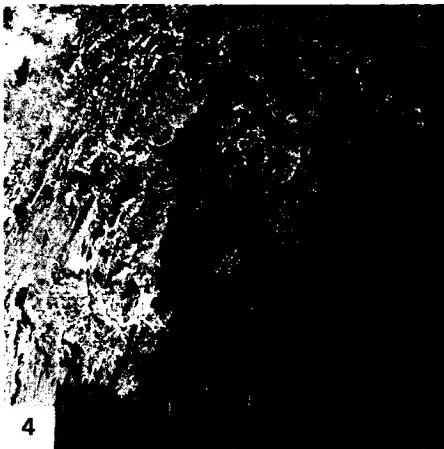
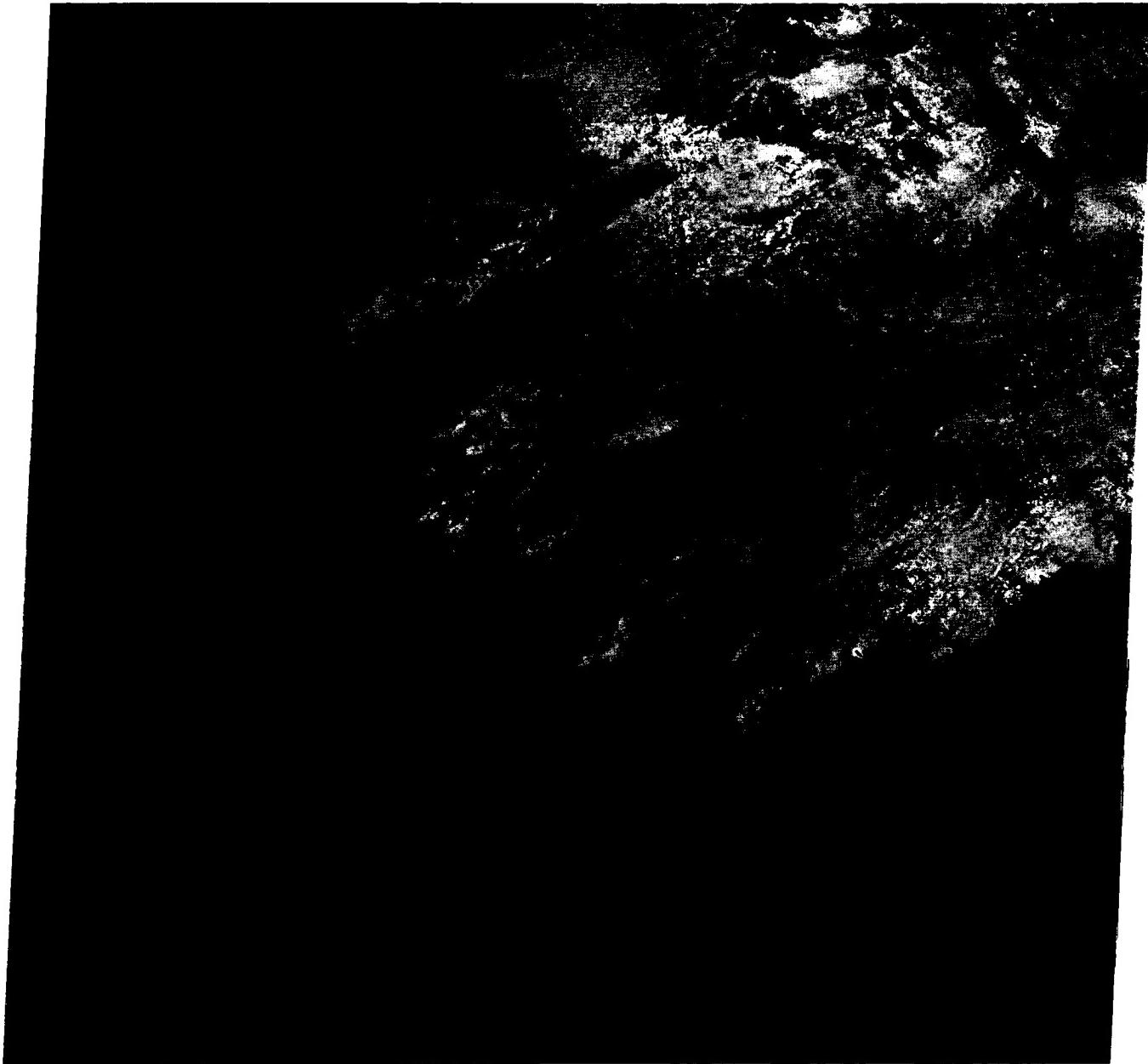
Ancient abrasion platforms are found at various places along this coast, some submerged and some emerged by amounts ranging from 3 to 9 m (Stephens, 1970, p. 140). Their age is uncertain, but they are generally being exhumed from beneath glacial drift or the periglacial "head." Their height has led to much speculation about the extent of postglacial isostatic uplift in the region and, thereby, the inferred thickness of the former ice cap on the mountains. If these shore features formed during last interglacial time, when the sea was a few meters higher than at present (see Plates C-2, C-4, and C-14), they may not have been significantly displaced.

Wave energy along this coast is refracted by the deep embayments. The small subsequent rivers follow the southwest-plunging strike valleys and enter the bays at their extreme inner ends. The wide flaring estuaries focus waves and currents to build some remarkable straight long *tombolos* and spits near the heads of bays, especially in Dingle Bay. These are among the few coastal depositional features to be seen on the image. The coast is a rather simple example of a fluvial landscape that was eroded on the strike ridges of an ancient mountain belt and was then torn apart and submerged (Figure C-7.3).

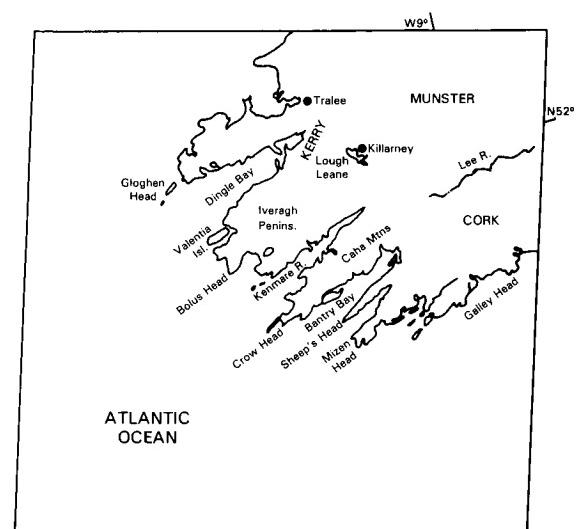
Very similar topography can be seen in the Landsat sub-scene of the Penobscot Bay region of the State of Maine (Figure C-7.4). Although that area was glaciated, the lineation is primarily of bedrock strike ridges. Neither Ireland nor Maine has *fjords*. Rather, these are *rias* or strike-controlled river valleys. **Landsat 2573-10492-6, August 17, 1976.**



ORIGINAL PAGE IS
OF POOR QUALITY



4



In the early part of the Mesozoic Era, some 200 Ma ago, an epicontinental ocean known as the Tethys stretched across southern Eurasia. Reef-building corals flourished in the warm Tethys Sea, and great thicknesses of limestone were deposited, interlayered with shale and sandstone. Later, these rocks were buried by younger sediments and folded into elongate anticlinal ridges and intervening synclines. During the main pulse of the Alpine mountain building, the fold belts were exhumed as the Dinaric Alps along the Adriatic south coast of Yugoslavia, seen in relation to the Italian coast to the west and the Albanian/Greek coast to its south in the HCMM image that makes up this Plate.

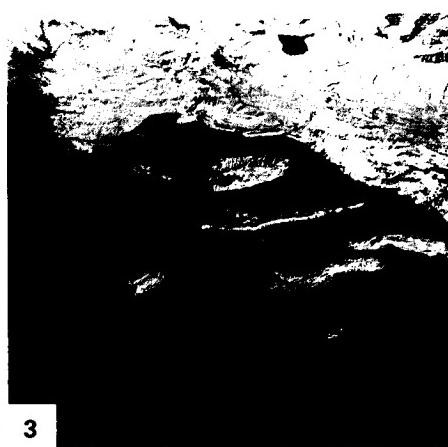
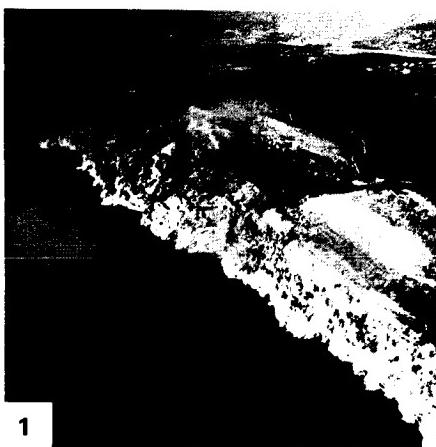
Limestone resists erosion in dry climates such as in the Mediterranean basin because most of the winter rain sinks underground. The landscape of the old district known as Dalmatia, now part of Yugoslavia, is the classic karst region of the world (Plate KL-5). The Dalmatian coast is, for the most part, a region of drowned karst. Aside from cliff cutting (Figure C-8.1), little marine modification of the subaerial karst landscape has occurred since it was partly submerged by the postglacial rise at sea level. Structurally controlled limestone ridges have been made into peninsulas and islands, evident along the coast near Dubrovnik (Figure C-8.2). Closely spaced gullies on the flanks of the ridges have been drowned to form other spectacular examples of skeleton islands (see Plate C-6 for a discussion of this phenomenon). The western end of Hvar Island and the small island west of it are the most notable examples (Landsat subimage, Figure C-8.3).

Millenniums of agriculture in the thin limestone soils of the Dalmatian coast have stripped off most of the soil, revealing

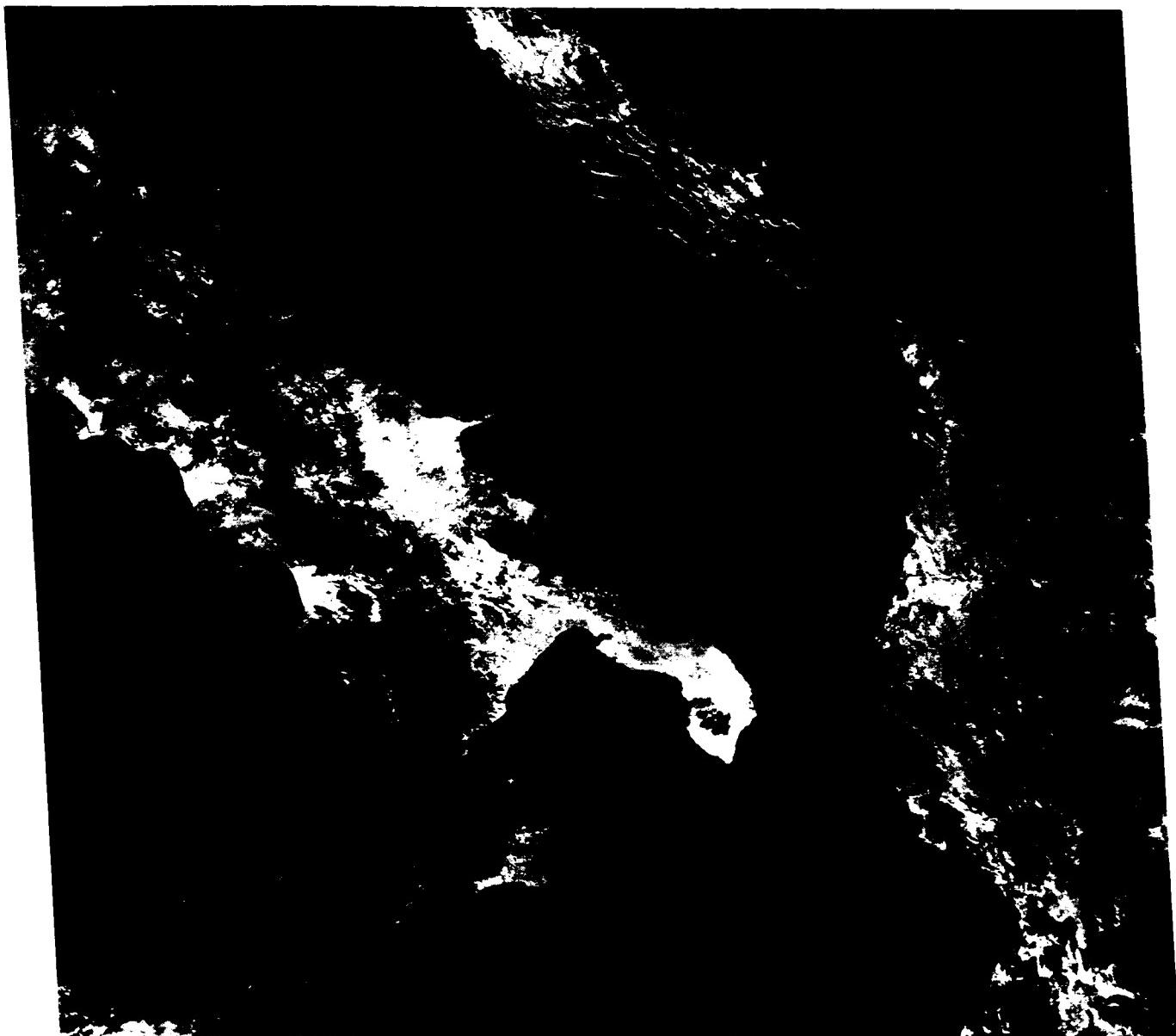
the structural intricacies of the rocks. Except for grazing and small terraced gardens and vineyards, most agriculture is now restricted to the alluvial soils of narrow floodplains and river deltas that now form fertile valleys between mountains that rise above them (Figure C-8.4).

The gently arcuate trends of the Dinaric folds are clearly traceable from the Yugoslav mainland onto the peninsulas and islands (Figure C-8.1). Although the structural deformation of the Dinaric Alps is older than that of the Makran coast (Plate C-9), the lineations parallel to the present Dalmatian shoreline indicate that this is a tectonically active region. The tendency of the few drowned valleys to zig-zag between perpendicularity and parallelism to the coast is another variant of the *ria* coast described in Plate C-7.

Except for small gravel spits and tombolos, there are no broad beaches along the Dalmatian coast. Because the limestone terrain is weathered primarily by solution, rivers do not carry sand and gravel to the sea. Furthermore, many of the rivers that drain the Dinaric Alps alternate between surface flow across alluvial plains and subsurface flow through cavern systems. The karst hydrology of the region is extremely complex, so that blockage of an underground channel can flood an alluvial valley for a year or two until the obstruction suddenly clears. The combination of a lack of alluvial sediments delivered to the coast by rivers and the lack of effective wave action on this narrow inland sea is not favorable for constructional coastal landforms. HCMM 0170-12020-2, October 13, 1978.



ORIGINAL PAGE IS
OF POOR QUALITY



4



PLATE C-9

"The Makran" is a traditional name for the desert northern coast of the Gulf of Oman and the Arabian Sea in eastern Iran and Pakistan. The Makran coast is on a converging tectonic plate margin, where oceanic lithosphere of the Arabian plate is subducting under the continental Eurasian plate. This is obviously a Pacific type of coast (p. 354) with folded and faulted mountain ridges trending parallel to the present shoreline. Seaward of the Pakistan portion of the Makran shown in this image, the Arabian Plate is subducting northward at a very shallow angle of about 2° , and is dragging Tertiary marine sediments many kilometers in thickness into an accretionary prism at the southern edge of the continent (White and Louden, 1983; Platt et al., 1985). The young sedimentary rocks are being scraped off the downgoing lithosphere and crumpled against the continental margin to form the wide belt of fold mountains that dominates the image. At the present coast, the process continues; the bold headlands at Jabal Zarain, Ras Ormara, and elsewhere are upthrust fault blocks of weakly consolidated mudstones and conglomerates of Miocene to Pleistocene age that are the lastest increments of land to the southern edge of Eurasia. In a 1945 earthquake, several new islands emerged along the Makran coast, including one at locality A in the image that is now obscured by muddy water around (and probably over) it. The cliffs of weakly consolidated geologically young sediments are so easily eroded that some sea cliffs are dangerous to approach by ship, for fear of rock falls and slides (Snead, 1969, p. 26).

Ras Ormara is an especially interesting example of a tombolo, or sand beach, that connects an island to the mainland (Figures C-9.1). The north-facing fault scarp, 300 m in height, is clearly visible on the Landsat image. The trends of the beach ridges on the mainland show that the headland was an island several kilometers offshore, toward which refracted waves gradually built beach ridges that tied the uplifted fault-block island to the mainland. Subsequently, intense erosion, especially from strong southwesterly wind and waves, has eroded much of the tombolo (Figure C-9.2). Coastal archeologic sites tens of kilometers inland have been cited as evidence that dramatic changes in this coastal outline have occurred only in the last 3000 to 5000 years (Snead, 1967). The next earthquake could create new islands or peninsulas anywhere on the coast. Fishermen claimed that part of the coast near Pasni was uplifted 5 m during the 1945 earthquake (Snead, 1967, p. 552).

Near the center of the image is a large coastal lagoon and salt flat called "Kalmat Khol." Its existence here is anomalous,

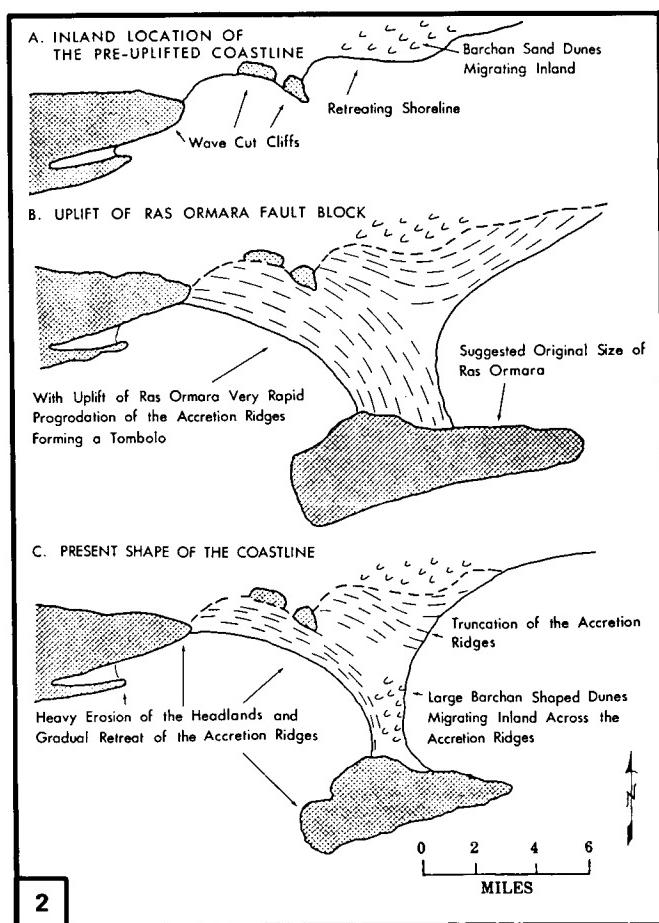


MAKRAN COAST, PAKISTAN

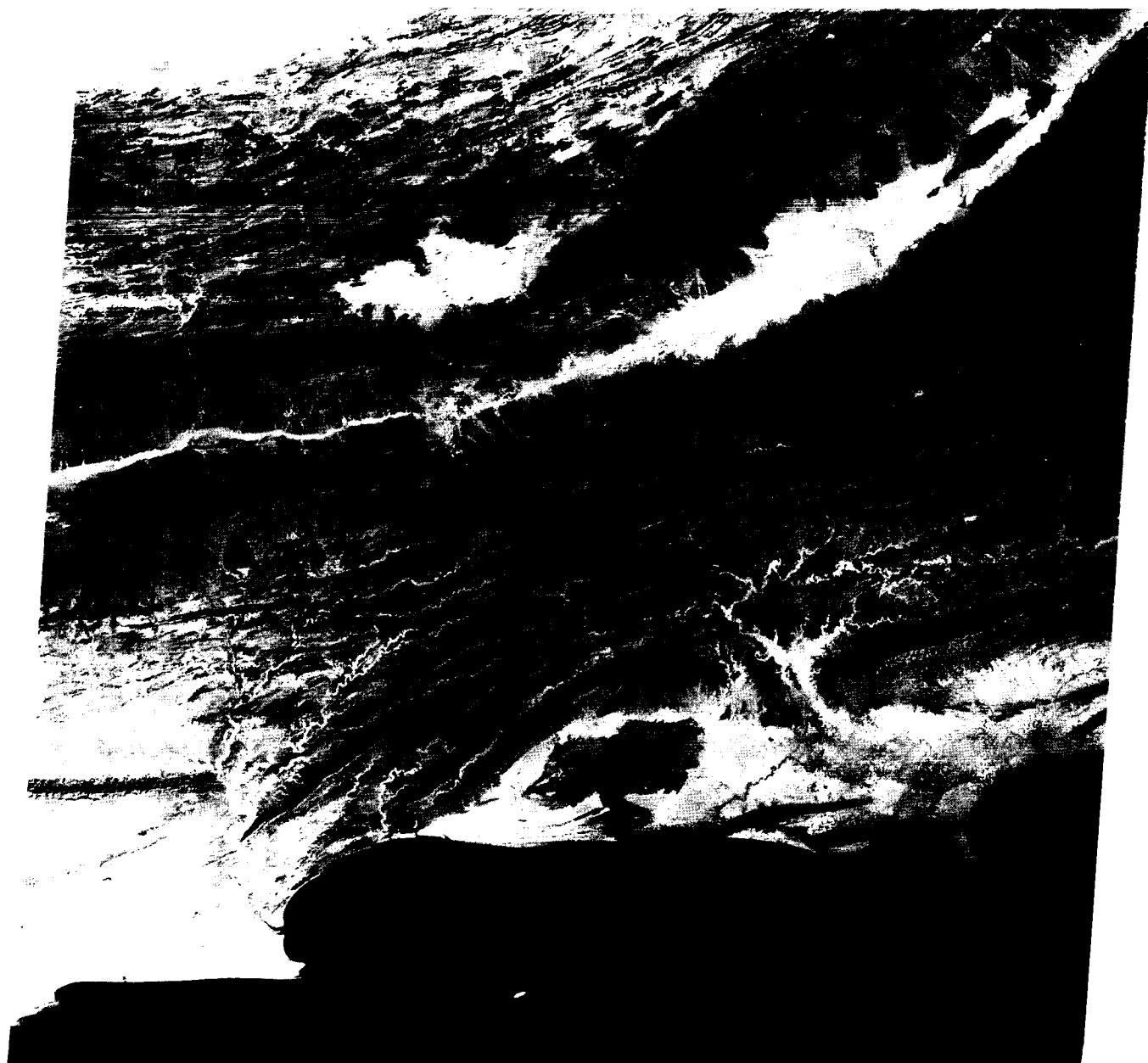
for it seems doomed to be either filled in by erosion of the surrounding mountains of soft mudstones or drained by continued tectonic uplift. The Basol River to the east could be diverted into the basin by tectonic uplift, hastening the infilling.

The rapid tempo of change on the Makran coast is aided by climatic as well as geologic factors. Strong southwest monsoon winds blow steadily for several months toward this coast, causing extended periods of high water and high waves sweeping in from the southwest. The swell patterns of the southwest monsoon reflect around headlands to create sweeping curves of beaches on both sides of headlands such as Ras Ormara (Figure C-9.3). The dominant beach drifting appears to be toward the east, so that the beach at Posni, in the lee of Jabal Zarain, develops a *zetaform* or logarithmic spiral shape (see Plate C-2). Erosion by wind-driven waves is undoubtably enhanced by tsunamis (seismic sea waves) such as the one 12 to 15 m in height that followed the 1945 earthquake (Snead, 1967, p. 551).

Powerful waves and currents, infrequent but intense flash floods, erodible young sedimentary rocks, and strong tectonic uplift combine to make this one of the most active and dramatic coastal regions of the Earth. Its outlines could change within the lifetimes of the readers of this book. **Landsat 1123-05441-5, November 23, 1972.**



ORIGINAL PAGE IS
OF POOR QUALITY



3

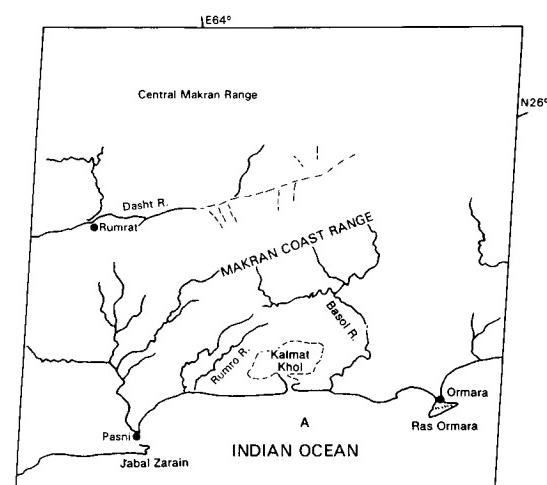


PLATE C-10

ORIGINAL PAGE IS
OF POOR QUALITY

The islands of New Zealand and their adjacent submarine pedestal are continental in deep structure, but are now surrounded by oceanic crust. The coasts of the two main islands include an amazing variety of landforms, from subtropical beaches in the north to fjords in the south. This scene and the following will illustrate two adjacent regions of the South Island that have very different coastal landscapes.

New Zealand has had a long and complex geologic history, but by Late Cretaceous time, most of the former relief had been eroded away (see also Plate T-58). Individual tectonic blocks tilted and submerged and were covered by shallow-water Tertiary marine sediments that buried most of the previous rocks. By Oligocene time, the New Zealand region was almost entirely submerged. Then about 30 Ma ago, the Kaikoura Orogeny began and continues to the present time. New Zealand and Japan are similar in that most of the relief is the result of uplift in the last few million years.

This view has three main topographic elements: (1) the snow-capped Southern Alps, the main mountain range of the South Island, with its fault-controlled glaciated valleys; (2) the alluvial Canterbury Plains; and (3) the eroded basalt dome of Banks Peninsula. The mountains are noted for active earthquakes along great right-lateral strike-slip faults, of which the Alpine Fault and the Hope Fault can be traced in the upper left part of the image. While the mountains were rising and eventually accumulating multiple mountain ice caps during the Pleistocene Epoch, the erosional debris was spreading eastward to build the Canterbury Plains. Most of the alluvium on the plains was deposited as outwash of relatively recent ice ages. The Rakaia, Waimakariri, Hurunui, and Waiau are bedload rivers, carrying mostly sand and gravel derived from glacial erosion.

CANTERBURY, NEW ZEALAND

The rivers deliver their massive loads to the east coast, but strong swells from the east and powerful longshore currents have prevented the building of deltas. At the time the image was made, the current north of Banks Peninsula was carrying plumes of sediment northward from the river mouths, bypassing numerous small headlands.

In relatively Late Pleistocene times, probably during a time of glacially lowered sea level, the volcanic Banks Peninsula was joined to the rest of the South Island by the prograding alluvial plain. The volcano was active from two major eruptive centers from about 12 to 5 Ma ago. Since then, it has been deeply eroded (Figure C-10.1). Both old calderas have been breached by erosion and are now submerged. The harbor town of Lyttleton, near Christchurch, and the original European settlement in New Zealand at Akaroa are each in one of the breached calderas.

South of Banks Peninsula is Lake Ellesmere, a shallow lagoon enclosed by a Holocene barrier spit. A similar but smaller lagoon is barely visible at the Christchurch city waterfront. Figure C-10.2 shows accretion (beach) ridges at Birdlings Flat along the north edge of Lake Ellesmere.

Banks Peninsula is noted for its plunging cliffs (Figure C-10.3), steep headlands with almost no abrasion platforms at their base. They reflect wave energy so efficiently that they are not being intensely eroded (Cotton, 1951). Their development is related to the multiple low sea levels of the Pleistocene Epoch, when fluvial and periglacial dissection of the basalt dome was graded to a now-submerged level. With the postglacial rise of sea level, the former subaerial cliffs were drowned as much as 35 to 55 m and now rise from water too deep to cause significant wave refraction and surf. Landsat 2192-21265, August 2, 1975.



1

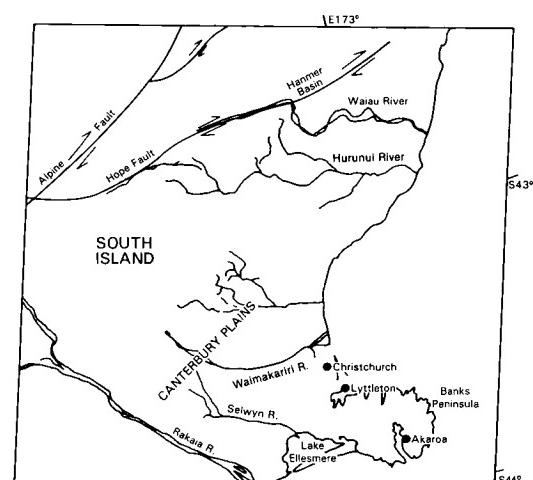


2

ORIGINAL PAGE
COLOR PHOTOGRAPH



3



C - 5

375

PLATE C-11

MARLBOROUGH SOUNDS AND COOK STRAIT, NEW ZEALAND

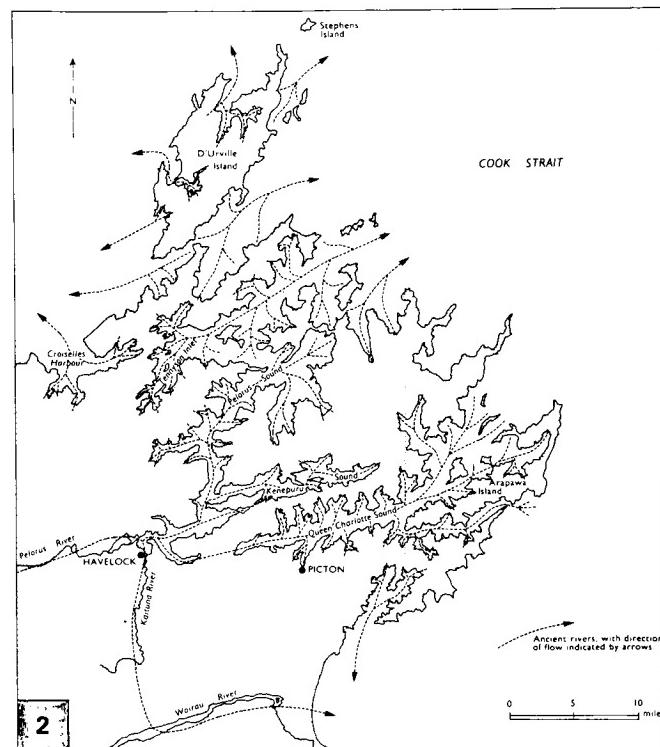
Cook Strait separates the North Island from the South Island of New Zealand. An aerial oblique view (Figure C-11.1) of the Strait shows Wellington on North Island in the foreground and the Marlborough Sounds on South Island near the top of the photograph. It is probably a very old geologic feature that predates the series of right lateral strike-slip faults that are followed by the valleys of the Wairau, Awatere, and Clarence Rivers. The Wairau Fault is a major northern segment of the great Alpine Fault of the South Island. The intricately dissected and drowned Marlborough Sounds region around Picton (Figure C-11.2) is estimated to be creeping northeastward along the Wairau Fault toward Wellington on the North Island at a rate of 6.3 mm per year (Stevens, 1974, p. 198). Cook Strait is thus gradually becoming Z-shaped.

The area around Wellington is actively rising, especially during earthquakes. Cape Turakirae may be rising at an average long-term rate of as much as 4 m per 1000 years (Wellman, 1967). It rose about 2.4 m during an earthquake in 1855, enabling farmers in the Wairarapa Valley to the east to thereafter drive cattle around the Cape to market in Wellington. The swampy tombolos that connect several peninsulas within the city of Wellington were also uplifted 1 to 2 m in 1855, creating much better sites for future city expansion and establishing the route for the present Marine Drive around the harbor (Stevens, 1974, p. 228).

The Marlborough Sounds region has submerged after it developed an intricate fluvial drainage pattern. According to one interpretation, much of the drainage was toward the southwest, so that the drowned northeastern heads of former valleys are now below their former southwestern mouths (Figure C-11.3). Note that there are relatively few islands in the Marlborough Sounds region. Most of the landscape is an intricate series of peninsulas, because the relatively steep gradient along the former subaerial ridge crests carries them completely below sea level in a short distance (Figure C-11.4). If the divides were more uniform in height, numerous small high areas on them would appear above sea level as chains of islands.

The rocks of Marlborough Sounds are schists and gray-wacke sandstones, relatively resistant to erosion but highly fractured so that they crumble in freezing climates. The region may have been subjected to periglacial conditions during the ice ages,

and perhaps intense weathering during times of lowered sea level helped to shape the landscape prior to drowning. The resulting skeleton islands and peninsulas are similar to those in the Falkland Islands (Plate C-6). If the former river valleys had flat longitudinal gradients, smooth sides between relatively sharp ridge crests, and semicircular "theater" heads, all typical of periglacial valleys, tilting and drowning could produce the observed landscape (Cotton, 1957, 1969). **Landsat 2335-21190-6, December 23, 1975.**



ORIGINAL PAGE IS
OF POOR QUALITY



4

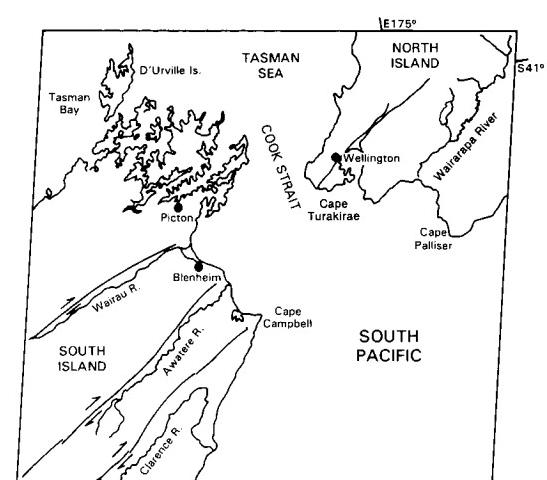


PLATE C-12

NORTHERN CHILE

At 18°30' S latitude, just south of the Chile/Peru border near the Chilean frontier city of Arica, the western coast of South America makes a sharp bend from its southeasterly trend in Peru to a nearly southerly direction. North of the bend, in Peru, alluvial fans drain the desert piedmont of the Andes directly to the Pacific Ocean. Only two small mountain blocks in the northwestern corner of the image obstruct the direct connection of alluvial fans to the shore zone (A). One of them is bisected by the lower course of the Rio Sama, reflecting a late Cenozoic history similar to that of the area farther south, in Chile (Tosdal et al., 1984).

The image covers the heart of the Atacama Desert, said to be the driest on Earth (2 mm in 30 years at Iquique). In many places, no measurable rain has ever fallen. Because of the cold ocean current offshore, coastal fogs provide moisture for a few highly specialized shrubs, but most of the ground is completely bare. Rain or snow falls in limited amounts in the mountains, however, and in the inland valleys (C), irrigated agriculture is possible.

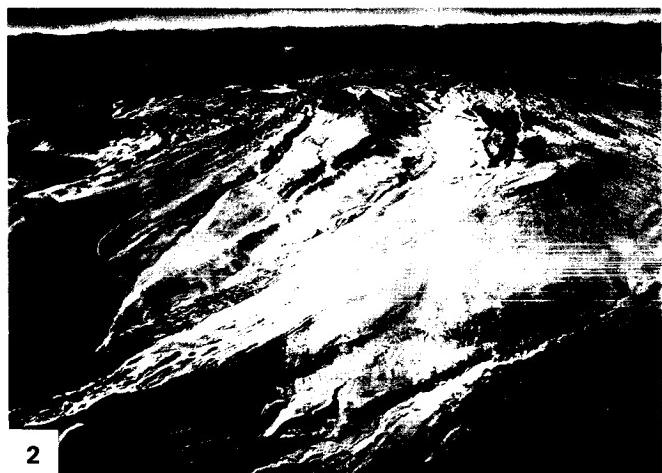
The sharp change in direction of the coast in Chile is controlled by the Cordillera de Costa (Coastal Range) that rises about 1000 m above sea level (B). On its seaward side, the Coastal Range has been eroded into a spectacular scarp (Figure C-12.1), in many places fully as high as the flattened summits of the Range. This scarp runs from Arica (18.5° S) to Taltal (25.5° S), a distance of more than 800 km. Its average height is about 700 m; in places, the relief from sea level may reach 2000 m. The cliff base commonly is almost at the coastline; typically, a narrow emergent abrasion platform has been cut into the scarp by waves (mainly during storms and tsunamis). The Coastal Range itself was beveled by early in the Cenozoic Era and has been uplifted only since the Miocene Epoch. The uplift created a barrier to the westward drainage of the Andes, which were experiencing tectonic uplift and massive explosive volcanism at the same time. For example, the large volcano in the lower right part of the scene is 4900 m high. The eroded sand, gravel, and volcanic ejecta (Figure C-12.2) from the Andes were trapped against the Coastal Range and filled the longitudinal tectonic valley on the western flank of the Andes to a depth of 900 to 1000 m (Erickson, 1981; Galli, 1967; Mortimer

and Saric 1972, 1975). In relatively recent geologic time, perhaps in the Pliocene or Pleistocene Epoch, the alluvial filling overtopped the Coastal Range in a few places. Having spilled over the mountains into the sea, the rivers cut deep gorges across the mountains and eroded headward across the longitudinal valley to the base of the Andes. The spectacular gorges or *quebradas* (Figure C-12.3) are over 800 m in depth near the coast, but the steep gradients of the gorge floors rise inland rapidly and the entrenched across the interior plains is no more than a few hundred meters. The cutting of the gorges across the Coastal Range may have been aided by coastal retreat under powerful wave attack.

The continental shelf off Northern Chile's coast is less than 10 km wide and may be the result of wave erosion across tectonic blocks similar to the exposed coastal ranges. An alternative hypothesis is that the present coast is controlled by north-south trending faults that have dropped the seaward side of the Coast Range below sea level. Brüggen (1950) considered the scarp to be primarily tectonic in origin. Mortimer and Saric (1972) contend that tectonic movement has only uplifted a scarp caused by continued marine erosion against a subsiding coastline. Paskoff (1980) treats the present cliffs as a modified fault scarp retreating inland by bench-cutting wave erosion from Miocene onward and influenced also by glacio-eustatic movements in the Quaternary.

Southward from the extreme southern edge of the view, the coast is reported to have flights of uplifted marine terraces cut into the cliffs. Apparently, erosion of the coastal cliffs has been so rapid in the northern section that all trace of terraces has been removed (Mortimer and Saric, 1972, p. 162).

The continental shelf is negligibly narrow along this part of the South American Coast. Alluvium carried to the coast by infrequent flash floods is either trapped in submarine canyons and transported into the deep Peru/Chile submarine trench, or is swept northward by powerful currents. The only large beach would be in the 30-km coastal segment in Peru from the Chilean border north to Rio Sama. **Landsat 1155-14102-6, December 25, 1972.**



ORIGINAL PAGE IS
OF POOR QUALITY



3

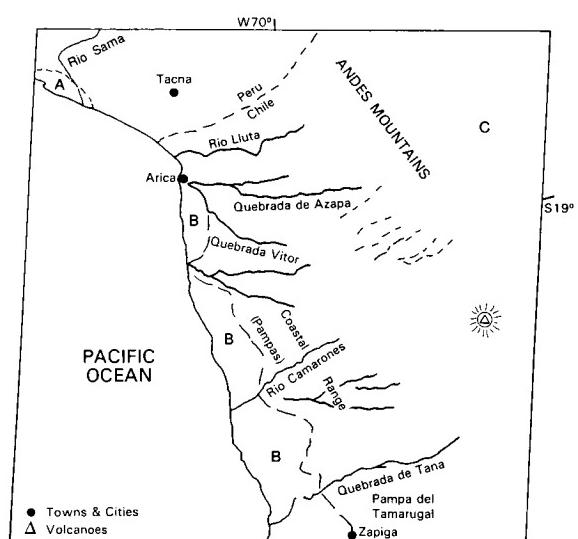


PLATE C-13

CAPE HATTERAS, NORTH CAROLINA

Plates C-13 through C-17 all show landforms at the edge of a broad continental shelf that has been repeatedly exposed and drowned during multiple glacially controlled sea-level fluctuations. This scene illustrates a gigantic cuspatate foreland on a trailing continental margin. This and the next two Plates are from the southeastern United States, and their sequence from Cape Hatteras southward to the Florida Everglades illustrates the progressive change from polycyclic clastic sand deposits in the north to biogenic carbonate sediment in the south. This northward oblique view was taken with a hand-held camera by Apollo 9 astronauts. It shows the North Carolina and Virginia coast from west of Morehead City, North Carolina, and Cape Lookout northward to Cape Henry and Norfolk, Virginia. The view is considerably foreshortened by the oblique angle.

Cape Hatteras (Figure C-13.1) is one of the several cuspatate forelands that project seaward from the nearly continuous chain of barrier islands and spits that extends from Long Island, New York, to Florida. The barrier spit that encloses Currituck and Albemarle Sounds southward from Cape Henry to Oregon Inlet is about 100 km long. It includes the high dunes at Kitty Hawk, from which the Wright brothers made their pioneering flights. In the 65-km distance from Oregon Inlet to Cape Hatteras, the barrier system projects even farther seaward to enclose Pamlico Sound, which is almost entirely less than 10 m deep (Pierce and Colquhoun, 1970, p. 3699). Seaward of Cape Hatteras, the submerged Diamond Shoals extend seaward almost to the edge of the continental shelf. The shoal may represent the retreat path of Cape Hatteras as sea level rose in the Holocene Epoch, at the end of the last ice age (Swift, 1969). The great swirl of turbid water southeast of Cape Hatteras in the image is a clue to the dangerous submerged sandbars and confused currents that have caused so many shipwrecks there. South of Cape Lookout to Myrtle Beach in South Carolina, the Barrier Islands lie close to the cuspatate mainland coast, as is sharply portrayed in the second Apollo 9 oblique view looking to the north (Figure C-13.2).

The segment of barrier that extends 120 km southwest from Cape Hatteras to Cape Lookout includes Ocracoke Island and the Core Banks, with several inlets and other locations of ephemeral washovers across the barrier system. This barrier segment seems less well nourished than the barriers north of Cape Hatteras. Another ridge of dangerous shoals and shifting currents extends southeastward from Cape Lookout.

The prominent eastward projection of the U.S. Atlantic coast at Cape Hatteras suggests an ancient tectonic or sedimentologic foundation for the barrier system. It is noteworthy that

emerged marine terraces of Late Tertiary age, far inland and as much as 60 m above present sea level, show a similar cuspatate shape. One of the numerous emerged Pleistocene barriers of the southeast Atlantic coast can be traced as a beach ridge through the lowlands inland from Albemarle and Pamlico Sounds, evident in the upper left corner of the Plate as a narrow light-toned line fringing the Dismal Swamp and other forest belts.

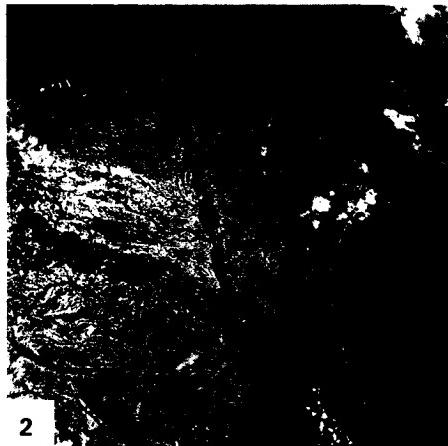
In southern South Carolina and Georgia, relatively young emerged fossil barrier islands converge within 20 to 30 km of the present shoreline and are separated by shallow lagoons or "sounds" that are mostly shallow and filled with the salt marsh grass, *Spartina alterniflora*. The barrier segments are dissected by estuarine rivers into short wide islands that look like sausage links. These are the Sea Islands (Figure C-13.3), where cotton and tobacco growing were introduced to the United States. Now many of them are developed as winter resorts or exclusive holiday communities (e.g., Hilton Head Island). The cores of the Sea Islands were barrier islands of the last interglacial age, when sea level was a few meters higher than now. Certainly, more than one episode of barrier building preceded the last full-glacial drop of sea level, when the coastal plain rivers extended across the exposed continental shelf and dissected these barriers into segments that became the Sea Islands when sea level rose again (Winkler and Howard, 1977). The general southward direction of sand transport is illustrated by the recurved spits (Figure C-13.4) on islands such as Ossabaw and St. Catherines.

The modern barrier system is partly underlain by an older but similar system (Pierce and Colquhoun, 1970). Perhaps during the last interglacial high sea level about 125 000 years ago, which in most parts of the world was a few meters above present sea level, the former barrier system was built. It was deeply weathered during the last ice age when it was exposed by lower sea level, but as the sea rose to its present level in Holocene time, the modern barrier was built against and partly on top of the older eroded system. As on so many other coasts, the present dynamic barrier system, which responds so subtly and quickly to storms and waves, is actually only the youngest in a long history of similar forms built on the coast.

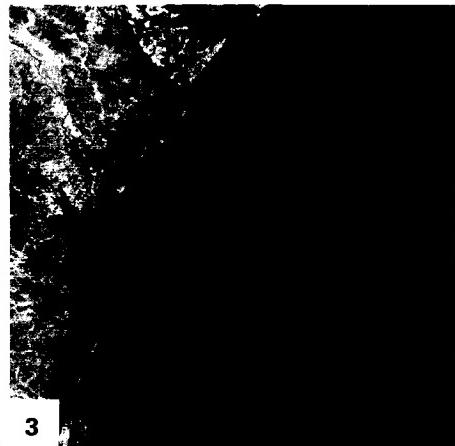
The mainline coast inland from the sounds is obviously drowned by the postglacial rise of sea level, but was not cut back or straightened by wave erosion, so that the barriers must have been in place during the submergence. Barriers such as these are not evidence of coastal emergence or uplift, but of inheritance from previous forms with constant reworking by modern processes. **Apollo 9 Photo AS-9-20-3128.**



1



2



3

ORIGINAL PAGE
COLOR PHOTOGRAPH

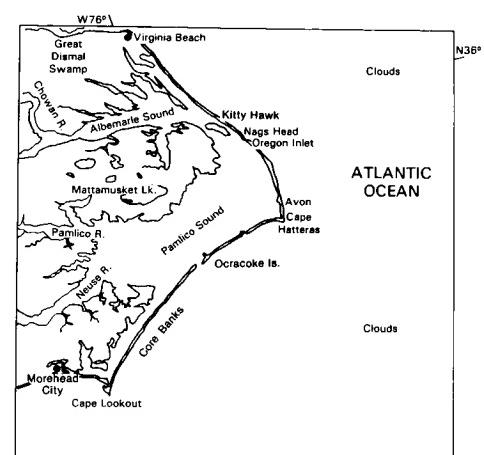
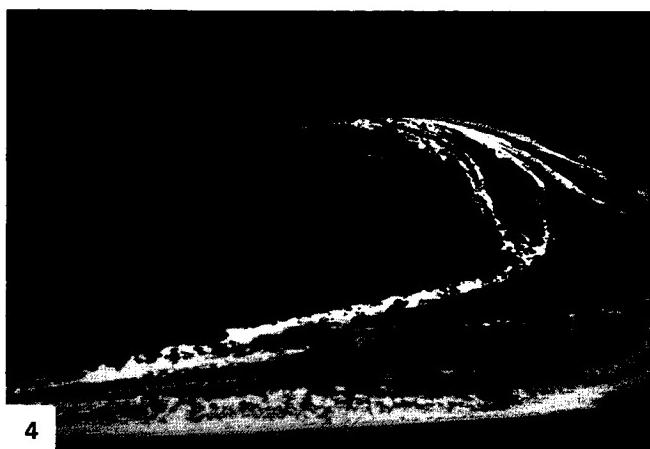
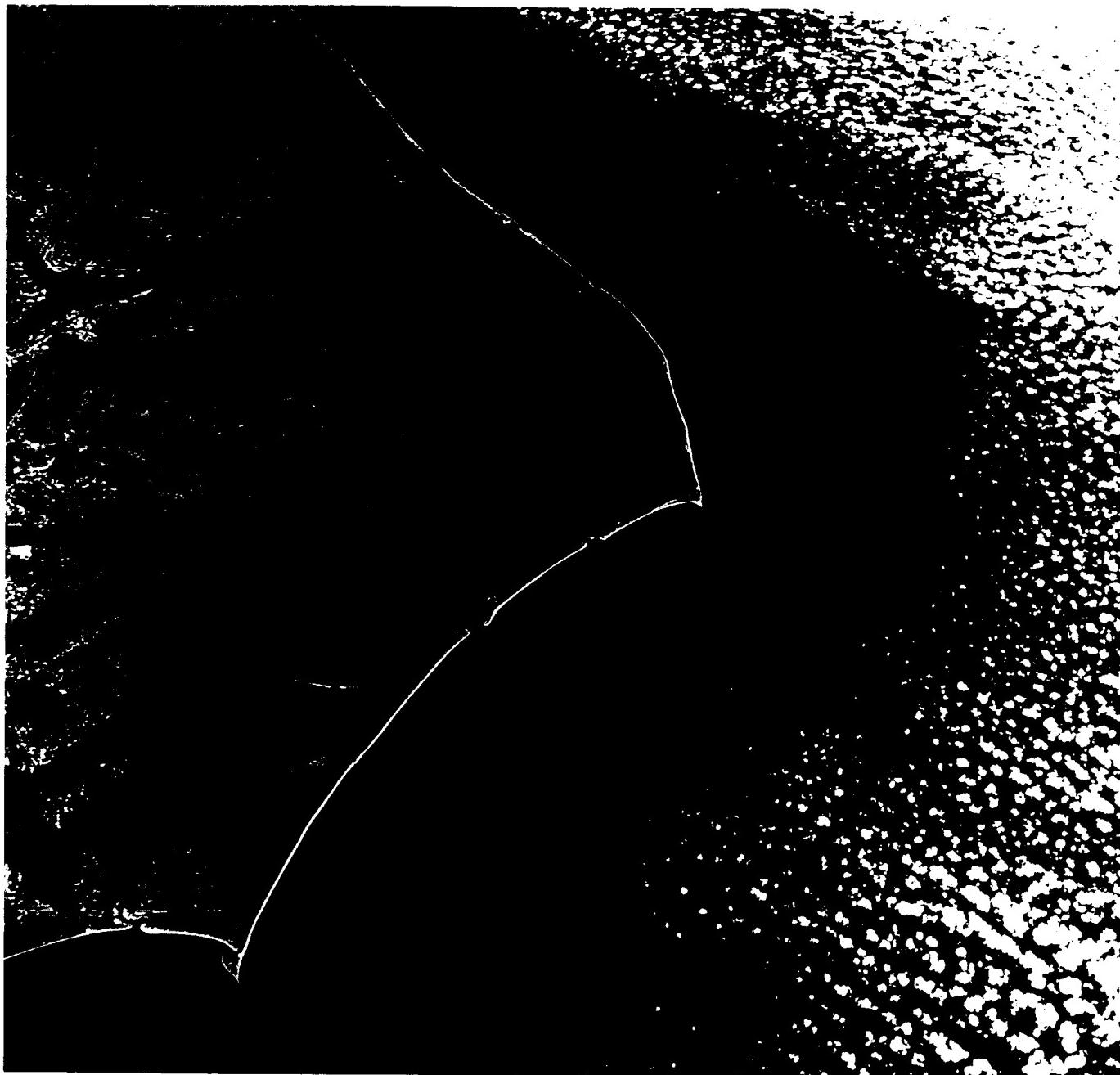


PLATE C-14

Cape Canaveral is the southernmost of the cuspat forelands on the U.S. Atlantic coast barrier system. It is the site of Cape Kennedy Air Force Station and NASA's Kennedy Space Center (KSC). The cuspat foreland has officially reverted to its traditional name after being called Cape Kennedy for a few years in the 1960s. Numerous rocket launch pads are visible in the false-color Landsat scene as uniformly spaced light patches along the shoreline of the Cape. Views of the coast up and down from the Cape appear in Figures C-14.1 and C-14.2. More details in and around KSC are visible in the Landsat RBV image reproduced in Figure C-14.3.

Cape Canaveral is approximately the southern limit of quartz-rich detrital sand transported southward from rivers that drain the coastal plain, the piedmont, and the Appalachian Mountains of the southeastern states. Most of the detrital sediment of Cape Canaveral is mixed with and bound together by weakly cemented biogenic limestone. Masses of broken mollusk shells cement easily by ground water to become *coquina*, a shelly conglomerate that may be strong enough to be used as a building material or to protect fossil beach ridges from later erosion. The weakly cemented mixture of detrital quartz and biogenic limestone is so resistant to erosion that several generations of the ancient beach ridges that predate Cape Canaveral can be easily traced in the view.

The oldest fossil shoreline is a series of detrital sand ridges that trend slightly east of south through western Orlando and Haines City. Rising 50 to 60 m above present sea level, these ridges are deeply weathered and leached of any former carbonate material. They may be as old as Pliocene or Late Miocene age (perhaps 3 to 5 Ma) (MacNeil, 1950). The sandy cover of central Florida frequently collapses into karst sinkholes in the underlying Ocala limestone, with disastrous results (Plate KL-4). The maze of lakes in the central part of the image are karst sinkholes, flooded by the generally high rainfall of the region and the low relief that inhibits ground-water movement.

A second series of fossil barrier ridges can be traced between Orlando and the St. Johns River. These have most recently been referred to as the Effingham Sequence, named for Effingham County in Georgia (Winkler and Howard, 1977). They are generally below 30 m altitude and have been correlated with the Wicomico and Waccamaw formations of Georgia and South Carolina. They are estimated to be of Early Pleistocene age,

CAPE CANAVERAL, FLORIDA

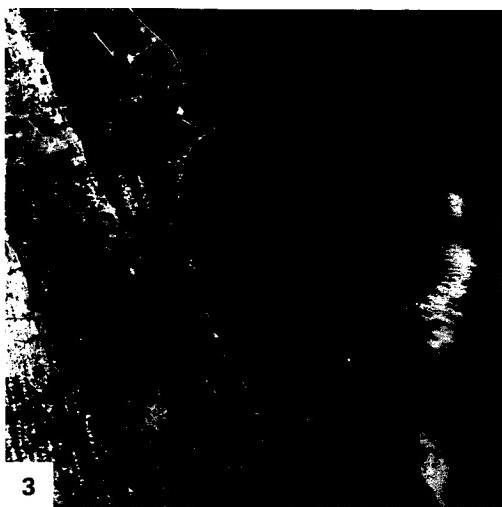
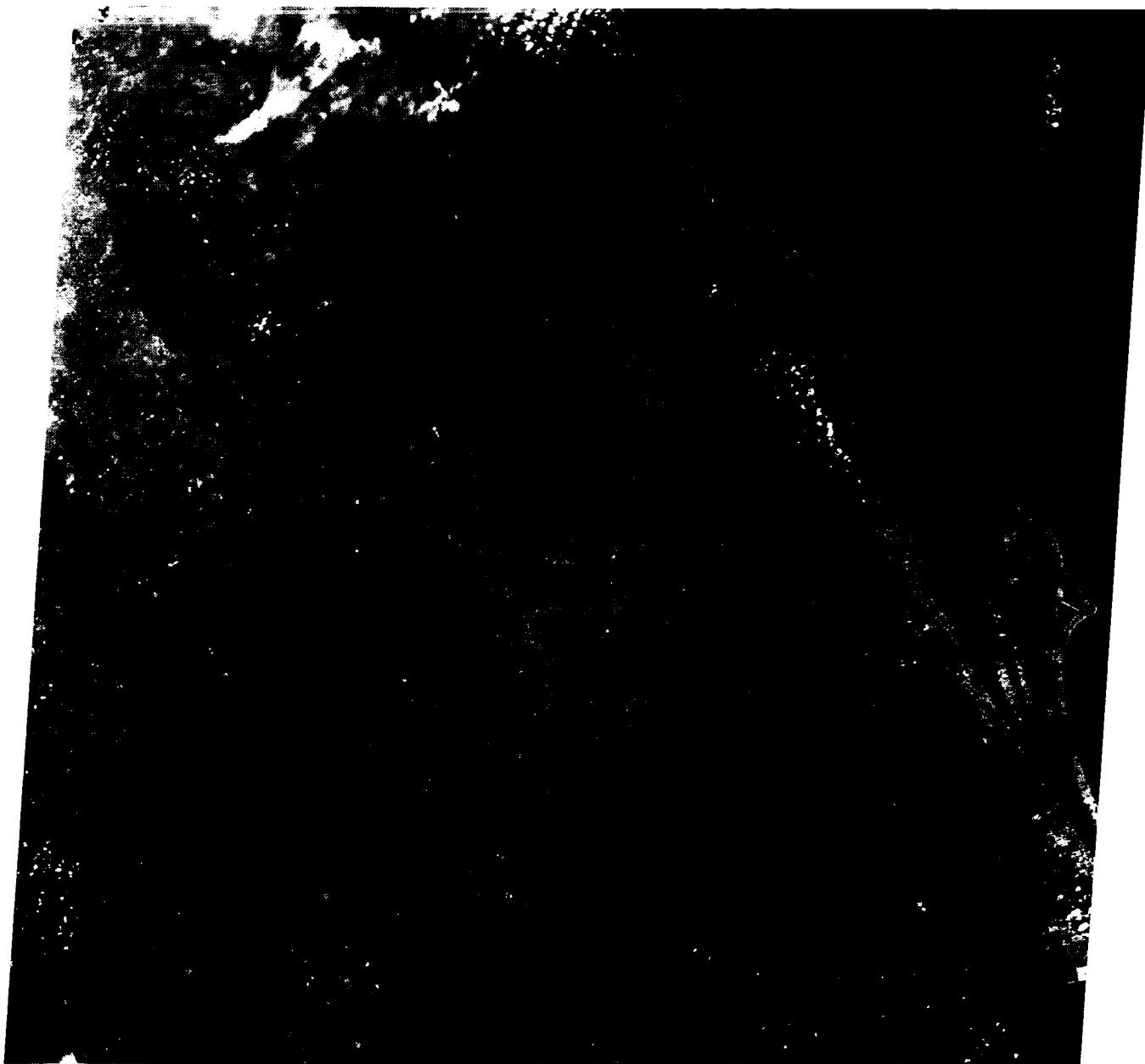
between 1.0 and 1.7 Ma old. The Effingham beach ridges are distinctive in that they show a series of cuspat forelands of dimension similar to Merritt Island and Cape Canaveral.

Between the St. Johns River and Indian River, and including Merritt Island, is the next younger series of ancient beach ridges. These ridges, named the Chatham Sequence by Winkler and Howard (1977), show a well-developed cuspat foreland in Merritt Island, now truncated by Cape Canaveral except where the modern barrier is deflected seaward by the resistant cemented coquina beach ridges at False Cape. A few radiometric dates on poorly preserved mollusk shells suggest that this sequence, now less than 10 m above sea level, is about 100,000 years old. It was probably built during the last interglacial interval when sea level was a few meters above the present level (Osmond et al., 1970). Although the older higher beach ridges inland require a slight amount of tectonic uplift over the past few million years, the Chatham Sequence could have been built during a higher sea level, rather than having been uplifted in the last 100,000 years. These are probably of the same ages as the ridges that control the Sea Islands of Georgia and South Carolina, and are buried under the modern barriers of Cape Hatteras.

Thus, as noted in Plate C-13, the modern barriers on the southeastern U.S. coast are only the latest of a long series of such forms that were built in the Tertiary Period as the coastal plain gradually accumulated sediment and prograded seaward. But during the Pleistocene Epoch, the repeated rise and fall of sea level through a range of 100 m in harmony with each ice age has complicated the longer term progradation. Each ice age exposed most of the shelf, and rivers extended their lower valleys nearly out to the shelf margin (Field and Duane, 1974). As sea level rose, the shoreline again migrated landward. Especially in the last 5000 to 6000 years, the most recent rise of sea level has driven older barrier systems landward across the shelf or overtapped them to form newer barriers near the transgressing shoreline. In many regions, the youngest Holocene barriers have been stabilized by older eroded barrier segments. Like the cuspat forelands of Cape Hatteras and the Sea Isles, the modern Cape Canaveral foreland has probably accreted and migrated southward in the last few thousand years, although massive construction at the Kennedy Space Center has now destroyed many of the prehistoric beach ridges on the Cape. **Landsat 1045-15275, September 9, 1972.**



ORIGINAL PAGE
COLOR PHOTOGRAPH



3

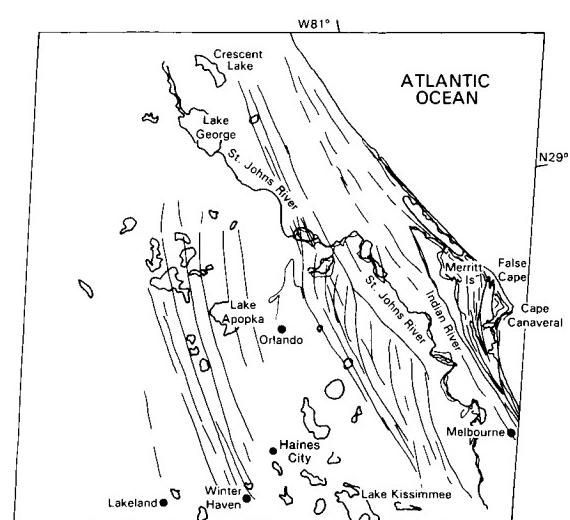


PLATE C-15

SOUTH FLORIDA

The southern tip of Florida is a limestone platform only a few feet above or below sea level. Its relation to the karstic sinkhole terrain of central Florida and to the shallow Bahamas carbonate platform beyond the deeper straits of Florida is clearly depicted in the HCMM scene shown as Figure C-15.1. For the last 100 million years, the continental crust here has slowly subsided, allowing new limestone to vertically accumulate at a net rate of 2 to 5 cm per 1000 years. During the ice ages, however, the Florida peninsula was emerged as a flat limestone plateau. Ground-water solution through the limestone produced a sponge-like *karst* terrain, with mazes of underground caverns and innumerable surface sinkholes (see Plate KL-4).

During the last interglacial age, about 125 000 years ago, sea level was higher than at present by as much as 6 m, and the climate was warmer than today. A warm shallow sea spread over the Florida peninsula and deposited a new layer of coralline, algal, and muddy limestone. The reef edge of most active coral growth was somewhat southeastward of the trend of the modern Florida Keys. Behind the reef, over most of Florida Bay and the Everglades, was a shallow carbonate bank, with isolated patch reefs. Just as today, hurricanes then probably tore reef limestone fragments from the reef margin and threw the abraded debris across the shallow lagoon floor. Algal-browsing fish, sponges, and boring organisms further comminuted the debris to limy mud.

In the last full-glacial period, culminating about 18 000 years ago, all of southern Florida was exposed a hundred or more meters above sea level. On a nearly flat surface relief (with occasional coralline mounds), the new layer of limestone developed sinkholes and caves, interconnected with older systems at depth. The area probably looked like the Yucatan Peninsula of today (Plate KL-3). Wave erosion during low sea level apparently removed the entire former reef southeast of the Keys and cut back into the back-reef and lagoon limestone.

By 7000 years ago, the edges of the Florida peninsula were again being submerged. By 4000 years ago, sea level was only a few meters below its present level, continuing its slow uniform rise. The eroded limestone surface supported a distinct vegetational and sedimentational zonation, which gives the area its fascinating modern landscape. Most of the land in the image is in Everglades National Park.

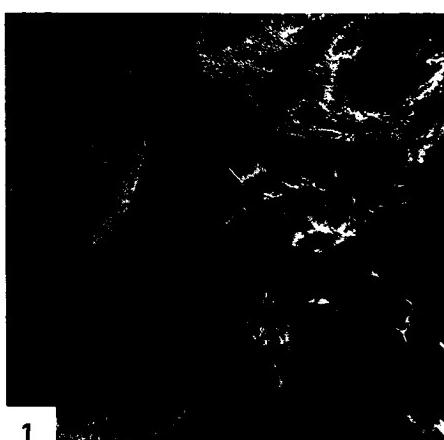
Under 1500 mm of annual precipitation, the highest part of south Florida is actually a low stable dome of water centered over Lake Okeechobee, well shown north of the Everglades on the HCMM scene (Figure C-15.1). The water drains radially to the coast, impeded by the thick growth of saw grass (*Juncus* sp.),

with no distinct channels carrying the flow. Rather, the water spreads seaward through the grass in a barely detectable current. Elongate streamlined *hammocks* of hardwood trees in the Everglades, which show white in the radar image, demonstrate that the major water movement in the Everglades is southward and westward in a great sweeping arc into Whitewater Bay.

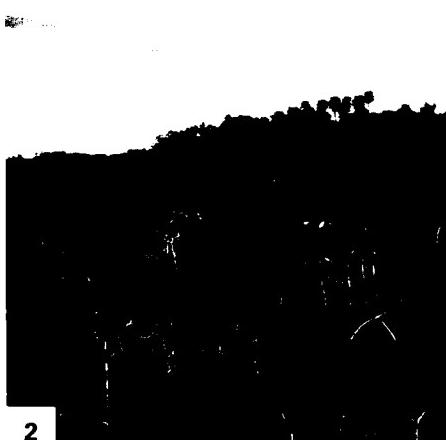
At the margin of the saw-grass prairie, sea water intrudes along tidal creeks and spreads onto the prairie surface. The salt-intolerant grasses are displaced by red mangrove (*Rhizophora mangle*; Figure C-15.2), which shows on the radar image as a light-colored zone.

Florida is near the northern limit of coral growth, and the modern reefs are fragmentary and incomplete. The modern Florida Keys (Figures C-15.3 and C-15.4) have some underwater reef tracts, but basically are only thin coral fringes and coral sand spits resting on the eroded foundation of the limestones of the last interglacial age. Behind the Keys, diverse shallow marine fauna and flora thrive in Florida Bay. Many of the organisms build limestone shells or supporting structures, while other predators destroy these frameworks. The net result is a shallow bay only 1 or 2 meters deep, with the distinctive reticulate network highlighted in the radar image of corroded algal-encrusted reef remnants separated by soft limy mud.

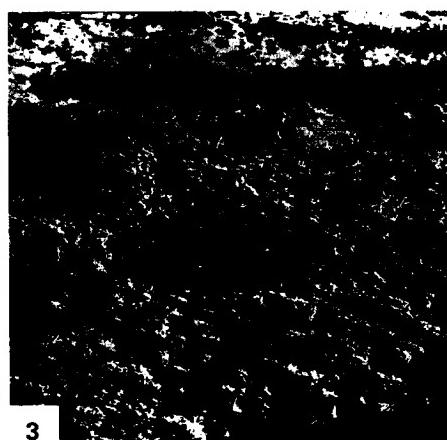
As sea level rises and continues to submerge southern Florida, each of the depositional environments migrates landward. The still-exposed area of last interglacial limestone is only about 1 m above sea level, but has suffered extensive urban development. Around it, peat deposits in the saw-grass prairies of the true Everglades slowly transgress onto the flanks of the exposed limestone. Simultaneously, the saline mud and peat of the mangrove swamps creep over the freshwater saw-grass peat. Finally, aided by hurricane winds and high water, the limy mud of Florida Bay is thrown onto and into the mangrove forest as the shoreline recedes. With time, the old limestone surface at any single point has been or will be covered first by a few centimeters to a meter or so of saw-grass peat, then mangrove peat and mud, and finally by shallow-water limy mud of Florida Bay. Numerous shallow boreholes in the Everglades have documented the succession, and radiocarbon dates on the basal peat confirm that the process has been continuing for at least the last 4000 years (Scholl and Stuiver, 1967). The future of terrestrial animals, including man, in southern Florida is gloomy on the time scale of the next few hundred or thousand years. But for aquatic species, from alligators to zebra fish, the future is bright. They can anticipate greatly extended environments. *Seasat SAR, Rev. 809, August 22, 1978.*



1



2



3

ORIGINAL PAGE IS
OF POOR QUALITY



4

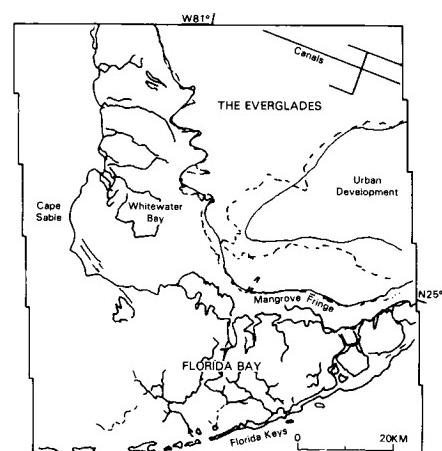


PLATE C-16**ORIGINAL PAGE
COLOR PHOTOGRAPH****GREAT BAHAMA BANK**

The Great Bahama Bank is a pile of coral reef limestone at least 4500 m thick that has been accumulating since Cretaceous time. The entire pile was deposited in warm shallow water, so the foundation crust must have been slowly subsiding at an average rate of at least 3.6 cm per 1000 years (Newell, 1955). The crustal block basement underneath the Bank is continental in structure and may have rifted from North America when that continent began to break off from Africa and the Atlantic Ocean originated.

The Bahama Bank is now separated from the mainland by the Straits of Florida, which reach depths of 760 m. The eastern edge of the Gulf Stream sweeps northward past the western margins of the Bank at a speed of 3 km per hour, about half as fast as the main current near Miami Beach. On the Atlantic Ocean side, the platform drops steeply to depths exceeding 4000 m just 20 km to the east. Depths within the bank proper are seldom greater than 6 meters.

Most bedrock under Great Bahama Bank is coral-reef limestone, as indicated by a deep well on Andros Island. The nearly vertical submarine cliff that forms the west bank edge must be built of Tertiary-age corals. It has the same form as the ribbon reefs of the Australian Great Barrier Reef (Plate C-18) or mid-oceanic atolls such as Jaluit atoll (Plate C-19). The west cliff descends abruptly to depths of 30 to 60 m, then less rapidly to the floor of the Straits of Florida. The loose shifting sands of the present Bahama Bank could not maintain such steep gradients.

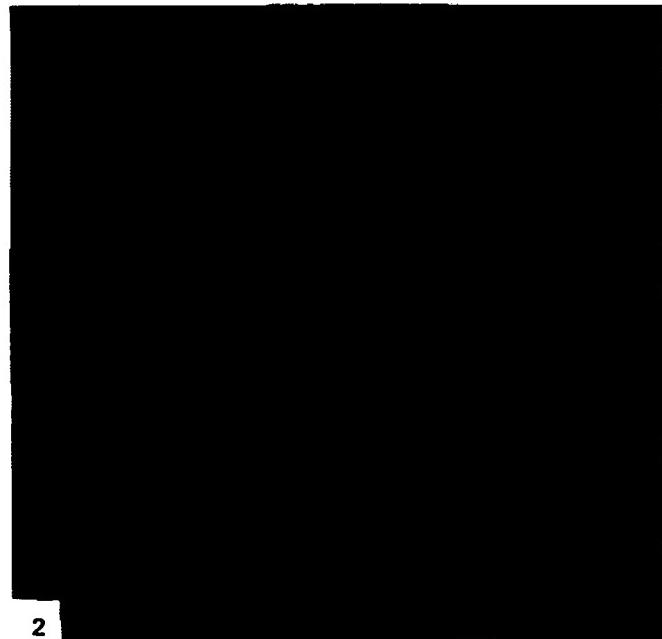
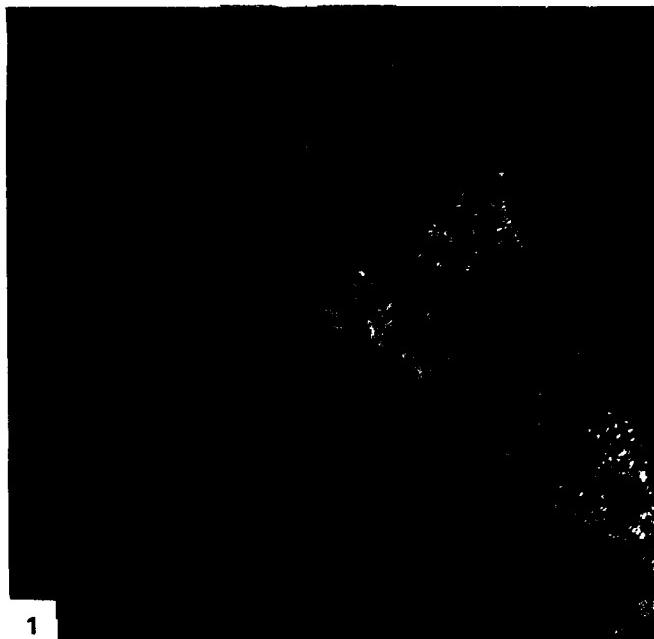
Various species of coral live on Great Bahama Bank, as they do in the nearshore zone of Florida, but their growth is so slow that they do not build significant reefs. Since the Pleistocene, this part of the Atlantic has been in the "marginal" zone of coral growth, where winter temperatures inhibit healthy coral growth. A more important limiting factor on the Bank is turbidity. No suspended detrital sediment from the continent reaches the Bahamas, accounting for the clear water in the Straits of Florida. However, the warm Gulf Stream surface water is supersaturated (by 40 percent) with dissolved calcium carbonate, and when the water washes up and over the bank rim, it is warmed. Agitation and evaporation cause massive chemical precipitation of a cloud

of aragonite crystals. These accrete concentrically on nuclei of shell or coral fragments, growing into oolites, which are sand-sized pellets with a layered structure similar to hailstones. The clouds of limy precipitate and shoals of oolitic sand effectively inhibit coral growth today.

Most of this oolitic sand originates within a few hundred meters of the bank margins, but currents distribute the sand into the interior of the bank. The small islands and cays are made up mainly of biogenic limy sand and mud derived from foraminifera, corals, mollusks, and calcareous plants (Illing, 1954; Newell, 1955).

During glacial ages, when sea level was about 120 m lower than at present, the Bahama Banks would have been great emerged flat-topped limestone plateau islands. Their surfaces were riddled with karst sinkholes and the oolitic sand was blown into giant dunes of *eolianite* sand that has now cemented. As sea level rose in Late Holocene time, the karst sinkholes have flooded (known as "blue holes"), and the islands such as North and South Bimini are the tops of Pleistocene eolianite dunes.

The Plate is an enlarged scene of the Bimini Islands at the northwest corner of the Great Bahama Bank (South Bimini is 83 km due east of Miami; see Figure C-15.1) taken from a Landsat-4 image made by the Thematic Mapper. Although this false-color image (Bands 1, 2, 4) was generated to emphasize shallow water and submerged shoals in realistic blue shades, the vegetation on the islands is in characteristic reds. Sandy Cay, an emerged barrier sand patch in lower center of Plate image, takes on the bright white color of oolitic sand. Figure C-16.1, a Landsat MSS image, depicts the largest Bahama Island, Andros, with its mangrove swamps. Sand sedimentation extends up to 100 km westward there, but the waters just to the east deepen to 2400 m in the Tongue of the Ocean, a channel that divides Andros from Nassau (upper right). Figure C-16.2 is an Apollo camera view of Eleuthera Island, with its shoals to the west, the Atlantic on the east, and another deep-water channel (Exuma Sound) to the south. Figure C-16.3 is an aerial view of a typical coral island (Stocking Island) in the Bahamas. **Landsat TM 40182-15125, January 18, 1983.**



ORIGINAL PAGE
COLOR PHOTOGRAPH

ORIGINAL PAGE
COLOR PHOTOGRAPH



3

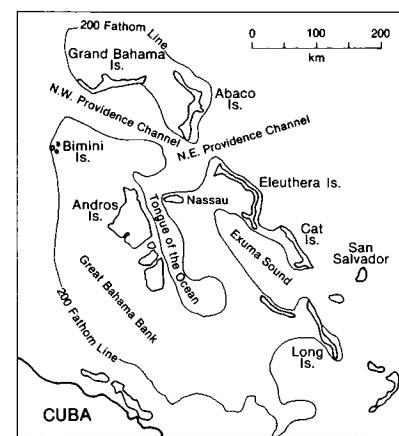


PLATE C-17

ORIGINAL PAGE IS
OF POOR QUALITY

BELIZE REEF TRACT

This false-color mosaic of three Landsat images covers the entire 230-km Caribbean coast of Belize (ex-British Honduras) from the Mexican border in Chetumal Bay on the north to Cabo Tres Puntas, Guatemala, on the south. Also shown at the right center is the Turneffe Islands, one of three atolls in the Caribbean seaward of the Belize barrier reef. This is the longest continuous coral reef in the Atlantic basin.

The continental shelf on which the Belize reefs are built is narrow (only 15 to 25 km in width) and tectonically active. North of the capital city of Belize, the northern shelf lagoon is generally less than 6 m deep; to the south of Belize city, the central channel of the southern shelf lagoon deepens to nearly 30 m (Purdy, 1974, p. 34). Chetumal Bay and the northern shelf lagoon are separated from the open sea by a long peninsula and a line of barrier islands (Figure C-17.1).

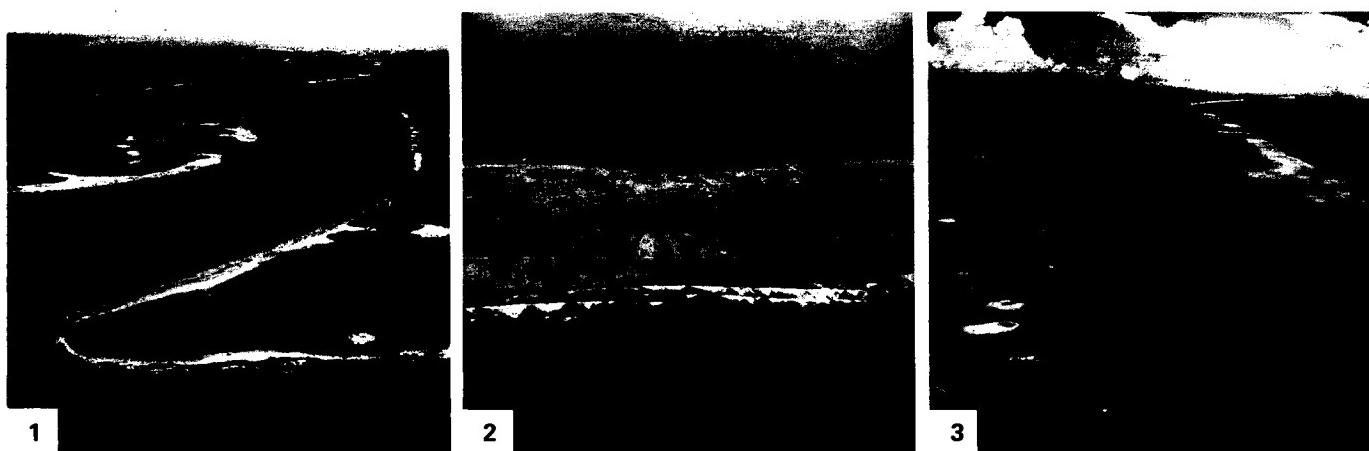
The southward deepening of the shelf lagoon and the progressive drowning of the outer platform suggest tectonic rotation down to the south. The modern reefs grow in the lagoon and on the distinct outer or barrier platform, which is a few kilometers wide (Figures C-17.2 and C-17.3). Both the barrier platform and the modern barrier reef on its seaward rim terminate in a J-shaped landward hook at the southern end of the reef tract. Seaward of the barrier reef, the water plunges to a depth of 180 m. During times of maximum glacial ice, when sea level was about 120 m lower than at present, the wall-like emerged margin of Turneffe atoll would have faced westward across a narrow channel to an equally steep emerged scarp on the outer platform barrier reef.

Unlike oceanic atolls such as Jaluit (Plate C-19) or the Great Bahama Bank (Plate C-16), the Belize reefs are not built on a thick accumulation of limestone on a subsiding platform. Rather, detrital continental shelf sediments have built the narrow shelf, with quartz sand dominating the mainland side of the shelf lagoon, clay-rich mud on the outer side of the lagoon, and carbonate mud on the shelf platform. On this "siliciclastic" foundation, the reefs have grown in relatively recent time, perhaps only in the Late Pleistocene (Choi and Ginsburg, 1982). The

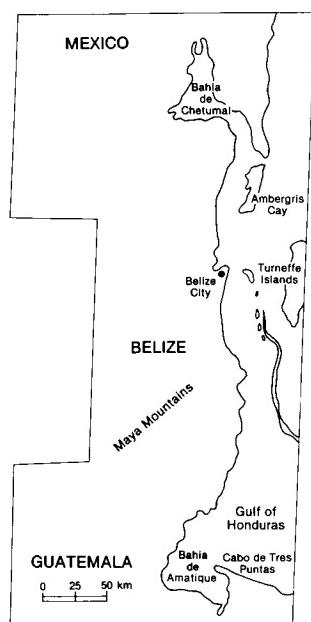
noncalcareous subreef sediments are exposed in the northern shelf lagoon and have been encountered in shallow borings under reefs in the southern shelf lagoon, seemingly confirming the recent southward tectonic tilt. One theory is that the former narrow continental shelf was largely subaerial, with fluvial sediments and landforms such as natural levees, deltas, and point bars on a floodplain. When this landscape subsided tectonically into the shelf lagoon, the higher parts of the fluvial landscape become the loci for initial reef growth (Choi and Ginsburg, 1982). Apparently, the outer barrier platform had a longer history of reef growth.

An alternate hypothesis for the distribution of modern reefs in the shelf lagoon and on the outer or barrier platform is that the modern reefs are growing on fault-controlled blocks of karst-weathered older reef limestone (Purdy, 1974). The intricate distribution of small shelf atolls inside the southern barrier reef suggests that their foundations were older limestone that, when exposed to humid tropical weathering during times of low sea level, was weathered into a maze of karst pinnacles and blind valleys. Seismic profiling and a few boreholes have confirmed that the modern reef is quite thin and closely reflects the relief of the substrate.

Both alternate hypotheses probably have some truth. The older siliciclastic foundation deepens to the south, and Holocene reefs are thicker to the south, supporting the idea that a former coastal plain has differentially subsided. However, if a former reef had been built during the last interglacial time, about 125 000 years ago, that reef would have subsequently died and been subaerially exposed by low sea level until only a few thousand years ago when the postglacial sea level again rose. If the weathered karst landscape on the old reef had subsided tectonically at the rate of only a few meters in 100 000 years, it would be covered by the modern sea, and corals would have found abundant surfaces on which to reestablish. Although corals are flourishing on the Belize reef today, it is probably not a very old landform. **Landsat Mosaic.**



ORIGINAL PAGE
COLOR PHOTOGRAPH



NORTHERN GREAT BARRIER REEF,
QUEENSLAND, AUSTRALIA

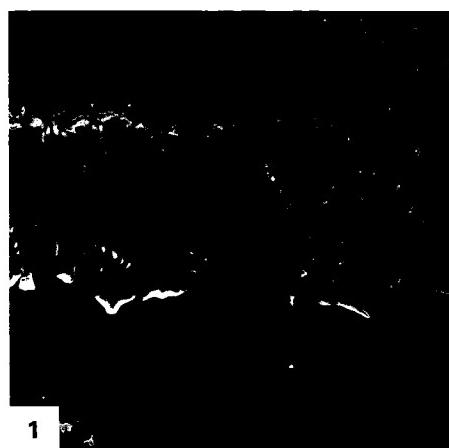
The Great Barrier Reef of Australia extends up the north-eastern coast of the continent from the Tropic of Capricorn (at the Cumberland Islands and Swain Reef, photographed from STS-8 (Shuttle; Figure C-18.1)) for 2300 km to Torres Strait, where it merges with the reefs along southern Papua New Guinea (as seen from Landsat-1 in Figure C-18.2). It includes thousands of individual reefs of a bewildering variety: patch reefs (Figure C-18.3), linear or ribbon reefs, crescentic reefs, submerged shoals, lagoonal reefs, and planar reefs (Hopley, 1982, p. 274). All the modern reefs have evolved in the last 6000 years since sea level returned to its approximate present position, but they are only thin veneers of recent coral limestone, usually less than 10 m thick, over older reefs, mostly constructed during the last interglacial age and then modified by karst solution during the long exposure of low sea level during the last ice age.

The segment of the Great Barrier Reef near Cape Melville in the image is typified by a ribbon reef (also called a wall reef or linear reef; Figure C-18.4) at the outer edge of the continental shelf. Farther south, the barrier reef system consists of large patch reefs or horseshoe-shaped crescentic reefs on a wider continental shelf. North of 16°S latitude, as in this view, the continental shelf becomes narrower, and the edge of the shelf is delineated by narrow ribbon reefs on which the powerful southeastern swell breaks in violence. The reef margin is so dangerous that few accurate soundings have been made, but divers have reported a depth of 400 m at a point 300 m seaward of Hicks Reef, along the right edge of this view (Veron and Hudson, 1978, p. 6). Depths of 1000 m are common within 1 km of the ribbon reefs, confirming that they define the edge of the continental shelf. Behind the ribbon reefs are a maze of submerged shoals, lagoonal reefs (those with a central atoll-like lagoon), and planar reefs (in which the central depression of a crescentic or lagoonal reef has been filled with coral debris to become a low-tide platform). The maximum depth among the shelf reefs is only 36 m. North of Cape Melville the

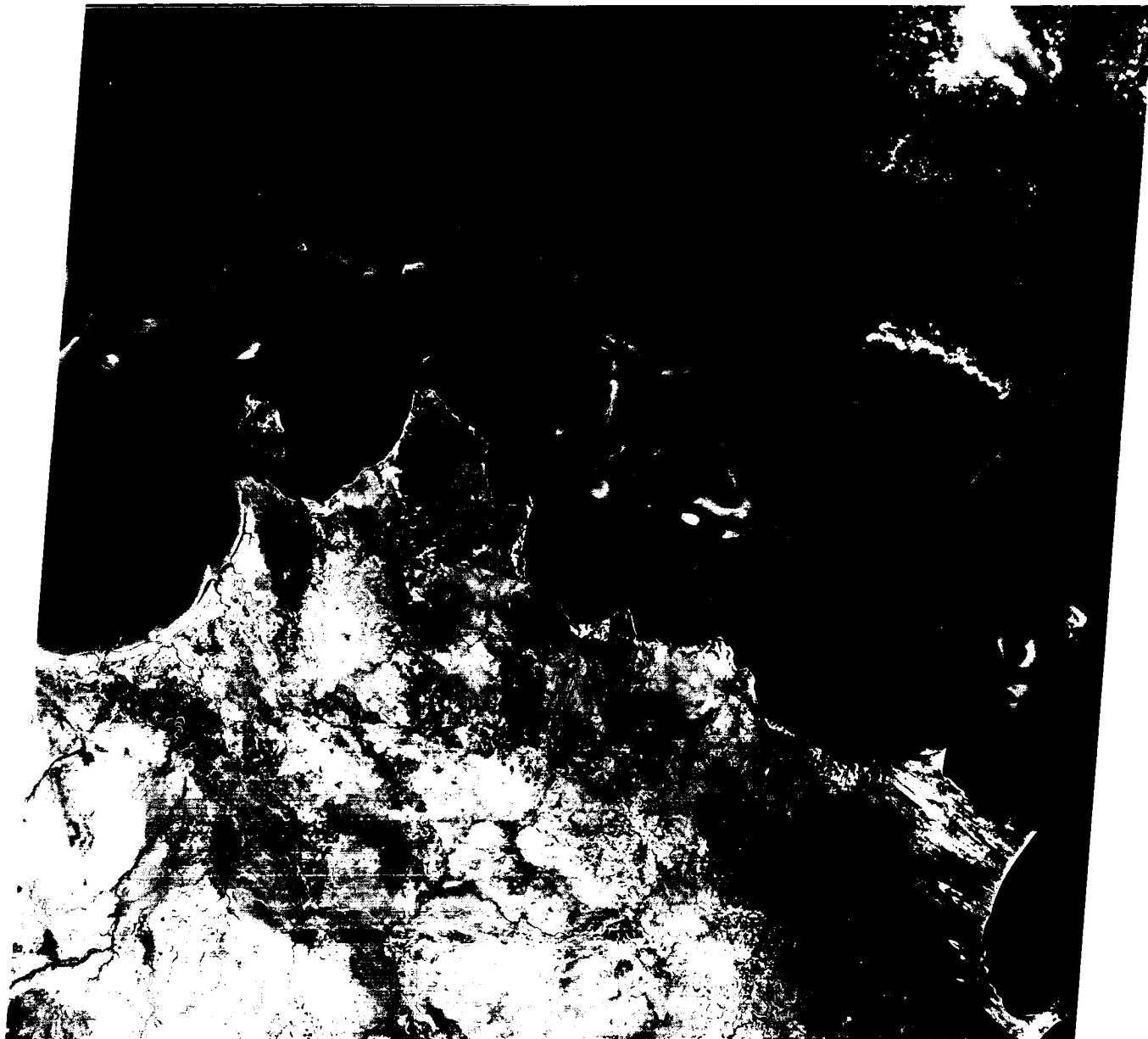
ribbon reef approaches to within 25 km of the mainland, the narrowest part of the channel behind the entire Great Barrier Reef.

Captain James Cook's discovery of the Great Barrier Reef was a near tragedy. He had sailed north for 1400 km along the mainland coast for many weeks in early 1770, unaware of the great reef system that was closing in on him from the east. On June 11, he went aground on Endeavour Reef near the place now named Cooktown, just southeast of this image (Hopley, 1982, p. 1). After beaching and repairing the ship, he threaded his way through the shelf reefs to Lizard Island, a granitic island that rises 360 m above sea level in the eastern part of the image. From the summit of Lizard Island, he planned a course that took him through the outer ribbon reef at Cooks Passage, at the extreme east edge of this image. It is ironic that, although the crew cheered at their harrowing escape from the Great Barrier Reef, after sailing north for a time in terrible weather, Cook was forced to run inside the reef once again. The tidal current miraculously swept *HMS Endeavour*, without any rudder control, back inside the reef through a pass. From that time on, Cook was able to navigate safely through the Torres Strait and north to Dutch settlements in present Indonesia. The first written description of the Great Barrier Reef is also one of the epics of maritime history.

Among the shelf islands of the northern Great Barrier Reef are a number of "low wooded islands," former patch reefs or lagoon reefs that have partially filled with storm beaches, coral debris, and dunes, and which now support mangrove swamps and tough woodland shrubs and trees typical of the northern Australia savanna. A cluster of these low wooded islands north of Cape Flattery includes Bewick, Howick, the Pethebridge Group, the Turtle Group, and Nymph Island. The ecology and geology of these unique reef islands were subjects of extended British research in 1928–1929 (Yonge, 1930). The northern Great Barrier Reef was again studied in 1973–1974 by a combined Australian, British, and U.S. team (Royal Society of London, 1978; Stoddart, 1978). **Landsat 1203-23543-5, February 11, 1973.**



ORIGINAL PAGE IS
OF POOR QUALITY



4

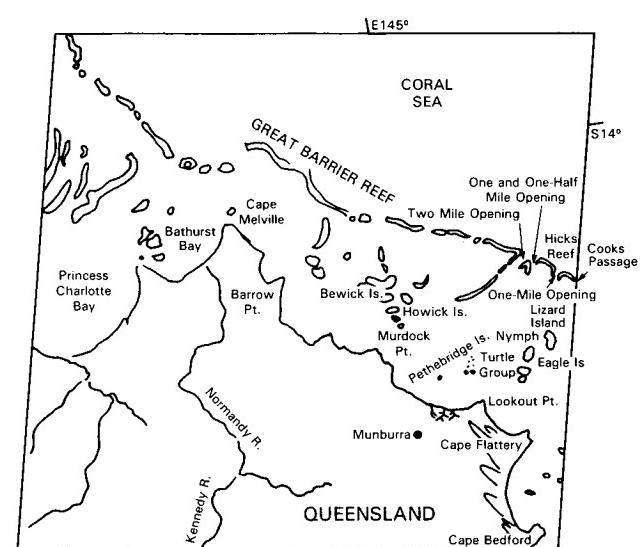


PLATE C-19

TROPICAL CORAL ISLANDS

Reef-building corals thrive in all mud-free shallow ocean water where surface water temperatures remain above 18 °C. The region includes almost all tropical oceans today and warm shallow subtropical seas. The coral polyps are pelagic until they settle on a hard substrate in clear water less than 70 m deep. Corals support symbiotic photosynthetic algae in their tissue, so that clear shallow water is essential for reef growth. There is such an extensive shallow water zone in the tropics today, especially among the island arcs of southeast Asia and the western Pacific basin, that one of the most fundamental divisions of coastal types is that between coralline and noncoralline coasts (Davies, 1980).

Indonesian island arcs are especially notable for reefs growing on active tectonic foundations. The upper image in the Plate montage shows the Toekang Besi archipelago that trends southeast into the Banda Sea from the southeast arm of Sulawesi (Celebes) Island. Hamilton (1979) suggested that the foundation of these islands is a fragment of continental crust torn from New Guinea, now almost 1000 km to the east. Umbgrove (1947, p. 762) noted a linear arrangement for the islands, with southeast-trending atolls on the southwest side, then a row of elevated islands, followed by another row of atolls, and finally on the northeast, a row of small islands with uplifted coral reef terraces. He interpreted the chains of atolls as growing on subsiding fault blocks or anticlinal ridges. The alternating belts of high and low islands certainly favors control by active tectonic lineaments, but the net movement has not been ascertained. (Uplift rather than subsidence is more likely.)

In the central Pacific are several chains of islands administratively called the U.S. Trust Territory of the Pacific Islands, or Micronesia. Covering a total oceanic area equal to that of the 48 conterminous United States, the total *land* area of Micronesia is less than two-thirds the size of Rhode Island. All but a few of the Micronesian islands are atolls, rising from oceanic depths to barely above sea level and enclosing lagoons that are commonly 30 to 40 m in depth (Wiens, 1962; Shepard, 1970). At the western end of Micronesia lies the Belau (Palau) fringing reefs located 900 km east of Mindanao in the Philippines (lower left image in Plate). This reef complex, which stretches about 160 km along a north-northeast line, consists of a group of islands along the east side of the lagoonal waters. The largest, Babelthuap, is about 50 km in length and has several peaks above 200 meters. In the Plate, these heavily vegetated islands show up as bright tones in the Band 7 image (left center), but the fringing atoll reefs are

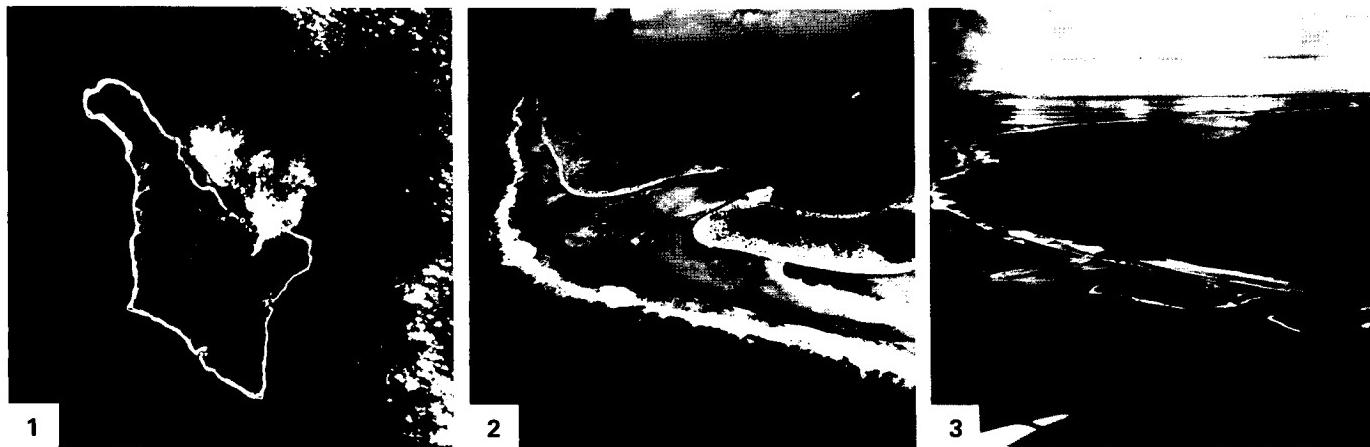
nearly invisible; in Band 4 (not shown), these reefs would stand out, but the islands would be difficult to pick out.

In eastern Micronesia, Jaluit atoll (Figure C-19.1, part of a Landsat image) in the Marshall Islands is typical of reef islands that enclose a lagoon without interior land. Jaluit is more elongate (55 by 36 km) and cuspatate than many Micronesian atolls. Southeast Pass and Southwest Pass are clearly visible at low tide because of the maze of smaller plug reefs that thrive inside the main reef rim, nourished by strong tidal currents at the inlets. Typhoons are common, and in 1958, one stripped many of the islets of their trees and soil (McKee, 1959). The northeast Trade Wind is dominant over Jaluit. Because ocean currents also come from the east, the eastern side has higher waves and stronger currents that encourage more vigorous growth on that side, which in turn provides more broken coral debris for storms to throw onto the reef flat. Inside the Jaluit lagoon are uncounted numbers of small pinnacle or patch reefs, some of which break surface above the 20- to 30-m deep floor.

Reefs also form a cluster of atolls in the Maldives Islands south of the tip of peninsular India (lower right image in Plate). These islands have built up along high points on the Chagos Laccadive Plateau that lies between the mid-Indian spreading ridge and the Chagos Trench.

Figures C-19.2 and C-19.3 are aerial views of Jaluit and Arno atolls, respectively, in the Marshall Islands.

The origin of oceanic atolls, which Darwin (1842) called "enigmatic" structures, has been one of the classic problems of geology. Most researchers now agree that atolls like Jaluit were established on former midocean basaltic volcanoes (some are now guyots) that originated near active spreading ridges but have since been displaced to their present positions. As new oceanic lithosphere is created at the ridge crest, it moves outward and cools. Thermal contraction is an adequate mechanism to explain how hot young oceanic lithosphere can form at shallow depths (2 to 3 km) near a spreading ridge and then move outward over the next 30 to 60 Ma while sinking to an average oceanic depth of 4 to 5 km. Darwin's theory that oceanic atolls began on slowly subsiding foundations has gradually been confirmed. Borings on Eniwetok atoll, near Jaluit, reached basalt basement at 1200 and 1400 m after penetrating shallow water reef limestone of Eocene age. During most of Cenozoic time, these atolls have maintained their surfaces in or close to the breaker zone while their foundation sank at a rate of a few centimeters per 1000 years. **Landsat Montage.**



ORIGINAL PAGE IS
OF POOR QUALITY

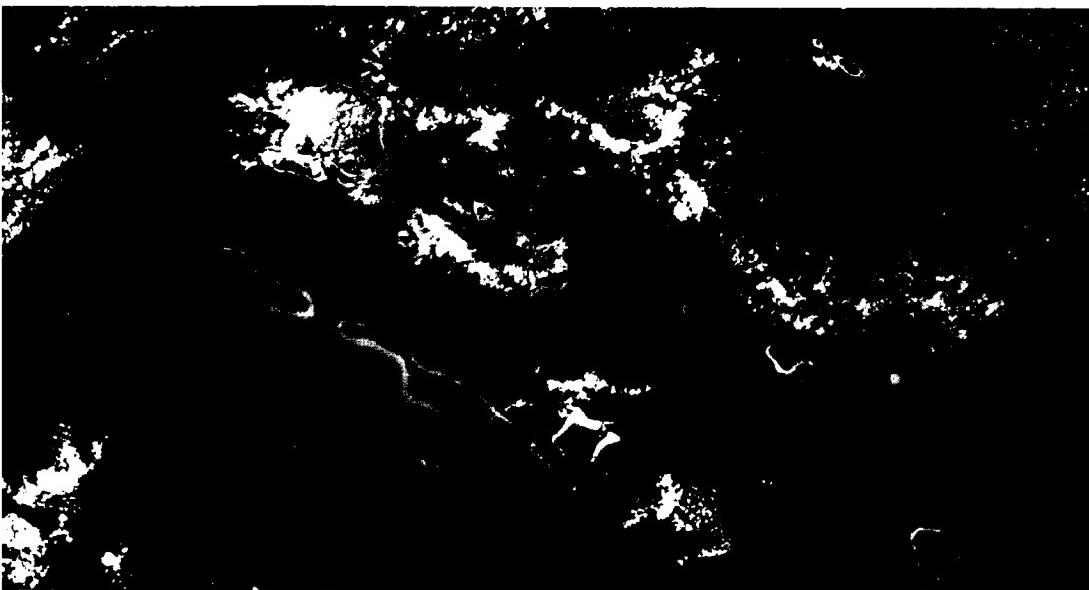


PLATE C-20

The Swan coastal plain around Perth in western Australia (Wilde and Low, 1975, 1980) illustrates one way in which faulting can influence a coastline. As is strikingly displayed in the Plate, the inner edge of a 20- to 30-km wide coastal zone stands out as a remarkably regular line; the present shore roughly follows the curvature of this line but shows cuspate indentations, promontories, a series of beach ridges, and lagoonal lakes developed in Late Pleistocene and Holocene times. The inner line is actually a scarp eroded back from several major fault planes. The longest of these is the Darling Fault, whose trace over 400 km is accentuated by the abrupt drop in heavy vegetation cover (Jarrah: *Eucalyptus sp.*) on the western edge of the plateau to the east, readily perceived in a Landsat mosaic (Figure C-20.1) of the region.

The physiography of southwestern Australia (Jutson, 1950) is dominated by the Darling Fault. This normal fault was initiated in the Early Paleozoic; geophysical work suggests that it has a cumulative displacement of about 10 km. The fault runs meridionally from well north of Perth to the southern coast. A second rupture—the Collie-Naturaliste Fault—arcs southwestward inland from Geographe Bay. Movement along this fault system in the Tertiary has been postulated, but no modern earthquakes can be traced to its subsurface extension. Uplift of the Yilgarn structural block is to the east of the fault, where the present surface attains altitudes averaging 300 m (maximum of 582 m at Mt. Cooke, one of many higher monadnocks). The ranges within the Darling Plateau are underlain by Precambrian crystalline rocks—mostly granites, migmatites, and banded gneisses—and basic volcanics are exposed in the south. The Darling Ranges today comprise an uplifted and dissected peneplain beneath which deep and intense weathering during the Late Mesozoic/Early Tertiary has led to lateritic and bauxitic regolith, together with some sands

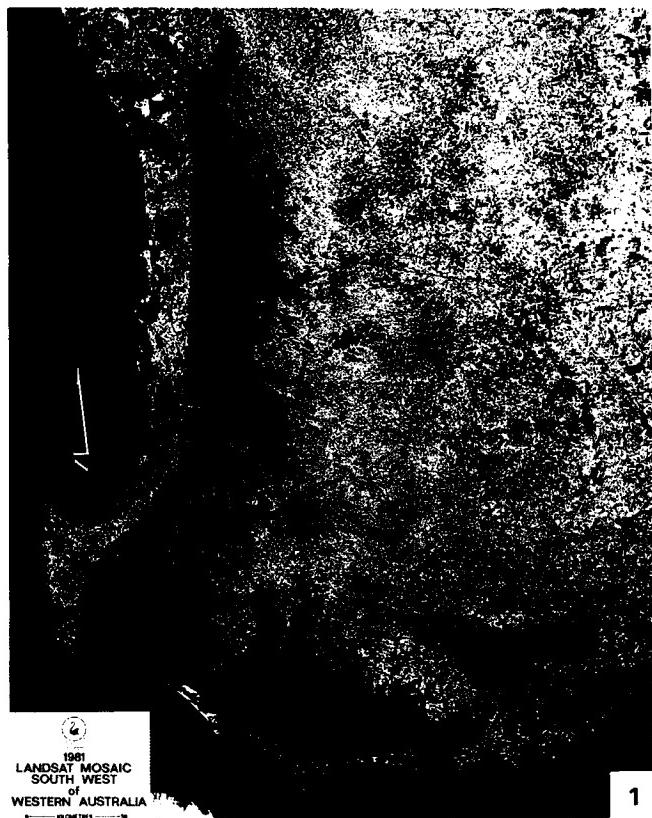
PERTH, AUSTRALIA

and conglomerates, that hardened on uplift and dessication. These duricrusts have since been strongly stripped away in the southern region, exposing fresh crystalline rock.

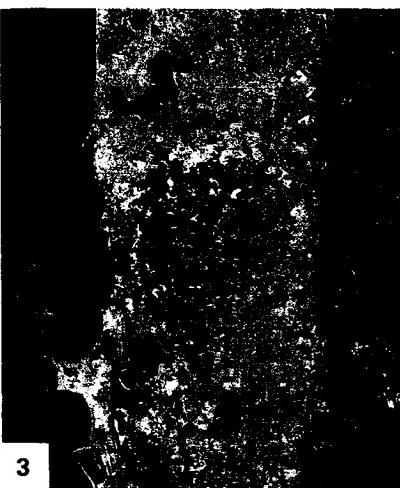
The Darling scarp varies in height from about 90 to 200 m. Streams to its east (controlled on the plateau by northwest-southeast jointing) incise through the scarp enroute to the Indian Ocean. The scarp itself, stepped in places, appears to be a fault-line surface eroded back perhaps 1 to 2 km from the present fault trace to the west.

The coastal plain (Figure C-20.2) tops the Perth Basin, which extends oceanward to the continental shelf. The major basin fill consists of sedimentary rocks, possibly exceeding 15 km in depth, that are sparsely exposed amid otherwise continuous Late Cenozoic (mainly Pleistocene) deposits (Playford et al., 1976). Elevations in the Swan coastal plain are generally below 75 m. Highest points are near the scarp, where alluvial fans have built up a piedmont zone. Moving westward, one encounters the Pinjarra Plain, an alluvial tract, then the Bassendean Dunes—low vegetated hills of quartzose sands—and finally the Coastal Belt—dominated by calcareous and siliceous dunes or ridges that can attain heights of 60 m above associated swales (Figure C-20.3). Offshore islands are sand dunes built during lower sea level some 5000 years ago. The subsequent rise in this level has cut low cliffs and beaches along the present coast and produced drowned estuaries and lagoons.

Isolated strandlines close to the Darling scarp indicate nearly complete inundations of the Swan plain during Pleistocene interglacial times (Churchill, 1959). The scarp itself thus served as a barrier to further inland invasion, but its erosion has been influenced more by fluvial processes than by marine action. (GCW: N. M. Short) Landsat 21189-01004-7, April 25, 1978.



ORIGINAL PAGE IS
OF POOR QUALITY



3

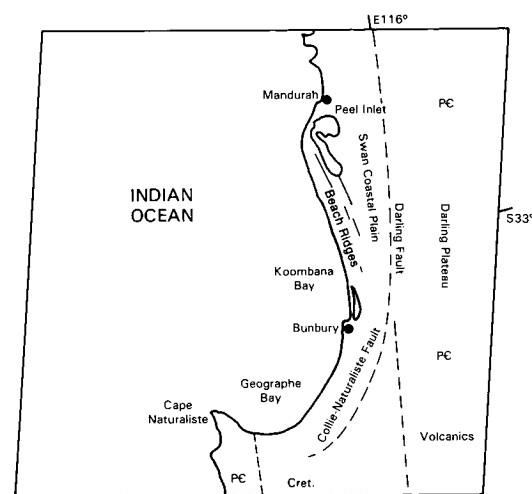


PLATE C-21

COASTAL EMBAYMENTS

Water incursions into semi-enclosed basins on the landward side of marine coasts contain salts in varying concentrations ranging from supersaturated to slightly brackish. The concentration depends on the degree of interchange (replenishment) between the open ocean and the land-locked waters, on evaporation rates, and on past history. This Plate treats three prominent examples as seen from space.

The Plate image shows most of the Gulf (Gol) of Kara-Bogaz along the east-central side of the Caspian Sea, itself a huge landlocked "lake" of slight salinity, but once a part of the Mediterranean system (Garbell, 1963). The Kara-Bogaz is the classic modern counterpart, although somewhat smaller, to some typical evaporite basins responsible for ancient salt deposits in the stratigraphic record. Its current dimensions cover an area of about 10000 km with a maximum depth of 3.5 m (Fairbridge, 1968), but the distribution of saline deposition beyond its periphery indicates a former area of more than 18000 km. Recent salinity determinations show an excess of 300‰ in the Gulf of Kara-Bogaz waters (compared with an average of 13‰ for the Caspian Sea and 35‰ for seawater), approximately the same as that of the Great Salt Lake (Plate KL-12). Deposition of salts is prodigious, with gypsum, epsomite, and halite being most common. In earlier times, mirabilite (a hydrous sodium sulphate) formed under conditions suggesting the cooler temperatures found in periglacial environments.

Sand spits developed by longshore currents in the Caspian Sea are responsible for the nearly complete oceanward enclosure of the embayment of the Gulf onto desert lowlands. Waters now enter the Kara-Bogaz through a narrow (300 m wide) and shallow inlet (A on the index map), but there is no reverse circulation. The arid climate in this part of the Turkmen Republic S.S.R. favors precipitation of salts. In the long term, the Kara-Bogaz is likely to vanish as an active sediment basin, but no significant change can be detected from comparing the 1972 image with a later one in 1977 (Figure C-21.1). Visual differences may be attributed to both the differences in MSS bands (5 for 1972;

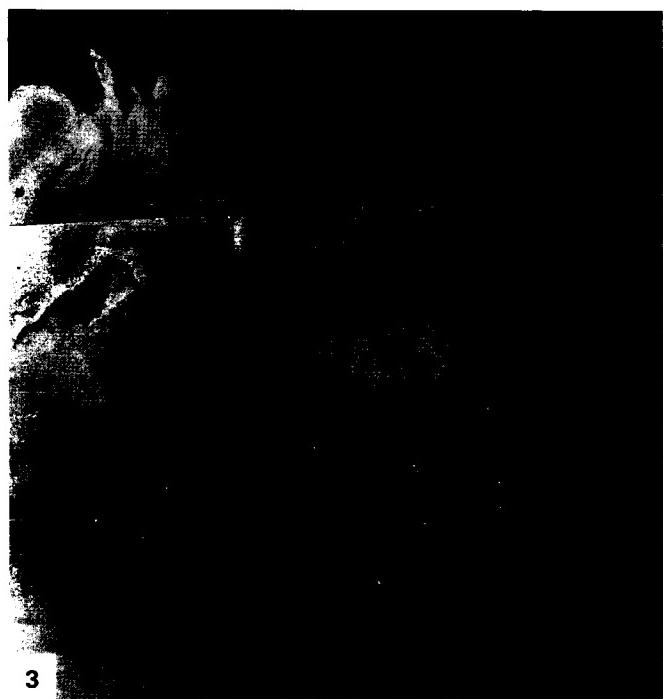
6 for 1977 image) and seasonal variability (December versus March).

Figure C-21.2 is a mosaic of parts of two images that focus on the southern Gulf of Venezuela (indented from the Caribbean Sea) and northern Lake Maracaibo in western Venezuela. These water bodies lie within a structural basin that localized extensive sedimentation throughout the Cenozoic (Sutton, 1946). Marine waters driven by tides invade the narrow strait of Maracaibo from the nearly sealed Tablazo Bay at the south end of the Gulf. This strait was probably the course of a river during times of lower sea level. Then, Maracaibo was a true freshwater lake, as revealed by samples from drilling into and around the lake in search of abundant oil in subsurface fields. The lake now supports low but variable salinity (typically less than 1‰ at the surface and 3‰ at depth), depending on influx of seasonally fluctuating rainwaters from land drainage. Outflow from the lake to the Bay and Gulf predominates during the wet season, but this usually reverses in dry times (Redfield, 1961).

In Figure C-21.3 (another Landsat two-image mosaic), a much different situation exists along the Arabian (Trucial) coast on the Persian Gulf (Evans et al., 1964). Adjoining this coast, in land near sea level, are several salt-encrusted depressions termed sabkhas (or sebkhas). These may receive fluids from tidal action, if near shore, from rainwater, or from shallow, often saline ground water. Two types of sabkhas are distinguishable: one coastal and the other inland (including playas of the southwestern United States, the kevirs of Iran, and shotts of northwest Africa). High evaporation rates are required to maintain sabkhas, and capillary action above shallow water tables resupplies saline inputs. Sabkhas along the Persian Gulf can result from residual waters introduced from higher sea levels during Holocene sea level changes. This may apply to the very large interior sabkha—Sabkhat Matti—seen in Figure C-21.3 to extend inland for more than 150 km from the Persian Gulf (just east of Qatar) into the Empty Quarter of Saudi Arabia. (GCW: N. M. Short) Landsat 1134-06425-5, December 4, 1972.



2



3

ORIGINAL PAGE IS
OF POOR QUALITY

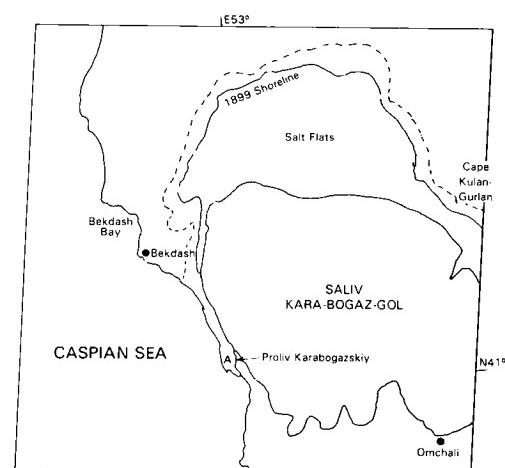


PLATE C-22

RANNS OF KUTCH, WESTERN INDIA

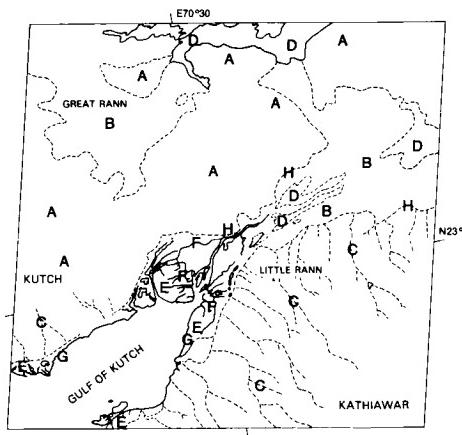
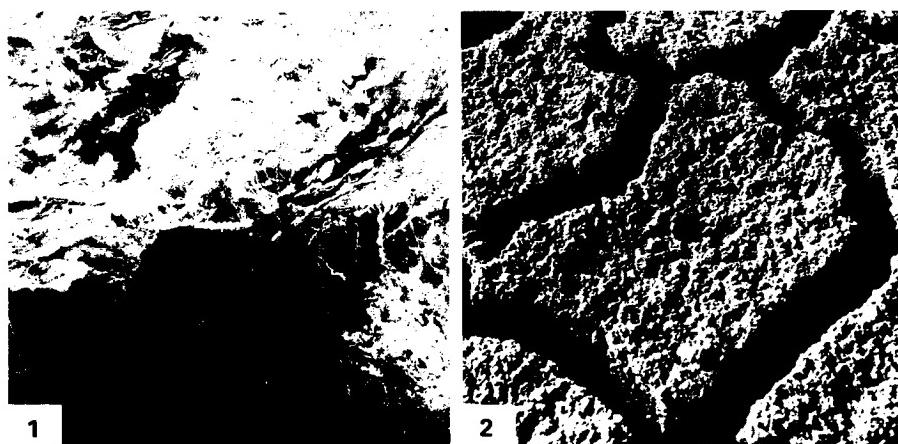
This two-frame mosaic shows both the Little Rann of Kutch and its larger counterpart, the Great Rann of Kutch, to the north-northwest. These coastal features consist of large low-relief plains on the southeastern flank of Pakistan's Indus River delta. These plains are separated by hills of pre-Quaternary rocks (A). The Great Rann of Kutch is on the Pakistan/India border just east of the India distributary mouths. The Little Rann of Kutch is located between the mainland of Kutch, forming the northern border for the Gulf of Kutch and Kathiawar to the south.

The Ranns of Kutch are believed to have a structural origin that has controlled their location. Faults that influenced the alignment of the pre-Quaternary rock outcrops trend west-northwest. Another family of faults, of which the Gulf of Kutch may be an expression, trends north-northeast. The aforementioned outcrops are thought to be horst blocks cut into segments by the north-northeast faults, while the Ranns themselves probably represent grabens. These tectonic depressions were once shallow marine gulfs after the last postglacial rise in sea level. Changes in nearby river courses (Indus, Nara, and other rivers of the western part of the Indo-Gangetic plain) caused the Ranns to become infilled with deltaic sediment, and they are now essentially broad salt-covered supratidal areas (sabkhas) that are inundated only part of the year (Glennie and Evans, 1976), as in this Plate image.

In lowland areas such as the Indus Delta to the west, the monsoonal cycle plays an important role in supplying water and sediment to the coastal plain. For the Ranns of Kutch, annual flooding by marine water and freshwater runoff from surrounding highlands occurs during the Southwest Monsoon, when marine water is forced up into the area by persistent strong winds. Including the Great Rann of Kutch, more than 30000 km² of lowlands are flooded annually. Most of this area is supratidal or above the normal high tide. However, when winds of the Southwest Monsoon, which blow from July to September, push marine water into the Gulf of Kutch and other estuary mouths along the coast under these conditions, salt water can be more than 2 m deep on the supratidal surface (B) (Platt, 1962). During this same period, rainfall in the area is maximized when moisture from the Arabian Sea is transported inland. Annual rainfall over the Ranns of Kutch ranges between 20 and 38 cm/yr, most of which falls during the Southwest Monsoon months. During these high-rainfall months, a number of small rivers to the

east bring both terrigenous sediment and fresh water to the eastern parts of the Ranns. Hills around the Little Rann of Kutch display an intricate drainage network (C), activated primarily during the Southwest Monsoon. The remaining months of the year are characterized by the high average temperatures and low humidity of a desert environment. Therefore, as the Southwest Monsoon subsides, waters recede from the supratidal areas, allowing the Ranns of Kutch to become regions of intense evaporation and subsequent deposition of evaporite minerals such as halite and gypsum typical of coastal sabkhas (Figure C-22.1). These surfaces of salt deposition (D) are clearly visible in this figure as white (high reflectance) areas on the scene. Figure C-22.2 is a closeup of a sabkha surface illustrating the salt deposition and desiccation cracks typical of sediments from this environmental setting. Unlike the broad supratidal plains of the well-studied western Persian Gulf, which are composed mainly of carbonate sediments and evaporite minerals, the Ranns of Kutch are accumulating sizeable quantities of terrigenous clays and silts, as well as halite and gypsum. Because of the high salinities and periods of dessication, most of the organisms that contribute skeletal carbonates to many of the world's intertidal and supratidal environments are not present in this setting.

After the Southwest Monsoons, a normal semidiurnal tide of approximately 3 m forces marine waters up the Gulf of Kutch and over muddy tidal flats (E) at its head and along its flanks. These mudflats are cut by intricate networks of meandering tidal channels (F) that are clearly visible in the scene. The clay-rich sediments comprising these mudflats are transported into the Gulf of Kutch by strong longshore currents from the mouths of the Indus River, to the northwest. The greatest influx of sediments coincides with strong winds of the Southwest Monsoon. However, the flux of fine-grained sediment into the gulf, which in turn is used for tidal flat accretion, is a constant process. Local wind waves rework the outwash fans of sediment that prograde along the margins of the Gulf of Kutch, leaving narrow and poorly developed beaches (G). A similar process occurs within the Ranns themselves. As they fill with water during the Southwest Monsoon, local wind waves create shoreline features such as beaches and small cliffs (H) along the Rann margins where the distal ends of outwash fans from surrounding hills become inundated and then modified by waves. (GCW: J. M. Coleman) Landsat 2294-05024-6 and 2294-05020-6, November 12, 1975.



ORIGINAL PAGE IS
OF POOR QUALITY



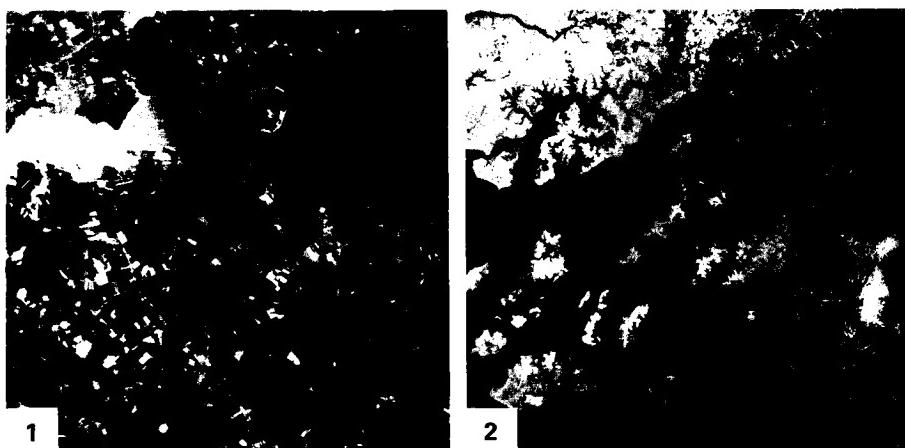
PLATE C-23

This two-image Landsat mosaic of the mid-Atlantic Coast includes the southern tip of New Jersey, the Delmarva (Delaware/Maryland/Virginia) peninsula, and the Norfolk/Virginia Beach area to the south. These major landforms are bounded by the Delaware and Chesapeake Bays, both drowned river valleys. The Chesapeake Bay, with its many tributaries, has a total tidal shoreline of approximately 1000 km almost equally divided between the states of Maryland and Virginia, making it the largest estuary in North America.

Estuaries are defined as semi-enclosed coastal bodies of water that freely connect with the ocean and within which seawater is measurably diluted with fresh water from runoff (Pritchard, 1967). The main source of freshwater input in the Chesapeake is the Susquehanna River, which drains a large watershed extending into Pennsylvania and New York. Other tributaries, such as the Potomac and James Rivers on its Western Shore, contribute substantial quantities of water, with the eastern shore tributaries adding only a little more. Salinity varies along the roughly north-south axis of this estuary from full-strength seawater (35‰) at the mouth to completely fresh water near the head north of Baltimore. Because of the brackish water conditions, estuaries teem with life, and many commercially and recreationally important finfish and shellfish are dependent on estuaries during at least some portion of their life cycle.

The tidal range in the Chesapeake Bay ranges from an average of 1 m at its mouth to less than 30 cm near its head. The Bay is generally very shallow, averaging 3 to 6 m deep, except for the narrow deep channel near the Western Shore, which represents the drowned river channel of the Susquehanna River. Because of its shallow depth and extremely long length (over 300 km), the astronomical tide takes over 12 hours to propagate from one end of the Bay to the other. Therefore, the Chesapeake Bay has the distinct characteristic of containing two high tides along its length (say at Norfolk, Virginia, and Baltimore, Maryland) at the same time.

Estuaries are ephemeral features on a geologic scale; lifetimes are usually limited to a few thousands to at most a few tens of thousands of years (Schubel, 1971). All present-day estuaries worldwide are thus very young geologically; they formed during the most recent rise in sea level, which began about 15000 years ago. Estuaries along the trailing edge of passive margin coasts, which are dominated by low, gently sloping wide coastal plains, were formed by the drowning of river valleys. Other estuaries have been created by tectonic processes (San Francisco Bay, California), by glacial ice motion (fjords of Norway and Sweden), and by development of barrier islands (Atlantic coast of Delmarva). A rise in sea level can prolong the lifetime of an estuary,



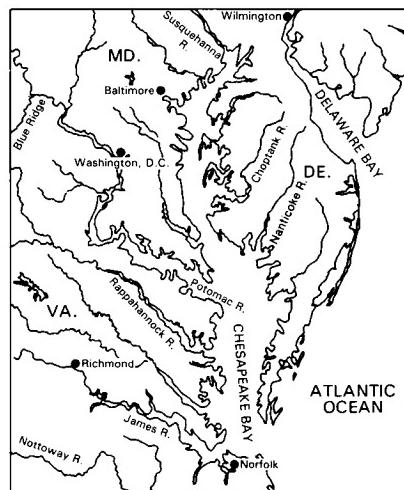
THE CHESAPEAKE BAY

but many large cities, such as Norfolk, Virginia, and Washington, D.C., would be inundated if the rise were to exceed a few meters.

With rising sea levels, low-lying regions are submerged. This has been the primary response of the shoreline along the Eastern Shore of the Chesapeake Bay. Here, farmlands are being slowly invaded (Figure C-23.1) by the brackish water so that cornfields are changed to marshlands (termed upland conversion). This landward migration of the salty waters and associated flora is presently occurring at rates of up to 1 m per year in low-sloped areas of the Eastern Shore. In addition, sea-level rise results in actual erosion of sediment along the outer edge of the land (the Bay shoreline). Depending on shore type, which ranges from low to fairly high cliffs of unconsolidated sediments along the Western Shore to generally low banks, beaches, and marshes along the Eastern Shore, there is a wide range of erosion rates. The highest rates of historic erosion approach 3 m per year, while the baywide average is 0.3 to 0.6 m per year, providing large quantities of sediment. The small marshy islands in the mid-Bay are rapidly eroding; some have disappeared completely in historic times. Other sources for Bay infilling result from landward transport of littoral sediments through the mouth by tidal and wave-generated currents and riverine inputs from the numerous tributaries, primarily the Susquehanna River.

Estuaries are clearly dominated by natural processes, but human activities can also affect the infilling of estuaries. Until recently, relatively poor soil conservation practices throughout the drainage basin of the Chesapeake Bay have greatly increased the sediment yield and hence sedimentation rates in nearshore areas. Such anthropogenic influences can shorten the lifetime of an estuary by a factor of 2 or more (Schubel, 1971).

The low-lying terrain of the West Africa coast has likewise been greatly influenced by the Holocene rise in sea level. Rivers have become tidal-influenced, converting them into a series of small estuaries and creating a very irregular coastline (Figure C-23.2). This coast is microtidal (<2 m) and semidiurnal, as is the U.S. mid-Atlantic Coast (Davies, 1980). The large estuary of the Geba River is quite similar to the Choptank and Nanticoke tributaries of the Chesapeake Bay. The abundant river discharge due to the high rainfall (2000 to 3000 mm/yr (Orme, 1982)) results in considerable flow of terrigenous sediments onto the continental shelf. Although the shore morphology is characterized as lowland coastal swamps and tidal creeks, the erosion-resistant rocks (Paleozoic cover over a Precambrian platform) form the irregular coastline of Guinea-Bissau, as well as the numerous offshore islands. (GCW: S. P. Leatherman) **Landsat 1079-15135-7 and 1080-15187, October 1972.**



ORIGINAL PAGE IS
OF POOR QUALITY



PLATE C-24

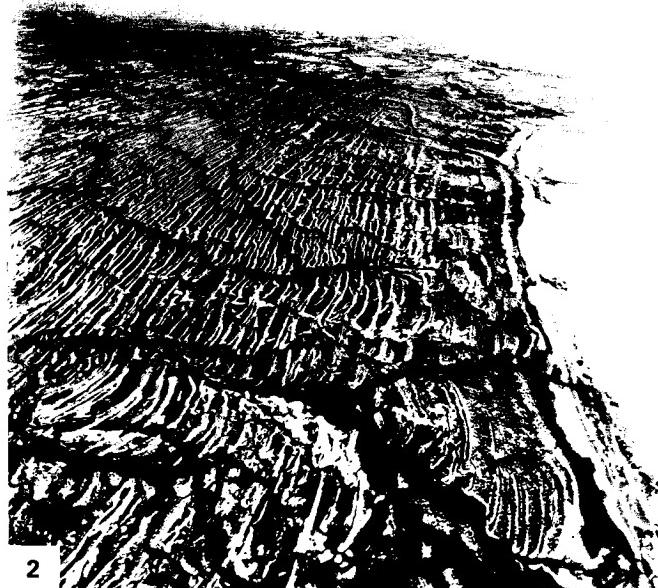
HUDSON BAY SHORELINES

One of the most convincing lines of evidence for major shifts in sea level during Pleistocene and Holocene times comes from elevated shorelines and other coastal features such as terraces now found inland from the present land/sea boundaries. Eustatic changes during those times are attributed to varying water volumes in the ocean basins as some of the seawater is incorporated in the ice caps during glacial advances or is returned as meltwater when glacial sheets retreat. However, shifting shorelines can also be driven by progressive rises or falls of the land surface as underlying crustal units move up or down in the gravity field in response to isostatic adjustments. One mechanism for this vertical motion stems from on-loading or off-loading of the crust by the sheer weight of overlying geologically brief masses of thick glacial ice. The sequence of shorelines along the Hudson and James Bays (Martini et al., 1980) is a classic example of the marks made by a retreating water body as the crust underneath rebounds from the off-loading of an ice sheet. In the Plate image, these multiple shores, whose positions are recorded by raised beach ridges, are brought into sharp perspective by the emphasizing effect of low Sun angle (14°) associated with the subarctic midwinter scene; in summertime imagery of the same area, these ridges are barely invisible.

As the great Wisconsin ice sheet retreated across Canada, the open seas invaded low regions of northern Canada, perhaps as early as 12000 years ago, entering from the present Hudson Straits and elsewhere. Marine water—named the Tyrrell Sea by H. A. Lee (1960)—spread over the central part of Canada, reaching a maximum extent some 8000 years ago at points 100 to 250 km inland from today's Hudson/James Bay shores. As the sea filled the crustal downwarp instigated by a major lobe of the Wisconsin glaciers, it interacted with remnants of the Laurentide ice sheet, in places producing distinctive drift deposits (washboard moraines) at contacts with the receding ice. Concurrently, the

land beneath the invading sea was rising in response to the isostatic rebound accompanying ice removal. The rate of crustal uplift was fast at first, on the order of 600 cm per century (Lee, 1960), but it diminished exponentially to rates that range between 70 to 120 cm per century. Thus, the coastline has emerged rapidly, forcing the Hudson Bay waters northward, but the net shift was being counterbalanced somewhat by the meltwater rise of sea level worldwide. Radiocarbon dating of invertebrate shells in the farthest inland beach ridges indicate that those southwest of James Bay are 6900 to 7200 years old. The innermost beaches in the Fort Severn group now stand at elevations of 175 to 200 m above the current surface of Hudson Bay.

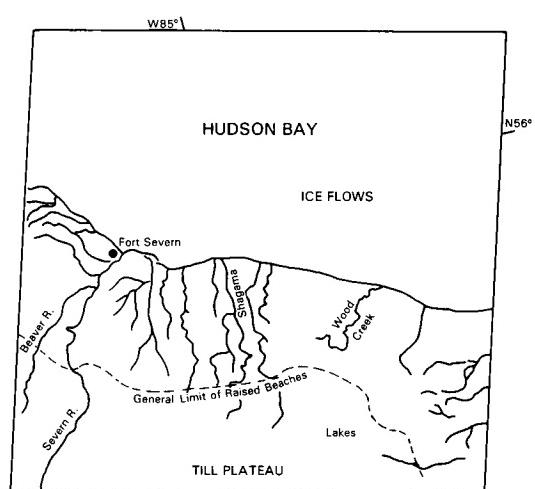
In the Plate scene, the area near the bottom (with ice-covered thermokarst-like lakes) is a till plateau, generally smooth and flat, with peat deposits, bogs, and fens along both elevated surfaces and drainage channels. To the north is the main zone of beach ridges. As many as 50 can be discerned from space in a 50- to 60-km wide stretch east and west of Fort Severn. These features are the dominant landform, as is evident in the oblique aerial photographs (Figures C-24.1 and C-24.2). The ridges, some 100 to 200 m in width, attain heights up to 7 m (Pala and Weischet, 1982). Spacing between ridges is greater, and those lower areas are typically filled with dark peat deposits. Close examination of a ridge *in situ* (Figure C-24.3) indicates it to be a mixture of cobbles, gravel, sand, and blue clay, representing the reworking by wave action of the till plains materials over which the sea regressed. Soils developed on the beach material (in which the exposed larger stones account for the bright reflectances in both the Landsat and aerial images) now support jack pine and spruce. Tidal flats and salt marshes persist along the present shores. (GCW: N. M. Short) **Landsat 40202-16184-4 (TM)**, February 3, 1983.



ORIGINAL PAGE IS
OF POOR QUALITY



3



REFERENCES

- Andersson, J. G., "Solifluction", a component of subaerial denudation, *J. Geol.*, **14**, 91-112, 1906.
- Bloom, A. L., *Geomorphology: A Systematic Analysis of Late Cenozoic Landforms*, 510 pp., Prentice-Hall, Englewood Cliffs, N. J., 1978.
- Brüggen, J., *Fundamentos de la Geología de Chile*, 374 pp., Santiago de Chile, Inst. Geogr. Militar, 1950.
- Choi, D. R., and R. N. Ginsburg, Siliciclastic foundations of Quaternary reefs in the southernmost Belize Lagoon, British Honduras, *Geol. Soc. Amer. Bull.*, **93**, 116-126, 1982.
- Churchill, D. M., Late Quaternary eustatic changes in the Swan River district, *Roy. Soc. West Australia Jour.*, **42**, 53-55, 1959.
- Clapperton, C. M., Evidence of cirque glaciation in the Falkland Islands, *J. Glaciology*, **10**, 121-125, 1971.
- Clark, J. A., An inverse problem in glacial geology: The reconstruction of glacier thinning in Glacier Bay, Alaska Between A.D. 1910 and 1960 from relative sea-level data, *J. Glaciology*, **18**, 481-503, 1977.
- Cotton, C. A., Sea cliffs of Banks Peninsula and Wellington: Some criteria for coastal classification, *New Zealand Geographer*, **7**, 103-120, 1951. (Republished in Collins, B. W., (Ed.), *Bold Coasts: Annotated Reprints of Selected Papers on Coastal Geomorphology, 1916-1969*, by C. A. Cotton, A. H. Reed, Wellington, New Zealand, pp. 84-98.)
- Cotton, C. A., Geomorphic contrasts in central New Zealand, *Tijdschrift van et Koninklijk Nederlandsch Aardrijkskundig Genootschap*, **74**, 248-253, 1957.
- Cotton, C. A., 1969, Skeleton islands of New Zealand and elsewhere, *Earth Science Jour.* (New Zealand), **3**, 61-76, 1969.
- Darwin, C., *The Structure and Distribution of Coral Reefs*, 1st Ed., London, 1842.
- Davies, J. L., *Geographical Variation in Coastal Development* 2nd Ed., 212 pp., Longman, New York, 1980.
- Davis, W. M., The coral reef problem, *Amer. Geographical Soc. Special Publ.*, **9**, 596 pp., 1928.
- Delaney, P. J. V., Quaternary geologic history of the coastal plain of Rio Grande do Sul, Brazil, Louisiana State University Coastal Studies Institute, Technical Report 18A, pp. 1-63, 1962.
- Delaney, P. J. V., Geology and geomorphology of the coastal plain of Rio Grande do Sul, Brazil and Northern Uruguay, Louisiana State University Coastal Studies Institute, Technical Report 18B, pp. 1-58, 1966.
- Erickson, G. E., Geology and origin of the Chilean nitrate deposits, *U.S. Geol. Surv. Prof. Paper*, **1188**, 37 pp., 1981.
- Evans, G., C. G. St. C. Kendall, and P. Skipwith, Origin of the coastal flats, the sabkha, of the Trucial Coast, Persian Gulf, *Nature*, **202**, 759-761, 1964.
- Fairbridge, R. W., Kara-Bogaz Gulf, in *Encyclopedia of Geomorphology*, edited by R. W. Fairbridge, pp. 579-581, Reinhold Book Co., New York, 1968.
- Field, M. E., and D. B. Duane, Geomorphology and sediments of the inner continental shelf, Cape Canaveral, Florida, U.S. Army, Corps of Engineers, Coastal Engineering Research Center, Technical Memorandum 42, 87 pp., 1974.
- Galli, O., Pediplain in northern Chile and the Andean uplift, *Science*, **158**, 653-654, 1967.
- Garbell, M. A., 1963, The sea that spills into a desert, *Sci. Amer.*, **209**, 94-100, 1963.
- Glennie, K. W., and G. Evans, A reconnaissance of the Recent sediments of the Ranns of Kutch, India, in *Sedimentology*, **23**, 625-647, 1976.
- Guilcher, A., Les Côtes à rias de Corée et leur évolution morphologique, *Annales de Géographie*, No. 472 (85th year), 641-671, 1976.
- Hamilton, W., Tectonics of the Indonesian region, *U.S. Geol. Surv. Prof. Paper*, **1078**, 345 pp., 1979.
- Hicks, S. D., and W. Shofnos, The determination of land emergence from sea level observations in southeast Alaska, *J. Geophys. Res.*, **70**, 3315-3320, 1965.
- Hopley, D., *Geomorphology of the Great Barrier Reef: Quaternary Development of Coral Reefs*, 453 pp., John Wiley, New York, 1982.
- Illing, L. V., Bahama calcareous sands, *Amer. Assn. of Petrol. Geol. Bull.*, **38**, 1-95, 1954.
- Inman, D. L., and B. M. Brush, The coastal challenge, *Science*, **181**, 20-32, 1973.
- Inman, D. L., and Nordstrom, C.E., On the tectonic and morphologic classification of coasts, *J. Geol.*, **79**, 1-21, 1971.
- Jutson, J. T., Physiography (geomorphology) of western Australia, *West Australia Geol. Surv. Bull.*, **95**, 1950.
- Lathram, E. H., Apparent right-lateral separation on Chatham Strait fault, southeastern Alaska, *Geol. Soc. Amer. Bull.*, **75**, 249-252, 1964.

- Lee, H. A., Late glacial and post-glacial Hudson Bay sea episode, *Science*, **131**, 1609-1611, 1960.
- MacNeil, F. S., Pleistocene shorelines in Florida and Georgia, *U.S. Geol. Surv. Prof. Paper*, **221-F**, 95-107, 1950.
- Martini, I. P., D. W. Cowell, and G. M. Wickware, Geomorphology of Southwest James Bay: A low energy emergent coast, in *Coastlines of Canada*, edited by S. B. McCann, pp. 293-301, Geol. Surv. Canada Paper 80-10, 1980.
- McKee, E. D., Storm sediments on a Pacific atoll, *J. Sedim. Petrol.*, **29**, 354-364, 1959.
- Mortimer, C., and N. Saric, Landform evolution in the coastal region of Tarpaca Province, Chile, *Revue de Géomorphologie Dynamique*, **21**, 162-170, 1972.
- Mortimer, C., and N. Saric, Cenozoic studies in northernmost Chile, *Geologische Rundschau*, **64**, 395-420, 1975.
- Newell, N. D., Bahamian platforms, *Geol. Soc. Amer. Special Paper*, **62**, 303-316, 1955.
- Orme A. R., Coastal Morphology of Africa, in *Encyclopedia of Beaches and Coastal Environments*, edited by M. L. Schwartz, pp. 17-32, Hutchinson Ross Publ. Co., Stroudsburg, Pennsylvania, 1982.
- Osmond, J. K., J. P. May, and W. F. Tanner, Age of the Cape Kennedy barrier-and-lagoon complex, *J. Geophys. Res.*, **75**, 469-479, 1970.
- Pala, S., and W. Weischet, Toward a physiographic analysis of the Hudson Bay-James Bay lowland, *Le Naturaliste Canadien*, **109**, 637-651, 1982.
- Paskoff, R. P., Late Cenozoic crustal movements and sea level variations in the coastal area of Northern Chile, in *Earth Rheology, Isostasy, and Eustasy*, edited by N. A. Morner, pp. 487-495, John Wiley, Chester, Sussex, 1980.
- Pierce, J. W., and D. J. Colquhoun, Holocene evolution of a portion of the North Carolina coast, *Geol. Soc. Amer. Bull.*, **81**, 3697-3714, 1970.
- Platt, L. B., The Rann of Kutch, *J. Sedim. Petrol.*, **32**, 92-98, 1962.
- Platt, J. P., J. K. Leggett, J. Young, H. Raza, and S. Alam, Large-scale sediment underplating in the Makran accretionary prism, *Geology*, **13**, 507-511, 1985.
- Playford, P. E., A. L. Cochbain, and G. H. Low, Geology of the Perth Basin, *West. Australian Geol. Surv. Bull.*, **124**, 1976.
- Pritchard, D. W., What is an estuary: Physical viewpoint, *Estuaries*, edited by G. H. Lauff, pp. 3-5, Amer. Assoc. Adv. Sci. Pub. 83, Washington, D.C., 1967.
- Purdy, E. G., Reef configurations: Cause and effect, in *Reefs in Space and Time*, edited by L. F. Laporte, pp. 9-76, Soc. Economic Paleontologists and Mineralogists Special Pub. 18, 1974.
- Redfield, A.C., The tidal system of Lake Maracaibo, *Limnol. Oceanogr.*, **6**, 1-12, 1961.
- Royal Society of London, 1978, The northern Great Barrier Reef, A Royal Society Discussion organized by D. R. Stoddart and Sir Maurice Yonge, F. R. S., held on January 28-29, 1976, The Royal Society, London: part A, 194 pp.; part B, 162 pp. (First published in *Phil. Trans. Roy. Soc. London: Series A*, **291**, 1-194; Series B, **284**, 1-162.)
- Scholl, D. W., and M. Stuiver, Recent submergence of southern Florida: A comparison with adjacent coasts and other eustatic data, *Geol. Soc. Amer. Bull.*, **78**, 437-454, 1967.
- Schubel, J. R., The estuarine environment, estuaries and estuarine sedimentation, Amer. Geol. Inst. Short Course Lecture Notes, Washington, D.C., 324 pp., 1971.
- Shepard, F. P., Lagoon topography of Caroline and Marshall Islands, *Geol. Soc. Amer. Bull.*, **81**, 1905-1914, 1970.
- Shepard, F. P., *Submarine Geology*, 3rd edition, 517 pp., Harper and Row, New York, 1973. (see Chapter 6 for coastal classification).
- Shepard, F. P., and H. R. Wanless, *Our Changing Coastlines*, 579 pp., McGraw Hill, New York, 1971.
- Snead, R. A., Recent morphological changes along the coast of West Pakistan, *Ann. Abs. Assn. Amer. Geographers*, **57**, 550-565, 1967.
- Snead, R. A., Physical geography reconnaissance: West Pakistan coastal zone, *University of New Mexico Publications in Geography*, No. 1, 55 pp., 1969.
- Stephens, N., The coastline of Ireland, in *Irish Geographical Studies Published in Honour of E. Estyn Evans*, pp. 125-145, The Queen's University of Belfast, Department of Geography, Belfast, North Ireland, 1970.
- Stevens, G. R., *Rugged Landscape: The Geology of Central New Zealand*, A. H. and A. W. Reed, 286 pp., Wellington, New Zealand, 1974.
- Stoddart, D. R., The Great Barrier Reef and the Great Barrier Reef Expedition 1973, *Phil. Trans. Roy. Soc. London, Series A*, **291**, 5-22, 1978.
- Suess, E., *Das Antlitz der Erde* (translated by H. B. C. Sollas, 604 pp., *The Face of the Earth*, Vol. 1, Clarendon Press, Oxford, 1904), 1888.
- Sutton, F. A., Geology of the Maracaibo Basin, *Bull. Amer. Assn. Petrol. Geologists*, **30**, 1621-1741, 1946.
- Swift, D. J. P., Inner shelf sedimentation: Processes and products, in *New Concepts of Continental Margin Sedimentation*, edited by D. J. Stanley, pp. 4-1-4-6, American Geological Institute, Washington, D.C., 1969.
- Tarr, R. S., and L. Martin, *Alaskan Glacier Studies*, 498 pp., National Geographic Society, Washington, D.C., 1914.
- Thom, B. G., G. M. Bowman, and P. S. Roy, Late Quaternary evolution of coastal sand barriers, Port Stephens-Myall Lakes area, central New South Wales, Australia, *Quaternary Research*, **15**, 345-364, 1981.

- Tosdal, R. M., A. H. Clark, and E. Farrar, Cenozoic polyphase landscape and tectonic evolution of the Cordillera Occidental, southernmost Peru, *Geol. Soc. Amer. Bull.*, **95**, 1318-1332, 1984.
- Umbgrove, J. H. F., Coral Reefs of the East Indies, *Geol. Soc. Amer. Bull.*, **58**, 729-778, 1947.
- Veron, J. E. N., and R. C. L. Hudson, Ribbon reefs of the northern region, *Phil. Trans. Roy. Soc. London, Series B*, **284**, 3-21, 1978.
- Wellman, H. W., Tilted marine beach ridges at Cape Turakirae, New Zealand, *J. Geoscience*, **10**, 123-129, 1967.
- White, R. S., and K. E. Louden, The Makran continental margin: Structure of a thickly sedimented convergent plate boundary, *Amer. Assn. Petrol. Geol. Mem.*, **34**, 499-518, 1983.
- Wiens, H. J., *Atoll Environment and Ecology*, 532 pp., Yale University Press, New Haven, 1962.
- Wilde, S. A., and G. H. Low, Explanatory note on the Perth 1:250000 geological sheet, Western Australia, *West. Australia Geol. Surv.*, 1975/76.
- Wilde, S. A., and G. H. Low, Explanatory note on the Pilbara 1:250000 geological sheet, Western Australia, *West. Australia Geol. Surv.*, 1980.
- Winkler, C. D., and J. D. Howard, Correlation of tectonically deformed shorelines on the southern Atlantic coastal plain, *Geology*, **5**, 123-127, 1977.
- Yonge, C. M., *A Year on the Great Barrier Reef*, 245 pp., Putnam, London, 1930.
- Zenkovich, V. P., *Processes of Coastal Development*, translated by D. E. Fry, 738 pp., Wiley, Interscience, New York, 1967.

KARST LANDFORMS AND LAKES

*Robert W. Blair, Jr.**

INTRODUCTION

This chapter is concerned with the recognition and origin of karst topography and certain types of lake basins and is not intended to be a comprehensive text-style dissertation on either karst or lakes. For more specific information, see Jennings (1971), Sweeting (1972), or Hutchinson (1957). The category of lakes, although a separate topic from karst, has been included because we believe that it does not warrant a special chapter and because the number of good images displaying karst is limited. The approach is by necessity a regional one, with little discussion related to landforms that are not observable from space.

KARST

Introduction

The term "karst" stems from the region Krs in Slovenia, now in northwestern Yugoslavia, which is typified by stony barren rock (Figure 7-1). The Indo-European word "kar" for rock and the Italian word "carso" evolved to the Germanized term "karst," which is now the accepted term for solution-derived landscapes like those just north and east of the Adriatic Sea.

Karstification is the geologic process of differential chemical and mechanical erosion by water on soluble bodies of rock, such as limestone, dolomite, gypsum, or salt, at or near the Earth's surface. Karstification is exhibited best on thick, fractured, and pure limestones in a humid environment in which the subsurface and surface are being modified simultaneously. The resulting karst morphology is usually characterized by dolines (sinkholes), hums (towers), caves, and a complex subsurface drainage system.

Factors in Karst Development

The development of karst terrain depends on the interplay of at least seven important factors in varying degrees. These are: lithology, structure, relief, hydrology, climate, vegetation, and time.

Lithology. Several lithologies are susceptible to karstification, but limestones and dolomites, owing to their solubility and nature of resistance and widespread distribution, are overwhelmingly dominant. According to Pettijohn (1975), 75 percent of the Earth's surface is covered with sedimentary rocks, and of that,

10 to 20 percent consists of limestones or dolomite. Karst morphology can occur on carbonates with less purity than 80 percent, but generally the purer the limestone, the better the development of karst morphology (Jennings, 1971). For example, the Cretaceous and Early Tertiary Dinaric karst limestones of Yugoslavia are 95 to 100 percent pure (Herak, 1972), and white limestone in Jamaica seldom exhibits less than 98 percent purity. Numerous compositional variations can exist in carbonates, and many of these are discussed in Sweeting (1972) and Jennings (1971).

In addition to the composition of limestone, the thickness of individual beds, the nature of interbeds, especially shaly beds, and lateral facies variations affect the style and degree of karstification. In the Dinaric Mountains, the depth of surface karstification is sometimes limited by impermeable beds which have aided the development of broad flat-floored valleys called poljes (Herak, 1972).

Structure. Structure is used here in the structural geologic sense and is concerned with the attitude and deformational effects of bedrock. Limestones and dolomites at or near the surface tend to deform by brittle fracture. This tendency to form complex joint sets is directly responsible for the secondary permeability required for the development of subsurface solution drainage and subsequent three-dimensional cave development. Vertical fractures usually manifest themselves at the surface and focus the solution processes along them. The influence of fracturing is paramount in southeast China, where thousands of square kilometers are affected by several consistent sets of joints (see Plate KL-1, karst of south China). Folding, in addition, may have the effect of isolating watersheds and directing ground-water flow. This has occurred in the Dinaric karst of Yugoslavia.

Large-scale structures or tectonics not only have led to the development of specific landforms like poljes but have also influenced the rates and degree of karstification. Most poljes, for example, are associated with boundary faults (Roglic, 1972). Uplift and deformation of a carbonate plateau accelerates the dissolution of the limestone because: (1) fracture density increases, (2) any elevation rise is usually accompanied by an increase in precipitation, and (3) increased relief increases piezometric surface gradients. These conditions can: (1) lead to solution-enlarged conduits along fracture planes, (2) impart to the limestone a high hydraulic conductivity, and (3) cause rapid fluctuations in the water table with accompanying accelerated solution (Fetter, 1980).

Relief. Topographic relief is the elevation difference between the highest and lowest points on the surface for a given area. The Julian Alps in the inner region of Yugoslavia have a topographic relief near 2000 m. This mountainous area is associated with an abundance of potholes and few caves. Both characteristics are thought to be a consequence of this high relief

*Department of Geology, Fort Lewis College, Durango, Colorado, 81301.

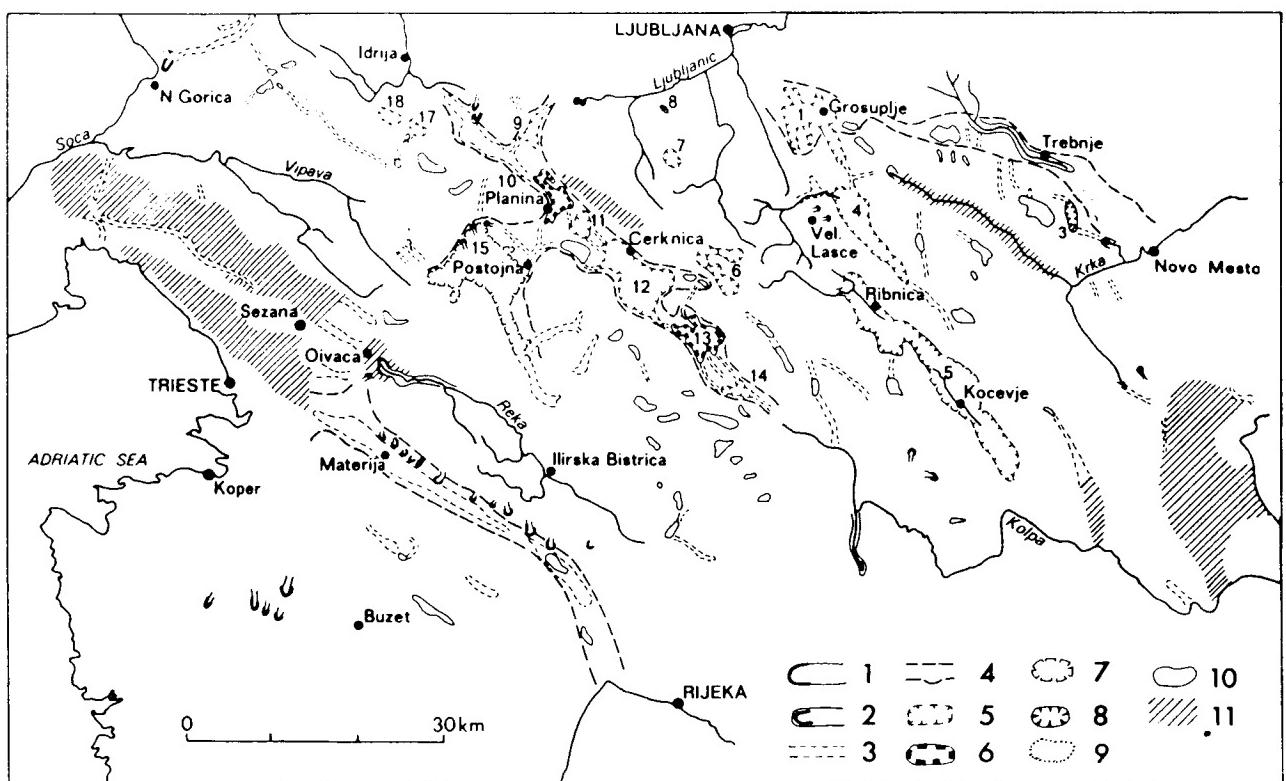
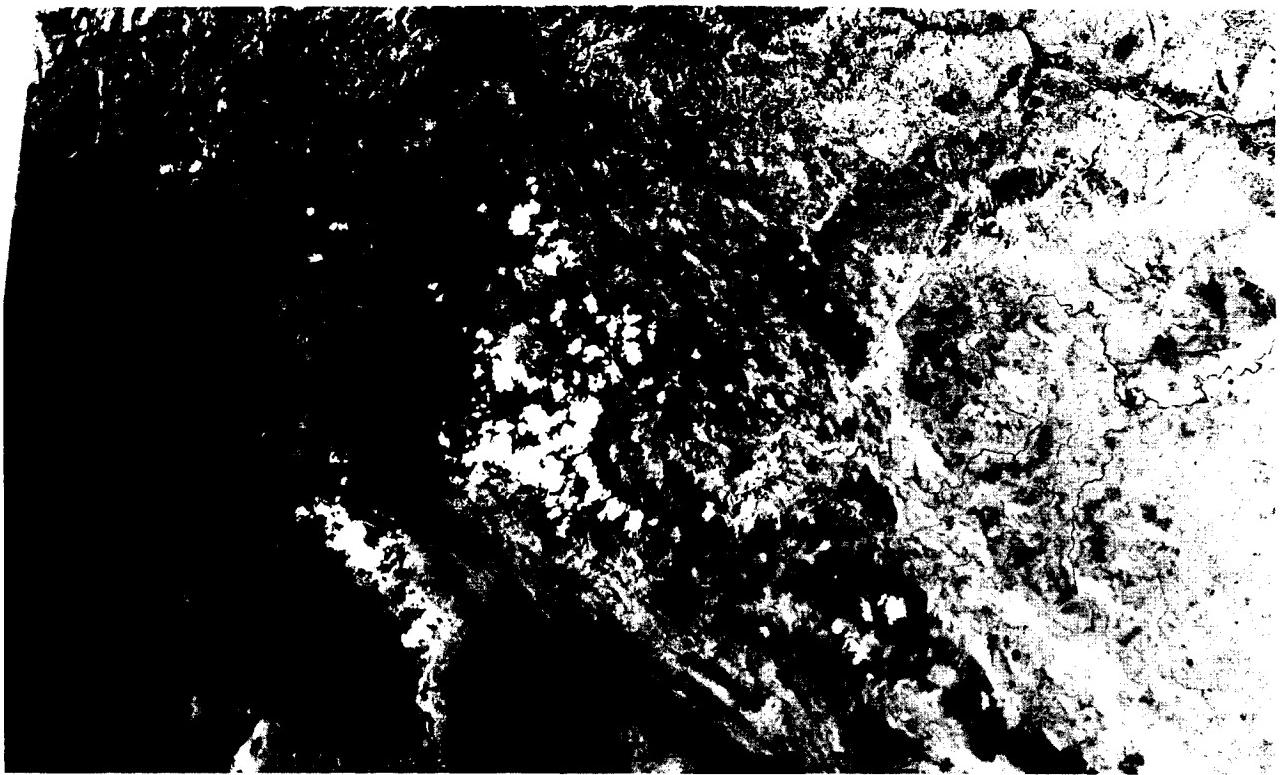
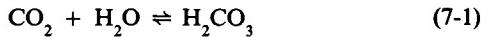


Figure 7-1. Part of Landsat image 30091-09094-7, June 8, 1978, showing the type locality region of karst topography in the Slovenian Dinaric Mountains of Yugoslavia. The map below, taken from an article by Demek et al. in *Geomorphology of Europe* (C. Embleton, Ed.) (1984) shows karstic features in approximately the same region. Numbers on the map refer to poljes: (1) Grosupeljsko, (3) Globodol, (4) Dobro, (5) Ribniško-kočevsko, (6) Bloke, (7) Rakitna, (8) Ponikve, (9) Logaško, (10) Planinsko, (11) Rakovsko, (12) Cerkniško, (13) Loško, (14) Babno, (15) Postojnsko, (17) Črnovrško, (18) Zadlog. Key to symbols: (1) blind valley, (2) pocket valley, (3) dry valley, (4) dry valley system, (5) border polje, (6) overflow polje, (7) peripheral polje, (8) dammed polje, (9) karst doline, (10) uvala, (11) karst plain (Demek et al., 1984).

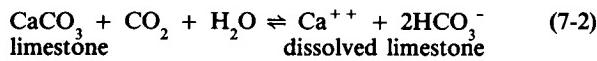
(Herak, 1972). Related to relief is the depth of the vadose zone, which is the vertical distance between the surface and the water table. In Florida, the vadose depth is small, as is the topographic relief. However, throughout low sea level stands during the Pleistocene, the increased depth of the vadose zone probably led to the development of a more extensive and efficient subsurface drainage system with an increase in dissolution along fractures and fissures. With the absence of the buoyancy effect of a high water table surface, the formation of collapse dolines may have been accelerated (see Plate KL-4, Florida karst). Even today the effects of water table drawdown due to excessive pumping have rendered some urban areas susceptible to the sudden and unexpected collapse of buried solution cavities. Such a collapse occurred in Winter Park, Florida, in May 1981.

Hydrogeology. Hydrogeology is concerned with the inter-relationships of geologic materials and processes with water (Fetter, 1980). The karstification process involves not only the solution of limestone but also the sometimes overlooked mechanical erosion of limestone. Because the solution chemistry of carbonates is well known (Jennings, 1971; Sweeting, 1972; Bogli, 1980), only a brief summary will be presented here.

The dissolution of limestone involves three principal components: carbon dioxide, water, and calcium carbonate. Initially, atmospheric carbon dioxide diffuses into the moisture within the air or soil and simultaneously becomes hydrated to form carbonic acid:



In the presence of limestone, carbonic acid dissolves the calcite. The reaction is often presented as:



The only water that is capable of dissolving limestone is aggressive water, which is water undersaturated with respect to dissolved carbonate. The time required for aggressive water in karst regions to be neutralized or to reach saturation equilibrium varies considerably, depending on a number of factors such as temperature, turbulence, variations in the partial pressure of carbon dioxide, dilution, presence of other acids, and surface area of limestone. To achieve equilibrium may require several days; however, laboratory studies suggest that most of the limestone dissolution resulting from an influx of fresh aggressive water may occur within minutes to a few hours (Sweeting, 1972; Jakucs, 1977; Ritter, 1978). Additional acids, such as organic acids from soils and most recently sulfuric and nitric acids from acid rain, will contribute to the dissolution of carbonate rocks.

Once saturation equilibrium is achieved, any change to warmer water temperatures or decreases in the partial pressure of carbon dioxide can drive equation 7-2 to the left, resulting in the deposition of calcium carbonate (see Figure 7-2).

Erosion rates have been calculated for many karst regions around the world and vary widely even within the same climatic zone (Smith and Atkinson, 1976).

Table 7-1 lists some of the calculated erosion rates for karst regions discussed in this chapter. Although these erosion rates are useful for comparative purposes, they are not indicative of the duration intensity of the erosion process. The dissolution of the limestone does not take place at a constant rate, but fluctuates with storm events that flood the karst surface and subsurface with undersaturated water. In other words, the actual dissolution occurs episodically with maximum peaks corresponding to surges in the karst water flow. In Jamaica, intense storm events result in subsurface flooding, and because the existing conduit system is not of sufficient size to handle excessive infiltration

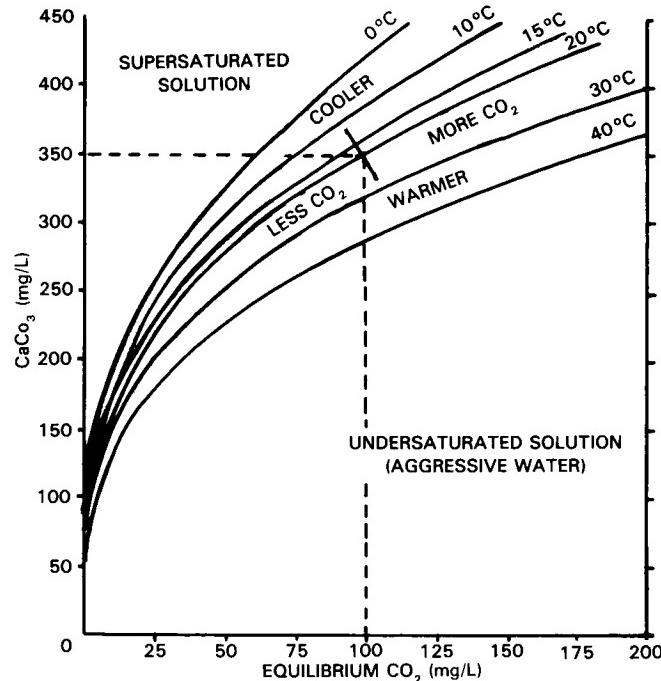


Figure 7-2. Saturation equilibrium curves for solution of calcium carbonate at selected temperatures as a function of carbon dioxide equilibrium in solution (modified after Jennings, 1971, p. 26).

Table 7-1
Erosion Rates for Image Areas Discussed

Location	Erosion Rate (m ³ /km ³ /yr)	Climate
Florida USA *	35, 5, 8	Tropical
Jamaica *	69, 39, 86, 96	Do
Yucatan, Mexico *	30, 16	Do
Guangxi, S. China†	120–300 (surface)	Do
Dinaric karst, Yugoslavia*	43, 63, 55, 67	Temperate
S. Nullarbor Plain, Australia‡	5 (surface)	Semiarid

*Smith and Atkinson, 1976.

† Daoxian, 1981.

[#]Lowry and Jennings, 1974.

rates, backfilling of caves and solution channels occurs with fresh undersaturated water (Versey, 1972). These flood events can be of the single-storm variety or may be seasonal, as with the winter flooding of poljes in Yugoslavia.

Because of the unusually high permeabilities and the periodic flooding associated with most karst regions, the water table correspondingly exhibits drastic fluctuations. This has been observed by many spelunkers. The water table in karst rock is frequently difficult to define, especially in free-flow carbonate aquifers that display a complex multitude of enlarged open conduits. The water table can occur at considerable depths below the land surface, especially in mountainous regions like the Dinaric Mountains, Yugoslavia. Water can also be perched under solution depressions above the water table or it may be discontinuous if the permeability is principally fracture-controlled (Fetter, 1980). Zones with few or no fractures yield little or no water.

in contrast to dense fracture zones that can potentially supply abundant water.

Climate. The best-developed karst regions of the world are found in tropical (e.g., Jamaica) and temperate (e.g., Yugoslavia) environments. Considerable discussion has evolved as to whether tropical or temperate environments are more conducive to karstification (Smith and Atkinson, 1976). Lehmann (1970), a strong advocate of climatic geomorphology, asserts that solutional erosion rates are more intense in the tropics because of greater rainfall and carbon dioxide production in soils at higher temperatures. In contrast, Corbel (1959) contends that the intensity is greater in cold humid climates where larger quantities of carbon dioxide can be absorbed by water. The higher the carbon dioxide absorption in water, the stronger is the resultant carbonic acid. However, because Corbel overlooked the rates of reaction, which slow down at lower temperatures, the levels of CO₂ content may be irrelevant (Embleton, 1985, personal communication).

The absorption of carbon dioxide is temperature-dependent so that cooler water for a given volume can absorb larger quantities of carbon dioxide. If the water temperature rises from 0 to 35 °C, the carbon dioxide saturation level will decrease between one-third to two-thirds (Jennings, 1971). Therefore, waters in cold climates can hold greater quantities of carbon dioxide in the ionic state, thus being more effective in dissolving limestone. However, more important than temperature is the partial pressure of carbon dioxide, which at sea level is relatively constant at 0.035 percent. The partial pressure of carbon dioxide in soil air can exceed that of the atmosphere from ten to several hundred times (Bogli, 1980). As a consequence, the presence and nature of soil cover can be far more important in karstification intensity than atmospheric air.

A study by Smith and Atkinson (1976) of comparative karst data from around the world indicates that mean annual runoff, rather than precipitation, is the principal parameter directly related to erosion rate. Temperature is believed to be important only with regard to its influence on supporting a continuous cover of soil and vegetation.

Vegetation. Arid karst regions, such as the Nullarbor Plain in Australia, are associated with sparse vegetation, thin soils, and therefore, a slowed rate of surface karstification. In contrast, if the existing soil and climate can support a dense vegetation cover, an intensified surface and subsurface karstification occurs, as observed in Jamaica and south China. Biogenic carbon dioxide, introduced to the soil by plant root systems and bacterial decay, is regarded as the most important control of solution erosion of limestones (Jennings, 1971).

Generally, where vegetation is most lush, the highest concentration of moisture, the highest biogenic activity, and the highest production rates of carbon dioxide occur. Under these conditions and free water circulation, the highest solution erosion rates can be achieved. Such conditions are found in both Jamaica and south China (Table 7-1). In Jamaica, the forest canopy has been cited as one of the prime factors responsible for the overdeepening of cockpits (Versey, 1972).

Time. The early karst studies of Cvijic and Grund at the turn of the 20th century were strongly influenced by the cyclic evolutionary teachings of Davis and Penck (Roglic, 1972). Thus, karst topography has been thought to evolve through stages of development beginning with fluvial action and the initial formation of dolines. As the surface drainage is slowly captured by swallow holes and the developing subsurface drainage, dolines coalesce to form uvalas, which, in turn, expand to poljes. This sequence is now considered to be antiquated, and according to Roglic, poljes are structurally controlled and are not related to uvalas.

It is questionable whether any two karst regions anywhere in the world have evolved sequentially in the same manner or even display identical morphological forms. Each karst region evolves

within its unique combination of dynamic and static factors. However, this does not preclude the comparison of areas of similar morphology in an attempt to evaluate common factors.

From the examples of Landsat imagery in this chapter, it becomes apparent that each region has developed its own morphologic signature. To understand the evolution of a given karst terrain, it is necessary to comprehend the roles of length of time, style, and intensity of the energy flow through the hydrologic system. Those karst regions with the largest potential energy, related to the thickness of the vadose zone, and kinetic energy, or flooding, will also exhibit a higher energy morphology more rapidly and more fully than regions of lower total energy. High-energy morphology can be manifested in the form of larger caves, increased relief, density, and magnitude of dolines, hums, flood deposits, and a more extensive underground solution network.

KARST FROM SPACE

Within the realm of geomorphology, each geologic process leaves its own imprint on the Earth's landscape, and each process will develop its own characteristic assemblage of landforms (Thornbury, 1969). For karst landscapes, this imprint is expressed as solution morphology on the regional scale. Because of the relatively large ground resolution distance of 79 m, many karst landforms cannot be discerned from Landsat MSS images; only the larger solution and fracture-controlled dolines and uvalas can be recognized. Thus, the advantage of the space perspective is not the identification or the recognition of individual landforms, but the collective pattern and texture they impart to a region of hundreds or thousands of square kilometers. This can occur only where given geologic processes and materials, such as carbonates, dominate a large region for a sufficient length of time.

The Landsat imagery discussed in this chapter has been chosen from the known karst regions of the world. Some well-researched regions are not included either because good imagery has not been available (e.g., New Guinea) or because man's overprint (e.g., Indiana, U.S.A.) is so dominant as to obscure natural topographic patterns.

A cursory examination of all the karst images reveals a number of features specifically associated with the solution process:

1. Lack of drainage patterns (all karst regions)
2. Dimpled pock-marked texture (Jamaica, Nullarbor Plain)
3. Fracture sets with developed relief (China)
4. Uniformly scattered residual karst hills (Yucatan, China)
5. Circular basins or lakes (Florida)
6. Large flat karst plains and poljes (Yugoslavia, China)

Most important is the absence of a well-developed integrated surface drainage. Indeed, for the Nullarbor Plain, Australia, and Yucatan, Mexico, it is difficult to identify any recognizable drainage. Major rivers can be seen to incise the south China carbonate plateaus, but there is a distinct lack of well-developed tributaries draining into the river channels.

Most karst areas exhibit a relatively homogeneous pock-marked or dimpled texture. In south China, this pattern is overprinted with solution-incised joint sets. In Florida, the pattern is expressed as numerous large water-filled collapsed basins.

Joint sets are not recognized in all karst areas at Landsat scale. This does not preclude the presence of joints, but merely points out that they may be obscured because: (1) joints are too closely spaced, (2) solution relief of joints is slight, (3) dense vegetation cover is present, or (4) joints may indeed be absent or sparse.

What accounts for the large differences observed in karst regions is not variation in the karst process, but variation in lithology, structure, and the overprint of other processes like fluvial, tectonic, eolian, and glacial, and variations in the energy flow through the karst system through time.

LAKE BASINS

Introduction

According to the American Heritage Dictionary (Dell Publishing Co., Inc., 1983), a lake is defined as "a large inland body of water." The interpretation of the word "large" is conjectural. For our purposes, a lake must be large enough to be recognizable on Landsat imagery, which is limited by the ground resolution distance of 79 m and 30 m for the MSS and TM sensors, respectively. It is because of the presence of water that we easily recognize and focus our attention on these geomorphic forms. To develop a lake requires two things: (1) geomorphic process(es) to form a depression, and (2) the proper hydrologic and climatic conditions to maintain a confined body of water on the Earth's surface.

Classification

Virtually every geomorphic process is capable of producing a depression either singly or in combination. A classification of lakes is, in essence, a classification of various geomorphic processes. Davis (1882) proposes a classification of lakes based on constructive, destructive, and obstructive processes, and Hutchinson (1957) presents a detailed classification system based on various geologic processes.

The following is a modified Hutchinson classification:

1. Tectonic processes
 - a. Epeirogeny (Caspian Sea, U.S.S.R.)
 - b. Tilting (Lake Kioga, East Africa)
 - c. Rifting (Lake Baikal, U.S.S.R.)
2. Volcanic processes
 - a. Caldera collapse (Lake Rotorua, New Zealand)
 - b. Explosion crater (Ruapehu Crater Lake, New Zealand)
 - c. Lava flow collapse (Yellowstone Lake, Montana, U.S.A.)
3. Colluvial processes
 - a. Catastrophic landslides (Earthquake Lake, Montana, U.S.A.)
 - b. Noncatastrophic slope failure (Goatswater, English Lake District, Britain)
4. Glacial processes
 - a. Ice-dammed lakes (ancient Lake Missoula, U.S.A.)
 - b. Glacial scour lakes (Lake Michigan, Michigan, U.S.A.)
 - c. Moraine-dammed lakes (Jenny Lake, Wyoming, U.S.A.)
 - d. Kettle lakes (Nushagak Lowlands, southeast Alaska, U.S.A.)
5. Solution processes
 - a. Dolines (lakes of north central Florida, U.S.A.)
 - b. Polje (Lake Scutari, Yugoslavia)

6. Fluvial processes

- a. Plunge pools (Castle Lake, Washington, U.S.A.)
- b. Oxbow lakes (Mississippi River floodplain, U.S.A.)

7. Coastal processes—Lagoons (Lake Ellesmere, New Zealand)

8. Eolian processes

- a. Dammed lakes (Moses Lake, Washington, U.S.A.)
- b. Interdune lakes (lakes in Nebraska Sandhills, U.S.A.)
- c. Deflation basins (Avenue Pan, Witwatersrand, South Africa)

9. Impact processes—Explosion crater (Chubb Lake, Canada)

10. Life processes

- a. Beaver dams (generally too small for Landsat)
- b. Manmade dams (Lake Nasser, Egypt)

Origin

One objective of this section is to study various lake basins observable from space, and from their geometry, geologic, and geomorphic associations, point out characteristics that could reveal information about their origin. The study of the origin of lakes can be segmented into two lines of inquiry: (1) causes of topographic depression, and (2) explanation for the presence of water. The first line of inquiry listed is more amenable to study through space imagery than the latter. Note that many depressions exist that do not contain water, and as a consequence, their presence may be overlooked.

Physical criteria useful in the analysis of lakes from space are shape, size, density, and nature of the surrounding terrain.

Shape. Lake shape in many instances can narrow the choices of geologic process responsible for an inland depression. Circular topographic basins, for instance, can be produced by collapse (dolines, calderas), by explosions (volcanic craters, meteoric impact), or from wind (deflation hollows). Circular lakes, associated with these processes and visible on Landsat imagery, include the doline lakes in north central Florida, the caldera lakes from Nicaragua, a volcanic crater lake at Crater Butte, California, an impact lake in Chubb Lake, Quebec, and the deflation hollow lakes found on the Llano Estacado, Texas.

The best-developed elliptical basin lakes are the Carolina Bays in North and South Carolina and the oriented lakes of Alaska. Surface wave erosion, aided by wind at right angles to the long axis, is believed to be the major controlling factor in their elongation (Kaczorowski, 1976).

Dammed drainage basins produce dendritic lake patterns. The dams may be natural or, more frequently, manmade. In 1959, Earthquake Lake formed as a result of the Hebgen Lake earthquake, which jolted into motion 20 million m³ of rock and debris that subsequently dammed the Madison River in southwestern Montana (Costa and Baker, 1981). Lake Kioga in East Africa formed after epeirogenic tilting reversed the drainage in a large watershed and caused the eventual flooding of the tributary valleys. Manmade reservoirs are especially abundant in the southeastern United States, but they may be found in virtually every country of the world.

Linear lakes, including many on the Canadian Shield (Figures 7-3A and B), are commonly imposed on fracture- or fault-controlled zones of weakness that localize streamflow or are gouged out by glacial scour. Triangular lake basins are found in the stabilized dune fields of Senegal. Rectangular lake basins have been noted in northwestern Yukon Territory, Canada; their

origin is unknown, but structure and permafrost probably play a role in their development. Lunate or oxbow lake basins are common along meandering river channels such as the Mississippi River. These lakes are formed from abandoned meanders, usually during flood cycles. Irregular or amoebic-shaped lake basins are frequently associated with glacial till and are caused by the differential melting of buried ice or by water filling the low points on a hummocky moraine. These lakes are common in north-central North America and in Scandinavia. Some lake basins are so irregular and abundant that they resemble ink-splatter patterns and can be found in Canada, in Scandinavia, and in Siberia where large areas of bedrock have been laid bare by continental ice sheets. Frozen tundra, bedrock structure, and differential erosion have contributed to their highly irregular pattern.

Size. Of the world's ten largest lake basins based on water surface area, six have a tectonic origin and four are glacially de-

rived (Smith, 1968). At various times during the Pleistocene, glacial lakes have grown in size and probably out-numbered large tectonic lakes. Lake Bonneville in the Basin and Range of Utah and Minchin Lake in Bolivia are examples. These pluvial lakes were large because the cooler climate during glacial periods favored the storage of surface water. The largest lake basins have developed in response to a regional stimulus in contrast to small isolated lakes that may result from local influences.

Density. The density of lake basins per unit area can again indicate the regionality of a geomorphic process. The tens of thousands of lakes in central Canada and north-central United States reveal the ubiquity of the glacial process. The Carolina Bays of the southeastern United States and the oriented lakes of Alaska exhibit the regional influence of wind and, in the case of Alaska, further influence by permafrost. With isolated small

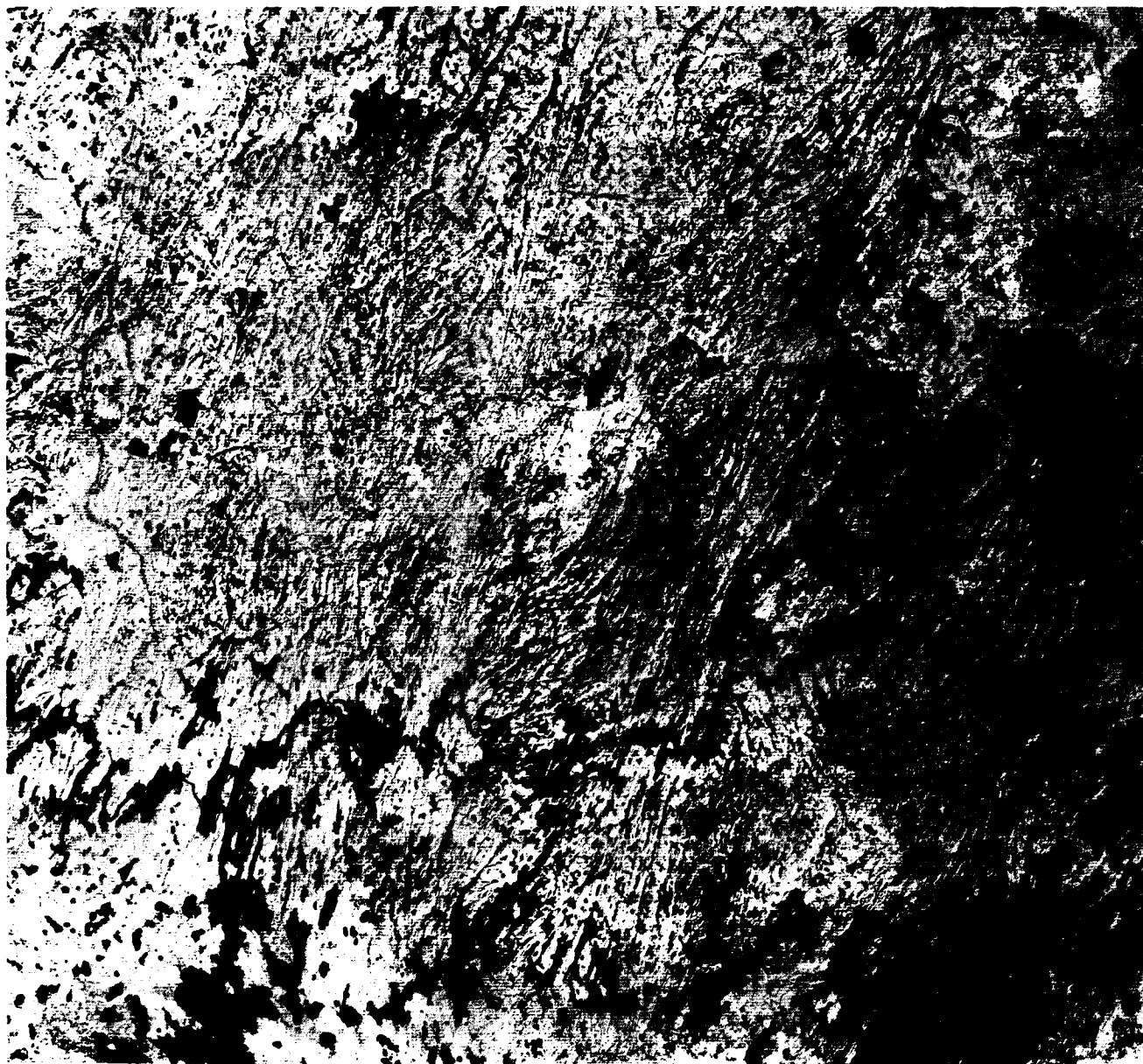


Figure 7-3A. This Landsat scene (1057-16305-7, September 18, 1972) shows numerous linear lakes produced by glacial scouring along fracture zones in Canadian Shield crystalline rocks in the Lac La Ronge area, central Saskatchewan.

**ORIGINAL PAGE IS
OF POOR QUALITY**

lakes, such as Earthquake Lake, Montana, local geomorphic processes must be examined to determine the lake's origin.

Associated Terrain. Clues to a lake's origin, as viewed on Landsat imagery, are frequently revealed by the regional overprint of a particular geomorphic process. The presence of dune fields in Senegal and glacial moraines in Quebec, Canada, and the abundance of volcanoes around Lake Nicaragua, all suggest to the observer a cause-and-effect relationship. Many rift lakes display straight-lined shores with angular bends mirrored on the opposite shore. Inland faults may parallel the lake edge and indicate a tectonic origin. Lake Tanganyika is an example. Lakes associated with the dimpled surface texture indicative of karst topography may well be water-filled dolines. The Dinaric Mountains of Yugoslavia have a few lakes of this variety. However, the most well-developed karst regions of the world as in Yugoslavia, south China, and Jamaica do not display abundant lakes. This is due,

in part, to the efficient infiltration of precipitation and a subterranean piezometric surface.

Time

Within our timeframe, lakes may develop catastrophically from volcanic eruptions, landslides, and earthquake activity, or they may form from slower acting processes like wind, glacial, and epeirogenic activity. However, it is important to emphasize that, geologically, lakes are temporary and form rapidly and decay quickly (Smith, 1968). Because most of the Earth's land surface is dominated by fluvial erosion, lakes that do occur are threatened with either capture and draining by expanding tributaries or infilling of sediment until the lake becomes extinct. The mere presence of a lake, then, demonstrates the dynamic restlessness of the Earth's surface.



Figure 7-3B. Aerial view of glacial scour lakes along fractures in the eastern Canadian Shield (Canadian Department of Energy, Mines, and Resources, A11607-84).

PLATE KL-1

KARST OF SOUTH CHINA

The portion of south China displayed in this Landsat image encompasses part of the most spectacular karst topography found anywhere on Earth. The carbonate rocks show up as the dark-toned areas on the image. Reference to karst in China is found frequently in early Chinese literature and is depicted in their art. This is not surprising because over 1.2 million km² of China is exposed karst. This solution topography is best developed in south China where carbonate rocks spanning from Late Precambrian to Triassic attain thicknesses of 3000 to 10000 m (Daoxian, 1981).

Carbonate rocks of the central Guangxi Province (this Plate) are characterized by a continuous age sequence from Devonian through Triassic with a cumulative thickness of 3000 m. Most of the exposed karst in the image displays the peak-cluster or cockpit-like morphology (Figure KL-1.1) that the Chinese call "Fengcong" (Daoxian, 1981). These grouped peaks and depressions share a common carbonate basement (see region A on index map) in which the solution is strongly controlled by jointing (Figure KL-1.2). Another common karst form is the Fenglin, or peak forest, which consists of multiple carbonate pillars sometimes separated by flat plains that can be of erosional or aggradational origin. These are common around Guilin (Figure KL-1.3), a tourist center approximately 130 km east of the image area. A region of similar terrain is located near the center right edge of the image (B on index map). Daoxian (1981) notes that, although much Fenglin topography is often associated with a later stage of development of the Fengcong topography, no such relationship has been documented. Indeed, Chinese studies (Daoxian, 1981) suggest that Fengcong may be the same age as Fenglin and that Fenglin does not necessarily pass through a Fengcong stage in its development. Still another variant are karst towers expressed as cone-shaped hills (Figure KL-1.4), equivalent to hums in Yugoslavian terminology (Plate KL-4).

The hydrology of the Fengcong differs from the Fenglin in that vertical infiltrating water through a thick vadose zone dominates in the former, whereas horizontal ground-water flow influences the latter (Daoxian, 1981).

A fundamental characteristic of the exposed or bare karst is its lack of a surface drainage network. Within this image of the central Guangxi Province, there are several main rivers, but there is a lack of tributary development. In this region, over 1000 underground streams with a cumulative discharge in excess of

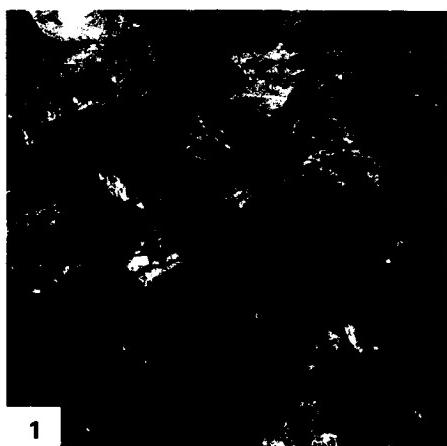
700 m³/s have been explored and thousands of caves have been detected or mapped (Daoxian, 1981, 1983).

The labyrinth of underground drainage channels drains most surface runoff through swallow holes and solution fissures. The surface and subsurface drainage have evolved together and are integrated. For instance, the Sanshi Polje (see index map), which is surrounded by cockpit-like karst, is drained by the Banmen underground stream through a swallow hole to the east. The Banmen subsurface stream flows for 10 km eastward into the Hongshui River. The efficiency of these underground drainage systems presents its own special set of problems related to flooding and droughts. Sixty-six to eighty percent of the south China rainfall is concentrated during the wet summer months of May through August. Its rapid loss to the subsurface drainage system often results in drought conditions, even though the annual precipitation is 1000 to 2000 mm (Daoxian, 1983).

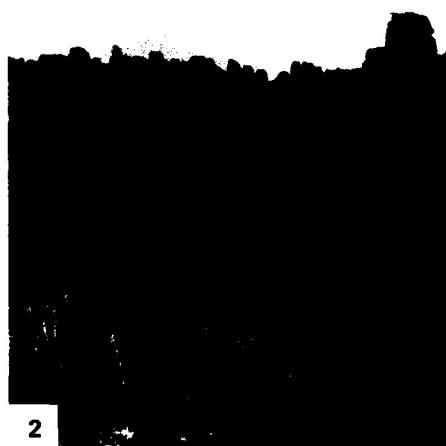
Why is the south China karst so much more spectacular than other karst areas of the world? The answer is not simple, but several distinct features set China karst apart. First is the huge thickness (exceeding 3000 m) of virtually uninterrupted sequences of massive crystalline limestone and dolomites over an area between 1 and 2 million km². Secondly, this area has undergone a slow epeirogenic uplift during the Cenozoic Era, exposing broad plateaus of gently dipping to horizontal carbonate strata (Sweeting, 1978).

Although pre-Cretaceous paleokarst exists in places, the dominant solution topography seen today developed during the Cenozoic. Recently, solution rates in the Guangxi Province have been measured at 0.12 to 0.3 mm/yr (Daoxian, 1981).

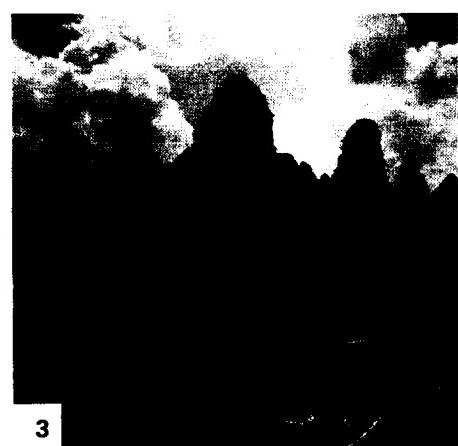
The concordance of summits forming the regional plateau-like surfaces, identified as the dark-toned areas on the image, are believed to represent an uplifted Late Cretaceous peneplain (Sweeting, 1978). The presence of regional jointing is seen as a crisscross pattern on the image and may represent conjugate shear fractures related to folding. Localized deformation has complicated the evolution and has increased the diversity of the karst topography. For example, the Sanshi Polje represents a faulted syncline and the karst topography around Guilin developed upon a downfolded sequence of Devonian limestones. **Landsat 1524-02432-7, December 29, 1973.**



1



2



3

ORIGINAL PAGE IS
OF POOR QUALITY



4

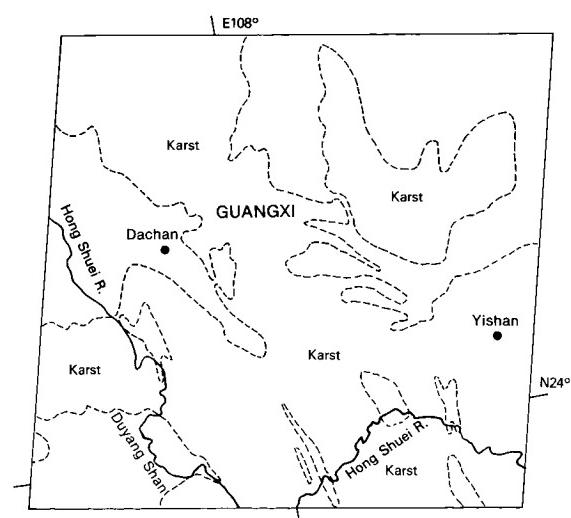


PLATE KL-2

JAMAICA

The Seasat image on the opposite page covers central Jamaica, one of the two most westerly islands of the Antillean Island Arc; the other is Cuba. This Seasat radar image has two advantages over Landsat images: (1) the radar beam at low depression angles tends to accentuate small-scale landforms, and (2) no cloud-free Landsat imagery of this tropical area is available.

Zans (1958) divided Jamaica into two physiographic regions based on structure, the Eastern Mountain Mass and the Main Block, the latter occupying two thirds of Jamaica. The Eastern Mountain Mass consists of Cretaceous and Lower Eocene clastic rocks with mafic and felsic intrusives (Versey, 1972). The Main Block represents a dissected limestone plateau with elevated inliers of sub-limestone and clastic rocks.

The oldest limestone unit, the Yellow Limestone Formation, was deposited over a large part of the Main Block during the Cretaceous and Tertiary strata. The Yellow Limestone consists of two impure limestone beds separated by bedded clastic rocks. From the middle Eocene to Lower Miocene, the clastic influx ceased, and the relatively pure White Limestone Formation was deposited primarily over the Main Block. The White Limestone displays the most widespread and best-developed karst topography on Jamaica (Sweeting, 1958) and can be readily identified on the image from the fine dimpled texture (see cockpit Plateaus region on index map).

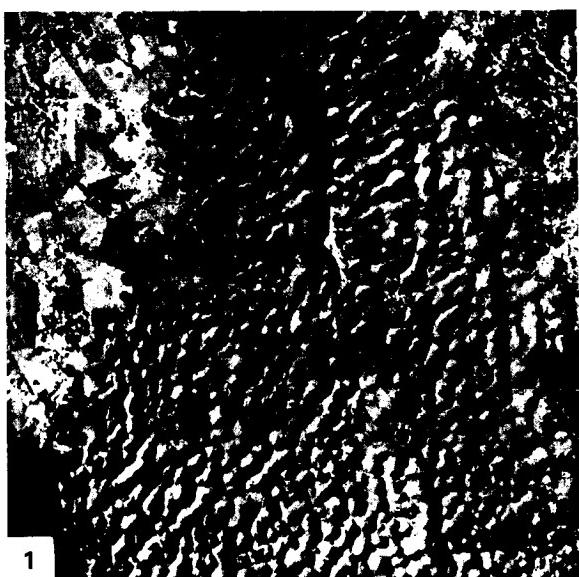
The White Limestone Formation rarely exceeds 460 m thickness; however, 1500 m has been observed (Versey, 1972). Several facies of this limestone have been mapped in the Cockpit Plateaus inland from the north coast. Along the north coast lies the Coastal Series which consists largely of a raised reef. Between the Coastal Series and White Limestone is the Montepelier Formation, a fine-grained calcareous detritus or chalk consisting dominantly of planktonic microfauna. Deformation of these chalks occurred by folding with few fractures. The chalk porosity is primary; therefore, water transmission is through the body of the rock rather than along solution channels (Versey, 1972).

In contrast with the coastal chalk, the limestone over central Jamaica is recrystallized into a dense rock with little primary porosity. Intense fracturing, however, has resulted in secondary porosity. A third facies mapped is characterized by a nodular or rubble texture (Versey, 1972).

Most of the karst topography can be traced back to the influence of a Late Tertiary block-faulting episode that cracked the limestone units into a three-dimensional fracture system. The two dominant fracture sets, one east-west and the other north-south, have had the most influence on karstification, but an oblique secondary set of fractures has, in places, left a strong overprint (Figure KL-2.1). The Duanvale Fault (see index map), the major east-west fault shown on the image, effectively marks the northern edge of the cockpit or kegel karst topography (Michael Day, written communication, 1985).

Beneath the Cockpit Plateaus (index map), ground-water drainage is principally through solution-enlarged joints and rubble zones. Many of these separate passages coalesce to produce master conduits. On rare occasions, high intensity storms will culminate in subsurface floods. The natural plumbing system is not designed to handle unusually large volumes of water; thus, the water backs up and causes radical fluctuations in the ground-water ponding and may lead to secondary surface flooding. It is quite possible that most of the work by solution is accomplished during these storm events. Corrosion is also accelerated because much of the coarse clastic debris carried off by overland flow is shuttled down through the subsurface channels.

A striking uniformity of fine dimpled texture exists over a very large segment of the radar image. This texture is directly due to the development of thousands of solution doline or cockpits on the White Limestone (Figures KL-2.1 and KL-2.2). Poljes with mogotes or residual karst hills can be found in northern Jamaica (Figure KL-2.3). Some controversy exists over the origin of cockpits, which nearly all exhibit solution deepening. An unanswered question concerns how much influence subsurface flow may have on their evolution. The dominating influence, however, is probably runoff and subsequent solution at the pit floor. Day (1976) found that every depression he examined in a study area along the north coast had an outlet. Very few of these outlets showed any evidence of collapse. The infiltration through these outlets was efficient, and only during intense storms did water back up and produce temporary ponds. Accelerated weathering and biologic activity generally occurs at those places that have the longest moisture residence times—in this instance, the cockpit floors. *Seasat SAR Rev. 0608, August 8, 1978.*



ORIGINAL PAGE IS
OF POOR QUALITY



3

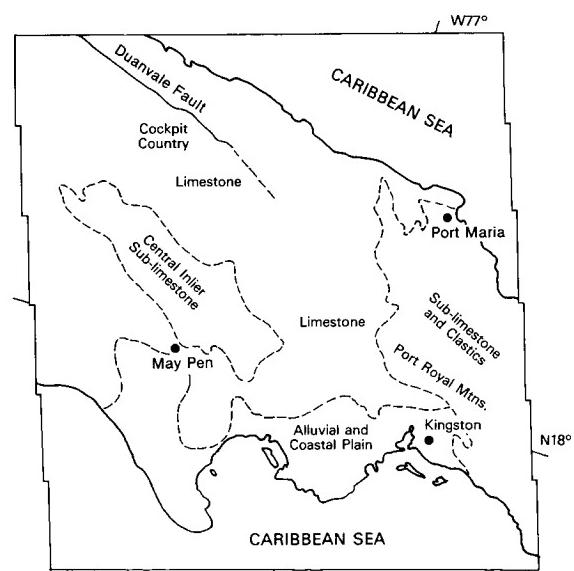


PLATE KL-3

This image includes part of the Yucatan Platform within the Yucatan Peninsula in the states of Campeche, Quintana Roo, and Yucatan. Although no coastline is exposed in the image area, it is surrounded on three sides by the sea. This part of Mexico receives between 1000 mm of rainfall near Merida and 1500 mm toward the south edge of the image. Nearly all of this rain falls between May and September. Of the total precipitation, approximately 85 percent returns to the atmosphere via evapotranspiration, while the remaining 15 percent infiltrates to the ground-water table (Hanshaw and Back, 1980). As can be seen from the image, no drainage network has developed over the region; thus, runoff is insignificant.

The Yucatan Peninsula and adjoining continental shelf (Campeche Bank) consist of relatively flat-lying Tertiary carbonates (Figure KL-3.1) covering some 350 000 km² of area (Weidie et al., 1978). The Campeche Bank extends about 200 km into the Gulf of Mexico both north and west of the peninsula. The narrow Caribbean shelf borders the peninsula to the east and rarely exceeds a few tens of km in width. The exposed Tertiary rocks attain thicknesses up to 1000 m in northwestern Yucatan and consist primarily of dolomites, limestones, and marls. Most of the surface rocks exposed in the image area are Eocene and Paleocene in age. Other ground scenes typical of karst terrain in the Yucatan are shown in Figures KL-3.2 and KL-3.3.

The most prominent structure in the region is the Ticul Fault and associated Sierra de Ticul escarpment, which trends N60W for about 200 km (see index map and image). Movement on the fault has probably been sporadic since the Late Cretaceous (Weidie et al., 1978). Sierra de Ticul is a series of hills, forming an arcuate ridge with a relief of nearly 50 m (West, 1967). The Sierra marks the boundary between the flattish Yucatan Plain to the north and the hilly Campeche region to the south. Most of the Yucatan Peninsula is dominated by karst topography (Figure KL-3.3) consisting of cenotes (steep-walled sinks that usually penetrate the water table), bare limestone platforms, aquadas (broad shallow solution basins), and resumideros (funnel-shaped conical depressions). The cenotes and aquadas are the two most important sources of water in the region, and as a consequence,

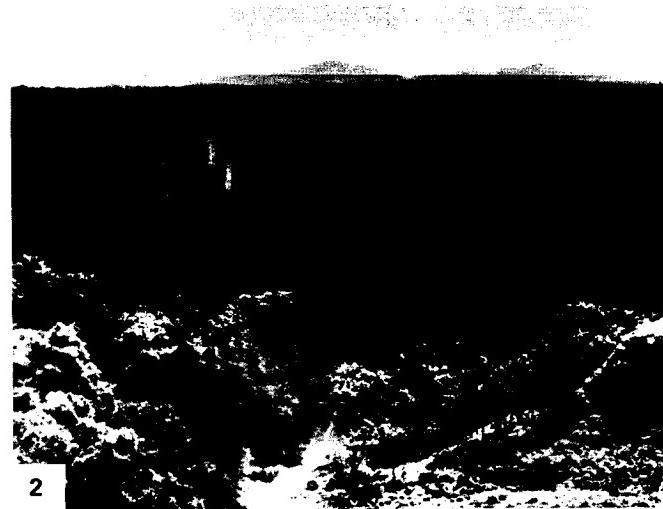
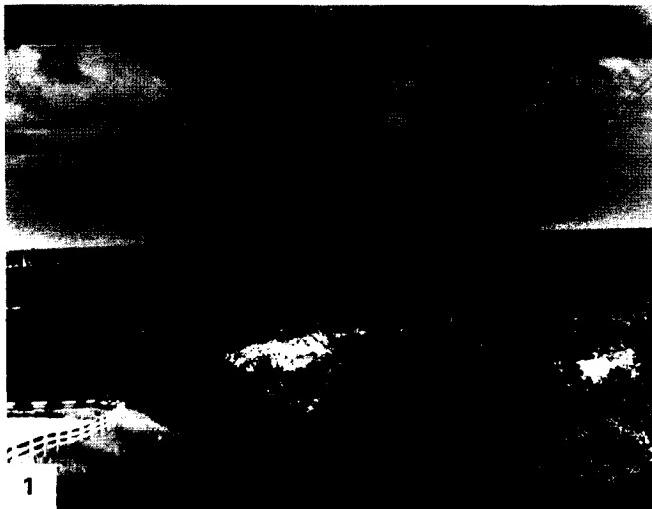
CENTRAL YUCATAN PENINSULA

most of the Mayan cultural development and population centers are found to be closely associated with these karst features. Where the limestone is not bare, it is covered with a thin terra rossa soil, usually less than 20 cm thick, developed on weathered limestone (Hanshaw and Back, 1980). Where bare limestone is exposed, it often exhibits deep solution channels or karren that can pose a problem for vehicular travel (West, 1967).

It is because of the karst that no surface drainage exists in the northern and central parts of the peninsula. The high porosity and permeability of the limestones provide for an efficient internal drainage (Southworth, 1984). The Yucatan Peninsula is similar to Florida because both have thick sequences of relatively flat-lying Tertiary limestones; however, in Yucatan, the lack of Upper Tertiary clays and marls overlying the limestone results in rapid infiltration or rainfall. The presence of an extensive interconnected subsurface drainage network is suggested by: (1) a gentle piezometric surface gradient that has been measured as 1.2 to 1.5 m above sea level in areas 80 km inland from the coast at an elevation of 30 m above sea level, (2) the lack of notable drawdown observed in heavily used wells, and (3) the young age of water dated from its C¹⁴ content (Hanshaw and Back, 1980).

Hanshaw and Back (1980) believe that chemical mass wasting in the zone of dispersion is perhaps the most important geomorphic process in the region. From their measurements on the concentration of dissolved solids, the surface in places could be lowered by as much as 340 mm/1000 yr. This figure is misleading, however, because much of the dissolution occurs along subterranean passageways.

The karst nature of the image area can be recognized by the lack of any developed drainage network and by the presence of residual karst knobs found south of Sierra de Ticul. Lago de Chichancanal (see index map) may be fracture-controlled like some of the lakes east of the image area that are influenced by the Holbox fracture system. Alignment of cenotes due to fracture control has also been documented in the eastern part of the peninsula (Southworth, 1984). **Landsat 21089-15115, January 15, 1978.**



ORIGINAL PAGE
COLOR PHOTOGRAPH

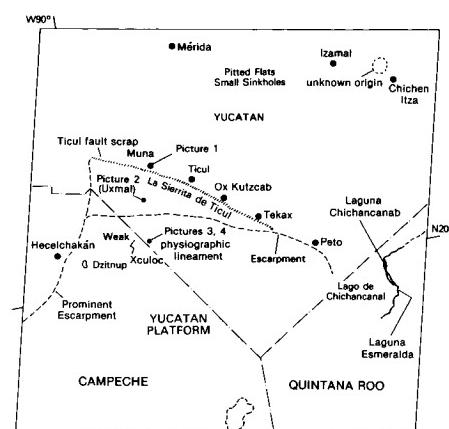
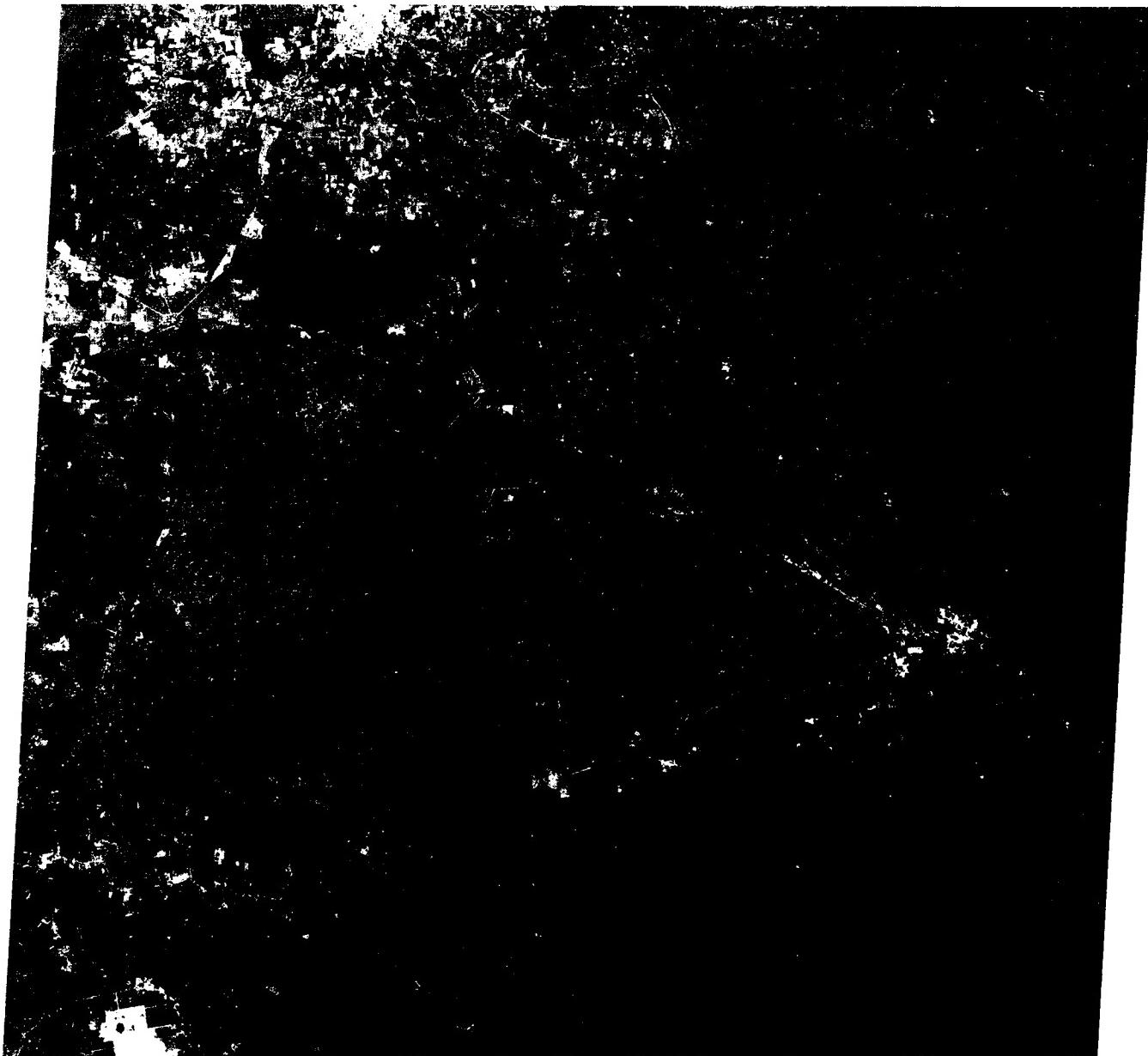


PLATE KL-4

FLORIDA KARST

West-central Florida, shown in the Landsat scene, is part of the Central or Mid-Peninsular Zone (geomorphic division of White, 1970). Florida karst is characterized by the abundance of depressions, many filled with water, and a lack of well-developed surface drainage pattern (Figure KL-4.1, A on index map). Florida is a carbonate plateau with limestones in the region comprising one of the best aquifer systems in the world. Tertiary limestones underlie all of Florida and regionally dip gently toward the south and west. The oldest rocks exposed are Middle Eocene (Avon Park Formation). The Tertiary limestones are some 300 m in thickness with numerous unconformities and facies relationships indicative of frequent marine regressions (Randazzo and Saroop, 1976). Significant diagenetic episodes involving dissolution and dolomitization (Randazzo and Hickey, 1978) have influenced karst development. Miocene and younger clastic sediments blanket the limestones in most areas of Florida.

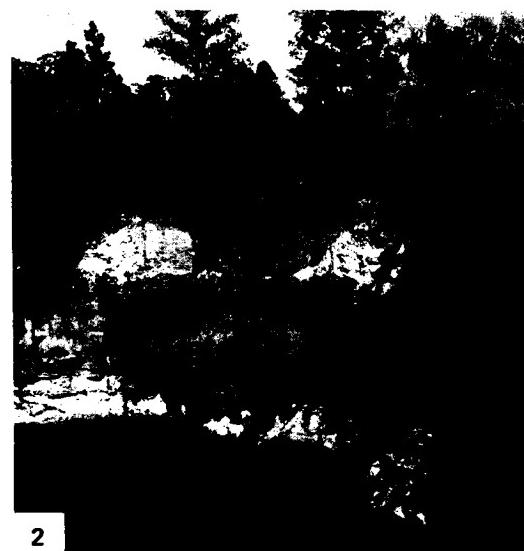
The topography of Florida included within the Landsat image is flat near the coast and becomes gently rolling towards the center. There is a lack of well-defined drainages and an abundance of rounded lake depressions, most of which contain water (Figure KL-4.1). These two characteristics are associated with an integrated subterranean drainage system, high water table, and collapsed depressions. Virtually all depressions seen on the Landsat image are dolines or sinkholes developed on the underlying limestones. Most dolines are shallow depressions, but some exhibit steep sides and contain lakes with depths greater than 25 m (Figure KL-4.2) (Sweeting, 1972). The greatest concentration of large lakes falls along the axis of the Central Lakes region (B on index map) and defines the region most influenced by the Ocala limestone. The Central Lakes region receives in excess of 100 cm/yr of precipitation and is the primary recharge area for the Floridian aquifer.

According to Windham and Campbell (1981) and Foose (1981), the subsidence and resultant sinkholes in Florida may occur when several conditions are met. These include a well-developed joint-controlled subsurface drainage network in limestone, a thin to moderate thickness of unconsolidated overburden, and a potentiometric surface below the unconfined water table. The

sequence of events that they envision begins with a lowering of the water table either from a drought or from excessive withdrawal of ground water from pumping. As the unconsolidated sediments and weathered debris that overlie the Tertiary limestones dry out, shrinkage cracks and cavities develop. Any subsequent vertical or horizontal percolation of water can enlarge and flush out these cavities through a process known as piping. Some of the unconsolidated sediment may drop directly into pre-existing dissolution cavities in the limestone and be carried away by the subsurface drainage system. When the overburden dries, it develops an internal strength capable of supporting itself, even over fairly large cavities. However, when the materials become rewetted from a rainy season or an unusually wet storm, the water weakens the material and gravity stoping can enlarge the cavity until the roof fails. The result is a conical sinkhole, the size of which is largely dependent on the thickness of overburden. The thicker the overburden is, the larger the sinkhole. Most of these depressions develop rapidly and unexpectedly as in Winter Park and Bartow, Florida (Figure KL-4.3 and index map).

Many of the sinkholes and cavernous networks in central Florida probably formed during low sea level stands during the Pleistocene. As the water table dropped in response to a lower sea level, unsupported roofs may have collapsed. Upon the return of high sea level and associated high water tables, further collapse may have ensued. Water now fills many of these sinks.

Several regions of Florida support a prolific number of small sinks (areas C on index map) and support as many as seven or more water-filled depressions per square kilometer. These subcircular regions appear to represent large but very shallow topographic basins with a relief of a meter or less. A shallow-surface water table in these regions is indicated not only from the presence of lakes but also from the darker tones associated with more lush and dense vegetation. Because of a dense lake concentration and small size, factors such as "perched" aquifers and distribution of clay lenses within the overburden are probably involved in their development (A. F. Randazzo, written communication, 1984). **Landsat 30244-15181-7, November 4, 1978.**



ORIGINAL PAGE IS
OF POOR QUALITY



3

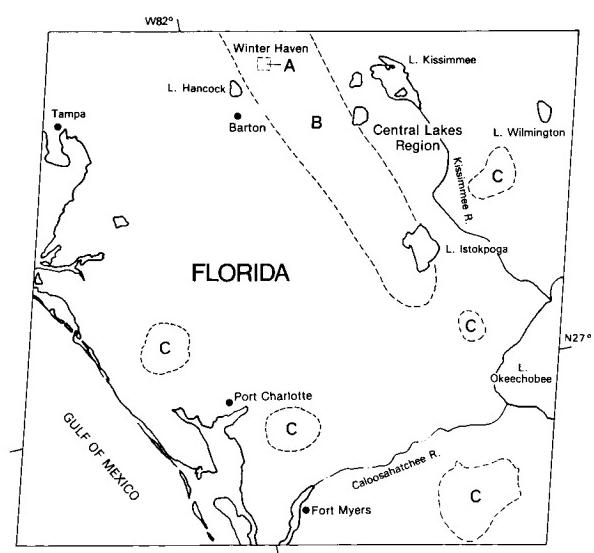


PLATE KL-5

SOUTHERN YUGOSLAVIA

The region of karst topography in Yugoslavia could rightly be called one of the type karst regions of the world because much of the pioneering work in karst began here. In fact, the term "karst" comes from the Slav word, "krs," and is associated with the limestone country in western Slovenia, Yugoslavia. Other terminology, such as doline, uvala, and polje, also originated here (Jennings, 1971).

Karst landscape covers principally the southwestern third of Yugoslavia. The karst country falls into three zones based on geographic setting and hydrogeology. These zones are: (1) the Adriatic insular and coastal region, (2) the high karst region of the Dinaric Mountains, and (3) the inner region. This Landsat image of southern Yugoslavia encompasses portions of the Adriatic insular, coastal, and high-karst regions; however, only in the high-karst area, or Dinaric Mountains (see index map), can karst be recognized on the image. The Dinaric Mountains display the most developed solution topography in the country.

The karst topography can be recognized by the dimpled nature of the land surface and the lack of integrated surface drainage (A on index map). With the exception of a few streams immediately adjacent to the coast, virtually all the drainage flows to the northeast into the Black Sea. From the Landsat image, drainage in much of the high-karst region is unrecognizable.

Most of the rocks in the Dinaric Mountains are late Paleozoic and Mesozoic limestones and dolomites, representing, for the most part, a shallow marine environment. The rest of Yugoslavia (eastern two-thirds) is characterized by clastic flysch-like sediments interbedded occasionally with limestone lenses.

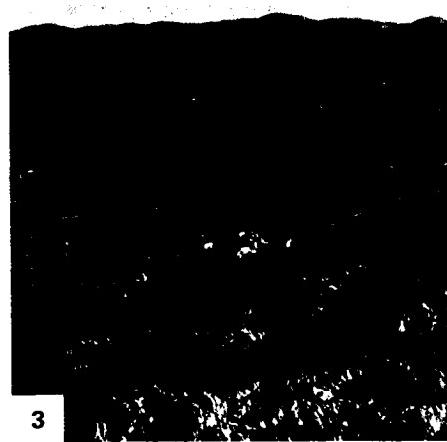
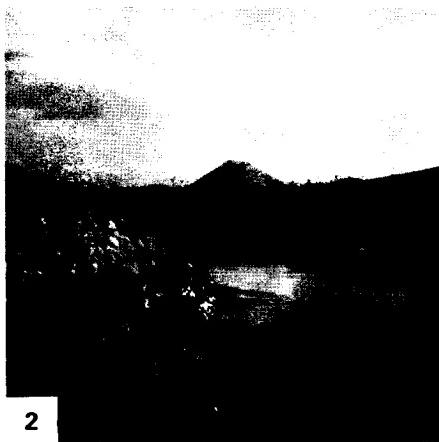
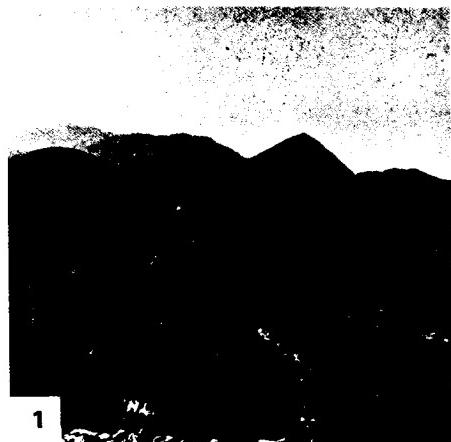
Structurally, the Dinaric Mountains have been interpreted in several ways: (1) a large overthrust sheet, (2) part of a meganticlinorium, and (3) a combination of all diastrophic disturbances (Herak, 1972). The presence of unconformities and deformed strata indicate that multiple phases of diastrophism have taken place, beginning in the Late Paleozoic and continuing sporadically through the Mesozoic era. It was not until the Late Cretaceous and Early Tertiary, however, that significant deformation and uplift had a major influence on the development of karst landforms.

Thus, the evolution of Yugoslavian karst was slow, but it continued with increasing volume and intensity with time (Herak, 1972). With each orogenic event from the Late Cretaceous on,

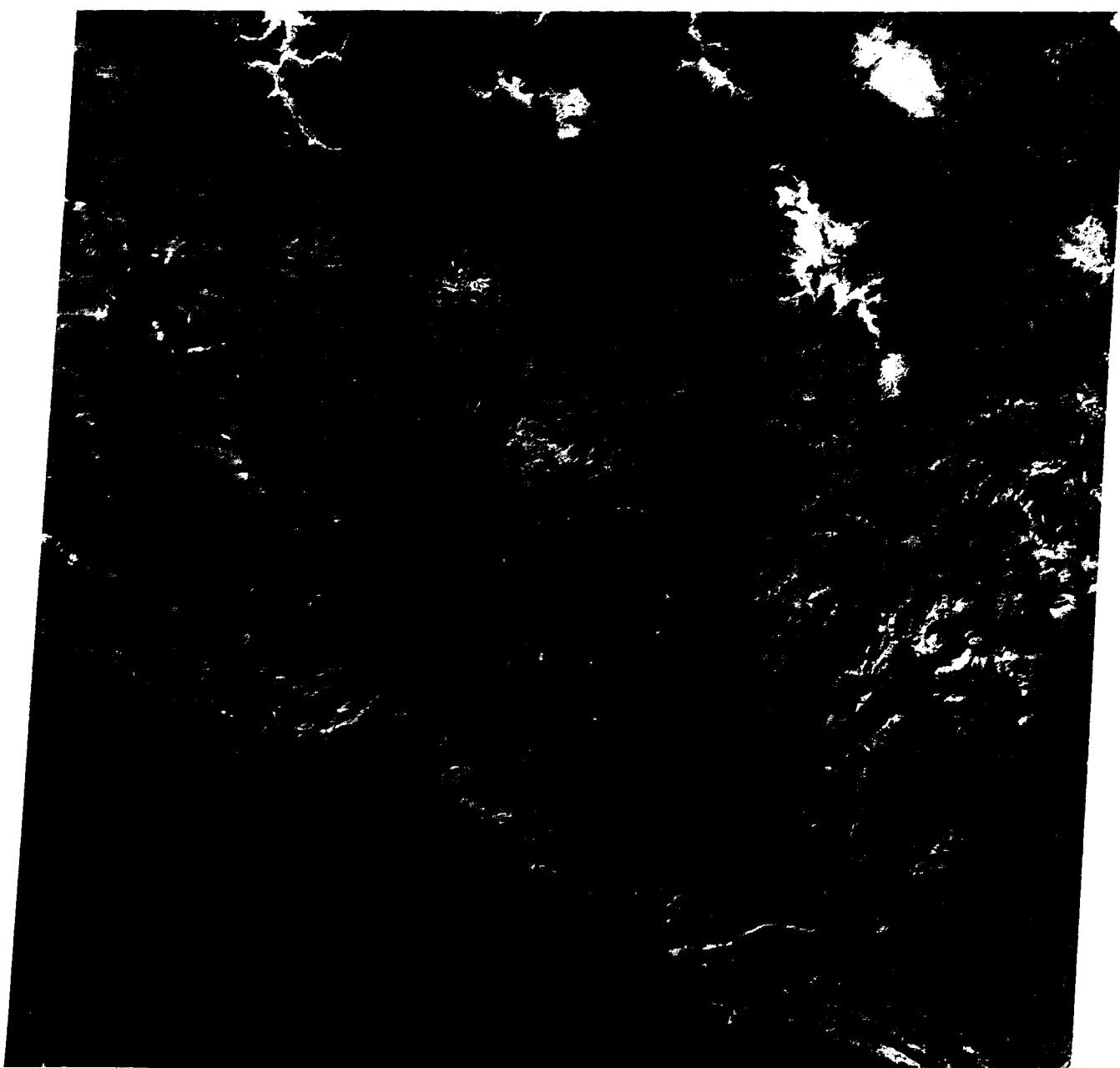
a different system of joints, fractures, and faults shattered the carbonate rocks to develop an intricate system of pathways for percolating ground water. Folding of the strata produced separate watersheds and barriers, resulting in the impoundment and concentration of water flow. Therefore, accompanying each uplift event was a renewed phase of karstification.

The Dinaric Mountain region is a veritable outdoor museum of karst landforms. Literally hundreds of examples of karen, dolines, pits, swallow holes (ponors), dry valleys, uvalas, poljes, karst plains, and caves are found in a variety of shapes and sizes. Because of their scale, most of these features cannot be picked out on the Landsat imagery, but collectively, they impart a unique textural signature. This signature is well displayed at "A" on the index map where the pitted, hummocky-looking surface is exposed northwest of Skadar Lake (lake). The nature of this topography can be grasped from Figure KL-5.1 and KL-5.2. Figure KL-5.1 shows dolines that impart a megapock-marked surface. These solution sinkholes developed in Mesozoic carbonates in the Biokovo Mountains immediately northwest of the image. Several poljes are included in the image area, but the best-developed one is the Popovo Polje (see index map and Figure KL-5.2), which displays the typical flat-floor and residual conical hills or hums on its surface. The term "hum" comes from the name of the village Hum found within the Popovo Polje (Figure KL-5.2). The side boundaries of many of the poljes are controlled by faulting. A hint of this can be seen from the northwest-southeast trend of structures associated with the Popovo Polje. Another polje, Polje Stasevica, shown in Figure KL-5.3, is located northwest of the image. Poljes may widen and coalesce to form distinct valleys such as one near Titograd (Figure KL-5.4).

The polje surfaces are frequently flooded during the autumn and winter and are dry during the summer (compare Popovo Polje (Figure KL-5.2) with Polje Stasevica (Figure KL-5.3)). The flooding cycle is highly dependent on climatic conditions and fracture solution permeability. Most of the water from the poljes infiltrates quickly to subsurface conduits where it flows freely through fracture-controlled solution channels. Water from one polje will frequently emerge in an adjacent polje only to be drawn into another subsurface hydrologic system (Herak, 1972). **Landsat 1104-08595-7, November 4, 1972.**



ORIGINAL PAGE IS
OF POOR QUALITY



4

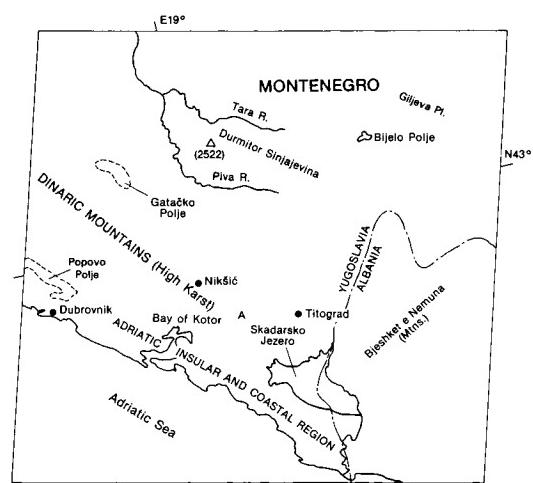


PLATE KL-6

NULLARBOR KARST, AUSTRALIA

The Nullarbor karst makes up an area encompassing about 200000 km² of southern Australia, which makes it one of the larger karst regions in the world. The Landsat image views only a portion of the south-central Bunda Plateau, which is treeless and is called the Nullarbor Plain. The Bunda Plateau is the positive surface expression of the Eucla structural basin, which is filled with over 600 m of Cretaceous and Tertiary marine sediments. The planar surface of the Bunda Plateau and associated Nullarbor Plain represent an emergent stable continental margin mantled with a uniform sheet of shelf sediments. The uppermost formation, the Nullarbor Limestone, is of Middle Miocene age and ranges in thickness from 15 to 60 m (Twidale, 1973). It is in this limestone that the Nullarbor karst is expressed.

The emerged sea cliff (Figure KL-6.1) of the Hampton Range exposes both the Nullarbor Limestone and the underlying older Abrakurrie Limestone. South of the sea cliff, the coastal plain is mantled with Late Tertiary and Quaternary marine sediments and shelly conglomerates.

The Nullarbor karst is unusual in that it represents an arid karst. The precipitation averages about 250 mm per year near the coast and decreases northward to about 150 mm, where the flat to gently rolling surface of the Nullarbor Limestone is sparsely vegetated with shrubs and grasses, particularly saltbushes and blue bushes. As might be suspected, this arid karst supports no surface streams (Figure KL-6.2). Any rainfall quickly disappears underground through joints and depressions exposed on the surface. The aridity is also responsible for the observed paucity of caves and dolines and the absence of larger karst features like uvalas and poljes.

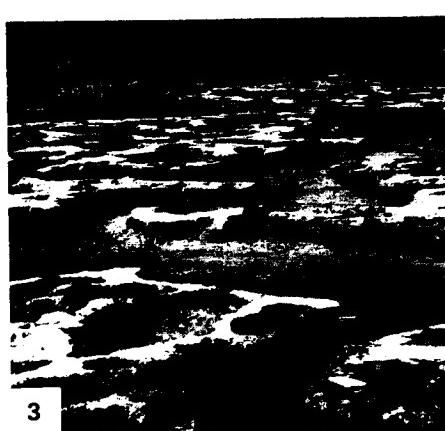
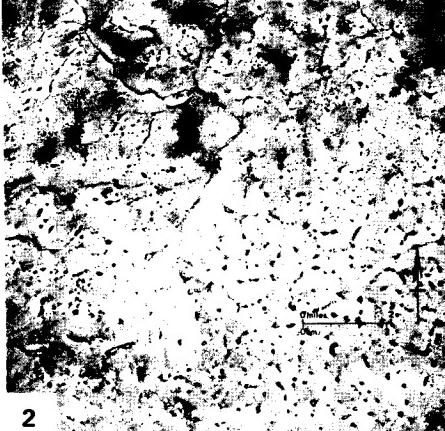
Denudation, primarily due to solution and minor wind deflation, averages 5 mm per 1000 years over the last 14 Ma since the landscape began to evolve (Lowry and Jennings, 1974). In the image area, Lowry and Jennings estimate that between 60 and 180 m of subaerial solution has taken place.

Several striking morphological features show clearly on the Landsat image, including one that is probably related to solution denudation. Besides the emerged and prominent sea cliff making up the Hampton Range, several fault traces, possibly Early Pleistocene, can be discriminated. These faults (see index map) exhibit scarps with a relief of 5 to 25 m on the surface. The ground view (Figure KL-6.2) and vertical aerial photos (Figures KL-6.3 and KL-6.4) show large-scale views of this topography. Karst and solution features show up as a distinctive ridge-and-corridor pattern (Figure KL-6.2), which imparts a rippled texture to the Nullarbor Plain in the image area. The low relief of 1.5 to 6 m stands out surprisingly well on the Landsat image. The corridors are flat-floored basins up to 1 km wide and several km long that show up as light tones because of a concentration of clays in the residual soil. The ridges of the same dimensions show darker tones because of a greater concentration of vegetation and associated darker soils. Lowry and Jennings (1974) regard differential solution of the limestone surface as the prime factor in the development of relief across this ridge-and-corridor topography. The distinct east-west trend of the corridors is apparently controlled by jointing; however, the exact nature of the cause and effect relationship remains unclear. The white areas near the coastline are coastal sand dunes.

Twidale (1973) summarizes the Nullarbor Plain as being:

1. An essentially original sedimentary surface modified by deflation and solution
2. A featureless surface because of simple geologic structure, resistant bedrock surface, and arid climate
3. An example of covered karst (thin soil cover)
4. A region in which karst development has been retarded on both the surface and subsurface
5. A surface with its greatest solutional activity probably occurring during wetter pluvial periods in the Pleistocene

Landsat 2083-00391-6, April 15, 1975.



ORIGINAL PAGE IS
OF POOR QUALITY

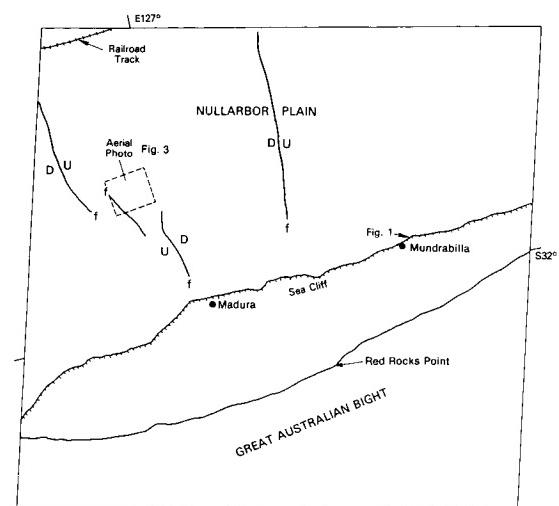
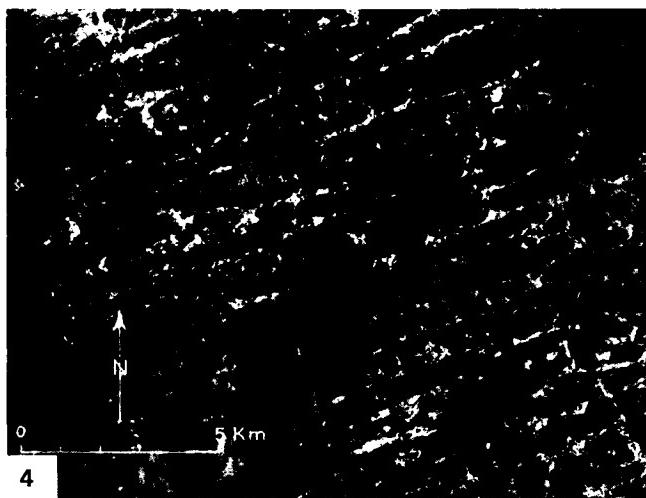
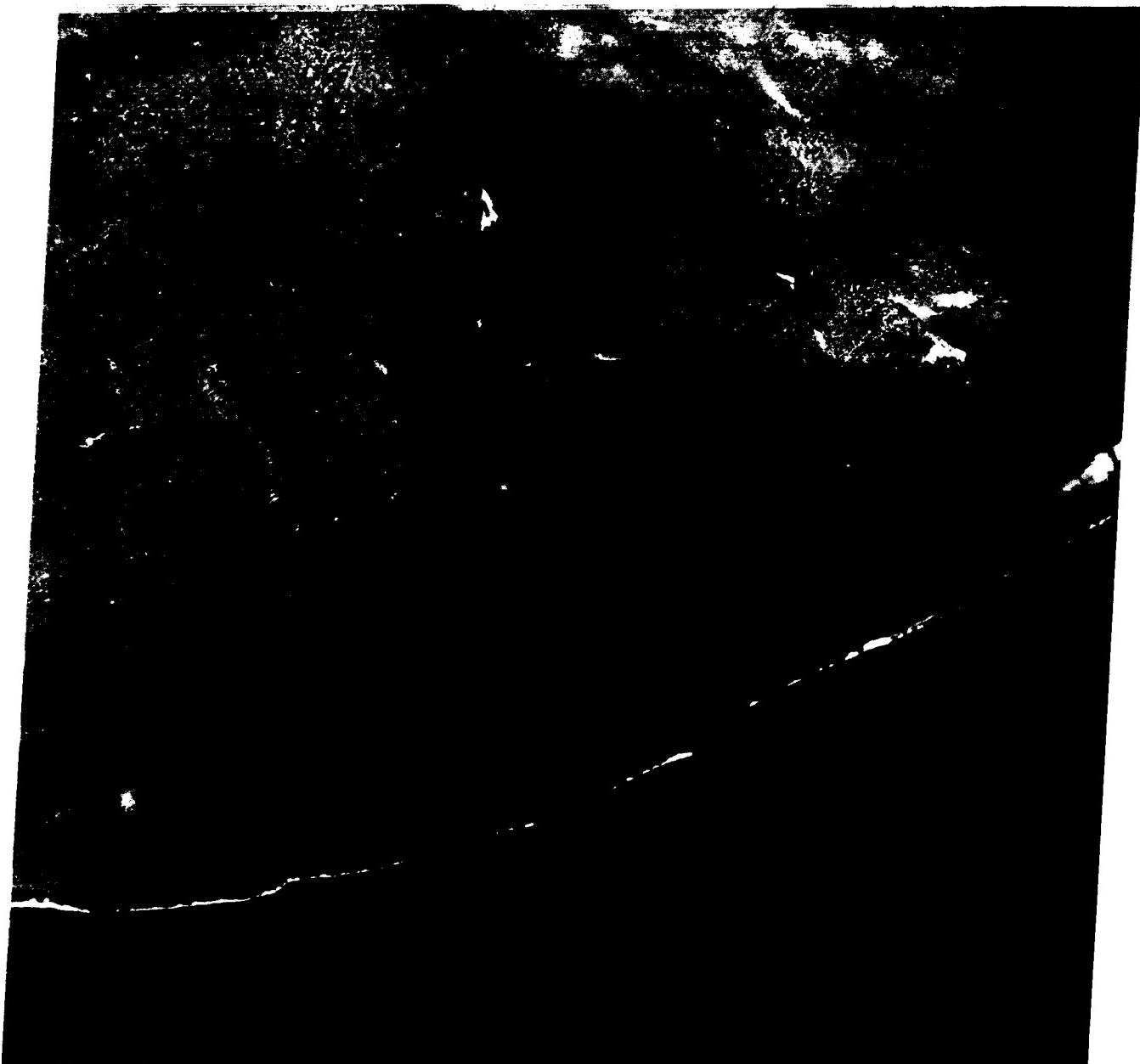


PLATE KL-7

FINGER LAKES OF ALASKA

Mertie (1938) classifies glacial lakes into four categories: (1) glaciotectonic lakes (influenced by faulting or folding of surface), (2) rock-basin lakes (including tarns or cirque lakes), (3) pit lakes (kettles formed by melting of ice beneath glacial till), and (4) barrier lakes (water impounded by end moraines). This image of southwest Alaska displays examples of all four lake types. The barrier lakes dominate and can be seen to finger out of the Tikchik Mountains to the east onto the Nushagak Lowlands. These lakes are dammed by bedrock overlain by end moraines that are discernible by the broad dark-toned areas east of the lakes (area A on index map). Because of the hummocky topography of the moraines at the eastern ends of the lakes, overflow channels have developed between lakes (e.g. note the channel between Lake Kulik and Lake Beverly).

These finger lakes (Figure KL-7.1) are similar to the finger lakes of New York State. Nuyakuk Lake, Alaska, and Seneca Lake, New York, for example, are similar in shape and area (both approximately 175 km²); however, they differ in depth (284 and 189 m, respectively). Curiously, many of the finger lakes in both Alaska and New York have a boxed or rectangular shoreline at the lake head, as can be seen on the northwest end of Lake Nerka (Figure KL-7.2). This is apparently due to the development of a delta across the valley floor.

Togiak Lake (Figure KL-7.3) is situated along the Togiak Fault and is an example of a glaciotectonic lake. The Togiak Fault is a major right lateral strike-slip fault (a continuation of the Denali-Farewell Fault) and shows evidence of recent activity (Hoare and Conrad, 1978). The lake lies at the northern end of a pull-apart basin into which the Quaternary alkali basalts were erupted (mostly south of the image area).

Rock-basin lakes are generally too small to be resolved by Landsat's multispectral scanner system, but careful examination of the image, especially west of the Togiak Fault in the Kilbuck Mountains, reveals a number of larger tarns occupying cirques.

Pit lakes or kettles appear on the image as small lakes scattered about in the morainal deposits to the east of the finger lakes. Figure KL-7.1 shows a few of these lakes on the far side of Lake

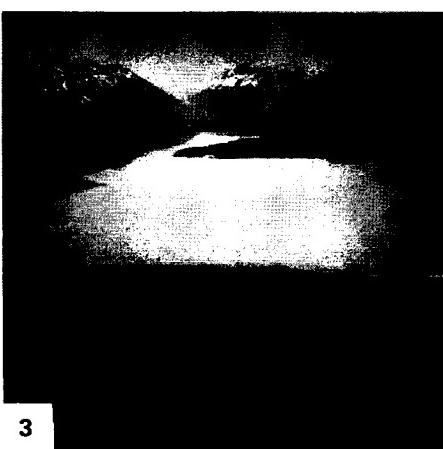
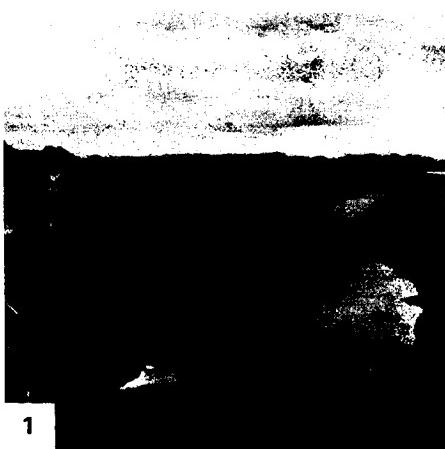
Chauekuktuli. Note the split-like projections (Figure KL-7.1) that mark one of the more recent end moraine deposits and glacial standstills.

The size of these finger lakes indicates that, during the Pleistocene, the Kilbuck and Tikchik Mountains supported a vast ice field that has since disappeared. There are still, however, a few remaining small active glaciers in the northern Tikchik range.

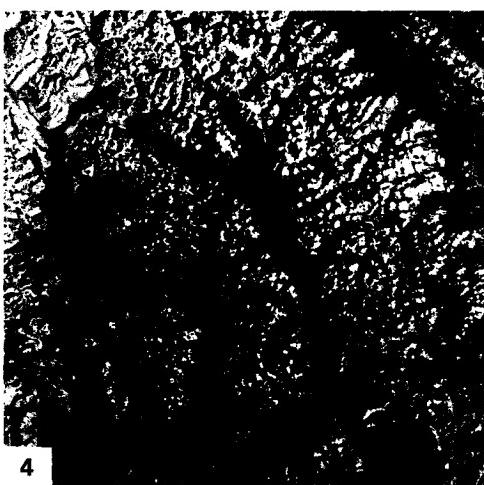
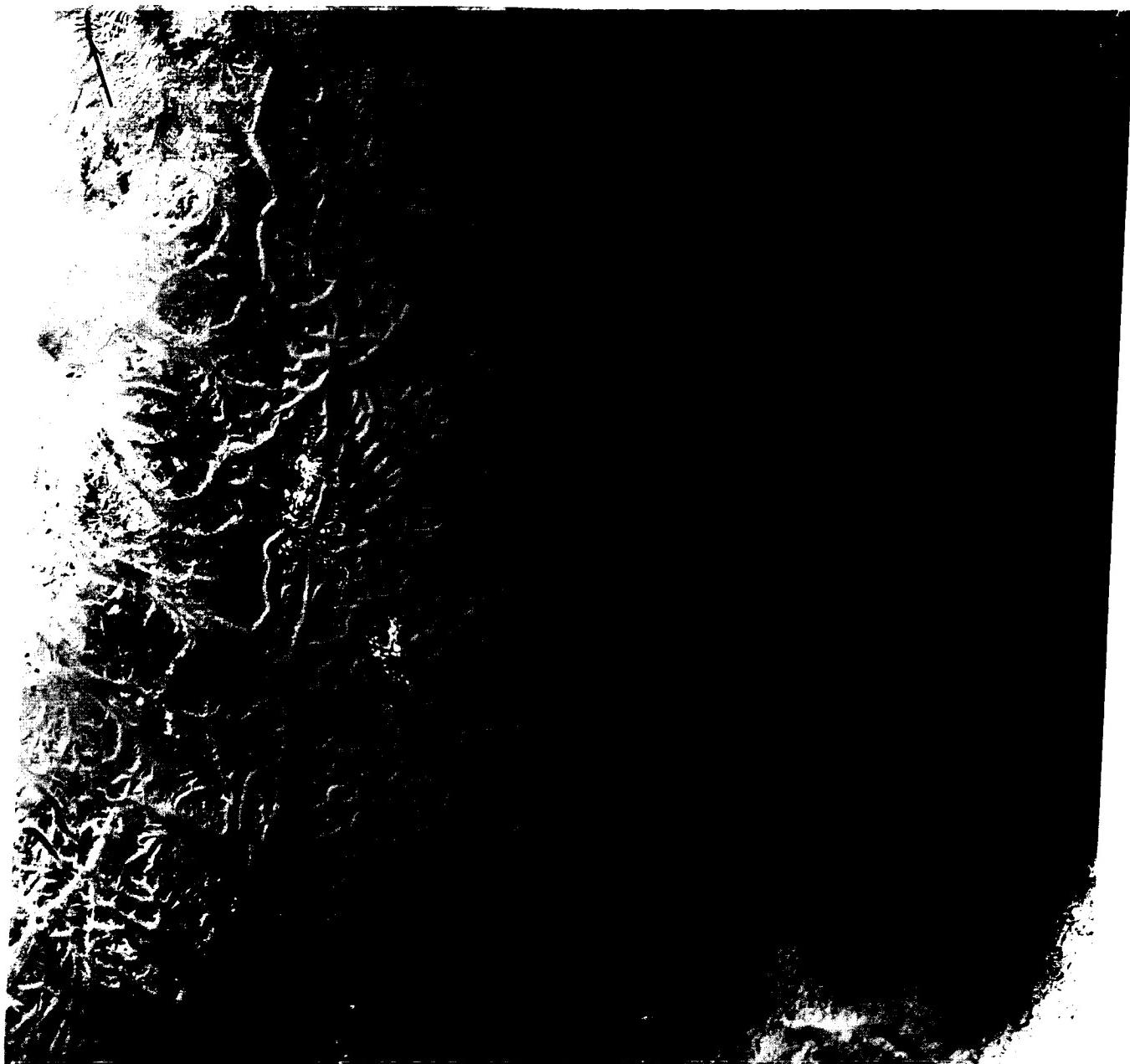
Mertie (1938) finds evidence of ice action high above Nuyakuk Lake, the largest finger lake, indicating an ice thickness of at least 900 m at the lake site during maximum glaciation. He also estimates that the ice moved eastward 65 km from the head of the lake. All outwash channels at that time drained east and south across the Nushagak Lowlands. As the glaciers ablated, the residual moraines altered the drainage and produced the dams that confined the lakes. A multitude of lake terraces of varying heights, ranging from 2 to 20 m above the present lake levels, suggest a complex adjustment of postglacial drainage.

The Nushagak Lowlands to the east of the finger lakes is blanketed with glacial outwash. The lowlands are underlain by nonresistant Cretaceous flysch in a structurally low region between the Tikchik Mountains and the Alaska Peninsula. The Tikchik and Kilbuck Mountains are underlain by a structurally complex assemblage of highly indurated volcanogenic rocks of prehnite-pumpellyite metamorphic facies (Steve Box, 1985, written communication). North of Nuyakuk Lake, the rocks are primarily interbedded volcanogenic graywacke and argillite of Mesozoic age (Steve Box, 1985, written communication). The structure is complex, and the lakes only locally follow the strike of bedding. Faults, cleavage, and regional jointing also influence the trends of the finger lakes.

Finger lakes are common in other mountainous regions where glaciation has widened and straightened preglacial drainage valleys. Some of these lakes can be remarkably long, as are Upper and Lower Arrow Lakes and Kootenay Lake, in southern British Columbia (Figure KL-7.4). **Landsat 1018-21200-6, August 10, 1972.**



ORIGINAL PAGE IS
OF POOR QUALITY



4

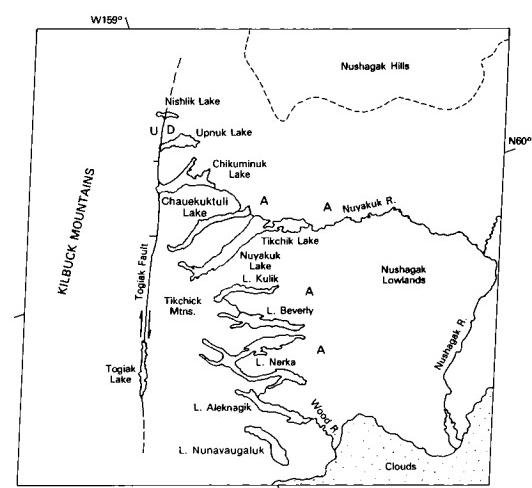


PLATE KL-8

LAKES OF THE OB RIVER VALLEY, SIBERIA

This Landsat scene is of the Ob River (Figure KL-8.1) about 170 km from where it enters the Obskaya Gulf, an arm off the Kara Sea (part of the Arctic Ocean). The river originates in the Altai Mountains near the Russian/Chinese border, where it then flows north for over 4000 km through the Western Siberian Lowland. The northern edge of the image is only 50 km south of the town of Salekhard, the largest nearby community. The Ob River is frozen about 220 days of the year but thaws in May and June (Suslov, 1961). These thaws are accompanied by ice jams that hinder navigation until late June. In general, the aridity of the Western Siberian Lowland increases from the west to the east. In this part of Siberia, the rainfall is 30 to 50 cm/yr, which falls mostly in the summer. The flatness of this part of Siberia is indicated by the gradient. In the last 2900 km of the Ob River's trek to the sea, it drops only 91 m (Suslov, 1961).

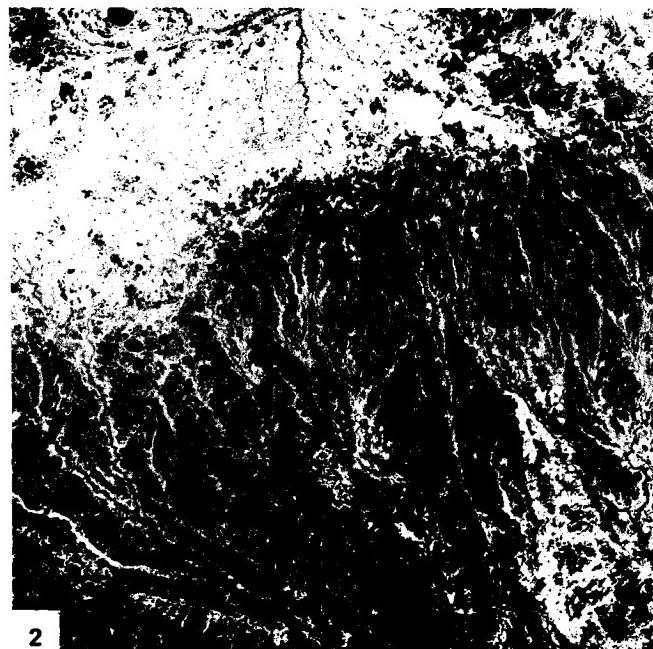
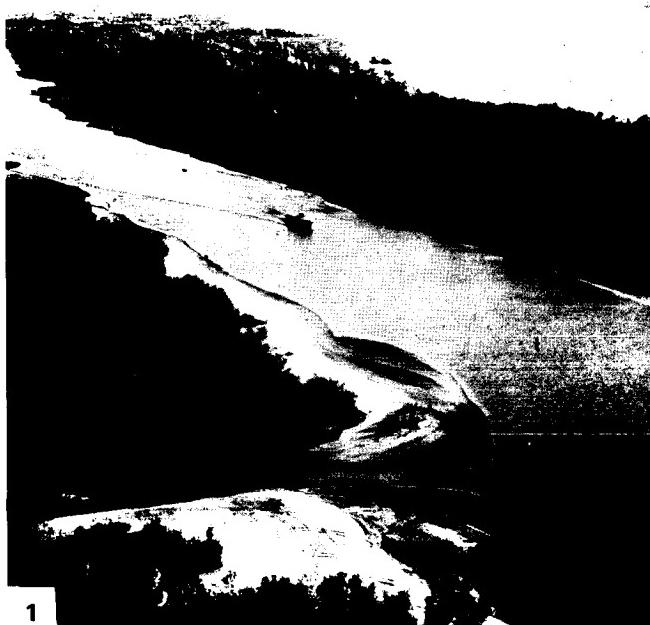
The Western Siberian Lowland is a structural basin with more than 1000 m of Tertiary cover overlying several thousand meters of Mesozoic and Paleozoic rocks. Few structures of any consequence are expressed topographically in the region, although some of the drainages in the plate image area appear to be influenced by fracture trends (index map). This region was inundated during the last glaciation by a vast glacial ice sheet that moved southeast. The image area is mantled with fluvial-glacial deposits and glacial moraines (Bush, 1985, written communication).

In this Landsat image, the Ob River displays a braided channel and anastomosing network across its floodplain. Numerous lakes are scattered both within the floodplain and just outside

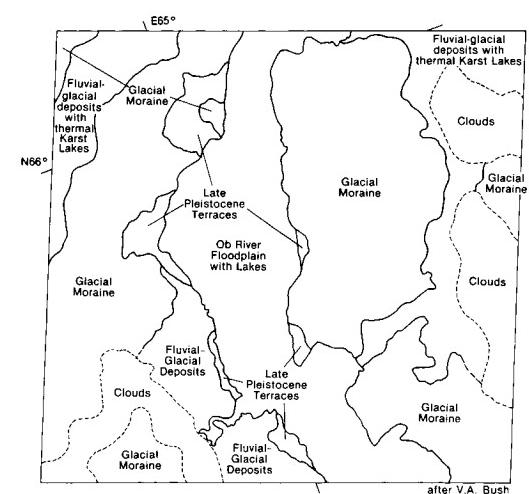
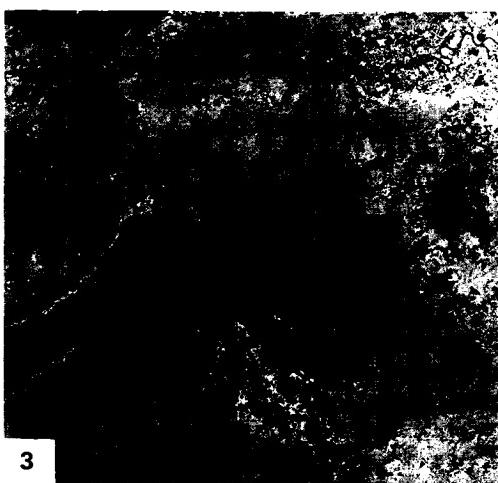
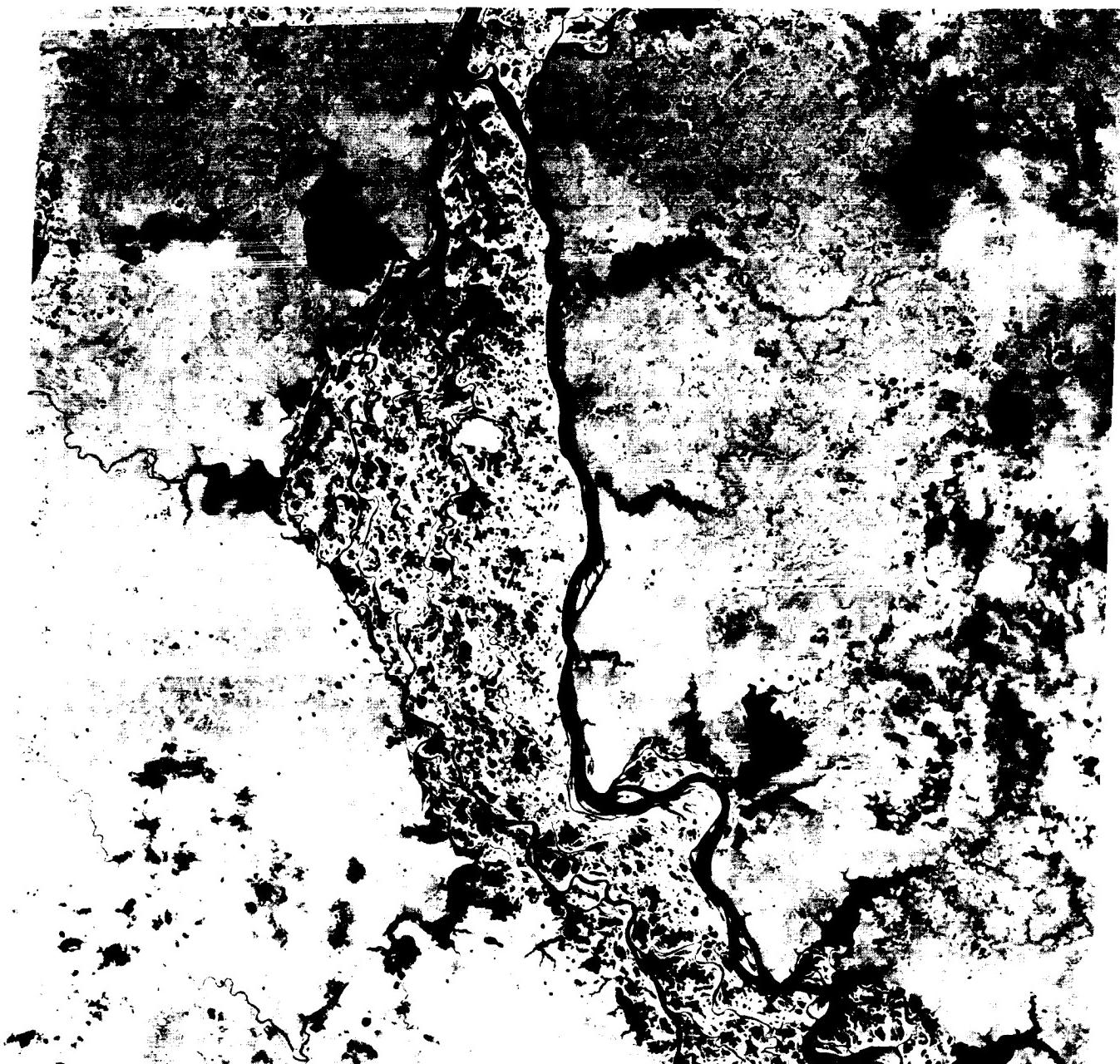
the floodplain. Suslov (1961) classifies the lakes within the Western Siberian Lowland as primary (geological origin), glacial (kettle lakes), alluvial (oxbow, abandoned high-water channels and crevasse lakes), peat-bog, and suffusion lakes (due to the winnowing out of fines and subsequent hydrocompaction). Most of the lakes displayed in the floodplain are probably abandoned high-water channels. Some crevasse lakes may also be evident (the large lakes around the periphery) and are possibly influenced by a natural levee system adjacent to the floodplain. Some of the lakes to the east and northwest of the image are thermokarst lakes, which are not recognized by Suslov, but have been noted by Bush (1985, written communication).

Thermal karst lakes form through the melting of ground ice accompanied by surface collapse to create a depression that subsequently fills with water (Washburn, 1980). This type of lake has been studied extensively in eastern Siberia near the Lena River (Czudek and Demek, 1970). A profusion of these lakes can be seen in Figure KL-8.2, a Landsat image taken southeast of the Plate image. The lakes in this figure are confined to the interfluves and are circular to slightly elliptical with the long axis trending east-west. The axis is perpendicular to the prevailing north wind (Suslov, 1961). These lakes bear a strong resemblance to the Carolina Bays found in North and South Carolina.

The thermal karst lakes in the Plate image are confined to fluvial-glacial deposits as mapped by Bush (1985, written communication). Similar lakes occupy the uplands around the Yenisey River to the northeast (Figure KL-8.3) as it enters the Yeniseyskiy Gulf on the Kara Sea. **Landsat 1387-06402-7, August 14, 1973.**



ORIGINAL PAGE IS
OF POOR QUALITY



ORIGINAL PAGE IS
OF POOR QUALITY

PLATE KL-9

ORIENTED LAKES, POINT BARROW, ALASKA

This Landsat scene covers a small portion of the Arctic Coastal Plain of Alaska. The Arctic Coastal Plain is underlain by flat-lying Late Cretaceous to Early Tertiary sandstones and shales with interbedded conglomerates and coal seams. This sedimentary pile has a thickness greater than 1000 m and is overlain by as much as 45 m of Late Tertiary to Quaternary unconsolidated clays, silts, gravel, and peat.

The most significant physiographic characteristic of this region of Alaska is the abundance of oriented thermokarst lakes that are associated with permafrost in northern Alaska. The Arctic Coastal Plain is included within the continuous permafrost region as defined by Péwé (1983). Within the Landsat scene, perennially frozen unconsolidated sediments are found only a few decimeters below the surface. This has the marked effect of limiting water flow to either surface runoff or within upper soil horizons. The permafrost zone extends to 680 m in depth in parts of northern Alaska (Péwé, 1984, written communication). Topographic relief in this region is generally less than 3 m, but along coastal bluffs, it can average 5 m.

Black and Barksdale (1949) estimated that from 50 to 70 percent of the coastal plain is dominated by lakes and marshy ponds. Between the lakes, the gently rolling surface is blanketed with a thick mat of vegetation consisting of lichens, mosses, grasses, sedges, shrubs, and occasional willows (Black and Barksdale, 1949), and there is a conspicuous absence of trees. The permafrost conditions exist because the annual mean temperature at Barrow is -12°C and subzero temperatures are recorded 320 days of the year. The prevailing winds are from the northeast for 11 months of the year, and in July, they blow from the southwest.

The oriented lakes of Alaska (Figures KL-9.1 and KL-9.2) are primarily confined to the Arctic Coastal Plain, although other oriented lakes are known to occur under similar environmental conditions such as in the vicinity of Old Crow in Yukon Territory. The shapes of the lakes have been described as elliptical, cigar-shaped, rectangular, ovoid, triangular, and compound (Black and Barksdale, 1949). The length-to-width ratios of the lakes vary from 1:1 to 5:1, but 2:1 to 3:1 dominates in the Barrow Region. Most lakes are 6 m deep or less, but some attain depths exceeding 20 m. The abundance of drained lake basins and former

extensions of existing lakes suggests that many lakes have been larger some time in the recent past.

Summer thawing affects the stability of the lake shore by causing collapse, slumping, caving, and erosion of the banks (Figure KL-9.3). A lake can enlarge through thawing and wave action at its banks and may be drained if the banks expand into a drainage system or topographic depression. The origin of the lakes is related to the frozen, fine-grained sediments that generally contain a volume of ice that exceeds the normal porosity of ice-free sediments. When thawing of the surface occurs, a depression results and a thaw lake has formed (Carson and Hussey, 1962).

Controversy still exists over the origin of the predominant N10-15°W orientation of the lakes. Black and Barksdale (1949) suggest that lake elongation may be due to a dominant north by northwest paleowind that has since shifted to the present-day northeast wind. The relatively recent age of several thousand years from radiocarbon dating and the fact that no lakes seem to be forming parallel to the existing wind direction support some other origin. Carson and Hussey (1962), after considerable field work, conclude that the northeast-southwest winds develop sublittoral shelves and bars along the major or longest axis (normal to wind direction) that insulate the banks from further thaw and subdue wave erosion. Deeper and warmer water has been found to be present near the ends of some of the elongated lakes, indicating that continued thaw and collapse will tend to accentuate or at least maintain the elliptical shape.

Furbringer and Naydn (Washburn, 1979) propose bedrock fracture control for lake orientation. Ice wedges oriented in a north by northwest direction (the same as bedrock fractures) have been observed, which upon thawing give rise to elongated lakes. The influence of maximum insolation at noon along a north-south axis may also aid in maintaining the elongation of lakes.

The final solution must take into account some of the observations seen from the Landsat image (namely, that the size and elongation of lakes tend to increase toward the coastline). The interior lakes are rounder and smaller. Some of the lakes to the eastern lower edge of the image are even elongated in a northwest-southwest direction. **Landsat 20182-21394-7, July 23, 1975.**



1



2

ORIGINAL PAGE IS
OF POOR QUALITY



3



PLATE KL-10

CAROLINA BAYS

This Landsat image covers a region that encompasses a portion of the Atlantic Coastal Plain in North and South Carolina. The most intriguing geomorphological features within the image are the Carolina Bays. These are shallow ovoid depressions with a northwest-southeast orientation. Most bays are ringed by a sand rim that is best developed on the southeast side. Some bays exhibit multiple rims. Careful examination of this Landsat image reveals more than 200 of these depressions (A on index map). Although they have been studied by geologists and geomorphologists for over a century, there is still no agreement as to their exact origin. These oriented depressions have a striking resemblance to the oriented lakes of Alaska (see Plate KL-9), but because there is no evidence that permafrost conditions ever existed this far south during the Pleistocene, processes other than permafrost must be considered.

Some of the hypotheses suggested for the formation of the bays are listed by Price (1968a, p. 103):

1. Spring basins
2. Sandbar dams of drowned valleys
3. Depressions dammed by giant sand ripples
4. Craters from a meteor swarm
5. Submarine scour by eddies, currents, or undertow
6. Segmentation of lagoons and formation of crescentic keys
7. Lakes in sand elongated in the direction of maximum wind velocity
8. Solution depressions, with wind-drift sand forming the rims
9. Solution depressions, with magnetic highs near bays due to redeposition of iron compounds leached from basins
10. Basins scoured out by confined gyroscopic eddies
11. Solution basins of artesian springs with lee dunes
12. Fish nests made by giant schools of fish waving their fins in unison over submarine artesian springs
13. Eolian blowouts (deflation)
14. Sinkholes over limestone solution areas, streamlined by ground water

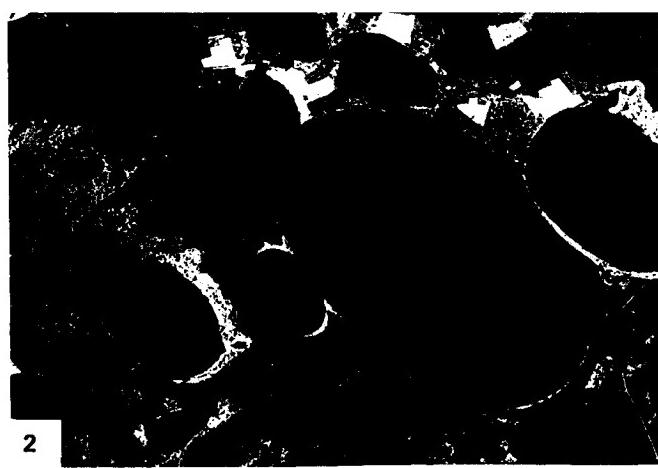
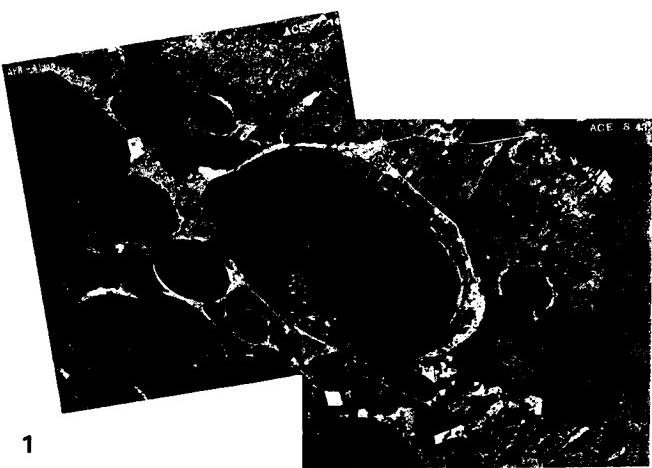
15. Oriented lakes of stabilized grassland, interridge swales of former beach plains and longitudinal dune fields, with some formed from basins in Pleistocene lagoons

With the exception of the deflation hypothesis (No. 13), the other proposed origins have been shown to be untenable (Kaczorowski, 1976). Thom (1970) in South Carolina was able to classify all bays within his study area into three topographic settings: (1) flat interfluviums, (2) dune depressions, and (3) terrace contacts. His study indicates that most of the bays are found to be concentrated on the interfluvium plains between entrenched stream valleys (see image; A on index map).

Dates obtained from organic fill within the bays indicate that their formation probably occurred between 7000 and 40000 years ago. Thom believes that the bays developed from shallow lakes during the Pleistocene, which, because of changing vegetation and drainage patterns and a dominant southwest wind, worked collectively to orient the bays normal to the wind direction. Surface wave action generated at right angles to the wind direction is believed to cause elongation in the northwest-southeast directions. Kaczorowski (1976) made a careful comparison of the oriented lakes in Chile and Alaska, and he corroborates Thom's conclusions.

No investigator has disputed the influence of eolian processes as an agent in bay formation. The question is whether the wind action is primary or secondary. The high reflectivity of the rim sand dunes outlines many of the bays on the Landsat image and can be clearly seen in the ancillary photos (Figures KL-10.1, KL-10.2, and KL-10.3). Many of the dunes are believed to be former longitudinal dunes that later, under the influence of more humid conditions, transformed into parabolic dunes or blowout crescent-shaped dunes with tails anchored by vegetation (Price, 1968b). Because today's dominant winds blow from the southwest, a more complex wind regime than that suggested by either Thom or Price must be invoked to account for the buildup of sand on the southeast ends.

Such wide variation exists among the half million lakes that no single hypothesis satisfactorily explains their origin. **Landsat 1080-15203-5 October 11, 1972..**



ORIGINAL PAGE IS
OF POOR QUALITY

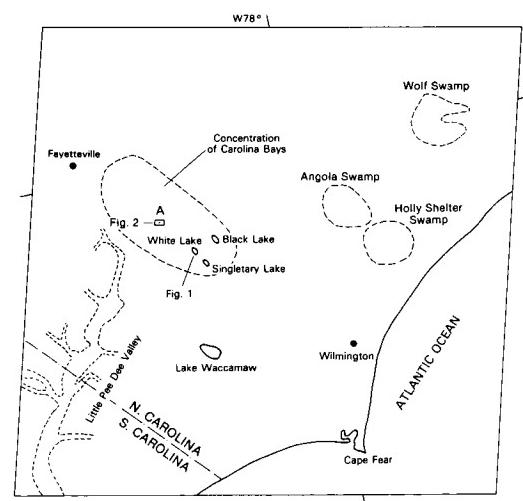
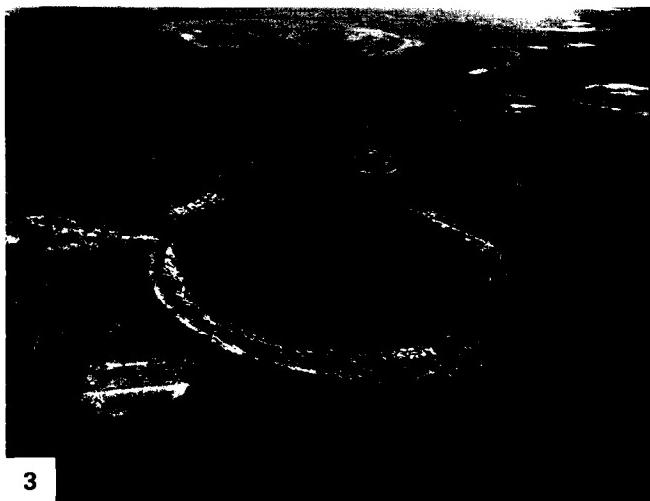
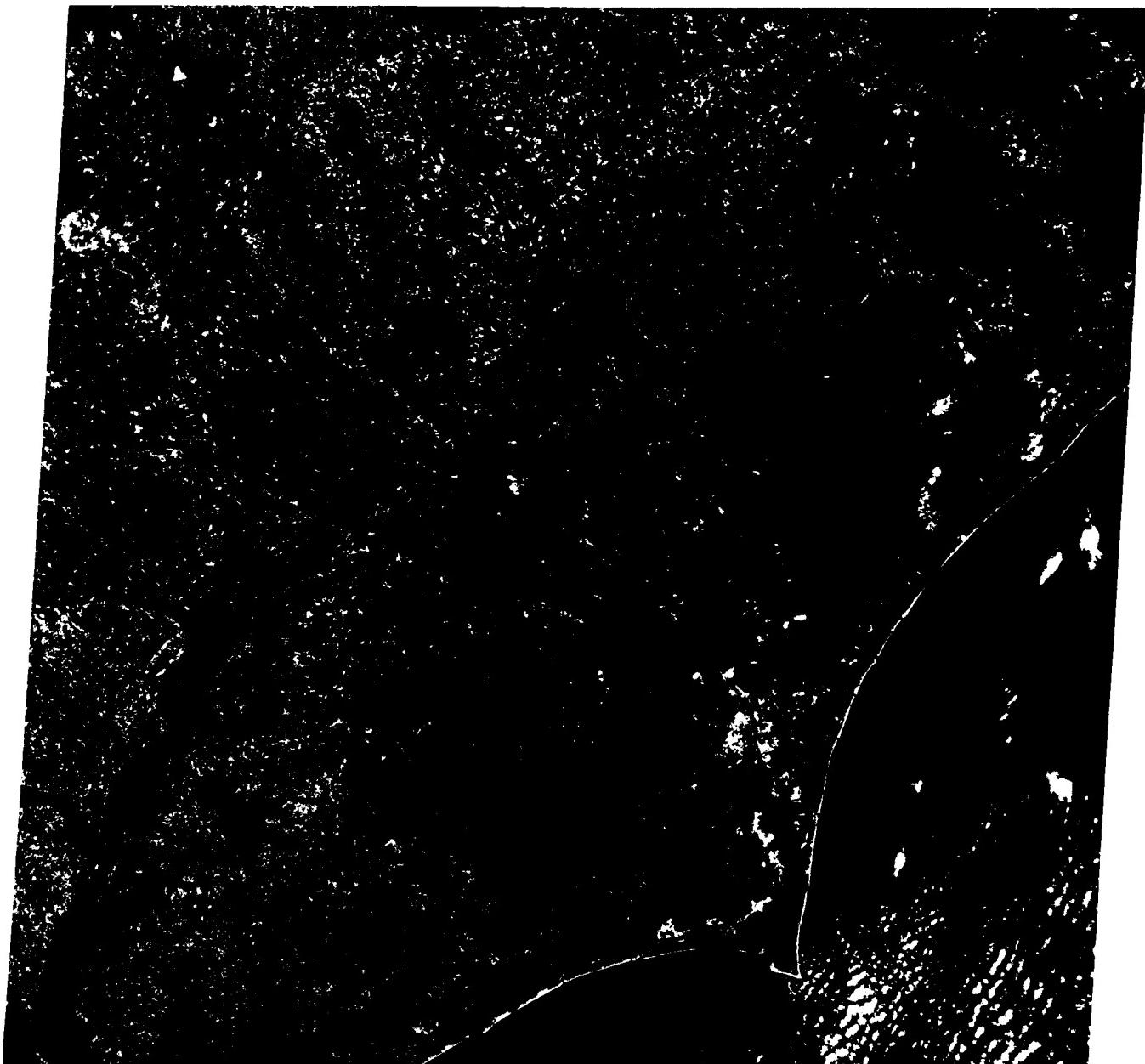


PLATE KL-11

This uncorrected Landsat mosaic illustrates the Beni Basin, which is located west of the Brazilian Shield between the northwest-trending Andean Cordilleras and the Brazilian border. This Basin, which covers most of northeastern Bolivia, constitutes the transition zone between the extensive cratonic region of the Brazilian Shield and the Andean Foredeep or piedmont. The drainage from this huge swamp area, one of the largest in the world, finds its way into the Rio Madeira, which joins the Amazonas River downstream from Manaus, Brazil. An unusual feature of the region is the large number of rectangular straight-edged, often aligned lakes that are contained in an area of roughly 250000 km².

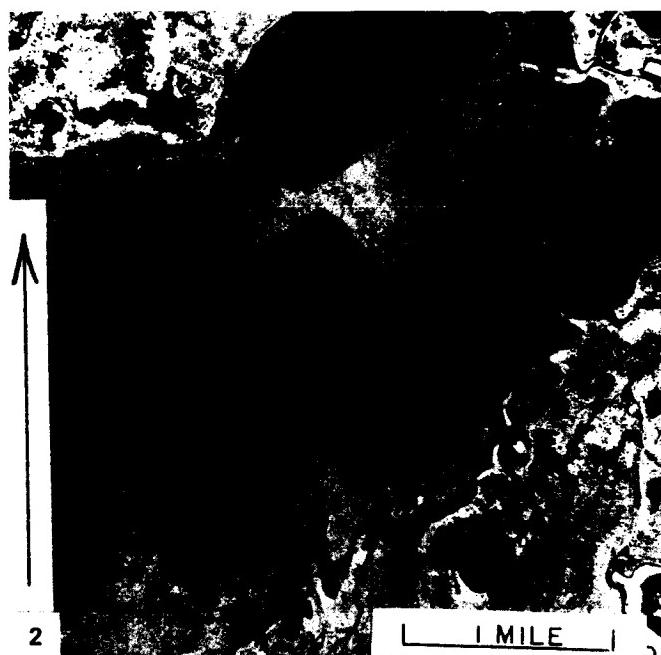
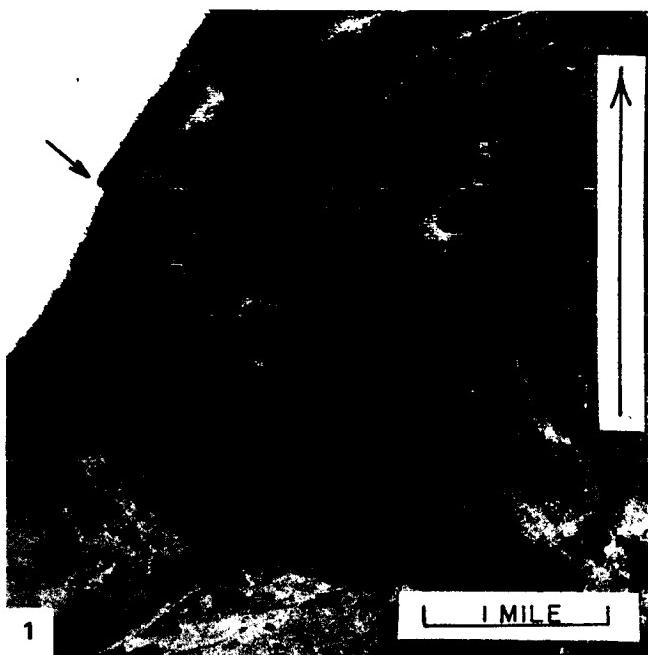
Unfortunately, very little geological information is available about this inaccessible area, which is impassable in the rainy season and, in the dry season, is traversable only by means of a few Indian trails. The only detailed publications of the region easily available in the literature are by Plafker (1964, 1974), who made use of partial airphoto coverage, limited ground surveys, and the results of several exploratory wells. According to Plafker, the Basin is exceptionally flat, the stream gradients are extremely low (less than 20 cm/km), and the water table is less than 1 meter from the surface. Most of the Basin is covered with grassland or reeds, the trees being restricted to the "higher" natural levees rising 1 meter above the plains. Based on soundings in seven lakes and reports from local inhabitants, Plafker (1964) reports that the lakes in cross section are steep-sided with shallow flat bottoms. The deepest lake (10 by 6 km) he sounded had a maximum depth of about 2.5 meters. Basement underneath the Basin sediments appears to be the Brazilian Shield, which plunges to a depth of over 5.5 km along the edge of the Foothills Belt. Seismic results indicate that sediments are flat, lying over a relatively smooth basement undisturbed by any large vertical faults. Stratigraphic drill holes show that the cover consists of poorly consolidated continental sediments of clay, sand, and silts of Quaternary and possible Late Tertiary ages.

BENI BASIN, BOLIVIA

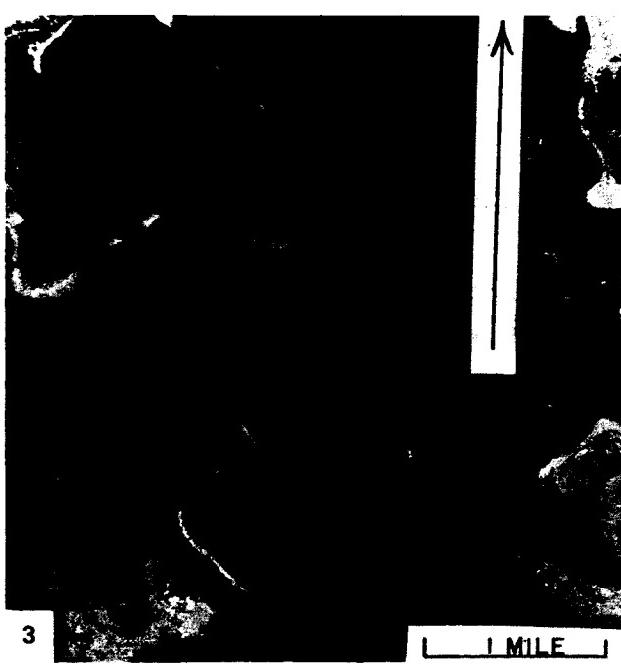
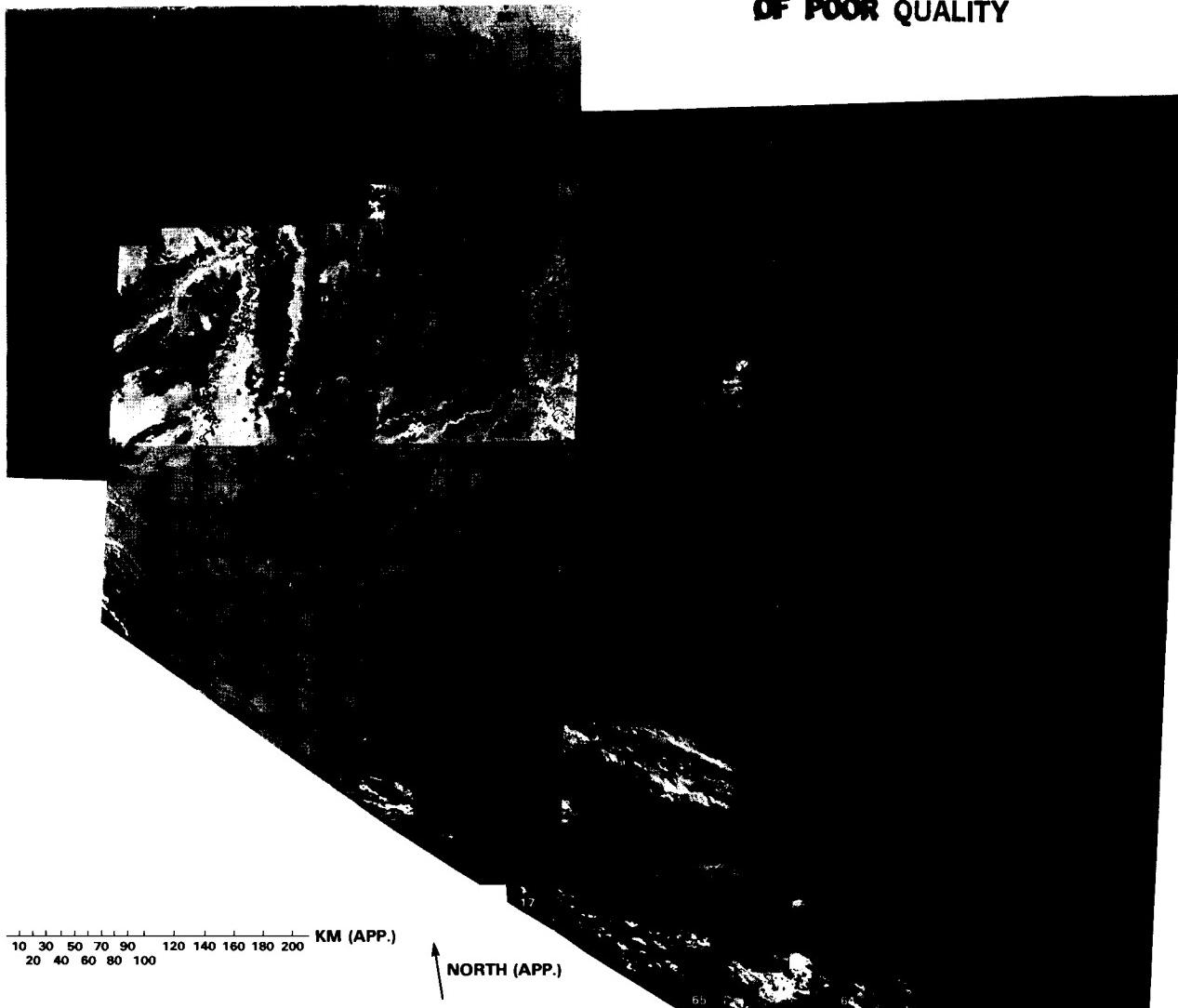
Because some of the lakes occur on the outcropping Brazilian Shield, their formation cannot be attributed to characteristics within the sedimentary column. Instead, it is believed that the Beni lakes reflect a basement (Shield) fracture pattern projected upward through the sediments. The regional drainage pattern further suggests that this fracture pattern has been enhanced by a broad, gentle tectonic uplift occurring across the basin. This upwarping would generate tensile conditions in the basement and facilitate subsidences or sags of fault-bounded basement blocks. The fracture pattern (and uplift) are also compatible with wrench-faulting induced by the faster western motion of the Brazilian Shield relative to the Andean Cordillera.

Globally, the Beni lakes, although unusual, are not unique. Clustered, oriented lakes occur in the Carolina Bays (Plate KL-10), along the Arctic Coastal Plain of Alaska (Plate KL-9), in the Mackenzie Delta of Canada (Plate D-10), and in northwestern Siberia (Plate KL-8). These lakes are generally oval or elliptical in horizontal section and basin-shaped in cross section. Although controversial, the formation of these lakes is attributed primarily to strong wind action, with the long axis of the lakes being perpendicular to the prevailing wind direction. Only the lakes in the Old Crow Plain of the Canadian Yukon closely resemble the Beni lakes. The Old Crow lakes occupy a much smaller area (approximately 7000 km²), but are strongly rectangular in shape with shallow flat bottoms.

Figures KL-11.1, KL-11.2, and KL-11.3 (courtesy of George Plafker) are high-altitude vertical airphotos of individual lakes. In Figure KL-11.2, a large lake cuts across an abandoned channel of the Rio Beni (large river on west side of Basin). The arrow indicates a lateral displacement of shoreline along a northwest-trending lineament. Figure KL-11.2 illustrates a region in the center of the lake region, and Figure KL-11.3 shows a lake near the margin of the Brazilian Shield. (GCW: R. Allenby) **Landsat Mosaic**.



ORIGINAL PAGE IS
OF POOR QUALITY



1 MILE

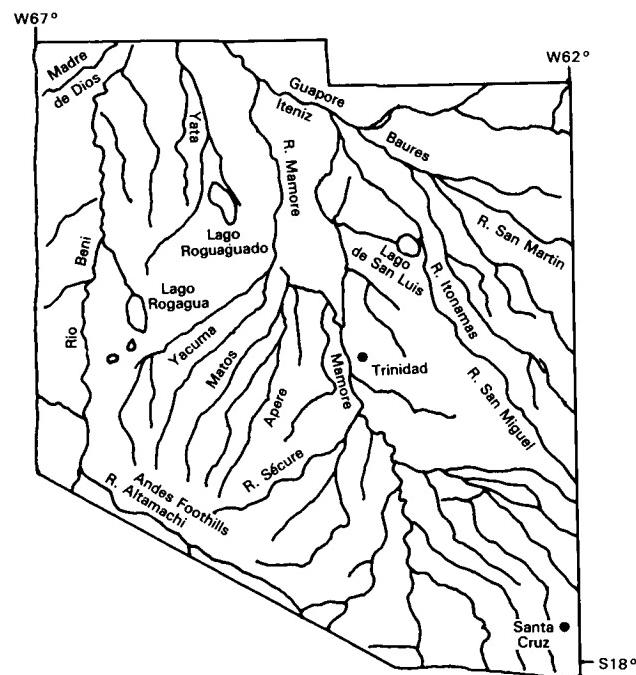


PLATE KL-12

One of the great pluvial lakes of North America is Lake Bonneville, which was first studied and reported in detail by G. K. Gilbert (1890). The modern remnants of this huge lake are the Great Salt Lake, Utah Lake, and Sevier Lake. This image of Utah includes the Utah Lake and the southern end of the Great Salt Lake. These two lakes lie at the northwestern edge of the Great Basin Section in the Basin and Range Province. The Wasatch Mountains front (see index map) marks the boundary between the Great Basin and the Middle Rocky Mountain Province to the east. For the most part, this mountain front conforms with the Wasatch dip-slip normal fault zone that can be traced for many kilometers both north and south of the image. The Wasatch fault scarp is a Late Cenozoic feature. Locally, it displaces moraines of the Bull Lake glaciation and other deposits (Figure KL-12.1). Some segments of the fault are considered to be active.

When Lake Bonneville expanded to its maximum size, it drowned at least 50 percent of the image area. A hint of this is given in Figure KL-12.2, a computer-generated shaded relief image of Utah made by the U. S. Geological Survey at Flagstaff using DMA topographic data tapes, in which the uniform flat tones along the left side of the image correspond roughly with areas likely to have been inundated. Several times in the past, the lake attained an area of about 51 700 km², nearly the size of present-day Lake Michigan, and maintained water depths of as much as 335 m (Morrison, 1965). Eardley et al. (1973) have analyzed in detail a 307-m core that penetrated lake sediments at Burmester, Utah, just south of the Great Salt Lake. The core records about 3 million years of history. Over the last 800 000 years, 28 episodes of subaerial exposure interrupted by lake-fill cycles have been identified. Most investigators agree that the high lake levels are associated with cool climatic intervals in which the volume of precipitation and runoff exceeds the evaporation. During warmer climatic episodes, the relationship was reversed.

There are more than a dozen distinct lake shorelines representing various lake stillstands (Thornbury, 1965). The shorelines form distinct benches or wave-cut platforms such as those along the northern flank of the Traverse Mountains (Figures KL-12.3 and KL-12.4). These former lake levels are usually associated with lake sediments, deltas, and calcareous tufa. The most significant of these shorelines are the Bonneville (1550 m) and Provo (1450 m), which represent the most recent of the high lake levels (Scott,

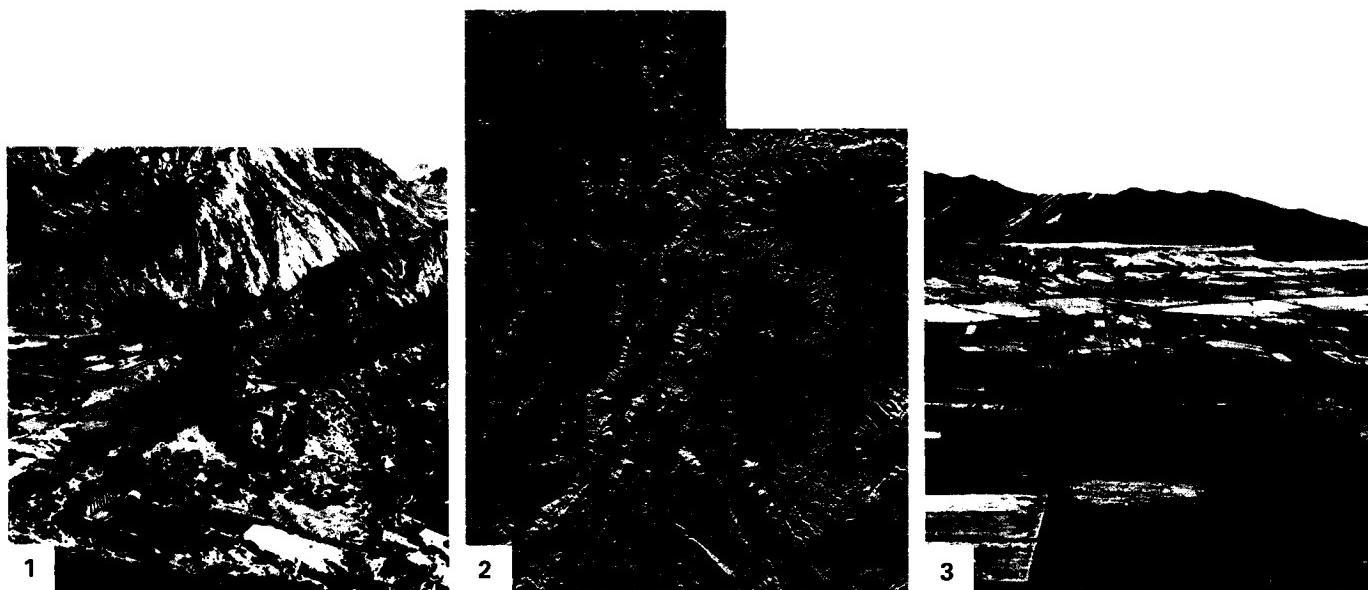
PLUVIAL LAKE BONNEVILLE

et al., 1983). The present level of the Great Salt Lake is about 1285 m, although this periodically fluctuates with the local variations in climate.

Although the shorelines are clearly displayed along much of the eastern margin of the lake basin, considerable controversy has developed over the sequence and timing of the last lake-filling episodes. From a low lake level 11 000 to 12 000 years ago, Morrison (1965) suggests that the lake rose to a 1450-m level 10 000 years ago. Scott (1979), however, shows some evidence that no such rise took place. The history of lake fluctuations is complex, especially when one considers that the last high lake episode would tend to either wipe out or modify features produced by preceding levels and that most of the lake deposits are very similar. The most recent chronostratigraphic work is based on amino acid dating of gastropod shells and radiocarbon dating of wood from lake sediments (Scott et al., 1983). The dates obtained indicate that, within the last 150 000 years, two major episodes of lake filling occurred. The earliest of the two fill cycles ended about 130 000 years ago and attained a high water level just below the present Bonneville shoreline. The Bonneville shoreline represents the highest water level reached during the last lake-fill cycle, which began about 25 000 years ago. This 1550-m level was reached approximately 16 000 years ago and was maintained for about 1500 years (Scott et al., 1983).

The end of the Bonneville stage is associated with the lake overflowing through an outlet into the Snake River drainage at Red Rock Pass in southern Idaho. Rapid downcutting ensued, resulting in the release of 1590 km³ of water, mostly over a period measured in weeks, to produce the Bonneville Flood (Malde, 1968). The readjusted lake level, 100 m below the Bonneville shorelines, was maintained for possibly 2000 years to create the Provo shoreline. This was followed by a steady decline of the lake level until 11 000 years ago when the water level was just 9 m above the present Great Salt Lake (Scott et al., 1983).

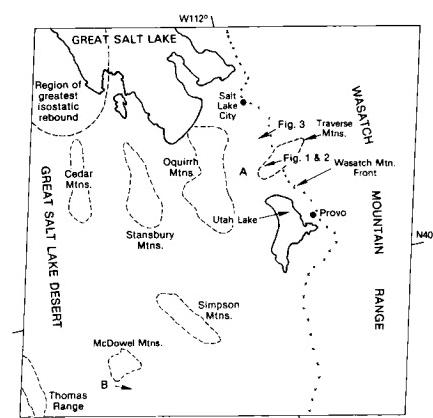
Former lake shorelines are not the kind of geomorphic feature that readily shows up at the scale of Landsat imagery; however, careful examination of the Plate image reveals the hint of shorelines in the Traverse Mountains (A on index map) and in the McDowell Mountains (B), showing the vast extent of the Pleistocene lake. **Landsat 10051-17420-7, September 12, 1972.**



ORIGINAL PAGE IS
OF POOR QUALITY



4



Salar de Uyuni and Salar de Coipasa are salt pans or playas in southwestern Bolivia that lie on the central Andean Altiplano at an altitude of over 3600 m. More than 75 playas exist in closed basins, making the Altiplano the largest basin of interior drainage in South America. However, Salar de Uyuni is by far the largest of these playas and is considered the largest playa in the world with an area of 9000 km² (Rettig et al., 1980).

This Landsat color image covers the southern part of the Altiplano Massif, a structurally depressed basin. It is bordered on the west by the Cordillera Occidental, a plateau located mainly in Chile that is comprised of Tertiary and Quaternary volcanics. To the east of the Altiplano is the Cordillera Oriental, a complexly folded and faulted stack of Phanerozoic sediments interlaced by subsequent intrusives. Northeast of the image, the Cordillera Oriental in Bolivia, known for its tin deposits, produces more than 16 percent of the world's tin (Kidron and Segal, 1981).

The Altiplano salars, in this image and south beyond the image, are partially filled with alluvial and glacial debris and are underlain by Tertiary and Quaternary rhyolitic ashflow tuffs (Figure KL-13.1). Numerous volcanoes can be identified (Figure KL-13.2), some attaining altitudes greater than 5300 m above sea level, such as Cerro Tumapa (see index map). To the south, a number of volcanoes rise more than 6000 m above sea level.

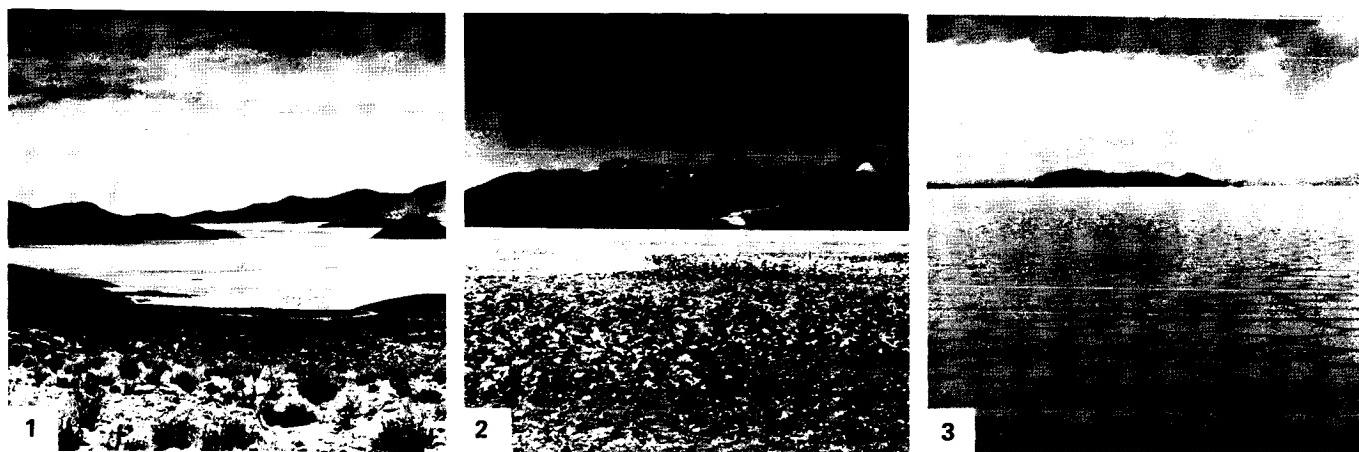
The image area is semiarid, with an average annual rainfall of about 300 mm. Thick deposits of evaporites suggest that this aridity has prevailed for several thousand years. The Salar de Uyuni is thought to have been a closed basin for the last 10000 years or since the last glacial stage (Rettig et al., 1980). At present, the only water inflow is from the Rio Grande de Lipez and from some small drainages to the east. At higher lake levels in the past, water from Salar de Coipasa, which is about 7 m higher, flowed into Salar de Uyuni. During the rainy season from December to March, the playas may be covered with brine to depths of 25 cm; however, during the dry season, the brine evaporates to a position at or below the surface.

The surface is an evaporite crust of predominantly halite that is very porous and 10 m thick in some places. The repeated wet/dry cycles have produced an exceptionally smooth surface with a relief measured in centimeters (Figure KL-13.3).

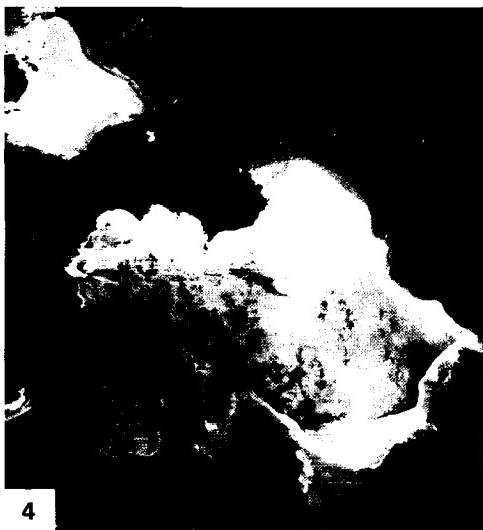
During the Late Pleistocene, most of the image area was drowned under a huge lake, called Lago Minchin, with a surface area probably exceeding 43000 km². This lake was the more southern of the two lakes known to exist then on the Altiplano Plateau. The northern lake, Lake Ballivian, included the present-day Lake Titicaca (see Plate KL-15). The southern lake finally diminished in size toward the end of the Pleistocene (15000 years B. P.) from 3760 m above sea level to 3720 m about 10000 years B. P. As the lake shrunk in size, large quantities of calcium carbonate were deposited to form marginal algal limestones. These limestones form terraces that mark the high lake levels (Erickson et al., 1978). The present elevation of Salar De Uyuni at 3653 m indicates that lake depths well over 100 m were attained during maximum lake size.

As the calcium carbonate was removed from the lake, the remaining water became progressively enriched in the more soluble saline components like chloride and sulfate. The resulting evaporites were concentrated with gypsum and finally halite, forming a zoned gypsum-halite crust (Erickson et al., 1978).

In the last few years, the southern Salar de Uyuni brines have been found to contain anomalous concentrations of lithium from 200 to 2000 ppm (Rettig et al., 1980). The source of the lithium is apparently derived from the drainage area of the Rio Grande de Lipez, which feeds into the playa. For many years, the playa has been the singular source of salt for Bolivia. More information on distribution of the salts in the salar is expressed in a color-ratio enhancement (4/5 = blue; 5/6 = green; 6/7 = red) of the subscene shown as Figure KL-13.4. Landsat 1243-13595, March 23, 1973.



ORIGINAL PAGE
COLOR PHOTOGRAPH



4

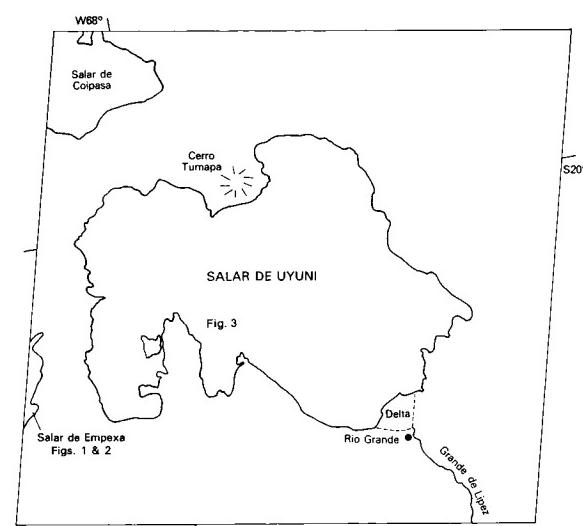


PLATE KL-14

LAKE BAIKAL

Lake Baikal lies in the southern part of eastern Siberia, U.S.S.R. It is the deepest continental body of water on Earth, having a maximum depth of 1741 m. Its area extends over 31 500 km², being about 636 km in length and averaging 48 km in width. This huge lake embodies one-fifth of the world's fresh water, which is as much as the five Great Lakes of the United States combined. The lake maintains an elevation of 454 m and is surrounded by mountains that rise to as high as 2900 m above sea level (Encyclopedia Britannica, 1980).

The lake is far enough north in latitude (N52°–N56°) that it is frozen from January through May. Annual precipitation there is 200 to 340 mm/yr, which falls mostly in July and August.

Much of the western edge of the lake is bounded by the Primovskiy Fault, which is clearly displayed on the image (see index map), and marks the boundary between the Siberian Platform to the northwest and the pre-Cenozoic Sayan/Baikal fold belt to the southeast (Zamarayev and Ruzhich, 1978). The shoreline on the west consists of cliffs and hills (Figures KL-14.1 and KL-14.2) that express the influence of this fault on the topography. Lake Baikal is located within a rift 2000 km in length and exhibits many of the same characteristics as the East African rift in Kenya (Logatchev et al., 1983). For example, both have anomalous heat flows, are bounded by major extensional fault systems, are associated with basaltic volcanism and deep-seated dike systems, display a thinning of the crust, and are zones of concentrated seismic activity (Logatchev et al., 1983). Lake Tanganyika (Figure KL-14.3), in the western arm of the African Rift, is in some respects an analog to Lake Baikal.

From the image, it can be seen that the lake boundaries conform to the tectonic fabric of the surrounding terrain (see index map), which, according to Zamarayev and Ruzhich (1978), predates the rift and may have influenced the rift orientation. The Baikal rift is not a simple rift valley, but is a complex system of block-faulted depressions. The lake occupies the southwestern part of the Baikal depression, which consists of three en echelon grabens separated by two topographic highs, one located south-

west on the Selenga Delta and the other along the Olkhon Island and Svyatoy Nos Peninsula (Tapponnier and Molnar, 1979).

Lake Baikal began to form at least by Late Oligocene to Early Miocene based on the Oligocene/Miocene sediments recovered from the rift floor (Tapponnier and Molnar, 1979), which would make the lake 20 to 25 million years old and thus, the oldest documented lake on Earth. Continental sediments in the Baikal depressions are subdivided into two series. The lower series consists of Oligocene to Early Pliocene clastics mixed with carbonates and coals. The upper series is Middle Pliocene to Quaternary in age and consists of coarser clastics (Logatchev et al., 1983). In places, the sedimentary rocks within the lake basin may attain thicknesses of up to 6000 m (Encyclopedia Britannica, 1980).

Cenozoic volcanism in the Baikal depression, whose total volume is less than 6000 km³ (20 times less than the volume found in the East African Rift in Kenya), is located principally along the margins or shoulders of the rift. Seismic studies by the Russians indicate that the crustal thickness within the Baikal Rift depression is about 35 km, whereas the shoulders display thicknesses of 42 to 46 km. Logatchev et al. (1983) suggest that plastic extension of as much as 15 km has taken place beneath the rift proper. The Baikal rift is believed to be the surface expression of a deep-seated asthenospheric upwelling and, because of its similarities to the Kenya rift, is believed to be an example of an active rift system.

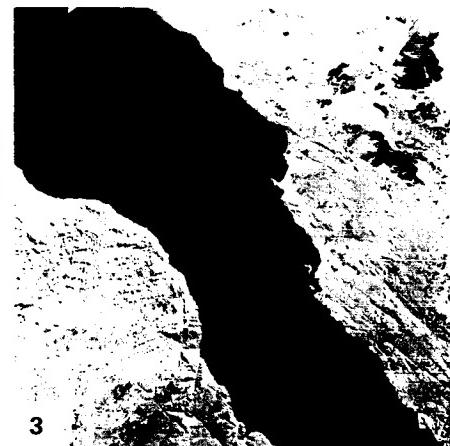
Baikal is one of three large lake systems in the Soviet Union. A second, the Aral Sea (Plate D-15), is the fourth largest lake in the world, but is quite shallow. A third, Lake Balkhash (Figure KL-14.4), is elongate (600 by 30 to 50 km) like Baikal, but is shallow (maximum depth 12 m) like Aral. Lake Balkhash occupies a shallow structural trough (graben?) backfilled with sediments carried in by the Ili River from the high Tian Shan along the Russian border. Despite lack of outlet drainage, the Balkhash waters have a low saline content (but high potassium), yet have led to conditions favoring precipitation of dolomite in modern times.
Landsat 2150-03123-5, June 21, 1975.



1

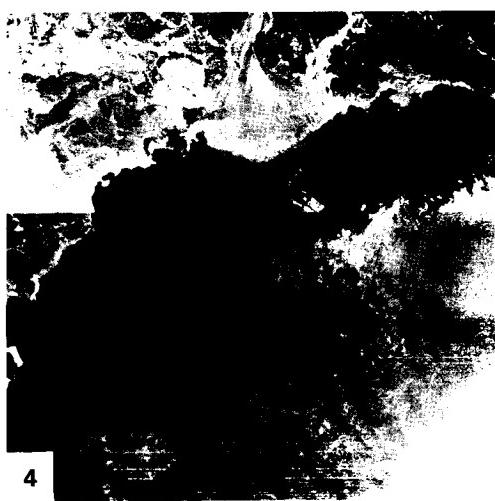


2

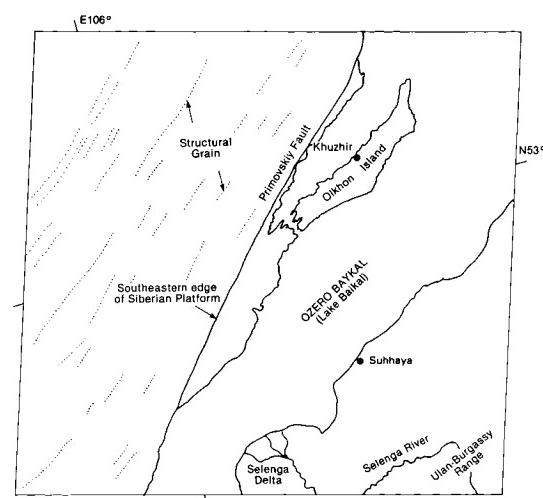


3

ORIGINAL PAGE
COLOR PHOTOGRAPH



4



Lake Titicaca lies within a structural depression elongated in a northwest-southeast direction and represents the most northern portion of the Altiplano of Peru and Bolivia. The snow-covered mountains seen in the northeastern portion of the image are part of the Cordillera Oriental, a mass of relatively competent Paleozoic black shales, slates, phyllites, and quartzites that have been crosscut by Tertiary intrusives. To the southwest of the lake, volcanic mountains lie within the Cordillera Occidental, a volcanic plateau. Along portions of the western lake edge, Tertiary andesite and basalt flows comprise the Sillapaca Group. The Altiplano represents an alluvial-lacustrine plain overlying Late Paleozoic through Tertiary sedimentary rocks.

Lake Titicaca is considered the largest and deepest lake in the world at comparable altitudes. It occupies an area of more than 8300 km², which is slightly less than the size of Jamaica. Its surface stands at an altitude of 3804 m, and its measured depth exceeds 300 m (Rettig et al., 1980). The lake is a freshwater body, in contrast to the Salar de Uyuni (Plate KL-13). The lake exhibits centripetal drainage and has only one outlet, the Rio Desaguadero at the southeastern end, which drains into Lake Poopo 270 km southeast of the image. Lake Poopo is one of many saline lakes on the Altiplano. In spite of receiving only 60 to 80 cm of precipitation per year, Lake Titicaca has been able to maintain its present level with only occasional fluctuations. This may be due, in part, to its receiving nearly all the precipitation during the summer. During the winter when the climate is dry, the evaporation rate is relatively low.

Lake strandlines, wave cut benches, and lacustrine sediments found about 100 m above the existing lake level are the erosional and depositional remnants of the ancestral Lake Ballivian. This Early Pleistocene lake was connected through Rio Desaguadero to the vast pre-Minchin Lake that existed at the same time to the south and encompassed today's Lake Poopo, Salar de Coipasa, and Salar de Uyuni.

Some early investigators (Steinmann, 1929; Oppenheim, 1945) suggest a glacial origin for Lake Titicaca; however, Newell (1949), who has published the most comprehensive study on the region, finds no evidence to support this hypothesis. In fact, no glacial deposits have been recognized below 4000 m of elevation. Newell, who did his work before the era of plate tectonics, found evidence that the Titicaca trough lies between opposing sets of high-angle overthrust faults produced by compression of the deep sedimentary basin beneath the lake. The present consensus about the causes of the compression is the westward drift of the South American Plate, which overrides the Nazca Plate along the Pacific margin. The disordered structure of the region is truncated by the remarkable Puna erosion surface 200 to 300 m above the lake level. This surface cuts across Early Tertiary and other rocks. As with many mobile belts, the latest orogenic episodes have been regional uparching, accompanied by block-faulting, with volcanism and hypabyssal intrusions dominant in the Western Cordillera near the continental margin (N. D. Newell, 1984, written communication).

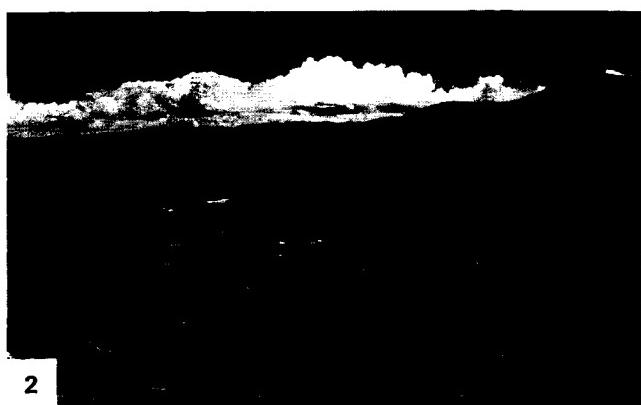
Recognition of the tectonic origin is suggested from close examination of the Landsat image. The northwest-southeast structural trend is quite evident on both sides of the lake at the northeast end. The drowned hogbacks accentuate this structural trend and indicate that fluvial erosion operated below the present lake level some time in the past (Figure KL-15.1). Further evidence of sublake level fluvial erosion is the entrenched canyon cut in bedrock at the Strait of Tiquina (Figure KL-15.2; Newell, 1949). A lower lake level evidently existed during more arid periods of the Pleistocene, probably during major interglacials.

Of interest is the oil field around Perin, which produced petroleum between 1906 and 1915 from pay horizons at 3800 m, making this the highest elevation producing zone in the world. Landsat 10443-14073-7, October 9, 1973.

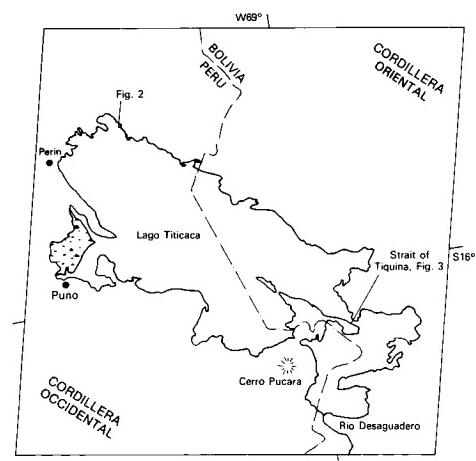


1

ORIGINAL PAGE IS
OF POOR QUALITY



2



REFERENCES

- Black, R. F., Thaw depressions and thaw lakes, a review, *Bulletyn Peryglacialny*, No. 19, 131-150, 1969.
- Black, R. F., and W. L. Barksdale, Oriented lakes of northern Alaska, *J. Geol.*, **57**, 105-118, 1949.
- Bloom, A. L., *Geomorphology: A Systematic Analysis of Late Cenozoic Landforms*, 510 pp., Prentice-Hall, Englewood Cliffs, New Jersey, 1978.
- Bogli, A., *Karst Hydrology and Physical Speleology*, translated by J. C. Schmid, 284 pp., Springer-Verlag, New York, 1980.
- Carson, C. E., and K. M. Hussey, The oriented lakes of arctic Alaska, *J. Geol.*, **70**, 417-439, 1962.
- Corbel, J., Erosion en terrain calcaire, *Annual Geogr.*, **366**, 97-120, 1959.
- Costa, J. E., and V. R. Baker, *Surficial Geology, Building with the Earth*, 498 pp., John Wiley, New York, 1981.
- Crittenden, M. D., Jr., New data on the isostatic deformation of Lake Bonneville, *U. S. Geol. Surv. Prof. Paper*, **454-E**, 31 pp., 1963.
- Czudek, T., and Demek, J., Thermokarst in Siberia and its influence on the development of lowland relief, *Quaternary Res.*, **1**, 103-120, 1970.
- Daoxian, Y., *A Brief Introduction to China's Research in Karst*, 14 pp., Guilin, People's Republic of China, Inst. of Karst Geology, Ministry of Geol. and Min. Resources, 1981.
- Daoxian, Y., *Problems of Environmental Protection of Karst Area*, 14 pp., Guilin, People's Republic of China, Inst. of Karst Geology, Ministry of Geol. and Min. Resources, 1983.
- Davis, W. M., On the classification of lake basins, *Proc. Boston Soc. Nat. Hist.*, **21**, 315-381, 1882.
- Day, M., The morphology and hydrology of some Jamaican karst depressions, *Earth Surface Processes*, **1**, 111-129, 1976.
- Demek, J., I. Garns, I. Vaptzarov, Balkan Peninsula, *Geomorphology of Europe*, edited by C. Embleton, pp. 374-386, Macmillan Publishers, London, 1984.
- Dell Publishing Co., Inc., *American Heritage Dictionary*, New York, 880 pp., 1983.
- Eardley A. J., et al., Lake cycles in the Bonneville Basin, Utah, *Geol. Soc. Amer. Bull.*, **84**, 211-216, 1973.
- Encyclopedia Britannica*, New York, **2**, p. 596, 1980.
- Ericksen, G. E., J. D. Vine, and A. Raul Ballon, Chemical composition and distribution of lithium-rich brines in Salar de Uyuni and nearby salars in southwestern Bolivia, *Energy*, **3**, 355-363, 1978.
- Fetter, C. W., Jr., *Applied Hydrogeology*, 488 pp., Charles E. Merrill Pub. Co., Columbus, Ohio, 1980.
- Foose, R. M., Anywhere sinking can be fast or slow, *Geotimes*, **26**, 21-24, 1981.
- Gilbert, G. K., Lake Bonneville, *U. S. Geol. Surv. Monograph*, **1**, 438 pp., 1890.
- Hanshaw, B. B., and W. Back, Chemical mass-wasting of the northern Yucatan Peninsula by groundwater dissolution, *Geology*, **8**, 222-224, 1980.
- Herak, M., Karst of Yugoslavia, in *Karst: Important Karst Regions of the Northern Hemisphere*, edited by M. Herak and V. T. Stringfield, pp. 25-83, Elsevier Pub. Co., New York, 1972.
- Hoare, J. M., and W. Conrad, *Geology of the Goodnews and Hagemeister Quadrangle, Alaska*, U. S. Geol. Surv. Open File Report, 789 pp., 1978.
- Hutchinson, G. E., *A Treatise on Limnology, Vol 1: Geography, Physics and Chemistry*, 1015 pp., John Wiley, New York, 1957.
- Jakucs, L., *Morphogenetics of Karst Regions*, 284 pp., John Wiley, Halsted Press, New York, 1977.
- Jennings, J. N., *Karst*, 252 pp., The M. I. T. Press, Cambridge, Massachusetts, 1971.
- Kaczorowski, R. T., Origin of the Carolina Bays, in *Terrigenous Clastic Depositional Environments, Some Modern Examples*, edited by M. O. Hayes and T. W. Kana, pp. II 16-II 36, Coastal Res. Div. of South Carolina, Technical Report 11-CRD, 1976.
- Kidron, M., and R. Segal, *The State of the World Atlas*, Pan Books, London, 1981.
- Lehmann, H., Kegelkarst and tropngrenze, *Tubinger Geogr. Stud.*, **34**, 107-112, 1970.
- Logatchev, N. A., Y. A. Zorin, and V. A. Rogozhina, Baikal Rift: active or passive? — Comparison of the Baikal and Kenya Rift zones, *Tectonophysics*, **94**, 223-240, 1983.
- Lowry, D. C., and J. N. Jennings, The Nullarbor karst of Australia, *Z. Geomorph.*, No. 18, 35-81, 1974.
- Malde, H. E., The catastrophic Late Pleistocene Bonneville Flood in the Snake River Plain, Idaho, *U.S. Geol. Surv. Prof. Paper*, **596**, 52 pp., 1968.

- Mertie, J. B., Jr., The Nushagak District, Alaska, *U. S. Geol. Surv. Bull.*, **903**, 96 pp., 1938.
- Morrison, R. B., Quaternary geology of the Great Basin, in *The Quaternary of the United States*, edited by H. E. Wright and D. G. Frey, pp. 265–285, Princeton Univ. Press, Princeton, New Jersey, 1965.
- Newell, N. D., Geology of the Lake Titicaca region, Peru and Bolivia, *Geol. Soc. Amer. Mem.*, **36**, 111 pp., 1949.
- Oppenheim, V., Las glaciaciones en el Peru, *Bol. Soc. Geol. Peru*, **18**, 37–43, 1945.
- Pettijohn, F. J., *Sedimentary Rocks*, 628 pp., Harper & Row, New York, 1975.
- Péwé, T. L., *The Periglacial Environment in North America During Wisconsin Time, in the Late Pleistocene*, edited by S. C. Porter, pp. 157–189, Univ. of Minnesota Press, Minneapolis, 1983.
- Plafker, G., Oriented lakes and lineaments of northeastern Bolivia, *Geol. Soc. Amer. Bull.*, **75**, 503–522, 1964.
- Plafker, G., Tectonic implications of oriented lakes and lineaments in northeastern Bolivia, in *Proc. First International Conf. on New Basement Tectonics*, edited by R. A. Hodgson, S. P. Gay, Jr., and J. Y. Benjamins, pp. 519–527, Utah Geological Assn. Pub. 5, 1974.
- Price, W. A., Carolina Bays, in *Encyclopedia of Geomorphology*, edited by R. W. Fairbridge, p. 784, Reinhold Book Corp., New York, 1968a.
- Price, W. A., Oriented lakes, in *Encyclopedia of Geomorphology*, edited by R. W. Fairbridge, pp. 784–796, Reinhold Book Corp., New York, 1968b.
- Prouty, W. F., Carolina Bays and their origin, *Geol. Soc. Amer. Bull.*, **63**, 167–224, 1952.
- Randazzo, A. F., and E. W. Hickey, Dolomitization in the Floridan Aquifer, *Amer. J. Sci.*, **278**, 1177–1184, 1978.
- Randazzo, A. F., and H. C. Saroop, Sedimentology and paleoecology of Middle Eocene carbonate shoreline sequences, Crystal River, Florida, U.S.A., *Sedimentary Geology*, **15**, 259–291, 1976.
- Rettig, S. L., B. F. Jones, and F. Risacher, Geochemical evolution of brines in the Salar of Uyuni, Bolivia, *Chem. Geol.*, **30**, 57–79, 1980.
- Ritter, D. F., *Process Geomorphology*, 600 pp., Wm. C. Brown, New York, 1978.
- Roglic, J., Historical review of morphologic concepts, in *Karst: Important Karst Regions of the Northern Hemisphere*, edited by M. Herak and V. T. Stringfield, pp. 1–18, Elsevier Pub. Co., Amsterdam, 1972.
- Scott, W. E., Evaluation of evidence for controversial rise of Lake Bonneville about 10,000 years ago (abstract), *Geol. Soc. Amer. Abst. with Programs*, **11**, 301–302, 1979.
- Scott, W. E., W. D. McCoy, R. R. Shroba, and M. Rukbin, Reinterpretation of the exposed record of the last two cycles of Lake Bonneville, Western United States, *Quaternary Res.*, **20**, 261–285, 1983.
- Smith, A. J., Lakes, in *Encyclopedia of Geomorphology*, edited by R. W. Fairbridge, pp. 598–603, Reinhold Book Corp., New York, 1968.
- Smith, D. I., and T. C. Atkinson, Process, landforms and climate in limestone regions, in *Geomorphology and Climate*, edited by E. Derbyshire, pp. 367–409, John Wiley, London, 1976.
- Southworth, C. S., Structural and hydrogeologic applications of remote sensing data, eastern Yucatan Peninsula, Mexico, in *Sinkholes: Their Geology, Engineering and Environmental Impact*, edited by B. F. Beck, pp. 59–64, A. A. Balkema, Boston, 1984.
- Steinmann, G., *Geologie von Peru*, Heidelberg, Germany, 448 pp., 1929.
- Suslov, S. P., *Physical Geography of Asiatic Russia*, 594 pp., W. H. Freeman, San Francisco, 1961.
- Sweeting, M. M., The karstlands of Jamaica, *Geographical J.*, **CXXIV**, 184–199, 1958.
- Sweeting, M. M., *Karst Landforms*, 362 pp., Macmillan Press, Ltd., London, 1972.
- Sweeting, M. M., Landscape of one-seventh of China, *Geographical Magazine*, **50**, 393–400, 1978.
- Tapponnier, P., and P. Molnar, Active faulting and Cenozoic tectonics of the Tien Shan, Mongolia, and Baykal Regions, *J. Geophys. Res.*, **84**, 3425–3459, 1979.
- Thom, B. G., Carolina Bays in Horry and Marion Counties, South Carolina, *Geol. Soc. Amer. Bull.*, **81**, 783–814, 1970.
- Thornbury, W. D., *Regional Geomorphology of the United States*, 605 pp., John Wiley, New York, 1965.
- Thornbury, W. D., *Principles of Geomorphology*, 594 pp., John Wiley, New York, 1969.
- Twidale, C. R., *Geomorphology, with Special Reference to Australia*, 406 pp., Thomas Nelson Australia, Sydney, Australia, 1973.
- Versey, H. R., Karst of Jamaica, in *Karst: Important Karst Regions of the Northern Hemisphere*, edited by M. Herak and V. T. Stringfield, pp. 445–466, Elsevier Pub. Co., New York, 1972.
- Washburn, A. L., *Geocryology: A Survey of Periglacial Processes and Environments*, 406 pp., Edward Arnold, London, 1979.
- Washburn, A. L., *Geocryology*, 406 pp., John Wiley, New York, 1980.
- Weidie, A. E., W. C. Ward, and R. H. Marshall, Geology of Yucatan Platform, in *Geology and Hydrology of Northeastern Yucatan*, edited by W. C. Ward and A. E. Weidie, pp. 3–29, New Orleans Geol. Soc., 1978.
- West, R. C., Physical geography of the Yucatan Platform, in *Yucatan Guidebook*, 2nd ed., edited by A. E. Weidie, pp. 58–63, New Orleans Geol. Soc., 1967.

White, W. A., The geomorphology of the Florida peninsula, *Florida Bur. Geol. Bull.*, 51, 164 pp., 1970.

Windham, S. R., and K. M. Campbell, In Florida, sinkholes follow the pattern, *Geotimes*, 26, 20-21, 1981.

Zamarayev, W. M., and V. V. Ruzhich, On relationships between the Baikal Rift and ancient structures, *Tectonophysics*, 45, 41-47, 1978.

Zans, V. A., Major structural features of Jamaica, in *Caribbean Geol. Conf., Report of 1st Meeting*, Antigua, British West Indies, Geol. Surv., Georgetown, 1958.

8

EOLIAN LANDFORMS

*Alta S. Walker**

GLOBAL ATMOSPHERIC CIRCULATION

We live at the bottom of a gaseous envelope that is gravitationally bound to the planet Earth. Our atmosphere is generally separated into two zones—the homosphere at low altitudes where mixing produces a uniform composition of gases, and the upper heterosphere. The homosphere consists of 78 percent nitrogen, 21 percent oxygen, and 0.9 percent argon. Water vapor, carbon dioxide (0.03%), and other molecules are present as minor constituents. The lowest layer of the homosphere, which contains about 80 to 90 percent of the mass of the atmosphere, is the troposphere, which is defined as the layer where temperature decreases with increasing elevation. Most of the Earth's weather occurs in the troposphere. The heterosphere is divided into four subzones, each with a distinct composition. Above the heterosphere is the exosphere, which is the top of the atmosphere. It begins about 600 km above the surface of the Earth and extends up to the altitude at which the average density of the atmosphere falls to the average density of the interplanetary medium. Using this criterion, the upper boundary of the atmosphere is about 20000 km above the surface of the Earth (Smith and West, 1983).

The circulation of a planetary atmosphere is a complex process because of rotation of the planet and inclination of its axis. The Earth's axis is inclined $23\frac{1}{2}$ ° from the ecliptic. Vertical rays of the Sun strike $23\frac{1}{2}$ °N latitude, the Tropic of Cancer, at summer solstice in late June. At winter solstice, the vertical rays strike $23\frac{1}{2}$ °S, the Tropic of Capricorn. The inclination of the axis causes seasonal changes in the global circulation system.

The circulation of the atmosphere is further affected by the rotation of the Earth, which introduces the Coriolis Effect. The Coriolis Effect illustrates Newton's first law: a body in motion will remain in motion in the same direction unless acted on by some outside force. The rotational velocity of a planet is zero at the poles and maximum at the equator. If a missile were fired true north from the equator, it would acquire the rotational velocity of the equator. As the missile progresses northward, it would retain the rotational velocity of the equator. This velocity would be greater than the rotational velocity of the Earth under it. Inasmuch as the Earth rotates west to east, the missile would be deflected toward the east. The Coriolis Effect causes moving objects to be deflected toward the right in the northern hemisphere and toward the left in the southern hemisphere.

The global circulation pattern of Earth is illustrated in Figure 8-1. The circulation of air between the hot equatorial region and the cold polar regions creates pressure belts that in-

fluence weather. In 1735, George Hadley suggested that one large convection cell existed in each hemisphere for a nonrotating Earth. According to Hadley, the simple convection cell consisted of hot air rising at the equator, cooling as it moves toward the poles, descending as cold air over the poles, and warming as it moves over the surface toward the equator.

In the zone between the equator and about 30° latitude, the surface atmospheric flow is toward the equator, and the flow aloft is poleward. This area is referred to as the Intertropical Convergence Zone (ITCZ). It is an equatorial low and is a zone of calms or light variable winds, known to mariners as the doldrums. The location of the ITCZ varies seasonally and has been measured as far north as 40°N during a northern hemisphere summer (Lutgens and Tarbuck, 1979). Its migration significantly modifies precipitation, with the length of the dry season depending primarily on the distance of an area from the ITCZ.

Around 30° latitude, the poleward airflow begins to subside in subtropical high-pressure belts. The subsiding air is relatively dry because its moisture has been released near the equator in the tropical rainforests. Near the center of this high-pressure zone of descending air, called the Horse Latitudes, the winds at the surface are weak and variable. The name for this area is believed to have been given by Colonial sailors who, when sometimes becalmed at these latitudes while crossing the oceans with horses as cargo, were forced to throw a few of them overboard to conserve water. Over the continents, this subsidence zone is the site of many of the world's deserts.

The subsiding air that then flows equatorward from the subtropical high-pressure belts is deflected toward the west in both hemispheres by the Coriolis Effect. Because wind direction is the direction from which the wind is blowing, these winds are referred to as the northeast trade winds in the northern hemisphere and the southeast trade winds in the southern hemisphere. The trade winds meet at the doldrums.

The poleward surface flow away from the equator beyond the Horse Latitudes produces winds referred to as westerlies. They meet easterlies from the polar highs at a subpolar low-convergence zone at about 50 to 60 degrees latitude.

The atmospheric circulation systems of other terrestrial planets with gaseous envelopes also depend on the orbit and inclination of the planets and the composition parameters of the atmospheres. Leovy (1977) finds that the atmosphere of Mars behaves like a rarefied version of the Earth's atmosphere. Because of its retrograde rotation and extremely high pressure, the atmospheric dynamics of Venus are considerably different from those of the Earth. Seasonal variations on Venus are negligible because of its small orbital eccentricity and the 3° inclination of its axis from the ecliptic. In addition, the 243-day rotation minimizes the Coriolis Effect. At cloud height, the atmosphere circulates around

*U.S. Geological Survey, Code MS 927, Reston, Virginia 22092.

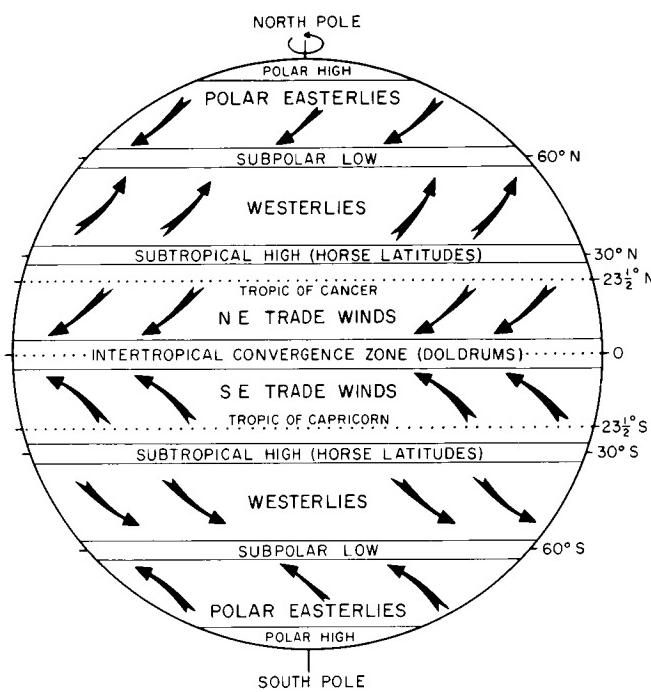


Figure 8-1. Global circulation patterns.

the planet in about 4 days. The complex global circulation patterns of the atmosphere of Venus are not fully understood (Schubert, 1983).

Fujita (1981) proposes that a planet's atmospheric motion be divided into five scales. The largest scale is the equator length, for the Earth, 40 000 km. The dimensions of the scales decrease by two orders of magnitude per scale, and the smallest scale on Earth has a maximum length of 40 cm.

Wind is a stream of air flowing because of a difference in atmospheric pressure between two points. Winds blow from areas of high pressure to areas of low pressure. Near the ground, wind is affected by friction and by changes in topography. Winds may be seasonal, sporadic, or diurnal. Their intensities on Earth range from gentle breezes to tornadoes with speeds in excess of 60 m/sec (Fujita, 1981).

A BRIEF INTRODUCTION TO DESERTS

Approximately one-third of the land surface of this planet is considered to be desert-barren land with meager rainfall that can support only sparse vegetation and a limited population. A widely accepted arid-zone classification system was suggested by Meigs (1953) and is shown in Figure 8-2.

Desert regions on Earth have been divided into three categories according to the amount of precipitation they receive. Extremely arid lands have at least 12 consecutive months without rainfall, arid lands have less than 250 mm of annual rainfall, and semiarid lands have a mean annual precipitation between 250 and 500 mm. Arid and extremely arid land are deserts, whereas semiarid grasslands generally are referred to as steppes. Savannas, which are treeless plains with distinct wet and dry seasons, lie between deserts and tropical rain forests.

Trade-Wind Deserts

The trade winds are two belts on the equatorial sides of the Horse Latitudes. As these surface winds move from higher

to lower latitudes, they become warmer. In addition to being dry, the winds dissipate cloud cover, allowing more sunlight to heat the land. Trade-wind deserts are sometimes referred to as low-latitude deserts.

Most of the major deserts of the world lie in areas crossed by the trade winds. The world's largest desert, the Sahara of North Africa, with a maximum recorded air temperature of 57 °C (Cooke and Warren, 1973), is a trade-wind desert. The Taklimakan Desert of China is predominantly a trade-wind desert although its northern and southern borders are in the rain shadows of two mountain ranges.

Midlatitude Deserts

The midlatitude deserts occur between 30 to 50° latitude, poleward of the subtropical high-pressure zones. They have a wide temperature range with lower winter temperatures than those found in trade-wind deserts. Midlatitude deserts normally develop far from the ocean in interior drainage basins. The Lut Desert in Iran and the Sonoran Desert in the United States and Mexico are midlatitude deserts.

Rain-Shadow Deserts

Rain-shadow deserts are created by mountain ranges that prevent moisture-rich clouds from reaching areas in the lee of the range. Rain or snow is precipitated as the air rises over the mountains, and a desert is formed on the lee-side "shadow" of the range. Rain-shadow deserts are recognized easily from space by the absence of vegetation on the lee side of the mountains. These deserts sometimes are called orographic deserts. The Turpan Depression, Plate E-24, is a rain-shadow desert.

Coastal Deserts

Coastal deserts generally are found on the western edges of continents near the tropics of Cancer and Capricorn. They have the smallest temperature range of all deserts (Meigs, 1966). These deserts are affected by cold ocean currents parallel to the coast. These currents create high-pressure zones that lower the temperatures and cause temperature inversions. In coastal deserts, local wind systems often override the trade winds. These deserts are, therefore, less stable than other deserts and are dependent on ocean currents (McCauley et al., 1977). Winter fogs, which reduce solar radiation and decrease the temperature, are frequent in coastal deserts. Many coastal sand dunes are relatively complex because they are at the interface of terrestrial, oceanic, and atmospheric systems (Pye, 1983). The world's driest desert is the Atacama of South America, a coastal desert shown on Plate E-10.

Monsoon Deserts

Changes in the position of the ITCZ lead to monsoons in low latitudes. The term monsoon is derived from an Arabic word meaning season and refers to a wind system with pronounced seasonal reversals. Monsoons develop in response to temperature variations between continents and oceans. The two major monsoon systems on Earth are in northern Australia and West Africa. Lesser monsoon systems affect the deserts of central Asia. The southeast trade winds of the southern Indian Ocean provide heavy summer rains in India when they move onshore. As the monsoon crosses India, it loses moisture on the eastern slopes of the Aravalli Range. The Rajasthan Desert of India and the Thar Desert of Pakistan (Plate E-21) are parts of a monsoon desert region west of the range.

Polar Deserts

Polar deserts are in currently nonglaciated areas with annual precipitation of less than 250 mm, and a mean warmest

month temperature of less than 10°C. The polar deserts on Earth, which have a total area of nearly 5 M km², generally consist of bedrock or gravel plains. Sand dunes are not prominent features, but snow dunes are common in areas where precipitation is locally more abundant.

Because most moisture in polar deserts is in the solid rather than the liquid state, there are differences between polar and other deserts (Pewé, 1974). Temperatures in polar deserts often fluctuate above and below the freezing point of water. Alternate freezing and thawing creates patterned textures, such as contraction polygons that may be 15 to 30 m in diameter. These sand-wedge polygons are not usually seen in other deserts.

Paleodeserts

Patterns characteristic of dunes in sand seas may be recognized on images even though they are located in presently nonarid environments (see, for example, Plate F-8). Many such relict dunes are in areas in which annual rainfall is now 700 to 1500 mm, and some extend into areas presently occupied by tropical rain forests (Goudie, 1983). Ancient sand seas, changing lake basins, archaeological data, relict fluvial topography, and vegetation analyses indicate that climatic conditions have changed over vast areas of the Earth. Goudie (1983) suggests that, during most cold phases of the Pleistocene, parts of the deserts were more arid than they are today. Sarnthein (1978) notes that 10 percent of the land between 30°N and 30°S is presently covered by sand seas. About 18000 years ago, sand seas in two vast belts occupied almost 50 percent of this land area. As today, tropical rain forests and savannas existed between the two belts.

Many sandstones are considered to be eolianites, sedimentary rock formed by consolidation of sediment deposited by wind. Some investigators hold that distinction between eolianites and certain fluvial sediments can be very difficult, but eolianites may often be recognized by large-scale cross bedding with high-angle dips, ripple marks, slump marks, and contorted bedding characteristic of dry sand (McKee, 1979a).

As described by Glennie (1970), vector analysis and stereographic plots may be used to determine prevailing paleowind directions when the dunes were formed. Bigarella (1972) considers that the paleolatitude of eolianites may also be determined. He refers to a latitude that marks the mean boundary between the trade winds and the westerlies as the "wheel-round latitude" (Bigarella, 1972, p. 41). This latitude is marked by a distinct change in the alignment of sand dunes and dune movement. He argues that the present wheel-round latitude in northern Africa is 25°N, but comments that other investigators have placed the Pleistocene wheel-round latitude at 15°N. This difference suggests a climatic boundary shift of more than 1000 km.

Arid-land geomorphic features are usually excellent indicators of paleoclimatic conditions. In some environments, however, differentiating between response to a global climatic change and response to regional uplift of an associated mountain range is difficult. Stoertz and Erickson (1974) address this problem by noting that regional uplift causes the crowding of playas, salt crusts, lake shores, and piedmont alluvial slopes in parts of Chilean basins. Other anomalies they observed in one basin include the presence of lake sediments along the eastern side high above the western playas and the diminishing height of terrace scarps around salt crusts toward the west. Climatic change, as opposed to regional uplift, is indicated by the absence of extensive and consistent regional asymmetry.

The Nebraska Sand Hills, Plate E-14, is an inactive, probably Holocene, 57 000-km² dune field in central Nebraska. The largest sand sea in the western hemisphere, it is presently stabilized by vegetation and has an annual precipitation of 406 to 610 mm (Ahlbrandt and Fryberger, 1980). These authors found the dunes to be of crescentic and dome types as high as 91 m. They have

a maximum thickness extending to 34 m below interdune surfaces. Present-day effective winds, calculated from weather station data, differ from paleowind regimes inferred from the internal structures of the dunes. A modern analog may be Lake Chad, Plate E-8, where large-scale crescentic dunes occur in an arid area in which the climate has changed episodically.

Although paleoeolian depositional features have been recognized widely, little work has been done until recently in recognizing paleoeolian erosional features. Only with the advent of space imagery was the regional extent of some eolian erosional features recognized (McCauley et al., 1977; Mainguet, 1983).

Martian Sand Seas

Although Mars has a diameter of about one-half that of Earth and a surface atmospheric pressure about 1 percent that of Earth, it has a north circumpolar sand sea with an area of at least 700 000 km², greater than the Empty Quarter, which is the largest sand sea on Earth (Breed et al., 1979b). The martian sand sea, Plate E-15, consists predominantly of crescentic dunes and is visible on plains south of the perennial ice cap of the north polar area. Smaller dune fields are found elsewhere on the planet, including inside many large craters in the north and south polar regions. Eolian depositional features of polar deserts on Earth are studied as analogs for martian geomorphology (Morris et al., 1972).

Eolian Processes on Venus

Venus is frequently called the Earth's twin because it is close to the Earth in radius, mass, density, and surface gravity. The relation is only sororal, however. Venus has a retrograde rotation period of 243 days, a mean surface temperature of 480°C, and a predominantly carbon dioxide atmosphere with a surface pressure almost 100 times that of the Earth.

Orbiting U.S. and Soviet spacecraft have acquired radar data of the surface of the planet, but due to low resolution, evidence for global eolian activity has not been noted yet. The Soviets have landed several spacecraft on the surface of the planet. Images from these landers generally show flat layered rocks centimeters in diameter. After examining several Venera images, Greeley and Iversen (1985) point to a bimodal-size distribution of the particles on the surface as indicative of fluid transport. Inasmuch as liquid water cannot exist on Venus, they assume that the fluid involved is the atmosphere.

DESERT FEATURES

The deserts of the world are not restricted by latitude, longitude, or elevation. The People's Republic of China has both the highest desert—the Qaidam Depression (3000 m above sea level)—and one of the lowest deserts—the Turpan Depression (100 m below sea level).

Only about 20 percent of the Earth's desert area is covered with sand (Holmes, 1965). Much of the sand collects in sand sheets and sand seas—vast regions of undulating dunes resembling an ocean surface caught in an instant of time. Sand seas are called ergs in North Africa (Wilson, 1973).

Nearly 50 percent of desert surfaces are plains where eolian deflation has exposed loose unsorted residual gravels predominantly of pebble size (4 to 64 mm in diameter) but with occasional cobbles (64 to 256 mm in diameter). An extensive flat desert surface composed of pebbles on bedrock is called a hamada. Bagnold (1941) calls coarse-grained residues remaining after the passage of sand a whaleback.

The remaining surfaces of arid lands are composed of fluvial deposits, including alluvial fans, playas, desert lakes and

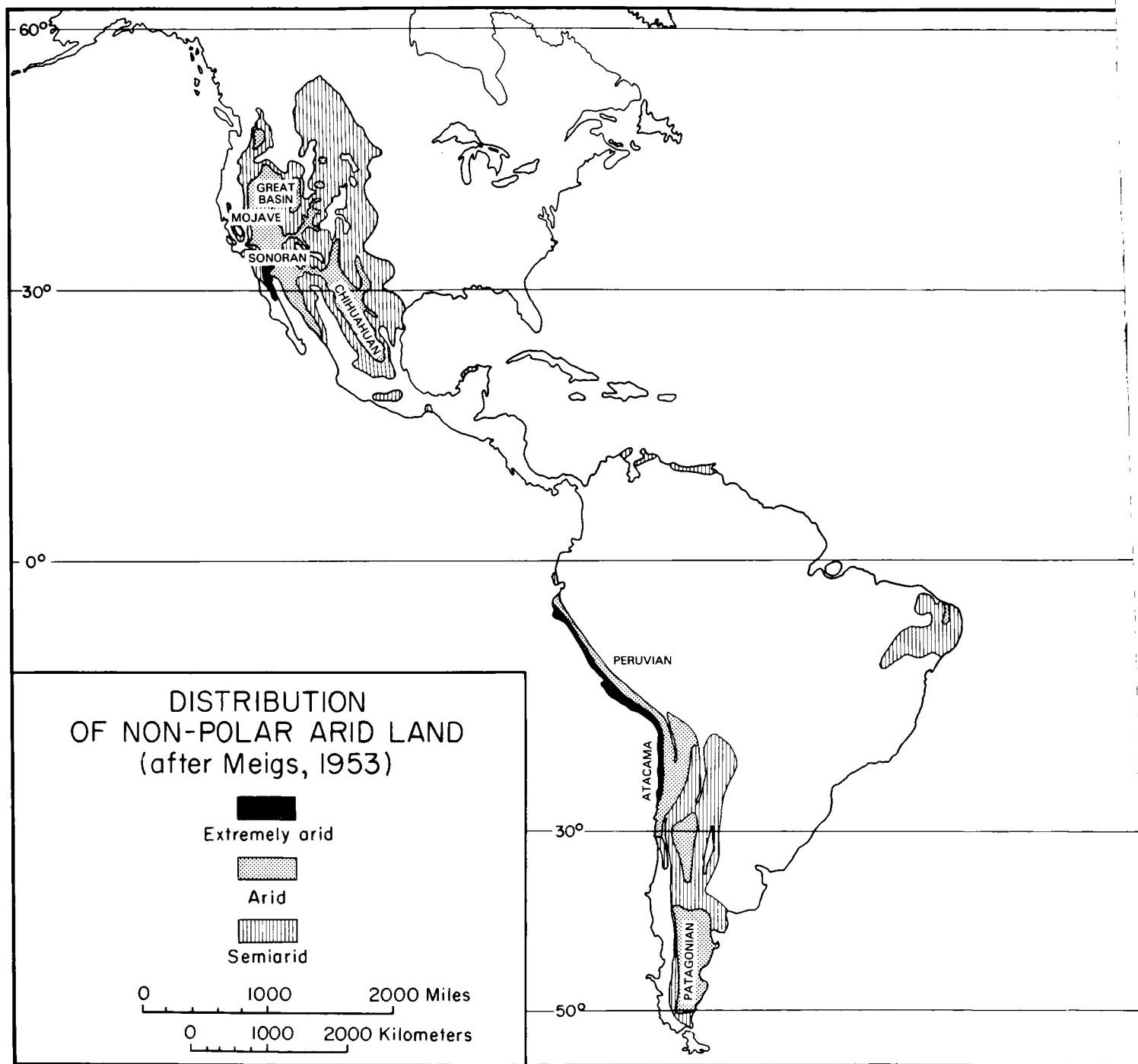


Figure 8-2. Nonpolar deserts of the world.

oases, and exposed bedrock outcrops and desert soils. Bedrock outcrops commonly stand up as inselbergs, which are small mountains surrounded by extensive erosional plains.

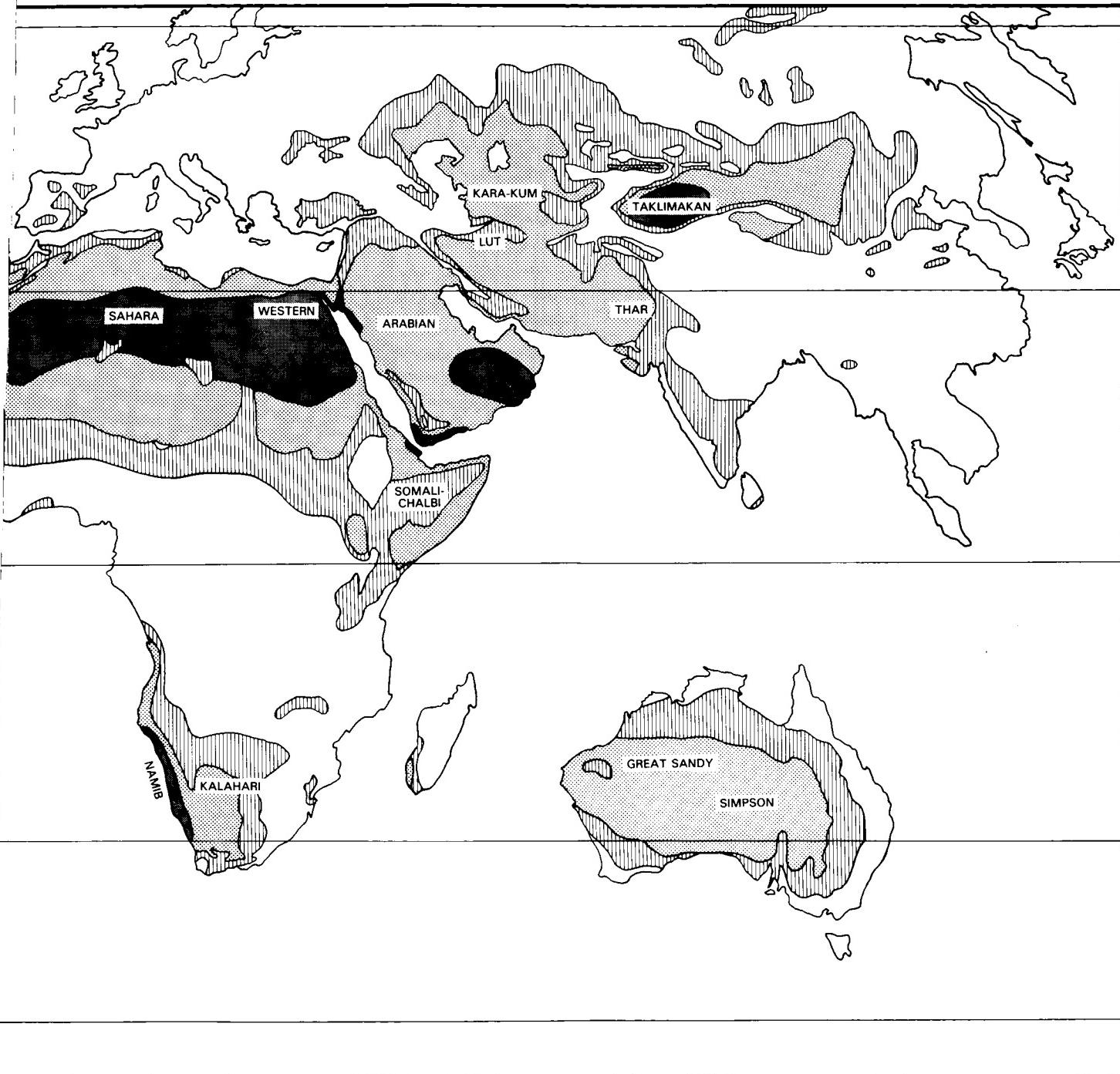
Soils and Caliche

Soils that form in an arid regime, in which the potential evapotranspiration exceeds the precipitation during most of the year, are termed "aridisols." They are predominantly mineral soils with a low organic content. The episodic accumulation of

water in some aridisols favors the development of distinct salt horizons. Calcium carbonate precipitated from solution may cement sand and gravel into hard horizons called "calcrete." Calcrete forms layers as thick as 50 m in the regoliths of some arid environments (Goudie and Wilkinson, 1977). As reported by Birkeland (1984), carbonate horizons in aridisols may be subdivided into morphological stages that correlate with the age of the parent material.

Caliche is a layer of secondary carbonate accumulation found in many aridisols. Believed to be of pedogenic origin,

ORIGINAL PAGE IS
OF POOR QUALITY



caliche commonly occurs as disseminated nodules or as coatings on mineral grains, and is formed by a complex interaction between water and carbon dioxide released by the decay of organic material or by plant roots during respiration. In areas of low rainfall, the caliche zone is close to the surface. As rainfall increases, however, it descends to greater depth. When annual rainfall exceeds 100 cm, caliche disappears from the soil profile (Blatt et al., 1980). Ancient caliche is difficult to recognize because it is susceptible to recrystallization and chemical changes by ground water.

Plants

Deserts typically have a plant cover that is sparse but of enormous diversity. The Sonoran Desert has the most complex desert vegetation (Crosswhite and Crosswhite, 1982). Most desert plants are xerophytes (drought- or salt-resisting plants), succulents (which store water in their leaves, roots, and stems), or phreatophytes (with long tap roots that penetrate the water table). Plant roots that anchor the soil inhibit deflation, and the stems and leaves of some plants check the surface velocity of sand-carrying

wind to prevent saltation and to cause deposition. A sand dune protected from wind by vegetation is referred to as a fixed dune.

Desert Water

Rain occasionally falls in deserts, and desert storms are often violent. In the Sahara Desert, 300 mm of rain were once recorded to have fallen within 24 hours. Large Saharan storms may have an intensity of precipitation of 1 mm/min (Cooke and Warren, 1973). As originally pointed out by Gerster (1960), more people drown in deserts than die of thirst.

Though deficient in precipitation, deserts receive runoff from ephemeral streams fed by rainfall and snow meltwater from adjacent higher elevation areas. They commonly transport considerable quantities of sediment for 1 or 2 days, filling the channel with a slurry of mud. A dry former stream channel is a wadi or arroyo. Although most deserts are locked into basins with interior drainage, a few deserts are crossed by "exotic" rivers that derive their water from outside the desert. Such rivers infiltrate and evaporate on their journeys through the deserts, but their volume is sufficient to maintain their integrity. The Nile, Colorado, and Yellow are exotic rivers.

Lakes form where rainfall or meltwater in interior drainage basins is sufficient. Desert lakes (playas) are generally shallow, temporary, and salty. Their water levels fluctuate and may dry up, leaving a salt crust or claypan. Because playa lakes are shallow and have a low bottom gradient, wind stress may cause the advance and retreat of lake waters over many square kilometers (Torgersen, 1984). Ground water feeds some desert lakes. Most playas in the United States are relics of Pleistocene lakes (Cooke and Warren, 1973). Playas are one of the arid landforms that may have been inherited from a wetter past and thus contain clues to climatic change (Street and Grove, 1976).

A large multilingual terminology describes desert-lake deposits. Investigators with experience in parts of the Middle East usually call a flat area of clay, silt, or sand encrusted with salt a sabkha (Glennie, 1970). In North America, it is a playa, salt pan, or hardpan. In South America, such a lake is a salina or salar. In parts of North Africa, it is a chott; and in the U.S.S.R., it is a solonchach. Glennie separates desert lakes into coastal and inland sabkhas (see Plate C-21). The former develop from seepage of ground water or where water flowing in wadis intermittently floods low-lying depressions. Coastal sabkhas, which he defines as coastal flat areas just above high tide, are characterized by algal mats and deposits of halite, gypsum, and dolomite.

Playas are potential sources of mineral wealth formed by evaporation (see Plate KL-13). In addition, their flat terrains make excellent runways for air and spacecraft. The Space Shuttle frequently lands on Rogers Lake Playa at Edwards Air Force Base, California.

EOLIAN EROSION

Wind erodes by deflation—the removal of loose, fine-grained incoherent particles by the turbulent eddy action of the wind—and by abrasion—the wearing down of surfaces by the grinding action of windborne particles.

Evaporation

Water is the base level for eolian erosion, in that it provides cohesion for surface particles, and thus prevents deflation. In a desert basin, wind blowing in a hot, dry atmosphere increases the rate of evaporation, the process by which a substance passes from the liquid or solid state to the vapor state. Evaporite deposits form in closed basins in which water flows with large quantities of salts. As water evaporates, minerals such as gypsum and various nitrates, chlorides, and borates are precipitated. The

minerals deposited depend on the temperature and composition of the saline waters at the time of crystallization. Many of these deposits are economically significant. Plate E-13 illustrates some evaporite deposits in the Great Basin Desert.

In describing evaporites, Blatt (1982) states that modern evaporite deposits and belts of higher salinity in the oceans tend to occur more frequently at about 30° latitude as a consequence of global circulation patterns. He suggests that fossil evaporite deposits may be used to narrow down paleolatitudes of associated ancient landforms developed on drifting terranes or continents.

Ventifacts

Wind uses saltating and suspended grains as agents of abrasion. During frictional contact, particles carried along flow lines and in centers of vorticity (Whitney, 1978) create grooves or depressions in material exposed on the ground in the path of the wind. Ventifacts are aerodynamically shaped rocks up to meters in size that have been cut, and sometimes polished, by the abrasive action of wind. McCauley et al. (1979) note that the pitted and fluted rocks in the Western Desert of Egypt resemble the pitted rocks seen at the Viking Lander sites on Mars. They surmise that susceptible materials on the martian surface may have been modified by a large amount of eolian erosion.

Blowouts

A blowout, which is a deflation basin, is a hollow formed by the removal of particles by wind. Blowouts generally remain small, but may enlarge up to kilometers in diameter. Glennie (1970) discusses a circular 2- to 3-km diameter blowout in Libya 60 to 70 m deep. Although he notes that a few short wadis drain into the hollow, he believes that the hollow was formed predominantly by the wind.

Yardangs

Yardangs are sculpted landforms streamlined by desert winds. Up to tens of meters high and kilometers long, yardangs are found in many deserts of the Earth and also on Mars (McCauley et al., 1977). Some investigators suggest that the Sphinx of Egypt was constructed out of a yardang. Yardangs were first described northwest of Lop Nur, China, by Swedish explorer Sven Hedin (1903). The photographs accompanying Plate E-25 show the Lop Nur yardangs carved from lakebed sediments. McCauley et al. (1977) show that yardangs can be carved in rocks of all types, including crystalline bedrock, and therefore are not limited to soft sediments as formerly supposed. In wind-tunnel simulations, Ward and Greeley (1984) find that yardangs form by abrasion concentrated at the windward end of a structure. Deflation and reverse air flow control the formation near the middle and downstream ends.

Mariner and Viking images show yardangs up to 50 km long and 200 m wide that lie in the equatorial region on Mars (Ward, 1979). Ward notes that the azimuths of some martian yardangs are not parallel to wind-streak directions, indicating that the yardangs were formed earlier by winds from a different direction than those that formed the adjacent, more recent wind streaks.

Desert Pavement

Most eolian deflation zones are composed of desert pavement, a sheet-like surface of rock fragments that remain after wind and sheetwash have removed the fine particles. The rock mantle in desert pavement protects the underlying material from deflation. Because stony deserts are ubiquitous, a diverse terminology describes their surfaces. Stony deserts in Africa are called

lag gravels or reg if fine material remains, or serir if no fine material is present. In Australia, a stony desert is a gibber, and in the People's Republic of China, it is a gobi. (The adjective "gobi" should not be confused with the Gobi Desert in the Mongolian People's Republic.) Most investigators consider that many of these stony desert plains are inherited from previous fluvial cycles and represent surfaces merely modified by winds.

Desert pavement is easily identified in space images (e.g., in Plate E-24, the Turpan Depression). Desert pavement enhances saltation due to the increased elastic rebound of grains bounding along the coarse surface (Greeley and Iversen, 1985).

Desert Varnish

Desert varnish is a dark shiny stain found on the surfaces of many desert rocks. Manganese, iron oxides, hydroxides, and clay minerals comprise most varnishes and provide the shine. These constituents are believed to come from sources external to the rocks. Many investigators consider atmospheric dust to be the source of the manganese found in the varnish. Dorn and Oberlander (1982) favor a biologic origin for desert varnish. These authors note that, although varnish is found predominantly in arid environments, it also occurs in alpine, arctic, fluvial, and other humid environments, and they prefer to use the term "rock varnish."

EOLIAN TRANSPORTATION

Particles are transported in the wind by suspension, saltation, and creep. In a classic work on the physics of windblown sand, Ralph Bagnold (1941) pointed out that an object falling from rest through any fluid (air, water, oil, etc.) will reach a constant terminal velocity of fall. The net force on an object as it falls is the result of the pull of gravity on the particle and the force of the fluid acting in the direction opposite to that of the fall. When these two forces are equal, the velocity of the object has reached a constant value—the terminal velocity of fall.

A lifted particle whose terminal velocity of fall is less than the velocity of upward eddy currents within a surface wind is susceptible to transport in suspension. For typical winds near the surface of the Earth, particles having diameters less than 0.20 mm may be kept in suspension and scattered as dust or haze.

With the advent of the space age, scientists can investigate eolian processes on planets having atmospheres of significantly different compositions and pressures. Although Mars and Venus have predominantly carbon dioxide atmospheres, the atmospheric surface pressure on Mars is nearly 100 times less than that of Earth, and the pressure on the surface of Venus is nearly 100 times greater than that of Earth. Iversen et al. (1976) and Greeley and Iversen (1985) have calculated a threshold friction speed, which is the minimum wind speed required to initiate particle motion for each planet. According to their calculations, a particle 0.1 cm in diameter would have a threshold friction speed of about 8 cm/sec on Venus, 60 cm/sec on Earth, and 600 cm/sec on Mars. These investigators calculate a particle diameter for the saltation-suspension boundary of 30, 52, and 210 microns for Venus, Earth, and Mars, respectively.

Saltation and Creep

Saltation is the downwind movement of particles through a series of jumps initiated by granular impact. The particles move in a curved path and strike the ground at angles between 10 to 16°. Bagnold (1941) found experimentally that saltation proceeds at one-half to one-third the speed of the wind and that the mean height of saltation of grains with an average size of 0.25 mm is less than 1 cm on Earth.

When a saltating grain impacts other grains on the surface, a fraction of the energy it has acquired is passed on to grains that are ejected upward and continue the saltation. However, most of the energy is dissipated among a large number of grains, and a slow forward surface creep of the surface grains is initiated. Through creep, a saltating particle can move a surface grain more than 200 times its own weight. Bagnold (1941) estimated that as much as 25 percent of grain movement in a desert is due to surface creep.

Dust and Loess

Dust storms are eolian turbidity currents. When rain falls from a cumulonimbus cloud, the air is cooled significantly as the precipitation passes through it. Because this air is cooler and denser than the surrounding air, it sinks. When it reaches the ground, this cold air is deflected forward, sweeping up surface debris in its turbulence. Dust storms have been reported since 1150 B.C. in China (Liu et al., 1981) and since biblical times in the Middle East (Péwé, 1981). Villages, crops, people, and possibly even climates are affected by dust storms. Peterson and Junge (1971) estimate that 500×10^6 tons of windblown dust are carried from deserts annually. McCauley et al. (1981) report that millions of tons of valuable topsoil were removed from the U.S. High Plains by a single dust storm in 1977. This was the first dust storm whose entire progression was recorded in satellite images. Their geostationary orbits and wide fields of view allow the NOAA meteorological satellites to monitor the entire course of regional and continental dust storms.

On Earth, great dust storms, called haboobs from the Arabic word for violent winds, sometimes rise to elevations around 2500 m and advance at speeds up to 200 m/sec (Idso et al., 1972; Idso, 1976). Some dust storms are intercontinental, a few may circle the globe (Péwé, 1981), and some may engulf entire planets. When Mariner 9 arrived at Mars in 1971, the planet was enshrouded in global dust. Dust storms on Mars have been observed to last up to 100 days. The poles and topographically high regions are the first to clear as the dust settles (Greeley, 1982).

Dust devils are small vortices that whirl around arid lands and are thought to be related to very intense local heating and instabilities (Cooke and Warren, 1973). Dust devils on Earth may extend up to 1 km high (Péwé, 1981). Using shadow measurement of Viking Orbiter images, Thomas and Gierasch (1985) recently identified 94 dust devils on Mars. They determine that some dust devils are up to 6 km high and suggest that dust devils are common near the subsolar point.

Péwé (1981) discusses two particle size ranges for dust. Dust devils, dust storms, and loess deposits are composed of particles 5 to 50 μm in diameter. Particles less than 10 μm in diameter are tropospherically sorted dust that moves as an aerosol and remains suspended in air until brought down by rainfall.

Loess is a deposit of homogeneous, nonstratified, and unconsolidated windblown silt that may bury the existing topography. The banks of slopes cut in dry loess generally stand vertically, but can slump when wet. The thickness and mean size of windblown silt varies inversely with distance from the dust source (Pye, 1984). The thickest known loess deposit, 335 m, is on the 300000 km² Loess Plateau in China (Derbyshire, 1983), a small portion of which is shown in Plate E-22 (see also Plates F-2 and F-3). In Europe and in the Americas, loess thicknesses may exceed 60 m, but 20 to 30 m is more common (Pye, 1984). As reported in Derbyshire (1983), geomagnetic and thermoluminescence dating of loess deposits fixes the times when the climatic conditions produced the environment of deposition. The majority of European and North American loess is of glacial and periglacial origin, and the loess of China is believed to have been produced from the deserts (Goudie, 1978; Pye, 1984).

EOLIAN DEPOSITION

Wind-deposited sand bodies are found in many parts of the Earth's deserts. Wilson (1973) contends that sand deposits occur in bed forms at three scales: ripples, dunes, and large sand bed forms that he calls draas. In addition, sand sheets are irregular accumulations surfaced by grains that may be too large for saltation. Sheets are low, flat, gently undulating sandy strips with no slipfaces (Tsoar, 1983). Sand sheets comprise approximately 40 percent of eolian depositional surfaces (Fryberger and Goudie, 1981). One of the largest sand sheets on Earth is the 60000-km² Selima Sand Sheet of southern Egypt and northern Sudan. Haynes (1982) describes it as absolutely flat in some places. He notes that active dunes are moving over the sand sheet.

Ripples

As the wind blows on a sand surface, the surface becomes rippled, with ripple crests and troughs being perpendicular to the wind direction. The mean length of jumps during saltation corresponds to the wavelength of ripples (Wilson, 1972). These wavelengths and the heights of the crests above the troughs increase with increasing wind velocity. In ripples, the coarsest materials collect at the crests. Bagnold (1941) reports that this characteristic distinguishes the small-scale surface ripples from large-scale dunes (see Figure E-11.1) in which the coarsest materials are generally in the troughs. Sharp (1963) distinguishes between sand ripples composed of grains with median diameters of 0.30 to 0.43 mm and granule ripples composed of grains with diameters greater than 1 mm.

Dunes

A dune is an accumulation of sediment blown by the wind into a mound or ridge. Dunes have gentle upwind slopes on the stoss, or wind-facing side. The downwind portion of the dune, on the lee slope, is commonly a steep avalanche slope referred to as a slipface; dunes may have more than one slipface. The slipface stands at the angle of repose, which is the maximum angle at which loose material is stable (30 to 34° for sand). Bagnold (1941) observed that the minimum height of a slipface is about 30 cm. The brink of the dune is the top of its slipface, which may or may not be at the highest point—the crest.

Sand particles are transported up the gentle stoss slope of the dune by saltation and creep. When a load of particles reaching the brink exceeds the angle of repose, a small avalanche takes place that reforms the slipface. As the avalanching continues, the dune migrates in the direction of the wind.

Bagnold (1941) recognized two basic dune types in the Egyptian desert, the crescentic dune, which he called barchan, and the linear dune, which he called longitudinal or seif (the Arabic word for sword). Local names have been applied to these and many other varieties of dunes in sandy deserts, which has resulted in a bewildering terminology. However, certain basic types that occur widely as small dunes were defined by McKee (1957, 1979a) on the basis of their internal structures as longitudinal, transverse, barchan, star, dome, and parabolic.

Breed and Grow (1979) showed that these basic types occur globally as very large "mega-dunes" that form the bulk of the Earth's sand seas. Based on a worldwide inventory of deserts using Landsat images and aerial and satellite photographs, these authors categorize dunes according to their shapes in plan view and the relative positions of their slipfaces, and classified them as linear, crescentic, dome, star, or parabolic. This classification system, which has global applicability and transcends regional language, was tailored for space observations and is used in this chapter.

Crescentic dunes are crescent-shaped mounds or segments of ridges (Figure 8-3a). Each segment is generally wider than it is long and is bounded on its concave side by a slipface. These dunes form under dominantly unidirectional winds and are referred to as barchan, barchanoid, or transverse by some writers. At the downwind ends of crescentic dunes are horns that have no slipfaces. Crescentic dunes move faster than any other dune type. A set of dunes was measured to move an average of 100 m per year between 1954 and 1959 in Ningxia Province, China (Li, 1962), and similar rates are recorded in the Western Desert of Egypt (Embabi, 1982). Breed and Grow (1979) note that the largest crescentic dunes are in the Taklimakan Desert, where their horn-to-horn mean width is 3.24 km. Movement of such large dunes is probably so slow that it is practically imperceptible over the short run. The most common dune form on Earth and on Mars is the crescentic (Breed et al., 1979a, 1979b).

Hills (1940) described unusual 6- to 10-m high crescentic dunes on the lee shores of some of the lakes in arid Australia. These dunes are generally composed of clay, and Hills called them lunettes. Langford-Smith (1982) suggests that lunettes are formed when seasonal exposure of saline lake beds induces clay particles to combine in aggregates. The aggregates are deflated from lake beds and deposited as clay dunes that form arcuate mounds along the downwind lake shore.

Linear dunes are straight or slightly sinuous longitudinally symmetrical sand ridges typically much longer than they are wide (Figure 8-3b). Slipfaces occur alternately on both sides (Tsoar, 1978). Linear dunes cover more area in the sand seas of Earth than any other dune type, but are rare on Mars (Breed et al., 1979b). These dunes have been called seif dunes, sand ridges, or longitudinal dunes.

Linear dunes may occur as isolated ridges, but they generally form sets of parallel ridges separated by kilometers of sand, gravel, or rocky interdune corridors. The origin of linear dunes is controversial. Bagnold (1941) suggested that a change in wind direction could preferentially advance one of the horns of the crescentic dune, forming a linear dune. Many workers have noted similarities between the axial alignment of linear dunes and the prevailing direction of the regional winds. Some conclude that linear dunes are built by unidirectional winds. Other investigators, such as McKee (1979b), Lancaster (1982), Tsoar (1983), and Breed et al. (1984), provide field evidence that many linear dunes are the product of bidirectional or multidirectional wind regimes and that the long axis of each dune extends in the resultant direction of sand movement.

Most deposition on linear dunes in bidirectional wind regimes is known to occur by lee-side accretion. The effect of dominance of a wind blowing from one direction rather than the other is to concentrate erosion and deposition at the same locations on the dune. If the wind regime becomes essentially unidirectional, Lancaster (1980) suggests that a linear dune would be reformed into a series of individual or linked crescentic dunes, as may be happening in the northern parts of the Namib sand sea (Plate E-9).

Linear dunes are commonly more than 100 km long (Breed et al., 1979a). Some linear dunes have "Y" connections (Plates E-17 and E-18). Langford-Smith (1982) reports measuring a linear dune in the Simpson Desert, Australia, that was longer than 300 km.

Linear dunes, as well as crescentic dunes, are known to form in submarine canyons. Valentine et al. (1984) investigated 3-m high linear dunes in a canyon on the continental shelf. Those dunes have 20-cm wavelength ripples subparallel to the slope of the walls on their gentle faces. These authors find that the crests are oriented across the canyon axis.

Star dunes are radially symmetrical pyramidal sand mounds with slipfaces on three or more arms that radiate from the high center part of the mound (Figure 8-3c). They tend to accumulate in areas with multiwind direction and are sometimes referred to

as ghords, pyramid dunes, radial dunes, or rhours. Star dunes grow upward rather than migrate laterally. According to Breed and Grow (1979), star dunes are the dominant dunes in the Grand Erg Oriental of the Sahara (Plate E-6). In other deserts, they occur around the margins of the sand seas, particularly near topographic barriers (Breed et al., 1979a, 1984). The highest sand dunes on Earth may be the star dunes in the Badain Jaran Desert of China, which are up to 500 m tall (Zhu et al., 1980).

Parabolic dunes are U-shaped mounds of sand with convex noses trailed by elongated arms. The nose and the arms are bounded by slipfaces on their outer convex sides (Figure 8-3d). They are sometimes called U-shaped, blowout, or hairpin dunes and are well known in coastal deserts. These dunes form in unidirectional wind regimes, but they are opposite to the geometry of crescentic dunes in that their horns point upwind. Although their elongated arms trail behind because they have been fixed by vegetation, the bulk of the sand migrates forward. The largest parabolic dune measured by Breed and Grow (1979) is near the Colombia/Venezuela border and has a trailing arm 12 km long. Parabolic dunes are illustrated in Plate E-21, the Thar Desert.

Blowout dunes are small (meter size) dunes that form downwind from deflation hollows—cup-shaped depressions or “blowouts” scooped out by wind erosion of a sand deposit. Many investigators suggest that blowouts evolve into parabolic dunes when a prevailing wind advances a section of the rim and vegetation stabilizes the arms (McKee, 1979b).

Dome dunes are semicircular mounds that lack slipfaces (Figure 8-3e). Small dome-shaped dunes are normally not visible on Landsat images, but a few large dome-shaped dunes have been observed. Plate E-1 shows some dome dunes in Saudi Arabia. Bigarella (1972) discusses one 137- by 128-m dome dune that is 5.5 m high.

Reversing dunes are a variety of any of the foregoing types that may occur wherever winds periodically reverse direction. These dunes typically have major and minor slipfaces oriented in opposite directions. They tend to grow in height but migrate only slowly, if at all. McKee (1979a) considers them to be intermediate in character between a star dune and a linear dune. Breed

et al. (1984) show reversing dunes that are modified crescentic dunes.

Simple, Compound, and Complex Dunes

Breed and Grow (1979) deduce that the foregoing dune types are scale-independent and occur in three forms—simple, compound, and complex. Simple dunes are basic forms with a minimum number of slipfaces that define the geometric type. They represent a wind regime that has not changed in intensity or direction since the formation of the dune. Compound dunes are large dunes on which smaller dunes of similar type and slipface orientation are superimposed. An example is a crescentic dune with smaller crescentic dunes on its gentle slope. Compound dunes probably represent a wind regime that has decreased in intensity, but not in direction, since the larger basal dune was formed. Possibly, however, the entire feature may be built by contemporaneous processes.

Complex dunes are combinations of two or more dune types. A crescentic dune with a star dune superimposed on its crest or a star dune with an arm evolving into a crescentic dune are examples of complex dunes. The most common complex dunes noted by Breed and Grow (1979) are linear or crescentic dunes with star dunes along their crests. Such complex dunes indicate that the wind regime has changed significantly with respect to intensity and direction. Understanding the parameters involved in the eolian regimes of complex dunes may provide evidence for the direction of paleoclimatic changes.

RESOURCES IN DESERTS

Some mineral deposits are improved, preserved, or created by geologic processes that occur as a consequence of an arid climate (Smith, 1977). Evaporation in arid lands is a process that may enrich mineral accumulation in lakes. Leaching of ore minerals and redeposition in zones near the water table may convert minerals to malleable grade ore. Of the 15 major mineral

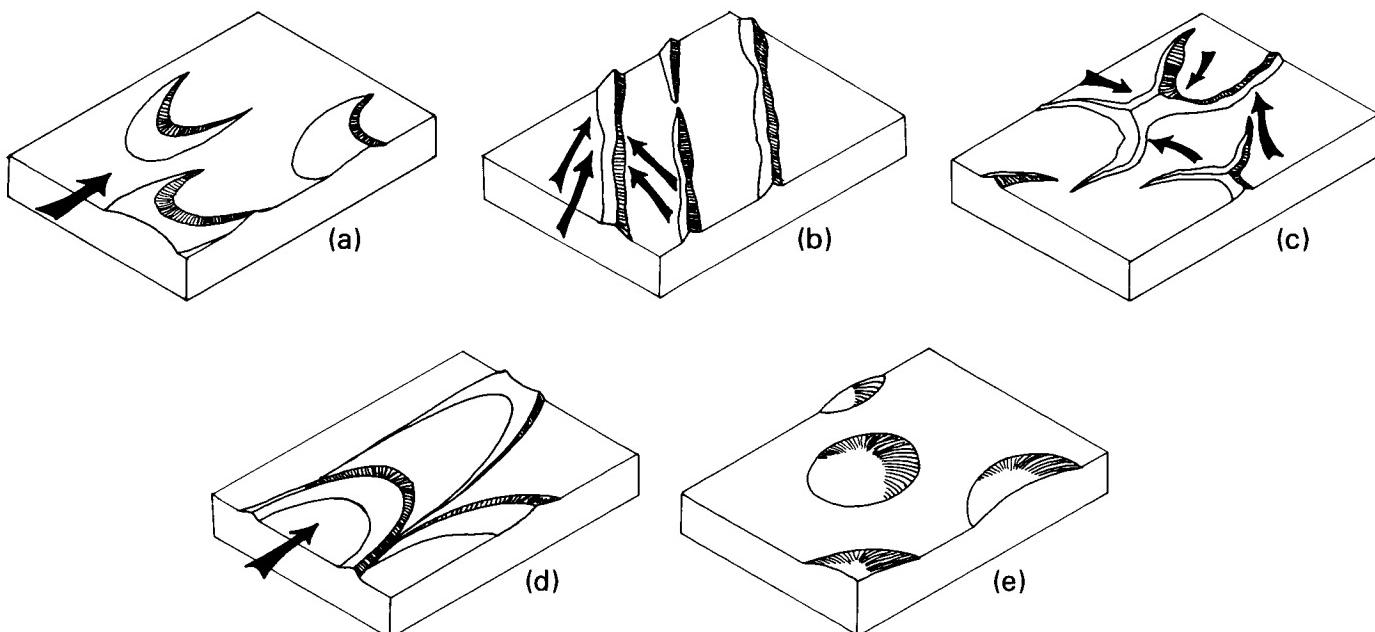


Figure 8-3. Dune forms: (a) crescentic dune, (b) linear dune, (c) star dune, (d) parabolic dune, and (e) dome dune. Arrows indicate wind direction.

deposits in the western hemisphere strongly affected by ground water, 13 are in deserts (Smith, 1977).

Minal mineral salts concentrate in sediments and near-surface brines formed by evaporation of inland bodies of water, often during geologically recent times. The known amount of available lithium in the world, for example, nearly doubled when the mineral was found in the saline deposits in the Qaidam Basin of west-central China. Landsat views of significant evaporite deposits are illustrated in Plate E-13, the Great Basin and Mojave Deserts, and Plate E-10, the Atacama Desert.

Owing to scarcity of vegetation, arid lands are especially amenable to spectral remote sensing. Limonitic rocks have a composition that may be identified readily from Landsat Multispectral Scanner (MSS) data. By extending the wavelength range of scanners further into the infrared, additional surface materials may be identified. Using airborne spectrometer surveys of the Mojave Desert, Raines et al. (1984) discovered three previously unknown molybdenum stockworks. Field reconnaissance should determine whether these finds are economically important.

The Landsat Thematic Mapper (TM) increases the capability to detect hydrothermally altered volcanic rocks in arid and semiarid lands. Kahle (1982) recognizes the presence of hydrous minerals using data from an airborne TM simulator sensor. She points out that recognition of hydrous phases sometimes allows mapping of hydrothermal alteration zones, which is important in economic mineral exploration. Podwysocki et al. (1984) investigated altered rocks in the Mojave Desert, drawing upon data digitally processed to enhance areas of hydrothermally altered volcanic rocks. They used a color-composite image composed of three band ratios to recognize several types of altered rock on the image. These investigators found that some deposits were confused with bleached altered rocks, thus indicating the necessity for field work to investigate the significance of TM anomalies.

REMOTE SENSING OF ARID LANDS

The world's deserts are generally isolated, inaccessible, and inhospitable. They are also excellent laboratories in which to study all aspects of eolian geomorphology and the interaction of wind with other elements of the environment.

Modern technology and new perspectives made available by remote sensing systems are proving to be especially helpful in the effort to understand arid lands. Landsat satellites provide excellent data with which to monitor temporal variations in a given area. For example, comparing data over a period of several years may indicate changes in eolian features or an increase or decrease in productive land near the desert fringes.

One of the most exciting results of the first Shuttle Imaging Radar System (SIR-A) is that images of the Western Desert in Egypt and the Sudan show buried fluvial topography, faults, and intrusive bodies that otherwise are concealed beneath sand sheets and dunes (see Plate I-3). Most of these features are not visible in the field. The radar signal that penetrates the loose, dry, surficial sediment is being used to find previously unknown archaeological sites and potential sources of potable water in the arid environment (McCauley et al., 1982; Schaber et al., 1986).

The high-resolution and forward overlap of the 30.5-cm focal-length lens on the Large Format Camera (LFC) allows investigators to acquire accurate topographic data previously unavailable for poorly mapped arid lands. Using stereo LFC photos, experimental topographic profiles have been constructed for the sand sea in the Namib Desert and for the Qattara Depression of the Western Desert of Egypt (Walker, 1986). Desert color, which often reflects the composition of exposed rock surfaces and sand and which may be a significant age marker for eolian sands on a regional and a local scale, also may be investigated with the mapping-quality natural-color photographs from the LFC.

Desert studies still are hampered in many regions by lack of accurate climatic data. Most desert weather stations are in oases surrounded by trees and buildings and have been subjected to many height and location changes throughout the duration of the station. Data from oases do not reflect data from the raw desert. In addition, a wide variety of instrumentation has been used. Measurements are recorded over varying lengths of time and in different formats, making them difficult to interpret and compare.

To overcome some of these problems in deserts of the American Southwest, the U.S. Geological Survey (USGS) established a Desert Winds Project to uniformly measure several key meteorologic parameters of arid lands (McCauley et al., 1984). This group has successfully established geometeorologic (Geomet) stations to measure windspeeds, including peak gusts, which do most of the geologic work. The stations also measure wind direction, precipitation, humidity, soil and air temperatures, barometric pressure, and blowing dust particles at specific heights above the surface by using low-maintenance automatic solar-powered sensors. Data are sampled at 6-minute intervals and transmitted every 30 minutes to a Geostationary Operational Environmental Satellite (GOES). From GOES, the data are transmitted in real time to a receiving station and are distributed to the USGS laboratory in Flagstaff, Arizona.

These investigators have been recording weather data from four different types of deserts in Arizona and will add a Geomet site in the Chihuahuan Desert in New Mexico. They have recorded a windstorm near Vicksburg, Arizona, with peak gusts of almost 144 km/hour (McCauley et al., 1984, p. 17). The investigators will combine analysis of quantitative meteorologic data acquired from the Geomet stations over several years with detailed geologic field studies and repetitive aerial and ground photographs and Landsat imagery. They will study long-term changes produced by wind in deserts of differing geologic and climatic types.

DESERTIFICATION

The main bodies of the world's great deserts were formed naturally by processes interacting over long periods of time. During those times, deserts expanded and shrunk independent of human activities. Evidence is abundant that large sand seas, now inactive because they are "fixed" by vegetation, once extended well beyond the present margins of core deserts, such as the Sahara. In some regions, deserts are separated sharply from the surrounding less arid areas by elevation changes that reflect structural differences in the regional geology. In other regions, the desert fringes, the transition to a more humid environment is gradational, and the desert border is difficult to define. These arid transition zones have very fragile, delicately balanced ecosystems. Hare (1983) discusses the desert fringes as a mosaic of microclimates in which small enclaves support vegetation that picks up heat from the hot winds. After rainfall, vegetation serves as a gigantic wet bulb and is distinctly cooler than its surroundings. He notes that, in areas having high livestock densities, the pounding of soil by hooves increases the proportion of fine material and reduces the percolation rate, thus encouraging wind and water erosion. Browsing by livestock and collection of firewood by man reduce or eliminate plant cover that provides good soil binding.

In these areas, and in similar semiarid environments, human activity is commonly superimposed on the natural processes that tend to shrink or expand deserts. These human activities may stress the ecosystem beyond its tolerance limit, resulting in general and semipermanent degradation of the land. This degradation of formerly productive land, referred to as desertification, is a complex process that can occur from different causes and at varying rates in different climatic regimes. Desertification may exacerbate a general climatic trend toward increasing aridity, or as some

investigators propose, it may initiate local climatic change (Charney, 1975; Charney et al., 1977).

The process of desertification was first brought to world attention in the 1930s when parts of the Great Plains of the United States turned into the Dust Bowl as a result of poor farming practices initiated during a "wet" cycle. Millions were forced to abandon their farms and their livelihoods. The term was popularized by Aubreville (1949). By 1973, drought that began in 1968 in the Sahelian countries of Africa was responsible for the deaths of between 100 000 and 250 000 individuals, the disruption of millions of other lives, and the collapse of the agricultural bases of five countries. More than \$200 million in cash and food were donated by private individuals, governments, and the United Nations in an effort to prevent mass starvation. Reining (1978) estimates that desertification affects more than 600 million people and one-third of the Earth's land surface. The 1977 UN Conference on Desertification estimated that $31.6 \times 10^6 \text{ km}^2$ of the surface of the Earth has been subjected to desertification (Kates et al., 1977). Cross (1983) concludes that the southern edge of the Sahara has expanded by $650 000 \text{ km}^2$ in the past 50 years.

Scientists at the Lanzhou Institute of Desert Research of the Chinese Academy of Sciences consider $170 000 \text{ km}^2$ in China to be desertified and an additional $170 000 \text{ km}^2$ to be in danger of desertification. They recently calculated that $50 000 \text{ km}^2$ of formerly productive land in China has been desertified within the past 50 years owing to misuse of the land. Chinese scientists refer to deserts that they think are entirely manmade as "sandy lands." Part of the Mu Us Sandy Land (Plate E-22) falls into this category.

Desertification does not proceed in linear, easily mappable patterns. Deserts advance erratically, forming patches on their borders. Areas far from deserts may quickly degrade to barren soil, rock, or sand through lack of sound land management practices. Desert encroachment does not occur because of a change in only one measurable parameter in a given area. Rather, it is a process to which many factors contribute. Usually, an area undergoing desertification is brought to public attention only after the process is well under way. Often little or no data are available to indicate the previous state of the ecosystem or the rate of degradation.

Landsat sensors provide extensive ($34 000 \text{ km}^2$ per image) repetitive coverage of the Earth's surface in uniform scale and in uniform format. The sensors provide data well suited for monitoring desertification. Using Landsat reflectance data, Otterman (1977) analyzed the impact of people and animals on the surface albedo of the Earth. Low albedo is a result of dark plant debris accumulating on the crusted soil surface, and a higher albedo is produced when collecting firewood and overgrazing results in a trampled, crumbled soil. Otterman believes that overgrazing has a significantly regional and global effect and may have raised the surface albedo of the Earth as much as 10 percent. Hare (1983) and Charney et al. (1977) argue that the feedback processes of albedo increase may intensify and extend drought, but may not induce permanent change.

In a review of the concept of desertification, Glantz and Orlovsky (1983) argue that the term has numerous definitions. Some researchers consider it a process of change, while other investigators view it as the end result of a process. Also, researchers are unable to agree as to where desertification can occur.

According to Glantz and Orlovsky (1983), some investigators consider climate to be the major contributor to desertification processes, with human factors contributing only a minor role. Other researchers reverse the significance, and a third group blames climate and humans equally. The importance of a long-

term climatic change, when compared to a few years of fluctuating precipitation, is not yet known. Certain investigators, as summarized in Kerr (1984), suggest that drought in the American Great Plains may be related to the superposition of an 18.6-year lunar cycle of changing declination and the 22-year sunspot cycle. Some investigators consider desertification to be irreversible during a season or a few seasons, but reversible on a scale of decades or centuries.

On a local level, individuals living on desertified land may do much to reclaim the land. The wind regime near the face of dunes can be interrupted by covering the dunes with large boulders to prevent sand from blowing. In another approach, meter-size straw grids are constructed to decrease the surface wind velocity on some dunes, as is illustrated in Plate E-23 of the Tengger Desert. Shrubs and trees planted within the grids are protected by the straw until they take root. In areas where some water is available, dunes have been stabilized with shrubs planted on the lower one-third of a dune's windward side. By decreasing the wind velocity, this vegetation prevents much of the sand from moving near the base of the dune. The higher velocity winds at the top of the dune level it off. Trees are then planted on top of the flattened dune.

Oases and farmland in windy terrain are sometimes protected by rimming the area with specially selected grasses and shrubs. Sand that manages to pass through the grass belts is caught in the adjacent forest belts, which are strips of poplars planted 50- to 100-m apart as windbreaks. Small plots of trees may be scattered inside oases to further stabilize the area. In China, a Green Wall is being planted in the northeast to protect the sandy lands. When complete, the Green Wall will be 5700 km long.

Efficient utilization of water resources and control of salinization are other effective tools for improving arid lands. Research is being done to exploit surface water resources, primarily seasonal runoff from adjacent highlands, to find and tap ground-water resources, and to develop effective irrigation procedures for arid lands. Other research on the reclamation of deserts is now focusing on how sand-fixing plants may be adapted to local environments and how the resources of grazing land and water may be effectively exploited without being overused.

CONCLUDING REMARKS

In a report comparing the agricultural situation in Africa and Asia, Norman (1985) notes that, although the rate of growth of food production in Asia increased by 20 percent from the 1960s to the 1970s, crop yields in Africa have not kept pace with population growth. During the 1970s, the population in Africa grew twice as fast as its food production. A new wave of desertification presently is threatening millions of people in the Sahel. According to Glantz (1980), solutions to several causes of desertification are known, but because of the political, economic, cultural, or social situation, they are not applied.

Dr. Mostafa Kamal Tolba, the Executive Director of the United Nations Environmental Programme, recently discussed the present Sahel drought (Tolba, 1984, p. 3):

"The message now is the same as it was in 1977: when we cope with desertification we can cope with drought. The difference between now and then is that now we have no excuse. The framework for applying the known remedies for desertification has existed for over six years; the suffering of the millions of poor in the semiarid regions should be on all our consciences."

PLATE E-1

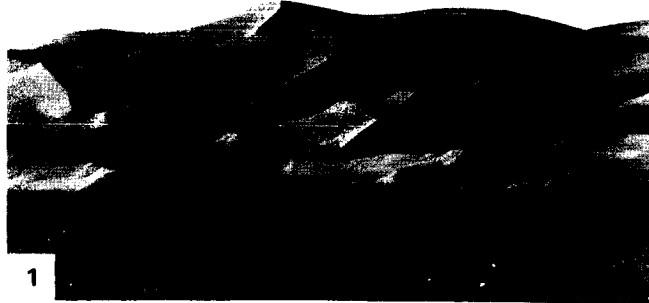
Dome dunes up to 150 m high (Holm, 1960) dominate this area of Saudi Arabia. As may be seen in the Plate and the figures, dome dunes are mounds of sand that lack external slipfaces.

The sand seas in the northern part of the Arabian Desert are divided into the Great Nafud, the Jafurah, and Dahna sand seas (Anton, 1983). Holm (1960) considers the primary sources of sand to be crystalline rocks exposed in the uplands. Sandstone outcrops and gravel plains are a secondary source. Holm suggests that the sands in the Arabian Peninsula accumulate in two large basins, the Great Nafud and the Rab'al Khali, the Empty Quarter. A 120-km long Dahna sand field connects the two basins.

Small elongate sand seas, called nefuds, subparallel to and west of the Dahna, are in this scene. The sand fields are about 20 km wide and are separated by 25-km wide hamadas that rise about 50 m above the dunes. As seen in the Plate, the western contacts between the sand fields and the hamadas are sharp, while the eastern contacts are generally gradational.

The hamadas and the gravel plains in the lower left of the Plate are vegetated sparsely along the wadis. Figure E-1.1 illustrates the dune/gravel contact near Al Hawtah. The ripples on the dunes are roughly perpendicular to the slipface that faces left in this photograph. Holm (1960) notes that the gravel plains are either alluvial or residual and are created from weathering and deflation of conglomerates. He believes that the Wadi ar Rimah was once continuous with Wadi al Batin, which is northeast of the scene. The wadis now are separated by the sand seas in the upper right of this Plate. Holm suggests that during the Pleistocene this river system reached the sea from the Tigris/Euphrates Valley. Eolian deflation has smoothed hamadas into flat, gently undulating surfaces.

Wilson (1973) reports that travelers find that hamadas are no more free from sand storms than are the surrounding sand seas. He mentions that hamada sand is only a thin veneer between pebbles of the desert pavement, or is found as drifts in low-elevation areas. The hamada in the upper right is composed predominantly of limestone, while the hamada between Thuwairat



1

DOME DUNES OF SAUDI ARABIA

and Sirr nefuds is composed of sandstones. The hamada continues past the alluvium of the Wadi. Lakes in this area tend to be in the western sections of the hamadas.

The westernmost rocks in the scene are granite. Sandstone lies between the granites and the Nefud Shudaibah. The contact between these rocks cannot be seen on the Plate. Dome dunes are common in these sand fields. North of the Wadi ar Rimah and Wadi al Batin dome dunes grade into linear dunes, as may be seen in the upper center of the Plate.

The dunes enlarge toward the east in each of the sand fields in this Plate. The domes decrease in size toward the south. As seen in the Plate, some of the domes are coalescing into composite dunes up to 5 km long and 1.5 km wide (Holm, 1953). Breed et al. (1979a) conclude that, with a mean diameter of 1.2 km, these are the largest dome dunes observed in their study. Holm (1953) notes that the dome dunes are elongated because of the prevalence of particular wind directions over other wind directions.

According to Anton (1983), the Dahna sand fields occupy a low topographic position and approximately follow the geological structure. Anton believes that this suggests a nearby sand source. He notes two paleosoils 1 and 2 m below the surface of the sand ridge in this area. This implies two humid periods in the environment.

Figure E-1.2 illustrates large dome dunes in the Empty Quarter of Saudi Arabia. Figure E-1.3 shows dome dunes present in the upper right of this Plate. The domes are about 1 km in diameter. As the figure illustrates, these dunes are complex with small crescentic dunes, showing the present dominate wind direction, on the rounded crests of the dome dunes. Adjacent dunes are separated by low ridges and deflation hollows. Breed and Grow (1979) interpret the dark gray spots on the ridges as oases. They point out that large dome-shaped dunes such as these are located at the far upwind margins of sand seas. Landsat 1137-07043-7, December 7, 1972.



2

ORIGINAL PAGE IS
OF POOR QUALITY

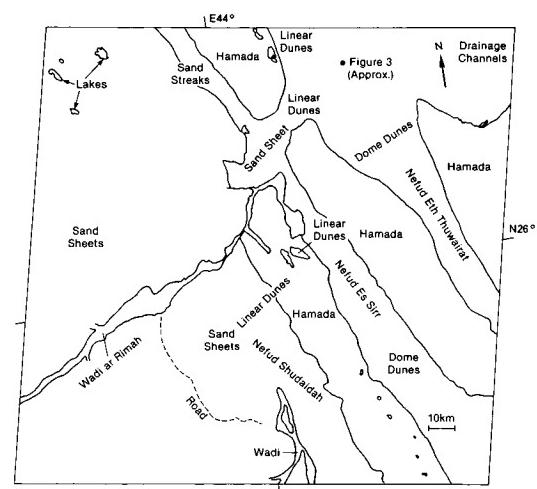
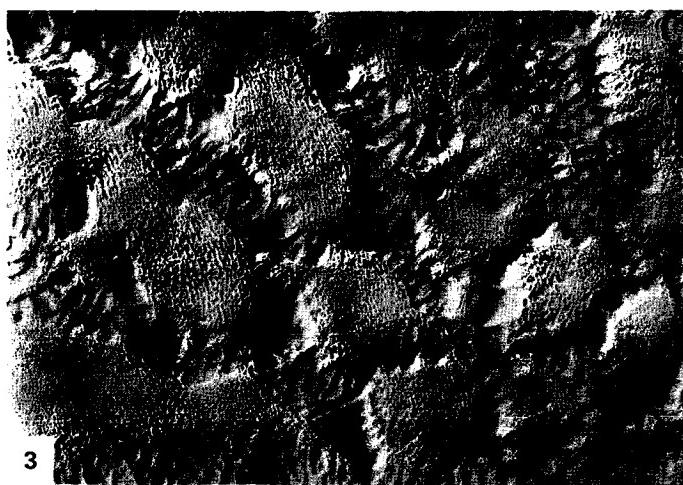


PLATE E-2

The largest active sand sea on Earth, with an area of 560000 km², is the Rub'al Khali, the Empty Quarter of southern Saudi Arabia. The eastern Empty Quarter is on a 300-km wide northeast plunging elongate basin of Tertiary age (Powers et al., 1966). The western desert overlies the Hadramawt segment of the Arabian Shelf, which has an average dip of 0°20' (Powers et al., 1966). The Empty Quarter is covered by an almost continuous eolian accumulation with only occasional remnants of older relief, gravel, or sabkha flats (Anton, 1983). Breed et al. (1979a) divide the Empty Quarter into three principal areas. The western half of the desert consists mainly of northeast-southwest-trending linear dunes. Star dunes dominate the east and south; crescentic dunes are in the northeast. All three of these dune regimes may be seen within this scene in eastern Saudi Arabia.

Most of the star dunes are of equal size and are equidistant. These are also noted on the bottom right of Figure E-2.1, a Return-Beam Vidicon (RBV) image that covers the bottom left of the Plate. Proceeding westward in this image, observe the elongation of the arms of the star dunes. The stoss side (gentle side, facing the dominant wind direction) of the dune is extended. Some of the dunes have coalesced into linear dunes with well-defined crescentic hooks at the western end. These are sometimes called fishhook dunes. The fishhook dunes are connected by northwest sand streaks.

Figure E-2.2, an aerial photograph, shows a 15-km wide area of the complex star dunes that occur in the lower right of the Plate. Note the crescentic dunes on the interdune areas and the linear dunes on the arms. A few of the star dunes in the photograph are isolated, but most are surrounded by small dunes.

Complex crescentic dunes, about 100 m tall, with star dunes on their faces dominate the northern half of the scene. Breed et al. (1979a) found that these crescentic dunes have a mean width (horn to horn) of 2.8 km, a mean length of 2.1 km, and a spacing of 2.6 km.

DUNES OF THE EMPTY QUARTER

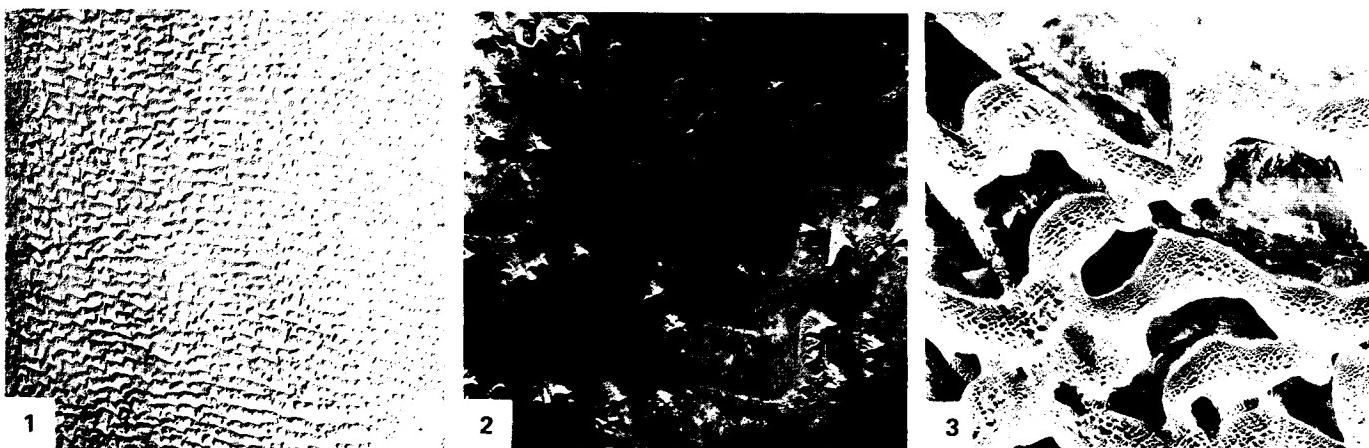
The amount of sand in this sand sea increases greatly to the northwest in this Plate scene. The dunes in this area are much longer and are coalescing. Sand, rather than bedrock or gravel, underlies the crescentic dunes. Where the dunes overlap, the sand sea overlies sand instead of gravel or bedrock. Compare this transition to the appearance of other sand seas in this chapter.

Figure E-2.3 is an aerial photograph of a 5-km wide area of compound crescentic dunes about 50 km north of this scene. The main slipfaces of these giant dunes are to the southeast. Note the interruption of the smaller crescentic dunes on their stoss sides where they coalesce. Breed and Grow (1979) call attention to small simple crescentic dunes on some of the dark interdune areas that they consider to be interdune sabkhas. Sabkhas, salt-encrusted playas of clay, silt, or sand, are seen in the light areas at the bottom right of the Plate.

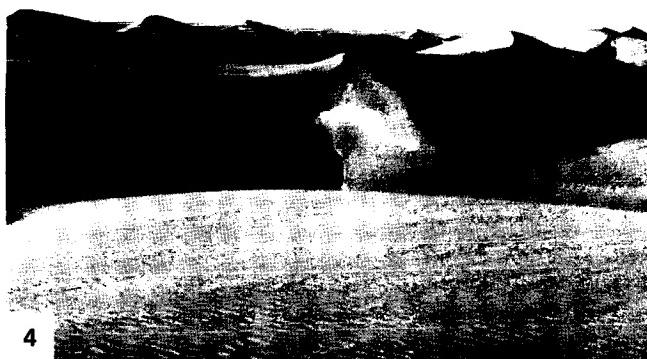
In this Plate scene and the far left margin of Figure E-2.1, the pattern sharply changes from large crescentic dunes to the east to sand sheets and small crescentic dunes to the west. Linear dunes appear near the bottom left of the Plate and dominate the region directly to the west. A change in relief may have caused this shift; this is speculative owing to lack of adequate topographic data.

In an area northwest of this Plate scene, Breed et al. (1979a) suggest that the small crescentic dunes may be migrating southward and overriding the larger compound crescentic dunes. If this is the case, it may mean that more sand became available rather rapidly at the source area, perhaps because of regional uplift or climatic changes, and the sand sea has not yet reached equilibrium.

Figure E-2.4 illustrates typical Empty Quarter dunes as seen at ground level. The light areas are very transient patches of salt. Landsat 1111-06195-7, November 11, 1972.



ORIGINAL PAGE IS
OF POOR QUALITY



4

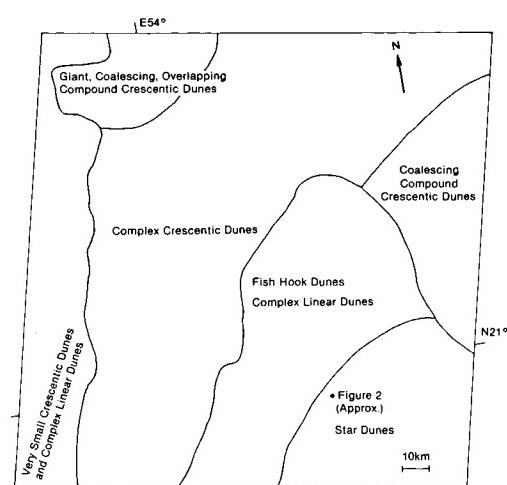


PLATE E-3

ERG CHECH AND YETTI EGLAB MASSIF

This Heat Capacity Mapping Mission (HCMM) daytime visible (Day-VIS) image shows parts of west-central Algeria, Mali, and Mauritania. In the scene, Erg Chech and the smaller Erg Iguidi and Erg Er Raoui encroach on the edges of the Yetti Eglab Massif. Erg Er Raoui is on the upper right between two dark northwest-southeast-trending hills. For convenience in comparing the Day-VIS image with the nighttime infrared (Night-IR) image in Plate E-4, point A, near the northeastern edge of the massif is marked on both index maps. Almost 15 Landsat images would be needed to cover the area imaged by HCMM. Plate E-5, a Landsat image of Erg Chech, is outlined on the right center of this HCMM image.

This Plate is in the Sahara of northern Africa. The world's largest desert, the Sahara is approximately equal in size to the contiguous United States. About 20 percent of the desert consists of numerous sand seas, referred to by the Arabic term "erg." The sand seas are confined to basins and are separated by plateaus, massifs, and low mountain ridges (Breed et al., 1979a). Although erg means sand sea, each linear dune is referred to as an erg on some old geologic maps.

Yetti Eglab is a hilly massif composed of granite (light gray) in the west and northeast. Precambrian shield rock (dark gray) is north of the granite. The dark material in the southeast is undifferentiated Cambrian and Ordovician rock, and the center of the massif is composed of various Paleozoic shield rocks (Legrand, 1981). The small black areas on the massif are standing bodies of water.

The dark northwest-trending hills in the upper right make up the Ougarta Range that consists of Ordovician and Silurian rocks (Legrand, 1981). Wadi Saoura, an ephemeral stream channel, cannot be distinguished directly north of the Ougarta Range, although it may be seen on Plate E-4, an HCMM Night-IR image.

Erg Er Raoui is a thin sand sea of linear dunes between the two series of hills of the Ougarta Range. The hills and bedrock separate it from the other sand seas. The linear sand dunes of the erg are separated by rock and gravel plains. Breed et al.

(1979a) map this sand sea as complex linear dunes with star dunes on their crests.

The southwest corner of Grand Erg Occidental is on the upper right of this Plate; the erg has a very bright surface and features within it cannot be distinguished. Compare this with Plate E-4.

Erg Chech, in a depression east of the massif, consists of compound and complex linear and star dunes. Rocks from the massif may be differentiated in the interdune areas on this image. Breed et al. (1979a) measure the dunes in the erg as having a mean width of 1.0 km and an interdunal spacing of 5.7 km. They find this wide spacing unusual when compared with the linear dunes of other deserts. The regularity of the interdunal spacing of Erg Chech on the east of the massif suggests a topographical control of the dunes by jointing or faulting on the massif. Breed et al. traced the linear dunes of Erg Chech southwestward into sand seas of Mali and Mauritania. They believe that this supports Wilson's (1971) contention that dunes such as these are "sand passing" dunes that transport sand great distances from basin to basin across the Sahara. The complex linear dunes on the western flank of the massif, Erg Iguidi, rapidly die out toward the south.

Figure E-3.1 is a hamada north of the Plate scene in Algeria surmounted by a dune field in the background. Garner (1974) examined this hamada and found that the clasts on the surface of the gravel desert are ventifacts.

A cuesta is a ramp or hill with a gentle slope on one side and a scarp on the other. The cuesta in Figure E-3.2 is northeast of this Plate near Beni-Abbes and shows linear erosion remnants from inclined Cambrian and Ordovician quartzites. Beds more resistant to erosion in the cuesta can be easily distinguished in the figure.

Compound star dunes of Algeria are visible in Figure E-3.3, an aerial photograph. Most of these dunes have four arms, and only two of the arms generally have star dunes on their flanks. The area in the foreground in this picture is a wadi. **HCMM A-A0309-13200-1 Day-VIS, March 1, 1979.**



1



2

ORIGINAL PAGE IS
OF POOR QUALITY

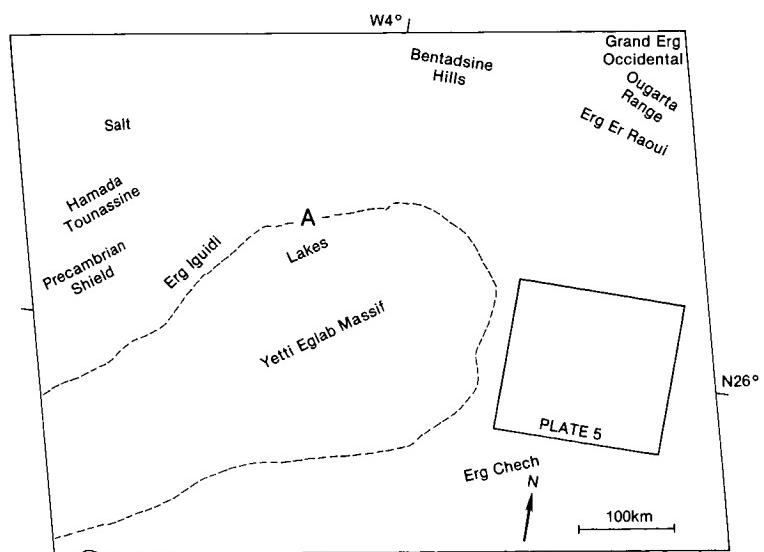
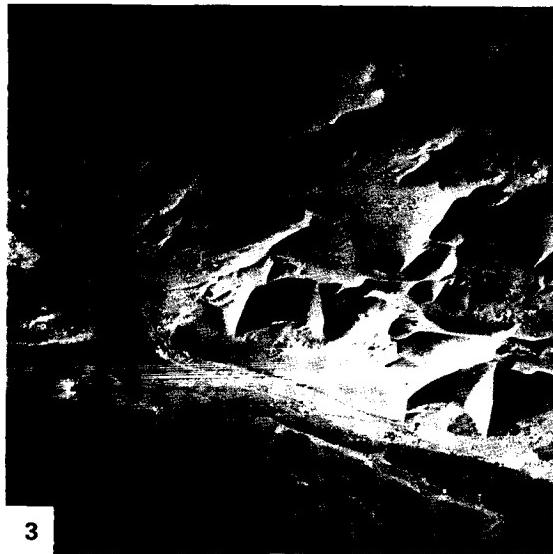
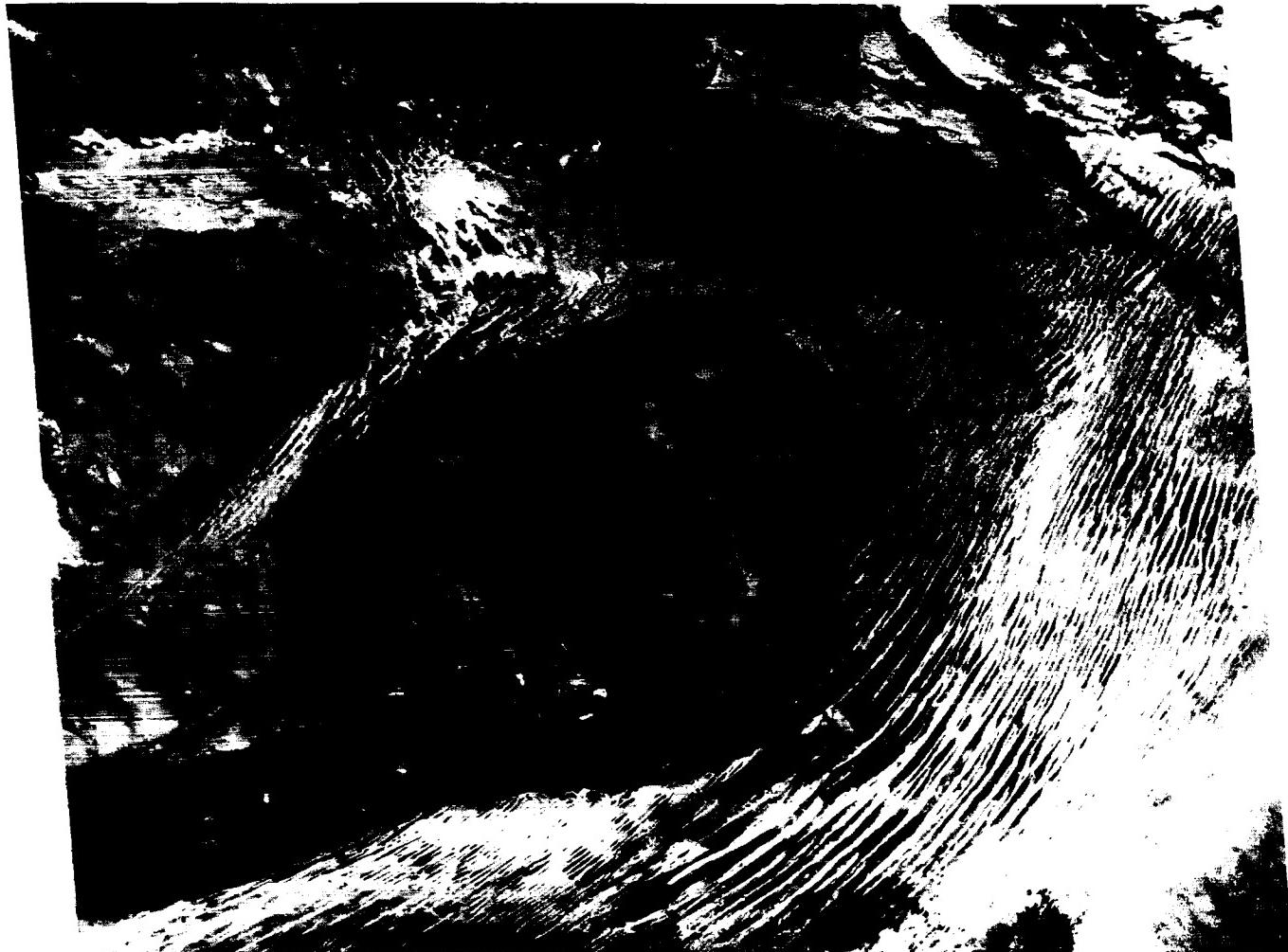


PLATE E-4

The central point of this HCMM Night-IR image of the Sahara Desert is northeast of that of the HCMM Day-VIS image of Plate E-3. The overlap is considerable, and it is interesting to compare them. A locale near the northeast edge of Yetti Eglab Massif is marked as point A on both images. Except for the black (cool) clouds on the upper left of this Plate, atmospheric effects are negligible in both images. The Landsat image on Plate E-5 of Erg Chech, is outlined on the lower right.

HCMM day data were collected when the spacecraft was in the ascending node (passing from south to north) at about 2 p.m. local time. For the night data, however, the spacecraft was in the descending node (passing from north to south) at about 2 a.m. local time. Because of the track coverage, a north-south line in the Day-VIS image trends toward the right in the image, while on a Night-IR image, the line trends left.

Few rock types of Yetti Eglab Massif can be discriminated because their thermal contrasts at night are not great. Several rock types in the massif may be discriminated by their gray tones on the Day-VIS image. Standing bodies of water are warm at night and extremely bright on HCMM Night-IR images. The sharp bright areas on the massif are small lakes, and they correspond with the sharp black lakes on the Day-VIS image. The diffuse light-gray areas near the lakes are probably marshes and are not seen on the Day-VIS image. The areas of these swamps are different on Night-IR images of other dates, indicating the response of moisture to the surface environment in the desert.

Compare the signatures of the rocks on the massif with those of the rocks of the Ougarta Range. Although the range rocks are relatively cool (dark) on Day-IR Images of this area, they are very warm (light) on this Night-IR image. Through comparing Day-VIS (Plate E-3), Day-IR (not included), and Night-IR images, more rock types are discriminated than can be discriminated on one type of image alone. However, field investigators are necessary to identify the rock types.

Most of the dunes south of 30°N in this image are much warmer (lighter) than the more sheltered interdunal areas. Because resolution on the thermal IR image is 600 m, as compared with 500 m on the VIS images, the dunes are not as sharp. The diffusive appearance of the dunes of eastern Erg Er Raoui and

GRAND ERG OCCIDENTAL

eastern Erg Chech is probably an atmospheric phenomenon. A topographic low may have created a warm air pocket. Some of the dunes directly southwest of the Ougarta Range are distinguishable in this image because of the contrast between the dune and the sheltered interdunal area, but in the Day-VIS image, they are indistinguishable.

The northern ends of many of the linear dunes in Erg Chech bend sharply to the west. A different rock type may be seen on the Day-VIS image where this occurs, and the turn may reflect a change in the wind direction resulting from an abrupt change in topography. The variations in rock types beneath these turning dunes are not apparent on the Night-IR image.

It is interesting to compare the Day-VIS and Night-IR appearance of the dunes of Erg Igoudi west of the massif. The westernmost dunes discernible on the Day-VIS image have a deeper gray signature than the other dunes. On the night image, the signatures are identical. Many dunes in the eastern part of Erg Igoudi are visible at night and are difficult to distinguish in the Day-VIS image. In the VIS image, the dunes appear to be similar in gray tone to the rocks in the massif and therefore indistinguishable from the massif. In contrast, the dunes are much warmer at night than the surrounding interdunal areas and are visible.

The southwest corner of Grand Erg Occidental (Great Western Sand Sea) is in the upper right of this image. Although the edge of the erg can be recognized by a subtle change in gray scale, the dunes mapped by Breed et al. (1979a) as star dunes cannot be distinguished on this HCMM image because of the poor resolution.

Examination of this area on Landsat indicates that the interdunal areas do not contrast in signature with the dunes, as they do in the ergs south of this erg. This also may be seen in Figures E-4.1 and E-4.2, ground photographs of the erg. The southwestern border of this erg, Wadi Daorua, is represented on the Plate image by a thin light-gray line. Outcrops on Hamada du Guir are seen in the light-colored areas west of the erg. Figure E-4.3, near Beni-Abbes, shows that hamada with the erg in the background. **HCMM 0141-02090-3 Night-IR, September 14, 1978.**



ORIGINAL PAGE IS
OF POOR QUALITY

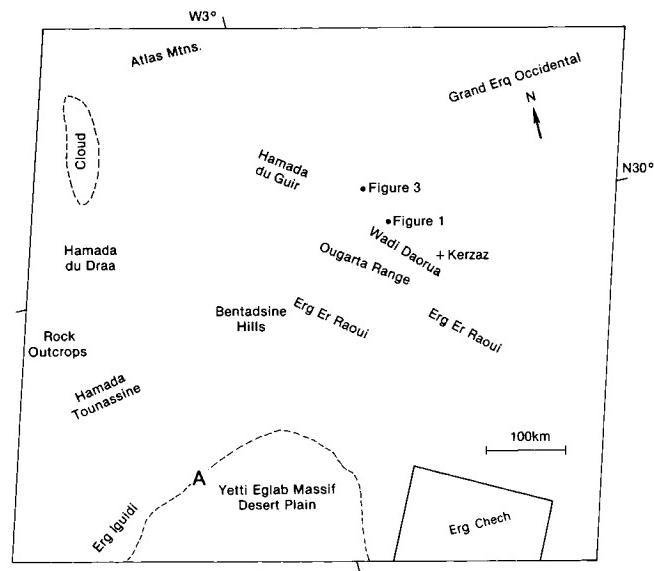
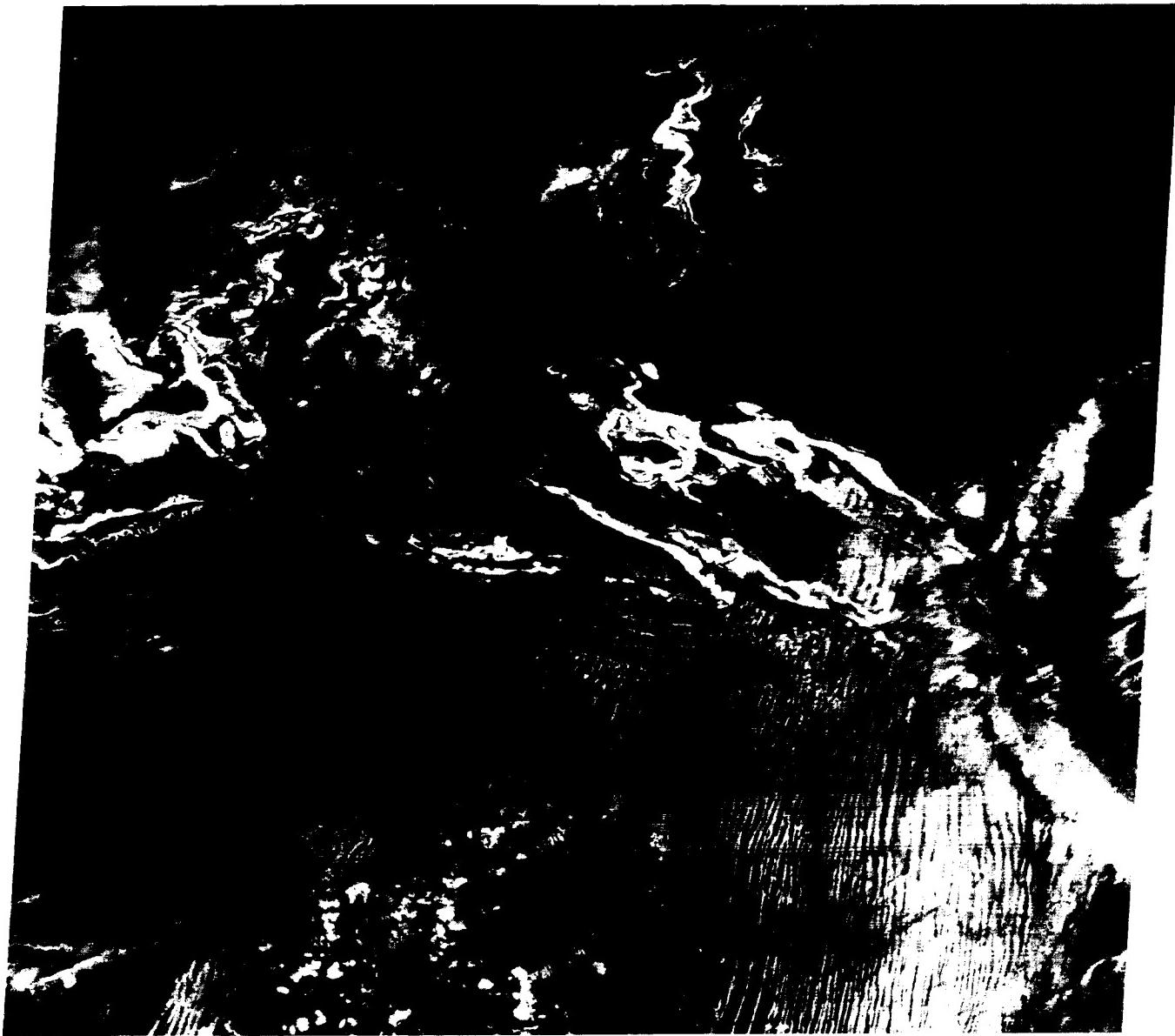


PLATE E-5

ORIGINAL PAGE IS
OF POOR QUALITY

ERG CHECH

Erg Chech, east of Yetti Eglab Massif in the central Sahara, is imaged in this Plate, in Plate E-3 (HCMM Day-VIS), and in Plate E-4 (HCMM Night-IR). On an ancient alluvial plain (Petrov, 1976), it is separated from Grand Erg Occidental by sand sheets and low hills such as the Ougarta Range, and from Grand Erg Oriental by the Tademait Plateau. Wilson (1973) suggests that this erg and the Simpson Desert, Australia, ergs are probably interdigitated with their source areas to a large extent. For most ergs, however, he holds that the center of mass must be downwind from the main mass of the source area.

Erg Chech consists of very widely spaced parallel compound and complex linear dunes. These southwest-trending dunes are asymmetrical, with the east side of the crest broader than the west side. Bedrock or gravel cover is visible in the dark interdune areas in the lower left. The black areas in the lower left of the Plate are water.

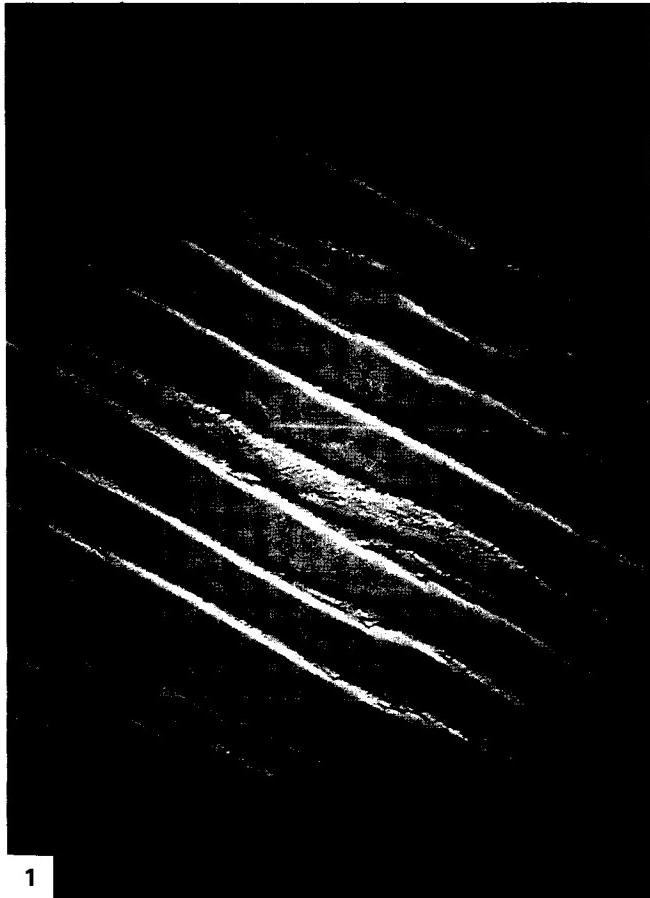
Compare the Plate with Figure E-5.1, a space photograph. It is more difficult to see any interdunal features on the photograph. In the field, this erg is quite red. The dunes in this figure are much wider than the linear dunes shown in Figures E-5.2 and E-5.3. Figure E-5.2 is an aerial photograph of the linear dunes in the erg. The dunes in this figure and Figure E-5.3, a Skylab photograph, show complex linear dunes with crescentic dunes on their crests.

Using Landsat, Breed et al. (1979a) measured the spatial parameters of dunes in the Erg Chech. They found the dunes to have a mean width of 1.0 km and an average spacing of 5.7 km.

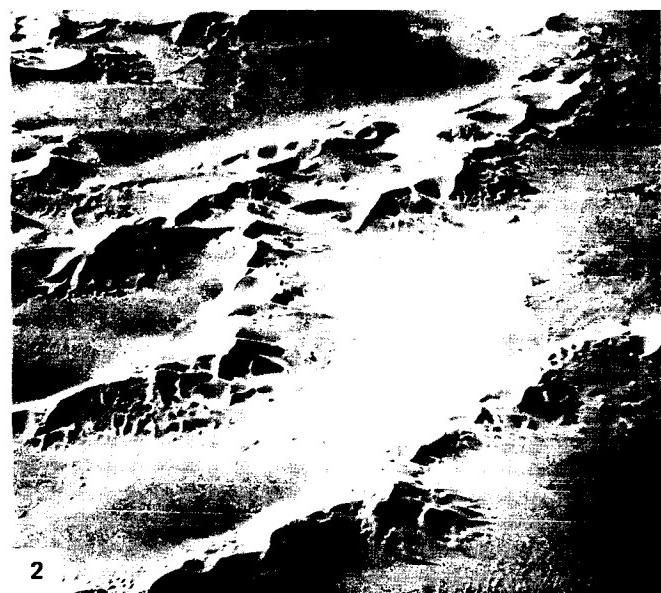
They consider the wide spacing unusual when compared with the linear dunes of other deserts. These investigators traced the linear dunes southwest onto sand seas of northwestern Mali and northeastern Mauritania.

Mainguet and Chemin (1983) suggest that the large interdune areas in Erg Chech indicate a very negative sand budget. They conclude that a negative sand budget occurs when the output of sand is greater than the input, and the sand sea thins. They contend that a large part of the exported sand is trapped in the Sahel, although some is blown into the Atlantic.

Figure E-5.4 shows linear dunes encroaching Nouakchott, capital of Mauritania. The area is southeast of the Plate. The mosque and farms at the edge of the photograph are becoming inundated by the sand sea. **Landsat 1565-10032-6 February 8, 1974.**



1



2



3

ORIGINAL PAGE IS
OF POOR QUALITY

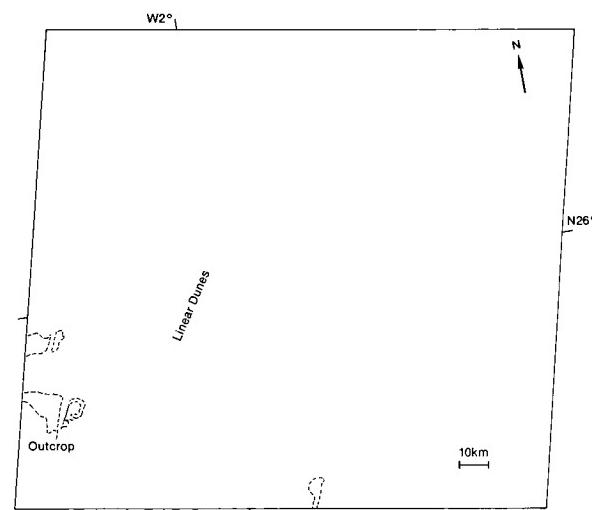
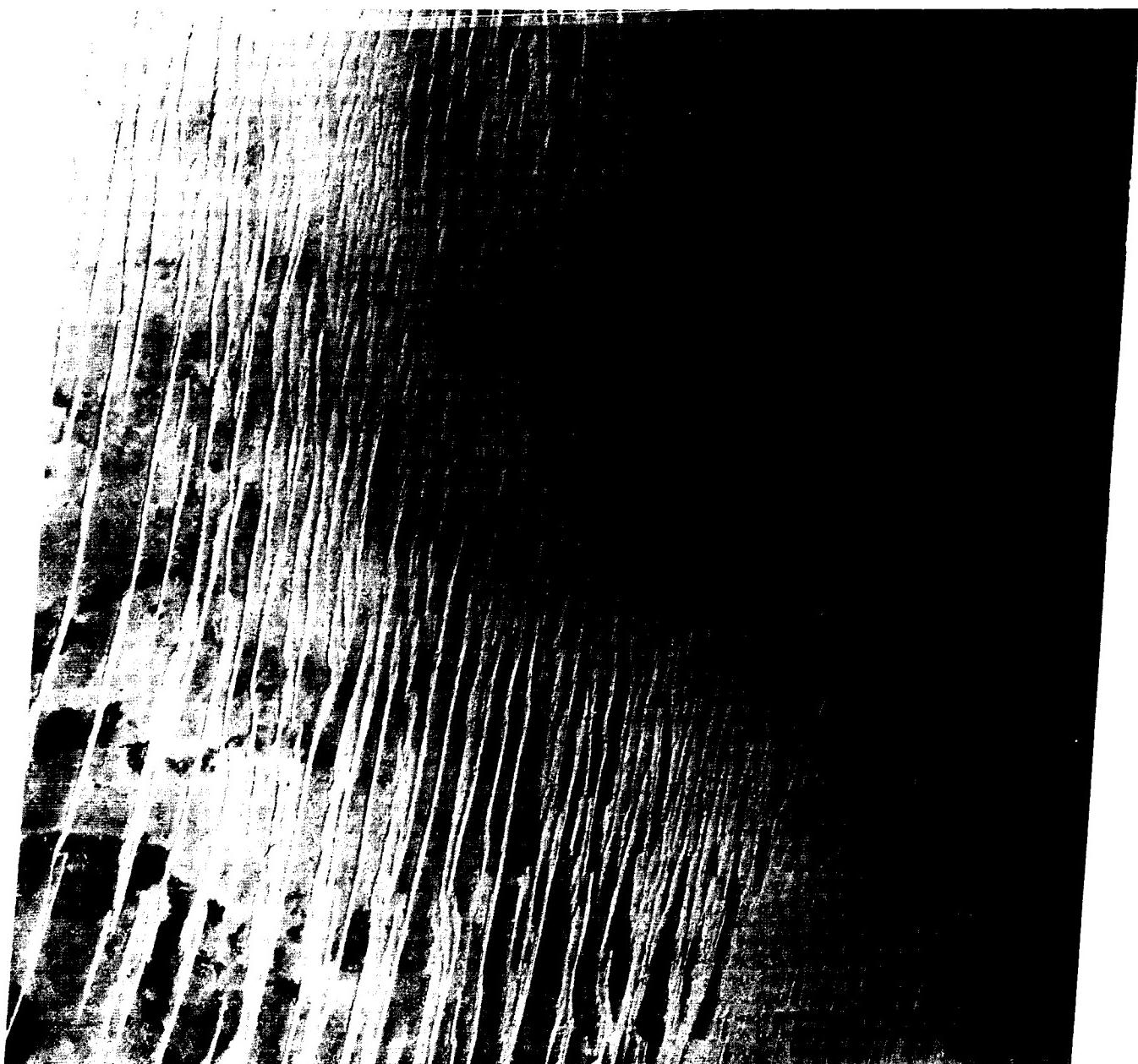


PLATE E-6

GRAND ERG ORIENTAL

Grand Erg Oriental is a 192000-km² sand sea east of Grand Erg Occidental in the central Sahara. The two sand seas are separated by 100 km of gravel desert. About 70 percent of Grand Erg Oriental is sand covered (Wilson, 1973).

A section of Tinrhert Hamada is visible beyond the southeast margin of Grand Erg Oriental. A few intermittent drainage channels mark the extension of streams that flow from the hamada into the sand sea. The light areas on the hamada are saline. Breed et al. (1979a) conclude that the abrupt southern boundary of the sand sea may be controlled topographically because the margin matches the 306-m contour line of the plateau slope. As Wilson (1973) notes, ergs are confined to basins and terminate at any pronounced break of slope.

The star dunes at the boundary appear much closer together and smaller than the dunes directly north in the sand sea. Star dunes are common in the northern Sahara. According to Wilson (1971, 1973), the isolated star dunes of the Grand Erg Oriental are not randomly distributed, but form at the nodes of crossing dune trends. The wind regime of Grand Erg Oriental is very complex, involving the northeast summer trade winds, temperate-zone and southwesterlies, northwesterly cyclonic winds, local thermal winds, and winds related to the sand seas, mountains, and massifs (Wilson, 1971). Wilson states that, although the wind regime is complex, resultant direction of sand flow is definite. He finds dunes without slipfaces in the coarser-grained interdune hollows. Breed et al. (1979a) trace the sand-passing dune trends westward into the Grand Erg Occidental, where the star dunes merge into complex linear dune chains.

The elevation decreases about 150 m from the border of the sand sea with the hamada to the upper left of this image. With

decreasing elevations, the star dunes become isolated and smaller. The interdunal spacing increases significantly. A tendency toward a slight east-west linear orientation becomes apparent in the upper left of the Plate where sand sheets dominate.

Breed et al. (1979a) measure the isolated star dunes and find a mean diameter between 0.7 km at the northern upwind side to 1.7 km at the southern margin just west of this image. The mean crest-to-crest distance ranges from 0.8 to 6.7 km in the north to from 1.5 to 3.1 km in the south.

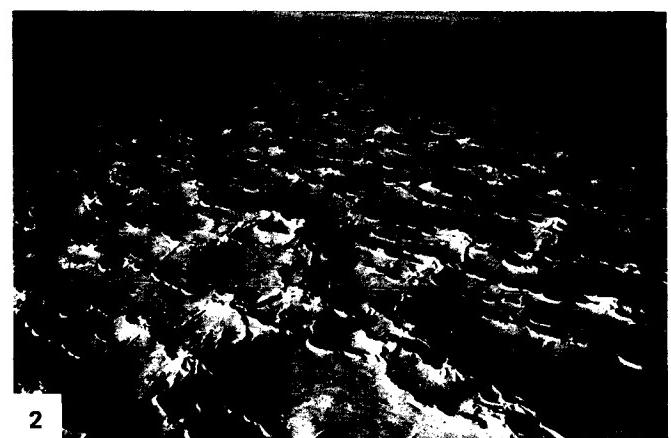
Wilson (1973) suggests that the sand is derived from deflation of alluvium from basins upwind of the sand sea. He estimates a net sand inflow of about six million tons annually for this sand sea. Based on a mean dune height of 117 m and a mean spreadout sand thickness of about 26 m, he infers that Grand Erg Oriental has had an active sand-blown life of 1350000 years.

Figures E-6.1 and E-6.2 are aerial photographs of Grand Erg Oriental. Tinrhert Hamada is in the right foreground of Figure E-6.1. The compound star dunes at the border are larger and closer together than the dunes within the sand sea, as can be seen on the Plate. Figure E-6.2 shows complex linear dunes just inside the southern border of the sea. Although most of the dunes are linear, a few star dunes may be seen in the left center of the photograph.

Figure E-6.3 is a Space Shuttle photograph of the erg a little southwest of the Landsat Plate image. Many of the linear star dunes in that photograph cross the bulk of the sand sea. The interdunal sand areas do not appear to be thick, and the boundary between the sand sea and the hamada is distinguished easily. **Landsat 1199-09323-7, February 7, 1973.**



1



2

ORIGINAL PAGE IS
OF POOR QUALITY

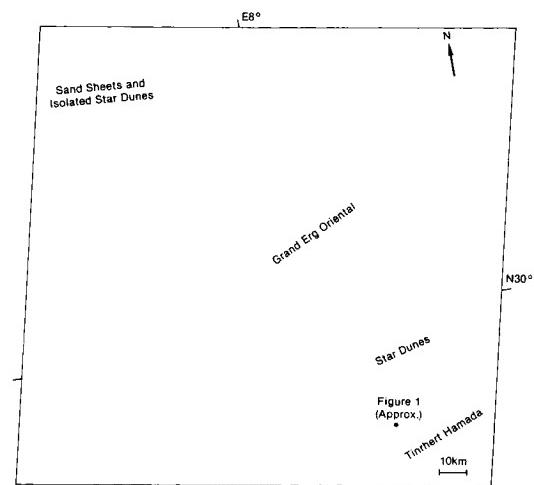
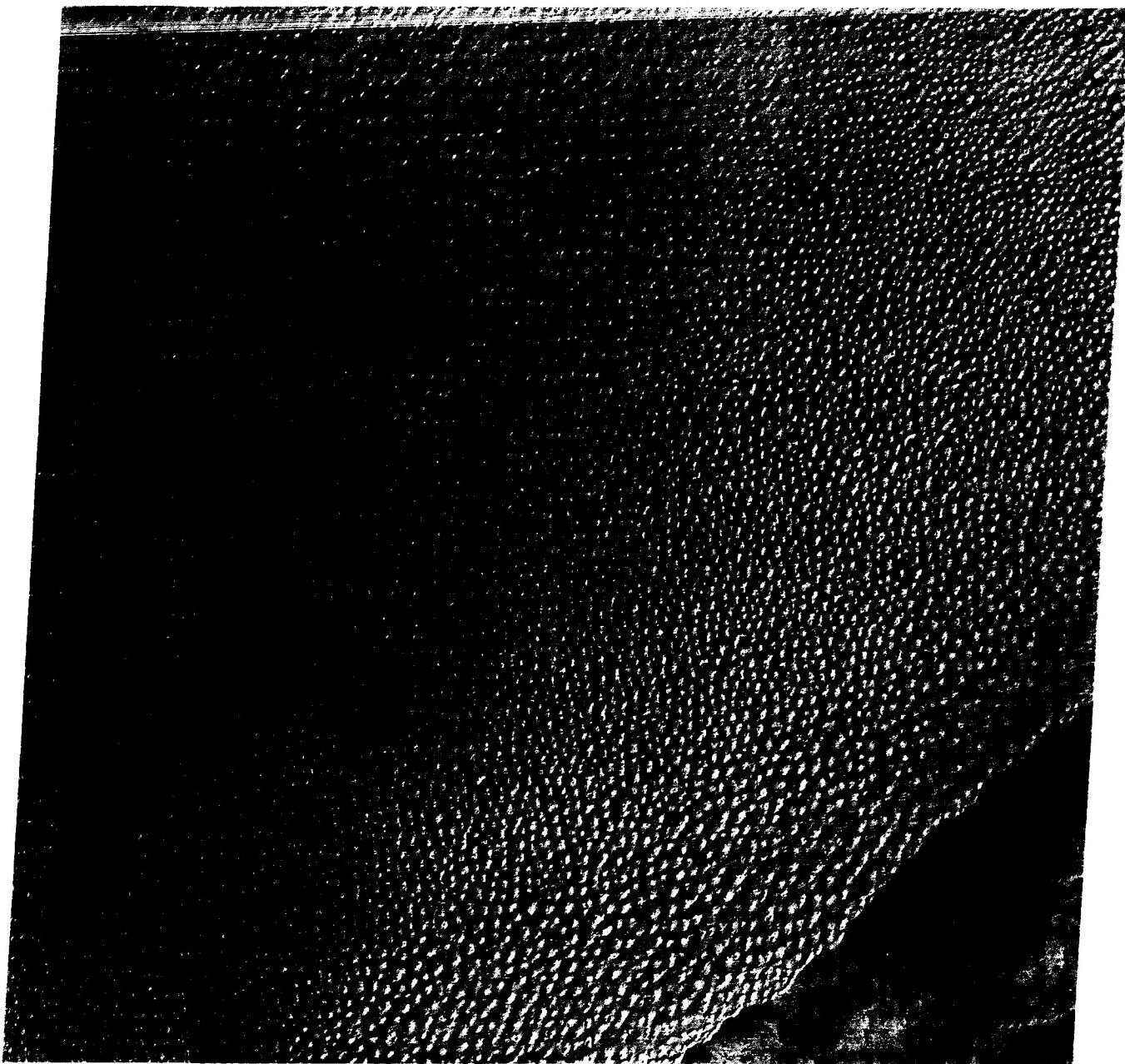


PLATE E-7

TANEZROUFT BASIN

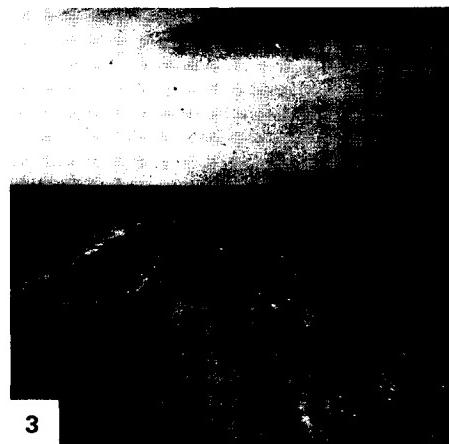
The Tanezrouft Basin is a geographical region in southern Algeria known as the "Land of Terror" because of its desolate landscape. The Tanezrouft is located in the south-central Sahara a few hundred kilometers southeast of Yetti Eglab Massif. The eastern border of Erg Chech, depicted in Plates E-3 and E-5, is near the basin. Reg, or gravel desert, dominates this Plate as it does about 70 percent of the Sahara. Reg stripes on the basin surface are illustrated in Figure E-7.1; note the oil rigs and trucks in the background. The hills at the bottom and right of the Plate are the foothills of the Ahaggar Plateau.

As reported by Cooke and Warren (1973), areas near this Plate record many climate extremes. Tamanrasset, Algeria, a few hundred kilometers to the east, has a range of annual precipitation between 6.4 and 159 mm; once, 44 mm of rain fell within 3 hours. Figure E-7.2 shows the terrain in the Ahaggar west of Tamanrasset. Tanezrouft, a small town a few kilometers west of this Plate, holds the regional record for the greatest daily variation of relative humidity, between 12 percent in July and 29 percent in November–December (Cooke and Warren, 1973, p. 12).

Two small ergs occur within this region. Erg Mehedjibat is made up of a cluster of small star dunes. Just the tip of Erg Tassegefif appears at the bottom. These ergs probably occupy the lowest elevations on the Plate. In addition, numerous small salt flats are scattered throughout the scene.

The concentric patterns that stand out in this Plate are deflation hollows scoured by eolian activity in slightly Paleozoic sedimentary rocks. Note the effects of differential deflation on the structures. Deflation basins are created wherever variations in lithology or cementation result in differing rates of rock-weathering and wind-aided removal of fines (Glennie, 1970). Considerable local relief develops even though fluvial activity is minimum. Cuestas, known in this part of the world as "tassilis," that formed from north-dipping rocks appear along margins of the darker rocks in the lower fourth of the Plate. In places, the erosion surface has beveled the strata to produce a banded floor pattern that corresponds to small segments of the concentric patterns of the deflation basins (Figure E-7.3). Figure E-7.4 is a hand-held Shuttle picture of a small dune field northeast of this Plate. The photograph covers an area of 120 km and shows star dunes west of Hagar Massif.

This Plate image was digitally processed to emphasize the contrast between the rock units. Figure E-7.5 is part of the same Plate image that was processed in the standard way by the EROS Data Center. Compare the equivalent areas of the two images. The digital data used to make the Plate image have been filtered and stretched to enhance certain features in the basin by changing the gray-scale step values. As a result, the rock exposed at the bottom of the Plate is extremely dark, and subtle features on the outcrop visible on Figure E-7.4 are not evident in the Plate. Similarly, the dunes in Erg Mehedjibat are better highlighted in the figure than in the Plate, where they are more saturated. Sometimes special processing done to improve information extraction and to bring out certain features causes loss of details not always recoverable by careful printing. Landsat 1112-09505, November 12, 1972.



ORIGINAL PAGE IS
OF POOR QUALITY

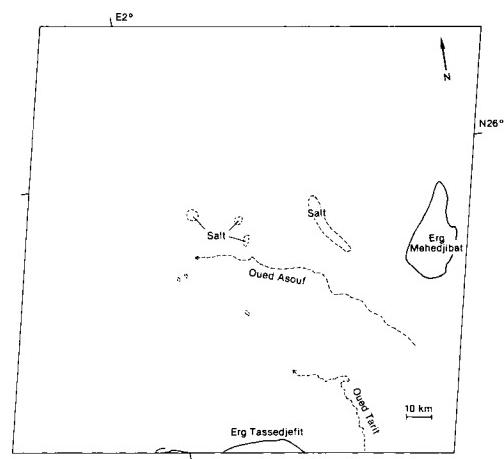
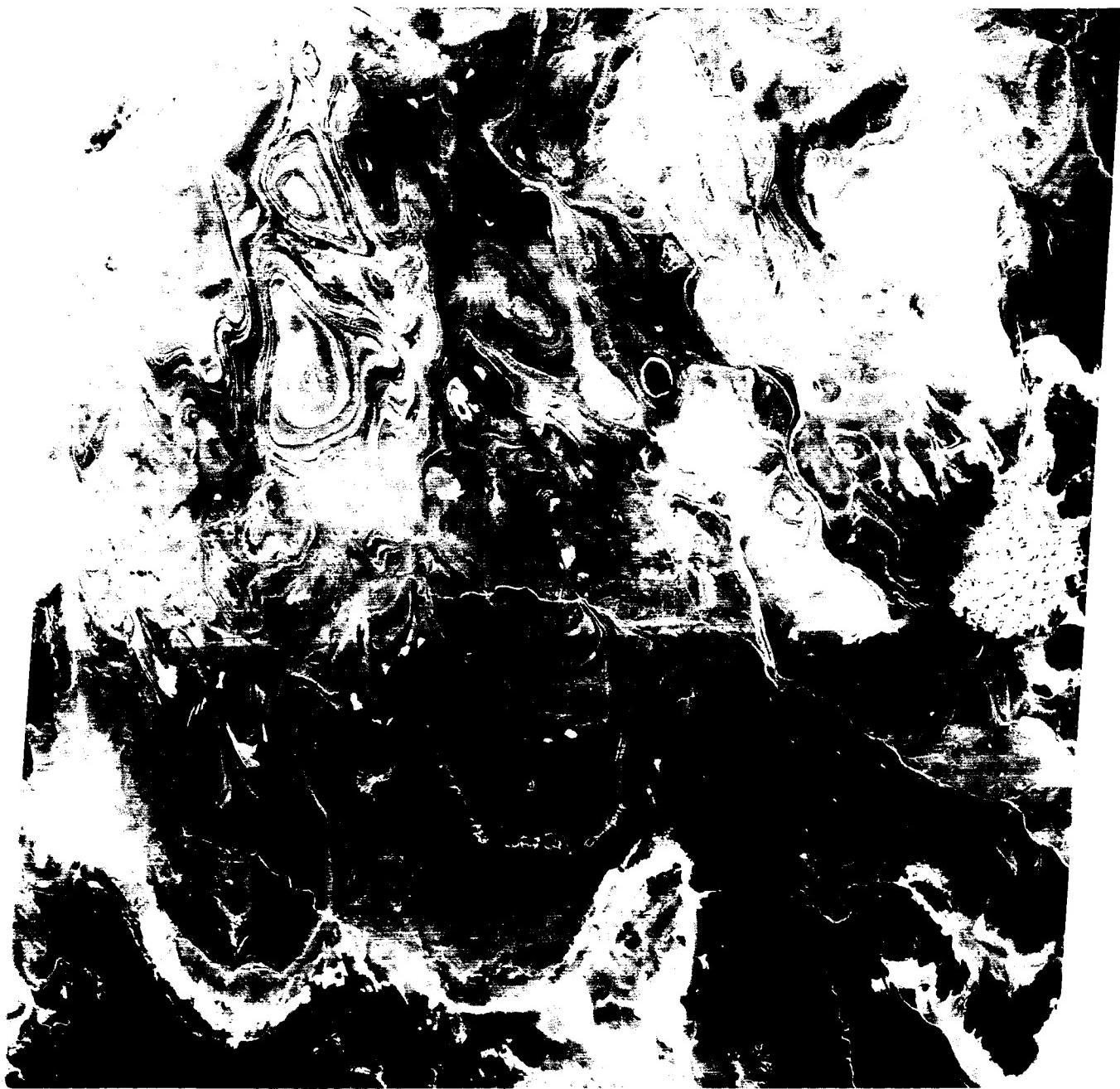


PLATE E-8

LAKE CHAD

This Plate images on the northeastern part of the 220-km wide Lake Chad in the Sahel, a semiarid zone south of the Sahara. The Sahel was afflicted by a severe drought in the late 1960s and early 1970s and is currently recovering from another drought. Faure and Gac (1981) fix a mean time of 31 years between each of the last three droughts in the Sahel. From this, they correctly predicted that the recent drought would end in 1985.

Lake Chad is slightly west of center of the Chad Basin, an extensive area of sand seas in Central Africa. Grove (1958) describes the present lake shore as having north-south-running ridges and hollows. Dunes form long closely spaced peninsulas and northwest-oriented lines of islands in the lake. The shoreline is illustrated in Figure E-8.1. The dunes are about 80 m high and, as can be seen on the Plate, are spaced 2 to 3 km apart. The interdune areas called bahrs, which become flooded during the rainy season, contain deposits and calcareous shales.

Lake Chad survives today in a savanna landscape distinguished from a humid and an arid environment by a highly seasonal rainfall (Thomas, 1971). As reported in Schneider et al. (1985), more than 90 percent of the annual rainfall occurs between June and September. The surface of the lake is highly responsive to climate change. Between 1964 and 1974, the surface of Lake Chad was diminished by a factor of 3 and its volume by a factor of 4 (Schneider et al., 1985). Due to evaporation and uneven water supplies, the surface area of the lake annually varies between 10000 and 25000 km² (Van Chi-Bonnardel, 1973).

Goudie and Wilkinson (1977) suggest that Lake Chad stood between 380 and 400 m above sea level around 55000 years ago. As drier conditions prevailed, dune fields were established until humid conditions returned. Nicholson (1980) notes that, from about 1600 until some time in the 18th century, the surface of the lake was about 4 m above the present level. Fluctuations of Lake Chad have been dated with pollen analysis and with human records, such as the Bornu Chronicals, which began before 1500. From these data, Nicholson concludes that, within the past several hundred years, the climate has changed significantly. She feels

that the lake level changes are clear examples of the expansion and contraction of the desert belt. Studying lake sediments, Servant and Servant-Vildary (1980) state that the first appearance of windblown sands in the Chad Basin was 2 or 3 Ma ago.

Extensive alluvial and lacustrine deposits near Lake Chad represent former shorelines at heights of 20 to 40 m above the present lake. An older lake, "Mega-Chad," appears to date from a pluvial period 10000 to 7000 years ago (Thomas, 1971). Grove (1970) notes that the shoreline of Mega-Chad had cut into a group of volcanic plugs of columnar rhyolite southeast of the present lake. These hills are illustrated on an aerial photograph (Figure E-8.2). From the ground, the Mega-Chad shoreline traces on the plugs mark a level some 40 m above the present lake shore.

Schneider et al. (1985) illustrate the recent Sahelian drought by comparing a 1972 Landsat image with more recent images. They note that by 1978 the northern basin of Lake Chad had all but disappeared.

Figure E-8.3 is a visible (left) and near-IR (right) Advanced Very High Resolution Radiometer (AVHRR) image of the Lake Chad area. AVHRR data are available daily from NOAA-7, with a resolution of about 1 km. The images cover a 1500-km swath. In the visible image, the lake bed is dark gray, and the shallow sediment-rich water is light gray. On the infrared image, the water is black and is surrounded by vegetation.

Schneider et al. (1985) map changes in vegetation over the Lake Chad region using a normalized vegetation index calculated by comparing the spectral response of an area on the AVHRR bands. These authors use AVHRR thermal infrared bands to generate temperature maps, from which they find that the southern basin is about 14 °C cooler than the adjacent desert and the northern basin is only about 4 °C cooler. The water and vegetation in the south account for this lower temperature. With its coarse resolution and daily coverage, the AVHRR system provides data that supplement Landsat data. **Landsat 50250-08534-4, November 6, 1984.**



ORIGINAL PAGE IS
OF POOR QUALITY

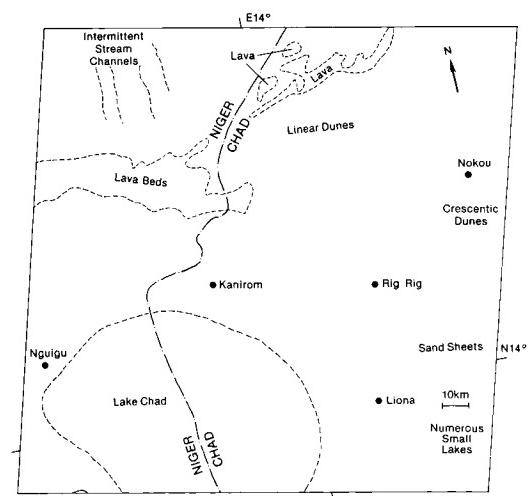
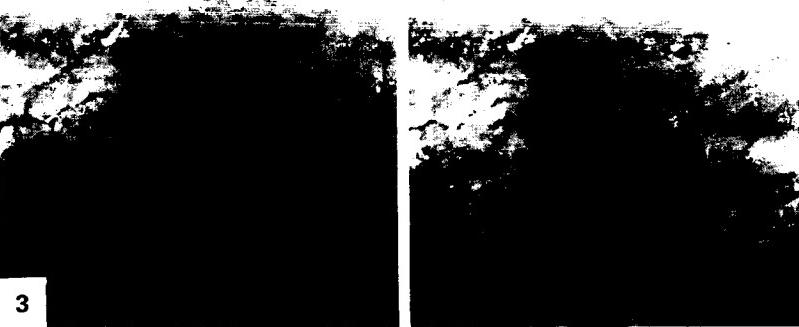


PLATE E-9

The Kuiseb River separates the 34000-km² sand sea in the south from the northern gravel deflation zone of the Namib Desert. Plate E-9 (two pages forward) is an LFC photograph of a 170- by 345-km area of the Namib Desert and environs. Two Landsat images (Figures E-9.1 at the north end of the LFC image and E-9.2 at the south end), computer-enhanced to bring out dune details, are reproduced below for comparison. This desert is bounded on the west by the Atlantic Ocean, with its north-flowing Benguela Current that controls the arid climate of the region. On the east, 80 to 140 km inland from the ocean, it is bounded by the Great Escarpment (see Figure 1-7) along the edge of higher terrain underlain by Paleozoic sedimentary rocks. Note the drainage patterns on the western side of the Great Escarpment. Playas fed by two ephemeral stream channels, Tsondab Vlei and Sossus Vlei, develop about halfway through the sand sea.

As summarized by Breed et al. (1979a), many investigators believe that the desert sands are derived mainly from fluvial sediment transported to the Namib coast by a perennial river about 300 km south of the Plate. The sediments are then transported north by longshore drift. Some of the sand near the coast is of marine origin, and a little sand is brought in from the Great Escarpment and beyond.

The Namib Platform is a Tertiary erosional surface formed on schists, quartzites, and granite intrusives (Breed et al., 1979a). The platform is exposed north of the Kuiseb River in the rock desert. Roads, outcrops, gravel plains, and sand sheets may be distinguished in the gravel desert. Structures and lineaments in the outcrops are indicated by their dark features. The relief of many features on the gravel desert can be estimated using the stereoscopic capacity of the LFC. Such data on elevation differences are generally unavailable in remote corners of the world.

Rossing, at the southern end of the elliptical structure north of the Khan River, is the location of one of the world's largest uranium deposits. Other minable minerals are found also in this area of the Namib. Extensive sheets of calcrete 1 to 30 m thick are exposed on the platform, leading Selby et al. (1979) to suggest that the climate has been considerably wetter for extended periods in the past.

The Kuiseb River passes through an incised valley in about the center of the Namib. Selby et al. (1979) note that the Kuiseb becomes progressively less entrenched away from the Great Escarpment. They point out that, although some flow occurs in the upper Kuiseb valley annually, it reaches the sea only once in every 8 or 9 years.

Selby et al. (1979) find calcium carbonate precipitates in an interdune area west of the Tsondab Vlei that they believe mark a small shallow lake. They date that lake at between 210000 to

NAMIB DESERT

240000 years ago. The surviving precipitates imply that the climate has been arid since then. The lake borders east of Narabeb cannot be distinguished on the LFC photograph, but it does show a large flat area with a disruption of the dune pattern that indicates the former course of the Tsondab River at the time it extended farther into the sand sea. Seely and Sandelowsky (1974) postulate that the Tsondab and other rivers from the Great Escarpment originally reached the Atlantic. The northward movement of the dunes truncated their channels.

There are three main dune types in the Namib Sand Sea. Breed et al. (1979a) and Lancaster (1983) describe a 5- to 30-km wide zone of compound crescentic coastal dunes (Figures E-9.3 and E-9.4). Crescentic dunes are common in coastal deserts with prevailing onshore winds. Note the two orders of ridge spacing in Figure E-9.3. In Figure E-9.4, morning sea fog, common in coastal deserts, moistens the dunes; the sea is toward the right.

Linear dunes have formed inland of the crescentic dunes, and star dunes occur locally near the vleis. Compound linear dunes, in the Namib, consist of groupings of 3 to 5 sinuous sharp-crested ridges, each 5 to 10 m high and spaced 120 to 150 m apart. The dunes in the southern sand sea are 25 to 40 m high. Each compound linear dune set is spaced 1.5 to 2 km apart (Lancaster, 1982). Compound linear dunes are seen in Figure E-9.5, an aerial oblique view of the Kuiseb River looking south over the gravel desert and the river to the 80- to 100-m tall linear dunes of the sand sea.

The complex linear dunes in the Plate are 50 to 150 m tall and 600 to 1000 m wide, with small star dunes and reversing dunes along their crests. Figure E-9.6 shows a large linear dune near Sossus Vlei. Lancaster (1982) notes that linear dunes in the east are effectively chains of star dunes. Below eastern slipfaces along the main ridge are small crescentic dunes that help to provide an en echelon pattern to the sinuous crest.

Figure E-9.7 depicts a complex star dune of the Namib. Small linear dunes are conspicuous between the two right arms of the main dune. Vegetated linear dunes to the left of this dune are encroaching on the adjacent star dune.

The influence of topography on wind pattern can be studied on the southeastern side of the inselberg directly south of Sossus Vlei at the bottom left of the Plate. Because winds there are deflected by the inselberg, the small dunes to the south reflect the complicated pattern of the wind regime. By using the stereo capability of the LFC, Walker (1985) constructed a profile of the Namib sand sea that shows a systematic increase in dune height and interdunal spacing with distance from the Great Escarpment. **Large Format Camera 1917, October 12, 1984.**

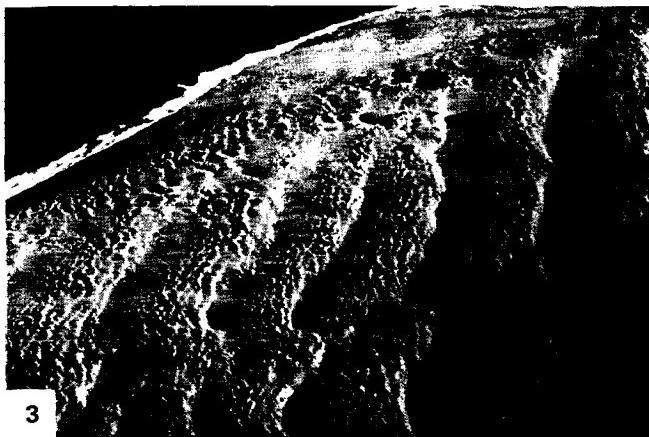


1



2

ORIGINAL PAGE IS
OF POOR QUALITY





**ORIGINAL PAGE IS
OF POOR QUALITY**

ORIGINAL PAGE IS
OF POOR QUALITY

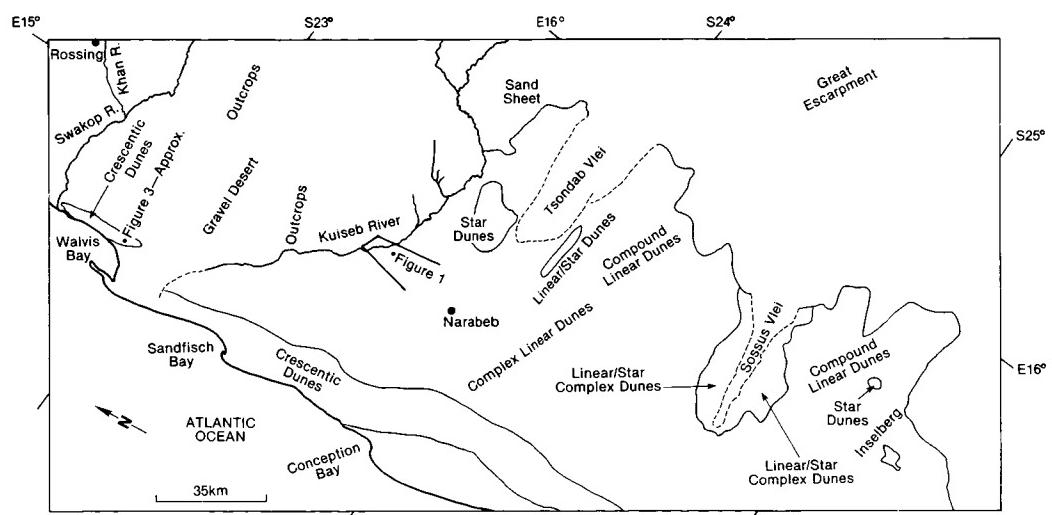


PLATE E-10

ATACAMA DESERT

The Atacama Desert is not only a trade-wind desert and a coastal desert affected by the north-flowing Peru Current, but is also a rain-shadow desert protected by the Andes Mountains. Many investigators consider it the driest desert on Earth. Compare this desert with the Namib Desert (Plate E-9), a coastal desert in western Africa at the same latitude. The Tropic of Capricorn passes through both deserts.

This Plate is near the center of the Atacama Desert (and south of the scene in Plate C-12). The dark tones along the right margin represent vegetation on the eastern slopes of some of the Andes Mountains.

The low Coastal Range is immediately east of the Pacific Ocean. Throughout much of this Plate, the shoreline is a wave-cut cliff with a maximum height of about 1000 m (Erickson, 1981). The drainage pattern from the Coastal Range is poorly defined. Note in Figure E-10.1 the influence of a mantle of dust that covers much of the range. The linear features in the foreground are open fissures formed during faulting.

The Central Valley separates the Andes from the Coastal Range. Alluvial fans in drainage deposits derived from the higher Andes dominate the surficial material of the valley. According to Erickson (1981), the valley contains alluvium and interbedded lacustrine sediments up to 900-m thick. The dense coastal fogs that cover the Coastal Range nearly every austral winter night do not extend to the Central Valley (Erickson, 1981).

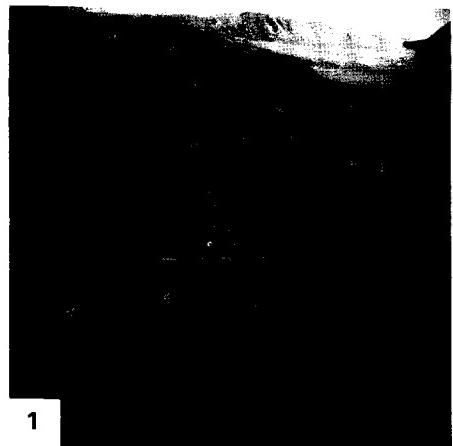
A small dune field lies directly north of this plate, and occasional large dunes have built up along the coast and even within the Coastal Range. Figure E-10.2 shows dunes near the coast directly north of this image. The slipface is toward the left. Except for these dunes, the Atacama is a region of eolian deflation and evaporation. Erickson (1981) points out that, due to variable diurnal and seasonal winds, eolian-transported material spreads evenly over the desert rather than forming dunes. He found about 100

closed basins in northern Chile, many of which contain salars (playas). The map of the playas north of the Loa River on the Plate are based on Erickson (1981). Figure E-10.3 is an eroded clay playa about 50 km north of the top of this Plate. Yardangs that formed in mudflows indicate fairly uniform wind direction. The large ridge on the far right is a mine refuse pile. Figure E-10.4 is also an eolian deflation zone and shows gypsum-rich soil on top of nitrate-rich caliche.

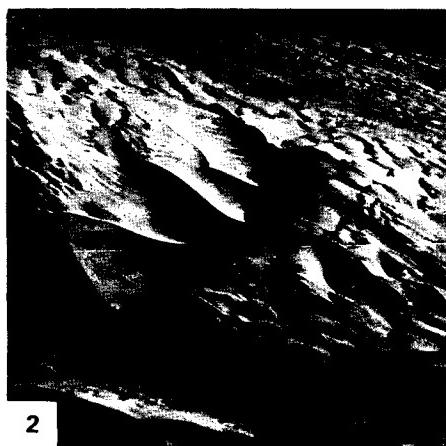
The Atacama Desert is unique among the deserts of the world in its great abundance of saline minerals. Sodium nitrate has been mined for explosives and fertilizer in the Atacama since the middle of the 19th century. Nearly 3 million metric tons were mined during World War I (Erickson, 1983).

The nitrate deposits are ubiquitous in the Atacama. The deposits are found on all types of topography and in all types of bedrock and unconsolidated sediments. Erickson (1983) distinguishes two types of nitrate ore: alluvial ore in which the saline minerals cement the unconsolidated sediments, and bedrock ore in which the minerals vein into bedrock. He suggests that most of the nitrates formed through fixation of atmospheric nitrogen by micro-organisms in playa lakes and moist soils. Periodic evaporation led to crystallization of saline minerals, after which leaching and redeposition bring about secondary enrichment. He indicates that the chief sources of the saline constituents are water-soluble saline minerals from the volcanoes in the Andes. The minerals were leached by ground water and carried into the desert by streams, ground water, and wind.

Erickson (1983) attributes the abundant nitrate deposits to the fact that the Atacama has had an extremely arid climate at least since the Middle Miocene time (10 to 15 Ma ago). Therefore, the present-day landscape has been modified only slightly, thus providing a long-time interval for depositional buildup of the nitrates. Landsat 2312-13514-7, November 30, 1975.



1



2



3

ORIGINAL PAGE IS
OF POOR QUALITY

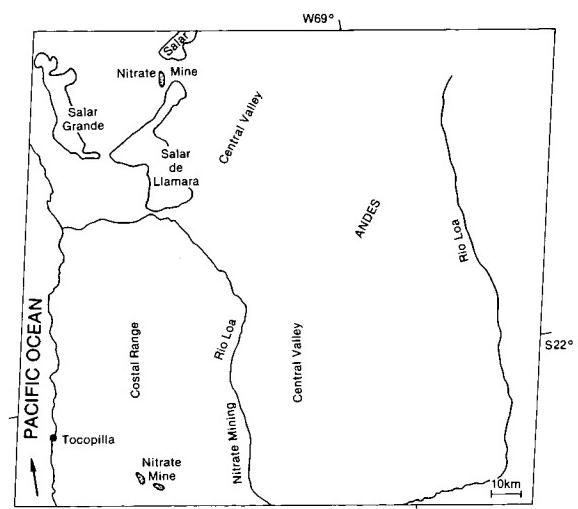
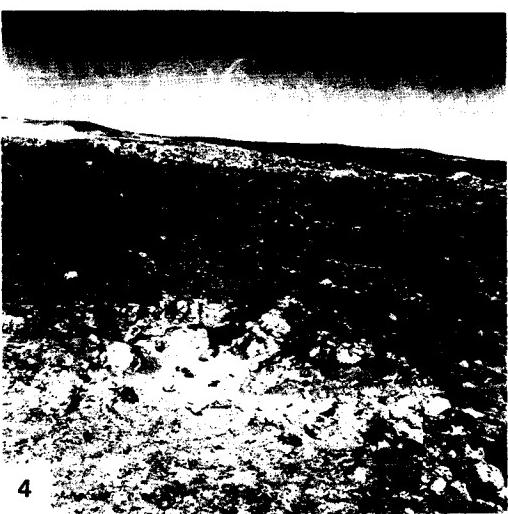


PLATE E-11

GRAN DESIERTO, SONORAN DESERT

The color Plate on the opposite page is an enlargement of part of a full Landsat TM image showing the Sonoran Desert of northwest Mexico and the adjacent Gulf of California. To set the context, the full scene, hereafter referred to as the "Plate scene," is reproduced at a smaller size below the color enlargement, along with an index map for the entire scene. The enlargement vividly portrays the details that can be extracted from TM images after additional computer processing.

The 310000-km² Sonoran Desert has more than 3800 km of sea coast. Considerably more than one half of the desert is within 80 km of a coast (Crosswhite and Crosswhite, 1982). According to these authors, the Gulf of California, bottom right in the Plate, was formed in the center of the present Sonoran Desert by tectonic rifting of the San Andreas fault system about 12 Ma ago. Faulting and tectonism created the basin and range topography characteristic of the Sonoran Desert (this Plate and Plate E-12) and of the Great Basin Desert (Plate E-13).

The present Colorado River delta forms inland from where the river empties into the Gulf of California (Plate D-12). The Gran Desierto sand sea lies in a basin about 60 m deep east of the Colorado River. Northwest-southeast-oriented mountain ranges typical of the Basin and Range Province stand both west of the Colorado River floodplain and east of the sand sea. The ranges are sharp-peaked and have broad alluvial fans.

Most of the rocks underlying the Gran Desierto are of igneous origin. The Sierra Pinacate, part of which appears along the right margin of the full scene (Figure E-11.1) from which the color Plate is extracted, is a large field of volcanoes (see Plate V-4). As summarized by May (1973), the Pinacate is of Quaternary age with small sections containing rocks of Tertiary age. Eruptive activity continued into the Holocene, but the field is presently dormant or possibly extinct. Cerro Pinacate, a ring just visible in the Plate, reaches an elevation 1000 m above the alluvial plain that surrounds the volcanic field.

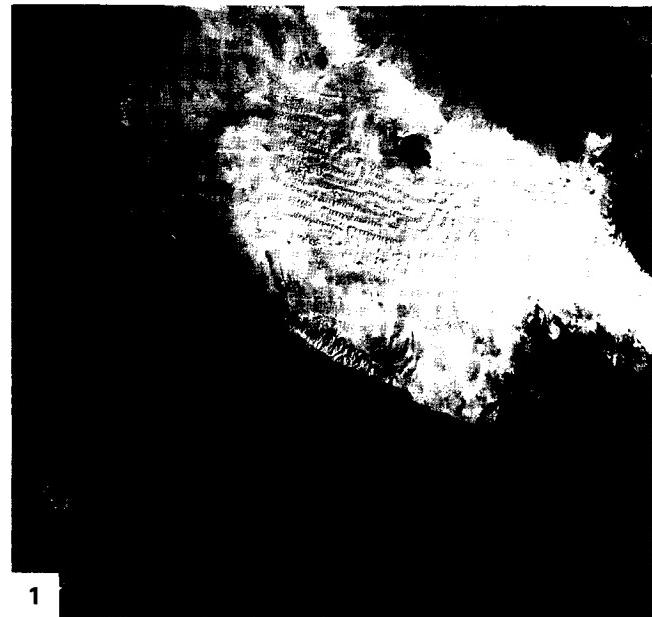
The sand sea overlies lava beds. According to May (1973), lava outcrops are constantly being buried or exposed on the sand

sea as the winds shift. The Sierra del Rosario within the sand sea is about 25 km long and 5 km wide. The range consists of granite with pegmatite dikes (May, 1973). The dunes around the Sierra del Rosario average 180 m in height (May, 1973). Simple, compound, and complex star dunes dominate the area. The complex star dunes southwest of the Sierra del Rosario consist of three to four arms and line up in a linear array. Below the southernmost linear-star dune array and on the one directly above it, crescentic and linear dunes are visible in the color image on the south-trending arm of the dune. Small linear and crescentic dunes lie in the interdunal areas. Simple star dunes are north and northwest of the complex dunes. Ripples on one of the star dunes appear in Figure E-11.2.

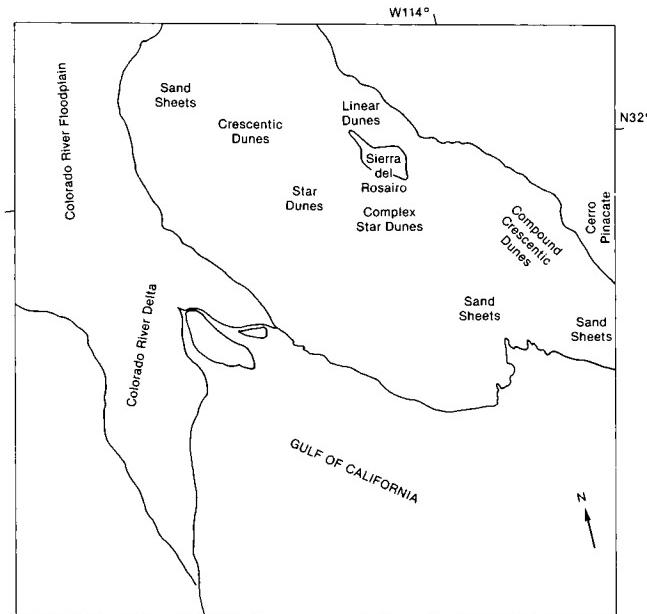
Figure E-11.3 shows rows of simple three-armed star dunes. Note the parallelism of the arms from dune to dune. Between the rows are compound transverse dunes of low relief. This dune array grades eastward into patterns of complex crescentic dunes crested with small star dunes. Still farther east near the Pinacate Field, they merge with compound crescentic dunes (Greeley et al., 1985).

Small linear dunes are distributed within the sand sheets north of the Sierra del Rosario. Isolated small star dunes also occur there. The change in dune orientation among the clusters reflects the change in wind direction due to elevation changes near the range. Proceeding west, these dunes grade into very small simple crescentic dunes close to the limit of resolution of the TM image.

Figure E-11.4 is an oblique aerial photograph showing the borders of the lava flow of the Pinacate lava field and the sand sea. This figure is just off the right center of the Plate scene. The compound crescentic dunes are superposed with compound transverse dunes. The southwest boundary of the lava shows a mixture of bright eolian material and dark volcanics. Eolian sediments cover the lava flow as a gradually thinning mantle (Greeley et al., 1985). **Landsat TM 40174-17392-7, January 6, 1983.**



1



ORIGINAL PAGE
COLOR PHOTOGRAPH

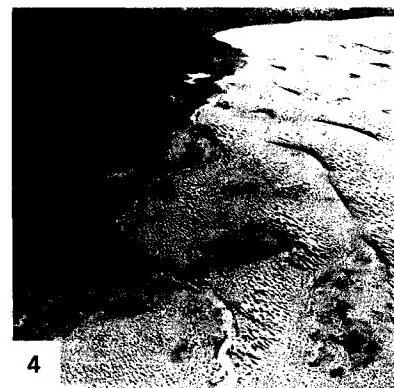
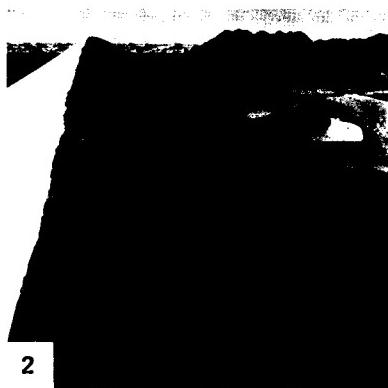
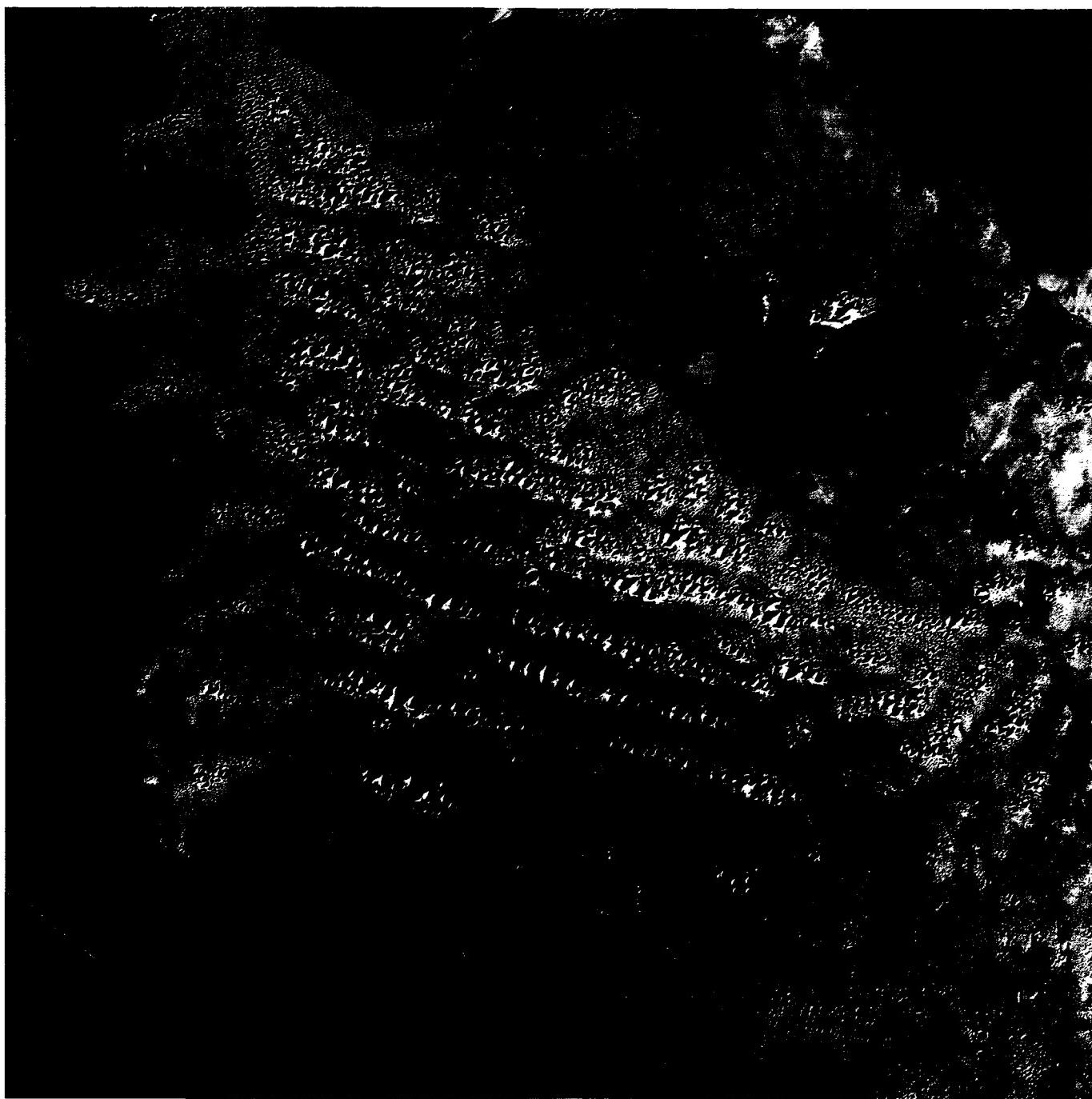


PLATE E-12

ORIGINAL PAGE IS
OF POOR QUALITY

SONORAN DESERT, ARIZONA

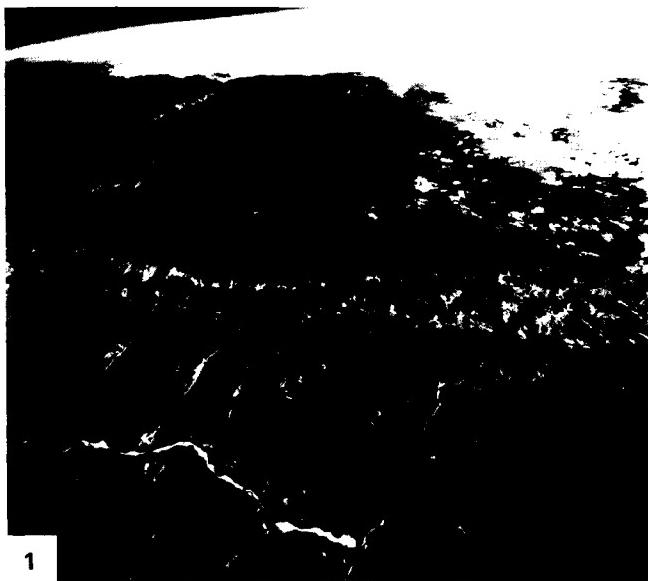
Deserts outside of North America generally form on stratified structural plains with horizontal bedrock or ancient alluvial plains that stretch for hundreds of kilometers (Petrov, 1976). The desert lands of western North America differ from most other deserts of the world in that they often contain closed depressions that hold well-preserved lacustrine terraces or pluvial lakes; many are within or adjacent to eroded structural plains or plateaus. Deep canyons, such as the Grand Canyon, and mountain ranges are associated with these deserts. Figure E-12.1 is a high-altitude oblique aerial photograph of a typical plateau desert of the U.S. Southwest—here the Moenkopi Plateau about 600 km north of the Plate. The Little Colorado River is on the front left. Small crescentic dunes are in most of the washes above the river. Their crests indicate that the dominant wind direction is from the bottom left in this figure. Red Rock Cliff is across the center of this picture, and linear dunes are on the plateau above the cliff. Dunes are rare in North American deserts, and fluvial processes dominate much of the landscapes. Compare the mountains and basins in this Plate and in Plate E-13, the Great Basin Desert, with Plates of other deserts throughout the world.

The Sonoran Desert is a subtropical desert and is the most complex of the North American deserts. Based on vegetation, Crosswhite and Crosswhite (1982) divide the Sonoran into seven region divisions and suggest that the Mojave Desert be considered an eighth division of the Sonoran Desert. Because of its biseasonal rainfall, short duration of cold weather, and topographic and

geologic diversity, the Sonoran Desert has the greatest variety of plants of any deserts on the Earth. Figure E-12.2 shows the giant saguaro, which is sometimes more than 15 m tall. This plant dots the Sonoran and reinforces a general concept of deserts as cacti-rich land.

Tucson, Arizona, is in the northeastern Sonoran Desert, in a province generally referred to as the Arizona Uplands. As is evident in the Plate image, no perennial streams flow near Tucson. Inasmuch as irrigable acreage in the Santa Cruz Valley is limited to the narrow floodplain, the average annual rainfall in the upper Santa Cruz basin is presently capable of recharging underground water supplies (Dunbar, 1968). Dunbar points out that Tucson is the largest city in the United States that is wholly dependent on ground water.

The Arizona Uplands is the most diverse province of the Sonoran because of an abundance of moisture and a 600-m variation in elevation. The effects of this elevation range and the moisture differences that together determine the complex vegetation are best seen in the compound alluvial fans next to the mountains in the province. These fans, sometimes called bajadas in North America, are gently inclined surfaces of deposition (Figure E-12.3). In this province, Hastings and Turner (1972) find that 40 percent or more of the higher reaches of bajada may be covered by woody and succulent perennials. Small plants grow beneath the low shrubs, and saguaros top them. **Landsat TM 40176-17270, January 8, 1983.**



1



2

ORIGINAL PAGE
COLOR PHOTOGRAPH

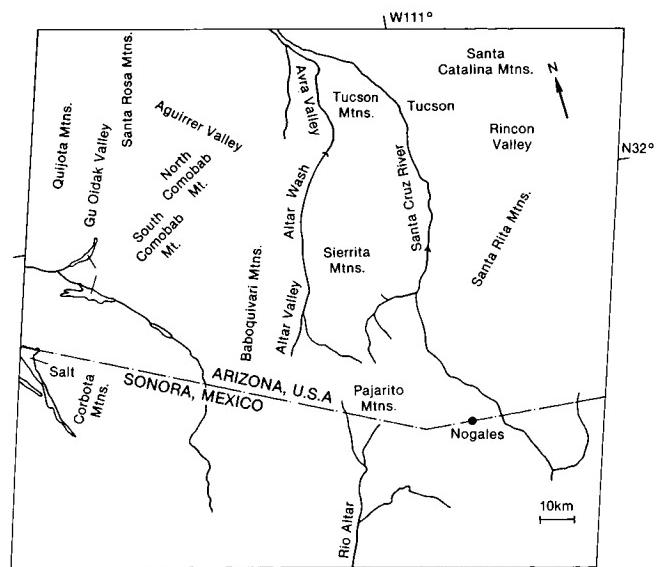


PLATE E-13

GREAT BASIN DESERT AND MOJAVE DESERT

The Garlock fault, near the bottom of the Plate image, is generally considered to be the geologic border between the Mojave Desert and the Great Basin Desert north of the Mojave (Hunt, 1974). The Mojave, the smallest North American desert, contains vegetation found in the Great Basin and in the Sonoran Desert, but in many respects, each of the three deserts has its own distinct flora (Rowlands et al., 1982).

The Great Basin contains more than 150 discrete desert basins; some, like the Amargosa Desert in this scene, named individually. These basins are separated by more than 160 mountain ranges (Morrison, 1965). With three exceptions, all basins in this province presently are closed (Hunt, 1974). Four major ranges of the Great Basin are shown in this Plate: the Argus Range, the Panamint Range, the Amargosa Range, and the Spring Mountains. All are oriented northwest-southeast and have the extensive alluvial plains flanking the basins. Compare the alluvial fans on each side of Death Valley. As seen in Figure E-13.1, an aerial photograph, the fans on the western side are about 10 km long, whereas many on the east are less than 1 km wide and have fewer stream channels. The difference indicates the structural control of the basins and illustrates the relatively rapid downdropping of the eastern side.

Fluctuations in lake levels are indicators of climate change. Most investigators refer to lakes enlarged during the Late Wisconsinan (25000 to 10000 years ago) as pluvial lakes (Smith and Street-Perrott, 1983). Several basins in the Great Basin group that once contained pluvial lakes are readily picked out in this Plate because dry playa lakes now occupy their centers. In the Late Quaternary, these lakes were members of a chain referred to as the Owens River system (Smith and Street-Perrott, 1983). The Owens River transported most of its water from the Sierra Nevada to Owens Lake, approximately 40 km west of Darwin Wash. After Owens Lake filled, water overflowed to China Lake in Indian Wells Valley. When filled, China Lake overflowed into Searles Lake (Smith, 1979).

The overflow from Searles Lake traveled south around Slate Range, then north into Panamint Valley where a 280-m deep lake formed during the most intense pluvial periods. Panamint Lake spilled into Death Valley via Wingate Pass, now a long dry wash between the Panamint Range and the hills south of the range. East of Death Valley, water from the ephemeral Amargosa

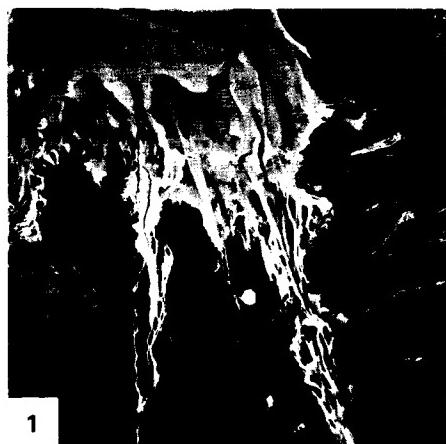
River drains into the valley today, as it did in the past. The channel is marked on the index map near its center and is easily traced on the TM image.

Badwater Basin, in the center of Death Valley, has an elevation of 86 m below sea level, the lowest elevation in the United States. Telescope Peak, about 20 km southwest of Badwater Basin, has an elevation of 3368 m. The striking contrast in local relief is indicated by the visible changes in the vegetation and geomorphology. Figure E-13.1 is a vertical aerial photograph of a 54-km wide area in Death Valley. The floor of the 5-km² salt pan in the upper center and left of this figure is the hottest and driest part of the United States.

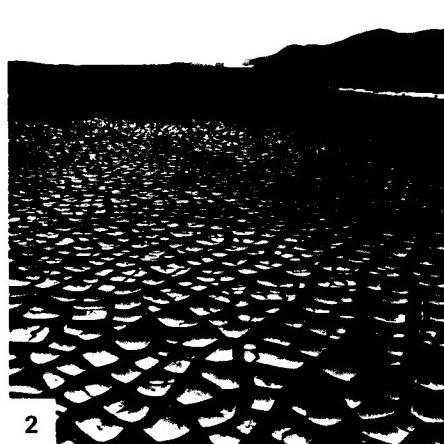
Searles Lake is a 100-km² dry pluvial lake. A 930-m core drilled to bedrock in the middle of the lake (Smith, 1984) recorded more than 3 Ma of change in the environment. It is the longest available record of nearly continuous deposition in a closed basin responsive to regional surface hydrologic regimes. The lacustrine deposits record nine distinct regimes. Smith (1984) notes that many coincide with changes in sea-surface temperatures in the tropical Atlantic, and possibly one or more changes in the Earth's orbit.

Salt bodies of Late Quaternary age in Searles Lake contain interstitial brines from which sodium, potassium, carbonate, sulfate, chloride, and borate products are extracted. Figure E-13.2 illustrates the geometric pattern of saline mud cracks at the lake. The total production value of chemicals from Searles Lake substantially exceeds \$1 billion (Smith, 1979). Production continues today, and evaporation ponds and plant discharge waters are easily visible as dark pools in the northern lake area in the Plate image.

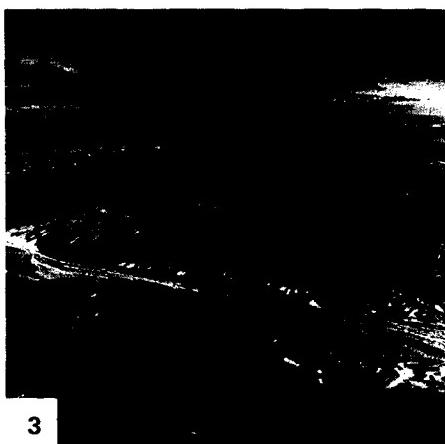
Figure E-13.3 is an oblique aerial photograph of a portion of the pluvial lake deposits in Searles Valley. Note the ancient lake strandlines in the foreground and the pluvial drainage patterns into the lake in the center of the figure. Searles Lake sediments are also visible in the foreground of Figure E-13.4. The Pinnacles, vertical tufa spikes up to 40 m tall, are in the right center. The Pinnacles are directly south of Searles Lake. Figure E-13.5 shows an evaporite pool on the left that has dried up. Remnants of the former pluvial lake sediments are on the right. The Argus Range is in the background. **Landsat TM 50022-17492-4, March 23, 1984.**



1

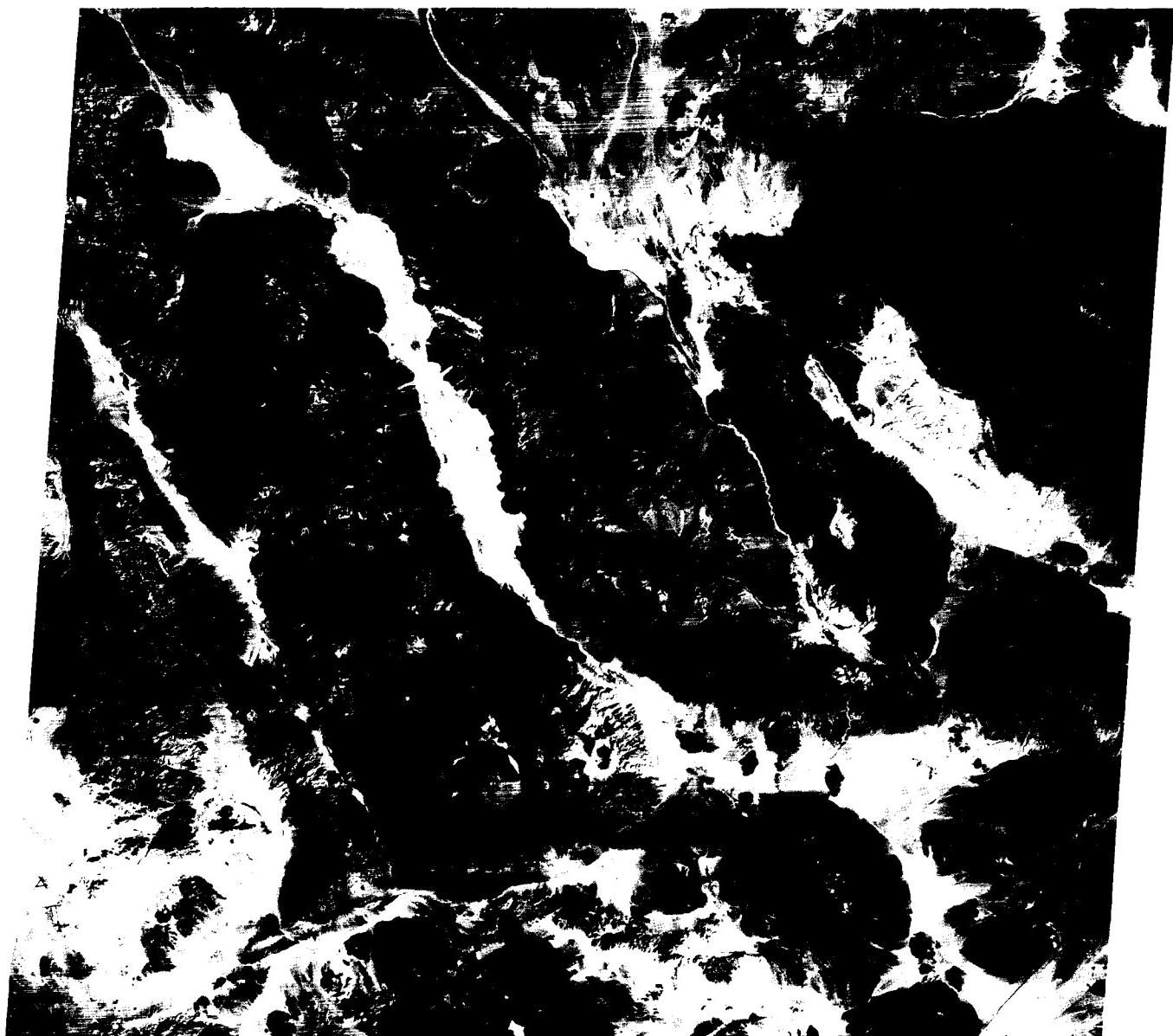


2

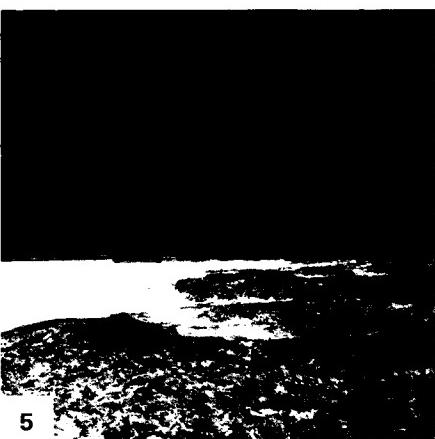


3

ORIGINAL PAGE IS
OF POOR QUALITY



4



5

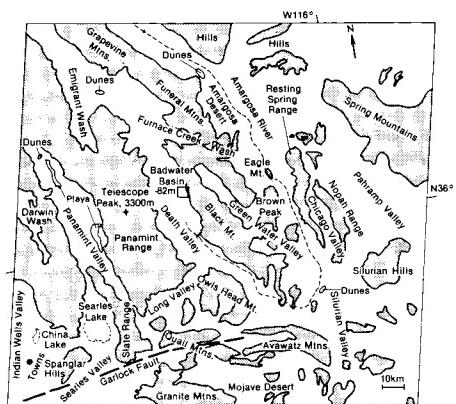


PLATE E-14

The 57000-km² Nebraska Sand Hills in central Nebraska is the largest dune field in the Western Hemisphere. It is bordered by the Niobrara River to the north, directly above this scene, and the North Platte and Platte Rivers to the south; loess borders the hills to the east; and the dunes overlie eroded remnants of the loess in the southeast. Ahlbrandt and Fryberger (1980) conclude that sands intercalated in the loess are probably fluvial rather than eolian. Precipitation in the sand sea varies between 406 mm/year in the west to 610 mm/year in the east (Ahlbrandt and Fryberger, 1980). These investigators analyzed basal sediments in a core and determined that the sand sea is of Holocene age. The Sand Hills presently are stabilized by grasses, as shown in Figures E-14.1 and E-14.2.

Ahlbrandt and Fryberger (1980) classify the dunes as simple or compound crescentic. They note that some of the large dunes (up to 90 m high), particularly those south of the Dismal River, superficially resemble linear dunes. Internal stratification of the dunes, however, indicates that they are crescentic in nature. These authors suggest that these dunes may represent an early stage of evolution from en echelon crescentic types to linear dunes. The evolution was frozen in time when the climate became more humid. This illustrates the importance of field investigations in interpreting remote sensing data. Ahlbrandt and Fryberger (1980) found that the interdune deposits differ from nearby dunes in composition, color, and texture. As can be seen in the Plate and in Figures E-14.2 and E-14.3, the interdune sediments are normally darker than the dune sands. Through laboratory analysis, these investigators determined that the interdune sediments are rich in organic matter and could produce petroleum on burial and heating.

Blowout and parabolic dunes are ubiquitous in the sand sea. Ahlbrandt and Fryberger (1980) interpret them to be secondary features that developed after the large dunes formed. Blowout dunes are smaller than the resolution of the TM image (30 m). Three blowouts, indicated by a crescent-shaped hollow devoid of vegetation except at the top, appear in Figure E-14.2.

Ahlbrandt and Fryberger (1980) measured the orientation of cross-beds within the dunes and found a general northwest-southeast drift of sand with a more southerly drift in the southeast. These investigators point to a wide discrepancy between the present wind regime and the dune field. They state that if the rainfall did not support vegetation, the sand sea would be active

NEBRASKA SAND HILLS

and, in some areas, the dune forms would be different from those existing today. They surmise that the nature of change in wind circulation from the time of dune-building to the present cannot be determined from available data.

The paleoclimatic record of the sand sea reveals the climate to have fluctuated from arid to more humid than present. According to Smith (1965), pollen analysis indicates the presence of a spruce forest 12600 years ago. The forest was succeeded abruptly by grassland and the numerous interdunal lakes of the present. These lakes may be seen in the upper center of the Plate image and in Figure E-14.3, a high-altitude aerial photograph. The lakes and grass suggest the presence of greater moisture than when the sand sea was formed. The dark areas on this photograph are not lakes, but may be swamps. About ten small lakes can be seen in the photograph and are indicated by a light-gray tone and a sharp contact with the grasses.

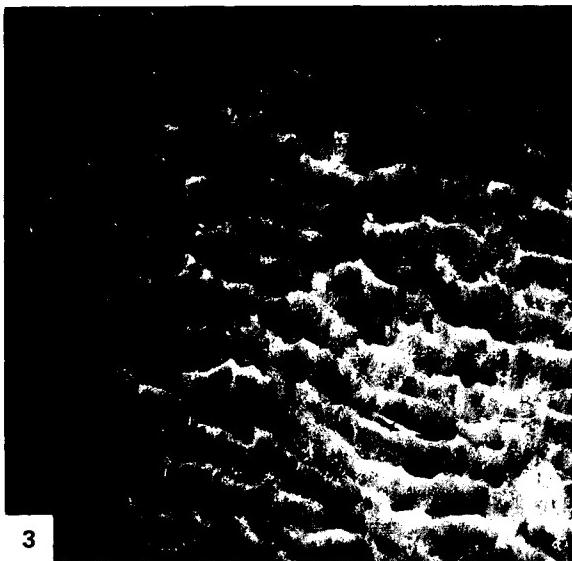
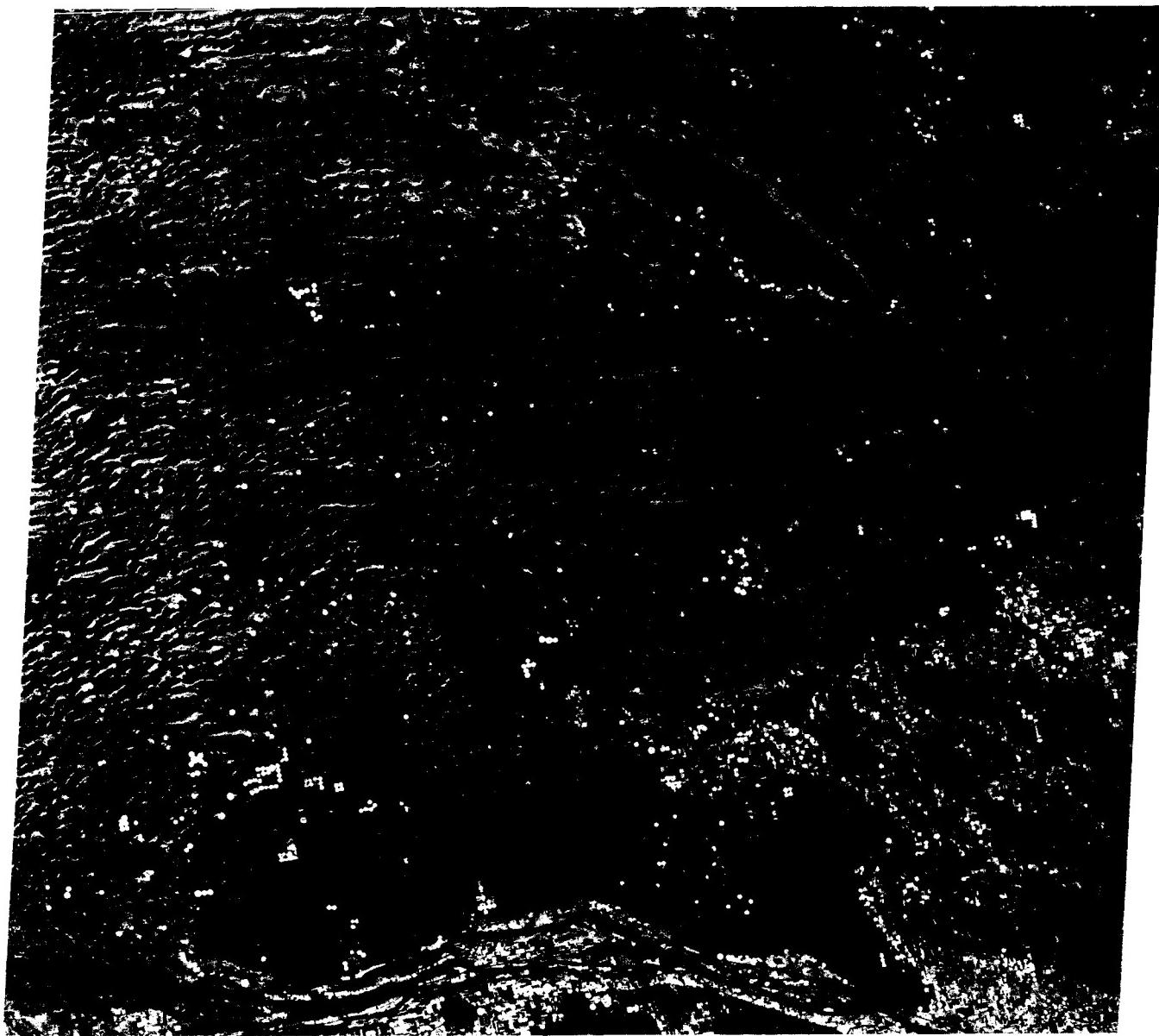
In some areas in the Sand Hills, Ahlbrandt and Fryberger (1980) observe that wind erosion has created yardangs. In the western Sand Hills (left of the Plate), denudation of dry salt-crusted interdunes occurs during the summer. These investigators cite water erosion as the most important cause of present landscape alteration. Rainfall helps form organic-rich interdunal deposits and aids in the development of thin soils on the dune sands.

Clusters of ancient sand dunes now in semihumid terrain, and playas which represent formerly large lakes, now in arid environments, indicate that climatic conditions have changed over vast areas of the Earth. Applying remote sensing data, we can determine the sedimentary characteristics that reflect variations in geomorphic and hydrologic processes as functions of climatic changes. Likewise, vegetation changes that correspond to climatic changes may be recorded and dated. With this approach, the paleoenvironment of the arid lands can often be reconstructed.

Ample evidence exists for climatic changes on the Earth's surface. Surficial features of arid lands are important indicators of such changes. By monitoring the surface from satellites, shifts in climate in arid lands can be followed over decades by observing changes in vegetation cover. Studies of this kind in the African Sahel using NOAA AVHRR imagery over a 5-year span have been reported by Tucker et al. (1985). Landsat TM-40141-16525-4, December 4, 1982.



ORIGINAL PAGE IS
OF POOR QUALITY



3

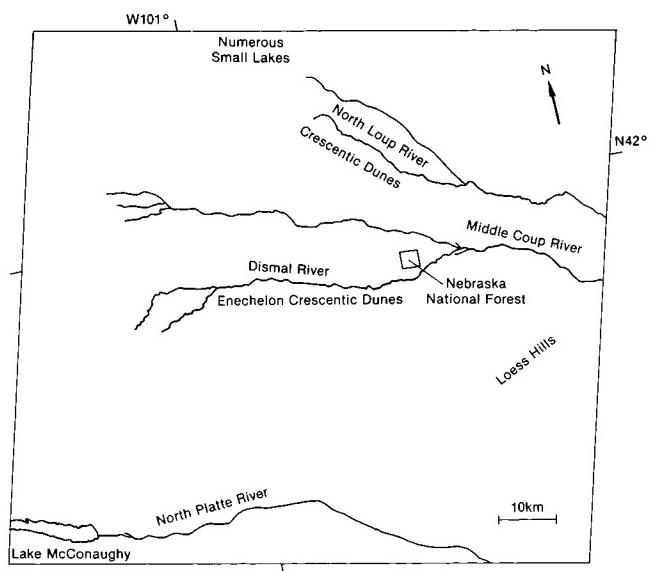


PLATE E-15

MARTIAN SAND SEAS

Evidence of eolian action on Mars was gathered first by the Mariner spacecraft series (1964–1972) and then by the two Viking Landers in 1976. Most scientists working with Mariner/Viking images refer to some eolian accumulation features on Mars as desert drifts rather than dunes because they appear to be remnants of formerly more expansive deposits. The constituent particles are probably silt- and clay-sized rather than sand-sized. Sharp and Malin (1984), however, argue for the presence of significant sand-sized particles on the surface. The features on Mars appear to be stabilized erosional remnants of a formerly more extensive cover rather than growing and moving sand dunes (Mutch and Jones, 1978).

Viking Lander 1 touched down on Chryse Planitia, Mars, on July 20, 1976, at the locality since designated the Thomas A. Mutch Memorial Station. This Plate image, acquired at 7:30 a.m. martian local time by the Viking Lander scanner, shows a ground panorama that covers about 100° , looking northeast on the left to southeast on the right. The Viking Lander 1 meteorology boom of a miniature weather station is in the center of the image. An eolian accumulation zone occupies the far left and an eolian deflation zone the right. This duality is similar to that of many deserts on Earth. The large boulder at the left is about 8 m from the lander and measures about 3 by 1 m. As seen in images of this boulder at higher Sun angles, it actually consists of two coarse-grained and banded boulders, leading to the suggestion reported in Mutch and Jones (1978) that it may be an impact breccia. Other Viking images indicate that the boulder, nicknamed "Big Joe" by Viking investigators, is capped with fine-grained material, possibly a remnant of dust that may have covered the entire area (Mutch and Jones, 1978).

Internal stratification of the drifts seen to the left of the boom and in the three ridges in the drift right-center of the boom suggest a number of depositional events. Mutch and Jones (1978) note that the most recent event is general erosion because the drifts in the Plate are well wind-scoured. Examining multitemporal data, these authors conclude that the apparently bright drifts in this Plate are actually dark drifts with a thin veneer of bright fine-grained dust.

The martian surface at the Mutch Memorial Station and at the Lander 2 site is peppered with angular blocks of many sizes. On close inspection, most of these rocks have small cavities that may be flutes created by scouring by sediment-laden current. They provide strong evidence of the importance of eolian activity on Mars (Garvin et al., 1981).

As the two Viking Landers collected surface and atmospheric data on the Martian surface, their companion Viking Orbiters collected images. The Viking Orbiter 1 periapsis of 300 km above the surface provided highest resolution images and shows features as small as 20 m.

The dune fields arise from global wind patterns that result in erosion of the equatorial and midlatitude regions and deposition in the circumpolar regions. Sand seas of varying size on Mars are most common in the north circumpolar areas. Mars also has numerous small crater-floor dune fields (McCauley, 1973; Tsoar et al., 1979; Breed et al., 1979b). Figure E-15.1 shows several crater-floor dune fields. The dune field in the large crater on the

upper right is 65 km long by 30 km wide. The streaks in this sand sea and along the edge of the crater to its left imply a wind from the east. According to Breed et al. (1979b), this bed-form pattern of massed crescentic dune ridges is typical of most crater-floor dune fields. Some of the crescentic dunes in Figure E-15.2 are more than 1 km wide. The asymmetry of the horns, with an elongated western horn, suggest a different secondary wind direction for these hooked crescentic dunes. The dark material that streaks from the horns may be dust recently blown from the dunes.

When comparing the scale ratios derived from measurements of width, length, and wavelength of crescentic dunes on Mars, Breed et al. (1979b) find that the circumpolar dunes are nearly identical in shape to the crater-floor dunes although the former are half their size. They suggest that the two dune areas are in dynamic equilibrium with depositional environments in widely separated areas on Mars. These authors propose that on Mars, as well as on Earth, dune patterns are topographically controlled.

Many investigators consider the Western Desert of Egypt, one of the most arid regions on Earth, to be a terrestrial analog to the surface of Mars (McCauley et al., 1979). Maxwell and El-Baz (1982) find dark streamlined streaks in orbital images of this desert similar in scale and form to streaks on the martian surface. They believe that the extreme aridity of southwestern Egypt makes it a martian analog both on the scale of orbital images and on the scale of millimeter-size rock pits.

Figure E-15.3 is a siliceous limestone ventifact from the Western Desert of Egypt. The arrow indicates the wind direction. Whitney (personal communication, 1985) notes that the subsidiary flow patterns beneath the main flow lines of wind deliver the abrasives to surfaces to shape and flute ventifacts. Figure E-15.4, also of the Western Desert, is a series of yardangs in siliceous limestone. These ventifacts and yardangs bear a striking resemblance to the fluted and pitted rocks imaged by the Viking Landers (McCauley et al., 1979). Whitney (1983) notes that the response of the wind to the shape of the feature on which it impinges is a significant factor in developing streamlined forms.

Ward (1979) suggests that the 50-km long, 1-km wide, and 200-m high ridges in the left of Figure E-15.5 are early-stage yardangs. They have deep wide troughs, but the ridges are not streamlined. He notes that these yardangs are oriented with their widest ends toward the east, indicating that the wind effectively came from that direction. Compare this high-resolution (20-m) image of martian yardangs with the 80-m resolution MSS image of the yardangs of the Lut Desert (Plate E-19).

Figure E-15.6 illustrates deposits of alternating layered ice and windblown dust near the north polar cap. According to Howard et al. (1982), layered deposits accumulate on the flat uplands and on the banded terrain of pole-facing trough walls. Erosion of pole-facing scarps (those facing upper left) expose layers previously deposited. Analysis of multitemporal data of martian polar stratigraphy suggests that annual and other periodic climatic changes due to orbit fluctuations occur on Mars (Howard et al., 1982). **Viking 11A097, August 3, 1976.**

ORIGINAL PAGE IS
OF POOR QUALITY

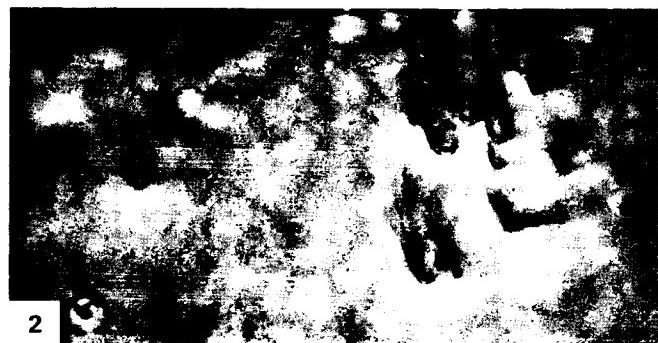


PLATE E-16

According to Morris et al. (1972), the Dry Valleys of Antarctica have been ice-free for thousands of years and are excellent analogs for martian geomorphology. Mean annual temperatures average -20°C ; the winter minimum temperature near Lake Vida was -51°C in 1960. Due to radiative imbalance, rock temperatures are known to exceed air temperatures. Morris et al. (1972) note that mean wind speeds are 10 to 15 km/hour. Ventifacts and pebble ridges commonly are positioned with their cut-and-polished surfaces facing west, the dominant wind direction.

The rocks are Upper Precambrian to Lower Paleozoic folded metasediments cut through with large sills and dikes. Morris et al. (1972) located a prominent field of transverse dunes perpendicular to the prevailing wind direction on the eastern end of lower Victoria Valley. They find beds of frozen snow and sand exposed beneath the mobile sand of the dunes. These are inconsistent with the present dune forms and suggest that they were deposited during austral winter months when winds blow from the west instead of the east.

Figure E-16.1, from an area near the center of the Plate, depicts a linear dune in the lower Victoria Valley. At the top of the dune is a 1-m thick cornice, which is an overhanging ledge of frozen sand and snow. As the dune dried out, the cornice disappeared.

Figure E-16.2 is an aerial photograph north of the Insul Range looking west up Victoria Valley. Crescentic dunes are moving right to left on patterned ground formed on glacial drift. The

DRY VALLEYS, ANTARCTICA

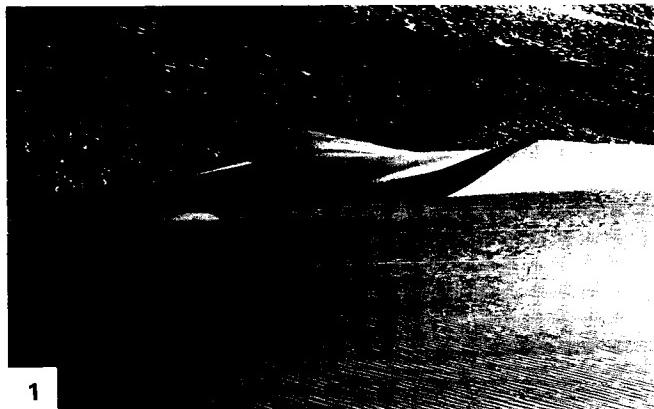
dunes are 5 to 10 m high, and the center dune is 250 to 300 m wide. Frozen sand beds crop out at the windward (right) side of the dunes.

Figure E-16.3 offers a closeup view of eolian features in the Dry Valley region. The rock hammer in the lower left shows the scale. The ripples indicate that the wind direction is right to left. Sand shadows to the left of the outcrop disturb the ripple pattern.

Cornices are at the crest of each of the linear dunes in Figure E-15.4. The cornices disappear as the upper surface of the dunes dry out. Victoria Lower Glacier is in the background of this figure. The dune in the foreground is encroaching on glacial drift.

Figure E-15.5 is a small-scale vertical aerial photograph of transverse sand dunes. Packard Glacier enters in the upper left. The windward face of the dunes lies to the right. After comparing this 1962 photograph with a 1970 photograph, Morris et al. (1972) found that the individual dunes had not moved or noticeably changed shaped in the 8 years between the photographs.

Southworth (1984) produced a Landsat color composite of the Dry Valley region with contrast enhancement and band ratioing of bands 4, 6, and 7. He was able to discriminate several lithologic units and could differentiate between alluvium and glacial drift by comparing differences in surface roughness and composition. **Landsat 2279-19361-7, October 28, 1975.**



1



2



3



4

ORIGINAL PAGE IS
OF POOR QUALITY

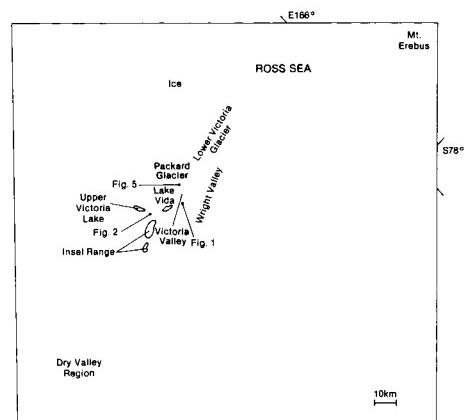
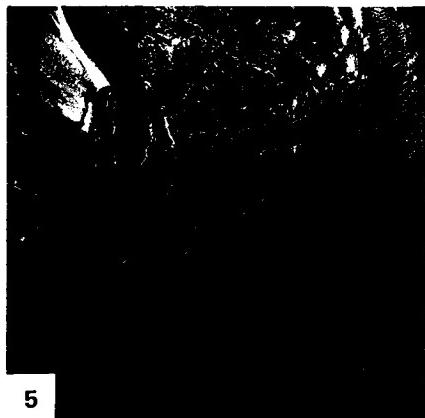
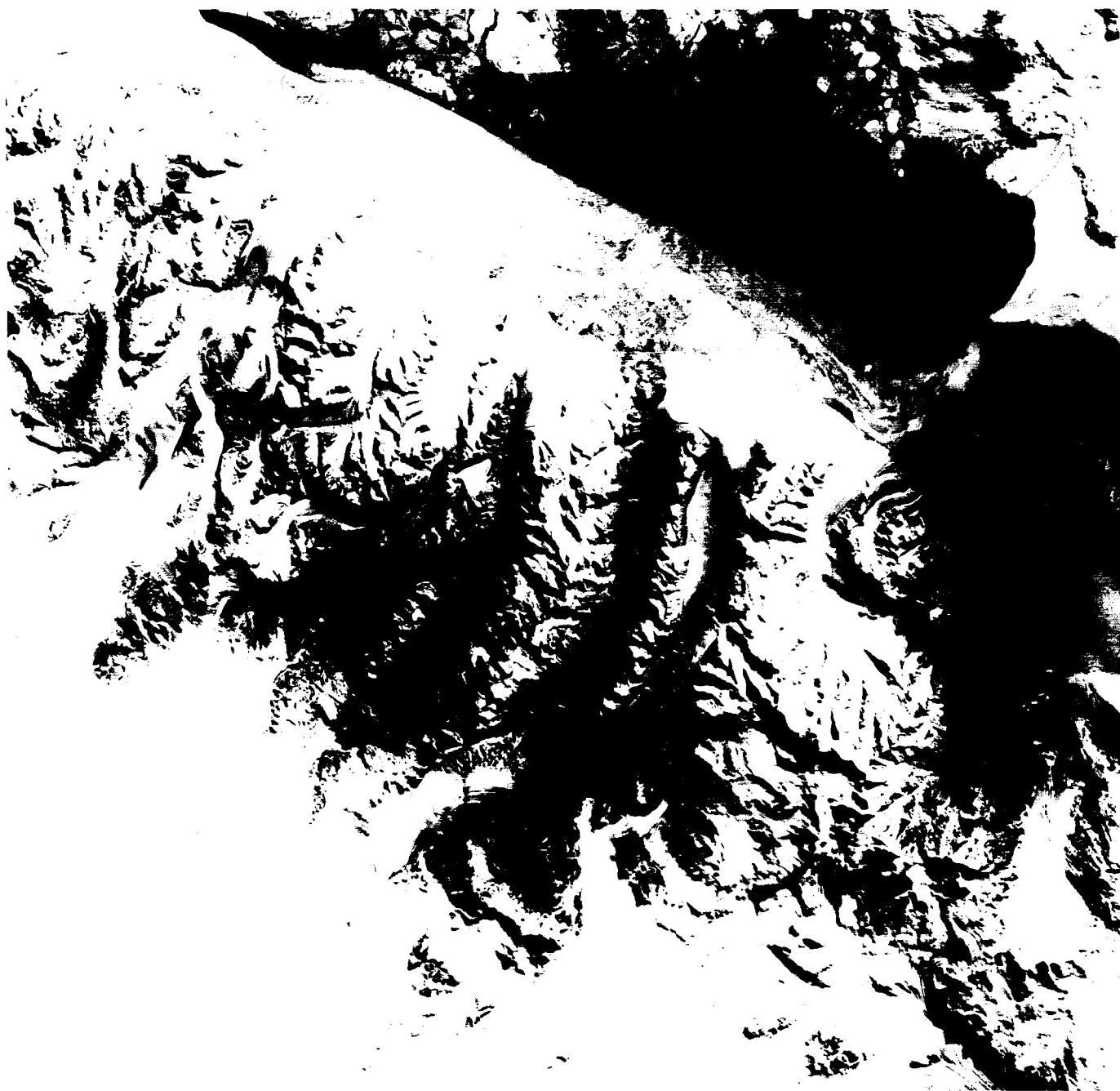


PLATE E-17

Approximately one-third of Australia is classified as arid, and another one-third is semiarid (Langford-Smith, 1982). Unlike other desert areas in the world, almost one-half of these deserts is composed of sand, of which about 50 percent are vegetated sand sheets (Figure E-17.1). Linear dunes dominate the remainder of the sand areas.

The Great Sandy Desert is a 360 000-km² expanse in northwestern Australia. As evident in this Plate, much of the desert consists of semifixed linear dunes. Because of the stability of the dunes and the suggestion of a developing soil profile created by the vegetation, some investigators refer to these dunes as sand ridges. They average 40 to 50 km long and reach to about 15 m in elevation (Petrov, 1976). The dune-free strips near the center of the Plate have slightly higher elevations and low mesas (Figure E-17.2).

From comparing the west-northwest-trending linear dunes on this Plate with those on Plate E-18, the Simpson Desert to the southeast, both deserts would appear to reflect a similar wind orientation. However, Langford-Smith (1982), after mapping the orientations of linear dunes throughout Australia, concludes that the pattern has a concentric orientation around the continent that conforms to a counterclockwise swirl for the major wind patterns within Australia.

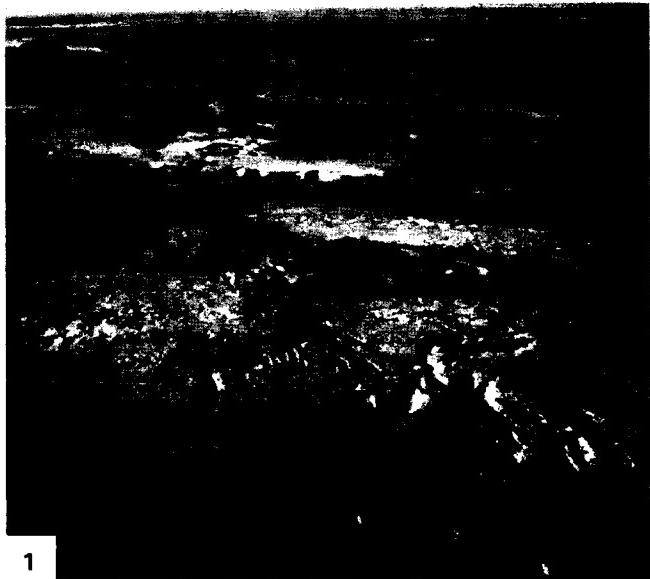
Figures E-17.3 and E-17.4 are linear dunes in the Great Victoria Desert south of the Great Sandy Desert. The vegetation in Figure E-17.3 changes between the slipfaces of the dunes and the interdunal corridor, which is possibly due to a composition change between the dunes and the interdunal areas. This is not the case in Figure E-17.4; note the Y joins of some of the dunes. As seen in these figures and on the Plate, the crests of the dunes are generally free of vegetation.

Langford-Smith (1982) states that no solid field evidence indicates the time of the initiation of the sand sheets and dunes. However, he feels that they are essentially Late Pleistocene in age. They extend well beyond the present desert as fixed dunes. Langford-Smith proposes that the dune pattern is the product

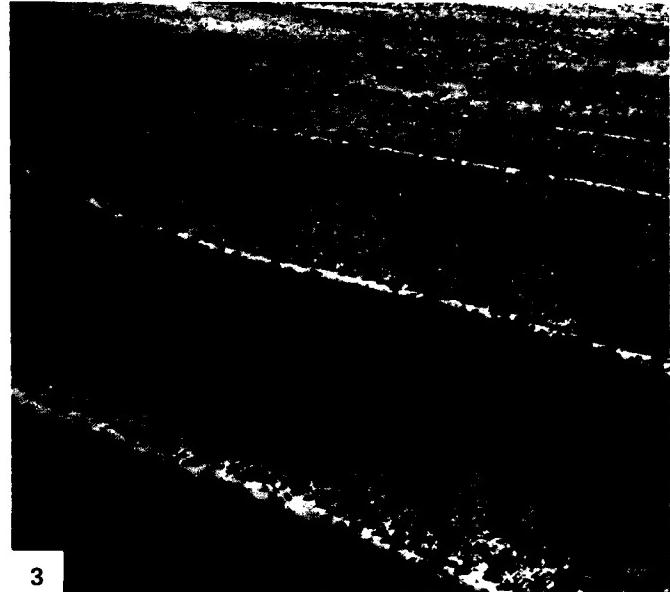
GREAT SANDY DESERT, AUSTRALIA

of eolian activity brought on by a dry climate related to glaciation elsewhere. He reports that a group of coastal dunes near the Great Sandy Desert extends beyond the present shoreline to at least 15 m below sea level, indicating drowning during postglacial sea-level rise.

Compare the Plate with Figure E-17.5, a vertical aerial photograph of a 20-km wide area located in the bottom left of the Plate. The conspicuous light-toned patches at the bottom of the photograph and similar patterns over much of the Plate were created by fires that burned the vegetation. Owing to the lower resolution of the Plate image, it is difficult to pair most of the linear dunes in the figure with those in the image. Landsat 20125-01100-7, May 27, 1975.

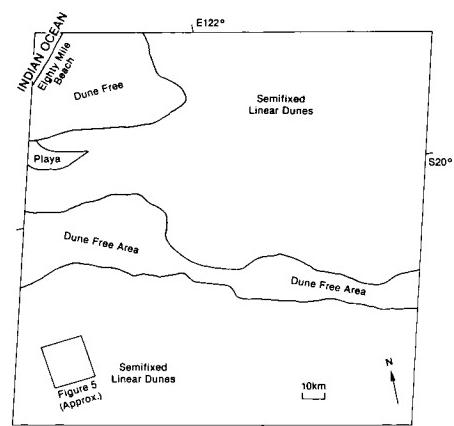
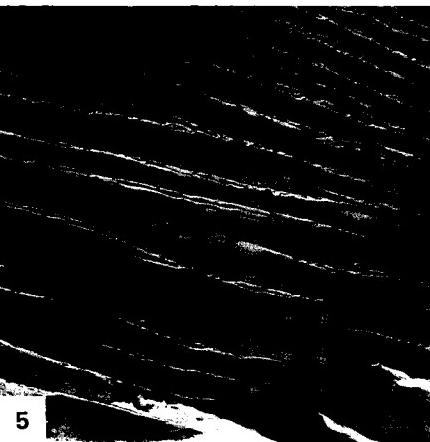
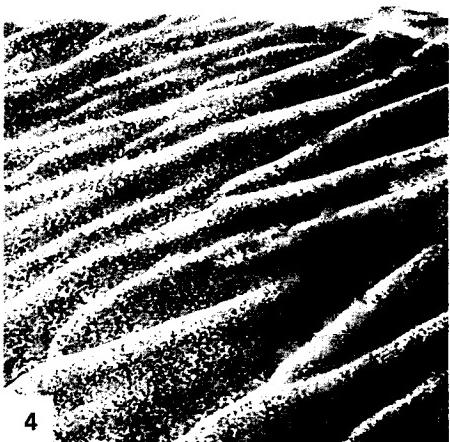
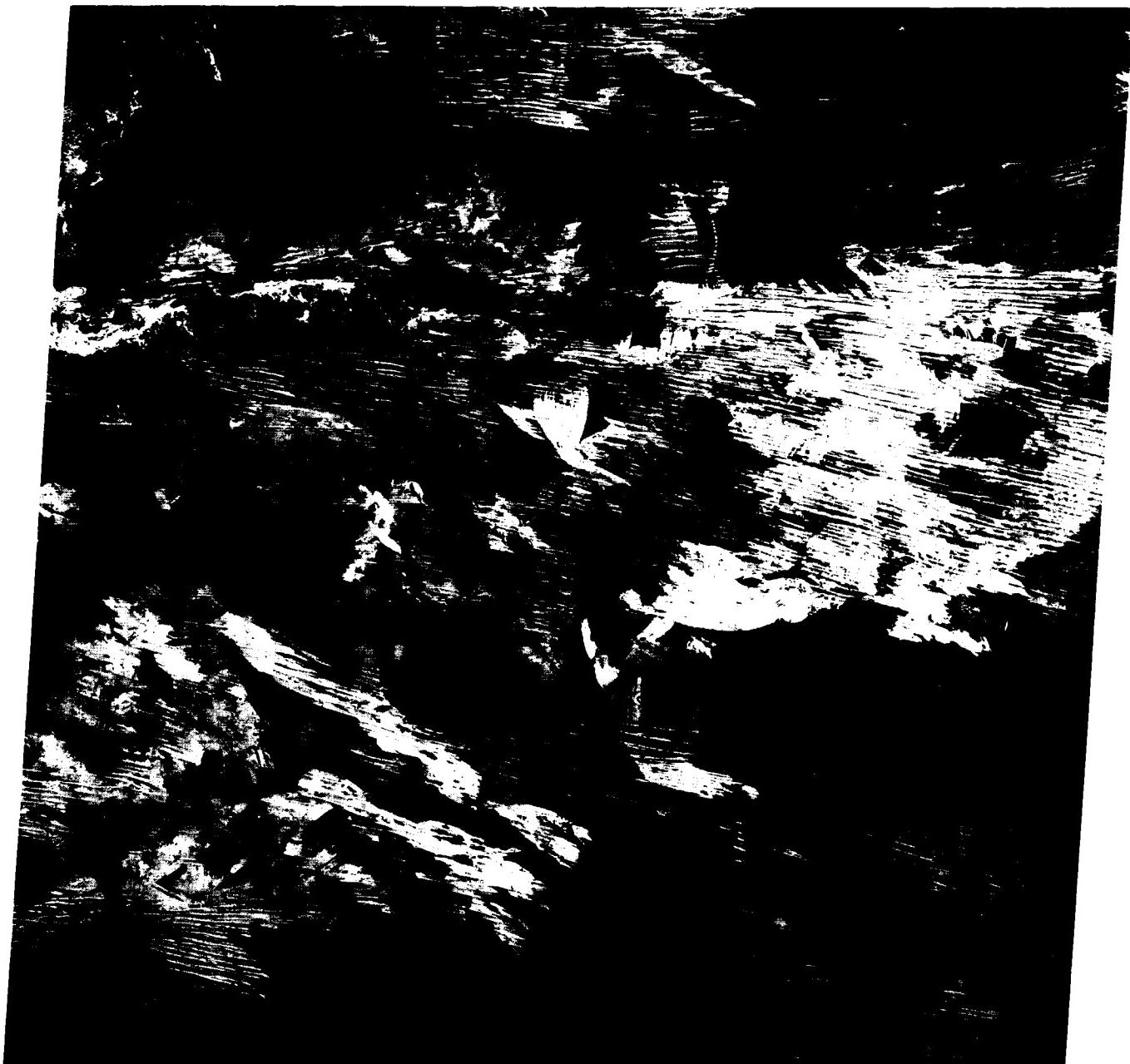


1



3

ORIGINAL PAGE IS
OF POOR QUALITY



The 300000-km² Simpson Desert is situated predominately within the Lake Eyre structural basin in central Australia (Twidale, 1980). This Plate scene is about 400 km northeast of Lake Eyre. With a surface area of 9300 km², Lake Eyre is one of the largest playas on Earth. Twidale (1980) suggests that it is bounded by a fault scarp and points out that it fills approximately twice a century. He affirms that, during the Late Pleistocene, a lake up to 17 m deep occupied an area at least three times larger than the present lake. He notes that the Simpson Desert sand sea is on the leeside of the main area of sediment accumulation in the Lake Eyre Basin.

The simple linear dunes (Figure E-18.1) in this sand sea are similar to the linear dunes in the Great Victoria Desert to the southwest and to the Great Sandy Desert to the northwest (Plate E-17). The individual dunes in the Simpson Desert are 10 to 38 m high and generally 160 to 200 m apart and may extend without a break for more than 300 km (Langford-Smith, 1982). The interdunal areas are generally more vegetated. The conspicuous light-toned patterns in the upper left of this Plate are similar to the burning patterns of the Great Sandy Desert visible in Plate E-17. Repetitive Landsat coverage shows these patterns to change over the years as the vegetation recovers. Salt playas have formed in less vegetated areas of the scene.

Figure E-18.2, looking south, shows the linear dunes advancing over the Late Pleistocene floodplain of the Diamantina River slightly northeast of this Plate. According to Twidale (1980), these dunes are migrating slowly to the north-northwest. He notes that, early in this century, some Simpson Desert dunes were advancing about 90 m per decade. He suggests that migration of wind-transported material from the many centers of alluvial and lacustrine sedimentation in the basin during the Late Pleistocene led to the development of the sand sea.

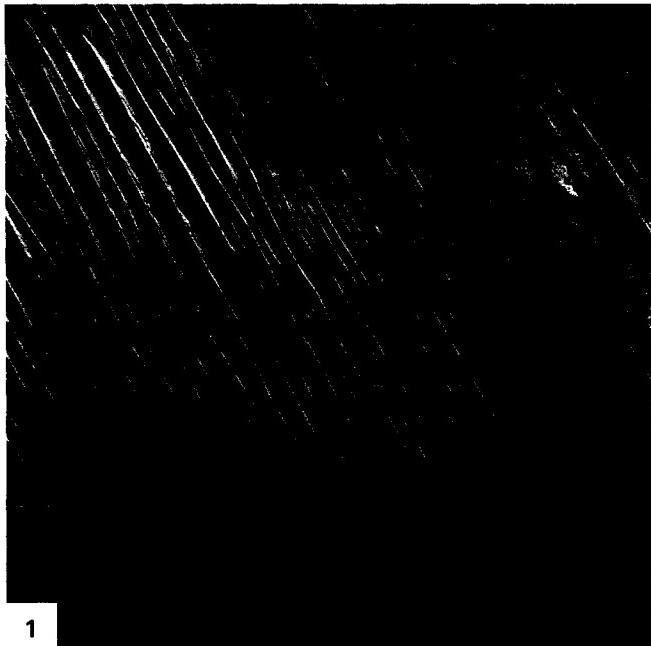
Twidale (1980) has observed a relationship between dune height and interdunal spacing taken in a direction normal to the dune trend. Note that the shorter dunes in the western Simpson

SIMPSON DESERT, AUSTRALIA

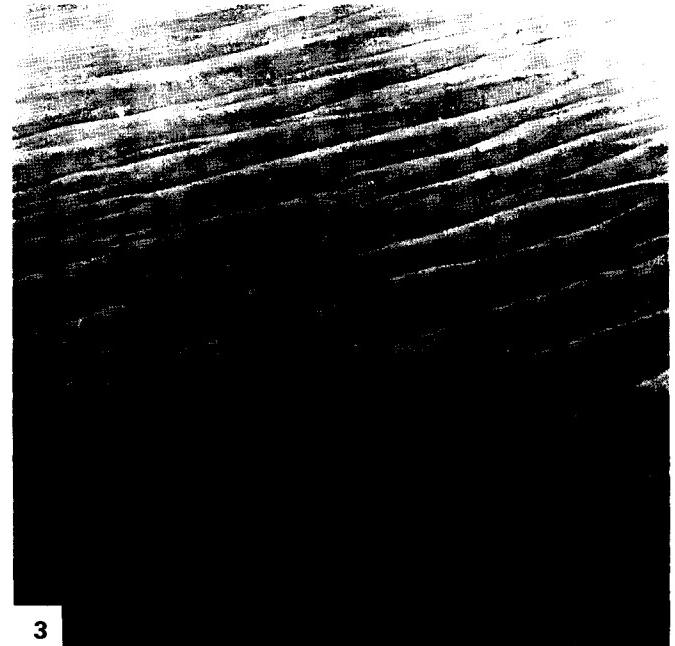
Desert are much farther apart than the taller dunes in the east. Figure E-18.3, a vertical aerial photograph, was taken directly north of this Plate. Field River is in the northeast of this photograph of a 20-km wide area. The interdunal spacing decreases toward the river as the dunes become smaller. East of the river, however, no decrease in dune size or interdunal spacing occurs as the river is approached; this may be due to topographic variations in the river floodplain.

Figure E-18.4 shows linear dunes approaching small playas east of Lake Eyre in the southern Simpson Desert. A landing strip parallel to the dunes is in the upper right. The dunes in the right of this photograph appear much wavier than the dunes on the left, which suggests topographic influence on the wind regime.

Figure E-18.5 is a stony desert, called a gibber plains in Australia, in a deflation zone immediately to the west of this Plate. Except for the vegetation, it is quite similar to the gobi in the Turpan Depression (Plate E-24). **Landsat 40090-00104-4, October 14, 1982.**

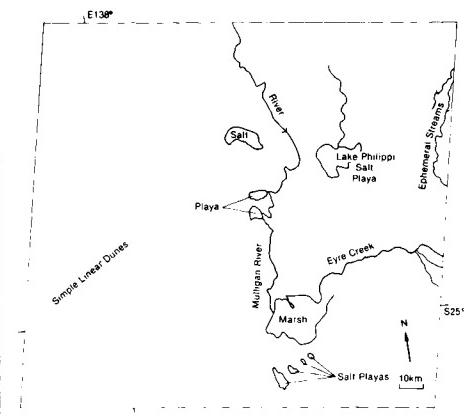
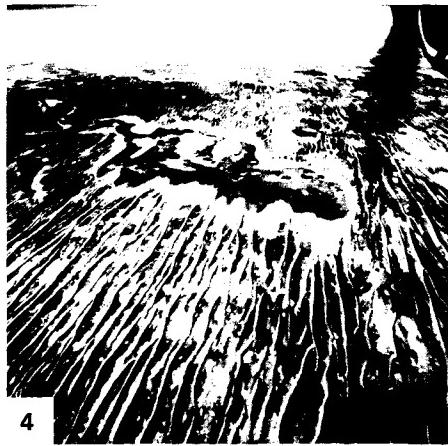
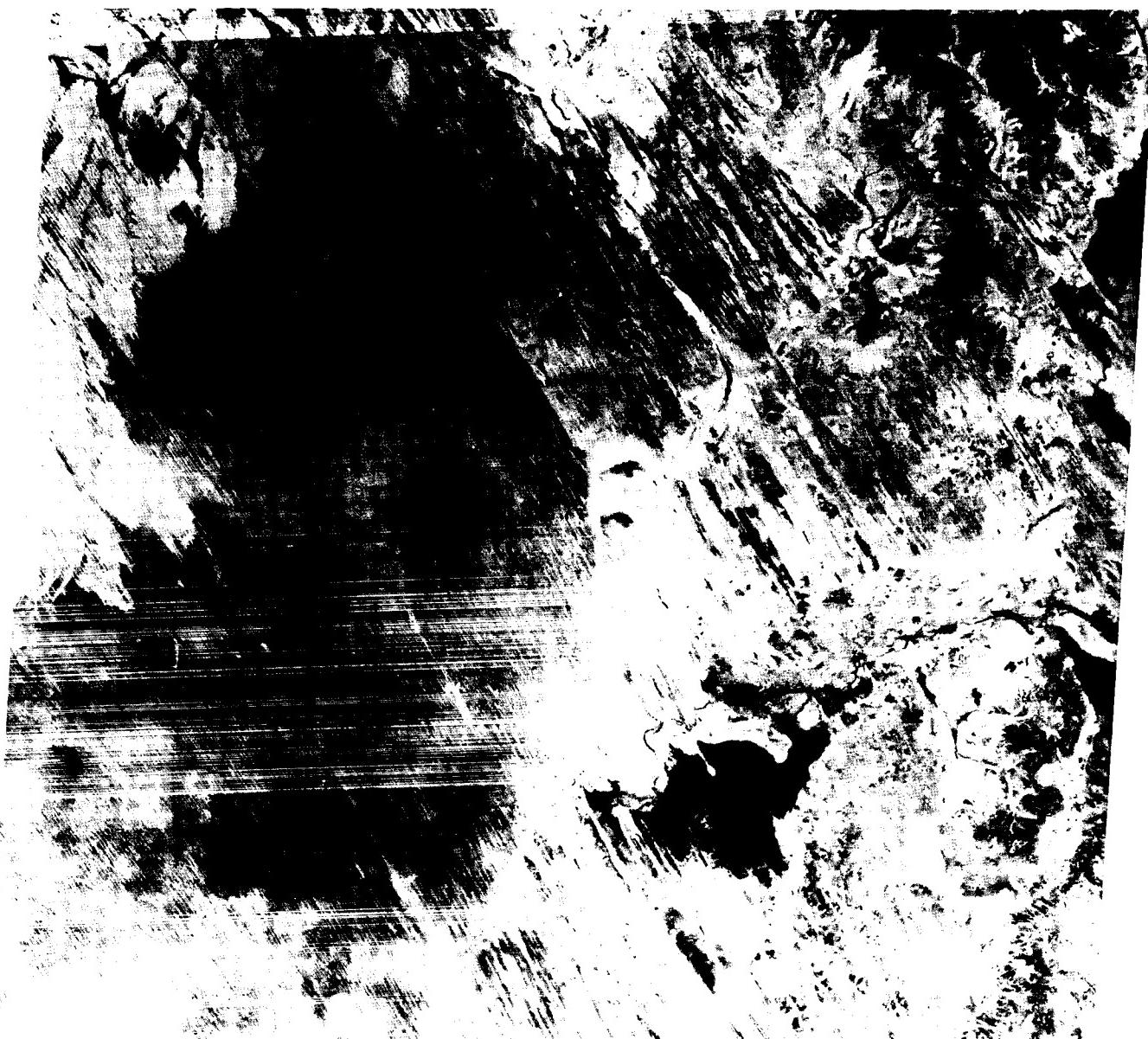


1



3

ORIGINAL PAGE IS
OF POOR QUALITY



YARDANGS OF THE LUT DESERT

The Lut Basin in southeastern Iran contains several ancient interior drainage systems separated by low ridges and residual mountains. Selivanov (1982) describes the recent paleoclimatology as alternations of wet and dry periods. He contends that these alternations, coupled with tectonic compression of the basin fill sediments into scarcely perceptible folds, resulted in unusual types of relief being formed during the second half of the Quaternary.

The yardangs up to 80 m high of the western Lut Desert, in the center of this Plate, are among the largest yardangs on Earth. They are carved out of the Lut Formation, a fine-grained horizontally bedded silty clay and limy gypsiferous sands with an estimated thickness of 135 to 200 m. Salt, gypsum, and silty clay encrust the unit (Krinsley, 1970).

These yardangs were described by Gabriel (1938) as deposits from Lut Lake that resemble desert cities separated by "boulevards." He notes that no erosion channels on the ground and no evidence of water erosion are found and that "the surface of the land had been formed merely by the wind" (p. 198).

The yardangs trend north-northwest, parallel to the prevailing winds, and are separated by 100 m or more of troughs. According to McCauley et al. (1977), the surfaces of the yardangs are covered by a layer of gypsiferous clay 10 to 15 cm thick. This clay layer swells when wet and prevents rainwash from penetrating the pronounced running-water-eroded gullies on the flanks of the yardangs.

As shown in Figures E-19.1 and E-19.2, oblique aerial photographs, only the broadest yardangs have flat or rounded summits. In the other yardangs, the ridges are narrow. Most of the yardangs in the foreground of Figure E-19.2 have similar widths. Figure E-19.3, a vertical aerial photograph of 10 km of the Lut yardangs, shows some of the relief on top of the yardangs. The spacing between many of the yardangs appears to be regular. On some of the yardangs, the horizontal bedding of the Lut Formation may be seen on the gullies.

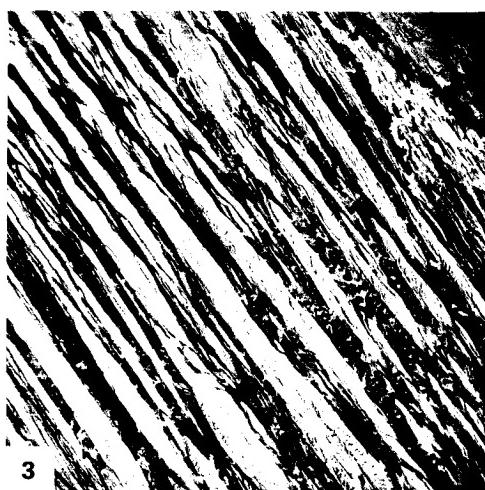
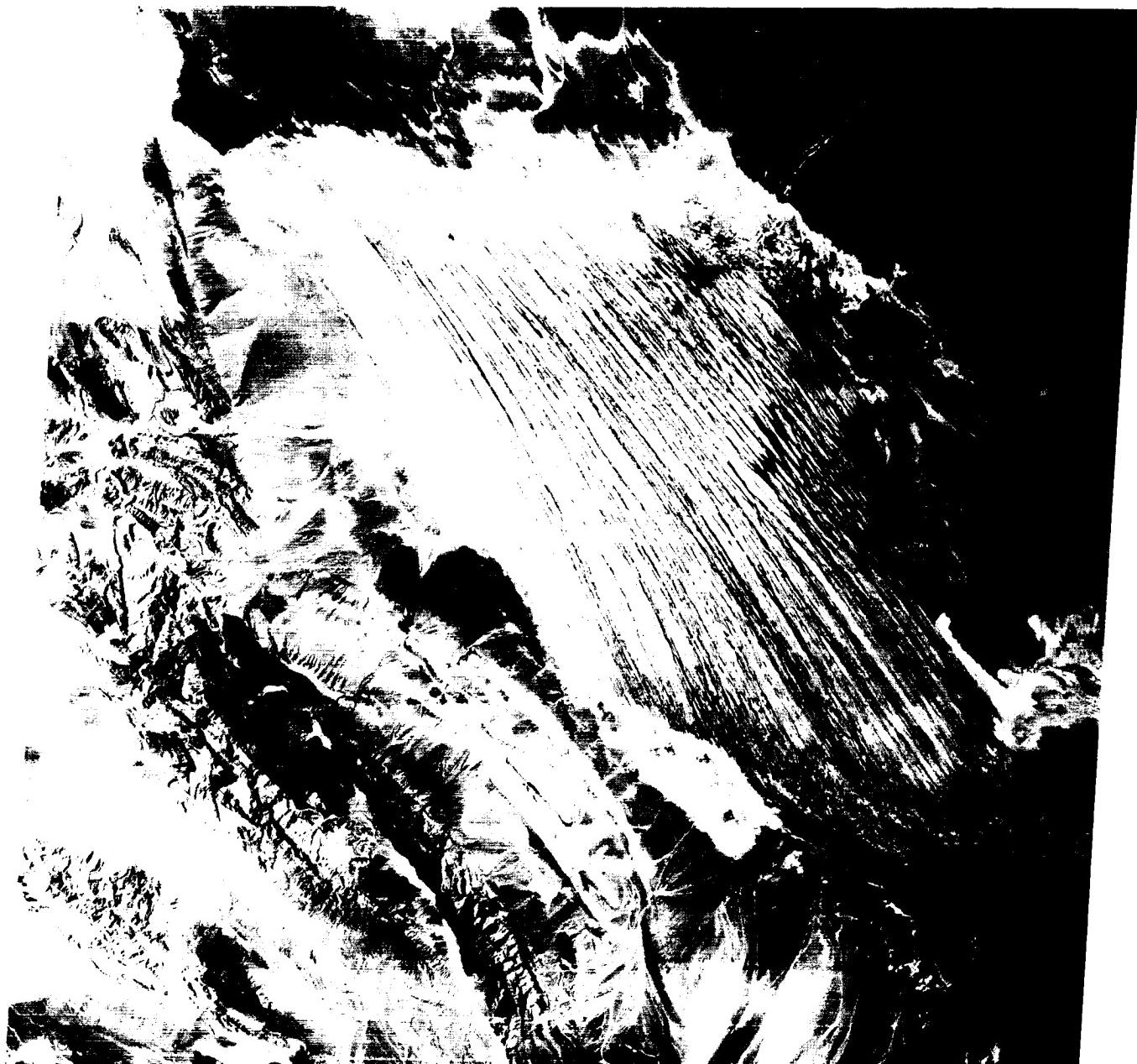
Note the small, scattered crescentic dunes on the troughs to the right of and behind the front central yardang in Figure E-19.2. The orientation of the dunes parallels the orientation of the yardangs, which suggests that the wind was coming from the direction of the foreground of this photograph. The salt stains in the furrows on the front yardang at the far left in this figure indicate that the floor of the yardang area has been flooded. This is mentioned by Dresch (1968), who notes that the base of the convex ridge slope makes a steep angle with the floor due to erosion from periodic floodwaters. The waters from the north penetrate the furrows and sap the base of the slopes to a height of 1 to 2 m.

As noted in the index map, the yardangs are bounded on the west by alluvium from the Kerman Mountains. Thrust faults and fractures cut through the Mesozoic sedimentary rocks in this range. The plateau of the Lut Formation bounds the field on the north and east. Buttes and small yardangs north of the field are separated from the Lut Formation by a scarp. Salt playas locally surround the yardang area. Their boundaries are actually mobile zones that shift with each flooding (Krinsley, 1970). The elongated salt-crusted playa southeast of Shahdad, in the left center of the Plate, is flooded periodically.

A few star dunes are found east of the yardang field. Star dunes are believed to form in areas where effective winds blow from several directions. Therefore, evidence exists for two wind regimes, an early strong NNW-SSE regime that created the yardangs, followed by a more recent multidirectional wind regime that created the star dunes. The relief of the yardangs probably controls the wind regime among the yardangs to create crescentic dunes, although star dunes exist above the yardang field. Southeast of the Lut Desert, yardangs are sand ridges that Krinsley (1970) believes are derived from materials excavated from the furrows between the yardangs. The sand ridges terminate in a sand sea in the eastern Lut Desert, which can be seen on Plate E-20. **Landsat 2592-05510-7, September 5, 1976.**



ORIGINAL PAGE IS
OF POOR QUALITY



3

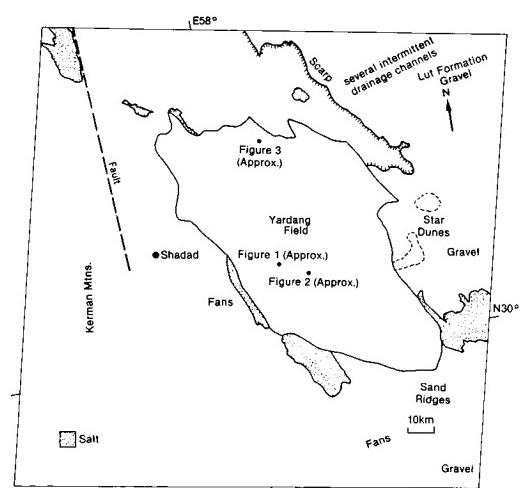


PLATE E-20

This 10000-km² sand sea in the southeastern Lut Desert is directly east of the yardangs described in Plate E-19. The eastern and southern edges of the yardang field are on the left in this Landsat image. The field has an elevation of less than 300 m above sea level; the elevation of the sand sea is about 600 m on the west, 900 m in the center, and 1200 m on the east.

The Lut Desert consists of several expansive basins separated by low ridges and residual mountains. The desert is on the Lut Block, a stable elongated fault-bounded structure about 900 km wide north-south and 200 to 250 km east-west. The block exhibits a simple tectonic structure with faulting, tilting, and gentle folding. Strong disturbances occur only near the junction of the block with the flysch zone in the east (Stocklin et al., 1972). The eastern border with the flysch zone is in the right of this image, and the western border is to the left of the yardangs in Plate E-19.

The youngest deposits in the basin are recent unconsolidated gravels that cover vast portions of the desert (Stocklin et al., 1972). The stony desert is locally called a dasht, and the Lut Desert is sometimes referred to as the Dasht-E-Lut. The gravel surfaces seen in the upper left and lower right are dissected by intermittent light-colored stream channels flowing into the basin. Krinsley (1970) states that the sand ridges between the dune field and the southeastern portion of the yardang area are derived from the excavation of the furrows between the yardangs.

A volcano with a small caldera is on the western edge of the sand sea. Dunes and a sand sheet are encroaching its lava field. A few small star dunes on the northeastern edge of the lava field and a large, simple three-armed star dune northwest of the volcano imply an older age for the volcano. The northeast and southwest arms of the star dune close to the volcano are in an orientation close to the star dune arms near the yardangs 40 km to the southwest. The third arms of the latter are northwest, while the third arm of the former is southeast. For the dune near the volcano, the arm is southeast. This may be because the volcano's topography creates a change in the orientation of the wind pattern around it.

Alfons Gabriel, one of the first explorers in this area, describes this sand sea as a "confused mass of impassable tangled dunes" (1938, pg. 148). He notes that the sands of this dune

SAND SEA IN LUT DESERT

field, with dunes up to 150 m tall, are of uniform size, are almost perfectly round, and have an admixture of volcanic material.

Figures E-20.1 and E-20.2 are photographs taken near the center of the dune field. They show sharp-crested complex star dunes with arms greatly elongated in two directions. A crescentic dune extends on to the arm of the left center star dune in Figure E-20.2. Figure E-20.3 is an aerial photograph of the northern portion of the dune field.

The dunes in this sand area are predominantly sharp-crested simple, compound, and complex star dunes. The northeast and southwest arms of the dunes dominate and are connected to give a linear orientation to the dunes. The wavelengths between the linear dune pattern increases toward the west as the elevation decreases. The edge of the sand sea is marked by individual small dunes and sand streaks. The dunes in the north grade into dome dunes and sand sheets. It appears that sand is encroaching on the dune field in the north. Although dunes in the north have the same orientation as the other dunes in the field, they appear subdued as if they are being covered by a sand sheet.

Subtle changes in the linear pattern of the dune field may reflect topographic differences in the basin. The linear pattern of the sand sea is subperpendicular to the pattern of the yardangs.

The slightly darker gray tone in the left-center of the sand sea and a difference in the sharpness of the arms suggest a change in composition of the dunes. Selivanov (1982) suggests that the sands of the Lut consist of deposits of different ages. Using aerial photographs, he observes that younger, more readily transported loose sands have covered older coarse sand now anchored by grasses.

Salt flats scattered throughout the image attest to the presence of playas and extensive coalescing fans that border them. Krinsley (1970) notes that the salty clay flats, with drainage patterns, and the waterlines at the base of some of the dunes of the sand sea indicate that a local shallow perched water table may reach the surface seasonally. One of the largest continuous salt flats and bolsans (Figure E-20.4) in Iran occurs some 300 km to the south around the Hāmān-e-Jaz Mūrlān in the intermontane basin between the Kerman Mountains (north) and the western end of the Baluchistan belt. **Landsat 2663-05425-7, November 15, 1976.**



1



2

ORIGINAL PAGE IS
OF POOR QUALITY

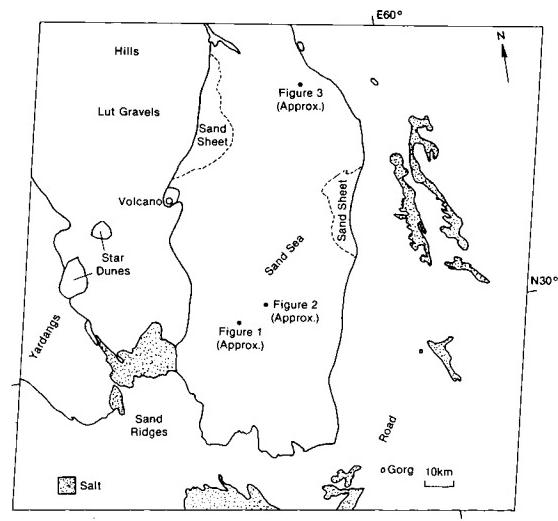
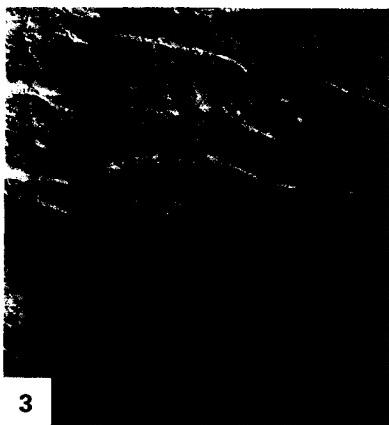


PLATE E-21

The Thar Desert includes a 214000-km² sand sea on the ancient alluvial plain of the Indus River in Pakistan and western India (Petrov, 1976). The desert is bound on the east by the Aravalli Range and on the west by the present Indus River floodplain. Canals that irrigate the farmland on the floodplain are easily seen in the Plate image.

The Thar is a monsoon desert. As described by Wasson et al. (1983), summer heating of the northern Indian subcontinent leads to an intense low-pressure zone fixed in position by the Himalayas. Because an air-pressure gradient is established, air and moisture are drawn from the south across the continental low. In September, wind direction changes, and the northeast monsoon begins. Winter circulation consists of outflow from a cold continental anticyclone. Temperatures and wind speed reach their maximum in May and June, with maximum rainfall in July and August. The average annual rainfall in the Thar ranges from less than 100 mm in the northwest to more than 400 mm in the southeast (Breed et al., 1979a). The strong winds of June and July are unidirectional over the Thar and are not impeded by rain.

Crescentic, linear, and parabolic dunes are visible in this image of the Thar. Compound parabolic dunes with many arms have been observed by Breed et al. (1979a) only in the Thar Desert. These dunes are particularly sharp northeast of Naya Chor near the center of the Plate. These investigators refer to compound parabolic dunes linked to adjacent dunes or with many arms as rake-shaped clusters. Parabolic dunes develop in areas where their arms are anchored by vegetation. Compare the dark vegetated parabolic dunes on the right center of the Plate with the light nonvegetated crescentic dunes in the upper left. Wasson et al. (1983) report that the dunes are 10 to 70 m high. They average 2.6 km long and 2.4 km wide (Breed et al., 1979a).

Linear dunes, some up to 30 m high, occur west of the parabolic dunes. Wasson et al. (1983) consider these linear dunes to be complex because crescentic dunes with convex centerpoints perpendicular to the southwest summer monsoon winds are superimposed on their crests and upper flanks. These secondary dunes are not visible in this scene. As reported in Wasson et al. (1983), some investigators conclude that the linear dunes are

THAR DESERT

derived from parabolic dunes by the winds eroding their noses. Some linear dunes may originate from a lee-side mound of unconsolidated material on the northeastern side of the Hakra Channel. The channel is an inactive distributary of the Indus on the floodplain in this image. Linear dunes extend downwind from the mound.

In the upper right of this Plate are small patches of sand sheets. West of the sand sheets are zones of nonvegetated crescentic dunes. Breed et al. (1979a) suggest that these are areas of modern eolian activity. In keeping with the wind regime of this desert, the crescents point in a northeast direction. Figure E-21.1 is an oblique aerial photograph of a cluster of small compound crescentic dunes west of the Plate scene. Small interdunal lakes are at some of the contacts between the linear and the crescentic dunes. The lakes are generally among the linear dunes, but a few exist within the crescentic dunes.

The small squares among the dunes in the upper left of the Plate are small farms (about 1 km² in area) irrigated by wells. Trees planted at the edges of the farms to protect the area from the wind may account for what is imaged on Landsat. That they are aligned in the same direction may indicate structural control of the ground water.

Figure E-21.2 is a vertical aerial photograph of a 10-km wide dune field west of this Plate. The slipfaces of these 1-km wavelength coalescing crescentic dunes are toward the northeast. Small interdunal sabkas are adjacent to some of the slipfaces in the upper right. Many blowouts are on the gentle faces of the dunes.

By using archaeological, thermoluminescence, and radiocarbon dating methods, Wasson et al. (1983) determined that dunes in the Thar Desert were stabilized during the Middle to Late Holocene. They consider that the dunes started accumulating during the last glacial maximum under the influence of a weak monsoon circulation. As the Earth warmed after the glaciation, the monsoon was reestablished, leading to stabilization. They also suggest that the dunes were partially vegetated during their formative phases. An example of semifixed dunes northeast of the Plate scene appears in Figure E-21.3. **Landsat 20781-04533-7, March 13, 1977.**

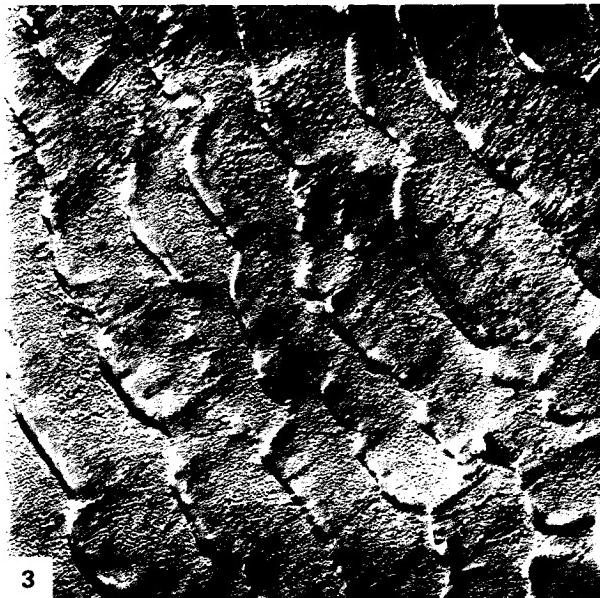
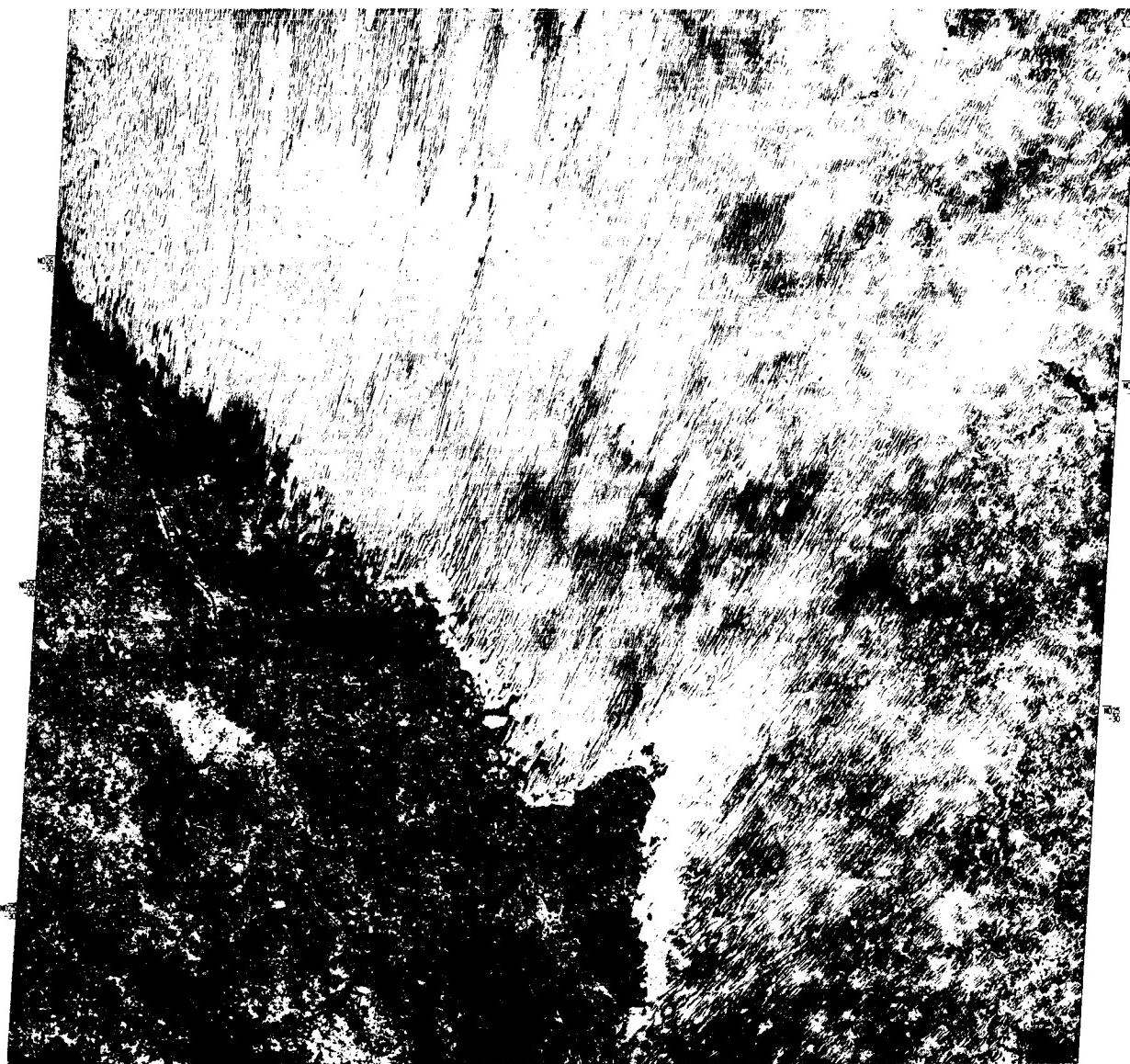


1



2

ORIGINAL PAGE IS
OF POOR QUALITY



3

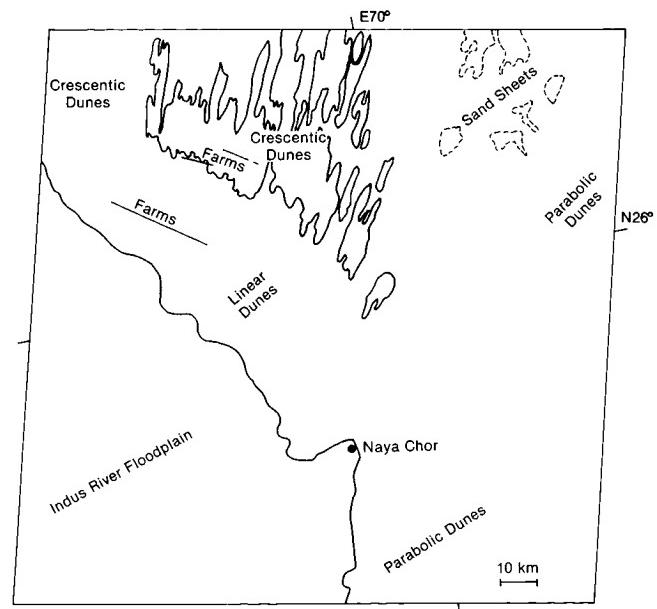


PLATE E-22

ORIGINAL PAGE IS OF POOR QUALITY

The Mu Us Sandy Land is a 32000-km² desert region on the Ordos Plain in central China. This low-relief desert reaches an elevation of about 2000 m above sea level. Dunes in the Mu Us average 3 to 5 m in height, but some may be as high as 20 m (Zhu et al., 1980). These authors map the dunes as crescentic and linear chains oriented toward the northeast. Inasmuch as these features are below the limit of resolution in the Landsat image, the Mu Us Sandy Land appears in this scene to consist of sand sheets. A few small linear dunes may be seen south of the stream in the left center of this Plate. The dark tone of some of the dunes suggests that they are semifixated (partly vegetated).

Because of the presence of archaeological ruins and other evidence of formerly wetter climates, many Chinese scientists consider some of the deserts in central and eastern China to be man-induced (Zhu et al., 1980), and sometimes refer to them as sandy lands. The Mu Us Sandy Land is cited frequently as one of the most desertified areas of China. Incursions of pastoralists since the 9th century B.C., exploitation of the floodplains of the Yellow River, and poor farming practices destroyed the delicately balanced ecosystem of the steppe environment and allowed the desert to encroach. Li (1979) reports that ruins of the capital of the Xia dynasty (2205–1766 B.C.) and 11 other large cities are now covered by the moving dunes of the Mu Us. As seen in this Plate, today the desert consists of large areas of irregularly shaped sand sheets and streaks interspersed with numerous small lakes, some of which are salty. Approximately 50 percent of the Mu Us is marshland or farmland covered with vegetation.

The eastern section of the Mu Us Sandy Land and the western section of the Loess Plateau of China are seen respectively in the left and right of the Plate. This Plate reveals a striking difference in drainage patterns between the Loess Plateau and the Mu Us Sandy Land. This also shows up in Figure E-22.1, a SIR-A radar image. The sandy areas in the Landsat image are light, whereas on the radar, they are dark. The streams on the right half of the Plate drain into the Yellow River, just a few kilometers east of the scene. Note how much sharper some of

MU US SANDY LAND, CHINA

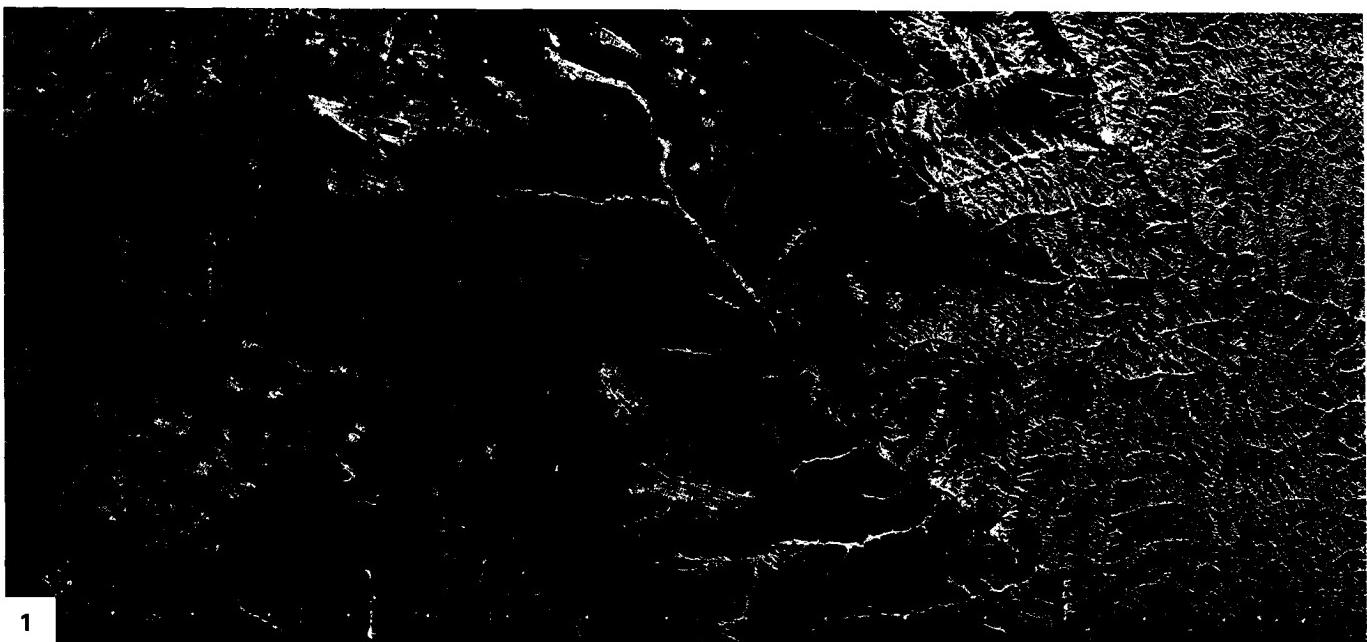
the drainage patterns are on the SIR; compare point A on the Landsat with the equivalent point on the radar. The reflectance differs sharply on the radar, perhaps because of a change in the slope or vegetation type of the stream channels.

In an effort to reclaim the sandy lands, the residents of the Mu Us have developed a method for stabilizing the dunes. First, shrubs are planted on the lower one-third of a dune's windward side. The vegetation lowers the wind velocity near the bottom of the dune and prevents much of the sand from moving up the dune. Higher velocity winds at the top of the dune level it off. Then trees are planted on top of the flattened dune. Within 5 years, this method of controlled planting can increase vegetation cover as much as 50 to 80 percent.

Another technique for reclaiming deserts used in many of the sandy lands of China is to build kuluns. These are exclosures to control grazing and to allow the land to recover from misuse. Pastures and forests inside the kuluns block the wind and improve the quality of the soil. Kuluns may be constructed to provide grazing or fodder, to control sand movement, or to turn swampy areas between dunes into productive land. Desert marshes may be upgraded by planting belts of tall trees perpendicular to the main wind direction, by planting grasses in the shelter of the trees, and by developing irrigation channels using the groundwater resources. Dunes inside a kulun may be leveled manually or by the wind, thus reducing the topographic relief.

Although the kuluns of the Mu Us are not visible in this Landsat image, they are scattered throughout the desert, as can be seen in the SIR-A image. Compare points B and C on the Plate and on the SIR image. In the SIR view, we may be seeing the barbed-wire fences that are creating the exclosures.

Figure E-22.2 is an oblique aerial photograph of the Loess Plateau acquired about 200 km east of this Plate. As in the Plate, the plateau is deeply dissected in a dendritic drainage pattern. Note how the streams are eroding the plains. **Landsat 30203-02430-7, September 24, 1978.**



ORIGINAL PAGE IS
OF POOR QUALITY



2

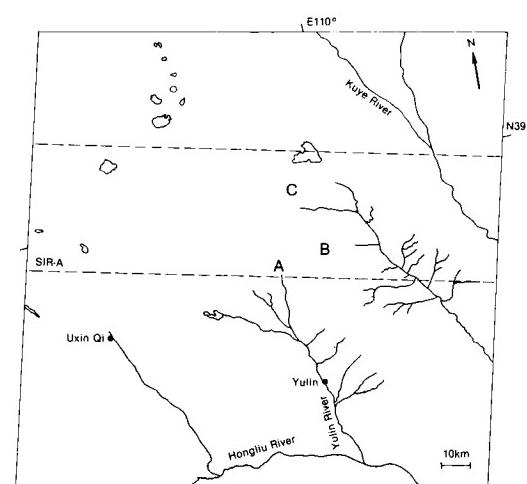


PLATE E-23

TENGGER DESERT

The 42 700-km² Tengger Desert is one of three deserts on the Alashan Plain in central China. The Tengger is in the upper half of this Plate. The Qilian Mountain range in the bottom half of the image is the southern boundary of the Tengger. The large river passing through the mountains and then through the Tengger is the Yellow River. Landsat-3 experienced an MSS line-drop problem late in its mission, and only the right two-thirds of this image was produced.

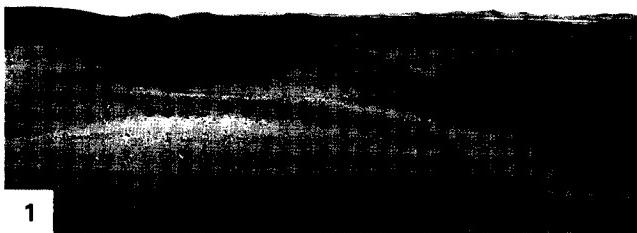
The wind in the Tengger is primarily from the northwest, and the dunes are moving toward the Yellow River. Only 7 percent of the dunes are fixed (Zhu et al., 1980). In the MSS rendition, this area of the Tengger appears to consist of sand sheets. Field investigations, however, reveal that these sand sheets are actually fields of small (5 to 10 m) complex crescentic dunes (Walker, 1982). The four people in the center of Figure E-23.1 are returning from a 3-day trip to a playa close to the center of the Tengger (slightly northwest of this Plate). At the playa, they collected a supply of salt for their village.

The Shapotou Desert Research Station, north of a bend in the Yellow River near the center of this Plate, was established in 1956 by Academia Sinica to develop and monitor methods to protect a major east-west railroad where it passes through the Tengger. The railroad is the dark line north of the river on the Plate. More than 40 km of track of this railroad are in the Tengger where dunes are moving as much as 15 m per year toward

the southeast. The track has been buried by sand several times in the past, resulting in serious accidents.

The research station personnel manually leveled dunes to provide experimental agricultural plots. Soil and plant analysis laboratories were built to monitor land changes. Engineering, mechanical, and biologic methods are being studied at the station to determine how best to reduce the damage of windblown sand to the railroad. The most effective method developed thus far is to supplement a planting program by constructing 1-m² straw grids on the dunes, as shown in Figures E-23.2 and E-23.3. The grid system, which is effective up to 7 years, lowers the surface wind velocity by 17 percent. Shrubs and trees planted within the grid are protected by the straw until they take root. Note in Figure E-23.3 that the grid system has changed the profiles of the dunes. Since the implementation of the grid system and planting program, the railroad has remained open, and no serious accidents have occurred.

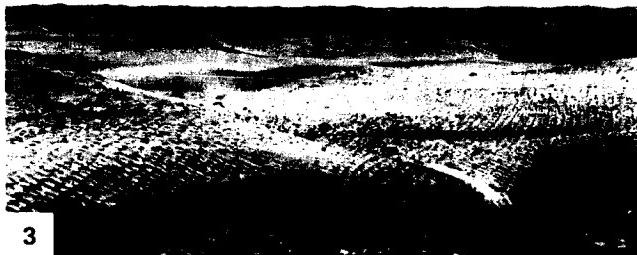
Figure E-23.4 is part of an RBV image of the Tengger Desert acquired the same day as the MSS image. The Shapotou Desert Research Station is at the bend of the Yellow River on the right. The linear dune structures of the Tengger are more easily seen on the higher resolution (30-m) RBV image. The sedimentary outcrops, barely discernible in the MSS Plate image, are also better defined. Vegetation surrounding the railroad appears as a dark line parallel to the tracks. **Landsat 30106-02481-7, December 15, 1980.**



1



2



3



4

ORIGINAL PAGE IS
OF POOR QUALITY

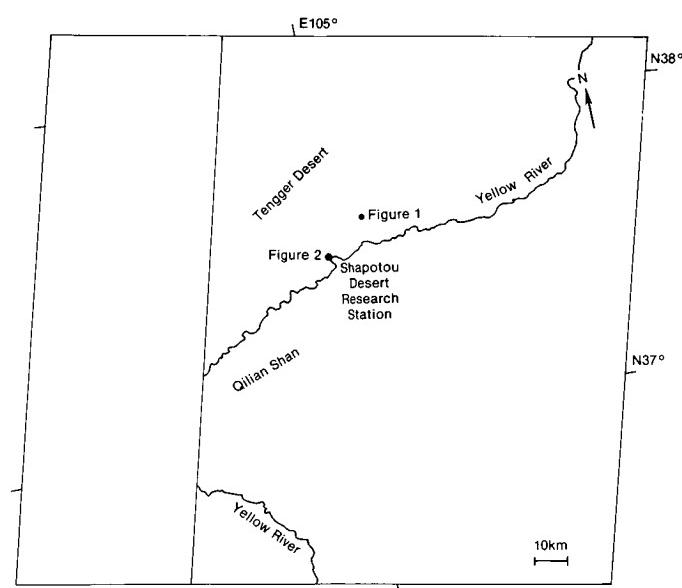


PLATE E-24

The Turpan Depression is a 50000-km² fault-formed interior drainage basin in Xinjiang Autonomous Region, People's Republic of China. The basin is bounded by the Tian Shan (Celestial Mountains), which are composed predominantly of quartzite and other metasediments. A small segment of the range south of the depression is seen at the bottom of this Plate, and the glaciated north range is above the center. The mountain topography creates a rain-shadow desert in the Turpan Depression. The windward north side of the Tian Shan has more ice, rain, and vegetation than the depression side of the range. Drainage channels are evident on the alluvial plain of the northern slopes, where glacial meltwater flows into the Junggar Basin.

Wind flows through gaps in the Tian Shan to the northeast and northwest of the depression. Much of the depression is a deflation zone composed of black gobi (regionally unsorted loose subangular to subrounded quartzite gravels) occupying an area 25 km wide in the north and 15 km wide in the south. The dark gravel desert dominates much of this Plate. Alluvium, artesian wells, spring-fed oases, and small lakes occupy the center of the basin. The maximum recorded ground temperature in the depression is 48.9°C (Xia and Hu, 1978).

Fifty years ago, winds with speeds greater than 36 m/sec carried sands that totally buried all the houses in the area of the Five Star People's Commune, and in 1961, a similar storm destroyed the entire wheat crop. To stop disasters such as these, the Chinese construct shield belts to reduce the wind velocity over the farm land.

The Huang Liu He State Farm in the northwestern part of the depression was begun in 1957 on gobi terrain 8 km south of the Turpan Railroad Station. Water is supplied by wells and by karez—horizontal underground tunnels that carry water from the Tian Shan into the depression. If the water were not shielded from the dry atmosphere, it would quickly evaporate. Wheat, sorghum, cotton, watermelon, grapes, and various vegetables grow on the farm.

TURPAN DEPRESSION

Figure E-24.1, looking north toward the Huang Liu He State Farm, is an example of the deflated gobi area. Note the flatness and equigranular pebbles. The farm is conspicuous in Figure E-24.2, the second principal component of digital data for this scene. Principal component analysis is designed to minimize the correlation among the Landsat bands. The second principal component emphasizes vegetation (Lodwick, 1979). The dark patch in the left center of the figure represents vegetation evident on the farm; the dark area at bottom right marks the oases in the center of the depression. In comparing this October 1972 image with an October 1980 Landsat image, a 12 percent increase in the productive area of the farm was noted (Walker and Liu, 1982).

An intermittent salt lake in the southern part of the basin, Aydingkol Hu, is difficult to locate on this image. The lake is the second lowest point on the surface of the Earth not covered by ocean (-154 m), and its location is represented by a dot on the map.

Much of the sand in the depression has been transported to Sand Mountain, a 2500-km² sand sea. The dune pattern in the sea reflects the atmospheric circulation pattern of the area. Masibroda (1952) notes that the northwest and north winds do not penetrate far onto the sea and that the northeast winds become considerably intensified and prevail over the area. The linear array of the complex linear dunes and sand sheets on the sea reflect the complex patterns described by Masibroda. Star dunes appear in the south center of the sand sea and dominate the northeast.

Flaming Hills (Figure E-24.3) is an anticlinal structure of Mesozoic and Cenozoic sandstone, conglomerate, and mudstone. This figure illustrates poorly consolidated sand dunes that were buried by water. The lake eroded the crests of the dunes and deposited a horizontal layer of siltstone above the sand. Following evaporation of the lake, dunes encroached and were deposited above the lake sediment (C. Breed, USGS, oral communication, 1982). More recently, fluvial erosion has exposed the section. Note that the dip of the cross-strata below the horizontal beds is slightly steeper than that of the strata above the bed. **Landsat 10073-04181-7, October 4, 1972.**

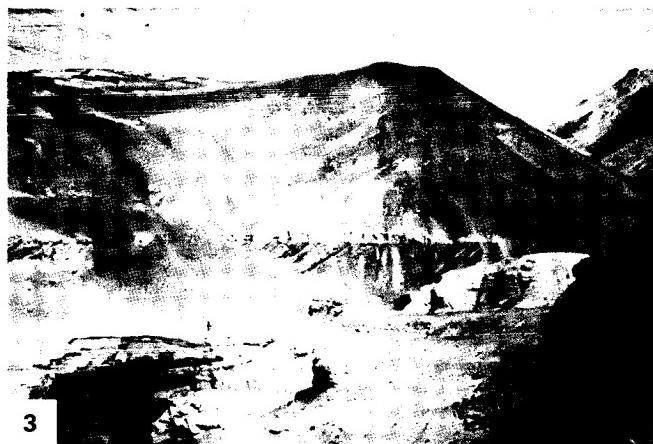
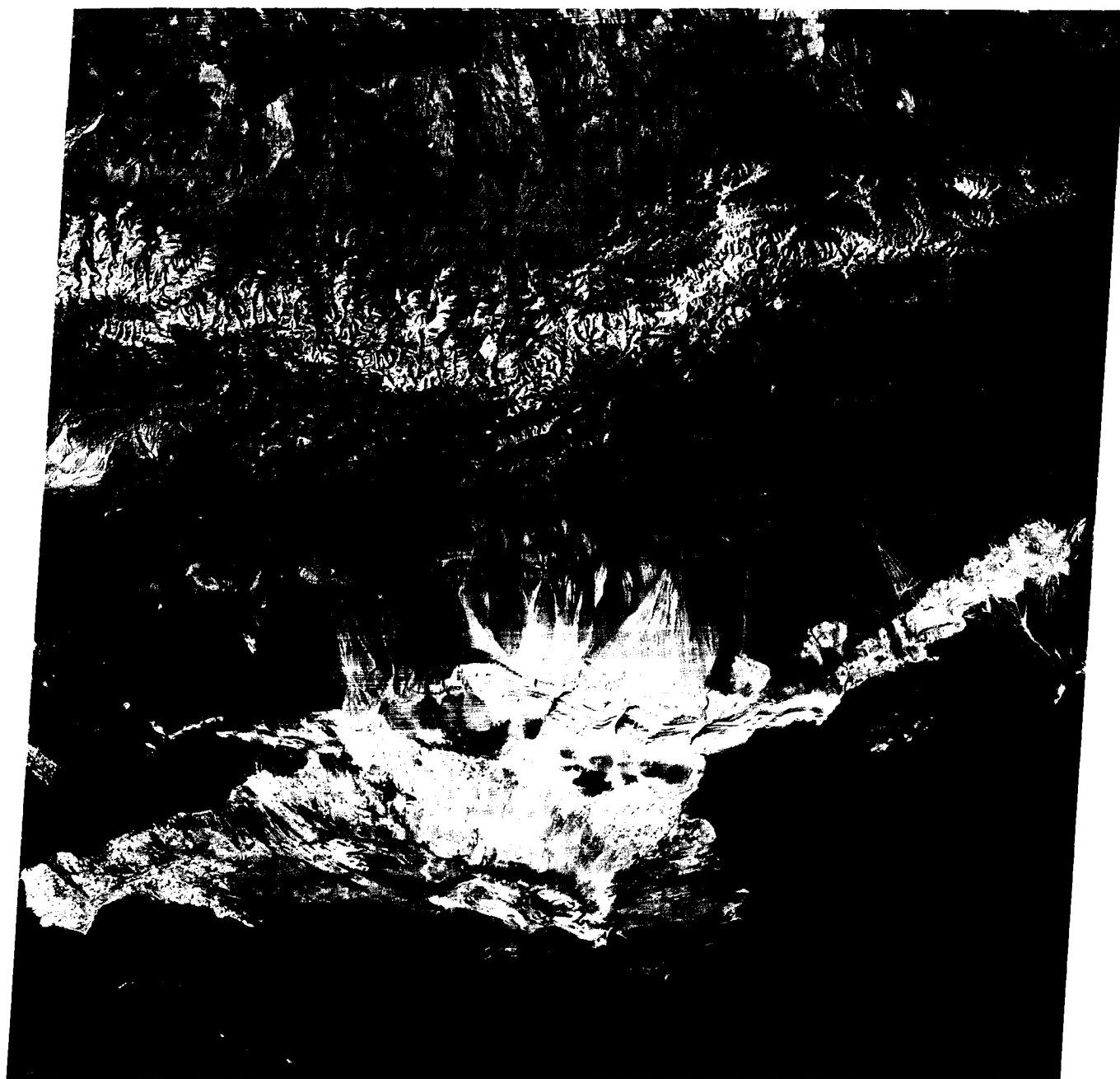


1



2

ORIGINAL PAGE IS
OF POOR QUALITY



3

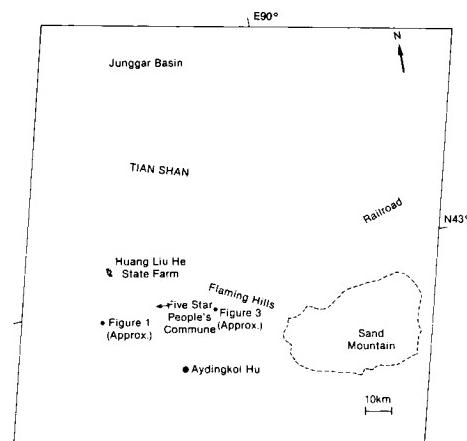


PLATE E-25

LOP NUR

Lop Nur, in the eastern Tarim Basin, was identified in ancient Chinese records and maps as a salt lake 150 km in diameter (Xia, 1982). Today, it is a totally dry lake bed with a salt crust 30 to 100 cm thick. The concentric rings created by the progressively shrinking shorelines of the lake resemble a giant ear when viewed from space. Water has probably most recently been in the dark center of the ear. The dark areas north of the ear are also lacustrine plains, perhaps containing some water at this time of year.

At an elevation of about 780 m above sea level, Lop Nur is the main drainage playa of the Tarim Basin. The Tarim River, Plate E-26, flows into Lop Nur. The mean annual precipitation at Lop Nur is generally less than 20 mm (Zhao and Xia, 1984).

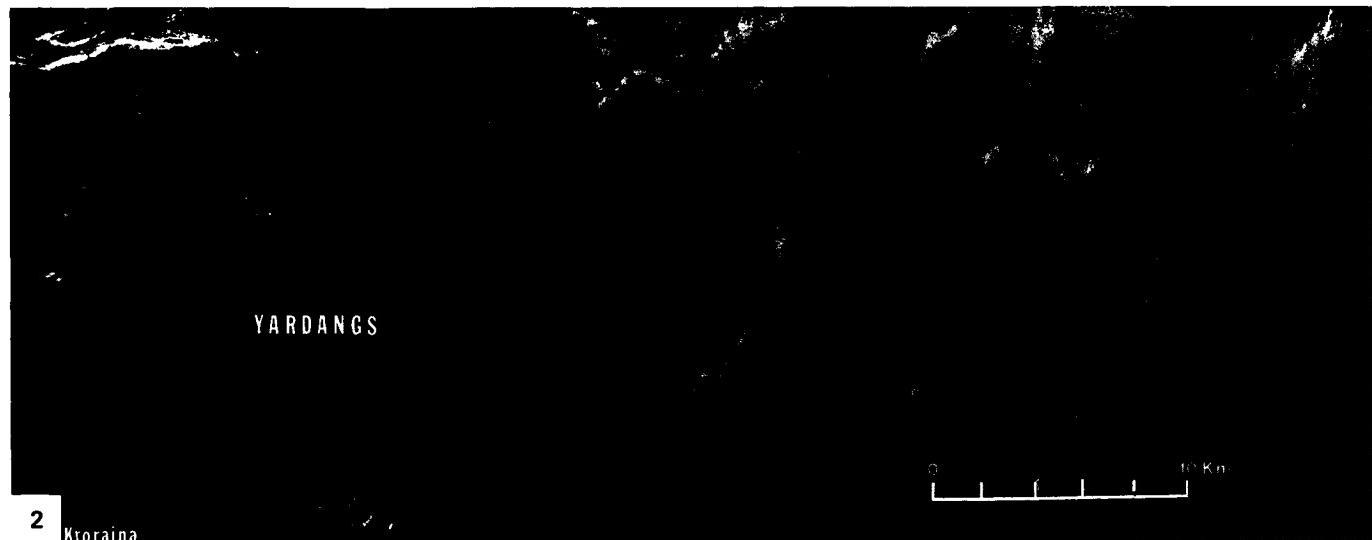
Yardangs, sculpted landforms streamlined by desert winds, were first described in this locality by Hedin (1903). The yardangs in Figure E-25.1 are near the ruins of Kroraïna in the center of the Plate. Note the heights of the yardangs and the flatness of the intervening depressions. Some of the horizontal beds have been undercut and have collapsed on the slope of the yardangs. Compare these yardangs with those on Plate E-19, the Lut Desert. Xia (1982) estimates that 5.3 m of surface was eroded in Lop Nur between 1919 and 1959, although this may be geographically and temporally a local phenomenon. He also points out that some of the yardangs extend in the apparent directions of former floodwaters of Lop Nur, and cites some evidence of floodwater erosion on the yardangs. He hypothesizes that water may have played a significant role in shaping these yardangs.

The influence of a northeasterly wind direction on elongation of the yardangs is readily apparent both on the Plate and in Figure E-25.2, a Space Shuttle radar image (SIR-A) of the area outlined on the index map. Although individual yardangs northwest of Lop Nur are discernible in the radar image, they are quite difficult to see on the Landsat image. Dark intermittent stream channels are likewise visible as they pass across the yardangs on the radar image.

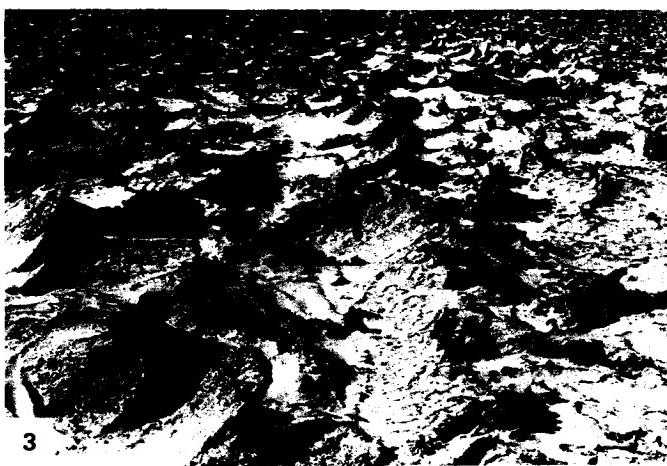
Until the 4th century A.D., Kroraïna, also known as Loulan, was a major stop on the Silk Road. Fish from rivers

emptying into Lop Nur, as well as cattle and game from the surrounding grasslands, fed this city of more than 10000 people (Mu, 1981). Today, the area is a desolate wasteland with a few ruins left to mark the once-flourishing metropolis that is still reachable only by camel.

Xia (1982) describes the Lop Nur area as an undulating crust of salt stretching in every direction. Figure E-25.3 illustrates the salt crust of the desert. Zhao and Xia (1984) note that salt crusts and saline soils occupy about 35 percent of the Lop Nur environment. **Landsat 1162-04134-7, January 1, 1973.**



ORIGINAL PAGE IS
OF POOR QUALITY



3

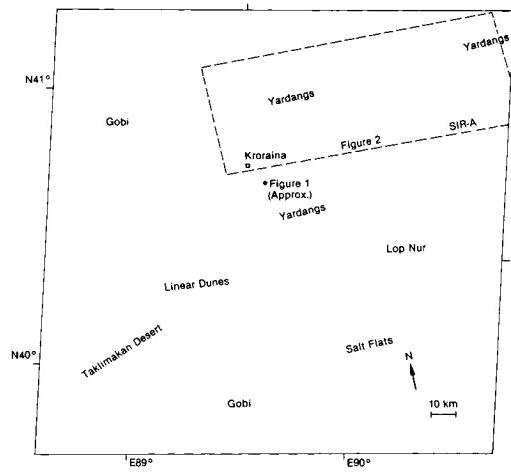


PLATE E-26

ORIGINAL PAGE IS
OF POOR QUALITY

TAKLIMAKAN DESERT

This Plate scene falls within the northeastern Taklimakan Desert of the Tarim Basin. Compare this Plate with Plate E-27, the color mosaic of the southwestern Taklimakan Desert, and with Plate E-25, Lop Nur, which is about 300 km east of this Plate. The Tian Shan Mountains are directly north of the Tarim River floodplain. The Qarqan River drains water from the Kunlun Shan, a mountain range at the southern border of the Tarim Basin.

Breed et al. (1979a) determined that the compound crescentic dunes in the center of this Plate are the largest such dunes in their worldwide study. The dunes have a mean horn-to-horn width of 3.2 km and a mean length of 2.2 km. They are spaced 3 km apart and average 100 to 150 m in height (Zhu et al., 1980).

Simple crescentic dunes in the right center of the Plate are encroaching westward over the large ridges (Breed et al., 1979a). Although these dunes are smaller, their orientation is identical to that of the larger dunes. Sand for these encroaching dunes may be derived from the floodplain of the intermittent Tarim River. The sand sheet north of these dunes also is encroaching on the large field, as can be seen by the muted crescentic dune forms under the sheet.

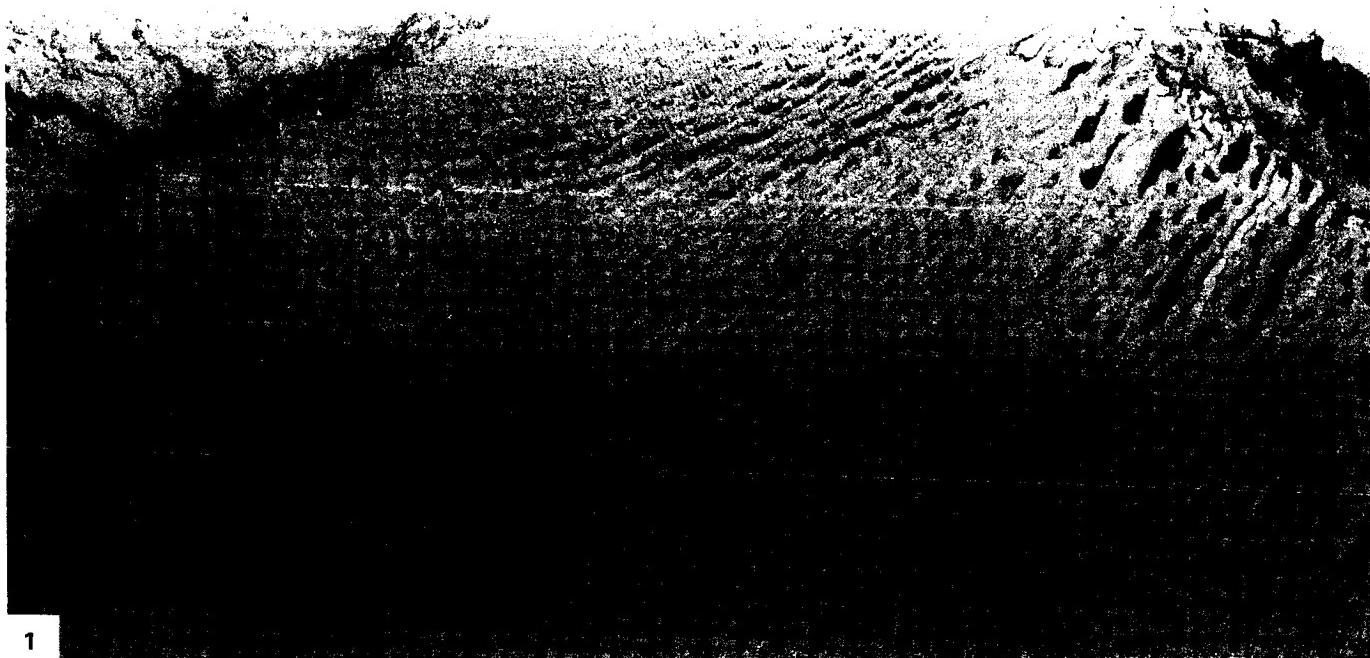
Parallel interdunal lakes at the upper left of the Plate are directly south of the small channel of the Tarim. The wide lakes north of the Tarim River are reservoirs.

Figure E-26.1 is a 50-km wide SIR-A radar strip of the interdunal lakes and the desert. In radar imagery, smooth water, being a specular reflector, normally is black because of low signal returns. However, this strip had to be printed as a negative because of film density problems, so that these lakes now appear as lighter gray tones. The longest lake and the two on the far left are outlined by former lake levels in the strip. Compare this with the former lake levels at Lop Nur on Plate E-25. The sharply defined dark areas near the lakes in the radar image are interdunal playas that remain dark in the Landsat image. The bright areas north of the lakes in the radar strip are irrigated farmland.

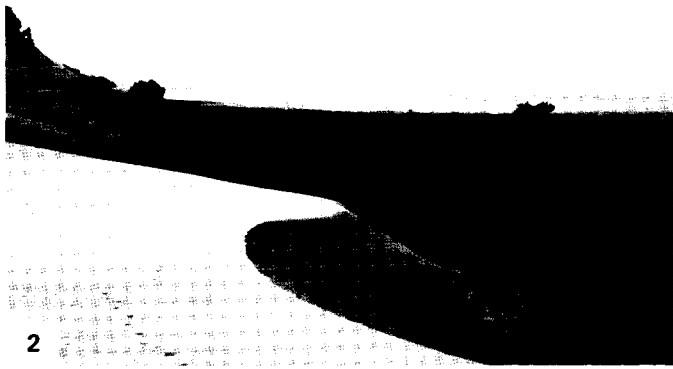
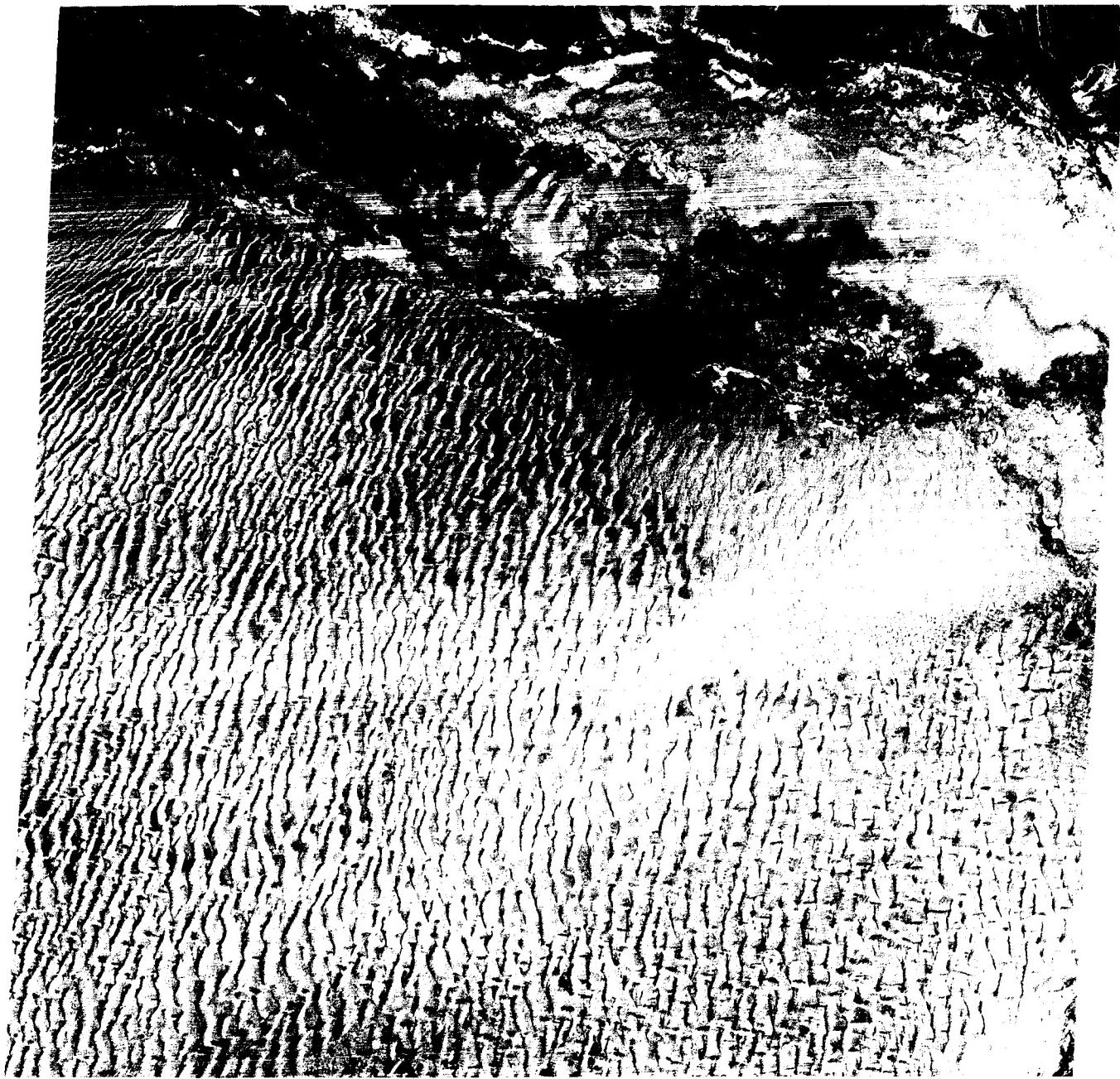
The return signals in the radar image display a notable difference between the dunes associated with the lakes and the smaller simple linear dunes west of the lakes. Dunes commonly have a dark response on radar images typical of smooth surfaces unless the dunes have slipfaces oriented normal to the incident radar beam (Blom and Elachi, 1981). Because the slipfaces of these small dunes are almost normal to the SIR-A flight path, they are much brighter in a radar display than the larger dunes among the lakes.

Observe the drainage pattern on the left side of the radar strip. Numerous buried drainage channels of the east-flowing Tarim River are readily visible in the radar image. Although one channel may be distinguished on a Landsat image directly west of this Plate, most of the other known channels cannot be recognized. That area is a sand sheet with occasional small dome-shaped dunes. Paleochannels of the Tarim River have been found about 80 km south of the present Tarim channel (Zhu, 1984). This image once again confirms the value of spaceborne radar for mapping paleodrainage channels.

When Sven Hedin investigated this area in 1905, he found a total of 35 lakes that the local inhabitants claimed were artificially made in the interdune depressions. Hedin (1905) questions the artificial origin of these lakes. Because some of the lakes were fed by the Tarim River through connecting channels, he deduced that they were once fresh but became brackish when the channel was severed. Hedin points out that the lakes are young because the Tarim River has only recently begun to flow through that region. The lakes are doomed to perish through either the advancing of the dunes or the instability of the river (Hedin, 1905, p. 83). As the Plate scene illustrates, few of the original 35 lakes remain 80 years after his work. Figure E-26.2 shows the dune/water boundary on one of the lakes on the Plate. Note the vegetation on the floodplain and on the dune to the far left. **Landsat 10074-04244-7, October 5, 1972.**



ORIGINAL PAGE IS
OF POOR QUALITY



2

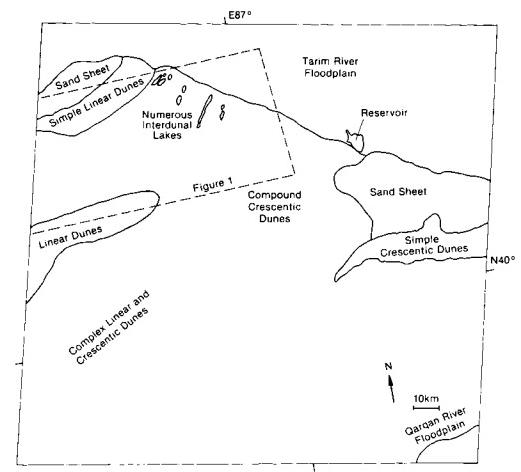


PLATE E-27

THE SOUTHWEST TAKLIMAKAN DESERT

This color mosaic contains a portion of the Tarim Basin in western China, one of the largest internal drainage basins in the world. The elliptical-shaped basin is bordered by the Tian Shan on the north and the Kunlun Shan and Altun Shan on the west and south. Parts of those mountains are glaciated. The basin grades into the Inner Mongolian Plateau on the northeast, and toward the east into Lop Nur, the large playa shown on Plate E-25. The elevation at Lop Nur is 780 m, but the western Tarim Basin rises to about 1560 m. As seen in the mosaic, most of the intermittent streams with headwaters south of the basin flow north from the Kunlun Shan into the desert. Farther east are the two non-north-flowing rivers in the basin—the Qarqan River that rims the southeastern edge, and the Tarim River that flows east along the northern border; these rivers appear in Plate E-26.

Two distinct deserts occupy the Tarim Basin. The smaller ($19\,500 \text{ km}^2$) Kumutage Desert east of Lop Nur is composed of gobi, sand sheets, and crescentic, linear, and star dunes 10 to 30 m in height. More than 100 km of Quaternary alluvium and marshland on the lacustrine plain of Lop Nur separate the Kumutage and the Taklimakan. With a total area of $337\,600 \text{ km}^2$, the Taklimakan Desert is the largest desert in China and one of the largest in the world. The name is derived from a minority language expression meaning "once you get in you can never get out." Gobi surfaces are located only along the southeastern and northern borders of the Taklimakan. Approximately 85 percent of the desert consists of moving sand dunes that average 100 to 150 m in height in the northeastern desert but locally may be as high as 200 m. Dunes along the periphery of the desert and in its western reaches are only 5 to 25 m tall (Zhu et al., 1980). Crescentic, linear, dome, and star dunes are found throughout the Taklimakan.

Explorer Fa Xian described the Taklimakan in A.D. 400 by saying, "In this desert there are a great many evil spirits and also hot winds; those who encounter them perish to a man. There are neither birds above nor beasts below. Gazing on all sides as far as the eye can reach in order to mark the track, no guidance is to be obtained save from the rotting bones of dead men, which point the way" (Giles, 1923).

Through analysis of the heavy minerals in the sands of the Taklimakan, Zhu (1984) determined that much of the desert sand is a product of weathering of the bedrock from the bordering mountains. These materials were transported into the basin by water and deposited in floodplains and river beds. He associates the average size of the sands with the grain size of the underlying deposits, and notes that wind presently dominates the activity of the Taklimakan. Zhu (1984) discusses two dominant wind regimes. Northeasterly winds dominate much of the desert, but winds from the northwest dominate the western Taklimakan. These two wind systems meet in the central-west part of the desert, resulting in a complex dune alignment.

This mosaic covers the Kunlun Mountains and a southwest section of the Tarim Basin. The snowfield decreases on the lee side of the range. Several intermittent streams fed from the Kunlun flow into the desert. Note the red vegetation on the oases and alluvial plains at the foot of the mountain. Some of the vegetation extends into the desert for some distance.

Sand sheets and gobi are common west of the Yarkant River. The small streams in that area in the Plate flow east onto the plain. One of the alluvial fans has been breached, and a small

second fan is being established on the northeastern end of the flank.

The Hotan River is formed by the joining of the Karakax on the west and the Ywungkax on the east. The Hotan is an exotic stream fed from the Kunlun. In the northern Tarim Basin, it merges into the Tarim River. The Hotan channel bed provides the only transportation system across the Tarim.

Note the extremely narrow 200-km long east-west range between the Hotan and the Yarkant Rivers. Its 100- to 300-m high escarpment is composed of red sandstone, shale, and gypsum. Because these beds dip toward the north, the south slope is steeper than the north. A map of the wind patterns in the Taklimakan indicates that the northeasterly wind pattern does not change direction when it passes over the range (Zhu et al., 1981).

Figure E-27.1 is a digitally enhanced Landsat image that encompasses this range. The pileup of sand against the windward side of the range is noteworthy. The simple linear dunes in the upper right of the figure coalesce westward into complex linear dunes with crescentic dunes on their crests. Sand sheets followed by crescentic dunes concentrate in the west. The sand sheets, which cross a break in the escarpment, may represent a paleo-drainage channel. Approaching the escarpment from the north, linear dunes merge into crescentic types. In the mosaic, it is evident that the simple linear dunes on the Yarkant River floodplain do not change their orientation as they cross the escarpment.

The dunes south of the escarpment illustrate the wind-shadow effect of this topographic barrier. Small dome dunes formed south of the escarpment, and as the distance from the escarpment increases, the domes begin to coalesce into complex linear dunes. This is more obvious below the western part of the escarpment because the Hotan floodplain has probably reduced the amount of sand. Figure E-27.2 depicts dome dunes of the Taklimakan. These dunes are described by Zhu (1984) as being 40 to 60 m tall with slipfaces approximately equal in length and width. As the figure illustrates, they are circular or elliptical in shape. Zhu states that dome dunes are irregularly distributed in the Taklimakan.

To the east, the two dominant wind directions in the Taklimakan Desert meet near the Keriya and Niya Rivers, resulting in a significant difference in dune types. The simple short linear dunes of the Hotan River floodplain grade into complex crescentic dunes and linear dunes. Note the wind-shadow effect of the small hills between the two rivers. It is easy to study the changing wind regime with the dune pattern.

A compound crescentic dune typical of the Taklimakan is illustrated in Figure E-27.3. The direction of the wind points toward the bottom of the aerial photograph. As the horn narrows, the orientation of the superimposed crescentic dune does not change. The linear dunes in Figure E-27.4 are sometimes called fishhook dunes because many of them terminate in a hook. This is particularly conspicuous in the bottom right of the figure. As illustrated in this Plate and in Plate E-26, linear dunes are one of the most widely distributed dune types in the Taklimakan (Zhu, 1984). Figure E-27.5 is an array of complex linear dunes with crescentic dunes superimposed both on the linear dunes and on the interdunal areas. These dunes are sometimes called scaled dune groupings or akle dunes because they resemble fish scales (Zhu, 1984). **Landsat Mosaic.**

ORIGINAL PAGE IS
OF POOR QUALITY



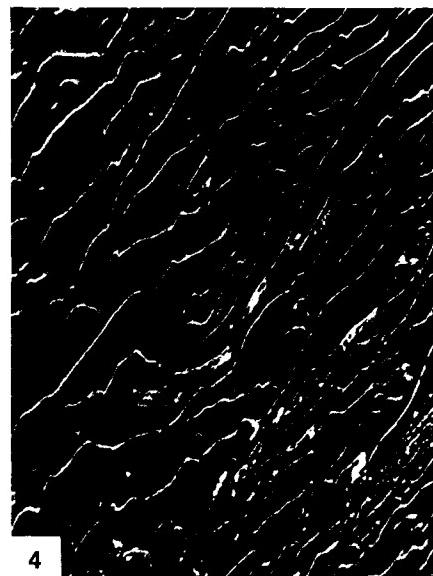
1



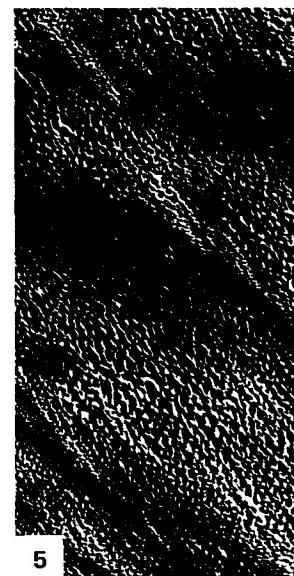
2



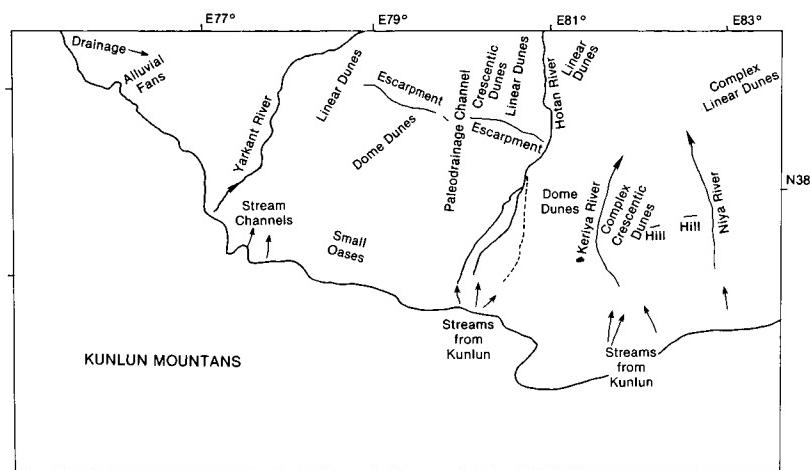
3

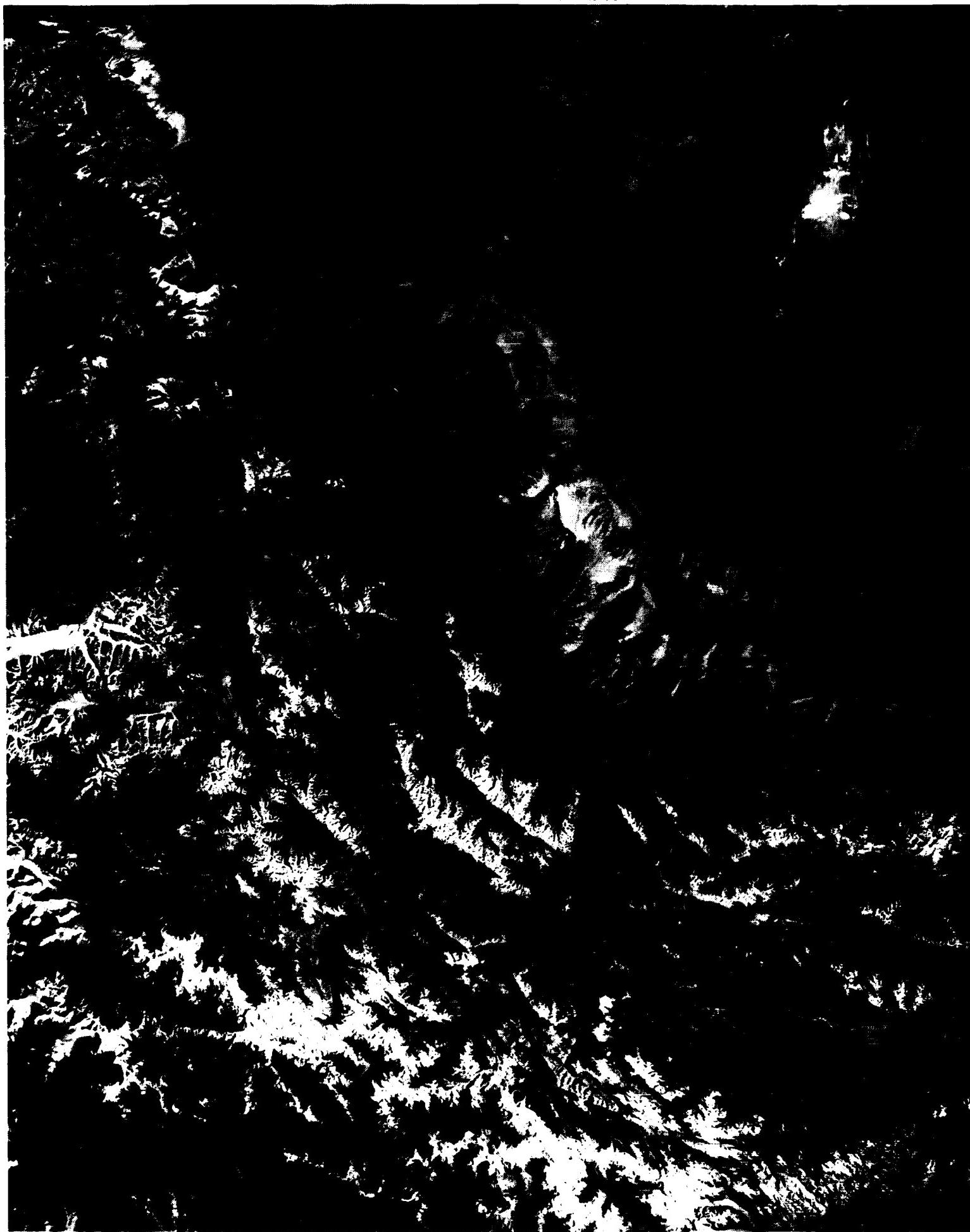


4



5





ORIGINAL PAGE
COLOR PHOTOGRAPH

REFERENCES

- Ahlbrandt, T. S., and S. G. Fryberger, 1980, Eolian deposits in the Nebraska Sand Hills, U.S. Geol. Surv. Prof. Paper, **1120A**, 1-24, 1980.
- Anton, D., Modern eolian deposits of the Eastern Province of Saudi Arabia, in *Eolian Sediments and Processes*, edited by M. E. Brookfield and T. S. Ahlbrandt, pp. 365-378, Elsevier, Amsterdam, 1983.
- Aubreville, A., Climats, Forêts et Desertification de l'Afrique Tropicale, Société d'Editions Géographiques Maritimes et Coloniales, Paris, France, 351 pp., 1949.
- Bagnold, R. A., *Physics of Blown Sand and Desert Dunes*, Methuen, London, 265 pp., 1941.
- Bigarella, J. J., Eolian environments: Their characteristics, recognition, and importance, in *Recognition of Ancient Sedimentary Environments*, edited by J. K. Rigby and W. K. Hamblin, pp. 12-62, Society of Economic Paleontologists and Mineralogists, Special Publication 16, 1972.
- Birkeland, P. W., Soils and Geomorphology, Oxford University Press, Oxford, 372 pp., 1984.
- Blatt, H., *Sedimentary Petrology*, W. H. Freeman and Co., San Francisco, California, 564 pp., 1982.
- Blatt, H., G. Middleton, and R. Murray, *Origin of Sedimentary Rocks*, Prentice-Hall, Englewood Cliffs, New Jersey, 782 pp., 1980.
- Blom, R., and C. Elachi, Spaceborne and airborne imaging radar observations of sand dunes, *J. Geophys. Res.*, **86**, 3061-3073, 1981.
- Breed, C. S., S. G. Fryberger, S. Andrews, C. McCauley, F. Lentz, D. Gebel, and K. Hortman, Regional studies of sand seas, using Landsat (ERTS) imagery, in A study of global sand seas, edited by E. D. McKee, *U.S. Geol. Surv. Prof. Paper*, **1052**, 305-397, 1979a.
- Breed, C. S., M. J. Grolier, and J. F. McCauley, Morphology and distribution of common 'sand' dunes on Mars: Comparison with the Earth, *J. Geophys. Res.*, **84**, 8183-8203, 1979b.
- Breed, C. S., and T. Grow, Morphology and distribution of dunes in sand seas observed by remote sensing, in A study of global sand seas, edited by E. D. McKee, *U.S. Geol. Surv. Prof. Paper*, **1052**, 253-302, 1979.
- Breed, C. S., J. F. McCauley, W. J. Breed, C. K. McCauley, and A. S. Cotera, Eolian (windformed) landscapes, in *Landscapes of Arizona*, edited by T. L. Smiley, J. D. Nations, T. L. Péwé, and J. P. Schafer, pp. 359-413, University Press, 1984.
- Charney, J. G., Dynamics of desert and drought in the Sahel, *Quart. J. Roy. Meteorol. Soc.*, **101**, 193-202, 1975.
- Charney, J. G., W. J. Quirk, S. H. Chow, and J. Kornfield, A comparative study of the effects of albedo change on drought in semi-arid regions, *J. Atmospheric Sciences*, **34**, 1366-1385, 1977.
- Cooke, R. U., and A. Warren, *Geomorphology in Deserts*, 374 pp., Univ. California Press, Berkeley, California, 1973.
- Cross, M., Last chance to save Africa's topsoil, *New Scientist*, **28**, 289-293, 1983.
- Crosswhite, F. S., and C. D. Crosswhite, The Sonoran Desert, in *Reference Handbook on the Deserts of North America*, edited by G. L. Bender, pp. 163-295, Greenwood Press, Connecticut, 1982.
- Derbyshire, E. D., On the morphology, sediments, and origin of the Loess Plateau of central China, in *Mega-Geomorphology*, edited by R. Gardner and H. Scoging, pp. 172-194, Clarendon Press, Oxford, 1983.
- Dorn, R. I., and T. M. Oberlander, Rock varnish, *Progress in Physical Geography*, **6**, 317-367, 1982.
- Dresch, M. J., Reconnaissance dans le Lut (Iran), *Bull. Assn. Géographique Francais*, Nos. 362-363, 143-153, 1968.
- Dunbar, R., *The Sonoran Desert—Its Geography, Economy, and People*, 426 pp., Univ. Arizona Press, Tucson, Arizona, 1968.
- Embabi, N. S., Barchans of the Kharga Depression, in *Desert Landforms of Southwest Egypt: A Basis for Comparison with Mars*, edited by F. El-Baz and T. A. Maxwell, pp. 141-155, NASA CR-3611, 1982.
- Erickson, G. E., Geology and origin of the Chilean nitrate deposits, *U.S. Geol. Surv. Prof. Paper*, **1188**, 37 pp., 1981.
- Erickson, G. E., The Chilean nitrate deposits, *American Scientist*, **71**, 366-374, 1983.
- Faure, H., and J.-Y. Gac, Will the Sahelian drought end in 1985?, *Nature*, **291**, 475-478, 1981.
- Fryberger, S., and A. S. Goudie, Arid geomorphology, *Progress in Physical Geography*, **5**, 420-428, 1981.
- Fujita, T. T., Tornadoes and downbursts in the context of generalized planetary scales, *J. Atmospheric Sciences*, **81**, 1511-1524, 1981.
- Gabriel, A., The southern Lut and Iranian Baluchistan, *Geographical J.*, **92**, 193-210, 1938.

- Garner, H. F., *The Origin of Landscapes*, 734 pp., Oxford Univ. Press, New York, 1974.
- Garvin, J. B., P. J. Mousginis-Mark, and J. W. Head, Characterization of rock populations on planetary surfaces: Techniques and a preliminary analysis of Mars and Venus, *The Moon and the Planets*, **24**, 335-387, 1981.
- Gerster, G. *Sahara—desert of destiny*, 302 pp., Coward-McCann, 1960.
- Giles, H. A. (translator), *The Travels of Fa-hsien (399-414 A.D.) or Record of the Buddhist Kingdoms*, 96 pp., Cambridge Univ. Press, 1923.
- Glantz, M. H., Man, state and the environment: An inquiry into whether solutions to desertification in the West African Sahel are known but not applied, *Canadian J. Development Studies*, **1**, 75-97, 1980.
- Glantz, M. H., and N. Orlorsky, Desertification, a review of the concept, *Desertification Control Bull.*, UNEP No. 9, 15-22, 1983.
- Glennie, K. W., *Desert Sedimentary Environments*, 222 pp., Elsevier Publishing Co., New York, 1970.
- Goudie, A. S., Dust storms and their geomorphological implications, *J. Arid Environments*, **1**, 291-310, 1978.
- Goudie, A., The arid Earth, in *Mega-Geomorphology*, edited by R. Gardner and H. Scoging, pp. 152-171, Clarendon Press, Oxford, 1983.
- Goudie, A., and J. Wilkinson, *The Warm Desert Environment*, 88 pp., Cambridge Univ. Press, Cambridge, England, 1977.
- Greeley, R., Aeolian modification of planetary surfaces, in *The Comparative Study of the Planets*, edited by A. Coradini and M. Fulchignoni, pp. 419-434, NATO, Reidel Publishing, Dordrecht, 1982.
- Greeley, R., P. R. Christensen, J. F. McHone, Y. Asmerom, and J. R. Zimbelman, *Analysis of the Gran Desierto-Pinacate Region, Sonora, Mexico, via Shuttle Imaging Radar*, 45 pp., NASA CR-177356, 1985.
- Greeley, R., and J. D. Iversen, *Wind as a Geological Process on Earth, Mars, Venus and Titan*, 333 pp., Cambridge Univ. Press, New York, 1985.
- Grove, A. T., The ancient erg of Hausal and similar formations on the south side of the Sahara, *Geographical J.*, **124**, 526-533, 1958.
- Grove, A. T., Rise and fall of Lake Chad, *Geographical Magazine*, **42**, 432-439, 1970.
- Hare, F. K., Climate on the desert fringe, in *Mega-Geomorphology*, edited by R. Gardner and H. Scoging, pp. 134-151, Clarendon Press, Oxford, 1983.
- Hastings, J. R., and R. M. Turner, *The Changing Mile—An Ecological Study of Vegetation Change with Time in the Lower Mile of an Arid and Semiarid Region*, 317 pp., Univ. Arizona Press, Tucson, Arizona, 1972.
- Haynes, C. V., Jr., Great Sand Sea and Selima Sand Sheet, Eastern Sahara: geochronology of desertification, *Science*, **217**, 629-633, 1982.
- Hedin, S., *Central Asia and Tibet*, 608 pp., Scribner's, New York, 1903.
- Hedin, S., The lakes beside the lower Tarim, *Amer. Geograph. Soc. Bull.*, **37**, 78-83, 1905.
- Hills, E. S., The lunette, a new landform of eolian origin, *Australian Geographer*, **3**, 15-21, 1940.
- Holm, D. A., Dome-shaped dunes of central Nejd, Saudi Arabia, in *Proc. 19th International Geological Congress*, pp. 107-112, Algiers, 1952, Comptes Rendus, sec 7, pt. 7, 1953.
- Holm, D. A., Desert geomorphology in the Arabian Peninsula, *Science*, **132**, 1369-1379, 1960.
- Holmes, A., *Principles of Physical Geology*, 1288 pp., Ronald Press Company, New York, 1965.
- Howard, A. D., J. A. Cutts, and K. R. Blasius, Stratigraphic relationships within martian polar cap deposits, *Icarus*, **50**, 161-215, 1982.
- Hunt, C. B., *Natural Regions of the United States and Canada*, 725 pp., W. H. Freeman and Co., San Francisco, 1974.
- Idso, S. B., Dust storms, *Scientific American*, **235**, 108-114, 1976.
- Idso, S. B., R. S. Ingram, and J. M. Pritchard, An American haboob, *Bull. Amer. Meteor. Soc.*, **53**, 930-935, 1972.
- Iversen, J. D., R. Greeley, and J. B. Pollack, Windblown dust on Earth, Mars and Venus, *J. Atmospheric Sciences*, **33**, 2425-2429, 1976.
- Kahle, A. B., Spectral remote sensing of rocks in arid lands in *Proc. Conf. on Remote Sensing of Arid and Semi-Arid Lands*, pp. 279-298, ERIM, Ann Arbor, Michigan, 1982.
- Kates, R. W., D. L. Johnson, and H. K. Johnson, Population, society, and desertification, in *UN Conference on Desertification, Desertification: Its Causes and Consequences*, pp. 261-317, Pergamon Press, Oxford, 1977.
- Kerr, R. A., The Moon influences western drought, *Science*, **224**, 587, 1984.
- Krinsley, D. B., *Geomorphological and Paleoclimatological Study of the Playas of Iran*, Vols. 1 and 2, 486 pp., U.S. Geol. Surv. Final Science Report, Contract PRO CP 70-800, 1970.
- Lancaster, N., The formation of sief dunes from barchans—Supporting evidence for Bagnold's model from the Namib Desert, *Zeitschrift für Geomorphologie, Neue folge*, **24**, 160-167, 1980.
- Lancaster, N., Linear dunes, *Progress in Physical Geography*, **6**, 475-503, 1982.
- Lancaster, N., Controls of dune morphology in the Namib Sand Sea, in *Eolian Sediments and Processes*, edited by M. E. Brookfield and T. S. Ahlbrandt, pp. 261-289, Elsevier, Amsterdam, 1983.

- Langford-Smith, T., The geomorphic history of the Australian deserts, *Striae*, **17**, 4-19, 1982.
- Legrand, P. N., Essai sur la paleogeographie du Silurien au Sahara Algerien, *Compagnie Francaise des Petroles, Notes et Memories*, No. 16, 9-24, 1981.
- Leovy, C. B., The atmosphere of Mars, *Scientific American*, **237**, 34-43, 1977.
- Li, H. F., The problems of desertification in China's semiarid region—Ordos, in *Proc. International Arid Lands Conf. on Plant Resources*, edited by J. R. Goodin and P. K. Northington, pp. 678-683, Texas University Press, Lubbock, Texas, 1979.
- Li, X. F., A survey of the desert in Hedong, Ningxia, in *Research on Sand Control*, pp. 391-421, Communist China, Sand Control Group of Academia Sinica, JPRS-19993, 1962.
- Liu, T. S., X. F. Gu, Z. S. An, and Y. X. Fan, The dust fall in Beijing, China on April 18, 1980, in *Desert dust: Origin, characteristics, and effect on man*, edited by T. L. Péwé, *Geol. Soc. Amer. Special Paper*, **186**, 149-157, 1981.
- Lodwick, G. D., Measuring ecological changes in multitemporal Landsat data using principal components, in *Proc. 13th International Symp. Remote Sensing of Environment*, pp. 1131-1141, ERIM, Ann Arbor, Michigan, 1979.
- Lutgens, F. T., and E. J. Tarbuck, *The Atmosphere, an Introduction to Meteorology*, 413 pp., Prentice-Hall, Englewood Cliffs, New Jersey, 1979.
- Mainguet, M., Tentative mega-morphological study of the Sahara, in *Mega-Geomorphology*, edited by R. Gardner and H. Scoging, pp. 113-133, Clarendon Press, Oxford, 1983.
- Mainguet, M., and M. C. Chemin, Sand seas of the Sahara and Sahel: An explanation of their thickness and sand dune type by the sand budget principle, in *Eolian Sediments and Processes*, edited by M. E. Brookfield and T. S. Ahlbrandt, pp. 353-363, Elsevier, Amsterdam, 1983.
- Masibroda, V. E., Eolian relief of the Turpan Depression and Western Bei Shan as a reflection of local circulation of the atmosphere, *Izvestia Akademii Nauk SSSR, Ser. Geograf No. 2*, pp. 25-35, 1952.
- Maxwell, T. A., and F. El-Baz, Analogs of martian eolian features in the western desert of Egypt, in *Desert Landforms of Southwest Egypt: A Basis for Comparison with Mars*, pp. 247-260, NASA CR-3611, 1982.
- May, L. A. *Geological Reconnaissance of the Gran Desierto Region, North-Western Sonora, Mexico*, Vol. 8, pp. 58-169, Arizona Academy of Science, 1973.
- McCauley, J. F., Mariner 9 evidence for wind erosion in the equatorial and mid-latitude regions of Mars, *J. Geophys. Res.*, **78**, 4123-4137, 1973.
- McCauley, J. F., C. S. Breed, F. El-Baz, M. I. Whitney, M. J. Grolier, and A. W. Ward, Pitted and fluted rocks in the Western Desert of Egypt: Viking comparisons, *J. Geophys. Res.*, **84**, 8222-8232, 1979.
- McCauley, J. F., C. S. Breed, M. J. Grolier, and D. J. MacKinnon, The U.S. dust storm of February 1977, in *Desert dust: Origin, characteristics, and effect on man*, edited by T. L. Péwé, *Geol. Soc. Amer. Special Paper*, **186**, 123-148, 1981.
- McCauley, J. F., M. J. Grolier, and C. S. Breed, Yardangs of Peru and other desert regions, U.S. Geol. Surv. Interagency Report, *Astrogeology 81*, 177 pp., 1977.
- McCauley, J. F., C. S. Breed, P. J. Helm, G. H. Billingsley, D. J. MacKinnon, M. J. Grolier, and C. K. McCauley, Report monitoring of processes that shape desert surfaces: The desert winds project, *U.S. Geol. Surv. Bull.*, **1634**, 19 pp., 1984.
- McCauley, J. F., G. G. Schaber, and C. S. Breed, Subsurface valleys and geoarchaeology of the Eastern Sahara revealed by shuttle radar, *Science*, **218**, 1004-1020, 1982.
- McKee, E. D., Primary structures in some recent sediments, *Amer. Assn. Petrol. Geol. Bull.*, **41**, 1704-1747, 1957.
- McKee, E. D., Ancient sandstones considered to be eolian, in *A study of global sand seas*, edited by E. D. McKee, *U.S. Geol. Surv. Prof. Paper*, **1052**, 187-238, 1979a.
- McKee, E. D., Introduction to a study of global sand seas, in *A study of global sand seas*, edited by E. D. McKee, *U.S. Geol. Surv. Prof. Paper*, **1052**, 1-20, 1979b.
- Meigs, P., World distribution of arid and semi-arid homoclimates, in *Reviews of Research on Arid Zone Hydrology*, pp. 203-209, UNESCO, Paris, Arid Zone Programme-1, 1953.
- Meigs, P., *Geography of Coastal Deserts*, 140 pp., UNESCO, Paris, Arid Zone Research 28, 1966.
- Morris, E. C., T. A. Mutch, and H. E. Holt, Atlas of geologic features in the dry valleys of South Victoria Land, Antarctica—Possible analogs of martian surface features, U.S. Geol. Surv. Interagency Report, *Astrogeology 52*, 156 pp., 1972.
- Morrison, R. B., Quaternary geology of the Great Basin, in *The Quaternary of the United States*, edited by H. E. Wright, Jr., and P. G. Frey, pp. 265-285, Princeton Univ. Press, Princeton, New Jersey, 1965.
- Mu Shunying, *In Search of the Lost City of Kroraina*, pp. 62-65, China Reconstructs, May 1981.
- Mutch, T. A., and K. L. Jones, *The Martian Landscape*, 160 pp., NASA SP-425, 1978.
- Nicholson, S. E., Saharan climate in historic times, in *The Sahara and the Nile*, edited by M. A. Williams and H. Faure, pp. 173-200, A. A. Balkema, Rotterdam, 1980.
- Norman, C. The technological challenge in Africa, *Science*, **227**, 616-617, 1985.
- Otterman, J., Anthropogenic impact on the albedo of the Earth, *Climate Change*, **1**, 137-155, 1977.
- Peterson, S. T., and C. E. Junge, Sources of particulate matter in the atmosphere, in *Man's Impact on the Climate*, edited by W. H. Matthews, W. W. Kellogg, and G. D. Robinson, pp. 310-320, M.I.T. Press, Cambridge, 1971.

- Petrov, M. P., *Deserts of the World*, 447 pp., John Wiley, New York, 1976.
- Péwé, T. L., Geomorphic processes in polar deserts, in *Polar deserts and modern man*, edited by T. Smiley and J. H. Zumberge, pp. 33-52, University of Arizona, Tucson, Arizona, 1974.
- Péwé, T. L., Desert dust: An overview, in *Desert Dust: Origin, Characteristics, and Effect on Man*, edited by T. L. Péwé, *Geol. Soc. Amer. Special Paper*, **186**, 1-10, 1981.
- Podwysocki, M. H., J. W. Salisbury, M. S. Power, and O. D. Jones, Evaluation of low-sun illuminated Landsat 4 Thematic Mapper data for mapping hydrothermally altered rocks, in *Proc. Conf. on Remote Sensing for Exploration Geology*, pp. 541-549, ERIM, Ann Arbor, Michigan, 1984.
- Powers, R. W., L. F. Ramirez, C. D. Redmond, and E. L. Elberg, Jr., Geology of the Arabian Peninsula—Sedimentary geology of Saudi Arabia, *U.S. Geol. Surv. Prof. Paper*, **560-D**, 147 pp., 1966.
- Pye, K., Coastal dunes, *Progress in physical Geography*, **7**, 531-557, 1983.
- Pye, K., Loess, *Progress in Physical Geography*, **8**, 176-217, 1984.
- Raines, G. L., D. B. Hoover, and W. E. Collins, Remote-sensing mineral discoveries in the Mojave Desert of California, in *Proc. Conf. on Remote Sensing for Exploration Geology*, pp. 16-17, ERIM, Ann Arbor, Michigan, 1984.
- Reining, P. (Ed.), *Handbook on Desertification Indicators*, 141 pp., American Association for the Advancement of Science, Washington, D.C., 1978.
- Rowlands, P., H. Johnson, E. Ritter, and A. Endo, The Mojave Desert, in *Reference Handbook on the Deserts of North America*, edited by G. L. Bender, pp. 103-145, Greenwood Press, Westport, Connecticut, 1982.
- Sarnthein, M., Sand deserts during glacial maximum and climatic optimum, *Nature*, **272**, 43-46, 1978.
- Schaber, G. G., J. F. McCauley, C. S. Breed, and G. Olhoeft, Space Shuttle Imaging Radar physical controls on signal penetration and subsurface scattering in the Eastern Sahara, *IEEE Geoscience and Remote Sensing*, in press, 1986.
- Schneider, S. R., D. F. McGinnis, Jr., and G. Stephens, Monitoring Africa's Lake Chad basin with Landsat and NOAA satellite data, *International J. Remote Sensing*, **6**, 59-73, 1985.
- Schubert, G., General circulation and the dynamical state of the Venus atmosphere, in *Venus*, edited by D. M. Hunten, L. Colin, T. M. Donahue, and V. I. Moroz, pp. 681-765, Univ. Arizona Press, Tucson, Arizona, 1983.
- Seely, M. K., and B. H. Sandelowsky, Dating the regression of a river's end point, *South Africa Archeological Soc. Bull.*, Goodwin Series, No. 2, 61-64, 1974.
- Selby, M. J., C. H. Hendy, and M. K. Seeley, A Late Quaternary lake in the central Namib Desert, Southern Africa, and some implications, *Paleogeography, Palaeoclimatology, Palaeoecology*, **26**, 37-41, 1979.
- Selivanov, E. I., The Dasht-E Lut desert of Iran, *Problemy Osvoenija Pustyn*, 14-19, 1982.
- Servant, M., and S. Servant-Vildary, L'environnement quaternaire du bassin du tchad, in *The Sahara and the Nile*, edited by M. A. Williams and H. Faure, pp. 133-162, A. A. Belkema, Rotterdam, 1980.
- Sharp, R. P., Wind ripples, *J. Geol.*, **71**, 617-636, 1963.
- Sharp, R. P., and M. C. Malin, Surface geology from Viking landers on Mars: A second look, *Geol. Soc. Amer. Bull.*, **95**, 1398-1412, 1984.
- Smith, G. I., Minerals in deserts, in *Proc. Conf. on Alternative Strategies for Desert Development and Management*, pp. 90-97, 1977.
- Smith, G. I., Subsurface stratigraphy and geochemistry of Late Quaternary evaporites, Searles Lake, California, *U.S. Geol. Surv. Prof. Paper*, **1043**, 130 pp., 1979.
- Smith, G. I., Paleohydrologic regimes in the Southwestern Great Basin, 0-3.2 my ago, compared with other long records of "global" climate, *Quart. Res.*, **22**, 1-17, 1984.
- Smith, G. I., and F. A. Street-Perrot, Pluvial lakes of the western United States, in *Late-Quaternary Environments of the United States*, edited by H. E. Wright, Jr., pp. 190-212, Univ. Minnesota Press, Minnesota, 1983.
- Smith, H. T. U., Dune morphology and chronology in central and western Nebraska, *J. Geol.*, **73**, 557-578, 1965.
- Smith, R. E., and G. C. West (compilers), Space and planetary environment space criteria guidelines for use in space vehicle development, Vol. 1, 1982 Rev., NASA TM-82478, 248 pp., 1983.
- Southworth, C. S., Spectral discrimination of bedrock and surficial geology of the Dry Valley region of Antarctica using computer-enhanced Landsat data, *Geol. Soc. Amer. Abstracts with Programs*, p. 663, 1984.
- Stocklin, J., J. Eftekhar-nezhad, and A. Hushmand-zadeh, *Central Lut Reconnaissance—East Iran*, 62 pp., Geological Survey of Iran, Report 22, 1972.
- Stoertz, G. E., and G. E. Erickson, Geology of salars in northern Chile, *U.S. Geol. Surv. Prof. Paper*, **811**, 65 pp., 1974.
- Street, F. A., and A. T. Grove, Environmental and climatic implications of Late Quaternary lake-level fluctuations in Africa, *Nature*, **261**, 385-390, 1976.
- Swift, J., *The Sahara*, 184 pp., Time-Life International, Amsterdam, 1975.
- Thomas, M., Savanna lands between desert and forest, *Geographical Magazine*, **44**, 185-189, 1971.
- Thomas, P., and P. Gierasch, Dust devils on Mars, in *Lunar and Planetary Science XVI*, p. 857, Lunar and Planetary Institute, Texas, 1985.
- Tolba, M. K., Desertification is stoppable, *Arid Lands Newsletter*, No. 21, 2-9, 1984.

- Torgersen, T., Wind effects on water and salt loss in playa lakes, *J. Hydrology*, **74**, 137–149, 1984.
- Tsoar, H., *The Dynamics of Longitudinal Dunes*, 171 pp., Final Technical Report, European Research Office, U.S. Army, 1978.
- Tsoar, H., Dynamic processes acting on a longitudinal (sief) sand dune, *Sedimentology*, **30**, 567–578, 1983.
- Tsoar, H., R. Greeley, and A. R. Peterfreund, Mars: the north polar sand sea and related wind patterns, *J. Geophys. Res.*, **84**, 8167–8182, 1979.
- Tucker, C. J., C. L. Van Praet, M. J. Sharman,, and G. Van Ittersum, Satellite remote sensing of total herbaceous biomass production of the Senegalese Sahel: 1980–1984, *Remote Sens. of Environment*, **17**, 233–249, 1985.
- Twidale, C. R., The Simpson Desert, Central Australia, *South African Geograph. J.*, **62**, 1–17, 1980.
- Valentine, P. G., R. A. Cooper, and J. R. Uzmann, Submarine sand dunes and sedimentary environments in Oceanographer Canyon, *J. Sedimentary Petrology*, **54**, 704–715, 1984.
- Van Chi-Bonnardel, R., *The Atlas of Africa*, 335 pp., Macmillan Publishing Co., New York, 1973.
- Walker, A. S., Deserts of China, *American Scientist*, **70**, 366–376, 1982.
- Walker, A. S., Large Format Camera photographs: A new tool for understanding arid environments, in *Proc. International Symp. on Exploration and Utilization of Natural Resources in Arid Lands*, Urumqi, China, in press, 1986.
- Walker, A. S., and S. Liu, Monitoring arid land changes in the Turpan Depression, People's Republic of China, in *Proc. Conf. on Remote Sensing of Arid and Semi-Arid Lands*, pp. 755–762, ERIM, Ann Arbor, Michigan, 1982.
- Wang, Y., and H. Song (Eds.), *Rock Desert, Gravel Desert; Sand Desert, Loess*, Shaanxi People's Art Publ. House, 1983.
- Ward, A. W., Yardangs on Mars: Evidence of recent wind erosion, *J. Geophys. Res.*, **84**, 8247–8266, 1979.
- Ward, A., and R. Greeley, Evolution of the yardangs at Rogers Lake, California, *Geol. Soc. Amer. Bull.*, **95**, 829–837, 1984.
- Wasson, R. J., S. N. Rajaguru, V. N. Misra, D. P. Agrawal, R. P. Dhir, A. K. Singhvi, and K. K. Rao, Geomorphology, late Quaternary stratigraphy and palaeoclimatology of the Thar dunefield, *Annals Geomorphology (Supplement)*, **45**, 117–151, 1983.
- Whitney, M. I., The role of vorticity in developing lineation by wind erosion, *Geol. Soc. Amer. Bull.*, **89**, 1–18, 1978.
- Whitney, M. I., Eolian features shaped by aerodynamic and vorticity processes, in *Eolian Sediments and Processes Developments in Sedimentology*, 38, edited by M. E. Brookfield and T. S. Ahlbrandt, pp. 223–246, Elsevier, Amsterdam, 1983.
- Wilson, I. G., Desert sandflow basins and a model for the development of ergs, *Geograph. J.*, **137**, 180–199, 1971.
- Wilson, I. G., Sand waves, *New Scientist*, **53**, 634–637, 1972.
- Wilson, I. G., Ergs, *Sedimentary Geology*, **10**, 77–106, 1973.
- Xia, X., *Probing the Mystery Lake: Lop Nur*, pp. 18–23, China Reconstructs, April 1982.
- Xia, X., and Y. K. Hu, *Turpan Basin*, 123 pp., Xinjiang People's Publishing House, Xinjiang (in Chinese), 1978.
- Zhao, S. and X. Xia, Evolution of the Lop Desert and the Lop Nur, *Geograph. J.*, **150**, 311–321, 1984.
- Zhu, Z., Aeolian landforms in the Taklimakan Desert, in *Deserts and Arid Lands*, edited by F. El-Baz, pp. 133–143, Martinus Nijhoff Publishers, the Hague, Netherlands, 1984.
- Zhu, Z. D., Z. P. Chen, Z. Wu, B. Y. Li, and G. C. Wu, *Study on the Geomorphology of Wind-Drift Sands in the Taklimakan Desert*, 110 pp., Science Publishing House, Beijing (in Chinese), 1981.
- Zhu, Z. D., Z. Wu, and S. Liu, *General Introduction to China's Deserts*, 132 pp., Science Publishing House, Beijing (in Chinese), 1980.

9

GLACIERS AND GLACIAL LANDFORMS

*Richard S. Williams, Jr.**

INTRODUCTION

This chapter discusses the use of satellite images in examining selectively, on a global basis, the effect on the Earth's surface of glaciers and glacial processes, especially the distribution and types of present-day glaciers, landforms resulting from glacial and fluvioglacial erosion and deposition during the Quaternary, and landforms resulting from active or relict periglacial processes. In many respects, this chapter is a space-age version of a similar review of glaciers and glacial landforms done by Shaler and Davis (1881) more than 100 years ago. Their pioneering work was one of the first publications to combine text with newly available ground photographs of glaciers and glacial landforms.

Nature of Glacial Phenomena

A glacier is a mass of ice ($\geq 0.1 \text{ km}^2$) that has its genesis on land and that represents a multiyear surplus of snowfall over snowmelt. According to Sugden and John (1976) and Flint (1971), perennial ice covers about 10 percent ($1.5 \times 10^7 \text{ km}^2$) of the land areas of the Earth (Table 9-1). Although glaciers are generally thought of as polar entities, as this table shows, they are also found in mountainous areas throughout the world, on all continents except Australia, and even at or near the Equator on high mountains in Africa, South America, and the East Indies.

Present-day glaciers and the deposits from more extensive glaciation in the geological past have considerable economic importance in many areas. In regions of limited precipitation during the growing season, such as parts of the western United States, glaciers are considered to be frozen freshwater reservoirs that release water during the drier summer months. In some semiarid areas, glaciers are of considerable economic importance in the irrigation of crops. In mountainous areas such as Switzerland, Norway, and Iceland, meltwater from glaciers is critical to the economic generation of hydroelectric power. Lakes and ponds are numerous where continental ice sheets once covered vast areas of North America, Europe, and Asia (Figure 9-1), and the glacial deposits in these regions act as major ground-water reservoirs. These deposits also have substantial economic value as sand and gravel for construction and are often the basis, as in the Commonwealth of Massachusetts, for the largest mineral industry in a state.

Within the past 3 million years, glaciers—in the form of ice caps and ice sheets—repeatedly expanded to cover about 29 percent (Flint, 1971) of the total land area of the Earth (Table

9-2). This land area includes most of Canada, all of New England, much of the upper Midwest, large areas of Alaska, most of Greenland, Iceland, Svalbard, other arctic islands, and Scandinavia, much of Great Britain and Ireland, and the western part of northern U.S.S.R. (Figure 9-1). Along mountainous coasts and high mountains of the interior in these areas, however, peaks and ridges would have protruded above the ice as nunataks. Parts of southern South America, central Asia, the Alps, and many other mountainous areas in Asia also experienced an increase in glacier extent. Glaciers in Antarctica likewise expanded somewhat, but more in ice thickness than in ice area because of the limiting effect of the surrounding oceans.

Although four or five major glacial advances have been identified by glacial geologists who have studied glacial deposits in Europe and North America, stratigraphic evidence from the Tjörnes area of northern Iceland suggests that as many as 10 major glacial advances may have occurred within the past 3 million years or during what is popularly referred to as the Ice Age (Einarsson et al., 1967). On the basis of paleomagnetostratigraphic studies in southwestern Iceland, Kristjánsson et al. (1980) stated "that at least 13 glaciations occurred in western and southwestern Iceland between 3.1 and 1.8 Ma ago." The correlation of oxygen isotope ratios from deep-sea cores with the results of statistical analyses of the periodicity of the three astronomical elements of the Earth's orbit confirmed the fact that many cycles of glacier advance and recession occurred during the Pleistocene (Imbrie and Imbrie, 1980).

At the present time, most of the glacial ice on the planet is encompassed in the two largest ice sheets, Antarctica (bottom of Figure 9-2) and Greenland (Figure G-1.3), which together contain an estimated 97 percent of all the glacial ice and 77 percent of the freshwater supply on Earth. During a maximum global advance of glaciers, however, it is estimated that North America contained volumetrically nearly as much ice as the present combined total of Antarctica and Greenland and that the sea level dropped by as much as 100 m (Flint, 1971).

Role of Satellite Surveillance in Glacial Studies

Until the launches in 1972, 1975, 1978, 1982, and 1984 of the five spacecraft in the Landsat series of Earth-resources satellites, glaciologists had no accurate means of measuring the areal extent of glacier ice on a global basis. Only Multispectral Scanner (MSS) images provided the worldwide coverage (except for the circular areas poleward of 81° north and south latitudes) needed for global geomorphological investigations. Coverage by higher resolution Landsat sensors (both TM and RBV at 30 m) has been more limited. Figure 9-3 is a Landsat-3 RBV image of the Rennick Glacier area of northern Victoria Land, Antarctica, showing the

*U.S. Geological Survey, Reston, Virginia 22092.

Table 9-1
Present Areal Extent of Glaciers*

Geographic Region	Approximate Area (km ²)	Subtotals (km ²)
South Polar Region		12 588 000
Antarctic Ice Sheet (excluding shelves)	12 535 000 [†]	
Other Antarctic Glaciers	50 000	
Subantarctic Islands	3 000	
North Polar Region		2 081 616
Greenland Ice Sheet	1 726 400	
Other Greenland Glaciers	76 200	
Canadian Arctic Archipelago	153 169	
Iceland	12 173	
Spitsbergen and Nordaustlandet	58 016	
Other Arctic Islands	55 658	
North American Continent		76 880
Alaska	51 476	
Other	25 404	
South American Cordillera		26 500
European Continent		9 276
Scandinavia	3 810	
Alps	3 600	
Caucasus	1 805	
Other	61	
Asian Continent		115 021
Himalaya	33 200	
Kun Lun Chains	16 700	
Karakoram and Ghujerab-Khunjerab Ranges	16 000	
Other	49 121	
African Continent		12
Pacific Region (including New Zealand)		1 015
Total		14 898 320

*From Sugden and John (1976), after Flint (1971).

[†]According to Drewry et al. (1982), the total area of the present-day Antarctic ice sheet (including ice shelves) is 13 586 380 km².

improved morphologic detail of many glaciological features: flow lines (f1), crevasses, (c), and nunataks (n), as compared with Landsat MSS images.

Landsat images provide a means for delineating the areal extent of ice sheets and ice caps, for determining the position of the termini of valley, outlet, and tidal glaciers, and for measuring the average speed of flow of some glaciers by a time-lapse method of sequential images on a common base of data for the entire globe. To take advantage of the vast amount of Landsat data of the glacierized regions of the planet, the U.S. Geological Survey (USGS), in association with more than 50 United States and foreign glaciologists and glacial geologists, is working on a project to prepare a satellite image atlas of glaciers of the world (Williams and Ferrigno, 1981). If Landsat-type surveys of the Earth are

continued for several decades, a means of monitoring long-term changes in glacier area will also become possible, thereby providing means for monitoring one potential effect of global climatic change (Williams and Svensson, 1983a; Williams, 1985).

Because of their availability for most of the land areas of Earth, Landsat images are the primary source of image data for this chapter. Most images or photographs acquired by manned spacecraft are concentrated in the low or middle latitudes because of the restricted orbital inclination of most manned spaceflight missions conducted by the United States. The orbital inclination of Skylab, for example, reached about as far north or south as any manned mission—to 50° north and south latitude—and more than 35000 photographs and images were acquired during the three occupations of the Skylab space station during 1973 and

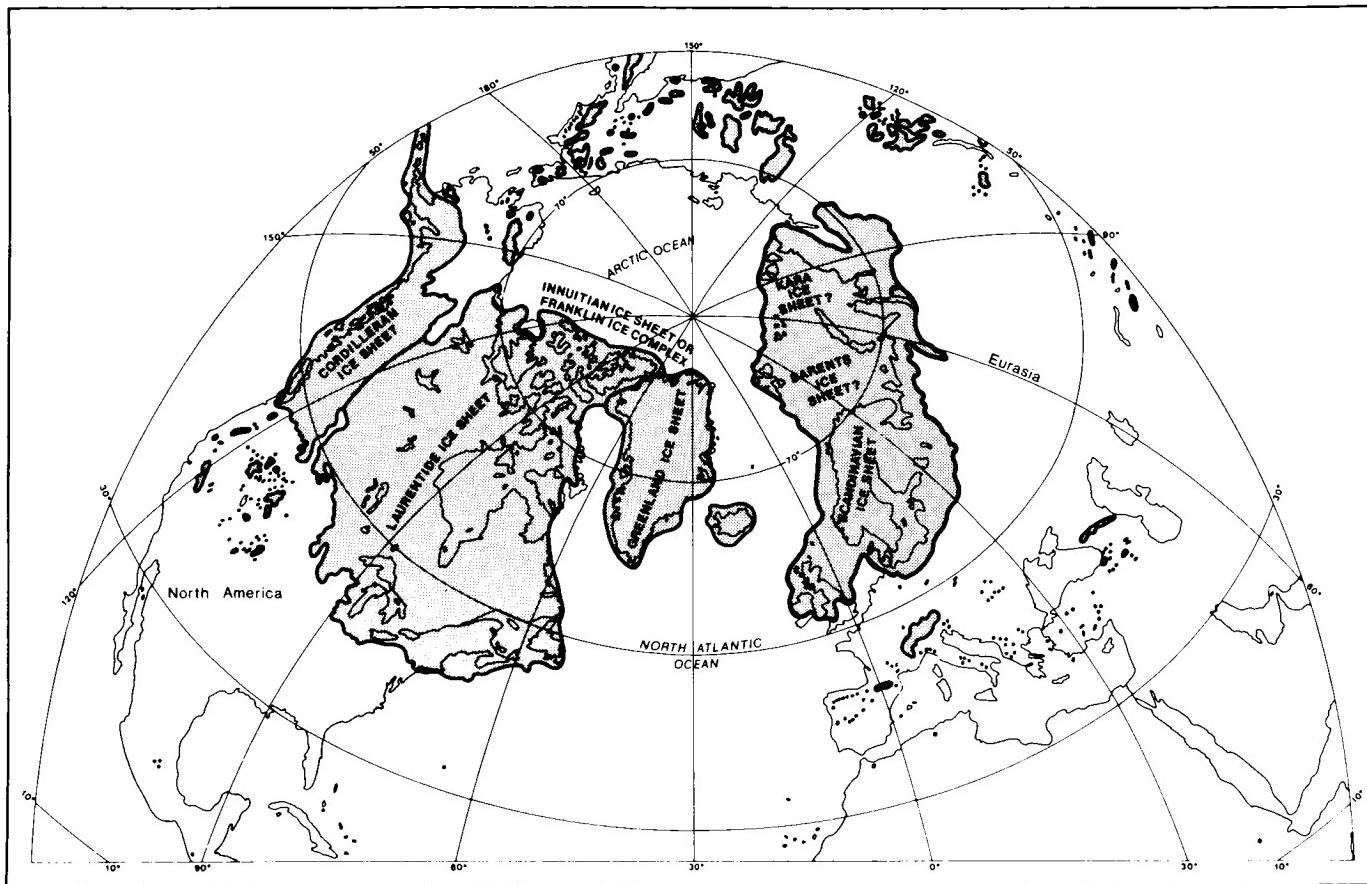


Figure 9-1. Postulated maximum areal extent of glacier ice in the north polar region during the Late Pleistocene Epoch (from Denton and Hughes, 1981a).

1974 (Southworth, 1983). The Synthetic Aperture Radar (SAR) on board Seasat operated intermittently from late June until early October 1978 in an orbit that reached to a maximum of 72° north and south latitude. During two missions, the Space Shuttle has acquired two large sets of Shuttle Imaging Radar data—SIR-A and SIR-B. Seasat SAR (Ford et al., 1980) and Shuttle SIR data, with pixel sizes up to 25 m, produced some excellent images of glaciers and glacial landforms. Some of the Seasat SAR images appear in this chapter.

The great value of image data acquired from Earth-orbiting spacecraft is that it gives scientists the capability to study and to monitor our planet on a global basis. In particular, the Landsat series has markedly broadened the availability of image data of the Earth's surface, so that geomorphologists now have two-dimensional image information of virtually the entire land area and many shallow sea areas of the planet. Local and regional geomorphological studies carried out since the 1930s have traditionally used stereopairs of vertical aerial photographs because of the analytical importance of viewing landforms in three dimensions, rather than two. Generally speaking, most satellite images portray the Earth's landforms in two dimensions, although low solar-angle illumination of the terrain can often provide an illusion of the third dimension. In many cases, the geomorphic analysis of landforms on satellite images in only two dimensions can be a drawback. Another drawback in the analysis of landforms on satellite images is that, on Landsat MSS images, for example, only landforms large enough to be represented by a few pixels can even be detected, and tens of pixels are needed for identifica-

tion. As a result, many types of landforms are simply not visible on Landsat images. In unknown or unfamiliar regions, the scientist using such images may not even be aware of what is "missing." For example, in a recent paper on Icelandic volcanoes, 27 discrete types of volcanoes can be identified in Iceland on vertical aerial photographs (Williams et al., 1983b), and only 6 of the 13 types of Icelandic basaltic volcanoes previously described by Thorarinsson (1959) could be unambiguously recognized on Landsat images (Williams et al., 1974).

It is important for geologists who use Landsat images for geomorphological, structural, tectonic, and other types of geological investigations to be aware of the limitations of such images, especially in the two-dimensional and in the spatial resolution aspects. The 26 Plates showing glaciers, glacial landforms, and periglacial landforms in this chapter describe features that are large enough to be delineated on Landsat or other types of satellite images and can be well portrayed in two dimensions.

GLACIERS AND GLACIER PHENOMENA

Glaciers form in any area in which a year-to-year surplus of snow occurs. Under such conditions, successive layers of snow are slowly compacted until the loose snowflakes form a mono-mineralogic (frozen H₂O) sedimentary deposit that gradually becomes more and more dense with increasing depth and age. When a density of 830 to 910 kg/m³ is reached, formation of ice occurs (Paterson, 1981). As the effect of gravity slowly deforms this mass of ice, a glacier is formed. A glacier therefore represents an

Table 9-2
Maximum Areal Extent of Glaciers During the Pleistocene*

Glaciated Region	Approximate Area (km ²)	Area Subtotals (km ²)
South Polar Region		13 810 000
Antarctic Ice Sheet	13 800 000	
Sub-Antarctic Islands	10 000	
North Polar Region		2 797 737
Greenland Ice Sheet	2 295 300	
Iceland and Jan Mayen Island	142 000	
Spitsbergen and Nordaustlandet	298 662	
Other Arctic islands	61 775	
North American Continent		16 217 091
Laurentide Ice Sheet	13 386 964	
Alaska	1 033 062	
Other	1 797 065	
South American Cordillera		870 000
European Continent		6 721 708
Scandinavian Ice Sheet	6 666 708	
Alps, Pyrenees, and other Continental Areas	39 000	
Caucasus	16 000	
Asian Continent		3 935 000
Himalaya and Other Mountains Outside U.S.S.R.	189 000	
Ural/Siberian Ice Sheets	2 707 000	
Mountains in Northeastern U.S.S.R.	707 000	
Mountains in Southern U.S.S.R.	332 000	
Africa		1 900
Pacific Region		30 000
Total		44 383 436

*From Flint (1971).

unusual type of metamorphic rock, being the result of deformation of what was originally a sedimentary rock.

Glaciers are of considerable scientific interest because of the extensive record of variations in atmospheric gases and aerosols contained within a vertical column of glacier ice. In optimum geographic locations, the record can extend over several hundred thousand years and provide specific information about variations in carbon dioxide (CO₂), the O¹⁸/O¹⁶ ratio (a measure of temperature in the lower atmosphere), variations in meteoritic infall rates, the occurrence of explosive volcanic activity through deposition of tephra, etc. The impact of the industrial revolution on the Earth's surface and atmosphere can also be determined through careful analyses of cores of glacier ice.

The fluctuation of glaciers, especially fluctuations in volume of glacier ice, is related to climatic variations (Williams, 1983d). Although the historical record of glacier fluctuation is not very lengthy in most glaciated regions, glaciers were known to have advanced during what is known as the "Little Ice Age"

(the period from the late 1500s to the late 1800s). There has been a general retreat of glaciers since the late 1800s until the late 1950s or early 1960s. Perhaps the best record of variation in climate during the past 1000 years is the proxy record of the mean annual change in Iceland's temperature compiled from Icelandic sources by various investigators (Figure 9-4; CIA, 1974, 1978). The later temperature record for Iceland shown in Figure 9-4 is from actual thermometric measurements. The glaciers of Iceland, several of which are used to illustrate glaciers, glaciological phenomena, and glacial landforms in this chapter, are of special value to understanding the link between climatic change and glacier fluctuation. At about 64° north latitude, Iceland's glaciers are especially sensitive to the climatic variation resulting from secular changes in the Earth's orbital history (eccentricity, tilt, and precession), which form the basis for the Milankovitch theory of glacier advance and recession (Imbrie and Imbrie, 1980).

As previously discussed, 10 percent of the present land area of our planet is covered by glacier ice. Glaciers comprise 2.15

percent of the total water supply of the planet, the second largest "reservoir" after the Earth's oceans, which are the biggest repository at 97.2 percent (Table 9-3). Glacier ice is represented by a special class of landforms called glaciers. Glaciers range in size from about 0.1 (Meier, 1974) to 13 586 380 km² (Antarctic ice sheet including ice shelves) (Drewry et al., 1982) and have been classified into several well-defined groups on the basis of morphology and physiographic setting. A glacier classification and description scheme (Table 9-4) was developed by the International Association of Scientific Hydrology (IASH) in 1970 (UNESCO,

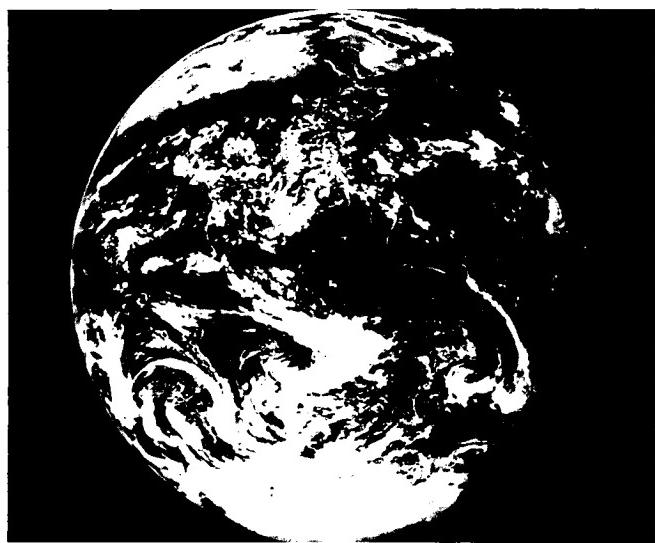


Figure 9-2. Apollo 17 photograph of the Earth showing most of the continent of Antarctica on the bottom of the globe.



Figure 9-3. Landsat RBV image of flow lines, crevasses, and nunataks on the lower part of the Rennick Glacier, Antarctica.

1970) for use in a computerized data archive for the World Glacier Inventory Project (Müller et al., 1977). The IASH classification and description guidelines are especially useful when using aerial photographs or satellite images to assist in determining the six parameters of a glacier.

Meier (1974) discussed three main types of glaciers: (1) continuous masses of ice moving outward in all directions, such as ice sheets or their much smaller counterparts, ice caps; (2) linear masses of ice constrained in their flow by topography, such as outlet glaciers, valley glaciers, cirque glaciers, and ice streams; and (3) cake-like masses of ice that spread laterally on level ground or in coastal areas, such as piedmont glaciers and ice shelves. Examples of each of these types of glaciers are presented in the Plates section. Two special subtypes of glaciers are also included—surging glaciers and tidal glaciers—because of the special effect they can have on modifying the preglacial landscape.

Glaciers are a peculiar type of landform because they can in turn modify the existing (preglacial) landscape, producing both erosional and depositional landforms. The process by which a glacier modifies the subglacial and adjacent landscape is by the

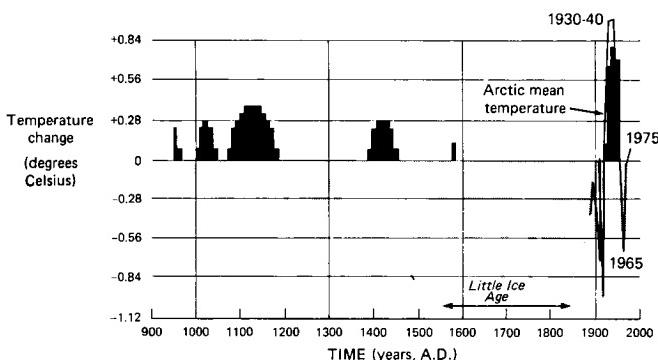


Figure 9-4. A 1000-year history of variations in Iceland's temperature compiled by various investigators from both proxy (historical records, chiefly old annals) and modern (thermometric) records (CIA, 1974, 1978; Thoroddsen, 1916, 1917).

Table 9-3
Estimated Percent by Volume of the Earth's Water Supply*

Reservoir	Percentage of Total Water Supply by Volume
Surface Water	(1.71 × 10 ⁻²)
Freshwater Lakes	9 × 10 ⁻³
Saline Lakes and Inland Seas	8 × 10 ⁻³
Average in Stream Channels	1 × 10 ⁻⁴
Subsurface Water	(6.25 × 10 ⁻¹)
Vadose Water (includes soil moisture)	5 × 10 ⁻³
Ground Water (within upper 0.8 km of the Earth's crust)	3.1 × 10 ⁻¹
Ground Water (deeper than 0.8 km)	3.1 × 10 ⁻¹
Other	(99.351)
Glacier Ice	2.15
Atmosphere	1 × 10 ⁻³
Oceans	97.2
Total	100

*U.S. Geological Survey (1976c).

Table 9-4
Glacier Classification and Description*

DIGIT 1 Primary classification	DIGIT 2 Form	DIGIT 3 Frontal characteristic	DIGIT 4 Longitudinal profile	DIGIT 5 Major source of nourishment	DIGIT 6 Activity of tongue
0 Uncertain or misc.	Uncertain or misc.	Normal or misc.	Uncertain or misc.	Uncertain or misc.	Uncertain
1 Continental ice sheet	Compound basins	Piedmont	Even; regular	Snow and/or drift snow	Marked retreat
2 Ice field	Compound basin	Expanded foot	Hanging	Avalanche ice and/or avalanche snow	Slight retreat
3 Ice cap	Simple basin	Lobed	Cascading	Superimposed ice	Stationary
4 Outlet glacier	Cirque	Calving	Icefall		Slight advance
5 Valley glacier	Niche	Coalescing noncontributing	Interrupted		Marked advance
6 Mountain glacier	Crater				Possible surge
7 Glacieret	Ice aprons				Known surge
8 Ice shelf	Groups of small units				Oscillating
9 Rock glacier	Remnant				

Digit 1 Primary Classification

0 Miscellaneous	Any not listed.
1 Continental ice sheet	Inundates areas of continental size.
2 Ice field	Ice masses of sheet or blanket type of a thickness not sufficient to obscure the subsurface topography.
3 Ice cap	Dome-shaped ice mass with radial flow.
4 Outlet glacier	Drains an ice sheet or ice cap, usually of valley glacier form; the catchment area may not be clearly delineated.
5 Valley glacier	Flows down a valley; the catchment area is well defined.
6 Mountain glacier	Cirque, niche, or crater type; includes ice aprons and groups of small units.
7 Glacieret and snowfield	A glacieret is a small ice mass of indefinite shape in hollows and river beds and on protected slopes developed from snow drifting, avalanching, and/or especially heavy accumulation in certain years; usually no marked flow pattern is visible and therefore no clear distinction from snowfield is possible. Exists for at least two consecutive summers.
8 Ice shelf	A floating ice sheet of considerable thickness attached to a coast, nourished by glacier(s); snow accumulation on its surface or bottom freezing.
9 Rock glacier	A glacier-shaped mass of angular rock in a cirque or valley either with interstitial ice, firn, and snow or covering the remnants of a glacier, moving slowly downslope.

*UNESCO (1970), Müller et al. (1977).

action of moving ice and by the deposition of till beneath and adjacent to the glacier. Glaciers also affect areas peripherally by discharging large amounts of sediment-laden meltwater. Some of the eolian deposits, called loess, are produced from erosion and redeposition of fine-grained sediment derived from glacial outwash. Erosion and deposition can also result from catastrophic outburst floods (*jökulhlaups*) caused by the failure of ice-dammed lakes or, more rarely, from subglacial volcanic eruptions or geothermal activity. The cold climate adjacent to glaciers usually fosters periglacial processes that produce special types of landforms as the result of the action of ground ice, including an unusual type of "glacier" composed of rock fragments and ice. Such a glacier is called a rock glacier.

Three special-topics dealing with glaciological phenomena that have proven to be especially amenable to delineation on Landsat images are included in this section of the introduction: the accumulation zone of a glacier, areas of blue ice in Antarctica, and subglacial volcanoes.

Glacier Mass Balance

The mass balance of a glacier is defined by Bates and Jackson (1980) as: "The change in mass (the difference between total accumulation and gross ablation) of a glacier over some defined interval of time, determined either as a value at a point, an average over an area, or the total mass change for the glacier. The units normally used are millimeters, meters, or cubic meters of water equivalent, but kilograms per square meter or kilograms are used by some." Mass-balance studies of glacier provide a measure of its condition. Is it gaining (positive) or losing (negative) mass? There are several ways to determine the mass balance of a glacier (Paterson, 1981), but all are labor-intensive and costly. As a result, the records of very few glaciers contain their mass balance in 1 year or over several years.

Studies of the Greenland Ice Sheet by Benson (1962) and of the ice caps and outlet glaciers of Axel Heiberg Island, Northwest Territories, Canada, by Müller (1962) led to the development of the concept of zonation of the accumulation zone of temperate glaciers and the relationship between the accumulation zone, firn line, equilibrium line, and ablation zone. If one can determine the late summer season snowline, which is a good approximation of the equilibrium line on temperate glaciers (Paterson, 1981), then the accumulation area ratio—the area of the accumulation area at the end of summer divided by the glacier's area—can be determined. As noted by Glen (1963) in Paterson (1981), "A rule of thumb is that an accumulation area ratio of about 0.7 corresponds to a net balance of zero." This means that aerial photographs and satellite images, if acquired at the optimum time in late summer, can be used to determine the accumulation area ratio of temperate glaciers. In fact, Østrem (1975) directly applied this concept to Landsat images of Norwegian glaciers. Østrem's work is an extension of the previous research by Meier and Post (1962), who first described the use of equilibrium line altitudes and accumulation area ratios, derived from aerial photographs, to infer the regional distribution of glacier mass balances.

Figure 9-5 is a Landsat MSS false-color composite image (1426-12070; September 22, 1973) of Vatnajökull ice cap and environs, Iceland. MSS bands 5, 6, and 7 were enhanced by special computer processing and were projected through yellow, red, and blue filters, respectively, to create a false-color composite image. The original computer-generated histograms of the spectral characteristics of the image fell into three groupings (trimodal), thereby permitting snow-covered areas, vegetation, and bare rock or soil to be processed independently. Each of these zones was stretched in each of the three MSS bands to encompass the full range of brightness and was then composited by the Image Processing Laboratory of the California Institute of Technology's Jet Propulsion Laboratory (Soha et al., 1976). This type of

computer-enhanced image of Vatnajökull (see also Plate G-6 for a standard Landsat false-color composite of Vatnajökull) appears to provide a good correlation of glacier color with the zones in the accumulation area and the ablation area shown schematically in Figure 9-6, a schematic representation of the zones in the accumulation zone of a glacier, the area up-glacier from the equilibrium line. Bare glacier ice is exposed down-glacier (to the right of the firn line in that figure). The ablation zone extends down-glacier from the equilibrium line (see Figure 9-5; from Björnsson, 1971, after Paterson, 1969, 1981). The concept of zonation in the accumulation area was developed by Benson (1962) from his work in Greenland and by Müller (1962) from his work on Axel Heiberg Island, Northwest Territories, Canada. On Vatnajökull, the colors apparently correlate as follows: light blue, the bare glacial ice of the ablation zone; orange, superposed ice, including the approximate position of the equilibrium line; black, soaked zone; dark gray, percolation zone; light blue-gray, dry-snow zone (Williams, 1983c).

Figure 9-7, an oblique aerial photograph (taken on August 17, 1973) of the terminus of Síðujökull, one of the outlet glaciers on the southwestern margin of Vatnajökull, shows the bare glacial ice of the ablation zone (see Figure 9-6) in the foreground. Last winter's snow, now mostly firn, is visible at higher elevations of the glacier lobe. Note the patterns produced by the ablation surface cutting across ice foliation (complex patterns of ice deformation outlined by tephra layers and seasonal dust layers due to flow processes up-glacier). At the end of the summer season, the demarcation between the bare ice and firn-covered ice is the approximate position of the equilibrium line on temperate glaciers. Figures 9-8 and 9-9 are a pair of oblique aerial photographs (taken on August 17, 1973) of another outlet glacier coming off Vatnajökull, Brúarjökull (see Plate G-10), that show the ablation zone from a different perspective. Figure 9-8, a high-angle oblique photograph, depicts a proglacial lake in the foreground, bare ice of the ablation zone in the middle background, and last winter's snow cover in the background. Figure 9-9, a low-angle oblique, shows bare glacial ice in the foreground with a supraglacial stream valley and channel in the foreground, the complex ice-fracture patterns, and wavy patterns of deformed tephra layers. Last winter's snow cover is visible in the far background. An August 1978 Landsat-3 RBV image of Brúarjökull that illustrates the transient snowline dividing the accumulation zone from the ablation zone is shown on Plate G-16.

Blue Ice

The term "blue ice" was introduced by the late Swedish glaciologist, Valter Schytt, during observations made on the 1949–1952 Norwegian/British/Swedish Antarctic Expedition to Queen Maud Land (V. Schytt, January 6, 1983, private communication; Schytt, 1961). He used the term to refer to areas of bare glacier ice. Such areas of blue ice primarily occur near the coast and in interior areas both upstream and downwind from nunataks, the peaks of mostly buried mountain ranges or isolated massifs. Blue ice is caused by ablation, which results mainly from sublimation, wind-scouring of the snow mantle, and surface polishing by wind-driven snow (Williams et al., 1983a). Bare glacial ice or blue ice also occur extensively in Greenland, especially during mid- to late summer, when the previous winter snowfall has melted from the margins of the ice sheet. Although much more limited areally, blue ice is also characteristic of the lower parts of valley and outlet glaciers and along the margins of ice caps in late summer.

The term "blue ice" has special significance in Antarctica, however. Since 1969, more than 6000 fragments of meteorites, including at least 600 individual meteorites, have been discovered in blue-ice areas of Antarctica. Many of these meteorite finds have included types that are exceedingly rare (Marvin, 1984), and

ORIGINAL PAGE
COLOR PHOTOGRAPH

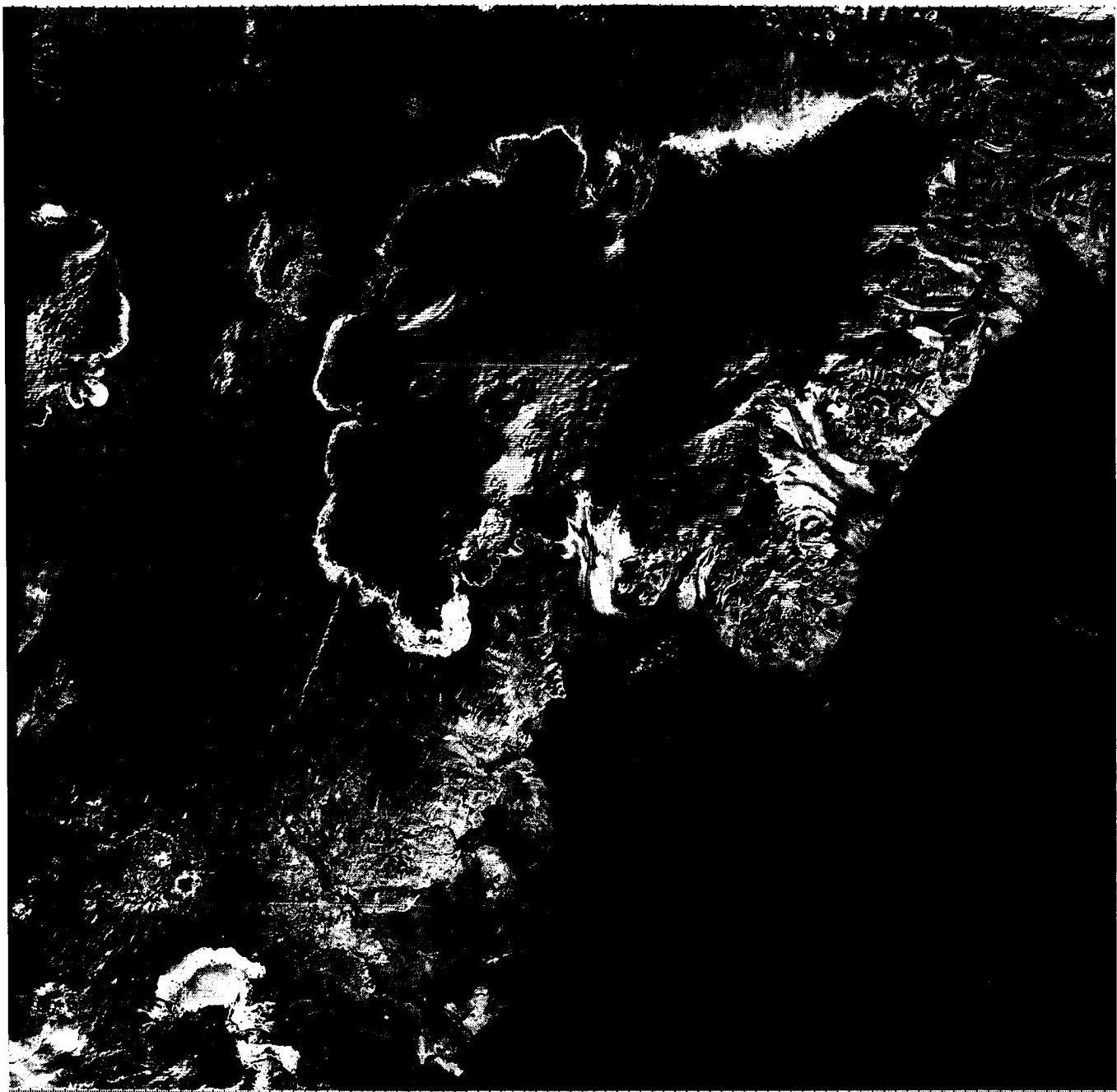


Figure 9-5. Landsat false-color (special) composite image of Vatnajökull, Iceland, showing the accumulation and ablation areas on the ice cap.

the full suite of specimens so far discovered provides an extraordinarily fine representation of the range of meteorite types that have reached the Earth's surface. Therefore, Antarctica has become the most important collecting area on our planet for meteorites.

Brown (1961) estimated the Earth's meteorite infall rate to be approximately one per square kilometer each million years. Basing his work on this figure, a model of the East Antarctic ice sheet, and other factors, Olsen (1981) estimated that at least 760 000 meteorites are likely to lie in the East Antarctic ice sheet. Most of those recovered to date in Antarctica have been found

in areas of blue ice, especially around nunataks or where the normal flow of glacier ice is impeded or stopped.

A U.S. Geological Survey colleague, Mark F. Meier (written communication, 1982), noted that "... meteorite concentrations pose interesting glaciological problems: I would expect that the highest concentrations would be found in areas combining high vertical strain rates with high ablation rates; areas of high strain rates might be predictable from the flow geometry, which might be identifiable on Landsat imagery." He also noted that the greater the ablation, the greater the volume of ice that would flow through meteorites. Thus, it is likely that concentrations of

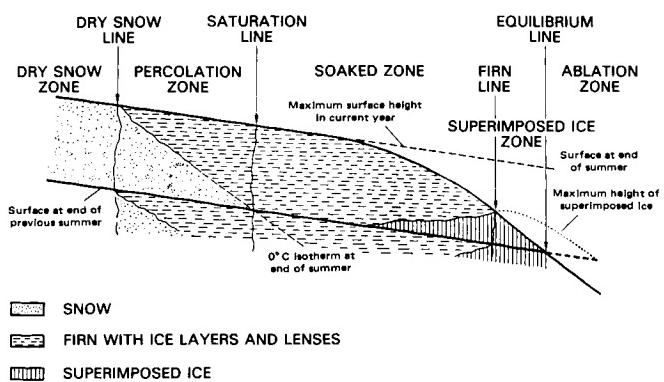


Figure 9-6. Schematic diagram of the subdivisions of the accumulation zone of a glacier (from Paterson, 1981).



Figure 9-7. Oblique, aerial photograph of the margin of Síðujökull, an outlet glacier from Vatnajökull, Iceland.

meteorites will be found in areas of blue ice, which can be identified not only from surface traverse and aerial reconnaissance, but also by systematic search of satellite imagery.

The launch of Landsat-1 in July 1972 provided the first opportunity for higher resolution satellite image coverage of Antarctica. Excellent Landsat images of the Queen Fabiola (Yamato) Mountains were acquired as early as December 1973. Later, the National Institute of Polar Research in Tokyo, Japan, published a 1:200000-scale Landsat image (*Working Map of the Meteorite Ice Field, Yamato Mountains, Antarctica*) (1976), which delineated areas of blue ice, nunataks, morainal debris, and spot elevations derived from ground surveys. In the identification of blue ice areas, MSS bands 6 and 7 are similar, with band 7 somewhat better than MSS band 6. MSS band 5, however, is best in areas of bedrock exposure (e.g., nunataks) for proper differentiation between areas of blue ice and either bedrock or morainic debris. On MSS bands 6 and 7, blue ice and rock usually have a similar spectral response. Mark F. Meier (written communication, 1982) suggested experimenting with computer-assisted analysis of different MSS bands because blue ice should be distinctive enough (spectrally) for a computer to identify with high accuracy (Williams et al., 1983a). Figures 9-10a and 9-10b are a Landsat-1 MSS false-color composite and its index map that cover the Queen Fabiola (Yamato) Mountains area, East Antarctica, which displays extensive areas of blue ice (bare glacier ice) around nunataks.



Figure 9-8. Oblique aerial photograph of the margin of Brúarjökull, a broad, surging outlet glacier from Vatnajökull, Iceland.



Figure 9-9. Oblique aerial photograph of the ablation zone of Brúarjökull, Iceland, showing contorted tephra layers and supra-glacial drainage.

and associated morainal debris. Landsat (and NOAA) images can be used to delineate areas of blue ice in Antarctica, some of which have proved to contain extraordinary accumulations of meteorites. Since 1969, Japanese scientists have collected 4813 meteorites within the blue-ice areas shown on this image or about 25 percent of the extant worldwide collection of meteorites.

During the 1982–1983 field season, a meteorite-collection effort in blue-ice exposures of the Allan Hills/“Elephant Moraine” areas of Victoria Land, West Antarctica, used a Landsat image to identify areas of blue ice, to plot traverses through and between blue-ice patches, and to locate collection points in a general sense. Precise geographic positions were established with a Magnavox Model MX1502 geociever in conjunction with overpasses of the Navy navigational satellite system (Cassidy et al., 1984; Williams et al., 1984). Meteorites were collected from each of the blue-ice areas identified on the Landsat image and were actually viewed in the field (T. K. Meunier, private communication). Figure 9-11 is a photograph of the cupped and scalloped surface of the blue ice in the “Elephant Moraine” area, Victoria Land, West Antarctica. Figure 9-12 shows the only meteorite so far recovered in situ within blue ice in Antarctica. This H-5 chondrite (ALH-82102) weighed 48 g (35-mm camera lens cap indicates scale). Figure 9-13 is a large H-5 chondrite (ALH-82103) that weighed 2.53 kg. This meteorite was one of the largest of the 113 collected during the 1982–1983 field season.

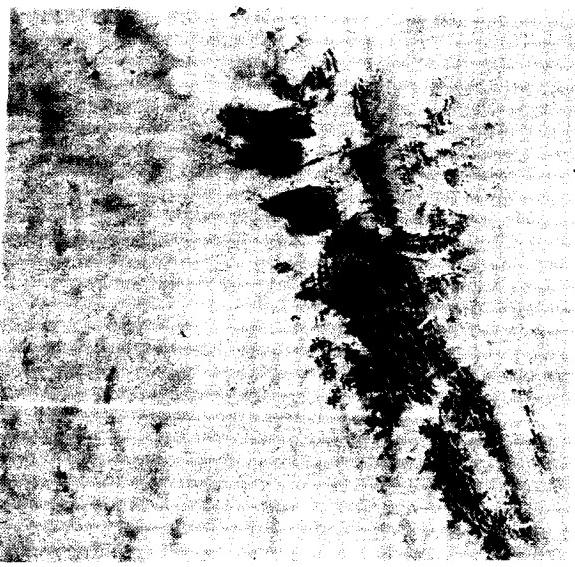


Figure 9-10a. Landsat image of the Queen Fabiola (Yamato) Mountain area, East Antarctica, showing extensive areas of "blue ice" (bare glacier ice) around nunataks and associated morainal debris.

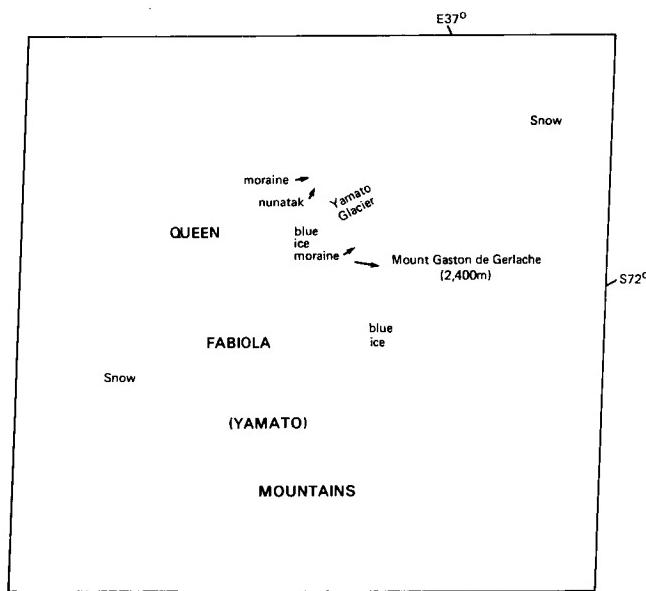


Figure 9-10b. Index map showing selected geographic, geomorphic, and glaciological features on Figure 9-10A.

Subglacial Volcanoes

In volcanically active regions with an extensive cover of glacier ice, volcanoes may be wholly or partly subglacial. Volcanoes and glaciers often coexist because areas of extensive volcanic activity tend to be regions of higher than normal elevation. Glacier-shrouded volcanoes with a history of volcanic activity include several volcanoes in Iceland; Mount Beerenberg on Jan Mayen (Island), Norway; Mount St. Helens (Plate V-8) (Brugman

and Post, 1982) and other volcanoes of the Cascade Mountains, northwestern United States; numerous volcanoes in Alaska, both on the mainland and along the Aleutian Islands arc (Plate V-9) (Post and Mayo, 1971); volcanoes on the Kamchatka Peninsula, U.S.S.R. (Plate V-25); and volcanoes in the Andes Mountains (including the Patagonian Ice Field) of South America (Plate V-14) and in Antarctica.

The eruption of a volcano under a glacier can produce a catastrophic outpouring of enormous quantities of water melted from the ice by the thermal energy. Perhaps best known from repeated occurrences in Iceland, where glacial-outburst floods are known as jökulhlaups, such extraordinary discharges of water represent a powerful geomorphic agent in regions in which glaciers and volcanoes coexist. Two ice caps in Iceland have had a lengthy historical record of jökulhlaups resulting from subglacial volcanic and/or geothermal activity and volcanic activity, respectively: Vatnajökull (Plate G-6) and Mýrdalsjökull (Plate G-22). Jökulhlaups from the Grímsvötn caldera (see Plate G-15, Figure 9-14, and the index map for Plate G-6) in the west-central part of Vatnajökull produced floods in the 50000 m³/s range several decades ago, but have dropped to the 10000 m³/s in recent years because of apparent thinning of the ice cap around the caldera (Björnsson, 1975; Tómasson, 1975). Figure 9-14 is an oblique aerial photograph of the 45-km² subglacial/subaerial caldera looking toward the east. Most of the jökulhlaups originating in the Grímsvötn caldera occur as the result of the lifting of the ice dam on the east side of the caldera whenever the subglacial lake in the caldera fills to a certain level. The input of water to the closed subglacial basin is believed to be from the melting of ice by subglacial geothermal activity and from seasonal ablation rather than in association with a volcanic eruption. The volcano Katla, which is located under the eastern part of Mýrdalsjökull (Plate G-22), was estimated by Thorarinsson (1957) to produce floods in excess of 100000 m³/s and perhaps as high as 200000 m³/s from eruptions. Other sites within Vatnajökull have also produced jökulhlaups from periodic volcanic and/or geothermal activity: Öraefajökull (Thorarinsson, 1956b) Kverkfjöll (Friedman et al., 1972), and the collapse calderas east of Hamarinn (Plates G-6 and G-15) (Thorarinsson et al., 1974).

Landsat images are especially well suited to show the morphology of large glacier-capped or glacier-shrouded volcanoes. Morphological changes on the surface of ice caps caused by subglacial volcanic and/or geothermal activity can also be well studied, if of large enough dimensions (Thorarinsson et al., 1974;

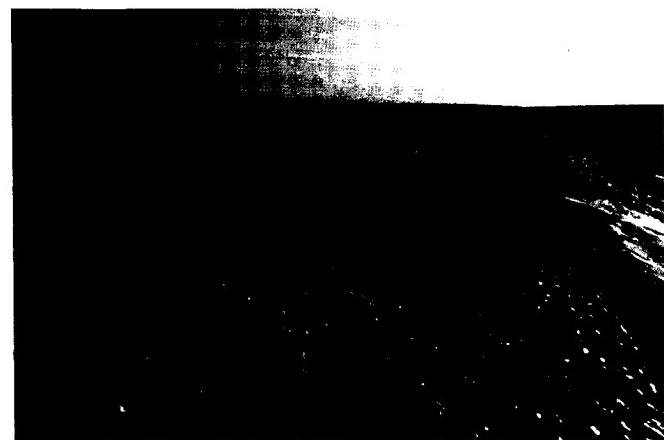


Figure 9-11. Photograph of blue-ice area in west Antarctica.

**ORIGINAL PAGE IS
OF POOR QUALITY**

Björnsson, 1975, 1976; and Tómasson, 1975) (see also Plates G-6 and G-15).

The continent of Antarctica and nearby offshore islands contain a number of volcanoes, only five of which are considered to be active (Simkin et al., 1981): the three stratovolcanoes—Mount Melbourne (in northern Victoria Land), Mount Berlin (in Marie Byrd Land), and Mount Erebus (on Ross Island; see Plate G-1)—and the two calderas—Mount Hampton (in Marie Byrd Land) and Deception Island (near the tip of the Antarctic Peninsula). The volcanoes of Buckle Island in the Balleny Islands, Penguin Island, Paulet Island, and Lindenbergs Island are also considered to be active on the basis of field studies (Simkin et al., 1981). Mount Erebus and Deception Island have historically been the most active, with at least 10 eruptions documented for each (Simkin et al., 1981).

A number of volcanoes in Antarctica have no known record of historic activity, but have well-developed summit craters or calderas. A variety of such volcanoes occur in West Antarctica in Marie Byrd Land between about 110 and 140° W longitude, either as isolated mountains or as a group of volcanoes within a mountain range. Landsat images are of particular value in providing two-dimensional morphological information on these volcanoes in West Antarctica.

Figure 9-15 is an enlarged part of a Landsat image of Mount Takahe volcano, which is centered at about 76°15' south latitude, 112°05' west longitude. Mount Takahe is a partially buried shield volcano, approximately 30 km in diameter and topped by an 8-km wide quasi-circular caldera. The highest elevation within the caldera is about 3460 m, and the surface elevation of the Antarctic ice sheet at the base of the volcano is about 1200 m (U.S. Geological Survey, 1976a). Figure 9-16 is an oblique (trimetrogon) aerial photograph of Mount Takahe, the type of data used by the U.S. Geological Survey to prepare the 1:250000 scale (Reconnaissance Series) maps of Antarctica.

Subglacial volcanic eruptions produce specialized types of landforms caused by the interaction of molten rock and meltwater from the surrounding glacier and the encapsulation of the volcanic activity by the glacier ice. In Iceland, where landforms formed from subglacial volcanic activity abound, two distinct types can be recognized: (1) landforms resulting from central eruptions of basaltic lava, and (2) landforms resulting from linear eruptions of basaltic lava (Williams et al., 1983b). Volcanic landforms formed in this way are composed of hyaloclastite breccias and pillow lavas, characteristic of the so-called Móberg Formation

in Icelandic. The linear landforms are called subglacial or móberg ridges, especially well depicted on Plate G-15 in the region between the southwestern part of Vatnajökull and the northeastern part of Mýrdalsjökull. The subglacial landform that results from a subglacial eruption is called a table mountain ("stapi" in Icelandic). Figure 9-17 is an oblique aerial photograph looking across the 1961 lava flows from the Askja caldera toward the prominent Herdubreid table mountain in north-central Iceland. Table mountains, such as Herdubreid in northeastern Iceland, often perforate the overlying ice sheet in the last phase of their development, thereby producing a normal subaerial lava-shield landform as a cap on a socle of hyaloclastite breccias and pillow lavas. In the case of Herdubreid, the base of the lava shield stands about 1000 m above the surrounding terrain and represents the thickness of the Pleistocene ice sheet in that part of Iceland when Herdubreid formed. Icelandic table mountains are the subglacial/subaerial counterparts of subaerial lava-shield volcanoes (Williams et al., 1983a). With Herdubreid as an example, it is easy to imagine what Mount Takahe (Figures 9-15 and 9-16) would look like if the surrounding ice sheet were to melt away.

EROSIONAL GLACIAL LANDFORMS

Some of the most spectacular landscapes on Earth, the so-called Alpine landscapes, are those formed by glacial and cold-climate processes, such as the Alps in France, Switzerland (Figure G-13.3), Italy, and Austria; the Grand Tetons in Wyoming (Figure 9-18), the Patagonian region of South America (Figure 9-19), the Himalaya in central Asia, and the fjords of Norway (Figure G-14.3) and other regions. Such landscapes derive their intrinsic beauty from the great local relief, the result of differential erosion by glacier ice. Figure 9-20 includes two schematic drawings by Davis (1909), which illustrate features associated with a mountainous region both during and after glaciation. Because of the two-dimensional aspect of most satellite images and photographs, this great relief (2000 to 3000 m from valley floor to mountain summit in some regions) is not appreciated. Such landscapes are best seen obliquely or from the ground aspect rather than from the vertical vantage point. Figure 9-18 shows the east side of the glacially eroded and cold-climate modified Grand Tetons in western Wyoming in June 1975. During the Pleistocene, the Grand Tetons served as the southwestern extension of a large ice cap that covered much of the Yellowstone National Park area,



Figure 9-12. Photograph of chondritic meteorite emerging at the ice-sheet surface, Allan Hills, Antarctica.



Figure 9-13. Photograph of large chondritic meteorite on the ice sheet surface, Allan Hills, Antarctica.



Figure 9-14. Oblique aerial photograph of the Grímsvötn subglacial/subaerial volcanic caldera, west-central Vatnajökull, Iceland.

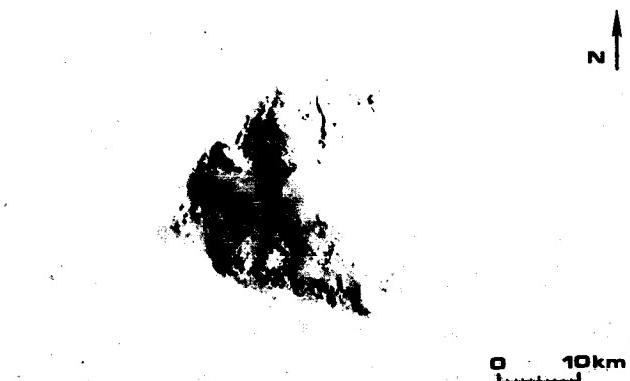


Figure 9-15. Landsat image of Mount Takahe, a partially buried shield volcano, West Antarctica.



Figure 9-16. Oblique aerial photograph of Mount Takahe volcano in West Antarctica.



Figure 9-17. Oblique aerial photograph of Herdubreid, a prominent table mountain in north-central Iceland.



Figure 9-18. Photograph of the east side of the glacially eroded Grand Tetons in western Wyoming.

and the highest elevations probably protruded above the glacier as nunataks. Only small glaciers remain today in cirques on the uppermost flanks of this mountain range. Figure 9-19 shows the glacially eroded and cold-climate-modified Fitz Roy/Torre massif (granitic intrusion) northwest of Lago Viedma; Patagonia, Argentina, in early April 1982, with a view of the eastern side of the massif showing Fitz Roy peak (3441 m) on the right and the spire of Cerro Torre (3128 m) on the left. During the Pleistocene, this region was covered by a large ice cap that extended along the southern Andes Mountains (see Figure G-4.2). The angular ridges (arêtes) and spires (horns) probably rose above the ice cap as nunataks. Examples from space of cirques, arêtes, glacial troughs, and fjords are presented in Plates G-12, G-13, G-14, and G-26.

Except for glacial outburst floods (*jökulhlaups*), landforms resulting from glaciofluvial erosion are generally too small to be characterized on satellite images. One example of landscape modification from such a catastrophic process, the Channeled Scabland of eastern Washington, is included in Chapter 4, Fluvial Landforms (Plate F-27).

DEPOSITIONAL GLACIAL LANDFORMS

In the erosional process of modifying the preglacier landscape by glacier ice and running water, glaciers pick up, carry, and deposit vast quantities of fragmental material derived from

the underlying surficial deposits, including deposits from previous glaciations, and bedrock. This fragmented material ranges from large blocks, often several to tens of meters in dimension, that are directly transported by glacier ice to very fine-grained material, called rock flour, that is transported in glacial streams or deposited directly from the glacier as a till matrix. On Landsat MSS false-color composite images, the color of proglacial lakes and streams that originate at glacier termini is a very characteristic robin's-egg blue, indicating the presence of glacial rock flour in suspension. The outwash plain (sandur) or valley floor downstream from the terminus of a glacier, when dry, becomes the source for downwind deposits of eolian material called loess.

Many varieties of landforms result from subglacial, supra-glacial, and marginal processes associated with glacial and glacio-fluvial deposition. Table 9-5 is a classification scheme for glacial and glaciofluvial deposits developed by Embleton and King (1975a).

Morainic landforms have been intensively studied by glacial geologists as relict landform features of the Pleistocene Epoch (Prest, 1968) and as active landforms associated with present-day glaciers. Figure 9-21, modified from Flint (1971), shows the characteristic morainic, till, and other landforms resulting from glacial and glaciofluvial processes associated with a valley or outlet glacier. Till is defined by Bates and Jackson (1980) as "dominantly unsorted and unstratified drift, generally unconsolidated, deposited directly by and underneath a glacier without subsequent reworking by meltwater, and consisting of a heterogeneous mixture of clay, silt, sand, gravel, and boulders ranging widely in size and shape." Till has replaced the now obsolete term, "ground moraine." Table 9-6, a classification scheme developed by Ritter (1978), shows a variety of morainal landforms.

Drumlins represent streamlined bedforms consisting of till which usually occur in groups of low (up to 60 m high) teardrop-shaped (in map view) hills (Scheidegger, 1970) (see Plate G-19).

Ritter (1978) discussed the depositional framework of ice-contact features on the basis of their setting (marginal or interior) and the type of glacial drift. He also included the two features (sandar and kettles) associated with the proglacial environment. Sandur (plural: sandar) is an Icelandic loanword used as a synonym for outwash plain (see Plate G-22).

Figure 9-22a, modified from Strahler (1960), shows the landforms associated with glacial, glaciofluvial, and glaciolacustrine processes at the margin of a glacier lobe of ice cap or ice sheets. Significant glaciofluvial ice-contact features include eskers and kames, but only the esker is large enough to be discernable on Landsat images (Slaney, 1981; Erling Lindstrom, 1985, written communication). Figure 9-22b is an oblique aerial photograph

looking north-northwest across the prominent esker located in Rörströmssjön, a lake in northwest Ångermanland, Sweden. The principal ice-stagnation landform visible on Landsat images is the kettle, which is usually occupied by a lake. The most dominant proglacial landform is the outwash plain or sandur (Figure 9-22a). Proglacial lakes (Plate G-23) commonly form at the edge of a lobe of glacier ice or at the terminus of a valley or outlet glacier. Such lakes become the sites for the deposition of deltas. Proglacial lakes are also important in the study of glacial stratigraphy because of the record of multiple cyclical (annual) sedimentary laminar couplets, called varves (Figure G-23.2), which form on their bottoms. Ephemeral ice-dammed lakes are also common at the edges of valley glaciers.

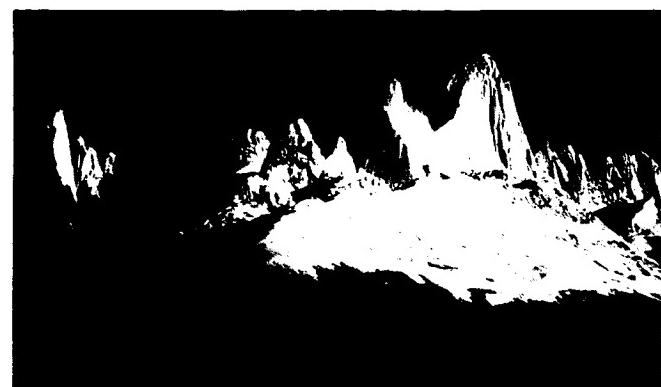
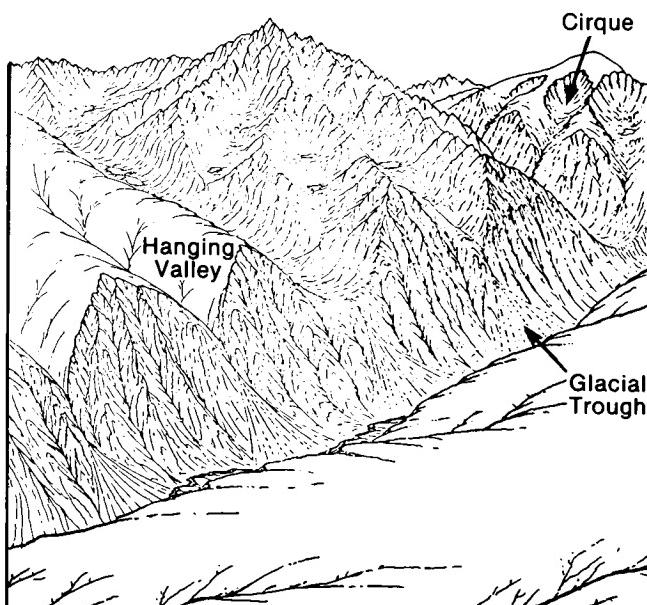
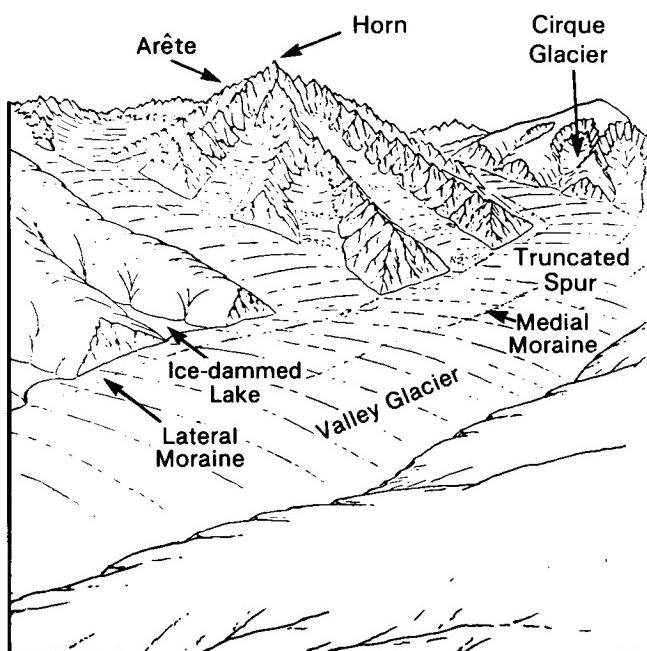


Figure 9-19. Photograph of the ice-modified Cerro Torre massif in Patagonia, Argentina.

Figure 9-20. Schematic drawings of the modification of a preexisting fluvial landscape by glacier erosion (after Davis, 1909).

Table 9-5
Classification of Glacial, Glaciofluvial, and Glaciolacustrine Deposits*

Stratified Drift	Unstratified Drift
Ice-contact deposits	Lodgement till (ground moraine)
Proglacial deposits	Ablation till (terminal, recessional, lateral, and ground moraine)
Lacustrine deposits	Pressure or squeeze till
Undermelt deposits	Push till (moraine)

*Modified from Embleton and King (1975a).

Glacial lakes are a common landscape element of glaciated terrains, especially in areas covered by ground moraine (Plate G-17). A common glacial lake is one that forms from the damming of a valley by a moraine. Glaciers may also overdeepen a valley through erosion; after the glacier recedes or disappears, such valleys may be filled by lakes. If overdeepening occurs in a coastal area, an arm of the ocean may occupy the valley, forming a fjord (see Plate G-14).

As already noted, deltas are common features in proglacial lakes. Much larger deltas can also form in lakes downstream from an active glacier or along the coast or in fjords from the enormous load of sediment discharged in glacial meltwaters from the terminus of a glacier.

An ice sheet represents a large surplus mass on the Earth's surface that may slowly depress the Earth's crust at a ratio of about 3:1 (3000 m of ice will deform the crust about 1000 m). After the ice sheet disappears, the crust will slowly restore itself in an isostatic process called glacial rebound. Along deglaciated coastal areas, a complex relationship exists between eustatic rise in sea level caused by the restoration of water to the oceans, new loading of the crust by the addition of sea water, and rebound resulting from the unloading of glacier ice. In some areas, the record of this rebound is preserved in a concentric series of strand lines (see Plate C-23).

PERIGLACIAL LANDFORMS

Periglacial landforms (Embleton and King, 1975b) form in cold-climate environments at high latitudes, on high mountains, and in proximity to glaciers. Although a number of landforms are associated with ground ice, such as hummocks, palsens (Friedman, et al., 1971), pingos, thermokarst, patterned (polygonal) ground, and rock glaciers, only two of these have dimensions large enough to be discernible at the spatial resolution of the Landsat MSS image (79-m pixel): thermokarst (Svensson, 1983), and rock glaciers. Figure 9-23 shows raised-edge, ice-wedge polygons on the northern coastal plain of Alaska near Barrow. The diameters of the polygons are 7 to 15 m, well below the spatial resolution capability of the Landsat MSS image. Aufeis (naled or icing), large surficial deposits of ice, can also be delineated on Landsat MSS images (Sloan et al., 1976). Figure 9-24 is an August 4, 1975, Landsat MSS band 6 image showing aufeis (naled) remnants that formed during the previous winter along the drainages of the Kuparuk, Echooka, Ivishak, and Shaviovik Rivers, northeastern Alaska. Determination of other periglacial features common in a cold-climate environment is generally in-

ferential, being derived from preexisting ancillary knowledge of the area encompassed by the Landsat image (Anderson et al., 1973). Thaw lakes (Table 9-7), special types of periglacial landforms resulting from thermokarst processes acting on perennially frozen ground or permafrost, are most evident on Landsat MSS images (Svensson, 1983) (Plate G-25). According to Péwé (1975), permafrost underlies about 20 percent of the land area of our planet and is especially widespread in the northern polar areas. Figure 9-25 shows the distribution of permafrost in the northern hemisphere (Péwé, 1975).

Editors Note:

Many of the glacial landforms, both erosional and depositional, and related features described in this introduction and shown in Figures 9-21 and 9-22 are difficult to pick out and identify in space imagery at Landsat-scale resolutions or less. Under the best of conditions, certain features are evident around active glaciers that are still producing them. Medial moraines on the glacial ice are easy to spot because of the sharp contrast between dark rock materials and bright ice, but lateral and terminal moraines, as well as kame terraces and some features in the outwash plains, are usually too small or dark or are lacking in relief to stand out. Deposits extending over wide regions covered by continental glaciers are frequently even more difficult to recognize despite their broad areal distribution. Even extensive terminal moraines are hard to discern unless they give rise to soils that display notably different spectral and physical properties. Eskers may appear conspicuous on the ground (Figure 9-22b) but seldom can be located, much less identified, even in glacial terrains where they may be commonplace. Drumlins, on the other hand, are often large enough in dimensions to be noted, especially where they occur in swarms (Plate G-19).

In addition to the foregoing factors (smallness, low relief, lack of contrast, and discontinuous distribution), vegetation cover (particularly in regions now heavily forested) and land-use practices (which effectively mask morainal features in much of the central and northern Great Plains) also prevent individual depositional features from being readily detected in Landsat imagery, even in some instances where they may predominate in a scene. As a rule, winter imagery is better for discriminating larger glacial features because the low Sun angle affords a natural enhancement as shadows call attention to small topographic differences (Plate

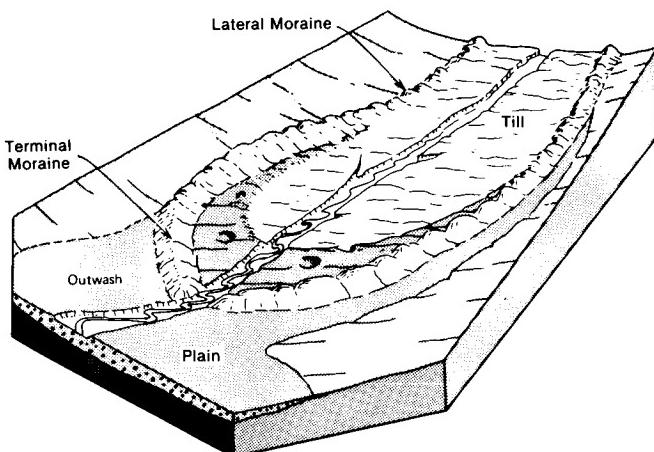
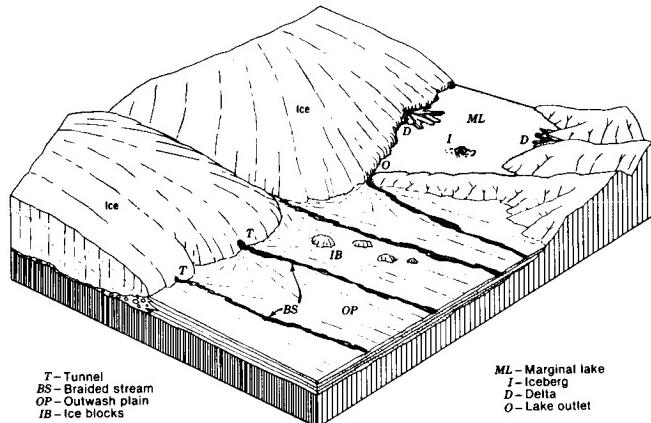


Figure 9-21. Characteristic morainal and other landforms resulting from glacial and fluvial deposition processes of a valley or outlet glacier (from Flint, 1971).

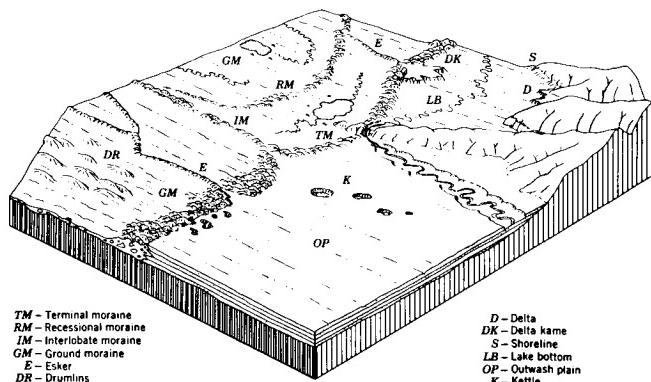
Table 9-6
Classification of Morainal Landforms

End Moraines	Moraines produced at front or sides of an actively flowing glacier.
Terminal moraines	Mark the farthest advance of an important glacial episode.
Lateral moraines	Deposited at or near the side margin of a valley glacier.
Recessional moraines	Formed at glacier front during temporary halt or readvance of ice in a period of general recession.
Till	Gently rolling surface formed of subglacial, englacial, or supraglacial debris released from glacier.
Interior and Minor Varieties	
Washboard moraines	Small parallel ridges oriented transverse to direction of ice movement.
Interlobate moraines	Formed at junction of two ice lobes.
Medial moraines	Elongate ridge developed at junction of two coalescing valley glaciers.

*Modified from Ritter (1978).



a. With the ice front more or less stationary (in relative equilibrium), various depositional features are built by meltwaters.



b. After the ice has wasted completely away, a variety of new landforms made under the ice are exposed to view.

Figure 9-22a. Landforms associated with glacial and fluvial glacial deposition processes at the margin of a glacier lobe of an ice cap or ice sheet (from Strahler, 1960).



Figure 9-22b. Oblique aerial photograph of esker in Rörströmsjön, northwest Ångermanland, Sweden (Photograph by Erling Lindstrom).

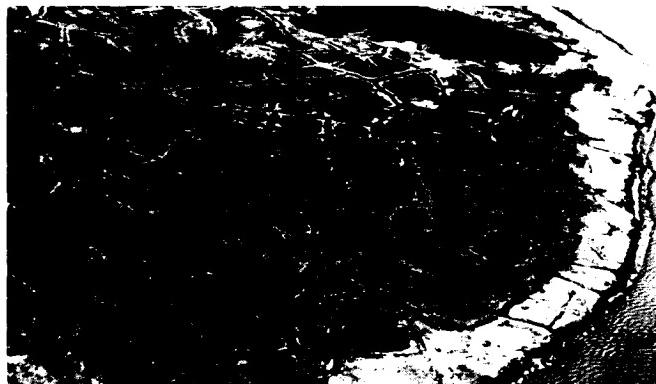


Figure 9-23. Oblique aerial photograph of ice-wedge polygons on the northern coastal plain of Alaska.

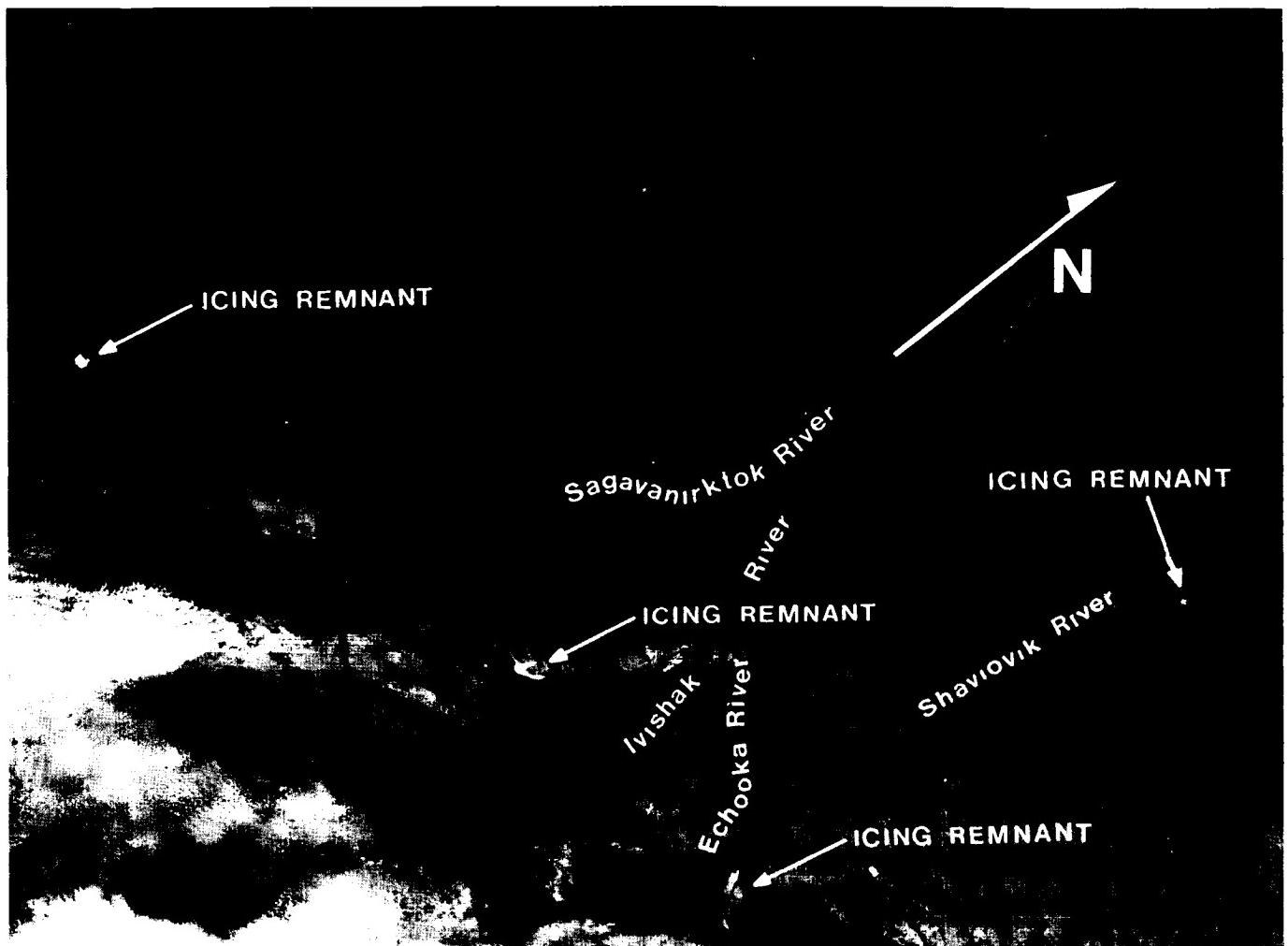


Figure 9-24. Landsat image of aufeis (naled) remnants (arrows) in northeastern Alaska.

Table 9-7
Classification of Common Types of Thermokarst Features*

Type	Formation	Features
Backwearing	By lateral erosion, by streams, lakes, or ocean	Gullies
		Thermocirques
		Thaw lakes
		Thermokarst mounds
Downwearing	By melting downward of ground ice. Usually develop as flat, shallow depressions in level areas.	Alases
		Thermokarst valleys

*From Ritter (1978).

ORIGINAL PAGE IS
OF POOR QUALITY

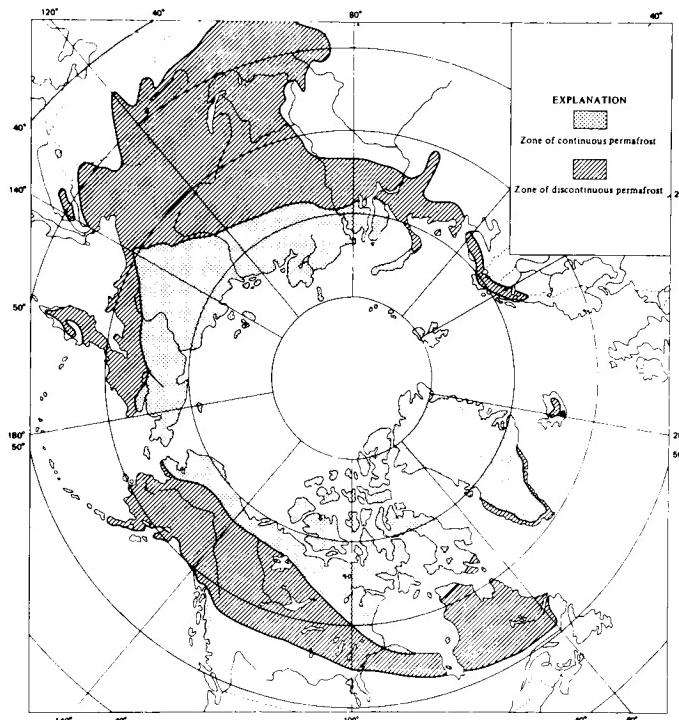


Figure 9-25. Map of permafrost distribution in the northern hemisphere (from Péwé, 1975).



Figure 9-26. (a) Crag and tail landforms in Québec, (b) glacial fluting in Manitoba, (c) multidirectional lineations in Ontario.

G-15). Although snow cover may inhibit recognition of some smaller glacial landforms, in some instances it aids in highlighting certain features ("fingerprint dusting" effect). Features that possess sharp spectral contrasts with their surroundings normally show up better in summer imagery. (October is generally an optimum time to look for glacial features in parts of the northern hemisphere such as the Canadian Shield.)

Landsat images (and mosaics therefrom) excel in providing synoptic information about one class of glacial features: aligned landforms and lineations imposed on the terrain by the passage of ice sheets across broad regions. Three Landsat images (interpreted by Canadian colleagues) illustrate this: In Figure 9-26a, showing a glaciated Precambrian surface in central Québec, a

pronounced lineation oriented to the southwest is produced by large crag-and-tail hills (especially evident in the lower left), possibly mixed with drumlins. Large-scale glacial fluting in Manitoba is emphasized in Figure 9-26b by ice formed in lakes and wetlands in the furrows; the direction of ice movement is obvious. Two directions of motion are evident in Figure 9-26c, a scene in Ontario south of Hudson Bay. In the right half of the image, mega-grooves running nearly north-south appear to be fluting (and possible iceberg gorge marks) in a flatlands composed of Paleozoic marine deposits. Pronounced northeast-southwest lineations in glacial cover over Precambrian bedrock in the left half of the image also appear to be glacial scouring effects that localize elongate lakes.

PLATE G-1

ORIGINAL PAGE IS
OF POOR QUALITY

An ice sheet is defined as "a mass of ice and snow of considerable thickness [>1000 m] and large area [>50000 km 2]. Ice sheets may be resting on rock [Plate G-1] or floating [Plate G-2]. Ice sheets of less than about 50000 square km resting on rock are called ice caps [Plate G-5]" (Armstrong et al., 1973). Of all the glacier ice on our planet today, only Antarctica and Greenland contain composite masses of glacier ice larger than 50000 km 2 (Table 9-1). During the Pleistocene, however, many regions contained composite masses of glacier ice that qualified as ice sheets (Table 9-2). In fact, the Laurentide Ice Sheet rivaled Antarctica in areal extent (Figure 9-1).

During a lunar mission, one of the Apollo 17 astronauts captured much of Antarctica on photographic film (Figure 9-2), becoming the first human to see most of that continent in one instant. For useful scientific information, however, polar-orbiting spacecraft, with various types of remote sensing devices, have been used to systematically acquire successive frames or strips of image data of Antarctica. This image data can be analyzed separately or in mosaic form. Drewry (1983) used Landsat images to correct parts of the coastline for the new 1:6000000-scale Scott Polar Research Institute base map of Antarctica. Many nations are using Landsat images to prepare planimetric image maps of Antarctica (Williams et al., 1982) and as base maps for geological maps (Wolmarans and Krynaauw, 1981; Tingey and Convine, 1982). Zwally et al. (1983) used mosaics of Nimbus 5 electrically scanned microwave radiometer (ESMR) images to prepare a monthly, seasonal, and year-to-year atlas of variations in sea-ice cover around Antarctica between 1973 and 1976.

Plate G-1 is a NOAA-6 advanced very high resolution radiometer (AVHRR) image of that part of Antarctica, including the primary logistical base (McMurdo Station), which is the center for scientific research by the United States. Only large-scale features can be discerned on this NOAA image, which spans a region about 1000 km wide. Part of the Ross Ice Shelf, Transantarctic Mountains, the so-called "dry valleys" area (e.g., Taylor Valley), Mount Erebus volcano, Drygalski ice tongue (the floating seaward extension of David Glacier), and the various outlet glaciers that originate in the inland ice can be seen on this image. The 5 steps (shades) of gray appearing as bands in the bottom left quadrant of the image are artifacts produced during image processing.



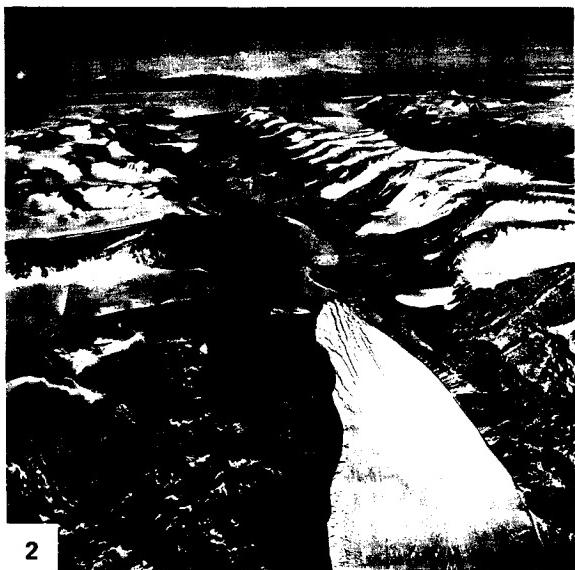
1

VICTORIA LAND, ANTARCTICA

Figure G-1.1 is a Landsat-1 MSS image of a small part of the area imaged in Plate G-1. Figure G-1.2 is an oblique aerial photograph of part of Taylor Valley (one of the "dry valleys" of Antarctica) looking toward the Mount Erebus volcano. Until the past decade, when vertical aerial photographs of selected sites in Antarctica began to be acquired, the trimetrogon camera (tricamera) configuration (one vertical camera, two oblique cameras) was the principal source of photographic data used to prepare maps of Antarctica. Because only about 20 percent of Antarctica has been mapped at scales of 1:250000 or larger (Swithinbank, 1980), much remains to be accomplished. Plate G-1 and Figures G-1.1 and G-1.2 represent a nested set of images of Antarctica, each providing different types and scales of information. NOAA images provide synoptic coverage (including around the South Pole where Landsat does not image), which is important to monitoring changes in coastline configuration and variations in sea ice, although microwave images would be superior because of the cloud-penetrating capability of microwave energy. If Antarctica were cloudfree, the polar convergence of Landsat orbits means that only about 520 images, instead of a total of 2514 nominal scenes, would be required to cover Antarctica from the coast to 81 °S latitude, assuming minimal sidelap of adjacent images.

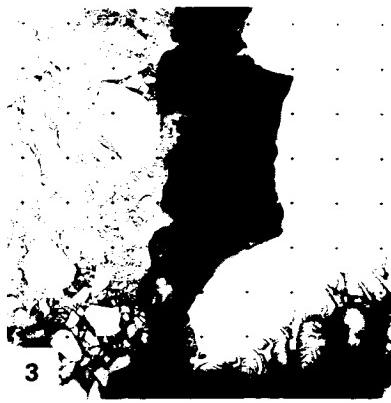
The great size of Antarctica presents a formidable barrier to gaining a better understanding of the geological, geophysical, and glaciological character of this continent. It is clear that the preparation of adequate base maps and other types of related studies of Antarctica will require major utilization of existing and future space technology (Swithinbank, 1983).

Figure G-1.3, from Williams and Ferrigno (1981), is a Landsat RBV band 2 image of northwestern Greenland. Taken on July 29, 1976, this image shows the well-defined edge of the Greenland Ice Sheet in the Inglefield Land area on the right and numerous outlet glaciers emptying into fjords. Several nunataks are visible on the southeast edge of the image. Sea ice fills the Kane Basin on the left, and part of Ellesmere Island, Northwest Territories, Canada, is visible in the lower left-hand corner of the image (see also Figure G-4.4). **NOAA 6 AVHRR, Ch. 2, 1812Z, February 27, 1980.**

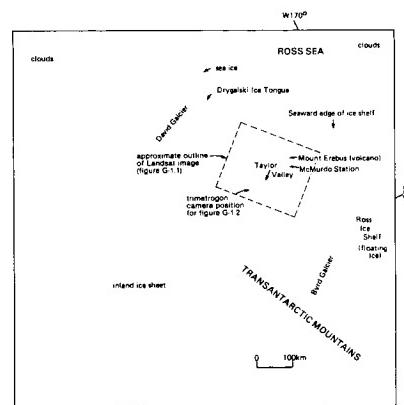


2

ORIGINAL PAGE IS
OF POOR QUALITY



3



ORIGINAL PAGE IS
OF POOR QUALITY

PLATE G-2

An ice shelf is defined as "a sheet of very thick ice, with a level or gently undulating surface, which is attached to the land along one side but most of which is afloat and bounded on the seaward side by a steep cliff (ice front) rising 2 to 50 m or more above sea level. Ice shelves have been formed along polar coasts (e.g., those of Antarctica, the Canadian Arctic islands, and Greenland), and they are generally of great breadth, some of them extending several hundreds of kilometers seaward from the coastline. They are nourished by annual snow accumulation and by seaward extension of land glaciers; limited areas may be aground" (Bates and Jackson, 1980).

Antarctic ice shelves front on 44 percent of the 31 876-km long coastline of Antarctica (Drewry et al., 1982). Figure G-2.1 shows the location of some of the ice shelves that fringe the periphery or fill coastal embayments in Antarctica, such as the Ross Ice Shelf.

Although ice shelves are most typical of various embayments around the coast of Antarctica, during the Pleistocene they were associated with the great ice sheets that formed over North America, Greenland, and the northern part of Eurasia, especially where edges of these ice sheets coalesced over large embayments. Denton and Hughes (1981b) suggest that ice shelves formed over parts of the Greenland, Norwegian, and Labrador Seas and even extended into the North Atlantic Ocean. Antarctica has several large ice shelves, such as the Ross (Plate G-1 and Figure G-1.1; this Plate and Figure G-2.2), Amery, Filchner, Ronne, and Larsen Ice Shelves, and several smaller ones, such as the Lazarev and Wordie Ice Shelves. According to Drewry (1983) the ice shelves of Antarctica cover 1 541 710 km², have a mean thickness of 475 m, and have a volume of 731 900 km³. The ice shelves represent 11.1 percent of the total area but only 0.02 percent of the volume of ice in Antarctica.

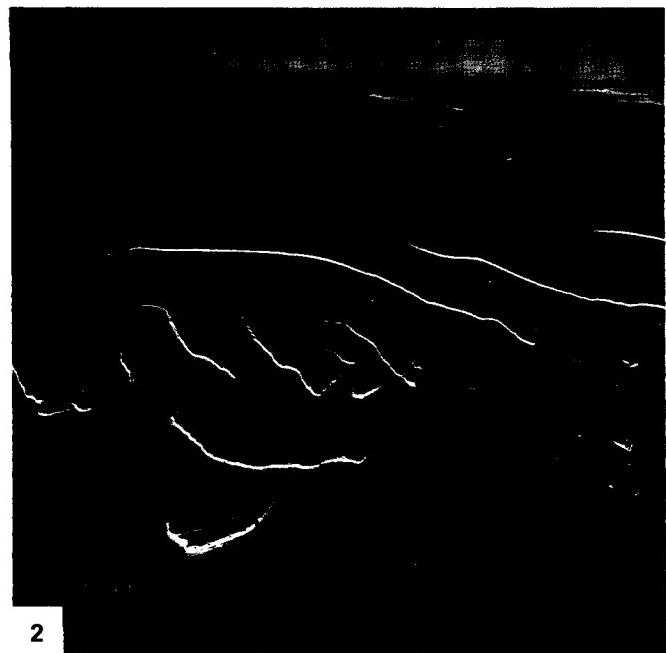
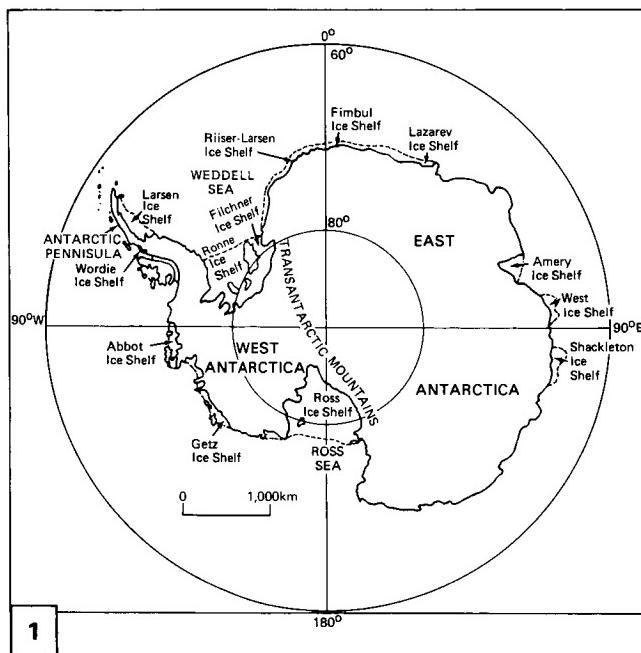
Plate G-2 is a NOAA-6 AVHRR image centered on the Ross Ice Shelf, Antarctica. This image overlaps another NOAA-6

ROSS ICE SHELF, ANTARCTICA

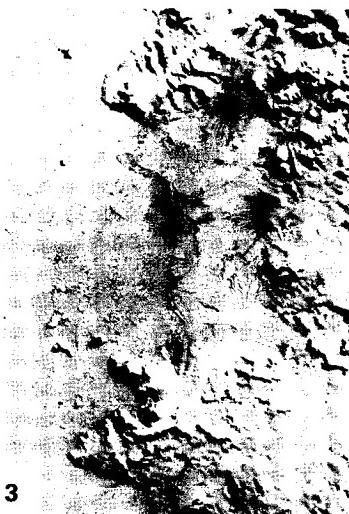
AVHRR image of the area (Plate G-1). The index map shows the principal glaciological and geographic features of the area encompassed by the image. The Ross Ice Shelf is bounded on the west and south by the Transantarctic Mountains through which enormous outlet glaciers, such as the Byrd (A) and Beardmore (B) Glaciers, feed the Ross Ice Shelf as they drain part of the East Antarctic ice sheet. On the east, the Ross Ice Shelf is fed by a series of five major ice streams (Figure G-3.1), A through E (from Drewry, 1983), which drain part of the West Antarctic ice sheet. Figure G-2.2 is an oblique aerial photograph of the ice front (floating edge of an ice shelf) along the northwestern margin of the Ross Ice Shelf on October 22, 1961. The open water of the Ross Sea is in the upper right background on Figure G-2.2. Tabular icebergs in the left foreground are "trapped" in sea ice (called fast ice when attached to the coast). The huge embayments of both the Ross and Weddell Seas are filled with large and complex ice shelves, which originate, in part, in the West Antarctic ice sheet; hence, these ice shelves share a common ice divide.

Ice shelves are considered to be the most metastable part of the Antarctic ice sheet in response to variations in global climate (Stuiver et al., 1981), and the ice shelves of the West Antarctic ice sheet are considered to be especially vulnerable (Hughes, 1973, 1975; Mercer, 1978).

The Wordie Ice Shelf on the southwest side of the Antarctic Peninsula has experienced a major retreat since the late 1940s. According to Doake (1982), who analyzed two successive Landsat images of the Wordie Ice Shelf acquired in 1974 and 1979 (Figure G-2.3), the ice front retreated up to 7 km during this interval, and the ice shelf was reduced in area by 250 km². Details of crevasses and other surface features on the shelf appear in this enlargement of a part of this 1979 Landsat image. **NOAA-6 AVHRR, Ch. 2, Orbit 7165, 13:42:15 UT, November 12, 1980.**



ORIGINAL PAGE IS
OF POOR QUALITY



3

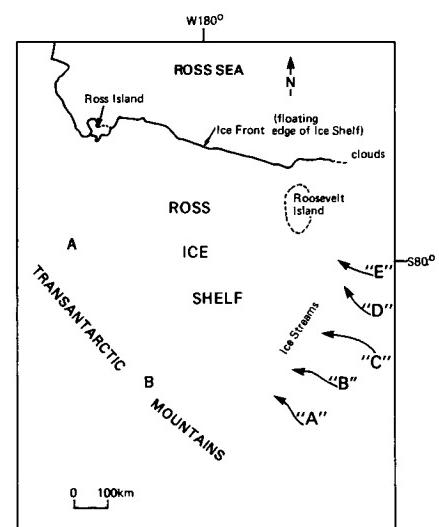


PLATE G-3

JAKOBSHAVNS ISBRAE, WESTERN GREENLAND

An ice stream is defined as "part of an ice sheet in which the ice flows more rapidly (than) and not necessarily in the same direction as the surrounding ice. The margins are sometimes clearly marked by a change in direction of the surface slope, but may be indistinct" (Armstrong et al., 1973). Bates and Jackson (1980) add the following to this definition: "usually flowing to the ocean or to an ice shelf and not constrained by exposed rock." The following discussion restricts the definition to apply only to well-defined, fast-flowing streams of ice within a larger ice sheet or ice cap.

Although large ice caps can have ice streams associated with outlet glaciers, ice streams are most commonly found in ice sheets. In Antarctica, ice streams are the primary sources of ice for the large ice shelves, especially those that feed the Ross Ice Shelf (Figure G-3.1) and the Ronne and Filchner Ice Shelves (Hughes, 1977). Ice streams are also common on the west coast of Greenland (Mercer, 1975b).

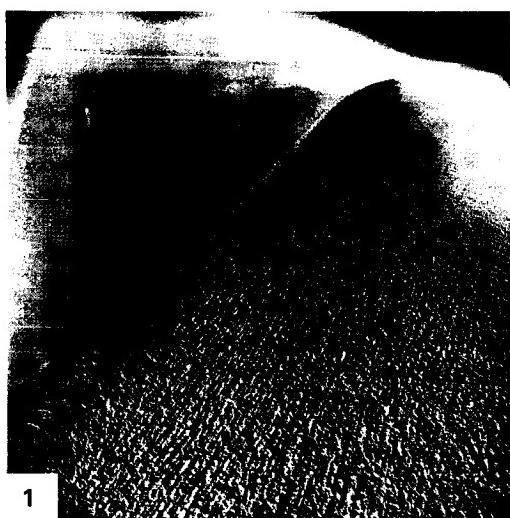
Plate G-3 is a Landsat image of Jakobshavns Isbrae (Sermeq kujatdelq, in Greenlandic), an important outlet glacier from the Greenland ice sheet on the west-central coast of Greenland. The terminus of Jakobshavns Isbrae is a prolific producer of icebergs that calve into Jakobshavns Isfjord (Stove et al., n.d.). Since 1850, the calving front of the outlet glacier has retreated approximately 25 km (Carboneau, 1968; Bauer, 1968). Hughes (1983) notes that "Jacobshavn Glacier is the fastest surging ice stream at the present time." Its terminus moves at the rate of about 7 km/yr or about 19 m/day. Hughes (1983) states that Jakobshavns Isbrae drains about 10 percent of the Greenland ice sheet and accounts for 42 percent of the total volume of ice discharge from the western margin of the Greenland ice sheet (Carboneau, 1968; Bauer, 1968). Hughes (1983) further notes that: "The most notable feature of the surface topography (of the ice sheet) is the large concave basin where the ice sheet funnels into Jacobshavn Glacier. A bedrock trough lies beneath this concave basin of converging flow, but has much less relief."

On the Landsat image, icebergs can be seen in Jakobshavns Isfjord, the production of which were the subject of an important study carried out with a sequential series of Landsat images (Stove et al., n.d.). Under this low Sun angle image, irregularities in the surface topography of the Greenland ice sheet are obvious, reflecting the presence of subglacial topographic relief. The ice stream is well defined from the 7-km wide terminus to about 100 km into the inland ice. Approximately 8 km up-glacier from the

terminus, Jakobshavns Isbrae travels northwest through a 4-km wide subglacial valley in the bordering subglacial mountains. Just down-glacier from this exit point from the subglacial valley where Jakobshavns Isbrae broadens to about 7 km, a tributary glacier feeds in from the north. Approximately 15 km farther up-glacier from the exit point, the ice stream changes direction (from northwest flow to west-southwest flow), and a sinuous path can be traced for another 80 km to the east-northeast in the inland ice. It is probable that the Jakobshavns ice stream is following a sinuous preglacial valley for at least 100 km. The distance from the outer coast of Greenland, at the western end Jakobshavns Isfjord, to the head of the Jakobshavns ice stream is about 150 km.

This 150-km long path of Jakobshavns Isbrae is comparable to the length of the longest nearly straight fjord in Greenland, Søndre Strømfjord (see Plate G-14). It is concluded that Jakobshavns Isbrae flows in a subglacial valley that, if ice cover were removed, would be almost identical to Søndre Strømfjord. Such comparisons show that ice streams are the dominant erosional agent in the creation of the fjord landform, especially in its inland parts.

As noted earlier, ice streams are important sources of ice for ice shelves in Antarctica. The index map of the Ross Ice Shelf, Antarctica (Plate G-2), shows five ice streams on its eastern margin. Figure G-3.1 is an oblique aerial photograph of the northern edge of Ice Stream "B" on the western margin of the Ross Ice Shelf, Antarctica (Plate G-2, index map). Note the abrupt difference in flow between the heavily crevassed, more rapidly moving ice of the ice stream on the right and the noncrevassed, slowly moving ice of the ice shelf on the left. Figure G-3.2 is a Landsat image of the upper part of the Jutulstraumen Glacier, an ice stream in Queen Maud Land, East Antarctica. The Jutulstraumen Glacier flows north (toward top of image) onto the Fimbul Ice Shelf through a subglacial trough between the Sverdrup Mountains on the east and the Ahlmann Ridge on the west. Figure G-3.3 is a Landsat image of the mouth of the Slessor Glacier, where the ice stream enters the east side of the Filchner Ice Shelf, East Antarctica, between the Shackleton Range on the south (bottom right) and Parry Point (angular promontory on the left), the southwestern extension of the Theron Mountains on the north. **Landsat 22087-14293-7, October 9, 1980.**



ORIGINAL PAGE IS
OF POOR QUALITY

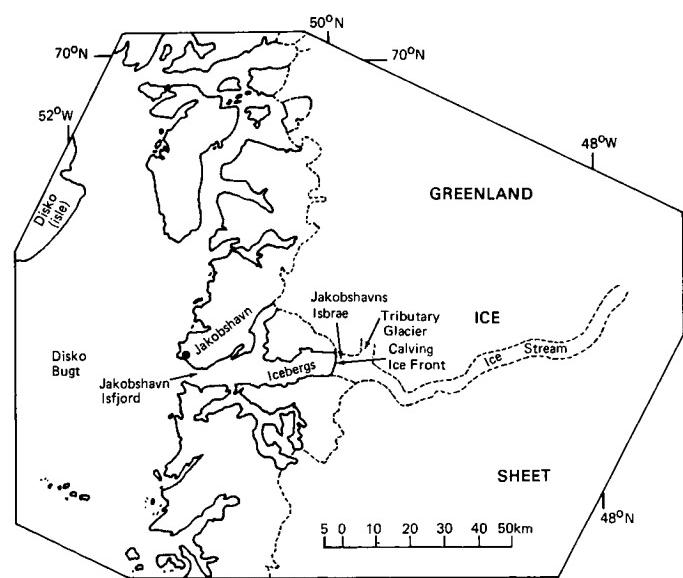


PLATE G-4

An ice field is defined as "an extensive mass of land ice covering a mountain region, consisting of many interconnected alpine and other types of glaciers, covering all but the highest peaks and ridges" (Bates and Jackson, 1980). The distinction between an ice cap (Plate G-5) and an ice field (Plate G-4) is the degree of burial of the landscape. Ice fields, for example, are common in the coastal mountain ranges of Alaska, where extensive masses of glacier ice partially cover the rugged mountain landscape and numerous outlet glaciers extend down-valley to the interior or coastal lowlands (Plate G-7). On the other hand, ice caps completely bury the underlying topography, although occasional nunataks may protrude through the ice cover, generally in the thinner marginal areas of the ice cap.

Ice fields tend to have long axes that extend along the crestal areas of mountain ranges; ice caps tend to be more circular or slightly elliptical. One of the classic ice fields on our planet is the Southern Patagonian ice field in the southern Andes of South America. It extends for about 300 km along the mountain divide and gives birth to numerous outlet glaciers (Mercer, 1967). The Southern Patagonian ice field is the principal remnant of a much larger ice sheet (large ice cap) that extended over a distance of about 2100 km and averaged about 250 km wide. The index map of the area shows the estimated extent of the Late Wisconsinan ice margins south of latitude 36° in southern South America. The largest black area is the present Southern Patagonian ice field shown in Plate G-4 (from Hollin and Schilling, 1981).

The ice fields and other glaciers of southern South America, especially those that are situated in the region between 46° and 56°S latitude, are not very well known. Access is difficult from the west; fierce storms are characteristic of the region, and only limited mapping has been accomplished. The long periods of overcast skies make the acquisition of aerial and satellite photographs or images that are suitable for mapping difficult and costly. Even during the 14 years of the Landsat program, comprehensive coverage of the glacierized areas south of about 50°S latitude is still lacking. Mercer (1967, pp. 136-137) described the Southern Patagonian ice field from available maps and his own observations:

"The southern Patagonian icefield is 360 km long and extends through about three degrees of latitude from 48°15'S to 51°20'S. Its greatest width between glacier termini is 90 km in latitude 48°50'S., but for much of its length it averages about 40 km. Outlet glaciers reach sea level in the fiords on the western side, many of which are choked with floating ice. On the east the largest glaciers calve into piedmont lakes at 185 m to 285 m above sea level."



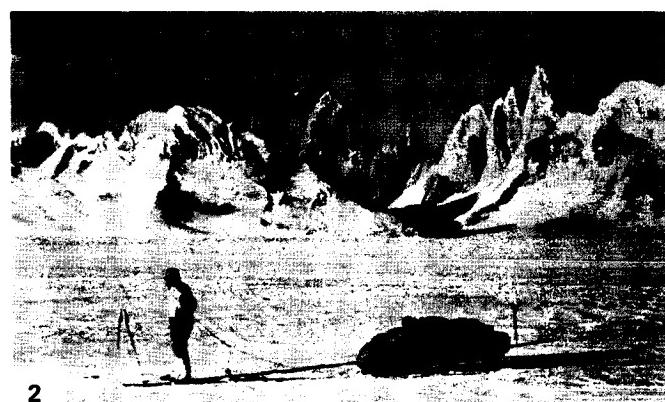
1

SOUTHERN PATAGONIAN ICE FIELD, CHILE AND ARGENTINA

Plate G-4 is an oblique color satellite photograph that provides the first complete coverage of most of the Southern Patagonian ice field, which sits astride the Andes Mountains along the Chile/Argentina border in southern South America. Numerous outlet glaciers with prominent medial moraines extend into fjords on the west and lakes on the east. Many lakes occupy valleys occupied by valley glaciers when the ice cover in the region expanded during the Pleistocene. The Plate photograph was acquired on March 10, 1978, by Soviet cosmonauts, G. M. Grechko and Yu. V. Romanenko, from the Salyut-6 spacecraft, as part of a series of glaciological research experiments designed by Vladimir M. Kotlyakov, a glaciologist with the Institute of Geography, Academy of Sciences of the U.S.S.R., in Moscow. This is one of 40 photographs taken of the ice fields and other glaciers in southern South America, several of which were analyzed in a paper by Desinov et al. (1980).

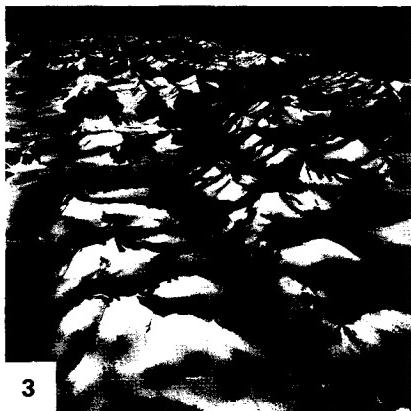
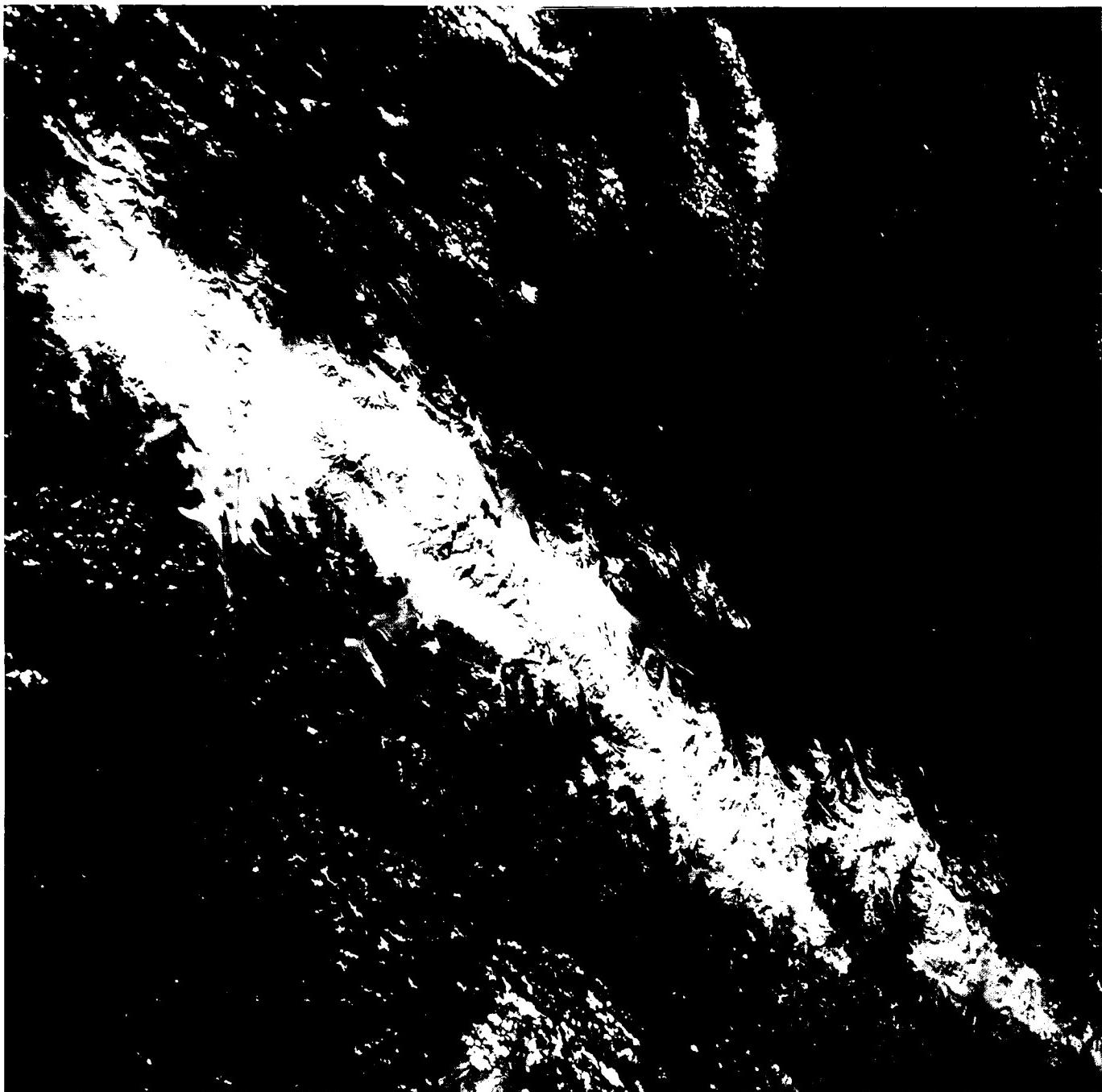
On the east side of this ice field, several outlet glaciers terminate in freshwater lakes: O'Higgins Glacier(A) in Lago O'Higgins, Viedma Glacier(B) in Lago Viedma, and Upsala Glacier(C) and Moreno Glacier(D) in Lago Argentino. Moreno Glacier has a history of surges across Canal de los Témpanos, an arm of Lago Argentino, which block the connection with another lake arm to the east (Brazo Rico). This produces flooding along the shore of Brazo Rico until the ice dam fails and the lake drains into Lago Argentino. Figure G-4.1 is a view in late October 1981 looking across Canal de los Témpanos and showing the terminus of the Moreno Glacier, Argentina, an outlet glacier on the east side of the Southern Patagonian Ice Field, after it has overridden the opposite shore. The ice dam closes off the connection between Canal de los Témpanos (foreground) and Brazo Rico (out of photograph to the left). The terminus is heavily crevassed and icebergs have calved from the vertical edge. The dark feature is probably the mouth of a tunnel formed by a subglacial stream. Figure G-4.2 is a view from the surface of the Southern Patagonian Ice Field looking east toward the western side of the Fitz Roy/Torre massif, with Cerro Fitz Roy (3441 m) on the left and the spire of Cerro Torre (3128 m) on the right (see also Figure 9-19).

Figure G-4.3 is an oblique aerial photograph of an ice field in the Victoria and Albert Mountains on the eastern part of Ellesmere Island in the Queen Elizabeth Islands area. Meltponds are visible on the prominent outlet glacier in the right background. Numerous nunataks, cirques, arêtes, and horns are visible throughout the ice field. The glacially sculptured landscape is now partially submerged by a more continuous cover of ice. The Kane Basin and Greenland are faintly visible in the distant background. Salyut 6 Photograph, March 10, 1973.



2

ORIGINAL PAGE
COLOR PHOTOGRAPH



3

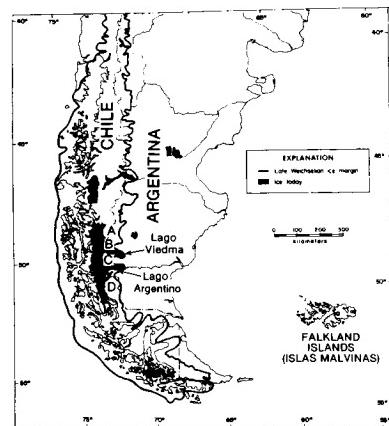


PLATE G-5

BARNES ICE CAP, BAFFIN ISLAND, NWT, CANADA

An ice cap is defined as "a dome-shaped glacier usually covering a highland area. Ice caps are considerably smaller in extent than ice sheets" (Armstrong et al., 1973). Armstrong et al. use a cutoff of 50000 km² to differentiate between ice sheets and ice caps. Figure G-5.1 (from Price, 1973) shows the evolution of isolated glaciers in a mountainous area, through development of a more extensive ice cap, to a large ice sheet.

Ice caps can be either small isolated domal masses of ice, such as the tiny (4.0 km²) ice cap on the volcano Ok in Iceland, quasi-circular or elongated composite masses of ice, such as Vatnajökull (8300 km²) in southeastern Iceland (Plate G-6), or more elongated masses of ice extending for 100 km or more.

An ice cap may have a smooth margin, such as the Barnes ice cap on Baffin Island in Canada seen in this Plate, or more typically, it may have various lobes that protrude into areas of low relief, called outlet glaciers, that extend down valleys from the main ice cap, such as the Vatnajökull ice cap in Iceland (Plate G-6).

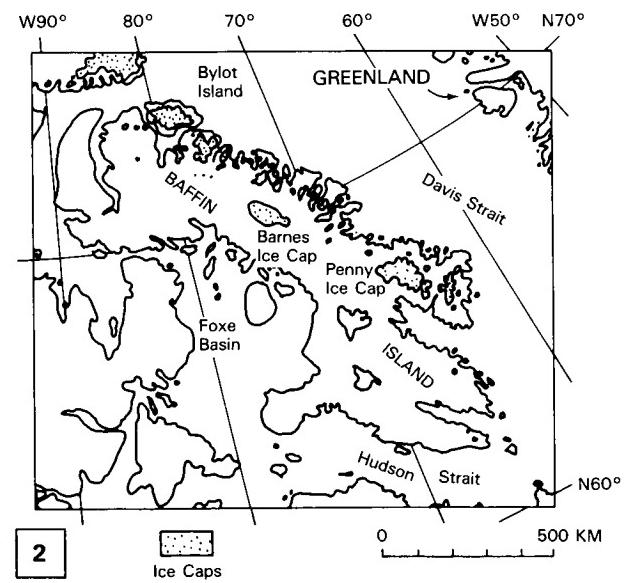
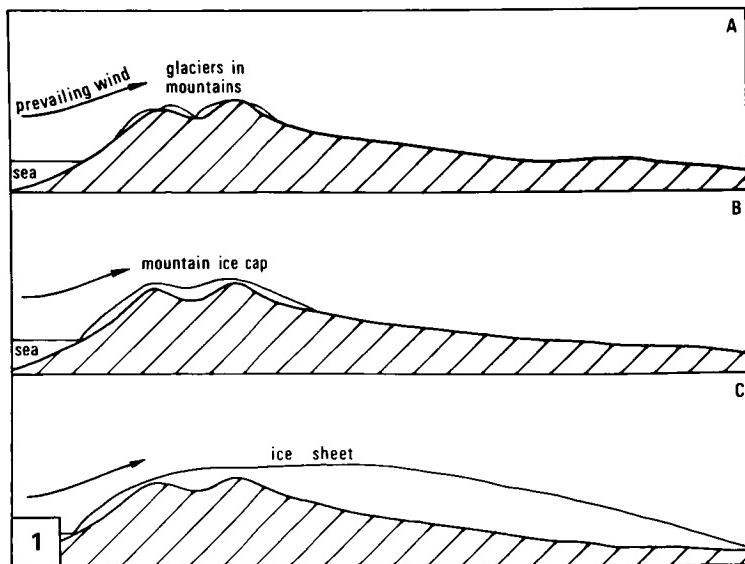
Plate G-5 is a Landsat image of the Barnes Ice Cap on the central part of Baffin Island, Northwest Territories, Canada (American Geographical Society Glacier Studies, 1975a). The Barnes Ice Cap lies 300 km southeast of the cirque glaciers on Bylot Island, which are discussed later in this section (Plate G-8), and 300 km northwest of the Penny Ice Cap in the southeastern part of Baffin Island. Figure G-5.2 is a locator map for the glaciers of Baffin Island. According to Mercer (1975a, p. 685), "Glaciers occur in the mountains along the north and east coasts of the island (Baffin Island), and less extensively in the interior. There are two large ice caps, Barnes on low ground in the interior of the island, and (the) Penny on the eastern mountains.... Other areas have extensive glaciers, some of which are small ice caps." Mercer (1975a), who uses Bird (1967) as a source, notes that Baffin Island has 36 830 km² covered by glaciers, about 7 percent of the island, and the Barnes and Penny Ice Caps are about equal in size, 5935 and 5960 km², respectively.

Mercer (1975a, p. 694) provides a description of the ice cap: "The Barnes Ice Cap is near the middle of Baffin Island, with its center at 70°10'N and 73°30'W. It occupies rolling coun-

try of relatively low relief, west of the main watershed of the island, with altitudes of up to nearly 550 m. The ice cap covers 5935 sq. km., and its main axis is 150 km. long, approximately parallel to the northwesterly trend of the island. It rests on the slightly dissected plateau of central Baffin Island. The broad, gently-sloping summit area of the main ice cap reaches 1130 m., and the lobe at the south end reaches 975 m. The gradients are nowhere steep, except locally at the margin. In the accumulation season, the ice surface is smooth and undulating; but at the height of summer, stream channels are a meter deep in the crest area and 9 m. deep near the margins."

On the Landsat image of the Barnes Ice Cap, numerous stream channels can be seen radiating away from the crestral area (divide) of the ice cap (A). Most of the ice cap has shed the accumulated snow from the previous winter, although either residual snowpack or a fresh snowfall covers a limited area at the highest elevations (B). Small ice caps (C), outlet glaciers (D), and numerous small cirque glaciers (E) can be seen to the east and northeast of the Barnes Ice Cap in the mountains that border Baffin Bay, which lies farther to the east just beyond the edge of the image. Well-developed fjords (F) have been eroded in these mountains by the expanded glaciation of the region during the Wisconsinan and earlier advances of glaciers. The Barnes Ice Cap also calves into several proglacial lakes along its terminus, especially into Conn and Bieler Lakes on the northeast and Generator (Figure G-5.3) and Blanchfield Lakes on the southeast and south, respectively. Figure G-5.3 is a view of the steep ice front on the southeast margin of the Barnes Ice Cap, where it terminates in Generator Lake. These lakes still have an ice cover on August 7, 1973.

Although not all Quaternary geologists agree with Mayewski et al. (1981), the latter consider the glaciers of Baffin Island to be remnants of an extensive ice sheet that covered much of the northern part of North America (see Figure 9-1). As the Laurentide Ice Sheet waned during the last stages of the Wisconsinan, it broke up into large isolated ice caps, some of which persisted into the Holocene. **Landsat 1380-16182-7, August 7, 1973.**



ORIGINAL PAGE IS
OF POOR QUALITY

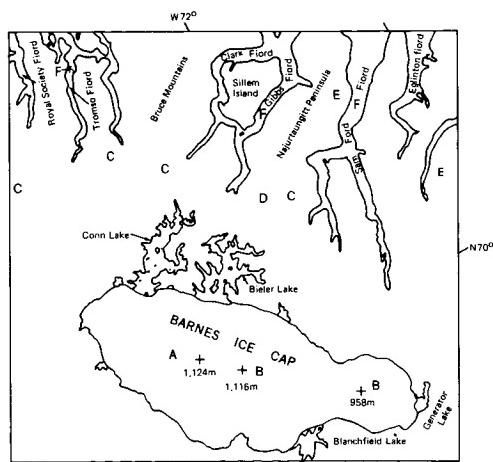


PLATE G-6

An outlet glacier can be defined as "a valley glacier which drains an inland ice sheet or ice cap and flows through a gap in peripheral mountains" (Armstrong et al., 1973). Outlet glaciers also include broad well-defined lobes of glacier ice that protrude from an ice cap or inland ice sheet and spread over areas of low relief.

Inland ice sheets, such as those of Greenland and Antarctica, have numerous outlet glaciers around their margins. Ice caps may have no outlet glaciers, such as the small ice cap on Ok in west-central Iceland, or may have a great many, such as the Vatnajökull ice cap in southeastern Iceland. Plate G-6 is a Landsat MSS false-color composite image of Iceland's largest ice cap, Vatnajökull (Williams et al., 1977), and the surrounding area including part of the Hofsjökull (upper left) and Mýrdalsjökull (bottom left) ice caps and all of the Tungafellsjökull ice cap (small one between Vatnajökull and Hofsjökull) (from Williams, 1983c). At 8300 km² (area calculated from this September 22, 1973, image), Vatnajökull is the largest of Iceland's 13 principal ice caps. It is a complex ice cap with 43 named outlet glaciers, either of the valley glacier type (especially prominent on the eastern, more mountainous part of Vatnajökull) or of the lobate type (more typical of the western part of Vatnajökull). The digitally enhanced Plate image captures far more glaciological features than are evident on the standard false-color composite image. The latter was made into an image map by the U.S. Geological Survey (1976b).

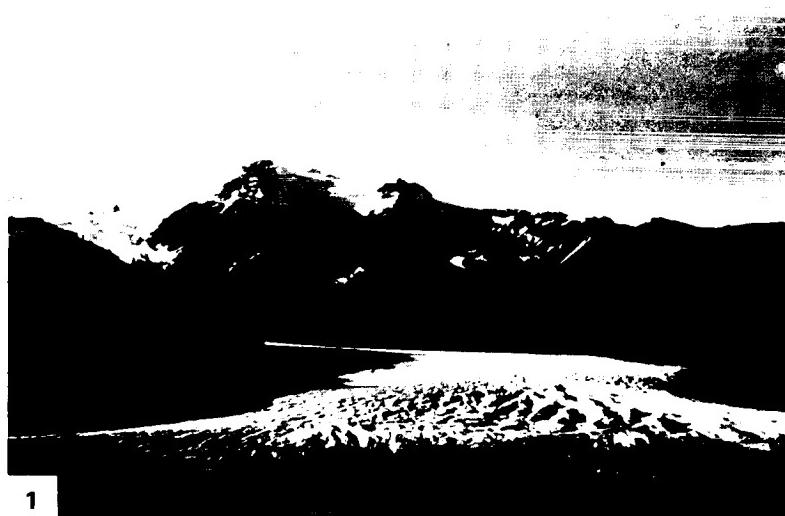
The index map shows some of the principal geographic, glaciological, and geological features associated with Vatnajökull and surrounding areas (Williams, 1976; Williams et al., 1974, 1975). This map also serves as a reference map for other types of glaciers and landforms associated with glaciers that are discussed in this chapter: the surging glacier, Eyjabakkajökull (A) (Plate G-10); the accumulation/ablation zone of a glacier (Figures 9-5 through 9-9) terminal and recessional moraines associated with Múlajökull (Figure G-15.1), one of the outlet glaciers from Hofsjökull; medial moraine at Breidamerkurjökull (C) (Plate G-16) lateral moraine at Kvíárjökull (D) (also Plate G-16); and outwash plain (including proglacial and ice-dammed lakes associated with the glacier, Skeidarárjökull (E) (Plate G-22). A sequence of Landsat images of Skeidarárjökull enabled a "time-lapse" calculation

VATNAJÖKULL, ICELAND

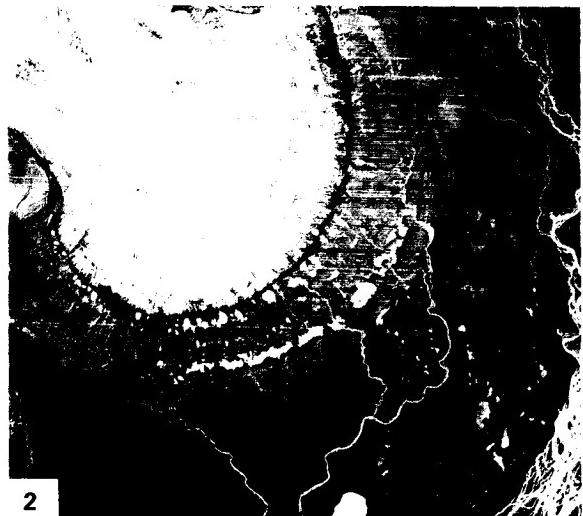
of its average velocity as 2 m per day over an 11-month interval (Williams et al., 1979). Figure G-6.1 is an oblique aerial photograph of Svinafellsjökull (F), one of Vatnajökull's 43 named outlet glaciers. Svinafellsjökull originates in the higher elevations of the glacier-capped stratovolcano, Öraefajökull, then descends to the Skeidararsandur outwash plain (Plate G-22) through a valley. In its lower reaches, it is indistinguishable from a valley glacier (Plate G-9). The crevassed terminus abuts a hummocky and complex series of terminal moraines in the foreground. The outermost terminal moraine, Stóralda, is considered by Thorarinsson (1956a) to have formed about 600 B.C. (See Plate G-16 for a Landsat-3 RBV image of this outlet glacier and others on the eastern margin of Vatnajökull.)

The western part of Vatnajökull has several sites of volcanic and geothermal activity. Grimsvötn ((G) on index map of Plate G-6) is a 30-km² subglacial volcano (see also Plate G-15 and Figure 9-14), the site of volcanic activity in 1934 and in 1983 (see also Figure 9-16 for dormant subglacial volcanoes in Antarctica). Kverkfjöll and Thórdarhyrna have also been sites of historic volcanic activity. Two collapse cauldrons, the result of subglacial geothermal activity, can be seen to the west of the Grimsvötn caldera (between Grimsvötn and Hamarinn) (Thorarinsson et al., 1974; Williams and Thorarinsson, 1974). These collapse cauldrons are even better delineated on a wintertime image of Vatnajökull (Plate G-15) (U.S. Geological Survey, 1977).

Figure G-6.2 is a vertical aerial photograph of Múlajökull, an outlet glacier from the Hofsjökull ice cap in central Iceland. Note the transverse and longitudinal crevasse patterns up-glacier from the terminus, the result of stress in the ice as Múlajökull splayes out in a near-piedmont glacier after it emerges from confinement in the valley (see Plate G-6). The concentric recessional moraines are shown in Figure G-15.1. Between the terminus and the innermost recessional moraine is till, probably including some buried dead ice, with many glacial and proglacial lakes. Figure G-6.3 is a Landsat image of the mouth of the Byrd Glacier, Antarctica, the Earth's largest outlet glacier in terms of discharge. The image shows the glacier as it crosses the Transantarctic Mountains to merge with the western edge of the Ross Ice Shelf. **Landsat 1426-12070, September 22, 1973.**

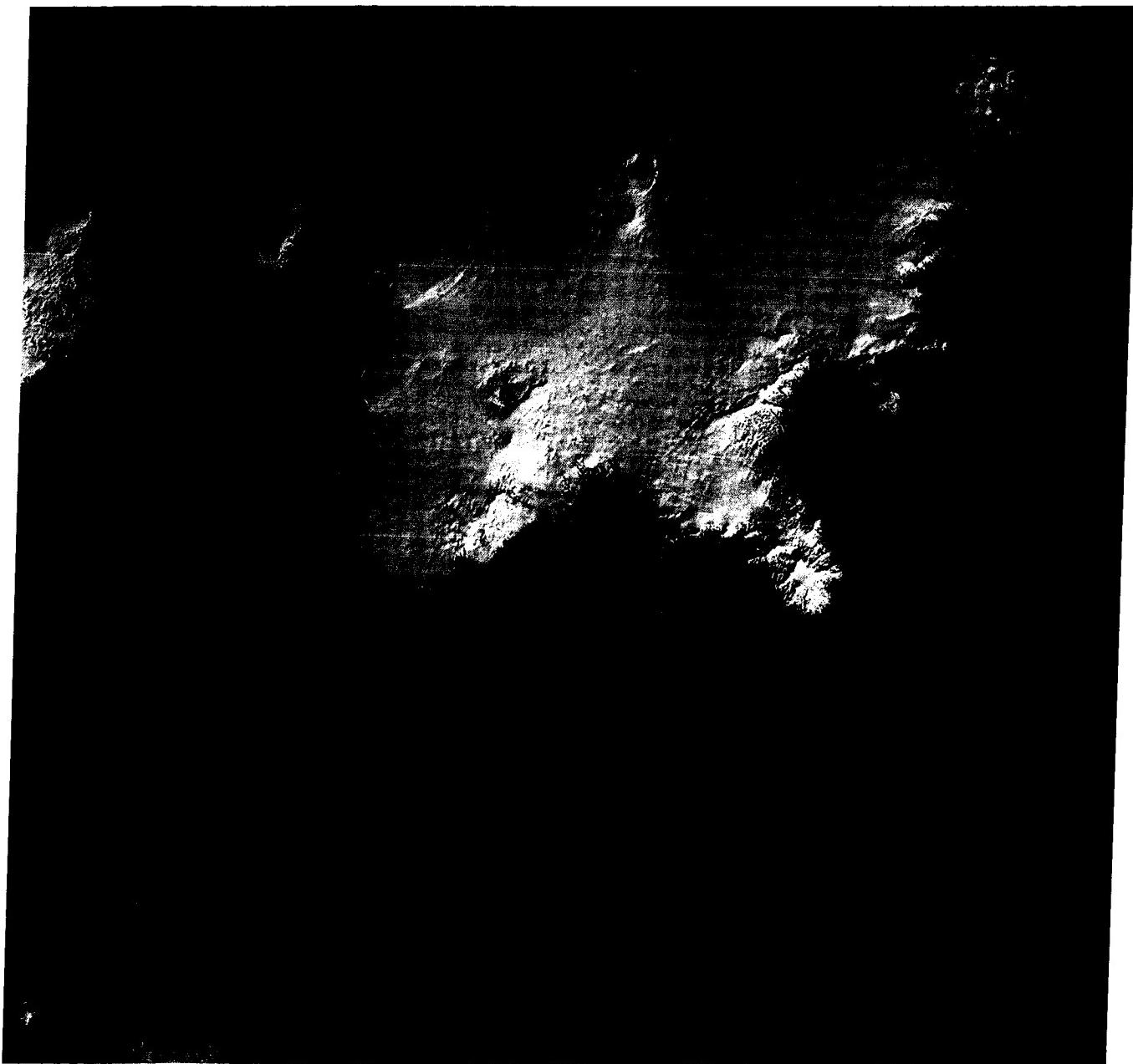


1



2

ORIGINAL PAGE
COLOR PHOTOGRAPH



3

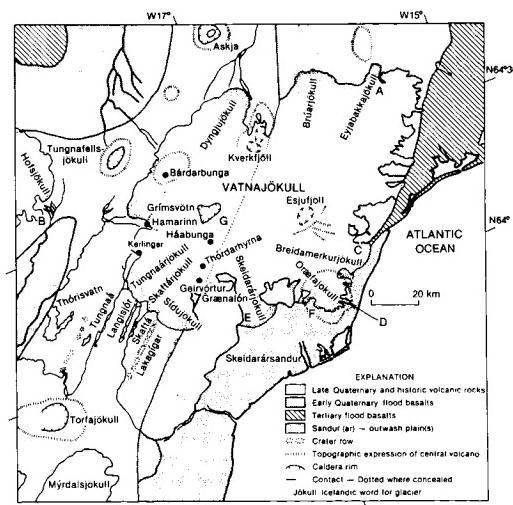


PLATE G-7

A piedmont glacier can be defined as "the lobe-shaped, expanded, terminal part of a valley glacier [see Plate G-9] spread out over broad lowlands at the base of mountains" (Armstrong et al., 1973). Piedmont glaciers are also associated with outlet glaciers and are common in glaciated mountainous areas fringed by a coastal plain or by a region of low relief. In Plate G-8, several valley glaciers on Bylot Island have an expanded, fan-shaped terminus typical of piedmont glaciers. In this Plate and Plate G-22, Skeidarárjökull, one of the many outlet glaciers from Vatnajökull, has the characteristic lobate form of piedmont glaciers at its terminus.

The classic type locality of the piedmont glacier, however, is the Malaspina Glacier in southeastern Alaska (Sharp, 1958b). Plate G-7 is a Landsat MSS image of the Malaspina Glacier. The Malaspina Glacier is an extremely complex glacier, deriving its ice from multiple highland sources, although its main source is the Seward Glacier, as seen in the index map of the area (from Sharp, 1958b). The Malaspina Glacier nearly reaches sea level at Sitkagi Bluffs on the Gulf of Alaska.

As Field (1975, p. 233) pointed out, "The Seward/Malaspina complex is a huge body of ice consisting of an extensive névé or icefield, the "upper" Seward Glacier, and a much narrower "lower" outlet glacier through which ice drains to the enormous piedmont of the Malaspina Glacier." Field (1975, p. 235) provides an additional description of the Malaspina Glacier: "The lobate piedmont fronts the coast from the bend of Yakutat Bay to Icy Bay, about 65 km., and from the coast northward to the mountain front its width is about 45 km.; its area is [about] 2195 km². Surface altitudes range from about 25 m. at the outer margin to about 600 m. at the lower end of the Seward Glacier, its main tributary. Other tributaries of considerable size, east to west, are: Hayden and Marvine Glaciers, east of the Seward Glacier, and Agassiz and Libbey Glaciers to the west."

"Seismic exploration shows that the glacier is 610 m thick and its basin extends as much as 300 m below sea level; the evidence indicates that the basin probably originated by central glacial erosion and peripheral deposition (Allen and Smith, 1953)."

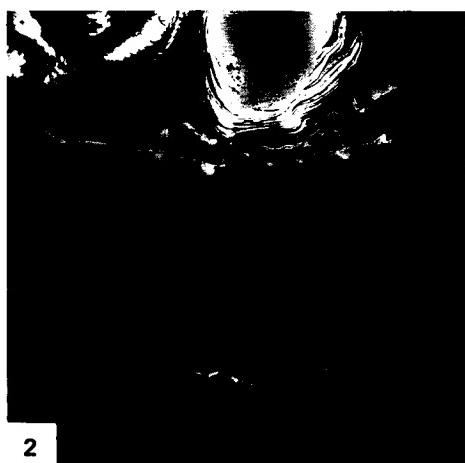
Only satellite images can provide a complete overview of the Malaspina Glacier because of its large area. Sharp (1958a), for example, had to compile a mosaic of about 100 vertical aerial photographs in his study of the contorted moraines. In this Plate, the three distinctly different parts of the Malaspina Glacier can be clearly delineated (see index map): (A) the western lobe, whose primary source is the Agassiz Glacier, 5 km wide where it exits

MALASPINA GLACIER, ALASKA

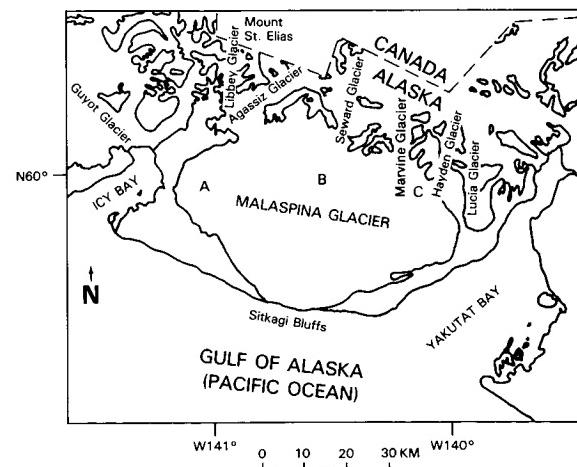
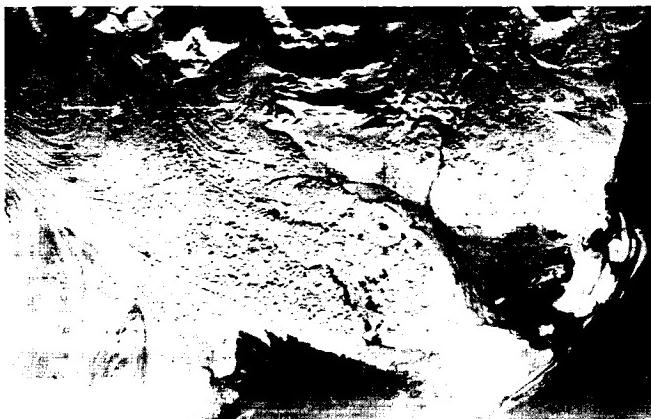
its valley; (B) the central lobe, whose source is the Seward Glacier, only 4 km wide where it leaves its valley; and (C) the smaller eastern lobe, whose source is the Hayden and Marvine Glaciers (index map).

The flow of such a huge volume of glacier ice through narrow valleys before fanning out on the coastal plain causes erratic variations in the velocity of glacier flow, manifested so clearly by the contorted moraines characteristic of the central lobe of the Malaspina Glacier (Figure G-7.1, an oblique aerial photograph of the eastern part of the Malaspina Glacier taken on August 15, 1969). Contorted moraines on a glacier are an indication of surge behavior. Field (1975, p. 236) notes that, "Post (1969) classified [a] tributary of the Agassiz, the entire Seward Glacier, the Hayden and Marvine Glaciers, and the eastern two-thirds of the Malaspina as surging glaciers." The contorted moraines of the eastern edge of the central lobe and the medial moraines along the boundary with the smaller eastern lobe are clearly shown. Mount St. Elias (5492 m) can be seen in the left background, just beyond where the Seward Glacier, the primary source of the Malaspina Glacier, exits from its valley.

The contorted moraines on the eastern side of the central lobe of the Malaspina Glacier have been investigated by Washburn (1935) and Sharp (1958a). They are especially well depicted on Landsat-3 RBV images such as the one obtained on June 11, 1981 (Figure G-7.2), showing the terminus of the Malaspina Glacier and the large contorted moraines that are characteristic of the central lobe. Contorted moraines are also visible on the western lobe. Note also the numerous proglacial lakes along the contact with debris-covered ice and the extensive "pitted" morainic debris in the interlobate area between the western and central lobes. Hall and Ormsby (1983) experimented with combining August 3, 1978, Seasat synthetic aperture radar (SAR) images (scene 05520276) with an August 24, 1979, Landsat image (21675-19482) of the Malaspina Glacier. They found that glacier flow patterns were best shown on the Landsat image, but that the SAR image showed many interlobate features because of radar's greater sensitivity to surface roughness (e.g., heavily crevassed areas), and the low reflectivity of the debris-covered surface made analysis of the Landsat image difficult. The same conclusion that Hall and Ormsby (1983) made with regard to the Seasat SAR image can also be reached by analyzing a side-looking airborne radar (SLAR or SLR) image (X-band) of the upper part of the Malaspina Glacier (Figure G-7.3). **Landsat 2956-19292-7, September 3, 1977.**



ORIGINAL PAGE IS
OF POOR QUALITY



A cirque glacier is defined as "a glacier which occupies a separate rounded recess which it has formed (or modified from a small gully) on a mountain side" (Armstrong et al., 1973). Cirque glaciers are the most common type of glacier found in glacierized mountain regions in temperate latitudes (see Figure G-8.1, from northern Iceland). The cirque erosional landform (see Plate G-12 and Figure 9-20) is also common in such regions and signifies the presence of a glacier at some time in the past. A cirque glacier that expands beyond its basin is in a transition to a valley glacier (Figure G-8.2). Once the cirque glacier expands down-valley, it has evolved into a true valley glacier (see Plate G-9 and Figure 9-20). Several cirque glaciers in the upper reaches of a valley may combine to produce a large composite valley glacier. The erosive power of the main valley glacier greatly exceeds that of the cirque glacier. After the glaciers disappear, the cirque and its downslope extension is left as a "hanging valley" (Figure 9-20) above the main valley.

This Plate is a Landsat MSS false-color composite image of Bylot Island and vicinity, Northwest Territories, Canada, showing cirque glaciers and valley glaciers. Bylot Island is centered at about $73^{\circ}15'N$ latitude and $78^{\circ}30'W$ longitude and is located to the east of the Borden Peninsula off the northeast part of Baffin Island (see Figure G-5.2). It is roughly diamond-shaped, about 180 km long and 110 km at its widest point. The maritime climate ensures an ample supply of snowfall to support the numerous glaciers that dominate the higher elevations of the island (American Geographical Society Glacier Studies, 1975a; Mercer, 1975a). There, the total area of glacial ice is about 4895 km² according to Bird (1967). Glaciers reach the sea on the northern coast at Maud Bight (A) and west of Cape Hay (B) and on the southern coast at the terminus of Sermilik Glacier (C); piedmont glaciers have also formed in several lowland areas, such as at (D). Not much information is known about fluctuations of the glaciers; however, Mercer (1975a), based on work by Falconer (1962), noted that glacier termini generally appear to be stationary or receding, except that the glacier (E) that occupies the valley inland from Bathurst Bay apparently advanced between 1948 and 1958.

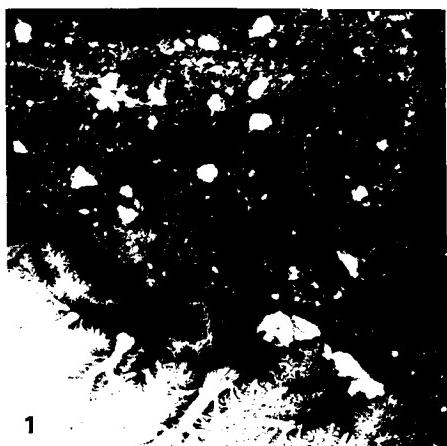
The rugged Byam Martin Mountains, with their resistant core of gneisses (Jackson, 1981), have been extensively modified by glacial erosion. The Landsat MSS image (Plate G-8) shows numerous glacier-filled cirques formed at the heads of valleys (F) and along the valley sides (G). In most cases, the cirque glacier has extended well beyond the cirque to become a true valley glacier (H). Cirques along valley sides are occupied by cirque glaciers that merge with the main valley glacier (I). If Bylot Island were

suddenly to be deglaciated, these valley-side glaciers would become hanging valleys.

Other features associated with glaciers and glacier erosion and deposition can be described from Plate G-8. The knife-edged ridge separating two cirques is called an arête (see also Plate G-12 and Figure 9-20), and numerous arêtes can be seen on the image, such as at (J). When valley glaciers reach lowlands and are no longer constrained by valley walls, their terminal part may spread out in a fan-shaped lobe called a piedmont glacier (D). Therefore, a cirque glacier may extend down-valley as a valley glacier (K) and then spread out over the lowlands as a piedmont glacier. Glacial outwash plains (sandar) (L) are well developed at Bathurst Bay and north of Cape Burney. A medial moraine is prominent on the terminal part of the glacier north of Cape Burney (M). A proglacial lake (N) associated with the small piedmont glacier south of Cape Liverpool has the distinctive robin's-egg blue color of glacial rock flour in suspension. All around the coast of Bylot Island, this distinctive blue signature of sediment-laden glacial meltwater can be seen (O). On the west coast of Bylot Island, two prominent glacial deltas are extending new land into Navy Board Inlet from sediment-laden glacial meltwater emanating from two major glacier systems in each valley (P). Across Navy Board Inlet, on the Borden Peninsula, two small unnamed ice caps and associated outlet glaciers are visible (Q).

Because of the narrow width and relatively low elevation of terminal and lateral moraines, such moraines can generally be only inferred on the Landsat MSS image. Figure G-8.1 is a Landsat-3 RBV of the northeast part of Bylot Island. Although the near threefold increase in spatial resolution make some glacial landforms and glaciological phenomena easier to discern, it does not markedly improve the capability of mapping moraines on Landsat images.

Figure G-8.2 is an oblique aerial photograph of three prominent cirque glaciers, with prominent bergschrunds (headwall crevasses) in the Muskwa Range of the Canadian Rockies, British Columbia, Canada, arêtes separating the cirques, and pyramidal peaks called horns. Note that most of the arêtes are at a fairly uniform level or Gipfelflur (summit plain). Icefalls are characterized by the zone of transverse crevasses where the glaciers exit their respective cirques. Figure G-8.3 is an oblique aerial photograph (August 15, 1981) of a small remnant of a cirque glacier on the northwestern side of Kerling. The cirque has been eroded in Tertiary flood basalts on the southeastern part of the Trollaskagi peninsula of northern Iceland. The view is looking southeast toward the table mountain, Herdubreid (Figure 9-17) in the distant background. Landsat 20204-16513, August 14, 1975.



1



2

ORIGINAL PAGE IS
OF POOR QUALITY

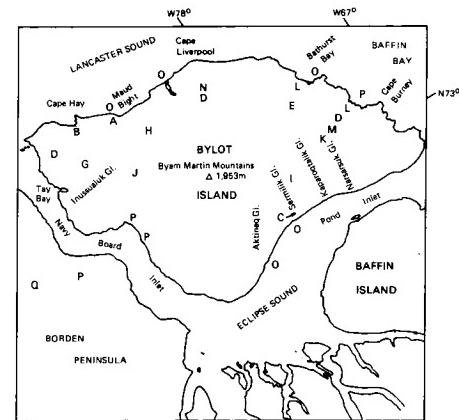
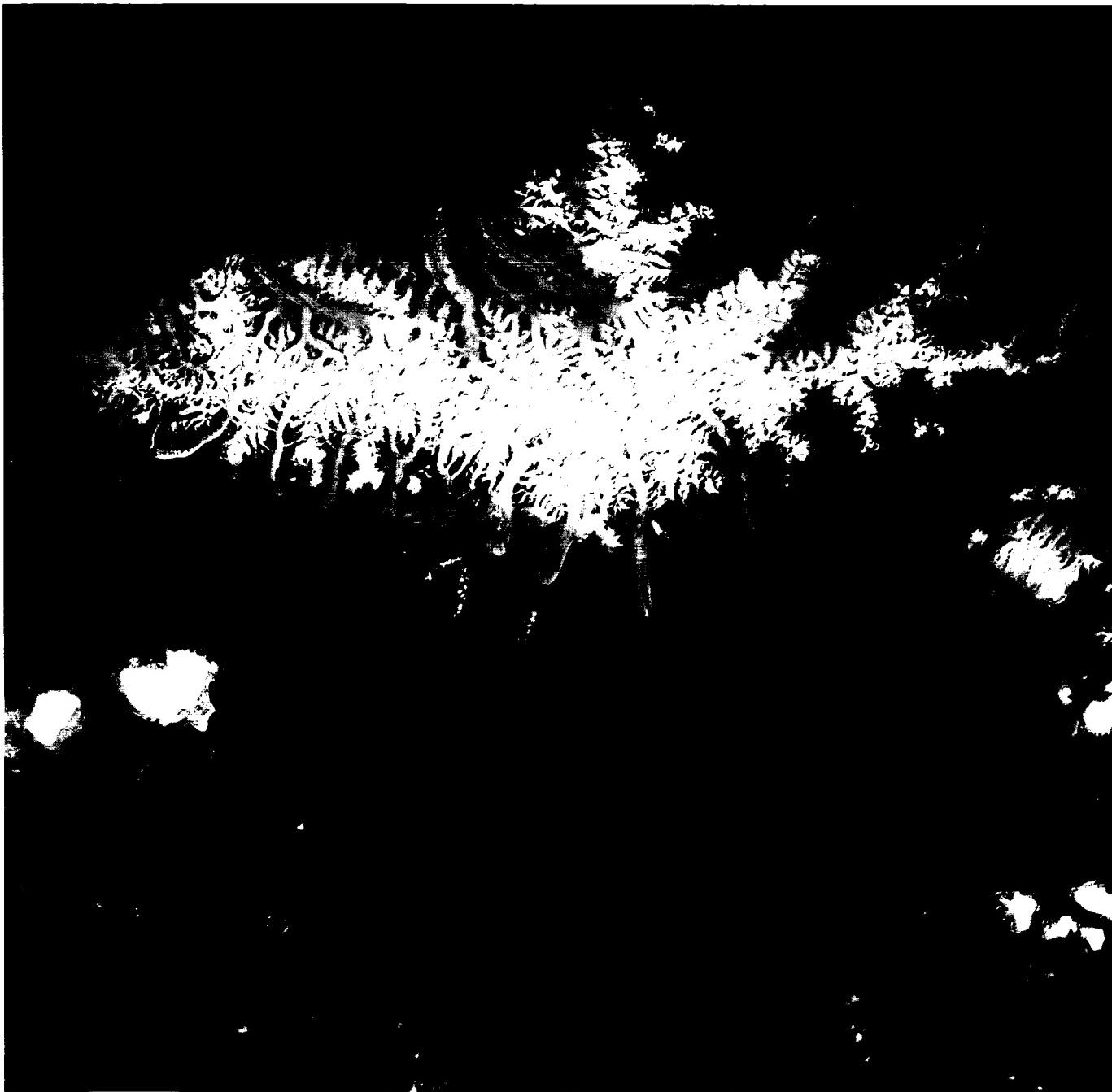


PLATE G-9

MOUNT McKINLEY, ALASKA RANGE, ALASKA

A valley glacier can be defined simply as "a glacier which flows down a valley" (Armstrong et al., 1973). A valley glacier can originate from one or more cirques (Plate G-8) or as an outlet glacier from an ice cap (Plate G-6) or ice sheet (Figure G-6.3). In either case, the glacier ice is constrained to flow within the walls of a valley—a valley that is usually initially created by preglacial stream erosion. Glacial troughs or U-shaped valleys (see Figure 9-20 and Plate G-13), typical landforms resulting from glacial and fluvioglacial erosion, will be discussed in Plates G-12 through G-14. A synonym for valley glacier is alpine glacier, because the latter is the dominant glacier type in the Alps of Europe. Bates and Jackson (1980) define an alpine glacier as "any glacier in a mountain range except an ice cap or ice sheet. It usually originates in a cirque and may flow down into a valley previously carved by a stream."

The higher elevations of the western part of the Alaska Range, especially in the segment that extends 60 km northeast and 90 km southeast of Mt. McKinley, give rise to a large number of valley glaciers that originate from numerous cirques (American Geographical Society Glacier Studies, 1975b). Plate G-9, a Landsat image of part of the western part of the Alaska Range, shows the many valley glaciers, both surging and nonsurging, that originate from cirques on the flanks of the Mt. McKinley massif. The index map shows the principal glaciers of the Mt. McKinley massif, and the overlapping outlines of the Landsat image and the Seasat SAR image (Figure G-9.1) (Denton and Field, 1975). The eight principal valley glaciers can be clearly seen on the southeast side of the western part of the Alaska Range. Three of these glaciers, the Tokositna, Lacuna, and Yentna Glaciers are classified as surging glaciers (Post, 1969) because of their peculiar flow characteristics. As was discussed by Meier (1976):

"Nonsurging glaciers, such as the Ruth and Kahiltna, flow at quite uniform rates of only a few centimeters or tens of centimeters per day, and the medial moraines—dark-colored strips of rock fragments stripped from mountains situated between tributary glaciers—are quite straight and uniform. On the other hand, such surging glaciers as the Tokositna, Lacuna, and especially the Yentna have wiggly folded moraines that result from alternating periods of near stagnation (lasting up to 50 yr) and of extremely high flow rates (lasting 1 to 3 yr when the ice may flow faster than 1.3 m/h.)"

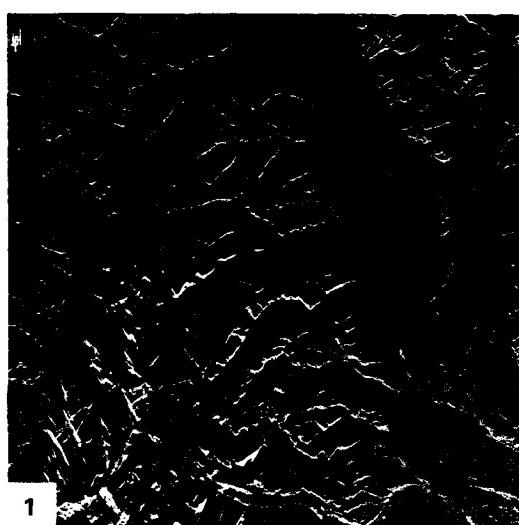
"The Tokositna Glacier had completed [in 1972] a surge that began in 1970. The Lacuna Glacier has been in a stagnant

condition for 40 or more yr, and its dirty mottled surface shows the effects of severe melting. The Yentna Glacier was first observed surging in 1972. This image shows its folded moraines displaced more than 1800 m down valley from their positions shown on recent maps and 1970 aerial photographs. Also visible on the Landsat image is a dark line (i.e., lateral moraine of Yentna Glacier) where the rapidly flowing Yentna Glacier has sheared across the stagnant ice of the Lacuna Glacier."

Figure G-9.1 is a digitally processed Seasat SAR image of the eastern half of the western part of the Alaska Range showing valley glaciers and associated glacial landforms. The SAR image overlaps the northeastern corner of the Landsat image, as can be seen on the index map. The Muldrow Glacier and the Eldridge, Ruth, and Tokositna Glaciers are the main valley glaciers shown on both images. Figure G-9.2, an oblique aerial photograph showing the upper reaches of the Eldridge Glacier on October 4, 1965, shows the coalescence of numerous tributary cirque glaciers that form this large valley glacier. It originates on the southeastern flanks of the Mt. McKinley massif. Mt. McKinley, the highest peak in North America (6195 m), is in the background.

The Seasat SAR image (Figure G-9.1) of part of the Alaska Range was analyzed by John Ford (written communication, 1983) and by Ford et al. (1980). Because radar images are more sensitive to topographic texture, the complex nature of the terminal moraine of both the Eldridge and Ruth (Figure G-9.3) Glaciers is well delineated. Ford (1984) was also able to delineate glacial lakes, fluted ridges, and drumlinized topography along the valleys of the Chulitna and Tokositna Rivers. Figure G-9.3 is an oblique aerial photograph of the terminus, complex terminal moraine, and outwash plain of the Ruth Glacier, a valley glacier that originates on the southern flank of the Mt. McKinley massif.

Hall and Ormsby (1983) did a comparative analysis of a Landsat image (30177-20455, August 29, 1978) of the Alaska Range and the Seasat SAR image (03800083, July 23, 1978) analyzed by Ford (1984). They found that Landsat and Seasat SAR images were equally useful in determining the position of glacier termini, delineation of medial moraines, and depiction of the terminal moraine areas. Landsat images can be used to determine the snowline, but Seasat SAR images cannot. **Landsat 30537-20443-7, August 24, 1979.**

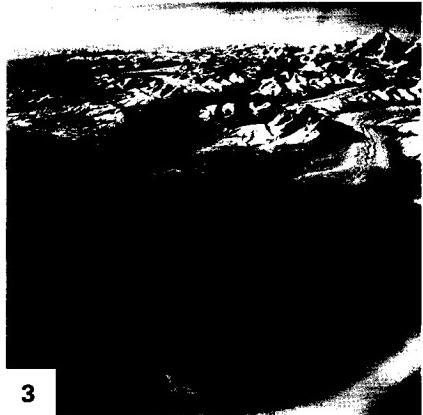


1



2

ORIGINAL PAGE IS
OF POOR QUALITY



3

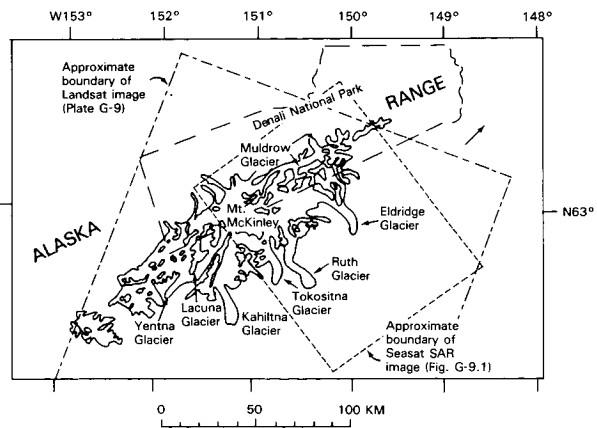


PLATE G-10

A surging glacier is defined as "a glacier that alternates periodically between brief periods (usually one to four years) of very rapid flow, called surges, and longer periods (usually 10 to 100 years) of near stagnation. During a surge, a large volume of ice from an ice-reservoir area is displaced downstream at speeds up to several meters per hour into an ice-receiving area, and the affected portion of the glacier is chaotically crevassed. Only in exceptional cases does the glacier advance beyond its former limit (of surge). In the interval between surges, the ice reservoir is slowly replenished by accumulation and normal ice flow, and the ice in the receiving area is greatly reduced by ablation" (Bates and Jackson, 1980).

A surging glacier is one in which the movement of the ice suddenly increases to several times its normal rate of flow, resulting in an abrupt advance of the terminus amounting to several kilometers or more over a period of a few months (Meier and Post, 1969). During the interval between surges, the lower part of the glacier is in a stagnant state. The surge occurs in the active part of the glacier, and the terminus advances over this zone of inactive ice or "deglaciated" terrain to reach about as far forward as the previous surge. Such precipitous advances may engulf parts of highways, railroads, or other manmade structures and dam adjacent valleys, producing ice-dammed lakes, as in the case of the Moreno Glacier, a surging outlet glacier of the northern Patagonian ice field (see Plate G-4 and Figure G-4.2). The failure of ice-dammed lakes can also cause serious flooding downstream (Williams, 1983d).

Surging glaciers can generally be identified on Landsat MSS images by the looped or crenulated character of medial moraines in the lower parts of such glaciers (Figure G-10.1). The eastern part of the Malaspina Glacier (see Plate G-7 and Figures G-7.1, G-7.2, and G-7.3) and the Tokositna, Lacuna, and Yentna Glaciers of the Mount McKinley massif, Alaska Range (see Plate G-9) are good examples of such contorted moraines. Krimmel et al. (1976) used a Landsat image to identify surging and non-surging glaciers in the Pamir Mountains of the Soviet Union. Post et al. (1976) used Landsat images to measure the motion of the Lowell and Tweedsmuir surging glaciers in the St. Elias Mountains of British Columbia, Canada; Williams (1983f) used successive Landsat images of the surging glacier, Eyjabakkajökull, Iceland, to measure cumulative advances of 1.0 and 2.8 km. Meier (1976) evaluated a Landsat image of the Mount McKinley massif and described three surging valley glaciers (Plate G-9).

A review paper of the distribution of surging glaciers in western North America was prepared by Post (1969). Thorarinsson has discussed those glaciers in Iceland that are known to have surged historically (1964, 1969).

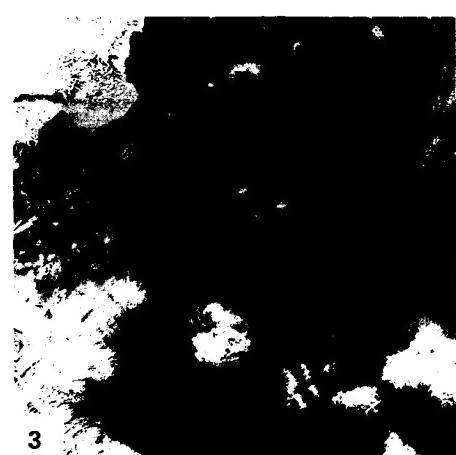
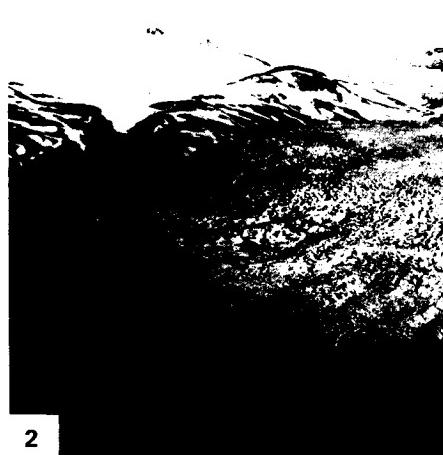
EYJABAKKAJÖKULL, ICELAND

Glacier advance has been noted on a number of sequential Landsat images of Iceland during 1972-1982 (Williams, 1983f). This Plate is a Landsat-3 RBV image of Eyjabakkajökull and Brúarjökull, two of the seven surging outlet glaciers of the Vatnajökull ice cap, Iceland (see Plate G-6). Brúarjökull is in a stagnant phase from its last surge of 8.0 km in 1963-1964 (Thorarinsson, 1969); Eyjabakkajökull is also in a stagnant phase from its 2.8-km surge in 1972-1973. Bare glacial ice of the ablation zone is visible on both glaciers. Figures 9-8 and G-10.2 are oblique aerial photographs of Brúarjökull and Eyjabakkajökull, respectively. Two small ice caps, Thrándarjökull (22 km²) and Hofsjökull (i Lóni), are located to the east of Eyjabakkajökull. A delta is building out into lake Lagarfljót from glacial sediment derived from Eyjabakkajökull. Part of the fjord, Berufjördur, is visible east of Thrándarjökull. Three other Icelandic ice caps, Drangajökull, Langjökull, and Hofsjökull have outlet glaciers that are known to surge (Clapperton, 1975).

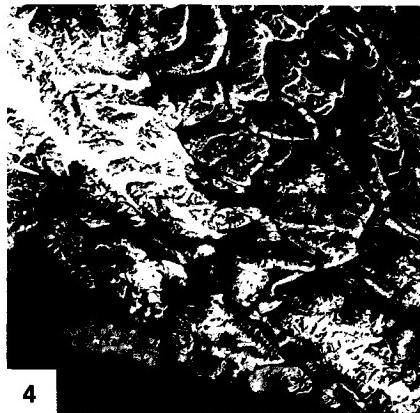
According to Thorarinsson (1969), the first recorded surge of Eyjabakkajökull occurred in 1890, when its terminus suddenly moved forward approximately 0.6 km. During 1972-1973, 82 years later, Eyjabakkajökull surged forward about 2.8 km. It began to surge in late August 1972, and the terminus had already advanced about 1 km by the time the first Landsat image of the area was acquired on October 14, 1972 (1083-12023) (Williams et al., 1974). A September 22, 1973, image (1426-12070; see Plate G-6) showed an additional advance of 1.8 km. Plate G-10 has nearly three times better spatial resolution than the MSS image (Plate G-6) and shows considerably more morphological detail (Williams, 1979; Williams and Ferrigno, 1981). Figure G-10.2 is an oblique aerial photograph looking south across the chaotically crevassed terminus of Eyjabakkajökull as it appeared on July 25, 1973, after it had completed its 2.8-km advance.

Figure G-10.1 is a vertical aerial photograph showing the characteristic contorted medial moraines near the terminus of the surging Klutlan Glacier, Yukon Territory, Canada. Figure G-10.3 is a Landsat image of surging, tidal, and outlet glaciers on four of the several islands of the Svalbard archipelago, Norway. Svalbard has many surging glaciers; Liestøl (in press) notes that 69 of Svalbard's glaciers have surged during the past century. Negribreen, on Spitsbergen, and Bråsvellbreen, on Nordaustlandet, are two surging glaciers that are visible on this image.

Figure G-10.4 is a Landsat image of the Lowell and Tweedsmuir surging glaciers on the western side of the St. Elias Mountains. Also visible is the Hubbard Glacier, a tidal glacier in a fjord in the left center margin of the image. Tidal glaciers are discussed in Plate G-11. Landsat 30157-11565-D, August 9, 1978.



ORIGINAL PAGE IS
OF POOR QUALITY



4

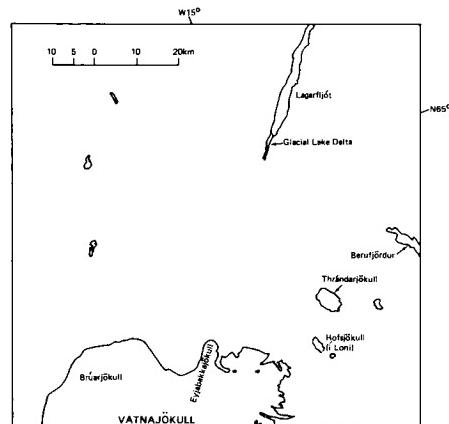


PLATE G-11

A tidal or tidewater glacier is defined as "a glacier that terminates in the sea, where it usually ends in an ice cliff from which icebergs are discharged" (Bates and Jackson, 1980). Tidal glaciers are some of the best-known glaciers in the world because of the relative ease of accessibility to their termini by the public via ship (e.g., Glacier Bay National Monument, Alaska) and because of their awesome beauty—great bluish white cliffs of ice that periodically spall off (calve) into the sea or fjord. Tidal glaciers were much more widespread during the Pleistocene, when many thousands of kilometers of the Antarctic ice sheet and the North American and Eurasian ice sheets terminated as tidal outlet glaciers or ice shelves in the ocean. Today, tidal glaciers are most common in Antarctica (Figure G-11.1; a Landsat view of Pine Island Glacier) (including the Sub-Antarctic islands), Greenland (see Figure G-1.3), Svalbard, Norway (Figure G-10.3), the Arctic islands of the Soviet Union, other Arctic islands, Arctic Canada, the Patagonian and Tierra del Fuego regions (see Plate G-4) of southern South America, and southern and southeastern Alaska.

Southeastern Alaska once had many tidal glaciers, but during the latter part of the Holocene, nearly all of these glaciers retreated well into the heads of their fjords, often in a catastrophic manner. The rapid disintegration of tidal glaciers has been particularly pronounced in the Glacier Bay National Monument area of southeastern Alaska, where a rapid retreat of most glacier termini has been discontinuously observed since the late 18th century. Field (1979) noted that the tidal glacier which had its terminus at the head of Glacier Bay has retreated more than 130 km since 1794. Muir Glacier, which once fully occupied an arm of Glacier Bay called Muir Inlet, retreated 36 km between 1892 and 1976 (Field, 1979).

Farther up the coast from Glacier Bay National Monument is Prince William Sound, a bay off the northern part of the Gulf of Alaska, into which flows one of the last of the great tidal glaciers of Alaska, the Columbia Glacier (Field, 1975). Plate G-11 is a Landsat-3 RBV image of the tidal Columbia Glacier, Prince William Sound, Alaska. The index map shows the location of the glacier and different velocities in m/annum (contour interval of 200 m/annum) measured along its length from its terminus to about 50 km up-glacier (Meier, 1983). The terminus of the glacier has retreated back from its terminal moraine at the head of the fjord and has begun a catastrophic retreat. Note the embayment that has formed in the central part of the terminus. Figure G-11.2 is an oblique aerial photo of the terminus of the

COLUMBIA GLACIER, ALASKA

Columbia Glacier, Prince Williams Sound, Alaska, in July 1976, showing its calving terminus, prominent medial moraines, and crevasse patterns. Figure G-11.3 is an annotated vertical aerial photograph, acquired on December 14, 1984, of Columbia Bay, Prince William Sound, showing successive recessional positions of the terminus of Columbia Glacier during the period August 26, 1978 - December 14, 1984.

Meier (1983) reports that "Columbia Glacier, near Valdez, Alaska, is a fast-flowing glacier of 1,100 km² area that terminates in an iceberg-calving terminus. Ice velocity at the terminus varies seasonally from 4 to 8 m/day, and it currently discharges about 2 km³/annum of icebergs. A fast-moving "ice stream" [Plate G-3] dominates the flow."

The slow retreat of a tidal glacier may suddenly accelerate if it retreats from an end moraine in shallow water to deeper water, resulting in the rapid disintegration of the lower reach of the glacier. Such a situation is occurring at Columbia Glacier, Alaska, where the rapid breakup of its terminus will probably discharge a large volume of small icebergs into Prince William Sound (Meier et al., 1980). If current, wind, and tidal conditions permit, many of these icebergs will drift into the main shipping channel from Valdez, the southern terminus of the trans-Alaska oil pipeline, and perhaps pose a hazard to the giant oil tankers that frequently transit Prince William Sound (Post, 1977).

The Columbia Glacier has been the subject of an intensive scientific study by the U.S. Geological Survey that began in 1974 (Post, 1975). During the course of the study, various types of remotely sensed data have been used, including periodic low-altitude oblique aerial photographs, high- and low-altitude vertical aerial photographs, water-depth determination with hydrographic soundings, Mini-Sparker and Lister Boomer surveys to determine submarine morphology of the terminal-moraine shoal, and airborne and surface radio-echosounding of glacier thickness (Meier et al., 1978). Iceberg plumes have also been mapped from specially enhanced Landsat images (Williams, 1983d).

Figure G-11.1 is a Landsat image of the Pine Island Glacier, an important tidal glacier in West Antarctica that discharges into Pine Island Bay. Williams et al. (1982), working from two Landsat images acquired 750 days apart, calculated an average speed of flow of the terminus of the Pine Island Glacier at 6 m per day. Therefore, this Antarctic tidal glacier flows at about the same speed as the intensively studied Columbia Glacier, an Alaskan tidal glacier. **Landsat 30174-20290-D, August 26, 1978.**



1



2

ORIGINAL PAGE IS
OF POOR QUALITY

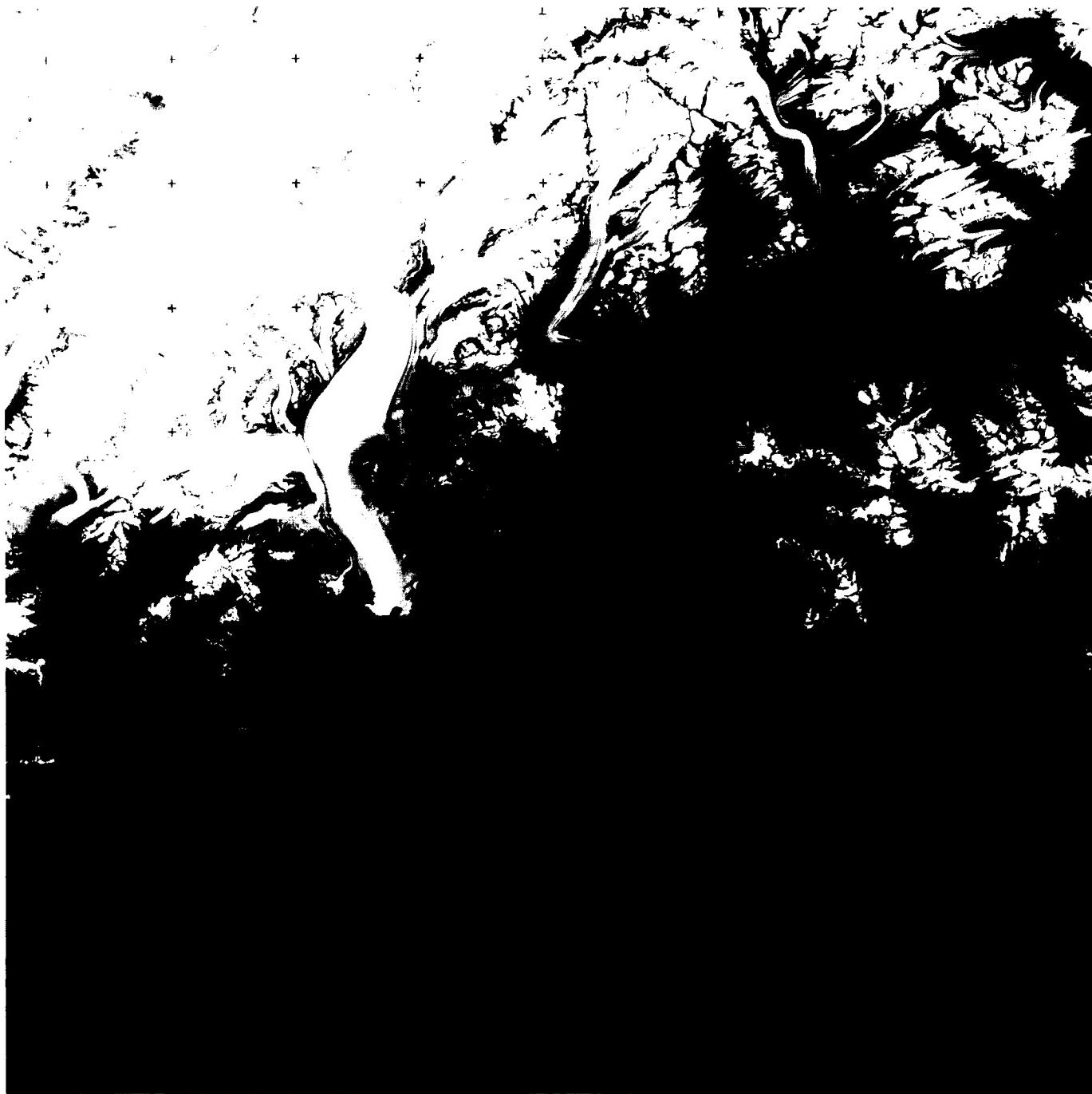


PLATE G-12

A cirque is "a deep steep-walled half-bowl-like recess or hollow, variously described as horseshoe- or crescent-shaped or semi-circular in plan, situated high on the side of a mountain and commonly at the head of a glacial valley, and produced by the erosive activity of a mountain glacier" (Bates and Jackson, 1980). During an active period of glaciation, a cirque is occupied by a cirque glacier or by the head of a valley glacier (see Plate G-8 and Figures G-8.1 and G-8.2). An arête is "a narrow serrate mountain crest or rocky sharp-edged ridge or spur, commonly present above the snowline in rugged mountains (as in the Swiss Alps) sculpted by glaciers, and resulting from the continued backward growth of the walls of adjoining cirques" (Bates and Jackson, 1980) (see also Figures 9-20, G-8.2 and G-12.1). A horn is "a high rocky sharp pointed peak with prominent faces and ridges, bounded by the intersecting walls of three or more cirques that have been cut back into the mountain by headward erosion of glaciers" (Bates and Jackson, 1980) (see Figures 9-20 and G-8.2.). An excellent discussion of the origin of cirques, arêtes, and horns is found in Embleton and King (1975a).

This Plate is a Landsat image of a part of the Ural Mountains of the Soviet Union showing the characteristic scalloped pattern of numerous cirques, some of which contain cirque glaciers. The intercirque ridges on the mountain sides and mountain crests have been eroded into the knife-like ridges (arêtes). Where three or more arêtes intersect, horns are present. The cirques, and associated arêtes and horns, can be readily identified on Landsat and other satellite images or photographs of equivalent or better spatial resolution (see also Figure G-26.2).

According to Horvath (1975), the Ural Mountains (Ural'skiy khrebet) contain a core of crystalline rocks with folded Paleozoic and Mesozoic rocks on the west. The area of the Ural Mountains included in this Plate is called the Subpolar Urals (Pripolarnyy Ural) with the highest mountain peak, Gora (Mount) Narodnaya, reaching 1894 m in elevation. The index map locates

URAL MOUNTAINS, U.S.S.R.

a few of the numerous cirques, arêtes, horns, and cirque glaciers that can be delineated on Plate G-12.

Figure G-12.2 is a Landsat-3 RBV image of part of the northern coast of East Antarctica ($40^{\circ}29'S$, $162^{\circ}31'E$) showing the northern part of the Bowers Mountains (peninsula) and the eastern part of the tidal terminus of the Rennick Glacier (Williams et al., 1982). The image was acquired at a solar elevation angle of only 6° . This low Sun angle highlights the subtle morphological details on the glaciers, such as crevasses and flow features, the topography of the peninsula, and the group of icebergs surrounded by sea ice offshore from the tip (Cape Cheetham) of the Stuhlinger Ice Piedmont. According to Armstrong et al. (1973), an ice piedmont is a variation of the piedmont glacier (Plate G-7) and is defined as "ice covering a coastal strip of low-lying land backed by mountains. The surface of an ice piedmont slopes gently seawards and may be anything from 1 to 50 km wide, fringing long stretches of coastline with ice cliffs. Ice piedmonts frequently merge into ice shelves [see Plate G-2]." Of particular interest are the shadows cast by the arêtes along the ridge crests on the western side of the peninsula. The solar azimuth angle is $65^{\circ}E$; because the ridges trend about $10^{\circ}W$, the illumination is nearly at right angles. The jagged nature of the arête landform is clearly evident in the shadows that are cast on the Rennick Glacier.

Figures G-12.1 and G-12.3 are a pair of oblique aerial photographs of cirques, cirque glaciers, arêtes, and horns that are characteristic of the southeastern coast of Greenland and often visible to airline passengers flying the Great Circle route between eastern United States and northern Europe. Fog banks fill most of the valleys in the two photographs. Figure 9-19 is a view of an ice-sculpted massif in the Patagonian region of South America. Compare the geometry of the shadows cast by the arêtes on Figure G-12.2 with Figures G-12.1, G-12.3, and 9-19. **Landsat 1330-07040-7, June 25, 1973.**



1



2

ORIGINAL PAGE IS
OF POOR QUALITY

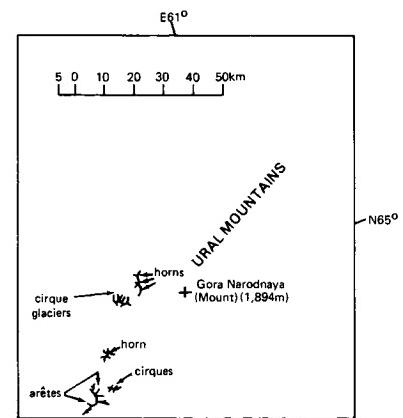


PLATE G-13

A glacial trough is "a deep, steep-sided *U-shaped valley* leading down from a cirque, and excavated by an alpine glacier that has widened, deepened, and straightened a preglacial river valley; e.g., Yosemite Valley, California" (Bates and Jackson, 1980). Although glacial troughs generally have a parabolic form in cross section, differential erosion by a glacier along the valley can result in a crossprofile that varies considerably from the U-shape. Embleton and King (1975a) give a thorough discussion of glaciated valleys and various theories, some controversial, about the formation of landforms associated with glaciated valleys. Linton (1963) classified glacial troughs into four major types: alpine, Icelandic, composite, and intrusive.

Figure 9-20 presents a schematic representation (from Davis, 1909) of the erosional evolution of a mountain range from preglacier to postglacier time. The left-hand sketch shows the main valley glacier and the tributaries with the same surface level. After the period of glaciation ends, the smaller tributary valleys are indicated in the right-hand sketch as suspended above the U-shaped main valley or glacial trough. The erosive power of the valley glacier also truncates the ridges between the tributary glaciers, leaving a characteristic flatiron appearance to the ends of these ridges after the valley glacier has melted (see Figure G-13.1).

This Plate is a subscene from a Landsat image of the mountainous peninsula, Tröllaskagi, between Eyjafjördur and Skagafjördur, two of several fjords that occur along the northwest, north, and east coasts of Iceland. Tröllaskagi has more than 100 alpine glaciers, primarily of the cirque and valley glacier type (Björnsson, 1980). In the previous section on cirques and arêtes (Plate G-12), it was noted that cirques and arêtes have a distinctive pattern on satellite images of glacierized areas, and Tröllaskagi clearly shows these two landforms, as well as numerous other landforms associated with glacial erosion. All the principal types of landforms resulting from glacial erosion visible on Landsat images appear in Plate G-13: cirques (A), cirque glaciers (B), arêtes (C), hanging valleys (D), glacial troughs or U-shaped valleys (E), and fjords (drowned U-shaped valleys) (F).

Tröllaskagi is underlain by tholeiitic plateau basalts of Tertiary age (Saemundsson, 1980) that have been subjected to

TRÖLLASKAGI, ICELAND

repeated periods of glaciation, perhaps as many as 10 distinct glaciations if based on the stratigraphic record on Tjörnes, the second peninsula to the east (Einarsson et al., 1967). During the Late Pleistocene, Eyjafjördur and Skagafjördur were occupied by large and powerful ice streams (see Plate G-3) that flowed within preglacial valleys and drained the central northern edge of the large ice sheet that covered most of Iceland. Because the Tröllaskagi peninsula was near the northern edge of the ice cap, some of the higher ridges may have been exposed as nunataks above the surrounding ice. Smaller glaciers would have fed the larger valley glaciers from tributary valleys. Figure G-13.1 is a ground photograph looking across Eyjafjördur at a group of hanging valleys on the southeast side of Hvammsfjall, which formerly contained small valley glaciers. These small valley glaciers were tributaries to the larger valley glacier that flowed down Hörgárdalur into the main ice stream in Eyjafjördur. Eyjafjördur is a fjord (Plate G-14) or a special type of glacial trough or U-shaped valley that was further inundated by rising sea level during the Holocene. The depth of Eyjafjördur opposite Hvammsfjall, which reaches an elevation of 1000 m on the west side, is 81 m. The elevation of the floors of the hanging valleys is about 500 m, giving approximately 600 m of relief between the floors of the hanging valleys and the bottom of Eyjafjördur. The bottom of the valley glacier in Hörgárdalur, another tributary glacier to the main ice stream, would have met the main ice stream in Eyjafjördur about 100 m above the bottom of the ice stream and about 400 m below the floors of the hanging valleys.

Figures G-13.2 and G-13.3 are two examples of glaciated valleys photographed in Canada and Switzerland, respectively. Figure G-13.2 shows a U-shaped valley in the Bridge River area of British Columbia. Figure G-13.3 depicts the glacially modified landscape of the Swiss Alps looking east from Riederapf, southern Switzerland, across the Rhône Valley toward Turbhorn (3244 m) and other peaks that border Switzerland and Italy. During the Pleistocene, this compound-glaciated valley (glacial trough) was occupied by a large glacier that was fed by many tributary glaciers. The horns and arêtes in the background probably rose above the ice as nunataks (see Figure G-4.3). **Landsat 22045-12124-7, August 28, 1980.**

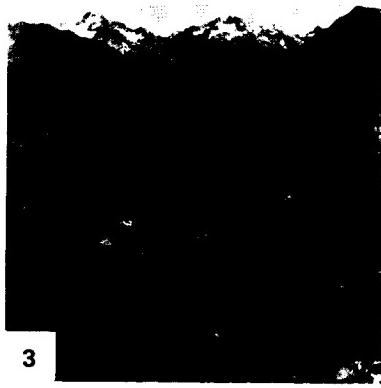


1



2

ORIGINAL PAGE IS
OF POOR QUALITY



3

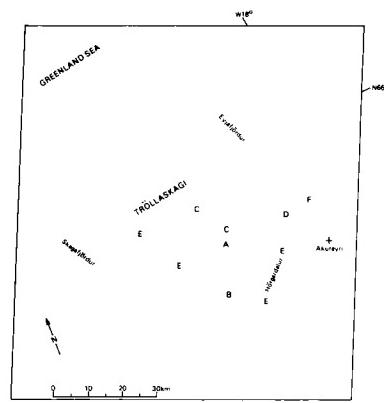


PLATE G-14

SØNDRE STRØMFJORD, WESTERN GREENLAND

A fjord is "a long narrow winding inlet or arm of the sea, U-shaped and steep-walled, generally several hundred meters deep, between high rocky cliffs or slopes along a mountainous coast; typically with a shallow sill or threshold of solid rock or earth material submerged near its mouth and becoming deeper inland." A fjord usually represents the seaward end of a deeply excavated glacial-trough valley that is partially [sic, further] submerged after the melting of the ice. Examples: along the glaciated coasts of [Chile, Iceland, British Columbia, New Zealand] Alaska, Greenland, and Norway" (Bates and Jackson, 1980). It should be emphasized that the ice stream which formed the fjord had already eroded the valley far below sea level and that the sea simply occupies this vacated glacial trough.

In the previous two Plates, various landforms associated with glacial erosion, which can be delineated on Landsat images, have been discussed: cirques, arêtes, glacial troughs, hanging valleys, and fjords. In the following discussion of the fjord landform, one should keep in mind that the cirque, glacial trough or U-shaped valley, hanging valley, and fjord are really only variations on the same theme and, in glaciated coastal areas, generally occur together (Plate G-13). A cirque is a bowl-shaped feature in a mountain ridge; a U-shaped valley or glacial trough is an erosional modification of a preexisting valley by a valley glacier originating in a cirque, an outlet glacier originating from an ice cap, or an ice stream originating from an ice sheet; and a fjord is a flooded glacial trough in a coastal region (Grosval'd and Glazovskiy, 1984).

This Plate is a false-color composite Landsat image of Søndre Strømfjord, one of the longest fjords in Greenland. Søndre Strømfjord extends for approximately 160 km in a north-easterly direction from its mouth at Davis Strait to the glacial delta at its head. The delta (B) is slowly infilling the fjord from glacial sediment derived from the Greenland Ice Sheet, the edge of which can be seen in the eastern part of the image.

It is likely that Søndre Strømfjord owes its location to a preexisting valley that had formed along a structural feature, such as a fault. In fact, structural (fracture-pattern) control of the fjords, lake basins, and glaciofluvial valleys is clearly evident on the Plate image because of their preferred orientations to the east or northeast. From the head and extending for about 90 km in a southwesterly direction, the fjord cuts across granodioritic gneisses (Escher, 1970; Escher and Watt, 1976). Glaciofluvial deposits occur from the edge of the Greenland Ice Sheet (A) across the delta (B) at the head of the fjord. Except for occasional marine deposits in the tributary valleys, the walls of the fjord are bare bedrock (Weidick, n.d.). Also at the edge of the ice sheet, three

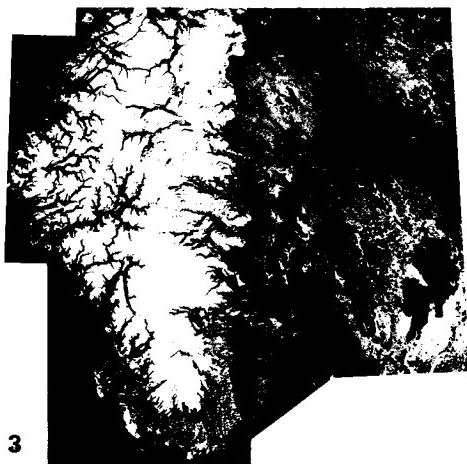
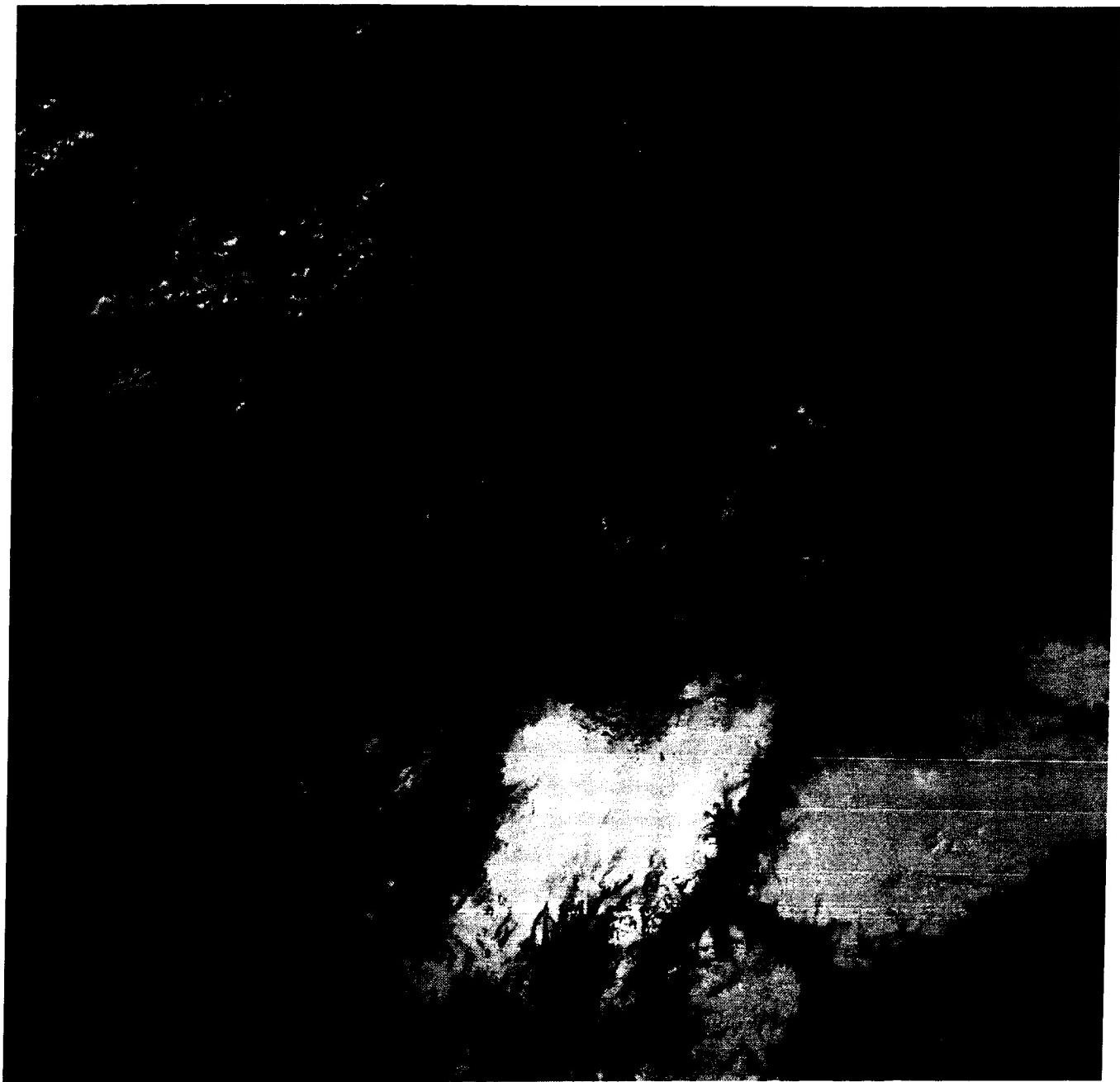
nunataks (D), medial moraines (E), and the terminal moraine (F) can be easily delineated.

During the Pleistocene, Søndre Strømfjord was once occupied by a fast-flowing ice stream within the main Greenland Ice Sheet that reached to the present coast and beyond. Sukkertoppen ice cap on the south would have coalesced into the main ice sheet and contributed part of its outflow down the present fjord during that time. A few of the outlet glaciers from the northwestern margin of Sukkertoppen extend toward the fjord, with the longest outlet glacier building a delta into the fjord at (C). A good modern analog to the setting of the Søndre Strømfjord ice stream during the Pleistocene is shown in Plate G-3, a Landsat image of the Jakobshavns Isbrae and ice stream. At the beginning of the Holocene (about 10 000 years B.P.), as the great ice sheets of the Pleistocene continued to melt away rapidly, sea level was approximately 75 m lower than at present. In western Greenland, sea level rose to inundate coastal areas before the land experienced delayed isostatic rebound from the loss of ice along the coastal margin. Crustal rebound produced reemergence of the land, so the relationship between sea level and the land has been complex during the last 10 millennia. The present sea level has further inundated the glacial trough of Søndre Strømfjord, thereby creating a spectacular long fjord. Most fjords are quite deep and represent substantial glacial erosion or bedrock well below present or even Pleistocene sea levels. The deepest known fjord, more than 2000 m below sea level, is in Antarctica. Sognefjord, Norway, has a maximum depth of 1308 m (Embleton and King, 1975a).

Figure G-14.1 is an aerial view of Søndre Strømfjord, about 120 km inland from its mouth, looking northeast along the fjord toward the head of the fjord, with the edge of the Greenland Ice Sheet visible about 70 km in the distant background. A layer of clouds lies just above the horizon. Figure G-14.2 is an aerial oblique view of a 20-km long fjord, Seydisfjördur, on the east coast of Iceland, which cuts through Tertiary plateau basalts. A hanging cirque is visible high up on the valley side east of the town of Seydisfjördur at the head of the fjord. The relief between the crests of the ridges and the bottom of the fjord is about 1000 m. Figure G-14.3 is a Landsat image mosaic of southern Norway and part of Sweden showing the classic region of fjords along the coast of Norway. The regional fracture patterns exercise a marked control on the orientation of fjords. The fjords are enhanced on the Landsat image because of residual snow cover in the highlands during May-June, 1973. **Landsat 21654-14185, August 3, 1979.**



ORIGINAL PAGE
COLOR PHOTOGRAPH



3

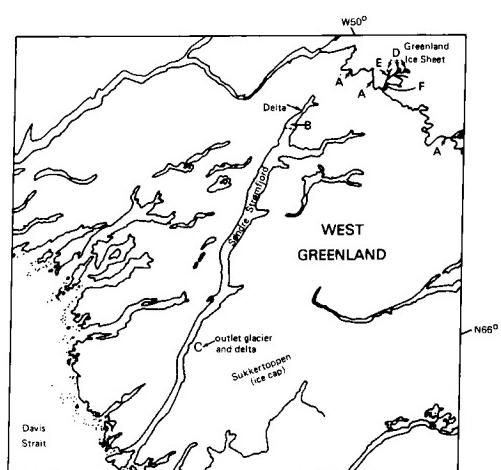


PLATE G-15

HOF SJÖKULL AND VATNAJÖKULL, ICELAND

A terminal moraine is "the end moraine, extending across a glacial valley as an arcuate or crescentic ridge, that marks the farthest advance or maximum extent of a glacier; the outermost end moraine of a glacier or ice sheet. It is formed at or near a more-or-less stationary edge, or at a place marking the cessation of an important glacial advance" (Bates and Jackson, 1980; see also Figures 9-21 and 9-22a). A recessional moraine is "an end or lateral moraine built during a temporary but significant pause in the final retreat of a glacier. Also, a moraine built during a slight or minor readvance of the ice front during a period of general recession" (Bates and Jackson, 1980; also Figure 9-22a).

The grouping by Ritter (1978) of terminal, recessional, and lateral moraines under the single category of end moraines (Table 9-6) was discussed in the introductory part of the section on glacial and fluvioglacial deposition (p. 533 of this chapter). Although lateral moraines grade into terminal and recessional moraines, they also extend for a considerable distance up-glacier along the valley walls of a valley or outlet glacier, as will be examined separately in Plate G-16.

Although terminal and lateral moraines can have considerable lateral extent, a few to many tens of kilometers or more, their cross-sectional dimension is usually only a few tens of meters, although some are several kilometers wide (Plate G-21). End moraines also have a pronounced third dimension, usually a few tens of meters, and can be easily mapped on stereopairs of aerial photographs. On Landsat MSS images, however, which are in two dimensions and have a picture element (pixel) of 79 m, end moraines are difficult to map. Except in a few rare cases, only Landsat images of glaciated areas acquired at a low solar elevation angle provide a good opportunity to delineate terminal and recessional moraines.

This Plate is a Landsat image of part of south-central and southeastern Iceland. The image was acquired at a solar elevation angle of only 7° and with much of the land snowcovered. Landforms with subtle morphologic expression, such as terminal, recessional, and medial moraines, stand out because of shadows cast by the low Sun angle. Various terminal and recessional moraines visible on Plate G-15 are associated with the Hofsjökull and Vatnajökull ice caps, as seen in the index map. (Consult the

index map for Plate G-6 for information on the geology and principal geographic features within the area encompassed by the image.)

Subglacial volcanic calderas are noted at Kverkfjöll and Grímsvötn, both of which are discussed briefly in the section on subglacial volcanoes (Figure 9-14). Collapse cauldrons caused by subglacial volcanic and/or geothermal activity are identified west of Grímsvötn. A comprehensive discussion of Plate G-15 is found in Williams and Thorarinsson (1974) and Thorarinsson et al. (1974). Plate G-6 is a Landsat MSS false-color composite of the same area in late summer, which should be used for comparison. Terminal moraines can be seen at the following outlet glaciers of Vatnajökull: a belt in front of Skeidarárjökull (A), single moraines in front of Sídujökull (B), on the northwest margin of Vatnajökull (C), and on the northeastern margin of Hofsjökull (D). Recessional moraines are visible at Mulajökull (E) (Figure G-15.1), a prominent outlet glacier of Hofsjökull, and along the eastern margin (F) of Hofsjökull (Figure G-15.2). Figure G-15.2 is a view looking north-northeast with the lobe of an outlet glacier in the left background. Note the V-shaped angle of the moraines, which resulted from the arcuate merger of two lobes from Hofsjökull. Arcuate medial moraines are visible on Dyngjujökull (G) (Figure G-16.2) and north of Breidamerkurjökull (H). On the late summer image of the area (Plate G-6), none of the end moraines can be detected, only the two medial moraines. The medial moraines are visible on summer images because the morainal material contrasts so sharply with the surrounding ice. On the wintertime image (Plate G-15), the medial moraines, although snow-covered, stand out sharply because of their relief, which is accentuated by the shadow cast by the low angle (7°) of solar illumination. Although of less relief than the medial moraines, the terminal and recessional moraines also are visible under the low solar angle of illumination.

Figure G-15.3 is a southward-looking view of a terminal moraine on the west side of the Greenland Ice Sheet approximately 40 km east of the head of Søndre Strømfjord described in the section on fjords (Plate G-14). The edge of the Greenland Ice Sheet, where the photograph was taken, is shown by that Plate. **Landsat 1192-12084-7, January 31, 1973.**

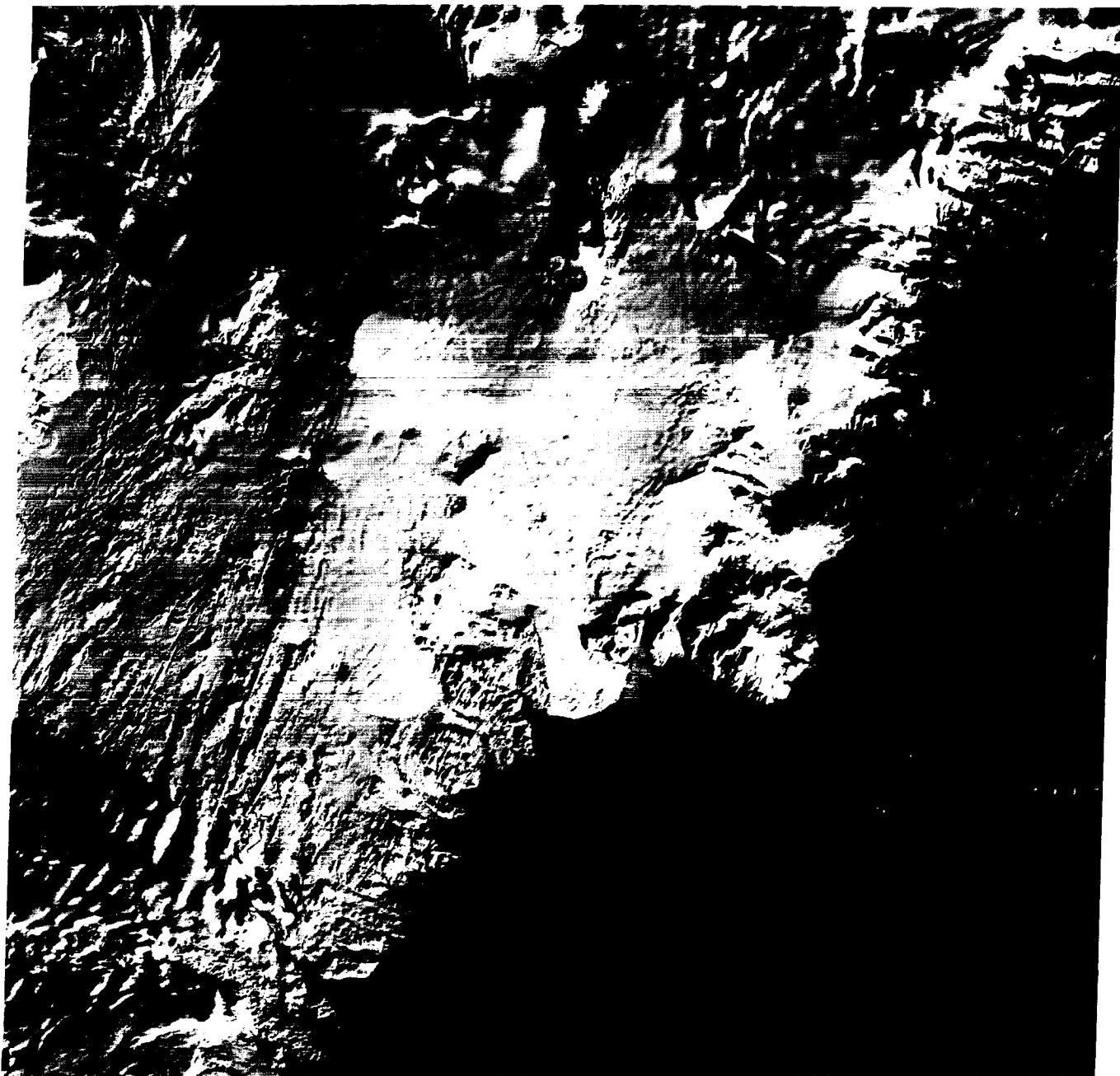


1



2

ORIGINAL PAGE IS
OF POOR QUALITY



3

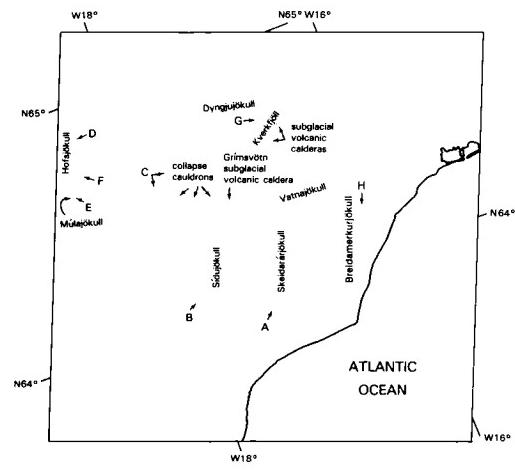


PLATE G-16

BREIDAMERKURJÖKULL, SOUTHEASTERN ICELAND

A lateral moraine is “(a) A low ridgelike moraine carried on, or deposited at or near, the side margin of a mountain glacier. It is composed chiefly of rock fragments loosened from the valley walls by glacial abrasion and plucking, or fallen onto the ice from the bordering slopes. (b) An end moraine built along the side margin of a glacial lobe occupying a valley” (Bates and Jackson, 1980).

A medial moraine is defined as “(a) An elongate moraine carried in or upon the middle (or near the margins) of a glacier and parallel to its sides (or lobes), usually formed by the merging of adjacent and inner lateral moraines below the junction of two coalescing valley (or outlet) glaciers. (b) A moraine formed by glacial abrasion of a rocky protuberance (nunatak) near the middle of a glacier and whose debris appears at the glacier surface in the ablation area” (Bates and Jackson, 1980).

Lateral moraines (Figure G-16.1; Steingletscher, Switzerland) grade into terminal moraines at the terminus of a glacier (Figure 9-21). On Landsat MSS images, lateral moraines are difficult to delineate because they are composed of the same materials as the valley walls and thus have comparable reflectivity. The same problem exists with Landsat-3 RBV images, even with a nearly threefold improvement in pixel resolution over the MSS image (30 m versus 79 m), but the greater resolution makes delineation somewhat more probable. When Plate G-16 is viewed at high magnification, very narrow ribbons of darker material can be distinguished at the margins of the Skaftafellsjökull and Svinafellsjökull outlet glaciers (see index map). The most distinctive lateral moraines, however, are those associated with the terminus (F) of Kvíárfjökkull, one of the outlet glaciers from Oraefajökull in the southern part of Vatnajökull (Williams, 1983e).

Medial moraines are characteristic glacier-surface features wherever two or more glaciers, valley or outlet, merge in their descent from higher to lower elevations. In this case, such a moraine represents the confluence of two lateral moraines (Figure G-16.2; Kaskawulsh Glacier, Yukon), which then continues as a medial (or interlobate) moraine (Figure G-16.3; Aletsch Glacier, Switzerland). A medial moraine is far easier to see on space imagery than lateral moraines because it is set against a high-contrast (white) background. Medial moraines are visible on several of the outlet glaciers of Vatnajökull, Iceland, especially those that flow as valley glaciers in the southeastern quadrant of the ice cap (see Plate G-6 and its index map). Of particular interest are the three pronounced medial moraines visible on the ablation area of Breidamerkurjökull, the largest outlet glacier that drains Vatnajökull on the southeastern part of the ice cap.

This Plate is a Landsat-3 RBV image that clearly shows the three principal and several minor medial moraines on Breidamerkurjökull. The largest medial moraine is called Esju-fjallarönd (A on the index map) because it originates from two nunataks in the Esjufjöll area (B). As the glacier flows around these two nunataks, material is eroded and carried down-glacier as a medial moraine. The first segment is about 8 km long from the smaller nunatak to where it joins another medial moraine below the larger nunatak. Both medial moraines, now joined, continue for nearly 14 km to the terminus of Breidamerkurjökull. In the upper part of the glacier, the medial moraine is very narrow, only about 100 m wide. Near the terminus of the glacier, however, it broadens to as much as 1 km or more (see also Figures G-16.1 and G-16.2). Two other medial moraines of Breidamerkurjökull are visible at (C) and (D). Prominent medial moraines can also be seen on Morsárfjökkull (E), Kvíárfjökkull (F), and Heinabergsjökull (G). Svinafellsjökull (H), one of the outlet glaciers from the Öraefajökull ice cap, was previously discussed in the section on outlet glaciers (Plate G-6).

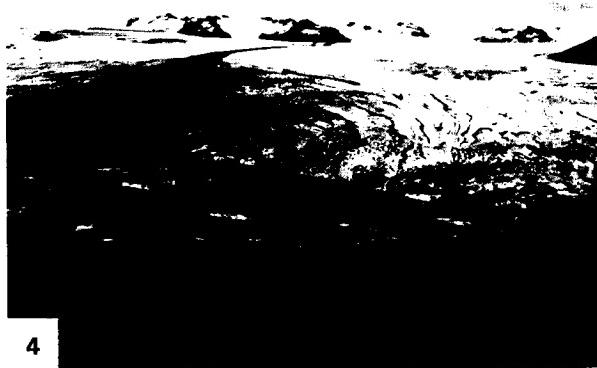
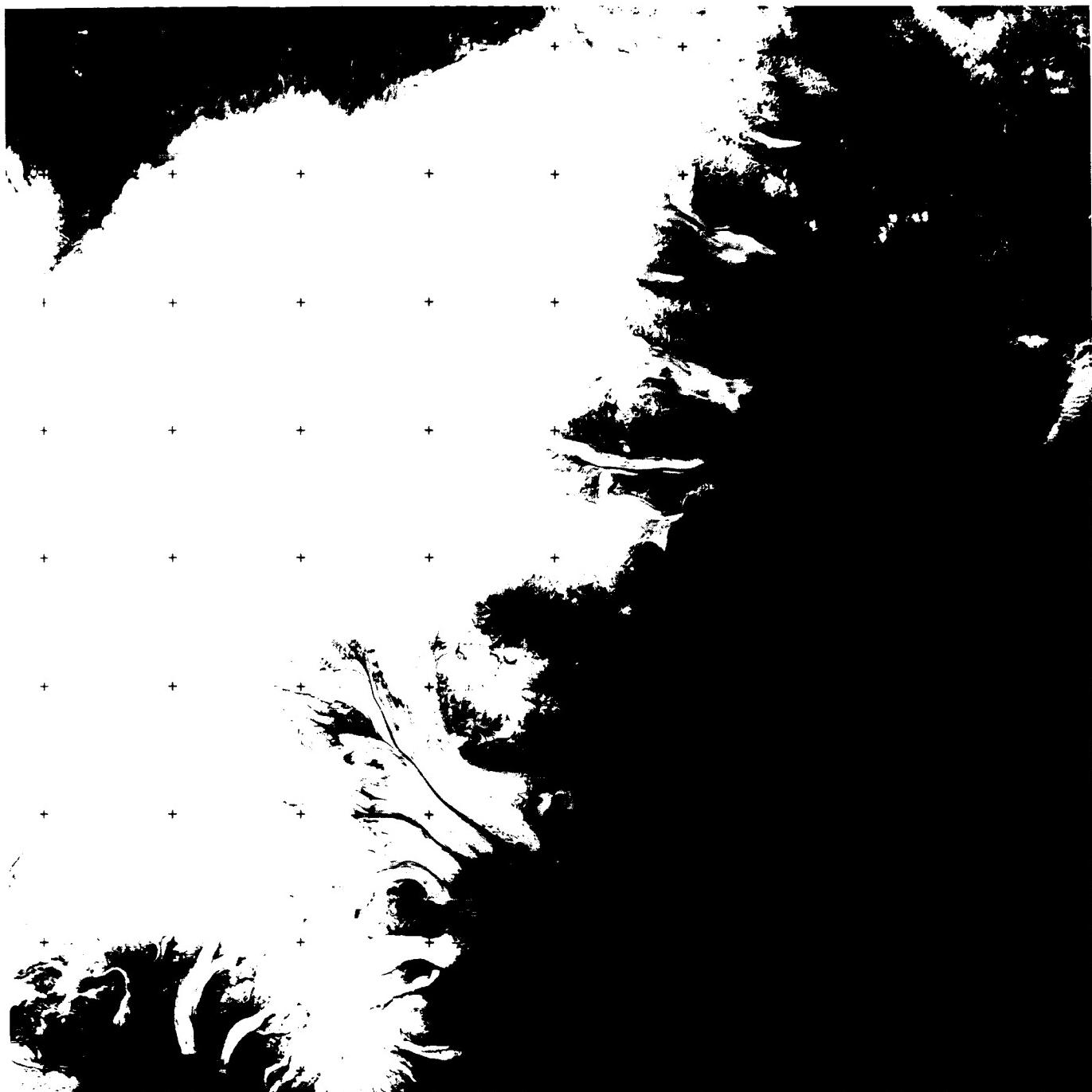
The outwash plain in front of Breidamerkurjökull is dominated by several large proglacial lakes (I), a subject discussed in Plate G-23. The largest of these proglacial lakes is Jökulsárlón (K), which is filled with icebergs, as can be seen on Plate G-16 and Figure G-16.4, an oblique photo that also shows part of the terminus of Breidamerkurjökull. Another large proglacial lake is also visible at the terminus of Hoffellsjökull (J). The transient snowline can be seen on Brúarfjökkull (L), the dividing line between the accumulation and ablation zones. (See the section on *Glacier Mass Balance* (Figures 9-5 through 9-9).) The upper part of the Skeidarásandur outwash plain is visible at (M).

The glacial geology of the evolving outwash plain of Breidamerkurjökull has been studied by students and faculty of the Department of Geography at the University of Glasgow, Scotland, since 1965, and this classical series of geomorphological studies (Howarth and Welch, 1969; University of Glasgow, 1982), based on geologic and photogrammetric methods, has been briefly summarized by Williams (1983b).

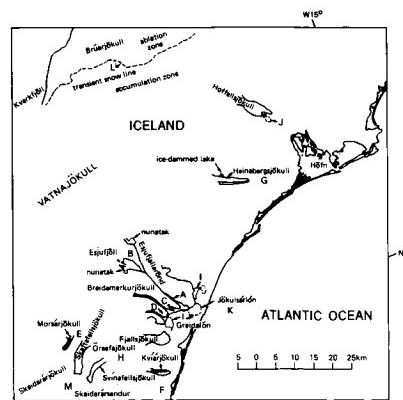
Figure G-16.1 is a ground view looking southwest at the eastern lateral moraine of the retreated Steingletscher near Sustenpass, Switzerland. Figure G-16.2 is an aerial photograph of the Kaskawulsh Glacier and tributary glaciers in the Yukon Territory, Canada, showing well-developed lateral and medial moraines. Medial moraines on the Grosser Aletschgletscher (Aletsch Glacier) in Switzerland appear in Figure G-16.3. **Landsat 30157-11572-B, August 8, 1978.**



ORIGINAL PAGE IS
OF POOR QUALITY



4



C - 7

569

PLATE G-17

SOUTHWESTERN SWEDEN

Ritter (1978) classifies morainal landforms into three basic groups (see Table 9-6): end moraines, including terminal (Plate G-15), lateral (Plate G-16), and recessional (Plate G-15); interior and minor varieties (medial, washboard, and interlobate (Plates G-15 and G-16)); and till. Bates and Jackson (1980) define till as "dominantly unsorted and unstratified drift, generally unconsolidated, deposited directly by and underneath a glacier without subsequent reworking by meltwater, and consisting of a heterogeneous mixture of clay, silt, sand, gravel, and boulders ranging widely in size and shape;" and define ground moraine (Figures 9-21 and 9-22a) as "an accumulation of till after it has been deposited or released from the ice during ablation, to form an extensive area of low relief devoid of transverse linear elements."

The "gently rolling surface" of till-covered (ground-moraine-covered) terrain is often characterized by numerous glacial lakes. Thornbury (1954) noted that: "It is undoubtedly true that glaciation has been responsible for the formation of more lakes than all other geomorphic processes combined."

This Plate is a Landsat image of a glaciated area in southwestern Sweden showing the numerous glacial lakes that have been created mainly by depositional processes associated with the recession of the Late Weichselian (Wisconsinan) ice sheet (Rudberg, 1984). Bolmen and Mockeln are two of the larger lakes (Lundquist et al., 1958). This glaciated region was one of the first Landsat-imaged areas to be investigated by an interdisciplinary group of Nordic scientists (Svensson et al., 1973).

Most of the region encompassed by the image is underlain by gneisses and granites (Magnusson et al., 1958). It is across this mainly granitic and gneissic bedrock that repeated advances and recessions of the Pleistocene Scandinavian ice sheets passed (see Figure 9-1), alternately eroding and depositing great quantities of glacial sediments (Rudberg, 1984).

In this part of Sweden, the ice sheet was between 2000 and 2500 m thick during its maximum extent at about 20000 years B.P. (Hughes et al., 1981). On the southern part of the west coast of Sweden, end moraines have radiocarbon dates of about 13000 years B.P. (Andersen, 1981). Since the ice-front deposits (Taberg-Levene) at the southwestern end of Lake Vättern have been radiocarbon dated at about 12000 years B.P., the entire region encompassed by the Landsat image was deglaciated from south-

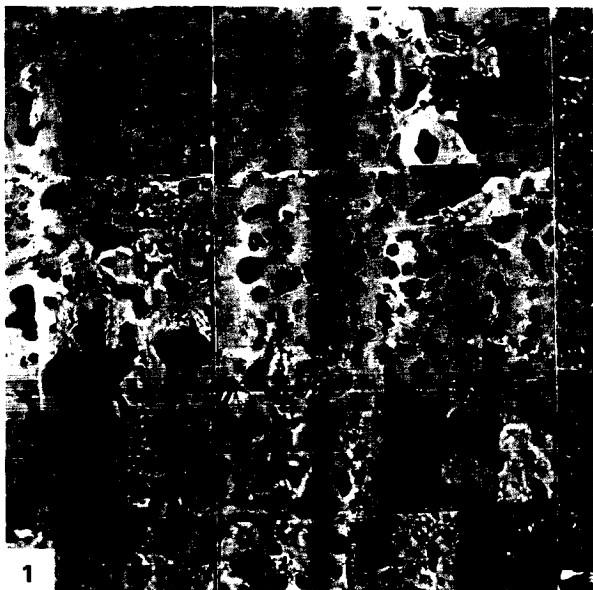
southwest to north-northwest in about 1000 years (Andersen, 1981).

In the waning stages of the last great Scandinavian Ice Sheet—the Weichselian—as the ice-sheet margin retreated across the area, an assortment of glacial deposits and landforms were laid down (Duphorn et al., 1970). According to Lundquist (1981), the area of the image lies within three morainal zones: on the west and northwest, on the south, and on the east and northeast. "On the west coast an end moraine zone of active, possibly cold-based ice, passes eastwards into a zone of ridges formed at the stagnancy of a formerly active, cold-based ice," and "a zone of subglacial features formed by active, warm-based ice."

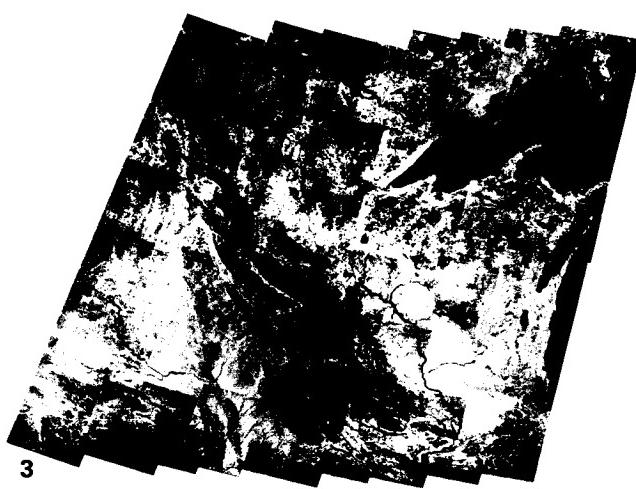
Most of the region included in the image is covered by till (ground moraine), drumlins, drumlinoid (Rogen) moraines, and linear glaciofluvial deposits such as eskers (Persson, 1972). However, around the bay at Laholmsbukten and extending northwest along the coast in a narrow band are marine deposits that have been uplifted by the rebound of the Fennoscandian shield in response to removal of the ice sheet. Throughout the area are limited exposures of bedrock. Larger bedrock outcrops occur on the west coast of Sweden from a point about half way between Laholmsbukten and the city of Göteborg.

Vast areas of the mid-continent of the northern United States and large areas of Canada are covered by till (ground moraine). Figure G-17.1 is a vertical aerial photograph of an area of hummocky till (ground moraine) in the province of Saskatchewan, Canada. Slaney (1981) has a brief section on glacial features in Canada that are visible on the various Landsat images included in his book; hummocky till (ground moraine) is delineated on five of these images. Figure G-17.2 is an oblique aerial photograph of ground moraine that has become visible following recession of the terminus of the Malaspina Glacier, a piedmont glacier (see Plate G-7) in Alaska. A proglacial lake with small morainal ridges is visible in the background. Figure G-17.3 is a Landsat mosaic of till (ground moraine) associated with the Des Moines lobe of the Laurentide Ice Sheet in north-central United States (see Figure 9-1) (Lucas and Taranik, 1977). The pronounced pattern of terminal and recessional moraines grades into till (ground moraine) to the northwest with the appearance of numerous glacial lakes.

Landsat 1041-09464-7, September 2, 1972.



ORIGINAL PAGE IS
OF POOR QUALITY



3

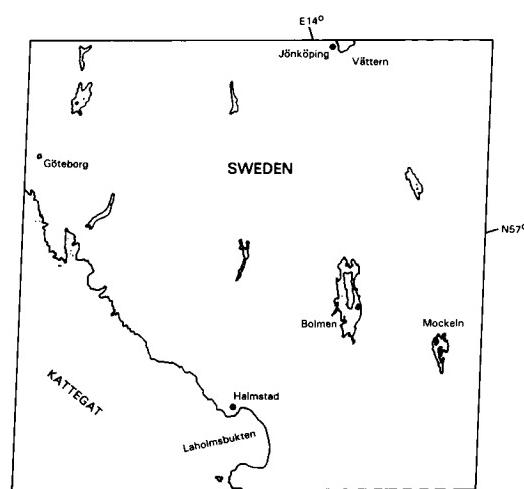


PLATE G-18

ABERDEEN LAKE, NORTHWEST TERRITORIES, CANADA

The District of Keewatin, in which this area is located, occupies that part of Canada's east-central Arctic which lies north of the Manitoba border to the Arctic Islands, and from the northwest side of Hudson Bay to 149°W longitude. It is an area of continuous permafrost. The tundra environment supports only low arctic vegetation such as small shrubs, heath plants, grasses, mosses, and lichens.

The entire area was glaciated during the Wisconsinan by continental glaciers that left varying amounts of drift cover. The direction of the ice flow can be deduced from features such as fluted till plains, drumlin fields, and striations, which indicate flow in two major directions. This has led to the Keewatin ice divide theory which states that an elongate center existed from Wager Bay through Baker Lake to just north of Ennadai Lake. Ice flowed to the northwest and southeast from the divide. Flow from the southern end of the divide was to the south. The divide is located to the east of the Landsat image.

The initial retreat of the glacier was to the north-northeast from northwestern Manitoba. Glacier ice remained with its margin just north of Ennadai Lake, causing proglacial lakes to form because the northward-flowing streams were blocked. With the recession of the glacier toward the ice divide, water flowed into the depressed region presently west of the current shoreline of Hudson Bay.

The Landsat image for this Plate was acquired in mid-June 1973. Seasonal ice is still visible on many of the lakes, especially Aberdeen Lake, located at the bottom of the image. Wisconsinan ice direction is very apparent from the elongation of the lakes in a north-northwest/south-southeast direction.

A supervised classification of the Landsat image (map below, on left) was conducted on a 30- by 40-km subscene centered just east of the east arm of Aberdeen Lake. This involved the

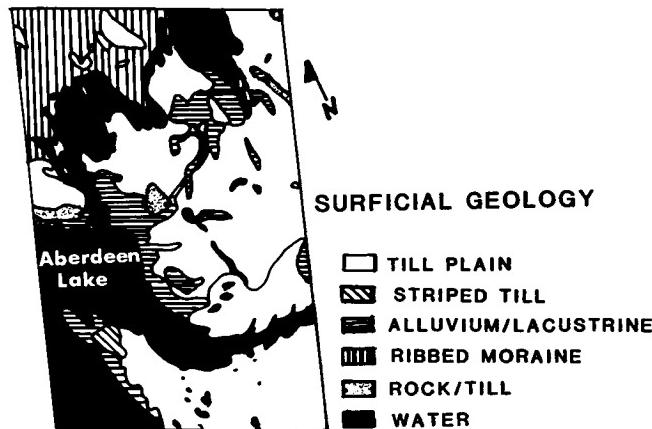
selection of training areas of known conditions for classification, which was based on field data and previously mapped information. The corresponding spectral values for each training unit were then used to classify the entire image. Figure G-18.1 shows an example of the rock/till class (site A on the Plate image). The vegetation in this type of terrain is discontinuous, consisting of mosses and lichens. The rock has been shattered by frost, leaving typical felsenmeier. The sandy till is generally less than 1 m thick.

The ribbed moraine shown in Figure G-18.2 (site B on the Plate image) has continuous vegetation consisting of scattered tufts of grasses, lichens, and mosses. The surficial material is sandy with little or no silt and clay.

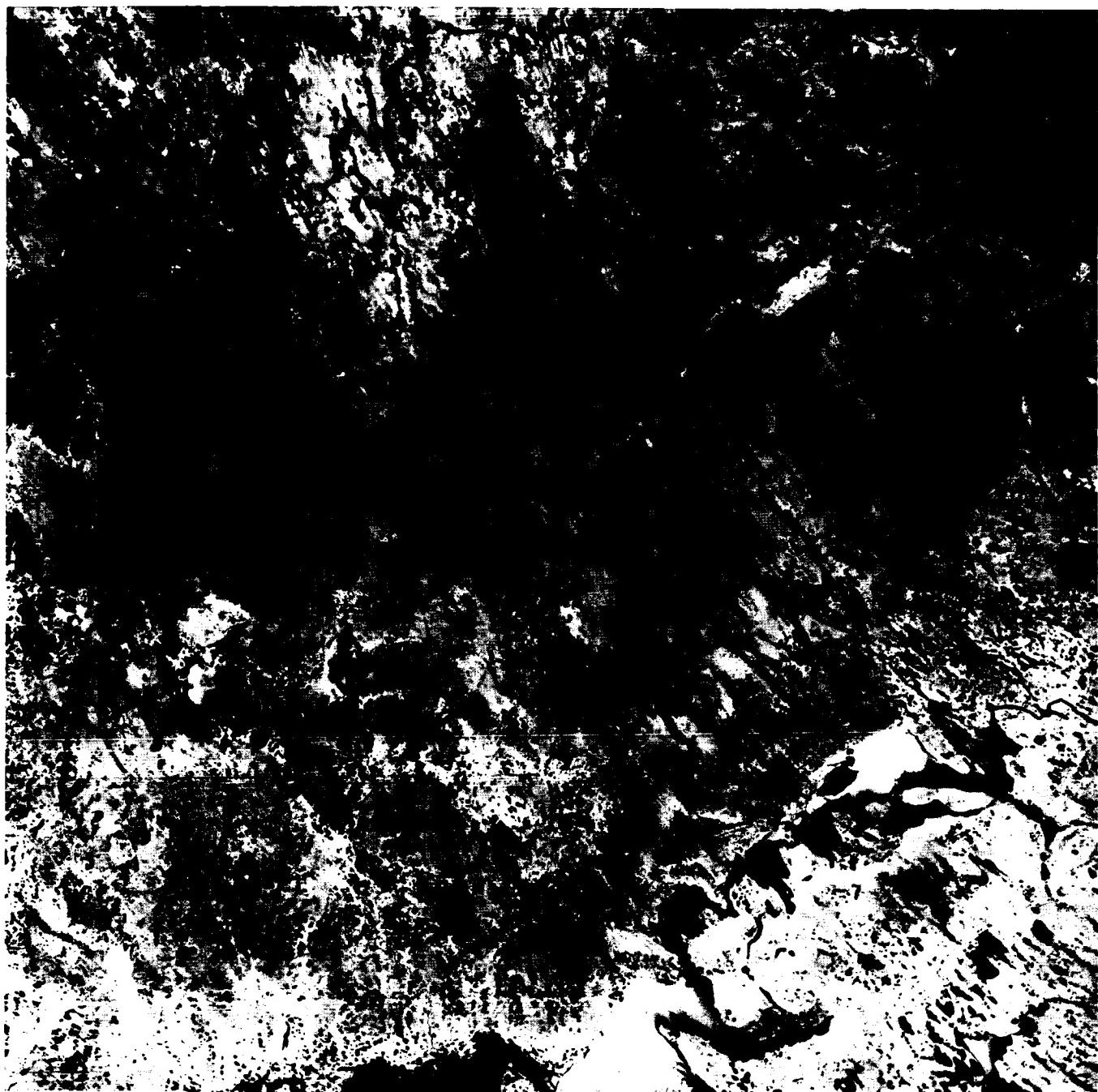
The till plain in the region is also sandy with sparse silt and clay. The till contains no apparent material differences, but has a striped appearance when viewed from low-level aerial photography. Vegetation on the till plain consists of a discontinuous cover of lichens and grasses in depressions and mosses in wetter areas. The striped till has the same type of vegetation cover.

The alluvium/lacustrine deposits are well-sorted sand with no silt and clay components, although some silts and clays occur in recent alluvial deposits. The vegetation cover is discontinuous particularly on beach ridges and scarps. Backshores and terraces have continuous vegetation consisting mainly of grasses (site C on Plate image).

It is important to note that, when using the Landsat data for mapping surficial geology and geomorphology in this type of terrain, it is the vegetation communities on the different types of deposits which enable the different units to be mapped. These grow in response to slope form, material, moisture, and micro-climatic influences that are strongly correlated with the surficial geology. (GCW: J. K. Hornsby) *Landsat 1339-17351-7, June 27, 1973.*



ORIGINAL PAGE IS
OF POOR QUALITY



2

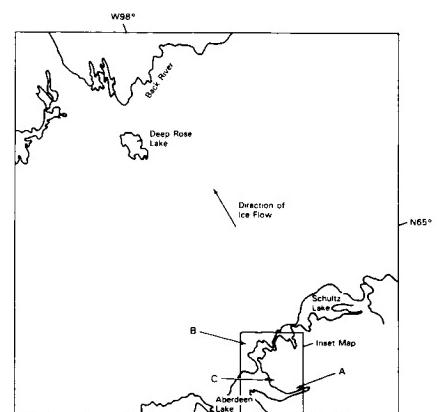


PLATE G-19

According to the definition given by Bates and Jackson (1980), a drumlin is "(a) A low, smoothly rounded, elongate oval hill, mound, or ridge of compact glacial till or less commonly, other kinds of (glacial) drift (sandy till, varved clay), built under the margin of the ice and shaped by its flow, or carved out of an older moraine by readvancing ice; its longer axis is parallel to the direction of movement of the ice. It usually has a blunt nose pointing in the direction from which the ice approached, and a gentler slope tapering in the other direction (Figure G-19.1). Height is 8-60 m, average 30 m; length is 400-2000 m, average 1500 m." Bates and Jackson (1980) also define drumlinoid as a near-drumlin and drumloid—a less symmetrically formed drumlin (Figure G-19.2); a drumlin field, also known as "basket-of-eggs topography," (Figure G-19.3) is defined as "a landscape characterized by swarms of closely spaced drumlins, distributed more or less en echelon, and commonly separated by small marshy tracts."

Drumlins are composed mainly of lodgement till and are associated with till (ground moraine) (see Table 9-6 and Figure 9-22a). Thornbury (1954) notes that there are four major areas of drumlin fields in North America. Flint (1971) provides an estimate of the number of drumlins in each of these areas: in southern New Hampshire and eastern Massachusetts (3000), in New York and Ontario south and north of Lake Ontario (10000), in Nova Scotia (2300), and in parts of Wisconsin (5000), Iowa, and Minnesota. Drumlin fields are also widespread in Europe, especially in Ireland (Figure G-19.3), Scotland, and England (Figure G-19.4), Germany, Sweden (Lundquist, 1981), and Finland. According to Sugden and John (1976), drumlins form in the marginal zone of active ice under dynamic conditions of extending flow at the glacier bed. Lundquist's (1981) work in Sweden and Prest's work (1968) in the Northwest Territories of Canada have shown that streamlined depositional landforms that form within the zone of active ice can be grouped into subzones. Prest's (1968) research, as discussed by Sugden and John (1976), determined that in the Northwest Territories a zone of drumlins is succeeded by a zone of elongated drumlinoid forms, then a zone of drumlinized ground moraine, followed by a fluted ground moraine, then a ground moraine zone, and then bedrock, as depositional processes eventually give way to erosional ones.

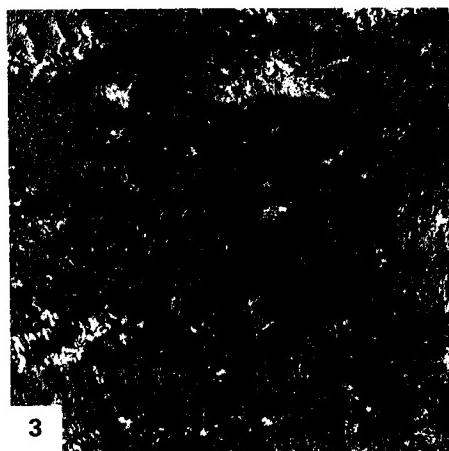
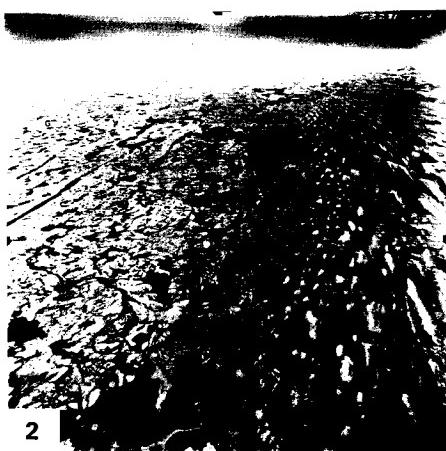
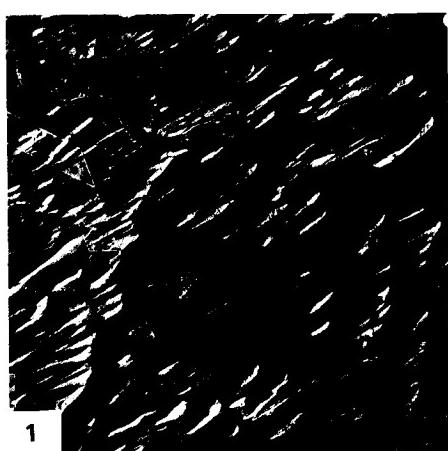
Drumlin fields are well displayed on Landsat images, although Ford (1984) has reported that a drumlin field in Ireland (Figure G-19.3) is much better delineated on Seasat SAR images than on Landsat images of the same area. Slaney (1981) includes six plates in which drumlinoid landforms can be delineated. Prest

WOLLASTON PENINSULA,
VICTORIA ISLAND, CANADA

(1983) and Mollard (1974) both contain excellent examples of aerial photographs (vertical and oblique for the former, stereoscopic pairs for the latter) of drumlins and drumlinoid landforms.

This Landsat Plate image of the Wollaston Peninsula, Victoria Island, Northwest Territories, Canada, clearly shows the full gradation of landforms from true drumlins to ground moraine in a single image. The diversity of morainal forms is evident in an oblique aerial photograph (Figure G-19.2; approximate position indicated by a "V" on the index map) looking eastward across the morainal zones. Both this photograph and the index map show (by letters) the following features: (A) streamlined drumlins, (B) short stubby drumlins, (C) drumlinoid landforms, (D) fluted ground moraines, (E) shear moraine, (F) Colville end moraine, and (G) hummocky moraine. Arrows show direction of glacier flow (east to west). (Delineation of the morainal zones and terminology are modified from Figure 37.2 in Sharpe (1984)). The peninsula is dominated by hummocky morainal deposits overlapped near the coast by marine deposits. The region containing the image was deglaciated between 12000 and 9000 years B.P.; it has subsequently been subjected to 400 to 500 m of rebound (Fremlin, 1974).

Figure G-19.1 is a vertical aerial photograph of a drumlin field with a few drumlinoid ridges and some fluting in northwest Saskatchewan, Canada. Eskers are prominent in the center and bottom left parts of the photograph. Glacier flow was from the northeast to the southwest (Prest, 1983; Mollard, 1974). Figure G-19.3 is a Seasat SAR image of part of the main drumlin field in northern Ireland. This is a classic area of "basket-of-eggs topography" and has been described by Duhorn et al. (1967), Davies et al. (1978), and Embleton (1984). As pointed out by Ford (1984), Seasat SAR images of glacial landforms have a considerable advantage over Landsat MSS images of the same area for geomorphic studies. This is primarily due to the threefold increase in spatial resolution, but in the MSS image used in the analysis by Ford, is also related to illumination angle. Ford was able to delineate four distinct classes of drumlinoid forms on the Seasat SAR image and only one on the Landsat MSS image. Figure G-19.4 (from Figure 13.8 in Sugden and John (1976)) shows the distribution of drumlin fields, ice-flow directions, and sources of ice in the United Kingdom and Ireland during the last or Weichselian (Wisconsinan) glaciation. The square shows the approximate outline of the Seasat SAR image in the center of the large drumlin field in Ireland. **Landsat 10371-18535, July 29, 1973.**



ORIGINAL PAGE
COLOR PHOTOGRAPH

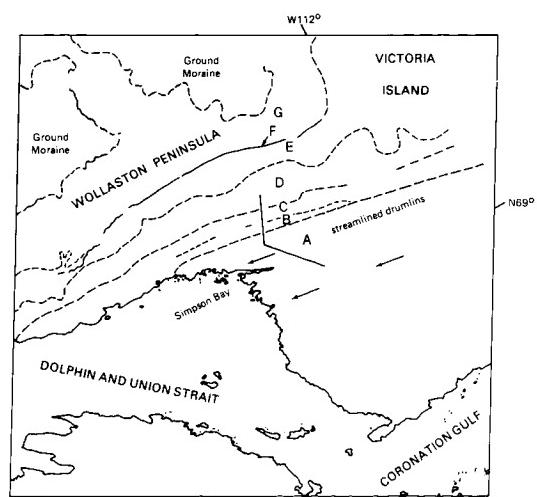
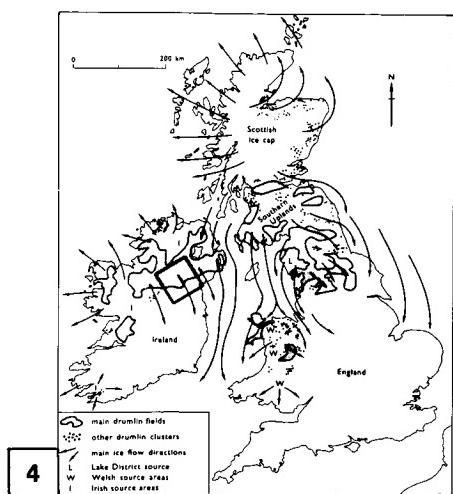
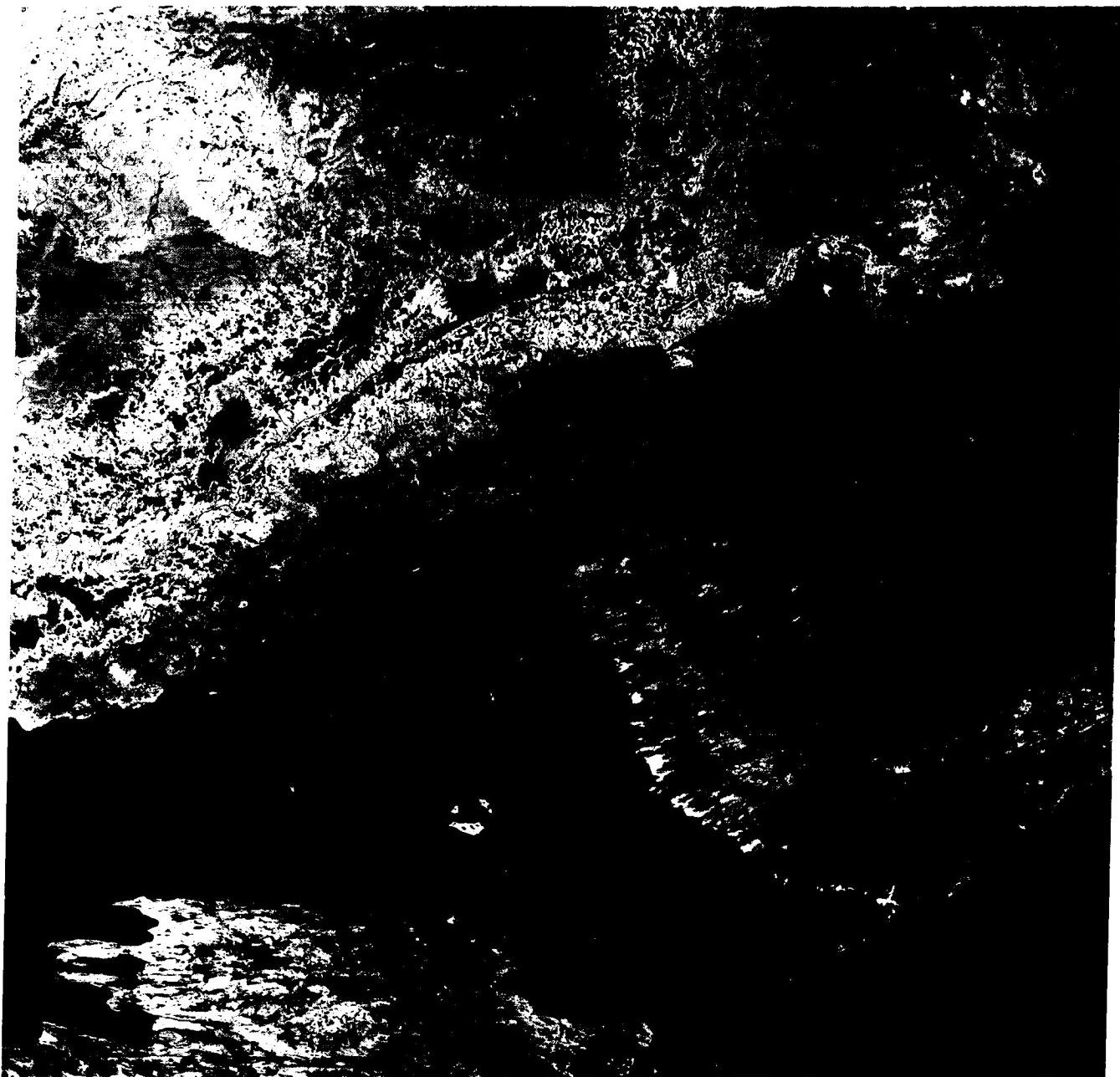


PLATE G-20

Located in the District of Franklin, King William Island presents glacial landforms typical of the Canadian Arctic Lowlands. The island had been totally glaciated during the Wisconsinan glaciation, leaving numerous glacial landforms related to major continental ice flows, stagnations and retreats of ice fronts, and later glacier surges. At the beginning of the Holocene, the entire island (highest elevation 30 m above sea level) was submerged by the sea, which reworked the original glacial landforms, washed the fine sediments from the prominent formations, and redeposited them in low-lying areas. The present vegetation belongs to the mid-Arctic ecosystem, and its distribution is closely related to drainage conditions.

The bedrock formations consist essentially of carbonate rocks—limestone, dolomite, sandy limestone, and sandy dolomite of Ordovician and Silurian age. Outcrops consisting of flat-lying beds 10 cm to 1 m thick are frost-shattered to a depth of several meters and are rubbly on the surface. Major rock outcrops are identified by "R" on the index map.

Unit 1 on that map shows flow patterns of continental glaciers. The ice-flow landforms (fluting and drumlins) consist of long ridges, commonly separated by elongated lakes that parallel the ridge crests, which indicate that ice advanced from the southeast, separating into northwest and northeast flows on either side of a major bedrock prominence. Northwest flow is believed to be the older of the two advances because some of the fluting forms southeast of the bedrock area have been overridden by northeastward flow. On the north tip of the island, the landforms show ice-flow transverse to flows south of the bedrock prominence. Large unvegetated areas (light tones on the Landsat imagery) are due to the removal of fine-grained materials by wave action during retreat of the sea, leaving a blanket of coarse-grained material unable to retain sufficient humidity to support vegetation. Figure G-20.1 is a close view of an unvegetated end-moraine ridge; although the boulders on the ridge are generally frost-shattered, a number of rounded rocks, shaped by wave action during the marine recession, are still intact. Because they are both composed of frost-shattered carbonate rocks, it is often difficult to differentiate bedrock ridges from till ridges.

Unit 2 covers an area of massive ice stagnation. The area is covered by a blanket of hummocky till containing numerous subcircular lakes. The poor drainage, due to the lack of relief and the presence of fine material, favors the presence of vegetation over most of the area. A large end moraine separates the southeast part of the stagnant ice topography from the fluted

KING WILLIAM ISLAND, CANADA

terrain of units 1 and 4. Note that the southern arm of the moraine has been reworked by the younger ice surge described in unit 4. Figure G-20.2 is an aerial view of the contact between the moraine and eskers (identified by an asterisk on the index map), the highest point on the island. Several levels of beaches were formed on the slopes of the morainic ridge during the marine regression (Figure G-20.3). The circular lakes on the foreground of the moraine (G-20.1) are typical kettle lakes formed by the collapse of drift over melting blocks of stagnant ice.

Unit 3 comprises several small ridges formed during a retreat of an ice front. The low-relief undulating ridges oriented in a southwest-northeast direction indicate that the ice front retreated toward the southeast. These recessional moraines were formed by successive retreats and stabilization of the ice front, the ridges corresponding to stable ice fronts and the troughs to ice recessions. Some of the older ice-flow patterns (similar to those of unit 1) are still visible underneath the more recent recessional moraines.

Unit 4 corresponds to a later glacier surge flowing in a northwest direction. The drumlin field on Adelaide Peninsula (southeast of the Landsat imagery) and northeast part of King William Island shows that the glacial flow was deflected to a more westerly direction as the glacier impinged on the frontal moraine that separates units 2 and 4. The drumlins are composed of till with a matrix that is fine enough to retain enough moisture to support vegetation. The low areas between drumlins, as well as the base of the drumlins, are covered by wet marine sediments. The drumlin field is bounded by a large rock outcrop located at the southwest tip of the island (light tone on the Landsat imagery). On the rock outcrop, the ice-flow features change slowly to more gravelly flutings that are unable to support vegetation, which explains their lighter tones.

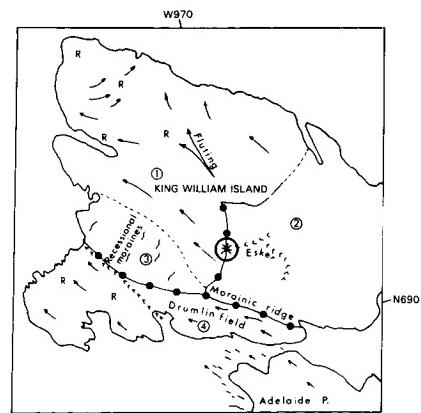
Because of the cold and semiarid conditions on King William Island, the vegetation is dependent on the nature of the soils and the drainage conditions. This strong control of vegetation patterns by even slight differences in soil moisture in this severe arctic environment facilitates the geological interpretation based on Landsat imagery by enhancing tonal differences among various landforms and soil types. Fieldwork and low-altitude air photography are still necessary for a detailed geomorphological study of King William Island, but the use of Landsat imagery permits the reconstruction of several phases of the Wisconsin glaciation by providing an overall view of the various glacial landforms. (GCW: J. R. Belanger) Landsat 20914-17165, July 24, 1977.



ORIGINAL PAGE IS
OF POOR QUALITY



3



The entire area of northwest Manitoba was glaciated during the last Wisconsinan stage and represents a typical region of continental glaciation. The latest movement was generally from a northeasterly direction and formed the Pas Moraine (4) approximately 10800 years B.P. Following a local readvance beyond the Pas Moraine, the ice melted and proglacial Lake Agassiz covered the ice-free portion of the area.

The scene can be subdivided into four broad areas based on surface deposits, bedrock geology, and vegetation:

1. This area is dominated by Precambrian volcanic, gneissic and granitic bedrock. Volcanic and gneissic rocks are characterized by linear and curvilinear ridges (A) representing fold systems that form a strongly rolling to hilly topography. Granitic rock types (B) usually form a more gentle topography or rounded hills. These bedrocks are covered by a mixed conifer and deciduous vegetation. Glacial erosion of the more resistant granitic and gneissic rocks of the Precambrian Shield produce a landscape of rounded knobs and hollows, streamlined roches moutonnées and crag and tail, and numerous ice-gouged lakes and valleys. Shallow sand till covers most of the area, with small lacustrine clay pockets occurring in valleys. Peat deposits, usually small in size, are found in depressions and are composed mainly of forest and sphagnum peat. Mining and forestry are the main economic activities. The bluish-green area at Flin Flon represents the toxic effects of the sulphurous fumes from the base metal smelter that has been in operation for several decades.

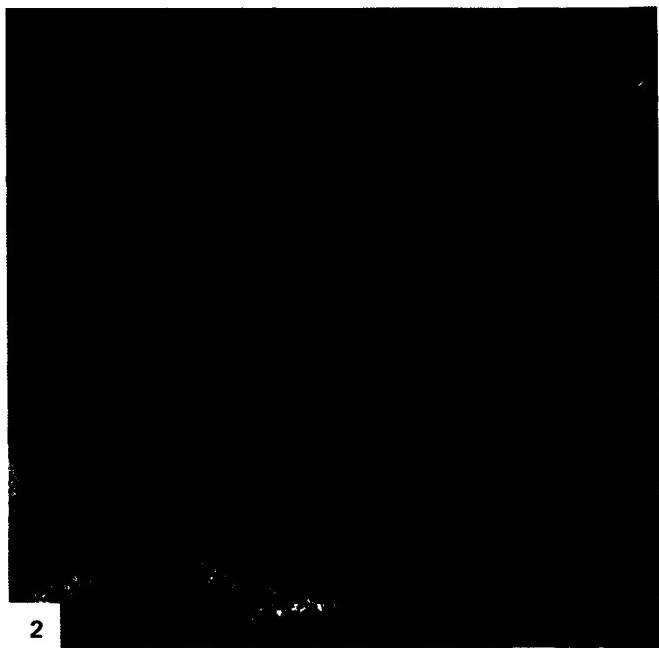
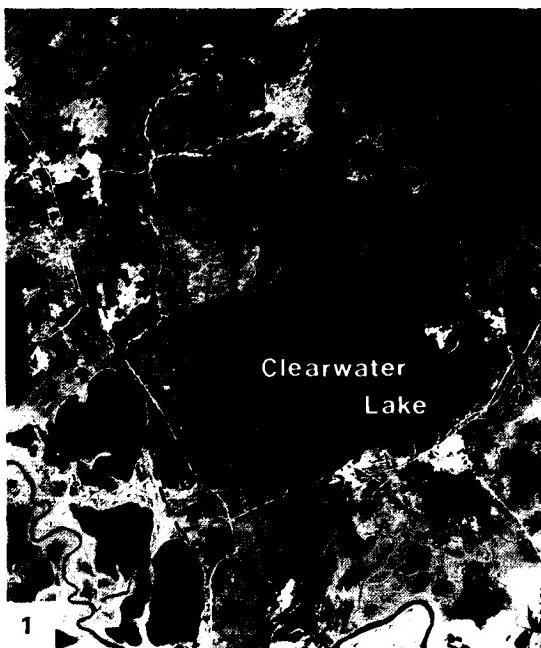
2. This area forms part of the Manitoba and Saskatchewan lowlands, which are underlain by glacial drift and flat bedded Ordovician dolomitic limestone. Unlike the bouldery, sandy till of the Precambrian Shield, the softer Paleozoic rocks in this region produce a silty clay till. Here, the lakes are larger and rounder, and the shorelines are more regular. Peatlands are extensive and occur as string bogs (C) and ribbed fens (D). Discontinuous permafrost occurs in peat plateaus and wooded palsen.

3. The Pasquia and Cedar Lake lowlands form an extensive alluvial and lacustrine plain that is divided by the Pas Moraine. The entire area was submerged by Lake Agassiz and has been modified by lacustrine and fluvial action. It includes part of the Saskatchewan River delta. Distributaries, channels,

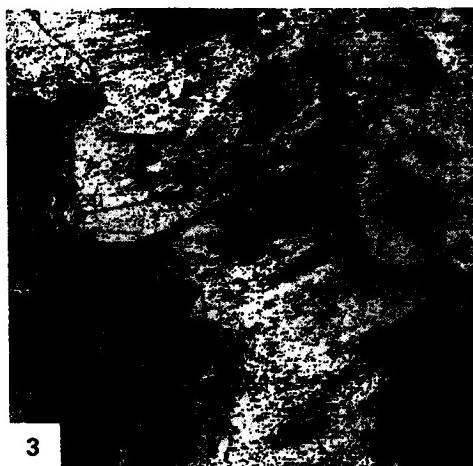
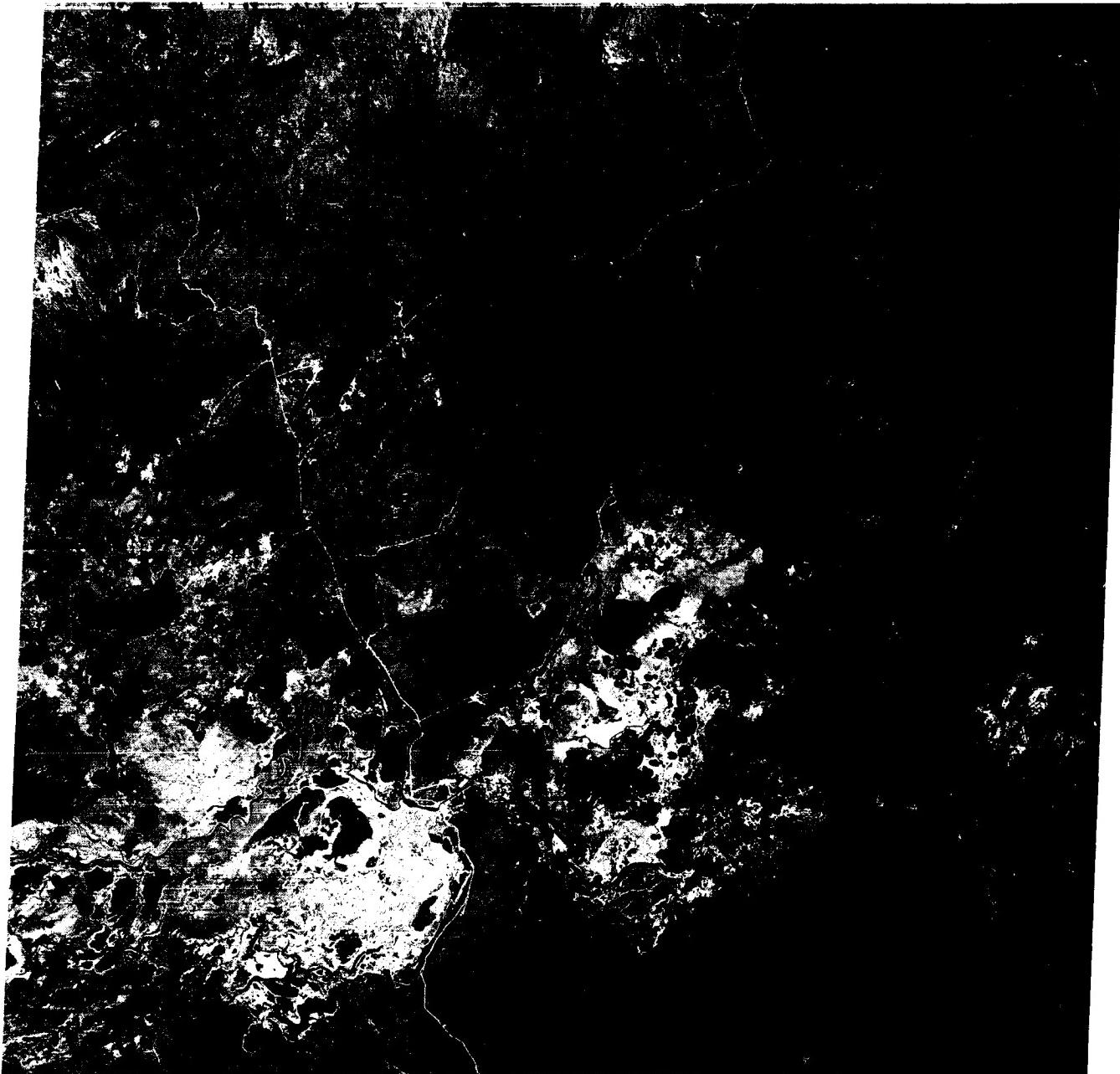
and natural levees (E) are evident from the image. In the Pasquia Basin, the alluvial floodplain is used as an area of improved pasture. The light blue at Cedar Lake represents suspended sediments stirred from the lake bottom, as well as sediment from erosion by the Saskatchewan River.

4. The Pas Moraine is a topographic high, arcuate in plan, and extends from Lake Winnipeg to 50 km north of the town of The Pas. This terminal moraine is the largest in Canada with a total length of approximately 225 km and a width varying from 6 to 30 km. The moraine is delineated on the Landsat scene and on the TM image (Figure G-21.1). The moraine front forms a south-to-west escarpment some 225 m high. It comprises an accumulation of till along the front of a bedrock escarpment. The subparallel lines indicated by (F) are glacial flutings on the Pas Moraine. These parallel grooves, with intervening ridges of glacial drift (Figure G-21.2) form fluted surfaces with gentle slopes and a relief of only a few meters. The drift-covered ridges support black spruce vegetation (dark tone), and the parallel grooves are peat-covered and support sedges, which produce a light tone on the color-infrared photographs and the Plate image. Several theories have been set forth to explain formation of these fluted terrains. These include (a) the erosion of the subglacial material by basal sliding in the submarginal zone where the bed is thawed; (b) the erosion of the underlying material by sliding on the sole of thrust blocks beneath the frozen bed zone; (c) the streamlining of subglacial blocks of material that were thrust up from below at the up-glacier edge of the frozen bed zone; and (d) the distribution of debris that is transported by the ice. Portions of the western edge of the Pas Moraine are flanked by Agassiz beach ridges that are mined for construction aggregates. The sand and gravel pits are shown as white spots (G) on the Plate image.

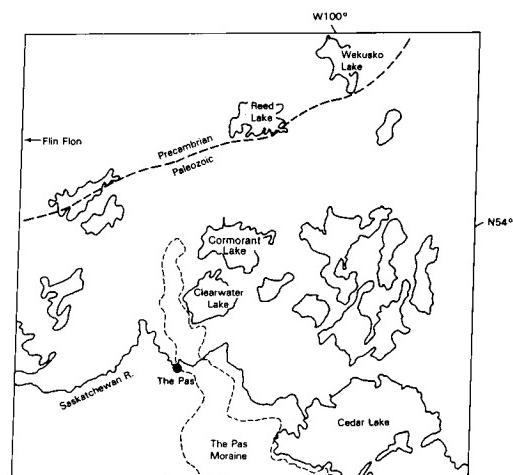
An unsupervised classification of a portion of the Pas Moraine (Figure G-21.3) shows the major spectral classes that correspond to landcover. Class (1) represents the open black spruce vegetation covering the Moraine; (2) the Saskatchewan river floodplain and delta; (3) areas of low black spruce bogs; (4) open fens; (5) algae-rich lakes; (6) muddy and turbid waters of the Saskatchewan River. (GCW: V. R. Singhroy) Landsat E-1335-17153-3, June 23, 1973.



ORIGINAL PAGE
COLOR PHOTOGRAPH



3

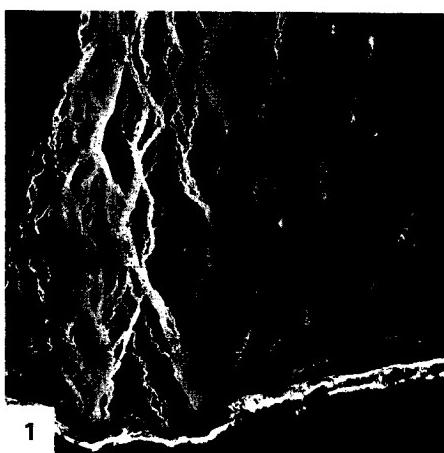


An outwash plain is defined as "a broad, gently sloping sheet of outwash deposited by meltwater streams flowing in front of or beyond a glacier, and formed by coalescing *outwash fans*" (Bates and Jackson, 1980). Bates and Jackson also define an outwash fan as "a fan-shaped accumulation of outwash deposited by meltwater streams in front of an end moraine of a glacier. Coalescing outwash fans form an *outwash plain*" (see Figures 9-21 and 9-22a). A synonym for outwash plain is sandur, an Icelandic loanword meaning the broad plain formed by the deposition of glacially derived sediments in front of the margin of a glacier. The sandur (sandar is the Icelandic plural) landform is especially well developed along the south-central coast of Iceland, particularly in the 110 km of the coastal plain that lies between the eastern margin of Mýrdalsjökull and Öraefajökull (see Figure G-23.1), the southernmost part of Vatnajökull (see also Plate G-6). Although deltas normally form at the seaward edge of an active sandur, such is not the case along the coast of Skeidarársandur because of intense wave action and strong littoral currents. (Note the deflection of sediment plumes on Plate G-22.) Any deltas that do form are ephemeral (Figure G-21.1).

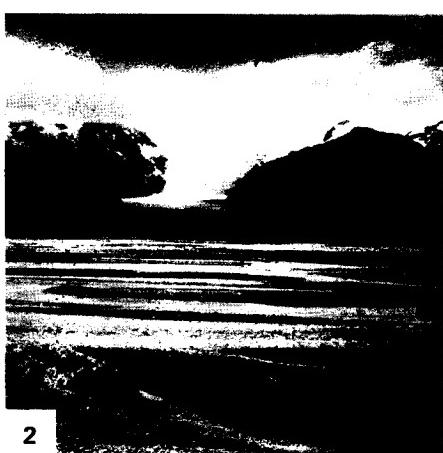
This Plate is a two-scene Landsat-3 RBV image mosaic of the 50-km wide Skeidarársandur, the largest of the four sandar (Mýrdalssandur, Medallandsandur, Brunasandur, and Skeidarársandur) between Mýrdalsjökull and Öraefajökull (Preusser, 1976). Enormous quantities of sediment-laden (silt, sand, and gravel) meltwater streams traverse these sandar from the margins of the outlet glaciers to the coast, especially during the late spring and summer months (A). The sediment-charged streams create an intricate pattern of anastomosing streams (A) (Figure G-22.1) before debouching into the sea. Figure 22-1 is a pair of vertical aerial photographs (photomosaic) of part of the southeastern part of the Skeidarársandur showing the anastomosing stream pattern characteristic of such glacial outwash plains and the ephemeral delta forming at the coast. At various points along the coast (B) sediment-laden glacial streams breach the barrier beach and discolor the ocean water with glacial rock flour (Figure G-22.1). A glacial delta may even build out into the sea in some places (C). On the eastern side of Skeidarársandur, meltwater is derived from the terminus of Skeidarárjökull and from the numerous outlet glaciers such as Skaftafellsjökull and Svinafellsjökull, which originate from the Öraefajökull ice cap (Plate G-16) and descend through valleys to the Skeidarársandur outwash plain. Figure G-22.2 is a photograph looking east-northeast across glacial streams (Skeidará) on the upper part of Skeidarársandur toward the terminus of the Svinafellsjökull outlet glacier (see also Figure G-6.1). On the western side of Skeidarársandur, meltwater

streams originate from the terminus of Skeidarárjökull and from Sídujökull. Proglacial lakes (D) can be seen in front of Skeidarárjökull. The ice-dammed lake Graenalón is visible at (E) (see Plate G-23). Glacial outwash plains along a coast usually have a very gentle slope from the terminus of the glacier down-valley or across a coastal plain to the sea, although the upper part can be relatively steep where the outwash material is much coarser. The upper part of Skeidarársandur, 25 km from the coast, lies close to the 100-m elevation contour, giving an average gradient of 4 m per kilometer.

Figure G-22.3 is a view looking across Mýrdalssandur toward Hjörleifshöfði, a Pleistocene palagonite mountain that lies about 5 km to the south-southeast. Hjörleifshöfði was probably at the coast at the time of the settlement of Iceland (ca. 874 A.D.), but is completely surrounded by glacial outwash deposits (dark-toned basaltic sediments) and now lies 3 km from the coast (Preusser, 1976). Note the extreme flatness of the topography in this part of the outwash plain, approximately 15 km south of the terminus of the Hofdabrekka jökull outlet glacier from Mýrdalsjökull. Small drumlins have been mapped in the outwash plain north of Mýrdalsjökull but are too small to be resolved on the Landsat-3 RBV image. Both Skeidarársandur and Mýrdalssandur have been subjected to repeated periods of catastrophic floods resulting from jökulhlaups. Icelandic jökulhlaups can originate from the failure of ice-dammed lakes (Thorarinsson, 1940) or from subglacial volcanic and/or geothermal activity (Björnsson, 1975, 1976). Maximum discharges across Skeidarársandur are now usually in the range of 1×10^4 m³/s from jökulhlaups originating in the Grímsvötn caldera (Figure 9-14) and estimated to be 2 to 3×10^5 m³/s across Mýrdalssandur from those originating in the subglacial Katla volcano within Mýrdalsjökull (Thorarinsson, 1957). Jökulhlaups affecting Skeidarársandur have also originated from Öraefajökull (Thorarinsson, 1956b) and from Graenalón (Plate G-23). In the image, it is possible to see two lakes west of Skaftárjökull and Sídujökull, Langisjór and Thórisvatn, which have quite different spectral (gray tone) characteristics. Because Langisjór is no longer receiving sediment-laden glacial meltwaters from the western edge of Vatnajökull, its waters are clear. Thórisvatn, also a ground-water lake, was also completely clear until large engineering projects associated with the development of hydroelectric power plants on the Tungnaá river diverted the course of the glacial Kaldakvísl river *into* the northern "outlet" of Thórisvatn to create a storage reservoir. Sediment in suspension (glacial rock flour) has now altered the natural condition of Thórisvatn. **Landsat 30517-11572 C and D, August 9, 1978.**



1



2



3

ORIGINAL PAGE IS
OF POOR QUALITY

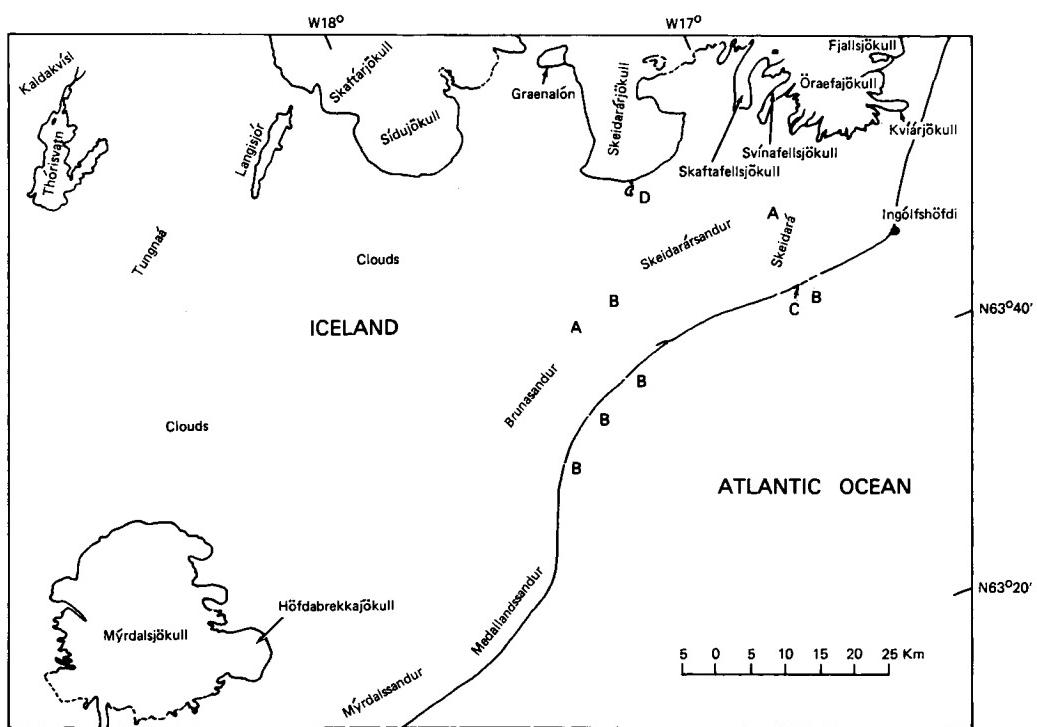


PLATE G-23

GRAENALÓN, SKEIDARÁRJÖKULL, ICELAND

A proglacial lake is "a lake formed just beyond the frontal margin of an advancing or retreating glacier, generally in direct contact with the ice" (Bates and Jackson, 1980). An ice-dammed (or glacier) lake is "a lake held in place by the damming of natural drainage by the edge or front of a glacier or ice sheet, as a lake ponded by glacier ice advancing across a valley, or a lake occurring along the margin of a continental ice sheet [or ice cap]" (Bates and Jackson, 1980) (see Figure 9-22a).

Ice-dammed lakes are of interest to both glaciologists and glacial geologists, especially those involved in the study of glaciologic hazards, because of the often ephemeral nature of the ice dam. Thinning or thickening and advance or recession of a glacier will cause changes in ice dams. Some ice-dammed lakes experience annual failures in the ice dams that cause extensive flooding downstream from rapid draining of the glacial lake. Such catastrophic floods are called jökulhlaups (an Icelandic loanword meaning glacier-outburst flood) and can sometimes result in extraordinary volumes of water discharged in short time periods (see Plate F-27, which describes the Channeled Scabland of eastern Washington). Jökulhlaups occur either as the result of the failure of ice-dammed lakes (Thorarinsson, 1940) or as the result of subglacial geothermal and/or volcanic activity (Björnsson, 1975, 1976). Ice-dammed lakes are also quite common in Alaska (Post and Mayo, 1971). Surging glaciers (Plate G-10) are especially apt to produce ice-dammed lakes because they often create ice dams on tributary valleys or by blocking main valleys (see Figure G-4.1).

This Plate is a Landsat-3 RBV image of the western half of the Vatnajökull ice cap, southeastern Iceland, showing the prominent ice-dammed lake (Graenalón) formed by a distributary valley glacier emanating from the Skeidarárjökull outlet glacier (Figure G-23.1). Figure G-23.1 is a view looking southeast across a glacier lobe, Graenalón, the 2.5-km wide ice dam, and the lower part of Skeidarárjökull toward the ice-shrouded stratovolcano, Öraefajökull (2119 m), 50 km in the distance. Graenalón experiences an annual fluctuation in lake level, beginning with a more or less steady rise during the melt season, followed by breaching of the ice dam at its southern margin in late summer and lowering of the lake level caused by partial draining. Floodwaters from the jökulhlaup travel down the western margin of Skeidarárjökull and debouch across the Skeidarársandur outwash plain. Rist (1974), in his discussion of the August 1973 jökulhlaup from Graenalón, used successive Landsat images to calculate a

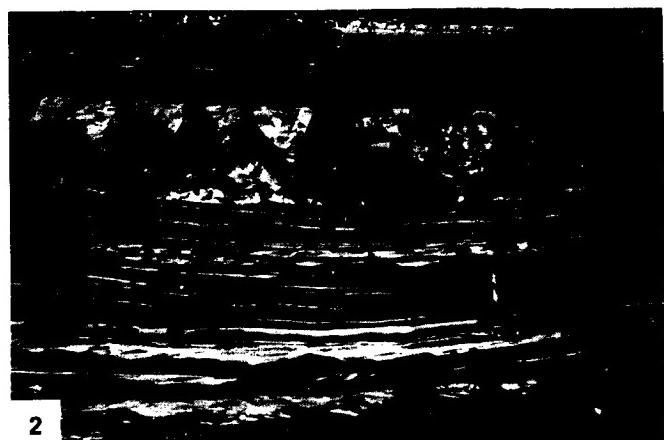
175-gigaliter reduction in volume of Graenalón after the jökulhlaup.

The index map for Plate G-23 pinpoints the following features: the ice-dammed lake, Graenalón (A); the ice dam (B) formed by a distributary valley glacier from Skeidarárjökull; a glacial delta (C) building out into Graenalón; medial moraine (D) on Skeidarárjökull; contorted tephra layers (E) used to calculate the rate of advance of Skeidarárjökull at 660 m per year determined from two successive Landsat images (Williams, 1983f), two proglacial lakes (F) west of Kerlingar; two proglacial lakes (G) west of Hamarinn; an arcuate medial moraine (H) on Dyngjújökull (Plate G-16) and recessional moraines and lakes developed in ground moraine in front of Múlajökull, an outlet glacier of Hofsjökull (I) (Plate G-15 and Figure G-15.1); subtle expression of recessional moraines (J) in the outwash plain of an eastern lobe of Hofsjökull (Plate G-15 and Figure 15-2); and a former proglacial lake, Langisjór (K). Proglacial and ice-dammed lakes in glaciated areas can usually be best recognized on Landsat MSS false-color composite images by their blue color (Plate G-6). Because Langisjór does not exhibit this blue color, it can now be classified as a ground-water lake. During the summer months, proglacial lakes receive copious amounts of fluvial-borne sediment, the coarser fraction from which settles quickly to the lake bottom; during the winter months, when the lake is ice-covered (see Plate G-15), finer-grained material, the so-called glacial rock flour, settles to the bottom, giving rise to the characteristic annual varve on the lake bottom. Figure G-23.2 shows varves deposited in a late Pleistocene or early Holocene proglacial lake north of the Torfajökull ice cap, southern Iceland. Note the thicker bed of massive sand with some pebbles above the hammer that probably represents the forward edge of coarser deltaic sediments.

Other proglacial and ice-dammed lakes are distributed around the margin of Vatnajökull as can be seen on Plates G-16 and G-22. Figure G-23.3 is an oblique aerial photograph of proglacial lakes along the terminus of the Breidamerkurjökull outlet glacier, southeastern Iceland. The Esjufjallarönd medial moraine (see Plate G-16) is visible in the left foreground. Jökulsárlón, the largest lake, is partly filled with icebergs. Glacial rock flour gives the proglacial lakes the characteristic milky white color. A plume of glacial rock flour also colors the Atlantic Ocean, where glacial rivers from the proglacial lakes are discharging into the sea. **Landsat RBV 30157-11572-A, August 9, 1978.**



1



2

ORIGINAL PAGE IS
OF POOR QUALITY



PLATE G-24

A kettle lake is defined as "a body of water occupying a kettle, as in a pitted outwash plain or in a kettle moraine" (Bates and Jackson, 1980). A kettle is defined as "a steep-sided, usually basin- or bowl-shaped hole or depression, commonly without surface drainage, in glacial-drift deposits (especially outwash and kame fields), often containing a lake (kettle lake) or swamp; formed by the melting of a large detached block of stagnant ice (left behind by a retreating glacier) that had been wholly or partly buried in the glacial drift. Kettles range in depth from about one meter to tens of meters and in diameter to as much as 13 km" (Bates and Jackson, 1980).

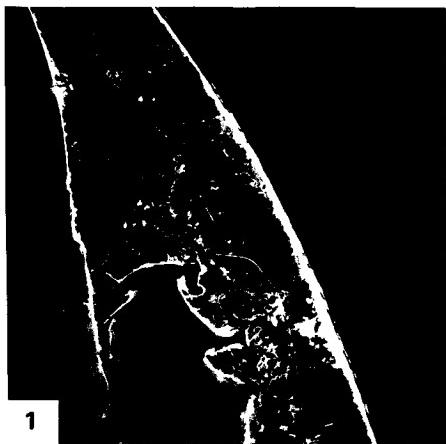
Figure G-24.1 shows a typical modern kettle still actively forming in an outwash plain of the upper Schuchert Dal of eastern Greenland. This kettle still contains part of the ice block whose melting is creating the depression. Kettle lakes are common features in the morainal and outwash deposits of surging glaciers because, after the surge is completed, a large area of fractured glacier ice becomes stagnant, usually for one or more decades until the next surge event.

This Plate is a Large-Format Camera (LFC) photograph (STS Mission 41-G) of the Cape Cod, Massachusetts, area and environs. The index map for southeastern Massachusetts locates the principal geographic place-names and areas of kettle lakes discussed in the text.

Cape Cod is a classic area of glacial and fluvioglacial deposition resulting from the interaction of three large lobes of the ice sheet that advanced over the Cape Cod area in Late Wisconsinan time and then gradually receded to the north (Oldale, 1976a, 1976b, 1982; Chamberlain, 1964; Strahler, 1966). Still-stands of the margins of these three lobes—Buzzards Bay lobe on the west, Cape Cod Bay lobe in the middle of Cape Cod, and South Channel lobe to the east—are marked by prominent ter-

CAPE COD, MASSACHUSETTS

minal moraines and/or a diversity of ice-contact and outwash deposits that range in thickness from 60 to 180 m (Oldale, 1976a). The area between Eastham and northern Truro is underlain by thick delta and outwash-plain deposits deposited in the interlobate area between the Cape Cod Bay and South Channel lobes as the main ice sheet retreated to the north and west (Oldale, 1976a, 1968; Oldale and Barlow, 1986; Koteff et al., 1967). At the margins of these thinning glacier lobes, copious quantities of morainal material became draped over buried stagnant ice, with outwash streams carrying debris onto and across the outwash plain. As the larger blocks of ice melted, numerous collapse depressions called kettles (Figure G-24.2) formed in the outwash plain. In the northern part of Wellfleet and the southern part of Truro, numerous kettles formed, many of which are now freshwater lakes, because the bottom of the kettle intersects the groundwater table (U.S. Geological Survey, 1972; Oldale, 1968). Figure G-24.3 is a vertical aerial photograph of this group of kettle lakes, which range in diameter from about 50 to 800 m (Gull Pond). Many of the kettles in this area do not intersect the ground-water table and are discernible only on topographic maps (U.S. Geological Survey, 1972) or on stereopairs of aerial photographs. Also, many of the kettle lakes do not completely fill their depressions or do not represent the actual irregular shape of a depression. For example, Great Pond (Figure G-24.2) partly fills an irregular kettle in association with four other smaller ponds. Its circular shape is mainly the result of post-kettle-formation processes, particularly reworking of the shores of Great Pond by wind and wave erosion of glacial deposits and redeposition as narrow sand bars between Great Pond and its four satellite ponds. Figure G-24.4 is a ground view of Round Pond, a water-filled kettle at the northern end of the group, near Truro. **Large-Format Camera 4107-0664, October 7, 1984.**



ORIGINAL PAGE IS
OF POOR QUALITY



4

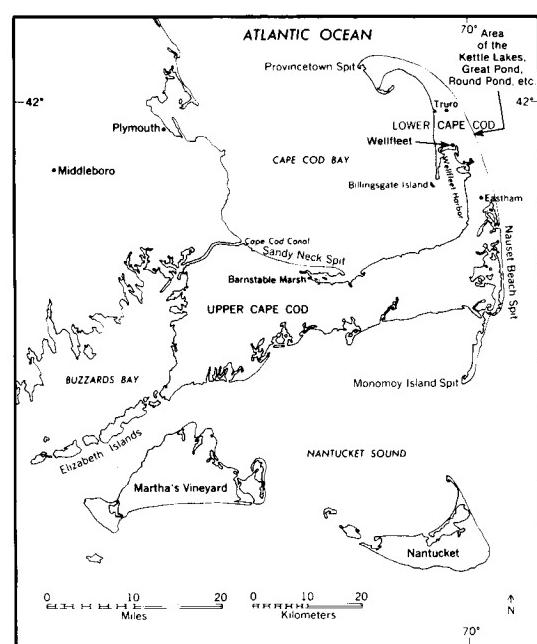


PLATE G-25

TUKTOYAKTUK PENINSULA, NWT, CANADA

Thermokarst is defined as "karstlike topographic features produced in a permafrost region by the local melting of ground ice and the subsequent settling of the ground. cf: glaciokarst" (Bates and Jackson, 1980). The area encompassed by the Plate image is situated northeast of the present mouth of the Mackenzie River in the northwestern part of the Northwest Territories. It shows well-developed thermokarst topography dominated by numerous thaw lakes. Thermokarst lakes and related features are particularly prominent features on the low-relief coastal plains (Figure G-25.1), peninsulas, and islands which border the Arctic Ocean (Figure G-25.2) and outside the floodplains of north-flowing rivers in northern Russia, such as along the Ob River (Figure G-25.3).

Figure G-25.1 is an oblique aerial photograph of thaw lakes on Bathurst Island, Northwest Territories, Canada, looking southwest across Polar Bear Pass. Figure G-25.2 is a Landsat MSS image of thaw lakes formed in ice-rich permafrost on the coastal plain south of Point Barrow, northern Alaska. Figure G-25.3 is a Landsat MSS image of thaw lakes in discontinuous permafrost beyond the floodplain of the Ob River, northern U.S.S.R. (see Plate KL-8).

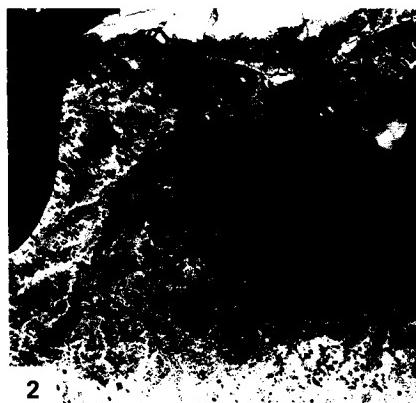
The Tuktoyaktuk Peninsula and the islands and linear landforms situated southwest of the peninsula are composed of Quaternary sediments; the remainder of the area is underlain by rocks of Cretaceous age (Fremlin, 1974). The area encompassed by the image, including the offshore submarine platform, was completely covered by glacial ice at the time of maximum extent of glaciation during the Pleistocene (Prest, 1983). In the Late Wisconsinan (the interval of the last ice sheet), however, the northern limit of the Laurentide Ice Sheet is considered to have extended along the southern edge of the Tuktoyaktuk Peninsula (Prest et al., 1967). Both the Tuktoyaktuk Peninsula and the northern and western part of the peninsula east of Liverpool Bay are composed of Wisconsinan outwash deposits. Ground moraine lies on the southwestern part of the Tuktoyaktuk Peninsula west of Campbell Island and the region from Nicholson Peninsula extending southwest through Rufus and Kaglik Lakes. Morainal ridges are visible southwest of Campbell and Thumb Islands. The remainder of the area south of Wood Bay is also mostly covered with ground moraine.

Tuktoyaktuk Peninsula contains numerous lakes formed through melting of the uppermost part of the underlying permafrost layer. Rampton and Bouchard (1975) noted that: "Permafrost-related processes, such as solifluction and soil creep, ice-wedge formation, frost shattering of boulders, pingo formation and the heaving of areas formerly covered by water bodies, have a major effect upon the landscape." This part of Canada lies

within the zone of continuous permafrost, which has been measured at more than 92 m in thickness about 200 km to the southwest (beyond the area of the image) at Inuvik (Brown, 1967), and 366 m thick in a well drilled on Richards Island, about 150 km to the west-southwest (Rampton and Bouchard, 1975). The peninsula is slowly being destroyed by the encroachment of the Beaufort Sea, which is progressively melting the upper part of the subaerial permafrost. Between McKinley Bay, Cape Dalhousie, and the easternmost part of the Tuktoyaktuk Peninsula, the coastline has a decidedly ragged appearance caused by the incorporation of older lake shorelines into the advancing new shoreline. "Coastal retreat is occurring as headland erosion and landward movement of spits and bars, which lie offshore or between headlands, occurs" (Rampton and Bouchard, 1975). In their geologic studies of the northwest coast of the Tuktoyaktuk Peninsula (about 70 km southwest of the western margin of the image), Rampton and Bouchard used sequential aerial photographs to measure the rate of coastal retreat. They found the average annual rate of retreat quite variable during the past 3 to 4 decades, ranging between 3.8 and 7.6 m per year. During one coastal storm in September 1970, a coastal bluff retreated 13.7 m in 1 day. Rapidly changing spits are also characteristic of the coast.

Submarine permafrost is present in the submerged coastal shelf; farther offshore, numerous submarine pingos have been mapped (Fremlin, 1974). Pingos also abound on the Tuktoyaktuk Peninsula and a belt extending west-southwest from Wood Bay (Brown, 1967). Although these and other periglacial landforms exist in the area, they cannot be resolved on Landsat MSS images.

Several other noteworthy geomorphic features that appear on the Landsat image should be noted. Large ice floes can be seen along the coast southeast of Cape Bathurst; smaller ice floes are present in the northwestern part of the image area in the Beaufort Sea. Several barrier beaches have formed on the northwest coast of the Tuktoyaktuk Peninsula, between Hutchinson Bay and Atkinson Point, at Atkinson Point, along the eastern shore of McKinley Bay, and at Cape Dalhousie. Spits have also formed at the tip of the Nicholson Peninsula on the southern part of Baillie Islands and at Cape Bathurst. Meanders are well developed on the lower reaches of the Anderson and Horton Rivers. The lowermost section of the Horton River represents an unusual geomorphic phenomenon. The advancing shoreline has "captured" the Horton River by intersecting one of the meander loops. The new mouth of the Horton River empties into the southwestern part of the Amundsen Gulf, where an arcuate delta has formed because of the limited wave energy. **Landsat 1005-20021-7, July 28, 1972.**



ORIGINAL PAGE IS
OF POOR QUALITY



3

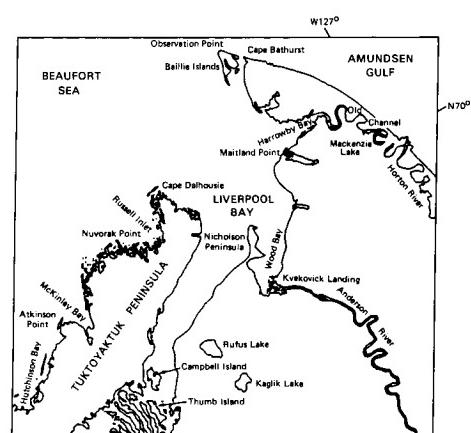


PLATE G-26*

WESTERN CHINA

South-central Asia contains mountain chains and basins whose average elevations lie higher than anywhere else in the world. This region is also one of the most tectonically active on Earth, with persistent rising of the crust to new heights. Temperatures at these higher altitudes are consistently low over most of this area expanse. Yet, examination of Landsat and Large-Format Camera images from selected localities throughout the region (e.g., Plates T-48, T-49, T-50, and E-27) reveal that extensive ice sheets are absent, and furthermore, some of the signs of major glaciation of the rugged terrain are either lacking or have been modified. This sparsity requires an explanation.

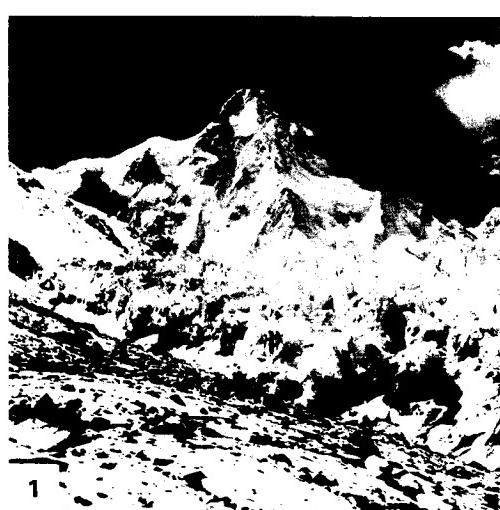
Perhaps the best example of the nature and extent of glaciation in this part of the world appears in this Plate. The scene lies in the Karakorum Shan, where Pakistan, India, and western-most China, southwest of the Taklimakan, come together. Included in the scene is the famed K-2 (or its Chinese name, Quogir Feng; 8611 m), second highest peak on the continents (Figure G-26.1) and reputedly more difficult to climb than Mt. Everest (Qomolangma Feng). Emanating from it and the nearby mountain ridges are a series of valley glaciers that include Ensugaite (Yinsukati), at 42 km the longest in China. In some instances, lower segments of the valleys hosting these glaciers appear in the image to have well-developed U-profiles, but at lower elevations there and in the mountains to the north, the valleys and particularly their tributaries seem to have narrow floodplains and sloping walls more akin to a V-shape. In areas not now being actively glaciated, older arêtes are indicated by knife-edge ridges, but cirques are not conspicuous in this image at Landsat resolution, although ground photographs indicate their presence. In the Nyainqntanglha Shan region some 1500 km to the east, modern glaciers also exist, as seen in the Landsat image shown in Figure G-26.2, but again, wide U-shaped valleys are uncommon relative to the more typical V-profiles cut into high mountains whose relief can exceed 4000 m. To the north in the Qilian Shan, active glaciers such as Laozugou (Figure G-26.3) descend through the steep-walled valleys widened by earlier glaciation.

Glaciation in West China has been described by Shi Yafeng and colleagues (1985, unpublished review/personal communica-

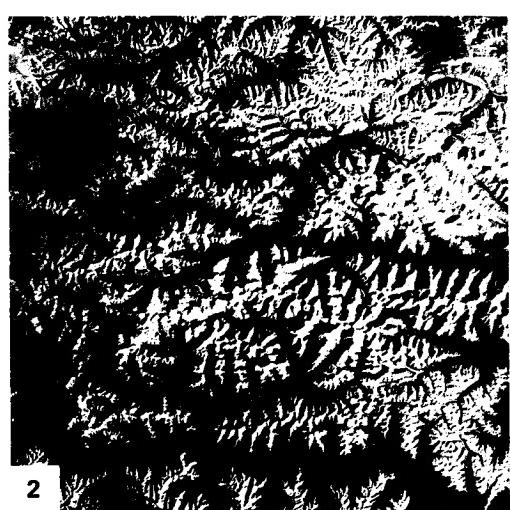
tion) and by Chi and Ren (1980). Glaciers persist today in the same mountain regions (Shans) but are notably diminished in area. The total area now occupied by glaciers in 56000 km², with the largest individual fields being the Himalaya Shan (11005 km²), Kunlun Shan (9973 km²), Tian Shan (9196 km²), Nyainqntanglha Shan (7536 km²), and Karakorum Shan (4650 km²). Chinese glaciologists recognize two major types of glaciers: (1) continental, which develop in regions in which precipitation ranges from 300 to 1000 mm per annum, the snowline is usually higher, and the mean air temperatures at the height of the snowline range between -6° and -15°C; (2) maritime, which represents regions in which weather conditions are strongly influenced by monsoonal precipitation ranging between 1000 and 2500 mm per annum and mean air temperatures at snowline stay at -2° to -4°C. (The second type is exemplified by glaciers in the Nyainqntanglha and Hengduan Shans.)

Shi and his colleagues at the Institute for Glaciology and Cryopedology in Lanzhou tie the glacial history of West China to a combination of climatic changes and increasing elevations in the Himalaya and other ranges in its trend, the Tibetan (Qinghai-Xizang) Plateau, and the fringing ranges to the north. From Early through Middle Pleistocene, two glaciations were driven by cold but humid climates as the region underwent continuing uplift. (Higher elevations may have been 2000 m lower than present.) Glaciation then was considerably more widespread than now, but no large continuous ice caps were formed. Valley glaciers, some with maximum lengths up to 100 to 200 km, did join in trellis-like networks. By the start of the Late Pleistocene, the climate had shifted to cold and dry as elevations generally rose. Two more glaciations have been recorded during this interval. Neoglacierization began in the Holocene, as permafrost conditions took over much of the entire region.

The relatively small number of glaciers surviving now in the "roof of the world" is explained by the general diminution of moisture available to provide snow from which to form ice by cold infiltration and congelation. The relief profiles characteristic of most of the higher mountains probably reflect the dominance of downcutting by streams and valley wall widening (decreasing slope angles) brought about by the high energetics of stream erosion that has modified older Pleistocene glacial topography. (*GCW: N. M. Short*) **Landsat 30135-04492, July 18, 1978.**

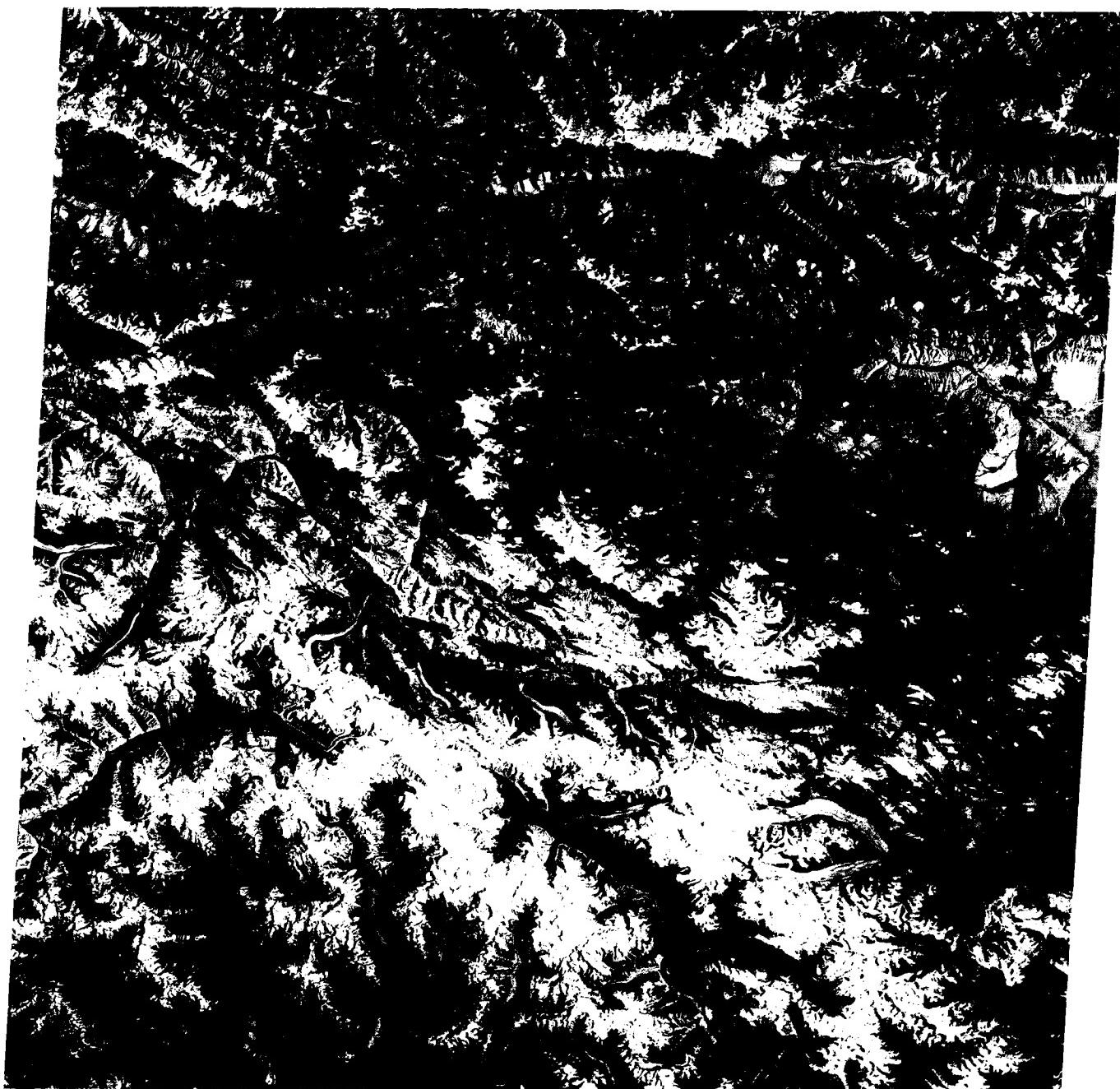


1

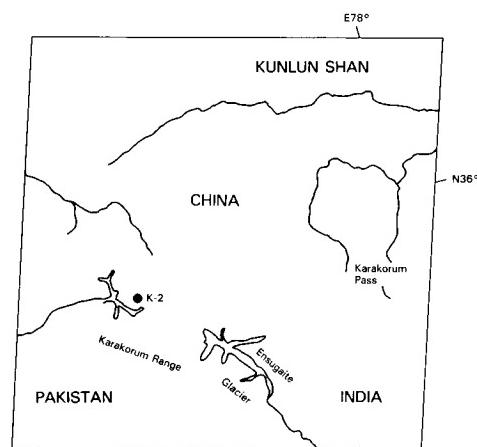


2

ORIGINAL PAGE
COLOR PHOTOGRAPH



3



REFERENCES

- Allen, C. R., and G. I. Smith, Seismic and gravity investigations on the Malaspina Glacier, Alaska, *Trans. American Geophysical Union*, **34**, 755-760, 1953.
- American Geographical Society Glacier Studies, Glaciers of Baffin Island, in *Atlas, Mountain Glaciers of the Northern Hemisphere*, edited by W. O. Field, Plate 37, Map 2.2 (dated April 1957), U.S. Army Corps of Engineers, Cold Regions Research and Engineering Laboratory, Technical Information Analysis Center, Hanover, New Hampshire, 1975a.
- American Geographical Society Glacier Studies, Glaciers of the Alaska Range: Mt. McKinley Area, in *Atlas, Mountain Glaciers of the Northern Hemisphere*, edited by W. O. Field, Plate 32, Map 1.4R (dated 1956, revised 1965), U.S. Army Corps of Engineers, Cold Regions Research and Engineering Laboratory, Technical Information Analysis Center, Hanover, New Hampshire, 1975b.
- Andersen, B. G., Late Weichselian ice sheets in Eurasia and Greenland, in *The Last Great Ice Sheets*, edited by G. H. Denton, and T. J. Hughes, pp. 1-65, John Wiley, New York, 1981.
- Anderson, D. M., W. K. Crowder, L. W. Gatto, R. K. Haugen, T. L. Marlar, H. L. McKim, and A. Petrone, An ERTS view of Alaska, Regional analysis of earth and water resources based on satellite imagery, U.S. Army Corps of Engineers, Cold Regions Research and Engineering Laboratory (CRREL), Hanover, New Hampshire, *Technical Report 241*, 51 pp., 1973.
- Armstrong, T., B. Roberts, and C. Swithinbank, *Illustrated Glossary of Snow and Ice*, 60 pp., Scott Polar Research Institute, Special Publication 4, Cambridge, 1973.
- Bates, R. L., and J. A. Jackson (Eds.), *Glossary of Geology*, 2nd Ed., 749 pp., American Geological Institute, Falls Church, Virginia, 1980.
- Bauer, A., Missions aériennes de reconnaissance au Groenland 1957-1958: Observations aériennes et terrestres, exploitation des photographies aériennes, détermination des vitesses des glaciers relâtant dans Disko Bugt et Umanak Fjord, *Expedition Glaciologique Internationale au Groenland*, **2**, No. 3, 116 pp., 1968.
- Benson, C. S., Stratigraphic studies in the snow and firn of the Greenland Ice Sheet: Snow, Ice, and Permafrost Research Establishment (SIPRE), U.S. Army Cold Regions Research and Engineering Laboratory (CRREL), *Research Report 70*, 93 pp. (published version of C. S. Benson's Ph.D. dissertation, 213 pp. (1960), Division of Geological Sciences, California Institute of Technology, Pasadena, California), 1962.
- Bird, J. B., *The Physiography of Arctic Canada, with Special Reference to the Area South of Parry Channel*, 336 pp., Johns Hopkins Press, Baltimore, 1967.
- Björnsson, H., Hugleidning um jöklarannsóknir á Íslandi, *Jökull*, **20** (1970), 15-26, 1971 (in Icelandic).
- Björnsson, H., Explanation of jökulhlaups from Grímsvötn, Vatnajökull, Iceland, *Jökull*, **24** (1974), 1-26, 1975.
- Björnsson, H., Subglacial water reservoirs, jökulhlaups and volcanic eruptions, *Jökull*, **25** (1975), 1-14, 1976.
- Björnsson, H., Glaciers in Iceland, *Jökull*, **29** (1979), 74-80, 1980.
- Brown, H., Addendum: The density and mass distribution of meteoritic bodies in the neighborhood of the Earth's orbit, *J. Geophys. Res.*, **66**, 1316-1317, 1961.
- Brown, R. J. E., *Permafrost in Canada: Geological Survey of Canada, Map 1246A*, Department of Energy, Mines and Resources, Ottawa, Ontario; scale 1:7 603 200, 1967.
- Brugman, M. M., and A. Post, Effects of volcanism on the glaciers of Mount St. Helens, U.S. Geol. Sur. Circ., **850-D**, 11 pp., 1982.
- Carbonnell, M., I. Nouvelles mesures photogrammétriques de la vitesse superficielle des glaciers du Groenland, *Expedition Glaciologique Internationale au Groenland*, **2**, 9-53, 1968.
- Cassidy, W. A., T. Meunier, V. Buchwald, and C. Thompson, Search for meteorites in the Allan Hills/Elephant Moraine area, 1982-1983, *Antarctic J. United States*, **18**, 81-82, 1984.
- Chamberlain, B. B., *These Fragile Outposts — A Geological Look at Cape Cod, Martha's Vineyard and Nantucket*, 327 pp., The Natural History Press, Garden City, New York, 1964.
- Chi, J., and B. Ren, *Glaciers in China*, Shanghai Scientific and Technical Publ., Shanghai, 1980.
- CIA, *A Study of Climatological Research as It Pertains to Intelligence Problems*, 36 pp., Office of Research and Development, Washington, D.C., 1974.
- CIA, *Polar Regions Atlas*, 66 pp., National Foreign Assessment Center, Washington, D.C., 1978.
- Clapperton, C. M., The debris content of surging glaciers in Svalbard and Iceland, *J. Glaciology*, **14**, 395-406, 1975.

- Davies, G. L. H., N. Stephens, and F. M. Syng, Ireland, in *The Geomorphology of the British Isles Series*, edited by E. H. Brown and K. Clayton, 250 pp., Methuen and Co., Ltd., London, 1978.
- Davis, W. M., The sculpture of mountains by glaciers, in *Geographical Essays*, edited by D. W. Johnson, pp. 617–634, Boston, Ginn and Co., 1909.
- Denton, G. H., and W. O. Field, 1975, Glaciers of the Alaska Range, in *Mountain Glaciers of the Northern Hemisphere*, Vol. 2, edited by W. O. Field, pp. 573–620, U.S. Army Cold Regions Research and Engineering Laboratory, Technical Information Analysis Center, Hanover, New Hampshire, 1975.
- Denton, G. H., and T. J. Hughes (Eds.), *The Last Great Ice Sheets*, 484 pp., John Wiley, New York, 1981a.
- Denton, G. H., and T. J. Hughes, The Arctic ice sheet: An outrageous hypothesis, in *The Last Great Ice Sheets*, edited by G. H. Denton and T. J. Hughes, pp. 437–467, John Wiley, New York, 1981b.
- Desinov, L. V., G. A. Nosenko, G. M. Grechko, A. S. Ivanchenkov, and V. M. Kotlyakov, Glaciological studies and experiments aboard the Salyut-6 orbital station, *Studies of the Earth from Space*, No. 1, 25–34 (in Russian), 1980.
- Doake, C. S. M., State of balance of the ice sheets in the Antarctic Peninsula, *Ann. Glaciology*, 3, 77–82, 1982.
- Drewry, D. J. (Ed.) *Antarctica: Glaciological and Geophysical Folio*, sheets 2–9, Scott Polar Research Institute, University of Cambridge, Cambridge, England, 1983.
- Drewry, D. J., S. R. Jordan, and E. Jankowski, Measured properties of the Antarctic ice sheet: Surface configuration, ice thickness, volume and bedrock characteristics, *Ann. Glaciology*, 3, 83–91, 1982.
- Duphorn, K., H. O. Grahle, and H. Schneider (Eds.), *International Quaternary Map of Europe*, Sheet 5, scale 1:2 500 000, Hannover, Bundesanstalt für Bodenforschung and UNESCO, INQUA-Commission for the International Quaternary Map of Europe, 1967.
- Duphorn, K., H. O. Grahle, and H. Schneider (Eds.), *International Quaternary Map of Europe*, Sheet 6, scale 1:2 500 000, Hannover, Bundesanstalt für Bodenforschung and UNESCO, INQUA-Commission for the International Quaternary Map of Europe, 1970.
- Einarsson, T., D. M. Hopkins, and R. R. Doell, The stratigraphy of Tjörnes, northern Iceland, and the history of the Bering land bridge, in *The Bering Land Bridge*, edited by D. M. Hopkins, pp. 312–325, Stanford University Press, Stanford, California, 1967.
- Embleton, C., Northern and central Ireland, in *Geomorphology of Europe*, edited by C. Embleton, pp. 125–131, Macmillan Publishers, London, 1984.
- Embleton, C., and C. A. M. King, Glacial geomorphology, in *Glacial and Periglacial Geomorphology*, Vol. 1, 2nd Ed., 573 pp., John Wiley, New York, 1975a.
- Embleton, C., and C. A. M. King, Periglacial geomorphology, in *Glacial and Periglacial Geomorphology*, Vol. 2, 2nd Ed., 203 pp., John Wiley, New York, 1975b.
- Escher, A. (compiler), *Tectonic/Geological Map of Greenland*, scale 1:2 500 000, Geological Survey of Greenland, Copenhagen, 1970.
- Escher, A., and W. S. Watt (Eds.), *Geology of Greenland*, 603 pp., Geological Survey of Greenland, Copenhagen, 1976.
- Falconer, G., Glaciers of northern Baffin and Bylot Islands, NWT, *Geographical Paper 33*, 31 pp., Geographical Branch, Department of Mines and Technical Surveys, Ottawa, Ontario, 1962.
- Field, W. O., Glaciers of the Chugach Mountains, in *Mountain Glaciers of the Northern Hemisphere*, Vol. 2, edited by W. O. Field, pp. 299–492, U.S. Army Corps of Engineers, Cold Regions Research and Engineering Laboratory, Technical Information Analysis Center, Hanover, New Hampshire, 1975.
- Field, W. O., Observations of glacier variations in Glacier Bay National Monument, in *Proc. First Conference on Scientific Research in the National Parks*, edited by R. M. Linn, pp. 803–808, National Park Service Transactions and Proceedings Series, No. 5, 1979.
- Flint, R. F., *Glacial and Quaternary Geology*, 892 pp., John Wiley, New York, 1971.
- Ford, J. P., Mapping of glacial landforms from Seasat radar images, *Quaternary Res.*, 22, 314–327, 1984.
- Ford, J. P., R. G. Blom, M. L. Bryan, M. I. Daily, T. H. Dixon, C. Elachi, and E. C. Xenos, Seasat views North America, the Caribbean, and western Europe with imaging radar, *JPL Publication 80-67*, 141 pp., Jet Propulsion Laboratory, California Institute of Technology, Pasadena, California, 1980.
- Fremlin, G. (Ed.), *The National Atlas of Canada*, 4th Ed. (revised), 254 plates, Department of Energy, Mines and Resources and Information Canada, Ottawa, The Macmillan Company of Canada Limited, Toronto, Ontario, 1974.
- Friedman, J. D., C. E. Johansson, N. Óskarsson, H. Svensson, S. Thorarinsson, and R. S. Williams, Jr., Observations on Icelandic polygon surfaces and palsas: Photo interpretation and field studies, *Geografiska Annaler*, 53A, 115–145, 1971.
- Friedman, J. D., R. S. Williams, Jr., S. Thorarinsson, and G. Pálason, Infrared emission from Kverkfjöll subglacial volcanic and geothermal area, Iceland, *Jökull*, 22, 27–43, 1972.
- Glen, J. W., Discussion of N. N. Pal'gov's paper: The relation between glacier retreat and the position of the firn line with special reference to the Zentralny Tuyuksu glaciers, *Bull. International Assn. Scientific Hydrology*, 8, p. 68, 1963.
- Grosval'd, M. E., and A. F. Glazovskiy, Glacial erosion of continental margins (the origins of fiords and troughs within glaciated shelves), *Polar Geography and Geology*, 8, 113–127, 1984.
- Hall, D. K., and J. P. Ormsby, Use of SEASAT synthetic aperture radar and LANDSAT multispectral scanner subsystem data for Alaskan glaciology studies, *J. Geophys. Res.*, 88, 1597–1607, 1983.
- Hollin, J. T., and D. H. Schilling, 1981, Late Wisconsin-Weichselian mountain glaciers and small ice caps, in *The Last Great Ice Sheets*, edited by G. H. Denton and T. J. Hughes, pp. 179–206, John Wiley, New York, 1981.

- Horvath, E. (compiler), Glaciers of Kol'skiy Poluostrov (Kola Peninsula), Ural'skiy Khrebet (Ural Mountains), and Poluostrov Taymyr (Taymyr Peninsula), in *Mountain Glaciers of the Northern Hemisphere*, Vol. 1., edited by W. O. Field, pp. 185-197, U.S. Army Corps of Engineers, Cold Regions Research and Engineering Laboratory, Technical Information Analysis Center, Hanover, New Hampshire, 1975.
- Howarth, P. J., and R. Welch, Breidamerkurjökull, Southeast Iceland, Department of Geography, University of Glasgow, Scotland; two map sheets (August 1945 and August 1965), scale 1:30000, 1969.
- Hughes, T. J., Is the West Antarctic ice sheet disintegrating?, *J. Geophys. Res.*, **78**, 7884-7910, 1973.
- Hughes, T. J., The West Antarctic ice sheet: Instability, disintegration, and initiation of ice ages, *Rev. Geophysics and Space Physics*, **13**, 502-526, 1975.
- Hughes, T. J., West Antarctic ice streams, *Rev. Geophysics and Space Physics*, **15**, 1-46, 1977.
- Hughes, T. J., The Jacobshavn Glacier ice drainage system, in *Workshop on the Jakobshavns Glacier (Greenland)*, pp. 36-50, held at Northwestern University, Evanston, Illinois, February 8-10, 1983, National Science Foundation, Division of Polar Programs, Washington, D.C., 1983.
- Hughes, T. J., G. H. Denton, B. G. Andersen, D. H. Schilling, J. L. Fastook, and C. S. Lingle, The last great ice sheets: A global view, in *The Last Great Ice Sheets*, edited by G. H. Denton and T. J. Hughes, pp. 263-317, John Wiley, New York, 1981.
- Imbrie, J. and J. Z. Imbrie, Modeling the climatic response to orbital variations, *Science*, **207**, 943-953, 1980.
- Jackson, G. D., Bylot Island, N.W.T. in *Landsat Images of Canada—A Geological Appraisal*, edited by V. R. Slaney, pp. 68-70, Geological Survey of Canada, Paper 80-15, 1981.
- Koteff, C., R. N. Oldale, and J. H. Hartshorn, Geologic map of the North Truro quadrangle, Barnstable County, Massachusetts, U.S. Geol. Surv. Geol. Quad. Map GQ-599, scale 1:24,000, 1967.
- Krimmel, R. M., A. Post, and M. F. Meier, Surging and non-surging glaciers in the Pamir Mountains, U.S.S.R., in *ERTS-1 A New Window on Our Planet*, edited by R. S. Williams, Jr., and W. D. Carter, pp. 178-179, U.S. Geol. Surv. Prof. Paper, **929**, 1976.
- Kristjánsson, L., J. B. Fridliefsson, and N. D. Watkins, Stratigraphy and paleomagnetism of the Esja, Eyrarfjall and Akrafjall mountains, SW-Iceland, in *Iceland Evolution, Active Tectonics, and Structure*, edited by W. Jacoby, A. Björnsson, and D. Moller, *J. Geophysics*, **47**, 31-42, 1980.
- Liestøl, Olav, Glaciers of Svalbard, Norway, in *Satellite image atlas of glaciers*, edited by R. S. Williams, Jr., and J. G. Ferrigno, U.S. Geol. Surv. Prof. Paper 1386-E, in press.
- Linton, D. L., The forms of glacial erosion, *Trans. Institute of British Geographers*, **33**, pp. 1-28, 1963.
- Lucas, J. R., and J. V. Taranik, Late Wisconsinan deglaciation of the northern Midwest interpreted from a springtime Landsat color mosaic (abstract), in *Proc. 11th International Symp. on Remote Sensing of Environment*, Vol. 2, pp. 991-992, Environmental Research Institute of Michigan, Ann Arbor, Michigan, 1977.
- Lundquist, G., K. E. Sahlstrom, J. Lundquist, E. Granlund, and E. Fromm, Karta över Sveriges jordarter (Quaternary deposits of Sweden), Ser. Ba, no. 17, scale 1:1000000, Sveriges Geologiska Undersökning, 1958.
- Lundquist, J., Moraine morphology-terminological remarks and regional aspects, *Geografiska Annaler*, **63A**, 127-138, 1981.
- Magnusson, N. H., B. Asklund, O. Kulling, G. Kautsky, J. Eklund, W. Larsson, P. H. Lundegårdh, S. Hjelmqvist, S. Gavelin, and O. Ödman, Karta över Sveriges bergrund (Pre-Quaternary rocks of Sweden), Ser. Ba, no. 16, scale, 1:1000000, Sveriges Geologiska Undersökning, 1958.
- Marvin, U. B., Meteorites on ice, *The Planetary Report*, **4**, 12-14, 1984.
- Mayewski, P. A., G. H. Denton, and T. J. Hughes, Late Wisconsin ice sheets in North America, in *The Last Great Ice Sheets*, edited by G. H. Denton and T. J. Hughes, pp. 67-178, John Wiley, New York, 1981.
- Meier, M. F., Ice sheets and glaciers, in *Encyclopedia Britannica*, 15th Ed., pp. 175-186, 1974.
- Meier, M. F., Monitoring the motion of surging glaciers in the Mount McKinley massif, Alaska, in *ERTS-1, A New Window on Our Planet*, edited by R. S. Williams, Jr., and W. D. Carter, pp. 185-187, U.S. Geol. Surv. Prof. Paper 929, 1976.
- Meier, M. F., The Columbia Glacier project and its relation to a Jakobshavns Glacier Research Program, in *Workshop on the Jakobshavns Glacier (Greenland)*, pp. 67-68, held at Northwestern University, Evanston, Illinois, February 8-10, 1983, National Science Foundation, Division of Polar Programs, Washington, D.C., 1983.
- Meier, M. F., and A. S. Post, Recent variations in mass net budgets of glaciers in western North America, in *Proc. Symp. on Variations of the Regime of Existing Glaciers*, edited by W. Ward, pp. 63-67, Obergurgl, Austria, International Assn. Scientific Hydrology Publication 58, 1962.
- Meier, M. F., and A. Post, What are glacier surges?, *Canadian J. Earth Sciences*, **6**, 807-817, 1969.
- Meier, M. F., A. Post, C. S. Brown, D. Frank, S. M. Hodge, L. R. Mayo, L. A. Rasmussen, E. A. Senear, W. G. Sikonia, D. C. Trabant, and R. D. Watts, Columbia Glacier progress report—December 1977, 78 pp., U.S. Geol. Surv. *Open-File Report 78-264*, 1978.
- Meier, M. F., L. A. Rasmussen, A. Post, C. S. Brown, W. G. Sikonia, R. A. Bindschadler, L. R. Mayo, and D. C. Trabant, Predicted timing of the disintegration of the lower reach of Columbia Glacier, Alaska, 47 pp., U.S. Geol. Surv. *Open-File Report 80-582*, 1980.
- Mercer, J. H., Southern hemisphere glacier atlas, *Technical Report 67-76-ES, Series ES-33*, 325 pp., by Amer. Geographical Society, New York, for the Earth Sciences Laboratory, U.S. Army Natick Laboratories, Natick, Massachusetts, 1967.

- Mercer, J. H., Glaciers of Baffin and Bylot Islands, in *Mountain Glaciers of the Northern Hemisphere*, Vol. 2, edited by W. O. Field, pp. 683-721, U.S. Army Corps of Engineers, Cold Regions Research and Engineering Laboratory, Technical Information Analysis Center, Hanover, New Hampshire, 1975a.
- Mercer, J. H., Glaciers of Greenland, in *Mountain Glaciers of the Northern Hemisphere*, Vol. 2, edited by W. O. Field, pp. 755-808, U.S. Army Corps of Engineers, Cold Regions Research and Engineering Laboratory, Technical Information Analysis Center, Hanover, New Hampshire, 1975b.
- Mercer, J. H., West Antarctic ice sheet and CO₂ greenhouse effect: A threat of disaster, *Nature*, **271**, 321-325, 1978.
- Molland, J. D., Landforms and surface materials of Canada; A stereoscopic airphoto atlas and glossary, A guide to terrain analysis for engineering, geological and environmental studies, J. D. Molland, Ph.D., Consultant, Airphoto Interpretation, Regina, Saskatchewan, looseleaf notebook, variously paginated by sections, 1974.
- Müller, F., Zonation in the accumulation area of the glaciers of Axel Heiberg Island, N.W.T., Canada, *J. Glaciology*, **4**, 302-313, 1962.
- Müller, F., T. Caflisch, and G. Müller, *Instructions for Compilation and Assemblage of Data for a World Glacier Inventory*, 28 pp., Temporary Technical Secretariat for World Glacier Inventory, International Commission on Snow and Ice, Swiss Federal Institute of Geography, Zürich, 1977.
- National Institute of Polar Research (Japan), (*Working Map of the Meteorite Ice Field, Yamato Mountains, Antarctica*, scale 1:200 000, National Institute of Polar Research, Tokyo, 1976.
- Oldale, R. N., Geologic map of the Wellfleet quadrangle, Barnstable County, Massachusetts, U.S. Geol. Surv. Geol. Quad. Map GQ-750, scale 1:24000, 1968.
- Oldale, R. N., Geologic History of Cape Cod, U.S. Geol. Surv. Scientific Leaflet No. INF-75-6, 24 pp., 1976a.
- Oldale, R. N., Generalized geologic map of Cape Cod, U.S. Geol. Surv. Open-File Report, 76-765, 23 pp. (includes 1:125 000-scale map), 1976b.
- Oldale, R. N., Pleistocene stratigraphy of Nantucket, Martha's Vineyard, the Elizabeth Islands, and Cape Cod, Massachusetts, in *Late Wisconsinan Glaciation of New England*, edited by G. J. Larson and B. D. Stone, pp. 1-34, Kendall-Hunt Publishing Co., Dubuque, Iowa, 1982.
- Oldale, R. N., and R. A. Barlow, Geologic map of Cape Cod and the islands, Massachusetts, U.S. Geol. Surv. Misc. Investigation Series, Map I-1763, scale 1:100000, 1986.
- Olsen, E.J., Estimates of total quantity of meteorites in the East Antarctica ice cap, *Nature*, **292**, 516-518, 1981.
- Østrem, G., ERTS data in glaciology—an effort to monitor glacier mass balance from satellite imagery, *J. Glaciology*, **15**, 403-414, 1975.
- Paterson, W. S. B., *The Physics of Glaciers*, 250 pp., Pergamon Press, New York, 1969.
- Paterson, W. S. B., *The Physics of Glaciers*, 2nd Ed., 380 pp., Pergamon Press, New York, 1981.
- Persson, T., Geomorphological studies in the south-Swedish highlands with special reference to the glacial forms, *Avhandlingar No. 66*, 91 pp., Meddelanden, Lund Universitet Geografiska Institution, 1972.
- Péwé, T. L., Quaternary Geology of Alaska, *U.S. Geol. Surv. Prof. Paper*, **835**, 145 pp., 1975.
- Post, A., Distribution of surging glaciers in western North America, *J. Glaciology*, **8**, 229-240, 1969.
- Post, A., Preliminary hydrography and historic terminal changes of Columbia Glacier Alaska, *Hydrologic Investigations Atlas HA-559* (3 sheets), U.S. Geol. Surv., 1975.
- Post, A., Reported observations of icebergs from Columbia Glacier in Valdez Arm and Columbia Bay, Alaska, during the summer of 1976, *Open-File Report 77-235*, 7 pp., U.S. Geol. Surv., 1977.
- Post, A., and L. R. Mayo, Glacier dammed lakes and outburst floods in Alaska, *Hydrologic Investigations Atlas HA-455* (3 sheets), U.S. Geol. Surv., 10 pp., 1971.
- Post, A., M. F. Meier, and L. R. Mayo, Measuring the motion of the Lowell and Tweedsmuir surging glaciers of British Columbia, Canada, in *ERTS-1, A New Window on Our Planet*, edited by R. S. Williams, Jr. and W. D. Carter, pp. 180-184, U.S. Geol. Surv. Prof. Paper 929, 1976.
- Prest, V. K., Nomenclature of moraines and ice-flow features as applied to the glacial map of Canada, *Paper 67-57*, 32 pp., Geological Survey of Canada, 1968.
- Prest, V. K., Canada's heritage of glacial features, *Miscellaneous Report 28*, 119 pp., Geological Survey of Canada, 1983.
- Prest, V. K., D. R. Grant, and V. N. Rampton (compilers), *Glacial map of Canada*; scale 1:5000000, Geological Survey of Canada, Map 1253A, Department of Energy, Mines and Resources, Ottawa, Ontario, 1967.
- Preusser, H., *The Landscapes of Iceland: Types and Regions*, 363 pp., Dr. W. Junk b.v., Publishers, The Hague, 1976.
- Price, R. J., 1973, *Glacial and Fluvioglacial Landforms*, 242 pp., Hafner Publishing Company, New York, 1973.
- Rampton, V. N., and M. Bouchard, Surficial geology of Tuktoyaktuk, District of Mackenzie, *Paper 74-53*, 17 pp., Geological Survey of Canada, 1975.
- Rist, S., Jökulhlápaannál 1971, 1972 og 1973, *Jökull*, **23** (1973), 55-60, 1974. (in Icelandic).
- Ritter, D. F., *Process Geomorphology*, 603 pp., Wm. C. Brown Company, Dubuque, Iowa, 1978.
- Rudberg, S., Finland, Sweden, and Norway, in *Geomorphology of Europe*, edited by C. Embleton, pp. 55-76, Macmillan Publishers, London, 1984.
- Saemundsson, K., Outline of the geology of Iceland, *Jökull*, **29** (1979) 7-28, 1980.

- Scheidegger, A. E., *Theoretical Geomorphology*, 435 pp., 2nd revised Ed., Springer-Verlag, New York, 1970.
- Schytt, V., Blue ice-fields, in *Glaciology II, E. Blue Ice-Fields, Moraine Features and Glacier Fluctuations*, Vol. 4, pp. 183–189, Norwegian-British-Swedish Antarctic Expedition, 1949–52: Scientific Results, Norsk Polarinstitutt, Oslo University Press, 1961.
- Shaler, N. S., and W. M. Davis, *Illustrations of the Earth's Surface: Glaciers*, 198 pp., J. R. Osgood and Co., Boston, 1881.
- Sharp, R. P., The latest major advance of Malaspina Glacier, Alaska, *Geograph. Rev.*, **48**, 16–26, 1958a.
- Sharp, R. P., Malaspina Glacier, Alaska, *Geol. Soc. Amer. Bull.*, **69**, 617–646, 1958b.
- Sharpe, D. R., Late Wisconsinan glaciation and deglaciation of Wollaston Peninsula, Victoria Island, Northwest Territories, in *Current Research, Part A; Paper 84-1A*, pp. 259–269, Geological Survey of Canada, 1984.
- Simkin, T., L. Siebert, L. McClelland, D. Bridge, C. Newhall, and J. H. Latter, *Volcanoes of the World*, 232 pp., Von Nostrand Reinhold Co., New York, 1981.
- Slaney, V. R., Landsat images of Canada—A geological appraisal, *Paper 80-15*, 102 pp., Geological Survey of Canada, 1981.
- Sloan, C. E., C. Zenone, and L. R. Mayo, Icings along the Trans-Alaska Pipeline route, *U.S. Geol. Surv. Prof. Paper*, **979**, 31 pp., 1976.
- Soha, J. M., A. R. Gillespie, M. J. Abrams, and D. P. Madura, Computer techniques for geological applications, in *Proc. Caltech/JPL Conf. on Image Processing Technology, JPL SP 43-30*, 4-1-4-21, Data Sources and Software for Commercial and Scientific Applications, California Institute of Technology, Pasadena, California, 1976.
- Southworth, C. S., Imaging sensor systems on spacecraft, in *Manual of Remote Sensing Vol. II*, 2nd Ed., edited by R. N. Colwell, pp. 1685–1696, American Society of Photogrammetry, Falls Church, Virginia, 1983.
- Stove, G. C., K. Green, R. V. Birnie, G. Davison, K. Bagot, M. Palmer, G. Kearn, P. F. S. Ritchie, and D. E. Sugden, *Monitoring Iceberg Production from West Greenland Tidewater Glaciers Using Landsat Data*, 32 pp., results of the AGRISPINE experiment for the Jakobshavn Isbrae, Macaulay Institute for Soil Research, Craigiebuckler, Aberdeen, Scotland, and the National Remote Sensing Centre, Space and New Concepts Department, Royal Aircraft Establishment, Farnborough, Hampshire, England, n.d. (1984?).
- Strahler, A. N., *Physical Geography*, 2nd Ed., 534 pp., John Wiley, New York, 1960.
- Strahler, A. N., *A Geologist's View of Cape Cod*, 115 pp., The Natural History Press, Garden City, New York, 1966.
- Stuiver, M., G. H. Denton, T. J. Hughes, and J. L. Fastook, History of the marine ice sheet in West Antarctica during the last glaciation: A working hypothesis, in *The Last Great Ice Sheets*, edited by G. H. Denton and T. J. Hughes, pp. 319–436, John Wiley, New York, 1981.
- Sugden, D. E., and B. S. John, *Glaciers and Landscapes: A Geomorphological Approach*, 376 pp., John Wiley, New York, 1976.
- Svensson, H., Permafrost, in *Manual of Remote Sensing Vol II*, 2nd Ed., edited by R. N. Colwell, pp. 1868–1869, American Society of Photogrammetry, Falls Church, Virginia, 1983.
- Svensson, H., K. Lidmar-Bergstrom, K. E. Bergsten, S. Behrens, S. W. Nordström, J. O. Mattsson, J. O. Lindquist, L. Améen, and N. Lewan, Experiences of ERTS-1 imagery in geographical studies, Lund Studies in Geography, Series A, Physical Geography, No. 55 (reprint of article published in Svensk Geografisk Årsbok, No. 49, pp. 117–170), 1973.
- Swithinbank, C. W. M., The problem of a glacier inventory of Antarctica: World glacier inventory in *Proc. Riederalp Workshop*, September 1978, pp. 229–236, International Association of Hydrological Sciences, Publication No. 126, 1980.
- Swithinbank, C., Towards an inventory of the great ice sheets, *Geografiska Annaler*, **65A**, 289–294, 1983.
- Thorarinsson, S., The icedammed lakes of Iceland with particular reference to their values as indicators of glacier oscillations, *Geografiska Annaler*, **21**, 216–242, 1940.
- Thorarinsson, S., On the variations of Svinafellsjökull, Skafafellsjökull, and Kviárjökull in Öraefi, *Jökull*, **6**, 1–15, 1956a.
- Thorarinsson, S., *The Thousand Years Struggle Against Ice and Fire*, Miscellaneous Paper No. 14, 52 pp., Museum of Natural History, Department of Geology and Geography, Reykjavik, 1956b.
- Thorarinsson, S., The jökulhlaup from the Katla area in 1955 compared with other jökulhlaups in Iceland, *Jökull*, **7**, 21–25, 1957.
- Thorarinsson, S., The postglacial volcanism, in *On the Geology and Geomorphology of Iceland*, edited by S. Thorarinsson, *Geografiska Annaler*, **41**, 143–150, 1959.
- Thorarinsson, S., Sudden advance of Vatnajökull outlet glaciers 1930–1964, *Jökull*, **14**, 76–89, 1964.
- Thorarinsson, S., Glacier surges in Iceland, with special reference to the surges of Brúarjökull (with discussion), *Canadian J. Earth Sciences*, **6**, 875–882, 1969.
- Thorarinsson, S., K. Saemundsson, and R. S. Williams, Jr., ERTS-1 image of Vatnajökull: Analysis of glaciological, structural, and volcanic features, *Jökull*, **23** (1973), 7–17, 1974.
- Thornbury, W. D., *Principles of Geomorphology*, 618 pp., John Wiley, New York, 1954.
- Thoroddsen, Th., Árferdi á Íslandi í thúsund ár, 432 pp., Hid Íslenska Fraedafjelag í Kaupmannahöfn, S. L. Möller, Copenhagen, 1916 (pt. 1) and 1917 (pt. 2) (in Icelandic).
- Tingey, R. J., and J. W. Convine (compilers), *Geology of Southern Prince Charles Mountains, Australian Antarctic Territory*, scale 1:500000, Bureau of Mineral Resources, Geology and Geophysics, Department of National Development and Energy, Canberra, 1982.

- Tómasson, H., Grímsvatnahlaup 1972, Mechanism and sediment discharge, *Jökull*, 24 (1974), 27–39, 1975.
- UNESCO, 1970, *Perennial Ice and Snow Masses: A Guide for Compilation and Assemblage of Data for a World Inventory*, 19 pp., United Nations Educational, Scientific, and Cultural Organization and International Association of Scientific Hydrology (IASI), 1970.
- University of Glasgow, *Breidamerkurjökull 1903–1980*, scale 1:200 000, (four maps—1903, 1945, 1965, 1980), Department of Geography, University of Glasgow, Scotland, 1982.
- U.S. Geological Survey, Wellfleet, Massachusetts, quadrangle map, scale 1:25 000, 1972.
- U.S. Geological Survey, *Mount Takahe*, Sheet ST 9-12/4 of Antarctic 1:250 000 Reconnaissance Series, 1976a.
- U.S. Geological Survey, *Vatnajökull, Iceland (Fall Scene)*, Landsat Image Format Series, N6359W01723, Experimental Printing, 1:500 000-scale, Reston, Virginia, 1976b.
- U.S. Geological Survey, Water of the world, *Scientific Leaflet INF-68-7*, 20 pp., Reston, Virginia, 1976c.
- U.S. Geological Survey, *Vatnajökull, Iceland (Winter Scene)*, Landsat Image Format Series, N6359W01723, Experimental Printing, 1:500 000-scale, Reston, Virginia, 1977.
- Washburn, B., Morainic bandings of Malaspina and other Alaskan glaciers, *Geol. Soc. Amer. Bull.*, 46, 1879–1889, 1935.
- Weidick, A. (compiler), *Quaternary Map of Greenland*, scale 1:2 000 000, The Geological Survey of Greenland, Copenhagen, n.d.
- Williams, R. S., Jr., Vatnajökull icecap, Iceland, in *U.S. Geol. Surv. Prof. Paper*, edited by R. S. Williams, Jr., and W. D. Carter, 188–193, 1976.
- Williams, R. S., Jr., Regional geologic mapping using Landsat 3 return beam vidicon images: Examples from Iceland and Cape Cod, Massachusetts (abstract), in *Abstracts with Programs, 1979 Annual Meetings, Geol. Soc. Amer.*, 11, pp. 541, 1979.
- Williams, R. S., Jr., *Glaciers: Clues to Future Climate?*, 22 pp., U.S. Geol. Surv. Scientific Leaflet, Reston, Virginia, 1983a.
- Williams, R. S., Jr. (contributing author), Remote sensing in glacial geology studies of the proglacial area of Breidmerkurjökull, southeastern Iceland, in *Manual of Remote Sensing*, Vol. II, 2nd Ed., edited by R. N. Colwell, pp. 1866–1868, American Society of Photogrammetry, Falls Church, Virginia, 1983b.
- Williams, R. S. Jr. (contributing author), Remote sensing of glaciers, in *Manual of Remote Sensing*, Vol. II, 2nd Ed., edited by R. N. Colwell, pp. 1852–1866, American Society of Photogrammetry, Falls Church, Virginia, 1983c.
- Williams, R. S., Jr. (contributing author), Remote sensing of glaciologic hazards, in *Manual of Remote Sensing*, Vol. II, 2nd Ed. edited by R. N. Colwell, pp. 1843–1846, American Society of Photogrammetry, Falls Church, Virginia, 1983d.
- Williams, R. S. Jr. (contributing author), Remote sensing of Kviárjökull outlet glacier, Iceland, in *Manual of Remote Sensing*, Vol. II, 2nd Ed., edited by R. N. Colwell, p. 1875, American Society of Photogrammetry, Falls Church, Virginia, 1983e.
- Williams, R. S., Jr., Satellite glaciology of Iceland, *Jökull*, 33, 3–12, 1983f.
- Williams, R. S., Jr., Monitoring the area and volume of ice caps and ice sheets: Present and future opportunities using satellite remote-sensing technology, in *Glaciers, Ice Sheets, and Sea Level: Effects of a CO₂-Induced Climatic Change*, pp. 232–240, National Academy Press, Washington, D.C., 1985.
- Williams, R. S., Jr., and J. G. Ferrigno, Satellite image atlas of the Earth's glaciers, in *Satellite Hydrology, Proc. Fifth Annual Wm. T. Pecora Memorial Symp. on Remote Sensing*, edited by M. Deutsch, D. R. Wiesner, and A. Rango, pp. 173–182, American Water Resources Association, Minneapolis, 1981.
- Williams, R. S., Jr., and H. Svensson, Glaciology, in *Manual of Remote Sensing*, Vol. II, 2nd Ed., edited by R. N. Colwell, pp. 1851–1869, American Society of Photogrammetry, Falls Church, Virginia, 1983a.
- Williams, R. S., Jr., and H. Svensson, Geomorphology, in *Manual of Remote Sensing*, Vol. II, 2nd Ed., edited by R. N. Colwell, pp. 1869–1878, American Society of Photogrammetry, Falls Church, Virginia, 1983b.
- Williams, R. S., Jr., and S. Thorarinsson, ERTS-1 image of Vatnajökull area: General comments, *Jökull*, 23 (1973), 1–6, 1974.
- Williams, R. S., Jr., Á. Bödvarsson, S. Fridriksson, G., Pálmarsson, S. Rist, H. Sigtryggsson, K. Saemundsson, S. Thorarinsson, and I. Thorsteinsson, Environmental studies of Iceland with ERTS-1 imagery, in *Proc. Ninth International Symp. Remote Sensing Environment*, Vol. 1, pp. 31–81, Environmental Research Institute of Michigan, Ann Arbor, Michigan, 1974.
- Williams, R. S., Jr., A. Bödvarsson, S. Rist, K. Saemundsson, and S. Thorarinsson, Glaciological studies in Iceland with ERTS-1 imagery (abstract), *J. Glaciology*, 15, 465–466, 1975.
- Williams, R. S., Jr., J. G. Ferrigno, T. M. Kent, and J. W. Schoonmaker, Jr., Landsat images and mosaics of Antarctica for mapping and glaciological studies, *Ann. Glaciology*, 3, 321–326, 1982.
- Williams, R. S., Jr., J. G. Ferrigno, and T. K. Meunier, Satellite glaciology project, *Antarctic Journal of the United States*, 18, 119–121, 1984.
- Williams, R. S., Jr., T. N. Mecklenburg, M. J. Abrams, and B. Gudmundsson, Conventional vs. computer-enhanced Landsat image maps of Vatnajökull, Iceland (abstract), in *Abstracts with Programs, 1977 Annual Meetings, Geol. Soc. Amer.*, 9, 1228–1229, 1977.
- Williams, R. S., Jr., T. K. Meunier, and J. G. Ferrigno, Blue ice, meteorites, and satellite imagery in Antarctica, *The Polar Record*, 21, 493–496, 1983a.
- Williams, R. S., Jr., S. Thorarinsson, H. Björnsson, and B. Gudmundsson, Dynamics of Iceland ice caps and glaciers (abstract), *J. Glaciology*, 24, 505–507, 1979.
- Williams, R. S., Jr., S. Thorarinsson, and E. C. Morris, Geomorphic classification of Icelandic volcanoes, *Jökull*, 33, 19–24, 1983b.

Wolmarans, G., and J. R. Krynauw (compilers), *Reconnaissance Geological Maps of the Ahlmannryggen, Borgmassivet, and Kirwanveggen Areas, Western Dronning Maud Land, Antarctica*, three satellite image map sheets, scale, 1:250000, South African Committee for Antarctic Research, Pretoria, 1981.

Zwally, H. J., J. C. Comiso, C. L. Parkinson, W. J. Campbell, F. D. Carsey, and P. Gloersen, *Antarctic Sea Ice, 1973-1976: Satellite Passive Microwave Observation*, 206 pp., NASA SP-459, National Aeronautics and Space Administration, Washington, D.C., 1983.

10

PLANETARY LANDFORMS

*Paul D. Lowman, Jr., and James B. Garvin**

With the achievement of space flight, geomorphology suddenly expanded its scope by orders of magnitude. As recently as the early 1960s, geomorphologists could study one planet directly and one satellite telescopically and could speculate on the dimly seen surface of Mars. Twenty-five years later, they are studying landforms on some 21 planetary bodies besides the Earth, ranging from Earth-sized Venus to the asteroid-sized satellites of Mars (which may in fact be captured asteroids). This chapter presents a small sample of these landforms, beginning with this introduction and summarizing the main factors that affect geomorphic evolution throughout the solar system. This summary draws heavily on reviews of planetary (extraterrestrial) geomorphology by Sharp (1974), Baker (1983), and Greeley (1985), in which the reader will find useful background material. The relative sizes of bodies covered in this chapter are illustrated in Figure 10-1; a useful summary of numerical data is presented by Beatty et al. (1982).

FACTORS AFFECTING GEOMORPHIC EVOLUTION

Mass

The most basic property of any body, its mass, is perhaps the leading single factor governing its geomorphology. Mass of a planetary body controls several other factors that are themselves critical, a major one being the retention or loss of atmosphere, which depends strongly on a planet's gravity field. It should be pointed out here (with the aid of Figure 10-2) that, for the inner planets, the general stage of crustal evolution reached is a strong function of mass. The Moon, smallest of the bodies tabulated, is the least-evolved and the least-active now, in contrast to the largest body shown, the Earth. With the notable exception of the volcanically active Galilean satellite, Io, which is continually heated by tidal friction, the dependence of tectonic and, to a large extent geomorphic, evolution on mass holds throughout the solar system, subject to other considerations that will be covered separately.

Location

The location of a planetary body with respect to its primary is another dominant factor in its evolution. The most obvious illustration is the great difference in composition between the inner and outer planets, which can be loosely grouped as silicate and

hydrogen planets (Lowman, 1976). The reason for this compositional dichotomy is primarily the temperature gradient in the primordial solar nebula, as shown by Lewis (1974). Another example is furnished by the Galilean satellites of Jupiter, which display a similar compositional variation. The innermost satellite, Io, is clearly a silicate body, judging from its density, while the outermost satellite, Callisto, must be largely ice. Pollack and Reynolds (1974) have suggested that these satellites, while accreting, were influenced by heat from Jupiter, which is within two orders of magnitude of being massive enough to sustain thermonuclear reactions.

Composition

The bulk composition of the bodies described here ranges from largely iron and Fe-Mg silicates (Mercury) to almost pure water ice (the Saturnian satellites). The small satellites of Mars, Phobos and Deimos, appear to consist of carbonaceous chondrite material. In the Earth/Moon binary planet system, the Moon is systematically low in volatiles compared to the Earth, and lunar rocks have been found to be almost completely water free. More subtle compositional differences among planets, such as radioactive element content, have probably had major effects on their geologic evolution. From a geomorphic viewpoint, the difference in water content is probably the most important factor governing landform development in the silicate planets, as we will see when discussing comparative geomorphology of Mars, the Moon, and Mercury.

Atmosphere

Closely related to water content in geomorphic importance is the presence or absence of an atmosphere, and on the bodies with atmospheres, the pressure, temperature, and composition of each atmosphere. Here too, the range in properties is startling. Venus has a carbon dioxide atmosphere, clouds of what appears to be sulfuric acid, and surface pressure on the order of 90 bars, while the Moon has so little atmosphere that the hydrogen nuclei of the solar wind reach the lunar surface directly. Mars has only a thin carbon dioxide atmosphere today, the highest surface pressures being less than 10 millibars, yet there is ample evidence of a much denser atmosphere in the past. Even now, the thin Martian atmosphere can sustain dust storms and major eolian erosion. The atmosphere of Titan, the only satellite that has one, appears to consist mainly of methane, so cold that there may be pools of liquid methane on the surface. The landforms of this surface, invisible through the opaque atmosphere, must be unimaginably alien.

*Geophysics Branch, Goddard Space Flight Center, Greenbelt, Maryland 20771.

ORIGINAL PAGE IS
OF POOR QUALITY

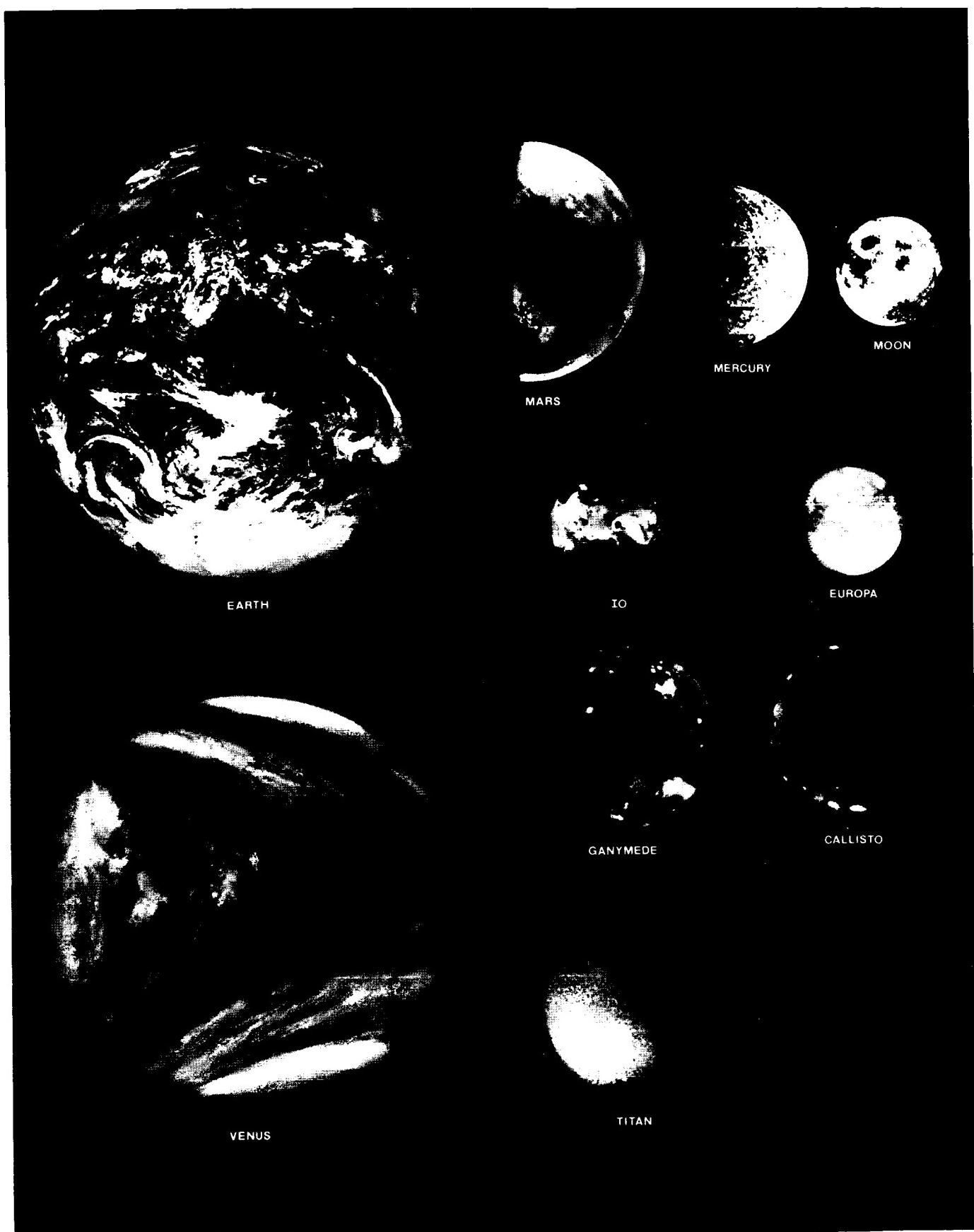


Figure 10-1. Photographic montage illustrating relative sizes of planets and satellites (Meszaros, 1983).

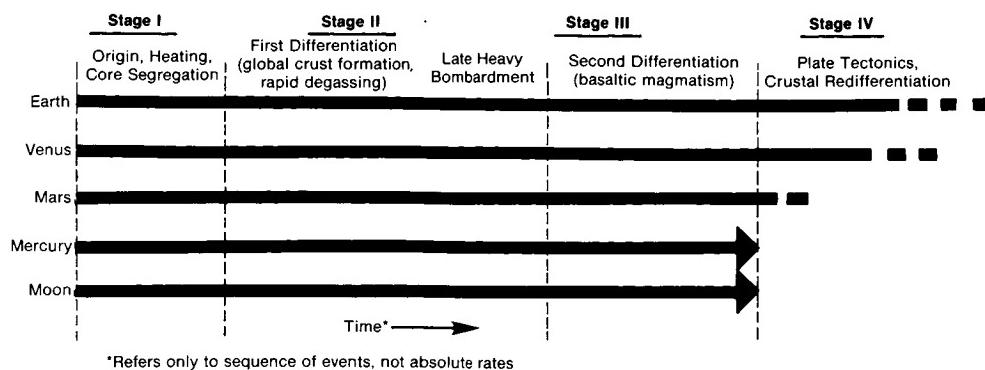


Figure 10-2. Comparative Crustal Evolution (Lowman, 1976).

Surface Temperature

Terrestrial geomorphology is greatly influenced, both directly and indirectly, by temperature. Temperatures encountered on the surfaces of planets and satellites discussed here cover a range of several hundred degrees Celsius. On Mercury, lead would melt in the daytime, whereas on Titan, the surface temperature is less than 100°K, close to the triple point of methane. Even on Mars, the temperature now rarely if ever gets above the freezing point of water, but in the past, near-surface temperatures have locally and temporarily permitted extensive melting of ground ice. Temperatures on the surface of Venus, Earth's near-twin in size, are around 450°C, high enough to affect the geothermal gradient and perhaps the nature of rock deformation. The extreme temperatures on Earth-like planets have undoubtedly had fundamental direct and indirect influence on the nature of planetary landforms, far more than we now realize.

Surface Gravity

The force of gravity at a planet's surface, a direct function of mass, has indirect geomorphic effects by governing the retention of an atmosphere and the surface pressure where one is present. By controlling internal pressure gradients, planetary gravity also affects geophysical phenomena such as magma generation and isostatic adjustment (although temperature is equally important). However, there can be many direct effects on geomorphic evolution from differences in surface gravity. On very small bodies, such as the ice satellites of Saturn, impact craters do not display the ejecta blankets typical of such craters on the Moon or Mars, probably because the ejecta spreads over extremely large areas. For the smallest bodies, such as Phobos and Deimos, escape velocity is so low (a few meters per second) that most impact ejecta is blown completely off, and may not return. Even on Io, larger than the Moon, escape velocity is so low that some of the material erupted from volcanoes goes into space, forming a torus around Jupiter. Geomorphologists studying extraterrestrial bodies must therefore keep in mind the fact that landscape evolution elsewhere may occur in far weaker gravitational fields than that of the Earth.

TIME SCALES IN EXTRATERRESTRIAL GEOLOGY

Although all the bodies in the solar system probably formed at about the same time (4.6 billion years ago), they have evolved geologically and geomorphically at drastically differing rates. Perhaps the most important generalization about planetary time scales is that many of these bodies remain in a very primitive stage of crustal evolution (Figure 10-2), corresponding to the earliest Archean on Earth. This is illustrated by the fact that the very first basalts collected on the Moon by the Apollo 11 crew turned

out to be 3.6 billion years old, nearly as old as the oldest known rocks anywhere on Earth. An even more dramatic illustration of the primitive state of the lunar surface comes from exposure ages of lunar samples (French, 1977), many of which are in the 100 million year range; sample 10017 had been lying on the surface in the same position for about 3 million years when it was picked up. Things happen much more rapidly on Mars, judging from terrain ages indicated by crater populations, but even Martian landforms are probably hundreds of millions or billions of years old. On the basis of Venera radar imagery (Lowman et al., 1985), it has been proposed that the present surface of Venus is similar to that of the Canadian Shield in the Proterozoic, when eruptions from what are now dike swarms produced huge floods of basalt. Extraterrestrial landforms, then, may represent features and stages of crustal evolution for which there is little or no evidence surviving on Earth; they are indeed fossil landscapes.

The foregoing comments on time scales should be qualified with two specific exceptions. Until 1979, it was believed that the Earth was the most geologically active solid body in the solar system, but in that year, the Voyager spacecraft returned the electrifying pictures showing nine erupting volcanoes on Io. These volcanoes are resurfacing the Ionian landscape while we watch, and it now takes title for the youngest land surface in the solar system. Reasons for this are discussed in the text for Plate P-13. Another exception to the great age of planetary landscapes may be Venus. Soviet Venera radar imagery has revealed only a small number of resolvable impact craters (on the order of 100 to 150), implying a geomorphic age roughly comparable to that of the Earth. The proposed similarity of Venusian topography to the Proterozoic Canadian Shield does not contradict this low age: Venus has apparently not undergone extensive fluvial erosion, while the Earth of course has. Landforms and rock types (chiefly tectonic and volcanic) preserved on Venus are thus considered to be similar to those long destroyed on Earth.

EXTRATERRESTRIAL LANDFORMS

It is appropriate to close this introduction on a cautionary note. There will be a natural tendency for geomorphologists to look for terrestrial analogs in the photographs of extraterrestrial landscapes presented here. There are of course many obvious analogs: the huge volcanoes of Mars are outsize replicas of those in Hawaii, landslides of the Valles Marineris can be matched by those in poorly engineered road cuts, and small lunar craters resemble craters formed by falling rockets. But it is almost certain that some, perhaps many, of the landforms found on other planets are unique to those planets, or at least have *no* terrestrial counterparts. Geomorphologists will do well to remember J. D. Bernal's aphorism: "The universe is not only stranger than we imagine, it is stranger than we *can* imagine."

PLATE P-1

TYCHO

Impact craters are the most common landforms in the solar system, though most people have never seen one on Earth because erosion and deposition have destroyed or covered nearly all the earlier ones. They occur on almost every solid planet and satellite and range in size from "zap pits" a few micrometers wide on returned lunar samples to basins thousands of kilometers rim to rim. In fact, much of the terrain on bodies such as the Moon and Mercury consists of little but craters or crater-related ejecta deposits.

The lunar crater, Tycho, the most obvious feature on the Earthward face of the full Moon because of its spectacular ray system, is easily visible with 7-power binoculars. It is equally conspicuous with Earth-based radar, being highly reflective, and with astronomical measurements of lunar surface temperature during solar eclipses, when Tycho retains its heat far better than its surroundings. Radar and thermal observations before the Lunar Orbiter mission that returned this image indicated that Tycho was probably a relatively young crater, whose anomalous physical properties were the result of exposed solid rock.

The Lunar Orbiter V view in Plate P-1 highlights the terrain of this 85-km wide crater, brought into sharp relief by the morning Sun coming from the right (Lowman, 1969). The crater has a circular raised rim surrounded by a blanket of debris ejected by the impact, an inner terraced wall, an extremely rough floor, and a central peak. These features will be described in order, beginning with the outermost and moving inward. An impact origin for the crater will be assumed here; this assumption will be justified later.

Much material blown out of Tycho during the catastrophic impact that formed it lies far beyond the limits of this image. Judging from the extent of the ray system (partly ejecta and secondary craters formed by ejecta), some material has traveled hundreds of kilometers. The nearer part of the ejecta blanket, shown in Figure P-1.1 (Lunar Orbiter V), appears to be partly solid debris and partly melted or fluidized material produced by the impact. The smooth-floored pond-like features, sometimes called "playas," probably represent the last deposits of impact melt that flowed to low spots in the ejecta blanket. A closeup view of the central part of Figure P-1.1, on the north flank of Tycho, is provided by a Surveyor VII surface picture (Figure P-1.2). Surveyor VII landed just southwest of the conspicuous playa at the center of Figure P-1.1, and the view is to the northeast toward it.

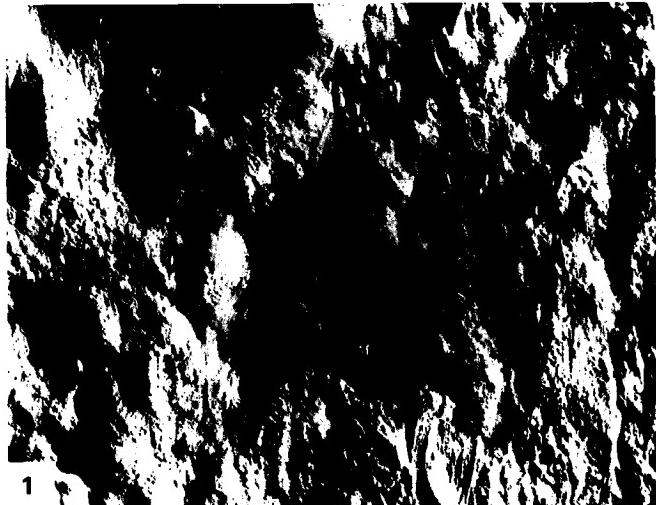
The inner rim and walls of Tycho clearly formed by slumping of material into the initial cavity, presumably only minutes after the impact. They have also in places collected fluidized or liquidified impact debris that flowed toward the floor (Figure P-1.3), as shown by another Lunar Orbiter V view. The crater floor is an extremely rugged terrain, suggesting a giant form of pahoehoe lava. Had this picture been obtained in 1950, many would have interpreted the floor as a solidified lava lake filling a volcanic crater. However, it now seems certain that all large impact craters are initially floored by thick layers of impact melt. An excellent terrestrial analog to Tycho is found in the Manicouagan structure of Quebec. This 65-km wide feature, seen on a Landsat view (Figure P-1.4), appears from its structure and mineralogy to be the eroded remnants of a Triassic impact crater formed in the Grenville Province about 210 million years ago (Glass, 1982). Most of the interior of the Manicouagan structure is a sheet of grossly homogeneous impact melt about 230 m thick. Its mineralogy, bulk chemistry, and strontium isotope ratios confirm that this sheet was formed by shock-melting of the Grenville basement, resulting in a pseudolava with the overall composition of a monzonite. Two hundred million years of erosion, including several glaciations, have smoothed out the floor of the former Manicouagan crater, but initially it must have looked like the

floor of Tycho does now. The absolute age of Tycho, incidentally, is probably over 100 Ma. (Taylor, 1982); one estimate from crater statistics is 700 Ma. But the near absence of tectonism and the slow rate of impact erosion have preserved its original morphology.

The central peak of Tycho, like those of most fresh craters over a few tens of kilometers wide, is morphologically analogous to the central peak of Manicouagan, an uplifted horst of anorthosite. Although the details of central peak formation by impact are not agreed upon, most workers argue for a combination of inward slumping and rebound, resulting in considerable uplift of the target rock. Isostatic adjustment probably plays a minor role in Tycho-like craters, but may become significant in circular mare basins displaying positive gravity anomalies (mascons).

Until the 1960s, many held that craters such as Tycho were lunar volcanoes, specifically calderas (Green, 1971). Now, origin by meteoritic or cometary impact is almost universally accepted, for the following reasons: direct evidence of shock metamorphism in lunar breccias; overwhelming collective evidence for the role of impact in the formation of small lunar craters and the lunar regolith at the six Apollo landing sites; and the existence of scores of comparable terrestrial craters (or their roots) whose impact origin is clearly shown by mineralogical criteria such as high-pressure phases, thermomorphic crystals, and crystallographic features. Finally, sizable asteroids are seen to cross the Earth/Moon orbit fairly frequently (Shoemaker and Hedin, 1978). In 3 billion years (the approximate time since lunar internal activity stopped), some such objects *must* have hit the Moon. If craters such as Tycho are not the scars of such encounters, where are the scars?

The most general objection now to a volcanic origin for Tycho-like craters comes from planetary missions such as the Mariner, Viking, and Voyager series. These spacecraft have transmitted pictures of what everyone agrees are extraterrestrial volcanoes, some visibly erupting (on Io). They differ in details and frequently in size from terrestrial examples, but they look like volcanoes—not like Tycho—and were immediately recognized as such. Therefore, the proponents of volcanic origin for lunar craters have in the end won while losing; there are dozens of fascinating extraterrestrial volcanoes for them to study. G-68-2958.



ORIGINAL PAGE IS
OF POOR QUALITY

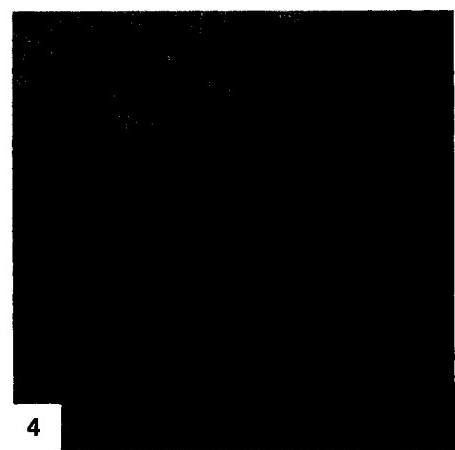
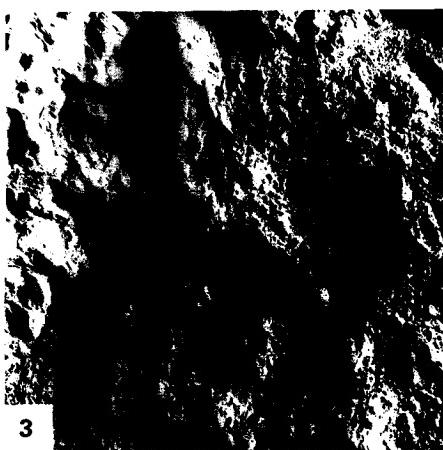


PLATE P-2

This view of Mare Imbrium, taken several decades ago with the 100-inch Mount Wilson telescope, is more valuable than ever because of the Apollo 15 mission, which landed at the foot of the Apennine Mountains. The two major divisions of the lunar surface, maria and highlands, are well displayed here. The maria as such will be covered in Plate P-3. This photo covers a *circular* mare (Imbrium itself) and parts of several *irregular* maria (Frigoris, Procellarum, Sinus Roris, and Sinus Aestuum). The lunar highlands, at top, are a mosaic of crater on crater, formed by impacts in the Moon's earliest crust. The highlands constitute most of the Moon's total area and underlie the mare basalts.

The most useful way to discuss the landforms of this area is to trace the evolution of the Imbrium area, using superposition and absolute dates from radiometric analyses. The first landforms produced were the impact craters of the highlands, excavated in a crust probably formed by igneous processes 4 to 4.5 billion years ago (Taylor, 1982). Most of this area resembled the northern highlands before the Imbrium Basin were formed.

The Imbrium Basin is essentially a very large impact crater. As visualized by Baldwin (1965), an asteroidal body probably a few tens of kilometers in diameter struck the Moon, producing a flash of light and throwing out an immense cloud of ejecta now forming the mountains ringing the basin. The Apennines are especially well displayed here. They grade into the Fra Mauro formation on which the Apollo 14 mission landed just off the Plate scene to the south (see Figure P-4.2). Radiometric dates of Fra Mauro samples indicate a major thermal event 3.8 billion years ago, presumably the Imbrium impact. The terrain at the Apollo 14 landing site is clearly shown in Figure P-2.1

The catastrophic impact produced a raised rim, visible in cross section in Figure P-2.2, looking south along the Apennine Front from the Apollo 15 spacecraft. The prominent ledge at left, Silver Spur (20 km away), shows gently dipping strata whose nature and origin are not understood. They may be layers of ejecta from pre-Imbrium impacts, or they may be some sort of igneous feature. The rounded topography of Silver Spur, formed in what

MARE IMBRIUM

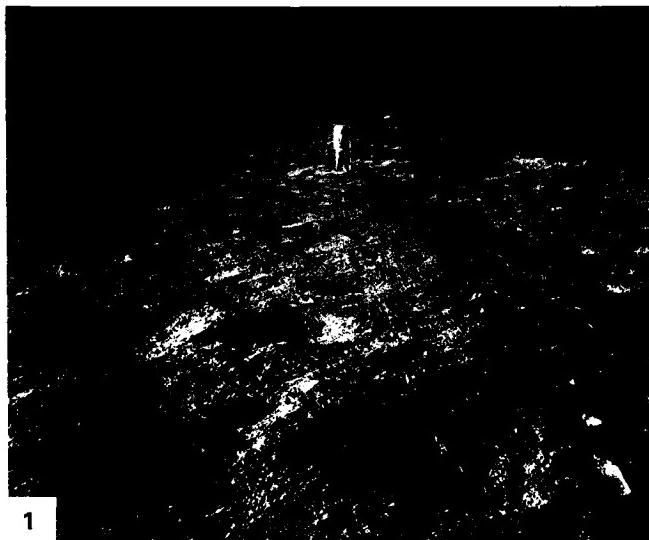
on Earth would be the early Archean, shows the extremely slow pace of lunar geomorphic processes.

Returning to the telescopic view, one can reconstruct the major postimpact stages in the evolution of Mare Imbrium. There was a short stage in which walls of the initial megacrater slumped back toward the depression. This is most obvious along the Apennine Front (lower right), which is basically a series of normal fault scarps. In the Apollo 15 orbital view (Figure P-2.3), one sees a number of concentric grabens representing postimpact tension fracturing. These grabens cut probable impact melt south of Autolycus, but not the mare basalts of the Palus Putredinus, and thus must be between 3.8 and 3.3 billion years old (the latter being the age of basalts from Hadley Base).

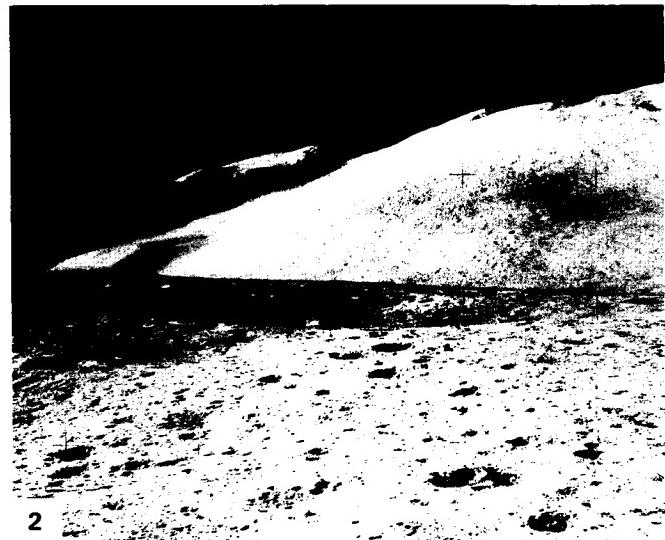
Another series of events involved the formation of several large craters, including Plato, Archimedes, and Sinus Iridum. These craters are obviously older than the Imbrium Basin, but older than the mare basalts. This physiographic relationship shows that the mare material could not be a simple impact melt.

Another interesting landform (also in Figure P-3.2) is Hadley Rille. It has been proposed that sinuous rilles of this sort are fluvial erosion channels dating from a time when the Moon had running water. This theory can now be discarded in view of the totally anhydrous nature of all lunar rocks sampled thus far. Another and more likely theory proposed by Cameron (1964) is that they were formed by ashflows; however, this proposal is weakened by the apparent absence of true ignimbrites on the Moon. The most likely theory, from both geomorphic and petrologic evidence, is that these rilles are unroofed lava tubes formed by drainage of the still-molten basalt (Greeley, 1971).

After the eruptions of mare basalt ceased, roughly 3 billion years ago, the internal evolution of Mare Imbrium was essentially complete. However, many spectacular impact craters have formed since then, so that few if any places on the Moon are free from the effects of impact. The Apollo 15 surface view (Figure P-2.2) gives a good closeup of the regolith formed on mare basalt by 3 billion years of small impacts. **View 263, Mount Wilson Observatory.**



1



2

ORIGINAL PAGE IS
OF POOR QUALITY

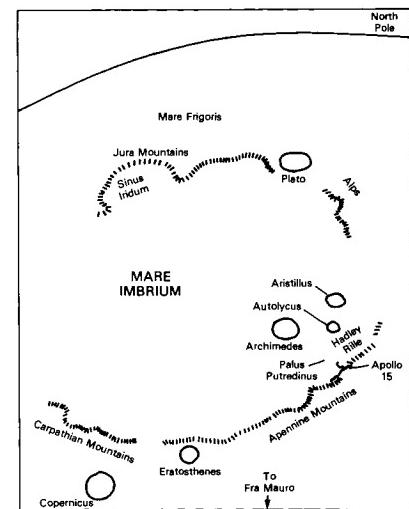
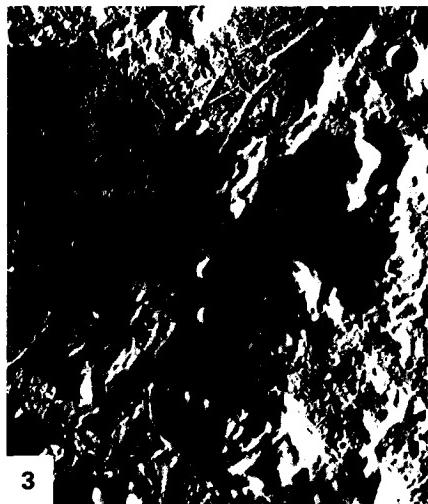
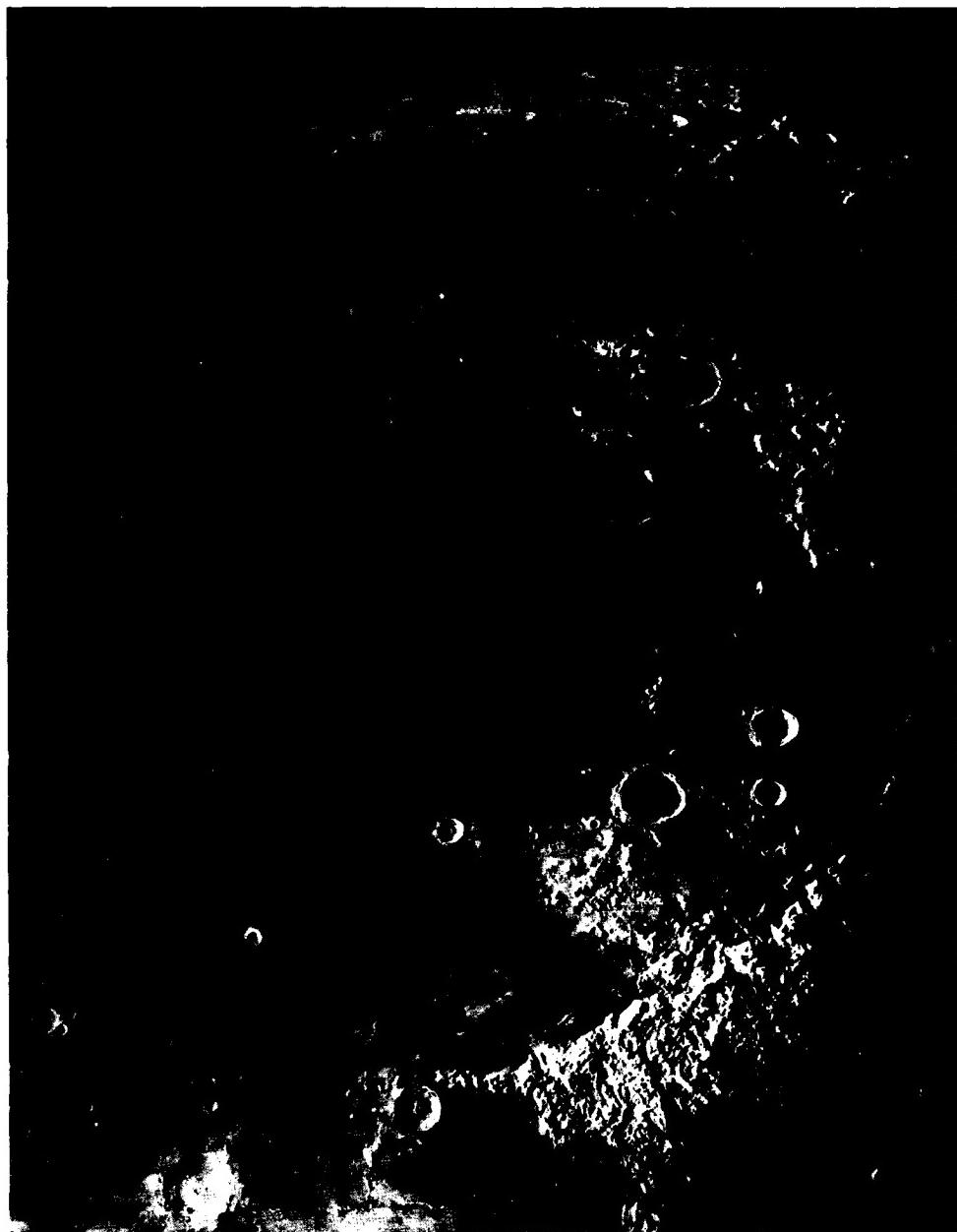


PLATE P-3

LUNAR MARIA

The lunar maria (Latin for seas) were considered oceans many centuries ago. We now know them to be immense basalt flows, ranging in age from roughly 3 to 4 billion years. These are discussed in relation to the photographic view from space, supplemented by closeup views taken by the Apollo astronauts on the Apollo 11 and 15 missions.

The main view (Plate P-3), taken looking west from the Apollo 10 spacecraft, shows Mare Tranquillitatis and what would become the Apollo 11 landing site. The low morning Sun brings out the topographic features of this typical mare area. The physiographic contrast between the rugged, heavily cratered highlands (top) and the lower, smoother maria is well displayed here. The primary reason for this contrast is the much lower density of large craters on the maria. However, it is clear that there are many craters on the maria, even as seen from orbital altitudes. The maria are in fact saturated with craters a few meters wide, as shown by an Apollo 12 surface view of Oceanus Procellarum (Figure P-3.1).

Returning to the orbital view of Mare Tranquillitatis, we see many mare ridges (also termed wrinkle ridges). The origin of these features is surprisingly little understood. Several different mechanisms have been proposed in two general categories—tectonic and igneous.

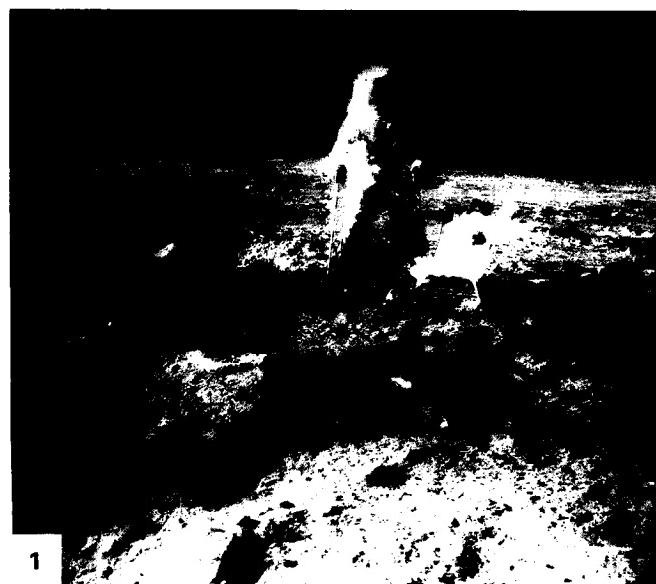
In the tectonic theories, the ridges are interpreted as folds, faults, or some combination of the two. In early USGS/NASA lunar mapping, the ridges were shown as anticlines, an interpretation since elaborated on by many workers. Solomon and Head (1979) have made perhaps the most extensive study of tectonic mechanisms and have shown that ridges in southern Mare Serenitatis probably resulted from global compression accompanying postmare cooling. This concept implies that the ridges are anticlines or possibly thrusts in places, expressed directly as topography.

Another explanation of the mare ridges is that they result partly or wholly from the intrusion or extrusion of magma (i.e., that they are basically igneous). One reason for this proposal is that in many places ridges grade into higher albedo rounded hills, suggesting viscous lava extrusions (O'Keefe et al., 1967). The ridges in such cases would form the fissures feeding these extrusions, although along most of the length, the magma did not break

through. One example of such relationships is visible here: the small hill on the mare ridge just above the prominent crater (Bruce) at the bottom of the picture. The tectonic and igneous theories for the ridges are not necessarily mutually exclusive since dikes may be permissively intruded along preexisting fractures as has happened on Earth.

Another mare landform is the sinuous rille. None are visible in the Mare Tranquillitatis scene, but a well-known example, Hadley Rille, appears in Figure P-2.1. Two surface views of Hadley Rille from Apollo 15 are shown in this Plate to discuss not the rille itself but the structure of the mare as exposed in its walls. The Apollo 15 landing site, Hadley Base, although not on a named mare, was on the Palus Putredinus, a relatively small area of basalt in the Imbrium Basin. This north-looking surface view (Figure P-3.2), showing mission commander David Scott standing with the Rover by the 300-m deep rille, also gives a good side view of the mare topography, emphasizing its levelness. A suggestion of layering is visible in the walls of the rille.

The layering is shown much better in another surface view (Figure P-3.3), looking at the southwest wall of Hadley Rille. This 40-m high cliff is one of the few good exposures of bedrock seen on the Apollo missions; most of the lunar surface is covered with the impact-generated regolith. This view reveals the layered structure of at least this mare area and may be reasonably representative of the maria in general, although the exposure itself is probably due to collapse of a lava tube as discussed in the Plate P-2 text. The layering is clearly of igneous origin and presumably represents several successive lava flows, even though intrusions cannot be ruled out. There are several reasons for presenting this particular view. Most important is that it at least suggests what has been inferred from other geologic relationships and from radiometric dates, namely that the maria were emplaced over a long time in many successive flows. They were not formed by one post-impact eruption or as an immense pool of impact melt. Furthermore, the Hadley Rille exposure is of geomorphic interest in demonstrating the superficial nature of the mare regolith. Unlike the highlands regolith, which extends to several kilometers depth (Short and Forman, 1972), the regolith on the maria is here demonstrably only a few meters deep, as shown by the fact that the igneous layers are not disrupted. 69-H-864.



ORIGINAL PAGE IS
OF POOR QUALITY

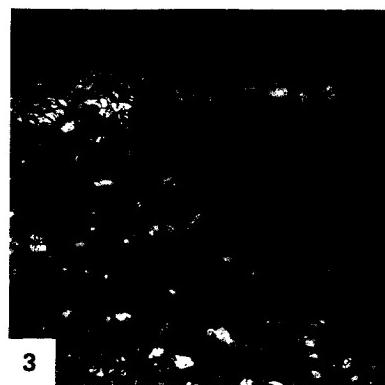


PLATE P-4

MERCURY—CALORIS BASIN

The planet Mercury was physiographically *terra incognita* before 1974, when Mariner 10 telemetered to Earth the first high-resolution photos of its surface (Murray et al., 1981). The instinctive reaction of those of us who saw those pictures as they were received was: "It's just like the Moon!" Perhaps the most striking analogy between lunar and Mercurian physiography was not evident until several pictures were mosaicked to show the Caloris Basin (Plate P-4), which appears to be a near-twin in size and topography to the Orientale Basin on the Moon (Figure P-4.1). This analogy will be illustrated with a view of the ejecta blanket from the Imbrium Basin (Figure P-4.2) and two close-up views of the Orientale Basin (Figures P-4.3 and P-4.4).

Turning first to the Texas-sized Caloris Basin, note that this collective term embraces several discrete terrain features. The heavily ridged area on the left, occupying roughly one-third of the picture, has been named Caloris Planitia (plains), and the arcuate mountains enclosing it, the Caloris Montes (mountains). The Caloris Planitia should be compared first with a previous view (Plate P-3) of Mare Tranquillitatis. It is obvious that the ridges criss-crossing Caloris Planitia are at least grossly similar to the mare ridges, raising the obvious question of whether the Mercurian plains are in fact maria and presumably lava flows.

The majority opinion is that they are and that Mercury has undergone a period of extensive basaltic volcanism analogous to that of the Moon (Strom, 1984). The Mercurian planitia are generally lower, smoother, and much less cratered than the Mercurian highlands (shown in Plate P-5), although there is no strong albedo contrast as displayed by the Moon. Reflection spectra of Mercury (Hapke, 1977) reveal features characteristic of pyroxenes, suggesting at least some compositional similarity in that pyroxenes are a major component of lunar basalts. Add to this the fact that similar ridges on the Moon are almost invariably found in mare terrain, then the evidence collectively strongly favors the interpretation that the Mercurian plains are lava flows. However, the possibility remains that they are some sort of impact ejecta analogous to the Cayley Formation of the Moon, and the nongeometric term "planitia" rather than "maria" is thus an appropriate one.

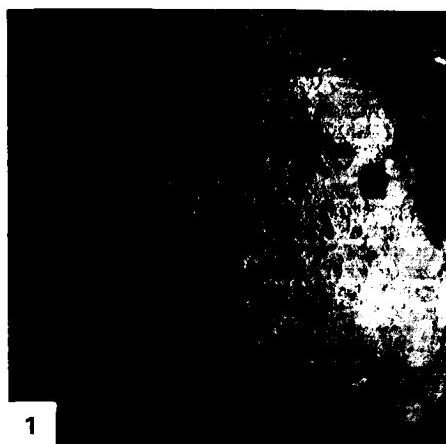
The Orientale Basin (Figure P-4.1) has long been recognized as a younger and better-preserved version of the Imbrium Basin and, by implication, is therefore an immense impact crater. Its physiography is relevant to possibly analogous features associated with the Caloris Basin. Look first at an Apollo east-looking view of the ejecta blanket south of Mare Imbrium (Figure P-4.2). This terrain, near the type locality of the Fra Mauro formation, shows the radiating hills and valleys typical of most of the mountains surrounding the Imbrium Basin. It should be compared with the

hills radiating from the Caloris Basin (Plate P-4). Although not as well preserved or displayed as the lunar terrain, Mercurian features fall clearly into the same general type of physiography and represent, by implication, the ejecta blanket from the Caloris Basin. However, there is an important difference between the Caloris and Orientale Basins, although this difference is not completely shown by the Mariner picture. Ejecta from the Orientale Basin (the Helvelius Formation) can be recognized in some directions several hundred kilometers from it (i.e., at least one basin diameter away). The ejecta from the Caloris Basin has apparently traveled much less distance. The obvious explanation for this is that, although Mercury and the Moon are superficially very similar, Mercury has a surface gravitational acceleration more than twice that of the Moon because of its much greater mass. Ejecta from Mercurian craters will therefore travel much less distance, other factors being equal, than on the Moon.

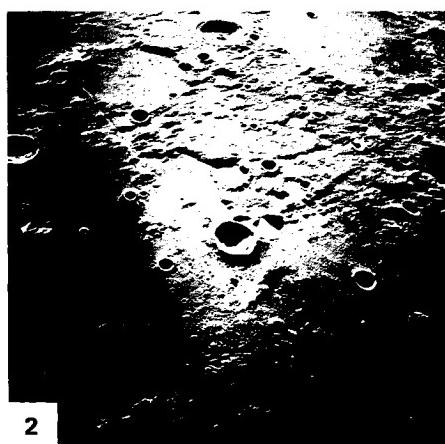
Although they are not strikingly similar to those of the Caloris Basin, the inner parts of the Orientale Basin are worth discussing briefly. The central part of the Orientale Basin is partly filled with mare material. Surrounding this area (Mare Orientale) is a broad ring of subdued hills, the Rook Mountains (Figure P-4.3). These hills are clearly younger than the adjacent mare area and have been mapped by USGS geologists as the Maunder Formation, interpreted as being chiefly impact melt, with occasional hills of prebasin bedrock projecting through it. Outward from the Maunder Formation (Figure P-4.4) is another concentric ring of material, which has been interpreted not as impact melt but as the inner facies of the ejecta blanket, which should correspond to some part of the terrain inside the Caloris Montes. Whether it does is left to the reader's judgement; however, it should be remembered that we are not seeing a complete cross section of the Caloris Basin and may be missing critical parts of it.

The Caloris Basin (left side of Plate P-4) differs from the Orientale Basin in that it contains polygonal blocks; there is nothing like this terrain on the Moon. However, comparable fracturing exists on Mars, with blocks of similar size. Their origin is unknown, although simple shrinkage (analogous to mud cracks) seems unlikely because of their size. Some sort of tectonic tension fracturing seems more likely; possibly, a similar explanation could apply to Mercury.

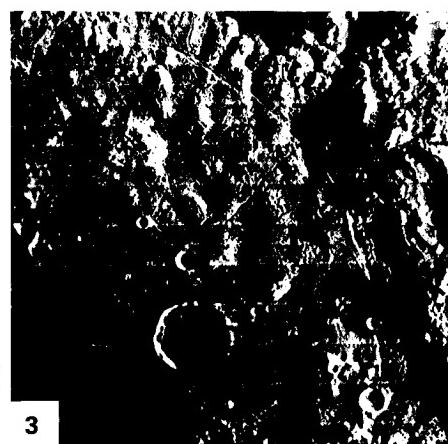
The discussion of the Caloris Basin has concentrated on similarities between Mercury and the Moon, but it is stressed that Mercury is internally quite different. Its high density (greater than that of the Earth if allowance is made for compression) clearly indicates a large iron core—unlike the Moon. Bruce Murray has characterized Mercury as "like the Moon on the outside, and like the Earth on the inside" (Murray et al., 1981). 74-H-536.



1



2



3

ORIGINAL PAGE IS
OF POOR QUALITY

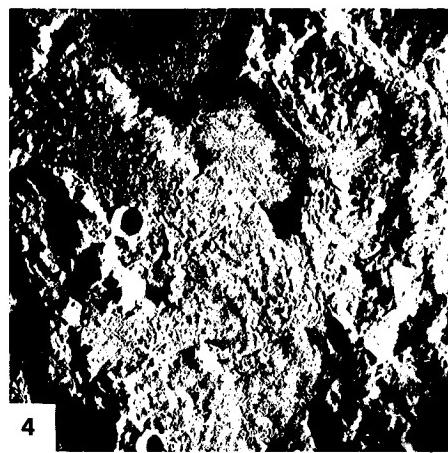
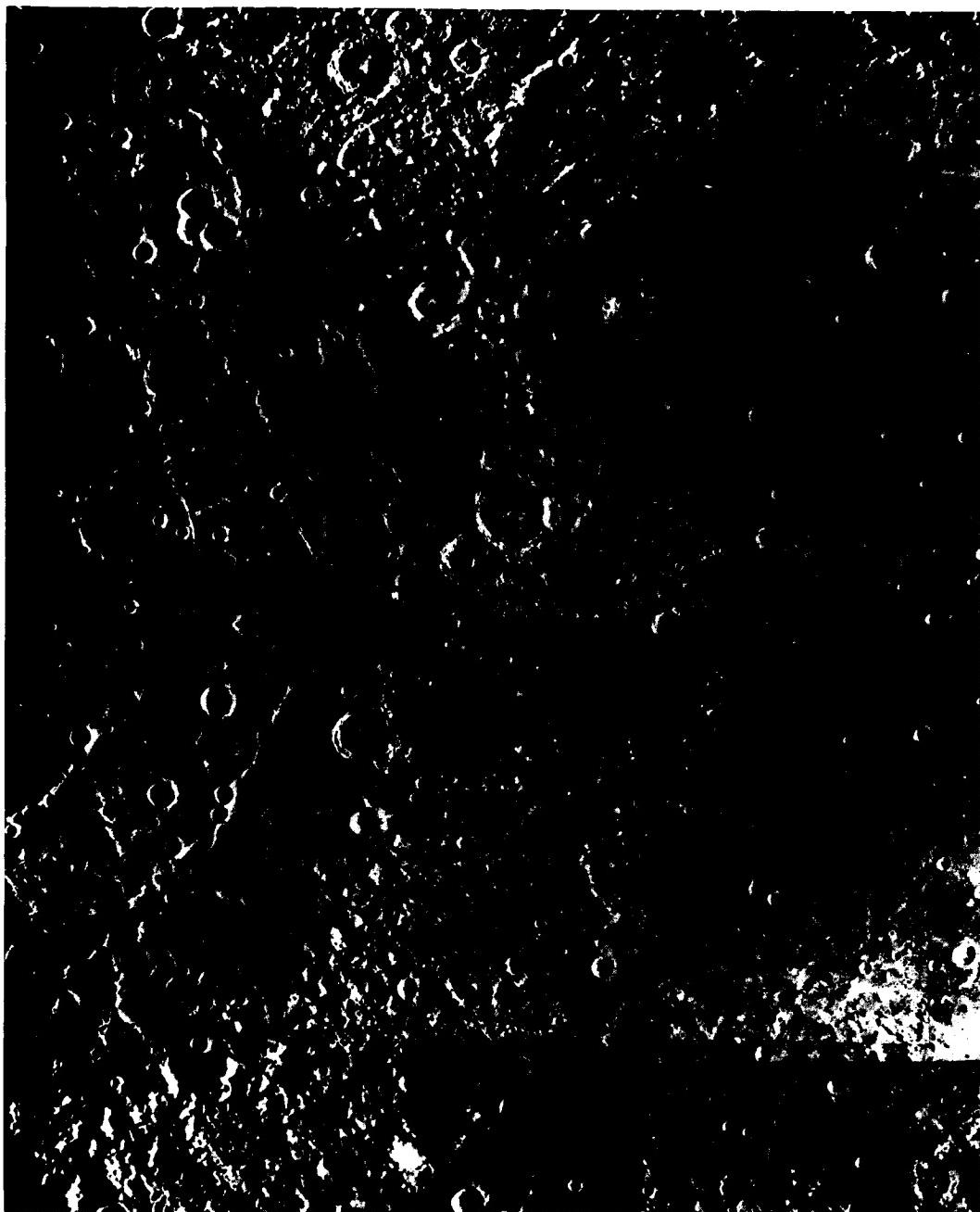
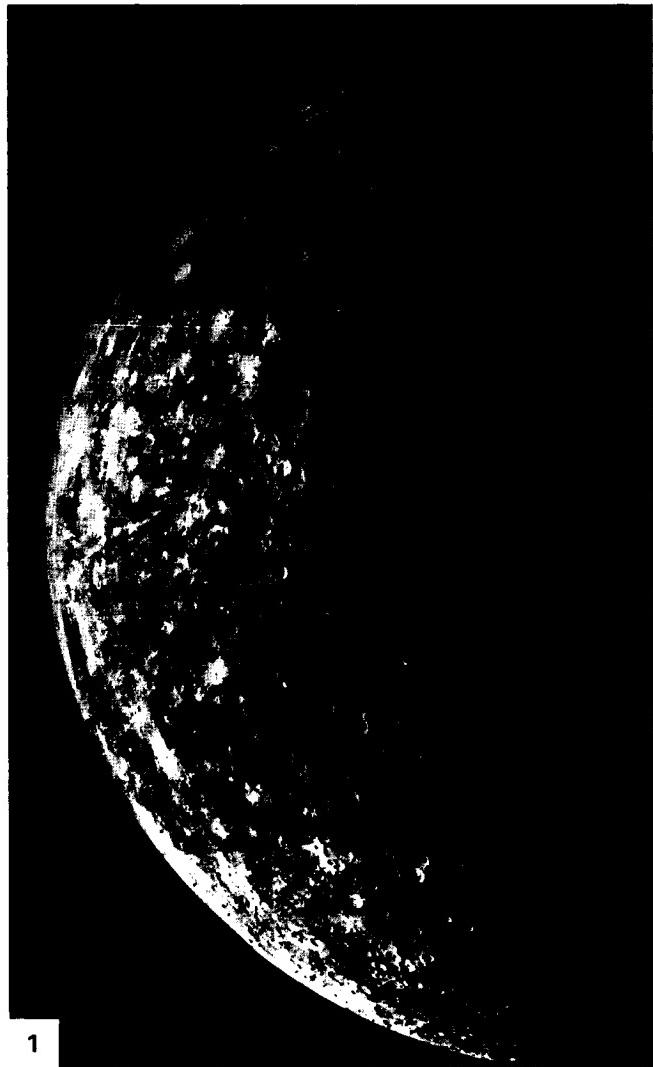


PLATE P-5

This view of Mercury (Plate P-5) covers an area near the terminator where the low Sun angle emphasizes topographic features around the 140-km wide crater Petrarch. The ancillary views show the same area as part of the "incoming side" (that first photographed on the initial Mariner 10 flyby; (Figure P-5.1) and at closer range (Figure P-5.2).

The dominant physiographic feature in the Plate view is the so-called "hilly and lineated terrain," whose chaotic nature has also given rise to the term "weird terrain." This rugged area is hard to explain by any known tectonic or geomorphic process and appears to be unique to Mercury. Two major possibilities are tectonism/volcanism or impact. The first is hard to argue for convincingly because of its vagueness and the evidence that it appears to have operated here only (although it must be remembered that we have seen only about half the surface of Mercury). The second possibility is an unusual one suggested by the fact that this area (roughly 30°S and 30°W) is antipodal to the Caloris Basin (i.e., on the opposite side of Mercury). If the Caloris Basin is an immense impact crater, the impact should have generated a series of strong surface waves spreading concentrically from the crater. In principle, these would have converged at about this



1

MERCURY—LINEATED TERRAIN

area, suggesting that this convergence point may have been subjected to strong shaking and mass wasting, producing the jumbled array of hills. A natural question is whether there is any lunar counterpart opposite the Orientale Basin. The answer appears to be no, but Mercury is internally very different from the Moon, and elastic wave propagation may have been correspondingly different. The large iron core of Mercury, for instance, may have reflected or refracted body waves. The question of how the aptly named "weird terrain" formed is obviously unanswered and remains a fruitful area for research.

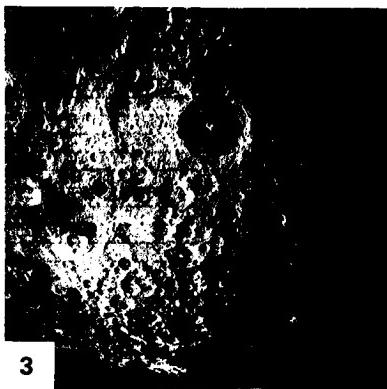
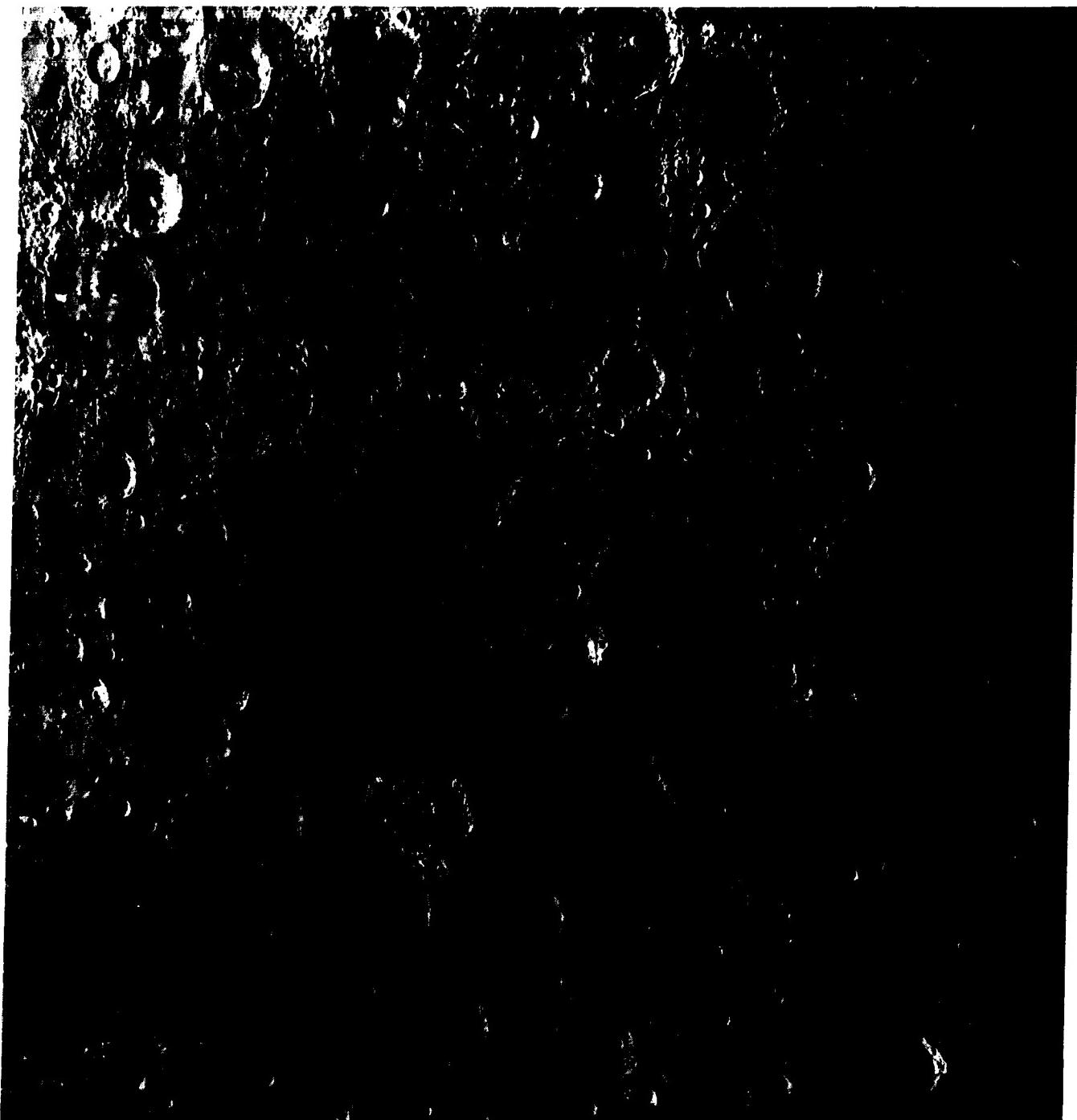
The Plate image also shows other uniquely Mercurian physiographic features. The most general one, well-known on the distant view (Figure P-5.1), is the high proportion of terrain not obviously cratered (with large craters); this area has been called the "intercrater plains." The intercrater plains correspond roughly, in relative age, to the lunar highlands, but their precise age cannot be pinned down. They constitute a type of terrain that cannot really be matched with the lunar highlands, which are saturated with large craters as shown in a Lunar Orbiter view (Figure P-5.3) of the Moon's far side centered on Tsiolkovsky. It seems fairly clear that the Mercurian intercrater plains represent a part of the early, but not primordial, crust whose formation overlapped the period of heavy cratering. There are several places on Mercury where lobate scarps on the intercrater plains, such as perhaps the Mirni Rupes (Figure P-5.2), overlap and apparently flow into craters. This suggests that the plains may have been formed by successive lava flows that were resurfacing the planet and obliterating craters. If correct, this possibility has important implications for planetology in that it may represent at least the last stages of formation of the earliest crust, which the writer has called the "first differentiation."

Other scarps, such as Vostok Rupes (Figure P-5.2), have been interpreted as reverse faults or thrusts. Martha Leake, in a 1981 Ph.D thesis, cited Strom's (1984) interpretation of Vostok Rupes as a thrust dipping 25 to 45 degrees to the east (right in this figure), that has shortened the crater, Guido d'Arezzo, by a 10-km westward heave along this thrust. Thrusts of this type are found elsewhere on Mercury and have generally been considered to be compressive features resulting from contraction of the planet. **75-H-83.**



2

ORIGINAL PAGE IS
OF POOR QUALITY



3

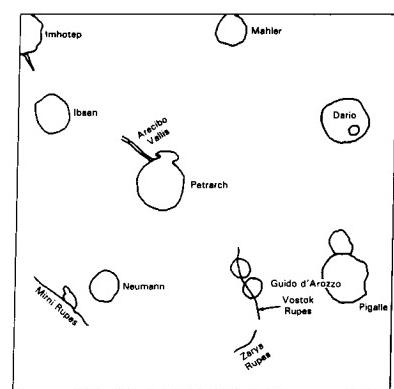


PLATE P-6

OLYMPUS MONS

The first systematic high-resolution imagery of all of Mars, from Mariner 9, showed that Martian geomorphology is far more complex and interesting than the Moon-like topography indicated by earlier missions. Only the most common of the many Martian landforms are treated in this and the next two Plates, beginning here with the largest volcano on Mars, Olympus Mons.

Lying on the Tharsis bulge, a large plateau, Olympus Mons is marked most obviously by its size (Meszaros, 1984). Although Alba Patera has a greater area, Olympus Mons, with a width of 650 km and a height of 26 km, leads in volume. Other members of the Tharsis volcanic province, (Figure P-6.1, from bottom: Arsia Mons, Pavonis Mons, and Ascraeus Mons) are similarly large compared to terrestrial counterparts; Ascraeus Mons, for example, covers about the same area as the basaltic Columbia Plateau, formed by many fissure eruptions.

Why are the Martian volcanoes so big? The answer is almost certainly something more fundamental than lower gravity or atmospheric pressure. Most authorities ascribe the difference to basic tectonic style. The absence of substantial strike-slip faulting, subduction, and folding indicates that Mars has not entered the plate tectonic stage (unless the Valles Marineris (Plate P-7) is considered to be made up of incipient rifts). If this interpretation is correct, there has been no major crustal motion on Mars, so that volcanoes stay fixed over their subsurface magma sources, unlike terrestrial oceanic volcanoes such as those of Hawaii. Their volcanic effluents can thus pile up into structures of immense size, rather than being distributed along chains.

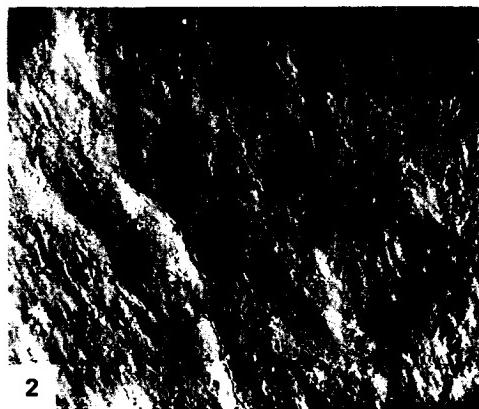
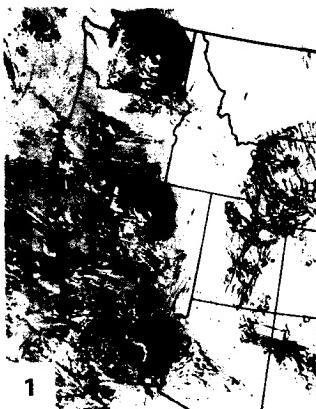
The morphology of Olympus Mons is typical of basaltic shield volcanoes: a broad upward-convex construct similar to terrestrial examples such as Mauna Loa except for its size. The low slopes of its flanks, only a few degrees, imply formation by a very fluid lava such as basalt. A close look at these flanks (Figure P-6.2), in a Mariner 9 view covering an area 50 km wide, shows terrain identical in all major respects to fresh basaltic lava flows on Earth. The sinuous channel in this area resembles many collapsed lava tubes in terrestrial volcanic fields (Murray et al., 1980); the reader will find it interesting to compare this feature with Hadley Rille (Figure P-3.2). An important aspect of the Martian lava flows as seen here is that, where individual flows can be traced, they are generally much longer and wider than terrestrial flows, which generally do not go more than a few tens of kilometers from their source volcanoes (although fissure eruptions do). As discussed by Carr (1982), this characteristic is probably the result of very high effusion rates for Martian basalts.

Northwest and north of Olympus Mons is a large aureole of ridged terrain (Figure P-6.3). This terrain is one of the most mysterious physiographic features on Mars, for which a wide range of origins has been proposed. As summarized by Morris

(1979), these include: (1) deeply eroded early lava flows, (2) eroded old shield volcanoes, (3) dissected ashflow tuffs, (4) magma-related crustal doming, fracturing, and erosion, (5) thrust sheets related to Olympus Mons, (6) subglacial lava flows, and (7) landslides. The ridged terrain is related to Olympus Mons in some way and is of roughly similar age, judging from impact crater counts (which must be used cautiously here because mass wasting could rapidly erode craters). Perhaps the most imaginative of the theories listed is that proposed by Hodges and Moore (1979), who find the ridged terrain similar to the table mountains of Iceland (Plate V-15). These consist largely of lavas and tuff breccias erupted under glacial ice several kilometers thick. Hodges and Moore further suggest that the unusual 5-km high scarp surrounding Olympus Mons expresses the former extent and thickness of this ice sheet, which confined the subaerial eruptions from the central vent.

The concept of Mars covered even partially with glacial ice is a fascinating one, but there is independent evidence for at least widespread subsurface ice in the form of very small Martian volcanoes (Frey and Jarosewich, 1982). As shown in Figure P-6.4, the northern plains contain thousands of subkilometer-wide cones with central craters. Although they resemble cinder cones, Allen (1979) and Frey and Jarosewich (1982) have shown that a more likely explanation is that these features are pseudocraters formed when lava flowed over water- or ice-saturated ground. Similar but somewhat smaller features are found in Iceland, where their origin is well established.

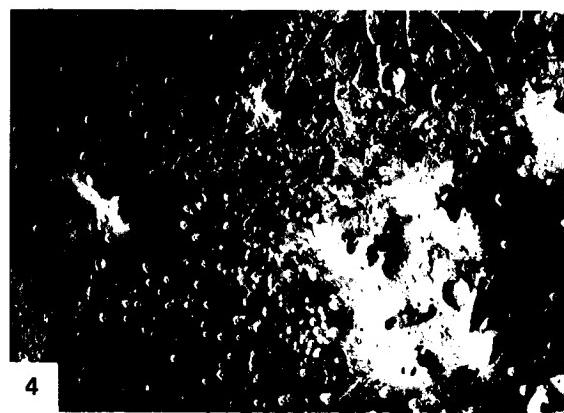
There is no good way to determine the absolute age of Olympus Mons, although the relative scarcity of impact craters suggests a low age. Wise (1977) has described the "crater number," the number of superposed impact craters greater than 1 kilometer wide per million square kilometers, as a convenient expression of the crater population. For a given flux of crater-forming objects, the crater number expresses the absolute age of a terrain; the problem is of course to find the correct flux for a given planet and to allow for crater destruction. Using Hartmann's (1977) model, Carr (1982) estimates the age of Olympus Mons to be about 400 million years, although he cautions that this may be only the age of the youngest flows, the main structure possibly having grown over billions of years. Nevertheless, even a 400 million year old landform would be ancient by terrestrial standards; study of photographs from Earth-orbiting spacecraft by Lowman (1981) indicates that volcanoes in humid climates seldom survive as recognizable features much longer than about 1 million years. Olympus Mons is a physiographically youthful volcano dating from roughly the Silurian Period. Like the Moon, Mars has evolved geomorphically with incredible slowness by terrestrial standards. 72-H-716.



ORIGINAL PAGE IS
OF POOR QUALITY



3



4

PLATE P-7

One of the most striking discoveries made by the Mariner 9 mission was the immense series of equatorial canyons, collectively named the Valles Marineris, shown in the Plate as a mosaic of Viking Orbiter images and in a USGS shaded relief map derived from the imagery (Figure P-7.1). The Valles Marineris would reach from almost coast to coast if it were in the United States; again, the most immediately obvious characteristic of Martian physiographic features is their great size. However, a number of terrestrial features are of comparable size and geometry; the East African rift valleys come to mind at once, and of course, the global system of terrestrial oceanic ridges are in aggregate much longer.

Before the details of the Valles Marineris are discussed, their regional relationships should be pointed out. The Valles are radial to the Tharsis uplift, which lies to the west, and slope off into low areas to the east (Figure P-7.1). There is a corresponding geomorphic gradation from dominantly tectonic valleys to those formed by fluvial processes. It will be helpful here, following Carr (1982), to distinguish between Martian "canyons" and "channels." "Canyon," as the term is applied to Mars, refers to features that do not form integrated drainage networks, consisting instead of segmented and frequently closed depressions showing little evidence of water erosion or deposition. They are inferred to be caused primarily by tectonism or subsidence. "Channel," in contrast, implies the opposite characteristics and, in turn, an origin by fluid erosion or deposition.

The Valles Marineris are a composite feature, formed by the interaction of several different geomorphic and tectonic processes. This composite nature is well illustrated by a classic Mariner 9 view (Figure P-7.2) of what has since been named Ius Chasma (from the Latin term for large canyon or chasm). This segment of the Valles Marineris is roughly 60 km wide and 2 to 3 km deep, and can be compared with a partial Landsat frame showing the Grand Canyon and Kaibab Plateau in an area 130 km wide (Figure P-7.3). The main part of Ius Chasma is agreed to be of tectonic origin, the canyon being fundamentally a graben. There are all gradations, however, from grabens to chains of craters such as those north of Ius Chasma. These craters presumably result from collapse of the surface material into underlying fissures, although similar crater chains on the Moon are generally interpreted as volcanic, probably diatremes. The question of just how much of the main canyon's volume is the direct result of faulting remains open. Some authors have proposed a Martian version of plate movement, with the tectonic part of the Valles Marineris resulting from horizontal (north-south) spreading. However, the majority view is that the walls were never in contact and that the movement has been primarily subsidence.

The tributary canyons of Ius Chasma are strikingly similar to those of the Grand Canyon, such as the Little Colorado River

VALLES MARINERIS

at far right in the Landsat view. Despite this similarity, the origin of the Martian tributaries is by no means understood. The terrestrial ones are clearly the result of water erosion, involving spring sapping and rain runoff. However, liquid water could not exist on Mars at this time or for a long time in the geologic past, leaving some sort of sapping as the most likely origin for the tributaries to Ius Chasma. Sharp and Malin (1975) have proposed such an origin, perhaps aided by dry mass wasting following the sublimation of ground ice. An interesting parallel between the Martian and terrestrial tributaries is the degree of fracture control shown by a few. The terrestrial examples are known to result from differential erosion along faults such as those extending southward along the Kaibab uplift.

Another section of Ius Chasma (Figure P-7.4), seen in a Viking view, shows the type of tributaries just discussed, but also shows another process by which the main graben has been enlarged (namely, landslides from the north wall). Similar landslides are visible in Tithonium Chasma to the north. These are large features, the area covered by the mosaic being about 300 km wide, and slope retreat by such landslides has clearly contributed substantially to the width of the main canyons. The reader may find it incidentally interesting to compare these undoubtedly landslides with the ridged terrain northwest of Olympus Mons, for which a landslide origin has also been proposed (Plate P-6). A nonrigorous but perhaps plausible argument against that proposed for the ridged terrain is simply that the landslides in Ius Chasma are instantly recognizable as such, and resemble terrestrial analogs in morphology and regional setting. Another class of feature shown in the Voyager mosaic is the series of east-west trending valleys between Ius and Tithonium Chasmas. These are clearly grabens, occasionally intersected by other grabens, and their location provides further support for the basically tectonic origin of the central part of the Valles Marineris.

The north wall of Ius Chasma, notably at the extreme right of Figure P-7.4, provides an interesting exposure of the subsurface structure of the Martian highlands. Several strata are visible that can be traced for many kilometers to the west (left). Similar strata have been seen on Viking photos elsewhere in the highlands. Their nature is unknown; the obvious possibilities are sedimentary or volcanic layering, or a combination of the two. They appear to be relatively undeformed, with near-horizontal dips, which would be consistent with the general absence of major crustal deformation commented on previously.

Before leaving this unusually interesting scene, we should call the reader's attention to the crater at bottom center, south of Ius Chasma. The lobate ejecta blanket around what is presumably an impact crater has no counterpart on the Moon or Mercury. 83-H-244.



ORIGINAL PAGE IS
OF POOR QUALITY

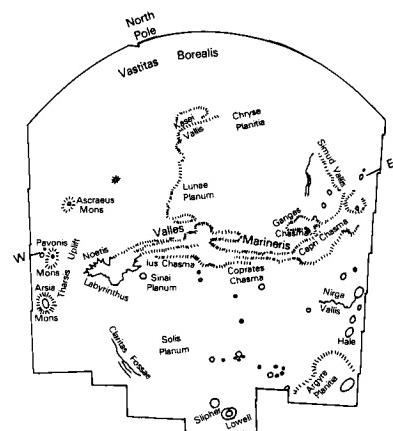
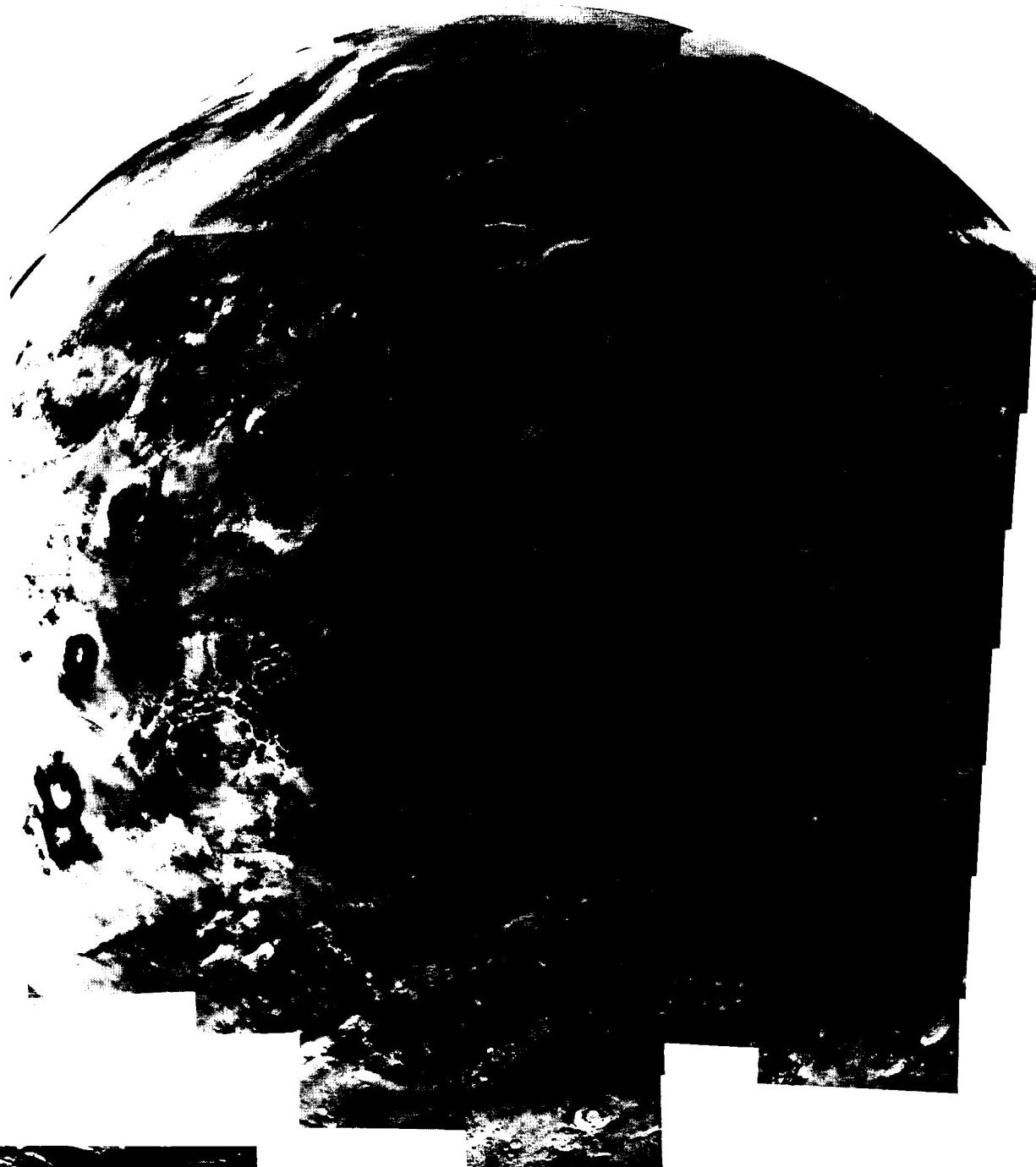


PLATE P-8

CHANNELS ON MARS

The Plate scene, showing an area of "outflow channels" (Carr, 1981; Baker, 1984) between Lunae Planum and Chryse Planitia, was chosen because it includes many features common to Martian channels in general. This Viking Orbiter mosaic covers an area about 300 km wide just west of the Viking 1 Lander site on Chryse Planitia (Figure P-8.1).

Martian channels have been grouped by Sharp and Malin (1975) into three main classes: *runoff*, *outflow*, and *fretted*. Runoff channels are both the most common and the most Earth-like fluvial erosion features on Mars, and are shown in Plate P-8 and Figure P-8.2, the latter covering the Nirgal Vallis. As described by Carr (1981), they "start small, increase in size downstream, and have tributaries." Those shown in Plate P-8 could be described as dendritic. Some runoff channels have only one valley, as in Figure P-8.2, except for a few small tributaries. Given enough time, these would presumably evolve into larger features like the main valley by headward erosion.

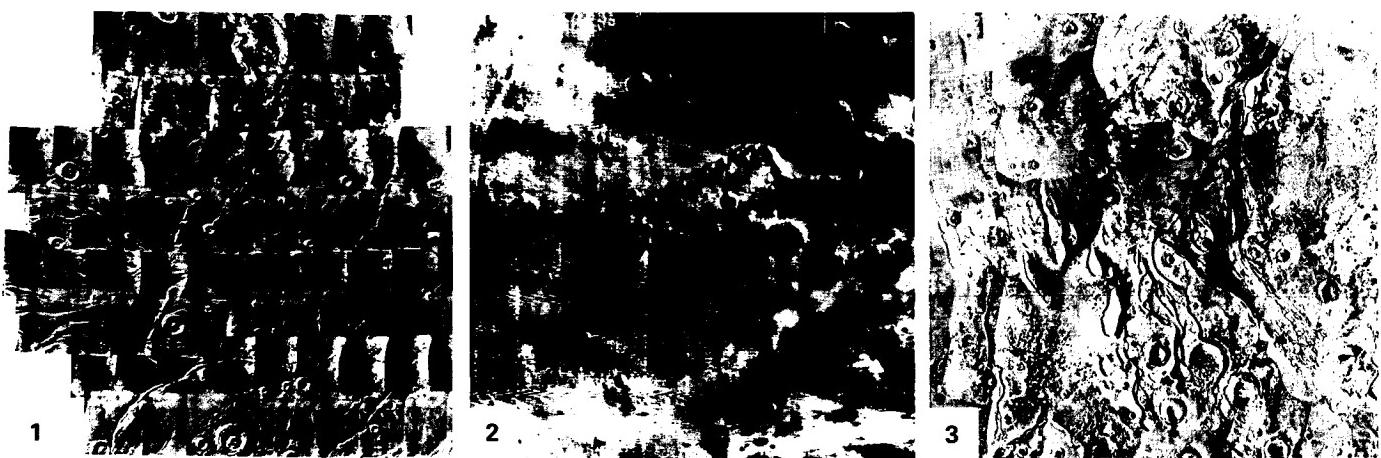
Despite their Earth-like appearance, the origin of runoff channels is debated. Various authors have proposed erosion by wind, lava, and even liquid hydrocarbons, but most evidence points firmly to water as the eroding agent. The exact mechanism is uncertain, the chief possibilities being direct erosion by rainfall or by ground-water seepage as discussed in Plate P-7 for the Valles Marineris tributaries. The two mechanisms are not necessarily mutually exclusive because infiltration of rain water could have occurred as it does on Earth (Carr, 1981).

An extremely important aspect of the runoff channels is their nearly complete restriction to the oldest part of the Martian landscape—the cratered terrain. Furthermore, as shown in this Plate, some craters are channeled and some channels are cratered, suggesting that formation of the early Martian atmosphere overlapped the later stages of crust formation and heavy cratering.

A fascinating possibility is that the terrain shown in this Plate is what the primordial landscape of the Earth looked like more than 4 billion years ago.

The outflow channels, shown in Figure P-8.3, were one of the most surprising discoveries made on Mars. Their resemblance to the Channeled Scablands of Washington (Plate F-27) suggests that catastrophic floods had once scoured the Martian surface. Since the surface pressure on Mars is now only a few millibars, even ponds could not last long before freezing or evaporating, much less floods. However, the existence of many other fluvial landforms now makes it clear that Mars once had a much denser atmosphere, since lost by one means or another, and flooding is now generally agreed upon. Some landforms, such as the segment of Kasei Vallis shown in Figure P-8.4 (a Viking Orbiter image), are so evocative that one can almost see the rushing water. However, the source of this water is, as for the runoff channels, unknown, although sudden massive release seems to be required. An outflow channel just north of Capri Chasma (Figure P-8.5) suggests a possible source. The channel originates in a canyon filled by chaotic terrain and grades into a scoured valley to the left, away from the cratered highlands. This relationship between chaotic terrains, canyons, and outflow channels is common and suggests that the release of subsurface water first formed chaotic terrain by slumping and then formed channels by erosion. Mechanisms proposed for this release include geothermal melting of ice and "breakout" of high-pressure water from confined aquifers (Carr, 1981), possibilities that are not necessarily exclusive.

Unlike the runoff channels, which are essentially confined to old cratered terrain, the outflow channels cut the younger mare-like plains as well. Therefore, they occurred in a substantially later period of Martian geologic history. **76-H-697.**



ORIGINAL PAGE IS
OF POOR QUALITY

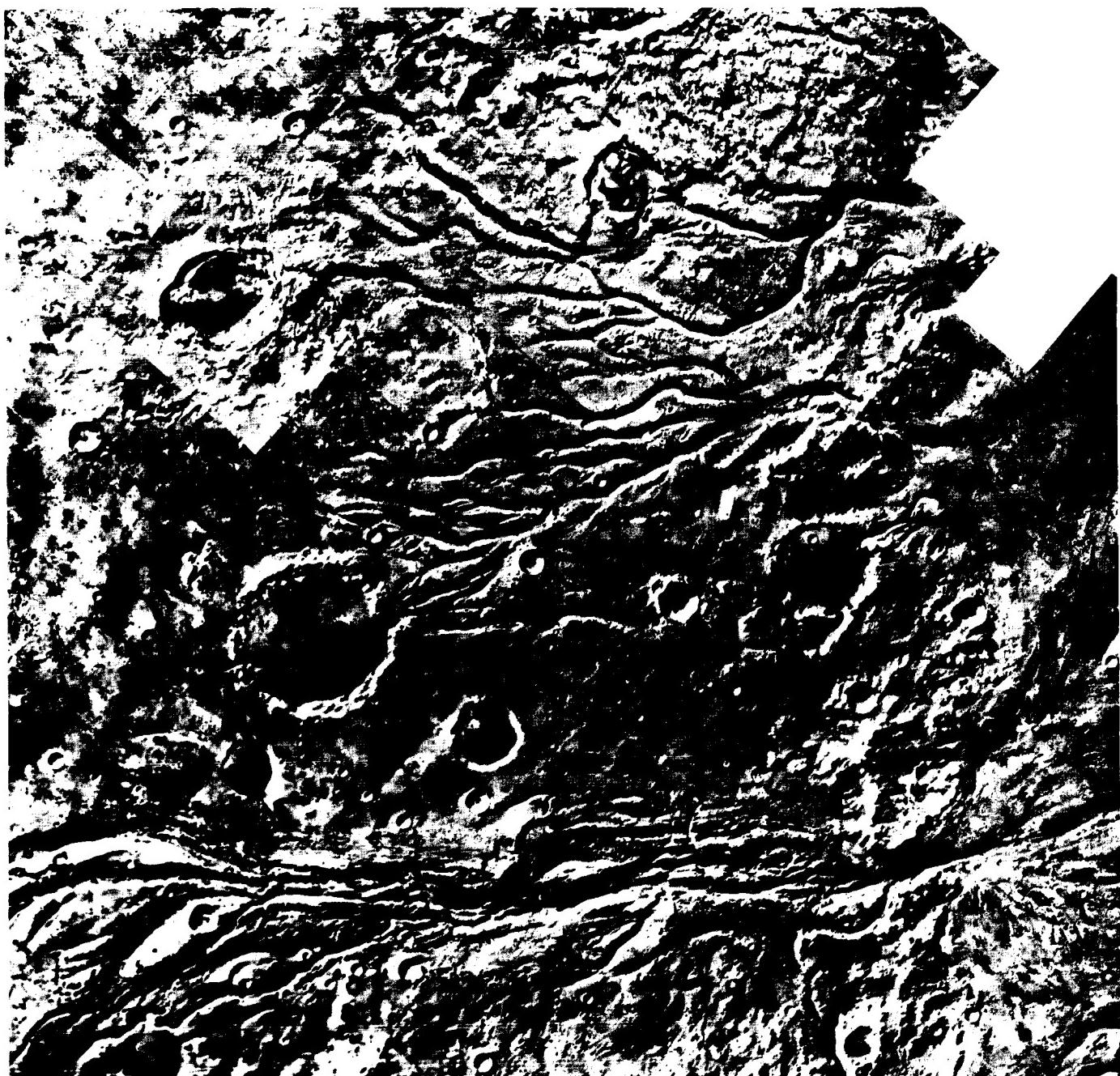


PLATE P-9

The two natural satellites of Mars, Phobos (Flight) and Deimos (Fear), were so small that they were not discovered until 1877 by Asaph Hall. Their landforms are of interest in several respects. First, these are the smallest objects, with mean diameters of 21 km for Phobos and 13 km for Deimos, as yet given a close look. Second, and the consequence of this small size, these bodies have so little mass that landforms have developed in the near absence of gravity; at the surface of Deimos, for example, the acceleration due to gravity is less than 0.1 percent that of the Earth. Third, the densities of both bodies combined with their low albedos virtually dictate a carbonaceous chondrite composition; these are therefore landforms on very primitive undifferentiated bodies. Finally, several lines of evidence strongly suggest that these "satellites" are actually captured asteroids, giving us a preview of asteroid geomorphology.

Plate P-9 shows Phobos as imaged by a Viking Orbiter from 612-km range (Carr, 1982); Figure P-9.1 shows Deimos as seen from 948-km range. Perhaps the most obvious geomorphic characteristic is the first-order one of shape: both are rough triaxial ellipsoids. Beyond that, both are heavily cratered. According to P. Thomas, cited by Carr (1981), their depth/diameter ratios and relative rim heights are similar to those of lunar craters, suggesting that, for impact craters in this size range, gravity has minor influence on shape. All the craters visible on both bodies are simple, without central peaks or multiple concentric rims. Although this may reflect the low gravity, it is more likely a simple function of size; Carr points out that, on the Moon, such features are found only in craters wider than about 20 km, and such craters obviously cannot be found on Phobos and Deimos. The largest crater on Phobos, Stickney (facing the viewer), is about 10 km wide; formation of a larger crater probably would have broken the satellite into pieces.

Probably the most puzzling landforms on Phobos are the grooves and crater chains shown in Plate P-9 and Figure P-9.2. Features of this sort on the Moon would be explained as tectonic or volcanic, probably both, but essentially internal in origin. It is hard to imagine internal activity in a body only 21 km wide, especially one of carbonaceous chondrite composition, and the most likely explanation is that they were formed by the impact that produced the crater Stickney. The main evidence for this is simply that, when mapped globally (or perhaps one should say ellipsoidally) the grooves are seen to radiate from Stickney, converging on the antipode. P. Thomas (1979) has examined these

PHOBOS AND DEIMOS

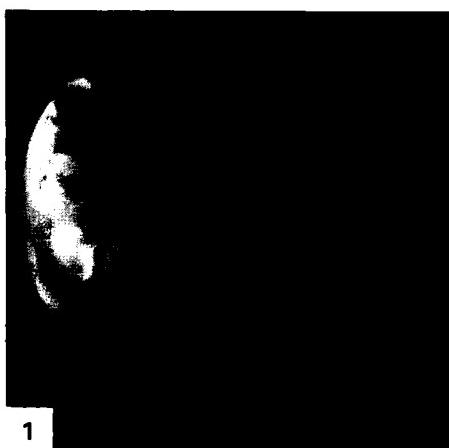
grooves and has concluded that their distribution and morphology suggest that they are essentially impact fractures. These fractures may have been modified by collapsing into them or by ejection of impact-generated steam—both processes that could produce chains of craters. Because carbonaceous chondrites contain several percent water of crystallization, impact-stimulated volcanism of some kind is conceivable.

Whatever their origin, the grooves on Phobos present a fascinating geomorphic puzzle, one for which the most promising approach thus far seems to have been basic geologic (or photo-geologic) mapping.

Another puzzling geomorphic characteristic of these small worlds is what appears to be thick regoliths on each, "thick" meaning 5 to 10 m for Deimos (Figure P-9.3) and up to 100 m for Phobos (Thomas, 1979). Formation of a regolith on heavily impacted bodies is now fairly well understood, owing to the Apollo investigations of the Moon. The dense crater population of the satellites of Mars clearly implies that regolith-forming processes have been active, but one would expect most of the ejecta from impact craters to be blown completely off because of the low gravity. However, the subdued outlines of craters and grooves (the latter on Phobos) imply that these are not bare rock surfaces, but are blanketed with debris.

Another enigmatic aspect of the regoliths is that the debris on Deimos appears to be more effective in subduing crater outlines than that on Phobos, suggesting that it may be thicker. From albedo markings on Deimos, Thomas has further shown that, despite the almost negligible surface gravity, mass wasting has taken place. Shaking by impacts or temperature changes may trigger creep; in any event, it is surprising to see gravity-dependent geomorphic processes at work even on this small satellite.

To summarize this description of geomorphology on Phobos and Deimos, these satellites furnish us with an end member, so to speak, in the family of solid bodies in the solar system. They are among the smallest ones for which high-resolution images have been obtained; they are geochemically primitive undifferentiated bodies that are probably close to carbonaceous chondrites in composition; and they have evolved geomorphically almost entirely by external processes. It is both surprising and gratifying that our understanding of planetary geomorphology is now great enough to provide at least plausible, though incomplete, accounts of how these strange small planetary bodies have evolved. **Viking Orbiter P20776.**



1



2



3

ORIGINAL PAGE IS
OF POOR QUALITY



The surface of Venus is impossible to observe optically because of its thick global cloud deck, but television panoramas of the terrain have now been obtained by the Soviet Venera 9, 10, 13, and 14 landers, which show small-scale geomorphology (Florensky et al., 1977; Florensky et al., 1983; Garvin et al., 1984). Large-scale landforms and global physiography have been surveyed with radar both by terrestrial radio telescopes and by orbiting spacecraft, which have revealed mountain ranges, volcanoes, plateaus, and mare-like terrains. Most recently, radar imagery with 1- to 2-km resolution has been acquired by Soviet Venera 15 and 16 spacecraft for about one quarter of the Venusian surface, above latitude 30°N. This imagery shows an amazing variety of landforms, ranging from huge concentric features (coronas) to strongly banded ridge and valley topography ("parquet" terrain). From 1978 to 1981, the American Pioneer Venus (PV) orbiter mapped 93 percent of the global topography at 30- to 110-km resolution, finding huge mountains (Figures P-10.1 and P-10.2) in the northern hemisphere 11 km above the dominant rolling plains. Collectively, these various investigations show Venus to be a tectonically and volcanically active world, presumably due in part to its large mass (90 percent that of the Earth).

The PV radar altimeter produced data on the topography, surface roughness (in RMS slopes from 1 to 10%), and reflectivity, shown on Mercator projections in Plate P-10 with 100-km resolution. The magnitude of the topographic slope on a horizontal baseline of about 100 km has been computed and compared with that of the Earth (Figure P-10.3). The surface of Venus has been classified into four topographic provinces. The lowlands, including the narrow cleft-like chasmata such as Artemis and Devana, make up about 25 percent of the surface area. Rolling plains, with elevations from 0 to 2 km relative to a 6051.0-km planetary radius, are globally dominant, comprising about 65 percent of the surface. The continent-like highlands, with elevations from 2 to 4.5 km, are about 7 percent of the surface and the mountainous regions are about 1 percent. The mountains include peaks 11 km high (Maxwell), contrasting with the highest terrestrial mountains, the Himalayas, which are only 8 km above sea level (although Hawaii is 13 km above the ocean floor).

Topographic slope distributions for Venus and Earth are shown in Figures P-10.2 and P-10.3 with cylindrical projections. The slopes are calculated from the planar topography gradient over 3 by 3° regions from 100-km resolution data. It is apparent that high terrestrial slopes are typical of continental margins and of features related to plate convergence or divergence. The only slopes on Venus approaching those of continental margins are the ones bordering Ishtar Terra. Highland margins have lower

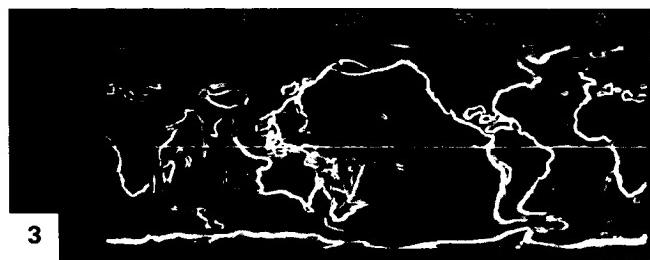
slopes. Flat areas, with 0° slopes, distinguish terrestrial platforms and cratons from Venusian highlands; detailed comparisons are given by Sharpton and Head (1985).

The radar-derived surface roughness (middle map, Plate P-10) represents the spatial distribution of facets (scatterers) at scales from about 20 cm to 20 m, and relates to the features observable in surface images from Venera landers (Figure P-10.4). The roughness, expressed as RMS slope, has been subdivided into smooth, moderate, and rough categories (increasing slopes). Most of Venus is smooth to moderately rough at meter scales, contrasting with the rougher surfaces of the Moon and Mars. There is an obvious correlation between meter-scale roughness and elevation, as might be expected, with roughness increasing systematically with elevation except for the Lakshmi plateau. This may be related to weathering rates or efficiency or to surface age. Higher features may be younger and thus fresher, with steep slopes preserved. Alternatively, if erosion processes on Venus increase surface roughness, higher regions would be older.

The reflectivity (bottom map, Plate P-10) has been measured from the radar echos. Reflectivity is strongly related to surface porosity and composition, the abundance of free metals (as in iron meteorites), graphite, and oxides and sulfides of Fe, Ti, Mn, Sn, Pb, and Cu being especially important. Minerals such as pyrite, hematite, ilmenite, and magnetite would therefore affect reflectivity very strongly. This range in reflectivity from 0.0 to 0.5 corresponds to materials ranging from poor conductors (e.g., very porous material) to excellent conductors with high dielectric constants. Reflectivity values less than 0.1 generally represent soils or weakly cemented materials such as the lunar regolith and eolian sands. Rocks generally fall in the 0.1 to 0.2 range, with a few dense or metal-rich rocks having values of 0.2 to 0.3 (high dielectric constants). Materials above 0.3 are extremely rich in free metals or other highly conductive materials. As shown on the map, there are extensive areas of high reflectivity, mostly mountainous, although a large area of high reflectivity is adjacent to the lowland Atalanta Planitia. In general, Venus appears to lack a globally continuous porous regolith like that of the Moon. The areas of high reflectivity may be volcanics with unusually high Fe or Ti contents, like some lunar basalts, or alteration products such as pyrite, hematite, or pyrolusite. Concentrations of free carbon, such as graphite, could also play a role. Such highly reflective surfaces have not been observed on the Moon or Mars thus far, and their nature is not understood. More knowledge about their relation to geologic structures is needed. NASA/Pioneer Venus; MIT and Brown University.



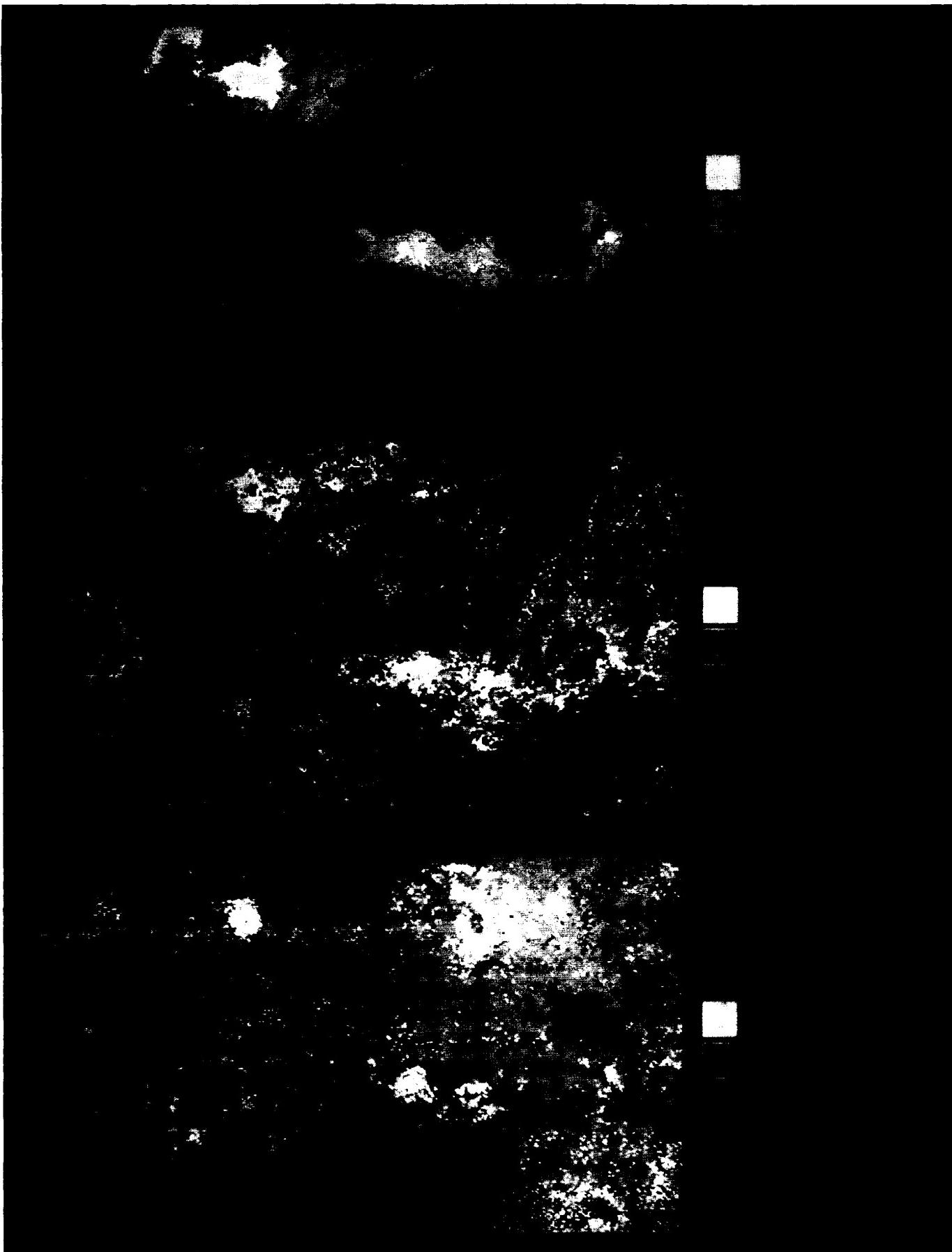
2



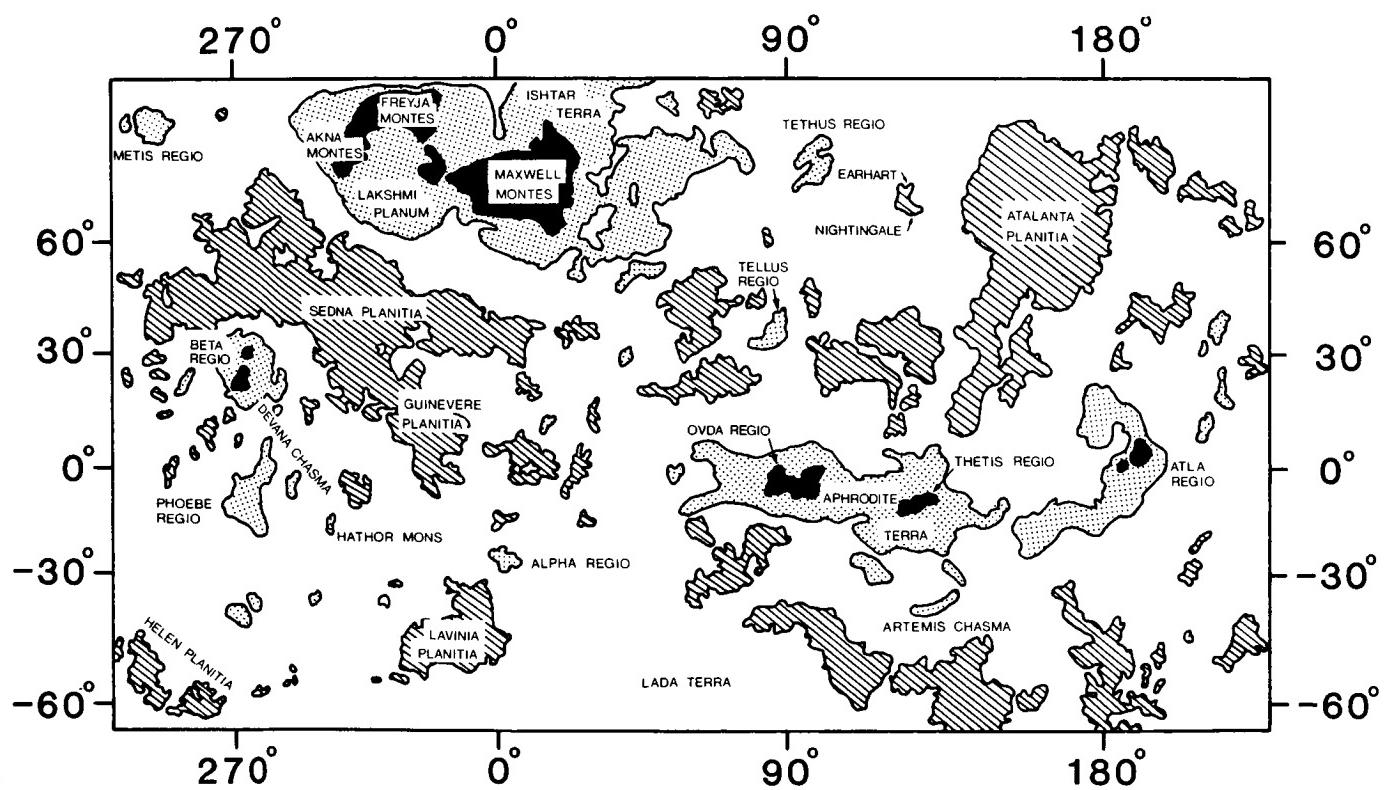
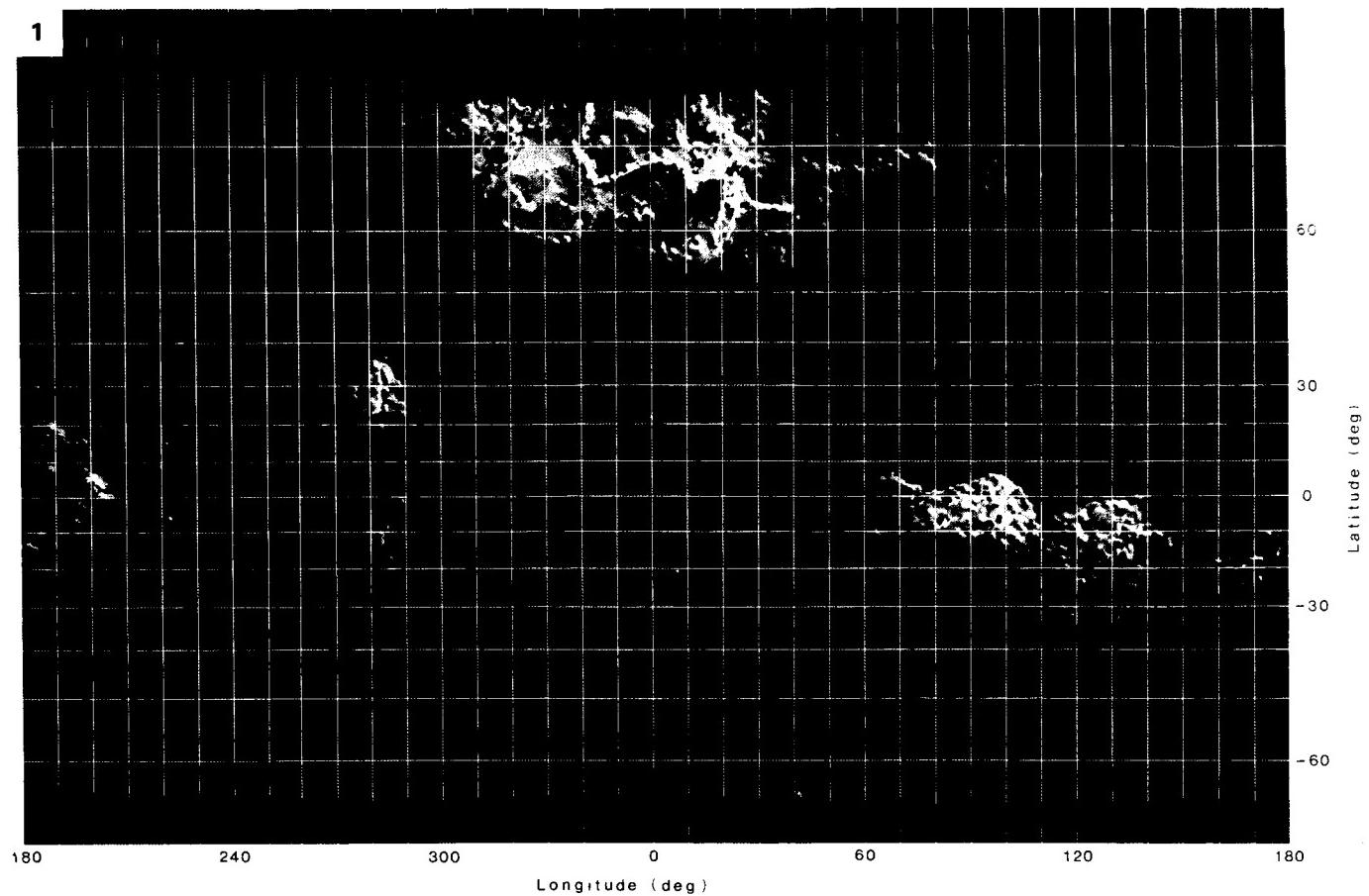
3

MERCATOR PROJECTION

ORIGINAL PAGE IS
OF POOR QUALITY



ORIGINAL PAGE
COLOR PHOTOGRAPH



ORIGINAL PAGE IS
OF POOR QUALITY

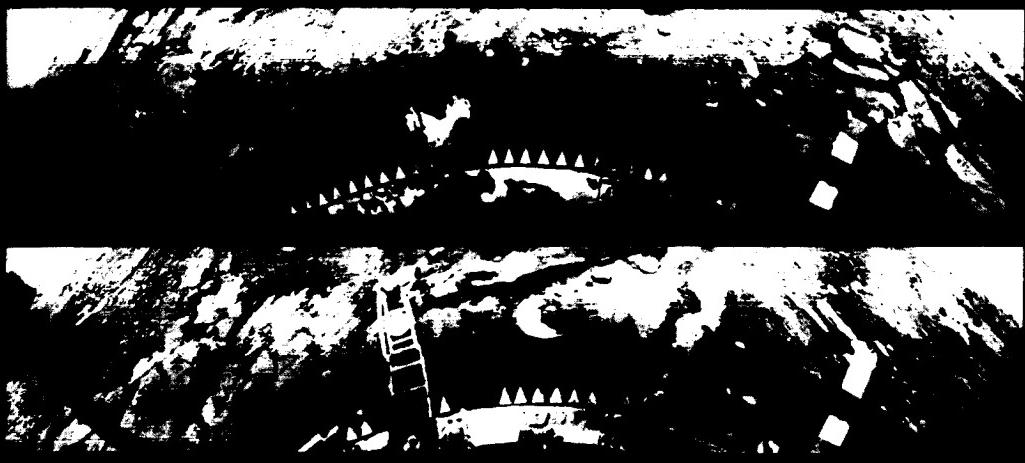
VENERA 9



VENERA 10



VENERA 13



VENERA 14



PLATE P-11

HIGH-RESOLUTION RADAR IMAGES OF VENUS

The high-resolution views of the Venusian surface on the next pair of pages have been obtained through the optically opaque atmosphere by radio telescopes at Arecibo, Puerto Rico, and Goldstone, California (Plate P-11, left), and by the Soviet Venera 15 and 16 spacecraft (Plate P-11, right). The highest resolution on these images ranges from 1 to 4 km. More important, however, is the radar incidence angle. Near-vertical incidence images, such as those from Venera 15 and 16 (5 to 15°) are sensitive to edges and small slopes, whereas higher angles (15 to 65°) are most sensitive to small-scale roughness that may be landform-specific. The left view of Plate P-11 (Arecibo radar) shows the Maxwell Montes region (Figure P-10.1) with 2-km resolution at a 65° incidence, resulting from Maxwell's 65°N latitude.

The banding of the Maxwell area, which has been the subject of much study (Campbell et al., 1983), may result from either extensional or compressional tectonism. Compression on Earth produces features such as fold belts and imbricate thrusts that might be analogous to the Maxwell banded terrain. Another possibility would appear to be flow structure resulting from very silicic lavas that, because of their high viscosity, frequently form ridges normal to the flow direction. However, these bands are 10 to 20 km wide (Campbell et al., 1983), far larger than any terrestrial analog.

The right image of Plate P-11, from Venera 15 and 16, shows a much larger area centered on Maxwell, with a 10° incidence angle (Barsukov et al., 1985). The circular crater shown on both views is Cleopatra Patera. Originally interpreted as a large caldera, it has more recently been proposed to be a multi-ringed impact crater with a central peak.

The currently favored model for the geologic evolution of this region calls for a complex multistage history involving tectonism (uplift, extension, compression), volcanism, and minor erosion. The physiography and great relief of Maxwell make it one of the most interesting regions on Venus, but it may be an unusual feature from a global viewpoint. Examples of more representative landforms and terrains are presented in Figures P-11.1 through P-11.4.

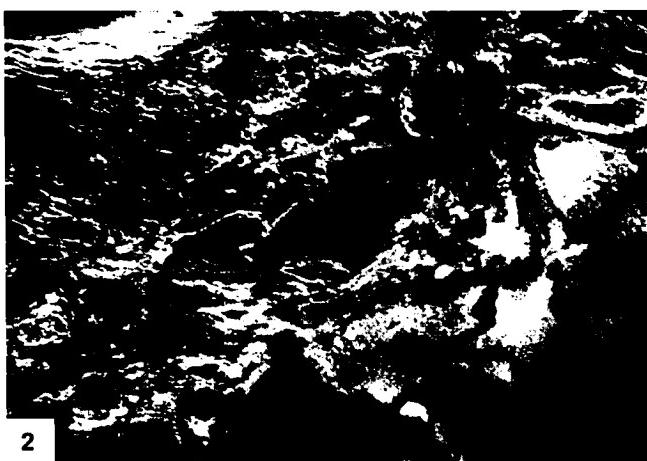
There is evidence that volcanic processes have operated on Venus as they have on other bodies. Figure P-11.1 is an Arecibo radar image of the summit region of Beta Regio. Beta has been interpreted as a large volcanic complex, including a shield structure (Theia Mons, at bottom), a rift zone, and another volcanic edifice (Rhea Mons, bright feature at top right). It may be analogous to the East African rift zone and associated volcanics. The flow-like features coming from Theia Mons are similar in dimen-

sions to terrestrial volcanic flows. Other evidence for volcanism on Venus can be seen on the plains in an Arecibo image (Figure P-11.2) of the area southeast of Lakshmi Plateau that shows what appear to be volcanic flows and source vents. Comparable features have also been identified on the Lakshmi Plateau itself (Plate P-11, right image).

In addition to unambiguous volcanic features, the higher plains of Venus commonly display a type of intensely lineated or banded terrain termed "parquet" by Soviet scientists because of its resemblance to certain types of wood flooring. The term "tessera" has since been adopted by the International Astronomical Union. Figure P-11.3, a Venera mosaic covering an area 600 by 850 km near Ishtar Terra, shows a large area of parquet terrain (using the original term). Several different terrestrial analogs for this terrain have been suggested, including Cenozoic folds such as the Sulaiman Range in Pakistan (Plate T-45) and midocean ridge-transform fault systems such as those in the eastern Pacific. Silicic lava flow structures have also been proposed, but as for those near Maxwell, the ridges of the parquet terrain are far larger than any known lava ridges.

A previously unknown Venusian landform, the "coronas," was discovered by the Venera 15/16 radar, as shown in Figure P-11.4. Most coronas are 100 to 300 km in diameter and are composed of concentric systems of faults or ridges. Like so many Venusian features, their origin is not understood, opinion being divided. They resemble the fracture patterns associated with large plutons on the Earth; the individual intrusions making up batholiths sometimes display structures of this type. The gross outline of the coronas is reminiscent of multiringed impact features. They might represent the Venus analog of modified impact features such as the Sudbury Basin of Ontario, in which intrusions and volcanism might have deformed the original crater to produce a corona. Still another view is that the coronas represent relaxed volcanic centers. Given the high temperatures at the surface of Venus, old (1 to 2 billion years) volcanic constructs could collapse by creep, leaving behind some type of corona structure.

Without subkilometer resolution radar images of these ambiguous features, conclusive statements about their origin must be deferred, presumably until 1988 when the Venus Radar Mapper (Magellan) arrives. At this point, it is certain that Venus, having a wide range of volcanic, tectonic, impact, and composite features, is more geographically diverse than the Moon and perhaps even Mars. **Left: Arecibo Observatory; right: U.S.S.R. Academy of Sciences.**

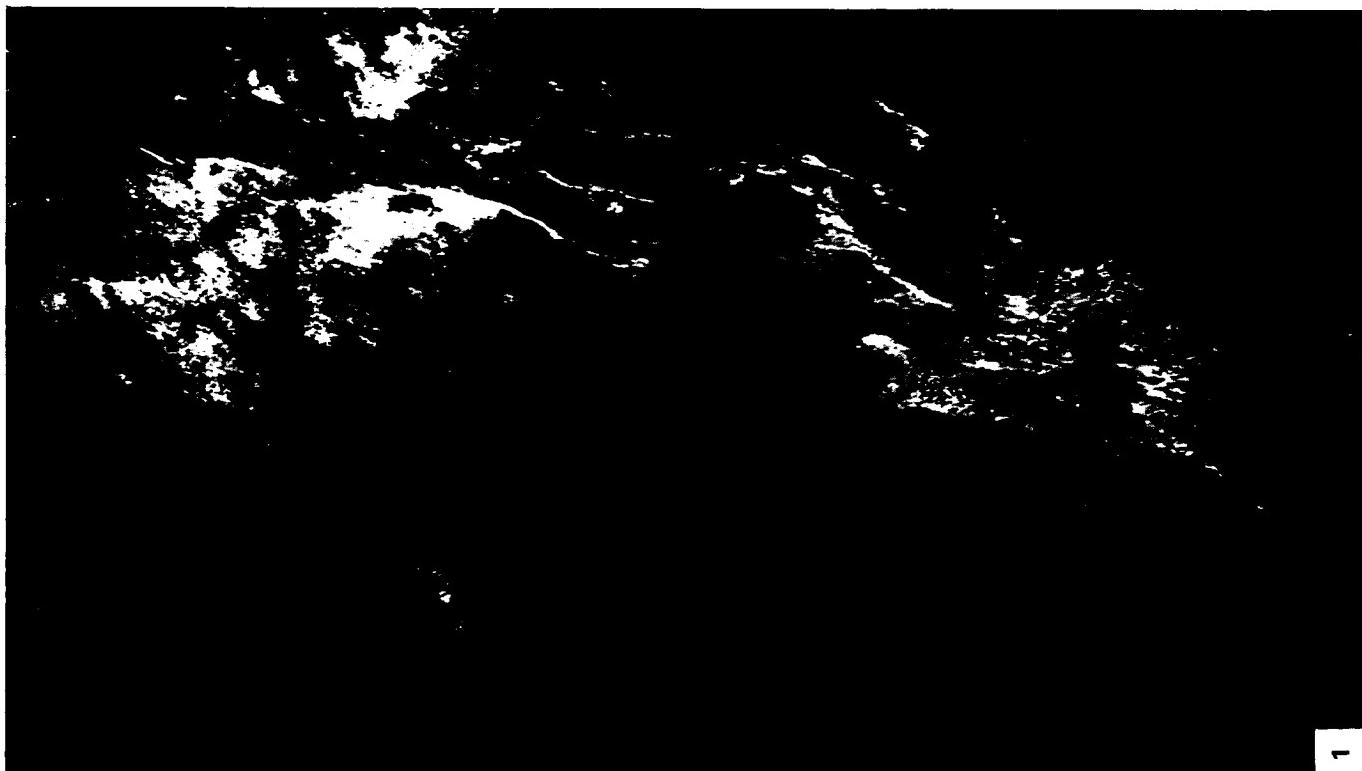


2

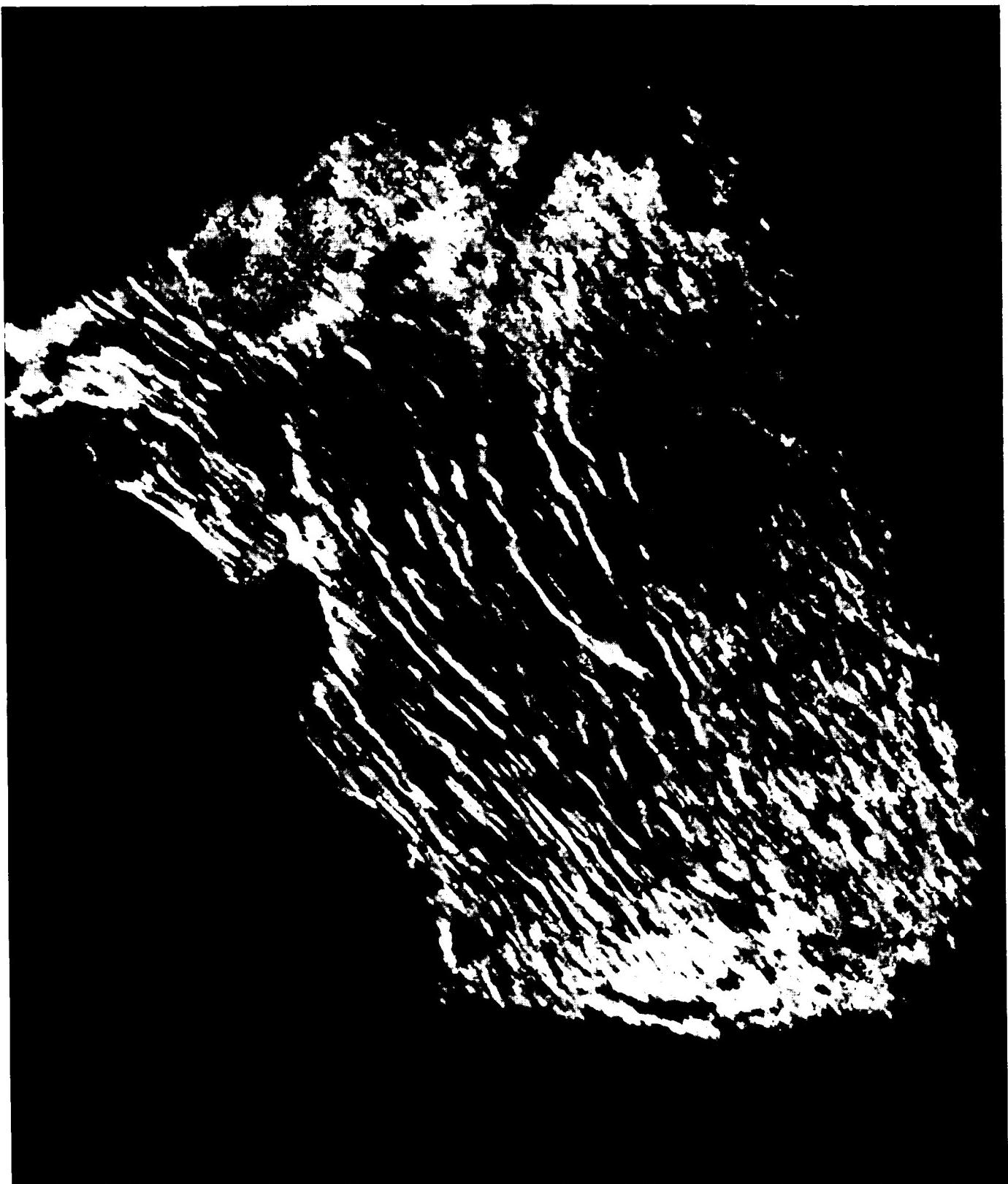


4

**ORIGINAL PAGE IS
OF POOR QUALITY**



**ORIGINAL PAGE IS
OF POOR QUALITY**



**ORIGINAL PAGE IS
OF POOR QUALITY**

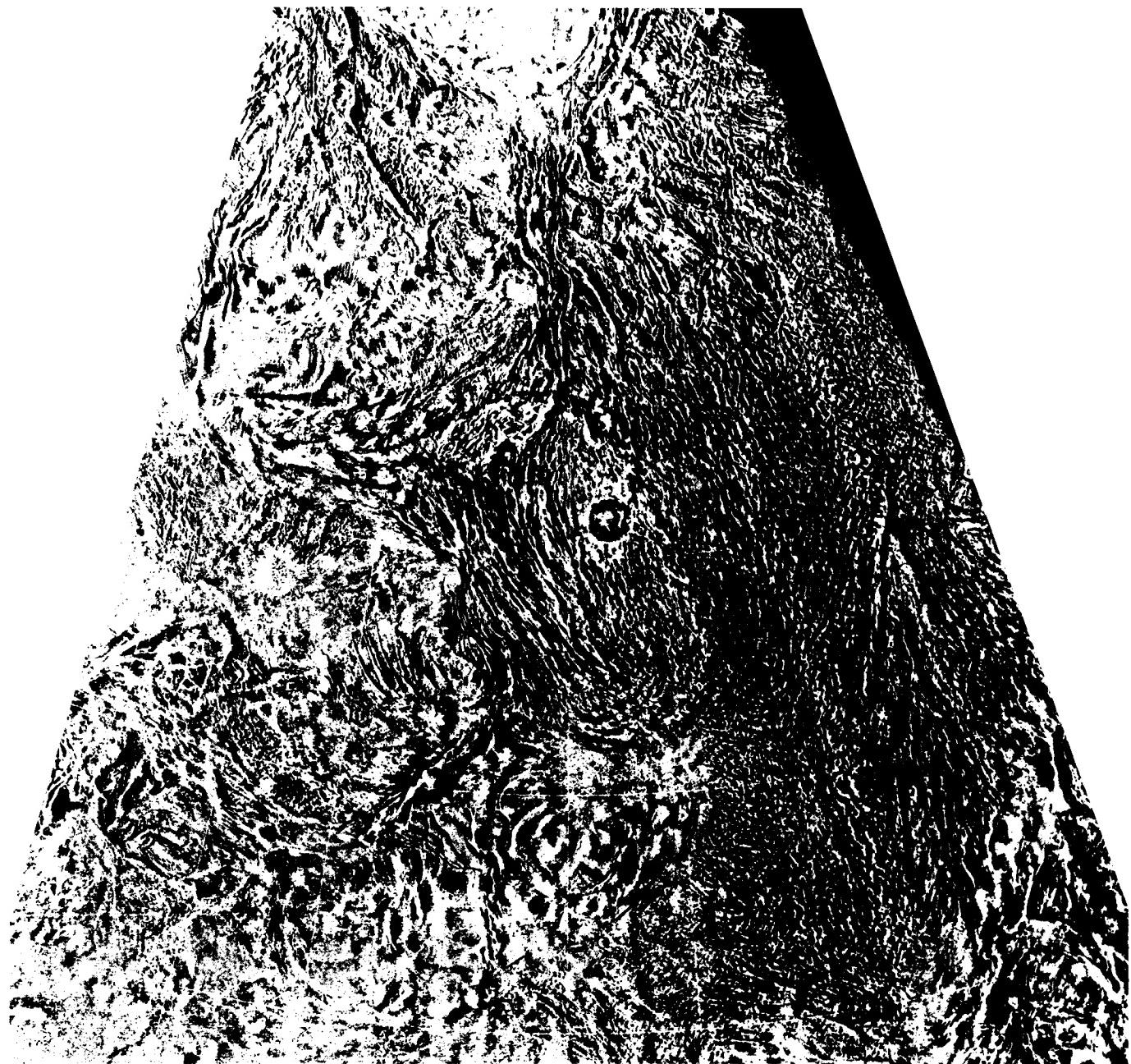


PLATE P-12

SATELLITES OF JUPITER

The four largest satellites of Jupiter, although visible from Earth with 7-power binoculars, were not seen close-up until 1979 when Voyagers 1 and 2 flew through the Jovian system. The variety and strangeness of landforms on these and the Saturnian satellites could hardly have been greater if the spacecraft had made interstellar flights and returned photographs of another solar system. The three icy Galilean satellites, shown in a composite view are discussed here; Io will be treated separately (Plate P-13).

The innermost of these three bodies, Europa, possesses a network of lines that are strikingly similar to prespacecraft renderings of Percival Lowell's fancied canals on Mars, at least in early distant views. At higher resolution, the terrain is revealed as criss-crossed with a complex network of intersecting lineaments cutting an otherwise smooth surface, with only a few craters. The lineaments, many of them hundreds of kilometers long, have little evident relief and are visible mainly because of albedo or color contrast. They have been intensively studied by many investigators; the following account is based primarily on the comprehensive treatment by B. K. Lucchitta (1981) and her colleagues.

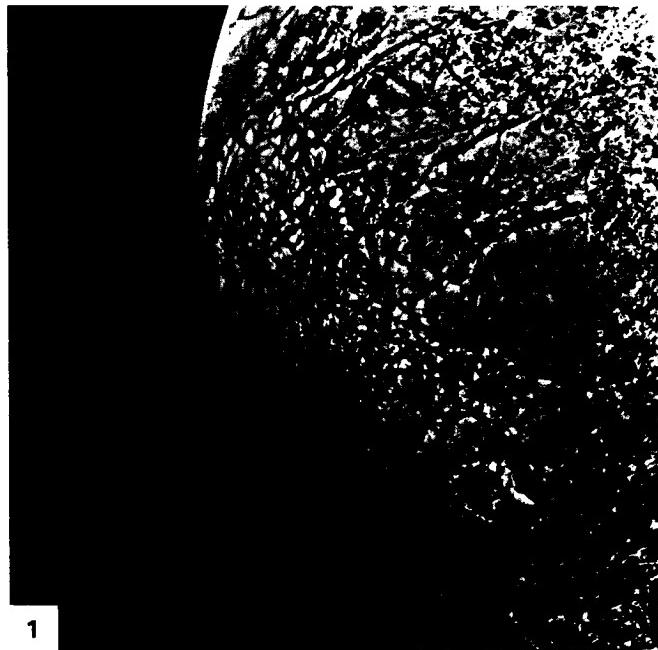
As shown in a closer view (Figure P-12.1), the most conspicuous lineaments are dark bands, generally with sharp edges and often wedge-shaped. They dominate the upper left part of the area shown here. Because they cut most other features, they are probably the youngest class of lineament and they appear to have been formed by local expansion and rotation of the crust, which is presumed to be impure water ice from reflection spectra. The wedge-shaped bands are concentrated near the point farthest from Jupiter, suggesting that they are in some way related to tidal deformation. In the lower right part of the image, parts of three gray bands are visible; when seen in broader perspective, they form concentric arcs around a common point in the southern hemisphere. They show some similarities to the dark wedge-shaped bands, but appear to be considerably older. They may represent parts of large circles, but there are so many ways that such features could originate (such as major impacts) that further speculation at this time seems fruitless. A third type of lineament, also curved, dominates the right side of the area shown here. These are ridges with at most a few hundred meters relief, best seen along the terminator. They sometimes form cycloidal patterns, but may locally grade into straight segments. Their azimuthal distribution, peaking in the northwest and northeast, suggests the regmatic shear pattern often postulated for the Earth, and Lucchitta et al. (1981) suggest they may have been formed as conjugate shears. The specific nature of the curved ridges is unclear; two possibilities are ice dikes and compressional structures (reverse faults or folds). A major problem in interpreting the Europan lineaments is uncertainty about the internal structure of the satellite. Its density implies a silicate interior, but it may have retained a liquid interior long after the outer ice crust formed. Tidal interactions, supplemented by internal radioactivity, have evidently led to resurfacing and renewed tectonism, as shown by the near absence of impact craters. It is obvious that study of Europan tectonics will be a fruitful one for many years, especially when better imagery is obtained from the Galileo mission in the late 1980s.

Ganymede (Figures P-12.2 and P-12.3) has a bulk density of 1.9 gm/cm^3 , implying a substantial ice fraction. The expectation that closeup views from Voyager would show some type of ice landscape proved correct. The surface is an intricate montage of dark cratered terrain (left part of Figure P-12.2), cut by a network of light-toned grooved terrain (right part of Figure P-12.2; left part of Figure P-12.3). The grooved terrain is clearly younger than the cratered terrain, as shown not only by its cross-cutting relationships but by its much lower crater density. The absolute ages of both have been estimated by Shoemaker and Wolfe (1980)

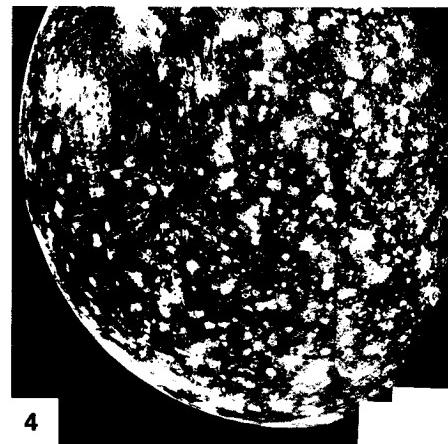
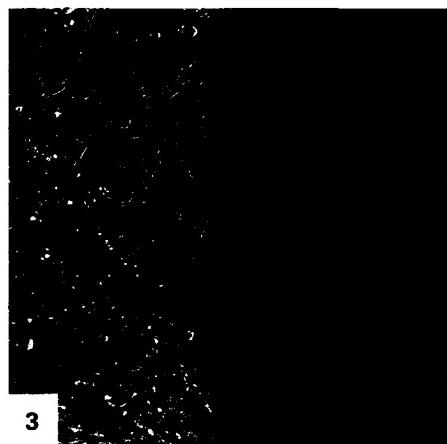
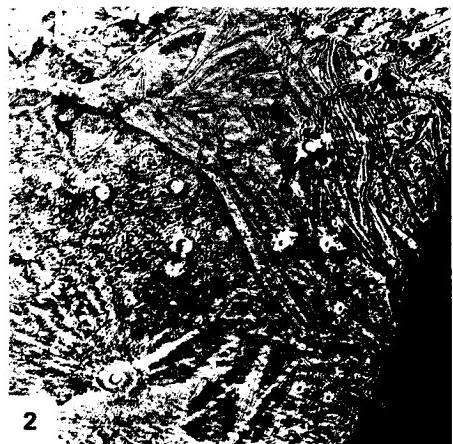
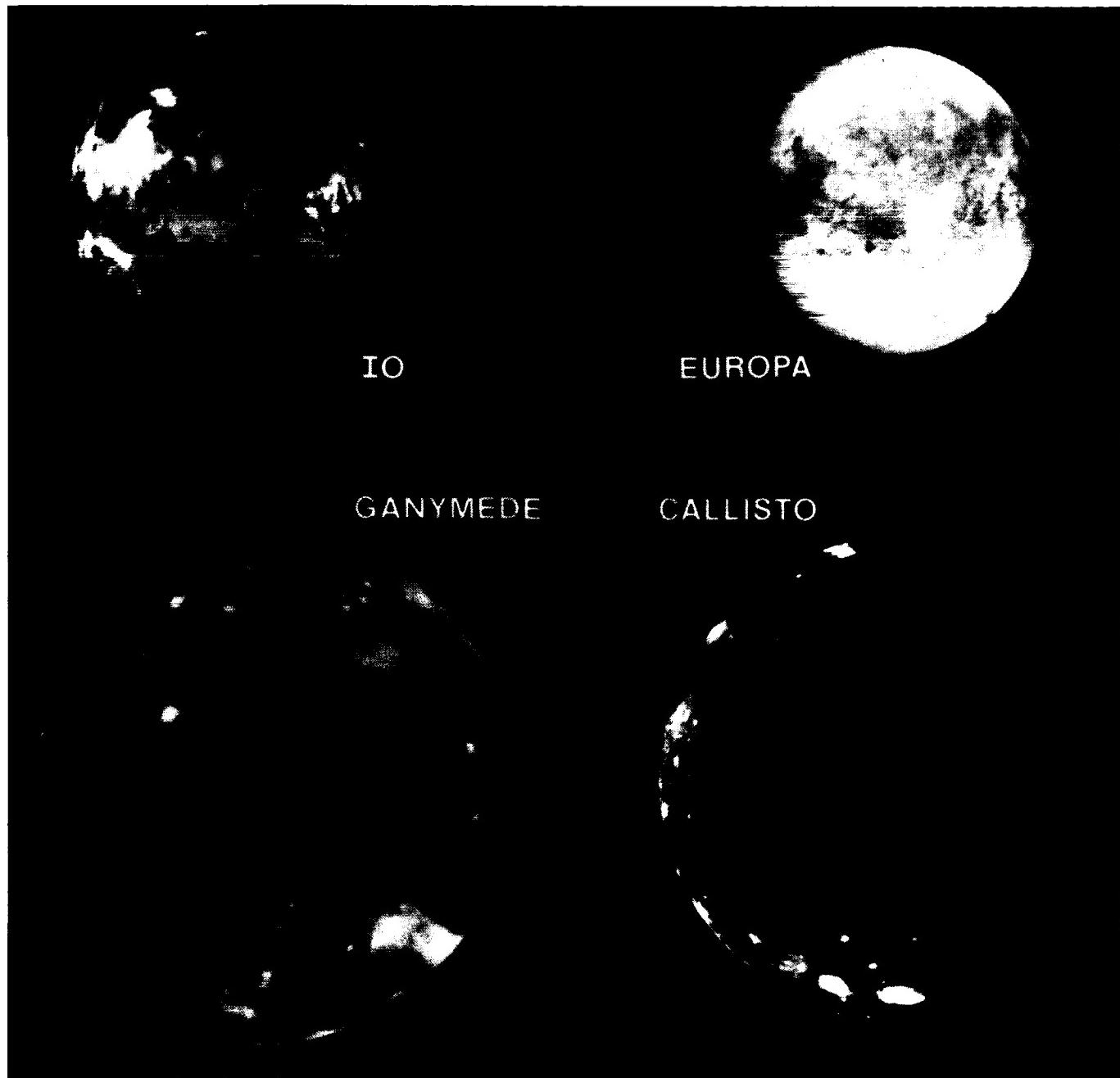
to be older than 3 billion years (i.e., in the same general range as the lunar surface).

The impact craters, although modified by plastic flow in the ice, are clearly recognizable cousins to the classic example, Tycho (Plate P-1). The grooved areas, or sulci (sing. sulcus), are unlike anything seen before the Voyager missions. They superficially resemble folded mountains such as the Appalachians or, more plausibly, the Zagros Mountains. However, the consensus of almost all investigators is that they are extensional structures of some type, probably families of normal faults that have formed repeatedly, producing the intricate superposition relationships noted in Figure P-12.3. Flow of water from the interior of Ganymede may have accompanied the faulting. It is tempting to draw a comparison between the grooved terrain and terrestrial spreading centers, Ganymede providing a type of ice/water analog to the basalt eruptions found on Earth. A more plausible analog may be the grooved terrain on Saturn's Enceladus (Figure P-14.3). This account has only touched on the fascinating variety of strange landforms seen on Ganymede; further examples are illustrated in the initial Voyager reports (Smith et al., 1979) and the summary by Johnson (1982).

The last of the Galilean satellites covered here is Callisto (Figure P-12.4), which is also the most primitive one. Callisto's density is close to that of Ganymede, suggesting that it too consists of a thick crust and mantle of ice over a silicate core. The landforms seen on Callisto favor such a structure; the terrain can be summarized as an extremely old one, saturated with craters formed in an icy crust (Smith et al., 1979). The closeup view shows general characteristics of this terrain, as well as the gigantic Valhalla ring structure. Valhalla superficially resembles the Orientale Basin on the Moon or the Caloris Basin on Mercury, and in fact, it is judged to be a large impact structure. However, it is morphologically very different, displaying little relief and no evidence of a distinct ejecta blanket. It is generally believed that the initial crater has nearly been erased by plastic flow of the ice, as has apparently happened to many smaller craters both on Callisto and Ganymede. 83-H-205.



**ORIGINAL PAGE
COLOR PHOTOGRAPH**



The innermost of Jupiter's large satellites, Io, deserves an entire caption. The Plate shows the full disk as Voyager 1 approached it; the three ancillary views cover regions included in the main view, with the same geographic orientation.

Io had been known to be peculiar for some years, but the first Voyager images astonished viewers. Apart from the bright orange colors, later proved by Young (1984) to be an artifact of the instrumentation, the terrain revealed was unlike that of any other planet or satellite. Most striking is the total absence of impact craters; Io is the only known solid body with none. This implies some type of rapid resurfacing process that must be obliterating impact craters, since cratering is obviously happening throughout the solar system now. The nature of this resurfacing process was quickly discovered when closeup views (Figure P-13.1) revealed unmistakable volcanic craters and flows. Even more surprising was the discovery by Voyager engineer, L. Morabito, of nine huge volcanic plumes (Plate P-13) coming from Io, which has turned out to be the most volcanically active body known. The fundamental cause of this activity is dissipation of tidal energy in Io. In a brilliant predictive paper, published just 3 days before the Voyager 1/Jupiter encounter, Peale et al. (1979) demonstrated that Europa perturbs Io into an unusually elliptical orbit around Jupiter. This in turn raises heat-producing body tides in Io, which, they predicted, would generate intense volcanism.

Geomorphically, the Ionian landscape appears to consist almost entirely of volcanic craters (patera), flows, or other volcanic deposits. The craters, such as those in Figure P-13.1 and P-13.2, tend to be relatively shallow and can best be termed "calderas." The lava flows resemble those on Earth. Because of their apparent reddish orange color, it was first believed that they were flows of elemental sulfur, which is red when initially melted. As mentioned previously, however, Young (1984) later showed that the true colors were chiefly pale yellows, and he argued convincingly that, although there is undoubtedly a flow of sulfur and sulfur dioxide on Io, the flows are not sulfur. These are thus landforms composed largely of silicate volcanics, as proposed by H. Masursky et al. (1979).

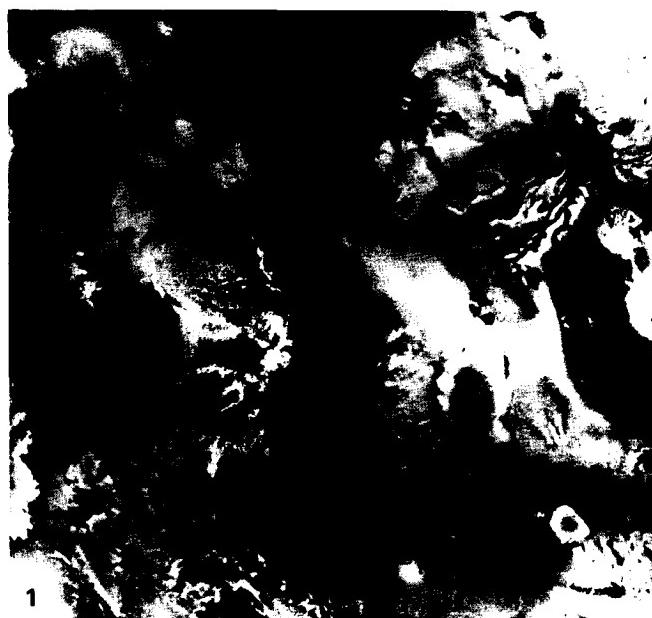
Much of the Ionian surface consists of plains with relatively low relief (Figures P-13.2 and P-13.3), clearly some type of vol-

canic deposits probably mantled with sulfur or sulfur dioxide. The total absence of impact craters indicates that the plains are extremely youthful, but it is not clear whether they formed from lava flows, pyroclastic deposition, or other processes. There is no doubt that at least some of the plains material is analogous to pyroclastic material, inasmuch as the huge volcanic plumes have been observed falling back onto the surface.

The origin of the topographic elevations, apart from the volcanoes, is even less clear. The angular mountains, such as Haemus Mons (Figure P-13.4), have relief of several kilometers and appear to be massifs or volcanic constructs of some sort. However, the mesas, composed of erosional remnants of layered plains (Figure P-13.2 and P-13.3) are even less understood. The most specific question is that of how their bounding scarps are produced (i.e., what the mechanism of slope retreat is). McCauley et al. (1979) have proposed that the scarps were produced by some type of sapping in which liquid sulfur dioxide plays a role analogous to that of water in terrestrial sapping. They interpreted the light-colored deposit around the mesa in Figure P-13.3 as a deposit of frozen SO₂ related to sapping. An alternative explanation proposed by Mouginis-Mark et al. (1984) is thermal erosion of the layered plains by lava flows.

Some scarps appear to be normal fault scarps, notably the long straight ones in Figure P-13.3, bounding depressions. The continual and intense internal heating of Io probably keeps much of its interior molten, and the lithosphere is probably only a few tens of kilometers thick. Under such conditions, extensional tectonism and normal faulting should be widespread.

The geomorphology of Io as it is now may resemble that of the very primitive Earth, which must have been much hotter and more active in the earliest Archean than it is now. The inferred partly molten interior and thin lithosphere of Io resemble most concepts of the early Earth; perhaps the geomorphology of both bodies was similar. At a later stage, when the Earth cooled enough to permit rain and fluvial erosion, its landscape may have resembled that of the channelled Martian highlands (Plate P-8). **Voyager P-21226.**



ORIGINAL PAGE IS
OF POOR QUALITY

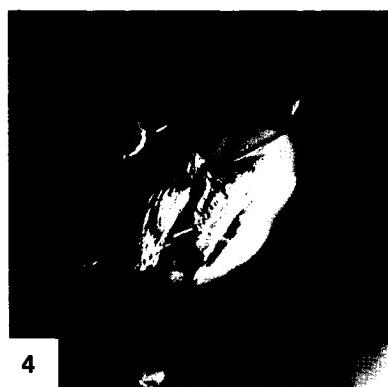
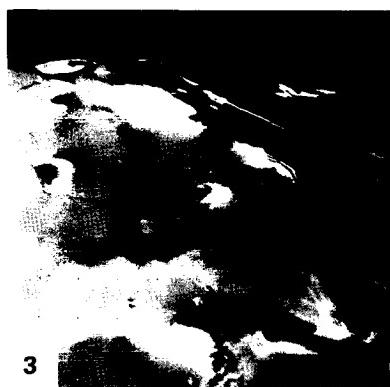
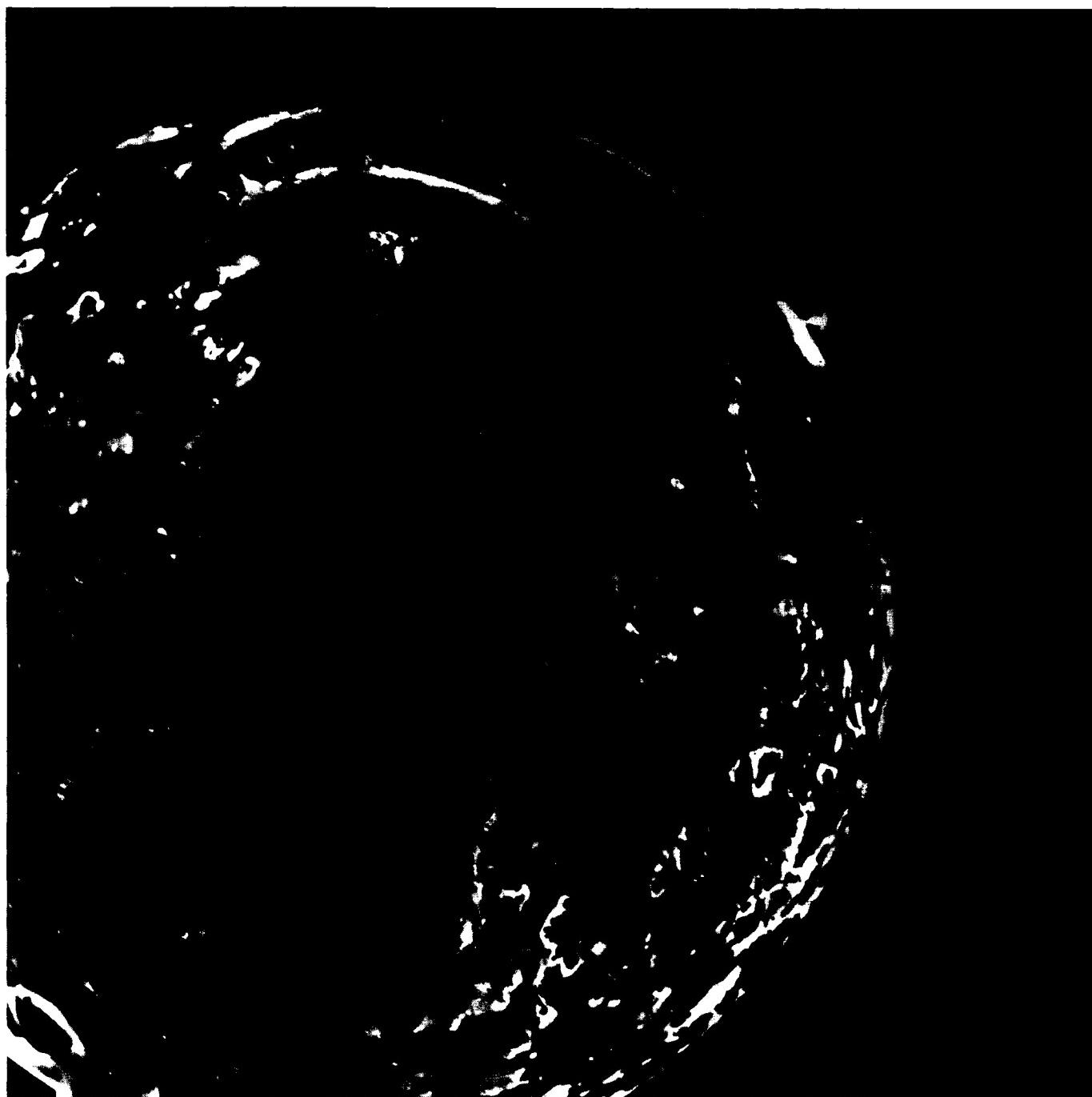


PLATE P-14

SATELLITES OF SATURN

The satellites of Saturn (except for Titan) can be called ice worlds. Their low densities and reflection spectra indicate that they are not only coated with water ice but must also be largely ice or water all the way through (probably mixed with dispersed silicates and perhaps ammonia in some). This bulk composition, although strange by terrestrial standards, is understandable in view of Saturn's great distance from the Sun. There is a striking compositional gradient in the solar system as a whole, from iron/silicate planets near the Sun to volatile-rich bodies farther out that consist mainly of hydrogen (the giant planets) or hydrogen compounds (the icy satellites, comets, and perhaps some asteroids). Unlike the Jovian system, the satellites of Saturn exhibit no obvious compositional gradient comparable to that from Io to Callisto, suggesting that the proto-Saturn was cooler than proto-Jupiter.

Geomorphically, the small Saturnian satellites provide examples of landforms produced on planets composed essentially of ice (Morrison, 1982). The term "ice" applies in a general sense inasmuch as the material making up the Saturnian satellites is probably not pure H₂O, but may include H₂O-NH₃, eutectics and, in deep interiors, high pressure H₂O polymorphs. Furthermore, the temperatures in Saturnian satellites may be far below those usually prevalent in terrestrial glaciers, and the physical properties may therefore be unfamiliar by terrestrial standards (Veverka, 1985).

Six of the medium-sized satellites of Saturn shown in the Plate (Meszaros, 1983) are superimposed on a disk representing the comparative size of Titan (5150-km diameter), the largest moon in the solar system. (Titan's surface is obscured by a thick opaque atmosphere.) The ice satellites exhibit a series of terrains ranging from highly cratered primitive terrains to those showing a considerable degree of resurfacing. The largest of these satellites, Rhea, is also the most heavily cratered (Figure P-14.1), as shown in this Voyager 1 view of the north polar region. However, the distribution of craters in this area is definitely nonuniform, with a much higher density of fresh-looking craters in the lower left part of the image (Smith et al., 1981). Smith et al. labeled the craters of the heavily cratered area Population I, formed by impacts in the early post-accretion period, and those of the other area Population II. They considered the different populations to result from different ages rather than differing impact rates, with a period of resurfacing that mantled the older craters at the upper right of the Plate (part of low albedo area).

The most clearly visible craters differ from those seen on Ganymede in that they show little evidence of flattening by ice flowage and are notably irregular or polygonal. This may indicate

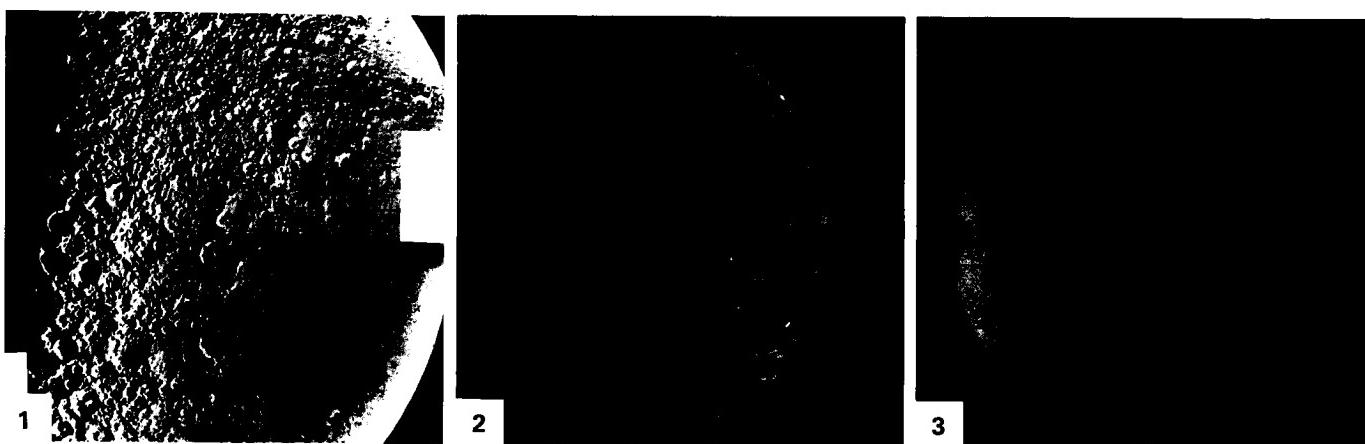
that the crust of Rhea became cold and solid early in its history. Distinct ejecta blankets around the craters are generally rare, owing to the lower gravity of Rhea, which permits ejecta to spread much farther than on the Moon, forming thinner ejecta blankets.

Dione has a markedly different topography (Figure P-14.2), including both impact and tectonic features. Three distinctly different types of terrain are visible here (Moore, 1984): heavily cratered terrain (right), cratered plains (left center), and smooth plains (upper left). The heavily cratered terrain is presumably the oldest, having been covered by internally expelled material to form the plains. Although the nature of the plains-forming material is unknown, it may have been erupted as a liquid, pyroclastic, or snow-like material. The term "volcanism" is generally applied to this resurfacing process, a curious term for a satellite whose surface temperature is now less than 100°K. However, the lava or ash analog was probably not a hot silicate liquid but water, ammonia, or organic compounds, with a significant fraction of rocky or carbonaceous material, as proposed by Plescia (1983).

The craters on Dione, almost certainly formed by impact during the post-accretionary period after the plains-forming events, resemble those on the terrestrial planets in that they have central peaks and raised rims. However, they are relatively shallow compared to similar-sized craters on silicate bodies, suggesting that viscous flow of the ice crust has flattened their initial forms.

The smooth high-albedo surface of a smaller Saturnian moon, Enceladus (Figure P-14.3), shows even stronger evidence of tectonic and volcanic activity. The resurfacing process inferred for Rhea and Dione went further here, producing substantial areas with no impact craters visible at a resolution of 2 km/line pair. This curious situation, reminiscent of Io, clearly implies relatively recent eruption of whatever the resurfacing material is, perhaps an ammonia/water mixture. Smith et al. (1981) estimated that such surfaces could not be over 1 billion years old, far from primordial. Squyres et al. (1983) suggest that tidal dissipation may, as in Io, have repeatedly melted the interior of Enceladus up to the present, augmented by radioactivity. They further suggest that the grooves may be extension fractures.

The dominant landform on Mimas is obviously the huge impact crater, Herschel (Figure P-14.4), whose size (130 km) approaches the diameter of the satellite (400 km). The presumed impact must have almost broken up the entire satellite. Mimas is also noted for the very high density of impact craters and, of all the Saturnian satellites, comes closest to representing a primordial crater-saturated terrain. The craters tend to be relatively deep, implying less viscous flow. 83-H-223.



ORIGINAL PAGE IS
OF POOR QUALITY

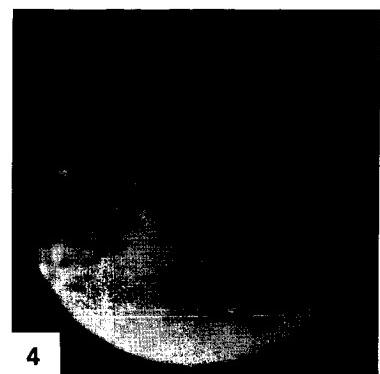
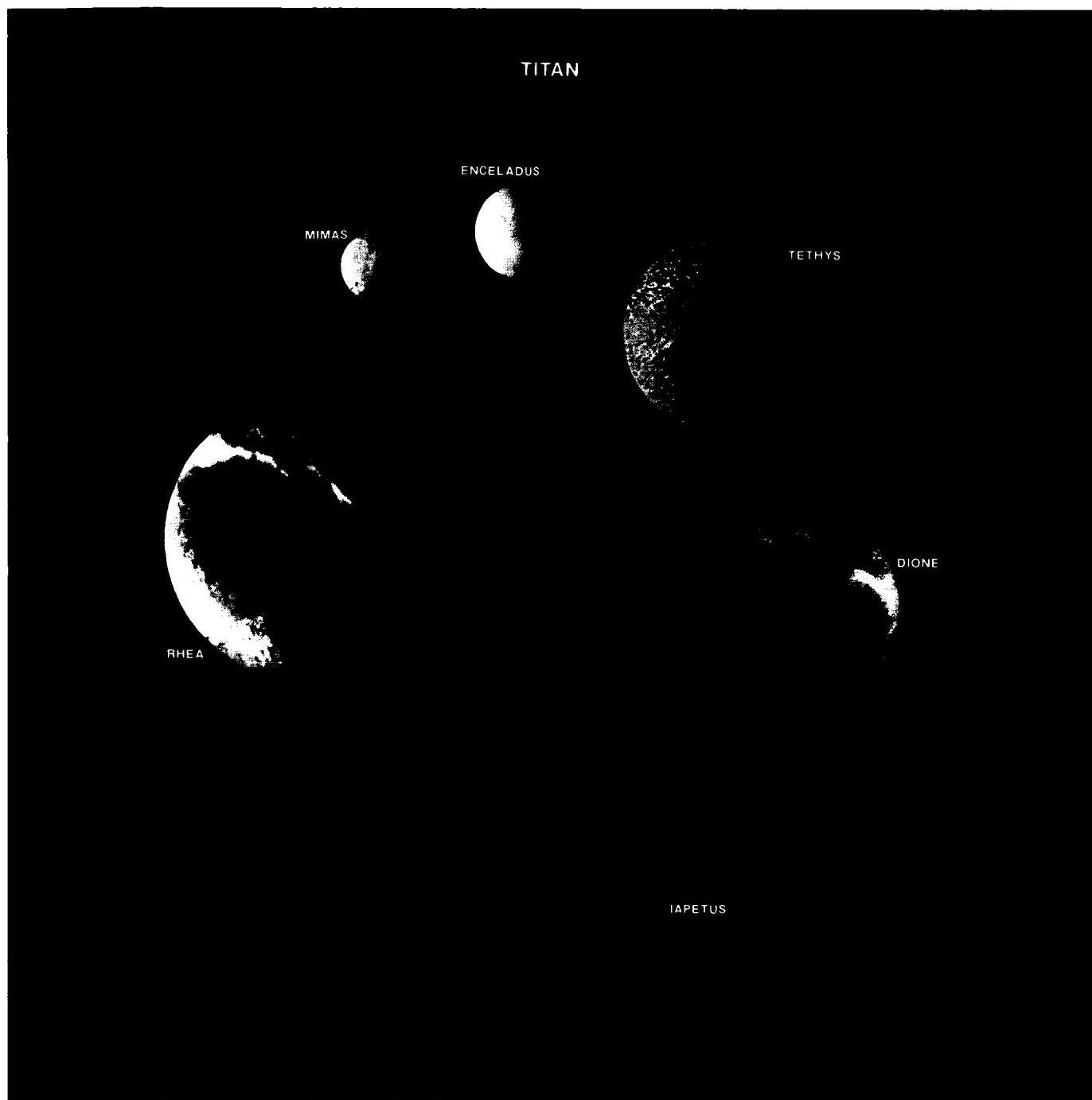


PLATE P-15

Until recently, the major satellites of Uranus appeared as little more than specks of light in the largest terrestrial telescopes. In January 1986, Voyager 2 passed by the Uranian system to make the detailed observations shown in this Plate. The highest resolution images of any outer-planet satellite were obtained for Miranda, the innermost large (480-km diameter) satellite in the system. A combination of spacecraft motion compensation, ground-based data reception, and computer-processing has yielded images of Miranda with 600- to 800-m resolution, as shown on the facing page. Preliminary findings hint at some fascinating, almost bizarre features on this satellite's surface.

The Plate image at the top shows much of Miranda at 3-km resolution. Distinctive brightness variations, perhaps analogous to those on Iapetus (Plate P-14), are evident. Two different terrain types—heavily cratered bright terrain and a topographically lower, darker grooved terrain arranged in oval to polygonal blotches—dominate the surface. Scarps and cliffs, sinuous troughs (canyons?), and deep clefts cutting the terrain suggest more geologic activity than expected for a small icy world. Figure P-15.1, an oblique view of Miranda, reveals steep high-angle faults that expose a vertical stratigraphy in the crust. Some sinuous scarps might represent thrust faults, suggesting severe horizontal motions of the crust. The grooves and troughs, a few km deep, reveal materials of different albedos, possibly indicating changes in composition or age. Diversity of fracture directions, along with the brightness variations, imply a long complex geologic history for this presumably older region of the Miranda surface. Figure P-15.2 illustrates differences in morphology between older heavily cratered terrain and dark grooved or chevron terrain. Patches of such grooved terrain were informally tabbed "racetrack," "flapjack," or "circus maximus" by Voyager scientists.

Figure P-15.3 offers more evidence of the intensity of both vertical and horizontal deformation on Miranda. A near-vertical, stratified scarp 8 to 10 km in height (upper right) represents the highest cliff known in the solar system (even exceeding the relief of the huge cliffs in Valles Marineris on Mars and more than three times the relief of the Grand Canyon). Vertical grooves (from shearing between fault blocks?) appear on the cliff face. Such a huge cliff, remaining intact, is quite surprising on a small icy body.

Troughs and ridges are well displayed in Figure P-15.4. Older complexly grooved terrain possessing intersecting curvilinear ridges and troughs is commonly truncated by younger

THE SATELLITES OF URANUS

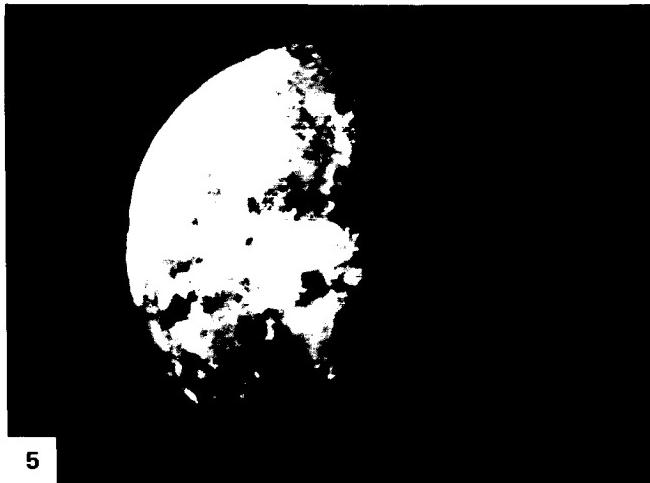
linear grooved terrain, similar to relationships observed on Jupiter's satellite, Ganymede (Figure P-12.2).

So far, only four bodies in the solar system show evidence of horizontal crustal movement: Earth, Mercury, Venus, and now Miranda. Internal heat in larger silicate planets was believed to be necessary to drive intense horizontal tectonism; yet Miranda, a low-density ice world, displays convincing signs of such processes. Voyager scientists speculate that Miranda might have been disrupted by giant impacts early in its history (perhaps 4 Ga ago) and later re-accreted heterogeneously. If this happened after some differentiation that separated heavier rock from ice and volatiles, a patchwork of terrains (such as the "flapjack" and "racetrack" types) would result as readjustments of crustal blocks of differing composition and physical properties occurred during continuing accretion.

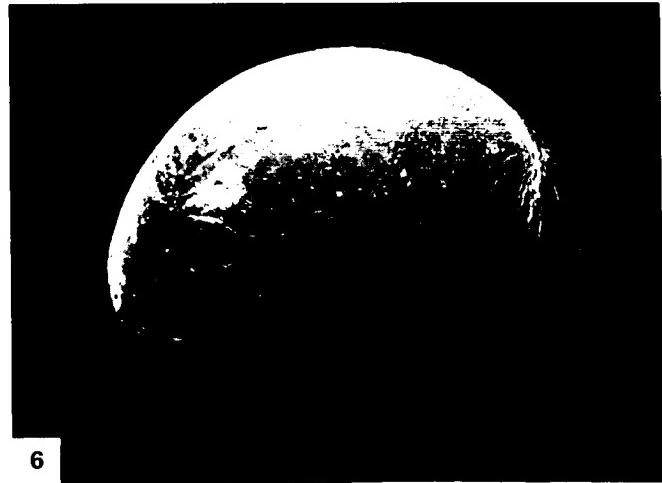
Second out from Uranus, Ariel (Figure P-15.5, below) displays no "racetracks" or "flapjacks," but has a variety of intriguing features. Although Ariel's surface superficially resembles several Saturnian satellites (especially Enceladus, Plate P-14), there are canyons on this 1200-km diameter Uranian moon that apparently have been flooded by ice volcanism. In the lower right of the figure, near the terminator, a series of valleys resembles glacially carved valleys on Earth. These valleys probably formed as grabens that were subsequently flooded, with later faulting and more flooding. Some sinuous features may have formed by thrusting in these flow-like deposits.

Figure P-15.6 is the best Voyager image of Oberon, the outermost larger Uranian satellite. At 12-km resolution, large impact craters with extremely bright rays of ejecta are conspicuous. In the center of Oberon's disc is an apparent impact crater with dark deposits on its floor adjacent to a large central peak. This material may be icy carbon-rich substances brought to the crater floor as impact melt. A 6-km high mountain is seen on the lower left limb. Thus, Oberon, too, hosts tantalizing geologic features that must await future visits for more detailed interpretation.

The Voyager observations of these unexpected features in the Uranian system once more astonished comparative planetologists, even after they had absorbed the surprising diversity of geologic features and processes found as this spacecraft provided first looks at the Jovian and Saturnian systems. No doubt still more surprises are in store when geoscientists obtain pictures of the Neptunian system during the Voyager flyby in August of 1989. **86-H-72.**

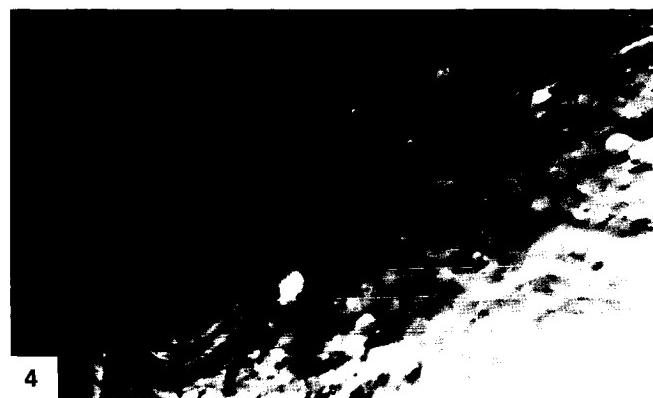
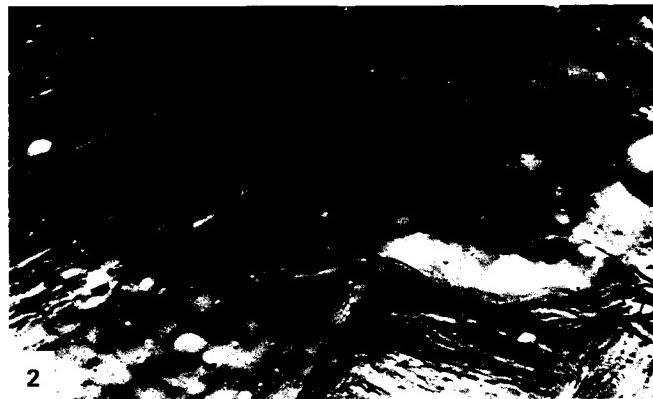


5



6

ORIGINAL PAGE IS
OF POOR QUALITY



REFERENCES

- Allen, C. C., Volcano-ice interactions on Mars, *J. Geophys. Res.*, **84**, 8048-8059, 1979.
- Baker, V. R., Planetary geomorphology, *J. Geol. Education*, **32**, 236-246, 1986.
- Baldwin, R. B., *A Fundamental Survey of the Moon*, 149 pp., McGraw-Hill, New York, 1965.
- Barsukov, V. L., et al., The geology and geomorphology of the Venus surface as revealed by the radar images obtained by Veneras 15 and 16, in *Proc. 16th Lunar and Planetary Science Conf.*, *J. Geophys. Res. Supplement*, in press, 1985.
- Beatty, J. K., B. O'Leary, and A. Chaikin, *The New Solar System*, 240 pp., Cambridge University Press, Cambridge, Massachusetts, 1981.
- Cameron, W. S., An interpretation of Schroter's Valley and other lunar sinuous rilles, *J. Geophys. Res.*, **69**, 2423-2430, 1964.
- Campbell, D. B., J. W. Head, J. K. Harmon, and A. A. Hine, Venus: Identification of banded terrain in the mountains of Ishtar Terra, *Science*, **221**, 644-647, 1983.
- Carr, M. H., *The Surface of Mars*, 232 pp., Yale University Press, New Haven, Connecticut, 1981.
- French, B. M., *The Moon Book*, 287 pp., Penguin Books, New York, 1977.
- Florensky, C. P., et al., The surface of Venus as revealed by Soviet Venera 9 and 10, *Geol. Soc. Amer. Bull.*, **88**, 1537-1546, 1977.
- Florensky, C. P., et al., Venera 13 and 14: Sedimentary Rocks on Venus?, *Science*, **221**, 57-59, 1983.
- Frey, H., and M. Jarosewich, Subkilometer Martian volcanoes: properties and possible terrestrial analogs, *J. Geophys. Res.*, **87**, 9867-9879, 1982.
- Garvin, J. B., et al., Venus: The Nature of the surface from Venera Panoramas, *J. Geophys. Res.*, **89**, 3381-3399, 1984.
- Glass, B. P., *Introduction to Planetary Geology*, 469 pp., Cambridge University Press, Cambridge, Massachusetts, 1982.
- Greeley, R., Lava tubes and channels in the lunar Marius Hills, *The Moon*, **3**, 289-314, 1971.
- Greeley, R., *Planetary Landscapes*, 265 pp., Allen and Unwin, London, 1985.
- Green, J., Copernicus as a lunar caldera, *J. Geophys. Res.*, **76**, 5719-5731, 1971.
- Hartmann, W. K., Cratering in the solar system, *Sci. American*, **236**, 84-99, 1977.
- Hapke, B., Interpretation of optical observations of Mercury and the Moon, *Physics of the Earth and Planetary Interiors*, **5**, 264-274, 1977.
- Head, J. W., et al., Surface characteristics of Venus derived from Pioneer Venus Altimetry, roughness and reflectivity measurements, *J. Geophys. Res.*, **85**, 6873-6885, 1985.
- Hodges, C. A., and H. J. Moore, Table mountains on Mars (Abs.), in *Lunar and Planetary Science IX*, pp. 521-525, Lunar and Planetary Institute, Houston, 1978.
- Hunten, D. M., L. Colin, T. M. Donahue, and V. I. Moroz (Eds.), *Venus*, 1143 pp., Univ. of Arizona Press, Tucson, Arizona, 1983.
- Johnson, T. V., The Galilean satellites, in *The New Solar System*, edited by J. K. Beatty, B. O'Leary, and A. Chaikin, pp. 143-160, Cambridge University Press, Cambridge, Massachusetts, 1982.
- Lewis, J. S., The chemistry of the solar system, *Sci. Amer.*, **230**, 51-65, 1974.
- Lowman, P. D., Jr., *Lunar Panorama*, 136 pp., Weltflugbild Reinhold A. Muller, Zurich, 1969.
- Lowman, P. D., Jr., Crustal evolution in silicate planets: implications for the origin of continents, *J. Geol.*, **84**, 1-26, 1976.
- Lowman, P. D., Jr., The origin and early evolution of continents, in *Proc. Third International Conf. on Basement Tectonics*, 275-286, 1981.
- Lowman, P. D., Jr., H. Frey, J. M. Garvin, and K. Goettel, Basaltic overplating on the Earth and Venus, submitted to *Nature*, 1986.
- Lucchitta, B. K., L. A. Soderblom, and H. M. Ferguson, Structures on Europa, in *Proc. 12th Lunar and Planet Sci. Conf.*, pp. 1555-1567, Pergamon Press, 1981.
- Masursky, H., G. G. Schaber, L. A. Soderblom, and R. G. Strom, Preliminary geological mapping of Io, *Nature*, **280**, 725-729, 1979.
- McCauley, J. F., B. A. Smith, and L. A. Soderblom, Erosional scarps on Io, *Nature*, **280**, 736-739, 1979.

- Meszaros, S. P., *Planetary Size Comparisons: A Photographic Study*, NASA TM-85017, 94 p., Goddard Space Flight Center, Greenbelt, Maryland, 1983.
- Moore, J. M., The tectonic and volcanic history of Dione, *Icarus*, **59**, 205–230, 1984.
- Moore, J. M., and J. L. Ahern, The geology of Tethys, *J. Geophys. Res.*, **88**, A577–A584, 1983.
- Morris, E. C., A pyroclastic origin for the aureole deposits of Olympus Mons, *NASA TM-82385*, pp. 252–254, 1979.
- Morrison, D., *Voyages to Saturn*, NASA SP-451, 225 pp., National Aeronautics and Space Administration, Washington, D.C., 1982.
- Mouginis-Mark, P. J., J. L. Whitford-Stark, and J. W. Head, New models for landform evolution on Io, pp. 32–33, in *Reports of Planetary Geology Program—1983*, NASA TM-86246, 1984.
- Murray, B., M. C. Malin, and R. Greeley, *Earthlike Planets*, 387 pp., W. H. Freeman, San Francisco, 1981.
- O'Keefe, J. A., P. D. Lowman, Jr., and W. S. Cameron, Lunar ring dikes from Lunar Orbiter I, *Science*, **155**, 77–79, 1967.
- Peale, S. J., P. Cassen, and R. T. Reynolds, Melting of Io by tidal dissipation, *Science*, **203**, 892–894, 1979.
- Plescia, J. G., The geology of Dione, *Icarus*, **56**, 255–277, 1983.
- Pollack, J., and R. T. Reynolds, Implications of Jupiter's early contraction history for the composition of the Galilean satellites, *Icarus*, **21**, 248–253, 1974.
- Sharp, R. P., Geomorphological processes on terrestrial planetary surfaces, *Ann. Rev. Earth and Planet Sci.*, **8**, 231–262, 1980.
- Sharp, R. P. and M. C. Malin, Channels on Mars, *Geol. Soc. Amer. Bull.*, **86**, 593–609, 1975.
- Sharpton, V. L., and J. W. Head, Analysis of regional slope characteristics on Venus and Earth, *J. Geophys. Res.*, **90**, 3733–3740, 1985.
- Shoemaker, E. M., and E. F. Helin, Earth-approaching asteroids: populations, origin, and compositional types, in *Asteroids: An Exploration Assessment*, NASA CP-2053, edited by D. Morrison and W. C. Wells, pp. 163–175. NASA Scientific and Technical Information Branch, Washington, D.C., 1978.
- Shoemaker, E. M., and R. F. Wolfe, Cratering time scales for the Galilean satellites, in *Satellites of Jupiter*, edited by D. Morrison, pp. 277–339, Univ. of Arizona Press, Tucson, 1982.
- Short, N. M., and M. L. Forman, Thickness of impact crater ejecta on lunar surface, *Modern Geology*, **3**, 69–91, 1972.
- Smith, B. A., et al., The Galilean satellites and Jupiter: Voyager 2 imaging science results, *Science*, **206**, 927–950, 1979.
- Smith, B. A., et al., Encounter with Saturn: Voyager 1 imaging science results, *Science*, **212**, 163–191, 1981.
- Solomon, S. C., and J. W. Head, Vertical movement in mare basins: relation to mare emplacement, basin tectonics, and lunar thermal history, *J. Geophys. Res.*, **84**, 1667–1682, 1979.
- Squyres, S. W., R. T. Reynolds, P. M. Cassen, and S. J. Peale, The evolution of Enceladus, *Icarus*, **53**, 319–331, 1983.
- Strom, R. G., Mercury, in *The Geology of the Terrestrial Planets*, edited by M. H. Carr, R. S. Saunders, R. G. Strom, and D. E. Wilhelms, NASA SP-469, pp. 13–55, NASA Scientific and Technical Information Branch, Washington, D.C., 1984.
- Taylor, S. R., *Planetary Science: A Lunar Perspective*, 481 pp., Houston, Lunar and Planetary Institute, 1982.
- Thomas, P., Surface features of Phobos and Deimos, *Icarus*, **40**, 223–243, 1979.
- Veverka, J., *Planetary Geology in the 1980s*, NASA SP-467, 187 pp., National Aeronautics and Space Administration, Washington, D.C., 1985.
- Wise, D. U., Timing of deformational events in the northern Tharsis bulge of Mars, *NASA TM X-2511*, pp. 59–60, 1977.
- Young, A. T., No sulfur flows on Io, *Icarus*, **58**, 197–226, 1984.

11

GEOMORPHOLOGICAL MAPPING

*Robert S. Hayden**

The study of landforms, their structure and development, includes the need to illustrate both the findings of an investigation and the character of the landforms investigated. Geomorphologists have used a variety of methods of illustration, including sketches, block diagrams, and various types of photography and other imagery, both from the ground and from the air, to show features of the Earth's land surface. The geomorphological map, in its various forms, represents recent efforts of many geomorphologists, including most European practitioners, to develop a method of graphical display of the features of the Earth's physical surface. These detailed maps have become, for them, not only a means of illustration, but a major research instrument in both theoretical and applied geomorphology (Figure 11-1).

Throughout the 19th century and into the early years of the 20th century, the study of landforms was dominated by a static descriptive physiography. Some investigators in Europe and the United States recognized the influence of dynamic forces on the landscape. In Switzerland, Agassiz saw the erosive power of ice in the Alps. John Wesley Powell recognized the force of water in the carving of the Grand Canyon. Ferdinand Hayden noted the presence of volcanism and the landscape-shaping power of endogenic force beneath the geysers and boiling mud pots of the Yellowstone volcanic region. G. K. Gilbert posed the idea of a landscape in dynamic equilibrium in his studies in the Henry Mountains in Utah. In 1899, with the publication of *The Geographical Cycle*, William Morris Davis introduced into the stagnant physiography of his time what King (1968) calls "a semblance of dynamism." Davis' concept of the "cycle of erosion" produced a radical change in geomorphology. It suggested forcefully that the landscape was dynamic and constantly evolving through a cycle of change due to the external forces of water and the atmosphere. Although his ideas have been extensively criticized and to some extent discredited in their original form, Davis' dynamic approach to the landscape has been indelibly stamped on geomorphology. A similar dynamism was introduced into French geomorphology at about the same time through the development of the "Geologie Dynamique." However, in practice, most geomorphological research continued to be dominated by a static descriptive physiography in which the landscape was described in writing, generally accompanied by artistic block diagrams drawn to illustrate the author's conclusions. Although these diagrams were often excellent illustrations of geomorphological processes, they tended to be idealized qualitative portraits rather than quantitatively verifiable graphic analyses of the landscape.

By the 1920s, photography had developed to a fairly high level of sophistication and should have been useful to geomorphologists. It was generally ignored in favor of block diagrams or given a very low rating as a research tool. There were a few early users of photography in landform study. As early as 1840, the Frenchman, J. Arago, suggested that photography could be useful in topographic mapping. The early photographers and balloonists, Nadar and Triboulet, experimented with aerial photography and the view it provided of the landscape. In 1899, Albert Heim published his photographs and observations made during a balloon flight over the Alps; he is probably the first person to use aerial photography in geomorphological research. During the first World War, aerial photographs were used to investigate terrain and map battlefield positions.

In the early part of the 20th century, until World War II, most geomorphological research was focused on specific sites or specific factors of the landscape rather than at the land from a comprehensive regional perspective. Fenneman's *Physiography of the Western United States* and *Physiography of the Eastern United States* (1931, 1938) were perhaps an exception, although his interests were primarily qualitative and descriptive and did not include quantitative factors by which landscapes might be analyzed and compared. Visualization of regional landscapes by means of physiographic or landform maps of the United States and elsewhere were drawn by Raisz, Lobeck, and others. These maps are intermediate between topographic and geomorphic units maps. As a form of block diagram, the physiographic map shows sketched perspective representation of actual landforms as envisioned from an oblique "birds-eye" view. Figure 11-2 reproduces a section of the physiographic map of Utah, prepared by M. Ridd.

World War II represented a fundamental divide for geomorphology both theoretically and technically. Great advances were made, technologically, in the use of aerial photographs and airphoto interpretation for the terrain analysis necessary for the highly mobile style of warfare that characterized World War II. Better photo equipment, films, and instrumentation for interpretation became available, increasing the ability to study landform features by means of aerial photographs. Quantitative analytical techniques, developed in other sciences, were applied to geomorphic research (e.g., Strahler, 1957). Geomorphologists, particularly in Europe, became interested in comprehensive regional analysis of landforms that considered together all the aspects and features of the landscape. Investigators realized that processes in landform development were more complex than the relatively simple Davisian cycle of uplift, downwearing to a peneplain, and rejuvenation. Questions were asked about the nature of past landform processes and their relationship to present processes. How could various landscapes be compared and contrasted with one another, and what were the significances of

*Department of Public Affairs (Geography Program), George Mason University, Fairfax, Virginia 22030.

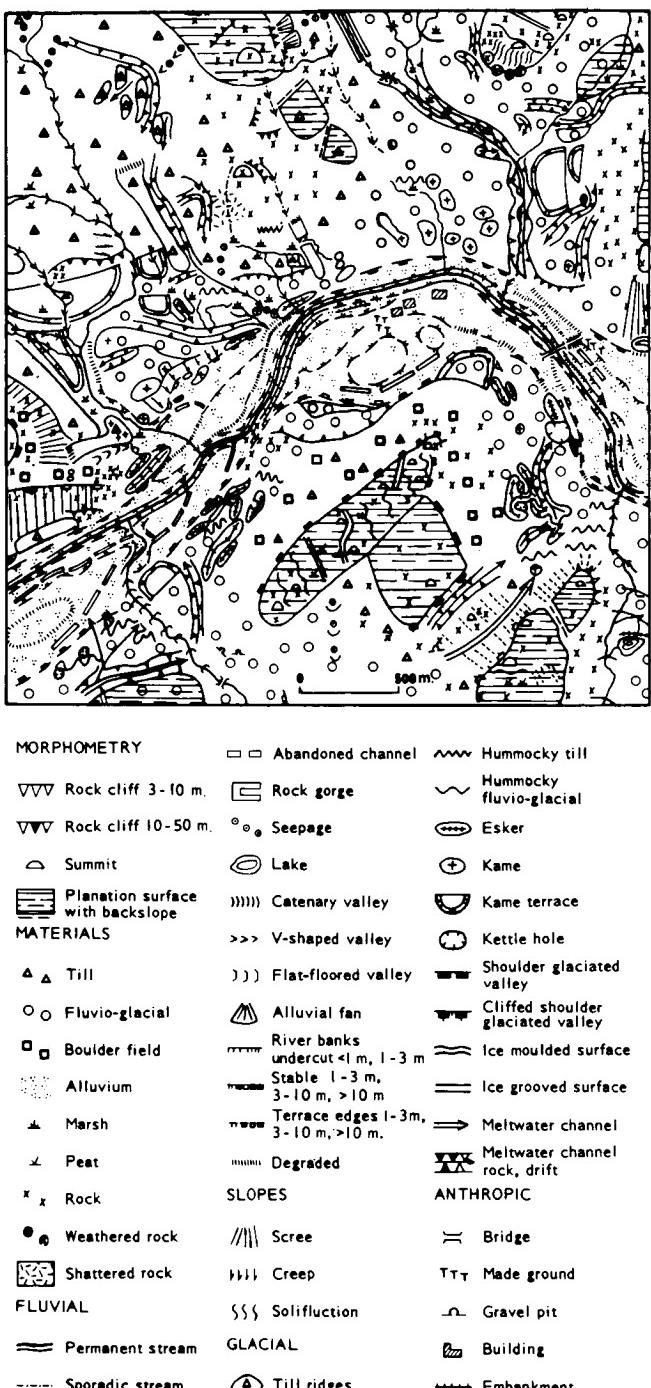


Figure 11-1. A sample area of the detailed geomorphological map of the upper Dee valley, Aberdeenshire, Scotland. Reprinted with permission from *Progress in Geomorphology*, Institute of British Geographers Special Publication No. 7, R. S. Crofts, "Detailed Geomorphological Mapping and Land Evaluation in Highland Scotland," 1974.

landforms and the influence of relief on such things as vegetation, hydrology, and the human cultural development of the area? From these and other questions arose the need for a new paradigm in geomorphology. Because the landscape was complex, in order to pursue orderly scientific research, geomorphologists sought

an objective scientific method of graphic portrayal of the complex factors of landforms. The qualitative descriptions and artistic diagrams of the physiographers did not provide the information necessary for detailed and accurate analytical studies of landforms. As Klimaszewski (1982) has said, "It was only after World War II that the preparation of detailed geomorphological maps on the basis of a systematic mapping of landforms was advanced as a need or even a necessity." In the 1950s and 1960s, the science of geomorphology became, in the words of Fairbridge (1968), "the analytic physiography of the Earth's surface," and the detailed geomorphological map became, in many countries, "the main research method in geomorphology" (Demek, 1982).

Research in modern analytic geomorphology has developed around five fundamental landform concepts:

1. Morphology: the appearance, shape, etc. of the landscape. (In Europe, the term "morphography" is often used.)
2. Morphometry: the measurements, dimensions, and slope values of landforms.
3. Morphogenesis: the origin of each landform.
4. Morphochronology: the age of each landform.
5. Morphodynamics: the land-forming processes presently active on the landscape or those that may become active in the future.

The graphic portrayal of these five concepts involves a complex and often difficult set of analytical and cartographic procedures. The development of theory, procedures, and cartographic legends has taken a great deal of time and effort, particularly by European geomorphologists, over the last 30 years. Although all agree on the need for detailed geomorphological maps in order to further geomorphological research and to enhance the value of geomorphology in applied landscape analysis, considerable disagreement exists as to the correct character and content of geomorphological maps.

Some of the earliest detailed geomorphological maps were published by Siegfried Passarge in 1914 in his *Morphological Atlas*. From that time to the end of World War II, a few detailed maps of local regions were published by some European geomorphologists and detailed geomorphological surveys were occasionally made, but it was not until the 18th Congress of the International Geographical Union (IGU) in Rio de Janeiro in 1956 that the importance of detailed geomorphological maps received international acknowledgment. Two years later, at the IGU congress in Stockholm, the Subcommission on Geomorphological Mapping was created and was given three tasks:

1. To introduce and develop the methodology of geomorphological mapping.
2. To adopt a uniform system for geomorphological mapping to ensure compatibility.
3. To demonstrate the applications of geomorphological mapping in local and regional economic planning in order to facilitate a rational utilization of the Earth's surface (Klimaszewski, 1982).

Before the establishment of the subcommission, detailed geomorphological maps were being prepared in a number of countries, including Switzerland, U.S.S.R., Poland, France, Czechoslovakia, Japan, Belgium, and Hungary. Because of national differences in content and methodology, the maps were

generally not comparable and were therefore of limited use for wider area geomorphological analysis. European geomorphologists recognized the need for a single unified technique, including a common legend, for comprehensive mapping. At a meeting of the subcommission in Krakow, Poland, in 1962, representatives of 15 countries established a set of guidelines for preparing geomorphological maps. These guidelines included (Klimaszewski, 1982):

1. Field work as a basic necessity with aerial photographs as a recommended tool.
2. Mapping at scales between 1:10000 and 1:100000 at which scales "relief and its peculiarities can be represented."
3. Mapping of all aspects of relief, including morphography, morphometry, morphogenesis, and morphochronology, so that the past, present, and future development of relief can be learned.
4. The use of both color and symbols to convey information.
5. The establishment of chronological order in the development of landforms.

6. The inclusion of lithological data.
7. The arrangement of the map legend in a genetic-chronological order.
8. The recognition that detailed geomorphological maps are essential for the future development of geomorphology.

The Subcommission on Geomorphological Mapping met regularly through the 1960s. In 1968, at the IGU Congress in New Delhi, India, it was upgraded to The Commission of Geomorphic Survey and Mapping and was charged with the responsibility of developing a Manual of Detailed Geomorphological Mapping and devising the legend for an International Geomorphological Map of Europe on a scale of 1:2500000. The legend, produced in collaboration with many geomorphologists from European countries, was published in 1971 (Bashenina et al., 1971). The Manual, a compilation of articles by 20 geomorphologists, was published in 1972 (Demek, 1972). The first of the 16 projected maps and accompanying texts was published in 1984 (Embleton, 1984).

In spite of the collaborative work by the Commission on Geomorphological Survey and Mapping, a great deal of diversity and disagreement still exists on the nature of geomorphological maps and their contents. The number of legends,

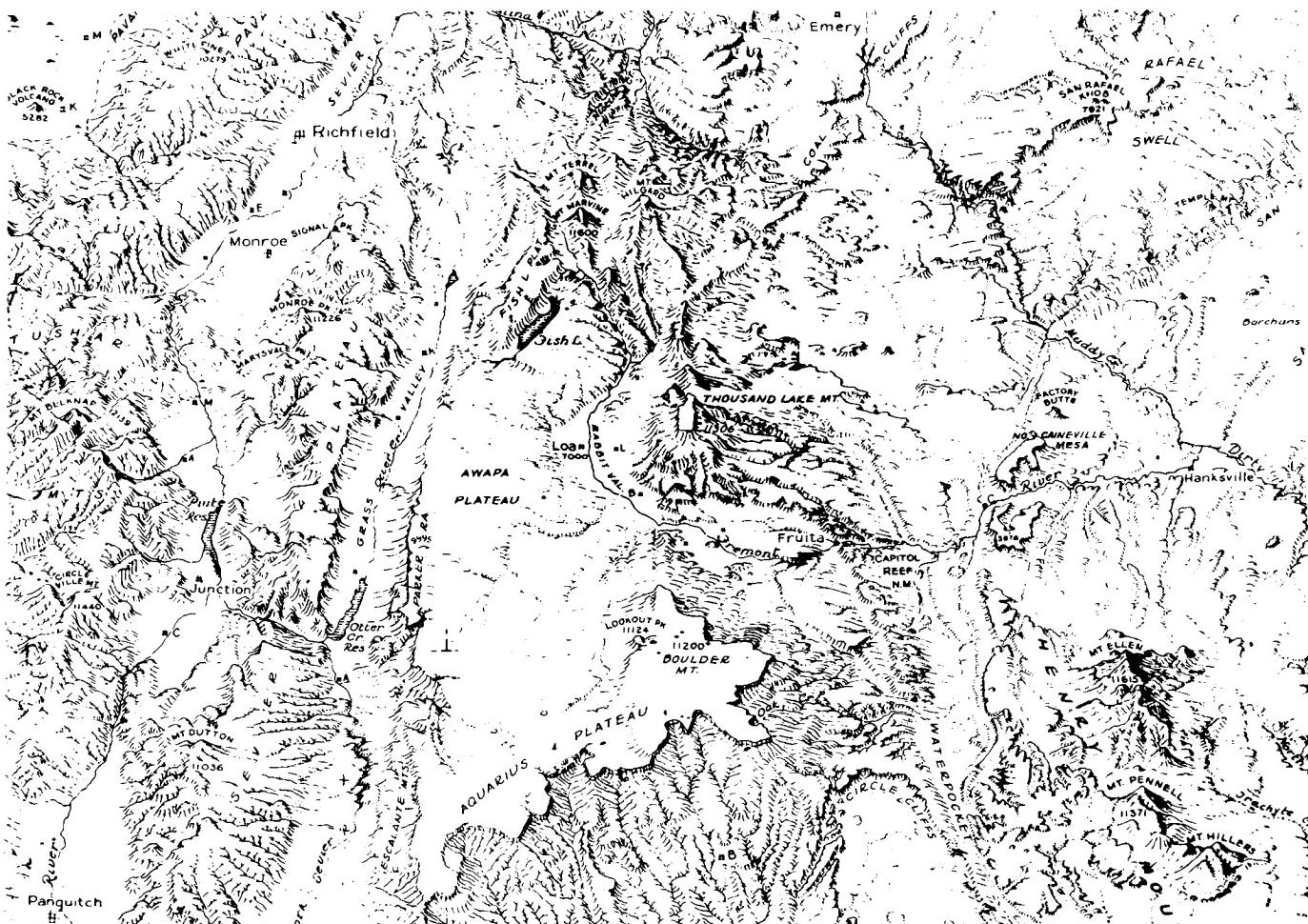


Figure 11-2. A part of the "Landforms of Utah" map prepared by Merrill K. Ridd.

representing different approaches and methodologies, has proliferated. For the most part, they represent a particular national or regional outlook and few, if any, meet all the requirements of comprehensive geomorphological mapping. Demek (1982) has pointed out that new developments in geomorphology since 1970 have substantially increased the theoretical and practical significance of geomorphological mapping. There is a better understanding of the competing interactions of endogenetic and exogenetic forces, due to both the new theories of global tectonics and the development of methods of investigating the Earth from space. A new emphasis on "ecological geomorphology" has related the understanding of landscape relief to human life and activity. New research methods have been introduced, particularly in relation to aerial photography, satellite imagery, and radar imagery, along with development of computers to analyze data and provide automated cartographic displays. Although there has been progress, serious problems remain. In addition to the problems of content and methodology, the question of appropriate scales, particularly in the case of small-scale large-area maps, has not been answered. It is important for the future of geomorphology that these questions be settled. Demek maintains that, until they are settled, "there can be no further progress in geomorphology as a science." Wright (1972) divides geomorphological maps into two generalized categories: "Landform Surveys" and "Special Feature Investigations." The first category covers the various types of detailed geomorphological maps. The second category includes specialized maps such as the "Terrain Analogues" of the U.S. Army, which analyze the land only in terms of its trafficability for military vehicles, or Hammond's (1954) "Small Scale Continental Landform Maps," which, although small-scale and regional in scope, are focused on "actual characteristics of the existing surface rather than genetic interpretations." Hammond's restricted view takes his work out of the realm of landform surveys.

GEOMORPHOLOGICAL MAPPING THEORY: DEVELOPMENT AND DIVERSITY

In different countries, the development of geomorphological mapping has followed different courses, partially due to the particular interests and emphases of geomorphologists and partially due to real or perceived differences in the landforms found in various regional settings. To date, most detailed geomorphological mapping has been done in Europe by European geomorphologists. In general, American practitioners have been primarily interested in special feature studies or the mapping of special factors of the landscape rather than the development of comprehensive studies. This low degree of interest in comprehensive studies may be due, in part, to a reduced interest in geography and its integrative emphasis in the United States. Some European geomorphologists, including French, Czechoslovakian, and Hungarian workers, have selected the lithological-structural unit as the basic element in landform analysis. Others, such as Polish, Russian, Rumanian, and German geomorphologists, consider the form as the basic unit. The *Manual of Detailed Geomorphological Mapping* and the *Legend to the International Map of Europe* on the scale 1:2500000 generally follow the Polish, Russian, and German convention. In Great Britain, geomorphologists developed an "empirical system" based on division of the landscape into "slopes and flats." Similar systems have been adopted by some Belgian and Canadian geomorphologists because they make it possible to give quantitative values to all landforms, generally at the expense of genesis and chronology. Some geomorphologists have attempted to combine approaches. In Australia, the Division of Land Research and Regional Survey of The Commonwealth Scientific and Industrial Research Organization (CSIRO) developed a system of geomorphological mapping for resource survey based on a concept of land units

and land systems. The concept was "aimed at providing both a basic and functional subdivision of landscape" (Christian and Stewart, 1968). A land unit was conceived as an area dominated by a land surface that had a similar genesis and now has similar topography, soils, vegetation, and climate. A land system was "an assembly of land units which are geographically and genetically related" (Christian, 1958). This system, which is particularly well adapted to rapid reconnaissance surveys of large areas based on information derived from aerial photographs, has been used to map large areas of Australia and New Guinea (Mabbutt and Stewart, 1963).

The development of the international legend, or "Unified Key," and its application to a projected international geomorphological map of Europe, of which the first sheet has now been published, is considered a step forward by most European geomorphologists, but much remains to be done. There is appreciation for, but currently no universal acceptance of, the Unified Key as the one legend to use. Demek (1982) points out the desirability of a single legend for geomorphological maps on various scales, but, he says, the legends proposed so far "do not meet all the requirements." In spite of the many differences, there is an underlying unity to terrain classification. All geomorphologists are concerned with identifying the simplest land unit with low variability, and all are attempting to combine these into a hierarchy of increasingly more complex regions (Gardiner, 1976).

GEOMORPHIC UNITS

Geomorphological mapping begins with the identification of the fundamental units that compose the landscape. Establishment of the nature and character of these units is critical to the success of any geomorphological research. However, there is no single agreed-upon unit that satisfies all types and all scales of research mapping. Miyogi et al. (1970) have described a geomorphic unit in general terms as "an individual, genetically homogeneous landform produced by a definite constructional or destructional geomorphic process." Most geomorphologists would agree with this definition as far as it goes, but would differ widely as to the descriptive characteristics of the genetically homogeneous landform. In addition, although most landforms may be considered as "genetically homogeneous" in terms of present processes, most landforms owe their characteristics, in part, to past processes of a different sort. Wright (1972) has pointed out that "...each part of the land surface is the end product of an evolution governed by parent geological material, geomorphological processes, past and present climate, and time." Most geomorphologists would agree that it is necessary to view the landscape in terms of recognizable patterns that are, to some degree, repetitive. As Gardiner (1976) has said, "units of land, however defined, recur in the landscape in recognizable patterns."

There are two general approaches to the question of geomorphic units, which Speight (1974) divides into a Landform Elements Model and a Landform Patterns Model. He sees the two approaches as complementary. Either model can be used to describe any piece of land, with the choice dependent on scale and the purpose of the mapping. In the Landform Elements Model, the units of landscape are compared to "a simply curved geometric surface without inflections," focused on slope and slope measurements. In the Landform Patterns Model, the land surface is seen as a "three-dimensional cyclic or repetitive phenomenon in which simpler elements recur at quasi-regular intervals in a definable pattern." Here the units are those elements that form the patterns. The Russian, Polish, and Czechoslovakian systems of geomorphological mapping are among those that follow the landform pattern model in which the basic units are morphostructures generally fitted into a nested classification of forms (Bashenina, 1978). British geomorphologists and some

others use a landform elements model that classifies the basic units of the landscape in geometric terms as facets and segments defined by slope and area measurements (Savidge, 1965). Other national groups have developed systems that follow some variation of the two models.

Differences in the identification of geomorphic units are significantly related to matters of regionalization and scale. At different scales, covering regions of different size, different features can be identified as basic homogeneous units. The choice of unit is dependent on the scale of analysis. Howard and Mitchell (1980) have said that the clearest and simplest basis of classification is "classification of landscapes into homogeneous units suitable to the mapping scale required for the particular purpose." A hierarchy of land units can be readily identified in most regions, depending on the scale of the mapping (Figure 11-3). The landscape is, in the words of Nicholayev (1974), "a multi-tiered geosystem." At each tier, different taxonomic individuals form the basic geomorphic units of the landscape. As broader regions are studied, at smaller scales, smaller features and processes often fade from view while larger features, imperceptible at larger scales, assume prominence.

Geomorphology is a complex subject with multiple approaches to geomorphological analysis and multiple scales of geomorphological mapping. The nature of the geomorphic unit is controlled by the model of analysis chosen and the scale of mapping required. The basic geomorphic unit is not a single feature or entity, but must be carefully selected to be essentially homogeneous and indivisible at the scale chosen. Although all generally agree that the basic geomorphic unit should be a homogeneous entity, it can be defined in terms of genetic or structural pattern, the approach followed by the IGU and most European geomorphologists, or in terms of location and dimensions of geometric elements, along the lines of the British system.

Most detailed geomorphological maps are developed for small areas on quite large scales, typically between 1:10000 and 1:50000. A major growing interest in geomorphology is the possibility of wide-area regional analysis of landforms. Such research requires the regionalization of geomorphological maps. A number of methods have been suggested by various workers through which a hierarchy of geomorphological regions can be developed (Gellert, 1972).

APPLICATIONS OF GEOMORPHOLOGICAL MAPPING

The modern detailed geomorphological map provides a unique means of displaying all of the various factors and features of the physical landscape in an orderly scientific fashion. Such a map is the one analytical research tool developed so far by which it is possible to approximate a portrayal of the Earth's complex surface and its dynamics. It has direct scientific value for research in theoretical geomorphology and likewise serves as a basis from which applied maps may be drawn, focused on special aspects of the landscape, to aid in a variety of different types of applied geomorphological research.

Detailed geomorphological mapping leads to a number of applications to basic scientific research essential to the continued growth and development of geomorphology. As Klimaszewski (1982) pointed out, mapping can:

1. Provide a precise picture of the dynamics of relief that will, in turn:
 - a. Enable the reconstruction of the development of relief
 - b. Provide the way to evaluate factors and processes of origin and transformation

2. Facilitate the search for connections between landforms
3. Enable regionalization
4. Facilitate the development of comparative studies
5. Provide a means of comparison between developed and developing landforms in areas of differing and of similar geologic structure and under varying climatic conditions
6. Serve as an aid in studying the role of climate in shaping the Earth's surface by distinguishing climatic types of relief

Barsch and Liedtke (1980) cite other scientific benefits from a program of detailed geomorphological mapping in West Germany, including a greatly increased data base from the necessary field work, an improvement and clarification of geomorphological terminology, enlargement of data processing capability, the intensification of morphodynamic studies, provision of geomorphological documentation in areas of intense development, and an increased cooperation between geomorphologists and other geoscientists.

The complex nature of detailed geomorphological maps tends to limit their usefulness beyond the area of technical geomorphology. As Barsch and Liedtke (1980) point out, these maps are "made by experts for experts." Tricart (1969) notes that "a genuine geomorphological map is an intricate document which can be read only by persons with adequate specialized training." All of these tend to render their information inaccessible to persons outside geomorphology. In spite of this, Tricart maintains that "Geomorphological surveys should constitute one of the basic elements in the preparation of development projects." According to Embleton (1985), geomorphological maps serve several valuable functions. He states that they are primarily "a visual information store." They can also serve to coordinate geomorphic research among workers with diverse concepts and approaches to the subject. In viewing geomorphological phenomena over a wide spatial context, as was required when preparing the IGU Geomorphological Map of Europe on the scale of 2.5 million, all researchers are subject to the discipline of working within an agreed international framework. In education, geomorphological maps can be used with other physical maps to "show the complex integration of the natural environment." Finally, in relation to remote sensing data, Embleton points out that an experienced geomorphologist, mapping the landscape, can more easily and reliably appreciate terrain types depicted on remote sensing images than the analyst without such a background.

A special value of geomorphological mapping lies in its application to particular problems, generally by the use of limited maps showing only those geomorphic features relevant to the particular question at hand. Such maps either are derived, by simplification, from the detailed maps, or are prepared using only the necessary data. Derivative maps are often the more desirable because it is always possible to refer back to the detailed maps should further information be needed.

Geomorphological maps are of great value in the general field of Environmental Management, particularly at the planning stage. Cook and Doornkamp (1974) found geomorphological maps to be of principal utility at the initial field investigation stage of analysis for environmental concerns. They also considered the maps to be valuable as the basis for a number of special-purpose maps useful in various stages of environmental management. Panizza (1978) created a series of geomorphological stability maps for areas of northern Italy, southern Italy, and east-central

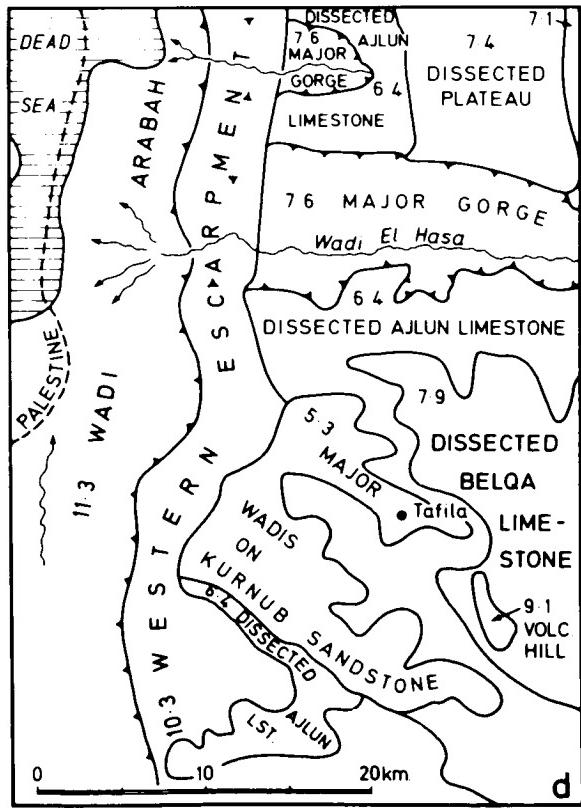
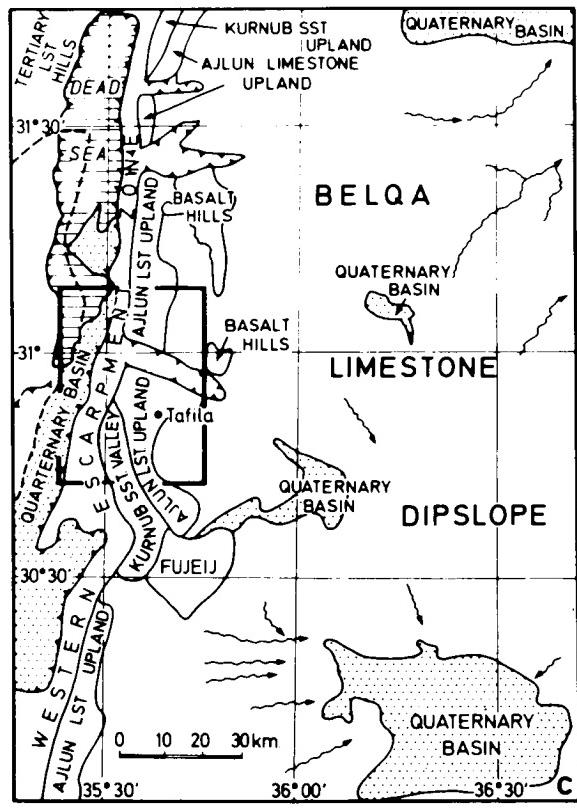
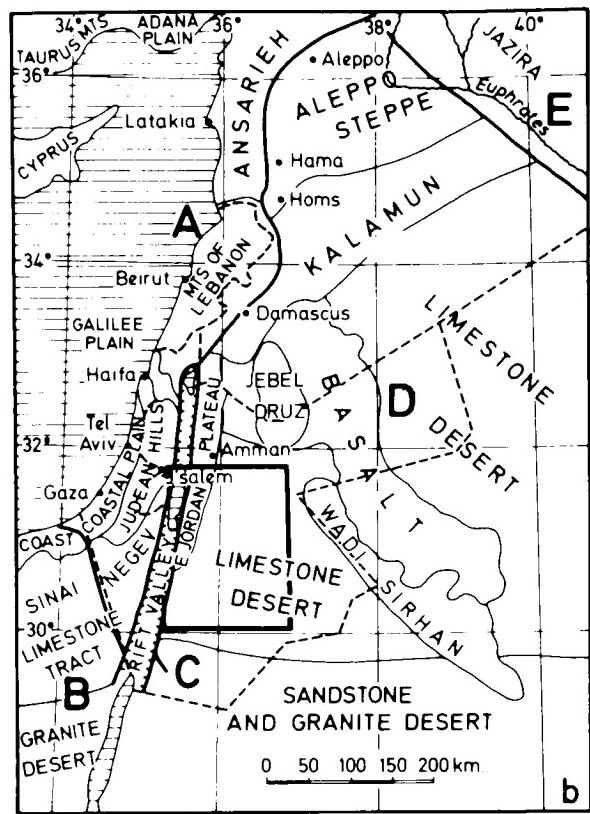
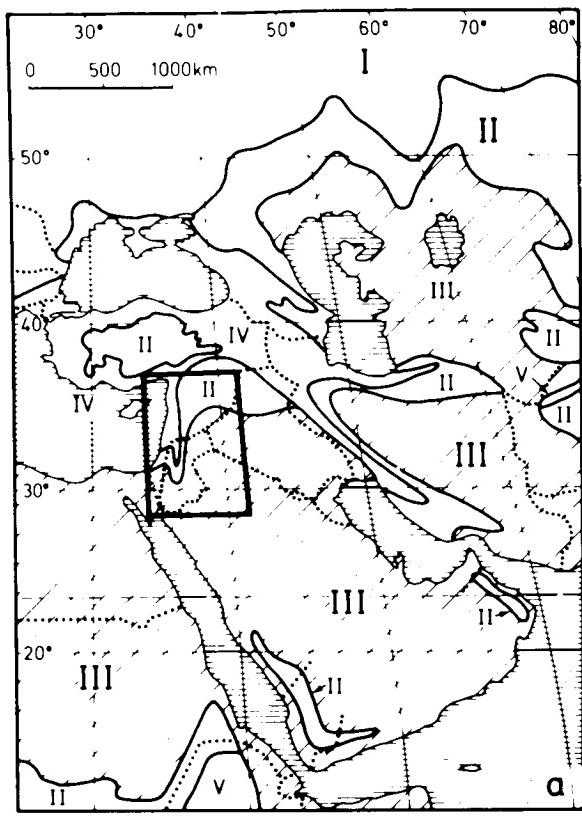


Figure 11-3. Four maps constituting a multiple-scale portrayal of the land unit hierarchy in the Near East showing climatic, geomorphic, and geologic features of the region and sections within it. Reprinted with permission from *Geoforum*, Vol. 11, J. A. Howard and C. W. Mitchell, "Phyto-Geomorphic Classification of the landscape," Pergamon Press, Ltd., 1980.

Nigeria. Their purpose was to aid in coherent land-use planning in sensitive areas. These were simplified maps based "on the one hand, on morphogenetic process causing instability and, on the other hand, on the lithology involved in degradation." The resulting maps were simple and easy to read, showing only the information relevant to stability (Figure 11-4). The stability maps were developed from detailed maps drawn after a full geomorphological survey which, Panizza says, "is a prerequisite to the development of maps useful for planning purposes." Geomorphological stability maps were also developed by Rosenfeld (1976) as environmental planning documents in connection with the development of a new township accommodating 800 to 1000 persons at Resolute Bay, Northwest Territories, Canada (Figure 11-5). In a periglacial environment, microfeatures of the area such as patterned ground, solifluction lobes, meltwater channels, and eustatic strandlines were mapped. The data were used to choose the best location among five alternative sites and to plan the use of open space in the community so as to avoid concentrated activities in areas of sensitive terrain. The purpose of the planning was not only to deal with the structural engineering concerns of construction in a difficult environment but also to use the land in such a way as to enhance the aesthetic quality of the community.

The application of comprehensive geomorphological surveying and mapping to environmental engineering concerns, such as highway planning and construction, is just beginning to take hold. Brunsden et al. (1975) say that "there is an obvious need for additional geomorphic information ... (beyond the geologic information generally utilized in highway planning) ... since surface form and the spatial pattern of geomorphological processes often influence the choice of a route." They see the use of different types of applied geomorphological maps at different stages of planning and construction. Small-scale maps can provide the regional analysis of an area that would be valuable at the initial

feasibility stage of planning. Large-scale small-area maps would be valuable for questions of site investigation and could help in forecasting behavior during and after construction.

THE ROLE OF REMOTE SENSING

Various techniques by which sections of the landscape can be viewed from a distance have been classified under the general term "Remote Sensing." For geomorphologists, these include aerial photography and satellite imagery, both photographic and telemetered, recorded at various wavelengths or bands of the electromagnetic spectrum. The wavelengths used have included several in the visible light range, several in the infrared range, and radar in the microwave range. Sound-wave studies, or sonar, and studies of regional variations in the Earth's magnetic field can also be classified as remote sensing. The use of side-scan sonar shows great promise for studying the geomorphology of the ocean floor. With the development of the *Geological Long Range Inclined Asdic (GLORIA)* by the National Institute of Oceanography in Great Britain, detailed studies of the deep ocean floor became possible (Laughton, 1980). A number of morphological studies using GLORIA have been made of midoceanic ridges (e.g., Searle, 1979; Searle and Laughton, 1981) and of submarine fan morphology below the deltas of several major rivers (Damuth et al., 1983). Geomorphological mapping of the deep ocean floor has recently been advanced with the development of

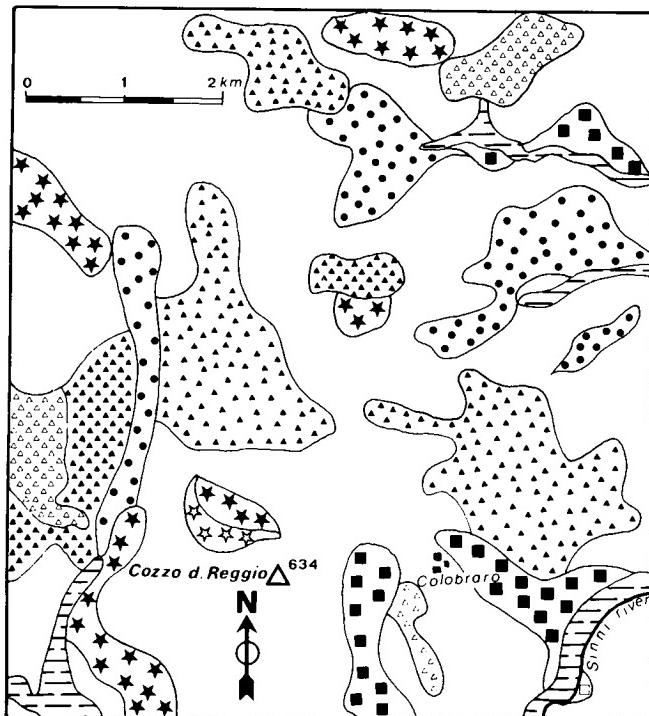


Figure 11-4. Part of a geomorphological stability map of the region of S. Giorgio L. and Colobraro in southern Italy extracted from a previously prepared detailed geomorphological map of the region. Reprinted with permission from *Geoforum*, Vol. 9, M. Panizza, "Analysis and Mapping of Geomorphological Processes in Environmental Management," Pergamon Press, Ltd., 1978.

PROCESSES	UNSTABLE AREAS	SYMBOLS
coastal	LIABLE TO FLOOD	[Symbol: horizontal lines]
	UNSTABLE FOR EROSION { in rocks in debris	{ [Symbol: stars] [Symbol: squares]
fluvial	LIABLE TO FLOOD	[Symbol: dashed lines]
	UNSTABLE FOR EROSION { in rocks in debris	{ [Symbol: squares] [Symbol: dots]
eolian	LIABLE TO SAND ACCUMULATION	[Symbol: curved arrows]
	LIABLE TO DEFATIATION	[Symbol: wavy lines]
superficial	LIABLE TO DEBRIS ACCUMULATION	[Symbol: inverted triangles]
	UNSTABLE FOR EROSION { in rocks in debris	{ [Symbol: triangles] [Symbol: diamonds]
slope	UNSTABLE FOR EROSION { in rocks in debris	{ [Symbol: circles] [Symbol: dots]
	LIABLE TO DEBRIS ACCUMULATION	[Symbol: crosses]
deep	UNSTABLE FOR EROSION { in rocks in debris	{ [Symbol: stars] [Symbol: double stars]
	LIABLE TO RAIN FLOOD	[Symbol: dotted lines]
various	LIABLE TO AVALANCHE FALL	[Symbol: diagonal lines]
	UNSTABLE FOR HUMAN ACTION	A
anthropogenic		

a combination side-scan sonar and seafloor mapping system (SeaMARC II) (e.g., Hussong and Fryer, 1983; Blackinton and Hussong, 1983; see also Chapter 13). Magnetic, gravity, and seismic studies customarily are not used in geomorphological research because the information they provide refers primarily to subsurface states; however, knowledge of the Earth's interior can sometimes assist in recognizing and interpreting surface phenomena (e.g., using gravity or magnetic anomalies to disclose the presence of a dike beneath a ridge; remanent magnetization anomalies were shown by Mahrer and Bradley (1983) to relate to morphology of alluvial fans on which arroyos have developed).

Working with aerial photographs, geomorphologists have been able to view sizable portions of the land surface at one time from a map perspective. Although individual aerial photographs are limited in area, the process of assembling groups of adjacent photos into a mosaic has provided a direct regional perspective of larger areas. The opportunity to see the landscape on a regional scale has often included the ability to perceive features that were not perceptible on site or on larger, more localized scales. Throughout the 1950s and 1960s, as the techniques of remote sensing were refined, as new film emulsions became available, and as the new technology of orbital imagery came on line, remote sensing became more and more a dominant factor in geomorphological research.

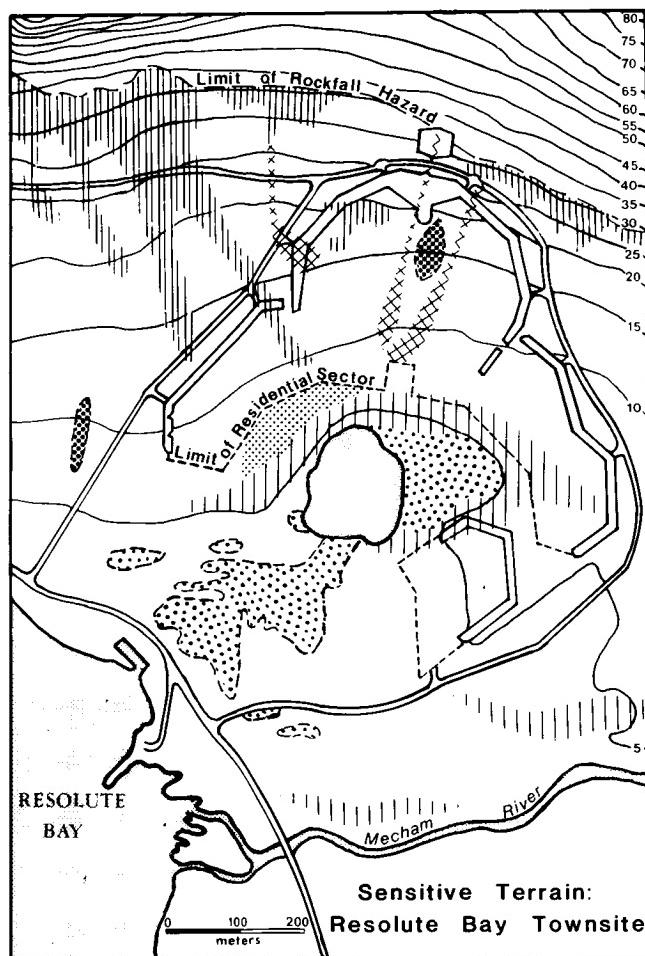


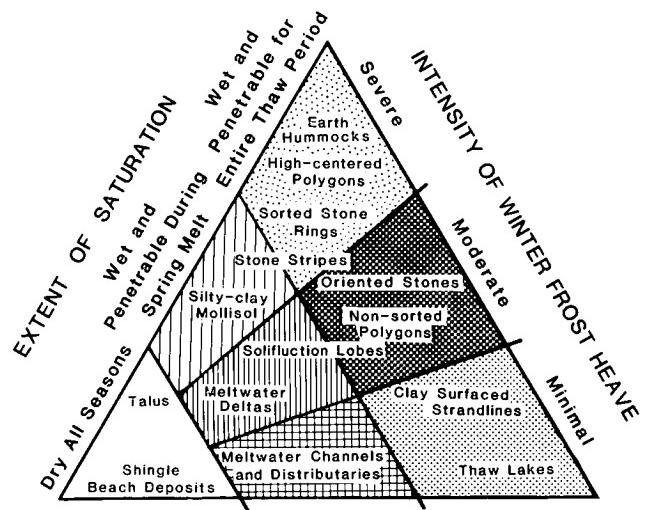
Figure 11-5. Terrain sensitivity map showing geomorphological characteristics of a landscape underlain by permafrost. The map was used for land-use planning at a new townsite. Symbols are identified in triangular diagram on right. Reprinted with permission from The Yearbook of the Association of Pacific Coast Geographers, Vol. 39, C. Rosenfeld, "Terrain Sensitivity of the Townsite at Resolute Bay, N.W.T.," 1977.

Today, as a general rule, the first step in a comprehensive geomorphological survey is the identification and mapping of geomorphic units, using aerial stereopairs of the area to be studied. From aerial photography, most of the morphology can be identified, and many of the questions of morphogenesis, such as denudational versus depositional processes, can be answered. Slope angles can be estimated and classified, and the relative relief of all but small features can be determined with acceptable accuracy. The geomorphologist goes to the field with the basic structure of the survey well outlined and mapped from aerial photographs.

The second step in the survey is the field work. The accuracy of the aerial photointerpretation must be checked on site, and measurements of small features must be made. Questions of morphochronology, such as the sequential history of terraces, must be ascertained. Remote sensing techniques, using aerial photographs, are valuable in providing the basic prefield framework of the study, but a complete, accurate geomorphic survey leading to true detailed geomorphological mapping requires extensive field work.

When the field work has been completed and the preliminary map has been thoroughly checked, the final detailed geomorphological map is drawn, generally in multiple colors using a complex symbology.

Orbital imagery, first in the form of photographs taken by astronauts and then as telemetered imagery from unmanned satellites, provided geomorphologists with a new perspective on the Earth's landscape. From the outset, great hope was expressed for its value, but to date, the importance of orbital imagery in providing new insights into the physical geography of our planet has not been unequivocally established. Over the past 10 to 15 years, geomorphologists have used orbital imagery of various types as the basis of geomorphological mapping with some success. Verstappen and vanZuidam (1970) used several types of orbital imagery available at the time to test its value in mapping a remote region of the central Sahara. With photos taken by Gemini and Apollo astronauts and telemetered imagery from Nimbus and ESSA satellites, they endeavored to develop geomorphological and geological reconnaissance maps of Lake Chad and of the Tibesti Massif. They concluded that the imagery then



available was useful "for discovering very large features and structures that may otherwise escape attention because of a lack of a comprehensive image." However, they felt that the imagery needed to be of higher resolution if it were to provide new information not already available by other means. Slaney (1974) looked at some of the first Earth Resources Technology Satellite (ERTS; now Landsat) imagery and found that its limited ground resolution would only be moderately useful for mapping purposes. He did find it helpful as an educational tool in reports, as a base map underlying other data, as a source of information in defining "broad targets of particular interest," and as a catalyst to provide "inspiration for new ideas and to promote further thoughts about established concepts." Palabekinoglu (1974), also studying data from ERTS-1, concluded that "intensive interpretation of the satellite imagery would help the geoscientist to become more familiar with the surface of our entire Earth." The problem of scale was considered a serious limiting factor in the usefulness of satellite imagery. Mukerjee (1982) said, "the small scale of orbital photographs limits the possibility of interpretation to major relief features only." On the other hand, Bedi (1982) found that geomorphological maps could be easily prepared from either aerial photographs or Landsat imagery "supplemented by nominal field work."

At the present time, one area in which satellite imagery seems to provide a definite advantage over aerial photography is in the realm of large-area small-scale geomorphological studies. The ability to perceive mega- and macro-structures, using mosaics of Landsat images, promises to provide new information and new mapping techniques. Astinov et al. (1976), in citing contributions of small-scale satellite imagery to geomorphology, point out that it has "changed our view of the formation of large relief forms." Bashenina and Tal'Skaya (1981) have used space imagery to construct a geomorphological map of the world on the scale of 1:15000000. They found the imagery to be very satisfactory as they were able to perceive all the information pertinent to a geomorphological map at this generalized scale (Figure 11-6). Canoba (1982) found that the perception level of Landsat Multispectral Scanner (MSS) imagery of the Argentine Pampa permitted the development of "a preliminary geomorphological map at a scale of 1:1000000 directly without going through a complete cartographic generalization process starting from larger scale maps." He found that, with adequate data from other sources, he was able to develop a good standard geomorphological map. Although the satellite imagery did not provide any unique information, the direct regional mapping procedure was valuable because of the savings in time, effort, and cost. As Rao and Bedi (1982) have said, "Remote sensing technology has reversed the conventional pattern of geomorphological surveys, where studies were carried out locally and then a regional picture was constructed. Now it is possible to do regional studies straight away on aerospace imagery and then the smaller areas selected for detailed work."

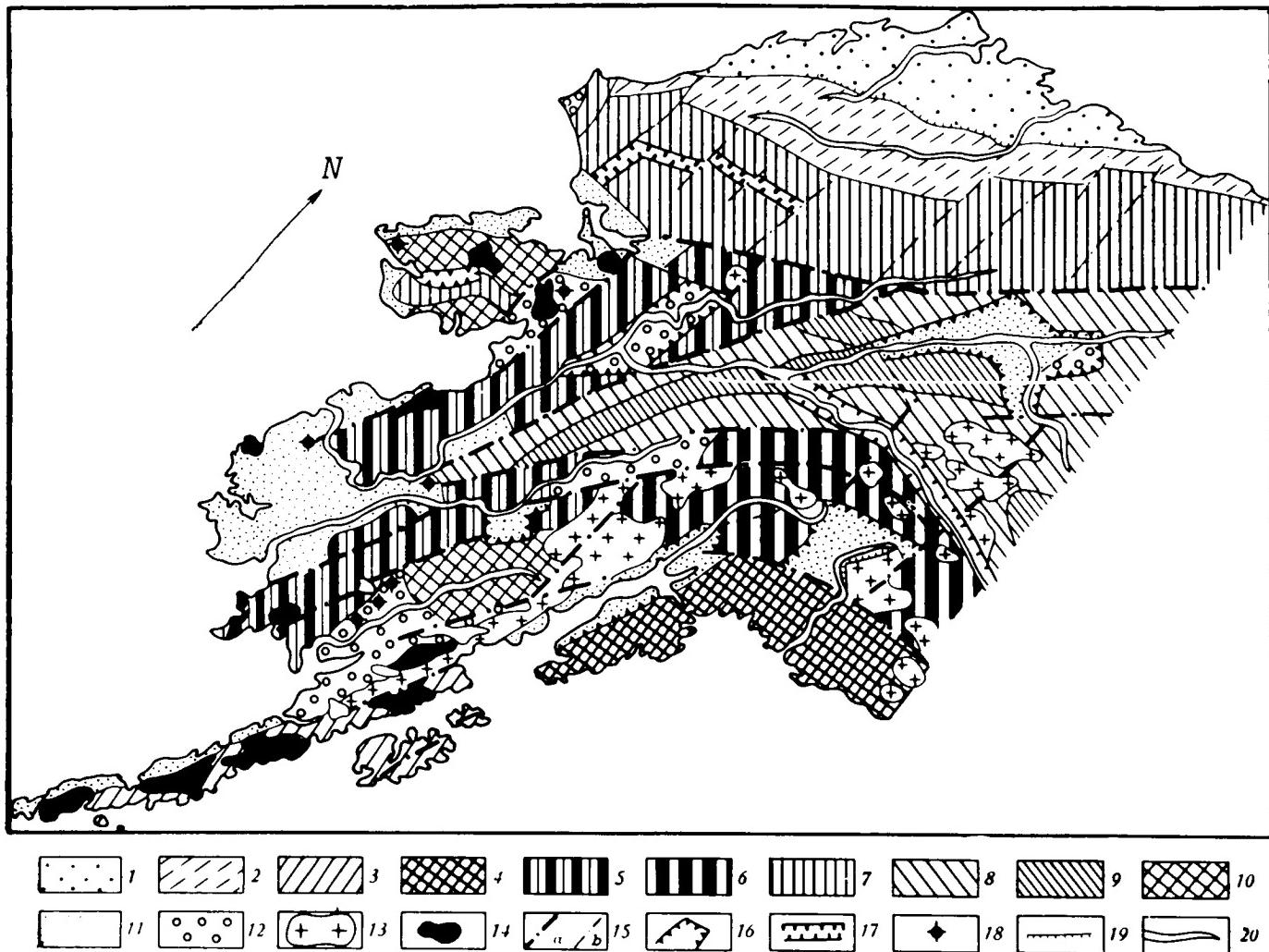
Studies in which Landsat imagery was the principal data base for classifying and mapping landforms began to appear in the literature by the mid-1970s. Among these were a classification of physiography from ERTS imagery (Ulaby and McNaughton, 1975), application of Landsat imagery to southwestern Turkey (Kayan and Klemas, 1978), and use of RBV imagery in geomorphic mapping of Kansas (Cochran and Browne, 1981). The work of Bedi (1982), already cited, involved mapping from Landsat images of several areas in India. A landforms map (Figure 11-7a) of part of New South Wales, Australia, produced by C. F. Pain (1985), modifies a landscape profile classification scheme (Figure 11-7b) developed by C. D. Ollier (1967) to generate a set of units that are well suited to analysis of a variety of terrains. Townshend (1981) describes an approach to regionalization of terrain using remotely sensed data from space.

Today, advances in the resolution of satellite imagery have increased its use in geomorphological mapping, particularly on small scales. However, it is still not clear how truly useful Landsat and other orbital imagery is in providing new data not available from other sources. Landsat imagery has proved valuable in providing pictures of areas in which, because of remoteness of location or political conditions, investigations by aircraft or on the ground are not possible. The use of radar imagery also promises to provide pictures of areas that are difficult to photograph due to cloud conditions. The real potential of satellite imagery is still to be realized. As geomorphologists have investigated landscapes from larger regional perspectives, they have found that, at different scale levels, different types of forms are evident. At the present time, most regional studies are viewed as generalizations from large-scale small areas to small-scale large areas. But regionalization is more than generalization. Regionalization through generalization is prone to the dangers of subjectivity. At each level of generalization, individual investigators must decide how to generalize, choosing what to include and what to eliminate from the analysis. A regional perspective from space provides an objective portrait, relatively free from unintentional bias. The regional view helps place individual landforms and individual processes into a wider geographic context. As previously mentioned, it has been impossible for geomorphologists to develop a single mapping key that satisfies the requirements of all regions at all scales. A major reason is that landforms differ significantly from region to region and require different cartographic symbolization. The proliferation of geomorphological mapping legends is a recognition of the complexity of geomorphological reality. It is relatively easy to classify individual geomorphic processes into a series of basic categories such as tectonic, fluvial, or eolian, but landforms are almost always the result of a complex mixture of processes interacting on the landscape. From the regional variations in the mix of geomorphic processes comes the multitude of often unique landforms that characterize the surface of the Earth. Space imagery provides a direct perspective of the regional mix. Through space imagery and the geomorphological mapping and analysis derived from it, we can have a better view of the integrated dynamics forming the surface of our planet.

GEOMORPHOLOGICAL MAPPING AND ANALYSIS OF THE COLORADO DELTA REGION

To further demonstrate the utility of Landsat imagery and the value of mapping from the regional perspective in geomorphological research, a regional geomorphological map of the Colorado River Delta Region in Mexico (Figure 11-8) has been developed from a black and white Landsat Band 7 MSS image of the area taken December 23, 1975 (see Plate D-12). The scale of the image and of the original map was approximately 1:330000, but it has been reduced here to about 1:850000. All of the units mapped can be perceived in the Landsat scene. Geomorphic units were defined by relatively obvious combinations of tone and texture in the scene. Identification of the character of the units, such as mountains, terraces, or sand dunes, was made by a combination of shape, tone, texture, and location context. Most of the boundaries between geomorphic units were relatively sharply defined by changes in tone. Terraces and the edges of some alluvial fans were also definable by change of tone. Faults and lineaments were mapped where obvious, and fault movement has been indicated where perceptible. Other features were also identified by shape, tone, and location context.

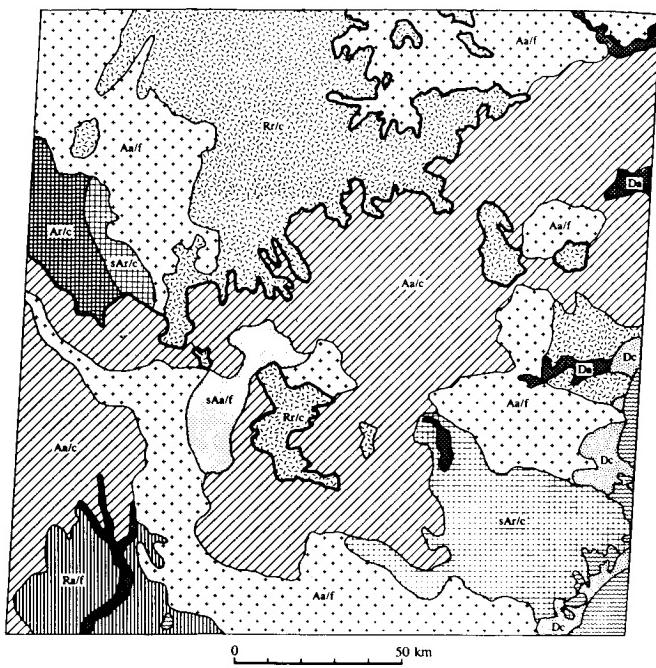
Some of the symbols used on the map, such as those for alluvial fans, terraces, and transverse dunes, were taken from the legend contained in the ITC system for Geomorphological Survey (Verstappen and vanZuidam, 1975). Others, such as those for



A geomorphologic units map of Alaska, prepared originally at 1:15000000. *Morphostructures: I. Continental platforms:* 1 — Depositional plains of platform downuckles on a basement lying at a great depth, and 2 — Denudational plains of homoclinal and locally dislocated strata. *II. Epigeosyncline orogenic belts:* 3 — Block-fold ranges and massifs, and 4 — Arch-fold-block and block-homoclinal ranges and massifs. *III. Orogenic belts formed by rifting:* 5 — Fold-block ranges and massifs on Mesozoic rocks, 6 — Arch-fold-block and block-overthrust ranges and massifs on Mesozoic rocks, 7 — Arch-block and block-homoclinal ranges and massifs on Paleozoic rocks, 8 — Block highlands inheriting median massifs, 9 — Ranges within highlands (complex horsts), and 10 — Uplands fragmented by differential block movements. *Plains of foredeeps and intermontane basins:* 11 — Depositional and 12 — Depositional/denudational and denudational. *Morphostructures of tectonic and igneous origin:* 13 — Ranges and massifs formed by horst development and igneous intrusions, and 14 — Ranges and massifs composed of volcanic rocks. *IV. Deep-seated faults:* 15a — Boundaries of deep-seated fault zones, and 15b — Deep-seated faults responsible for the block character of morphostructures. *V. Minor morphostructures and individual landforms:* 16 — Depressions formed by grabens, 17 — Rift depressions, 18 — Horst massifs formed by igneous intrusions, 19 — Denudation scarps, and 20 — Major river valleys.

Figure 11-6. Morphostructural map of Alaska drawn from space imagery. Reprinted with permission from *The Soviet Journal of Remote Sensing*, No. 6, N. V. Bashenina and N. N. Tal'Skaya, "Space Imagery Analysis for a Geomorphological Map of the World," 1981.

**ORIGINAL PAGE IS
OF POOR QUALITY**



LEGEND:

Erosional landforms

- With structural control
 - ridge and V valley forms (sAa)
 - dissected surfaces (sRa, sFa)
 - surfaces with remnant ridges (sAr, sAf)
 - plateaux and plainlands (sRr)
- Without structural control
 - ridge and V valley forms (Aa)
 - dissected surfaces (Ra, Fa)
 - surfaces with remnant ridges (Ar, Af)
 - plateaux and plainlands (Rr)

Depositional landforms

- Inland
 - alluvial plains
 - fans(Da)
- Coastal
 - coastal lowlands(Dc)

Note: Letters in brackets are suggested mapping symbols, taken in part from Ollier (1967). An s prefix is used to denote landforms with structural control, and a c or an f after a diagonal stroke refers to coarse and fine textures.

Figure 11-7a. A geomorphic units map of an area in eastern New South Wales, prepared from Landsat MSS scene 2045-23005-7. Units are defined in legend (from Pain, 1985).

salt pans and for the geothermal field, were made up because the ITC system had no symbols for these features. In most European geomorphological mapping systems, geomorphic units or lithology or both are indicated by color. Since this map is entirely black and white, patterns for the geomorphic units were chosen that could be easily drawn and would stand out clearly on the completed map. Lithological identification was made from *The Reconnaissance Geological Map of the State of Baja California* by Gastil et al. (1975). Other ancillary information was drawn from books and articles by Lowman (1968), Merifield and Lamar (1975), and Thompson (1968). It should be emphasized that this map was drawn entirely as a desk exercise. No field work was undertaken either to check the accuracy of the analysis or to supply additional information. It is possible that errors of identification would be discovered and certain that additional morphometric information could be gained from field investigation.

The northern end of the Gulf of California tectonic trough contains the delta of a major river system, but unlike many other deltas, different active geomorphic processes compete for dominance with the deltaic processes. From the perspective of the basic order of the processes operating in the region, it would be better entitled "an active tectonic trough, in an area of strong structural control, within an arid climate region that contains a major river delta."

The geomorphological region is bordered on the west by the Sierra Juarez and Sierra San Pedro Martir, a section of the Peninsular Ranges that extend southward from near Los Angeles to form the backbone of Baja California. The eastern side is bordered by the Tinajas Altas Ranges of Arizona. The ranges on both sides of the trough are formed of Mesozoic granitic rocks. The north end of the region, including the Salton Sea and the Imperial Valley, are outside of the mapped area. The southern boundary of the region is formed by the Gulf of California. The Sierra Pinacate volcanic field (Plate V-4) lies off the image just to the southeast of the mapped area.

Mountain ranges within the trough are a complex mixture of age and lithology. A small volcanic center, consisting of an inactive cinder cone and surrounding geothermal field, is located at Cerro Prieto. Here the Mexican government has constructed a 75-megawatt geothermal power station, its cooling reservoir clearly visible on the Landsat image. Alignment of the volcanic center and surface manifestations of the San Jacinto fault system in the delta flat, perceptible as variations in tone and shape of agricultural fields on Landsat, may indicate a relationship between volcanism and faulting in the area (Merifield and Lamar, 1975).

Several faults or fault systems and a number of lineaments, which may or may not be faults, were mapped from the image. The Sierra de Los Cucapas has four distinct northwest-southeast-trending lineaments that are undoubtedly faults. Two of these show clear offsets characteristic of right lateral strike-slip movement. The prominent Agua Blanca fault is easily recognized as a gash across the eroded and dissected upland region west of Valle de la Trinidad. This is known to be a strike-slip fault, although it is difficult to confirm any offsets in this particular scene.

The climate of the region is arid, with two distinct arid climatic subregimes operating in different parts of the area. To the east and south of the delta is the Sonoran Mesa, which is a desert dominated by eolian geomorphic processes. The central

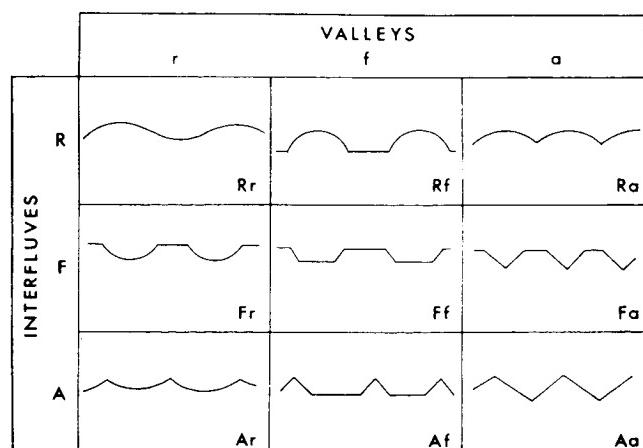


Figure 11-7b. A classification of generalized landscape profiles in which R(r) = round, F(f) = flat, and A(a) = angular, for interfluve (capital letter) and valley (lowercase letter) profiles (from Ollier, 1967).

portion, west and south of the Sierra del Rosario, is an extensive sand sea with long ridges of prominent transverse dunes oriented with the prevailing wind (See Plate E-11). A dark spot in the north-central portion of the desert is an anomalous lake in this very dry region. Merifield and Lamar (1975) suggest that the lake may be caused by the impoundment of ground water behind a fault. The geology of the Sonoran Mesa is poorly understood, but Thompson (1968) suggests that the desert sands may represent a possible topset facies of an early Colorado River Delta. Although the mesa is predominantly eolian, one section, close to the foot of the delta, shows significant scarp retreat due to fluvial erosion. The western side of the trough is controlled by arid climate fluvial processes with little visible evidence of eolian activity. The piedmont slopes appear to be dominated by pediment

erosion with accumulations of sediment, probably sand, on fluvial terraces and alluvial fans south of the Sierra Pinta and north of the Sierra de la Tinaja. Within these ranges, the pediments show markedly less fan activity, or possibly, these areas may have more of a vegetative cover, accounting in part for the darker tones on the image. There are two playas in this area—the Laguna Salada and the Valle de San Felipe. The Laguna Salada appears to be quite separate from the Colorado Delta in form and process, in spite of relative proximity. Separated from the delta and deltaic processes by the Sierra de Los Cucapas, it seems to derive its water and sediment as runoff and erosion from the adjacent mountains. The Valle de San Felipe appears to be a classic desert basin of interior drainage. Sediment and water move from the mountains, across the pediment to the playa, where the water evaporates.

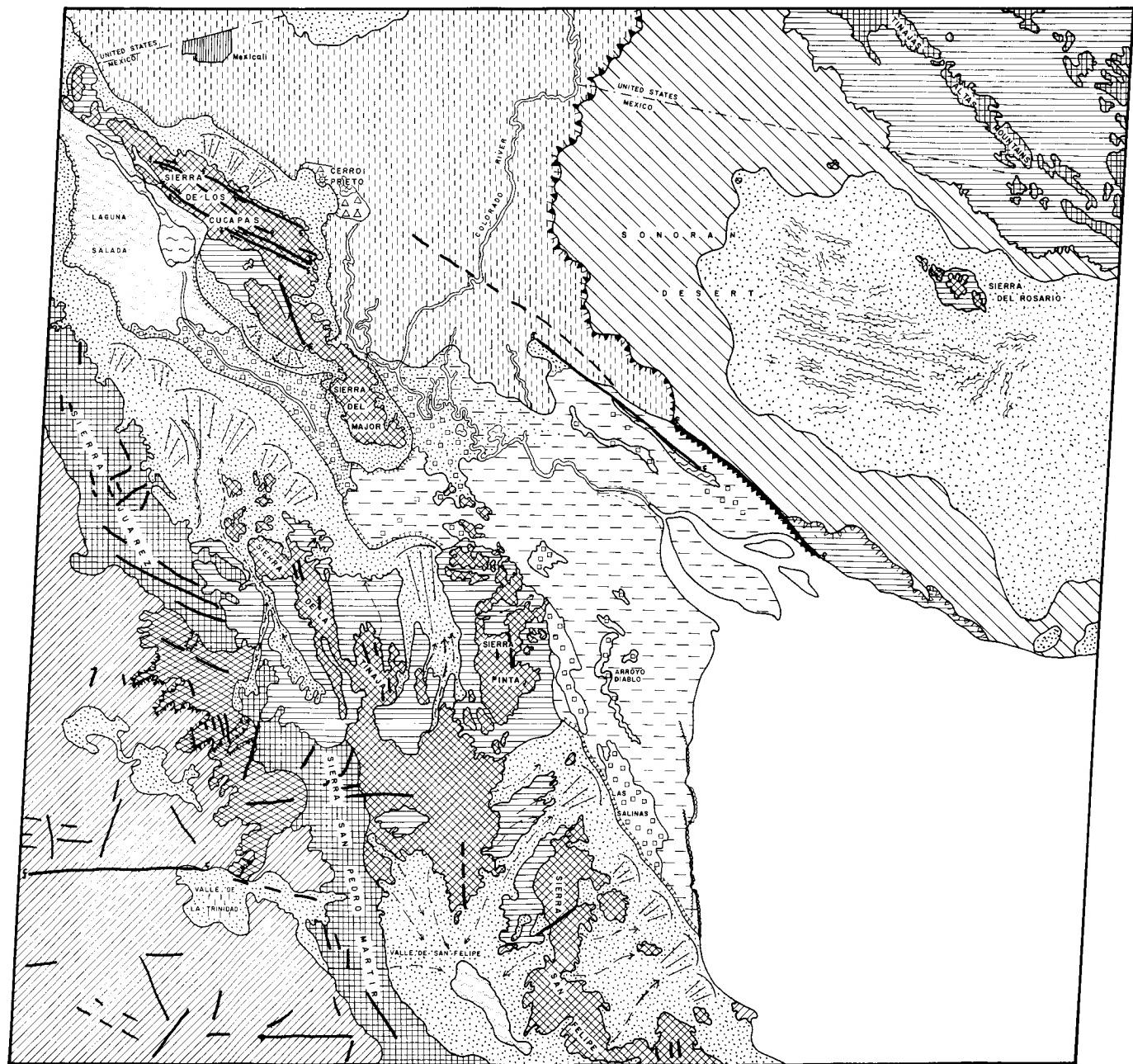


Figure 11-8a. Geomorphological units map of the Colorado delta region, Baja California, drawn from Landsat MSS Band 7 image.

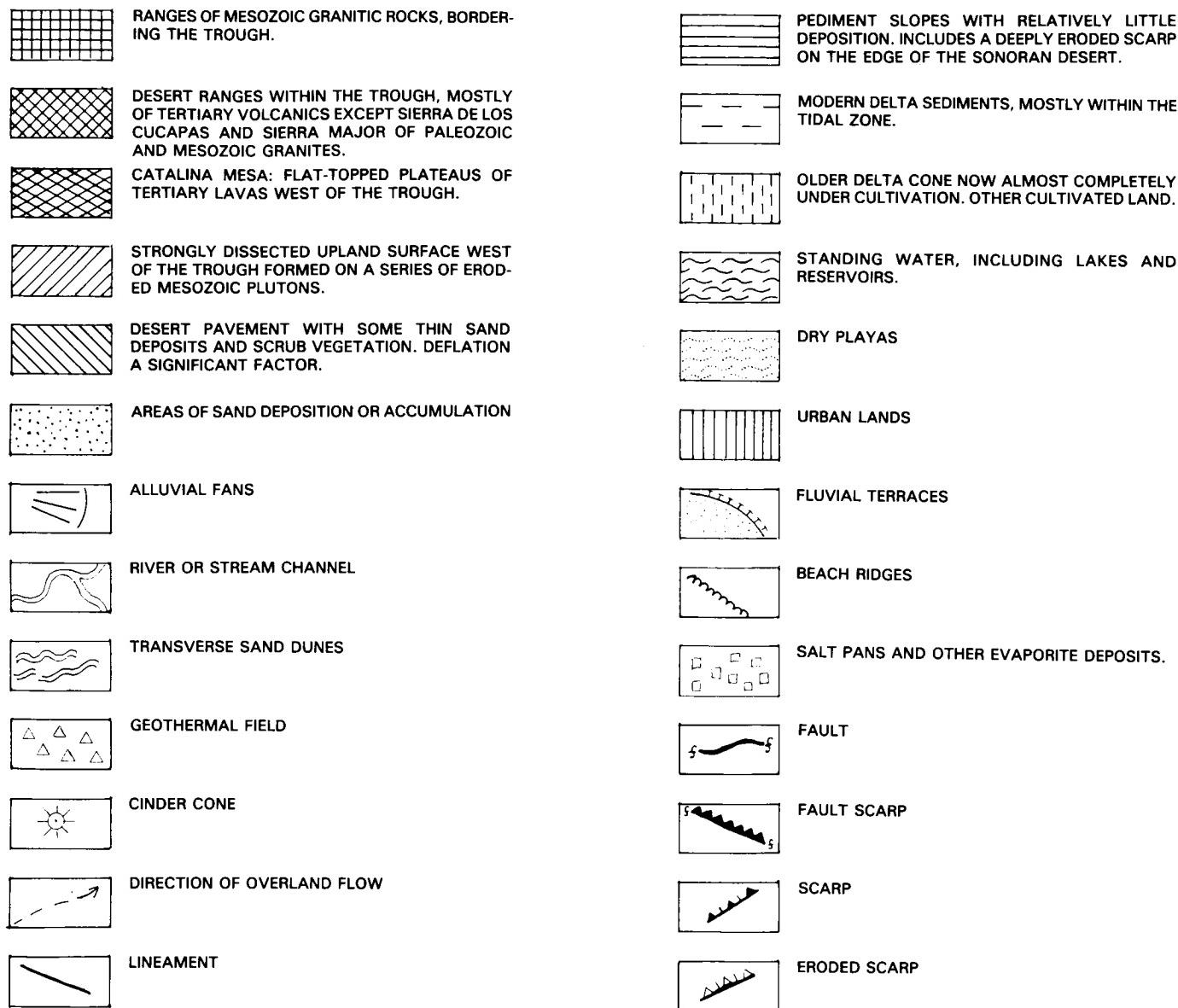


Figure 11-8b. Legend for the geomorphological units of the Colorado delta region, Baja California.

Evidently, the Colorado River Delta (see also Plate D-12) has been rigidly controlled by structure throughout its history. The river enters the trough near Yuma, Arizona, and has built an extensive delta cone against the Sierra de Los Cucapas and the Sierra Major. Sediment distribution basically follows two directions—northward toward the Salton Trough and southward toward the Gulf of California. The normal direction of the river flow appears to have been southward with occasional, probably relatively short, excursions toward the north. Thompson (1968) states that it is likely that such diversions toward the north occurred several times during the past 1500 years, with the overflow spilling back toward the Gulf of California near Cerro Prieto. Abrupt scalloped edges of the alluvial fans on the north side of Sierra de Los Cucapas mark the paleochannel from the Salton Trough to the Gulf of California. Development of alluvial fans on the north side of the Sierra de Los Cucapas and the almost complete lack of fans along the eastern side of the mountains indicate the relative dominance of deltaic deposition on the south

limb of the cone, while fan deposition was possible during the relatively long periods without any delta action on that side. South and east of the Sierra Major, the modern delta is predominantly a tidal flat where the principal active geomorphic process is the reworking of sediments in a littoral marine environment characterized by large tidal ranges and generally weak wave action within the relatively protected Gulf of California. Tidal ranges on the delta are from 6 to 9 m at various locations. The Landsat scene apparently shows the time of low tide. The range of tidal action, up to the Sierra Major, can be identified by the dark tones of the tidal flat. A number of areas of evaporite deposits show clearly as bright locations on the image due to the high reflectance of the salt. The snakelike "Arroyo Diablo" is apparently a stream channel from an earlier stage of delta development. "Las Salinas," a salt pan with thick evaporite deposits, against the southwestern end of the piedmont terrace, has been mined for salt in the past. A series of prominent beach ridges, built of sand and broken shells, stands out as white lines

along the southern edge of the delta. On the north side of the delta are several evaporite deposits associated with old stream channels and a linear stretch of standing water that is apparently tied to activity along the San Jacinto fault in 1934. On a 1966 Gemini photograph of the same area, this feature appears to be entirely dry and filled with evaporites (Lowman, 1968).

Coastlines to either side of the modern delta appear to be undergoing active marine erosion. The scalloped appearance of the coast of the Sonoran Mesa south of the delta is indicative of active erosion, as is the arcuate character of the coastline east of the Sierra San Felipe. Thompson (1968) says that recent coastal erosion has removed most of the sediments on the seaward side of the easternmost San Felipe peaks, although their former presence is attested to by a distinctive rim of mud, capped by alluvial gravels, along the edge of the peak.

There are several strong indications of the influence of human activity on the geomorphology of the delta. The older delta cone, which was, under natural conditions, a desert, is now almost entirely under cultivation. One of the most obvious results of human activity is the manifestly underfit character of the present river in relation to its delta. A large portion of the natural flow of the river is now diverted to areas outside the Colorado basin from locations upstream. In addition, most of the river's sediment load has been trapped upstream in Lake Meade since 1935. Even though effects of continued sediment deprivation cannot be evaluated from a single scene, the sequential analysis of the same scene over several years should reveal changes in the delta due to tidal erosion.

At smaller scales, covering larger areas, regional geomorphic systems can be seen as subsystems nested into one or more larger regional systems of differing geomorphological character. The complexity of the Colorado Delta region is due, in part, to its location at the intersection of two larger geomorphic systems, each controlled by a different mix of geomorphological processes. It is a nested subregion of the Colorado River Drainage Basin, a fluvial system in a predominantly mountainous setting, and of the Gulf of California, an active tectonic system in a largely marine environment.

Few, if any, geomorphic systems exist in isolation. Even such seemingly isolated regions as the Hawaiian Islands do not stand alone. They are bound into the tectonic processes of the Pacific Ocean Basin and are influenced by midocean marine processes and subtropical climate.

GEOMORPHOLOGICAL MAPPING OF THE TUCSON AREA

A geomorphological map of the area from Tucson, Arizona, southward past Nogales into northern Mexico and westward by about 100 miles was developed from a Landsat 4 Thematic Mapper (TM) scene obtained on January 8, 1983 (Figure 11-9). The original map was produced by photointerpretation techniques on a scale of 1:250000 using black and white images of bands 3, 5, 6, and 7 and a color image composited from bands 2, 3, and 4 (see Plate F-9). Other sources used in this mapping were the U.S. Geological Survey (USGS) 1:250000 topographic sheets of the area, used principally to identify the names of places and features, and a geologic map of the state of Arizona used to identify the lithology. The symbols used on the map were generally taken from the ITC system for Geomorphological Survey, and contrasting geometric patterns were used to display different geomorphological units. Again, the map was not checked out in the field. Before this or any other geomorphic units map produced by remote sensing techniques is used for definitive research, it should be field-checked for accuracy.

Band 7, in the shortwave infrared range, was used to draw the basic map as it was judged to provide the clearest definition

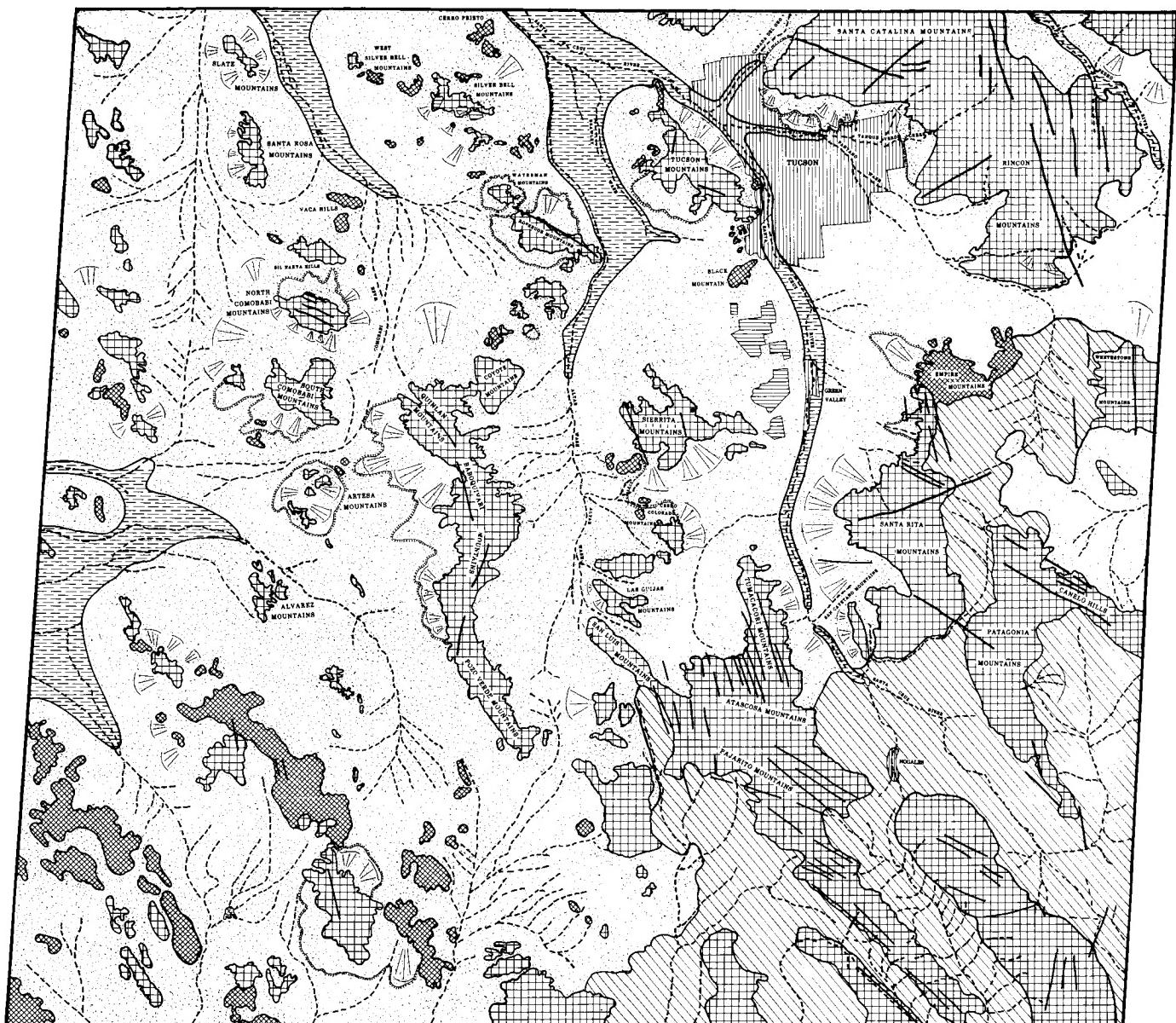
of various geomorphic features. Images from the other bands and the color composite were used for comparison to refine the definition of various mapped features. Drainage features were quite clear on all bands, although band 6, even with its lower (120 m) resolution, better highlighted the master channels of the area. This was helpful in deciding how much of the drainage pattern to map in an area laced with a fine network of ephemeral channels. Band 6, in the thermal infrared region of the spectrum, was also particularly useful in defining breaks in slope indicating the division between mountain and pediment features. Cultural features, including urban and agricultural areas and strip mines, showed most clearly on the color-composite image.

Tucson is located in the Basin and Range Physiographic Province, a large region covering much of the southwestern United States and parts of northern Mexico. The province is characterized by numerous small linear ranges of block-faulted mountains separated by low pediments and playas. In this scene, two types of mountain ranges are evident. Most of the ranges are sharp-crested mountains of mixed lithology but composed primarily of Cretaceous to Early Tertiary crystalline rocks. These are interspersed with some Paleozoic and Precambrian units and some segments of Middle Tertiary volcanics. The other mountain ranges have rounded crests and are composed mostly of Middle Tertiary volcanics. The difference between the two types of mountain ranges shows up quite clearly on the imagery. The two different types of mountains can be clearly identified on the Tucson city subscene (Figure 11-10). The Santa Catalina Mountains in the upper right-hand portion of the subscene are sharp-crested mountains (recently classed as a metamorphic core complex) composed of mostly Cretaceous crystalline rocks with some Paleozoic units. Black Mountain southwest of Tucson is a prominent, relatively low rounded mountain formed of Middle Tertiary volcanics. The Tucson Mountains west of the city are of mixed lithology with the central core formed on crystalline rocks and the northward extension of the Tertiary volcanics. Lithological differences would require field work for identification, but the geomorphological distinctions between the two types of lithology can be distinguished on the imagery.

In addition to the two dominant types of mountains, there are also several small ranges of folded sedimentary rocks in the western portion of the general scene. Alluvial fans and terraces were mapped wherever there appeared to be an obvious slope break. Some of the terraces and pediment fans are especially large, particularly north of Tucson against the Santa Catalina Mountains and along the Canada del Oro. An exhumed bedrock pediment borders the Santa Catalina Mountains along the east side of the Canada del Oro (Figure 11-11). This shows up very clearly on the Tucson subscene. Within the scene are two distinctly different areas that may be parts of separate subregions within the Basin and Range Province. South and east of the Empire, Santa Rita, and Tumacacori Ranges, the mountains are quite close together, and the pediments between them appear to have relatively steep slopes dominated by active gullying into the Gila Conglomerate that forms the cover in this area. The valley bottoms appear to contain relatively little alluvium. The boundary of this area closely coincides with the western boundary of the section of the Basin and Range Province that Fenneman (1931, page 380) titled "The Mexican Highland."

Throughout the remainder of the scene, the mountains are more widely spaced and are separated by pediments with low slopes and considerable alluvial fill. Wide drywashes characterize the valley bottoms. Low-relief floodplains were mapped along the sides of the Santa Cruz River and some other areas identified by a greater concentration of vegetation. These were also the areas containing agricultural development. Lineaments were mapped where evident on the scene. Some of these lineaments probably represent fault traces, but none were mapped as faults because evidence of displacement could not be resolved on the imagery.

ORIGINAL PAGE IS
OF POOR QUALITY



TUCSON ARIZONA REGION

GEOGRAPHICAL UNITS



Scale 1:250,000

- | | | |
|---|---|---------------------------------|
| Sharp crested mountains formed primarily on intrusive rocks of upper Cretaceous to early Tertiary age. | Alluvial terraces with evident slope breaks. | Lineaments and Faults |
| Rounded mountains and hills formed mainly on late Cretaceous volcanics with some late Cretaceous sedimentary rocks. | Low relief flood plains and other areas of frequent overland flow. Some of these areas are under cultivation. | Streams and washes, mostly dry. |
| Eroded pediments and fans with low slopes, formed mainly on quaternary alluvial gravels. | Disturbed strip mining lands | Alluvial fans |
| Eroded pediments with moderate slopes and evident deep gullying, found mostly in areas covered by the Gila conglomerate and other stream and lake deposits. | Urban lands | Standing water. |

Figure 11-9. Geomorphological units map of the Tucson, Arizona, region drawn from a Landsat Thematic Mapper image. The original scale of the map is 1:250000.

**ORIGINAL PAGE
COLOR PHOTOGRAPH**

There are two quite prominent Quaternary fault scarps cutting across the Madera Canyon alluvial fan, a prominent feature extending northwestward from the Santa Rita Mountains southeast of Green Valley. These scarps are visible on an aerial photograph (Figure 11-12), but cannot be detected on the Landsat image. It is possible that, on another image of the area taken at a different time with a different Sun angle, these fault scarps might show up.

The geomorphology of the Tucson/Nogales area is much less diverse than that of the Colorado Delta region. However, this area also has its own complexity. Mapping the area from satellite imagery displays the boundary between two sections of the Basin and Range Province better than Fenneman could ever

have hoped and clearly shows a significant part of the uniformity and the diversity of process and form that characterize the region.

SUMMATION

Geomorphological processes seldom "sit for portraits." They can be best studied through their resulting landforms. At small-scale regional levels, landform patterns and distribution are surrogates through which the integration of many geomorphological processes can be studied. Regional geomorphological mapping from space imagery promises to become a powerful tool

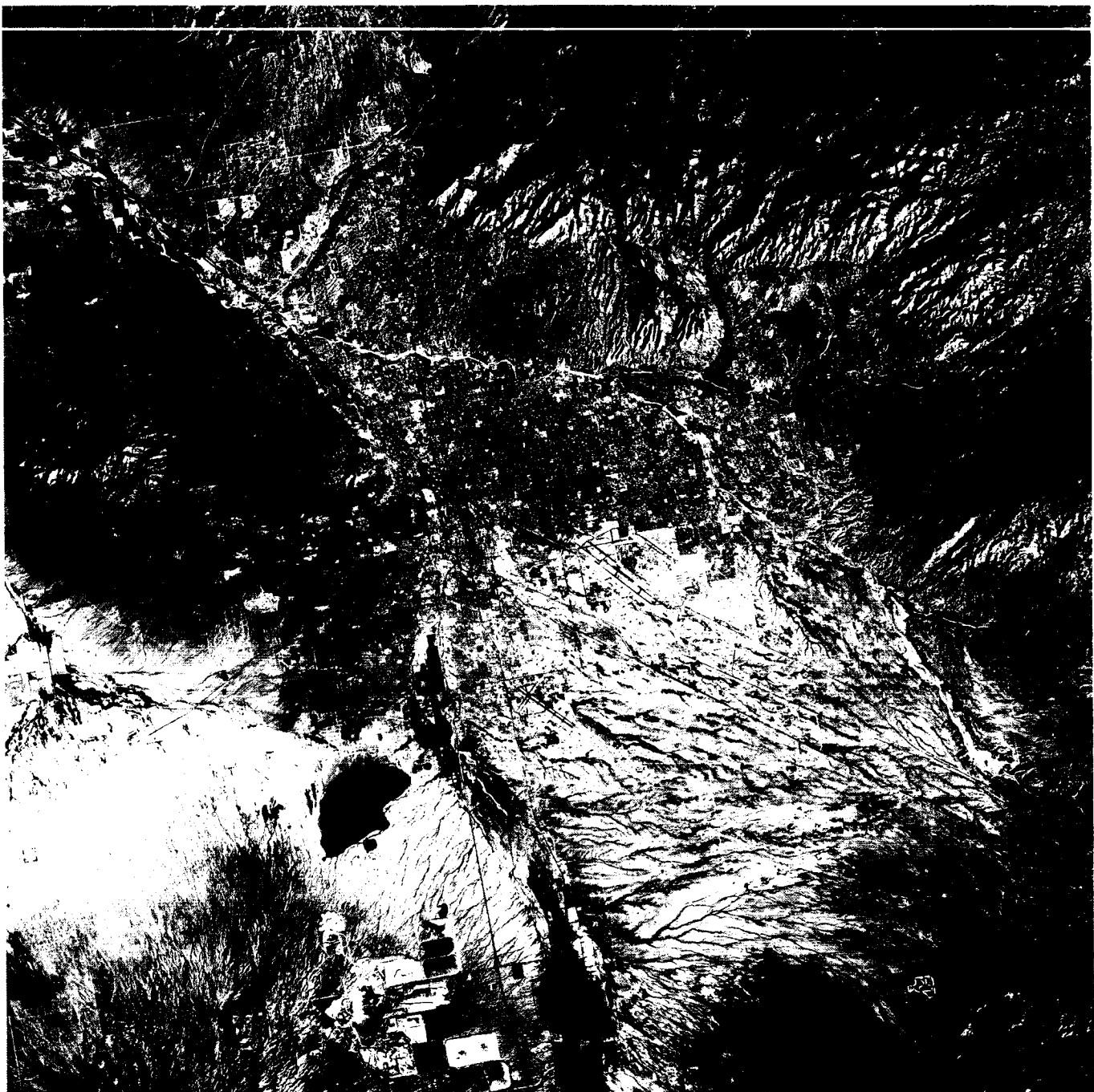


Figure 11-10. False-color composite Landsat Thematic Mapper image subscene of Tucson, Arizona, and environs.



Figure 11-11. Oblique aerial photograph taken near Tucson, Arizona, looking west from the *Canada del Oro* along an exhumed bedrock pediment at the foot of the *Santa Catalina Mountains*. Note stream terraces. Photograph by Peter Kresan.

for the study. Space imagery is limited by scale and resolution in the amount of detailed information it can provide. As resolution is improved and new techniques, such as stereoscopic viewing, become available, space imagery will yield more information about particular locations. The small-scale and large-areal



Figure 11-12. Oblique aerial photograph looking southeast at the *Madeira Canyon* alluvial fan south of Tucson, Arizona. Photograph by Peter Kresan.

coverage of space imagery is one of its principal advantages. The primary value of space imagery for geomorphology lies not in the amount of detail it reveals, but in the broad perspective of regions of the Earth's surface it provides. A regional geomorphology based on this broad perspective is a needed complement to detailed geomorphology focused on particular landforms and landform types, dominated by often diverse processes within relatively limited areas. Such a regional geomorphology should be concerned not with the multiplication of detail, but with the multiplicity of processes that, acting together, give each landform and each landform region its uniqueness. Space imagery offers the synoptic overview, and regional geomorphological mapping provides the technique by which geomorphologists can investigate the complex interactions of geomorphic processes that have formed and are modifying the dynamic surface of the Earth.

REFERENCES

- Astinov, V. I., B. N. Mozaev, V. G. Mozaeva, and N. V. Skublova, Remote sensing and origin of large relief forms, in *Geomorphology and Palaeogeography*, pp. 255–258, XXIII International Geographical Congress, Moscow, 1976.
- Barsch, D., and H. Liedtke, Principles, Scientific Value and Practical Applicability of the Geomorphological Map of the Federal Republic of Germany at the Scale 1:25 000 (GMK25) and 1:100 000 (GMK100), pp. 296–313, *Zeitschrift für Geomorphologie Supplementband* 36, Berlin, 1980.
- Bashenina, N. V., Principles of Geomorphological Classification, in *Guide to Medium Scale Geomorphological Mapping*, edited by J. Demek and C. Embleton, pp. 20–24, Schweizerbarts, Stuttgart, 1978.
- Bashenina, N. V. et al., Legend to the International Geomorphological Map of Europe 1:2 500 000 IGU Commission on Geomorphic Survey and Mapping, Czechoslovak Academy of Sciences, Institute of Geography, Brno, 1971.
- Bashenina, N. V., and N. N. Tal'Skaya, Space imagery analysis for a geomorphological map of the world, *Soviet J. Remote Sensing*, No. 6, 861–871, 1981.
- Bedi, N., Applied geomorphic studies on Landsat imagery in *Perspectives in Geomorphology, Vol. III—Applied Geomorphology*, edited by H. S. Sharma, pp. 251–269, Concept Publishing Co., New Delhi, India, 1982.
- Blackinton, J. G., and D. M. Hussong, First results from a combination side-scan sonar and seafloor mapping system (SeAMARC II), paper presented at 15th Annual Offshore Technology Conference, Houston, Texas, May 2–5, 1983.
- Brunsdon, D., J. C. Doornkamp, P. G. Fookes, D. K. C. Jones, and J. M. H. Kelly, Large scale geomorphological mapping and highway engineering design, *Quar. J. Eng. Geol.*, **8**, 227–253, 1975.
- Canoba, C. A., Geomorphological mapping using Landsat imagery: A case study in Argentina, *ITC J.*, **1982-3**, 324–329, 1982.
- Christian, C. S., Concept of land units and land systems, in *Proc. Ninth Pacific Science Conf. of Pacific Science Assn.*, **20**, 74–81, 1958.
- Christian, C. S., and G. A. Stewart, Aerial surveys and integrated surveys, in *Proc. Toulouse Conf. on Natural Resources Research*, pp. 223–280, UNESCO, Paris, France, 1968.
- Cochran, G. R., and G. H. Browne, Geomorphic mapping from Landsat-3 Return Beam Vidicon (RBV) imagery, *Photogramm. Eng. Remote Sens.*, **47**(8), 1205–1213, 1981.
- Cook, R. U., and J. C. Doornkamp, *Geomorphology in Environmental Management: An Introduction*, 413 pp., Clarendon Press, Oxford, 1974.
- Crofts, R. S., Detailed geomorphological mapping and land evaluation in highland Scotland, in *Progress in Geomorphology*, edited by E. H. Brown and R. S. Waters, pp. 231–249, Institute of British Geographers, Special Publ. 7, 1974.
- Damuth, J. F., V. Kolla, B. D. Flood, B. O. Kowsmann, M. C. Monteiro, M. A. Gorini, J. J. C. Palma, and R. H. Belderson, Distributary channel meandering and bifurcation patterns on the Amazon deep-sea fan as revealed by long-range side-scan sonar (GLORIA), *Geology*, **11**, 94–98, 1983.
- Davis, W. M., The geographical cycle, *Geographical J.*, **14**, 481–503, 1899.
- Demek, J., (Ed.), *Manual for Detailed Geomorphological Mapping*, 320 pp., IGU Commission on Geomorphic Survey and Mapping, Academia, Prague, 1972.
- Demek, J., Geomorphological mapping: progress and problems in *Perspectives in Geomorphology, Vol. III—Applied Geomorphology*, edited by H. S. Sharma, pp. 221–235, Concept Publishing Co., New Delhi, India, 1982.
- Demek, J., and C. Embleton, (Ed.), *Guide to Medium Scale Geomorphological Mapping*, 348 pp., Schweizerbarts, Stuttgart, 1978.
- Embleton, C., (Ed.), *Geomorphology of Europe*, 429 pp., Macmillan, London, 1984.
- Embleton, C., Techniques, problems and uses of mega-geomorphological mapping, in *Global Mega-Geomorphology*, edited by R.S. Hayden, pp. 84–88, NASA CP-2312, 1985.
- Fairbridge, R. W., Kara-Bogaz-Gulf, in *Encyclopedia of Geomorphology*, edited by R. W. Fairbridge, pp. 579–581, Reinhold Book Corp., New York, 1968.
- Fenneman, N. H., (1931–1938) *Physiography of Eastern United States and Physiography of Western United States*, McGraw-Hill, New York, 1931–1938.
- Gardiner, V., Land evaluation and the numerical delimitation of natural regions, *Geografia Polonica*, **34**, 11–30, 1976.
- Garrison, L. E., N. H. Kenyon, and A. H. Bouma, Channel systems and lobe construction in the Mississippi Fan, *Geo-Marine Letters*, pp. 31–39, March–June 1982.
- Gastil, R. G., R. P. Phillips, and E. C. Allison, Reconnaissance Geologic Map of the State of Baja California, *Geol. Soc. Amer. Mem.*, **140**, Plate 1A, 1975.

- Gellert, J. F., Principles of geomorphological regionalization and encoding of geomorphological characteristics for computer processing of data, in *Perspectives in Geomorphology, Vol. III—Applied Geomorphology*, edited by H. S. Sharma, pp. 237–242, Concept Publishing Co., New Delhi, India, 1972.
- Hammond, E. H., Small scale continental landform maps, *Annals AAG*, **44**, 34–42, 1954.
- Howard, J. A., and C. W. Mitchell, Phyto-geomorphic classification of landscape, *Geoforum*, **11**, 85–106, 1980.
- Hussong, D. M., and P. Fryer, Back-arc seamounts and the SeaMARC II Seafloor Mapping System, *EOS*, **64**, 627–632, 1983.
- Kayan, I., and V. Klemas, Application of Landsat imagery to studies of structural geology and geomorphology of Mentes region of southwestern Turkey, *Remote Sens. Environ.*, **7**, 51–60, 1978.
- King, L., Geomorphology, in *Encyclopedia of Geomorphology*, edited by R. W. Fairbridge, p. 403, Reinhold Book Corp., 1968.
- Klimaszewski, M., Detailed geomorphological maps, *ITC J.*, **1982–3**, 265–271, 1982.
- Laughton, A. S., The first decade of GLORIA, *Annual Report Institute of Oceanographic Sciences—1980*, pp. 60–85, Surrey, England, 1980.
- Lowman, P. D., *Space Panorama*, Weltflugbild, Zurich, Switzerland, 1968.
- Mabbutt, J. H., and G. A. Stewart, Application of geomorphology in resources surveys in Australia and New Guinea, *Revue de Géomorphologie Dynamique*, **14**, pp. 97–109, 1963.
- Mahrer, K. O., and C. Bradley, Magnetic terrain anomalies from arroyos in an alluvial fan, Amer. Geophys. Union, 1983 Fall Meeting, *Eos*, **64**, 684, November 8, 1983.
- Merifield, P. M., and D. L. Lamar, Faults on Skylab Imagery of the Salton Trough Area, Southern California, Technical Report 75-1, NASA Lyndon B. Johnson Space Center, Houston, Texas, 23 pp., 1975.
- Miyogi, D., S. K. Sarkar, and S. Mallick, Geomorphic mapping in the plains of West Bengal, India, *Selected Papers, Vol. I—Physical Geography*, pp. 89–94, XXI International Geographical Congress, India 1968, National Committee for Geography, Calcutta, 1970.
- Mukerjee, S., Remote sensing in geomorphological mapping, in *Perspectives in Geomorphology, Vol. III—Applied Geomorphology*, edited by H. S. Sharma, pp. 271–277, Concept Publishing Co., New Delhi, India, 1982.
- Nicholayev, V. A., Principles of a landscape classification, *Soviet Geography: Review and Translation*, **15**, 654–661, 1974.
- Ollier, C. D., The great escarpment of eastern Australia: Tectonic and geomorphic significance, *Geol. Soc. Australia J.*, **29**, 13–23, 1982.
- Pain, C. F., Mapping of landforms from Landsat imagery; An example from New South Wales, Australia, *Remote Sens. Environ.*, **17**, 55–65, 1985.
- Palabekinoglu, S. ERTS-1 imagery: The valuable tool of geoscientists, in *Proc. Symp. Remote Sensing and Photointerpretation*, International Society for Photogrammetry Commission, **VII**, 597–609, 1974.
- Panizza, M., Analysis and mapping of geomorphological processes in environmental management, *Geoforum*, **9**, 1–15, 1978.
- Rao, K. R. and N. Bedi, Remote sensing for geomorphology, in *Perspectives in Geomorphology, Vol. I—Recent Trends*, pp. 401–417, Concept Publishing Co., New Delhi, India, 1982.
- Rosenfield, C. L., Terrain sensitivity mapping at Resolute Bay, N.W.T., in *Association of Pacific Geographers Yearbook*, **39**, 77–87, 1976.
- Savigear, R. A. G., A Technique of Morphological Mapping, *Annals AAG*, **55(3)**, 514–538, 1965.
- Searle, R. C., Side-scan sonar studies of North Atlantic fracture zones, *J. Geo. Soc. London*, **136**, 283–292, 1979.
- Searle, R. C., and A. S. Laughton, Fine scale sonar study of tectonics and volcanism on the Reykjanes Ridge, *Oceanologica Acta*, Actes 26^e Congrès International de Géologie, Colloque Géologie des Oceans, Paris, 7–17, juil, 1980, pp. 5–13, 1981.
- Slaney, V. R., Satellite imagery applied to earth science, in *Proc. Symp. Remote Sensing and Photointerpretation*, International Society for Photogrammetry Commission, **VII**, 555–571, 1974.
- Speight, J. G., A parametric approach to landform regions, *Progress in Geomorphology*, pp. 213–229, Institute of British Geographers Special Publ. 7, 1974.
- St-Onge, D., Geomorphic Maps, in *Encyclopedia of Geomorphology*, edited by R. W. Fairbridge, pp. 388–403, Reinhold Book Corp., 1968.
- Strahler, A. N., Quantitative Analysis of Watershed Geomorphology, *Amer. Geophys. Union Trans.*, **38 (6)**, 913–920, 1957.
- Thompson, R. W., Tidal flat sedimentation on the Colorado River Delta, Northwestern Gulf of California, *Geo. Soc. Amer. Mem.*, **107**, 1968.
- Townshend, J. R. G., Regionalization of terrain and remotely sensed data, in *Terrain Analysis and Remote Sensing*, edited by J. R. G. Townshend, pp. 109–132, George Allen and Unwin, London, 1981.
- Tricart, J., Cartographic aspects of geomorphological surveys in relation to development programs, *World Cartography*, **9**, pp. 75–83, U.N. Department of Economic and Social Affairs, New York, 1969.
- Ulaby, F. T., and J. McNaughton, Classification of physiography from ERTS imagery, *Photogramm. Eng. Remote Sens.*, **41**, 1019–1027, 1975.
- Verstappen, H. T., *Remote Sensing in Geomorphology*, Elsevier Scientific, New York, 1977.
- Verstappen, H. T., and R. A. vanZuidam, ITC system of geomorphological survey, in *ITC Textbook of Photo-Interpretation, Vol. VII: Use of Aerial Photographs*, International Institute for Aerial Survey and Earth Sciences, Delft, The Netherlands, 1968.

Verstappen, H. T., and R. A. vanZuidam, Orbital photography and the geosciences: A geomorphological example from the Central Sahara, *Geoforum*, **2**, 33–47, 1970.

Wright, R. L., Principles in a geomorphological approach to land classification, *Zeitschrift für Geomorphologie*, **16** (4), 351–373, 1972.

12

GLOBAL GEOMORPHOLOGY: OUTLOOK FOR THE FUTURE

Robert S. Hayden,* Robert W. Blair, Jr.,† James Garvin‡, and Nicholas M. Short‡

Views of Earth from space have provided mankind with new insights into the nature of our world, an appreciation of its place within the Solar System, and a fuller comprehension of the marvelous complexity of our planetary surface. As a result, Earth science is on the verge of a revolution in geomorphologic research. Over the last two decades, new technologies born from the space program have generated a rapidly expanding volume of geomorphic information. Specifically, observations from orbital satellites and manned orbital and space flights have given scientists a synoptic view of Earth previously impossible to obtain. It is now feasible to observe and study repetitively large-area land features up to continental dimensions through the medium of spaceborne imagery. Pictures at various scales, taken by remote sensors that utilize spectral bands in the visible, infrared, and microwave (radar) ranges, have opened new realms for quantitative geomorphological investigation. Moreover, we can now analyze the Earth from the planetary perspective. In this new context, Earth becomes just one of a number of celestial bodies of varying size and composition in the Solar System, some of which have their own distinct geomorphic character. The space images and other photographs presented in this book amply illustrate the value of observing the Earth's geomorphology from the same global vantage point that has successfully revealed the landscapes of other Earth-like planets.

In the latter part of the 19th century and the first decades of the 20th century, some early geomorphologists (e.g., G. K. Gilbert, 1877; W. M. Davis, 1899; W. Penck, 1924; N. Fenneman, 1938; J. T. Hack, 1960) extended their investigation of the Earth's land surface to megalevels. Thus, a global framework often underlay their postulates and theories on the formation and development of the Earth's varied landscapes. Their ideas dominated geomorphic research and contributed much to the advancement of knowledge concerning the systematic characteristics of the Earth's land surfaces. In the 1950s and 1960s, the emphasis in geomorphological research shifted toward more quantitative and replicable investigations in which accurate measurements of features and processes were made in order to reinforce general theories and their implications. As a result, the emphasis in geomorphology evolved toward micro-geomorphology, focusing on the quantitative evaluation of elements of small landform features

accessible to the investigator in the field. Although high-resolution aerial photography was often used as a tool in these investigations, it was seldom the principal vehicle in any study.

Beginning in the late 1950s, a series of quantum leaps both in available technology and in the understanding of terrestrial surfaces have fostered a new outlook in geomorphology. These advances pointed toward the need for a renewed emphasis on the mega (i.e., global) approach to studies of the Earth's landscapes. Prompted by research goals during the International Geophysical Year, by 1959 marine scientists had revolutionized the understanding of the ocean floor. Their discoveries led to the realization that the ocean floor was a varied complex of landform systems dominated by volcanic and sedimentary/erosional processes. The ocean floor, making up more than 70 percent of the planetary surface, has become an enlarging area of geomorphological interest, especially in the last 15 years. New technology now makes possible ever closer scrutiny of the varied geomorphic features of the ocean floor (Figure 12-1). In the 1960s, photographs taken by orbiting astronauts, culminating in the startling views of the full Earth from the Moon, have made us aware of the value of viewing our own planet from space. Since 1972, when Landsat-1 (ERTS-1) was launched, there has been a constantly growing supply of pictures with improving resolution, in a number

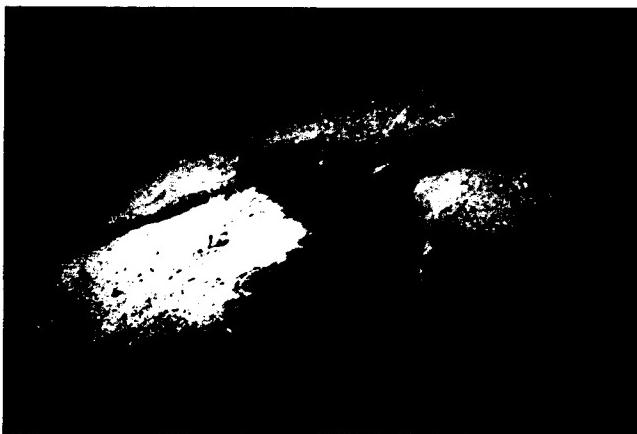


Figure 12-1. Rift Valley in the East Pacific Rise near 13°N, obtained during a dive of the CYANA submersible (CYANA in 1972); courtesy of R. Hekinian.

*Department of Public Affairs (Geography Program), George Mason University, Fairfax, Virginia 22030.

†Department of Geology, Fort Lewis College, Durango, Colorado 81301.

‡Geophysics Branch, Code 622, Goddard Space Flight Center, Greenbelt, Maryland 20771.

of spectral bands, covering nearly all the land areas of the Earth. The recent developments in radar imaging, through Seasat and Shuttle Imaging Radar (SIR-A, SIR-B), as well as advanced airborne systems such as MARS (Gelnett and Gardner, 1979), supplement the geomorphic data base with images in the microwave range, some showing regions seldom covered by Landsat due to persistent cloud cover (e.g., Amazon Basin; New Guinea). Other systems, including the recently tested Large-Format Camera (LFC) and some still to be tried (e.g., Shuttle laser altimeter), promise more geomorphic information in the near future.

To date, geomorphologists have made relatively limited use of satellite data that offer the global overview provided by spaceborne imagery. There are, for instance, no published studies that attempt to reexamine and confirm or refute, using the synoptic view from space, the older theories of landscape evolution derived from the early qualitative studies. The most extensive use of geomorphology from the perspective of space has been by planetary geologists. These specialists apply geomorphic principles in interpreting and mapping planetary surfaces and in developing theories of landscape evolution for the Moon, Mars, Mercury, Venus, and some of the moons of Jupiter and Saturn solely from space images (Glass, 1982; Short, 1975). Planetary geologists have taken this approach out of necessity. Although a small amount of *in-situ* surface data has been obtained for a few local areas of the Moon, Mars, and Venus, the hostility of the surface environments on those bodies to human life precludes extensive manned surface investigations in the foreseeable future. This has forced greater reliance on unmanned and orbital surveillance of these surfaces. The techniques developed for such exploration can also be profitably applied to terrestrial landforms. The advent of this new space and oceanographic technology, particularly the imaging systems, means that a mega-geomorphological investigation of the Earth is possible and amply justified.

MEGA-GEOMORPHOLOGY

In March 1981, at a conference sponsored by the British Geomorphological Research Group, geomorphologists coined the term "mega-geomorphology" (Gardner and Scoging, 1983) to describe the study of landforms and landscapes from subcontinental to global scales; by implication, the space perspective is desirable but not always necessary. The primary thrust of this conference was the regional distribution of landforms, especially in relation to those processes that formed them. Four years later, in January 1985, 30 geomorphologists from the United States, Great Britain, and Australia gathered for a workshop held at a conference center outside Tucson, Arizona, by invitation of NASA and the International Union of Geological Sciences. The objectives were to review the nature of global mega-geomorphology and to consider its present status and future place within the scientific study of landforms (Hayden, 1985). The workshop participants represented a broad range of specialties including glacial geology, marine geology, coastal studies, eolian processes, landscape evolution, fluvial processes, tectonic geomorphology, resource exploration, physical geography, remote sensing, and planetary geology. From the deliberations of the Tucson Workshop participants, it was soon evident that, despite the wide diversity of specialties, there was a complementary range of interests. Participants felt they were witnessing the beginnings of a "New Global Geomorphology built on expanded scales of concern in both space and time" (Baker and Head, 1985). They concluded that mega-geomorphology has now come into focus: "first, because geomorphology has recently been presented with exciting new techniques, most notably the rapidly developing technology of remote sensing. Second, these tools have arrived at a time when geomorphology is reassessing its role by defining or rediscovering important research thrusts. Third, geomorphologists are increas-

ingly leaving their specialty niches to pursue broad interdisciplinary concerns with tectonic, paleoclimatic, and even extraterrestrial ramifications" (Baker and Head, 1985).

STUDIES OF THE EARTH FROM SPACE

Landform investigations at continental scales require a regional outlook that can best be provided by images with viewing areas of tens to hundreds of kilometers on a side. In addition, the availability of multispectral images and temporal coverage at a variety of scales broadens the research by providing multiple data sets for analysis. Few studies have taken advantage of the mammoth amount of image data available. Those that do strongly demonstrate the potential of space imagery in geomorphological investigations.

Breed and Grow (1979) and Breed et al. (1979) relied on Landsat imagery to classify global sand seas. Dunes in major desert regions of the world were classified according to their external shape and slipface orientations as noted from Landsat imagery, Skylab, and aerial photographs. The types of dunes thus classified are, in order of global abundance, linear, crescentic, star, parabolic, and dome. Walker has carried forward this study of deserts and their associated sand seas in Chapter 8 of this volume.

Molnar and Tapponnier (1977) applied the synoptic views obtainable from Landsat imagery to the interpretation of the Himalayan and associated mountain ranges in the Tibetan plateaus of India and China (Plate T-48). They demonstrated that strike-slip faulting is pervasive throughout Tibet and southwestern China and might account for the suggested 2000-km northward movement of India into Eurasia during the last 40 million years. The key to putting this interpretation together was the ability to "see" the region from the vantage of space.

Brosse and Scanvic (1976) investigated the Villefranche-de-Rouergue zone in the southwestern portion of the Massif Central of France, using a variety of imagery obtained from satellites, stratospheric balloons, and aircraft at different scales and different spectral bands. Satellite imagery at a scale of 1:1000000 revealed a large regional ring structure within the Villefranche granite. Drawing on progressively larger scale imagery, Brosse and Scanvic mapped the orientation and distribution of fracture systems that are virtually unrecognizable on the ground owing to a lack of outcrops.

Lowman et al. (1986) used Landsat imagery (Plate T-15) to study fractures on the Canadian Shield in a test of the regmatic shear hypothesis, which suggests that the Earth's crust is fractured by a regular system of orthogonal shears resulting from global stress conditions early in the Earth's history. The results of the study, which included field investigation of some of the mapped fractures, demonstrated that the fracture patterns do not convincingly confirm the regmatic fracture hypothesis. They also found evidence in the patterns to suggest detachment and rotation of different regions of the shield at various times during the Precambrian.

Another recent study, involving Seasat Radar imagery (SAR), was published by John Ford (1984). It concentrated on the identification and classification of drumlins in Ireland (Plate G-19), as well as an examination of flow patterns in valley glaciers in Alaska. Ford was able to measure effectively the width/length ratios of drumlins. From this, he classified the drumlin fields into four categories: (1) subcircular hills, (2) broad ovoid drumlins, (3) long ovoid drumlins, and (4) ridges. The higher spatial resolution of the SAR (25 m compared to 79 m for Landsat) provided detail not visible on Landsat. Seasat imagery of Alaskan valley glaciers displayed medial moraines and variations of ice-surface roughness due to supraglacial till. This enabled Ford to decipher the flow patterns and flow history of glaciers such as the Columbia Glacier. Ford observed that repetitive radar imaging coverage facilitates a time-lapse record and would permit regional

ORIGINAL PAGE IS
OF POOR QUALITY

monitoring of glacial movements. RADARSAT, a Canadian system scheduled for launch in 1992, hopes to take advantage of this fact.

Robinove (1978) and Baker (1983) utilized repetitive coverage of specific regions from Landsat to demonstrate the usefulness of the imagery in evaluating catastrophic floods like that which occurred in the Coopers Creek drainage of Queensland and South Australia on February 6, 1974. A comparison of before and after images indicated that the floodplain in places was 60 km in width (Plate F-15). A similar study was applied to the Mississippi River flood of March 1973 by Morrison and White (1976).

Schneider et al. (1979) employed enhanced nighttime thermal infrared imagery from the Advanced Very High Resolution Radiometer (AVHRR) on NOAA polar-orbiting satellites to map drainage patterns and landforms over large areas at a spatial resolution of about 0.9 km. A geometrically corrected, computer-enhanced AVHRR image of North and South Dakota and the surrounding area obtained on the night of October 19, 1977, provides an excellent large-area portrait of the landforms and drainage of the region (Figure 12-2). The AVHRR detects transient surface thermal patterns, so that images obtained at another time of the year (e.g., wet versus dry seasons) might be quite different.

The Selima Sand Sheet in the southwestern desert near the border between Egypt and Sudan is a vast flat sand-covered region. Landsat views of the area disclose nothing unique about the region. Field observations also exposed little more than a flat featureless desert. However, in 1981, the SIR-A (Shuttle Imaging Radar) imagery indicated buried geomorphic detail never before seen (Plate I-3). The radar signal (23-cm wavelength) penetrated

through 1 meter or more of overlying dry sand to reveal an ancient drainage network trending to the southwest toward Lake Chad that must have rivaled the modern Nile in its discharge characteristics (McCauley et al., 1982). Recognition of the subsurface drainage was largely contingent on the presence of buried materials such as caliche nodules, having higher dielectric properties than dry sand, that mark the edges of the channels.

In September of 1983, during Space Shuttle mission STS-8, astronauts photographed a massive dust storm over northwestern Argentina (Francis and Rashka, 1983). Eolian particles, derived from fine-grained continental red beds and gypsum salt flats (salars) in the southern Puna, produced red and white dust plumes that could be traced hundreds of kilometers downwind. Documentation of these dust storms has confirmed the hypothesis that much of the landscape in this region is of eolian origin. It also identified the probable source of the loess that mantles the Argentine Pampas and demonstrated that the silt accumulation is an ongoing process (Bloom, 1985).

Detailed studies of the geomorphic features of the ocean floor at synoptic scales are only just commencing as oceanographers and marine geologists develop new technologies appropriate to operation in a marine environment. The recent development of narrow-beam echo-sounding equipment coupled with computer-controlled swath-mapping systems and the development of high-resolution deep-towed side-scan sonar such as GLORIA (Geological Long Range Inclined Asdic) and SeaMARC I and II (Sea Mapping and Remote Characterization) hold forth the promise of a rapid increase in accurate and detailed knowledge of the deep ocean floor (Bryan, 1985).

Between 1969 and 1980, the British Institute of Oceanographic Sciences obtained sonograms of more than 1 percent of the ocean floor using GLORIA, a long-range side-scan sonar instrument operated in much the same way as a spaceborne radar imaging system (Laughton, 1980). High-quality acoustic backscatter pictures were secured from a variety of terrains on both the continental shelf and the deep ocean floor. Recognition of numerous volcanic features, such as the Taney Seamount west of California (Figure 12-3), has been possible with such systems.

Damuth et al. (1983, 1985) used GLORIA to investigate the Amazon deep-sea fan on the continental rise off the coast



Figure 12-2. A NOAA AVHRR nighttime thermal image (October 19, 1977) of much of North and South Dakota and part of the southern Canadian Great Plains. The Missouri River roughly divides the left and right sides of the image. Lakes Manitoba and Winnipeg are in the upper right corner. Note more dissected plains terrain west of the Missouri River, with the image equivalent to approximately 900 km.

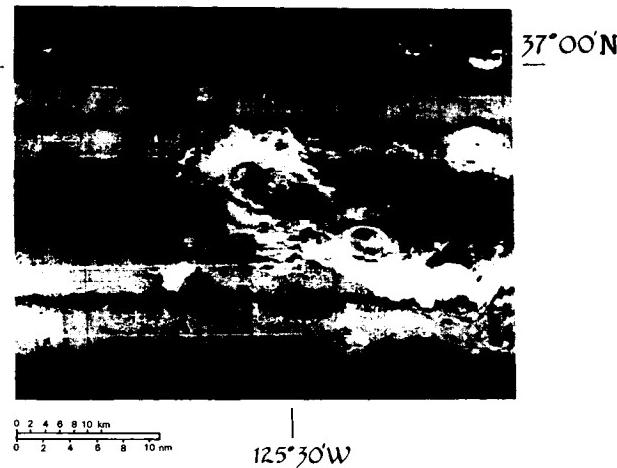


Figure 12-3. GLORIA sonogram of the Taney Seamount west of the California coast (courtesy of J. V. Gardner, USGS).

of northeastern Brazil. They discovered a complex of meandering channels, levees, and oxbows comparable in size and appearance to those of mature fluvial systems on land (Figure 12-4). Development of such a complex would seem to require conditions similar to those found in meandering fluvial systems on land, including a relatively continuous high-volume flow of sediment through the channels. This is contrary to the traditional view that deep-sea fan features result from intermittent turbidity flows.

SeaMARC is a combination side-scan sonar and bathymetric mapping system. It provides the means to construct ocean floor images at 10-m resolution and 10-km swath width (Blackinton and Hussong, 1983). Using images from SeaMARC I, McGregor and Lockwood (1985) mapped the extensively gullied South Wilmington submarine canyon and other features of the continental slope east of New Jersey (Figure 12-5). Hussong and Fryer (1983) combined SeaMARC II images into a photomosaic of a chain of submarine volcanoes in the northern Mariana island arc, deriving from this a bathymetric map with a contour interval of 100 m. They synthesized a consistent geologic interpretation based on integrated information from the mosaic and the bathymetric map. The SeaMARC technology has the potential not only for imaging the ocean floor but also for the analysis of the processes acting to form the observed features. Another important contribution to global submarine geomorphology was the demonstration by Marsh et al. (1985) that variations in ocean surface topography mapped from high-resolution Seasat altimeter data are expressions of gravitational differences related to sea-bottom morphology and hence tend to mirror most of the major seafloor landforms and topographic features such as mid-ocean ridges (Figure 12-6).

QUANTITATIVE GEOMORPHOLOGY FROM SPACE

The regional analysis of the Earth's surface by overhead observations came into its own with the routine acquisition after World War II of aerial photography—especially effective when quality aerial photomosaics were end products (see Figure T-2.2 for an example). From the vantage of space, astronauts and cosmonauts, during early orbital missions, took photographs of

ground scenes that covered significant parts, or even all, of physiographic provinces. Unmanned Earth-observing satellites have given us almost complete visual coverage of the terrestrial surface in image format at scales and resolutions that permit them to supplement, or even substitute for, aerial and space photography. This large-area coverage offers new approaches to interpreting the evolution of landscape by integrating collections of landforms, rather than individual ones, seen in context with one

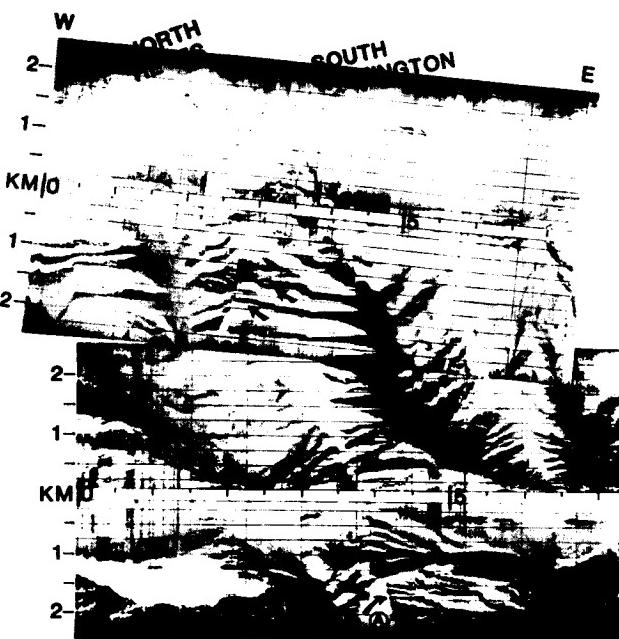


Figure 12-5. SeaMARC I sonogram of the South Wilmington and North Heyes submarine canyons east of New Jersey (courtesy of B. McGregor, USGS).

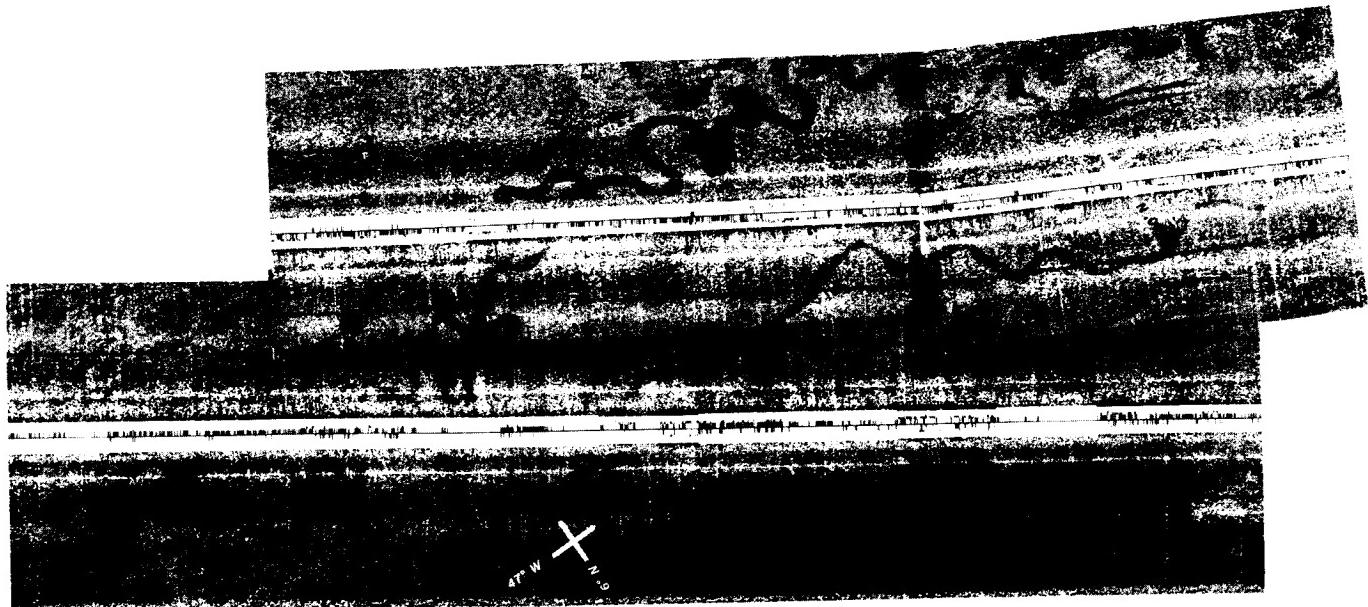


Figure 12-4. GLORIA long-range side-scan sonograph mosaic showing meandering distributary channels on the Amazon deep-sea fan (Lamont-Doherty Geological Observatory of Columbia University).



Figure 12-6. Surface topography of the world from Seasat Radar, imaging the underlying morphology of the seafloor (courtesy of J. Marsh, Goddard Space Flight Center, NASA).

another and with the various processes acting over a broad region. However, the main uses of both aerial and space imagery have been limited thus far to getting a "mental picture" of the landscape as an overview and as aids in making geologic and other types of maps describing and classifying the underlying geologic units, their structural states, and their topographic expression. Specifically, in geomorphology, most quantitative measurements from aerial photographs have been directed toward drainage network definition, determination of slopes and other geometric parameters, and change detection resulting from certain dynamic processes (e.g., shifting sand seas). Rather surprisingly, quantitative geomorphic analysis of assemblages of landforms seen advantageously in space imagery has not yet come into its own—a conclusion reached from any literature survey of results from the Landsat, Seasat, and other satellite or airborne sensor systems developed for terrestrial observations, and strongly inferred in several working group summaries at the Tucson Workshop.

As implied in the opening section, and aptly summarized by B. Lucchitta (1983, p. 1905), regional geomorphic analysis from space, incorporating quantitative measures as a prime method for both data gathering and information extraction, has been far more extensively applied to geological investigations of other planetary bodies. Most such planetary exploration begins with observations of a planet's *surface*, sometimes initially through a telescope, and eventually from orbiters with imaging instruments. As in the case with Landsat, the most *obvious* surface features first perceived by any interpreter of planetary imagery are landforms and related geomorphic phenomena. Using the method of *comparative planetology*, those landforms that seemingly have terrestrial counterparts are identified and analyzed. This allows deductions concerning processes that acted to develop them to be drawn. Maps of the planetary surfaces are produced by photointerpretive techniques; these maps tend to be a mix of landform types and stratigraphic units whose sequential relations and relative ages are assessed by principles of superposition and crosscutting (especially on planets where the effects of impact cratering remain dominant) and by crater (frequency) counts. Fields of view, scales, and resolutions for the surface im-

ages are similar in range to those acquired from Earth-observing satellites. A variety of sophisticated mensuration techniques has evolved over the years to extract quantitative data needed to improve our understanding of the nature, origin, and history of planetary bodies. This mode of planetary investigation has assumed great importance because, in nearly all cases, the chance to significantly increase the scope of knowledge through traditional ground studies (particularly with rock sampling) has of necessity been very restricted (even the manned and unmanned excursions on the lunar surface have touched only a tiny fraction of the Moon's surface). Thus, quantitative geomorphology as applied to large areas has taken a vital role in *extraterrestrial* exploration; the ability to conduct onsite field studies over most of the Earth's land areas has probably impaired the application of quantitative techniques to space imagery simply because measurements can usually be made by other means (notwithstanding the fact that *some* measurements can be carried out more rapidly and inexpensively on the space products).

At this point, a definition of quantitative geomorphology is in order. In an excellent review paper on "Development of Quantitative Geomorphology" for the Centennial Special Volume 1 published in 1985 by the Geological Society of America, Marie Morisawa defines this subfield of geomorphology as "the application of mathematics and statistical techniques to the study of landforms, their description and the processes by which they are created and changed. It includes also the application of physical and chemical theories to the analysis of landscapes." Morisawa further states that measurements by themselves do not constitute a quantitative study. Rigorous statistical treatment of data, scaled-down analog modeling, computer simulations, and systems analysis procedures can enter into the quantitative treatment of a geomorphic problem. Quantification of landform characteristics by means of *morphometry* has become a standard approach.

In Morisawa's summary of the historical origins of modern quantitative geomorphology, she states that the "quantitative revolution . . . dates from the publication of Horton's classic paper in 1945" in which some innovative methods for analyzing

the development and functional systematics of drainage basins were devised and tested. These included stream network topological analysis, dimensional analysis, and an ordering methodology. This "revolution," supported by other quantitative studies in the early postwar period, in effect refocused the scale and scope of approach to landforms analysis downward from the "large area" or "regional" level of Davis, Penck, and others to the more manageable dimensions of study sites as small as quadrangles, segments of stream valleys, and even small clusters of individual landforms. Because of a strong dependence on measurements close-in or at a limited number of scattered sample sites, the emphasis shifted to studies in the field over areas that were commonly much smaller than geomorphic provinces. "Regional" gradually was supplanted by "local."

During the last 40 years, geomorphologists and physical geographers have concentrated much of their research on aspects of landform development that depend heavily on appropriate quantitative measures and tests. Most studies are process-oriented. The list of quantitative techniques and accomplishments from their use is long and impressive, as succinctly surveyed by Morisawa (1985). Some selected examples suffice here to illustrate the kinds of studies that typify the present state of quantitative geomorphology:

1. Measurement of rates of overland flow
2. Relation of channel morphology to sediment transport
3. Verification of Horton's Laws
4. Topological characteristics of tributary/mainstream junction angles
5. The graded stream as an open steady-state system
6. Changes in slope angle, profile, and other geometric properties with time
7. Thresholds of slope failure; rates of downslope movements
8. Quantitative controls by sand supply, wind strength, and vegetation on dune formation, shape, and migration
9. Effects of ice dynamics on drumlin (streamlining) shape
10. Geometry of beachforms as functions of wave dynamics, sediment load, etc.

Some of these quantitative outputs have a feedback influence on other fields of geology. For example, a mainstay of tectonic geomorphology involves time-dependent measures of modifications of Pleistocene/Holocene fault scarps and related nearby surficial changes to deduce some indication of the time intervals between slip events. This can be translated to an estimate of frequency of recurrence of major earthquakes, a topic of extreme concern both to seismologists and to earthquake engineers.

Perusal of the foregoing list and other examples cited by Morisawa leads to the conclusion that some, perhaps most, of these conventional quantitative studies are not "do-able" primarily, if at all, through space observations or, for that matter, through the use of aerial photographs. They depend essentially on ground-based procedures and commonly require site access for collection of materials, gaging of rates, and intimate inspection of telltale signs at the outcrop level. There are exceptions of course: stream network analysis, dune migration patterns and rates, beachform transitions, and others can be done directly or at least can be assisted by the instantaneous samplings of surface appearance afforded by aerial and space images. Furthermore, repetitive coverage facilitates measurements of time-dependent

changes in morphology of assemblages of landforms over areas or even regions rather than isolated points.

The question now becomes this: Does the paucity of reported studies of landforms using space imagery as a data base for quantitative measurements imply some inherent shortcomings or limitations in the type of data source? If the answer is no, the logical followup question is: What kinds of meaningful measurements can be done and, a corollary, must improvements be made in the imagery (mainly in the sensors that acquire the data and the processing that generates the end products) to entice geomorphologists to start utilizing the space observation data in a more quantitative way? Neither question is resolved in this book. No master plan for carrying out constructive measurements and devising new models is put forth. But, perhaps, the way(s) to introduce quantification will be suggested to interested geomorphologists by the pictorial and descriptive overviews of regional landforms that are the theme of the gallery chapters and are touched upon in Chapters 1 and 11. In short, although the full potential for quantitative studies of landforms from space has yet to be demonstrated, it is hoped that this book will inspire the geomorphology community to begin to develop appropriate approaches to image analysis that rely on effective measurements.

Some work along these lines, carried on in the past several years, offers clues to what can be done with quantitative geomorphology at the regional level and how to go about it. A few examples with illustrations should clarify this issue.

Most likely, the key component in future quantitative studies of space imagery and other relevant kinds of data at regional scales will be the computer—a tool at last coming into its own for geomorphic analysis. Although some measurements can be extracted from space or aerial images (usually as transparencies on a light table) by employing customary photointerpretive methodology, much more information ultimately can be gleaned through computer processing. Surface data retrieved by remote sensors, especially scanners or CCD-based multilinear array detectors, are digitized on board space platforms and received in that mode, or if sent back as analog signals, these data too can be digitized; even photographs themselves can be converted by digitizing sensors (either line scanners or vidicons) any time after acquisition. In any case, the result is a sequence of numbers representing the sensed scene. For a Landsat image, these consist of an X-Y array (in successive raster-like scan lines) of sample points called pixels (*picture elements*), each containing some measure of a quantity (normally *radiance*, either as reflectance or emittance) emanating from an area on the Earth's surface. When played back by an image-recording device, the digitized quantity values (commonly displayed on film as density variations (gray levels)) in their correct spatial positions produce a "picture" composed of spatial patterns defined by varying gray tones or by colors if multispectral image sets are superimposed and projected through color filters. More details about these fundamental ideas of image production from remote sensor data are reviewed in Appendix A. The main point to master now is that modern sensing technology can quantify geomorphic features seen at a distance—from which many kinds of numerical manipulations may then be executed.

Since most geomorphologists still feel more comfortable with pictures or images, one group of optional operations on these numbers during image processing will often be beneficial to their needs. These come under the category of *enhancement techniques* and include contrast-stretching, density slicing, and spatial filtering. To elucidate the value of enhancement in revealing more geomorphic details, consider the examples of spatial filtering presented in Figures 12-7a-d. Other, more specialized operations are described by such terms as ratioing, principal components analysis, differencing (for change detection), and geometric corrections. Mapping of varieties of features or classes (landforms, geologic units, landcover types, etc.) can be carried out by statis-

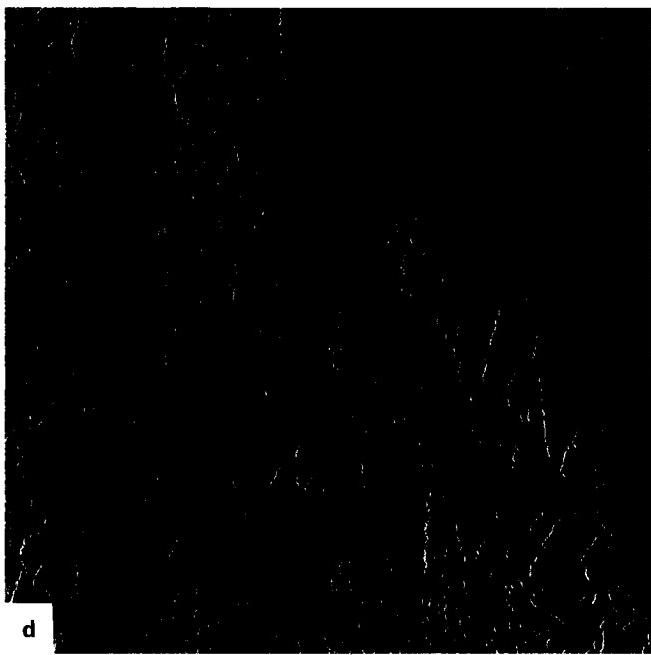
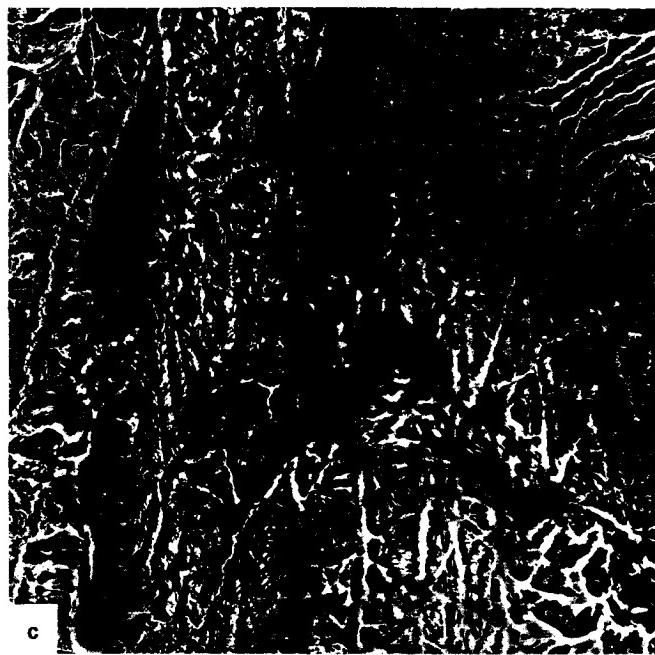
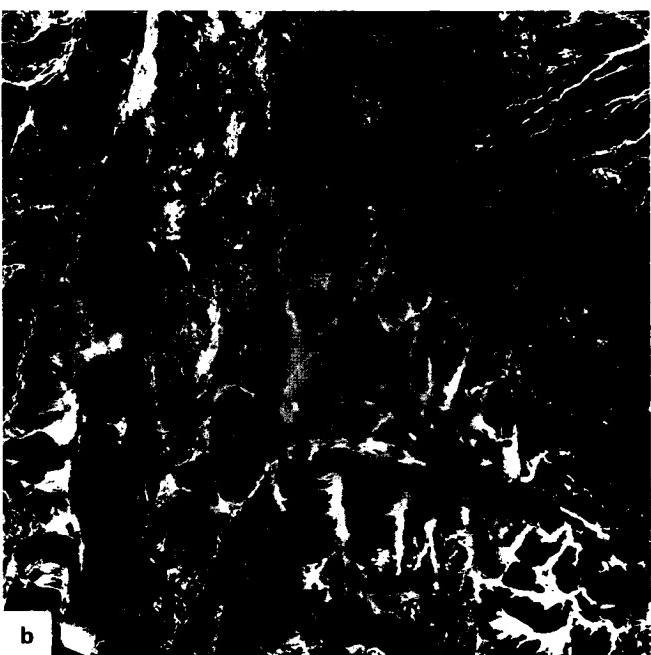


Figure 12-7. (a) Part of a Landsat-1 scene (1342-07430-7) of an area in southwest Jordan (see Plate F-4) that has been contrast-stretched by computer processing; (b) the same scene after data have been high-pass filtered (101 by 101 pixel box); (c) modification of the scene by further filtering (31 by 31 box); (d) generation of an edge-enhanced image of the Jordanian scene by the horizontal derivative method. Images courtesy of P. Chavez, Jr., U.S. Geological Survey, Flagstaff, Arizona.

tically based classification procedures. Several of these operations are discussed at some depth in Appendix A. Still other techniques, collected under the heading of *pattern recognition*, an automated approach to identifying objects and classes by their spatial configuration, boundary characteristics, contextual surroundings, tonal and textural aspects, and sizes, can in principle be adapted to discriminating, recognizing, and interrelating geomorphic entities. All of the above are directed toward a prime goal—to make

the information in the data (be they numbers alone or in images) more obvious, more accessible, and more amenable to integration with other types of data.

Data merging promises to open up new horizons in geomorphic analysis. Consider the following four examples. First, topographic maps can easily be digitized, storing elevations and other information for ready retrieval to reproduce the maps, as well as to create derivative maps. Computer routines exist to plot the

contours in a quasi-three-dimensional mode with the ability to rotate the resulting scene into any aspect or perspective desired. Or, images resembling shaded relief maps can be generated from digital terrain tapes, in which not only aspect but also direction and angle of illumination might be varied (Figures 12-8a-b). New information is presented in each individual rendition. This technique works especially well in emphasizing fractures and other types of lineaments inasmuch as linear features oriented perpendicular to the illumination direction (particularly at low angles) are highlighted relative to those features progressively more aligned to that direction.

The second example illustrates how a Landsat image can be converted into a format "dear to the heart" of any geomorphologist (i.e., one capable of being viewed in relief or three dimensions). Again, using digital elevation tapes, the Landsat pixels are individually shifted in position proportional to some slope function derived from the merged elevation data to yield a second image in which the perspective is equivalent to that of a stereo pair. This pseudo-stereo product (Figure 12-9a) can be made from any kind of data set that can be contoured. Thus, a sense of relief on a Landsat pictorial background is generated in Figure 12-9b from contoured thermal data; gravity, aeromagnetic, subsurface structural data are also treatable in this way.

The third case combines elements of the first two (Figure 12-10). Here, a small part of a Landsat scene of the Alaska Range has been altered into the three-dimensional state and then viewed obliquely, as though one were photographing the scene from an aircraft. Now at last, the geoscientist can take an aerial reconnaissance field trip from the comfort of a laboratory desk chair seated before a monitor—a simulated flight through the Grand Canyon has been produced by computer that engenders the stunning illusion of actually being airborne.

The last example describes a derivative map made from digitized terrain data but one that also can be constructed from calculations of slope steepness using stereo data from such systems as the French SPOT, the Large Format Camera, or the limited sidelap coverage from Landsat. Figure 12-11a is a shaded relief map generated from 1-km² resolution cell elevation data contained in digitized (NOAA) 30-sec topographic elevation tapes. The area shown includes several accretionary terranes in and around the Klamath Mountains of southwest Oregon. In Figure 12-11b, several ranges of slope steepness have been assigned levels of gray. The resulting pattern instantly singles out sections in the region with topographic ruggedness quite different from other

sections. These differences are in part related to the varying resistances of underlying geologic units to erosion and to their structural configurations, both in turn governing to some extent the elevations of the terrains, the gradient-influenced energetics of stream-cutting, and the interactions between mass-wasting and slope stability. These patterns can be compared (e.g., by overlaying) with other types of (digitized) maps (themselves reducible to patterns with varying degrees of detail), including maps of accretionary terranes. Explanatory correlations may then be made by "eyeball" or, better yet, through statistical tests to assess the contributions of pertinent variables to disclose other relations.

When analyzed together, multiple sets of data, including different thematic maps, are valuable aids to geoscientists in better understanding geologic phenomena—particularly process interactions and genetic factors associated with such diverse subjects as orebody formation, location of oil pools, likelihood of earthquakes or volcanic eruptions, trends in sedimentary facies variation, and distributions of multiple intrusions. Some of these topics are practical in nature and involve economic decision-making; others are more strictly scientific. The rapid growth of computer technology in the last decade has fostered a new systems approach to handling and integrating diverse data sets. (In the past, maps of several kinds for the same area were simply spread out side by side on a table and compared visually back and forth.) This approach frequently is referred to as a *Geomorphic Information System* or GIS (see Chapter 7 in Short, 1982). Any map showing some type of information about the Earth's surface or interior horizons can be subdivided into location cells (referenced to X-Y or X-Y-Z space), and information presented by the map pertaining to each cell can be encoded into a data base. Each map can be reconstructed and manipulated on a computer display; in some instances, direct overlays of one or more maps can be superimposed on a selected base map. More important, entirely new types of maps can be generated from varieties of data in the location cells. For practical uses, these maps serve as the end products of a decision-making or interpretation process; for example, a *suitability* map might pinpoint the optimum places to drill for ground water. Essential to their use is an appropriate mathematical or conceptual *model* that draws on the varieties of data available to execute the process. Figure 12-12 is a simplified example of a GIS analysis that uses multivariate data to define the best (highest numbers) place(s) for some type of site selection. In Figures 12-13a-c, three examples of theme or ordinal ranking maps of geomorphic relevance, as generated from a multiple data

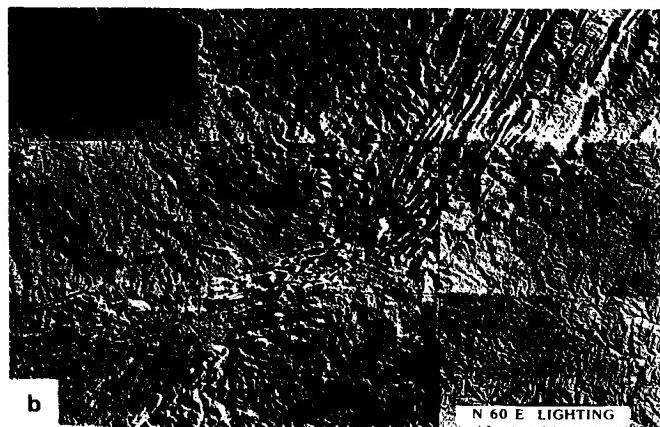
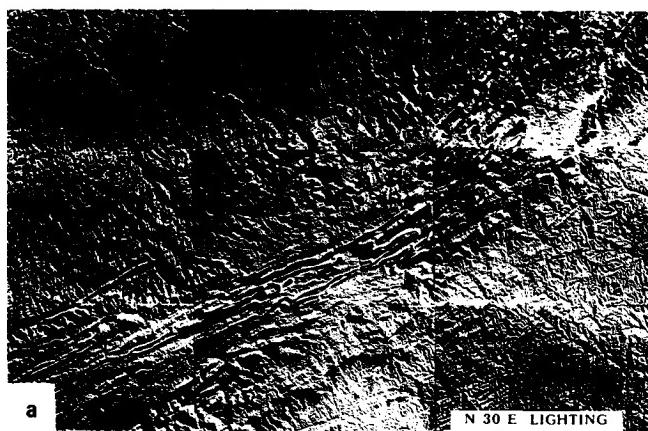


Figure 12-8. (a) One of a pair of images of the southern Appalachian Mountains around Roanoke, Virginia (see Figure T-11.5) made by photographing a mosaic of raised relief maps that are illuminated from the side (obliquely) from different azimuths (here, N30°E) and elevation angles to enhance certain linear directions; (b) same as (a) except that illumination direction is from N60°E (Wise et al., 1985).

base and color-coded for image output, illustrate the power of the GIS approach. The potential of a GIS for conducting various geomorphic analyses in a systematic, quantitative way should be almost self-evident. The role of space imagery in such a system is twofold. First, the images are often the best data base on which to fold in data of other kinds for display. Second, updates over time, yielding multitemporal data, are often needed in many kinds of studies, including some of a geomorphic character; continuously operating observatories such as the Landsats since 1972 provide both a time base for comparison and a constant source of new, timely data.

This section of the chapter has been included to convince the reader of just one straightforward idea: space imagery (and attendant data) offers exceptional possibilities for expanding (or, more frankly, returning) quantitative geomorphic analysis to a regional level, especially in view of the new computer technologies now evolving (e.g., incorporation of *expert systems* (in the field of Artificial Intelligence) to improve decision-making capability). Future studies of *Geomorphology from Space* will lead to a higher quality of results as this approach is followed.

NEW DIRECTIONS FOR GEOMORPHOLOGY

"One of the lessons from space is to 'think big'" (Sharp, 1980). This expresses a major new direction for geomorphology, the "global perspective," which ought to complement existing knowledge from meso- and micro-geomorphic investigations. At the Tucson Workshop, four concepts provided an investigative framework pointing the way toward future directions in geomor-

phology. These are: (1) Global Geomorphology, (2) Inheritance and Evolution, (3) Process Thresholds, and (4) Planetary Perspectives. These concepts are not inherently independent of one another, but form interconnected themes for approaching the future of geomorphological research. The Tucson Workshop agreed on a number of major questions around which global concerns should be centered (Douglas, 1985). Eight of these are discussed below.

The first four questions deal with the Earth's surface from an essentially static aspect, whereas the next four require sequential imaging to detect changes over time. The last of these addresses a state of the Earth that no one wishes to observe except as demonstrated through an artificial scenario. This question of effects of nuclear war on surface environments was only alluded to at the Tucson Workshop, but it remains one of potential significance in this age of atomic weapons. All of these questions are prone to solutions that fall back on space technology to give a global perspective—in other words, viewing the Earth as a single complex dynamic system—a planet.

1. *How does the surface of the whole Earth look at the planetary scale?* The key words here are the "whole Earth" because we must include the ocean floor for which there still is only rudimentary knowledge with respect to detailed surface morphology. GLORIA, SeaMARC and Seasat are the pioneer systems that will contribute to a global view.

2. *What are the significant major landform units to consider in mega-geomorphologic mapping, and how do these units*



a



b

Figure 12-9. (a) A pseudo-stereo pair for a segment of the Atlas Mountains of Morocco (see Figure T-30.4) produced by merging digital topographic data with digitized Landsat data; (b) a merge between digitized thermal data (daytime temperatures) obtained by the HCMM satellite and the same Landsat image seen in (a); compare stereoscopically the apparent relief from thermal variations with the exaggerated natural relief derived from the topographic data set.

ORIGINAL PAGE
COLOR PHOTOGRAPH

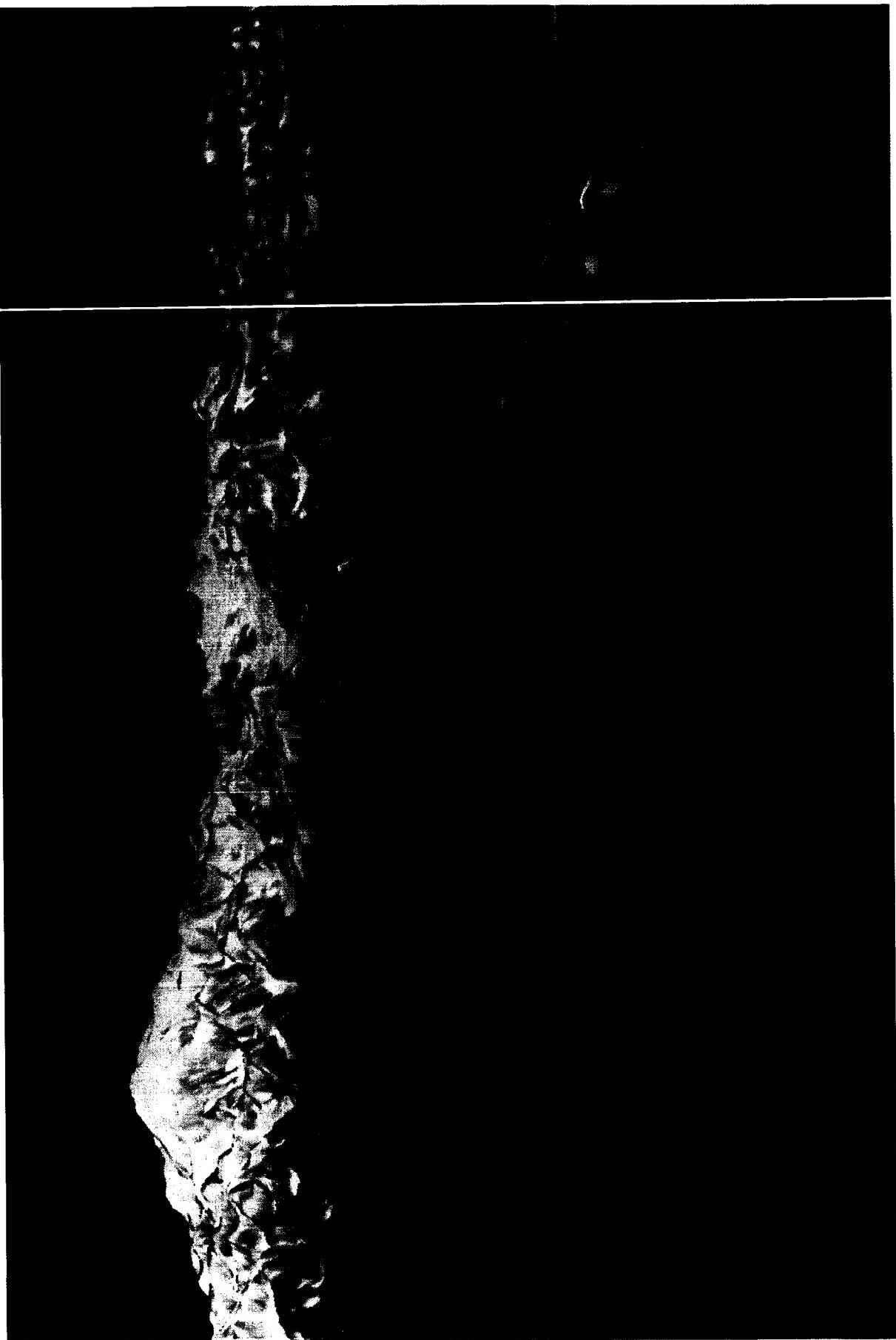


Figure 12-10. A computer-generated perspective view of Mt. McKinley as though seen from an elevation 4800 m above the Tokositna River in Alaska, produced by combining Landsat data with digital elevation data. Courtesy of National Mapping Division, U.S. Geological Survey, EROS Data Center, Sioux Falls, South Dakota.

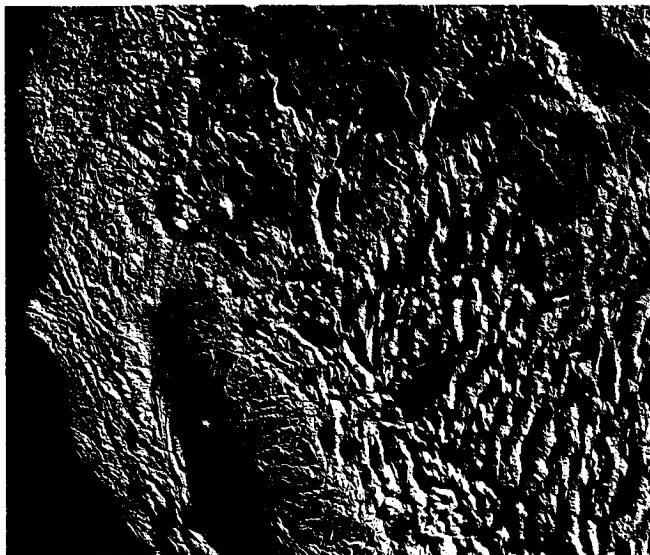


Figure 12-11a. A shaded relief map of parts of several states in the western United States produced from 1-km² cell data contained in digitized 30-sec topographic elevation tapes.

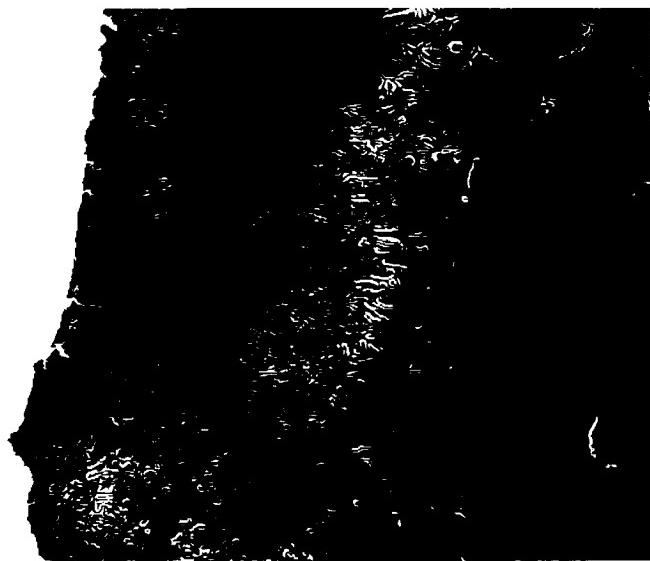


Figure 12-11b. A generalized slope steepness map (steeper slopes shown in lighter gray tones) for an area within the Klamath Mountains in Oregon, derived from the topographic data referred to in (a).

relate to their formation? The analysis of Earth's surficial features has by necessity been conducted from "the bottom up." Our understanding of the genesis of landforms is built up by extrapolating from field observations across boundaries of ever higher physiographic units (local, regional) to yield a synthesis of landform distribution at continental and global scales. So far, the global scale has been limited in achievable details to the 30 percent of the Earth's (land) surface exposed to direct observation. In contrast, the whole-planet approach used by planetary geologists has out of necessity proceeded from "the top down"

by progressively extending the global view into smaller regional segments as spatial resolution has improved. If the Earth were to be mapped using a "top down" approach, is it possible to identify large geomorphic units not heretofore recognized? The question of how local-scale information fits into the regional picture generated by the synoptic "top down" method has now become elevated in its importance. Both approaches must mesh if the new synoptic perspective of mega-geomorphology is to revolutionize the study of landforms.

3. Do landforms converge to some common type(s)? Some landforms may be produced by more than one cause. Perhaps the best examples of this are planation surfaces that may be formed by a variety of processes such as glacial, weathering, or marine. Globally, what is the distribution of these surfaces, and how do they relate to one another in terms of process and age? Can the principle of equifinality, which states that landforms from diverse processes tend to converge toward a similar form (von

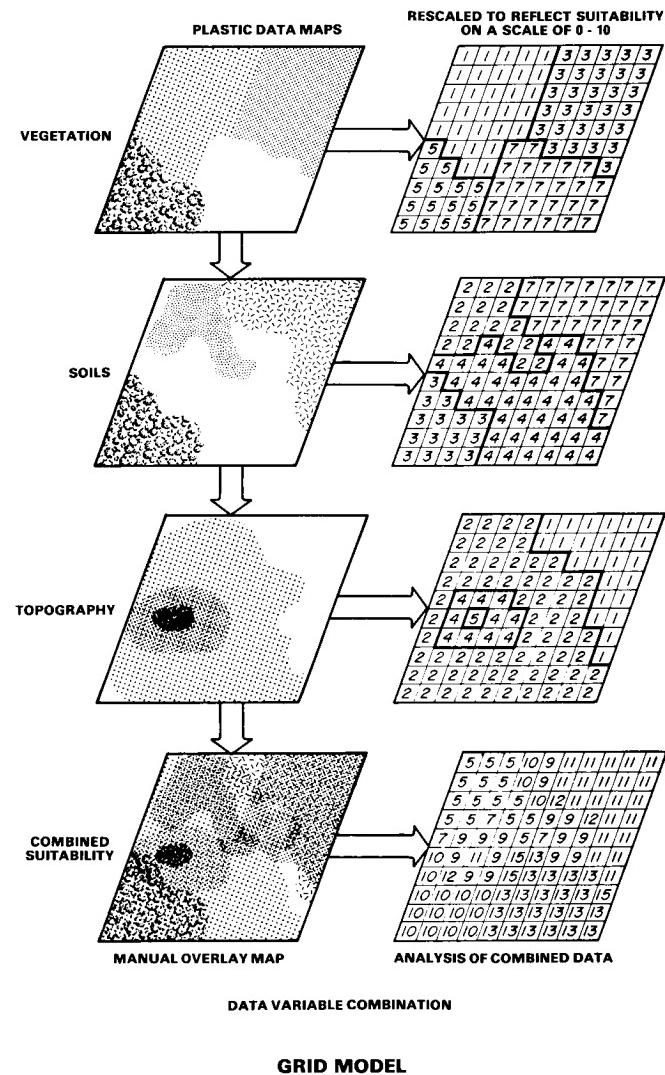
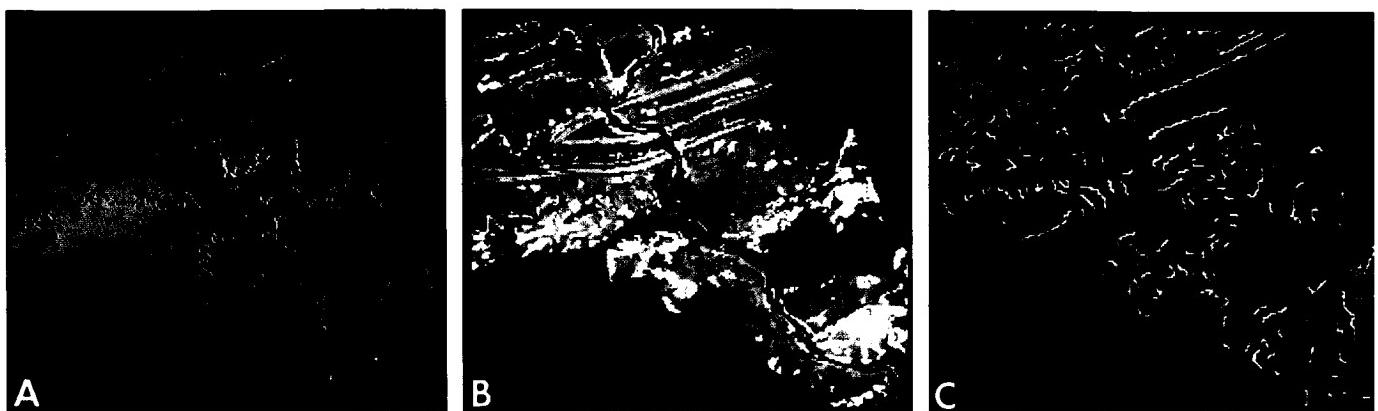


Figure 12-12. Diagram illustrating the steps involved in obtaining a Site Suitability map by conducting a Geographic Information System (GIS) analysis; 15 denotes maximum suitability (Short, 1982).

ORIGINAL PAGE
COLOR PHOTOGRAPH



a. Landforms

<i>Red:</i>	<i>Urban</i>
<i>Dark blue:</i>	<i>Water</i>
<i>Brown:</i>	<i>Plateau</i>
<i>Purple:</i>	<i>Mountain top</i>
<i>Dark green:</i>	<i>Steep slope</i>
<i>Light green:</i>	<i>Valley bottom</i>
<i>White:</i>	<i>Depression</i>
<i>Aqua:</i>	<i>Floodplain</i>

b. Slope

<i>White:</i>	<i>0-3 %</i>
<i>Light green:</i>	<i>3-8 %</i>
<i>Dark green:</i>	<i>8-15 %</i>
<i>Purple:</i>	<i>15-25 %</i>
<i>Yellow:</i>	<i>> 25 %</i>
<i>Red:</i>	<i>Urban</i>
<i>Dark blue:</i>	<i>Water</i>

c. Stream Order

<i>Dark blue:</i>	<i>1st order</i>
<i>Orange:</i>	<i>2nd order</i>
<i>Aqua:</i>	<i>3rd order</i>
<i>Light blue:</i>	<i>4th order</i>
<i>Yellow:</i>	<i>5th order</i>
<i>White:</i>	<i>6th order</i>
<i>Purple:</i>	<i>7th order</i>
<i>Red:</i>	<i>8th order</i>

Figure 12-13. Thematic maps produced by GIS processing of digital data in an electric utilities company information base and covering the area around Harrisburg, Pennsylvania (including the Susquehanna River and the Blue Mountain ridge of the folded Appalachians (Short, 1982)).

Bertalanffy, 1950; Chorley, 1962), be supported by space imagery? And, can the planation surfaces be distinguished from some depositional surface that may look similar?

4. What is the global extent to exogenetic and endogenetic landforms? For the first time, geomorphologists are in a position to accurately catalog the areal distribution of various exogenetic landforms such as sand dunes, regs, deltas, moraines, drainage basins, and karst topography and endogenetic landforms like volcanoes, faults, and various types of mountains. This task has yet to be done in the detail now possible with all the various types of imagery available for inspection. Today entire continents can be inventoried—tomorrow the ocean floor. Such a catalog is necessary to fully grasp the complex dynamics of global surface processes with time.

5. What is the relationship between climatic fluctuations and land-surface changes? The influence of climatic fluctuations on landforms has been considerable in a number of local situations, particularly in terms of droughts and floods. Repetitive satellite coverage can furnish valuable information on the broader significance of climate-induced changes and should also assist in making the important separation between man-induced effects and natural change.

6. Can the changes in geomorphic processes stemming from the modification of ground cover by human action be distinguished; if so, how? Man is a manipulator. He has influenced his surroundings from his earliest existence, but as technology has evolved, so has man's impact on the surface environment. Soil erosion, desertification, and deforestation, for example, are

three major problems confronting mankind in the next decades. At this time, only isolated studies and monitoring programs have been mounted to address the modification of ground cover. It is desirable to have in the immediate future a "global watch" program for overseeing and monitoring changes in vegetation as they occur upon our continents. Satellite monitoring is the key to this global watch.

7. What will be the geomorphic effects if half the world's population is living in cities by the year 2000? The world's population is doubling approximately every 40 years (Brown, 1984), and most of this occurs within the urban environment; thus, it is estimated that by the year 2000 over half of the world's inhabitants will live in urban areas. As population centers grow, a price must be paid in increasing pollution, more disturbance of natural runoff, greater strains on existing croplands, and a reduction in arable lands. Cities and their artificial environments place an ever-increasing demand on the world's resources. When combined, these changes and others will affect erosion rates, delta building, channel stability, weathering rates, and even the global climate through the increase in atmospheric carbon dioxide. With space-borne imagery, we are gradually acquiring a global data base, "a state of the globe," with which to make comparisons in the future to determine the rates and consequences of man's incessant bent for dominance of this planet.

8. What would be the outcome of a nuclear winter on the distribution and rates of geomorphic processes? God forbid that geoscientists should ever be placed in a position of having to evaluate the effect of a nuclear winter on the Earth. However, it would be prudent to develop a theoretical scenario if only to corroborate ongoing studies of the life-threatening and other negative events

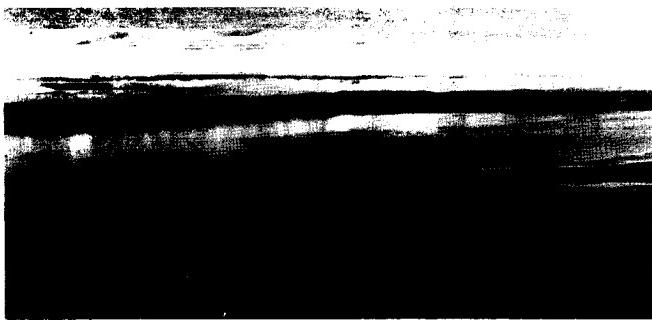


Figure 12-14a. Aerial photograph of Elgygytgyn Crater, north-eastern Siberia, U.S.S.R. (courtesy of B. Ivanov).

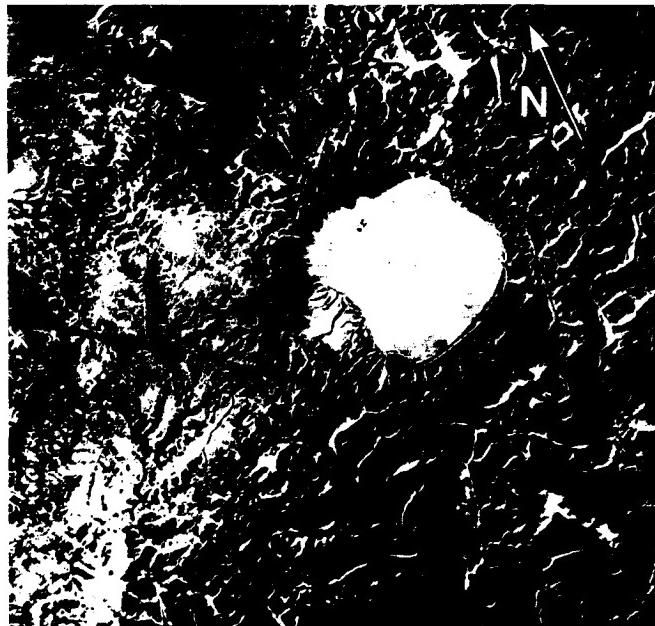


Figure 12-14c. Landsat MSS image of Elgygytgyn Crater and surrounding region.

that would follow a nuclear holocaust.* Because the effects would be global, the planetary perspective opens up a logical strategy from which to develop such a study.

A plausible analog to nuclear winter could come out of investigations of past climatic effects arising from the impact of large extraterrestrial objects (mainly asteroids), particularly those that excavate craters greater than 20 km in diameter. Recently, considerable attention has been focused on a number of Phanerozoic large-impact structures because of their possible causal relationship with major extinctions in the biological record (e.g., Cretaceous/Tertiary at 65 Ma and Eocene/Oligocene at 34 Ma; Silver



Figure 12-14b. Seasat radar image of Elgygytgyn Crater and the surrounding region.

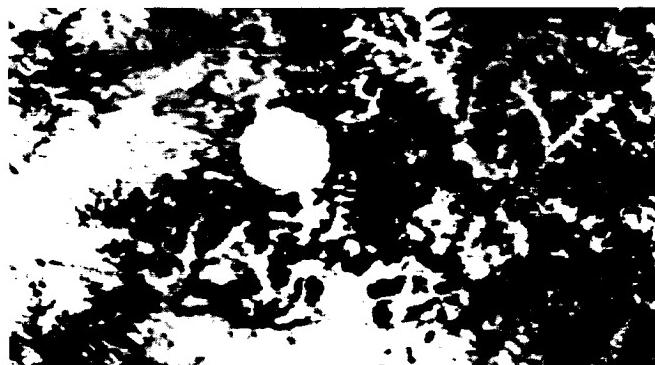


Figure 12-14d. HCMM image of Elgygytgyn Crater and surrounding region.

and Schultz, 1982). The most recent (approximately 3 Ma) large-impact structure is the Elgygytgyn crater in the Chukotka region of the far-eastern U.S.S.R. Although slightly glaciated, this 23-km diameter structure is reasonably well preserved for an Arctic landform. The crater is dominated by a fault-bounded rectangular lake approximately 18 km in width. Fieldwork by Gurov and colleagues (1979, 1982) has identified the diagnostic signs of a tremendous impact event, including high-pressure quartz phases and impact melt bombs. Attention was originally focused on Elgygytgyn when Landsat images suggested an impact origin for the remote feature (Dietz, 1977). Elgygytgyn is located above the Arctic Circle in an eroded volcanic terrain (Cenozoic tuffs and flows), several hundred kilometers from the nearest town. The four images in Figure 12-14 are views of the giant crater at different scales. The first (Figure 12-14a) is an oblique airphoto with a 1-m resolution. The other three were acquired from space-based systems. The 25-m resolution Seasat radar image (Figure 12-14b) provides comparable information to the 79-m resolution Landsat MSS image (Figure 12-14c). The HCMM scene (Figure 12-14d), at 500-m resolution, reveals less about the crater than

*An imaginative assessment of one geologic consequence of a full-scale nuclear war was devised by E. C. Prosh and A. D. McCracken, "Post-apocalypse Stratigraphy: Some Considerations and Proposals," *Geology*, 13, 4-5, January 1985.

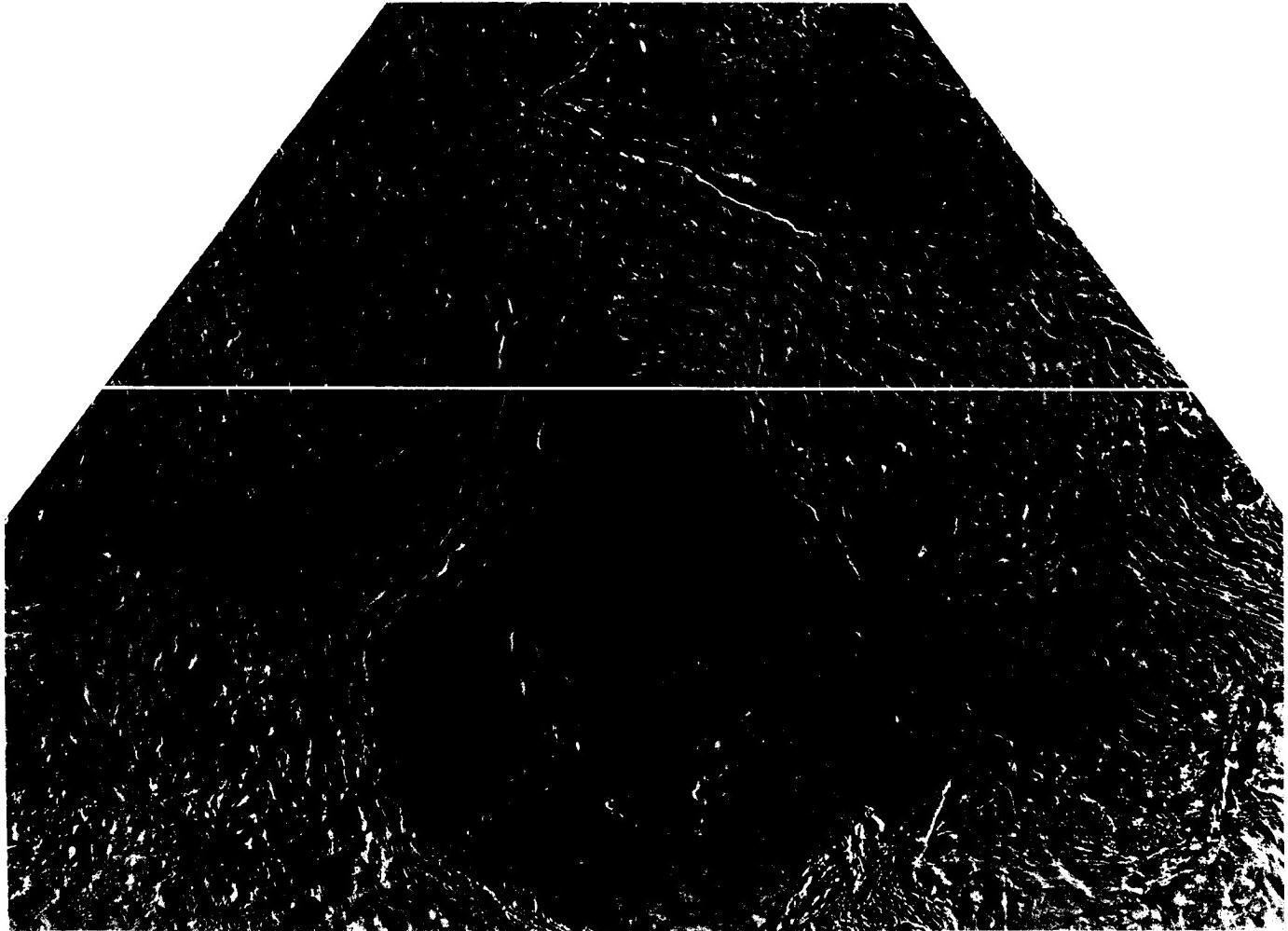


Figure 12-15a. Venera 15/16 radar image of Lakshmi Plateau and surrounding region of Venus.

it does about the regional erosional pattern. Impacts of the same magnitude as that which created Elgygytgyn could have produced transient "nuclear winters" that might have accelerated the onset of periodic global ice ages (Silver and Schultz, 1982). Analyses of available remote sensing data for the Elgygytgyn region (Garvin and Grieve, 1986) and the environs of other well-preserved giant impact features suggest that widespread climatic effects are not unreasonable in spite of the lack of extensive geomorphic effects. Even though many of the obvious geomorphic effects of large impacts can be eroded away in tens of millions of years (e.g., most of the surface ejecta around Elgygytgyn has been removed in only 3 Ma), impact craters retain some of their characteristic geomorphic expression for longer periods of time, attesting to the immense energies involved in their formation. Geomorphic studies of such structures at several scales could shed new light on catastrophic geologic events and their role in the geomorphological evolution of the Earth's surface.

Besides the questions related to global geomorphology, numerous other topics were addressed at the Tucson Workshop. For example, geomorphological studies of landscape evolution and inheritance have dwelled primarily on the Quaternary and Recent changes that are generally assumed to dominate most of the Earth's present landscapes. The workshop questioned this lat-

ter assumption by pointing out that landforms of great age are being recognized as more common and extensive than previously believed (Twidale, 1985). Ancient exhumed surfaces have been recognized in shield areas and in some of the older orogenic belts, where for part of their history, they remained buried until now reexposed by erosion. There are also epigene features, many of Mesozoic age, which had never been buried but have resisted alteration by weathering and other processes over very long time periods. Etchplains formed of resistant rock at a weathering front are more widely distributed than had been previously suspected. At the workshop, the point was raised but not answered as to whether space imagery can be used to assess the true extent of these ancient landforms and the reasons for their survival.

The concept of thresholds has increased in importance in geomorphological investigations (Ritter, 1985). The idea stems from the premise that boundary conditions exist within geomorphic systems beyond which different processes become dominant or existing processes change in rate and magnitude. For example, if pristine river water remains clear after running over a sandy bed, the boundary conditions leading to erosion presumably were not surpassed. But an increase in volume, gradient, or other factors, bringing about a rise in velocity, may carry the system across the threshold boundary conditions, causing sand particles to be

ORIGINAL PAGE IS
OF POOR QUALITY



Figure 12-15b. GLORIA sonogram of Charlie Gibbs Fracture Zone, an active transform fault on the Mid-Atlantic Ridge.

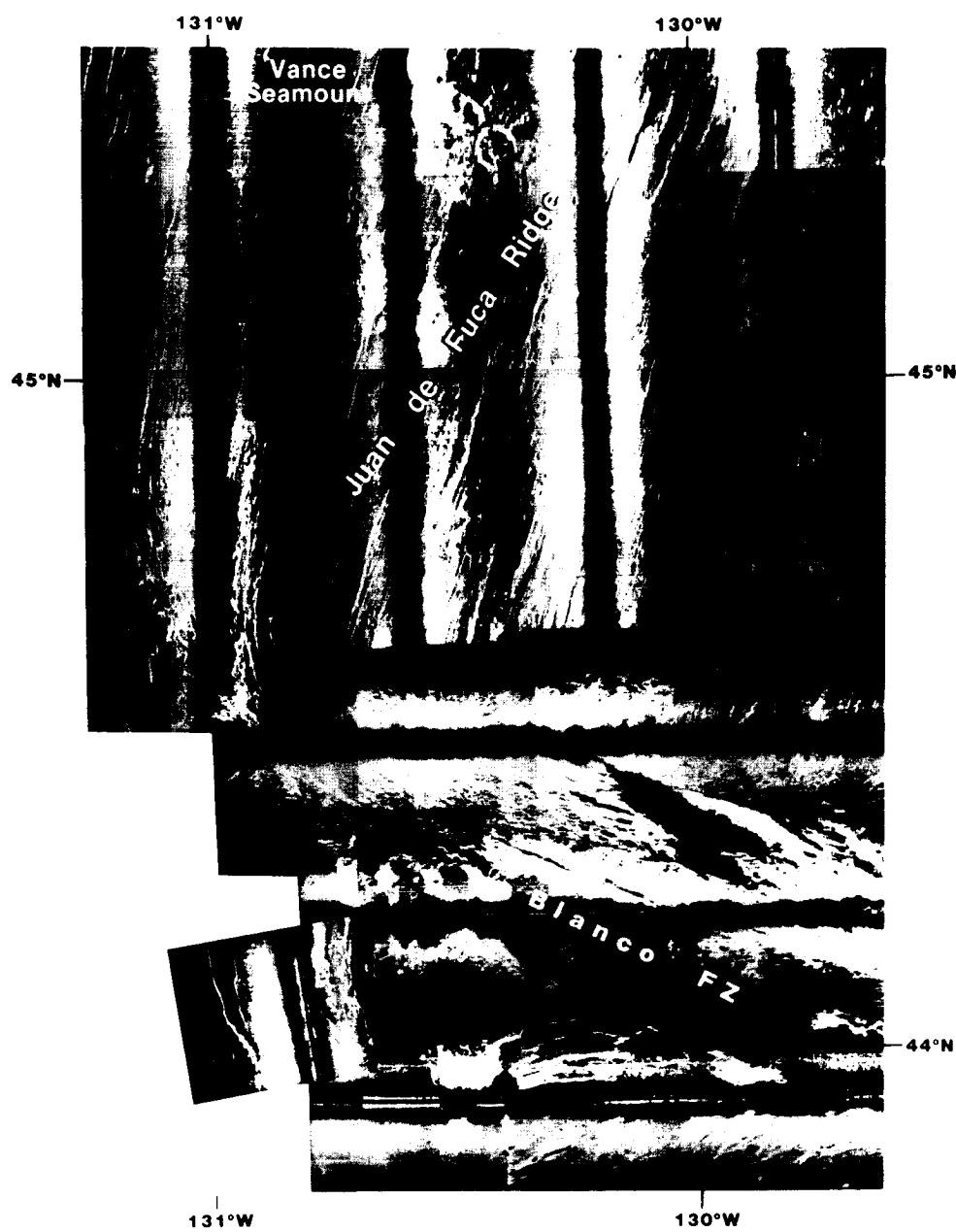


Figure 12-15c. GLORIA side-scan sonogram of the Juan de Fuca Ridge, Vance Seamount, and Blanck Fracture Zone off the Washington Coast.

picked up and moved. The perception of thresholds on a regional scale from space is a real challenge, but is not out of the question. For example, the Columbia Glacier near Valdez, Alaska (Plate G-11), has been retreating slowly for years, producing a moderate number of icebergs. Then, in 1981, a sudden increase in the production of icebergs, to such an extent that it jeopardized existing sea lanes (Kelly, 1981), forced some threshold boundary condition to be surpassed. In this instance, it was the unlocking of the Columbia glacier from a bedrock knob that had anchored and added stability to the ice stream. When unlocked, the snout of the glacier underwent an increased breakup rate with the fjord. Monitoring the iceberg density from space could have pinpointed the time of threshold change even had it occurred in some remote region of the world. The space perspective assists the investigator in observing where and possibly when threshold boundaries have been exceeded, but will probably not allow the scientist to determine the complex causes of the change without going into the field for closer examination. Although an indepth comprehension of thresholds and long-term geomorphic changes appears unattainable at present, geomorphologists can begin to initiate long-term experiments, some not coming to fruition for a century or more, that can nevertheless serve as an important contribution to future geomorphic research (Williams, 1985).

For geomorphologists to study the Earth from the planetary perspective, the effort requires more than the simple incorporation of satellite and other space imagery into their methods. The Tucson Workshop singled out the need for a fundamental philosophical change of direction so that, in the future, the Earth will be perceived as a planet like any other Solar System body (Rossbacher, 1985). Through exploration of the Moon and other planets of the Solar System, we have become aware of the immense variety of landform types, scales, and ages that exist. A major focus in the study of planetary landforms is the identification of terrestrial analogs, thus enabling investigators to adopt hypotheses pertaining to their origin and to the processes involved. Consider, for example, the recent Soviet radar imagery of the Lakshmi Plateau and its surrounding area on Venus (Figure 12-15a). This scene shows linear faults or fractures similar to terrestrial features such as the Charlie Gibbs Fracture zone, an active transform fault along the mid-Atlantic ridge south of Iceland (Figure 12-15b), and the Juan de Fuca Ridge and Vance Seamount

(Figure 12-15c) in the Pacific Ocean west of Washington State. However, it is dangerous to apply Earth-derived models directly to explain various planetary landforms because the other planets depart from the Earth in many important environmental parameters such as atmospheric bulk composition and pressure, water content and state, degree of tectonism, and lithologic materials. The images of the planets, however, have given us "snapshots" back into time of processes, such as impact cratering, that dominated the early Solar System and may have been intermittently important in more recent eras.

CONCLUDING STATEMENT

For almost as long as the human race has existed on Earth, people have expressed a curiosity about the nature of their surroundings. They have sought to learn more about the landscapes upon which they live and processes by which those landscapes formed and continue to evolve. Until recently, a person's view has been limited to what could be observed, on site, about the immediate surroundings. Moreover, the vistas were restricted to samplings of less than one-third of the total planetary surface seen normally from the ground up. Now new technologies growing out of space exploration, some of whose products are well portrayed by the illustrations in this book, offer exceptional opportunities to study and analyze the Earth from above. This takes advantage of the synoptic planetary view to gain new insights into the nature of Earth, its place in the Solar System, and the multiple processes by which its landscapes have been formed. With the new technologies for charting the ocean floor, the entire planet is being opened to careful scientific investigation. The challenge of the Earth Sciences is to make effective use of appropriate new technologies to gain the broadest possible understanding of the Earth and its features. In a world becoming more crowded because of the rapid expansion of the human population, with its concomitant threat to other creatures that share this planet with man, the study of geomorphology from space has a vital and exciting role to play in understanding more fully the nature of Earth. This promises assurance that habitability of land and sea can be preserved and enhanced for the future of all Earth's creatures.

REFERENCES

- Baker, V. R., Large-scale fluvial paleohydrology, in *Background to Paleohydrology*, edited by K. L. Gregory, pp. 453-478, John Wiley, New York, 1983.
- Baker, V. R., and H. W. Head III, Workshop Summary, Conclusions and Recommendations, in *Global Mega-Geomorphology*, edited by R. S. Hayden, pp. 113-120, NASA CP-2312, 1985.
- Blackinton, J. G., and D. M. Hussong, First results from a combination side-scan sonar and seafloor mapping system (SeaMARC II), paper presented at the *15th Annual Offshore Technology Conference*, Houston, Texas, May 2-5, 1983.
- Bloom, A. L., Andean examples of mega-geomorphology themes, in *Global Mega-Geomorphology*, edited by R. S. Hayden, pp. 44-45, NASA CP-2312, 1985.
- Breed, C. S., S. C. Fryberger, S. Andrews, C. McCauley, F. Lenhardt, D. Gebel, and K. Horstman, Regional studies of sand seas using Landsat (ERTS) imagery, *U.S. Geol. Surv. Prof. Paper*, **1052**, 305-397, 1979.
- Breed, C. S., and T. Grow, Morphology and distribution of dunes in sand seas observed by remote sensing, *U.S. Geol. Surv. Prof. Paper*, **1052**, 253-302, 1979.
- Brosse, J. M., and J. Y. Scanvic, Role de L'Echelle Dans L'Apport de la Teledetection en Geologie Structurale, in *Journees de Teledetection du G.D.T.A.*, Toulouse, France, October 25-28, 1976.
- Brown, L. R., Stabilizing population, in *State of the World—1984*, edited by L. R. Brown, pp. 20-34, Worldwatch Institute, Washington, D.C., 1984.
- Bryan, W., Deep sea mega-geomorphology: Progress and problems, in *Global Mega-Geomorphology*, edited by R. S. Hayden, pp. 54-55, NASA CP-2312, 1985.
- Chorley, R. J., Geomorphology and general systems theory, *U.S. Geol. Surv. Prof. Paper*, **500-B**, 10 pp., 1962.
- Damuth, J. E., and R. D. Flood, Amazon fan, Atlantic Ocean, in *Frontiers in Sedimentary Geology: Submarine Fans and Related Turbidite Systems*, edited by A. H. Bouma, N. E. Barnes, and W. R. Normark, pp. 97-106, Springer-Verlag, New York, 1985.
- Damuth, J. E., V. Kolla, R. D. Flood, R. O. Kowsmann, M. C. Monteiro, M. A. Gorini, J. J. C. Palma, and R. H. Belderson, Distributary channel meandering and bifurcation patterns on the Amazon deep-sea fan as revealed by long-range side-scan sonar (GLORIA), *Geology*, **11**, 94-98, 1983.
- Davis, W. M., The geographical cycle, *Geogr. J.*, **XIV**, 481-504, 1899.
- Dietz, R., Elgygytgyn Crater, Siberia: Probable source of Australian tektite field, *Meteoritics*, **12**, 145-157, 1977.
- Douglas, I., Report of the Working Group on Global Geomorphology, in *Global Mega-Geomorphology*, edited by R. S. Hayden, pp. 101-104, NASA CP-2312, 1985.
- Fenneman, N., *Physiography of Western United States*, 534 pp., McGraw-Hill, New York, 1931.
- Fenneman, N., *Physiography of Eastern United States*, 714 pp., McGraw-Hill, New York, 1938.
- Ford, J. P., Mapping of glacial landforms from Seasat Radar images, *Quaternary Res.*, **22**, 314-327, 1984.
- Francis, P. W., and D. Rashka, Space Shuttle studies of aeolian processes in the Andes, *EOS*, **64**, 745, 1983.
- Gardner, R. A. M., and H. Scoging (Eds.), *Mega-Geomorphology*, Clarendon Press, Oxford, 1983.
- Garvin, J. B., and R. A. F. Grieve, A remote sensing perspective of the Elgygytgyn impact crater (abstract), in *Proc. 17th Lunar Planetary Science Conf.*, pp. 251-252, L. P. I., Houston, Texas, March 17-21, 1986.
- Gelnett, R. H., and J. V. Gardner, Use of radar for ground water exploration in Nigeria, West Africa, in *Proc. 13th Internat. Symp. on Remote Sensing of Environment*, 1979.
- Gilbert, G. K., *Report on the Geology of the Henry Mountains*, 170 pp., U.S. Government Printing Office, Washington, D.C., 1877.
- Glass, B. P., *Introduction to Planetary Geology*, 469 pp., Cambridge Univ. Press, Cambridge, Massachusetts, 1982.
- Gurov, E. O., and E. P. Gurova, Some regularities of the areal spreading of fractures around Elgygytgyn impact crater (abstract), in *Proc. 13th Lunar Planetary Science Conf.*, pp. 291-292, L.P.I., Houston, Texas, 1982.
- Gurov, E. O., A. Valter, E. P. Gurova, and F. I. Kotlovskaya, Elgygytgyn impact crater (abstract), in *Proc. 10th Lunar Planetary Science Conf.*, pp. 479-481, 1979.
- Hack, J. T., Interpretation of erosional topography in humid temperate regions, *Amer. J. Sci.*, **258-A**, 80-97, 1960.
- Hayden, R. S. (Ed.), *Global Mega-Geomorphology*, 126 pp., NASA CP-2312, 1985.

- Hussong, D. M., and P. Fryer, Back-arc seamounts and the SeaMARC II seafloor mapping system, *EOS Trans., AGU*, **64**, No. 45, 1983.
- Kelly, D., Alaskan glacier speeds retreat and iceberg production, *U.S. Geol. Surv. News Release*, 3 pp., December 7, 1981.
- Laughton, A. S., The first decade of GLORIA, in *Annual Report of Institute of Oceanographic Sciences for 1980*, pp. 60–85, Great Britain, 1980.
- Lowman, P. D., N. M. Short, P. J. Whiting, A. M. Lohman, and G. Lee, Fracture patterns of the Canadian Shield: Implications for plate tectonics and the regmatic shear theory, in press, 1986.
- Lucchitta, B., Terrestrial analogs of extraterrestrial landforms, in *Manual of Remote Sensing*, 2nd Ed., Vol. 2, edited by R. N. Colwell, p. 1905, Amer. Soc. of Photogrammetry, 1983.
- Marsh, J. G., A. C. Brenner, B. D. Beckley, and T. V. Martin, Global mean sea surface based upon the Seasat altimeter data, *J. Geophys. Res.*, in press, 1985.
- McCauley, J. F., G. G. Schaber, C. S. Breed, M. J. Grolier, C. V. Haynes, B. Issawi, C. Elachi, and R. Blom, Sub-surface valleys and geoarcheology of the Eastern Sahara revealed by Shuttle radar, *Science*, **218**, 1004–1034, 1982.
- McGregor, B. A., and M. Lockwood, *Mapping and Research in the Exclusive Economic Zone*, 40 pp., Dept. of Interior, USGS, and NOAA, 1985.
- Molnar, P., and P. Tapponnier, The collision between India and Eurasia, *Scientific Amer.*, **236**, 30–41, 1977.
- Morisawa, M., Development of quantitative geomorphology, in *Centennial Special Volume I*, pp. 79–107, Geol. Soc. of America, 1985.
- Morrison, R. B., and P. G. White, Monitoring flood inundation in ERTS-1, in *A New Window on Our Planet*, edited by R. S. Williams, Jr., and W. D. Carter, pp. 196–208, *U.S. Geol. Surv. Prof. Paper*, **929**, 1976.
- Penck, W., *Morphological Analysis of Landforms*, translated in 1953 from the 1924 version by H. Czech and K. C. Boswell, 430 pp., Macmillan, London, 1924.
- Ritter, D., Regional landform thresholds, in *Global Mega-Geomorphology*, edited by R. S. Hayden, pp. 23–26, NASA CP-2312, 1985.
- Robinove, C. J., Interpretation of a Landsat image of an unusual flood phenomenon in Australia, *Remote Sensing of Environment*, **7**, 219–225, 1978.
- Rossbacher, L., Report of the Working Group on Planetary Perspectives, in *Global Mega-Geomorphology*, edited by R. S. Hayden, pp. 109–110, NASA CP-2312, 1985.
- Schneider, S. R., D. F. McGinnis, Jr., and J. A. Pritchard, Use of satellite infrared data for geomorphology studies, *Remote Sensing of Environment*, **8**, 313–330, 1979.
- Sharp, R. P., Geomorphological processes on terrestrial planetary surfaces, *Annual Rev. of Earth and Planetary Sci.*, **8**, 231–261, 1980.
- Short, N. M., *Planetary Geology*, 361 pp., Prentice-Hall, Englewood Cliffs, New Jersey, 1975.
- Short, N. M., *Landsat Tutorial Workbook*, 533 pp., NASA RP-1078, U.S. Govt. Printing Office, Washington, D.C., 1982.
- Silver, L. T., and P. H. Schultz (Eds.), *Geological Implications of Impacts of Large Asteroids and Comets on Earth*, 528 pp., GSA Special Paper 190, 1982.
- Twidale, C. R., Report of the Working Group on Landscape Inheritance, in *Global Mega-Geomorphology*, edited by R. S. Hayden, p. 105, NASA CP-2312, 1985.
- von Bertalanffy, L., The theory of open systems in physics and biology, *Science*, **111**, 23–29, 1950.
- Williams, R. S., Jr., Report of the Working Group on Process Thresholds, in *Global Mega-Geomorphology*, edited by R. S. Hayden, pp. 106–108, NASA CP-2312, 1985.
- Wise, D. U., L. T. Grady, and F. Salvani, Topographic lineament domains of the Appalachians: Some new methods and techniques for paleostress analysis, 1985 International Geoscience and Remote Sensing Symposium, Univ. of Massachusetts, *IEEE Digest*, **1**, 125–130, 1985.

EPILOGUE

Even as typesetting for this book neared completion, a dramatic event took place that promises to open up a new vista for the practice of geomorphological observations from space. On the night of February 21, 1986, in French Guiana along the Atlantic coast, a French Ariane rocket successfully launched a new Earth-observing satellite known as SPOT (Système Probatoire pour l'Observation de la Terre). This system is especially suited to the study of terrestrial landforms in the synoptic mode, already demonstrated as scientifically valuable from similar NASA missions, but with the added advantage of providing oblique and stereographic images of the Earth's surface. Developed by the Centre National d'Etudes Spatiales (CNES), France, in cooperation with Belgium and Sweden, SPOT will provide a variety of image and computer-compatible tape products to a worldwide community of users through two primary outlets—SPOT IMAGE of France (Toulouse) and SPOT Image Corporation (Reston, Virginia, U.S.A.)—as well as numerous SPOT distributors located in many countries of the world.

The SPOT satellite operates in a sun-synchronous, near-polar orbit at a nominal altitude of 832 km. Its repeat cycle over the same track is 26 days (yielding 369 tracks per orbital cycle). The next track immediately to the west of a given track is overflown 5 days after the adjacent eastern one. Local solar time in the descending node at the equator is 10:30 a.m.

The payload is a pair of identical sensors known as "high-resolution visible" (HRV) instruments. Each HRV covers a ground swath width of 60 km; operating side by side, the HRVs achieve an effective ground swath of 117 km (slight sidelap). The basic instrument consists of the technologically advanced "push-broom" scanner that comprises a linear array of 6000 charge-coupled device (CCD) detectors. All detectors (each representing a pixel in the resulting image) are activated simultaneously by incoming radiation; a mechanically oscillating mirror is not needed because the charge on each device is "read" electronically in sequence. An image is produced from the signals received from the CCD linear array as it moves forward in orbit to produce a succession of lines.

The HRV can function simultaneously in two modes: the panchromatic mode comprises a single band in the 0.51- to 0.73- μm range of the visible spectrum; the multispectral mode consists of three bands in the intervals 0.50 to 0.59, 0.61 to 0.68, and 0.79 to 0.89 μm (just within the near infrared). Separation of incoming radiation into these spectral bands is accomplished by a beam-splitter assembly at the focal plane. Effective resolution at nadir is 20 m for the multispectral mode and 10 m for the

panchromatic mode. The three-band mode permits registration of each band through color filters to generate a false-color composite.

An innovation on SPOT not found on the Landsats is a movable mirror that allows off-nadir viewing across track (normal to the orbital path) over an angular range of $\pm 27^\circ$. Movement is in incremental steps so that intermediate angles can be set. This pointable mirror capability increases the options for viewing areas within a 950-km wide corridor at greater frequencies than those allowed by the 26-day revisit cycle. Depending on latitude, an area can be imaged at least twice during a week (seven times per cycle at the equator; more often at higher latitudes). SPOT offers the first opportunity for global off-nadir imagery using a digital sensor. Judging from experience with hand-held photographs taken by astronauts, oblique images of Earth from space present yet another invaluable perspective for describing and interpreting landforms by their topographic signatures. This off-nadir function of the HRV also permits stereo imagery to be acquired. The same area is viewed at different angles from different orbits so that the two images constitute a stereo pair. Of course, this side-looking stereo will not match the registration and photogrammetric calibration obtainable from nadir-looking systems (e.g., the Large Format Camera). Likewise, cloud cover will frequently compromise the stereo expression of the scene, but the large number of passes over an area during the lifetime of the satellite ensure a high likelihood of obtaining stereo pairs with minimum cloud cover and at similar seasonal times. Eventually, stereo coverage of nearly all of the Earth's land surface is now a realistic possibility before the end of this century.

SPOT has already obtained a large number of scenes of much of the world. (Data are telemetered (downlinked) in real time to some receiving stations already on line; tape recorders permit data acquired outside the station range to be sent back later.) Those shown on the next two pages are indicative of the products offered by SPOT. Of special interest to all geomorphologists are the stereo images of an African site. Compare this set to the computer-generated stereo image from Landsat shown in Figure 12-9a.

The emergence of SPOT on the international scene represents still another important step forward in the analysis of the Earth's land surfaces and exploration for its resources. It is hoped that the study of the Earth from space will become as commonplace tomorrow as photogrammetry and ground-truthing are today.

ORIGINAL PAGE
COLOR PHOTOGRAPH

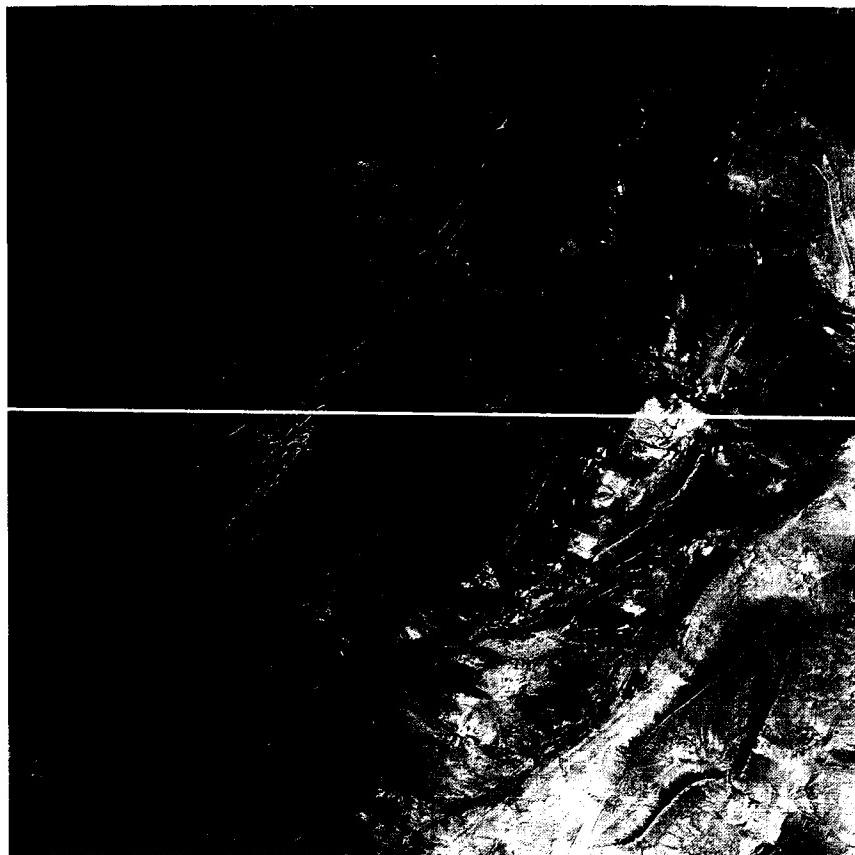


Figure 1. A false-color composite of a 60-km wide scene of part of the Atlas Mountains of North Africa (see Plate T-30) produced by CNES-IGN from the three-band (multispectral mode) HRV sensor (20-m resolution) on the SPOT satellite. This was the first color version released by SPOT Image, Inc. after launch; the color balance has since been modified for this product, but the original version is reproduced here for esthetic reasons (acquired February 23, 1986).



Figure 2. Another SPOT false-color composite image showing the entire Gran Canaria, an island volcano in the Canary Islands several hundred kilometers west of the Moroccan coast off North Africa. Scene dimensions are approximately 50 by 50 km (acquired February 24, 1986).

ORIGINAL PAGE IS
OF POOR QUALITY

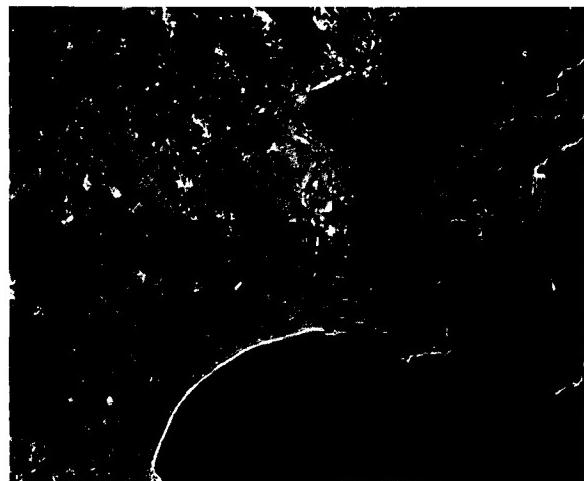


Figure 3. A subscene (covering approximately 13 km on a side) of Nice, France, and environs, imaged on February 23, 1986, by the HRV panchromatic mode (10-m resolution) scanner on the SPOT satellite. Note details in the urban sections of the image.

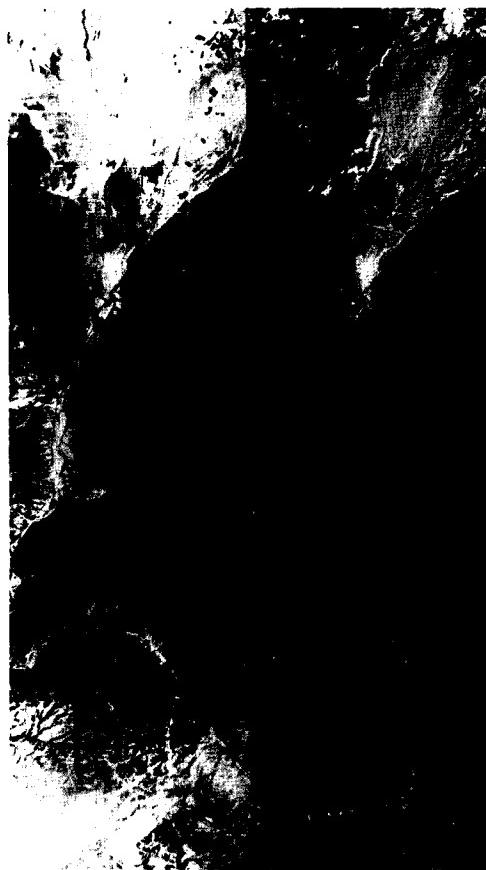


Figure 4. Two stereo pairs selected from parts of two adjacent scenes of a plateau-escarpment-plains near the Libyan/Tunisian border (N 32 00 ; E 11 10) by the SPOT HRV panchromatic scanner on February 24 and 25, 1986. The strips are mounted with spacings that favor use of a pocket stereoscope or the unaided eye. For the left image, the HRV was pointed east at an incidence angle of 24° (off nadir); for the right image, that angle was 10° off nadir ("looking" to the west). The faint vertical lines are artifacts of initial processing.

Appendix A

Remote Sensing Principles Applied to Space Imagery

*Nicholas M. Short**

To provide a better understanding of the interpretation and limitations of space imagery, this appendix presents a brief survey of relevant principles of remote sensing and of those spaceborne sensors that provide images in this book (Table A-1). For a more

indepth discussion of remote sensing, the reader is referred to Lillesand and Kieffer (1979), Lintz and Simonett (1976), Sabins (1978), Short (1982), Siegal and Gillespie (1980), and the second edition of the Manual of Remote Sensing (1983).

Table A-1
Satellite Systems Providing Useful Geomorphic Images

Vehicle/Sensor	Spectral Bands (μm)	Nominal Spatial Resolution (m)	Areal Coverage (km)	Frequency of Coverage	Data Center
Landsat 1, 2, 3, 4, 5/MSS	0.5–0.6 0.6–0.7 0.7–0.8 0.8–1.1	79	34 000 km ²	Once every 18 days	EROS Data Center (EDC)
Landsat 3 RBV	0.50–0.75	30	98 × 98 km		EDC
Landsat 4, 5/TM	0.45–0.52 0.52–0.60 0.63–0.69 0.76–0.90 1.55–1.75 2.08–2.30 10.40–12.55	30	185 × 185 km	16 days	EDC
Heat Capacity Mapping Mission (HCMM)	0.5–1.1 10.5–12.5	500 600	700-km Swath	3 days	NASA/GSFC
Seasat SAR	1.35 GHz (L-Band)	25	100-km Swath	As scheduled	JPL/NOAA
STS (Shuttle) SIR-A	L-Band	25–100	100–200-km Swath	As scheduled	JPL/NOAA
Tiros N/AVHRR	4, 5 Visible Bands, IR, Thermal IR	1100–4000	Subcontinental	12–24 hr	NOAA/NESS
Large-Format Camera	Panchromatic, Stereo	10	Continental (480 × 180 km)	As scheduled	EDC/NSSDC

*Geophysics Branch (Code 622), Goddard Space Flight Center, Greenbelt, Maryland, 20771.

~~PRECEDING PAGE BLANK NOT FILMED~~

~~PRECEDING PAGE BLANK NOT FILMED~~

~~PRECEDING PAGE BLANK NOT FILMED~~

REMOTE SENSING AND ELECTROMAGNETIC RADIATION

Remote sensing as a technology refers to the acquisition of data and derivative information about objects, classes, or materials located at some distance from the sensors by sampling radiation from selected regions (wavebands) of the electromagnetic (EM) spectrum. For sensors mounted on moving platforms (e.g., aircraft and satellites) operating in or above the Earth's atmosphere, the principal sensing regions are in the visible, reflected near-infrared, thermal infrared, and microwave/radar regions of the EM spectrum (Figure A-1). The particular wavelengths (or frequencies) detectable by visible/infrared sensors depend in large measure on the extent to which the waveband radiation is absorbed, scattered, or otherwise modified by the atmosphere ("windows of transparency" concept). The radiation measured from space platforms is usually secondary in that it is reflected or emitted energy generated from molecular interactions between incoming radiation (irradiance) and the Earth material being sensed. Common primary energy sources include the Sun or active radiation-generating devices such as radar; sensed thermal radiation from the Earth's surface results from both internal heat sources and the heating effect of solar radiation. Because most materials absorb radiation over the sensed parts of the EM spectrum, only fractions of the incoming radiation (typically, 1/20th (for water) to 4/5ths (sand) in the reflected region) are returned to the sensor.

The spectral character of the source radiation depends on how it is generated. A spectral distribution plot shows the variation with wavelength of irradiance levels, usually measured as intensity or power functions (illustrated for solar irradiance in Figure A-2). This distribution is initially modified as incoming radiation interacts with the atmosphere. It is then further changed through interaction with the surficial materials (to depths ranging from micrometers to a few meters, depending on wavelength),

and the returned fraction is altered once more as it passes back through the atmosphere. Finally, the sensor itself modifies the returned radiation according to the response characteristics of the radiation-sensitive detectors. The end result is a spectral signature for each sampled section of the sensed surface, which is made by plotting the intensity or power variations of the final signal as a function of wavelength (Figure A-3). For the wavebands commonly used, the greatest modification is imparted by the interactions involving the ground materials, so that the signature is generally diagnostic of the particular substances or of objects composed of them. Targets of interest at the Earth's surface are usually an intimate mix of several materials (e.g., soil clays and rock particles, as well as water, air, and organic substances) or even several classes of materials such as soil plus trees plus grass

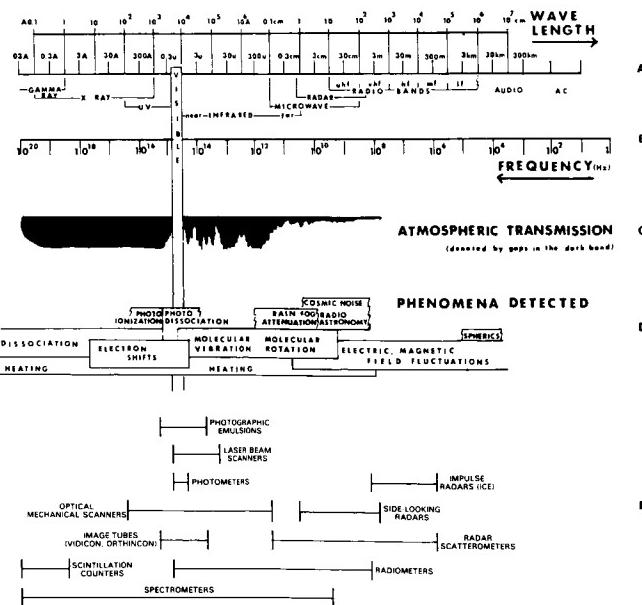


Figure A-1. The electromagnetic spectrum, atmospheric windows, and spectral operating range of sensors; modified from R. Colwell (upper diagram) and from *Remote Sensing of Environment*, J. Lintz, Jr., and D. S. Simonett (Eds.), 1976, with permission of the publisher, Addison-Wesley, Reading, Massachusetts (lower diagram, E).

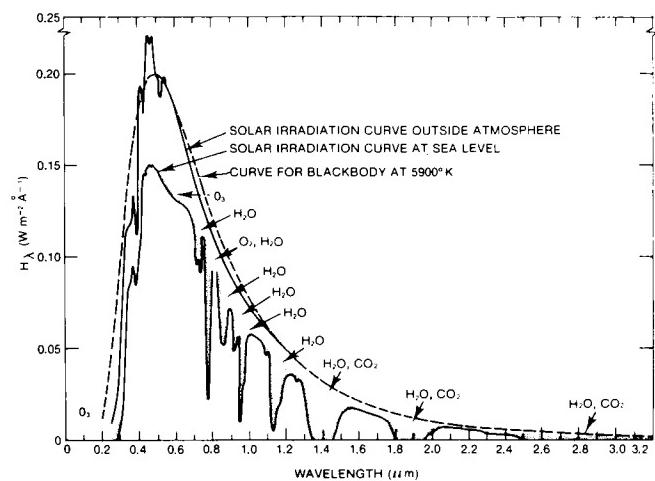


Figure A-2. Solar irradiation curves, showing location of atmospheric absorption bands; from *Handbook of Geophysics and Space Environments*, S. Valley (Ed.), copyright © 1965 McGraw-Hill (published with permission of McGraw-Hill Book Company).

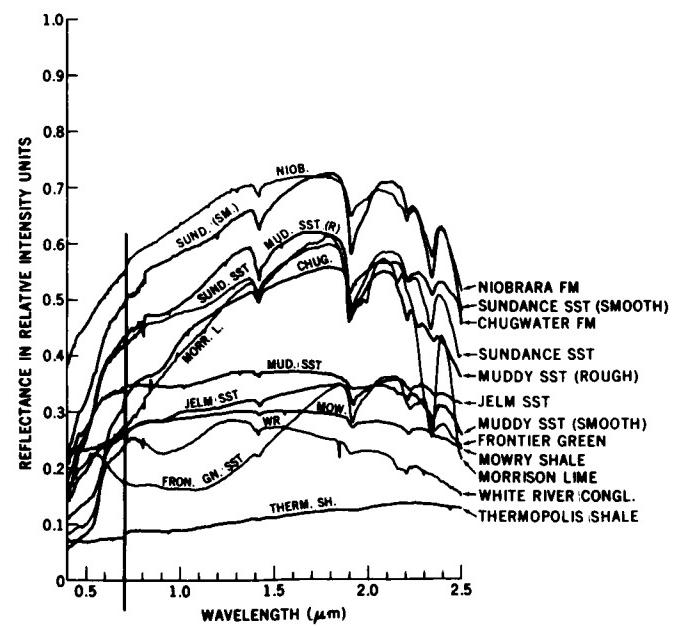


Figure A-3. Reflectance spectra of Wyoming rock stratigraphic units.

plus manmade objects that are grouped together in an area of the ground. The size of the sampled area (target) is specified by the spatial resolution limit of the sensor (its instantaneous field of view as determined by the sensor's optics, electronics, etc.). On an image, this "area" is represented by the picture element (called a pixel); the pixel size for a Landsat Multispectral Scanner (MSS) scene is 79 m, and each full scene (for a band) is made up of 7.5 million pixels.

Spectral signatures obtained with a spectrometer, which uses a grating or prism to disperse a radiation continuum into discrete wavelengths, appear as continuous plots. More commonly, the detector/counter system operating in a moving sensor is capable of measuring only the radiation distributed over a finite wavelength interval or band. Band limits are determined by the transmission characteristics of a filter that passes only radiation of certain wavelengths. The detector integrates the distribution of spectroradiance into a single intensity/power value. If the radiation distribution is sampled at several intervals, the plots of these single values for their respective wavebands resemble a histogram (Figure A-4) that crudely approximates the spectrometer-produced signature. The more spectral bands sampled over a given spectral region, the closer the resultant signature will be to the characteristic signature of the object or material sensed.

REMOTE SENSING INSTRUMENTATION

The most common types of remote sensors are radiometers, multispectral scanners, spectrometers, and film cameras. The first two convert radiation (photons) emanating from each surface target into electrical signals whose magnitudes are proportional to the spectroradiance in the intervals (bands) sensed. The surface is usually sampled sequentially, as by a mirror scanning from side to side while the sensor moves forward on its platform. Each pixel contributes the collective radiation from the materials within it to the record as a single discrete quantity so that the converted signal is a measure of the combined ground target variation from one successive pixel area to the next. After being recorded, the signals can be played back into a device that generates a sweeping light beam whose intensity varies in proportion to the photon variations from pixel to pixel. The beam output is, in a sense, a series of light pulses, each equivalent to an average value for an individual ground target. Because the signal pulses were collected as an array of XY space in relation to their successively sensed target positions, the individual values can be displayed as a sequential series of points (pixels) of varying intensity. The image display may be on a television monitor, a film (pixels are represented by diffuse clusters of silver grains), or a sheet of paper

on which pixel intensities are indicated by alphanumeric characters or by spots of variable densities or sizes (exemplified by a newspaper photograph). Any of these displays produces an image of the sensed scene comprising the variations in tonal densities of the different objects or classes within it in their correct relative positions. Normally, scanning spectrometers must dwell on a single target long enough for the full spectral interval to be traversed and hence cannot be operated from a moving platform unless the target is tracked (as was done by an astronaut on Skylab). This type of spectrometer presents the spectral signature as a continuous curve on a strip chart or plate. Fixed prism or grating spectrometers usually show discrete spectral wavelengths as a dispersed sequence of lines (images of a slit aperture). The Jet Propulsion Laboratory has developed an airborne imaging spectrometer that uses a slit to pass radiation from the ground onto a multilinear array charge-coupled detector (CCD) to sense successive areas along a moving track. The film camera differs from the sequential sensor types in that it allows the radiation from all surface targets sensed at the same instant to strike the film (recorder) simultaneously in their correct positions as determined by the optics of the system.

A set of multispectral images is produced by breaking the image-forming radiation into discrete spectral intervals through the use of waveband filters (or other light dispersion or selection devices). If a surface material has high reflectance or emittance in some given interval, it will be recorded as a light (bright) tone on a positive film-based image. Conversely, a dark tone represents a low reflectance or emittance. Because the same material normally has varying values of reflectance or emittance in different spectral regions, it will produce some characteristic gray level (on film) in the image for each particular waveband. Different materials give rise to different gray levels in any set of waveband images, thus creating the varying tonal patterns that spatially define classes, objects, or features. Multispectral images of the same scene are characterized by different tonal levels for the various classes from one band to the next.

REMOTE SENSING DATA DISPLAYS

Before Landsat and similar multispectral systems were developed, the principal remote sensing data displays were nearly always aerial photographs. Aerial cameras typically employ panchromatic films that use the visible region of the spectrum from about 0.40 to 0.70 micrometers (μm). Use of a yellow haze (minus blue) filter, which prevents energy transmission below 0.51 μm , narrows the actual waveband interval to 0.51 to 0.70 μm in black and white aerial photography. Color aerial photographs are recorded on natural color or false-color infrared film. These operate on the color subtraction principle, in which the three color substrates or layers of a negative on development are yellow, magenta, and cyan, being sensitive to blue, green, and red light, respectively. However, when producing a "color composite" from individual waveband images, the color additive principle applies. Three such images are needed to make a multispectral color composite. Multiband photography utilizes several cameras, each consisting of a bore-sighted lens and a color filter that transmits a specific spectral interval or band through the optical train onto black and white film.

For each band, the film records the scene objects as various gray tones related to the visible colors (or other radiation) variably transmitted and absorbed by the particular filter. Suppose two objects, one red and the other green, are photographed by three bore-sighted cameras. Each camera's lens would be focused on its own film, with one fronted by a blue filter, the second by a green filter, and the third by a red filter. When all three lens shutters are triggered together, light from the red object (mostly in the 0.6- to 0.7- μm interval) will only pass through the red filter (being absorbed to varying extents by the blue and green filters).

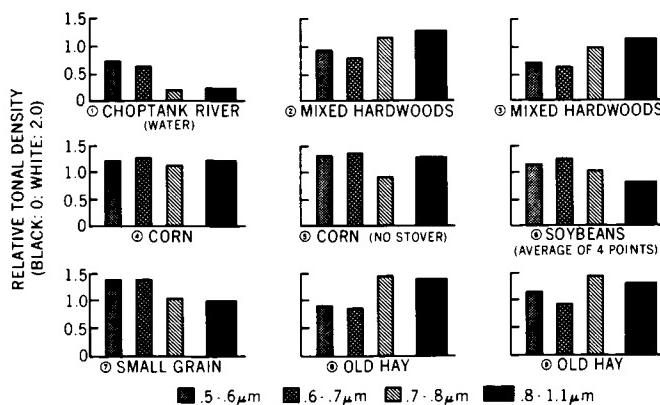


Figure A-4. Relative densities of ground class MSS signatures of nine cover types in the Choptank River, Maryland, area.

In the red filter camera, the shape of the object is reproduced as a light-toned pattern set off against dark (equivalent to non-red) surroundings. For cameras that record this object through green and blue filters, the red light object is absorbed, reproducing its presence on film as a dark tone. The green object is likewise recorded as light-toned only on the green filter/film combination. Obviously, a blue object, if in the scene, would have appeared in light tones only on the blue filter/film product. Non-primary colors would likewise be rendered as various gray tones in the three images, at levels depending on their relative transmission through each filter (e.g., yellow light normally will be only partially absorbed by red and green filters).

Color-composite photographs can be produced by passing white light successively through a primary color filter and each respective black and white transparency after all three images are superimposed and registered to one another on a color-sensitive film. The red-band image activates red color on the color film if projected through a red filter; light tones (clear in a transparency) representing red objects pass red-filtered light onto the film while screening out blue and green objects (dark or opaque in a transparency). Analogous results for blue and green objects (or a color mix) are obtained with blue and green filters. The resulting composite is a natural color photograph. When an infrared band transparency is projected through a red filter, and red and green bands through green and blue filters, respectively, vegetation, in particular, which is highly reflective (very bright) in the infrared, moderately reflective in the green, and low in the red because of absorption of red light by chlorophyll, will appear red in the color composite (little blue and almost no green contribution). Thus, in a false-color composite, red is almost always a reliable indicator of vegetation. Light-colored rocks or sand, which are generally bright in the infrared, red, and green bands, will be rendered whitish (with color tints) on false-color film because about equal amounts of blue, green, and red light (additively producing white) are transmitted through the light film tones associated with their spatial patterns. Specific gray tones in each of several multispectral band images or diagnostic colors in natural or false-color images can be used along with shape or textural patterns to identify particular classes of surface features or materials that compose them, as summarized in Table A-2.

MULTISPECTRAL SCANNER IMAGES

Images produced by the MSS on Landsats 1 through 5 and the Thematic Mapper (TM) on Landsats 4 and 5 use the image production system previously described. The MSS senses four contiguous spectral bands that cover sequentially the wavelength intervals from 0.5 to 1.1 μm ; the TM includes three bands that cover nearly the same intervals as the MSS, together with a blue band and two additional bands in the near infrared (wavelengths not overlapping) and one in the thermal infrared. In those new near-infrared band intervals, many rock/soil materials are more reflective than vegetation, but certain materials (e.g., clays) show absorption in one or both bands. Examples of several TM band images reproduced in Figure A-5 are typical of multispectral images. Various combinations of three bands and color filters can produce a variety of color composites, some rather exotic and unfamiliar to most geoscientists (e.g., Panel 6 in Figure A-5).

Reflectances, emittances, and other radiation parameters measured by spaceborne sensors, after conversion to electrical signals, are commonly digitized on board before transmission to receiving stations. The digital numbers representing the radiance values can then be reconverted to analog signals introduced into image-writing devices that generate the individual band (black and white) images; the numbers can also be retained in digital format on computer-compatible tapes (CCTs). Minicomputer processing of the digitized data, using a variety of software-based special functions, yields new insights into the nature of the Earth's

surface materials. If numerical reflectance values for any two MSS or TM bands are ratioed, new sets of numbers result that often indicate the identities of the materials. Thus, red-colored mineral alteration zones should produce a high value when their red band digital numbers (DNs) are ratioed to (divided by) their green band values. Other ratio values can be used to vary a beam intensity to generate a film product whose gray levels are proportional to the values. Combinations of band-ratio images and color filters give rise to distinctive color composites in which certain materials tend to stand apart in distinctive colors (see Figure T-8.1, for an example). A similar approach can be followed with images produced from Principal Components data. (See the *Landsat Tutorial Workbook* (Short, 1982) for details of the above techniques.)

Experience has shown that the larger geomorphic landforms are about equally well displayed in any of the four Landsat MSS band images and probably any of the six reflectance TM band images. However, expression of landforms in the TM thermal band image may be notably different, with lower overall contrast and lower resolution. On those images, shadows and Sun-facing slopes in mountainous terrain generally correspond to cool and warm (dark and light-toned) patterns. The tonal patterns in the reflectance band images show up best in semiarid to arid country, where vegetation is sparse to absent. Small-scale landforms and associated surface materials, such as fan outwash, can often be better discriminated from other landforms and materials by using select spectral bands, different color-composite combinations, or special process (e.g., ratio) images. In general, because the two infrared bands (6 and 7) on the MSS commonly show the best tonal contrast, they are used for the bulk of the black and white Landsat images comprising most of the gallery in this book. Bands 5 and 7 on TM frequently are even better, particularly in accentuating contrast, and are exemplified in several Plates. Specific information on the acquisition dates and conditions, band(s) used in the black and white and color images, and other characteristics of the Landsat MSS and TM, Heat Capacity Mapping Mission (HCMM), Seasat SAR, Shuttle Imaging Radar (SIR-A), and other space images shown in this book are documented in Appendix B. Guidelines for characterizing and interpreting thermal and radar space images that appear in this book are briefly surveyed in the following paragraphs; the reader is directed to Table A-1 for information on the systems pertinent to those images and to the *Landsat Tutorial Workbook* (Short, 1982) for a fuller discussion of the nature of these images.

THERMAL INFRARED

Thermal images are derived from sensors that detect emitted radiation within the 3- to 5- and 8- to 14- μm regions of the EM spectrum. The sensors measure radiant rather than kinetic temperatures; the values are less than direct contact (thermometer) temperatures by amounts determined by the emissivity (μ) of the surface materials. (Most rocks have emissivities ranging from 0.80 to 0.95.) The perceived radiant temperatures represent the effects of diurnal (daily) heating by the Sun's rays and subsequent cooling at night; internal sources of heat add only a small thermal contribution. The temperature variations during a heating/cooling cycle are largely controlled by the thermal inertia* of each ground constituent in the top meter or so (of soil, rock, or water), plus the influence of vegetation. Low thermal inertias result in large temperature differences over the cycle; high inertias involve small changes. Thermal inertia decreases with decreasing conductivity, density, and heat capacity. By convention, low radiant temperatures are shown as dark tones in a thermal image, with higher

*Thermal inertia is defined as the resistance of a material to temperature change during a full heating/cooling cycle.

Table A-2
Identification of Land Cover Categories

Category	Best MSS Bands	Salient Characteristics
a. Clear Water	7	Black tone in black and white and color.
b. Silty Water	4, 7	Dark in 7; bluish in color.
c. Nonforested Coastal Wetlands	7	Dark gray tone between black water and light gray land; blocky pinks, reds, blues, and blacks.
d. Deciduous Forests	5, 7	Very dark tone in 5, light in 7; dark red.
e. Coniferous Forest	5, 7	Mottled medium to dark gray in 7, very dark in 5, and brownish-red and subdued tone in color.
f. Defoliated Forest	5, 7	Lighter tone in 5, darker in 7, and grayish to brownish-red in color, relative to normal vegetation.
g. Mixed Forest	4, 7	Combination of blotchy gray tones; mottled pinks, reds, and brownish-red.
h. Grasslands (in growth)	5, 7	Light tone in black and white; pinkish-red.
i. Croplands and Pasture	5, 7	Medium gray in 5, light in 7, and pinkish to moderate red in color depending on growth stage.
j. Moist Ground	7	Irregular darker gray tones (broad); darker colors.
k. Soils—Bare Rock—Fallow Fields	4, 5, 7	Depends on surface composition and extent of vegetative cover. If barren or exposed, may be brighter in 4 and 5 than in 7. Red soils and red rock in shades of yellow; gray soil and rock dark bluish; rock outcrops associated with large landforms and structure.
l. Faults and Fractures	5, 7	Linear (straight to curved), often discontinuous; interrupts topography; sometimes vegetated.
m. Sand and Beaches	4, 5	Bright in all bands; white, bluish, to light buff.
n. Stripped Land—Pits and Quarries	4, 5	Similar to beaches—usually not near large water bodies; often mottled, depending on reclamation.
o. Urban Areas: Commercial Industrial	5, 7	Usually light-toned in 5, dark in 7; mottled bluish-gray with whitish and reddish specks.
p. Urban Areas: Residential	5, 7	Mottled gray, with street patterns visible; pinkish to reddish.
q. Transportation	5, 7	Linear patterns; dirt and concrete roads light in 5; asphalt dark in 7.

temperatures being lighter. The HCMM thermal sensor produces day and night temperature distribution images of the Earth's land and sea surfaces, as well as thermal inertia images derived from these and the visible band image.

RADAR

Radar (radio detection and ranging) operates as an active system that provides its own illumination (thus it is all-weather and nighttime capable) as discrete pulses of energy in frequencies that lie within the microwave region of the EM spectrum. Wavebands in common use are the K-band (wavelength: 1.1 to 1.7 cm), X-band (2.4 to 3.8 cm), and L-band (15.0 to 30.0 cm). The effective resolution of a radar sensor depends on the mode of operation, physical dimensions of the antenna that transmits and receives signals, and subsequent data processing. Airborne systems

usually use a linear real aperture antenna (5 to 6 meters long) and direct the radar beam off to the side of the aircraft (normal to flight path), hence the term "Side Looking Airborne Radar" (SLAR). Spaceborne systems, and some that are mounted on aircraft, use a smaller antenna that functions on the synthetic aperture principle, hence Synthetic Aperture Radar (SAR). (The SAR applies the Doppler effect to analyze variable frequencies that arise from relative motions between the sensor platform and ground targets.)

The typical mode of operation and character of signal return for a radar system are depicted in Figure A-6. The outward-sweeping beam scans a strip of surface elongated normal to the azimuthal direction of flight. Its length is set by the depression angle (measured from the horizontal) downrange along the look direction. Its complement, the incidence angle, is measured from the vertical. Photons in the energy burst interact with the ground

ORIGINAL PAGE
COLOR PHOTOGRAPH

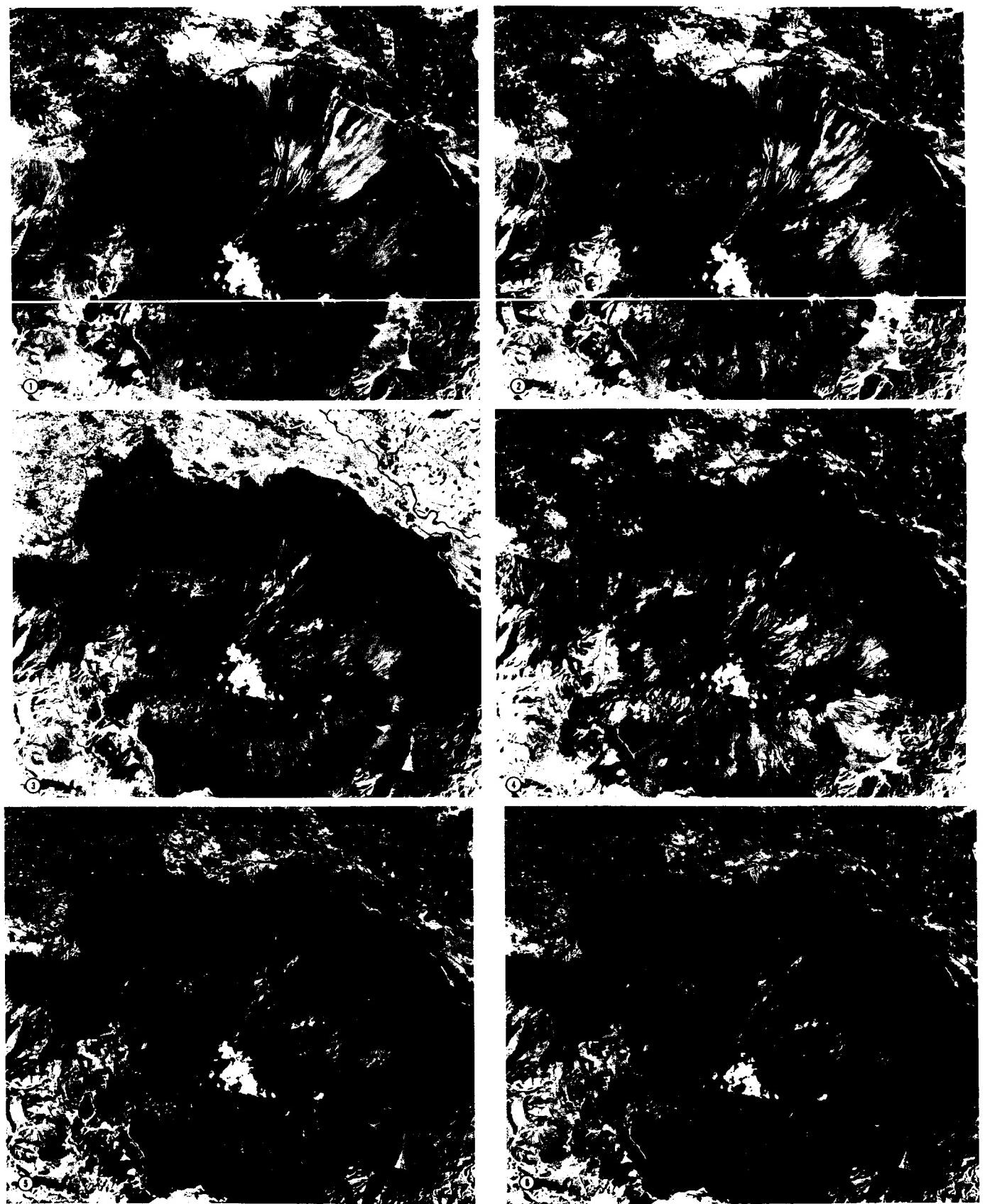


Figure A-5. Computer-enhanced subscenes of the Thematic Mapper image of Mount Ararat in eastern Turkey (see Plate V-17) illustrating different bands and color-composite images: (1) Band 2; (2) Band 3; (3) Band 4; (4) Band 5; (5) Bands 2 (blue), 3 (green), and 4 (red); (6) Bands 1 (blue), 4 (green), and 5 (red).

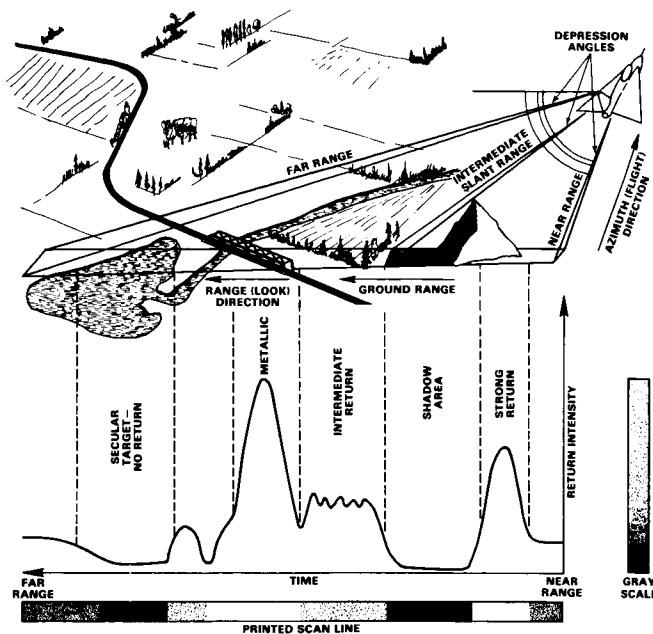


Figure A-6. Schematic diagram showing radar beam terminology and characteristics of returned signals from different ground features (modified from Sabins, 1978).

targets, creating new radiation, some of which is returned to the antenna where it is converted to an amplified electrical signal. The strength of that signal depends on a number of variables, mainly the geometry (shape) of the surface, the physical roughness of the surface relative to the wavelength of the pulse transmitted, and the dielectric constant of each material present in the target area. In the schematic diagram, the sensor-facing slope of the hill sends back considerable energy to the radar receiver, but the opposite slope is not illuminated by the beam, which causes a dark shadow. Plants and other vegetation scatter the radiation from their leafy surfaces, but a moderate amount is returned to the radar. The metal bridge consists of planar surfaces and corners, some oriented to efficiently return a high fraction of the beam. However, water, if not churned up by waves, acts as a specular reflector that redirects the radiation away from the receiver.

If surface roughness (as from pebbles or pits) has average dimensions much different (usually larger) than the radar wavelength, it acts to produce considerable backscatter that results in a strong (bright) signal return; a smooth surface relative to the radar wavelength generates a weak (dark) signal because of significant specular reflection away from the sensor. Likewise, because leaves may or may not interfere with the radar waves, depending on leaf size and on the radar wavelength, some tree canopies can be penetrated. Clouds are "transparent" because cloud-vapor droplets are too small to interact with most radar wavebands. However, ice crystals and raindrops may backscatter a signal. Reflection of radar radiation back to the antenna increases as the relative dielectric constant becomes smaller (3 to 16 for rocks and soils and 80 for pure water); a dry soil or sand (very low dielectric) permits penetration to depths of meters in some cases.

Radar images can be generated on recording devices from the electrical signals whose magnitudes are proportional to the returned radiation intensities. By convention, strong signal returns are printed as light tones and weak ones as dark tones (Figure A-7). Because of the proximity of airborne radars to the ground



Figure A-7. SAR image of central Pennsylvania, acquired during an ascending orbit (1260) on September 28, 1978, as processed on the digital correlator system at the Jet Propulsion Laboratory.

(as contrasted to the far greater distance of the Sun to a local surface on Earth), the geometry of radar-sensed features (such as hills) on the ground is more prone to distortions than that in images obtained with natural illumination. Distortions also vary as the depression angle changes from near to far range. Close in, foreshortening is expressed by an imposed asymmetry on forms such as ridges, so that the radar-facing slopes appear to steepen (the bright pattern becomes narrower) and the back slope broadens (dark pattern wider); this effect diminishes with decreasing depression angle. In the extreme, the facing slope appears to "layover" if its foreslope is greater than the look angle.

IMAGE ENHANCEMENT OF GEOMORPHIC SCENES

Many of the space images appearing throughout this book have been subjected to special computer-processing to more sharply define the geomorphic features and other geologic information that led to their selection. Although various techniques and operations can be applied to the data from which these images are constructed (see Condit and Chavez (1979) for a succinct summary of digital image processing or Short (1982) for a more in-depth review), several known collectively as *image enhancements* are generally the most useful to geomorphologists simply because they tend to improve the spatial display and characteristics of landforms in a scene. These are described briefly in this section, with emphasis on integrating the computer into the enhancement option.

Any experienced photographer is fully aware of the value of imparting an optimal *contrast*, or levels and spread of tone distribution, to a photograph. This usually involves expanding the number of discernible gray levels; the process is called contrast-stretching. The result is a picture both pleasing to the eye and, in scientific photography, effective in increasing the information content. At one or more stages in the entire photographic process, contrast can be influenced by various factors: at the time of picture-taking, such conditions as film type used, lens filters, illumination, and other exposure variables; in processing and printing, film development conditions, filters, properties of the printing paper, and exposure times.

The printing of a Landsat image is also affected by similar factors, but the importance of the film negative generated from the digital data is often paramount. Superior contrast can be introduced at some stage of negative production by manipulating the range of radiances (usually as reflectances) emanating from the scene and modified by the sensor. These radiances, expressed as digital numbers (DNs), fall within a range defined by gain settings and other sensor characteristics. For a Landsat MSS data set, the levels of brightness that can be detected by the sensor are digitized over a DN range of $(2^n - 1; n = 1 \text{ to } 8)$ or 0 to 225. Now, suppose the normally gaussian distribution of DNs representing the radiances from a given scene, after those are quantified and digitized, is 40 to 110. A photographic negative made to image this spread of values might have a limited range of gray levels within a particular film used, depending on the gamma (density transfer function) of the characteristic curve (X-Y plot of density D versus log exposure E) chosen; in other words, the negative may be "flat" and would produce a low-contrast positive print. Using an appropriate program, a computer can systematically expand (or contract, for a scene marked by a wide spread of radiances) the DN range so that a new negative will contain more of the gray levels that potentially are available within the density response capability of the film or print paper. (Of course, the benefits of such a stretch can be reduced by ineffective photo-processing afterward.) "Before" and "after" images following stretch-processing by computer are exemplified in Figures A-8a-b. Various kinds of numerical stretching are possible in computer-based processing, including linear, stepwise linear, logarithmic, and probability distribution function expansions or contractions. Similar principles of stretching underlie the moderation of contrast on electronic image displays (such as a television monitor).

Another enhancement approach involves combining sequential DNs within a specified range into a single gray level or density. Adjacent DN ranges over the total distribution are treated in like manner, thus reducing the variation of many individual brightness values to a new set of much fewer values. This method, known as density slicing, produces a simplified pattern of varying tones in a black and white image; each composite gray level can likewise be assigned a discrete color to visually enhance the image display by color coding. Sometimes a surface feature, such as a landform type, has a unique or characteristic tonal signature

and a narrow range of gray tones, allowing it to be separated as a particular pattern by slicing its mean level and spread from other levels.

A powerful enhancement technique that sharpens an image and can selectively bring out or delineate boundaries is addressed under the general term of *spatial filtering*. In any X-Y array of brightness values, like that of pixels in an image, the changing value can be considered to vary in a spatial as well as a radiance sense. This spatial variability can be expressed as frequencies (number of cycles of change over a given distance). A low spatial frequency represents gradual changes in the quantity (e.g., DNs) over a large areal extent of contiguous pixels; high spatial frequency results from rapid changes as only a few pixels in an area of the array are traversed. Variable line spacings in resolution test patterns are an artificial example of differing frequencies. (This can also be related to the concept of Modulation Transfer Function (MTF) that is a fundamental property of films or images.) Any image (or a complex harmonic wave) can be separated into discrete spatial frequency components by the mathematical technique known as Fourier Analysis.

Spatial filtering of an image can be done by scanning vidicons equipped with special functions; alternatively, the input data (DNs) from which images are derived after scanning (as by an MSS) are run through algorithm-based "filters" in a computer program designed to screen out or diminish certain frequencies and pass or emphasize other frequencies. To do this, a traveling "window" or "box" consisting of an array of $n \times m$ (line and sample) pixels is set up. This, in effect, creates a new value for each pixel as it passes during the computations into the center point of the moving array; the new DN for each such pixel depends on the brightness value frequency distribution of its neighboring pixels in the array size chosen. A low-pass filter ("band-pass" when the image data come from a spectral interval or band) tends to respond to features (including separated natural landforms such as dunes, divides, streams, fracture-controlled lakes, and series of folds) whose sizes and recurrence intervals (spacing) are larger than the averaging array (i.e., high-frequency spacings are not picked up). A high-pass filter reacts to features having dimensions and spacings smaller than the array. The new set of pixel values resulting from this will enhance (sharpen) those features whose periodicity or scale allows them to be enhanced. This filtered data set can be converted directly into a new image or can be combined (restored) with another image (such as the original one with its particular tonal patterns). The new image is usually contrast-stretched in the process to bring out density differences among the pixels in the array. Linear features such as rock or stratigraphic contacts and lineaments thus emphasized are said to be edge-enhanced. An example from the spatial filtering process is presented in Figure A-8c.

Although not an enhancement process in the strict sense, the ratioing of brightness values in one spectral band to those of equivalent pixels in another band yields a new set of DNs from which another image can be generated (Figure A-8d). For MSS data, this allows comparisons of relative reflectances between spectral intervals. Consider a ratio of bands A to B: a high value for A reflectances and a low for B produces a high ratio whose DNs would give rise to light-gray tones; conversely, low A and high B values cause low ratios and dark tones; similar A and B values lead to intermediate tones. Three sets of ratio images (e.g., A/B, C/A, D/B) can be combined into color composites with various colors often diagnostic of particular materials.

Identification of objects or features and materials by one of several methods of computer-directed *classification* can be treated as another means of the information extraction that is the ultimate goal of enhancement. The essence of the concept underlying classification is this: each identifiable class of object/material is considered to have one or more distinguishing properties with certain statistical parameters (usually means and

ORIGINAL PAGE IS
OF POOR QUALITY

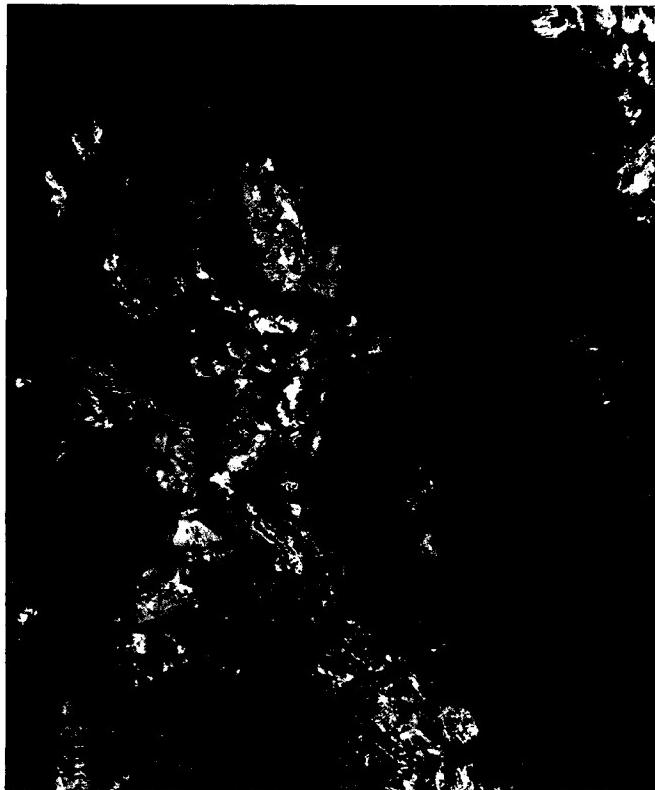
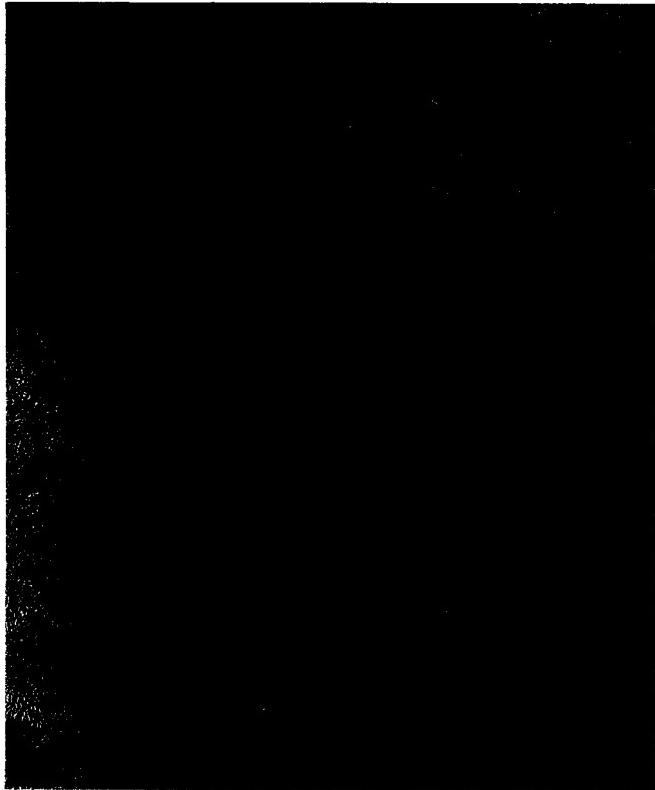
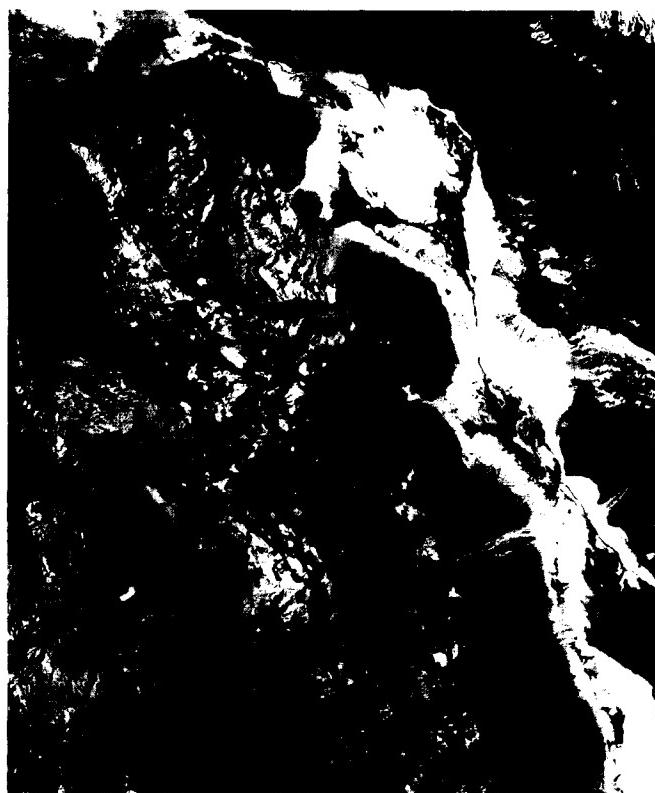
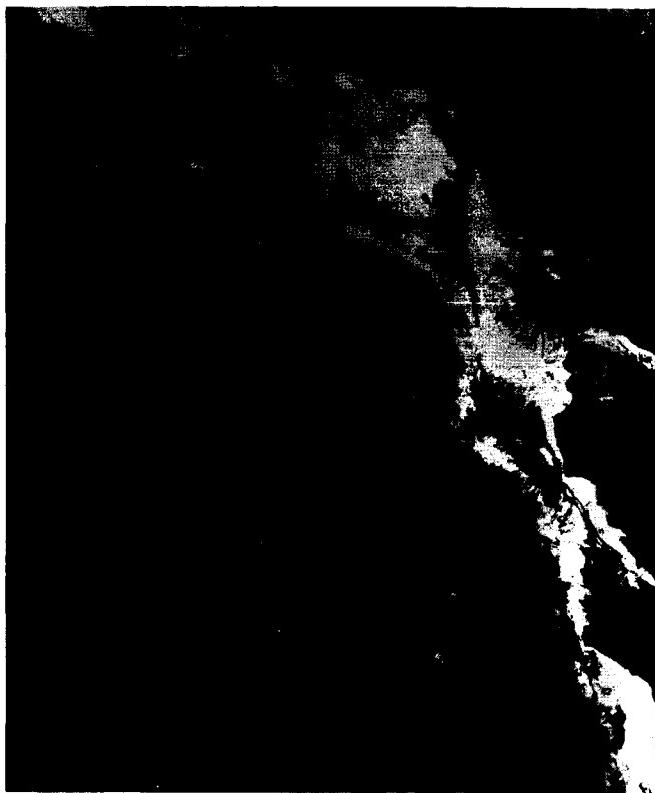


Figure A-8. Four products of image enhancement of a Landsat-5 Thematic Mapper subscene (50114-17550, June 23, 1984) of the Death Valley, California, area (see Plate T-5): (a) band 3 "raw" product (minimal enhancement), (b) band 3 gaussian stretch, (c) band 3 high-pass filter plus stretch, and (d) band 3/4 ratio.

variances) that can be demonstrated to be different (statistically) for other classes set up or recognizable in the data set being analyzed (such as natural terrains or land cover on a planetary surface). The classification program clusters property data into separable numerical sets (unsupervised classification) or obtains data characteristic of each known class in the scene by sampling those data at specific training sites (supervised classification). Once the specific classes are established from a fraction of the total sample points (e.g., pixels in an image), then all other (still unknown) sample points are assigned to some given class, identified by comparing their parametric characteristics (within the bounds of the statistical limits chosen) to those of the classes defined initially. Each unknown point is thus matched up with the class whose selected property or properties (e.g., radiance in an MSS image) is stochastically closest to it.

Classification of a Landsat image is usually based on spectral properties. An example of a geologic scene classified into rock/stratigraphic units by sampling the reflectances of each recognizable formation appears in Figure A-9. Other classifications can be devised to include spatial information (pattern recognition); although this has seldom been done yet for the geomorphic content of space imagery, in principle, it could be readily accomplished.



SUPERVISED CLASSIFICATION IMAGE FOR TM
SUMMER WATERPOCKET SUBSCENE: 7 BANDS USED;
IN THIS VERSION NO ALLUVIUM WAS MAPPED ON
THE BLUEGATE MEMBER.

SITE 9	
ALLUVIUM	
MASUK Sh	
EMERY SST	
BLUEGATE Sh	
FERRON Sst	
TUNUNK Sh	
DAKOTA Sst	
MORRISON Fm	
SUMMERTIME/	
SALT WASH	
ENTRADA Sst	
CARMEL Fm	
NAVAJO Sst	
KAYENTA Fm	
WINGATE Sst	
UPPER CHINLE Fm	
LOWER CHINLE Fm	
SHINARUMP Cong L.	
UPPER MOENKOPPI Fm	
LOWER MOENKOPPI Fm	
VEGETATION	
WATER	

Figure A-9. Classification of a Landsat-5 Thematic Mapper sub-scene of the Waterpocket Fold (monocline) between Circle Cliffs and the Henry Mountains (see Plate F-6); classes are stratigraphic formations; training sites selected from several U.S. Geological Survey maps (Short and Marcell, 1985).

CLOSING REMARK

This necessarily brief exposition of the principles of remote sensing was designed to introduce those unfamiliar with interpreting sensor-created images to those main ideas needed to appreciate the varieties of space and aircraft multispectral, thermal, and radar images appearing throughout this book. For a fuller understanding, consult any of the references cited in the introductory paragraph of this Appendix.

REFERENCES

- Condit, C. D., and P. S. Chavez, Jr., Basic concepts of computerized digital image processing for geologists, *U.S. Geol. Surv. Bull.*, 1462, 16 pp., 1979.
- Lillesand, T., and R. W. Kieffer, *Remote Sensing and Image Interpretation*, 612 pp., John Wiley, New York, 1979.
- Lintz, J., Jr., and D. S. Simonett, *Remote Sensing of Environment*, 694 pp., Addison-Wesley Publ. Co., Reading, Massachusetts, 1976.
- Manual of Remote Sensing*, 2nd Ed. (R. N. Colwell, Editor-in-Chief), Amer. Soc. of Photogrammetry, Falls Church, Virginia, 1983.
- Sabins, F., *Remote Sensing: A Better View*, 426 pp., W. H. Freeman & Co., San Francisco, California, 1978.
- Short, N. M., *The Landsat Tutorial Workbook*, 553 pp., NASA RP-1078, U.S. Govt. Printing Office, Washington, D.C., 1982.
- Short, N. M., and R. Marcell, New results for geologic units mapping of Utah test sites using Landsat TM data, *ERIM Fourth Thematic Mapper Conference*, San Francisco, Calif., in press, 1985.
- Short, N. M., and L. M. Stuart, Jr., *The Heat Capacity Mapping Mission (HCMM) Anthology*, 264 pp., NASA SP-465, U.S. Govt. Printing Office, Washington, D.C., 1983.
- Siegel, B. S., and A. R. Gillespie (Eds.), *Remote Sensing in Geology*, 702 pp., John Wiley, New York, 1980.

Appendix B

Sources of Illustrations and Tables Appearing in This Book

This Appendix records the sources of all space images, aerial photographs, ground and aerial views of landscapes and outcrops, line drawings, and other illustrations. Tables from publications are acknowledged below each one. The purpose of this listing is two-fold: (1) to give proper acknowledgment and thanks to all contributors, and (2) to provide adequate information to any reader wishing to contact the source individual or organization to seek a copy of the illustration or additional facts about it.

Because of the large number of illustrations appearing in *Geomorphology from Space*, the method of acknowledgment is, of necessity, concise and uses abbreviations wherever expedient. The overall scheme of this system is divided into three parts: (1) a list of the source of each illustration or table, arranged by chapter, with those in the gallery chapters (2 through 10) given in two parts—a group found in the introductory section of a chapter and then those used in each Plate; (2) a list of addresses for each source, organized alphabetically by the name of the individual contributor or by the organization providing the illustration; and (3) special lists of: (a) Guest Caption Writers, (b) University of Maryland students who supplied background information for Plates in the Tectonic Landforms chapter, and (c) required copyright statements.

More than 95 percent of all illustrations found in this book have been adequately registered by source and identifying numbers where appropriate. A few remain completely unidentified (referred to as *source or ID unknown*) or poorly documented. For these latter and some other illustrations, full accreditation has proved to be quite difficult because of insufficient supporting information from the contributors (e.g., a few individuals who supplied 35-mm slides failed to label them or even orient them appropriately). To those receiving incomplete (or possibly incorrect) credit, we offer sincere regrets, but ask their indulgence in view of the tremendous task involved in keeping track of the more than 2000 photographs and space imagery considered for the book.

Guidelines for interpreting the source listings are as follows:

1. All non-Plate illustrations are recorded by a pair of numbers: the chapter number-figure number (e.g., 6-4).

2. All Plate illustrations (excluding the index maps, which were prepared by Malcolm Tarlton and others at the Goddard Space Flight Center (GSFC)) are listed by letter-number, using the scheme described on page xiv. The ID for the Plate image itself (first in each entry) is set in boldface type.

3. Most of the space imagery is recorded by a number and/or other descriptive information. By learning the identifying numbers of word descriptors for each system, the reader can readily recognize which system is involved; to wit, descriptors for nearly every system source encountered in the list:

- a. Landsat MSS imagery (for Landsats 1, 2, and 3) is normally identified by a numerical sequence such as:

1347-07902-7	(Landsat 1)
2238-16433-5	(Landsat 2)
30148-22195-4	(Landsat 3)

A fifth digit in the first number set is inserted after the initial digit by some suppliers of Landsat 1 and 2 images (e.g., Earth Satellite Corporation; certain international receiving stations). The final digit -4 (5, 6, or 7) refers to the specific Multispectral Scanner (MSS) band for a black-and-white image. The notation "(C)" at the end of the sequence refers to a color composite. (A C used with mosaics or other types of illustrations indicates a color version.)

- b. Landsat-3 Return-Beam Vidicon (RBV) image IDs can be readily recognized by the replacement of the final digit by A, B, C, or D, which specifies the quadrant of an equivalent MSS frame (e.g., 30133-15321-B).

- c. Landsat IDs with the left set of 5 numbers beginning with either 4 or 5 (e.g., 40322-) are associated with the Thematic Mapper (TM) sensor on either Landsat 4 or 5; no MSS images from these spacecraft are included in this book.
- d. Landsat mosaics consisting of only two images normally will have the pair identified as above; if more than two images are used, none will be identified.
- e. An ID numerical sequence given as Oxxx-xxxx-x is reserved for Heat Capacity Mapping Mission (HCMM) imagery. The last digit (-x) will be 1, 2, or 3, depending on whether it is a Day Visible (1), Day Thermal IR (2), or Night Thermal IR (3) scene.
- f. Images identified by "LFC" and up to 4 digits refer to photographs taken with the Large Format Camera on STS-xx.
- g. The nomenclature "SAR Rev" followed by a number indicates an image acquired by the Synthetic Aperture Radar on the Seasat mission; "Rev" stands for revolution.
- h. The nomenclature "SIR-A Data Take" plus number refers to the Shuttle Imaging Radar system on the STS-2 mission (November 1981).
- i. Some photographs taken with handheld cameras by astronauts during Space Shuttle missions are identified with a letter-number sequence (e.g., S-9-3223 (the 9th STS flight)); some later STS flights use a different identifying system based on a combination of launchpad number and particular mission in a given year. Several photographs received from the Johnson Space Center were not fully identified.
- j. The identifier "NOAA" and additional letters/numbers normally is associated with meteorological satellites operated by the National Oceanographic and Atmospheric Administration, Satellite Data Services Division, Washington, D.C. 20233.
- k. Some Gemini and Apollo photographs contributed by Paul Lowman and others at GSFC had proper IDs, as evident from their entries. However, several lacked such IDs, and no convenient means to track them were available.
- l. Most images of planetary bodies in Chapter 10 were obtained from photograph files at the News and Information Branch, Public Affairs Division, NASA Headquarters. These are identified by a description such as 81-H-432 (first number = year; H = Headquarters; second number = picture number). Some images were acquired from NSSDC or JPL; see guideline 10.
- 4. Wherever appropriate (and available), the date on which an image/photo was taken is added after stating the ~~photographer or the spacecraft~~ system ID (e.g., 1234-16302-7: 6/26/73).
- 5. For illustrations copied directly from a book or a periodical, the author(s) (or in several instances, the book title), followed by the date of publication identifies the source. The full identification of that source appears in the references at the end of the appropriate chapter. In many instances, the illustration is copyrighted. The symbol © is then added to the entry; see Part 3 for any additional copyright statements.
- 6. For most illustrations submitted by individuals, the identification consists of listing only the contributor's name. Complete addresses of contributors are given in Part 2 of this appendix. Some individuals have coded their photographs by a number or some other descriptor. A few have provided numbered illustrations on a commercial basis.
- 7. Some photographs were purchased for the book from the Photo Library of the U.S. Geological Survey in Denver. These can be recognized by the following combination: Name of the photographer (commonly a well-known geoscientist), a number, and "USGS-PL."
- 8. A similar situation exists for two other sources—the National Park Service (NPS) and the National Geographic Society (NGS)—except that no charges were made for the contributions. These are credited by listing the name of the photographer(s) followed by NPS or NGS. Check Part 2 for addresses of the organizations.
- 9. Whenever possible, aerial photographs are identified by both source and specific flight, roll, and frame numbers. One group of aerial photographs comes from a collection available from the U.S. Geological Survey; this group is indicated by the descriptor "USGS-APA," where APA stands for Aerial Photograph Atlas (see USGS publications *Professional Papers 590 and 591*).

10. In addition to the many individuals and organizations named in Part 1 as sources (with addresses in Part 2), a number of organizations have served as sources frequently enough to be identified in Part 1 by a series of letters as initials. There is one exception: if, at the end of each entry for Landsat or HCMM images, no source is given in this manner, that source is the Landsat Image Processing Facility at GSFC. The other common sources, identified by initials (with addresses in Part 2), are:

CCRS	= Canadian Center for Remote Sensing (Canada)
CSIRO	= Commonwealth Science and Industrial Research Organization (Australia)
EDC	= EROS Data Center
ESC	= Earth Satellite Corporation
IPF	= Image Processing Facility (USGS Flagstaff)
JPL	= Jet Propulsion Laboratory
JSC	= Johnson Space Center
LRC	= Langley Research Center
NAPL	= National Air Photo Library (Canada)
NGS	= National Geographic Society
NPS	= National Park Service
NOAA	= National Oceanographic and Atmospheric Admin.
NSSDC	= National Space Science Data Center (GSFC)
USGS	= U.S. Geological Survey, at the following locations: Denver, Colorado; Flagstaff, Arizona; Menlo Park, California; Reston-National Center, Virginia.

PART 1 SOURCES

Chapter 1: Introduction

I-1: Carey, 1962, ©; **I-2:** V. Baker; **I-3:** V. Baker; **I-4:** 1285-17445, 5/4/73; **I-5:** F. Sabins, 1983, ©; **I-6:** V. Baker; **I-7:** 50116-08031-4

I-1: Ls mosaic, ESC; **I-1.1:** J. Shelton; **I-1.2:** S. W. Lohman, 655, USGS-PL; **I.3:** D. Carroll, 10, USGS-PL; **I-1.4:** J. S. Bradley

I-2: 10171-06530 (C), 1/10/73, ESC; **I-2.1:** H. Blodget

I-3: USGS Flagstaff/JPL; **I-3.1:** C. Elachi, JPL; **I-3.2:** SIR-A Data Take; **I-3.3:** C. Elachi, JPL

I-4: 1373-00364(C), 7/31/73; **I-4.1, I-4.2, I-4.4, I-4.5, I-4.6:** V. Baker; **I-4.2:**

Chapter 2: Tectonic Landforms

2-1: P. D. Lowman, Jr.; **2-2:** Tapponnier and Molnar, 1975, ©

T-1: National Geographic Society; **T-1.1:** E. Paylor, JPL

T-2: Mosaic, U.S. Soil Conservation Service; **T-2.1:** J. R. Balsey, 28, USGS-PL; **T-2.2:** Aero Service; **T-2.3:** 0546-20060-1; **T-2.4:** Apollo 9-21-3263, JSC

T-3: 40145-18084(C), 12/8/82, ESC; **T-3.1:** USGS-PIO 68-49f; **T-3.2:** J. Shelton, 5247; **T-3.3:** STS-17; **T-3.4:** J. Everett

T-4: Mosaic, USGS Flagstaff IPF; **T-4.1:** J. Shelton, 3851; **T-4.2:** J. Shelton, 682

T-5: 40012-17495(C), 11/12/82; **T-5.1:** Skylab; **T-5.2:** 50114-17501(C), 6/23/84; **T-5.3:** C. B. Hunt, 917, USGS-PL; **T-5.4:** USGS APA Calif 24B

T-6: 0528-19310-1, 10/6/1979; **T-6.1:** 0171-20260-1, 10/14/78; **T-6.2:** 5239-17083-5, 12/14/75; **T-6.3:** T. S. Lovering, 5a, USGS-PL; **T-6.4:** T. S. Lovering, 6a, USGS-PL

T-7: 1068-17364(C), 9/29/72, ESC; **T-7.1:** J. Shelton, 1561; **T-7.2:** 2693-17073-6, 12/15/76, EDC; **T-7.3:** LFC 2041, 10/6/78

T-8: Mosaic, ESC; **T-8.1:** 1408-17294(C), ESC; **T-8.2:** J. R. Balsey, 3 USGS-PL; **T-8.3:** 20885-17101-7, 8/29/76, ESC; **T-8.4:** J. Shelton, 1972

T-9: 036-10540-3, 6/1/78; **T-9.1:** Monger et al., 1982, ©; **T-9.2:** A. Dunn; **T-9.3:** 2182-18183-7, 7/23/75; **T-9.4:** BC 762:108, British Columbia Air Photo Library

T-10: Mosaic, Soil Conservation Service: **T-10.1:** 1103-20513-7, 11/3/72; **T-10.2:** 1103-20504-7, 11/3/72; **T-10.3:** K. Dean; **T-10.4:** M. Meier, 2, USGS-PL

T-11: 0570-17380-1, 11/17/79 (map from Hatcher and Viele, 1982), ©; **T-11.1:** 0153-18160-2, 9/26/78; **T-11.2:** 21401-5, 2/11/79, EDC; **T-11.3:** 40102-15062-5, 10/26/82; **T-11.4:** 40114-15333-4, 11/7/82; **T-11.5:** Landsat, ID unknown

T-12: 50202-15222(C), 9/19/84, ESC; **T-12.1:** SAR Rev 759, 8/19/78, JPL; **T-12.2:** J. Hornsby; **T-12.3:** J. Shelton, 40E

T-13: Ls mosaic 1858-15300-7 and 1858-15303-7, 11/28/74; **T-13.1:** SAR Rev 407, 5/15/80, JPL; **T-13.2:** R. Frear, NPS

T-14: 1146-16300-7, 12/16/72, ESC; **T-14.1:** H. C. Macdonald; **T-14.2:** SAR Rev 795, 8/21/78

- T-15:** 1443-15322-7, 10/18/73; T-15.1 and T-15.2: Lowman et al., 1986; T-15.3: N. M. Short; T-15.4: 40100-15182-5, 10/4/82
- T-16:** 1438-15013-6, 10/4/73, CCRS; T-16.1: 40184-14522-4, 1/16/83; T-16.2: A11503-97, NAPL (Can.); T-16.3: T 185-R-35, NAPL (Can.); T-16.4: ID unknown
- T-17:** 1206-18381-7, 2/14/73; T-17.1: Lowman et al., 1986; T-17.2: T 481-L-19, NAPL (Can.); T-17.3: A5120-105R, Canadian Royal Air Force; T-17.4: 10436-18132-7, CCRS
- T-18:** 20943-18161-7, 8/22/77, ESC; T-18.1: T420L-22, NAPI (Can.); T-18.2: 420 R-16, NAPI (Can.); T-18.3: A16203-115, NAPL (Can.)
- T-19:** 1508-16410-6, 12/13/73; T-19.1: Zona 77A-1834, 20 F 7, L. M. Mitre-Salazar; T-19.2: J. Shelton, 6011; T-19.3: Zona 85A 1353 15 F 31, L. M. Mitre-Salazar
- T-20:** Ls mosaic, ESC; T-20.1: 21447-13371-7, 1/8/79, ESC; T-20.2: S. J. Prucha
- T-21:** Ls mosaic, R. Allenby; T-21.1: 2130-13412-6, 6/1/75; T-21.2: 20148-13421-7, 6/18/75; T-21.3: Apollo 7 AS-7-7-1826, JSC; T-21.4: 1244-14065-7, 3/14/73, ESC
- T-22:** 2194-14351-6, 8/4/75; T-22.1: H. Garner; T-22.2: W. Zeil; T-22.3: R. Allenby; T-22.4: 20382-13442-7, 2/8/76, ESC
- T-23:** 1233-10564-7, 3/13/73; T-23.1: E. Kristoff, NGS; T-23.2: P. D. Lowman, Jr.; T-23.3: SAR Rev 719, 8/16/78, JPL
- T-24:** Ls mosaic, H. R. Hopkins; T-24.1: J. Ballais; T-24.2: 1147-08163-7, 12/17/72; T-24.3: 1327-06312-7, 6/15/73
- T-25:** Ls mosaic, Westerman Sat Map, ©; (courtesy L. Beckel) (accompanying map from Spencer, 1977, ©); T-25.1: C. Embleton; T-25.2: C. Burchfiel; T-25.3: Swissair 20643; T-25.4: L. Beckel; T-25.5: 50155-09272-6, 8/8/84; T-25.6: L. Beckel
- T-26:** 1078-09555-7, 10/9/72; T-26.1: M. E. Perret, 94-35; T-26.2: aerial photo 3327-3328 (source unknown); T-26.3: M. E. Perret; T-26.4: 1078-09553-5, 10/9/72
- T-27:** 1102-08491-7, 11/2/72; T-27.1: C. Burchfiel; T-27.2: L. Faugeres; T-27.3: C. Burchfiel
- T-28:** 2922-06040-7, 8/1/77; T-28.1: 1389-06515-7, 8/16/73; T-28.2: Sovfoto-Eastfoto, ©; T-28.3: 2084-07161-7, 4/16/75
- T-29:** 1221-02505-6, 3/1/73; T-29.1: 1365-02500-7, 7/23/73; T-29.2: D. Conger, NGS; T-29.3: 1244-01374-7, 3/24/73; T-29.4: 30961-23111-B, 10/21/80
- T-30:** Ls subscene 10103-10413V(C), 11/3/72, ESC; T-30.1: 0230-13520-1, 12/18/78; T-30.2: L. Bogart; T-30.3: R. Snead; T-30.4: 10551-10253-7, 1/25/74, ESC; T-30.5: 1115-10060-7, 11/15/72
- T-31:** STS-17, JSC; T-31.1: 2369-10291-5, 11/20/80; T-31.2: C. Monod; T-31.3: Monod and Pomerol, 1973, ©
- T-32:** 1382-08205(C), 8/9/73; T-32.1: R. Snead; T-32.2: C. Twidale; T-32.3: J. Manning; T-32.4: 50086-07463-4, 6/16/84
- T-33:** 10230-07370(C), 3/10/73, ESC; T-33.1: 365, Geol. Surv. S. Africa; T-33.2: C. Twidale; T-33.3: 278, Geol. Surv. S. Africa; T-33.4: 2151-07074-7, 6/22/75
- T-34:** 10103-07291-7, 11/7/72, ESC; T-34.1: 1390-07214-5, 8/17/73; T-34.2: Stagman, 1978, ©; T-34.3: 10049-07272-7, 9/10/72, ESC
- T-35:** Ls mosaic, W. Smith; T-35.1: G. McCall; T-35.2: E. Kristoff, NGS; T-35.3: W. Moore, NGS
- T-36:** Ls mosaic, NASA/General Electric; T-36.1: 50044-07003-4, 4/14/84; T-36.2: E. Kristoff, NGS; T-36.3: H. Tazieff (H. Garner, 1974, ©); T-36.4: 50044-07003-4, 4/14/84
- T-37:** Apollo 7 7-5-1623, JSC; T-37.1: 1090-07433-7, 10/21/72, USGS-Flagstaff IPF; T-37.2: F. Bender, 3, USGS-PL; T-37.3: R. Snead; T-37.4: F. Bender, 9, USGS-PL
- T-38:** Ls mosaic, ESC; T-38.1: Apollo-Soyuz AST-9-564
- T-39:** Ls mosaic, ESC; T-39.1: Sengor and Yilmaz, 1981, ©; T-39.2: Earthquake Information Bull. 225, USGS-PL; T-39.3: 2248-07247-7, 9/27/75 and 2229-07214-7, 9/8/75
- T-40:** Ls mosaic, ERIM, prepared for USGS-Reston; T-40.1: W. Greenwood; T-40.2: H. Blodget
- T-41:** 10127-06080(C), 11/27/72, ESC; T-41.1 and T-41.2: D. Rothery; T-41.3: LFC 223, 10/6/84
- T-42:** Ls mosaic, ESC; T-42.1: 10220-06241(C), 2/28/73, ESC; T-42.2: Gemini, ID unknown; T-42.3: USGS APA Iran-7-B; T-42.4, T-42.5, and T-42.6: T. Oberlander and Hunting Surveys, Inc., ©; T-42.7: J. T. Daniels; T-42.8: 30945-06213-D, 10/5/78; T-42.9: 20549-06534-7, 7/24/76
- T-43:** Ls mosaic, R. Lawrence/R. O. Rogers, Oregon St. Univ.; T-43.1: STS-17; T-43.2: 30554-05193-7, 9/9/79; T-43.3: 20838-05065-7, 5/9/77, ESC; T-43.4, T-43.5, T-43.6, and T-43.7: R. Lawrence
- T-44:** 30212-05203(C), 10/3/78; ESC; T-43.1: SIR-A Data Take 35-36, 11/14/81; T-43.2: K. DeJong; T-43.3: 30283-05151-7, 12/13/78; ESC
- T-45:** 30283-05144(C), 12/13/78, ESC; T-45.1 and T-45.2: K. DeJong

T-46: 20691-04550(C), 12/13/76, ESC; T-46.1, T-46.2, and T-46.3: K. DeJong

T-47: 2719-04125-6, 1/10/77; T-47.1, T-47.2, and T-47.3: S. Drury; T-47.4: 1107-04133-5, 11/7/72

T-48: STS-17, S7-120-022; T-48.1: LFC 534; T-48.2: LFC 173; T-48.3: Chi and Ren, 1980; T-48.4: 1216-0413307, 2/24/73, T-48.5: C. Burchfiel; T-48.6: Chi and Ren, 1980; T-48.7: LFC 503; T-48.8: STS, Mission ID unknown; T-48.9: 20711-03245(C)

T-49: 1206-05000-7, 2/14/73; T-49.1: SIR-A Data Take 28, 11/14/81; T-49.2: Chi and Ren, 1980; T-49.3: 2746-04565-7, 2/6/77; T-49.4: V. Trifonov

T-50: LFC 168, 10/6/84; T-50.1: 1074-04253, 10/5/72; T-50.2: 1128-04250-6, 11/28/72; T-50.3: 1482-03493-7, 11/17/73; T-50.4: Chi and Ren, 1980

T-51: Ls mosaic, EDC; T-51.1, T-51.2, T-51.3, and T-51.4: B. Bailey

T-52: 2305-02370-6, 11/25/75; T-52.1: 2647-02280-6, 10/30/76, and 1488-02415-6, 11/23/73; T-52.2: 1523-02331-7, 12/28/73

T-53: 1547-03112-7, 1/21/74; T-53.1: 1531-03232-7 and 1531-03235-7, 1/5/74; T-53.2: J. Rock, NGS

T-54: 1112-01120-7, 11/12/72; T-54.1 and T-54.2: M. Sano; T-54.3: 2232-00470-7, 9/11/75

T-55: Ls mosaic, Dept. Lands & Surveys, Western Australia; Geol. Map of Australia, 1:2500000, 1974-76, compiled by W. D. Palfreyman, Bur. of Mineral Resources, Geology, and Geophysics, Canberra, ©; T-55.1: 1148-01282(C), 12/18/72; T-55.2: subscene 1148-01282-5, 12/18/72, CSIRO; T-55.3: F-50-8, Run 5, 127 (1:86000), Div. National Mapping, Australia; T-55.4: SIR-A Data Take 38, 11/14/81; T-55.5: C. Twidale; T-55.6: J. Manning; T-55.7 and T-55.8: C. Twidale

T-56: 1377-00573(C), 8/4/73, CSIRO; Geol. Map of Western Australia, 1:1900000, 1970, Dept. Lands and Surveys, Western Australia, ©; T-56.1: Ls Mosaic, Dept. Lands and Surveys, Western Australia; T-56.2: E52-6, Run 2, 7233 (1:86000), Div. National Mapping, Australia; T-56.3: C. Finkl, Jr.

T-57: 22144-23514-7, 12/5/80, ESC; T-57.1, T-57.2, and T-57.3: C. Twidale

T-58: 0050-03010-2, 6/15/78; T-58.1: R. Blair, Jr.; T-58.2: 30180-21335-7, 9/1/78; T-58.3 and T-58.4: D. Homer, N. Zealand Geol. Surv.

T-59: 21395-08373(C), 11/17/78, ESC; T-59.1: MARS SLAR image, ©; T-59.2: WRS 237-77, N. Parada, INPE; T-59.3: 1109-09343-7, 11/9/72; T-59.4: J. Ballais

T-60: Egypt = SIR-A Data Take 28, 11/14/81; 1180-07444-7, and 1180-07442-7, 1/19/73; Mali = SIR-A Data Take 29-30, 11/14/81; 1490-09501-7, 11/25/78; T-60.1: 1106-09183-7, 11/6/72; T-60.2: 281214-121742-7, 6/29/83, N. Parada, INPE; T-60.3: 10177-07293-7, 1/16/73, ESC

T-61: Landsat images and other figures, courtesy J. McHone

Chapter 3: Volcanic Landforms

3-1: 1097-04465-5, 10/28/72; **3-2:** Press and Siever, 1982, © (adapted from R. G. Schmidt and H. R. Shaw, USGS); **3-3:** 1825-17294-7, 10/26/72

V-1: 0171-20240-1, 10/14/78; **V-1.1:** 0171-20240-2, 10/14/78; **V-1.2** and **V-1.3:** J. Shelton; **V-1.4:** 40123-17061-5, 11/16/72, ESC

V-2: 10856-11/26/74, ESC; **V-2.1:** Apollo 9 AS-9-20-3141, JSC; **V-2.2:** J. Shelton, **V-2.3:** R. Bailey, USGS-Reston

V-3: 1103-17323-5, 11/3/72; **V-3.1** and **V-3.2:** J. McCauley; **V-3.3:** SAR Rev 322, 7/19/78; **V-3.4:** R. Sutton

V-4: 40199-17332-5, 1/31/83; **V-4.1:** T. Nichols; **V-4.2:** D. Roddy; **V-4.3:** 40183-17332-6, 1/15/83

V-5: Mosaic of U.S., Soil Conservation Service; **V-5.1:** F. Jones, 29, USGS-PL; **V-5.2:** PIO-80-96a, USGS-PIO; **V-5.3:** 6719, Oregon St. Highway Dept.; **V-5.4:** PIO-78-173, USGS-PIO

V-6: 1094-18215-7, 10/25/72; **V-6.1:** H. Cornwall, 86, USGS-PL; **V-6.2:** Landsat-1, ID unknown; **V-6.3:** 65-90, Oregon St. Dept. Geol. & Min. Ind.

V-7: 1358-17471(C), 7/16/73, EDC; **V-7.1:** 40392-18133-4, 8/12/83; **V-7.2:** R. Greeley; **V-7.3:** J. Shelton; **V-7.4:** USGS APA Idaho 5-A

V-8: 22017-18144 (subscene), 7/31/80; **V-8.1:** USGS APA Wash. 7-B; **V-8.2:** K. Ronnholm, ©; **V-8.3** and **V-8.4:** C. Rosenfeld; **V-8.5:** PIO-80-130C, USGS-PIO; **V-8.6:** PIO-80-126C, USGS-PIO; **V-8.7:** NOAA, GOES-West, 1233 26081 KB7, 5/18/80; **V-8.8:** 80-55-095, EDC (USGS); **V-8.9:** MSH PP 1250 103, USGS-PL; **V-8.10:** 50140-18245-3, 6/19/80, **V-8.11** and **V-8.12:** C. Bohn; **V-8.13** and **V-8.14:** C. Rosenfeld; **V-8.15:** PIO-81-239, USGS-PIO; **V-8.16:** 50140-18245-6, 6/19/80, GSFC

V-9: 30341-20591-5, 2/9/79, EDC; **V-9.1:** Radar mosaic 1:250000, MARS SLAR, ©, courtesy A. Kovar, USGS-Reston; **V-9.2:** M. Williams, NPS; **V-9.3:** SAR Rev 0605, JPL

V-10: 1203-20180-6 and 1203-20182-6, 2/11/73; **V-10.1:** U.S. Air Force 38525; **V-10.2:** USGS APA Hawaii 7-C; **V-10.3:** USGS, ID unknown

V-11: 1816-16430-5, 10/17/74; V-11.1: R. Snead; V-11.2: Texas Bur. Econ. Geol.; V-11.3: G. K. Gilbert, 2337, USGS-PL; V-11.4: G. Gahan, NGS

V-12: 21449-15304-7, 1/12/79, EDC; V-12.1: SIR-A Data Take 18, 11/13/81, JPL; V-12.2: Nagle et al., 1977, ©

V-13: 30624-15340-7, 11/19/79, EDC; V-13.1: SIR-A Data Take 37, 11/14/81, JPL; V-13.2: U.S. Air Force

V-14: 2419-13440-7, 3/16/76, EDC; V-14.1: L. O'Callaghan; V-14.2: STS-8, SO8-36-1387; V-14.3: 2436-13433-7, 4/2/76, EDC; V-14.4: K. Segerstrom, 602, USGS PL

V-15: 1392-12191-7, 8/19/73; V-15.1: R. Williams, Jr.; V-15.2 and V-15.3: S. Thorarinsson; V-15.4: J. Friedman, USGS-Denver

V-16: Ls subscene 04-465-07140(C), 4/23/83, Telespazio; V-16.1: Ls subscene, ID unknown, Telespazio; V-16.2 and V-16.3: Carnegie Geophysical Laboratory, Washington, D.C.; V-16.4: Ls subscene, ID unknown, 6/16/77, Telespazio

V-17: 50209-07140(C), 9/26/84; V-17.1: O. Erol; V-17.2: 10084-07062-7, 10/15/72, ESC; V-17.3: SIR-A Data Take 35, 11/14/81, JPL

V-18: 2367-08343-7, 1/26/76, ESC; V-18.1: D. Busch; V-18.2: A. Pesce; V-18.3: 1190-08433-6, 1/29/73; V-18.4: STS-17, SO9-45-2162, JSC

V-19: 2368-07040-6, 1/25/76, EDC V-19.1: G. McCall; V-19.2: 1191-07115-7, 1/30/73; V-19.4: Source unknown

V-20: 50081-07314-4, 5/21/84, EDC; V-20.1: Republic S. Africa Geol. Surv.; V-20.2: A. De Villiers; V-20.3: 2116-07141-7, 5/18/75

V-21: LFC 1330, 10/9/84; V-21.1: Earthquake Info. Bull. Photo 435, USGS-PL; V-21.1 and V-21.3: H. Tazieff (see H. Garner, 1974, ©)

V-22: 1446-07195(C), 10/12/73; V-22.1 and V-22.2: H. Blodget; V-22.3: 1160-07323-7, 12/30/72; V-22.4: Geol. Map of Al Madinah Quadrangle, Sheet 24-D, 1981, Kingdom of Saudi Arabia, Ministry of Petroleum and Mineral Resources

V-23: 30278-04492-5, 12/8/78, EDC; V-23.1, V-23.2, and V-22.3: C. Ollier; V-23.4: 2362-04404, 1/19/76, EDC

V-24: 30277-01130-5, 12/7/78, EDC; V-24.1: M. Morisawa; V-24.2: Japan Air Lines; V-24.3: 1145-00542-7, 12/15/72; V-24.4: M. Sano

V-25: 1477-23542-5, 11/12/73; V-25.1, V-25.2, and V-25.3: A. E. Sviatlovsky (see V. Trifonov); V-25.4: 1047-00025-7 and 1047-00031-7, 9/8/72; V-25.5: STS 9-31-109

V-26: 10067-02145-7, 9/28/72, ESC; V-26.1: W. Hamilton, 549, USGS-PL; V-26.2: Dept. Information, Repub. Indonesia; V-26.2: SIR-A Data Take 35-36, 11/14/81

V-27: 30844-21121-6, 6/26/80, EDC; V-27.1 and V-27.2: D. Homer, New Zealand Geol. Surv.; V-27.3: S. N. Beatus, New Zealand Geol. Surv.

Chapter 4: Fluvial Landforms

4-1: Howard, 1967, ©; **4-2:** SIR-A Data Take 24C, 11/13/81; **4-3:** 2436-08080-7; **4-4:** V. Baker, **4-5:** Schumm and Kahn (1975), ©

F-1: 21711-16314-7, 9/29/79; F-1.1 and F-1.2: V. Baker; F-1.3: USGS APA Texas 5-B

F-2: 1524-02394-7, 12/29/73; F-2.1: 2287-02344-7, 11/5/75; F-2.2: SIR-A Data Take 38, 11/14/81; F-2.3: USGS APA China 1-A

F-3: 30597-02293-7, 10/29/79, ESC; F-3.1: 1525-02455-7, 10/30/73; F-3.2: B. Dale, NGS; F-3.3: C. Burchfiel

F-4: 30289-07322-6, 12/19/78; F-4.1: LFC 230; F-4.2: 30972-07122(C), 11/1/80

F-5: 1167-06324-6, 1/6/73; F-5.1: 2362-06242-5, 1/9/76; F-5.2: STS-17-36-36; F-5.3: 1186-06381-7, 1/25/73, USGS-Flagstaff IPL; F-5.4: 30346-06100-6, 2/14/79

F-6: 30194-17091-A, 9/5/78; F-6.1: J. Shelton; F-6.2: J. Bradley; F-6.3: R. Snead; F-6.4: Source unknown

F-7: 1284-17384(C), 5/3/73; F-7.1: J. Shelton, 920; F-7.2: J. Shelton, 67:545, F-7.3: TM subscene 40183-17321(C), 4/19/83

F-8: 21446-13324-7, 1/9/79; F-8.1: K. Lee; F-8.2: Vargas (Venezuelan Airlines); F-8.3: SIR-A Data Take 34, 11/14/81; F-8.4: 1177-14255-7, 1/16/73

F-9: 40176-17270(C), 1/8/83; F-9.1, F-9.2, and F-9.3: P. Kresan

F-10: 0344-19040-1, 4/5/79; F-10.1: 0344-19040-2, 4/5/79; F-10.2: 40037-16033-4, 8/22/82; F-10.3: USGS APA Miss. 2-C; F-10.4: Apollo 9 9-22-3454

F-11: 1344-21290-7, 7/2/73; F-11.1: Source unknown; F-11.2: J. Coleman; F-11.3: T. Mortensen; F-11.4: Source unknown

F-12: 1408-20430-7, 9/4/73; F-12.1: T. Péwé, 849, USGS-PL; F-12.2: T. Péwé, 844, USGS-PL; F-12.3: J. Williams, 7e, USGS-PL; F-12.4: 1102-20441, 11/2/72

F-13: 1123-04010-5, 11/23/72; F-13.1: J. Coleman; F-13.2: Source unknown; F-13.3: J. Coleman

F-14: 30170-23570-B, 8/22/78; F-14.1: V. Baker; F-14.2: R. Goodman, NGS; F-14.3 and F-14.4: Div. of National Mapping, Australia

F-15: 1563-23530(C), 2/6/74; F-15.1: V. Baker; F-15.2: Div. of National Mapping, Australia; F-15.3: G. Taylor

F-16: 1519-02131-7, 12/24/73, F-16.1: 2464-02165-6, 4/30/76, EDC; F-16.2, F-16.3, and F-16.4: V Baker

F-17: 1127-06065-7, 11/27/72; F-17.1, F-17.2, and F-17.3: J. Coleman

F-18: 1400-04352-7, 8/27/73; F-18.1: 2621-03235-6, 10/4/76; F-18.2: 1191-03332-7, 1/30/73; F-18.3: 10127-06083-7, 11/27/72, ESC

F-19: 2751-03455-7, 2/11/77; F-19.1, F-19.2, and F-19.3: N. D. Smith

F-20: 1061-10104(C), 9/22/72; F-20.1: N. MacLeod; F-20.2: Apollo 9 9-19-3052; F-20.3 and F-20.4: N. MacLeod

F-21: 281149-125759-7 and 281149-125824-7, 5/29/81, Parada, INPE; F-21.1: 281132-130308, 6/30/83, Parada, INPE; F-21.2: M. J. Costa

F-22: 77212-13081-7, 7/31/77, ESC; F-22.1: Sternberg, 1975, ©; F-22.2: 1126-13013-5, 11/26/72; F-22.3 and F-22.4: L. McIntyre, NGS

F-23: 50115-13475(C), 6/14/77; F-23.1: 1008-13481-7, 7/31/72; F-23.2: V. Baker

F-24: Top = SIR-A Data Take 24C, 11/13/81, Middle = Map by V. Baker, Bottom = Brazilian RADAM image NA-19-Z-C; F-24.1: 50129-14022-4, 7/8/84; F-24.2: 50126-08320-4, 8/5/84

F-25: 78224-14193-7, 8/12/78; F-25.1: SIR-A Data Take 34, 11/14/81; F-25.2: R. Snead

F-26: Ls mosaic, H. Blodget and GSFC/GE; F-26.1: USGS Aerial Photo 4-9-77 GS VECK 0948; F-26.2: J. Shelton, 1715

F-27: 1381-18142-7, 8/8/73; F-27.1: J. Shelton, 6235; F-27.2: J. Shelton, 5595, F-27.3: J. Shelton, 5599

Chapter 5: Deltaic Landforms

5-1: A. Defense Mapping Satellite; B. STS-4-37-654; C. Landsat ID unknown; D. 30263-03242-5 and 30263-03235-5, 11/23/78

D-1: 1177-16023-5, 1/16/73; D-1.1: J. Coleman, unpublished report, ©; D-1.2: Kolb and Van Lopik, 1966; D-1.3: J. Coleman; D-1.4: H. Roberts; D-1.5: 40188-15552(C) subscene, 1/15/83; F-1.6: USGS APA LA-8; F-1.7, F-1.8, F-1.9, and F-1.10: J. Coleman

D-2: 2904-07510-7 and 2904-07504-7, 8/14/77; D-2.1 and D-2.2: J. Coleman

D-3: 30303-03454-6 and 30303-03450-6, 1/2/79; D-3.1: 30303-03454-4, 1/2/79; D-3.2: J. Coleman

D-4: STS-01004, 11/21/81; Thailand Landsat Receiving Station, Courtesy MacDonald, Dettwiler and Assoc., Inc.; D-4.1 and D-4.2: J. Coleman

D-5: 30067-01462, 5/11/78, ESC; D-5.1 and D-5.2: J. Coleman; D-5.3: 2368-01364-5, 10/21/76

D-6: 1520-02210-5, 12/25/73, R. Haydn, ZGF; D-6.1: J. Coleman; D-6.2: H. J. Walker

D-7: 1163-02450-7, 1/3/73; D-7.1: W. Garrett, NGS; D-7.2 and D-7.3: J. Coleman and U.S. Dept. of Defense

D-8: Ls mosaic 50115-06582-4, 6/24/84 and 50122-07044-4, 7/1/84; EDC; D-8.1: STS 51B-31-060, JSC; D-8.2: J. Coleman

D-9: 2505-21303-7, 6/10/76, EDC; D-9.1: 21477-21245-6, 2/7/79; D-9.2: J. Coleman; D-9.3: W. Dupre

D-10: 21985-20125(C), CCRS; D-10.1: J. Coleman; D-10.2: 1457-20123-7, 10/23/73; D-10.3 and D-10.4: J. Coleman

D-11: 1368-03062-7, 7/23/73; D-11.1 and D-11.2: Suslov, 1961, ©; D-11.3: J. Coleman; D-11.4: 1397-05524-7, 8/24/73

D-12: 2335-17311-7, 12/25/75, EDC; D-12.1: J. Shelton; D-12.2 and D-12.3: L. D. Meckel and Co.

D-13: 2653-06291(C), 12/30/80, R. Haydn, ZGF; D-13.1: Apollo 7-6-1699; D-13.2 and D-13.3: R. Snead

D-14: 1228-05274-7, 3/8/73; D-14.1: R. Snead; D-14.2 and D-14.3: J. T. Wells

D-15: 1310-06192(C), 5/29/73; D-15.1: V. Trifonov; D-15.2 and D-15.3: J. Coleman

Chapter 6: Coastal Landforms

6-1 and 6-2: Inman and Nordstrom, 1971, ©

C-1: 1100-01435-5, 10/31/72; C-1.1, C-1.2, and C-1.3: D. W. Park

C-2: 2263-23006-6, 10/12/75, EDC; C-2.1 and C-2.2: C. Pain; C-2.3: Div. of National Mapping, Australia; C-2.4: R. Snead

C-3: 1069-00442(C), 9/30/72; C-3.1: 10102-00281-7, 2/11/72; C-3.2: Div. of National Mapping, Australia; C-3.3: D. Gibson; C-3.4: R. Snead

- C-4:** 21468-12235-6, 1/29/79, EDC; C-4.1: 2376-16172-7, 2/2/76; EDC; C-4.2: K. W. Glennie; C-4.3: 278030-114110-7, Parada, INPE; C-4.4: K. W. Glennie
- C-5:** 1775-19330-7, 9/16/74; C-5.1: R. Snead; C-5.2: A. Dunn; C-5.3: R. Churchill; C-5.4: 2350-10073-6, 7/5/76, EDC
- C-6:** 31510-12502-6, 4/23/82, EDC; C-6.1, C-6.2, and C-6.3: S. M. Harrison/C. Swithinbank
- C-7:** 2573-10472-6, 8/17/76, EDC, C-7.1 and C-7.2: R. Snead; C-7.3: Irish Tourist Board; C-7.4: 1472-14530-7, 11/10/73
- C-8:** 0170-12000-2, 10/13/78; C-8.1 and C-8.2: R. Snead; C-8.3: 30197-09003-7, 9/18/78, EDC; C-8.4: R. Snead
- C-9:** 1123-05441-5, 11/23/72; C-9.1, C-9.2, and C-9.3: R. Snead
- C-10:** 2192-21265(C), 8/2/75; C-10.1: U.S. Navy; C-10.2: R. Kirk in Snead, 1967, ©; C-10.3: New Zealand Geol. Surv., A 109
- C-11:** 2335-21190-6, 12/23/75, EDC; C-11.1: Royal New Zealand Air Force in Stevens, 1974, ©; C-11.2: Stevens, 1974, ©; C-11.3 and C-11.4: L. Homer, New Zealand Geol. Surv.
- C-12:** 1155-14102-6, 12/25/72; C-12.1, C-12.2, and C-12.3: S. Araya Vergara
- C-13:** Apollo 9 AS9-20-3128, JSC; C-13.1: M. Morisawa; C-13.2: Apollo 9 AS9-21-3271, JSC; C-13.3: 2437-15112-7, 4/3/76; C-13.4: S. Leatherman
- C-14:** 1045-15275-15275(C), 9/6/72; C-14.1 and C-14.2: NPS; C-14.3: 30009-15095-A, 3/14/78
- C-15:** SAR Rev. 809, 8/22/78, JPL; C-15.1: 0192-18330-1, 11/4/78; C-15.2: J. Ford; C-15.3: J. Shelton, 9544; C-15.4: C. Finkl, Jr.
- C-16:** 40182-15125(C), 1/18/83; C-16.1: 1510-15093(C), 12/15/73; C-16.2: Apollo, ID unknown; C-16.3: B. A. Stewart, NGS
- C-17:** Ls mosaic, ESC; C-17.1, C-17.2, and C-17.3: R. Ginsburg
- C-18:** 1203-23543-5, 2/11/73; C-18.1: STS-18, JSC; C-18.2: 1026-00035-5, 8/18/72; C-18.3: D. Hopley, 1982, ©; C-18.4: Div. of National Mapping, Australia
- C-19:** Top = 1112-01234-5, 11/12/79; Lower left = 2013-00365-4, 2/4/75; Lower right = 30258-04415-5, 11/18/79; C-19.1: 30244-22173-5, 11/4/78; EDC; C-19.2: C. G. Johnson, 2, USGS-PL; C-19.4: W. Moore, NGS
- C-20:** 21189-01004-7, 4/25/78, ESC; C-20.1, C-20.2, and C-20.3: Dept. of Lands and Surveys, W. Australia
- C-21:** 1134-06425-5, 12/4/72; C-21.1: 2778-06150-6, 3/10/77; C-21.2: 21327-14061-7 and 21327-14063-7, 9/10/78; C-21.3: 1199-06302-5 and 1199-06302-5, 12/19/72
- C-22:** Ls mosaic 2294-05020-6 and 2294-05024-6, 11/12/75; C-22.1: 1136-05162-5, 12/6/72; C-22.2: J. Coleman
- C-23:** Ls mosaic 1079-15135-7, 10/10/72 and 1080-15187-7, 10/11/72; C-23.1: U-2 photo 00025 0083, Ames Research Ctr.; C-23.2: 2046-10404-7, 3/9/75, EDC
- C-24:** 40202-16184-4, 2/3/83; C-24.1: Nat. Air Photo Library, Canada; C-24.2: Photo 83255, Geol. Surv. of Canada

Chapter 7: Karst Landscapes and Lakes

- 7-1:** 30091-09094-7 (subset), 6/8/78; map from J. Demek in C. Embleton, 1982, ©; **7-2:** Jennings, 1971, ©; **7-3:** A. 1057-16305-7, 9/18/72; B. A116797-84, Nat. Air Photo Library, Canada
- KL-1:** 1524-02432-7, 12/29/73; K-1.1 and K-1.2: Karst in China, 1976; KL-1.3: Chinese postcard; KL-1.4: Karst in China, 1976
- KL-2:** SAR Rev 608, 8/8/78; JPL; KL-2.1: M. Sweeting, 1958, ©; KL-2.2 and KL-2.3: M. Day
- KL-3:** 21089-15115(C), 1/15/78, ESC; KL-3.1, KL-3.2, and KL-3.3: S. Prucha
- KL-4:** 30244-15181-7, 11/4/78, EDC; KL-4.1: USGS Topographic Map; KL-4.2: G. Espenshade, 51, USGS-PL; KL-4.3: USGS
- KL-5:** 1104-08595-7, 11/4/72; KL-5.1: I. Bralic in M. Herak, 1972; KL-5.2: P. S. Williams; KL-5.3: S. Božičević in M. Herak, 1972; KL-5.4: C. Rosenfeld
- KL-6:** 2083-00391-6, 4/15/75; EDC; KL-6.1: Lowry and Jennings, 1974; KL-6.2 and KL-6.3: C. Twidale; KL-6.4: Lowry and Jennings, 1974
- KL-7:** 1018-21200-6, 8/10/72; KL-7.1 and KL-7.2: J. B. Mertie, Jr., 1938, KL-7.3: K. Dean; KL-7.4: 1381-18133-7, 8/8/73
- KL-8:** 1387-06402-7, 8/14/73; KL-8.1: Sovfoto-Eastfoto, ©; KL-8.2: 1397-05551-7, 8/24/73; KL-8.3: 1397-05540-7, 8/24/73
- KL-9:** 20182-21394-7, 7/23/75, ESC; KL-9.1: Black and Barksdale, 1949, ©; KL-9.2: Hopkins et al., 1955, ©; KL-9.3: Black and Barksdale, 1949, ©
- KL-10:** 1080-15203-5, 10/11/72; KL-10.1 and KL-10.2: W. Prouty, 1952, ©; KL-10.3: J. Shelton, 1686
- KL-11:** Ls mosaic, R. Allenby; KL-11.1, KL-11.2, KL-11.3: G. Plafker

KL-12: 10051-17420-7, 9/12/72, ESC; KL-12.1: A. Granger in R. Morrison, 1965, ©; KL-12.2: USGS-Flagstaff; KL-12.3: Thornbury, 1965, ©; KL-12.4: Hamblin, 1985, ©

KL-13: 1243-13595(C), 3/23/73; KL-13.1, KL-13.2, and KL-13.3: G. Erickson; KL-13.4: 1243-13595(C), subscene, JPL

KL-14: 2150-03123-5, 6/21/75, EDC; KL-14.1: Sovfoto-Eastfoto, ©; KL-14.2: V. Trifonov; KL-14.3: 30087-08444-6, 6/1/79; KL-14.4: Ls mosaic 21304-04496-6 and 21304-04500-6, 8/18/78

KL-15: 10443-14073-7, 10/9/73, ESC; KL-15.1, KL-15.2, and KL-15.3: N. D. Newell

Chapter 8: Eolian Landforms

8-1: A. Walker, modified from various sources; **8-2:** P. Meigs, 1953, ©; **8-3:** A. Walker, modified from various sources

E-1: 1137-07043-7, 12/7/72, EDC; E-1.1: J. Briggs; E-1.2: E. G. Friesen; E-1.3: 11241-WSA-68, Dept. of Defense aerial photo, from Breed and Grow in McKee, 1979, ©

E-2: 1111-06195-7, 11/11/72, USGS-Flagstaff IPF; E-2.1: 31030-05565-C, 12/29/80; E-2.2: E. D. McKee (original from T. Nichols), 148, USGS-PL; E-2.3: Dept. of Defense aerial photo, from Breed and Grow in McKee, 1979; E-2.4: J. Briggs

E-3: 0309-13200-1, 3/1/79; E-3.1 and E-3.2: H. Garner; E-3.3: L. Bogart

E-4: 0141-02090-3, 9/14/78; E-4.1, E-4.2, and E-4.3: H. Garner

E-5: 1565-10032-6, 2/8/74, E-5.1: ID unknown; E-5.2: L. Bogart; E-5.3: E. D. McKee, 139, USGS-PL; E-5.4: G. Gerster

E-6: 1199-09323-7, 2/3/73, EDC; E-6.1 and E-6.2: L. Bogart; E-6.3: ID unknown

E-7: 1112-09505-7, 11/12/72, R. Haydn, ZGF; E-7.1: D. Busche; E-7.2: L. Bogart; E-7.3: D. Busche; E-7.4: STS-5-40-1168; E-7.5: 1112-09505-7, 11/12/72

E-8: 50250-08534-4, 11/6/84; E-8.1 and E-8.2: A. T. Grove; E-8.3: NOAA AVHRR (courtesy D. McGinnis)

E-9: LFC 1917, 10/11/84; E-9.1: 22287-08131-5, 4/27/81; E-9.2: 1202-08224-5, 7/17/77; E-9.3: N. Lancaster; E-9.4: G. Gerster; E-9.5: N. Lancaster; E-9.6 and E-9.7: G. Gerster

E-10: 2312-13514-7, 11/30/75; E-10.1, E-10.2, E-10.3, and E-10.4: G. Erickson

E-11: 40174-17392(C), 1/6/83; E-11.1: 40174-17392-7, 1/6/83; E-11.2: P. Kresan; E-11.3: D. H. Ball, 2334-A; E-11.4: D. H. Ball, 2339-A

E-12: 40176-17270-7, 1/8/83; E-12.1: I. Luchitta; E-12.2 and E-12.3: J. Olsen

E-13: 50022-17492-4, 3/23/84; E-13.1: Dept. of Defense aerial photo 246-A (courtesy A. Winograd, USGS-Reston); E-13.2: Kerr-McGee Co.; E-13.3 and E-13.4: G. I. Smith; E-13.5: A. Walker

E-14: 40141-16525-4, 12/4/82; E-14.1: R. Churchill; E-14.2: N. H. Darton, 366, USGS-PL; E-14.3: U-2 aerial photo, Ames Research Center

E-15: 11A097/014, JPL; E-15.1: 510A46, NSSDC; E-15.2: 544B05, NSSDC; E-15.3 and E-15.4: M. Whitney; E-15.5: 044B37, NSSDC; E-15.6: 056B86, NSSDC

E-16: 2279-19361-7, 10/28/75, EDC; E-16.1, E-16.2, E-16.3, and E-16.4: E. Morris; E-16.5: Aerial photo TMA 961, Victoria Valley

E-17: 20125-01100-7, 5/27/75, ESC; E-17.1: D. Gibson (C. Ollier); E-17.2: C. Twidale; E-17.3 and E-17.4: R. Giles/C. Twidale; E-17.5: Aerial photo (1:86000) Run 6, No. 5232, Div. of National Mapping, Australia (submitted by C. Twidale)

E-18: 40090-00104-4, 10/14/82; E-18.1: Aerial photo (1:86000) Run 6, No. 046, Div. of National Mapping, Australia (submitted by C. Twidale); E-18.1: C. Twidale; E-18.2: E. D. McKee (original by T. Nichols), USGS-PL

E-19: 2592-05510-7, 9/5/76; E-19.1 and E-19.2: J. T. Daniels; E-19.3: USGS

E-20: 2663-05425-7, 11/15/76; E-20.1 and E-20.2: J. T. Daniels; E-20.3: H. Pohn

E-21: 20781-04533-7, 3/13/77, ESC; E-21.1: R. Snead; E-21.2: C. S. Breed; E-21.3: USGS APA Pakistan 1-A

E-22: 30203-02430-7, 9/24/78, EDC; E-22.1: SIR-A Data Take 28, 11/14/84; E-22.2: Wang and Song, 1983

E-23: 30106-02481-7, 12/15/80, EDC; E-23.1, E-23.2, and E-23.3: A. Walker; E-23.4: 31016-02481-C, 12/15/80, EDC

E-24: 10073-04181-7, 10/4/72, ESC; E-24.1: A. Walker; E-24.2: 11073-04181-7, 10/4/72; E-24.3: A. Walker

E-25: 1162-04134-7, 1/1/73; E-25.1: Xia Xuncheng; E-25.2: SIR-A Data Take 28, 11/14/84, E-25.3: A. Walker

E-26: 10074-04244-7, 10/5/72, ESC; E-26.1: SIR-A Data Take 28, 11/14/84; E-26.2: Zhao Songqiao

E-27: Landsat mosaic, ESC; E-27.1: 20255-04411-7, 10/4/75; E-27.2, E-27.3, E-27.4, and E-27.5: Zhu Zhenda

Chapter 9: Glaciers and Glacial Landforms

9-1: Denton and Hughes, 1981; **9-2:** NASA 72-HC-928; **9-3:** 30928-20440-C, 9/18/80; **9-4:** CIA; **9-5:** 1426-02070(C), 9/23/73, JPL; **9-6:** Paterson, 1981; **9-7:** R. Williams, Jr., I-73-4-22; **9-8:** R. Williams, Jr., I-73-27-32-1; **9-9:** R. Williams, Jr., I-73-27-32; **9-10:** 1511-05240(C), 12/16/73, EDC; **9-11:** T. Meunier, 83-Jan83H3-17; **9-12:** T. Meunier, 82-Mar83W2-5; **9-13:** T. Meunier, 83-Jan83H4-35; **9-14:** B. Turner, I-73-5A-1; **9-15:** 1119-14280-7, 11/19/72; EDC; **9-16:** U.S Navy, USGS-PL TMA 1718F33 (No. 22); **9-17:** R. Williams, Jr., I-73-29-10; **9-18:** R. Williams, Jr., Jun75WS-37; **9-19:** P. Skvarca, Oct. '81; **9-20:** W. Davis, 1909; **9-21:** R. Flint, 1971; **9-22A:** Strahler, 1960; **9-22B:** E. Lindstrom; **9-23:** I. Péwé, 845, USGS-PL; **9-24:** 1377-21112-6, 8/4/73, **9-25:** R. I. Lewellen, in Péwé, 1975; **9-26:** 1377-21116-6, 8/4/73, EDC, in Sloan et al., 1976; **9-27:** Péwé, 1975

G-1: NOAA-6 AVHRR, 1812 UT, 2/27/80; **G-1.1:** 1174-19433-7, 1/13/73, EDC; **G-1.2:** TMA 540, F 31 (No. 250), USGS-PL; **G-1.3:** 2554-17283-2 (RBV), 7/29/76, EDC

G-2: NOAA-6 AVHRR; Ch. 2, Orbit 7165, 13:42:15 UT, 11/12/80; **G-2.1:** Modified from Swithinbank, 1980; **G-2.2:** TMA F 33 (No. 14), USGS-PL; **G-2.3:** 30335-12253-7, 2/3/79, EDC

G-3: 22087-14293-7, 10/9/80, EDC; **G-3.1:** U.S. Navy photo 10, Can 4145, 2/14/47, USGS-PL; **G-3.2:** 2281-07424-7, 10/30/75, EDC; **G-3.3:** 1476-07164-6, 11/11/76

G-4: Salyut 6 Photo (C), 3/10/73, courtesy U. M. Kotlyakov; **G-4.1** and **G-4.2:** P. Skvarca; **G-4.3:** T 400L-201 NAPL (Can.)

G-5: 10380-16182-7, 8/7/73, CCRS; **G-5.1:** R. J. Price, 1973; **G-5.2:** Mercer, 1975 (Plate 37, map 2.2); **G-5.3:** W. Melhorn

G-6: 1426-12070(C), 9/22/73, EDC **G-6.1:** Solarfilma HF; **G-6.2:** U.S. Air Force photo M-436, Roll 96, Frame 10063, 8/12/60, courtesy Iceland Geodetic Survey; **G-6.3:** 1542-18435-7, 1/16/74, EDC

G-7: 2955-19292-7, 9/3/77, EDC; **G-7.1:** Sharp, 1958b; **G-7.2:** A. Post, 425, USGS-PL; **G-7.3:** 31194-19494-C, 6/11/81, EDC; **G-7.4:** SLAR image, C. Rosenfeld

G-8: 20204-16513(C), 8/14/75, CCRS; **G-8.1:** R. Williams, Jr.; **G-8.2:** A. Dunn; **G-8.3:** 30173-16525-B, 8/25/78, EDC

G-9: 30537-20443-7, 8/24/79, ESC; **G-9.1:** SAR Rev 380, JPL; **G-9.2** and **G-9.3:** R. Hudson, U.S. Air Force Cambridge Res. Lab.

G-10: 30157-11565-D, 8/9/78, EDC; **G-10.1:** A15728-63, NAPL (Can.); **G-10.2:** R. Williams, Jr., I-73-27-5; **G-10.3:** 2542-111575-7, 7/18/76, EDC

G-11: 30174-20290-D, 8/26/78, EDC; **G-11.1:** 1185-13570-7, 1/24/73, EDC; **G-11.2:** L. R. Mayo; **G-11.3:** USGS-PIO 85-04

G-12: 1337-07040-7, 6/25/73, EDC; **G-12.1:** R. Williams, Jr., I-7; **G-12.2:** 30927-20382-C, 9/17/80, EDC; **G-12.3:** R. Williams, Jr., I-9

G-13: 22045-07040-7, 8/28/80, CCRS; **G-13.1:** R. Williams, Jr., 1-81-160 = -9; **G-13.2:** Photo 82964, Geol. Surv. of Canada; **G-13.3:** Switzerland, source unknown

G-14: 21654-14185(C), 8/3/79, CCRS; **G-14.1:** R. Williams, Jr.; **G-14.2:** Iceland Geodetic Survey; **G-14.3:** J. Skorve

G-15: 1192-12084-7, 1/31/73, EDC; **G-15.1** and **G-15.2:** R. Williams, Jr.; **G-15.3:** R. Williams, Jr., photo 100A

G-16: 30157-11572-B, 8/18/78, EDC; **G-16.1:** R. Williams, Jr., 1-73-28-14; **G-16.2:** A 15517-52, NAPL (Can.); **G-16.3:** R. Williams, Jr., S-78-5-7; **G-16.4:** Solarfilma Hf, photo 18/5

G-17: 1041-09464-7, 9/2/72, EDC; **G-17.1:** A 11991-1, NAPL (Can.); **G-17.2:** D. J. Miller, 1342, USGS-PL; **G-17.3:** USGS/EDC

G-18: 1339-17351-7, 6/27/73, CCRS; **G-18.1** and **G-18.2:** J. K. Hornsby

G-19: 10371-18535(C), 7/29/73, CCRS; **G-19.1:** A 14509-2, NAPL (Can.); **G-19.2:** T 328L-204, NAPL (Can.); **G-19.3:** SAR Rev 791, JPL

G-20: 21699-151808-7, 7/24/77, CCRS; **G-20.1,** **G-20.2,** and **G-20.3:** J. R. Belanger

G-21: 1335-17513(C), 6/23/73, CCRS; **G-21.1,** **G-21.2,** and **G-21.3:** V. Singhroy

G-22: Mosaic, 30157-11572-C & D, 8/9/78; EDC; **G-22.1:** Mission 445, Roll 115, Frames 12564/12565, U.S. Air Force/DIA; **G-22.2:** R. Williams, Jr., I-77-13-14; **G-22.3:** R. Williams, Jr., I-77-23-20

G-23: 30157-11572-A, 8/9/78, EDC; **G-23.2:** R. Williams, Jr., I-73-33-13; **G-23.2:** R. Williams, Jr., I-68-1287; **G-23.3:** Photo 2568, Iceland Geodetic Survey

G-24: LFC 664, 10/7/84, EDC; **G-24.1:** J. P. Schafer, USGS-Reston; **G-24.2:** R. N. Oldale, USGS-Woods Hole; **G-24.3:** USGS, NECR, Roll 2, Frame 37; **G-24.4:** R. N. Oldale, USGS-Woods Hole

G-25: 1005-20021-7, 7/28/72, EDC; **G-25.1:** Photo 201950, Geol. Surv. of Canada; **G-25.2:** 2901-21175-7, 7/12/77, EDC; **G-25.3:** 1387-06402-7, 8/14/73

G-26: 30135-04492(C), 7/18/78, ESC; **G-26.1:** Chi and Ren, 1980; **G-26.2:** 2711-03231-7, 1/2/77; **G-26.3:** Chi and Ren, 1980; **G-26.4:** Shi et al., 1980

Chapter 10: Planetary Landforms

10.1: Meszaros, 1983; **10.2:** Lowman, 1976, ©

P-1: NSSDC G-68-295B; P-1.1: NASA 67-H-1651; P-1.2: NASA 68-H-17; P-1.3: NASA 67-H-1407; P-1.4: 1636-14585-7, CCRS

P-2: Mount Wilson Observatory, View 263, Calif. Inst. of Technol.; P-2.1: NASA 71-H-1441; NASA 71-H-386; P-2.2 NSSDC AS 15-11748; P-2.4: GSFC, original artwork

P-3: NASA 69-H-864; P-3.1: NSSDC AS-12-49-7319; P-3.2: NSSDC S-71-51735; P-3.3: NSSDC AS 15-12157

P-4: NASA 74-H-536; P-4.1: Lunar Orbiter IV-187M, LRC; P-4.2: NASA 69-H-1863; P-4.3: Lunar Orbiter IV-187H2, LRC; P-4.4: Lunar Orbiter IV-181H2, LRC

P-5: NASA 75-H-83; P-5.1 NASA 74-H-239; P-5.2: NSSDC Mariner X 11-15; P-5.3: NASA 67-H-328; P-5.4: GSFC, original artwork

P-6: NASA 72-H-716; P-6.1: NASA 84-H-599; P-6.2: NSSDC Mariner IX 4133-96; P-6.3: NASA 74-H-647; P-6.4: NSSDC Viking Orbiter 072402

P-7: NASA 83-H-244; P-7.1: NASA 84-H-595; P-7.2: NASA 72-H-63; P-7.3: 1284-17384-6; P-7.4: NSSDC Viking Orbiter P-17708

P-8: NASA 76-H-697; P-8.1: Viking Orbiter, P-17002, JPL; P-8.2: NASA 72-H-109; P-8.3: NASA 84-H-430; P-8.4: Viking Orbiter 519 410, JPL; P-8.5: NASA 76-H-522

P-9: Viking Orbiter P-20776, JPL; P-9.1: NSSDC Viking Orbiter 428 B22; P-9.2: NSSDC Viking Orbiter 423 B63; P-9.3: NSSDC Viking Orbiter 039 B84

P-10: NASA/Pioneer Venus, MIT and Brown University; P-10.1: NASA/Pioneer Venus and Brown University; P-10.2 and P-10.3: V. L. Sharpton and J. W. Head, Brown University; P-10.4: NASA 83-H-254

P-11: Upper = Arecibo Observatory (D. B. Campbell); Lower = U.S.S.R. Academy of Sciences (Academician O. Rzhiga); P-11.1 and P-11.2: Arecibo Observatory (D. B. Campbell; also J. W. Head, Brown Univ.); P-11.3 and P-11.4: U.S.S.R. Academy of Sciences (Academician O. Rzhiga)

P-12: NASA 83-HC-205; P-12.1: NSSDC 1195V2-001; P-12.2: NSSDC 0891V1+100; P-12.3: NSSDC 0979V+100; P-12.4: NASA 79-H-432

P-13: P-21209, JPL; P-13.1: NSSDC 0041V1+000; P-13.2: NSSDC 0079V1+000; P-13.3: NSSDC 0101V1+000; P-13.4: NSSDC 0157V1+000

P-14: NASA 83-H-223; P-14.1: ID unknown; P-14.2: Voyager 1-5-49, JPL; P-14.3: NSSDC, Voyager 23956

P-15: NASA 86-H-72 (P-29510); P-15.1: NASA 86-H-75 (P-29513); P-15.2: NASA 86-H-77 (P-29515); P-15.3: NASA 86-H-74 (P-29512); P-15.4: NASA 86-H-76 (P-29514); P-15.5: 86-H-82 (P-29250); P-15.6: 86-H-110 (P-29501)

Chapter 11: Geomorphological Mapping

11-1: A. S. Crofts, 1974, ©; **11-2:** M. K. Ridd; **11-3:** Howard and Mitchell, 1980, ©; **11-4:** Panizza, 1978; **11.5:** C. Rosenfeld, 1977, ©; **11-6:** Bashenina and Tal'skaya, 1981, ©; **11-7:** A = C. Pain, 1985, ©; B = C. Ollier, 1967, ©; **11-8:** A and B = R. Hayden; **11-9:** R. Hayden; **11-10:** Subset from 40176-17270(C), 1/8/76; **11-11** and **11-12:** P. Kresan

Chapter 12: Global Geomorphology

12-1: R. Hekinian; **12-2:** NOAA AVHRR, ID unknown; **12-3:** J. V. Gardner, USGS-Reston; **12-4:** W. Ryan, Lamont-Doherty Observatory; **12-6:** B. McGregor, USGS-Reston; **12-7:** A, B, C, and D = P. Chavez; **12-8:** Wise et al., 1985, ©; **12-9:** R. Haydn, ZGF; **12-10:** National Mapping Division, USGS-EDC; **12-11:** A = Generated by M. Kobrick, JPL, from 30-s average elevation data for the U.S., NOAA Nat. Geophys. Data Center, Boulder, Colorado; B = J. Garvin; **12-12** and **12-13:** Short, 1982; **12-14:** A = B. Ivanov; B = 1350-23470-7, 7/8/73; C = SAR Rev 578, 8/6/78 (mosaic by J. Garvin); D = 031-01010-1, 5/27/78; **12-15:** A = U.S.S.R. Academy of Sciences (courtesy Academician O. Rzhiga); B and C = B. McGregor, USGS-Reston

Appendix A: Remote Sensing Principles

A-1 through **A-7:** Short, 1982; **A-8:** M. Abrams, JPL; **A-9:** Short and Marcell, 1985

PART 2 ADDRESSES OF CONTRIBUTORS

Aero Service, Western Geophysical Co. of America, 8100 Westpark Dr., Houston, TX 77063

Richard Allenby, Code 622, Goddard Space Flight Center, Greenbelt, MD 20771

Ames Research Center, Mountain Home, CA 94035

J. F. Araya Vergara, Departamento de Geografia, Universidad de Chile, Cas. 3387, Santiago, Chile

Bryan Bailey, EROS Data Center, Sioux Falls, SD 57198

Victor R. Baker, Dept. of Geosciences, University of Arizona, Tucson, AZ 85721

- D. H. Ball, Dept. of Geosciences, University of Arizona, Tucson, AZ 85721
- J. L. Ballais, Dept. de Geographie, Universite de Caen, 14032 Caen, France
- Lothar Beckel, Ahornstrasse 12, A-4820 Bad Ischl, Austria
- J. Belanger, Geological Survey of Canada, 601 Booth St., Ottawa, Ontario, Canada
- Robert W. Blair, Jr., Dept. of Geology, Fort Lewis College, Durango, CO 81301
- Herbert Blodget, Code 622, Goddard Space Flight Center, Greenbelt, MD 20771
- Lowell Bogart, P.O. Box 761, Port Townsend, WA 98388
- Charles Bohn, Code 632, Goddard Space Flight Center, Greenbelt, MD 20771
- J. S. Bradley, Amoco Production Company, 4502 East 41st St., P.O. Box 591, Tulsa, OK 74102
- Carol S. Breed, U.S. Geological Survey, Flagstaff, AZ 86001
- J. Briggs, SCS Engineers, Inc., 11260 Roger Bacon Dr., Reston, VA 22090
- British Columbia Airphoto Library, Victoria, B.C., Canada
- B. C. Burchfiel, Dept. of Earth, Atmospheric and Planetary Sciences, Massachusetts Inst. of Technology, Cambridge, MA 02139
- Detlef Busche, Geographisches Institut der Universität Würzburg, D-8700 Würzburg am Hubland, West Germany
- Canada Centre for Remote Sensing, 2464 Sheffield Road, Ottawa, Ontario K1A 0Y7, Canada
- Carnegie Geophysical Laboratory, Washington, D.C.
- Pat Chavez, U.S. Geological Survey, Flagstaff, AZ 86001
- Robert R. Churchill, Dept. of Geography, Middlebury College, Middlebury, VT 05753
- James Coleman, Coastal Studies Inst., Louisiana State University, Baton Rouge, LA 70803
- Mario Jorge Costa, Companhia de Pesquisa de Recursos Minerais—CPRM, Avenida Pasteur, 404, Rio de Janeiro, Brazil
- CSIRO, Mineral Research Laboratories, P.O. Box 136, North Ryde, N.S.W., Australia 2113
- J. T. S. Daniels, Carr Boyd Minerals Ltd., P.O. Box 6049, Hay Street East, Perth, Western Australia 6000, Australia
- M. Day, Dept. of Geography, Univ. of Wisconsin-Milwaukee, Milwaukee, WI 53201
- Kenneson Dean, Geophysical Institute, University of Alaska, C. T. Avery Bldg., Fairbanks, AL 99701
- Kees A. DeJong, Dept. of Geology, University of Cincinnati, Cincinnati, OH 45221
- Braam De Villiers, Dept. of Geography, Potchefstroomse Universiteit, 2520 Potchefstroom, Republic of South Africa
- Division of National Mapping, Department of Resources and Energy, Bureau of Mineral Resources, Geology and Geophysics, Dept. of National Development, P.O. Box 378, Canberra City, A.C.T. 2601, Australia
- Ian Douglas, Dept. of Geography, University of Manchester, Manchester M13 9PL, England
- S. A. Drury, Dept. of Earth Sciences, The Open University, Walton Hall, Milton Keynes, MK7 6AA, Buckinghamshire, England
- Anthony Dunn, 1623 Russian Jack No. 2, Anchorage, AL 99504
- William Dupre, Dept. of Geosciences, University of Houston, Houston, TX 77004
- Earth Satellite Corporation, 7222 47th St., Bethesda, MD 20815
- Clifford Embleton, Faculty of Science (Geography), University of London (Kings College) Strand, London, WC2R 2LS, England
- George E. Erickson, U.S. Dept. of the Interior, U.S. Geological Survey, National Center, Reston, VA 22092
- Oğuz Erol, Ankara Universitesi, Ankara, Turkey
- EROS Data Center, Sioux Falls, SD 57198
- John R. Everett, Earth Satellite Corporation, 7222 47th St., Bethesda, MD 20815
- L. Faugeres, 35 Rue de la Nahniere, 91600 Savigny sur Orge, France
- Charles W. Finkl, Jr., Center for Coastal Research, 1312 East Las Olas Blvd., P.O. Box 2473, Colee Sta., Fort Lauderdale, FL 33303
- John P. Ford, Jet Propulsion Laboratory, Calif. Inst. of Technology, 4800 Oak Grove Dr., Pasadena, CA 91109

- Jules Friedman, U.S. Geological Survey, Denver Federal Center, Denver, CO
- Elwood Friesen, 1641 Biscay Circle, Aurora, CO 80011
- H. E. Garner, Dept. of Geological Sciences, Rutgers State University, Newark, NJ 07102
- Geological Survey of Canada, Photographic Library, Room 510, 601 Booth St., Ottawa, Ontario, Canada
- Geological Survey, Republic of South Africa, Private Bag X122, Pretoria 0001, South Africa
- Geological Survey of Zimbabwe, Ministry of Mines and Lands, P.O. Box 8039, Causeway, Salisbury, Zimbabwe
- G. Gerster, Tobelhusstrasse 8126, Zumilon-Zurich, Switzerland
- D. Gibson (see C. Ollier)
- Robert N. Ginsburg, Rosenstiel School of Marine and Atmospheric Science, University of Miami, Fisher Island Station, Miami Beach, FL 33139
- K. W. Glennie, c/o Shell Intern. Petrol. Mij, EP/13, Oostduinlaan 75, Den Hague, The Netherlands
- Ronald Greeley, Dept. of Geology, Arizona State University, Tempe, AZ 85281
- William Greenwood, U.S. Geological Survey, National Center, Reston, VA 22090
- A. T. Grove, African Studies Center, Free School Lane, Cambridge, England
- S. M. Harrison (see C. Swithinbank)
- Robert S. Hayden, Dept. of Public Affairs (Geography), George Mason University, Fairfax, VA 22030
- Rupert Haydn, Zentralstelle für Geo-Photogrammetrie und Fernerkundung (ZGS), Luisenstrasse 37, 8000 München 2, West Germany
- R. Hekinian, Institut Francais de Recherche pour l'Exploitation de la Mer (IFREMER), Centre de Brest, B.P. No. 337, 29273 Brest Cedex, France
- H. R. Hopkins, Exxon Production Research Co., P.O. Box 2189, Houston, TX 77001
- John Hornsby, Intera Technologies Ltd., 717 Belfast Rd., Ottawa, Ontario K1A 0Y7, Canada
- Henry J. Houghton, Office of the Surveyor General, Cathedral Avenue, Perth, Western Australia 6000, Australia
- Hunting Geology and Geophysics Ltd., Elstree Way, Boreham Wood-Herts WD6-1SB, England
- R. Hudson, U.S. Air Force Cambridge Research Laboratory, Bedford, MA
- J. F. Huntington, Div. of Mineral Physics, CSIRO, P.O. Box 136, North Ryde, N.S.W., Australia
- Iceland Geodetic Survey, Reykjavik, Iceland
- Indonesian Dept. of Information, Jakarta, Indonesia
- Irish Tourist Board, 757 3rd Avenue, New York, NY 10017
- Boris A. Ivanov, O. Y. Schmidt Institute of the Physics of the Earth, U.S.S.R. Academy of Sciences, Moscow 123810, U.S.S.R.
- Japan Air Lines, 655 Fifth Avenue, New York, NY 10022
- Jet Propulsion Laboratory, California Inst. of Technology, 4800 Oak Grove Dr., Pasadena, CA 91109
- Johnson Space Center, Houston, TX 77058
- Allan Kovar, U.S. Geological Survey, National Center, Reston, VA 22090
- Peter Kresan, Dept. of Geosciences, University of Arizona, Tucson, AZ 85721
- C. Lallemand, Institut Francais du Pétrole, B.P. 311, 92506 Rueil Malmaison, France
- N. Lancaster, Desert Ecological Research Unit, Box 953, Walvis Bay 9190, SWA/Namibia
- Robert D. Lawrence, Dept. of Geology, Oregon State University, Corvallis, OR 97331
- Stephen Leatherman, Dept. of Geography, University of Maryland, College Park, MD 20742
- Erling Lindström, Dept. of Physical Geography, Uppsala University, Box 554, S-751 22, Uppsala, Sweden
- Paul D. Lowman, Jr., Code 622, Goddard Space Flight Center, Greenbelt, MD 20771
- Ivo Luchitta, U.S. Geological Survey, Flagstaff, AZ 86001
- Harold C. MacDonald, Dept. of Geology, University of Arkansas, Fayetteville, AR 72204
- MacDonald, Dettwiler, & Assoc., Ltd., 3751 Shell Road, Richmond, British Columbia V6X 2Z9, Canada
- Norman S. MacLeod, 7212 Maple Ave., Chevy Chase, MD 20015
- John C. Manning, P.O. Box 13470, Las Vegas, NV 89112

- MARS Associates, Inc., 3644 East McDowell Rd., Phoenix, AZ 85008
- L. R. Mayo, U.S. Geological Survey, Fairbanks, AL
- G. J. H. McCall, University of Western Australia, Nedlands, Australia
- John S. McCauley, U.S. Geological Survey, Flagstaff, AZ 86001
- Ken McCracken/Michael Hornbrook, Div. of Mineral Physics, CSIRO, P.O. Box 136, North Ryde, N.S.W., Australia 2113
- John F. McHone, Dept. of Geology, 245 Natural History Bldg., 1304 West Green Street, University of Illinois, Urbana, IL 61801
- L. D. Meckel and Co., 2723 Sackett Dr., Houston, TX 77098
- W. N. Melhorn, Dept. of Geosciences, Purdue University, West Lafayette, IN 74907
- T. K. Meunier, U.S. Geological Survey, National Center, Reston, VA 22092
- Luis M. Mitre-Salazar, Instituto de Geología, Apartado Postal 70-296, Ciudad Universitaria, 04510 Mexico D.F.
- Marie Morisawa, Dept. of Geological Sciences, State University of New York—Binghamton, NY 13901
- Elliot Morris, U.S. Geological Survey, Flagstaff, AZ 86001
- Tom Mortensen, P.O. Box 100663, Anchorage, AL 99510
- Mukang Han, Dept. of Geography, Peking University, Beijing, Peoples Republic of China
- Fred Nagle, Dept. of Geology, P.O. Box 249176, University of Miami, Coral Gables, FL 33124
- National Air Photo Library, Department of Energy, Mines and Resources, 615 Booth St., Ottawa, Ontario K1A OE9, Canada
- National Geographic Society, 17th and M St., N.W., Washington, D.C. 20036
- National Oceanographic and Atmospheric Administration, National Climate Center, Satellite Data Services Branch, World Weather Bldg., 5200 Auth Rd., Washington, D.C. 20233
- National Park Service (U.S. Dept. of the Interior), Photographic Library, P.O. Box 37127, Washington, D.C. 20013
- N. D. Newell, American Museum of Natural History, New York, NY
- New Zealand Geological Survey, Dept. of Scientific and Industrial Research, P.O. Box 30 368, Lower Hutt, New Zealand
- Tad Nichols, 5545 Camino Escuela, Tucson, AZ
- Theodore M. Oberlander, Dept of Geography, University of California, Berkeley, CA 94720
- L. O'Callaghan (see D. Rothery)
- Clifford Ollier, Bureau of Mineral Resources, Geology, and Geophysics, Dept. of National Development and Energy, P.O. Box 378, Canberra City, A.C.T. 2601, Australia
- J. Olsen, Dept. of Anthropology, University of Arizona, Tucson, AZ 85721
- Oregon Dept. of Geology and Mineral Industries, Portland, OR
- Oregon State Highway Department, Portland, OR
- Colin F. Pain, School of Geography, The University of New South Wales, P.O. Box 1, Kensington, N.S.W., Australia 2033
- Nelson de Jesus Parada, Director General, INPE—Instituto de Pesquisas Espaciais, C.P. 515, 12200 — São José dos Campos — SP, Brazil
- Dong Won Park, Dept. of Geography, Seoul National University, Seoul 151, Korea
- Roland P. Paskoff, Dept. of Geography, University of Lyon II, Lyon, France
- E. Paylor, Jet Propulsion Laboratory, 4800 Oak Grove Dr., Pasadena, CA 91109
- Maurice E. Perret, Dept. of Geography/Geology, University of Wisconsin/Stevens Point, Stevens Point, WI 54481
- Angelo Pesce, P.O. Box 661, Tripoli, Libya
- George Plafker, U.S. Geological Survey, National Center, Reston, VA 22090
- Howard Pohn, U.S. Geological Survey, National Center, Reston, VA 22090
- Stephen J. Prucha, Earth Satellite Corporation, 7222 47th St., Bethesda, MD 20815
- Merrill K. Ridd, University of Utah Research Inst., 420 Chipeta Way, Salt Lake City, UT 84108
- Harry H. Roberts, Coastal Studies Inst., Louisiana State University, Baton Rouge, LA 70803

- Charles Robinove, U.S. Geological Survey, National Center, Reston, VA 22090
- D. J. Roddy, U.S. Geological Survey, Flagstaff, AZ 86001
- Keith Ronholm, Remote Measurement Systems, 2633 Eastlake Ave., East, Suite 206, Seattle, WA 98102
- Charles Rosenfeld, Dept. of Geography, Oregon State University, Corvallis, OR 97331
- David Rothery, Dept. of Earth Science, The Open University, Wallon Hall, Milton Keynes, MK76AA, Buckinghamshire England
- Floyd F. Sabins, Jr., Chevron Oil Field Research Co., La Habra, CA 90631
- Guillermo P. Salas, Consejo de Recursos Naturales No Renovables, Niños Heroes 139, Mexico 7, D.F., Mexico
- M. Sano, Earth Resources Satellite Data Center, No. 39 Mori-Bldg 4-5 Azubuda 2 Chome Minato-ku, Tokyo 106, Japan
- Roger Searle, Inst. of Oceanographic Sciences, Wormley, Godalming, Surrey, GUB 5UB, England
- John S. Shelton, P.O. Box 48, La Jolla, CA 92038
- Shi Yafeng, Lanzhou Inst. of Glaciology and Cryopedology, Academica Sinica, Lanzhou, Peoples Republic of China
- Vernon Singhroy, Ontario Centre for Remote Sensing, Ontario Ministry of Natural Resources, 800 Bay St., Toronto, Ontario, M5S 1Z8, Canada
- J. Skorve, University of Oslo, Oslo, Norway
- Pedro Skvarca, Instituto Antártico Argentino, Cerrito 1248, 1010 Buenos Aires, Argentina
- G. I. Smith, U.S. Geological Survey, 345 Middlefield Rd., Menlo Park, CA 94025
- Norman D. Smith, Dept. of Geological Sciences, University of Illinois—Chicago, Chicago, IL 60680
- Robert L. Smith, U.S. Geological Survey, National Center, Reston, VA 22092
- William L. Smith, Spectral Data Corp., 1901 N. Moore St., Suite 1000, Arlington, VA 22209
- Rodman E. Snead, Dept. of Geography, The University of New Mexico, Albuquerque, NM 87131
- Soil Conservation Service, Cartographic Div., Federal Center, Bldg. 1, Hyattsville, MD 20782
- Solarfilma hf., Thingholsstraeti 27, 101 Reykjavik, Iceland
- Sovfoto-Eastfoto Agency, 25 West 43rd St., New York, NY
- R. Sutton, U.S. Geological Survey, Flagstaff, AZ 86001
- Swissair, Public Relations, Zurich (Kloten) Airport, Switzerland
- Charles Swithinbank, British Antarctic Survey, High Cross Madingley Road, Cambridge, CB3 OET, England
- Graham Taylor, School of Applied Science, Canberra College of Advanced Education, P.O. Box 1, Belconnen A.C.T., Australia 2616
- H. Tazieff (see H. Garner)
- Telespazio, European Space Agency, Via Galileo Galilei 000 44, Frascati, Italy
- Texas Bureau of Economic Geology, University of Texas, Austin, TX
- Sigurdur Thorarinsson, Museum of Natural History, Reykjavik, Iceland
- Vladimir G. Trifonov, Geological Institute, U.S.S.R. Academy of Sciences, Pyzhevsky Pereolok 7, Moscow 109-107, U.S.S.R.
- B. B. Turner, U.S. Air Force Cambridge Research Laboratory, Bedford, MA
- C. R. Twidale, Department of Geography, University of Adelaide, Box 498 GPO, Adelaide, South Australia 5001, Australia
- U.S. Geological Survey, Image Processing Facility, Flagstaff, AZ 86001
- U.S. Geological Survey, National Oceanographic Information Center, National Center, Reston, VA 22092
- U.S. Geological Survey, Photographic Library, Denver, CO 80225
- U.S. Geological Survey, Public Information Office, National Center, Reston, VA 22092
- Vargas, Venezuelan Airlines
- Alta Walker, U.S. Geological Survey, National Center, Reston, VA 22092
- H. J. Walker, Coastal Studies Inst., Louisiana State University, Baton Rouge, LA 70803
- J. T. Wells, Inst. of Marine Science, 3407 Arendel St., Morehead City, NC 28557
- Westerman Sat Photo, Anstatt Georg Westerman, Braunschweig, West Germany

Marion Whitney, Box 277, Shepherd, MI 48883

P. S. Williams, Dept. of Geography, University of Auckland, Auckland, New Zealand

Richard S. Williams, Jr., U.S. Geological Survey, National Center, Reston, VA 22092

Charles Wood, Johnson Space Center, Houston, TX 77058

Xia Xuncheng, Inst. of Biology, Soil and Desert Research, Academica Sinica, Urumqi, Peoples Republic of China

Werner Zeil, Institut für Geologie u. Paleontologie, Technische Universität Berlin, Hardenbergstrasse 42, D-1000, Berlin, West Germany

Zhao Songqiao, Inst. of Remote Sensing Application, Academica Sinica, Beijing, Peoples Republic of China

Zhu Zhenda, Director, Inst. of Desert Research, Academica Sinica, Lanzhou, Gansu, Peoples Republic of China

PART 3 SPECIAL LISTS

Guest Caption Writers

Richard Allenby, Code 622, NASA, Goddard Space Flight Center, Greenbelt, MD (Plates T-21 and KL-11)

J. Belanger, Geological Survey of Canada, Ottawa, Canada (Plate G-20)

Herbert Blodget, Code 622, NASA, Goddard Space Flight Center, Greenbelt, MD (Plate T-40)

Kees A. DeJong, Dept. of Geology, University of Cincinnati, Cincinnati, OH (Plates T-44, T-45, and T-46)

Jon E. Dykstra, Earth Satellite Corporation, Bethesda, MD (Plates T-41, T-42, T-43, and T-44)

John Hornsby, Intera Technologies, Ottawa, Canada (Plate G-18)

Mary M. Kennedy, 10994 W. Exposition Place, Lakewood, CO (Plate V-10)

Robert Lawrence, Dept. of Geology, Oregon State University, Corvallis, OR (Plate T-43)

Stephen P. Leatherman, Dept. of Geography, University of Maryland, College Park, MD (Plate C-23)

Ira S. Merin, Earth Satellite Corporation, Bethesda, MD (Plate T-39)

Richard C. Michael, Earth Satellite Corporation, Bethesda, MD (Plates T-49, T-50, and T-51)

Stephen J. Prucha, Earth Satellite Corporation, Bethesda, MD (Plates T-20 and T-21)

Orville R. Russell, Earth Satellite Corporation, Bethesda, MD (Plates T-18, T-37, and T-38)

Vernon R. Singhroy, Ontario Center for Remote Sensing, Toronto, Canada (Plate G-21)

James R. Underwood, Dept. of Geology, Kansas State University, Manhattan, KS (Plate T-31)

Permissions List

The following organizations or individuals holding copyrights to illustrations or tables used in this book have requested a general citation identifying the publications, authors, and other source information pertinent to the material used. In some instances, an additional specific statement of permission is required, as shown in parentheses with each such listing. For certain citations, the required author permission has also been obtained. To conserve space, the full publication listing is not reproduced here; the reader may certify this by examining the reference section of the relevant chapter in this book as indicated by the figure or table number. A few copyrighted sources (given by © in Part 1 of this appendix) did not ask for a specific permission statement.

1. American Association for the Advancement of Science
1333 H Street NW
Washington, D.C. 20005
2-2: Fig. 4, Molnar and Tapponnier, 1975
(Copyright, 1975)
2. American Association of Petroleum Geologists
1444 South Boulder Avenue
Tulsa, OK 74119-3604
1-5: Fig. 4, Sabins, 1983
4-1: Figs. 1 and 2, Howard, 1967
3. Edward Arnold Publishers, Ltd.
41 Bedford Square
London WC1B 3DQ England
Table 9-1: Sugden and John, 1976 (Published by J. Wiley and Sons, New York)
4. Australian National University Press
(Pergamon Press Australia Pty. Ltd.)
19a Boundary Street
Rushcutters Bay, NSW, Australia
7-2: Fig. 4, Jennings, 1971

5. Wm. C. Brown Co. Publishers
2460 Kerper Blvd.
Dubuque, Iowa 52001
Tables 10.2 and 11.3: Ritter, 1978 (All rights reserved. Reprinted by permission.)
6. Earth Satellite Corporation
7222 47th Street
Bethesda, MD 20815
(All images appearing in this book are copyrighted.)
7. Elsevier Science Publ. Co., Inc.
52 Vanderbilt Avenue
New York, NY 10017
KL-5.1: Fig. 5, I. Bralic, in Herak, 1972, from Herak and Stringfield, 1972
KL-5.3: Fig. 12S. Božičević, in Herak, 1972, from Herak and Stringfield, 1972
11-7A: Figs. 2 and 5, Pain, 1985
8. Elsevier Science Publ.
B. V. Post Office Box 330
1000 AH Amsterdam
The Netherlands
T-39: Fig. 6I, Sengor and Yilmaz, 1976
9. Energy, Mines and Resources Canada
Surveys and Mapping Branch
615 Booth Street
Ottawa, Ontario K1A 0E9, Canada
T-16.2: A 11503-97
T-16.3: T 185-R-35
T-17.2: T 481-L-19
T-17.3: A 5120-105R
T-18.1: T 420-L-22
T-18.3: A 16203-115
C-24.1: ID Unknown
G-4.3: T 400L-201 (Copyright, 1950)
G-10.1: A 15728-63 (Copyright, 1957)
G-16.2: A 15517-52 (Copyright, 1956)
G-17.1: A 11991-1 (Copyright, 1949)
G-19.1: A 14509-2 (Copyright, 1954)
G-19.2: T 328-204 (Copyright, 1949)
(These aerial photographs copyright for years indicated; Her Majesty the Queen in right of Canada reproduced from the collection of the National Air Photo Library with permission of Energy, Mines and Resources Canada.)
10. La Fondation Scientifique de la Géologie et de ses applications
Siège Social: 94, avenue de Lattre de Tassigny
F 54000 Nancy, France
T-31: Monod and Pomeral, 1973
11. W. H. Freeman and Co. Publ.
41 Madison Avenue
New York, NY 10010
3-2: Fig. 16.1, Press and Siever, 1982
D-11.2: Fig. 5-5, Suslov, 1965
12. Gebrüder Borntraeger
Johannesstra Be 3A
D-7000 Stuttgart 1
West Germany
KL-6.1: Plate 3, Lowry and Jennings, 1974
KL-6.4: Plate 5, Lowry and Jennings, 1974
13. Geological Society of America
3300 Penrose Place
P. O. Box 9140
Boulder, CO 80301
T-2: Fig. 1, Monger et al., 1982
T-11: Fig. 1, Hatcher and Viele, 1982
4-5: Fig. 6, Schumm and Kahn, 1972
KL-10.1: Prouty, 1952
KL-10.2: Prouty, 1952
14. Geological Society of Australia
10 Martin Place
Sydney NSW 2000
Australia
11-7.B: Ollier, 1967
15. Director General
Geological Survey of Canada
Department of Energy, Mines and Resources
601 Booth Street
Ottawa, Ontario K2A 0E8
Canada
C-24.2: Photo 83255
G-13.2: Photo 82964
G-25.1: Photo 201950
16. Geological Society of India
BBD Press
Bangalore 560-053
India
1-1: Fig. 2, Carey, 1962
17. Geological Survey of Zimbabwe
P. O. Box 8039, Causeway
Salisbury, Zimbabwe
T-34.2: Plate V, Stagman, 1978
18. Ginn Press
Ginn and Company
191 Spring Street
Lexington, MA 02173
G-7: Figs. 98 and 99, Davis, 1909

19. Gordon and Breach
Harwood Academic Publishers
50 W. 23rd Street
New York, NY 10010
11-6: Fig. 5, Bashenina and Tal'skaya, 1981
20. Hunting Geology and Geophysics Ltd. (Hunting Surveys)
Elstree Way
Boreham Wood-Hert WD6-1SB
England
T-42.4, T-42.5, T-42.6: Oberlander, 1965
21. Iceland Geodetic Survey
Laugaveg 178
Sími 81611
Reykjavík, Iceland
G-14.2: Slide 2660
G-23.3: Slide 2568
22. International Assoc. of Hydrological Sciences
Institute of Hydrology
Maclean Building
Crownmarsh Gifford
Wallingford, Berkshire OX10 8BB
England
Table 9-4: Table 1, UNESCO, 1970
23. Longman Group Ltd.
Longman House
Bun Mill, Harlow
Essex CM20 2JE
England
G-5.1: Fig. 87, Price, 1973
24. The Macmillan Press, Ltd.
4 Little Essex Street
London, WC2R 3LS
6-1: Fig. 16.3, Demek et al., in Embleton, 1984
25. McGraw-Hill Book Company
1221 Avenue of the Americas
New York, NY 10020
T-25: Fig. 23.3, Spencer, 1977
26. MIT Press
28 Carleton Street
Cambridge, MA 02142
7-2: Jennings, 1972
27. National Geographic Society
17th and M Street, NW
Washington, D.C. 20036
(All maps and photographs in this book attributed to NGS are copyrighted by the Society; used with permission, photographer identified in citation.)
28. Oxford University Press
200 Madison Avenue
New York, NY 10016
Figs. 3.82, 3.91, 6.49, 6.51, and 9.3 in Garner, 1974
29. Pergamon Press
Maxwell House, Fairview Park
Elmsford, NY 10523
9-6: Paterson, 1981
11-3: Fig. 11, Howard and Mitchell, 1980
11-4: Fig. 12, Panizza, 1978
30. Princeton University Press
41 William Street
Princeton, NJ 08540
KL-12.1: A. Grainger, in Morrison, 1965
31. A. H. and A. W. Reed Ltd.
182 Wakefield Street
Wellington, New Zealand
C-11.1: Fig. 13.41, Stevens, 1972
C-11.2: Fig. 13.42, Stevens, 1972
32. Sólarfilma hf
Thingholtsstraeti 27
101 Reykjavík, Iceland
G-6.1: Slide 1/2 (1962), S. Snorrason, photographer
G-16.4: Slide 18/5 (1962), S. Snorrason, photographer
33. Springer-Verlag New York, Inc.
175 Fifth Avenue
New York, NY 10010
The following appear in Green and Short, 1971
(original sources identified in Part 2, App. B):
V-2.3: Plate 167 B
V-3.4: 73 A
V-4.1: 92 B
V-4.2: 49 A
V-7.3: 97 A
V-15.4: 30 A
V-16.3: 36 B
V-18.2: 20 A
V-19.1: 21 B
V-26.2: 31 A
V-27.3: 36 A
34. Franz Steiner Verlag Gmb H
Friedrichstrasse 24
Postfache 5529
D-6200 Wiesbaden
West Germany
F-22.1: Sternberg, 1975

35. The University of Chicago Press
5801 S. Ellis Avenue
Chicago, IL 60637

Table 4-1: Milliman and Meade, 1983
6-1 and 6-2: Figs. 4 and 5, Inman and Nordstrom, 1971

36. Anstatt Georg Westerman
(Westerman Sat Photo)
Braunschieg, West Germany
T-25: Landsat mosaic

37. John Wiley and Sons, Inc.
605 Third Avenue
New York, NY 10158
Table 3-1: Adapted from Rittman, 1962
C-18.3: Hopley, 1982
KL-12.3: Fig. 24.13, Thornbury, 1965
9-1: Fig. on p. viii, Denton and Hughes, 1981
G-4: Fig. 3-6, Denton and Hughes, 1981
G-19.4: Fig. 13.8, Sugden and John, 1976
9-21: Fig. 8-1, Flint, 1971
9-22A: Fig. 26.16, Strahler, 1960
Table 9-2: Table 4-C, Flint, 1971
Table 9-5: Table 13.1, Embleton and King, 1975

Structural Geology Students

The following students in the Spring 1984 class in Structural Geology (Geol. 341) at the University of Maryland—College Park (Paul D. Lowman, Jr., Instructor) are gratefully acknowledged for their assistance in researching background material for many of the Plates comprising the Tectonic Landforms Chapter:

Deborah Bradley	Andrea Mongeon
Kathleen Burch	Elizabeth Montgomerie
April Cannon	Ernest Monti
Thomas Davis	Diana Obler
Donovan Duggan	Charles O'Carroll
Steven Eichenger	Clifford Oliver
Judith Elkins	Judith Owens
Kenneth Emerick	Daniel Pazdersky
Lisa Ettlinger	Mark Pedersen
David Falatko	Cynthia Poston
Alan Fisk	Winston Riley
John Fleming	George Sauer
David Greenan	Brenda Seylar
Andrew Hartten	Thomas Skelly
Mark Hensler	Adam Smith
Deborah Knox	Timothy Stacy
Mohanjeet Kohli	Robert Tucci
James Lang	Michael Tuttle
Gregory Lee	Edward Udelson
Alan Levine	Mark Watson
Hollis Mason	Patricia Watterson
Tom McCollum	Michelle Webb
Dennis McElrath	Kathleen Wehnes
Joseph Mickum	Ellen Wilson
David Miller	Pablo Yanez

INDEX

Abandoned delta, Bangladesh and India, 328
Aberdeen Lake, Canada, 572
Active delta, Bangladesh and India, 326
Adelaide rift, Australia, 166
Aden, 268
Adirondack Mountains, New York, 52
Adriatic coast, 370
Aerial photographs, use of, 637
Afar Depression, Africa, 108
Afar Triangle, volcanism, 234
Afar Triple Junction, Africa, 108
African Rift, Landsat mosaic, 106
African Rift Valley, 234
Ahaggar Mountains, Algeria, 170
Air Mountains, Niger, 172
Alaska
 Aleutian Arc, 210
 Columbia Glacier, 558
 Colville River, 280
 Finger Lakes, 426
 geomorphic map, 646
 Glacier Bay, 364
 Malaspina Glacier, 550, 570
 mosaic, 50
 Mount McKinley, 554, 666
 oriented lakes, 430
 Alaska Range, 554
 Yukon River, 282
 Yukon River delta, 338
Aletsch Glacier, Switzerland, 568
Aleutian Arc, Alaska, 210
Aleutian Trench, 210
Algeria, Tanezrouft Basin, 470
Alice Springs Orogeny, 20
Alluvial fans, Brazil, 300
Alluvial fans
 California, 40
 China, 294
 India, 296
 Iran, 292
 Jordan, 266
 Madera Canyon, Arizona, 276
Alpine Fault, New Zealand, 168, 374
Alpine glaciation
 Alaska, 50
 Colorado, 42
Alpine glaciers, China, 588
Alps
 European, 82, 86
 Landsat mosaic

 tectonic history, 82
Altiplano, Bolivia, 438, 442
Altyn Tagh fault zone, China, 150
Amadeus Basin, Australia, 8
Amargosa Desert, 484
Amazon deep-sea fan, 659
Amazon River (Solimões River), Brazil, 255, 302, 304
Amu Darya River delta, U.S.S.R., 350
Anastomosing channel, 258, 290, 338, 304
Anastomosing distributaries, Mackenzie River delta, 340
Anatolian Transform Faults, Turkey, 114
Ancient landscapes, 8
Andean Cordillera, Peru, 76
Andean Foreland, 308
Andean Mountains, 308
 volcanism, 220
Andesite Line, Central America, 216
Andros Island, Bahama, 386
Angel Falls, Venezuela, 274
Annular drainage, South Dakota, 44
Antarctica
 deserts, 490
 Pine Island Glacier, 558
 Ross Ice Shelf, 540
 Victoria Land, 538
Anti Atlas Mountains, Morocco, 94
Anu Darya River delta, U.S.S.R., 319
Appalachian Mountains, 52
Appalachian Plateau, fluvial dissection, 310
Arabian Sea, 348
Arabian Shield, volcanism, 236
Aral Sea 350, 440
Arctic Archipelago, 68
Arctic Coastal Plain, Alaska, 280
Arete, Ural Mountains, 560
Argentina
 dust storm, 659
 Patagonian ice field, 544
Arica Elbow, Bolivia, 74
Arid lands, remote sensing, 456
Ariel, 632
Arizona
 Grand Canyon, 272
 Pinacate volcanic field, 198
 San Francisco Mountains, 196
 Sonoran Desert, 482
 Tucson Mountains, 276
Arrow Canyon Range, Nevada, 38
Assam Plateau, 284
Atacama Desert, Chile, 378, 478
Atacama fault, Chile, 74
Atlantic type coast
 Falkland Islands, 366
 Ireland, 368
Atlas Mountains, North Africa, 676
Atolls, Coral Islands, 392
Australia
 Amadeus Basin, 20
 Burke and Hamilton Rivers, 286
 central, 20
 coastline New South Wales, 358
 Cobourg Peninsula, 360
 Cooper Creek, 288
 Finders Range, 166
 geomorphic mapping, 647
 Great Barrier Reef, 390
 Great Sandy Desert, 492
 Kimberley Plateau, 164
 Macdonnell Range, 20
 Nullarbor karst, 424
 Simpson Desert, 494
 western coastline, 394
Australian Shield, 158
Baffin Island, Canada, 546
Baikal rift, U.S.S.R., 440
Bajada, California, 40
Belize delta, 320
Balkan Alpine system, 88
Bangladesh, Ganges/Brahmaputra
 Rivers delta, 326, 328
Banks Peninsula, New Zealand, 374
Barnes Ice Cap, Baffin Island, Canada, 546
Barrier islands, North Carolina, 380
Barrier ridges, Florida, 382
Bartow, Florida, 420
Basin and Range, 32, 36, 198, 276
Bathurst Island, 68
Bay of Bengal, 326
 beaches, transgressive, Brazil, 324
Bear Province, Canada, 66
Belize reef tract, 388
Bengal Basin, Bangladesh and India, 326
Beni Basin, Bolivia, 434
Bering Sea, Alaska, 338
Big Bend, Texas, 214
Big Horn Basin, Wyoming, 42, 46

- Bimini Islands, 386
 Birdfoot delta, 320
 Black Canyon, Colorado, 12
 Black Hills, South Dakota, 44
 Blue ice, 527
Bolivia
 Madre de Dios River, 306
 oriented lakes, 434
 Salar de Uyuni, 438
Bolivian Andes, 74
Book Cliffs, Utah, 44
Border Ranges Fault, Alaska, 50
Bornhardts
 South Africa, 100
 Zimbabwe, 104
Brahmaputra River, 284
Brahmaputra/Ganges Rivers delta,
 Bangladesh and India, 326, 328
Braided channel,
 Ganges/Brahmaputra, 326
Braided river pattern, 257, 282
Brazil
 alluvial fan, 300
 Amazon River, 304
 coastline, 362
 Manaus, 302
 Rio de Janeiro, 362
 Rio Grande do Sul, 362
 Rio Taquari, 300
 São Francisco River, 324
 Solimões River, 306
Breidamerkurjökull, Iceland, 568
Brooks Range, Alaska, 50
Bucaramanga fault system, Columbia,
 72
Burke River, Australia, 286
Burma Ranges, 138
Bushveld Complex, South Africa, 102
Butsuzo Tectonic Line, Japan, 240
Bylot Island, Canada, 552

Caledonian Front, Scotland, 78
California
 Coast Ranges, 36
 Mojave Desert, 484
Callisto, 626
Caloris Basin, Mercury, 606
Canada
 Aberdeen Lake, 572
 Barnes Ice Cap, 546
 Bylot Island, 552
 drumlins, 574
 glacial drift, 576
 glacial fluting, 576, 578
 King William Island, 576
 Mackenzie River delta, 340
 thermokarst, 586
 Tuktoyaktuk Peninsula, 586
 Wollaston Peninsula, 574
 Canadian Shield, 27, 62, 64, 66, 658
 Canary Islands, 676
 Canterbury Plains, New Zealand, 168

 Canton (Hsi, Pearl) River delta,
 China, 332
Canyonlands, Utah, 12
Canyons, Mars, 612
Cape Canaveral, Florida, 382
Cape Cod, Massachusetts, 584
Cape Hatteras, North Carolina, 380
Captain James Cook, 390
Carolina Bays, North Carolina, 432
Carson Sink, Nevada, 38
Cascade Range, 32, 202
Cascade system, 4
Casco Bay, Maine, 368
Caspian Sea, U.S.S.R., 336, 396
Cataract Canyon, Utah, 270
Catskills Mountains, New York, 56
Caucasus, U.S.S.R., 90
Centripetal drainage, Jordan, 266
Centotes, Mexico, 418
Central America, volcanism, 216
Central Nevada Shear Zone, 38
Chaco Canyon, New Mexico, 12
Chad, Tibesti Mountains, 228
Chaman fault, Afghanistan, 126
Chang Jiang (Yangtze River), China,
 290
Chang Jiang (Yangtze River) delta,
 China, 319, 330
Channel Country, Australia, 286
Channel patterns, 256
Channeled Scabland, Washington, 312
Chatham Strait fault, Alaska, 364
Cheniers
 Colorado River delta, 344
 Ganges/Brahmaputra Rivers delta,
 328
 Vietnam, 334
Chesapeake Bay, Virginia, 400
Chile
 Atacama Desert, 378, 478
 coastline, 378
 Patagonian ice field, 544
China
 alluvial fans, 294
 alpine glaciers, 588
 Chang Jiang (Yangtze) River delta,
 330
 Hsi (Pearl) River delta, 332
 karst, 414
 Loess Plateau, 262
 Lop Nur, 508
 Mu Us Sandy Land, 500
 Qaidam Basin, 150
 Red River fault zone, 154
 Sichuan Basin, 152
 strike-slip faults, 146
 Taklimakan Desert, 510, 512
 Tengger Desert, 504
 Tian Shan, 144
 Turpan Depression, 506
 Yangtze River, 290
 Yunnan Province, 154

Choctaw thrust, 60
Chugach Mountains, Alaska, 50
Cirque glacier
 Bylot Island, 552
 Greenland, 560
Cirque
 Greenland, 560
 Ural Mountains, 560
Clearwater Lakes, Quebec, Canada,
 174
Climatic geomorphology, 4, 8
Coast Ranges, California, 32, 34, 48
Coastal deserts, 448
Coastal embayments, U.S.S.R., 396
Coastal landforms, 353
Coastal Plain, Alaska, 430
Coastal plain, Swan Plain, Australia,
 394
Coastline, defined, 353
Coasts
 Adriatic, 370
 Belize, 388
 Cape Canaveral, Florida, 382
 Chile, 378
 classification, 353
 Falkland Islands, 366
 Florida Keys, 384
 Great Bahama Bank, 386
 Hudson Bay, 402
 Kara-Bogas, U.S.S.R., 396
 Korea, 356
 morphological classification, 355
 New South Wales, Australia, 358
 North Carolina, 378
 Perth, Australia, 394
 Rio de Janeiro, Brazil, 362
 South Island, New Zealand, 374
 Southwest Ireland, 368
 tectonic classification, 354
 Virginia, Maryland, 400
Cobourg Peninsula, Northern
 Territory, Australia, 360
Cockpit karst, Jamaica, 416
Cocos Ridge, 218
Collision coasts, 353
Colombia, Sierra Nevada de Santa
 Marta, 72
Colorado Plateau, 12, 32, 270
Colorado River, 12, 270, 272
Colorado River Delta
 geomorphic map, 645
 Mexico, 319, 344
Columbia Glacier, Alaska, 558
Columbia Plateau, 32, 200, 202, 204,
 312
Colville River, Alaska, 280
Colville River delta, Alaska, 338
Compound dunes, 455
Congo River, Africa, 306
Cook Strait, New Zealand, 376
Cooper Creek, Australia, 288, 659
Copper River, Alaska, 280

- Coral Islands, atolls, 392
 Cordillera Blanca, Peru, 76
 Cordillera Central, Peru, 76
 Cordillera, geologic evolution, 32
 Cordillera Negra, Peru, 76
 Cordillera Occidental, 438, 442
 Cordillera Oriental, 438, 442
 Cordilleran accretionary terranes, 48
 Coriolis effect, 447
 Cornwallis fold belt, 68
 Cottonball Basin, 40
 Crater Lake, Oregon, 202
 Craters of the Moon, Idaho, 204
 Crescentic dunes, 454
 - Saudi Arabia, 458
 Crevasse splays, Mackenzie River delta, 340
 Cross-folding, India, 136
 Cuddapah Basin, 136
 Cuesta (côtes)
 - France, 80
 - North Africa, 464
 - Saudi Arabia, 16
 Cumberland Plateau, 58
 Cuspate spits, Brazil, 362

 Dalmatian coast, 370
 Damara Mountain Belt, Namibia, 100
 Danakil Depression, 108
 Danube River delta, Romania, 319, 324
 Darling Fault, Australia, 394
 Dasht-E-Lut, Iran, 498
 Dead Sea, 110, 112, 266, 642
 Death Valley, California, 34, 40, 484
 Deccan Plateau, India, 238
 Defiance Upwarp, Arizona, 12
 Deimos, Martian moon, 616
 Delta, Colorado River Delta, 645
 Delta plain, Alaska, 338
 Delta plain, Amu Darya River delta, U.S.S.R., 350
 Delta plain, Lena River delta, 342
 Deltas
 - environments, 319
 - factors in development, 317
 - landforms, 317
 Denali fault, Alaska, 50
 Dendritic drainage, 255
 - South Yemen, 268
 Desert pavement, 452
 Desert soils, 450
 Desert varnish, 453
 Desertification, 456
 Deserts, 447
 - Algeria, 470
 - Antarctica, 490
 - Atacama Desert, 478
 - blowouts, 452
 - dunes, 454
 - erosion, 452
 - features, 449
 Grand Erg Occidental, 464
 Grand Erg Oriental, 468
 Great Sandy Desert, Australia, 492
 Lake Chad, 472
 Lop Nur, China, 508
 Lut Desert, Iran, 496
 Mars, 449, 488
 Mojave Desert, California, 484
 Mu Us Sandy Land, China, 502
 Namib Desert, 474
 plants, 451
 remote sensing, 456
 resources, 455
 Saudi Arabia, 458
 Simpson Desert, Australia, 494
 Sonoran Desert, Arizona, 482
 Sonoran Desert, Mexico, 480
 Taklimakan Desert, China, 510, 512
 Tengger Desert, China, 504
 Thar Desert, India/Pakistan, 500
 Turpan Depression, China, 506
 types, 448
 Venus, 449
 water, 452
 yardangs, 452
 Devils River, Texas, 260
 Differential erosion, 42
 Dinaric Mountains, Yugoslavia, 422
 Dinarides, 82
 Dione, 630
 Distributaries, Mississippi River delta, 320
 Distributary channels, Mali, 298
 Distributary pattern, 258
 Dome dunes, 455
 - Saudi Arabia, 458
 Dongting Swamp, China, 290
 Drainage basins, 255
 Drainage density, 255, 260
 Drainage patterns, 255
 - classification, 257
 Drumlins
 - Canada, 574, 576
 - Ireland, 574, 658
 - Sweden, 570
 Dry Falls, Washington, 312
 Dry Valleys, Antarctica, 490
 Dunefield, Nafud-Qunayfidhah, Saudi Arabia, 16
 Dunes, 658
 - crescentic, 454
 - dome, 455
 - linear, 454
 - Nebraska Sand Hills, 486
 - parabolic, 455, 486
 - simple, compound, complex, 455
 - star, 454
 Dynamic equilibrium, 4

 East African rift, 440
 East China Sea, delta, 330
 East Pacific Rise, 31
 Edwards Plateau, Texas, 260
 Elat, Israel-Jordan, 266
 Electromagnetic radiation, 680
 Elgygytgyn Crater, Siberia, U.S.S.R., 669
 Ellesmere Island, 544
 Emi Koussi, Chad, 230
 Empty Quarter, Saudi Arabia, 460
 Enceladus, 630
 End moraine
 - Greenland, 566
 - Iceland, 566
 Endogenic landforms, 27
 Eolian, atmospheric circulation, 447
 Eolian deposition, 454
 Eolian landforms, 447
 Eolian processes, erosion, 452
 Eolian transportation, 453
 Equifinality, 4, 667
 Equilibrium, 4
 Erg Chech, central Sahara, 462, 466
 Escarpment, Red Sea, 118
 - South Africa, 232
 Estuaries, Chesapeake Bay, 400
 Estuary, Hsi (Pearl) River, China, 332
 Euphrates River, Iraq, 346
 Europa, 626
 Everglades, Florida, 384
 Extraterrestrial landforms, 599
 Eyjabakkajökull, Iceland, 556

 Fairweather fault, Alaska, 364
 Falkland Islands, coast, 366
 Fandelta, Iran, 292
 Feedback system, 4
 Felsenmeer, Canada, 68
 Fen He (Fen River), China, 264
 Flinders Range, Australia, 166
 Finger Lakes, Alaska, 426
 Finke River Gorge, Australia, 20
 Fjord, Greenland, 564
 - Norway, 364, 564
 Flinders River, Australia, 6
 Flood basalts, India, 238
 Floodplains, 259
 Florida, Cape Canaveral coast, 382
 Florida karst, 420
 Florida Keys, 384
 Fluvial
 - classification, 256
 - Edwards Plateau, 260
 - flood, 288
 - landforms, 255
 - meandering, 278
 - South Yemen, 268
 - structural influence, 255
 Fold belt
 - Himalaya, 134
 - Iran, 122
 Fracture orientations, Grenville Front, 62

- France
 Nice, 677
 Paris Basin, 80
 Franciscan mélange, 34
 French Alps, 83
 Frenchman Mountains, Nevada, 38
 Furnace Creek fault zone, 40
- Galapagos Archipelago, 218
 Ganges River, India/Nepal, 296
 Ganges/Brahmaputra River, 255
 Ganges/Brahmaputra Rivers delta
 Bangladesh and India, 319, 326, 328
 Ganymede, 626
 Garlock fault, California 40, 484
 Geomorphic analysis, 4, 5
 Geomorphic classification, 2
 Geomorphic concepts, 3
 Geomorphic Information System (GIS), 664
 Geomorphic map
 Alaska, 646
 Colorado River Delta, 648
 New South Wales, 647
 Tucson, Arizona, 648
 Geomorphic mapping, 8
 Geomorphic maps, guidelines, 639
 Geomorphic processes, 2
 Geomorphic scale, 1, 2
 Geomorphic studies, 3
 Geomorphic surfaces, 8, 10
 Geomorphic systems, 4
 Geomorphic thresholds, 670
 Geomorphic units mapping, 640
 Geomorphological mapping, 637
 applications, 641
 theory, 640
 use of remote sensing, 643
 Geomorphology
 future of, 657
 landform concepts, 638
 new directions, 665
 study from space, 658
 Glacial cirque, 560
 Glacial deposits, classification, 534
 Glacial drift
 Canada, 572, 576
 Sweden, 570
 Glacial erosion
 Canada, 64, 578
 Scotland, 78
 Glacial fluting, Canada, 576, 578
 Glacial lakes
 classification, 426
 Sweden, 570
 Glacial landforms, 521
 depositional, 532
 erosional, 531
 Glacial trough
 Canada, 562
 Iceland, 562
- Switzerland, 562
 Glacier Bay, Alaska, 364
 Glaciers, 521
 accumulation zone, 529
 Alaska, 50
 blue ice, 527
 cirque glacier, 552
 classification, 526
 ice cap, 546
 ice field, 544
 mass balance, 527
 nature of, 521
 outlet, 548
 piedmont, 550
 Pleistocene areal extent, 524
 present areal extent, 522
 satellite surveillance, 521
 surging, 556
 tidal, 558
 valley glacier, 554
 Victoria Land, Antarctica, 538
 Glen Canyon, Utah, 270
 Global geomorphology, future of, 657
 Global habitability, 8
 GLORIA, 671, 659
 Goosenecks, Utah, 12
 Gosses Bluff Astrobleme, Australia, 20
 Graenalón, Iceland, 582
 Gran Desierto, Mexico, 480
 Grand Canyon, Arizona, 272
 Grand Erg Occidental, North Africa, 464
 Grand Erg Oriental, central Sahara, 468
 Grand Mesa, Colorado, 12
 Great Bahama Bank, 386
 Great Barrier Reef, Australia, 390
 Great Basin, 40
 Great Basin Desert, 484
 Great Basin, Nevada, 38
 Great Dike, Zimbabwe, 104
 Great Escarpment, South Africa, 100, 232
 Great Glen fault, Scotland, 78
 Great Karroo Basin, South Africa, 232
 Great Rift Valley, Africa, 230
 Great Salt Lake, Utah, 436
 Great Sandy Desert, Australia, 492
 Great Slave Lake, Canada, 66
 Great Smoky Mountains, North Carolina, 53
 Greece, Balkan Alps, 88
 Green Mountains, Vermont, 52
 Green River, Utah, 12
 Greenland Ice Sheet, 538, 566
 ice stream, 542
 Søndre Strømfjord, 564
 Grenville Front, Canada, 62
 Grenville Province, Canada, 62, 64
 Guatemala, volcanism, 216
 Gulf of Aden, 234
- Gulf of Aqaba, 110
 Gulf of California, Mexico, 344
 Gulf of Kutch, 398
 Gulf of Suez, 110
 Gunnison River, Colorado, 12
- Hadley Rille, Moon, 604
 Hamersley Range, Australia, 158
 Hamilton River, Australia, 286
 Hammocks, Florida, 384
 Hawaii, volcanism, 212
 Hawaiian volcanism, 187
 HCMM image,
 Appalachian Mountains, 52
 Cordilleran, 48
 Rocky Mountains, 42
 New Zealand, South Island, 168
 North Africa, 94
 Southwestern U.S., 192
- Heat Capacity Mapping Mission (*see* HCMM)
- Helvetic Alps, 82, 83
 Henry Mountains, Utah, 12, 270
 Highland Boundary Fracture Zone, Scotland, 78
 Himalaya, foothills, 134
 Himalayan Front, 138
 Hopi Buttes, Arizona, 196
 Hofsjökull, Iceland, 566
 Horn, Ural Mountains, 560
 Hotspot, Hawaii, 212
 Hsi (Pearl) River delta, China, 332, 319
 Huang He (Yellow River), China, 255, 262, 264
 Huang He (Yellow) River delta, China, 318
 Huasteca Canyon, Mexico, 70
 Hudson Bay shorelines, Canada, 402
 Hum, Yugoslavia, 422
- Ice cap
 Barnes Ice Cap, 546
 Vatnajökull, Iceland, 528
 Iceland, 548
- Ice field, Patagonia, 544
 Ice floes, Canada, 586
 Ice sheet, Antarctica, 538
 Ice shelf, Antarctica, 540
 Ice stream, Greenland, 542
 Iceland
 Breidamerkurjökull, 568
 Eyjabakkajökull, 556
 Graenalón, skeidararjökull, 582
 Hofsjökull, 566
 jökulhláups, 580
 outwash plain, 580
 proglacial lake, 582
 Skeidarársandur, 580
 Trollaskagi, 562
 Vatnajökull, 548, 566
 volcanism, 222

- Icelandic volcanism, 187
 Idaho, Craters of the Moon, 204
 Ilhas Islands, Brazil, 306
 Image enhancement, 686
 Impact cratering, 11
 Impact craters
 Mercury, 606, 608
 Moon, 600, 602
 Impact structures, 174
 India
 alluvial fans, 296
 Deccan Plateau, 238
 Ganges/Bangladesh and India, 328
 Ganges/Brahmaputra Rivers delta, 326
 Indian Shield, 136
 Landsat mosaic, 326
 Ranns of Kutch, 398
 Thar Desert, 500
 Indonesian arc system, 246
 Indonesian terrain, 9
 Indus River delta, 398
 Indus River delta, Pakistan, 319, 348
 Indus suture, 138
 Inland delta, Mali, 298
 Intermontane Basins, Wyoming, 46
 Internal drainage, Jordan, 266
 Io, 628
 Iran
 fluvial features, 292
 Lut Desert, 496
 yardangs, 496
 Zagros Mountains, 122
 Iraq, Shatt El Arab delta, 346
 Ireland
 coast, 368
 drumlins, 574
 Irrawaddy River delta, Burma, 318
 Isostatic rebound, Canada, 402
 Israel, Elat, 266
 Italy, Mount Etna, 224

 Jakobshavns Isbrae, Greenland, 542
 Jamaica, karst, 416
 James Range, Australia, 10
 James River, Virginia, 400
 Japan
 Median Tectonic Line, 156
 volcanism, 240
 Japurá River, Brazil, 306
 Java, volcanism, 246
 Jemez Mountains, New Mexico, 194
 Jibal Tuwayq escarpment, Saudi Arabia, 16
 Jökulhlaups, Iceland, 580
 Jordan
 landform map, 642
 Qa Al Jafr, 266
 Juan de Fuca Ridge, 671
 Jupiter, satellites of, 626
 Jura Mountains, 82, 86
 Jura Plateau, 86

 K-2, Himalaya, 588
 Kaapvaal Craton
 South Africa, 102
 Zimbabwe, 104
 Kamchatka Peninsula, U.S.S.R., 242
 Kara Sea, U.S.S.R., 342
 Kara-Bogas, Turkmen Republic, U.S.S.R., 396
 Karakoram fault, 138
 Karoo System, South Africa, 10
 Karst
 Australia, 424
 climate, 410
 Dinaric Mountains, Yugoslavia, 408
 erosion rates, 409
 factors in development, 407
 Florida, 420
 hydrogeology, 409
 Jamaica, 416
 landscapes, 407
 lithology, 407
 relief, 407
 saturation equilibrium, 409
 South China, 414
 space perspective, 410
 structure, 407
 time, 410
 karst towers, China, 414
 vegetation, 410
 Yucatan, Mexico, 418
 Yugoslavia, 422
 Kashgar Ku-Che fold belt, Tian Shan, 144
 Katmaian volcanism, 187
 Kenai Mountains, Alaska, 50
 Kettle lake, Cape Cod, Massachusetts, 584
 Kettleman Hills, California, 36
 Khomas Highlands plateau, Namibia, 100
 Kilauea, Hawaii, 212
 Kilbuck Mountains, 426
 Kimberley Plateau, Australia, 164
 King William Island, Canada, 576
 Kirthar Ranges, Pakistan, 130
 Klutlan Glacier, Canada, 556
 Klyuchevskaya volcano, U.S.S.R., 242
 Kohat, Himalaya, 134
 Koppies, South Africa, 232
 Korea, coastline, 356
 Kosi Fan, India, 296
 Kosi River, 296
 Kunlun fault, China, 146, 150
 Kunlun fault, Himalaya, 138
 Kyushu, Japan, 240
 Kyzyl Kum desert, U.S.S.R., 350

 La Sal Mountains, Utah, 12
 Labrador Trough, Canada, 64
 Lafourche delta, 320
 Lagoa dos Patos, Brazil, 362
 Lake Ashanti, Bosumtwi (Ghana), 174

 Lake Baikal, U.S.S.R., 440
 Lake Balkhash, U.S.S.R., 440
 Lake Bonneville, Utah, 436
 Lake Chad, Sahel, 472
 Lake Eyre, Australia, 286, 494
 Lake Titicaca, Peru, 442
 Lake Yamma Yamma, Australia, 288
 Lakes
 Alaska, 426
 Bolivia, 434, 438
 Carolina Bays, 432
 classification, 411
 density, 412
 Lake Baikal, 440
 Lake Titicaca, 442
 Mackenzie River delta, Alaska, 324
 oriented, Alaska, 430
 origin, 411
 pluvial, 436
 shape, 411
 size, 412
 thermoskarst, U.S.S.R., 428
 time, 413
 Landform concepts, 638
 Landsat imagery, 28
 Landsat mosaic
 African Rift, 106
 Ganges/Brahmaputra Rivers delta, 326
 Middle East, 112
 Pacific Northwest, 200
 Southwest Asia, 126
 Turkey, 114
 Laptev Sea, U.S.S.R., 342
 Laramide Orogeny, 12
 Large Format Camera, 236
 Lateral moraine
 Canada, 568
 Iceland, 568
 Switzerland, 568
 Lebanon, 112
 landform map, 642
 Lena River delta, U.S.S.R., 319, 342
 Levant Fault, Middle East, 112
 Libya, 677
 Linear dunes, 454, 492
 Lineated terrain, Mercury, 608
 Loch Ness, Scotland, 78
 Loess Plateau, China, 262, 502
 Logancha, U.S.S.R., 174
 Lop Nur, China, 508
 Louisiana, Mississippi River, 278
 Lunar landforms, 599
 Lunar maria, 604
 Lut Desert, Iran, 496

 MacDonald fault, Canada, 66
 Mackenzie River delta, Canada, 319, 324, 340
 Macon Ridge, Louisiana, 278
 Madagascar, Tananarive block, 80
 Madre de Dios River, Bolivia, 306

- Main Boundary Fault, Himalayan Front, 138
- Maine, Casco Bay, 368
- Makran coast, Pakistan, 372
- Makran Ranges, Southwest Asia, 126
- Makteir desert, Mauritania, 98
- Malagasy Republic, Madagascar, 80
- Malaspina Glacier, Alaska, 550, 570
- Mali, Niger River, 298
- Manaus, Brazil, 302
- Mangrove swamp, Australia, 360
- Manicouagan, Quebec, Canada, 174
- Manitoba, Canada, 578
- Marble Canyon, Arizona, 272
- Mare Imbrium, Moon, 602
- Mare Tranquillitatis, Moon, 604
- Marginal sea coasts, 353
- Marlborough Sounds, New Zealand, 376
- Mars
- Olympus Mons, 610
 - outflow channels, 614
 - Valles Marineris, 612
- Marshall Islands, atolls, 392
- Martian moons, Phobos, Deimos, 616
- Martian sand seas, 449, 488
- Maryland, Chesapeake Bay, 400
- Massachusetts, Cape Cod, 584
- Mauna Kea, Hawaii, 212
- Mauna Loa, Hawaii, 212
- Mauritania, Richât structure, 98
- Meandering channel, Ganges/Brahmaputra River, 328
- Meandering pattern, 257
- Medial moraine
- Iceland, 568
 - Switzerland, 568
- Median Tectonic Line, Japan, 156, 240
- Mediterranean, volcanism, 224
- Mega-geomorphology, 1, 658
- Mekong River delta, Vietnam, 319, 334
- Merapi, Indonesia, 246
- Mercury
- Caloris Basin, 606
 - lineated terrain, 608
- Mesa Verde, Colorado, 12
- Meteor impact
- examples, 174
 - Mauritania, 98
- Meteorites, Antarctica, 527
- Mexico
- Colorado River delta, 344
 - karst, Yucatan, 418
 - Sierra Madre Oriental, 70
 - Sonoran Desert, 480
- Micronesia, atolls, 392
- Mid-Atlantic ridge, 222
- Middle East, Landsat mosaic, 112
- Midlatitude deserts, 448
- Mimas, 630
- Miranda, 632
- Mississippi River, 278
- Mississippi River delta, U.S.A., 319, 320
- Moine thrust, Scotland, 78
- Mojave Desert, 6, 484
- Monsoon deserts, 448
- Monument Upwarp, Utah, 12
- Moon
- Apennines, 602
 - lunar maria, 604
 - Mare Imbrium, 602
 - Tycho, 600
- Moraines, classification, 535
- Morocco, Anti Atlas Mountains, 94
- Morphostructural analysis, 5
- Mount Ararat, Turkey, 226
- Mount Aso, Japan, 240
- Mount Egmont, New Zealand, 248
- Mount Erebus, Antarctica, 538
- Mount Etna, Italy, 224
- Mount Mazama, Oregon, 202
- Mount McKinley, Alaska, 554, 666
- Mount St. Helens, Washington, 206
- Mt. Everest, Nepal, 138
- Mt. Fuji, Japan, 240
- Mt. Kenya, Africa, 106, 230
- Mt. Kilimanjaro, Africa, 106
- Mt. McKinley, Alaska, 50
- Mu Us Sandy Land, China, 502
- Multispectral scanner images, 682
- Nacimiento Fault, New Mexico, 194
- Nain Province, 64
- Namib Desert, South Africa, 474
- Namibia
- Damara Mountain Belt, 100
 - sedimentary basin, 80
- Nanga Parbat, 126
- Nebraska Sand Hills, 486
- New Mexico, Valles Caldera, 194
- New South Wales, Australia, 647
- New Zealand
- Alpine Fault, 168
 - Marlborough Sounds, 376
 - volcanism, 248
 - Canterbury coast, 374
- Ngauruhoe, New Zealand, 248
- Niger, Air Mountains, 173
- Niger River, Mali, 298
- Nigerian shield, 170
- Nile delta, Egypt, 317, 318
- North Carolina
- coastline, 378
 - oriented lakes, 432
- Northwest Territories, Canada, 66
- Norway, fjords, 364, 564
- Nubian sandstone, 18
- Nullarbor Plain, Australia, 424
- Oklahoma, Ouachita Mountains, 60
- Ob River Valley, Siberia, U.S.S.R.,
- 428
- Oberon, 632
- Oca fault, 72
- Ohio River, Ohio, 310
- Olduvai Gorge, Africa, 230
- Olympic Mountains, 32
- Olympus Mons, Mars, 610
- Oman, ophiolites, 120
- Ophiolites
- Cyprus, 120
 - Oman, 120
- Ord River, Australia, 164
- Oregon, volcanism, 202
- Oriented lakes
- Alaska, 430
 - Bolivia, 434
 - Carolina Bays, 432
- Ouachita Mountain fold belt, 60
- Outflow channels, Mars, 614
- Outlet glacier
- Iceland, 548
 - Vatnajökull, Iceland, 529
- Outwash plain, Iceland, 580
- Pacific Coastal Plain Province, 216
- Pacific Northwest, Landsat mosaic, 200
- Pacific type coasts, 354
- Alaska, 364
 - Pakistan, 372
- Padre Island barrier, Texas, 362
- Pakistan
- Indus River delta, 348
 - Landsat mosaic, 126
 - Makran coast, 372
 - Zob Valley, 130
 - Zinda Pir, 132
- Paleochannels, 18, 259
- Paleodeserts, 449
- Palimpsest, 27
- Pamirs, 126
- Pamlico Sound, North Carolina, 378
- Panamint Range, California, 40
- Pantanal Plains, Brazil, 300
- Parabolic dunes, 455
- Thar Desert, India, 500
- Paradox Valley, Colorado, 12
- Paraguay River, Brazil, 300
- Paredon basin, Mexico, 70
- Paris Basin, France, 80
- Parry Island fold belt, 68
- Patagonia, ice field, 544
- Patterned ground, 5
- Lena River delta, 342
- Pearl (Hsi) River delta, China, 332
- Pecos River, Texas, 260
- Peléan volcanism, 187
- Pennine Alps, 82, 86
- Periglacial, 5
- Periglacial landforms, 534
- Permafrost, 5
- Alaska, 430

- Canada, 586
 distribution, 537
 Persian Gulf, 396
 Iraq, 346
 Perth, Australia, 394
 Peru
 Andean Cordillera, 76
 Andean Mountains, 220
 Lake Titicaca, 442
 Ucayali River, 308
 Phobos, Martian moon, 616
 Physiography, 1
 Piedmont glacier, Alaska, 550
 Pilbara block, Australia, 158
 Pinacate lava field, 480
 Pinacate volcanic field, Arizona, 198
 Pindus Mountains, Greece, 88
 Pine Island Glacier, Antarctica, 558
 Pine Mountain Thrust, Kentucky, 58
 Pingos, Mackenzie River delta, 340
 Plain of Reeds, Vietnam, 334
 Planation surfaces, 8, 10
 Planetary geomorphology, 10
 Planetary landforms, 597
 Planetary surfaces, 11
 Planets
 atmosphere, 597
 composition, 597
 crustal evolution, 597
 geomorphic evolution, 597
 gravity, 597
 relative size, 597
 surface temperature, 598
 time scales, 599
 Plate collision, 30
 Plate-tectonic classification, 30
 Plateau basalts, India, 238
 Playa lakes, Iran, 292
 Playas, Nevada, 38
 Plinian volcanism, 187
 Plutons, 172
 Pluvial episodes, 18
 Pluvial fans, Jordan, 266
 Pluvial lake, Lake Bonneville, Utah, 436
 Po Basin, 82
 Point Barrow, Alaska, 430
 Polar deserts, 448
 Polje, Yugoslavia, 422
 Potato Hills, 60
 Potomac River, Maryland, 400
 Potosí, Bolivia, 74
 Powder River Basin, Wyoming, 42
 Pre-Alps, 82
 Primary coasts, 353
 Process studies, 4
 Proglacial lake, Iceland, 582
 Puna Plateau, Andean Mountains, 220
 Qa Al Jafr, Israel-Jordan, 266
 Qaidam Basin, China, 150
 Qilian Shan Mountains, China, 294
 Quantitative geomorphology, 5, 660
 Queensland, Australia, 6
 Radar, 683
 Radar imagery, Venus, 618, 622
 Rain-shadow deserts, 448
 Ramgarh, India, 174
 Ranns of Kutch, India, 398
 Rectangular drainage, 255
 Algeria, 170
 Red River fault zone, China, 154
 Red Sea, 110, 236
 Red Sea escarpment, 118
 Reef distribution, hypotheses, 388
 Regmatic shears, 658
 Remote sensing
 data displays, 681
 EM radiation, 680
 image enhancement, 686
 instrumentation, 681
 land cover categories, 683
 mapping applications, 643
 MSS, 682
 principles of, 679
 radar, 683
 thermal infrared, 68
 Rhea coasts, 630
 Rhodesia (*also see* Zimbabwe), 104
 Ria coast
 Adriatic Sea, 370
 Ireland, 368
 Korea, 356
 Richât structure, Mauritania, 98
 Rifting, 31
 Rio Caroní, Venezuela, 274
 Rio Grande do Sul, Brazil, 362
 Rio Huallaga, Peru, 76
 Rio Magdalena, Colombia, 72
 Rio Maranon, Peru, 76
 Rio Negro, Brazil, 302
 Rio Santa Valley, Peru, 76
 Rio Taquari fan, Brazil, 300
 Rivers, largest, 256
 Riyadh, Saudi Arabia, 16
 Roan Cliffs, Utah, 44
 Rock glaciers, 5
 Rock Springs Uplift, 46
 Rocky Mountain Trench, 48
 Rocky Mountains, 32, 42
 Romania, Danube River delta, 324
 Ross Ice Shelf, Antarctica, 540
 Rub Al Khali basin, Arabia, 118
 Sabkha, 398
 Iran, 292
 Persian Gulf, 396
 Sahara Desert
 Erg Chech, 462, 466
 Grand Erg Occidental, 464
 Grand Erg Oriental, 468
 Lake Chad, 472
 Tanezrouft Basin, Algeria, 470
 Salar de Coipasa, Bolivia, 438
 Salar de Uyuni, Bolivia, 438
 Salton Sea, 34
 San Andreas fault, 34, 36
 San Francisco Mountains, Arizona, 196
 San Juan Mountains, Colorado, 12, 42
 San Rafael Swell, Utah, 12, 44
 Sand sea
 Ad Dahna, Saudi Arabia, 16
 Lut Desert, Iran, 498
 Sand sheet, Sudan, 18
 Sand spit, Brazil, 362
 Sandia Mountains, New Mexico, 12
 Sandur, Iceland, 580
 Santa Marta fault system, Colombia, 72
 São Francisco River, Brazil, 324
 Satellite systems, 679
 Saturn, satellites of, 630
 Saudi Arabia
 dome dunes, 458
 Riyadh, 16
 star, crescentic dunes, 460
 volcanism, 236
 Scale, 1
 Scottish Highlands, 78
 Sea of Galilee, 112
 SeaMARC I, 659
 Searles Lake, 484
 Seasat, glaciers, Alaska, 554
 Secondary coasts, 353
 Selima Sand Sheet, North Africa, 7, 18, 659
 Semail Ophiolites, Oman, 120
 Serengeti Plain, Africa, 230
 Serra Da Cangalha, Brazil, 174
 Serranía de Perija, Colombia, 72
 Seto inland sea, Japan, 156
 Shanghai, China, 330
 Shanxi Province, China, 262
 Shatt el Arab delta, Iraq, 319, 346
 Shield volcano
 Hawaii, 212
 Iceland, 222
 Olympus Mons, Mars, 610
 Shields, 31
 Shields, cratonic, 170
 Shillong Plateau, 284
 Shoreline, defined, 353
 Shuttle Imaging Radar (*see* SIR-A)
 Siberian Lowland, 428
 Siberian Ranges, 92
 Sibi, Pakistan, 130
 Sibi Trough, Pakistan, 130
 Sichuan Basin, China, 152
 Sierra Madre Oriental, Mexico, 70
 Sierra Nevada de Santa Marta, Colombia, 72
 Sierra Nevada Mountains, 34
 Sierra Nevada province, 32

- Sierrita de Ticul, Mexico, 418
 Sills, South Africa, 232
 Simpson Desert, Australia, 494
 Sinkholes, Florida, 420
 SIR-A, 7, 9
 Brazil, 306
 Sudan, 18
 Skeidarárjökull, Iceland, 582
 Skeidarársandur, Iceland, 580
 Slave Province, Canada, 66
 Smoky Mountains, Tennessee, 58
 Snake River Plains, Idaho, 204
 Solifluction, Falkland Islands, 366
 Solimões River, Brazil, 302, 304, 306
 Søndre Strømfjord, Greenland, 564
 Sonoran Desert
 Arizona, 482
 Mexico, 480
 South Africa
 Namib Desert, 474
 Transvaal, 102
 volcanism, 232
 South China Sea, Mekong River delta, 334
 South Yemen, 268
 Southern Alps, New Zealand, 168
 Southern Arabian Shield, 118
 Southwest Asia, Landsat mosaic, 126
 Space technology, 6
 Spits
 Canada, 586
 North Carolina, 380
 sand, cuspatate, 362
 SPOT, 675
 Star dunes, 454
 Grand Erg Oriental, 468
 Saudi Arabia, 458
 Steady state, 4
 Stream piracy, Siberian Ranges, 92
 Strike-slip fault, Western China, 146
 Strombolian volcanism, 187
 Structural geomorphology, 5
 Stuctural dome, Mauritania, 98
 Subdelta, Mississippi River delta, 320
 Subglacial volcanoes, 530
 Sui anticline, Pakistan, 132
 Sui gas field, Pakistan, 130
 Sulaiman Ranges, Pakistan, 130
 Sunda Volcanic Arc, Indonesia, 246
 Superimposed rivers, Appalachian
 Mountains, 56
 Surging glacier, Iceland, 556
 Susquehanna River, Maryland, 400
 Suture zone, Southwest Asia, 126
 Sweden
 drumlins, 570
 glacial lakes, 570
 Swiss Plain, 82
 Switzerland, moraines, 568
 Système Probatoire pour l'Observation
 de la Terre (SPOT), 675
 Systems approach, 4
- Taklimakan Desert, China, 510, 512
 Talemzane, Algeria, 174
 Tanezrouft Basin, Algeria, 470
 Tanzania, volcanism, 230
 Tarim basin, China, 144, 146, 294,
 508, 510, 512
 Taupo Volcanic Zone, New Zealand,
 248
 Teays River, West Virginia, 310
 Tectonic classification, 30
 Tectonic geomorphology, 8
 Tectonic history, 30
 Tectonic landforms, 27
 Tectonic studies, 28
 Tectonic, volcanic activity, global, 28
 Tengger Desert, China, 504
 Tenoumer Crater, Mauritania, 174
 Terminal moraine, Iceland, 566
 Terraces, 259
 Tethys Sea, 30, 370
 Texas
 Big Bend, 214
 Edwards Plateau, 260
 Thar Desert, India/Pakistan, 500
 The Spider, Australia, 174
 Themokarst, Alaska, 430
 Thermal infrared, 682
 Thermokarst, 5
 Canada, 586
 classification, 536
 U.S.S.R., 428
 Threshold, 4
 Tian Shan
 China, 146, 294
 Sashgar Ku-Che fold belt, 144
 Tibesti Mountains, Chad, 228
 Tibet Plateau, 138, 146, 658
 Ticul Fault, Mexico, 418
 Tidal channels
 Ganges/Brahmaputra Rivers delta,
 328
 Indus River delta, 348
 Iraq, 346
 Tidal flats, Alaska, 338
 Tidal glaciers, 558
 Tidal mudflats, Vietnam, 334
 Tigris River, Iraq, 346
 Tikchik Mountains, 426
 Till plain, Canada, 572
 Time scales, 2
 Titan, 630
 Tokositna Glacier, Alaska, 554
 Tombolos
 Ireland, 368
 Pakistan, 372
 Tongariro, New Zealand, 248
 Tors, Ireland, 368
 Trade Wind deserts, 448
 Trailing-edge coasts, 353
 Transform fault, 36
 Transvaal, South Africa, 102
 Trellis drainage, 255
- Appalachian Mountains, 52, 56
 Oklahoma, 60
 South Yemen, 268
 Wyoming, 46
 Yukon, Alaska, 338
 Triple Junction, Afar Triangle, 108
 Tröllaskagi, Iceland, 562
 Troodos Massif, Cyprus, 120
 Tucson, Arizona, 276
 geomorphic map, 651
 Tuggerah Lake, Australia, 358
 Tuktoyaktuk Peninsula, Canada, 586
 Tundra delta, Yenisey River delta, 342
 Turkey
 Anatolian Faults, 114
 Landsat mosaic, 114
 Mount Ararat, 226
 Turpan Depression, China, 506
 Tycho, Moon, 600
- U-shaped glacial valleys, 562
 Ucayali River, Peru, 308
 Uinta Mountains, Utah, 46
 Unaweep Canyon, Colorado, 12
 Uncompahgre Plateau, Colorado, 12
 United States
 southwestern mosaic, 34
 western mosaic, 32
 Ural Mountains, U.S.S.R., 90, 560
 Uranus, satellites of, 632
 U.S.S.R.
 Amu Darya River delta, 350
 Elgygytgyn Crater, 669
 Lake Baikal, 440
 Lena River delta, 342
 Peter the Great Ridge, 144
 Pikkommunizma, 144
 Siberian Ranges, 92
 thermokarst, 428
 Ural Mountains, 90, 560
 Volga River delta, 336
 Yenisey River delta, 342
- Utah
 fluvial dissection, 270
 Lake Bonneville, 436
 San Rafael Swell, 44
 Utah Lake, Utah, 436
- Valles Caldera, New Mexico, 12, 194
 Valles Marineris, Mars, 612
 Valley and Ridge fold belt, 53, 56, 58
 valley glacier, Alaska, 554
 Vance Seamount, 671
 Vatnajökull, Iceland, 548, 566
 Venezuela
 Angel Falls, 274
 fluvial imprint, 274
 Ventifacts, 452
 Venus, 618
 radar imagery, 622
 Verkhoyanskiy Range, U.S.S.R., 92
 Vesuvian volcanism, 187

- Victoria Island, Canada, 574
 Victoria Land, Antarctica, 538
 Victoria Valley, Antarctica, 490
 Vietnam, Mekong River delta, 334
 Villefranche-de-Rouergue, France, 658
 Virginia, Chesapeake Bay, 400
 Volcanic landforms, 185
 Volcanism
 Afar Triangle, 236
 Andean Mountains, 220
 Arabia, 236
 Chad, 230
 classification, 186
 Colorado Plateau, 196
 East Africa, 230
 general, 185
 Iceland, 222
 India, 238
 Japan, 240
 Java, 246
 landform classification, 188
 Mars, 610
 Mediterranean, 224
 New Zealand, 248
 Pacific Northwest, 200
 subglacial, 530
 Southwestern U.S., 192
 surface features, 190
 Turkey, 226
 types of eruptions, 187
 U.S.S.R., 242
 Volga River delta, U.S.S.R., 319, 336
 Vulcanian volcanism, 187
 Walker Lane shear zone, 38
 Washington
 Channeled Scabland, 312
 Mount St. Helens, 206
 Water supply, Earth, 525
 Waterpocket Fold, Utah, 12
 West Falkland Island, 366
 Wind gap, Appalachians, 58
 Wind River Basin, Wyoming, 46
 Wind River Mountains, Wyoming, 42
 Winter Park, Florida, 420
 Witwatersrand, South Africa, 102
 Wollaston Peninsula, Canada, 574
 Wyoming, Intermontane Basins, 46
 Wyoming Overthrust Belt, 46
 Yangtze (Chang Jiang) River, China,
 152, 290
 Yangtze (Chang Jiang) River delta,
 China, 319, 330
 Yardangs, 452
 China, 508
 Lut Desert, Iran, 496
 Yazoo Basin, Louisiana, 278
 Yellow River (Huang He), China, 255,
 262, 264
 Yellow Sea, 356
 Yemen, central, 268
 Yenisey River delta, U.S.S.R., 342
 Yetti Eqlab Massif, North Africa, 462
 Yilgarn Block, Australia, 158
 Yucatan Peninsula, karst, 418
 Yugoslavia
 coastline, 370
 karst, 422
 Yukon River, Alaska, 282
 Yukon River delta, Alaska, 319, 338
 Zagros Mountains, Iran, 122
 Zaire River, Africa, 306
 Zetaform beach
 Australia, 358
 Pakistan, 372
 Zhamanshin, U.S.S.R., 174
 Zhob Valley, Pakistan, 130
 Zimbabwe, Great Dike, 104
 Zinda Pir, Pakistan, 132

LOCATION OF PLATE IMAGES

